W. Haase
S. Wróbel (Eds.)

Relaxation Phenomena

Liquid Crystals, Magnetic Systems, Polymers, High-Tc Superconductors, Metallic Glasses

Springer

Relaxation Phenomena

Springer-Verlag Berlin Heidelberg GmbH

W. Haase · S. Wróbel (Eds.)

Relaxation Phenomena

Liquid Crystals, Magnetic Systems, Polymers, High-T_C Superconductors, Metallic Glasses

With 412 Figures and 30 Tables

Springer

Professor Dr. Wolfgang Haase
Darmstadt University of Technology
Institute of Physical Chemistry
Petersenstr. 20
64287 Darmstadt, Germany
Email: *haase@chemie.tu-darmstadt.de*

Professor Dr. Stanislaw Wróbel
Jagellonian University Krakow
Institute for Physics
ul. Reymonta 4
30-049 Krakow, Poland
Email: *uwrobel@if.uj.edu.pl*
or *stanislaw-wrobel@wp.pl*

ISBN 978-3-642-07924-5

Library of Congress Cataloging-in-Publication Data

Relaxation phenomena : liquid crystals, magnetic systems, polymers, high-Tc superconductors, metallic glasses / W. Haase, S. Wróbel (eds.).
p. cm.
Includes bibliographical references and index.

1. Relaxation phenomena. I. Haase, W. (Wolfgang) II. Wróbel, S. (Stanislaw)
QC173.4.R44R47 2003
530.4'16--dc21 2003050473
ISBN 978-3-642-07924-5 ISBN 978-3-662-09747-2 (eBook)
DOI 10.1007/978-3-662-09747-2

This work is subject to copyright. All rights are reserved, whether the whole or part of the material is concerned, specifically the rights of translation, reprinting, reuse of illustrations, recitation, broadcasting, reproduction on microfilm or in any other way, and storage in data banks. Duplication of this publication or parts thereof is permitted only under the provisions of the German Copyright Law of September 9, 1965, in its current version, and permission for use must always be obtained from Springer-Verlag Berlin Heidelberg GmbH.
Violations are liable for prosecution under the German Copyright Law.

© Springer-Verlag Berlin Heidelberg

Originally published by Springer-Verlag Berlin Heidelberg New York in 2003

The use of designations, trademarks, etc. in this publication does not imply, even in the absence of a specific statement, that such names are exempt from the relevant protective laws and regulations and therefore free for general use.

Cover Design: design & production, Heidelberg
Typesetting: Springer-Verlag and LE-TEX GbR, Leipzig using a Springer LATEX macro packege

Printed on acid-free paper 52/3141/YL 5 4 3 2 1 0

My contributions are dedicated to the memory of my beloved daughter Berit; she deceased unexpectedly on October 12, 2000, soon after closing our workshop in Zakopane, October 8–11, 2000.

Wolfgang Haase

Preface

During the last three decades many new as well as extended classes of organic and inorganic materials, some of which being of hybrid type, have been synthesized. Among them are those the contributors of this book are dealing with. In parallel to this, new technologies have been developed such as active matrix addressed liquid crystal displays (TFT-LCD), new types of sensors like thermographic sheets employed in science, industry and medicine, organic light emitting diodes (OLEDs), SQUIDs etc. At the same time the techniques for characterizing both the materials and technological products have become very fast and highly precise. For example, today measuring a dielectric spectrum over a broad frequency range with a high density of experimental points per decade requires a few minutes time, sometimes just a few seconds, but before it would have taken weeks or even months. Nowadays one is able to create an enormous amount of data points but there is a real problem how to reach the real message, the truth?

To answer such questions, after some years of a very efficient and successful bilateral co-operation between our two research groups in Darmstadt and in Cracow, in the early 1990s an idea appeared to discuss all such intriguing problems with our colleagues and friends from many countries in the friendly atmosphere of the nice vacation resort of Zakopane in the Tatra Mountains. Therefore our first workshop was organized there in 1993 and repeated at the same place in 1995 and 2000, interchanged with Darmstadt in 1998 and finally again in 2002. These kinds of meetings were well received as shown by the participation of the leading scientists in the field of materials science and by graduate students and postdoctoral fellows from all over the world.

Since the last Zakopane meeting in 2000 an idea has grown to evidence the discussions on all these topics in a book in order to distribute the results to a larger scientific community. Therefore we have invited the participants to contribute to the book, and we were amazed by the great involvement and the willingness as well as nice co-operation of all the authors whose contributions are published in this book.

The topics in this book seem in some aspects quite different and, of course, they were individually selected: Liquid crystals, molecular magnets, polymers, high-T_c-superconductors, and metallic glasses – the common subject of which is relaxation behavior. Why do we think one can present these topics in one book? The answer is that it often happens that scientists involved in these fields use the same well-substantiated physical models, but they present their points of view sometimes in quite different perspective. We as editors shall try to find common aspects of the relaxation behaviors observed in the different fields, because relaxation phenomena play an interdisciplinary role important for physicists, chemists, biophysicists, materials scientists, and electronic engineers etc.

The contributions are written by theorists and experimenters, i.e. by physicists, chemists and materials scientists, all of which oriented on materials, usable for interested specialists or beginners in the entire field. In some contributions relaxation phenomena do not always play a leading role. This is because we wanted to present the experiment, the theory and the materials side of the relaxation processes.

The content of this book is as follows:

In Part I the dielectric relaxation spectroscopy methods are described as very powerful tools for studying the dynamics and electrical structure of the systems studied. As far as magnetic relaxation and properties are concerned the AC susceptibility methods are presented including electron spin resonance spectroscopy. Some other specific methods are parts of the following related chapters.

One may ask why we do not include in this book aspects of nuclear magnetic resonance techniques? The answer is twofold: first of all there are so many well written articles and books available in this field, and secondly, if we had presented this powerful method and the results adequately, indeed much more space would have been needed. Nevertheless, some other methods (or fields) are even not included. Some scattering techniques, mechanical methods, others spectroscopic techniques, and kinetics etc. are also missing: A choice had to be made.

Part II deals with relaxation processes in liquid crystals (calamitic and discotic ones) as well as their composites. Some fundamental aspects of nematic liquid crystals (like nematics under pressure) are presented, ferroelectric and antiferroelectric liquid crystals are specially considered as new materials, as well as metallomesogens.

Part III presents selected aspects of relaxation processes in magnetic systems. Only particular topics dealt with in our groups are discussed, which are by no means representative for the entire field of magnetism.

Finally Part IV includes aspects of High-T_c-superconductors, nonlinear optical polymers incorporating some more experimental methods, and at the end there are metallic glasses showing an interesting relaxation behavior of great practical importance.

As editors we should inform the readers that SI unit system is not consequently used throughout the book because of practical purposes. Another confusions may arise due to using in some contributions different symbols for the same physical quantities/processes in order to keep individual styles of the authors.

When starting our work on the book we considered presenting to the scientific community a useful and at the same time inexpensive book. We therefore decided together with the publisher to ask for contributions in LaTeX version. This created a lot of problems and we are thankful to all authors for their patience. Many people were helping us to solve different technical problems. In particular we would like to thank Dr. Maria Krygowska-Doniec, Dr. Evgeni Loginov, and Jan Wróbel for supporting us in converting the Word documents into LaTeX.

We would like to warmly thank all authors not only for their patience but also for their great enthusiasm to contribute and for so many substantial hints and important suggestions. At this point we express our gratitude to all reviewers of the manuscripts. It was hard work to come up with such a huge amount of contributions in a rather limited time.

Our deep thanks go to Springer Publishers and in particular to Dr. Marion Hertel for her patience and substantial help. We also would like to thank Mrs. Christine Moisa and Mrs. Jacqueline Lenz for their nice co-operation.

Finally we would like to thank both of our families for their continuous support.

Now we hope what has been done and presented herewith shall be of some help to the readers, especially students and young scientists. We are awaiting your questions and comments.

Darmstadt, Cracow,
October 2002

Wolfgang Haase
Stanisław Wróbel

Contents

Introduction. Relaxation Phenomena in Physics and Chemistry 1
1 General remarks and basic formulas 1
2 Selected examples 3
2.1 Dielectric relaxation 3
2.2 Relaxation processes in magnetic systems 5
2.3 Spin-spin and spin-lattice relaxation 5
2.4 Fast chemical processes 6
2.5 Nonlinear dielectric behavior 7
2.6 Relaxation effect in electrolytes 8
3 Time and frequency domains of relaxation processes 8
References 9

Part I Experimental Methods for Investigating Relaxation Phenomena in Condensed Matter

1 Dielectric Relaxation Spectroscopy 13
1.1 Frequency domain dielectric spectroscopy 13
1.1.1 Dielectric spectroscopy of molecular and collective processes 13
Complex dielectric permittivity 13
Dielectric spectroscopy of liquid crystals 14
1.1.2 Macroscopic models of dielectric spectra 15
Debye model 15
Cole–Cole model 20
Havriliak Negami model 21
1.1.3 Relaxation function and dielectric spectra 22
1.1.4 Dielectric spectrometer 23
Apparatus 23
Sample and cell preparation 23
Vacuum controlled experiment 25

1.1.5 A simple model of Maxwell–Wagner relaxation 27
Two layer dielectric 27
SHDR process 30
1.1.6 Dielectric spectroscopy of ionic diffusion 31
1.1.7 Summary 32
References 33
1.2 Dielectric time domain spectroscopy 35
1.2.1 Introduction 35
1.2.2 Fourier transformation 36
1.2.3 Single reflection 37
1.2.4 The total transmission method 40
1.2.5 The open circuit total reflection method 44
1.2.6 Admittance analysis and bilinear calibration 46
1.2.7 Conclusion 50
References 50
1.3 Nonlinear dielectric spectroscopy 51
1.3.1 Introduction 51
1.3.2 Theoretical background of the nonlinear dielectric spectroscopy 53
1.3.3 Nonlinear dielectric relaxation in non-interacting dipolar systems 57
1.3.4 Nonlinear dielectric relaxation due to chemical rate processes in liquids 60
1.3.5 Summary 70
References 70
1.4 Dielectric relaxation processes in condensed matter under pressure 71
1.4.1 Usefulness of high pressure studies and the equation of state 71
1.4.1.1 Establishment of phase diagrams 71
1.4.1.2 pVT measurements 73
1.4.1.3 Entropy separation 74
1.4.1.4 Volume dependence of the clearing line 75
1.4.1.5 Density dependencies of the dielectric relaxation and the order parameter 75
1.4.2 Experimental methods 75
1.4.3 Dielectric relaxation and activation quantities 78
1.4.4 Selected results 80
1.4.5 Summary 84
References 84

2 Dynamic Susceptibility of Magnetic Systems 89
2.1 Dynamic susceptibility of paramagnetic and exchange-coupled spin systems 89
2.1.1 Introduction 89

2.1.2 Magnetic susceptibility in alternating magnetic field .. 90
2.1.2.1 Real and imaginary components of χ_{AC} 90
2.1.2.2 AC susceptometer 92
2.1.3 Relaxation in oscillating magnetic field 92
2.1.4 Relaxation processes in paramagnets 95
2.1.4.1 Spin-lattice relaxation 95
2.1.4.2 Spin–spin relaxation 96
2.1.5 Long-range ordered magnets 97
2.1.5.1 Dynamics of domain walls 97
2.1.5.2 Loss mechanisms 98
2.1.6 Some experimental results for ferro-, ferri- and antiferromagnets 99
2.1.6.1 Ferrites 99
2.1.6.2 Hard magnets 101
2.1.6.3 Rare earth metals 101
2.1.6.4 Weak magnets 104
2.1.7 Spin–glasses and spin–glass–like magnets 105
2.1.8 Superparamagnetic particles and high–spin molecules . 108
2.1.9 Summary 110
References 111
2.2 Dynamic susceptibility in heavy–fermion systems and related materials probed by electron spin resonance 112
2.2.1 Introduction 112
2.2.2 ESR in metals 114
2.2.3 Microscopic probes for the dynamic susceptibility 116
2.2.4 The Kondo lattices CeM_2X_2 119
2.2.4.1 Heavy Fermi liquid and intermediate valence . 120
2.2.4.2 Competition of magnetism and heavy Fermi liquid 123
2.2.5 Kondo insulators 127
2.2.6 Summary and outlook 129
References 132

3 Relaxation Phenomena in High-T_c Superconductors: Experimental Methods and Results 137
3.1 Introduction 137
3.2 Experimental techniques 138
3.2.1 Mössbauer spectroscopy 138
3.2.1.1 Isomer shift 140
3.2.1.2 Quadrupole splitting 140
3.2.1.3 Magnetic hyperfine field 140
3.2.1.4 Relaxation phenomena 141
3.2.2 μ^+SR spectroscopy 142
3.2.3 Neutron techniques 144
3.2.3.1 Neutron diffraction 145
3.2.3.2 Inelastic neutron scattering 145

3.3 Experimental results 146
3.3.1 $La_{2-x}Sr_xCuO_4$ compounds 146
3.3.2 $RBa_2Cu_3O_{6+d}$ compounds (R = rare earth metals and Y) 148
3.3.3 $Y_{1-x}Ca_xBa_2Cu_3O_{6+d}$ compounds 155
3.4 Summary 157
References 157

Part II Relaxation Phenomena in Liquid Crystals

4 Non-chiral Calamitic Liquid Crystals 163
4.1 Introduction to dielectric relaxation in anisotropic fluids 163
4.1.1 Isotropic fluids 163
4.1.2 Anisotropic fluids 168
4.1.3 Nematic liquid crystals 174
4.1.4 Conclusions 178
References 180
4.2 Molecular rotations in liquid crystals as seen by the dielectric spectroscopy method 181
4.2.1 Introduction 181
4.2.2 Rigid rod-like molecules in the nematic medium 183
4.2.3 Low frequency relaxation process in the nematic phase and the order parameter 185
4.2.4 Molecular rotations around the long axes. Influence of molecule flexibility 192
4.2.5 Relaxation in the smectic phases 195
4.2.6 Influence of pressure on the relaxation processes in LC phases 198
4.2.7 Summary 202
References 202
4.3 Computer simulations of polar liquid crystals 204
4.3.1 Introduction 204
4.3.2 Liquid crystalline phases and dipolar ordering 205
4.3.3 Models of interacting liquid crystalline molecules 208
4.3.3.1 Pair potentials for liquid crystalline molecules 209
4.3.3.2 Gay–Berne pair potential 211
4.3.4 Computer simulations with dipoles 216
4.3.4.1 Ewald summation technique for dipolar interactions 217
4.3.4.2 Reaction field method 219
4.3.4.3 Further computational details 221
4.3.5 Structure analysis 221

4.3.5.1 Singlet distribution functions and order parameters . . . 222
4.3.5.2 Pair distribution functions . . . 224
4.3.5.3 Three-body distribution functions . . . 226
4.3.6 Hard particles with dipoles . . . 227
4.3.7 Dipolar Gay–Berne systems . . . 227
4.3.7.1 Central dipole moments . . . 228
4.3.7.2 Intermediate and terminal dipole moments . . 231
4.3.8 Towards realistic simulations . . . 233
References . . . 233
4.4 Dielectric properties of liquid crystalline polysiloxane doped with dichroic dye . . . 236
4.4.1 Introduction . . . 236
4.4.2 Probe preparation and thermodynamical data . . . 238
4.4.3 Dielectric relaxation . . . 242
4.4.3.1 Experimental technique . . . 242
4.4.3.2 Dielectric relaxation in pure PS6 . . . 244
4.4.3.3 Dielectric relaxation of PS6 doped with dichroic dye . . . 248
4.4.3.4 Dielectric relaxation parameters . . . 250
4.4.4 Summary and conclusions . . . 252
References . . . 253

5 Ferro- and Antiferroelectric Liquid Crystals . . . 257
5.1 Modeling of ferroelectric and antiferroelectric liquid crystals . . . 257
5.1.1 Introduction . . . 257
5.1.2 Phenomenological models of ferroelectric liquid crystals . . . 258
5.1.3 Phenomenological models of antiferroelectric liquid crystals . . . 261
5.1.4 Discrete models . . . 263
5.1.5 Discrete phenomenological model of antiferroelectric liquid crystals . . . 265
5.1.5.1 Intra-layer interactions . . . 265
5.1.5.2 Interactions between nearest layers (NN) . . . 266
5.1.5.3 Interactions with next nearest layers (NNN) . 270
5.1.5.4 Free energy . . . 271
5.1.5.5 Structures and phase sequences . . . 272
5.1.6 Summary . . . 273
References . . . 273
5.2 Switching processes in ferroelectric liquid crystals: Theoretical aspects . . . 274
5.2.1 Introduction . . . 274
5.2.2 Polarization reversal in thick films . . . 275

5.2.2.1 Non-stationary solution for applied dc electric field . . . 275
5.2.2.2 Non-stationary solutions for applied ac electric field . . . 276
5.2.3 High frequency switching of the ferroelectric with a deformed helix . . . 278
5.2.4 Bistability in confined ferroelectric films . . . 280
5.2.5 Inclinations of smectic planes and dislocation walls . . . 283
5.2.6 Ferroelectric domains in the smectic-C* films . . . 286
5.2.7 Relaxation frequencies and strengths of the domain modes . . . 288
5.2.7.1 Relaxation frequencies of the bulk and surface modes . . . 288
5.2.7.2 Relaxation strengths of the bulk and surface modes . . . 289
5.2.7.3 Elimination of the ferroelectric domains by a strong field . . . 291
5.2.7.4 Surface orientational relaxation in the ferroelectric smectic . . . 291
5.2.8 Problem of hysteresis-free electro-optical switching . . . 293
5.2.8.1 Observations and models of the V-shaped electro-optical switching . . . 293
5.2.8.2 Basic equations and assumptions . . . 296
5.2.8.3 Switching of the cell with a low conductivity FLC and an additional low resistance . . . 298
5.2.8.4 Hysteresis-free switching for high frequency voltage applied to the cell . . . 301
5.2.9 Conclusions . . . 307
References . . . 308
5.3 Dielectric properties of ferroelectric liquid crystals in finite samples and near the transitions to the hexatic phases 309
5.3.1 Introduction . . . 309
5.3.2 Dielectric response of SmC* phase in planar samples . . . 310
5.3.2.1 Phenomenological description of helicoidal and twisted structures . . . 311
5.3.2.2 Dynamic dielectric response . . . 312
5.3.2.3 Pinned SmA phase . . . 315
5.3.2.4 Experimental results . . . 316
5.3.2.5 Conclusions . . . 320
5.3.3 Dielectric behavior of ferroelectric and antiferroelectric liquid crystals near the transition to the hexatic phases . . . 320
5.3.3.1 Simple phenomenological description . . . 321
5.3.3.2 Properties of modes found experimentally in ferroelectric materials . . . 327

5.3.3.3 Transition to the hexatic phase in antiferroelectric liquid crystals 328
5.3.4 Summary 330
References 331
5.4 Systems with competing synclinic-anticlinic interactions 332
5.4.1 Introduction 332
5.4.2 Theoretical modelling 333
5.4.2.1 Free energy 334
5.4.2.2 Stable phases and their structures 336
5.4.3 Experiment 341
5.4.3.1 Phase transitions 342
5.4.3.2 Structure and properties 343
5.4.3.3 General phase diagram for the antiferroelectric system 352
5.4.4 Comparison of theoretical results and experimental observations 353
5.4.5 Conclusions 358
References 358
5.5 Dielectric study of collective and molecular dynamics in glass-forming chiral low-molecular-weight liquid crystals 361
5.5.1 Introduction 361
5.5.2 Experimental 362
5.5.3 Results and discussion 363
5.5.4 Summary and conclusions 374
References 375
5.6 Dielectric properties and switching processes in ferroelectric liquid crystals based composites 376
5.6.1 Introduction 376
5.6.2 Microstructures of FLC based composites 377
5.6.2.1 Structures and preparation of MFLC 377
5.6.2.2 Preparation of PDFLC films and structures of FLC droplets 378
5.6.3 Electrooptics of PDFLC films 381
5.6.3.1 Electrooptical modulation due to electrically controlled light scattering effect 381
5.6.3.2 Saturation voltage of PDFLC films 387
5.6.3.3 Dynamics of electrooptic response of PDFLC films 390
5.6.4 Effects of confined geometry in MFLC and PDFLC . . . 393
5.6.4.1 Dielectric properties of MFLC, PDFLC and bulk FLC. 393
5.6.4.2 Basic parameters of confined FLC's 396
5.6.5 Summary 397
References 398

5.7 Dielectric behavior of phases formed by bent-shaped molecules 400
5.7.1 Introduction . . . 400
5.7.1.1 General remarks . . . 400
5.7.1.2 Dielectric measurements . . . 403
5.7.2 The B_1 phase . . . 404
5.7.3 The B_2 phase . . . 407
5.7.4 The CP_A phase . . . 412
5.7.5 The B_3 phase . . . 413
5.7.6 The B_4 phase . . . 414
5.7.7 The B_5 phase . . . 415
5.7.8 The B_6 phase . . . 416
5.7.9 The B_7 phase . . . 417
5.7.10 The transition between classical and banana phases . . 418
5.7.11 Summary . . . 420
References . . . 421
5.8 Electrooptical studies of relaxation processes in ferroelectric liquid crystals . . . 422
5.8.1 Introduction . . . 422
5.8.2 The coupling between the electric field and the spontaneous polarization . . . 423
5.8.2.1 Deformation of a helical smectic liquid crystal 425
5.8.3 Ferroelectric liquid crystals in weak electric fields . . . 427
5.8.3.1 Dielectric response . . . 427
5.8.3.2 Optical response . . . 428
5.8.3.3 Correlation between the dielectric and electrooptic responses . . . 432
5.8.4 Antiferroelectric liquid crystals in the electric field . . . 433
5.8.4.1 Optical response . . . 434
5.8.4.2 Angular dependence . . . 436
5.8.4.3 Separation of the second harmonic components . . . 437
5.8.5 Frequency dependence . . . 438
5.8.6 Experimental procedures . . . 440
5.8.7 Comparison of dielectric and electrooptic methods . . . 441
5.8.8 Summary . . . 443
References . . . 443
5.9 Infrared studies of the orientational order and dynamics of molecules in ferroelectric and antiferroelectric liquid crystals . . 445
5.9.1 Introduction . . . 445
5.9.2 Determination of the absorbance profile and the segmental tilt angle of the molecule . . . 446
5.9.3 Effect of electric field in the SmC* phase . . . 449
5.9.4 Calculations of the absorbance components and of the distribution function . . . 451
5.9.4.1 Uniaxial phase . . . 452

5.9.4.2 Ferroelectric phase – a model with the tilt fluctuation . . . 453
5.9.4.3 Biased rotation of the 12OBBB8 molecule in in the SmC^*_A and SmC^* phases . . . 454
5.9.4.4 Antiferroelectric and ferroelectric phase – a model with tilt and phase fluctuation . . . 457
5.9.5 Dynamics of the electric field induced molecular reorientation . . . 462
5.9.6 Summary . . . 466
References . . . 467
5.10 On the dielectric relaxation in the antiferroelectric phase and sub-phase Alpha . . . 468
5.10.1 Introduction . . . 468
5.10.2 Experimental . . . 469
5.10.3 Dielectric studies . . . 470
5.10.3.1 Static dielectric permittivity . . . 470
5.10.3.2 Evidence of SmA^*, SmC^* and SmC^*_α phases . 471
5.10.3.3 Substantiation of the SmC^*_A phase . . . 477
5.10.4 Conclusions . . . 483
References . . . 484
5.11 Dielectric and electrooptic studies of MHPOBC analogues . . . 485
5.11.1 Introduction . . . 485
5.11.2 Calorimetric and dielectric studies . . . 489
5.11.2.1 Phase transitions . . . 490
5.11.2.2 Dielectric properties . . . 492
5.11.2.3 Bias field influence on the dielectric spectra . . 495
5.11.2.4 Data processing of the dielectric spectra and discussion . . . 497
5.11.3 Discussion of collective and molecular processes . . . 500
5.11.4 Some aspects of electrical and optical behavior . . . 501
5.11.4.1 Reversal current method . . . 502
5.11.4.2 Spontaneous polarization . . . 502
5.11.4.3 Tilt angle . . . 505
5.11.4.4 Critical voltage . . . 506
5.11.5 Summary . . . 506
References . . . 507

6 Calamitic and Discotic Metallomesogens . . . 511
6.1 Dielectric study of smectic and columnar ferroelectric metallomesogens . . . 511
6.1.1 Introduction . . . 511
6.1.2 Experimental . . . 513
6.1.3 Results and discussion . . . 514
6.1.3.1 Calamitic compounds . . . 514
6.1.3.2 Discotic compounds . . . 522

6.1.4 Summary and conclusions . . . 528
References . . . 529
6.2 Relaxation processes in columnar phases of vanadyl complexes . . . 530
6.2.1 Introduction . . . 530
6.2.2 Thermoanalytical, structural and magnetic investigations . . . 532
6.2.2.1 DSC and polarizing optical microscopy . . . 532
6.2.2.2 X-ray diffractometry . . . 534
6.2.2.3 Magnetic properties . . . 535
6.2.3 Dielectric and electrooptical investigation . . . 537
6.2.3.1 Experimental . . . 537
Dielectric spectroscopy . . . 537
Electrooptical measurements . . . 538
6.2.3.2 Results and discussion . . . 539
Conductivity . . . 539
Dielectric relaxation processes . . . 539
Reversal current and switching experiments . . 543
6.2.4 Summary . . . 543
References . . . 546

Part III Special Aspects of Relaxation Phenomena in Magnetic Systems

7 Magnetic Properties and ESR Behavior of Some Molecular Compounds Containing Copper(II) Trimers with the Quartet Spin Ground State . . . 549
7.1 Introduction . . . 549
7.2 Review of used experimental methods . . . 550
7.3 Results and discussion . . . 551
7.3.1 Magnetic studies . . . 551
7.3.1.1 Linear trimers . . . 551
7.3.1.2 Nonlinear trimers . . . 554
7.3.2 ESR studies of compounds with linear trimers . . . 558
7.4 Summary . . . 566
References . . . 567

8 Magnetic Properties and Relaxations Processes in Manganese(III)-Porphyrins-TCNE-Systems . . . 569
8.1 Introduction . . . 569
8.2 Experimental . . . 572
8.3 Results . . . 573
8.4 Discussion . . . 581
8.5 Summary . . . 583
References . . . 584

9 Dipolar Interaction and Three-Dimensional Magnetic Ordering of some Chain and Layered Compounds 587
9.1 Introduction 587
9.2 Selected experimental results 589
9.2.1 Mn-porphyrin based charge-transfer complexes 589
9.2.2 Hydroxide-based layered compounds 591
9.3 Model for the dipolar interaction between ferrimagnetic chains or layers 594
9.3.1 Chain compounds with very large interchain spacing .. 595
9.3.2 Layered compounds with very large interlayer spacing . 602
9.3.3 Conclusions about the model 606
9.4 Summary 606
References 607

10 Electron Delocalization in Dimeric Mixed-Valence Systems . 609
10.1 Introduction 609
10.2 Electronic interactions 609
10.3 Vibronic interactions: PKS model 611
10.4 Vibronic interactions: Piepho type of vibrations 614
10.5 MV iron dimer in the presence of both types of vibrations 615
10.5.1 Model 615
10.5.2 Analysis. Intervalence absorption band 619
10.5.3 Magnetic behavior 623
10.6 Summary 625
References 626

Part IV Relaxation Phenomena in High-T_c Superconducting Systems, Nonlinear Optical Polymers and Metallic Glasses

11 High-T_c Superconductors 629
11.1 Superconductivity suppression and critical currents in the $R_{1-x}Pr_xBa_2Cu_3O_{7-\delta}$ systems (R = Ho, Y) 629
11.1.1 Introduction 629
11.1.2 Experimental 630
11.1.3 Electrical resistance study and discussion of the mechanism of the superconductivity suppression 630
11.1.4 AC magnetic susceptibility studies 633
11.1.4.1 Intergrain critical currents 635
11.1.4.2 Study of the flux creep 636
11.1.5 Hysteresis loops and intragranular critical current 638
11.1.6 Concluding remarks 640
References 641
11.2 Vortex dynamics and magnetic relaxation in high-T_c superconductors 642

11.2.1 Introduction . . . 642
11.2.1.1 Abrikosov flux line lattice . . . 642
11.2.1.2 Vortices in layered HTSC . . . 643
11.2.2 Dynamics of vortices . . . 645
11.2.2.1 Flux creep . . . 645
11.2.2.2 The critical state . . . 646
11.2.2.3 Relaxation effects in hysteresis loop . . . 647
11.2.3 Logarithmic dependence of magnetization on time for limited H, T and t . . . 649
11.2.3.1 TAFM model, linear $U(j)$ . . . 649
11.2.3.2 Magnetization relaxation rate . . . 650
11.2.4 Non-logarithmic magnetization decay for extended H, T and t . . . 653
11.2.4.1 Non-linear $U(j)$ . . . 653
11.2.4.2 Collective flux creep model . . . 655
11.2.5 Complex AC susceptibility of HT_c superconductors . . . 657
11.2.5.1 Intra- and intergranular contributions to χ' and χ'' . . . 657
11.2.5.2 Frequency dependence and flux creep at grain boundaries . . . 659
11.2.5.3 AC response in strong DC magnetic field . . . 661
11.2.6 Summary . . . 662
References . . . 663

12 Relaxation Phenomena in Nonlinear Optical Polymers . . . 667
12.1 Introduction . . . 667
12.2 Physical background . . . 668
12.2.1 NLO susceptibility and effects . . . 668
12.2.2 Organic NLO materials . . . 669
12.2.3 Poled NLO polymers . . . 669
12.2.4 Stark effect (Electroabsorption) . . . 670
12.2.5 Piezoelectric effect . . . 672
12.3 The stability of polar order after poling . . . 673
12.3.1 Experimental methods . . . 673
12.3.2 The relaxation of SHG and acoustoelectric response . . 676
12.3.3 Discussion of poling stability . . . 678
12.4 Electroabsorption spectroscopy as a tool for relaxation measurements . . . 682
12.4.1 Experimental technique . . . 682
12.4.2 Electroabsorption spectroscopy with variable modulation frequency . . . 683
12.4.3 Internal electric field in NLO films . . . 687
12.5 Summary . . . 689
References . . . 690

13 Relaxation Processes in Two- and Three-Component Metallic Glasses 693
13.1 Introduction 693
13.2 Description of the relaxation phenomena 695
13.3 Experimental 697
13.4 Results and discussion 699
13.5 Summary and conclusion 704
References 705

Index 707

List of Contributors

Maria A. Athanassopoulou
Sect. 6.2
Darmstadt University of Technology
Institute of Physical Chemistry
Petersenstr. 20
64287 Darmstadt, Germany
Maria.athanassopoulou
@t-online.de

Maria Bałanda
Sect. 2.1, Chap. 8, Sects. 11.1, 11.2
The H. Niewodniczański Institute
of Nuclear Physics
Radzikowskiego 152
31-342 Kraków, Poland
Maria.Balanda@ifj.edu.pl

Danuta Bauman
Sect. 4.4
Faculty of Technical Physics
Poznan University of Technology
Nieszawska 13a
60-965 Poznań, Poland
bauman@phys.put.poznan.pl

Mojca Čepič
Sects. 5.1, 5.4
Josef Stefan Institute
Jamova 39
1000 Ljubljana, Slovenia
mojca.cepic@ijs.si

Grzegorz Cholewiak
Sect. 4.3
M. Smoluchowski Institute of Physics
Jagellonian University
ul. Reymonta 4
30-059 Kraków, Poland
ufcholew@th.if.uj.edu.pl

Milorad Davidović
Chap. 13
The Vinča Institute
of Nuclear Sciences
P.O. Box 522
11000 Belgrade, Yugoslavia
and
Faculty of Electrical Engineering
P.O. Box 8116
11000 Belgrade, Yugoslavia
davidm@vin.bg.ac.yu

Rosario de la Fuente
Sects. 5.5, 6.1
Departmento de Física Aplicada II
Facultad de Ciencias
Universidad del País Vasaco
Apdo. 644
48080 Bilbao, Spain
wdpfular@lg.ehu.es

Redouane Douali
Sect. 5.10
Laboratoire d'Etude des Matériaux
et des Composants
pour l'Electronique
E.A. 2601
Université du Littoral
Côte d'Opale
50 Rue Ferdinand Buisson, B.P. 717
62228 Calais, France
Douali@opale.univ-littoral.fr

Marc Drillon
Chap. 9
IPCMS
23 Rue du Loess
67037 Strasbourg, France
marc.drillon@ipcms.u-strasbg.fr

Frederic Dubois
Sect. 5.10
Laboratoire d'Etude des Matériaux
et des Composants
pour l'Electronique
E.A. 2601
Université du Littoral
Côte d'Oplale
50 Rue Ferdinand Buisson, B.P. 717
62228 Calais, France
dubois@univ-littoral.fr

David A. Dunmur
Sect. 4.1
Department of Chemistry and
Southampton Liquid Crystal
Institute
University of Southampton
Spouthampton SO17 1BJ, U.K.
d.a.dunmur@soton.ac.uk

Andrzej Fąfara
Sect. 5.11
Jagellonian University
M. Smoluchowski Institute of Physics
Reymonta 4
30-059 Kraków, Poland
anfafara@poczta.onet.pl

Karsten Falk
Chap. 8
Darmstadt University of Technology
Institute of Physical Chemistry
Petersenstr. 20
64287 Darmstadt, Germany
Kafalk@hrz2.tu-darmstadt.de

Bo Gestblom
Sect. 1.2
Department of Physics
Uppsala University
75121 Uppsala, Sweden
bo.gestblom@fysik.uu.se

Milada Glogarová
Sect. 5.3
Institute of Physics
Academy of Sciences
of the Czech Republic
Na Slovance 2
18040 Prague, Czech Republic
Glogarova@fzu.cz

Ewa Górecka
Sect. 5.4
Department of Chemistry
Warsaw University
Al. Zwirki i Wigury
02-089 Warsaw, Poland
Ewa.Gorecka@ipcms.u-strasbg.fr

Wolfgang Haase
Sects. 5.6, 5.11, 6.2,
Chaps. 7, 8, 9, 12
Darmstadt University of Technology
Institute of Physical Chemistry
Petersenstr. 20
64287 Darmstadt, Germany
haase@chemie.tu-darmstadt.de

Monika Heinrich
Sect. 2.2
Institute of Physics
Univerisity of Augsburg
Experimental Physics V
Universitätsstr. 1
86159 Augsburg, Germany
monika.heinrich
@physik.uni-augsburg.de

Louis Hellemans
Sect. 1.3
Department of Chemistry
Catholic University of Leuven
Celestijnenlaan 200 D
3001 Leuven, Belgium
louis
@lcbdiris.fys.kuleuven.ac.be

Jan Jadżyn
Sect. 1.3
Institute of Molecular Physics
Polish Academy of Sciences
ul. Smoluchowskiego 17
60-179 Poznań, Poland
Jadzyn@ifmpan.poznan.pl

Miguel Ángel Pérez Jubindo
Sects. 5.5, 6.1
Departamento de Física Aplicada II
Facultad de Ciencias
Universidad des País Vasco
Apdo. 644
48080 Bilbao, Spain
wdppejum@lg.ehu.es

Przemysław Kędziora
Sect. 1.3
Institute of Molecular Physics
Polish Academy of Sciences
ul. Smoluchowskiego 17
60-179 Poznań, Poland
Kedziora@ifmpan.poznan.pl

Dirk Kilian
Sect 6.2
Darmstadt University of Technology
Institute of Physical Chemistry
Petersenstr. 20
64287 Darmstadt, Germany
dirk.kilian@kuraray-kse.com

Antonio Kocot
Sect. 5.9
Institute of Physics
University of Silesia
Uniwersytecka 4
40-007 Katowice, Poland
kocot@us.edu.pl

Horst Kresse
Sect. 5.7
Martin-Luther-University Halle
Institute of Physical Chemistry
Mühlpforte 1
06108 Halle, Germany
Kresse@chemie.uni-halle.de

Hans-Albrecht Krug von Nidda
Sect. 2.2
Institute of Physics
University of Augsburg
Experimental Physics
Universitätsstr. 1
86159 Augsburg, Germany
Hans-Albrecht.Krug
@physik.uni-augsburg.de

Wojciech Kuczyński
Sect 5.8
Instiute of Molecular Physics
Polish Academy of Sciences
Smoluchowskiego 17
60179 Poznań, Poland
wkucz@ifmpan.poznan.pl

Christian Legrand
Sect. 5.10
Laboratoire d'Etude des Matériaux
et des Composants
pour l'Electronique
E.A. 2601
Université du Littoral
Côte d'Opale
50 Rue Ferdinand Buisson, B.P. 717
62228 Calais, France
legrand@univ-littoral.fr

Alois Loidl
Sect. 2.2
Institute of Physics
University of Augsburg
Experimental Physics V
Universitätsstr. 1
86159 Augsburg, Germany
alois.loidl
@physik.uni-augsburg.de

Lech Longa
Sect. 4.3
M. Smoluchowski Institute of Physics
Jagellonian University
ul. Reymonta 4
30-059 Kraków, Poland
lech@zfs.if.uj.edu.pl

Monika Marzec
Sect. 5.11
M. Smoluchowski Institute of Physics
Jagellonian University
ul. Reymonta 4
30-059 Kraków, Poland
ufmarzec@if.uj.edu.pl

Huu Tinh Nguyen
Sect. 5.10
Centre de Recherche Paul Pascal
Université de Bordeaux I
Avenue Schweitzer
33600 Pessac, France
tinh@crpp.u-bordeaux.fr

Sergei M. Ostrovsky
Chaps. 9, 10
Darmstadt University of Technology
Institute of Physical Chemistry
Petersenstr. 20
64287 Darmstadt, Germany
sm_ostrovsky@yahoo.com

Pierre Panissod
Chap. 9
Institute de Physique
et Chimie des Materiaux
de Strasbourg
UMR 75040 du CNRS
Rue du Loess
67037 Strasbourg, France
Pierre.Panissod
@ipcms.u-strasbg.fr

Sergei A. Pikin
Sect. 5.2
Institute of Crystallography
Russian Academy of Sciences
Leninsky prospect 59
117333 Moscow, Russia
pikin@ns.crys.ras.ru

Damian Pociecha
Sect. 5.4
Department of Chemistry
Warsaw University
Al. Zwirkii Wigury
02-089 Warsaw, Poland
pociu@chem.aw.edu.pl

Eugene Pozhidaev
Sect. 5.6
P.N. Lebedev Physical Institute
Russian Academy of Sciences
Leninsky prospect 53
119991 Moscow, Russia
epozhidaev@mail.ru

Blanca Ros
Sect. 5.5
Departamento de Química Orgánica
Facultad de Ciencias-ICMA
Universidad de Zaragoza-CSIC
50009 Zaragoza, Spain
bros@posta.unizar.es

Ivan Rychetský
Sect. 5.3
Institute of Physics
Academy of Sciences
of the Czech Republic
Na Slovance 2
18040 Prague, Czech Republic
rychet@fzu.cz

José Luis Serrano
Sects. 5.5, 6.1
Departamento de Química Orgánica
Facultad de Ciencias-ICMA
Universidad de Zaragoza-CSIC
50009 Zaragoza, Spain
joseluis@posta.unizar.es

Teresa Sierra
Sect. 6.1
Departamento de Química Orgánica
Facultad de Ciencias-ICMA
Universidad de Zaragoza-CSIC
50009 Zaragoza, Spain
tsierra@posta.unizar.es

Timothy Swager
Sect. 6.2
Department of Chemistry
Massachusetts Institute
of Technology
Cambridge
MA 02139-4307, USA
tswager@mit.edu

Andrzey Szytuła
Chap. 3
M. Smoluchowski Institute of Physics
Jagellonian University
ul. Reymonta 4
30-059 Kraków, Poland
szytula@if.uj.edu.pl

Predrag Tomić
Chap. 13
Energoinvest
Research and Development Sector
Factory Birač, Zvornik
Republic of Srpska, Bosnia and
Herzegovina
tomic@rstel.net

Zbiegniew Tomkowicz
Chap. 7, 8, Sect. 11.1
M. Smoluchowski Institute of Physics
Jagellonian University
ul. Reymonta 4
30-059 Kraków, Poland
tomkowic@castor.if.uj.edu.pl

Hans-Rainer Trebin
Sect. 4.3
Institute of Theoretical
und Applied Physics
University Stuttgart
Pfaffenwaldring 57
70550 Stuttgart, Germany
trebin
@itap.physik.uni-stuttgart.de

Stanisław Urban
Sects. 1.4, 4.2
M. Smoluchowski Institute of Physics
Jagellonian University
ul. Reymonta 4
30-059 Kraków, Poland
ufurban@cyf-kr.edu.pl

Natasa Vaupotič
Sect. 5.4
University of Maribor
Faculty of Education
Department of Physics
Koroska 160
2000 Maribor
Slovenia
natasa.vaupotic@uni-mb.sl

Thomas Weyrauch
Chap. 12
Darmstadt University of Technology
Institute of Physical Chemistry
Petersenstr. 20
64287 Darmstadt, Germany
weyrauch@mdo.net

Eryk Wolarz
Sect. 4.4
Faculty of Technical Physics
Poznan University of Technology
Nieszawska 13a
60-965 Poznan, Poland
wolarz@phys.put.poznan.pl

Roman Wrzalik
Sect. 5.9
Institute of Physics
University of Silesia
Uniwersytecka 4
40-007 Katowice, Poland
kocot@us.edu.pl

Stanisław Wróbel
Sects. 1.1, 5.11, 6.2
M. Smoluchowski Institute of Physics
Jagellonian University
ul. Reymonta 4
30-059 Kraków, Poland
ufwrobel@if.uj.edu.pl

Albert Würflinger
Sects. 1.4, 4.2
Institute of Physical Chemistry II
Ruhr University
44780 Bochum, Germany
albert.wuerflinger
@ruhr-uni-bochum.de

Bostjan Žekš
Sect. 5.1
Josef Stefan Institute
Jamova 39
1000 Ljubljana, Slovenia
and
Slovenian Academy
of Science and Arts
Novi trg 3
1000 Ljubljana, Slovenia
bostjan.zeks
@biofiz.mf.uni-lj.si

Introduction. Relaxation Phenomena in Physics and Chemistry

W. Haase and S. Wróbel

1 General remarks and basic formulas

Relaxation studies are important for many systems like liquids, glasses, anisotropic mesophases, disordered solids, magnetic materials etc. Within this book, a variety of examples of relaxation processes will be discussed.

What one can learn from the studies of relaxation in general? We receive information about the relaxation time τ (or the **relaxation frequency** $\boldsymbol{f_r}$), activation energies and entropies, the temperature and/or pressure dependencies. The question whether there are single or multiple relaxation processes (or a continuous distribution) involved will be discussed.

Another question arises when we deal with macroscopic or with microscopic properties. Generally speaking, the quantities obtained from the experiments described within this book and from the data processing are in any way the macroscopic ones, but how are they related to intrinsic (microscopic), molecular, atomic or spin properties? For instance, the **microscopic relaxation time** $\boldsymbol{\tau_i}$ (or correlation time) relates to the mean square angular deviation of a molecule along a time period. Neglecting internal polarization or internal forces due to the matrix it is most likely that the **macroscopic relaxation time** $\boldsymbol{\tau}$ is of the order of magnitude of the molecular (or microscopic) correlation time. Assuming that some internal forces are present due to the surrounding matrix like dipolar interaction, hydrogen bridges etc., our data are then specific only for the molecules embedded in the matrix.

Let us now shortly present a few basic relations to derive some specific **relaxation functions.**

When a system being in equilibrium is influenced by an external field **S**, as a consequence, the equilibrium state does not exist any more. If the process for reaching a new equilibrium state is much longer than the time, the field **S** affects this system, we are dealing with a **relaxation process**. This process follows first order kinetics. The time constant τ is the time needed for increasing (1a) (or decreasing (1b)) the related property R to $R_0(1-e)$ (or R_0/e) where R_0 is the initial value R; τ is the **relaxation time** for the

system. These two types of the well-known **relaxation function are** given by (1a) and (1b).

$$R(t) = R_0 \left(1 - \exp\left(-\frac{t}{\tau}\right)\right) , \tag{1a}$$

$$R(t) = R_0 \cdot \exp\left(-\frac{t}{\tau}\right) , \tag{1b}$$

where t denotes time.

Figure 1 demonstrates a typical relaxation process for the increase of the property R.

The step function $F(t-t')$ for **S** can be defined by assuming $F(t-t') = 0$ for $t < t'$ and $F(t-t') = 1$ for $t > t'$ [1, 2]. This leads to the formula:

$$S(t) = S_1 + (S_2 - S_1)F(t-t') . \tag{2}$$

The property $R(t)$ influenced by the field **S** changes with time according to the equation:

$$R(t) = \xi S_2 - \xi(S_2 - S_1)G_p(t-t') \qquad \text{for} \quad t \geq t' , \tag{3}$$

where ξ is a property, which will be defined later.

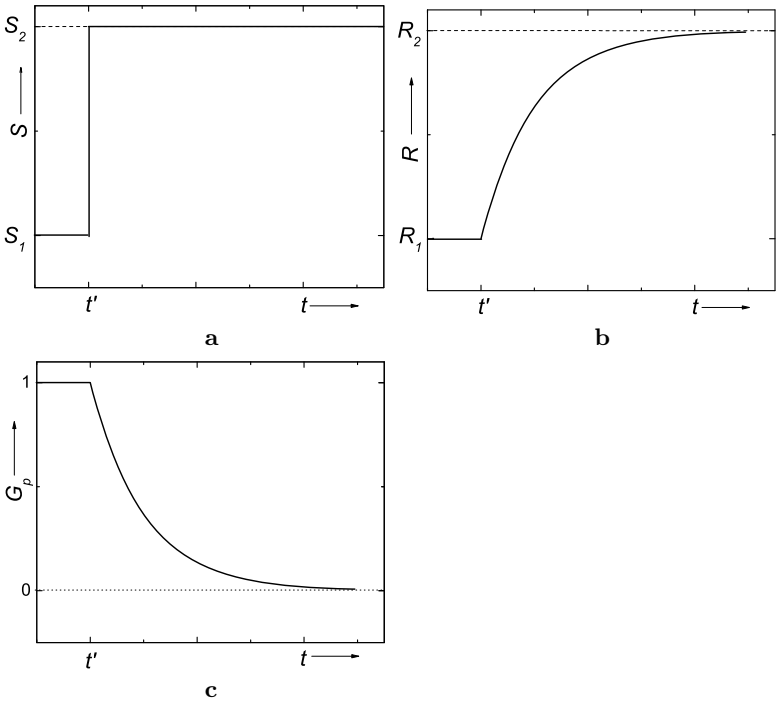

Fig. 1. (**a**) The step function $F(t-t')$ for an external force **S**, (**b**) response function for R, (**c**) decay function $G_p(t-t')$ after removing the force

Let us assume the field **S** is a pulse function with superposition of two (4) or more (5) arbitrary functions,

$$R(t) = \xi S\left(-G_p(t - t_1 + \Delta t)\right) + G_p(t - t_1)\ , \tag{4}$$

$$R(t) = \xi \sum_i S_i\left[-G_p(t - t_i + \Delta t) + G_p(t - t_i)\right]\ . \tag{5}$$

If for $S \neq 0$ the time iterval Δt goes to zero, $\Delta t \to 0$, we arrive at

$$R(t) = \xi \int_0^t -S(t')\left[\frac{\partial G_p(t - t')}{\partial(t - t')}\right]dt' = \xi \int_0^t S(t')g_p(t - t')dt'\ , \tag{6}$$

where $g_p(t - t')$ is the pulse response function of $R(t)$. There is a relation between the decay function $G_p(t - t')$ and the pulse response function:

$$g_p(t - t') = -\frac{\partial}{\partial t}G_p(t - t') \quad \text{with} \int_0^\infty g_p(t)dt = 1\ . \tag{7}$$

The quantity ξ is in general a complex property, $\xi^* = \xi' - i\xi''$, where ξ' represents the real, dispersion part and ξ'' the imaginary absorption part and $i = \sqrt{-1}$.

One can prove [2–6] that ξ' and ξ'' are linked together *via* the Kramers–Kronig relation:

$$\begin{aligned}\xi'(\omega) &= \xi'(\infty) + \frac{2}{\pi}\int_0^\infty \frac{\xi''(\omega')\omega'}{\omega'^2 - \omega^2}d\omega' \\ \xi''(\omega) &= -\frac{2\omega}{\pi}\int_0^\infty \frac{\xi'(\omega') - \xi'(\infty)}{\omega'^2 - \omega^2}d\omega'\ ,\end{aligned} \tag{8}$$

where ω' is a dummy variable substituting the frequency ω.

These relations are very important from a physical standpoint because they show that the quantitiy ξ' can be derived from ξ'' and *vice versa* with the consequence of obtaining the same information. Practically it is much better to measure both components to have better statistics and better substantiation of the process studied.

It should be mentioned that the Kramers-Kronig relations are always valid for any complex quantity like dielectric permittivity, magnetic susceptibility, polarizability, complex Faraday rotation and so on. In the following section we are going to present some representative examples.

2 Selected examples

2.1 Dielectric relaxation

If we now consider the electric dipole relaxation, we are dealing with the external electric field $\mathbf{E}(t)$ instead of $\mathbf{S}(t)$, the polarization $\mathbf{P}(t)$ instead of

$R(t)$ and $\varepsilon_0\chi$ instead of ξ. Here we can write:

$$\mathbf{P} = \mathbf{P}_{ind} + \mathbf{P}_{or} = \varepsilon_0\chi\mathbf{E} = \varepsilon_\circ(\varepsilon - 1)\mathbf{E} \,. \tag{9}$$

$\mathbf{P}_{ind}$ is the induced polarization, $\mathbf{P}_{or}$ the dipole orientational (or dipolar) polarization, ε_0 the dielectric permittivity of free space, $\chi = \varepsilon - 1$ the dielectric susceptibility, ε the dielectric permittivity. ε is in general a complex function [1–5], $\varepsilon^* = \varepsilon' - i\varepsilon''$, with the real ε' as dispersion and the imaginary ε'' as absorption component.

The time scale for the induced polarization is $\sim 10^{-16}$ s, whereas for the dipolar reorientation it can be between 10 s and $\sim 10^{-12}$ s. Therefore in reality we deal with several decay functions and, as a consequence, with several relaxation times for $\mathbf{P}$.

For a harmonically oscillating field, $\mathbf{P}$ is related to $\mathbf{E}(t) = \mathbf{E}_0 \exp(-i\omega t)$ via (10), where ω is the circular frequency,

$$\mathbf{P}(t) = \varepsilon_0 \left(\varepsilon^*(\omega) - 1\right) \mathbf{E}_\circ \exp(-i\omega t) \,. \tag{10}$$

The complex dielectric permittivity for the oscillating field is given by:

$$\varepsilon^*(\omega) = \varepsilon(\infty) + (\varepsilon(0) - \varepsilon(\infty)) \wedge_{i\omega} (g_p(t)) \;. \tag{11}$$

Here $\wedge_{i\omega}(g_p(t))$ is the Laplace transformed $g_p(t)$. Let us consider the decay process of the dipole relaxation after switching off the field $\mathbf{E}$ assuming there is only one dipole relaxation time τ. One can then receive for the following relation:

$$g_{p,\mu}(t) = -\frac{dG_{p,\mu}(t)}{dt} = \frac{1}{\tau}\exp\left(-\frac{t}{\tau}\right) \,, \tag{12}$$

where the $g_{p,\mu}(t)$ function fulfills the condition:

$$\int_0^\infty \frac{1}{\tau}\exp\left(-\frac{t}{\tau}\right) d\tau = 1 \,. \tag{13}$$

By combining (1a) or (1b) with (11) we receive the well-known Debye-type relaxation function:

$$\varepsilon^*(\omega) = \varepsilon(\infty) + (\varepsilon(0) - \varepsilon(\infty)) \frac{1}{1 + i\omega\tau} \,, \tag{14}$$

which can be split into the real and the imaginary part, as shown, e.g. in Sect. 1.1.

Instead of the Debye-single relaxation function one can use modified equations for non single processes (see Sect. 1.1). Other relaxation functions, e.g. with stretched exponentials [4–8], are presented in this book (Weyrauch and Haase – Chap. 12).

2.2 Relaxation processes in magnetic systems

Now we switch to relaxation processes in case of magnetic spins. This subject will be in detail presented in Sect. 2.1 by M. Balanda.

Instead of the dielectric polarization **P** in (9), we deal with the magnetization **M** which in case of linear approximation is proportional to the external magnetic field applied **H** (15). The proportionality is given by the magnetic susceptibility χ

$$\mathbf{M} = \chi \mathbf{H} \,. \tag{15}$$

χ can be treated as dependent on the external field strength and frequency.

The low frequency limit of the differential susceptibility, known as χ_T, is the isothermal susceptibility. Here the magnetic spins are in thermal contact with the surrounding.

At high frequencies the magnetic moments are unable to follow the field applied. Therefore we are dealing here with the case of no coupling between magnetic spins and the surrounding. This high frequency limit is therefore quoted as adiabatic susceptibility χ_S. This exactly lead to the Debye equation for magnetic system given by

$$\chi^*(\omega) = \chi_S + (\chi_T - \chi_S)\frac{1}{1 + i\omega\tau} \,, \tag{16}$$

where $\chi^* = \chi' - i\chi''$; in turn χ' is the dispersion, and χ'' is the absorption process, discussed in detail in Sect. 2.1.

Note the Debye equations (14) and (16) are valid for single relaxation processes only. If there is a distribution of relaxation times, one can use different Cole–Cole type equations (see Sects. 1.1 and 2.1). In fact by plotting ε'' versus ε' in the dielectric case one speaks of a Cole–Cole diagram, whereas people dealing with magnetism use the term Argand diagram by plotting χ'' versus χ'. The term Argand diagram is sometimes used in dielectric spectroscopy as well (Sect. 1.1).

2.3 Spin-spin and spin-lattice relaxation

Because of the importance of these two terms, and not only for NMR processes, we shall shortly introduce them.

In the thermal equilibrium the vector of magnetization is parallel to the z axis. Soon after applying a 90° pulse, the vector of magnetization rotates in the xy-plane and has an equal number of nuclear α and β spins. As a consequence the nuclear spins are no longer in thermal equilibrium. The process of returning to the thermal equilibrium is called spin relaxation. There are two mechanisms of relaxations:

The z component of the magnetization M_z tends to reach the equilibrium value $M_{z,0}$ with a time constant T_1:

$$M_z(t) - M_{z,0} \propto \exp\left(-\frac{t}{T_1}\right) . \tag{17}$$

T_1 is called longitudinal relaxation time and it is known as the spin-lattice relaxation time because this relaxation process consists in energy exchange between the spin and lattice reservoirs.

In thermal equilibrium the spins are randomized but not longer after applying a pulse. The time of getting back to an equilibrium by spin redistribution is the transversal or spin-spin relaxation time T_2 (18)

$$M_x(t) \propto \exp\left(-\frac{t}{T_2}\right) . \tag{18}$$

Note both processes are of the first order type.

In case of paramagnetic systems, the energy exchange between magnetic moments and the lattice is *via* spin-orbit coupling (see Sect. 2.1).

2.4 Fast chemical processes

For investigating fast chemical processes, one method became of essential importance, the so-called relaxation method [9]. The chemical reaction in equilibrium can be instantly disturbed either by changing temperature, pressure or electric field. Due to this there are such terms as temperature, pressure or field jump method. In Fig. 2a an abrupt temperature jump is presented. As one example a property proportional to the change of concentration can be the change of the optical absorption Ab, is measured over the time t.

Let us assume a reaction given by (19) is in the new equilibrium state.

$$A + B \underset{k_{-1}}{\overset{k_1}{\rightleftarrows}} C . \tag{19}$$

$[A]_\infty$, $[B]_\infty$, and $[C]_\infty$ are the concentrations in the new equilibrium. Then we get

$$\frac{d[C]}{dz} = k_1[A]_\infty[B]_\infty - k_{-1}[C]_\infty = 0 . \tag{20}$$

After the temperature jump has been applied to the system in the old equilibrium with the concentrations $[A]_0$, $[B]_0$, and $[C]_0$ the actual concentrations are $[A]_\infty + x = [A]$, $[B]_\infty + x = [B]$, $[C]_\infty - x = [C]$. x is proportional to the actual deviation of the system from the new equilibrium; $x_0 = [C]_\infty - [C_0]$. The problem can be treated mathematically, and after some steps and neglecting the term x^2 we arrive at

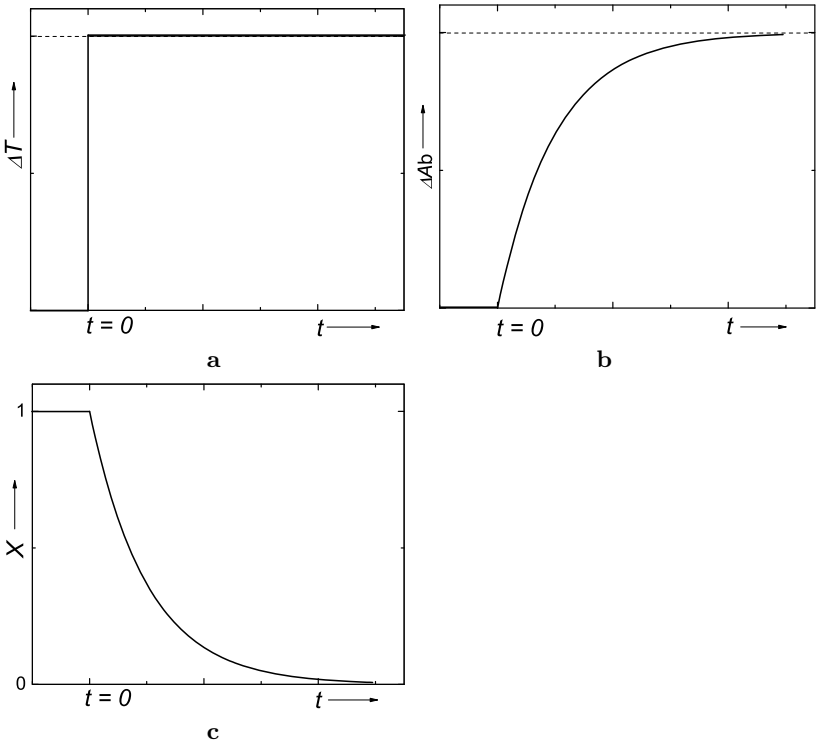

Fig. 2. Temperature jump method. (**a**) Time dependence of temperature, (**b**) Time dependence of optical absorption, (**c**) change of x (see text) with time

$$\frac{dx}{dt} \approx -k \cdot x \quad \text{with} \quad k = k_1 \left([A]_\infty + [B]_\infty\right) + k_{-1} \; . \tag{21}$$

This essential is a kinetics of first order described by:

$$x = x_0 \cdot \exp(-kt) \quad \text{and} \quad \Delta\,[C] \propto \Delta Ab \propto x_0(1 - \exp(-kt)) \; . \tag{22}$$

Equation (22) can be compared with (1a) and (1b) by adequately substituting $k = \frac{1}{\tau}$. The increase in the absorption, e.g. in the visible range, is proportional to the increase of the concentration of C.

It should be mentioned here, that any property proportional to the concentration of C, can be measured instead of the absorption.

2.5 Nonlinear dielectric behavior

An interesting method for investigating chemical reactions is presented in Sect. 1.3 by Jadżyn et al. [10] who are using nonlinear dielectric spectroscopy for this purpose. In this method, the chemical equilibrium can be affected by a small alternating electric field $\mathbf{E}(t)$ in presence of a strong static field $\mathbf{E}_\circ$.

Using this method dimerization processes, e.g. for 2-pyrrolidinone in benzene could be investigated or the self-association of cholesterol in carbon tetrachloride (see Sect. 1.3).

2.6 Relaxation effect in electrolytes

As a last example the so-called relaxation effect in electrolytes will shortly be presented. Here due to the transport of ions in the electric field an asymmetry in the ionic clouds takes place, say the clouds of opposite charges around an ion have no longer spherical symmetry. The time scale for renewing the spherical surrounding with new particles of opposite charges is called the relaxation time and the process relaxation process. The theory goes back to Debye, Hückel and Onsager [11, 12] interpreting the process to be essentially of the first order and following the equation:

$$g(x(t)) \sim \exp\left(-\frac{t}{\tau}\right) . \tag{23}$$

where $g(x(t))$ is a weighted function which is zero for $\tau = 0$. After Einstein and Smoluchowski the mean path squared of ion migration and the relaxation time τ are interconnected by

$$\overline{(\Delta x)^2} = \frac{2k_B T\tau}{R}, \tag{24}$$

where R is the radius of diffusing particles. Relaxation of ions being the origin of the low frequency relaxation in the sub-hertz frequency range is discussed in Sect. 1.1.

3 Time and frequency domains of relaxation processes

Figure 3 presents a schematic view of frequency domains of the selected experimental techniques used to study different relaxation processes. FT-IR-TRS (Fourier Transform Infrared Time Resolved Spectroscopy) is a method for studying the fastest relaxation processes, like reorientation around the long molecular axis in liquid crystals (discussed in Sect. 5.9 by Kocot). Transmission and reflection time domain methods are described in Sect. 1.2 by Gestblom. Frequency response analyzers are used to study collective and molecular processes and they are described in many chapters of this book. The electro-absorption method is described in Chap. 12 by Weyrauch and Haase. There are many other methods described in the book but not included in this diagram. QNS method is used to study fast molecular processes [13, 14]. However, this method is not incorporated in this book.

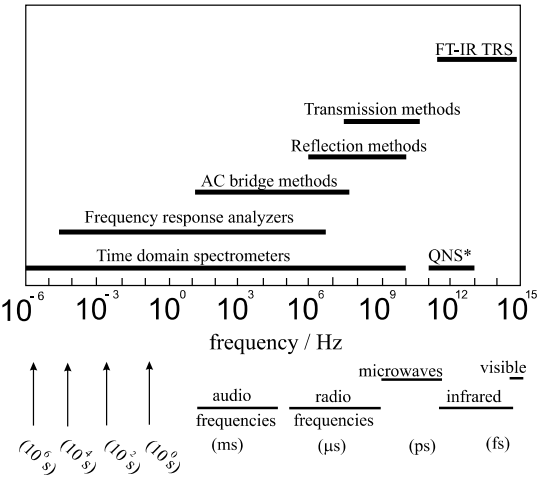

Fig. 3. Frequency domains and time windows for different experimental methods. *QNS = Quasi-elastic Neutron Scattering [13, 14]

References

1. C.F.J. Böttcher, O.C. van Belle, P. Bordewijk, A. Rip: *Theory of Electric Polarization*, Vol. I. Dielectrics in Static Fields, Elsevier, Amsterdam – London – New York 1973
2. C.F.J. Böttcher and P. Bordewijk: *Theory of Electric Polarization*, Vol. II. Dielectrics in time-dependent fields, Elsevier, Amsterdam – London – New York 1973
3. N. Hill, W.E. Vaughan, A.H. Price and M. Davies: *Dielectric Properties and Molecular Behavior*, Van Nostrand, London 1969
4. A.K. Jonscher: *Dielectric Relaxation in Solids*, Chelsea Dielectric Press, London 1983
5. B.K.P. Scaife: *Principles of Dielectrics*, Clarendon Press, Oxford 1998
6. V.I. Gaiduk: *Principles of Relaxation Dynamics of Polar Molecules*, World Scientific, Singapore, New Jersey, London, Hong Kong 1999
7. F.Gouda: Ph.D.thesis, Chalmers Univ. of Technology, Gothenburg 1992
8. M.Pfeiffer: Ph.D. thesis, Technische Hochschule Darmstadt 1993
9. M. Eigen, L. De Maeyer: In: *Techniques of Organic Chemistry*, Vol. VIII, Part 2, ed. by S.L. Fries, A. Weissberger (Interscience, New York 1961) p. 895
10. J.Jadżyn and W. Hellemans: Ber. Bunsenges. Phys. Chem. **97**, 205 (1993)
11. G. Kortüm: *Lehrbuch der Elektrochemie*, Verlag Chemie GmbH, Weinheim 1972
12. W.T. Coffey, Y.P. Kalmykov, S.V. Titov: 'Itinerant Oscillator Models of Fluids'. In: *Advances in Chemical Physics, Vol. **126***. Ed. by I. Prigogine and Stuart A. Rice (John Wiley and Sons, Inc., N.Y. 2003) pp. 131–186
13. J.A. Janik, T. Riste: Chapter 17 In: *Methods of Experimental Physics Vol. **23**, part B*. Ed. by K. Shold and D.D. Price (Academic Press, 1987)
14. J.A. Janik, J.M. Janik: Mol. Mat. **1**, 255 (1992)

Part I

Experimental Methods for Investigating Relaxation Phenomena in Condensed Matter

1

Dielectric Relaxation Spectroscopy

1.1 Frequency domain dielectric spectroscopy

S. Wróbel

1.1.1 Dielectric spectroscopy of molecular and collective processes

Complex dielectric permittivity

Nowadays dielectric spectroscopy covers the frequency range from 10^{-6} Hz to 10^{10} Hz by using computer controlled impedance analyzers [1–10], network analyzers as well as time domain spectrometers [11, 12]. At higher frequencies (above 10 GHz) one should use wave-guides, which means that for each frequency a separate apparatus is necessary to perform accurate dielectric measurements.

This contribution is devoted to linear dielectric response. Here the time dependent polarization $\mathbf{P}(t)$ of the sample, being induced by a weak measuring electric field $\mathbf{E}(t)$, is proportional to the field:

$$\mathbf{P}\left(t\right) = \varepsilon_0 \left(\varepsilon^* - 1\right) \mathbf{E}\left(t\right) \ , \tag{1.1}$$

where

$$\mathbf{E}(t) = \mathbf{E}_0 \exp\left(-i\omega t\right)$$

is a sinusoidal electric field applied to the Dielectric Under Test (DUT) and ε^* is the complex dielectric permittivity, ω is the angular frequency, $2\pi f$, and f in turn is the frequency of measuring electric field displayed in the channel A of most impedance analyzers, and ε_0 is the dielectric permittivity of free space, $\varepsilon_0 = 8.854187817$ pF/m. In linear dielectric spectroscopy the amplitude of the measuring electric field should be chosen so that it does not suppress the structure of DUT, for instance, the helicoidal structure of the SmC^* phase. It is worth pointing out that for anisotropic systems like crystalline solids

the complex dielectric permittivity is a tensor quantity, having at least two principal components. In dielectric spectroscopy one measures the complex dielectric permittivity:

$$\varepsilon^*(\omega) = \varepsilon'(\omega) - i\varepsilon''(\omega) - i\frac{\sigma}{\varepsilon_0\omega} , \tag{1.2}$$

where σ is conductivity related to Ohmic resistance of DUT, ε' and ε'' are, respectively, the real and imaginary parts of the complex dielectric permittivity, and $i = \sqrt{-1}$.

There are two borderline values of the dielectric permittivity: $\varepsilon'(\omega \to 0) \equiv \varepsilon(0)$ is the static dielectric permittivity (or traditionally dielectric constant) and $\varepsilon'(\omega \to \infty) = \varepsilon(\infty)$ is the high frequency limit of the dielectric permittivity. For non-polar materials the dielectric permittivity is equal to $\varepsilon(\infty)$ in the frequency range from ca. 100 kHz to the far infrared region, i.e. to about 10^{13} Hz. For polar liquids, mesomorphic systems like liquid crystals and plastic crystals and orientationally disordered crystals (ODICs) the reorientation of permanent dipole moments leads to the dielectric absorption in the microwave or radio frequency ranges. It can be shown [13] that $\varepsilon''(\omega)$ is connected with the energy (W) absorbed per unit volume of DUT by the formula:

$$W = \frac{1}{2}\varepsilon_o \left(E_0\right)^2 \omega\varepsilon'' \left(\omega\right) . \tag{1.3}$$

This equation is the basic principle of the microwave oven where microwaves are absorbed mostly by reorientation polar water molecules present in food products.

The principles of dielectric physics, dielectric spectroscopy and dielectric materials are described in books and review articles [13–27]. The most extended works on dielectric relaxation in condensed matter are by Böttcher and Bordewijk [13, 27], Daniel [17] and Hill et al. [18].

Dielectric spectroscopy of liquid crystals

In the case of liquid crystals (LCs) dielectric investigations are very interesting due to the fact that the dielectric permittivity is a tensor quantity [28–31]. For uniaxial LCs it has the form:

$$\hat{\varepsilon} = \begin{pmatrix} \varepsilon^*_\perp & 0 & 0 \\ 0 & \varepsilon^*_\perp & 0 \\ 0 & 0 & \varepsilon^*_{||} \end{pmatrix} \tag{1.4}$$

Both principal components of the dielectric permittivity tensor show different frequency dependencies and temperature dependencies as well [30–33]. For achiral liquid crystalline systems the dielectric spectrum consists of two molecular contributions [32–35] connected with the reorientation of molecules around the short or long molecular axis. For the purpose of this contribution

we shall call these processes S-process and L-process, respectively. These two processes also contribute to the dielectric spectra of ferroelectric liquid crystals (FLCs) and antiferroelectric liquid crystals (AFLCs). They are not frozen out even in highly ordered smectics. Studying molecular processes versus temperature one can learn more about the origin of ferroelectricity in FLCs as well as in classical ferroelectrics. The dielectric spectra of calamitic liquid crystals are discussed in detail in this book by Dunmur (Sect. 4.1), Urban and Würflinger (Sects. 1.4 and 4.2).

1.1.2 Macroscopic models of dielectric spectra

Debye model

One of the methods to study dielectric behavior of a material consists in measuring the complex dielectric permittivity (1.3) versus frequency at constant temperature and ambient pressure. In this way one obtains the dielectric spectrum in the frequency domain. That is why this method is called frequency domain dielectric spectroscopy (FDDS). Dielectric studies at varying temperature can usually be easily performed. Dielectric studies under high pressures are also being done for liquid crystals [35] and plastic crystals [36] (see Sect. 1.4 of this book by Würflinger and Urban) as well as for ferroelectric liquid crystals [37]. Using FDDS one obtains an absorption peak in a certain frequency range. In the case of polar liquids and plastic crystals it usually appears in the microwave frequency range (100 MHz–100 GHz) whereas for LCs and FLCs the dielectric absorption shows up also at radio frequencies.

In the plots of both components of the complex dielectric permittivity vs. f on the logarithmic scale one obtains a typical dielectric spectrum (Fig. 1.1). The frequency dependence of $\varepsilon'(\log f)$ is known in the literature as the dispersion curve whereas $\varepsilon''(\log f)$ is called the absorption curve due to accompanying energy absorption (see (1.3)).

In Fig. 1.1 one can see the dielectric spectrum obtained for one of the antiferroelectric liquid crystals. The frequency at which $\varepsilon''(\omega)$ reaches its maximum is known as critical (or relaxation) frequency. In many cases the dielectric spectrum can be described by the Debye-type formula:

$$\varepsilon^* = \varepsilon' - i\varepsilon'' = \varepsilon(\infty) + \frac{\varepsilon(0) - \varepsilon(\infty)}{1 + i\omega\tau}\,, \tag{1.5}$$

where τ is the dielectric relaxation time related to the critical frequency (f_c) by the equation:

$$\tau = \frac{1}{2\pi f_c}\,. \tag{1.6}$$

The Debye equation (1.5) can be split into two separate formulas:

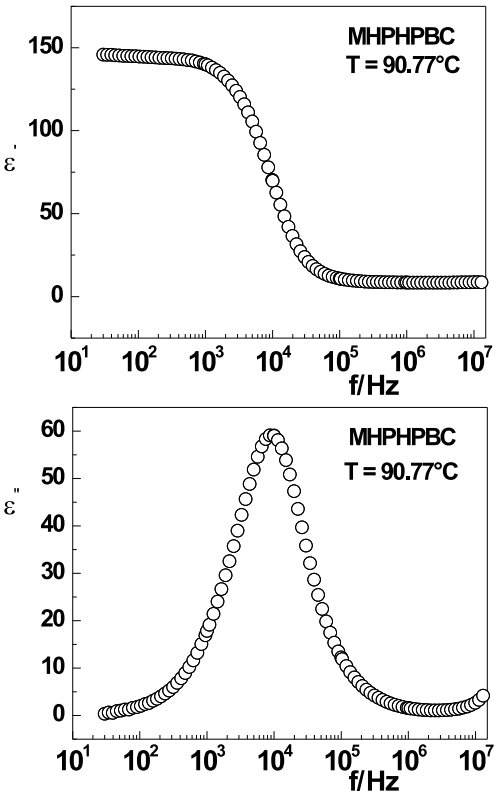

Fig. 1.1. Exemplary dielectric spectrum seen in the frequency window of HP 4192A impedance analyzer. The spectrum was obtained for SmC* and is due to the collective so-called Goldstone mode (GM) process

$$\varepsilon'(\omega) = \varepsilon(\infty) + \frac{\varepsilon(0) - \varepsilon(\infty)}{1 + (\omega\tau)^2}\,, \tag{1.7a}$$

$$\varepsilon''(\omega) = \frac{(\varepsilon(0) - \varepsilon(\infty))\omega\tau}{1 + (\omega\tau)^2}\,, \tag{1.7b}$$

where (1.7a) describes the dispersion and (1.7b) the absorption curve. One can see that $\varepsilon''(\omega)$ reaches its maximum at the critical frequency (ω_c), i.e.:

$$\varepsilon''(\omega_c) = \varepsilon''_{\max} = \frac{\varepsilon(0) - \varepsilon(\infty)}{2}\,, \tag{1.7c}$$

where the difference $\varepsilon(0) - \varepsilon(\infty) \equiv \Delta\varepsilon$ is the so-called dielectric increment or dielectric strength.

Based on the Onsager model [17–19, 22, 24, 26, 27] the dielectric strength depends on the microscopic parameters as follows:

Table 1.1. Molecular structure and phase diagrams of the compounds studied in the scope of this chapter. Temperature in °C

SUBSTANCES

No.	Compound	Phase diagram	in short
1.	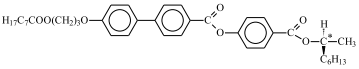	Is 105 SmA 92 SmC* 89 SmC^*_A 42 Cr.	**MHPHPBC**
2.	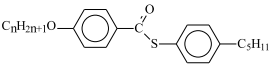	Cr.39(SmJ)SmC 60 SmA 63 N 85 Is	**10OS5**
3.	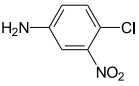	Cr2 - 31.3 Cr1 97 Is	**NCA**
4.	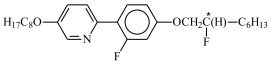	Cr.1 29 SmC* 47 N* 63 Is	**FFP**

$$\Delta\varepsilon = \varepsilon\,(0) - \varepsilon\,(\infty) = \frac{3\varepsilon\,(0)}{2\varepsilon\,(0) + \varepsilon\,(\infty)} \cdot \left(\frac{\varepsilon\,(0) + 2}{3}\right)^2 \frac{4\pi N_0 \mu^2}{3k_B T}\,, \tag{1.8}$$

In case of a simple molecular structure one can compute the dipole moment μ from the temperature dependence of the dielectric strength. However, it is difficult to estimate dipole moments for complicated molecules as often is the case for LCs or polymers. It is due to the complicated electrical structure (several permanent dipole moments) and the flexibility of such molecules. To calculate the effective permanent dipole moment in such cases one needs a model incorporating group dipolar moments and intra-molecular dynamics (see Minkin et al. [24] and Davies [25]).

There is another alternative way for presentation of dielectric spectra, namely, one can plot on the complex plain ε'' vs. ε'. In this way one obtains the so-called Cole–Cole plot (or Cole–Cole diagram). Such plots are also known as Argand's diagrams. Each point (ε', ε'') on the Cole–Cole plot represents the complex dielectric permittivity obtained at a certain frequency. For the Debye-type process the Cole–Cole plot is a semicircle with the center lying on the ε' axis. Note that on the Cole–Cole diagram both axes (ε' and ε'') should have the same unit. Otherwise the Cole–Cole plot would be artificially swollen or flatten.

Figure 1.2 shows a Cole–Cole plot. There are two particular points (vectors) on the complex plain – one is $\varepsilon^* = \varepsilon\,(0)$ and the other $\varepsilon^* = \varepsilon\,(\infty)$. The first vector represents the static dielectric permittivity which occurs to be a very important material constant whereas the second one can be connected with the refractive index squared by the equation [18, 27]: $\varepsilon(\infty) \cong 1.05\,n^2$.

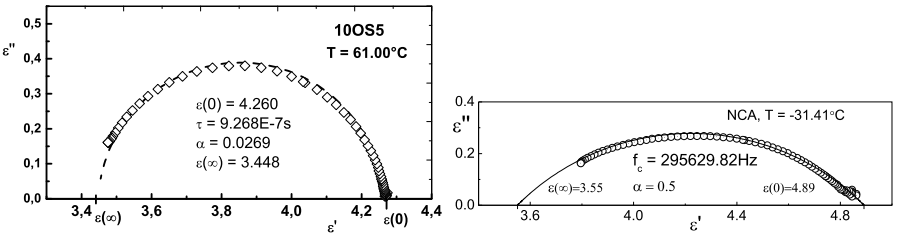

a **b**

Fig. 1.2. Exemplary Cole–Cole plots for **(a)** a Debye-type spectrum ($\alpha = 0$) obtained for the liquid crystalline phase of 10OS5 (Tab. 1.1) and for **(b)** Cole–Cole spectrum ($\alpha = 0.45$) acquired for NCA (Table 1.1) in its rotationally disordered phase

A more general relation between the dielectric permittivity and the refractive index is given by the Maxwell equation [13, 18]:

$$\varepsilon^*(\omega) = n^*(\omega)^2 = (n - ik)^2 = n^2 + k^2 - i2kn \,, \tag{1.9}$$

where n^* is a complex refractive index, n – real part of refractive index and k is the absorption coefficient. Equation (1.9) connects two physical quantities. The $\varepsilon^*(\omega)$ describes the dielectric properties at low frequencies whereas the refractive index was treated as a quantity characteristic for the optical frequency range. The Maxwell equation (1.9) relates then the formalism used to describe the dielectric behavior at low frequencies with that developed for the visible range. The complex refractive index is used for description of optical properties of semiconductors [38–40], in which case it displays pronounced values and reach spectrum in the optical frequency range. Please keep in mind that the refractive index is not a tensor quantity. In other words the dielectric permittivity is a more general physical quantity in describing the dielectric and optical behavior of materials.

Usually by using impedance analyzers one measures experimentally capacity $C(\omega)$ of the cell filled with a DUT and the loss tangent:

$$C(\omega) = \varepsilon_0 \varepsilon'(\omega) C_0 \,, \tag{1.10a}$$

$$\tan\delta(\omega) = \frac{\varepsilon''(\omega)}{\varepsilon'(\omega)} \,, \tag{1.10b}$$

where C_0 is the capacity of the empty cell and ε' the real part of the complex dielectric permittivity of DUT.

It is worth mentioning that the Debye equation written in terms of the loss tangent has the form:

$$\tan\delta(\omega) = \frac{(\varepsilon(0) - \varepsilon(\infty))\omega\tau}{\varepsilon(0) + \varepsilon(\infty)(\omega\tau)^2} \,. \tag{1.11}$$

Figure 1.3 presents $\tan\delta$ as a function of $\log f$ obtained for the Goldstone mode (GM) dielectric relaxation spectrum in the ferroelectric SmC* phase.

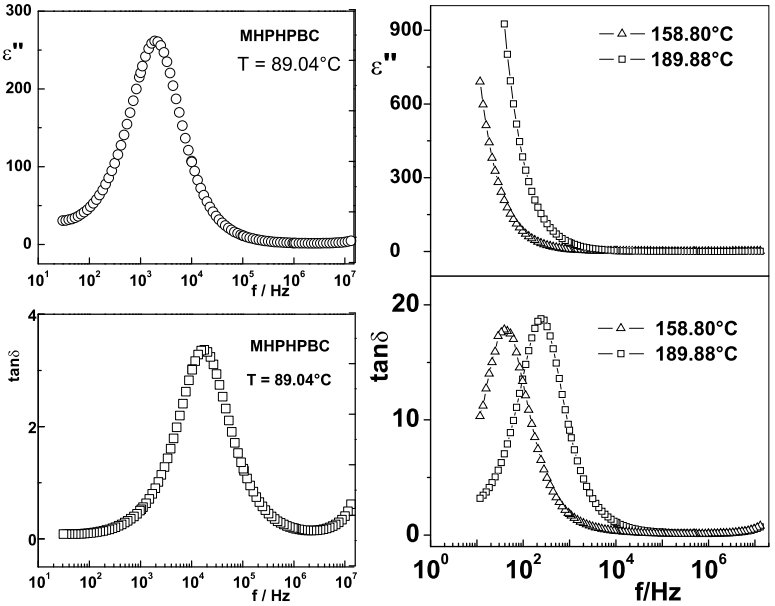

Fig. 1.3. (a) $\tan\delta$ and ε'' vs. $\log_{10} f$ obtained for the SmC* phase of MHPHPBC, **(b)** dielectric spectrum obtained at two temperatures for one of the vanadyl complexes (**1**(12), see Sect. 6.2 by Haase et al.)

Note that the position of the maximum of $\tan\delta$ does not coincide with the position of the maximum of $\varepsilon''(f)$. The former is shifted to higher frequencies by factor of $\sqrt{\varepsilon(0)/\varepsilon(\infty)}$. So, the relation between the critical frequency f_c and the frequency of $\tan\delta_{\max}$ ($f_{\max}$) is as follows:

$$f_{\max} = \sqrt{\frac{\varepsilon\,(0)}{\varepsilon\,(\infty)}} f_c\,. \tag{1.12}$$

As a consequence of (1.12) there is a pronounced shift effect for FLCs and highly polar materials for which this factor may be as large as 100 or even higher. As seen in Fig. 1.3b for some dielectrics showing very high dielectric permittivity at low frequencies, like columnar phases of metallomesogenes [41–43], the maximum of the dielectric losses may not be seen in the frequency window of the apparatus employed. On the other hand, $\tan\delta(\log_{10} f)$ may show a nice absorption peak (Fig. 1.3b).

It is a real problem to overcome in FDDS studies on FLCs or in general on materials showing very large dielectric permittivity in the sub-hertz frequency range. In many cases one observes a nice peak for $\tan\delta$ and after transformation of the dielectric spectrum into the dielectric loss $\varepsilon''(f)$ only the right-hand side part of the spectrum shows up due to the shift of the absorption curve

to low frequencies. So, for systems displaying very high dielectric permittivity at low frequencies due to collective processes like GM one should measure the dielectric spectrum in the widest frequency range possible. Sometimes it is even better to work with the $\tan\delta(f)$ dielectric spectrum only. The absorption peak which shows up at higher frequencies for $\tan\delta(f)$ after transformation to $\varepsilon''(f)$ via (1.11) may not be seen at all within the spectrometer's frequency window because of the large $\varepsilon''(f)$ maximum shift to lower frequencies. For instance, in the case of vanadyl complexes the dielectric absorption peak is shifted to the sub-hertz frequency range (Fig. 1.3b).

Cole–Cole model

Dielectric spectroscopy detects stochastic reorientation of molecular dipole moments and collective fluctuations of spontaneous polarization in paraelectric, ferroelectric, ferrielectric and antiferroelectric liquid crystals. For liquids and solid rotator phases of organic polar compounds [13, 18, 36] the dielectric spectrum is usually of a Debye-type. However, some systems composed of flexible molecules [1, 2, 16, 18, 21, 24] and some disordered solid phases [14, 19, 44, 45] exhibit broad dielectric spectra(check Fig. 1.2b), and can be described [17–19, 21] by the Cole–Cole function:

$$\varepsilon^* = \varepsilon' - i\varepsilon'' = \varepsilon(\infty) + \frac{\varepsilon(0) - \varepsilon(\infty)}{1 + (i\omega\tau_o)^{1-\alpha}} - i\frac{\sigma}{\varepsilon_o\omega}\,, \tag{1.13a}$$

which can be separated into two components:

$$\varepsilon'(\omega) = \varepsilon(\infty) + \frac{1}{2}\Delta\varepsilon \frac{1 + (\omega\tau_o)^{1-\alpha}\sin\left(\frac{1}{2}\pi\alpha\right)}{1 + 2(\omega\tau_o)^{1-\alpha}\sin\left(\frac{1}{2}\pi\alpha\right) + (\omega\tau_o)^{2(1-\alpha)}}\,, \tag{1.13b}$$

$$\varepsilon''(\omega) = \Delta\varepsilon \frac{1 + (\omega\tau_o)^{1-\alpha}\cos\left(\frac{1}{2}\pi\alpha\right)}{1 + 2(\omega\tau_o)^{1-\alpha}\sin\left(\frac{1}{2}\pi\alpha\right) + (\omega\tau_o)^{2(1-\alpha)}} + \frac{\sigma}{\varepsilon_o\omega}\,, \tag{1.13c}$$

where $\Delta\varepsilon = \varepsilon(0) - \varepsilon(\infty)$ is the dielectric strength, α is a parameter responsible for symmetric distribution of the relaxation times and τ_0 is in this case the most probable relaxation time. In (1.13a) the conductivity term is added to classical Cole–Cole function. It is worth pointing out here that the maximum value of $\varepsilon''(\omega)$ depends on the value of the α parameter according to the formula:

$$\varepsilon''(\omega_c) = \varepsilon''_{\max} = \frac{\varepsilon(0) - \varepsilon(\infty)}{2}\frac{\cos\frac{1}{2}\alpha\pi}{1 + \sin\frac{1}{2}\alpha\pi}\,. \tag{1.14a}$$

For small values of the α parameter ($\alpha < 0.1$) one can use the formula:

$$\varepsilon''_{\max} \cong \frac{\varepsilon(0) - \varepsilon(\infty)}{2 + \alpha\pi}\,, \tag{1.14b}$$

so for non-Debye dielectric relaxation processes the absorption peak is lower and broader. The dielectric relaxation time τ_o is connected with the critical frequency ω_{oc}:

$$\tau_o = \frac{1}{\omega_{oc}} , \tag{1.14c}$$

which is due to the symmetric distribution of the relaxation times. As seen (Fig. 1.2a) the dielectric spectrum is in this case broader and the Cole–Cole plot is now an arc with the center lying below the ε' axis.

Havriliak Negami model

A more general function [13, 18] was proposed by Havriliak and Negami:

$$\varepsilon^* = \varepsilon' - i\varepsilon'' = \varepsilon(\infty) + \frac{\varepsilon(0) - \varepsilon(\infty)}{\left[1 + (i\omega\tau_o)^{1-\alpha}\right]^{\beta}} - i\frac{\sigma}{\varepsilon_0\omega} , \tag{1.15a}$$

which can be written as two components in the following way:

$$\varepsilon' = \varepsilon(\infty) + \Delta\varepsilon \frac{\cos(\beta\varphi)}{\left[1 + 2(\omega\tau_o)^{1-\alpha}\sin\left(\frac{1}{2}\pi\alpha\right) + (\omega\tau_o)^{2(1-\alpha)}\right]^{\beta/2}} , \tag{1.15b}$$

$$\varepsilon'' = \Delta\varepsilon \frac{\sin(\beta\varphi)}{\left[1 + 2(\omega\tau_o)^{1-\alpha}\sin\left(\frac{1}{2}\pi\alpha\right) + (\omega\tau_o)^{2(1-\alpha)}\right]^{\beta/2}} + \frac{\sigma}{\varepsilon_o\omega} , \tag{1.15c}$$

where

$$\varphi = \arctan\left\{(\omega\tau_o)^{1-\alpha}\cos\left(\frac{1}{2}\pi\alpha\right) \Big/ \left[1 + (\omega\tau_o)^{1-\alpha}\sin\left(\frac{1}{2}\pi\alpha\right)\right]\right\} \tag{1.15d}$$

and

$$\tau_o = \frac{1}{\omega_c}\left[\tan\left(\frac{\pi}{2(\beta+1)}\right)\right]^{1/\alpha} . \tag{1.15e}$$

This new parameter β deforms the Cole–Cole diagram to a skewed arc. Relaxation processes that could be described by this kind of function were observed for polymers, some disordered solids and also LCs as well as AFLCs. As we shall see later some of the dielectric relaxation processes observed in FLCs and AFLCs are pure Debye-type processes, i.e. $\alpha = 0$ and $\beta = 1$ [46–58].

There are some other macroscopic models proposed and used widely for data processing, e.g. Cole–Davidson, Fuoss–Kirkwood [13, 18], Jonscher [19, 20], and so on.

1.1.3 Relaxation function and dielectric spectra

For simple polar liquids or plastic crystals the linear polarization induced after switching on the external electric field increases exponentially in time. After switching off the external electric field the polarization decays exponentially. To describe the dielectric relaxation process in time domain one can introduce the so-called relaxation function:

$$\Phi(t) = (\varepsilon(0) - \varepsilon(\infty)) \exp\left(-\frac{t}{\tau}\right) . \tag{1.16}$$

The Fourier transformation of this function gives the Debye equation (1.5) that describes the dielectric spectrum in the frequency domain.

The relaxation function for strongly bounded electrons in atoms as well as ions in ionic crystals is a sinusoidal function:

$$\Phi(t) = A_o \sin(\omega_o t) , \tag{1.17}$$

where ω_o is the resonant frequency which depends on the elastic constant and reduced mass of the two interacting particles. Such a function is valid only for harmonic systems. After Fourier transformation of this function one obtains typical pure resonant absorption. For real systems the relaxation function has the following form [14]:

$$\Phi(t) = A_o \exp\left(-\frac{t}{\tau}\right) \sin(\omega_o t + \varphi_o) , \tag{1.18}$$

the Fourier transformation of which gives a broadened resonance absorption maximum.

$$\varepsilon^*(\omega) - \varepsilon(\infty) = \frac{1}{2}\Delta\varepsilon_0 \left[\frac{1 - i\omega_o\tau}{1 - i(\omega_o + \omega)\tau} + \frac{1 + i\omega_o\tau}{1 + i(\omega_o - \omega)\tau}\right] , \tag{1.19}$$

where $\Delta\varepsilon_0 = A_o\tau\cos\varphi_o$ and $\omega_o\tau = -\tan\varphi_o$.

The broadening comes from anharmonic processes (phonon-phonon and/or phonon-electron interactions) [38–40] that take place especially at higher temperatures, i.e. in less ordered systems.

For ionic crystals the resonant absorption gives a large contribution to dielectric permittivity. The respective absorption takes place in infrared frequency range, i.e. from 10^{11} to 10^{13} Hz. The static dielectric permittivity $\varepsilon(0)$ and the high frequency limit $\varepsilon(\infty)$ fulfill one of the most fundamental formulas [38–40] in the physics of dielectrics:

$$\omega_L = \sqrt{\frac{\varepsilon(0)}{\varepsilon(\infty)}}\omega_T , \tag{1.20}$$

where ω_L and ω_T are the frequencies of longitudinal and transverse phonons in ionic crystals. Equation (1.20) is known as Lyddane–Sachs–Teller equation.

Resonant absorption takes place also in solid phases of the systems built by highly polar molecules incorporating, e.g. –C≡N or NO_2 groups. In mesomorphic phases – like plastic crystals, liquid crystals – and also in liquids this resonant absorption (known in the literature as Poley absorption) is a broad spectrum showing up at the borderline between microwave and infrared frequency range. Its Cole–Cole plot resembles an Argand graph known in physics as a way for presenting resonances. As a result there is a continuous transition from the resonance processes to relaxation processes which is present in case of strongly anharmonic systems.

1.1.4 Dielectric spectrometer

Apparatus

Nowadays many laboratories have real dielectric spectrometers covering the frequency range from 10^{-5} Hz to 10^{9} Hz.

As an example, the Condensed Matter Group in the Institute of Physical Chemistry of the Darmstadt University of Technology is equipped [1, 2, 5, 41] with the following set-ups:

1° HP 4192A Impedance Analyzer covering the frequency range from 5 Hz to 13 MHz,
2° HP 4191A Impedance Analyzer (1 MHz–1000 MHz) and
3° Schlumberger Solartron 1250 Frequency Response Analyzer(10^{-6} Hz to 30 kHz) in conjunction with a self-constructed amplifier based on the so-called Chelsea Dielectric Interface principle.

A EUROTHERM 818 controller allows for temperature stabilization for the dielectric measurements from room temperature to 200 °C. Figure 1.4a shows a schematic drawing of the set-up used for the intermediate frequency range. Using such FDDS set-up many calamitic liquid crystals [5, 7, 11, 48–51, 57, 59] columnar mesophases of discotic liquid crystals [41–43] as well as few mixtures [5, 50, 51], showing ferroelectric and antiferroelectric phases, have been investigated. Most of our dielectric relaxation spectroscopy studies were carried out by using cells with gold-coated electrodes.

Sample and cell preparation

For dielectric studies the capacitors were prepared by inserting the samples between the two parallel-plane low-resistance gold electrodes ($< 5\Omega$/sq.). The electrodes are deposited on planar quartz glass having dimensions of $7 \times 13 \times 3$ mm^3 (Fig. 1.4b) separated in most cases by mica spacers (Fig. 1.4c) having a thickness between 10 and 100 µm. Before assembling the empty cell both electrodes and mica spacers should be cleaned with acetone and flushed with a stream of hot air as to remove dust particles and water.

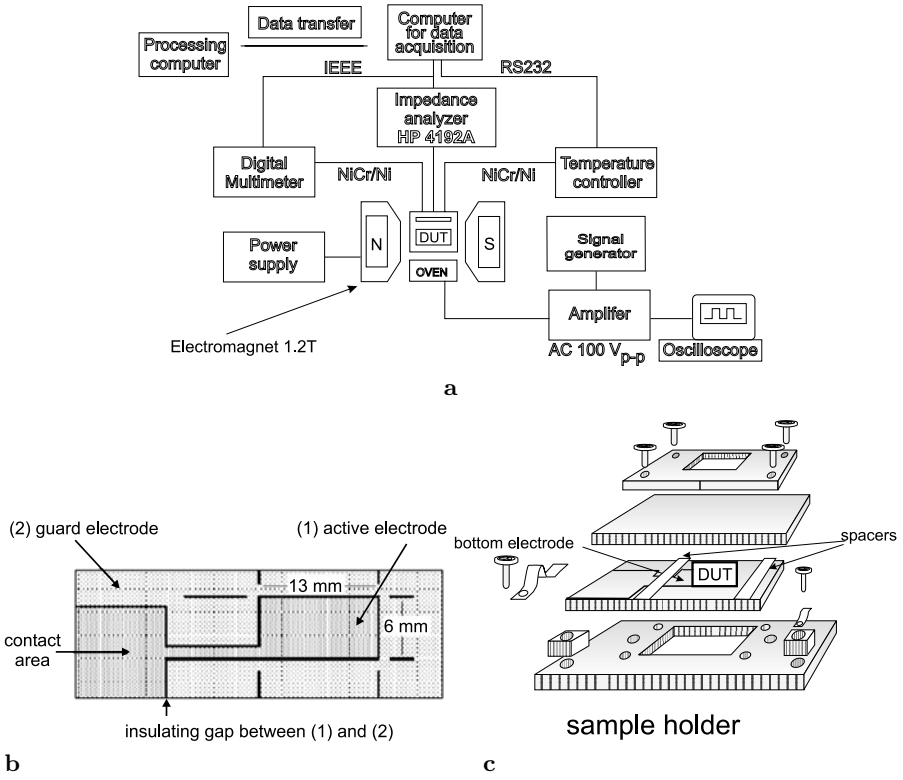

Fig. 1.4. (a) Schematic block diagram of the dielectric spectrometer for intermediate frequency range, **(b)** Schematic drawing of gold-coated electrode, **(c)** Scheme of the sample holder for gold electrodes

The capacity of the empty cell was strictly linear over the temperature range of our investigations (Fig. 1.5a). Firstly, the dielectric spectra are measured for the empty cell at a few temperatures in the temperature range in which the investigated compound is going to be studied.
The cells are then calibrated using a toluene reference (purified for spectroscopy) over the temperature range of 10 to 50 °C (Fig. 1.5b). The capacitors are filled with samples that have been heated into their isotropic phase under vacuum to expel entrapped gases and residual solvents.

For some samples, e.g. metallo-mesogenes, it is advisable to fill the capacitor under vacuum at temperatures slightly above the clearing temperatures by taking advantage of the gravity and capillary induced flow. One should add that vacuum also protects samples if one does dielectric studies in the low temperature range below room temperatures. Instead of vacuum protection one can apply inert gases like dry nitrogen or argon. The filling process is usually monitored by the HP 4192A self-balancing impedance analyzer operating at e.g. 100 kHz and is generally complete within a few minutes

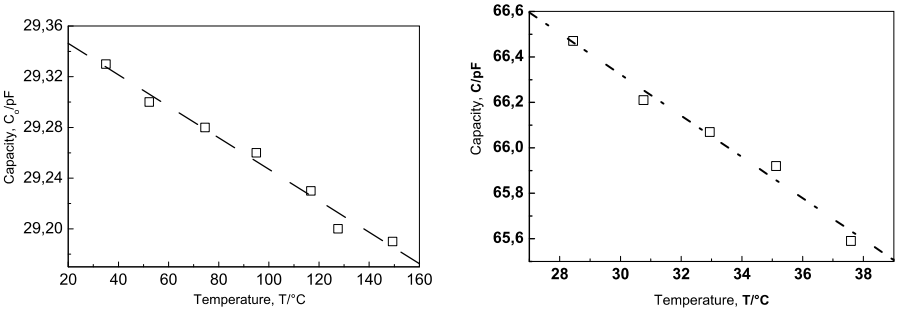

a **b**

Fig. 1.5. (a) Capacity of the empty cell vs. temperature, **(b)** capacity of the cell filled with toluene vs. temperature

time. The complete filling of the cells was indicated from a saturation of the dielectric permittivity. One can also monitor the filling process watching the cell under the polarizing microscope. In the case of gold electrodes one can watch the gap between guard electrode and the active one. Once filled the cells are being slowly cooled down under vacuum. The samples are investigated using FDDS from 10 mHz to 13 MHz, and in some cases to 1 GHz.

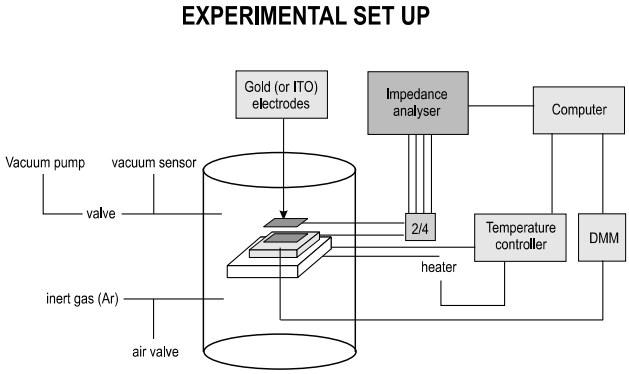

Fig. 1.6. Dielectric cell in vacuum (or inert gas) for dielectric investigations of vanadyl complexes

Vacuum controlled experiment

The dielectric spectra are measured over the frequency range from 10 Hz to 10 MHz with 15 to 40 experimental points per decade. A total number of 10 points per decade was used for the sub-hertz frequency range experiments. The reproducibility of all dielectric data is excellent when using vac-

uum (Fig. 1.6) to prevent, for instance, from oxidative degradation of the sample. In FDDS studies the stability of samples is very important as measurements of the dielectric spectra in a wide temperature range may last even a few days, especially, in the sub-hertz frequency range.

Time domain spectroscopy (TDS) was used in the Institute of Physics, Uppsala University, to study molecular relaxation processes [11, 48, 51], which show up between 10 MHz and 10 GHz. Right from the beginning the low-frequency dielectric relaxation process was studied more accurately as the low frequency bridges [28, 32, 45] allowed one to obtain many experimental points on the Cole–Cole plot or on dispersion and absorption curves. Nowadays lots of experimental results in the higher frequency ranges are available due to employing the apparatus mentioned above or some more sophisticated network analyzers. As an example the dielectric spectra obtained for trans,trans-4,4′-dipentyl-(1a,1′-bicyclohexyl)-4β-carbonitrile (CCN-55) [57, 58] by using a dielectric spectrometer based on the HP 4192A and HP 4191A bridges will be presented below.

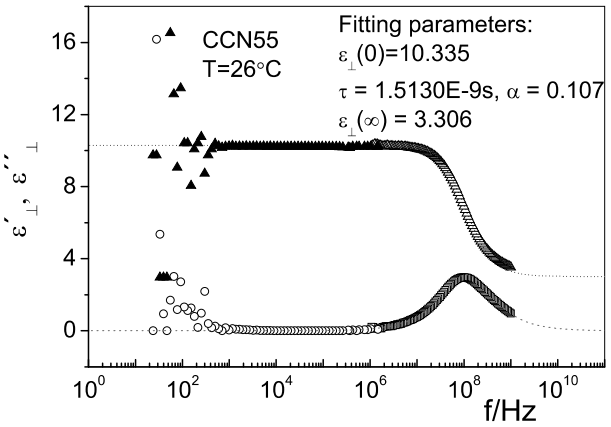

Fig. 1.7. Dielectric spectrum obtained in a wide frequency range for the nematic phase of CCN-55

Figure 1.7 clearly demonstrates the material exhibits a high value of the perpendicular component of the dielectric permittivity. There is very good evidence of the dielectric spectrum of Cole–Cole type for $\varepsilon^*_\perp(\omega)$, therefore the data were processed by fitting the Cole–Cole (1.7a) function. Practically only one process is dielectrically active namely the relaxation process connected with the reorientation of the strong CN-dipolar group, situated perpendicular

to the molecule's long axes, around the long axis (L-process). However, the value of the α parameter suggests that there are other relaxation processes involved. The second process may come from the librational motion of the molecule around its long axis which usually gives the so-called Poley absorption showing up at the border line between the microwave and far infrared frequency range.

1.1.5 A simple model of Maxwell–Wagner relaxation

Two layer dielectric

In many dielectric polar and non-polar materials one observes an enhanced dielectric absorption in the low frequency range. Usually this absorption is proportional to conductivity and inversely proportional to frequency:

$$\varepsilon_i''(\omega) = \frac{\sigma}{\varepsilon_o \omega} \,. \tag{1.21}$$

Such an equation is valid for thick layers of a dielectric material which is homogenous. For heterogeneous systems one observes additionally a low frequency dielectric relaxation process which overlaps the conductivity absorption given by (1.21). Below we shall give a simple model for Maxwell–Wagner relaxation showing up in the case of thin layers of dielectrics between electrodes covered with insulating polymer layer.

Recently some interesting dielectric results were obtained for FFP material (3-octyloxy-6-(2-fluoro-4-(2-fluoro-octyloxy)phenyl)-pyridin, see Tab. 1.1) at low frequencies by using a special cell with one electrode covered with a thick polymer layer [59]. Optically well aligned samples were prepared by coating the polymer on one of the electrodes and rubbing (Fig. 1.8).

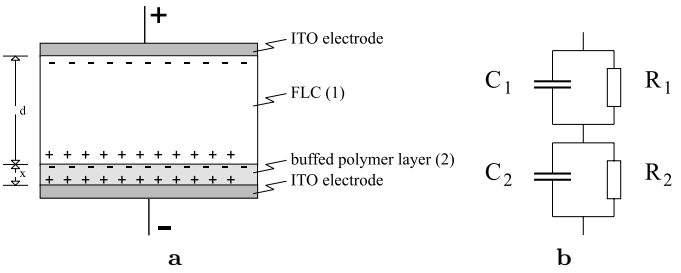

Fig. 1.8. (a) Model of the capacitor filled with two layers of dielectrics, **(b)** an electrical circuit substituting two-layer dielectric

Highly conducting indium tin oxide (ITO) with sheet resistance of 20Ω coated on optically flat glass substrates was used for electrodes which allows one to control the optical alignment of the liquid crystal molecules as well as to study

the dielectric relaxation processes in a wide frequency range. The measurement capacitor is filled with the FLC material which forms 2.5 μm–thick layer. One of its ITO electrodes (Fig. 1.8a) is covered with a buffed polymer layer the thickness of which is ca. 1000 Å. A charge accumulation effect was obtained by thick polymer coatings ($x = 0.1$ μm) with strong rubbing strength, which was done by keeping the minimum distance between the glass substrates and the rubbing block, wrapped up with a velvet cloth.

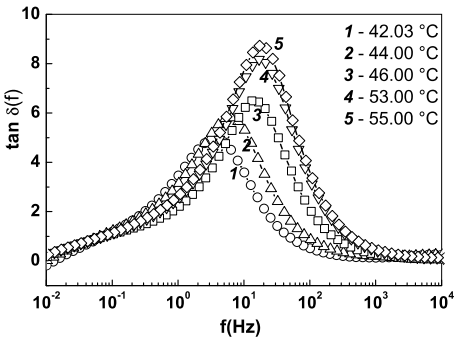

a

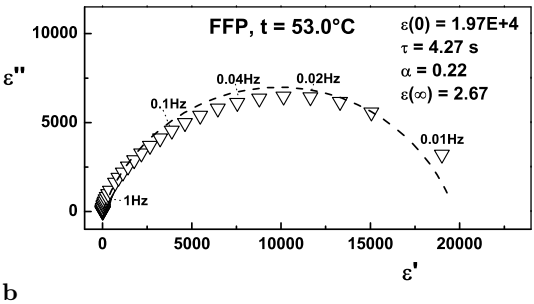

b

Fig. 1.9. (a) $\tan\delta(f)$ obtained for the ferroelectric phase of FFP, **(b)** Cole–Cole representation of the sub-hertz dielectric relaxation measured for FFP in the N* phase by Schlumberger Solartron 1250 FRA. Dashed line is a fit of the second term of (1.22) to the experimental points

The low frequency dielectric spectrum will be discussed in terms of the formula being a sum of the Debye and the Cole–Cole functions:

$$\varepsilon^*_\perp = \varepsilon'_\perp - i\varepsilon''_\perp = \varepsilon_{\perp\infty} + \frac{\Delta\varepsilon_{GM}}{1 + i\omega\,\tau_{GM}} + \frac{\Delta\varepsilon_{SH}}{1 + (i\omega\,\tau_o)^{1-\alpha}} - i\frac{\sigma_\perp}{\varepsilon_o\omega}\,, \qquad (1.22)$$

where $\Delta\varepsilon_{GM}$ is the GM contribution to the dielectric spectrum and $\Delta\varepsilon_{SH}$ is due to sub-hertz frequency relaxation.

How could we obtain a relaxation equation for a two-layer system? The two layer system can be treated as two parallel plate capacitors connected in

series (Fig. 1.8b). So, one can write the following equation for the effective capacitance:

$$C^{-1} = C_1^{-1} + C_2^{-1} \,, \tag{1.23}$$

where both capacities can be respectively expressed by:

$$C_1 = \varepsilon_0 \varepsilon_1^* \frac{S}{d_0 - x} \,, \tag{1.24a}$$

$$C_2 = \varepsilon_0 \varepsilon_2^* \frac{S}{x} \,, \tag{1.24b}$$

where ε_1* and ε_2* are the complex dielectric permittivities of the FLC material and buffed polymer layer, respectively. S denotes the surface of the ITO electrode, d_o – the distance between the ITO electrodes and x – the thickness of the polymer layer (Fig. 1.8a). Introducing (1.24a) and (1.24b) into (1.23) one obtains:

$$C = \varepsilon_0 C_o \frac{\varepsilon_1^* \varepsilon_2^* d_o}{x\varepsilon_1^* + (d_o - x)\varepsilon_2^*} \equiv \varepsilon_0 C_o \varepsilon^* \,, \tag{1.25}$$

where C_o is the capacity of the empty condenser and ε^* is the effective complex dielectric permittivity of the two-layer dielectric system. The complex dielectric permittivities of the FLC layer and buffed polymer layer at low sub-hertz frequencies can be written as:

$$\varepsilon_1^* = \varepsilon_1' - i\frac{\sigma_1}{\varepsilon_o \omega} \,, \tag{1.26a}$$

and

$$\varepsilon_2^* = \varepsilon_2' - i\frac{\sigma_2}{\varepsilon_o \omega} \,, \tag{1.26b}$$

respectively, where σ_1 and σ_2 are respective conductivities and ω is the angular frequency of the measuring electric field. By introducing (1.26a) and (1.26b) into (1.25) one arrives at:

$$\varepsilon^* = \frac{(\varepsilon_2' - i\frac{\sigma_2}{\varepsilon_o \omega})/\kappa}{1 + \frac{\varepsilon_1'\varepsilon_2' + \sigma_1\sigma_2/\varepsilon_o^2\omega^2}{\varepsilon_1'^2 + \sigma_1^2/\varepsilon_o^2\omega^2} + i\kappa^{-1}\frac{\sigma_1\varepsilon_2' - \sigma_2\varepsilon_1'}{(\varepsilon_1'^2 + \sigma_1^2/\varepsilon_o^2\omega^2)\omega}} \,, \tag{1.27}$$

where $\kappa = x/d$.

As seen it is a complex dielectric relaxation process. So, one should make additional assumptions to get a simpler final formula. Let us consider the following case: $\sigma_2 = 0$, $\varepsilon_1^2 \ll \sigma_1^2/\omega^2$, $\varepsilon_2^* = \varepsilon_2'$, $\varepsilon_1' = 0$, which means that FLC layer has much higher conductivity than the buffed polymer layer. For the system under discussion one obtains from (1.27) a simple Debye-type relaxation formula:

$$\varepsilon^* = \frac{\varepsilon_2^*/\kappa}{1 + (i\omega\tau_o)^{1-\alpha}} \equiv \frac{\Delta\varepsilon_{SH}}{1 + (i\omega\tau_o)^{1-\alpha}} \,, \tag{1.28a}$$

where

$$\tau_o = \varepsilon_2'/\kappa\sigma_1 \ , \tag{1.28b}$$

and α parameter is introduced here because heterogeneous dielectrics show always distribution of the relaxation time.

SHDR process

As is seen both the dielectric relaxation time and the dielectric increment depend not only on dielectric permittivities and conductivities but they are also functions of the parameter κ. The second term in (1.22) is just (1.28a) which is substantiated by the two-layer model presented. The α parameter has to be introduced because the sub-hertz dielectric relaxation (SHDR) spectrum appears to be a more complex process. One should add here one comment. In a few papers by Uehara, Hanakai, Hatano, Saito and Murashiro [53] there is a discussion about the low-frequency relaxation they observed and described by the following term:

$$\Delta\varepsilon^* \approx \frac{1}{(i\omega\tau_o)^{\gamma}} \ . \tag{1.29}$$

This equation can be easily obtained from (1.28a) by assuming $\omega\tau_o \gg 1$ and $\gamma \equiv 1 - \alpha$. It means that the low frequency dielectric absorption in the case of heterogeneous systems is affected by the dielectric relaxation process, the relaxation time of which depends not only on conductivity but also on the geometry of the sample.

The influence of thin layers on static dielectric permittivities was recognized in earlier dielectric experiments. In the case of FLCs it creates a low frequency process which could be sometimes assigned as a new ferroelectric mode. As was mentioned above this mode shows up even in the cholesteric and isotropic phases [59]. Its relaxation time must be connected with the mobility of ions which cause interfacial polarization. This effect is known in the literature as Maxwell–Wagner relaxation [13, 17] showing up in heterogeneous systems. One should add that whenever $\omega\tau_o \approx 1$ the second relaxation term in (1.22) overwhelms the dielectric spectrum due to the factor $d_o/x \approx 10\ \mu\text{m}/0.1\ \mu\text{m} = 100$.

The dielectric relaxation method clearly detects the charge accumulation. It is known that in surface stabilized ferroelectric liquid crystal (SSFLC) cells, the surface bistability is lost mostly due to the accumulation of free charges at the interface between the FLC medium and the insulating alignment layers, which depends on their nature and found to be very high in Nylon 6/6 polymer. It is also known that the use of high spontaneous polarization FLC materials improves the switching speed, but destroys the bistability due to charge accumulation.

It was found that the sub-hertz frequency dielectric relaxation process is bias field dependent showing that the charges accumulated between the

insulating alignment layer and the ferroelectric liquid crystal material can be annulled by the bias field [59].

1.1.6 Dielectric spectroscopy of ionic diffusion

Dielectric spectrometers operating in the sub-hertz frequency range allow one to study the dynamics of ions present in a dielectric material. Figure 1.10 shows the dielectric spectrum obtained for a liquid crystalline mixture doped with ions.

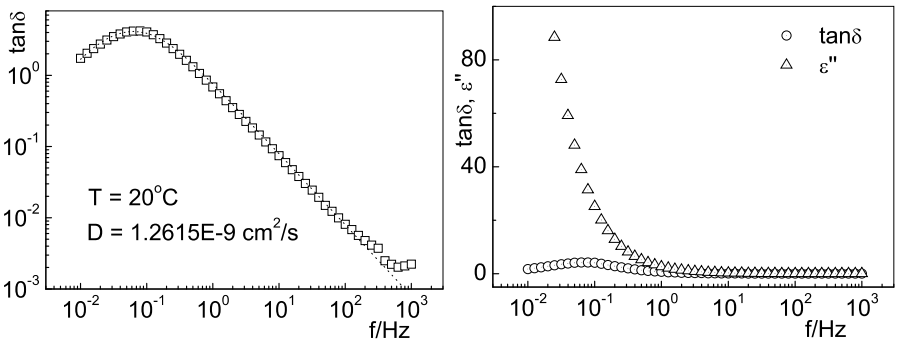

a **b**

Fig. 1.10. (a) $\tan\delta(f)$ dielectric spectrum acquired for the nematic phase doped with 1.000 ppm PCH-3N.O.F; **(b)** ε'' and $\tan\delta$ versus frequency

Sawada et al. [60, 61] have derived equations for real and imaginary parts of complex dielectric permittivity due to an ionic contribution. The theory developed by Sawada et al. give the following formulas for the real and imaginary parts of the complex dielectric permittivity:

$$\varepsilon'_I = -\left(\frac{4\pi q^2 D}{\omega k_B T R(\omega)}\right)\left\{\frac{1+2e^{R(\omega)}\sin R(\omega) - e^{2R(\omega)}}{1+2e^{R(\omega)}\cos R(\omega) + e^{2R(\omega)}}\right\}, \tag{1.30a}$$

$$\varepsilon''_I = \left(\frac{4\pi n q^2 D}{\omega k_B T}\right)\left\{1 + \frac{1-2e^{R(\omega)}\sin R(\omega) - e^{2R(\omega)}}{R(\omega)\left[1+2e^{R(\omega)}\cos R(\omega) + e^{2R(\omega)}\right]}\right\}, \tag{1.30b}$$

where n is the number of ions per unit volume, k_B – Boltzmann constant, T – absolute temperature, $R(\omega) = d\sqrt{\omega/2D}$ where in turn D is a diffusion coefficient and d is the thickness of the sample. These equations were obtained on the basis of a one-dimensional diffusion model of ions in a dielectric material.

The model predicts a low frequency (sub-hertz) dielectric relaxation process for dielectric materials with some ion concentration. Real dielectrics are not free from ions. So, such a relaxation process might be expected for all real dielectric materials. Another interesting result of the model under discussion is that both components of the dielectric permittivity are thickness

dependent. Figure 1.10 illustrates the experimental results obtained by Darius et al. [62, 63].

1.1.7 Summary

Summing up one should point out that dielectric spectroscopy has greatly been developed during the last three decades.

Frequency domain dielectric spectroscopy (FDDS) is often used to study dielectric properties of new materials for science and technology. Using FDDS one can evaluate on one hand the static dielectric permittivity ($\varepsilon(0)$), the high frequency limit of the dielectric permittivity ($\varepsilon(\infty)$) and such molecular parameters as: permanent dipole moment and polarizability – on the other hand, real dielectric spectroscopy consisting in measurements of the complex dielectric permittivity ($\varepsilon^* = \varepsilon' - i\varepsilon''$) in a wide frequency range, say from 1 mHz to 10 GHz. It allows one to study the diffusion coefficients of ions, present in real dielectric materials, collective and molecular dielectric relaxation processes. The former comes from components of polarization vectors whereas the latter results from molecular reorientation around different axes and/or from intra-molecular motion. All these processes lead to dielectric relaxation processes falling within the wide frequency range. Especially, new FLCs and AFLCs display a rich dielectric spectrum.

In dielectric spectroscopy studies one cannot cover the whole frequency range using one dielectric spectrometer. To cover the range mentioned at the beginning one should use several dielectric spectrometers in the frequency range up to ca. 1 GHz.

Above 3 GHz band one can use either TDS method (see Sect. 1.2 by B. Gestblom) or traditional standing wave method.

Each of these frequency ranges needs a separate apparatus, measurement cells and computer programs for data acquisition and processing. Each experimental technique has its own technology of cell preparation.

Acknowledgments

The author likes to thank Drs. F.-J. Bormuth, M. Pfeiffer, S. Hiller, D. Kilian, D. Ganzke, A.M. Biradar, Prof. W. Haase and Prof. S. Urban for their help and many fruitful discussions on dielectric spectroscopy. Drs. M. Marzec, M. Makrenek and A. Fąfara as well as undergraduate and graduate students are acknowledged for the help in data processing and preparation of some figures. I am also grateful to the DLR Büro in Bonn and KBN in Warsaw for financial support during my stay at the Darmstadt University of Technology in scope of the German-Polish Project (Pol-N-85-94).

References

1. W. Haase, H. Pranoto, F.-J. Bormuth: Ber. Bunsenges. Phys. Chem. **89**, 1229 (1985)
2. F.-J. Bormuth: Ph.D. Thesis, Technische Hochschule, Darmstadt 1988
3. C. Legrand: Ph.D. Thesis, Universite de Lille, Lille 1983
4. J.P. Parneix, C. Legrand: Ferroelectrics **88**, 199 (1998)
5. A.M. Biradar, S. Wróbel, W. Haase: Phys. Rev. A **39**, 2693 (1989) and references therein
6. F. Kremer, A. Schönfeld, A. Hofman, R. Zentel, H. Poths: Polym. Adv. Techn. **3**, 249 (1992)
7. M. Pfeiffer, G. Soto, S. Wróbel, W. Haase, R. Twieg, K. Betterton: Ferroelectrics **121**, 55 (1991)
8. F. Kremer, S.U. Vallerin, R. Zentel, Adv. Mater. **2**, 145 (1990)
9. M. Pfeiffer: Ph.D. Thesis, Technische Hochschule, Darmstadt 1993
10. H. Kresse, S. Tschierske, A. Hohmuth, C. Stützer, W. Weissflog: Liq. Cryst. **20**, 715 (1996)
11. B. Gestblom, S. Wróbel: Liq. Crystals **18**, 31 (1995) and references therein
12. J. Chruściel, S. Wróbel, B. Gestblom, W. Haase: "Molecular Dynamics and Phase Transitions Studied by Dielectric Methods". In: *Modern Topics in Liquid Crystals. From Neutron Scattering to Ferroelectricity.* Ed. by A. Buka (World Scientific, Singapore – New Jersey – London – Hong Kong 1993) pp. 31–54
13. C.F.J. Böttcher and P. Bordewijk: *Theory of Electric Polarization*, Vol.II: Dielectrics in time-dependent fields, Elsevier, Amsterdam – London – N.Y. 1973
14. H. Fröhlich: *Theory of Dielectrics*, Oxford University Press, London 1958
15. A.R. von Hippel: *Dielectric Materials and Applications*, Chapman and Hall, London 1954
16. C.P. Smyth: *Dielectric Behavior and Structure*, McGraw-Hill, N.Y. 1955
17. V.V. Daniel: *Dielectric Relaxation*, Academic Press, London and N.Y. 1967
18. N. Hill, W.E. Vaughan, A.H. Price and M. Davies: *Dielectric Properties and Molecular Behavior*, Van Nostrand, London 1969
19. A.K. Jonscher: *Dielectric Relaxation in Solids*, Chelsea Dielectric Press, London 1983
20. A.K. Jonscher: "Limitting Losses in Dielectrics". In: *IEEE Transactions on Dielectrics and Electrical Insulation. Recent Development in Dielectric and related Phenomena.* Eds. J. Ulański, L. Okrasa, R. Gerhard-Multhaupt, G. Bąk (IEEE Dielectrics and Electrical Insulation Society) Vol. **8**, No. 3, pp. 345–351 (2001)
21. A.R. von Hippel: *Dielectrics and Waves*, New York 1959
22. B.K.P. Scaife: *Principles of Dielectrics*, Clarendon Press, Oxford 1998
23. V.I. Gaiduk: *Principles of Relaxation Dynamics of Polar Molecules*, World Scientific, Singapore – New Jersey – London – Hong Kong 1999
24. V.I. Minkin, O.A. Osipov, Y.A. Zhdanov: *Dipole Moments in Organic Chemistry*, New York – London 1970
25. M. Davies: *Some Electrical and Optical Aspects of Molecular Behaviour*, Pergamon Press, Headigton Hill Hall, Oxford 1965
26. J.C. Anderson: *Dielectrics*, Chapman and Hall, London 1964
27. C.F.J. Böttcher, O.C. van Belle, P. Bordewijk, A. Rip: *Theory of Electric Polarization*, Vol. I. Dielectrics in Static Fields, Elsevier, Amsterdam – London – New York 1973

28. W. Maier, G. Meier: Z. Naturforsch. **16a**, 262 (1961)
29. G. Meier, A. Saupe: Mol. Cryst. Liq. Cryst. **1**, 515 (1966)
30. A. Axmann: Z. Naturforsch. **21a**, 615 (1966)
31. W.H. de Jeu, Th.W. Lathouwers: Z. Naturforsch. **29a**, 905 (1974)
32. H. Kresse: in Advances in Liquid Crystals, Ed.G.H. Brown, **6**, 109 (1983)
33. J. Jadżyn, Ch. Legrand, G. Czechowski, D. Bauman: Liq. Crystals **24**, 689 (1998)
34. K. Chłędowska, D. Chruściel, J.A. Janik, J.M. Janik, H. Stettin, K. Otnes, T. Stanek, S. Urban, S. Wróbel: Liq. Crystals **3**, 1339 (1988)
35. S. Urban and A. Würflinger: Adv. Chem. Phys. **98**, 143 (1997)
36. A. Würflinger: Int. Rev. Phys. Chem. **12**, 89 (1993)
37. A. Schönhals, F. Kremer: J. Non-Cryst. Solids **336**, 172 (1994)
38. Ch. Kittel: *Introduction to Solid State Physics*, John Wiley and Sons, Inc., New York 1998
39. N.W. Ashcroft, N.D. Mermin: *Solid State Physics*, Holt, Rinehardt and Winston 1976
40. H. Ibach, H. Lüth: *Solid-State Physics. An Introduction to Principles of Materials Science*, Springer-Verlag, Berlin-Heidlberg 1995
41. D. Kilian: Ph.D. Thesis, Darmstadt University of Technology, Darmstadt 1999
42. D. Kilian, D. Knawby, M.A. Athanassopoulou, S.T. Trzaska, T.M. Swager, S. Wróbel, W. Haase: Liq. Crystals **27**, 509 (2000)
43. W. Haase, D. Kilian, M.A. Athanassopoulou, D. Knawby, T.M. Swager, S. Wróbel: Liq. Crystals **29**, 133 (2002)
44. S. Wróbel, B.T. Gowda, W. Haase: J. Chem Phys. **106**(10), 5904 (1997)
45. V.K. Agarwal, A.H. Price: Mol. Cryst. Liq. Cryst. **98**, 193 (1983) and references therein
46. J. Hatano, Y. Hanakai, H. Furue, H. Uehara, S. Saito and K. Murashiro, Jpn. J. Appl. Phys. **33**, 5498 (1994)
47. S. Merino, M.R. de la Fuente, Y. González, M.A. Pérez Jubindo, M.B. Ros, J.A. Puértolas: Phys. Rev. E. **54**, 5169 (1996)
48. A. Fąfara, B. Gestblom, S. Wróbel, R. Dąbrowski, W. Drzewiński, D. Kilian, W. Haase: Ferroelectrics **212**, 79 (1998)
49. M. Marzec, R. Dąbrowski, A. Fąfara, W. Haase, S. Wróbel: Ferroelectrics **180**, 55 (1996)
50. M. Marzec: Ph.D. Thesis, Jagiellonian University, Kraków 1997
51. A. Fąfara: Ph.D. Thesis, Jagiellonian University, Kraków 2001
52. K.L. Ngai, E. Riande, G.B. Wright (eds.): Proceedings of the Second International Discussion Meeting on Relaxations in Complex Systems, Alicante, J. Non-Cryst. Solids 172–174 (1994)
53. H. Uehara, Y. Hanakai, J. Hatano, S. Saito, K. Murashiro: Jpn. J. Appl. Phys. **34**, 5424 (1995)
54. M. Buivydas, S.T. Lagerwall, F. Gouda, R. Dübal, A. Takeichi: Ferroelectrics **212**, 55 (1998).
55. F. Gouda: Ph.D. Thesis, Goeteborg 1997
56. H. Kresse, H. Schmalfuss, W. Weissflog, C. Tschierske, A. Hauser: Mol. Cryst. Liq. Cryst. **366**, 505 (2001)
57. D. Ganzke: Ph.D. Thesis, Darmstadt University of Technology, Darmstadt 2002
58. D. Ganzke, S. Wróbel, W. Haase: Mol. Cryst. Liq. Cryst., submitted

59. A.M. Biradar, D. Kilian, S. Wróbel, W. Haase: Liq. Cryst. **27**, 509 (2000)
60. A. Sawada, Y. Nakazono, K. Tarumi, S. Naemura: Mol. Cryst. Liq. Cryst. **318**, 225 (1998)
61. A. Sawada, K. Tarumi, S. Naemura: Jpn. J. Appl. Phys. **38**, 1418 (1999); *ibid.* 1423
62. M. Darius, T. Jacob, B. Rieger, W. Haase: 4th Workshop on Relaxation phenomena in Dielectric, Magnetic and Superconducting Materials, Zakopane 2000
63. M. Darius: Ph.D. Thesis, Darmstadt University of Technology, Darmstadt 2002

1.2 Dielectric time domain spectroscopy

B. Gestblom

1.2.1 Introduction

Transient methods have been used for a long time in the study of dielectric relaxation processes, when times of order milliseconds or longer are of interest [1]. The advent of time domain reflectometers opened the possibility to use time domain techniques also in the measurement of dielectric properties at high frequencies. A wide frequency range in the MHz and GHz region can then be covered in a single measurement. Several dielectric time domain spectroscopic (TDS) techniques have been developed since the pioneering work by Fellner-Feldegg [2]. Early reviews of different methods have been given by Suggett [3], van Gemert [4], Clarkson et al. [5] and Cole [6]. Later development, in particular of the method of total reflection against an open circuit, was summarised in a paper by Cole et al. in 1989 [7]. Recent instrumental development has been presented by Feldman et al. [8].

TDS is based on the study of the influence on the shape of a step pulse propagating in a coaxial line when it interacts with a dielectric sample. Either the shape of a pulse transmitted through a sample, or the shape of the pulse reflected from the sample, can be studied. If the incident pulse is called $v_0(t)$ and the transmitted(reflected) pulse $r(t)$ it is known from the theory of linear response that $r(t)$ is related to the $v_0(t)$ by the convolution equation

$$r(t) = \int_{-\infty}^{t} v_0(x)h(t-x)dx \; . \tag{1.31}$$

Here $h(t)$ is the response function in the time domain to a pulse excitation. A Fourier transformation of (1.31) into the frequency domain leads to

$$R(\omega) = H(\omega) \cdot V_0(\omega) \; , \tag{1.32}$$

where the Fourier transforms of the two pulses $r(t)$ and $v_0(t)$ are defined by

$$R(\omega) = \int_{-\infty}^{\infty} r(t)e^{-i\omega t}dt \quad \text{and} \quad V_0(\omega) = \int_{-\infty}^{\infty} v_0(t)e^{-i\omega t}dt \; . \tag{1.33}$$

The actual form of the transfer function $H(\omega)$ will depend on the experimental sample arrangement and can be obtained from transmission line theory; a few relevant examples will be given below. $H(\omega)$ will be a function of the complex dielectric permittivity $\varepsilon(\omega) = \varepsilon'(\omega) - i\varepsilon''(\omega)$ of the sample, and the solution of (1.32) will then in principle give the dielectric permittivity at any chosen frequency.

The principle of an experimental TDS set-up is given in Fig. 1.11. A pulse generator repetitively transmits a step pulse, which propagates along a low loss coaxial line. The pulse shape is monitored with a sampling oscilloscope, which will also store the pulse shape for further numerical processing by a PC. As indicated in the figure the dielectric sample is for transmission methods put in front of the oscilloscope sampling head, while for the reflection methods it will be put beyond the sampling head. The different methods have their advantages and disadvantages as will be discussed below.

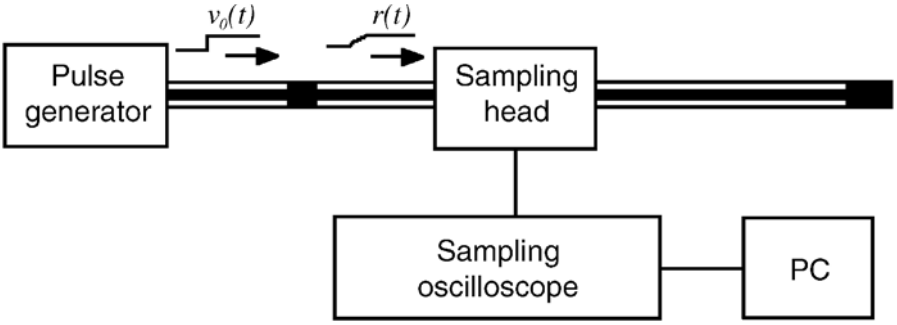

Fig. 1.11. Schematic drawing of the TDS set-up. Shadowed regions show the sample for transmission and reflection measurements respectively

1.2.2 Fourier transformation

The sampling oscilloscope will sample and store the pulse shapes at regular time intervals, the number of sampling points typically being $N = 2^{10}$. With a pulse shape $f(t)$ that is sampled at regular time intervals Δt the integral in (1.33) can be worked out by a discrete Fourier transform procedure,

$$F(\omega) = \Delta t \sum_{n=1}^{\infty} f(n\Delta t) e^{-i\omega n \Delta t} \,. \tag{1.34}$$

According to the Shannon sampling theorem the discrete transform in (1.34) gives the true transform of the function if the frequency is limited to $\omega < \pi/\Delta t$. In using the discrete transform to approximate (1.33) aliasing errors may be introduced if the sampling density is too low. Estimates of the necessary

sampling densities for typical TDS line shapes have been given [9] and it has been shown that the Samulon formula [10], (1.35), is accurate up to frequencies of the order of 10 GHz for sampling time intervals of 20 ps.

As seen in Fig. 1.11 the TDS pulse shapes are not generally time limited and a direct use of (1.34) will introduce serious truncation errors. In the Samulon modification of the discrete transform as given below (1.35), a differentiation of the pulse shape is performed [10]. This will remove truncation errors provided the pulse shape has reached a constant level within the time window used.

$$F(\omega) = \frac{\Delta t}{1 - e^{-i\omega\Delta t}} \sum_{n=1}^{\infty} \{f(n\Delta t) - f\left((n-1)\Delta t\right)\} \cdot e^{-i\omega n\Delta t} \,. \tag{1.35}$$

In dielectric spectroscopy a logarithmic frequency scale is frequently used in presentation of data. The fast Fourier algorithm, which calculates the transform at regularly spaced frequencies is then less suitable, and for TDS work the Samulon equation has been found convenient since frequencies can be chosen freely.

A crucial point in the evaluation of the Fourier transforms is the establishment of a common time origin for the two pulses. From (1.33) it is seen that a time shift of, for instance, $r(t)$ by δt will cause a phase shift in the transform according to

$$R'(\omega) = R(\omega)e^{-i\omega\delta t} \tag{1.36}$$

leading to a phase error $\Delta\phi = \omega\delta t$ in the calculation of the transfer function $H(\omega)$ from the experimental data.

Time base drifts between the recording of the two pulse shapes can therefore not be allowed. One way to solve the problem for a dual channel sampling oscilloscope with too large time base drift has been to use a power splitter after the pulse generator. A time reference pulse can then be monitored in one channel separately from the actual measuring pulse shapes in the other channel [11, 12]. The problem with the slow drift of the time base in the oscilloscope is then eliminated since the two channels are interlocked. Recent developments in sampling techniques have reduced the time base drift in oscilloscopes to such a level that the separate time reference channel can be discarded.

1.2.3 Single reflection

In the single reflection method the sample fills such a long section of a coaxial line that only the reflection from the front interface of the sample is recorded. Further reflections from the back interface are delayed to such an extent that they can be kept outside the time window used in recording the pulse shapes. The available time window will put a lower limit on the frequencies to be used

in the Fourier transforms, while the rise time of the step pulse and the high frequency limit of the sampling oscilloscope give an upper limit.

If the empty coaxial line has a characteristic impedance Z_0 the dielectric filled section will have the impedance $Z = Z_0/\sqrt{\varepsilon}$. The transfer function $H(\omega)$ will in this case be the reflection coefficient $\rho = R(\omega)/V_0(\omega)$ which is given by

$$\rho = \frac{Z - Z_0}{Z + Z_0} = \frac{\mathbf{1} - \sqrt{\varepsilon}}{\mathbf{1} + \sqrt{\varepsilon}} \,. \tag{1.37}$$

The dielectric spectrum can thus be directly obtained from the Fourier transformation of the pulse shapes and the calculation of the reflection coefficient ρ at the different frequencies. In practice the incoming pulse shape is not measured directly but rather by putting a short at exactly the same position as the air-dielectric interface, thus recording the reflected pulse $-v_0(t)$.

The single reflection method has the advantage of giving a reflection coefficient of magnitude $0.3 < |\rho| < 1$ over the whole frequency spectrum present in the incident pulse. It can thus be considered a true wide frequency method if sufficient accuracy in ρ can be achieved. The demand on the measurement accuracy in amplitude and phase of $\rho = |\rho|\, e^{i\phi}$ is best visualized by drawing equireflection lines in the $\varepsilon', \varepsilon''$ plane, Fig. 1.12. From this diagram a rough value of $\varepsilon = \varepsilon' - i\varepsilon''$ can be deduced from a given reflection coefficient. For a non-dispersive medium for which $\varepsilon'' = 0$, the reflection coefficient ρ is negative, giving a phase angle 180°. For a dispersive medium which can be described by a Cole–Cole plot in the diagram, it is seen that the additional phase change can hardly exceed 20°. The diagram also shows how a phase error in the reflection coefficient, due to a time origin error, will influence the

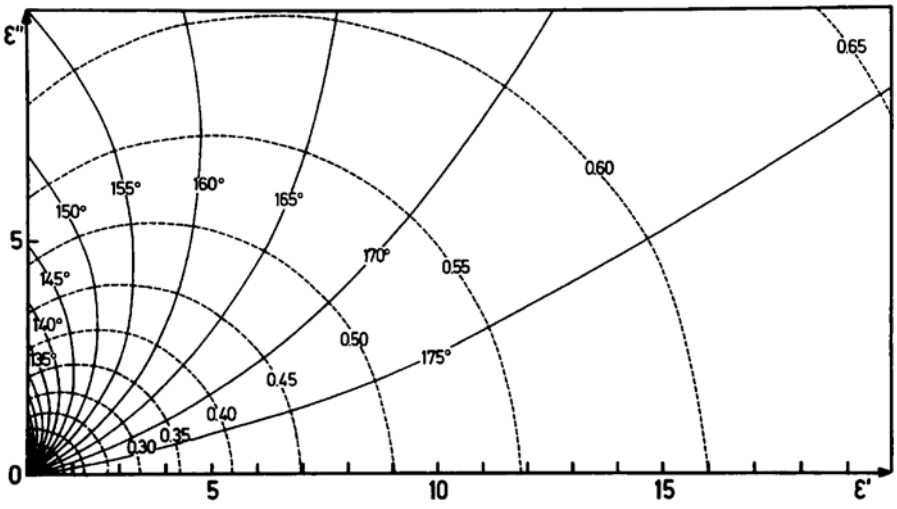

Fig. 1.12. Equireflection lines from the single reflection coefficient. The broken and full lines show constant amplitude and phase of ρ. Reproduced from [9]

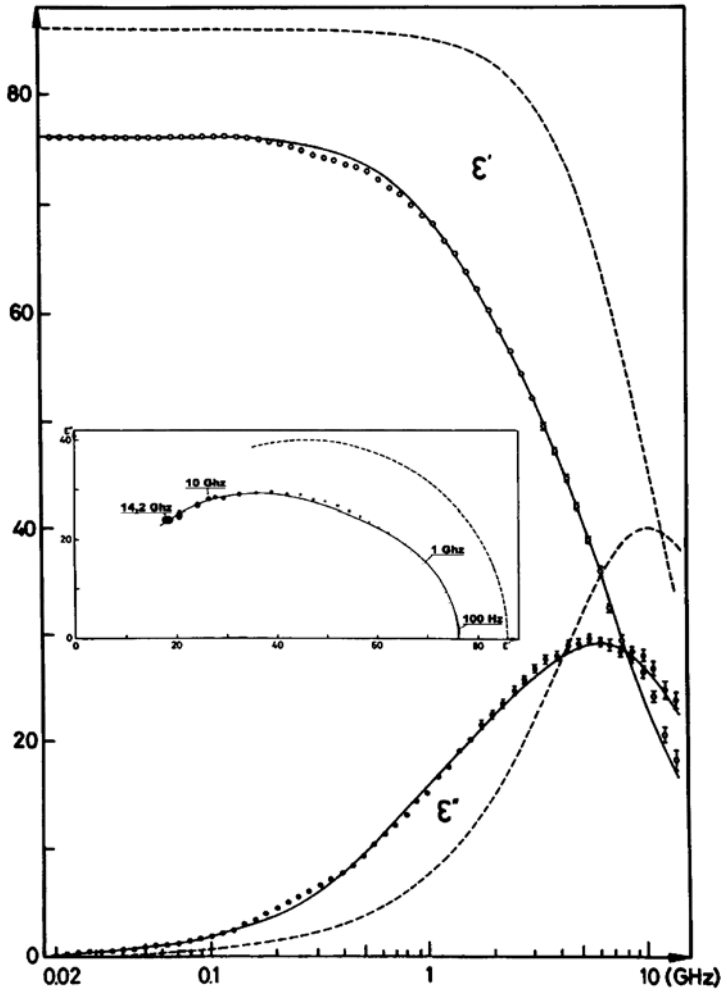

Fig. 1.13. Permittivity spectrum of an aqueous 2 M glucose solution at 5°C from single reflection measurements. The full lines give the fit to a two relaxation time Debye model function. The broken lines show the reference spectrum of pure water. Reproduced from [13]

calculated permittivity. Consider for instance the case that $\delta t = 1$ ps, which will at 10 GHz give a phase uncertainty $\Delta\phi = 3.6°$. As seen from the diagram this leads to large errors in the calculated permittivity, the problem becoming aggravated with increasing permittivity. Uncertainty in the amplitude of the reflection coefficient will similarly influence the calculated permittivity. This uncertainty can however be reduced by repeated scans of pulse shapes and signal averaging.

An application of the single reflection method also to a high permittivity system like an aqueous solution of glucose is illustrated in Fig. 1.13 [13]. In this case the reflected pulse from the solution was compared with that from pure water, for which the dielectric spectrum is well known.

Equations (1.32) and (1.37) then lead to

$$\frac{1-\sqrt{\varepsilon}}{1+\sqrt{\varepsilon}} = \frac{1-\sqrt{\varepsilon_W}}{1+\sqrt{\varepsilon_W}} \cdot \frac{R(\omega)}{R_W(\omega)} \,, \tag{1.38}$$

where ε_W is the permittivity of pure water and $R(\omega)$ and $R_W(\omega)$ are the transforms of the pulses reflected from the unknown and from pure water respectively.

Figure 1.13 shows that accurate permittivities are obtained over the whole frequency range up to 14 GHz. Judging from the data at 10 GHz the quoted error bars correspond to a phase uncertainty $\Delta\phi = 0.1°$, i.e. a time reference uncertainty as small as 0.03 ps. The full line shows the fit to a two relaxation time Debye model function

$$\varepsilon = \varepsilon_\infty + \frac{\varepsilon_1 - \varepsilon_\infty}{1+i\omega\tau_1} + \frac{\varepsilon_s - \varepsilon_1}{1+i\omega\tau_2} \tag{1.39}$$

with parameters ε_s=76.1, ε_1 = 54.9, ε_∞ =5.7 , τ_1 =21 ps and τ_2=98 ps. The interpretation would be to attribute τ_1 to bulk water while τ_2 is attributed to the relaxation in the modified water of the hydrated glucose complex.

1.2.4 The total transmission method

In this method the pulse transmitted through the sample carries the information about its dielectric properties. The general form of pulse shapes is given in Fig. 1.11. A sample cell suitable for liquids consists of a section of the coaxial line closed off by teflon beads [14]. These are dimensioned to give impedance match and a minimum of spurious reflections in the measuring cell. Holes are drilled in the line to allow the injection, removal and cleaning of the cell without disassembling. The cell length d is of order 1 cm, and so short that it allows the observation of all of the multiply transmitted pulse within the time window used.

The transfer function $H(\omega)$ in (1.32) is in this case given by

$$\frac{R(\omega)}{V_0(\omega)} = \frac{\left(1-\rho^2\right)\ e^{-\frac{i\omega d}{c}\sqrt{\varepsilon}}}{1-\rho^2 e^{-\frac{i2\omega d}{c}\sqrt{\varepsilon}}} \,. \tag{1.40}$$

Here d is the length of the cell, c is the speed of light in vacuum, while ρ is as above defined by $\rho = (1-\sqrt{\varepsilon})\,/\,(1+\sqrt{\varepsilon})$.

In a total transmission TDS experiment the pulse transmitted through the sample, $r(t)$, is not compared to the incoming pulse but rather to the pulse

transmitted through the same cell with air, $r_1(t)$. We then obtain as working equation for the total transmission coefficient

$$T(\omega) = \frac{R(\omega)}{R_1(\omega)} = \frac{\left(1-\rho^2\right)\ e^{-\frac{i\omega d}{c}\left(\sqrt{\varepsilon}-1\right)}}{1-\rho^2 e^{-i\,\frac{2\omega d}{c}\sqrt{\varepsilon}}}\ . \tag{1.41}$$

Equation (1.41) cannot be solved for ε in closed form but has to be solved numerically by an iterative numeric procedure, e.g. the Newton-Raphson iteration scheme. The implication of this transcendental equation in ε can be visualized by diagrams of equitransmission lines for different values of $\omega d/c$ [15]. Figure 1.14 shows such a diagram for the case $\omega d/c = 1$. The dominant term in the transmission coefficient is the exponential term $e^{-(i\omega d/c)\left(\sqrt{\varepsilon}-1\right)}$. Large phase shifts are introduced, and the permittivity calculated from a given transmission coefficient is less susceptible to phase errors compared the case of the single reflection method. E.g. a time reference uncertainty of 1 ps will at 1 GHz lead to a transmission coefficient uncertainty of 0.36°. With a cell length of 5 cm, $\omega d/c = 1$ and we can see from Fig. 1.14 that such a phase uncertainty will lead to an uncertainty $\Delta\varepsilon' \approx 0.04$, while ε'' is hardly affected.

An error source in total transmission TDS is the occurrence of an extra rereflected pulse due to a slight impedance mismatch between the coaxial line and the oscilloscope sampling head. Preferably this spurious pulse should be kept outside the observation time window by a proper choice of coaxial line lengths. The influence of these extra reflections can also be reduced by using as reference the pulse $r_r(t)$ transmitted through a cell filled with known

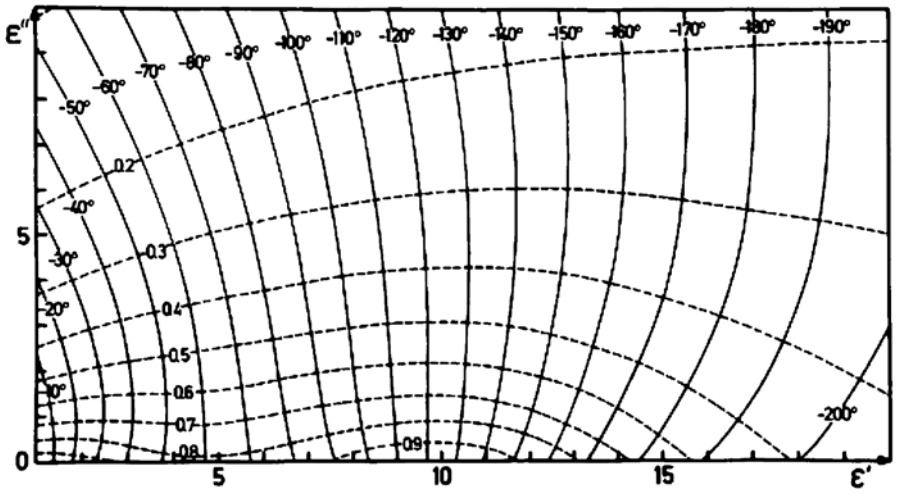

Fig. 1.14. Equitransmission lines from the total transmission coefficient T for $\omega d/c = 1$. The broken and full lines show constant amplitude and phase of T. Reproduced from [15]

dielectric properties not too different from those of the sample under study. The permittivity is then calculated by solving the equation

$$\frac{R(\omega)}{R_r(\omega)} = \frac{T(\omega)}{T_r(\omega)} \,. \tag{1.42}$$

$T(\omega)$ for the unknown is defined by (1.41) and $T_r(\omega)$ is calculated from the same equation from the known permittivity spectrum $\varepsilon_r(\omega)$ of the reference liquid. This procedure is suitable e.g. in the study of solutions, where the natural reference liquid then is the pure solvent.

As an example of measurement with the total transmission method, Fig. 1.15 shows the permittivity spectrum of pure octanol and a solution of octanol containing 1 % (w/w) water. The cell length in this measurement was 40 mm and the observation time window 20 ns. As seen from the figure the small amount of water has a strong effect on the alcohol spectrum, with a lowering of the static permittivity together with a shortening of the main relaxation time [16]. Other alcohol-water systems have been studied with TDS and the structural implications from the studies discussed in several papers [17–21].

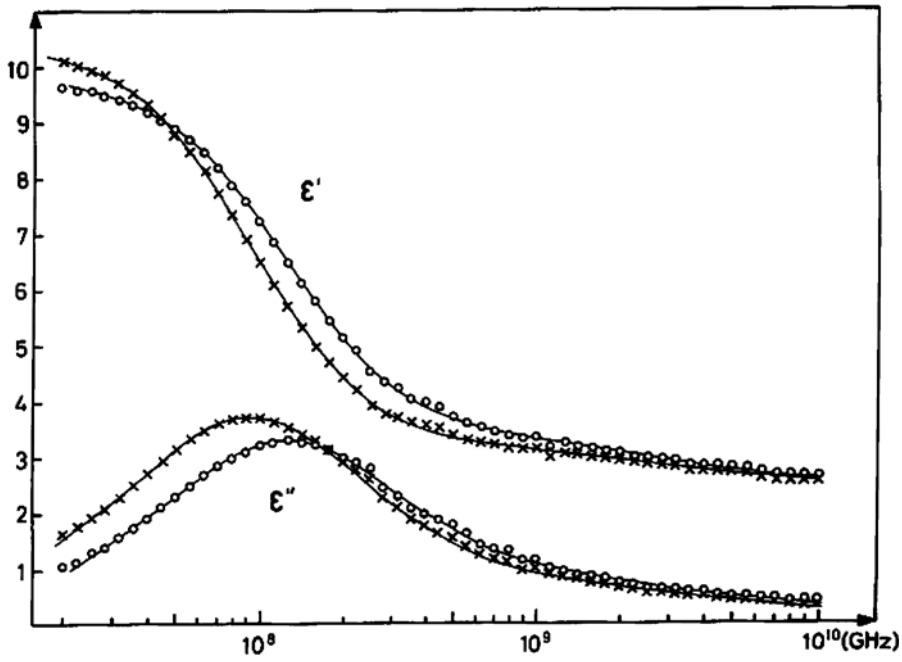

Fig. 1.15. The permittivity spectra of pure octanol(x) and octanol containing 1%(w/w) water(o). The full lines show the fit to a two relaxation time Debye model function. Reproduced from [16]

In dielectrics showing dc conductivity σ, the measured total permittivity is given by

$$\varepsilon_t(\omega) = \varepsilon - i\sigma/\omega\varepsilon_0 \ , \tag{1.43}$$

where $\varepsilon_0 = 8.854 \times 10^{-12}$ F/m is the empty space permittivity constant. To obtain the dipolar part $\varepsilon(\omega)$ of the total permittivity spectrum $\varepsilon_t(\omega)$, it should therefore be corrected for the conductivity contribution.

In applying the total transmission method to a conducting sample the pulse transmitted through the sample will not reach the final level of the incident step pulse. Instead its final level will show an offset which can be used to directly obtain the conductivity σ.
The asymptotic value of the time domain transmission coefficient is given by

$$t_\infty = \lim_{t\to\infty} \frac{r(t)}{r_1(t)} = \lim_{\omega\to 0} \ T(\omega) \ . \tag{1.44}$$

Inserting (1.43) into (1.41) and letting $\omega\to 0$ one obtains

$$t_\infty = \frac{1}{1 + \frac{\sigma d}{2\varepsilon_0 c}} \tag{1.45}$$

The time domain data will thus immediately give the dc conductivity σ.

As an example of the application of the total transmission method to the study of an electrolyte is shown the spectrum of a solution of Bu_4NClO_4 in dichloromethane, Fig. 1.16. The cell length was 20 mm and the time window 20 ns. A dispersion is observed around 1 GHz and the corresponding absorption maximum in ε'' is clearly brought out after correction for the conductivity

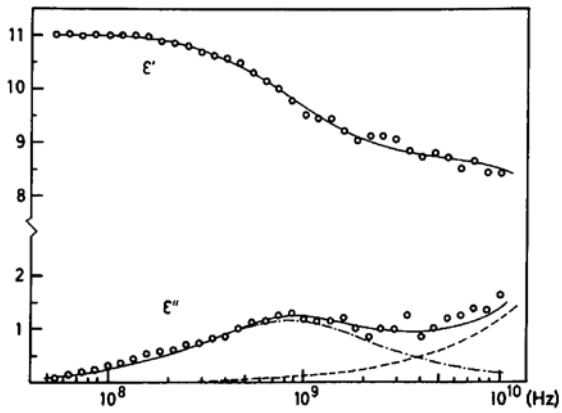

Fig. 1.16. Permittivity spectrum of a 0.0395 M solution of Bu_4NClO_4 in dichloromethane. The conductivity contribution has been subtracted. The full line shows the fit to a two relaxation time Debye model function. Reproduced from [22]

term. This dispersion is attributed to the presence of ion pairs in the solution. The full line gives a fit to the two relaxation time model function (1.39), while the broken lines show the decomposition of ε'' into the two relaxation processes. The tail of the high frequency dispersion is ascribed to the solvent relaxation with a relaxation time $\tau_2 = 2$ ps while the ion pair relaxation time $\tau_1 = 0.19$ ns. A discussion of the dielectric TDS data of this and other salts in dichloromethane has been given in relation to conductivity studies of the same electrolytes [22].

1.2.5 The open circuit total reflection method

In the single reflection method discussed above the sample length has to be long to ensure that no reflections from the rear interface of the dielectric are included in the observed reflected pulse shape. In the total reflection methods the sample length is shortened to allow the observation of the complete reflected pulse shape, including all rereflections within the sample. Of the different ways of terminating the line, we shall here only consider the case where the sample is put at the end of an open coaxial line as illustrated in Fig. 1.17. The general shape of the reflected pulse $r(t)$ for an input step pulse is illustrated in the figure, as well as a schematic sample cell. The cell is readily realized from standard coaxial components [7, 23]. This open-ended cell requires only a small amount of substance compared with the single reflection scheme and is easy to fill, empty and clean.

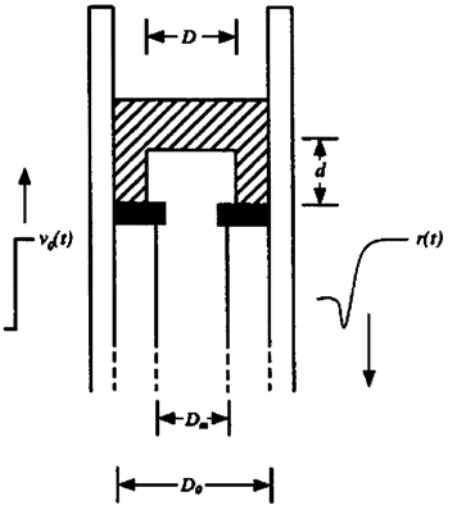

Fig. 1.17. Schematic drawing of a sample cell for reflection measurements. Stripes indicate the dielectric sample. Bottom section is a 50 Ω precision coaxial line

The transfer function $H(\omega)$ is in this case the reflection coefficient

$$S_{11}(\omega) = \frac{R(\omega)}{V_0(\omega)} = \frac{\rho + e^{-\frac{i2\omega d}{c}\sqrt{\varepsilon}}}{1 + \rho e^{-\frac{i2\omega d}{c}\sqrt{\varepsilon}}} \,. \tag{1.46}$$

The cell length d in this equation is slightly larger than the physical length of the centre pin, due to fringing field effects. If the centre pin has a diameter different from that of the centre conductor of an impedance matched line, ρ is in this case given by

$$\rho = \frac{1 - \gamma\sqrt{\varepsilon}}{1 + \gamma\sqrt{\varepsilon}} \,. \tag{1.47}$$

The factor γ is determined by the characteristic impedance ratio Z_0/Z_0' of the matched coaxial line with inner and outer diameters D_m and D_o to that of a line with the centre pin diameter D, $\gamma = \ln(D_o/D_m)/\ln(D_o/D)$.

If the pulse $r(t)$ reflected from the cell filled with a dielectric is not compared to the incoming pulse $v_0(t)$ but rather to the pulse $r_1(t)$ reflected from the empty cell we obtain a reflection coefficient

$$S = R(\omega)/R_1(\omega) = \frac{\rho + e^{-\frac{i2\omega d\sqrt{\varepsilon}}{c}}}{1 + \rho e^{-\frac{i2\omega d}{c}\sqrt{\varepsilon}}} \cdot \frac{\left(1 + \gamma + (1-\gamma)e^{-i\,\frac{2\omega d}{c}}\right)}{\left(1 - \gamma + (1+\gamma)e^{-i\,\frac{2\omega d}{c}}\right)} \,. \tag{1.48}$$

Again the reflection coefficient S is a transcendental equation in ε which can be solved numerically, e.g. by the Newton-Raphson procedure. The implications of (1.48) can be visualized by plotting equireflection lines. This is illustrated in Fig. 1.18 which shows the loci of constant phase and amplitude for S in the ε', ε'' plane for the case $\gamma = 1$ and $\omega d/c = 0.5$.

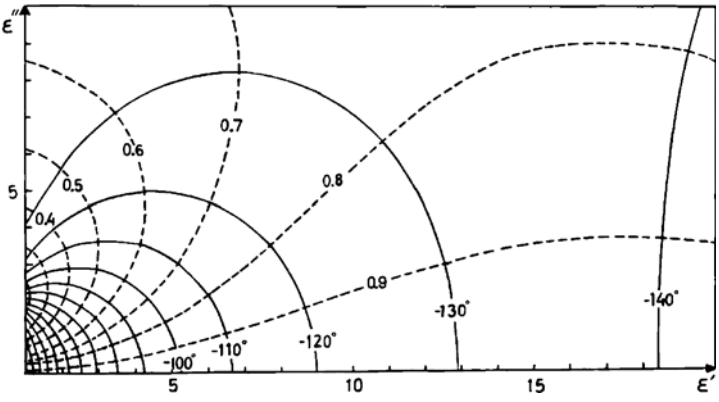

Fig. 1.18. Equireflection lines from the total reflection coefficient S for $\omega d/c = 0.5$. The broken and full lines show constant amplitude and phase of S

As seen from this diagram the solution of (1.48) becomes very sensitive to errors in the experimental values of the reflection coefficient S when $|\omega d\sqrt{\varepsilon}/c|$ approaches $\pi/2$, i.e. the quarter wavelength condition. The sample length should therefore be chosen short enough to ensure that $|\omega d\sqrt{\varepsilon}/c| < 1$ within the frequency range of interest.

Influence of imperfections in the line can be reduced by comparing the pulse reflected from the unknown $r(t)$ to that reflected from a reference sample with known dielectric properties $r_r(t)$. The unknown permittivity spectrum $\varepsilon(\omega)$ is then obtained by solving the equation

$$R(\omega)/R_r(\omega) = S(\varepsilon)/S(\varepsilon_r) \,, \tag{1.49}$$

where $S(\varepsilon_r)$ is calculated from (1.48) from the known dielectric spectrum $\varepsilon_r(\omega)$ of the reference liquid.

In the case of a sample showing dc conductivity σ the reflected pulse will not reach the final level of the incoming pulse. If a sufficiently long time window is used to allow the complete decay of all dielectric processes, the conductivity can also in this case be obtained directly from the time domain data. The asymptotic value of the ratio of time domain reflection data is related to the frequency domain reflection coefficient by

$$s_\infty = \lim_{t\to\infty} \frac{r(t)}{r_1(t)} = \lim_{\omega\to 0} S(\omega) \,. \tag{1.50}$$

Insertion of (1.48) and letting $\omega\to 0$ leads to

$$s_\infty = \frac{1 - \frac{\sigma\gamma d}{\varepsilon_0 c}}{1 + \frac{\sigma\gamma d}{\varepsilon_0 c}} \,. \tag{1.51}$$

An offset of the final pulse level is therefore a direct indication of dc conductivity in the sample, the offset also directly giving the conductivity.

1.2.6 Admittance analysis and bilinear calibration

R.H. Cole [7] has given an admittance analysis of the method of reflection against an open-ended cell, which also incorporates a calibration scheme that will take care of imperfections in coaxial lines and connectors. The input admittance Y of a termination of the coaxial line is given by

$$\frac{Y}{G} = \frac{V_0(\omega) - R(\omega)}{V_0(\omega) + R(\omega)} \,, \tag{1.52}$$

where $V_0(\omega)$ and $R(\omega)$ are the input and reflected voltages respectively and G is the characteristic admittance of the line. As discussed above $V_0(\omega)$ is generally not recorded in a TDS measurement, but rather the reflection from a suitable reference or empty cell. The difference in admittance between an unknown Y_x and a reference Y_r can then be written

$$\frac{Y_x}{G} - \frac{Y_r}{G} = \frac{1 - \left(\frac{Y_r}{G}\right)^2 \delta'}{1 + \frac{Y_r}{G}\delta'} \,, \tag{1.53}$$

where

$$\delta' = \frac{R_r(\omega) - R_x(\omega)}{R_r(\omega) + R_x(\omega)} \,. \tag{1.54}$$

$R_r(\omega)$ and $R_x(\omega)$ are the reflected voltages from the reference and unknown sample respectively.

For any passive network the admittance at one point can be written as a bilinear form of the admittance measured at another point. This is also true for a coaxial line system as in Fig. 1.11 where the actual recording of voltages is done at the sampling head and not at the line termination. This leads to the consequence that

$$Y_x - Y_r = \frac{a'\delta' + c'}{1 - b'\delta'} \,, \tag{1.55}$$

where the reflected voltages can be measured at any point in the coaxial line system. The parameters a', b' and c' can be determined by calibration with known standards.

For an open-ended cell filled with a dielectric of permittivity ε insertion of the reflection coefficient $S_{11} = R(\omega)/V_0(\omega)$ according to (1.46) gives for the admittance

$$\frac{Y}{G} = \frac{1 - S_{11}}{1 + S_{11}} = \frac{i\omega\gamma d}{c} \frac{\varepsilon}{z \cot\, z} \,, \tag{1.56}$$

where $z = \frac{\omega\, d}{c}\sqrt{\varepsilon}$.

For sample lengths such that $|z| < 1$ a series expansion can be made giving

$$z \cot\, z = 1 - \frac{1}{3}z^2 - \frac{1}{45}z^4 \,. \tag{1.57}$$

If we keep only the first term in this series expansion, i.e. for low frequencies, (1.41) and (1.56) give for the permittivity the simple expression

$$\varepsilon = \frac{c}{i\omega\gamma d} \frac{V_0(\omega) - R(\omega)}{V_0(\omega) + R(\omega)} \,, \tag{1.58}$$

which can be used as basis to evaluate the spectrum [24].

An improvement on this expression is obtained if further terms are kept in the series expansion. Keeping terms up to ω^4 the admittance is

$$\frac{Y}{G} = \frac{i\omega\gamma d}{c} \frac{\varepsilon}{1 - \frac{1}{3}\left(\frac{\omega d}{c}\right)^2 \varepsilon} \,, \tag{1.59}$$

i.e. ε can be written as a bilinear form (BLF) in Y. This implies that the difference between the permittivity of an unknown ε_x and that of a reference sam-

ple ε_r can be written as a new bilinear form in $Y_x - Y_r$, i.e. $\varepsilon_x - \varepsilon_r = \mathrm{BLF}(Y_x - Y_r)$ which according to (1.55) is a bilinear form in δ'. The permittivity of the unknown can consequently be obtained from

$$\varepsilon_x - \varepsilon_r = \frac{a''\,\delta' + c''}{1 - b''\,\delta'} \,, \tag{1.60}$$

where δ' is given by (1.54). The coefficients a'', b'' and c'' can be determined by standard samples with known permittivities.

If $R_r(\omega)$ is the reflected signal from an empty cell, $\varepsilon_r = 1$ and $c'' = 0$, leading as a working equation to the following simple bilinear form for the permittivity of the unknown

$$\varepsilon_x = \frac{1 + (1 + A)\delta}{1 - B\delta} \,. \tag{1.61}$$

Here

$$\delta = \frac{c}{i\omega\gamma d} \, \frac{(R_1(\omega) - R_x(\omega))}{(R_1(\omega) + R_x(\omega))} \,, \tag{1.62}$$

i.e. the term $i\omega\gamma d/c$ has been incorporated in the definition of δ as suggested by the simple first order expression (1.58).

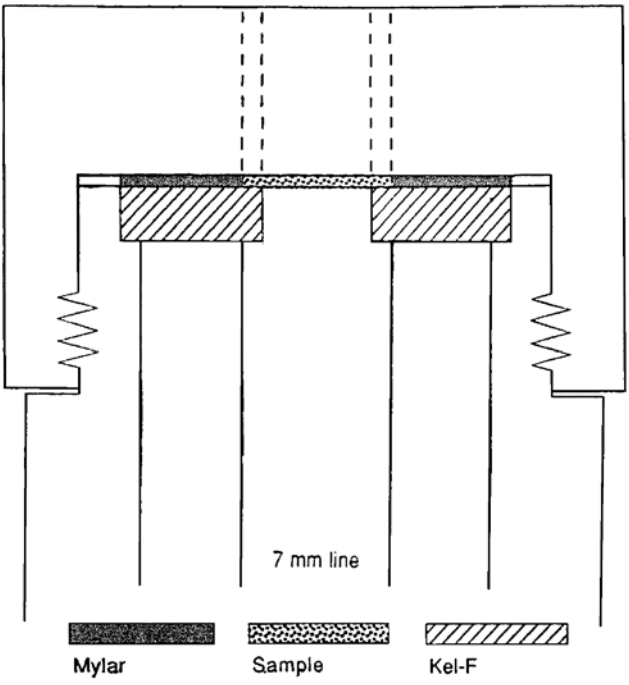

Fig. 1.19. A 7-mm line thin end capacitance cell

With δ as defined in (1.62) the calibration parameters A and B will be small in the limit of low frequencies. The cell constant γd can be determined by a standard liquid with known static permittivity. The calibration parameters A and B are complex and depend on frequency, $A(\omega) = A'(\omega) + iA''(\omega)$ and $B(\omega) = B'(\omega) + iB''(\omega)$. They can be determined by the use of two standard substances with known permittivity spectra, and a solution of the equation system for A and B implied by (1.61). In the choice of reference liquids it is preferable to choose two substances with lower and higher permittivity respectively, compared to that of the unknown. A number of suitable reference liquids, which span a large permittivity range have been given by Cole et al. [7].

Compared to the use of (1.48), the bilinear procedure leading to (1.61) has the advantage that once the calibration parameters are determined, the permittivity is directly obtainable from the transforms of the signals reflected from the empty and filled cell respectively. The calibration scheme will also in principle remove errors from imperfections in line and cell. As implied by (1.60) the bilinear calibration scheme can be used also with the reflected signal from a sample with known dielectric spectrum $\varepsilon_r(\omega)$ as reference.

A cell design found useful for applications in the study of liquid crystals is shown in Fig. 1.19 [25]. The dielectric is here injected into a thin end capac-

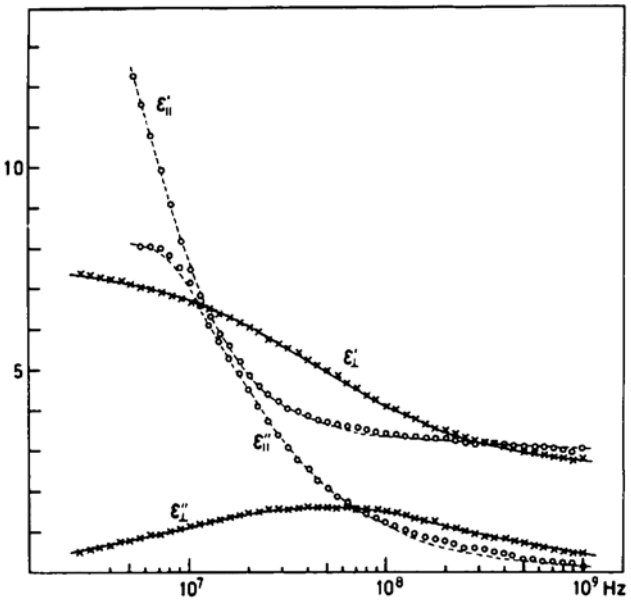

Fig. 1.20. The permittivity spectra of 4-*n*-pentyl-4′-cyanobiphenyl at 30 °C obtained for both principal directions of the oriented nematic phase. Reproduced from [25]

itance cell, which terminates a 7-mm coaxial line. A thin spacer determines the thickness of the cell. The bilinear analysis is valid and (1.61) can be used to determine the permittivity spectrum. The thin cell will give the same signal response as a coaxial cell with length of order 1 cm, but with a small fraction of substance needed to fill the cell. For liquid crystals it is valuable to study the permittivity spectra in the presence of orienting external electric or magnetic fields in order to obtain tensorial properties. The thin cell makes it possible to apply a strong orienting electric field, with a voltage sufficiently low not to ruin the sampling heads of the oscilloscope which register the pulse shapes. The end capacitor cell also allows the application of an orienting magnetic field both perpendicular and in parallel to the measuring electric field. As an example is given in Fig. 1.20 the permittivity spectrum of 4-*n*-pentyl-4′-cyanobiphenyl in the nematic phase at 30 °C with orienting electric and magnetic fields. The sample thickness was 50 μm, corresponding to a coaxial cell length of 1 cm. The relaxation times from a fit to a Cole–Cole model function are 3.5 ns and 30 ns for the two orientations respectively.

1.2.7 Conclusion

The time domain methods offer the opportunity to measure dielectric properties over a wide frequency range with a single measurement. The computational work involved in the transformation from time domain to the frequency domain is no longer an obstacle, the necessary numerical work handled by a PC in a few seconds. The accuracy obtained is comparable to that obtained with frequency domain methods.

Besides the TDS methods described here, other sample cell arrangements have been tried as can be found in the reviews [2–8], in particular should be mentioned the method of total reflection against a sample terminated by a matched line [26, 27]. In the use of TDS to the study of liquid systems the total transmission and total reflection methods seem to be the most generally applicable. The bilinear calibration method of Cole [7] will remove the influence of coaxial line imperfections, and also has the advantage of giving the permittivity directly without the need for solving a transcendental equation in ε. A few illustrative examples of the different methods have been given above, a large number of other applications of TDS can be found in a review by Feldman et al. [28].

References

1. N. Hill, W.E. Vaughan, A.H. Price, M. Davies: *Dielectric properties and molecular behaviour*, Van Nostrand, New York (1969)
2. H. Fellner-Feldegg: J. Phys. Chem. **61**, 616 (1969)
3. A. Suggett: In: *Dielectric and Related Molecular Processes* Vol. 1, editor M. Davies, Chemical Society London (1972), p. 100

4. M.J.C. van Gemert: Philips. Res. Rep. **28**, 530 (1973)
5. T.S. Clarkson, L. Glasser, R.W. Tuxworth, G. Williams: Adv. Mol. Relaxation Processes, **10**, 173 (1977)
6. R.H. Cole: Ann. Rev. Phys. Chem. **28**, 283 (1977)
7. R.H. Cole, J.G. Berberian, S. Mashimo, G. Chryssikos, A. Burns, E. Tombari: J. Appl. Phys. **77**, 793 (1989)
8. Y. Feldman, A. Andrianov, E. Polygalov, I. Ermolina, G. Romanychev, Y. Zuev, B. Milgotin: Rev. Sci. Instrum. **67**, 3208 (1996)
9. B. Gestblom, E. Noreland: J. Phys. Chem. **80**, 1631 (1976)
10. H.A. Samulon: Proc. IRE **39**, 175 (1951)
11. B. Gestblom, B. Jonsson: J. Phys. E: Sci. Instrum. **13**, 1067 (1980)
12. R.H. Cole, S. Mashimo, P. Winsor: J. Phys. Chem. **84**, 786 (1980)
13. B. Gestblom, E. Noreland: J. Phys. Chem. **88**, 664 (1984)
14. B. Gestblom, H. Elmgren: Chem. Phys. Letters **90**, 412 (1982)
15. B. Gestblom, E. Noreland: J. Phys. Chem **81**, 782 (1977)
16. B. Gestblom, J. Sjöblom: Acta. Chem. Scand. **A38**, 47 (1984)
17. J.P. Perl, D.T. Wasan, P. Winsor, R.H. Cole: J. Mol. Liquids **28**, 103 (1984)
18. S. Mashimo, S. Kuwabara, S. Yagihara, K. Higasi: J. Chem. Phys. **90**, 3292 (1989)
19. S. Mashimo, T. Umehara, H. Redlin: J. Chem. Phys. **95**, 6257 (1991)
20. B. Gestblom, J. Sjöblom: Acta. Chem. Scand. **A38**, 575 (1984)
21. D. Bertolini, M. Cassettari, G. Salvetti, E. Tombari, S. Veronesi: J. Non-Cryst. Solids **131-133**, 1169 (1991)
22. B. Gestblom, J. Songstad: Acta. Chem. Scand. **B41**, 396 (1987)
23. N. Shinyashiki, N. Asaka, S. Mashimo, S. Yagihara, N. Sasaki: Biopolymers **29**, 1185 (1990)
24. S. Mashimo, T. Umehara, T. Ota, S. Kuwabara, N. Shinyashaki, S. Yagihara: J. Mol. Liquids **36**, 135 (1987)
25. B. Gestblom, S. Wróbel: Liq. Cryst. **18**, 31 (1995)
26. A.W.J. Dawkins, R.J. Sheppard, E.H. Grant: J. Phys. E: Sci. Instrum. **12**, 1091 (1979)
27. R. Chahine, T.H. Bose: J. Chem. Phys. **72**, 808 (1980)
28. Y. Feldman, Y. Zuev, E.A. Polygalov, V.D. Fedotov: Colloid. Polym. Sci. **270**, 768 (1992)

1.3 Nonlinear dielectric spectroscopy

J. Jadżyn, P. Kędziora, and L. Hellemans

1.3.1 Introduction

When dipolar molecules are brought in an electric field, they experience a torque which tends to align them with the field direction. This orienting action is competing with the randomizing effect of molecular collisions, inferring a weight factor in Boltzmann's law for the angular distribution of the type $\exp(\boldsymbol{\mu} \cdot \mathbf{E}/k_B T)$. In the exponent appears the ratio of two energies: first, the energy $-\mu E \cos\theta$ acquired by a polar molecule with dipole moment $\boldsymbol{\mu}$

oriented at an angle θ with respect to the field $\mathbf{E}$, and second, the thermal energy k_BT. Usually, this ratio is very small so that any degree of ordering induced by the external field would become noticeable only for a very large number of particles, not for individual dipoles. While the total polarization $\mathbf{P}$ measures the electric moment per unit volume, the orientational part of the polarization $\mathbf{P}_{\text{or}}$ linked to the reorientation of the permanent dipoles by the field, is composed of the microscopic contribution of all polar particles as follows

$$\mathbf{P}_{\text{or}} = N\langle\boldsymbol{\mu}\rangle \ , \tag{1.63}$$

wherein N is the number density of the particles and $\langle\boldsymbol{\mu}\rangle$ is the molecular moment vector averaged over all possible orientations of the particle. In the absence of a field $\langle\boldsymbol{\mu}\rangle$ vanishes unless spontaneous order would exist. The quantity $\langle\boldsymbol{\mu}\rangle$ is to be understood as the projection of the average dipole moment on the orienting field vector, whose direction is defined by unit vector $\mathbf{e}$. Hence

$$\langle\boldsymbol{\mu}\rangle = \langle\boldsymbol{\mu}\cdot\mathbf{e}\rangle\mathbf{e} = \mu\langle\cos\theta\rangle\mathbf{e} \ , \tag{1.64}$$

assuming μ to be independent of the field. Next, $\langle\cos\theta\rangle$ is computed according to Boltzmann's law as follows

$$\langle\cos\theta\rangle = \frac{\int_0^\pi \cos\theta\exp(\mu E\cos\theta/k_BT)\sin\theta\,d\theta}{A} \ , \tag{1.65}$$

where A is a normalizing factor given by

$$A = \int_0^\pi \exp(\mu E\cos\theta/k_BT)\sin\theta\,d\theta \ , \tag{1.66}$$

and $\sin\theta\,d\theta$ represents the differential of the pertinent orientational variable [1]. The solution of the integral in (1.65) is known as one of the Langevin functions which for not too strong fields may be expanded into the following series:

$$\langle\cos\theta\rangle = \frac{1}{3}\left(\frac{\mu E}{k_BT}\right) - \frac{1}{45}\left(\frac{\mu E}{k_BT}\right)^3 + \ldots \tag{1.67}$$

Indeed, the result illustrates that for small values of $\mu E/k_BT$ the average angle θ will deviate only slightly from $\pi/2$, which is the situation encountered in field-free conditions when looking for order with respect to any given direction. Deviation from linear behavior with the field strength is even more difficult to perceive. Note that in the expansion only terms in *odd powers of* E are included. Even terms in E would be inconsistent with the directional character of the polarization.

For the case of non-interacting particles in a gas at moderate pressure, as opposed to denser media, the field experienced by the particles is practically equal to the externally applied field $\mathbf{E}$.

At this point we like to include the induced polarization $\mathbf{P}_{\text{ind}}$ in the expression of the total dipole density

$$\mathbf{P} = \mathbf{P}_{\text{ind}} + \mathbf{P}_{\text{or}} = N(\alpha \cdot \mathbf{E} + \langle \boldsymbol{\mu} \rangle) \ , \tag{1.68}$$

where α is the polarizability tensor and $\alpha \cdot \mathbf{E}$ the induced moment. The above expressions lead to

$$\mathbf{P} = N \left[\alpha \cdot \mathbf{E} + \frac{\mu^2}{3k_B T} \mathbf{E} - \frac{\mu^4 E^2}{45(k_B T)^3} \mathbf{E} + \ldots \right] \ , \tag{1.69}$$

which represents the electric polarization in a collection of particles under high field conditions, neglecting higher order terms of the polarizability. It is apparent that the increase of the polarization with field strength levels off at stronger fields.

1.3.2 Theoretical background of the nonlinear dielectric spectroscopy

From now on we shall assume the molecules to be isotropically polarizable so that α is reduced to a scalar quantity. In this way nonlinear effects related to the Kerr effect will be excluded from the present analysis.

In the following we shall modify the basic expression in (1.69) to apply to denser media where the field actually seen by the dipoles is quite different from the externally applied field. Traditionally the dipolar particles are considered to occupy spherical cavities embedded in a continuous dielectric medium with permittivity $\varepsilon_0 \varepsilon$. From electrostatics it may be shown that the field in such a cavity $\mathbf{E}_{\text{cav}}$ is related to the macroscopic field by

$$\mathbf{E}_{\text{cav}} = \frac{3\varepsilon}{2\varepsilon + 1} \mathbf{E} \ . \tag{1.70}$$

This is the first mechanism operating to distinguish macroscopic from microscopic fields. A second reason for their difference lies in the fact that the dense surroundings of the particles become polarized not only by the external field but also by the inhomogeneous fields carried by the permanent and induced moments within the cavity, producing in turn extra field components in the cavity. Onsager has noted that in so far as the ensuing *reaction field* is due to a permanent dipole moment, it cannot rotate the moment as both will always have the same direction [2].

Therefore, the effective field $\mathbf{E}_{\text{i}}$ that polarizes the particle by charge distortion and which is known as the internal field, is larger than the directing field $\mathbf{E}_{\text{d}}$ that effectively reorients the dipole; in condensed media both these fields are stronger than the externally applied field. Consequently, (1.69) must be rewritten as follows

$$\mathbf{P} = N \left[\alpha \mathbf{E}_{\text{i}} + \frac{\mu^2}{3k_B T} \mathbf{E}_{\text{d}} - \frac{\mu^4 E_{\text{d}}^2}{45(k_B T)^3} \mathbf{E}_{\text{d}} + \ldots \right] \ . \tag{1.71}$$

We shall now relate $\mathbf{E}_{\text{i}}$ and $\mathbf{E}_{\text{d}}$ to the external field $\mathbf{E}$. A general expression for the reaction field $\mathbf{R}$ shows that it is proportional to the sum of the permanent

dipole moment and the extra moment that this field induced in the polarizable dipolar molecule [2]:

$$\mathbf{R} = f(\boldsymbol{\mu} + \alpha\mathbf{R}) \ . \tag{1.72}$$

The proportionality constant f is known as the reaction field factor. Again from electrostatics it may be shown that f is given by:

$$f = \frac{1}{4\pi\varepsilon_0}\frac{1}{a^3}\frac{2(\varepsilon-1)}{2\varepsilon+1} \ , \tag{1.73}$$

with a the radius of the cavity and ε_0 the permittivity of free space. Onsager has proposed that a can be calculated from the particle density according to:

$$N = \frac{1}{(4\pi/3)a^3} \ . \tag{1.74}$$

To obtain $\mathbf{E}_\mathrm{d}$, the reaction field corresponding to its induced moment must be added to the cavity field

$$\mathbf{E}_\mathrm{d} = \mathbf{E}_\mathrm{cav} + f\alpha\mathbf{E}_\mathrm{d} \ , \tag{1.75}$$

so that by using (1.70) the required relation between $\mathbf{E}_\mathrm{d}$ and $\mathbf{E}$ is found:

$$\mathbf{E}_\mathrm{d} = \frac{1}{1-f\alpha}\frac{3\varepsilon}{2\varepsilon+1}\mathbf{E} \ . \tag{1.76}$$

Onsager has demonstrated that the difference between the internal and directing fields is due to the reaction field associated with the permanent dipole moment. Therefore

$$\mathbf{E}_\mathrm{i} = \mathbf{E}_\mathrm{d} + \langle\mathbf{R}\rangle \ , \tag{1.77}$$

where $\langle\mathbf{R}\rangle$ is the reaction field averaged over all possible orientations of the dipole. It may be written as follows

$$\langle\mathbf{R}\rangle = f(\langle\boldsymbol{\mu}\rangle + \alpha\langle\mathbf{R}\rangle) = \frac{f}{1-f\alpha}\langle\boldsymbol{\mu}\rangle \ , \tag{1.78}$$

so that with the help of (1.64) and (1.67) one obtains

$$\mathbf{E}_\mathrm{i} = \mathbf{E}_\mathrm{d}\left[1 + \frac{f}{1-f\alpha}\left(\frac{\mu^2}{3k_BT} - \frac{\mu^4E_\mathrm{d}^2}{45(k_BT)^3} + \ldots\right)\right] \ , \tag{1.79}$$

wherein the deviations from linear behavior are included explicitly. In (1.71) the microscopic fields can now be written in terms of the external field. If the macroscopic definition of the total polarization is chosen as

$$\mathbf{P} = \varepsilon_0(\varepsilon_E - 1)\mathbf{E} \ , \tag{1.80}$$

with $\varepsilon_0\varepsilon_E$ the permittivity of the dielectric at field strength E, we find after eliminating the field from the equation that

$$\varepsilon_0(\varepsilon_E - 1) = N\left[\alpha + \frac{1}{1-f\alpha}\left(\frac{\mu^2}{3k_BT} - \frac{\mu^4E_\mathrm{d}^2}{45(k_BT)^3}\right)\right]\frac{1}{1-f\alpha}\frac{3\varepsilon}{2\varepsilon+1} \ . \tag{1.81}$$

In the present expression, the first order correction for nonlinearity has been carried through in a coherent fashion. The distinction between ε_E and ε is immaterial at this point, the nonlinearity generally leading to no more than a very small correction of the permittivity. Now we still need to make the factor $1/(1 - f\alpha)$ explicit. At this stage it is advantageous to introduce the Clausius-Mossotti relation expressing the polarizability in terms of the optical permittivity $\varepsilon_0\varepsilon_\infty$, which is determined at such high frequencies of the measuring field that the permanent dipole moments cannot contribute to the polarization. The relation reads:

$$\frac{\varepsilon_\infty - 1}{\varepsilon_\infty + 2} = \frac{N}{3\varepsilon_0}\alpha \ . \tag{1.82}$$

By using (1.74) to eliminate a^3 from (1.73) and subsequently multiplying it by α, we have an expression for $f\alpha$ which leads to

$$\frac{1}{1 - f\alpha} = \frac{\varepsilon_\infty + 2}{3}\frac{2\varepsilon + 1}{2\varepsilon + \varepsilon_\infty} \ . \tag{1.83}$$

With the help of this result, (1.81) becomes

$$\frac{\varepsilon_0(\varepsilon - 1)}{\varepsilon} = N\frac{\varepsilon_\infty + 2}{2\varepsilon + \varepsilon_\infty}\left[\alpha + \frac{(2\varepsilon + 1)(\varepsilon_\infty + 2)}{2\varepsilon + \varepsilon_\infty}\left(\frac{\mu^2}{9k_BT} - \frac{\mu^4 E_\mathrm{d}^2}{135(k_BT)^3}\right)\right] \tag{1.84}$$

which is one form of the classical Onsager equation except for the correction term due to nonlinearity. When this equation is applied to high frequency measurements from which contributions due to the permanent moments are absent, the Clausius-Mossotti equation is duly recovered. Using it once more to eliminate the polarizability, we finally obtain

$$\frac{\varepsilon_0(\varepsilon - \varepsilon_\infty)}{\varepsilon} = N\frac{(\varepsilon_\infty + 2)^2}{2\varepsilon + \varepsilon_\infty}\left(\frac{\mu^2}{9k_BT} - \frac{\mu^4 E_\mathrm{d}^2}{135(k_BT)^3}\right) \ . \tag{1.85}$$

At low field strength, when E_d tends to zero, the result is Onsager's successful expression for the determination of the permanent dipole moment of non-associating molecules in the liquid phase. After collecting all terms in ε of (1.85) at the left hand side, the modified equation may be read as a series expansion in ε of the function $F(\varepsilon) = \varepsilon_0(\varepsilon - \varepsilon_\infty)(2\varepsilon + \varepsilon_\infty)/\varepsilon$ for which we have

$$F(\varepsilon) = F(\varepsilon)_{\varepsilon_{E\to 0}} + \left(\frac{\partial F(\varepsilon)}{\partial \varepsilon}\right)_{\varepsilon_{E\to 0}} (\varepsilon_E - \varepsilon_{E\to 0}) \ . \tag{1.86}$$

Equating terms in the reshuffled (1.85) and (1.86), as Barriol and Greffe [3] have suggested, produces

$$\left(\frac{\partial F(\varepsilon)}{\partial \varepsilon}\right)_{\varepsilon_{E\to 0}} (\varepsilon_E - \varepsilon_{E\to 0}) = -N(\varepsilon_\infty + 2)^2\frac{\mu^4 E_\mathrm{d}^2}{135(k_BT)^3} \ , \tag{1.87}$$

which finally leads to

$$\varepsilon_0(\varepsilon_E - \varepsilon_{E\to 0}) = \varepsilon_0 \Delta\varepsilon_{\mathrm{L}} = -N \frac{(\varepsilon_\infty + 2)^4 \varepsilon^4}{(2\varepsilon^2 + \varepsilon_\infty^2)(2\varepsilon + \varepsilon_\infty)^2} \frac{\mu^4 E^2}{135(k_B T)^3} \tag{1.88}$$

upon introducing the derivative of $F(\varepsilon)$ and replacing E_d in terms of E according to (1.76) and (1.83). We like to think of this expression as the Onsager description of the *first order orientational nonlinear dielectric behavior* in E^2 applicable to dipolar dense fluids (Langevin effect, $\Delta\varepsilon_{\mathrm{L}}$). This result has been obtained by Kielich long ago [4] and was derived once more by Thiébaut [5] and by Barriol and Greffe [3].

In practice, electric measurements provide the derivative $(\partial P/\partial E)$ rather than the polarization itself. Accordingly, an expression for the nonlinear dielectric effect $\Delta\varepsilon_{\mathrm{L}}$ is obtained by comparing the derivative obtained at high field strength with that noted at zero field:

$$\left(\frac{\partial P}{\partial E}\right)_E - \left(\frac{\partial P}{\partial E}\right)_{E\to 0} = \varepsilon_0 \Delta\varepsilon_{\mathrm{L}} = -N \frac{(\varepsilon_\infty + 2)^4 \varepsilon^4}{(2\varepsilon^2 + \varepsilon_\infty^2)(2\varepsilon + \varepsilon_\infty)^2} \frac{\mu^4 E^2}{45(k_B T)^3} \,, \tag{1.89}$$

the derivatives purposely being defined as the permittivity $\varepsilon_0\varepsilon$ of the dielectric, with ε_0 the permittivity of free space. It should be noted here that because in (1.69) the electric field strength occurs in a third power, experimental values of $\Delta\varepsilon_{\mathrm{L}}$ – measured as a difference of $(\partial P/\partial E)$ terms at various field strengths – are 3 times as large as $\Delta\varepsilon_{\mathrm{L}}$ given in (1.88) which was calculated as the difference of (P/E) terms.

Equation (1.89) provides a quantitative description of the onset of the *saturation effect of dipolar molecules* in strong electric fields. The negative sign of $\Delta\varepsilon_{\mathrm{L}}$ reflects the increasing difficulty that particles have to adjust their orientation to the measuring field while being restrained by higher and higher superimposed fields. It is customary practice in the nonlinear dielectric effect (NDE) work to probe the polarization of a system with a weak alternating field while switching a high constant field on and off [6–8].

Presented here the experimental results of the nonlinear dielectric increment $\Delta\varepsilon_{\mathrm{L}}$ were obtained as a difference of $(\partial P/\partial E)$ terms, as shown in Fig. 1.21. The dipolar liquid, placed in the plane measuring cell, was subjected to the two electric fields: a quasistatic field (85 Hz) of high amplitude ($E_0 = 1.1 \cdot 10^7$ V/m) and a weak (measuring) field E. As the frequency of the latter can be changed, the *nonlinear dielectric spectrum* can be recorded. In the used set-up the frequency range of the measuring field $E(\omega)$ was from 100 kHz to about 3 GHz [8–10]. The frequency dependent permittivity increment has, in generally, the complex form

$$\Delta\varepsilon_{\mathrm{L}}^*(\omega) = \Delta\varepsilon_{\mathrm{L}}'(\omega) + i\Delta\varepsilon_{\mathrm{L}}''(\omega) \,, \tag{1.90}$$

where $\Delta\varepsilon_{\mathrm{L}}'(\omega)$ and $\Delta\varepsilon_{\mathrm{L}}''(\omega)$ are the real and imaginary parts of the increment, respectively. The static value of the increment is described by (1.89).

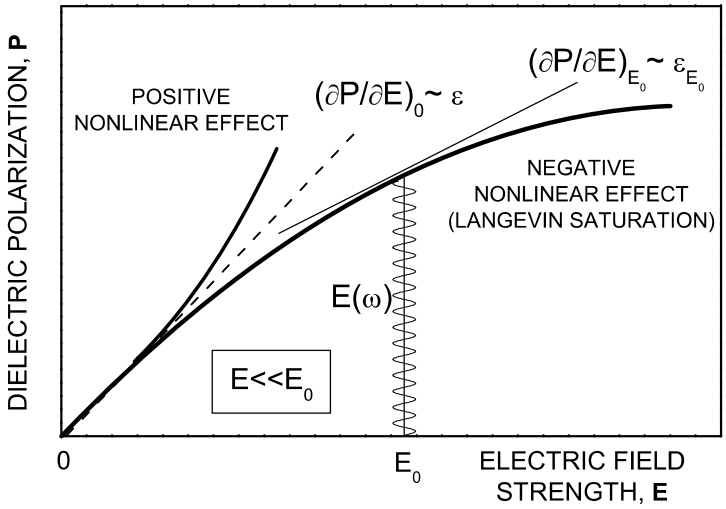

Fig. 1.21. Strong electric field causes a nonlinearity in the dielectric polarization vs. field strength dependence. The effect is measured with a weak a.c. electric field $E(\omega)$. For non-interacting dipolar systems the Langevin saturation effect leads to a negative value of the permittivity increment $\Delta\varepsilon_{\mathrm{L}}$

1.3.3 Nonlinear dielectric relaxation in non-interacting dipolar systems

The Langevin saturation phenomenon can be investigated only for non interacting dipolar systems. The dipolar interactions lead to molecular aggregates, which (as we will show latter) in presence of strong electric field, can give a positive contribution to the nonlinear dielectric increment.

The experimental results presented in Figs. 1.22 and 1.23 have been obtained for diluted solutions of 4.4′-*n*-hexylcyanobiphenyl (C_6H_{13}–Ph–Ph–C≡N, 6CB) and 4-(trans-4′-*n*-hexylcyclohexyl)isothiocyanatobenzene (C_6H_{13}–C_yH_x–Ph–N=C=S, 6CHBT) in benzene. Dilution of a dipolar substance in a nonpolar medium is an efficient way for the reduction of dipole-dipole interactions. Unfortunately, a decrease of the dipole number in the unit volume leads simultaneously to a decrease of the measured signal amplitude. The concentration of dipoles in our experiments (1% in molar fraction) was the compromise between the effectiveness of the dipole-dipole interactions reduction and the limit of the measuring apparatus sensitivity.

A theoretical description of the frequency dependence of the nonlinear dielectric phenomenon caused by the saturation of the dipoles orientation in strong electric fields has been proposed by Coffey and Paranjape [12], Kasprowicz-Kielich and coworkers [13–16] and Kimura and Hayakawa [17]. The theories concern the isotropic dielectrics containing N mutually non-interacting dipolar, axially symmetric molecules, with the dipole moment vector

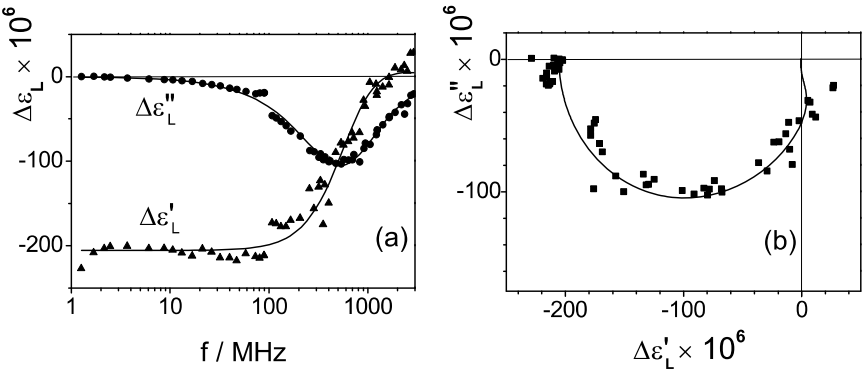

Fig. 1.22. Nonlinear dipolar relaxation spectrum (**a**) and nonlinear Cole–Cole plot (**b**) for 6CB solution in benzene. Molar fraction of 6CB: $x = 0.0107$, $E_0 = 1.1 \cdot 10^7$ V/m, $T = 25°$C. Solid lines represent the Coffey-Kielich equations (1.91) and (1.92) for $L = -2.01 \cdot 10^{-4}$ and $\tau = 0.2$ ns [11]

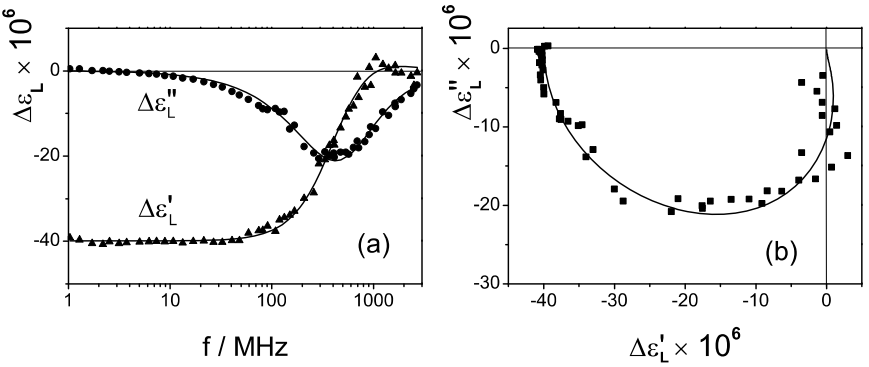

Fig. 1.23. Nonlinear dipolar relaxation spectrum (**a**) and nonlinear Cole–Cole plot (**b**) for 6CHBT solution in benzene. Molar fraction of 6CHBT: $x = 0.0108$, $E_0 = 1.1 \cdot 10^7$ V/m, $T = 25\,°$C. Solid lines represent the Coffey-Kielich equations (1.91) and (1.92) for $L = -0.40 \cdot 10^{-4}$ and $\tau = 0.2$ ns [11]

parallel to the axis of symmetry. The rotational relaxation of such an assembly, placed in a strong electric field, is described by the extended Debye rotational diffusion model [18–21].

Despite of the different basis of the Debye model extension to the nonlinear case, all theories give quantitatively similar predictions for the frequency dependence of the increment $\Delta\varepsilon_{\mathrm{L}}^{*}$. In particular, the most general theory, proposed by Kielich et al. [14], covering a great variety of nonlinear effects, predicts exactly the same dependence $\Delta\varepsilon_{\mathrm{L}}^{*}(\omega)$ as the theory of Coffey and Paranjape [12].

Here we will use the following Coffey-Kielich equations [12, 13]:

$$\Delta\varepsilon'_{\mathrm{L}} = L\frac{1}{1+\omega^2\tau^2}F_1(\omega)\ ,$$
$$\Delta\varepsilon''_{\mathrm{L}} = L\frac{\omega\tau}{1+\omega^2\tau^2}F_2(\omega)\ , \tag{1.91}$$

where τ is the relaxation time, $F_1(\omega)$ and $F_2(\omega)$ refer to the nonlinearity of the dipolar relaxation process and are given by

$$F_1(\omega) = \frac{27+\omega^2\tau^2-2\omega^4\tau^4}{3(1+\omega^2\tau^2)(9+\omega^2\tau^2)}\ ,$$
$$F_2(\omega) = \frac{42+19\omega^2\tau^2+\omega^4\tau^4}{3(1+\omega^2\tau^2)(9+\omega^2\tau^2)}\ . \tag{1.92}$$

The quantity L in (1.91) denotes the strength of the nonlinear dielectric increment and is equal to the static value of the increment given by (1.89) (the high frequency value of the increment ($\Delta\varepsilon_{\mathrm{L}\infty}$) is equal to zero).

From the static value of the nonlinear increment $L(=\Delta\varepsilon_{\mathrm{L}})$ one can evaluate the dipole moment of rotating molecules (1.89). The data presented in Table 1.2 indicate that, for both 6CB and 6CHBT, the dipole moment values (μ_{calc}) calculated from (1.89) are not too far from the values resulting from the linear polarization measurements in diluted solutions. The small difference of $\mu_{\mathrm{exp}} - \mu_{\mathrm{calc}} \approx 0.6\,D$ shows that for the concentration of $\sim 1\%$ (in molar fraction) the dipole-dipole association is not completely eliminated. This conclusion agrees with the results obtained by Dunmur et al. [22].

Table 1.2. Values of linear[a] and nonlinear dielectric data for the diluted solutions of 6CB and 6CHBT in benzene at 25 °C (the molar fraction of dipolar compound is equal 0.01)

	6CB	6CHBT
τ(ns)	0.205	0.254
L	$-2.01\cdot10^{-4}$	$-0.40\cdot10^{-4}$
$\mu_{\mathrm{calc}}(D)$	4.2	2.9
$\mu_{\mathrm{exp}}(D)$	4.8–4.9 [22]	3.48 [23]
ε_{s}	2.66	2.48

[a] $\varepsilon_\infty = 2.278$, density $\rho = 0.881$ g/cm^3 (for both solutions)

The strong dependence of the Langevin nonlinear effect on the dipole moment of molecular rotators ($L \sim \mu^4$) is illustrated in Fig. 1.24, where two nonlinear Cole–Cole plots corresponding to the 6CB and 6CHBT molecules are compared. The difference in the dipole moment values of these two molecules is relatively small and is equal to $\sim 1.3\,D$.

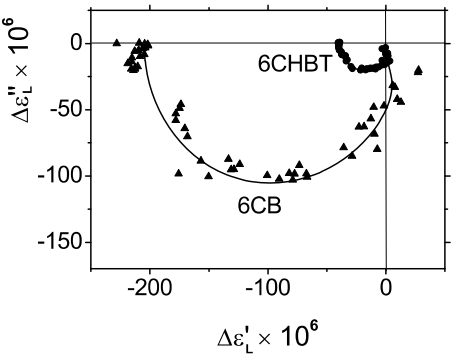

Fig. 1.24. Comparison of the Cole–Cole plots for two molecular rotators with different values of the dipole moment: $\mu_{6\mathrm{CB}} = 4.2\,D$, $\mu_{6\mathrm{CHBT}} = 2.9\,D$ [11]

Since a strong electric field applied to a dipolar liquid causes a partial ordering of dipoles and hampers the thermal rotation, one can expect an influence of the field intensity on the relaxation time. It has been shown by Coffey et al. [24] that the difference between the relaxation time obtained from nonlinear (τ) and linear (τ_D) dipolar relaxation spectroscopies depends on the ratio ξ of the electric energy of dipoles (μE_0) and the thermal energy $k_B T$. The theory predicts that for a small ξ value ($\xi \ll 1$), τ and τ_D should be equal to each other [25]. In our experiment the ξ value is $\sim 4 \cdot 10^{-2}$, thus one can expect that τ and τ_D are close to each other.

1.3.4 Nonlinear dielectric relaxation due to chemical rate processes in liquids

For the molecular systems, in which the chemical reactions occur, and the polarity of both sides of the reaction partners is different, the strong electric field shifts the equilibrium toward the more polar species. The shift measured with a weak a.c. electric field shown the relaxation which reflects the rate of the reaction.

Let us assume that the following chemical reaction occurs:

$$v_1 R_1 + v_2 R_2 + \ldots + v_j R_j \rightleftharpoons v_{j+1} P_{j+1} + \ldots + v_c P_c. \tag{1.93}$$

Any change in the number of moles n_i of the reaction partners is given by

$$\frac{dn_1}{v_1} = \frac{dn_2}{v_2} = \ldots = \frac{dn_c}{v_c} = d\xi \ , \tag{1.94}$$

where ξ denotes here the extent of reaction, while v_i are the appropriate stoichiometric coefficients in (1.93) (positive for products P, and negative for reactants R). When this system is placed in an external electric field, the Gibbs energy $G(T, p, E, \xi)$ has the following form [26, 27]

$$dG = -SdT + Vdp - MdE - Ad\xi \ . \tag{1.95}$$

The affinity

$$A = -\sum_i v_i \mu_i \tag{1.96}$$

connects the chemical potentials μ_i of all reaction partners. At equilibrium $A = 0$. The dependence of μ_i on the concentrations c_i has the form

$$\mu_i = \mu_i^0 + RT \ln(c_i f_i), \tag{1.97}$$

where μ_i^0 are the standard values of the chemical potential, and f_i are the activity coefficients. From (1.96) and (1.97) one obtains

$$A = RT \ln K - RT \sum_i v_i \ln c_i, \tag{1.98}$$

where

$$\ln K = \ln K^* - \sum_i v_i \ln f_i \ ,$$

$$K^* = \exp\left[-\frac{\sum v_i \mu_i^0}{RT}\right] . \tag{1.99}$$

K^* is the thermodynamic equilibrium constant of reaction (1.93); for ideal solutions ($f_i = 1$) it is equal to the effective equilibrium constant K. In isothermic-isobaric conditions, (1.95) leads to

$$\left(\frac{\partial A}{\partial E}\right)_{T,p} = \left(\frac{\partial M}{\partial \xi}\right)_{T,p} \equiv \Delta M \ . \tag{1.100}$$

This is the basic thermodynamic relation describing the influence of an electric field on chemical transformation. It relates four variables: on the one hand extensive (M) and intensive (E) quantities of electric energy, and on other hand extensive (A) and intensive (ξ) quantities of chemical free energy of the process studied. ΔM describes a change in total dipole moment M resulting from a shift of equilibrium (1.93), at constant T, p and high field E. Equations (1.98) and (1.100) (omitting electrostriction effects) give

$$\left(\frac{\partial \ln K}{\partial E}\right)_{T,p,\xi} = \frac{\Delta M}{RT} \ . \tag{1.101}$$

Since

$$\Delta M \equiv \left(\frac{\partial M}{\partial \xi}\right)_{T,p,E} = \varepsilon_0 E V \left(\frac{\partial \varepsilon}{\partial \xi}\right)_{T,p,E} \ , \tag{1.102}$$

Equation (1.101) shows that the change in equilibrium constant depends non-linearly on the electric field strength. The effect vanishes when $E \to 0$. The chemical equilibrium can be perturbed by a small alternating field dE only when an additional static field E_0 of high strength is applied (Fig. 1.25). In an experiment it reveals itself as the *field induced positive increment of the electric permittivity* $\Delta\varepsilon$, which relaxes in a frequency range dependent on the

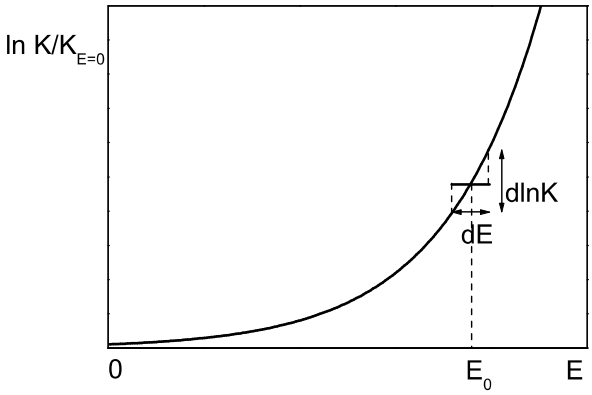

Fig. 1.25. Simultaneous influence of the two electric fields: strong static field E_0 and weak h.f. field E on the equilibrium constant of dipolar chemical reaction

rate of the chemical process. In practice, as we discussed before, the nonlinear dielectric effect measures the difference between the electric permittivity in strong and weak electric field; $\varepsilon(E_0)$ is here defined as

$$\varepsilon_0 \varepsilon(E_0) = \left(\frac{\partial D}{\partial E}\right)_{E_0} . \tag{1.103}$$

In the presence of a field-dependent chemical reaction, D is a complex function of the field strength $D = D[E, \xi(E)]$, and for $p,\ T = \text{const}$ (1.103) has the following form:

$$\varepsilon_0 \varepsilon(E_0) = \left[\left(\frac{\partial D}{\partial E}\right)_{\xi} + \left(\frac{\partial D}{\partial \xi}\right)\left(\frac{\partial \xi}{\partial E}\right)\right]_{E_0} . \tag{1.104}$$

The first right hand side term of (1.104) is a function of the chemical composition ξ and corresponds to the new equilibrium in strong electric field conditions. Since the new equilibrium state differs only slightly from the initial one, even for the highest fields possible ($E_0 \sim 10^5$ V/cm), this term can be approximated by the two first terms of a MacLaurin's series [9, 28]

$$\left(\frac{\partial D}{\partial E}\right)_{\xi(E_0)} = \left(\frac{\partial D}{\partial E}\right)_{\xi(0)} + \left[\frac{\partial}{\partial \xi}\left(\frac{\partial D}{\partial E}\right)\right]_{\xi(0)} \Delta\xi \ , \tag{1.105}$$

where

$$\Delta\xi = \xi(E_0) - \xi(0)$$

and

$$\frac{\partial}{\partial \xi}\left(\frac{\partial D}{\partial E}\right)_{\xi(0)} = \varepsilon_0 \left(\frac{\partial \varepsilon}{\partial \xi}\right)_E . \tag{1.106}$$

The increment of the electric permittivity caused by a strong electric field may now be expressed as

$$\varepsilon(E_0) - \varepsilon(0) \equiv \Delta\varepsilon = \frac{1}{\varepsilon_0}\left[\left(\frac{\partial D}{\partial E}\right)_{E_0} - \left(\frac{\partial D}{\partial E}\right)_0\right]_{\xi(0)} + \left(\frac{\partial D}{\partial \xi}\right)_E \Delta\xi + \frac{1}{\varepsilon_0}\left[\left(\frac{\partial D}{\partial \xi}\right)_E \left(\frac{\partial \xi}{\partial E}\right)\right]_{E_0} \tag{1.107}$$

or in simplified form as

$$\Delta\varepsilon = \Delta\varepsilon_{\mathrm{L}} + \Delta\varepsilon^0 + \Delta\varepsilon(\omega). \tag{1.108}$$

The term $\Delta\varepsilon_{\mathrm{L}}$ of this sum describes the orientation of permanent dipoles hindered by a strong electric field, i.e. Langevin's dielectric saturation (see (1.89)).

The two remaining terms of (1.108) are connected with the *field induced chemical transformations* and are always positive. They are designated as $\Delta\varepsilon^0$ and $\Delta\varepsilon(\omega)$ because of their different dependence on the frequency of the measuring field dE. $\Delta\varepsilon^0$ results from the equilibrium shift produced by the static field E_0 and is measurable by the small alternating field dE up to frequencies where *orientational relaxation* begins. $\Delta\varepsilon(\omega)$ is a consequence of the perturbation of the chemical equilibrium by the small measuring field dE and disappears above frequencies corresponding to *chemical relaxation* (Fig. 1.26).

The change in the extent of reaction ξ can be calculated by integration:

$$\Delta\xi = \int_0^{E_0} \left(\frac{\partial \xi}{\partial E}\right)_A dE, \tag{1.109}$$

where the derivative $(\partial\xi/\partial E)_A$ is equal to [26, 29]:

$$\left(\frac{\partial \xi}{\partial E}\right)_A = -\frac{(\partial A/\partial E)_\xi}{(\partial A/\partial \xi)_E} = -\frac{(\partial M/\partial \xi)_E}{(\partial A/\partial \xi)_E} = -\frac{\Delta M}{\Delta A}\ . \tag{1.110}$$

From (1.96) and (1.102) one obtains

$$\Delta\varepsilon^0 = \frac{\Gamma}{2RT}\varepsilon_0 V \left(\frac{\partial \varepsilon}{\partial \xi}\right)_E^2 E_0^2\ , \tag{1.111}$$

where Γ indicates the extent of perturbation possible in view of the actual equilibrium concentrations $\bar{c}_i$:

$$\Gamma = \left(\sum_i \frac{v_i^2}{\bar{c}_i}\right)^{-1}.$$

The analogous calculation of $\Delta\varepsilon(\omega)$ gives

$$\Delta\varepsilon(\omega) = \frac{\Gamma}{RT}\varepsilon_0 V \left(\frac{\partial \varepsilon}{\partial \xi}\right)_E^2 E_0^2\ \Phi(\omega)\ , \tag{1.112}$$

where $\Phi(\omega)$ represents the complex relaxation function $1/(1+i\omega\tau)$ with τ the relaxation time of the chemical process.

Equations (1.111) and (1.112) show that the low-amplitude measuring field gives a twice as large contribution to the chemical part of the electric permittivity increment (1.112) as the strong field E_0 itself (1.111). At first, it might be surprising but one should remember that, in essence, the permittivity change is given by the derivative of the nonlinear terms of the polarization with respect to the field.

The final expression for the *chemical contribution to the field induced increment of the electric permittivity* has the following form

$$\Delta\varepsilon^*_{ch} = \Delta\varepsilon^0 + \Delta\varepsilon(\omega) = \frac{\varepsilon_0 \Gamma V^2}{RT} \left(\frac{\partial\varepsilon}{\partial\xi}\right)^2_E E_0 \left[\frac{1}{2} + \Phi(\omega)\right]. \tag{1.113}$$

The calculation of the derivative $(\partial\varepsilon/\partial\xi)_E$ requires an assumption concerning the local field in dielectrics. It has been obtained from Onsager's model [2]:

$$\left(\frac{\partial\varepsilon}{\partial\xi}\right)_E = \frac{\varepsilon^2(n^2+2)^2}{n^4+2\varepsilon^2} \frac{1}{9\varepsilon_0 RT} \frac{N}{V} \sum_i v_i \mu_i^2. \tag{1.114}$$

Taking into account (1.102), expression (1.113) takes the following form

$$\Delta\varepsilon^*_{ch} = \frac{\Gamma}{\varepsilon_0 RT} (\Delta M)^2 \left[\frac{1}{2} + \Phi(\omega)\right]. \tag{1.115}$$

Thus, the total complex increment of electric permittivity equals

$$\Delta\varepsilon^* \equiv \Delta\varepsilon' - i\Delta\varepsilon'' = L + \frac{\Gamma}{\varepsilon_0 RT} (\Delta M)^2 \left[\frac{1}{2} + \frac{1}{1+i\omega\tau}\right] \tag{1.116}$$

with the following real and imaginary parts:

$$\begin{aligned} \Delta\varepsilon' &= L + \frac{1}{2}B + \frac{B}{1+\omega^2\tau^2}, \\ \Delta\varepsilon'' &= B\frac{\omega\tau}{1+\omega^2\tau^2}, \end{aligned} \tag{1.117}$$

where

$$B = \frac{\Gamma(\Delta M)^2}{\varepsilon_0 RT} \left[\frac{1}{2} + \frac{1}{1+i\omega\tau}\right]. \tag{1.118}$$

The elimination of $\omega\tau$ from (1.117) gives the equation of a semi-circle

$$[\Delta\varepsilon'']^2 + [\Delta\varepsilon' - (L+B)]^2 = \left[\frac{1}{2}B\right]^2. \tag{1.119}$$

The frequency dependence of $\Delta\varepsilon'$ and $\Delta\varepsilon''$ (1.117) as well as the corresponding Cole–Cole plot (1.119) for a dipolar system with one kind of chemical transformation are shown in Fig. 1.26.

Two examples presented hereafter illustrate the usefulness of the nonlinear dielectric spectroscopy in studies of the kinetics of some chemical reactions. The first example concerns one of the simplest reaction in liquids: the dimerization due to the hydrogen bonds:

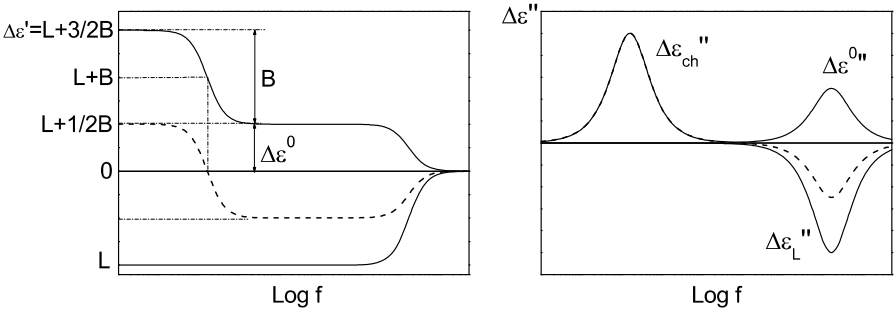

Fig. 1.26. Plot illustrating Debye's behavior of the nonlinear dielectric effect in a system with one type of chemical equilibrium. B represents the *chemical effect* (positive) caused by the low-amplitude measuring field (in the presence of static field E_0) and $L+\Delta\varepsilon^0$ sum of *orientational* (negative) and *chemical* (positive) effects; both caused by strong static field E_0

$$2 \text{ monomer} \underset{k_2}{\overset{k_1}{\rightleftharpoons}} \text{dimer} \ , \quad K = k_1/k_2 \tag{1.120}$$

with K the dimerization constant and k_1 and k_2 the rate constants for association and dissociation, respectively.

Figure 1.27 presents the nonlinear dielectric spectra for solutions of 2-pyrrolidinone in benzene. Due to *cis*-configuration of the peptide group $\mathrm{CO \cdot NH}$ in 2-pyrrolidinone molecule

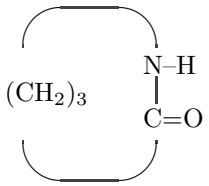

the interaction with other molecules leads mainly to formation of cyclic dimers with essentially compensated dipole moment. For such an association mechanism the relation between $1/\tau$ and the concentration of the monomer C_M is simply given by [30]

$$1/\tau = 4k_1 C_\mathrm{M} + k_2 \ . \tag{1.121}$$

This equation can be transformed to give a linear relationship between $1/\tau^2$ and the molar concentration C_0 of lactam:

$$1/\tau^2 = 8k_1 k_2 C_0 + k_2^2 \ . \tag{1.122}$$

A fit of the relaxation time data for small concentrations ($C_0 < 0.06$ mol/L) to this equation is presented in the inset of Fig. 1.28 and leads to $k_1 = (99 \pm 15) \cdot 10^8\,\mathrm{M^{-1}s^{-1}}$, close to the limit of a diffusion-controlled process, $k_2 = (1.44 \pm 0.22) \cdot 10^8\,\mathrm{s^{-1}}$ and $K = 69 \pm 15\,\mathrm{M^{-1}}$. The amplitudes of the

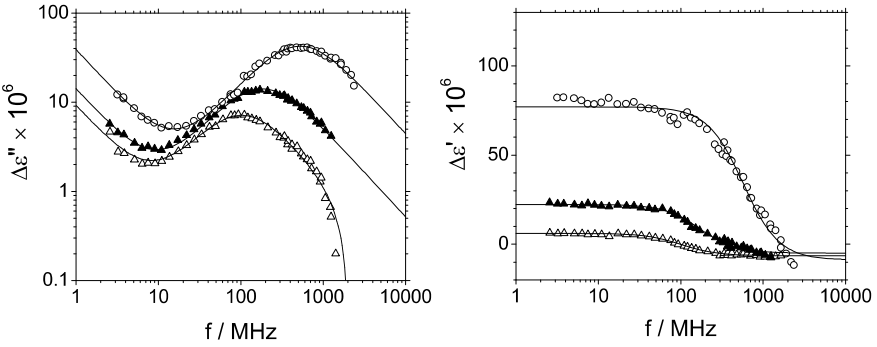

Fig. 1.27. NDE spectra for three concentrations $C_0 = 0.0405$ mol/L (open triangles), 0.119 mol/L (filled triangles), and 0.538 mol/L (open circles) of 2-pyrrolidinone in benzene at 25 °C, recorded at a field strength of 110 kV/cm. The line drawn through the data points represents a linear least-squares fit to a single Debye-type relaxation function describing chemical relaxation. For the smallest concentrations an extra Debye-type relaxation function with negative amplitude describing the Langevin term was added [10]

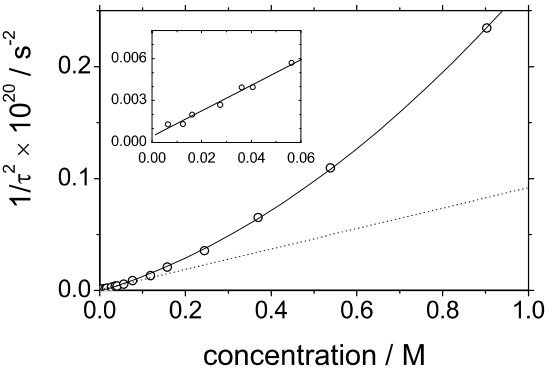

Fig. 1.28. Plot of the reciprocal of the relaxation time squared, $1/\tau^2$, against formal concentration C_0 for solutions of 2-pyrrolidinone in benzene at 25°C. The solid line is drawn with the parameters of a simultaneous fitting of the relaxation times and the perturbation amplitudes according to (1.123); the dotted line represents an extrapolation of the linear fit in the inset, which shows data at low concentrations ($C_0 < 0.06$ mol/L) where the solid line represents a linear fit according to (1.122) [10]

chemical relaxation spectra lead to values of $\Gamma(\sum \nu_i \mu_i^2)^2$ which in the case of a simple dimerization model can be written as

$$\Gamma \left(\sum \nu_i \mu_i^2 \right)^2 = \frac{1}{8K} \left(\frac{1 + 4KC_0}{(1 + 8KC_0)^{1/2}} - 1 \right) (-2\mu_{\mathrm{M}}^2 + \mu_{\mathrm{D}}^2)^2 \ . \qquad (1.123)$$

The dipole moments of the monomer and dimer are μ_{M} and μ_{D}, respectively. A fit of the chemical amplitudes to this equation over the same concentration region is presented in the inset of Fig. 1.29 and leads to $K = 42 \pm 12 M^{-1}$ and $(\sum \nu_i \mu_i^2)^2 = 661 \pm 37 D^4$. This latter value could imply that $\mu_{\mathrm{M}} = 5.1D$ when assuming $\mu_{\mathrm{D}} = 0D$, but such a value of monomer dipole moment is too high, so that $\mu_{\mathrm{D}} > 0D$. The values for the dimerization constant obtained from both sets of data points do not vary significantly. The literature values [31–34] for the dimerization constant for 2-pyrrolidinone in benzene are situated in the region 25–82 M^{-1}. Hofmann [35] reports $\sum \nu_i \mu_i^2 \approx \pm 29.6 D^2$ and the following kinetic parameters for the dimerization of ϵ-caprolactam in benzene solutions: $k_1 = (50 \pm 1) \cdot 10^8\,\mathrm{M}^{-1}\mathrm{s}^{-1}$ and $k_2 = (2.2 \pm 0.1) \cdot 10^8 \mathrm{s}^{-1}$, but the author did not analyze his NDE spectra $\Delta\varepsilon''/\varepsilon$ taking into account the contribution of orientational relaxation. Introducing a negative contribution, related to the reorientation of the dipoles, to the fitting function of the nonlinear spectrum lowers the observed chemical relaxation times and increases the value of k_1 in the present work.

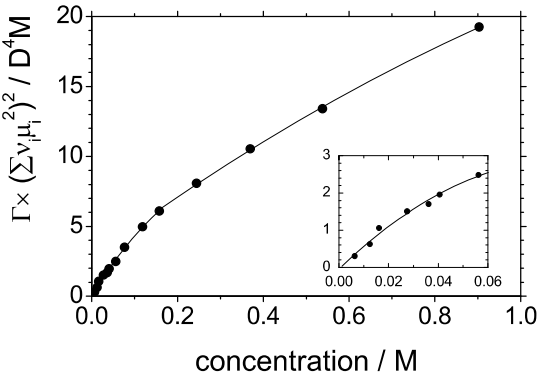

Fig. 1.29. Plot of the perturbation amplitude $\Gamma(\sum \nu_i \mu_i^2)^2$ against formal concentration C_0 for solutions of 2-pyrrolidinone in benzene at 25 °C. The solid line is drawn with the parameters of a simultaneous fitting of the relaxation times and the perturbation amplitudes according to (1.123). The inset shows the perturbation amplitudes for low concentrations ($C_0 < 0.06$ mol/L) with the solid line representing a fit according to (1.123) [10]

When looking at the total concentration range measured, it is clear that the linear relationship to (1.122) between $1/\tau^2$ and C_0 no longer holds experimentally (Fig. 1.28), suggesting the existence of higher multimers. This would be in agreement with other studies [33] in which is postulated an association mechanism including tetramers as well as dimers. However, this assumption is in contradiction with the observation that the chemical relaxation spectra can be described by a single Debye relaxation processes, meaning that only a single-step process becomes visible in the NDE spectra. Moreover, Walmsley [32]

studied the system for concentrations up to 2 mol/L and found that the only associated species is the cyclic dimer. The author determined a dimerization constant $K = 33 \pm 5M^{-1}$ and dipole moment values $\mu_{\mathrm{M}} = 3.91 \pm 0.20D$ for the monomer and $\mu_{\mathrm{D}} = 2.06 \pm 0.23D$ for the dimer. A fit of the nonlinear dielectric amplitudes to (1.123) gives a very good theory-experiment consistency for concentrations up to about 0.4 mol/L, leading to $K = 34 \pm 5M^{-1}$ and $(\sum \nu_i \mu_i^2)^2 = 636 \pm 28D^4$ (implying $\mu_{\mathrm{D}} = 2.3D$ if $\mu_{\mathrm{M}} = 3.9D$ is assumed) in excellent agreement with the findings of the former author. Accordingly, the dynamic measurements seem to be a much sensitive tool to discriminate between different association models.

The second example concerns the more complex self-association picture presented by cholesterol in solutions. IR spectroscopic, Raman, dielectric and thermodynamic studies [36–41] have shown that ability of cholesterol to self-association, despite its bulky hydrocarbon radical, is unexpectedly strong. Dielectric polarization measurements show [36] that the self-association of cholesterol in nonpolar solvents mainly leads to the formation of cyclic species with considerably compensated dipole moments. So, it is a system in which the equilibria should be perturbed by an electric field. However, because the coexistence of many different equilibria (seen in IR spectra), one cannot expect here a simple image of chemical relaxation.

The results of nonlinear dielectric relaxation studies of cholesterol solutions in CCl_4 are presented in Fig. 1.30. The chemical relaxation related to the perturbation of the cholesterol self-association equilibria comprises a considerably wider frequency range than predicted by the ideal (Debye-type) relaxation (which is observed in the systems with one type of chemical reaction). The plots of $\Delta\varepsilon'$ against $\log f$ (f = frequency) are centrosymmetric with respect to the point where $f_r = (2\pi\tau_0)^{-1}$, and the plots of $\Delta\varepsilon''$ are symmetric with respect to the vertical line through $f_r = (2\pi\tau_0)^{-1}$. In the $\Delta\varepsilon''$ against $\Delta\varepsilon'$ plots, the experimental points lie on semi-circles with their

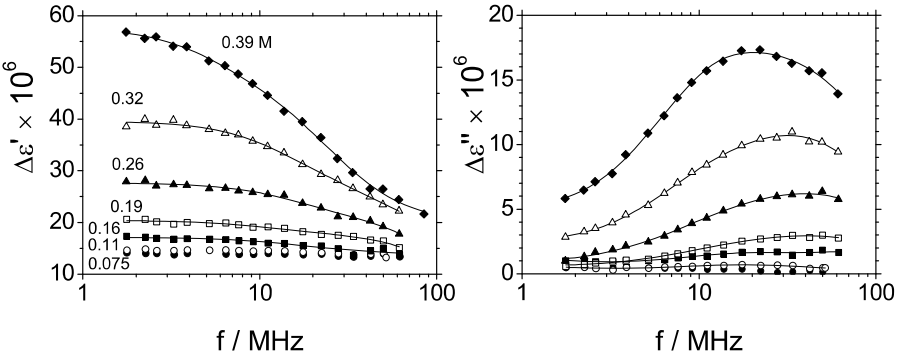

Fig. 1.30. Relaxation of the nonlinear dielectric effect for solutions of cholesterol in CCl_4. $E_0 = 109.4$ kV/cm, f = frequency. Solid lines are fitted on the basis of (1.125) and (1.126). The value of parameter α is equal 0.16 ± 0.04 [36, 42]

centers depressed below the $\Delta\varepsilon'' = 0$ axis. Such a behavior is well known for orientational dielectric relaxation. It can be observed in many solids and polymers, in which various dipolar species relaxe simultaneously. Such experimental behavior is described by the empirical Cole–Cole equation [43]. The system is then characterized by a spectrum of dielectric relaxation times.

For describing chemical relaxation spectra obtained for cholesterol solutions we proposed the following modification of (1.116):

$$\Delta\varepsilon^* \equiv \Delta\varepsilon' - i\Delta\varepsilon'' = L + \frac{\Gamma}{\varepsilon_0 RT}(\Delta M)^2 \left[\frac{1}{2} + \frac{1}{1 + (i\omega\tau_0)^{1-\alpha}}\right] , \qquad (1.124)$$

where α is an empirical constant, $0 \leq \alpha \leq 1$; for $\alpha = 0$ this formula gives (1.116). The separation of the real and imaginary parts of (1.124) gives:

$$\Delta\varepsilon' = L + \frac{B}{2} + B \frac{1 + (\omega\tau_0)^{1-\alpha} \sin\frac{\alpha\pi}{2}}{1 + (\omega\tau_0)^{2(1-\alpha)} + 2(\omega\tau_0)^{1-\alpha} \sin\frac{\alpha\pi}{2}} , \qquad (1.125)$$

$$\Delta\varepsilon'' = B \frac{(\omega\tau_0)^{1-\alpha} \cos\frac{\alpha\pi}{2}}{1 + (\omega\tau_0)^{2(\alpha-1)} + 2(\omega\tau_0)^{1-\alpha} \sin\frac{\alpha\pi}{2}} . \qquad (1.126)$$

Elimination of $\omega\tau_0$ from the above equations gives

$$\left[\Delta\varepsilon'' + (L + B)\tan\frac{\alpha\pi}{2}\right]^2 + (\Delta\varepsilon' - (L + B))^2 = \left[\frac{B}{2\cos\frac{\alpha\pi}{2}}\right]^2 . \qquad (1.127)$$

The solid lines in Fig. 1.30 represent the dependence described by (1.125) and (1.126).

The critical chemical relaxation time τ_0, corresponding to the maximum losses, changes with the concentration of cholesterol (Fig. 1.31) – a fact undoubtedly related to the varying degree of self-association. The increase of the cholesterol concentration causes the formation of cyclic multimers of greater number of molecules with longer times of chemical relaxation. When the concentration of cholesterol is decreasing, τ_0 tends to the value designated as τ_∞. This time describes the chemical relaxation of the simplest reaction sensitive to the electric field. It seems, however, that it is not related to the first self-association step-dimerization. Numerous data indicate that for molecules

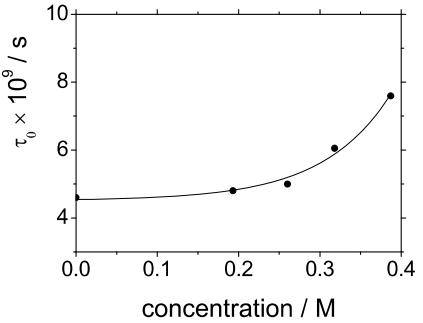

Fig. 1.31. Dependence of the chemical relaxation time on the cholesterol concentration [42]

of the R–OH type, the dimerization gives zero contribution to the chemical part of the nonlinear dielectric effect. This is connected with the fact that the dipolar polarizability of the dimer $(ROH)_2$ is close to that of two monomers ($\mu^2_{\mathrm{dim}} \approx 2\mu^2_{\mathrm{mon}}$) [44]. In such cases, the equilibrium $A_1 + A_1 \rightleftharpoons A_2$ cannot be perturbed by the electric field.

The chemical relaxation time τ_0 determined in our experiments describes the system as a whole. However, there are many coupled equilibria in solution and each of them is characterized by an appropriate time constant. The determination of these particular relaxation times, though vital, is impossible on the basis of our data.

1.3.5 Summary

The presented results show an analogy in the formal description of the relaxation processes observed in the linear and nonlinear dielectric spectroscopies. i) The reorientation of one type of dipoles corresponds, in the formal description, to the perturbation of one kind of chemical reaction. Both phenomena are described with the Debye-type function. ii) Various dipolar species relaxing simultaneously manifest themselves in the linear dielectric spectroscopy as the Cole–Cole distribution of the relaxation times with an analogy to the chemical relaxation due to simultaneous perturbation of many chemical reactions by an electric field of high intensity.

References

1. C.J.F. Böttcher: *Theory of Electric Polarization*, Vol. 1 (Elsevier Sci. Publ. Co., Amsterdam 1973)
2. L. Onsager: J. Am. Chem. Soc. **58**, 1486 (1936)
3. J. Barriol, J.L. Greffe: J. Chim. Phys. **66**, 575 (1969)
4. S. Kielich: Acta Phys. Polon. **17**, 239 (1958)
5. J. M. Thiébaut: Thesis, Université de Nancy I, (1968)
6. J. Małecki: J. Chem. Soc. Faraday Trans. II **72**, 1214 (1976)
7. S.J. Rzoska, J. Zioło, A. Drozd-Rzoska: Phys. Rev. E **56**, 2578 (1997)
8. M. Vints, L. Hellemans: I.E.E. Conf. Publ. **289**, 340 (1988)
9. L. Hellemans, L. De Maeyer: J. Chem. Phys. **63**, 3490 (1975)
10. K. De Smet, P. Kędziora, J. Jadżyn, L. Hellemans: J. Phys. Chem. **100**, 7662 (1996)
11. P. Kędziora, J. Jadżyn, K. De Smet, L. Hellemans: Chem. Phys. Lett. **289**, 541 (1998)
12. W.T. Coffey, B.V. Paranjape: Proc. R. Ir. Acad. **78**, 17 (1978)
13. B. Kasprowicz-Kielich, S. Kielich: Adv. Mol. Relaxation Proc. **7**, 275 (1975)
14. B. Kasprowicz-Kielich, S. Kielich, J.R. Lalanne: In: *Molecular Motions in Liquids*, ed. by J. Lascombe (D. Reidel, Dodrecht 1974) pp. 563–573
15. W. Alexiewicz, B. Kasprowicz-Kielich: 'Relaxation Theory of Nonlinear Processes in the Smoluchowski Rotational Diffusion Approximation'. In: *Modern Nonlinear Optics*, Part 1, ed. by M. Evans, S. Kielich (Wiley, New York 1993) pp. 1–50

16. W. Alexiewicz: Mol. Phys. **83**, 245 (1994)
17. Y. Kimura, R. Hayakawa: Jpn. J. Appl. Phys. **31**, 3387 (1992)
18. W.T. Coffey: In: *Dynamical Processes in Condensed Matter*, ed. by M.W. Evans (Wiley, New York 1985) pp. 69–252
19. B.K.P. Scaife: *Principles of Dielectrics* (Oxford University Press, Oxford 1989).
20. W.T. Coffey, J.L. Dejardin, Y.P. Kalmykov, S.V. Titov: Phys. Rev. E **54**, 6462 (1996)
21. Y.P. Kalmykov: Phys. Rev. E **65**, 021101 (2001)
22. D.A. Dunmur, M.R. Manterfield, W.H. Miller, J.K. Dunleavy: Mol. Cryst. Liq. Cryst. **45**, 127 (1978)
23. P. Kędziora, J. Jadżyn: Mol. Cryst. Liq. Cryst. **192**, 31 (1990)
24. W.T. Coffey, Y.P. Kalmykov, K.P. Quinn: J. Chem. Phys. **96**, 5471 (1992)
25. K. De Smet, L. Hellemans, J.F. Rouleau, R. Corteau, T.K. Bose: Phys. Rev. E **57**, 1384 (1998)
26. K. Bergmann, M. Eigen, L. De Maeyer: Ber. Bunsenges. Phys. Chem. **67**, 819 (1963)
27. G. Schwarz: J. Phys. Chem. **71**, 4021 (1967)
28. R. Nackaerts, L. De Maeyer, L. Hellemans: J. Electrostat. **7**, 169 (1979)
29. E.G. Guggenheim: *Thermodynamics* (North-Holland, Amsterdam 1967)
30. M. Eigen, L. De Maeyer: In: *Techniques of Organic Chemistry*, Vol. VIII, Part 2, ed. by S.L. Friess, A. Weissberger (Interscience, New York 1961) p. 895
31. R. Huisgen, H. Walz: Chem. Ber. **89**, 2616 (1956)
32. J.A. Walmsley: J. Phys. Chem. **82**, 2031 (1978)
33. J. Jadżyn, J. Małecki, C. Jadżyn: J. Phys. Chem. **82**, 2128 (1978)
34. J.-M. Dumas, M. Guerin, A. Kribii: J. Chim. Phys. **81**, 333 (1984)
35. R.F.W. Hofmann: J. Phys. Chem. **78**, 2341 (1974)
36. J. Jadżyn, L. Hellemans: Acta Phys. Polon. **A67**, 1093 (1985)
37. F.S. Parker, K.R. Bhaskar: Biochemistry **7**, 1286 (1980)
38. J.J. Feher, L.D. Wright, D.B. McCormick: J. Phys. Chem. **78**, 250 (1974)
39. M. Kunst, D. van Duijn, P. Bordewijk: Z. Naturforsch. **A34**, 369 (1979)
40. P. Mercier, C. Sandorfy, D. Vocelle: J. Phys. Chem. **87**, 3070 (1983)
41. M. Costas, D. Patterson: J. Chem. Soc., Faraday Trans. I **81**, 655 (1985)
42. J. Jadżyn, L. Hellemans: Ber. Bunsenges. Phys. Chem. **97**, 205 (1993)
43. K.S. Cole, R.H. Cole: J. Chem. Phys. **9**, 341 (1941)
44. J. Jadżyn, B. Żywucki, K.Prałat: Acta Phys. Polon. **A68**, 833 (1985)
45. C.J.F. Böttcher, P. Bordewijk: *Theory of Electric Polarization*, Vol. 2 (Elsevier, Amsterdam 1978)

1.4 Dielectric relaxation processes in condensed matter under pressure

A. Würflinger and S. Urban

1.4.1 Usefulness of high pressure studies and the equation of state

1.4.1.1 Establishment of phase diagrams

Pressure is an important parameter in materials science: it induces phase transformations, it confines the coexistence range of particular phases, it

changes the intermolecular distance thus altering the intermolecular potential. The high compressibility of molecular and liquid crystals make these materials excellent systems for studying the influence of moderate pressures on various physical and chemical properties [1]. Liquid crystals exhibit a wealth of polymorphism, where often pressure-induced or pressure-limited phases are observed. Therefore the application of pressure is indispensable for a full description of the phase behaviour. Many high-pressure devices are described in literature in order to establish phase diagrams or to investigate pecularities such as reentrant or multicritical phenomena [2–7]. In particular thermal methods [8–10] (differential thermal analysis, DTA [11–14], differential scanning calorimetry, DSC [15–17], and thermobarometry [6, 18, 19]) are widely used to detect phase transitions.

Using DTA or DSC, pressure-induced nematic phases (between different smectic and isotropic phases) have been found recently in 4-*n*-decyloxy-4′-cyanobiphenyl (10OCB) [16], 5-*n*-decyl-2-(4′-isothiocyanatophenyl)-1,3-dioxane (10DBT) [20], *n*-octyl-isothio-cyanato-biphenyl (8BT) [21], and in some longer *n*-alkylcyanobiphenyls [22]. These findings corroborate that the nematic state is in general favoured with increasing pressure. Broadening of the nematic phase region was also observed for other not rod-like liquid crystals [19, 23, 24]. For smectic compounds both pressure-induced and pressure-limited phases are reported [2, 25–27]. Peculiar pressure effects are also noted for cubic, columnar and banana-shaped phases [12, 28–30].

In Fig. 1.32 we present examples of a pressure-induced nematic phase in 8BT and a pressure-limited smectic A phase in 2,3-dicyano-4-hexyloxyphenyl-trans-4-butyl-cyclohexane-1-carboxylate (CNCN). In the figure for 8BT transitions between crystal (Cr), smectic (crystal) E (CrE), and the isotropic phase (Is) are displayed. At high pressures the clearing line splits, and above a triple point (389 K, 190 MPa) a new phase appears that was interpreted as a nematic phase [21]. This was recently corroborated by pVT measurements (cf. next chapter) [31]. In Fig. 1.32b CNCN exhibits a smectic A phase, S_A, which is pressure-limited below a triple point of 135 MPa and

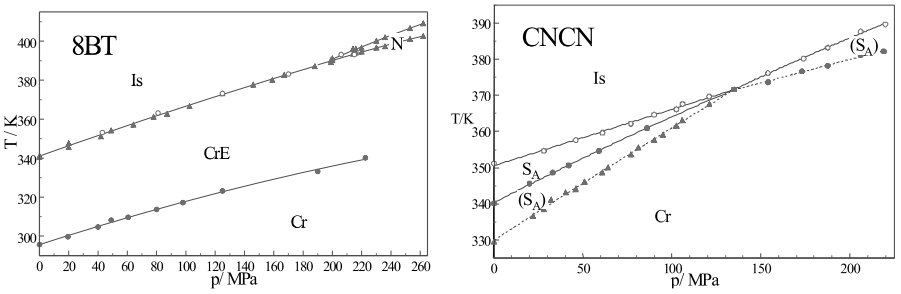

Fig. 1.32. (**a**) Phase diagram of 8BT, △ • DTA, ○ pVT (**b**) Phase diagram of CNCN

371 K [26]. The smectic phase can be distinctly supercooled, thus the smectic phase region may be considerably extended to lower temperatures and to higher pressures, indicated in the figure as (S_A). This metastable smectic phase exists above the triple point as well. Such a behaviour was also observed for 4-cyanobenzyl-5-(4-*n*-octyloxybenzoyl-oxy)-2-undecyloxybenzoate [25].

1.4.1.2 *pVT* measurements

Moreover is the knowledge of the equation of state necessary for a full discussion of physical properties. The intermolecular distance can be varied in high-pressure experiments, in particular isothermal, isobaric, and isochoric state changes can be distinguished. It will be shown below that relaxation properties depend significantly on the pathway chosen. The density change along a phase transition yields useful information about the configurational entropy and the volume dependence of the intermolecular potential.

Experimental methods for density and pVT measurements are described in [2, 3, 9, 32]. The classical method of measuring volume changes by a moving piston was recently improved and applied to the study of various liquid crystals [20, 25, 33, 34]. As an example we show in Fig. 1.33 a volume-pressure plot for 8BT [31]. The steps in the isotherms present the volume change due to the transition CrE → Is. At the highest temperature an additional small step is visible, corroborating the splitting of the clearing line as detected by DTA. In Fig. 1.33b the phase diagram is shown together with several isochores both for the smectic and isotropic phase, which have been calculated from the pVT data. The lower right part of the phase region belongs to the supercooled or superpressurized smectic E phase. Clearly, the slope of the isochoric lines $(\partial p/\partial T)_V$, is larger than the slope $(\partial p/\partial T)_{tr}$ of the CrE → Is transition line. These features will be discussed in the following chapters.

Many pVT data were established by Japanese researchers using also the displacement of a piston [35–38]. Instead of a moving piston a bellows cell

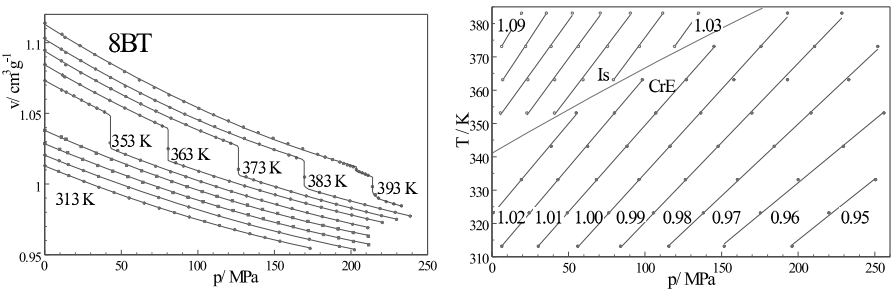

Fig. 1.33. (**a**) Specific volumes of 8BT as a function of pressure (**b**) Isochores for the smectic and isotropic phases of 8BT in steps of 0.01 cm^3g^{-1}

may be employed [39–41], but its use for solid phases is limited. Kuss employed a piezometer with mercury separation [42]. Horn et al. determined pVT data from high-pressure refractive index measurements [43]. The Clausius-Clapeyron equation enables to calculate enthalpy and entropy changes from the volume steps measured along a phase transition. It is very difficult to measure the pressure dependence of transition enthalpies in a straightforward way [44].

1.4.1.3 Entropy separation

Using standard thermodynamics the entropy change, ΔS_{tr}, accompanying a phase transition can be split into a constant-volume (configurational), $\Delta S_{tr,V}$, and a volume-dependent (dilational), ΔS_{dil}, part:

$$\Delta S_{tr} = \Delta S_{tr,V} + \Delta S_{dil} = \Delta S_{tr,V} + (\partial p/\partial T)_V \cdot \Delta V_{tr} \ .$$

This equation may be rearranged in combining it with the Clausius-Clapeyron equation: $\Delta S_{tr} = (\partial p/\partial T)_{tr} \cdot \Delta V_{tr}$, yielding

$$\Delta S_{tr,V} \equiv \Delta S_{\mathrm{conf}} = [(\partial p/\partial T)_{tr} - (\partial p/\partial T)_V]\, \Delta V_{tr} \ , \text{ or}$$
$$\Delta S_{\mathrm{conf}}/\Delta S_{tr} = [(\partial p/\partial T)_{tr} - (\partial p/\partial T)_V] \,/\, (\partial p/\partial T)_{tr}$$

The difference of the slope of the phase transition line and the slope of isochores determines the entropy splitting. If the isochores in a neighbouring phase go parallel to the phase line (which means that the density remains constant in that phase along the phase boundary), then the configurational part of the entropy change is zero and ΔS_{tr} is totally volume-dependent. The more the slopes $(\partial p/\partial T)_{tr}$ and $(\partial p/\partial T)_V$ differ, the larger is the configurational part.

There is some discussion in the literature about the significance of this approach, which anticipates a metastable supercooled or superpressurized state [39, 45–49]. Karasz et al. [47] have shown that the entropy separation depends on the path chosen, and consequently isochores for the phase above or below the phase line have to be considered. Usually $(\partial p/\partial T)_V$ of the liquid phase is taken for the melting process (or clearing transition in case of liquid crystals). However, it should be checked, whether the slopes of the isochoric lines are similar in both the high- and low-temperature phase [33, 49].

This entropy separation concept has been widely employed for the nematic-isotropic transition of liquid crystals [6, 19, 24, 33, 34, 39, 43, 49–52] and recently also for the smectic-isotropic transition [20, 25, 31]. For rod-like nematogens the configurational part amounts approximately to half of the total entropy change. For laterally aryl-branched liquid crystals significantly larger configurational entropies have been found [25, 34]. On the other hand, much smaller values are reported for dilaterally substituted nematogens that was interpreted with a lower minimum density required for the nematic order [19]. Molecules which are more bulky and flexible have a larger excluded volumen

that results in a stronger volume dependence of the entropy. Comparison of recent results shows that $\Delta S_{\mathrm{conf}}/\Delta S_{tr}$ depends more on the molecular shape of the molecules than on whether a nematic-isotropic or smectic-isotropic transition is considered.

1.4.1.4 Volume dependence of the clearing line

pVT measurements enable also to analyse the interaction potential involved in the clearing transition [20, 31, 33, 35–38, 40, 41, 43, 49–51, 53–55]. After Maier and Saupe the clearing temperature is expressed as a power law: $T_{\mathrm{NI}} \sim V^{-\gamma}$, where $\gamma = 2$ results from considering only the attractive part of the interaction potential [56]. The exponent γ can be derived from the volume dependence of the clearing line: $\gamma = -\partial \ln T_{\mathrm{NI}}/\partial \ln V_{\mathrm{NI}}$. Experimental results show that γ is distinctly larger than 2 which means that the repulsive interaction part cannot be neglected. Recently this approach was also employed to the smectic – isotropic transition [20, 31].

1.4.1.5 Density dependencies of the dielectric relaxation and the order parameter

Both theoretical and experimental studies on the order parameter S and nematic potential q in nematic phases reveal that the equation of state provides a better understanding of the roles of attractive and repulsive molecular interactions [54, 57–61]. The relation $q \sim S$ (which follows from the Maier-Saupe theory) is roughly fulfilled for isobaric, but not for isochoric state changes [61]. This behaviour can be better understood in the light of a thermodynamic treatment [58].

The pressure dependence of the relaxation time is expressed as the so-called activation volume which can be roughly understood as the extra space needed for a reorientation of a particular internal motion. The energy barrier against a rotation can be evaluated along isobaric (activation enthalpy) and isochoric (activation energy) changes. The difference provides useful information about the steric effects associated with the dynamic process [61–63].

1.4.2 Experimental methods

The measurement of dielectric properties is described in textbooks and review articles [64–67]. High-pressure experiments are reviewed in [54, 68], for other recent high pressure studies see [5, 60, 69–76]. We mention a few problems arising in dielectric measurements under high pressure. In any case the substance to be studied must be separated from the pressure medium, if compressed gases or fluids are used to create the pressure. Contamination of the sample with the compressed fluid may significantly alter the measured properties. Furthermore chemical reactions of the measured substance with the

material of the capacitor and its sealings has to be avoided. The deformation of the capacitor and the occurrence of pressure gradients has to be taken into account. For the study of anisotropic systems (for liquid crystalline phases at least two different components of the dielectric tensor have to be considered) special devices must be designed which allow to align the sample.

As an example we mention a set-up described in [60], see Fig. 1.34. The capacitor is emerged in a high-pressure vessel made of copper beryllium alloy. The pressure is transmitted by compressed oil. In previous dielectric measurements the pressure was created by compressed gases [54, 77]. This was advantageous in that the hysteresis pressure was negligible and the measurements could easily be extended to low temperatures. However, it was difficult to avoid a slow diffusion of the pressurized gas into the sample, although the cylindrical dielectric cell was closed by a moving piston and additional sealings. The new device enables one to attain higher temperatures (up to $\sim$ 400 K) and to perform repeated runs with the same sample similarly to

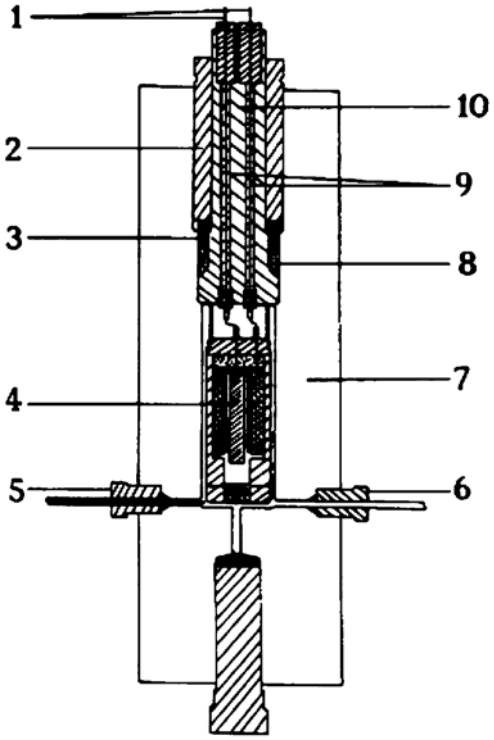

Fig. 1.34. High pressure set up for dielectric measurements – 1: connections for the electrical leads, 2: screw, 3: pressure ring, 4: three terminal capacitor, 5: screw with thermo-couple, 6: inlet for the pressurizing medium, 7: high pressure vessel, 8: sealing, 9: electrical feed-through, 10: Bridgman piston

the improved high-pressure dilatometer [34]. The highest pressure attainable is 230 MPa. For measuring the dielectric constant of nematic phases the sample is aligned by superimposing a bias field. Thus $\varepsilon_{||}$ can be obtained for nematogens whose dipole moment lies mainly parallel to the long molecular axis.

Another interesting high-pressure set-up was established by Urban [69], see Fig. 1.35. The high-pressure vessel is built with non-magnetic material that allows to apply a magnetic field for orienting the sample. The dielectric cell consists of a parallel-plate capacitor, in order to achieve a definite orientation of the magnetic field (0.6 T), either parallel or perpendicular to the nematic director (by turning the electromagnet by 90°). Thus also the perpendicular component $\varepsilon_{\perp}$ can be determined. Again the pressure is created by compressed oil. Instead of a moving piston the sample holder is sealed

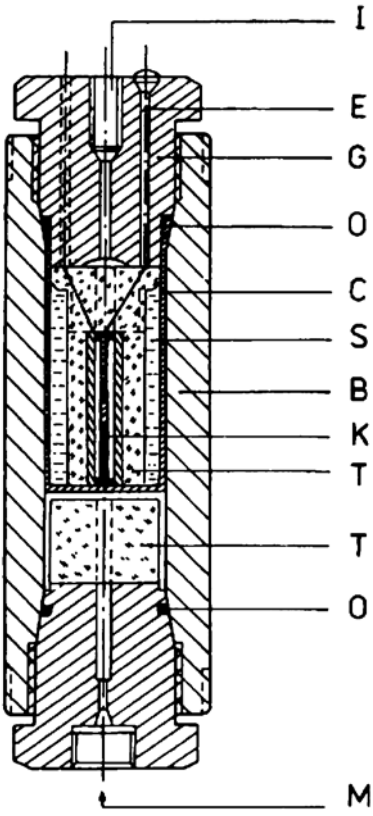

Fig. 1.35. B – corps of beryllium bronze, G – plug of beryllium bronze, I – sample inlet, E – electrical feed-through, C – cylindrical capsule of plastic material, S – sample, K – parallel-plate capacitor, T – teflon parts, O – o-rings, M – pressurizing oil inlet

by a screw plug which closes simultaneously the high-pressure corps. The apparatus is used up to 150 MPa and 350 K.

Lee et al. [73] report on a high pressure coaxial probe for measuring the dielectric spectra from 200 MHz to 18 GHz up to pressures of 18 MPa. The open-ended probe design is presented in Fig. 1.36. A semirigid coaxial cable (model EZ 86/M17, Suhner) was used that had a 50 Ω characteristic impedance and a usable bandwith of 60 GHz. A length of high pressure copper tubing jacket was soldered onto the coaxial cable. High pressure test runs were performed up to 22 MPa.

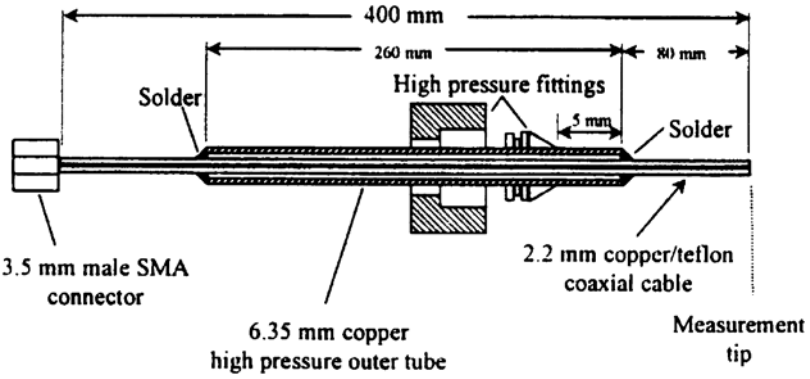

Fig. 1.36. High pressure coaxial probe

1.4.3 Dielectric relaxation and activation quantities

From the measurements of the frequency-dependent permittivity the static dielectric constant (ε_s) and the relaxation time τ are obtained. In the simplest case of a single relaxation time the complex permittivity, $\varepsilon^* = \varepsilon' - \mathrm{i}\varepsilon''$ can be described with the Debye equation [78]. In general deviations from the Debye behaviour occur, and correspondingly the loss curves have to be fitted to extensions, such as the equation of Havriliak-Negami or Jonscher:

$$\text{Havriliak-Negami:} \quad \varepsilon^*(\omega) - \varepsilon_\infty = \frac{\varepsilon_s - \varepsilon_\infty}{\left[1 + (i\omega\tau_0)^{1-\alpha}\right]^\beta}$$

$$\text{Jonscher:} \quad \varepsilon''(\omega) = \frac{A}{(\omega/\omega_p)^{-m} + (\omega/\omega_p)^{1-n}}$$

The equation after Havriliak-Negami contains Cole–Cole ($\beta = 1$), Cole-Davidson ($\alpha = 0$), and Debye ($\alpha = 0$ and $\beta = 1$) as special cases. In these equations τ_0 and $1/\omega_p$ mean the principal relaxtion time around the maximum of a distribution of relaxation times. It is convenient to define the relaxtion

time $\tau = 1/\omega_{\max}$ from the maximum of the loss curve that does not necessarily coincide with τ_0 (this is only the case for Debye and Cole–Cole). For the evaluation of τ and the fitting with respect to the adjustable parameters ε_∞, α, β, τ_o, A, m, n, ω_p see [79]. Before the fitting an eventual contribution from ionic conductivity has to be subtracted.

The temperature and pressure dependence of the relaxation time τ is usually treated in the frame of rate theories [64, 80]. The most popular presentation of the temperature dependence employes the Arrhenius equation provided that $\ln \tau$ is a linear function of $1/T$. This can be easily checked by an appropriate plot, the slope of which yields the activation enthalpy:

$$\Delta^{\#}H = R \left(\frac{\partial \ln \tau}{\partial (1/T)} \right)_p$$

This activation quantity, $\Delta^{\#}H$, is often called activation energy (in atmospheric pressure measurements). However, for the "high-pressure community" the activation energy, $\Delta^{\#}U$, is retained for the temperature dependence of τ at constant volume:

$$\Delta^{\#}U = R \left(\frac{\partial \ln \tau}{\partial (1/T)} \right)_V = \Delta^{\#}H - T \left(\frac{\partial p}{\partial T} \right)_V \Delta^{\#}V$$

where the activation volume, $\Delta^{\#}V$, expresses the pressure dependence of the relaxation time:

$$\Delta^{\#}V = RT \left(\frac{\partial \ln \tau}{\partial p} \right)_T .$$

The relation between $\Delta^{\#}H$ and $\Delta^{\#}U$ may be checked, if $(\partial p/\partial T)_V = \alpha/\beta$ has been calculated from pVT data or if α (thermal expansivity) and β (compressibility) are available from other sources. This was done for 5CB and 5PCH (Table 5, [54, p.181]) resulting in good agreement within the limits of experimental errors.

It will be shown below that $\Delta^{\#}H$ and $\Delta^{\#}U$ may be significantly different (see also Sect. 4.2.6 in [81]). Many relationships between the activation parameters have been established and discussed [54, 64, 68, 82]. For the discussion of density effects the comparison of the slopes $(\partial p/\partial T)_V$ and $(\partial p/\partial T)_\tau = \Delta^{\#}H/\left(T\Delta^{\#}V\right)$ is interesting, resulting in the expression:

$$\Delta^{\#}U = T \left[\left(\frac{\partial p}{\partial T} \right)_\tau - \left(\frac{\partial p}{\partial T} \right)_V \right] \Delta^{\#}V .$$

When the two thermal pressure coefficients are equal, then the (isochoric) activation energy is zero and the relaxation process is strongly density-dependent.

Another important relation expresses the volume dependence of the relaxation time:

$$\left(\frac{\partial \ln \tau}{\partial \ln V}\right)_T = -\frac{\Delta^{\#} V}{\beta RT} ,$$

where β is the compressibility [83]. The last equations show that the dependencies of both the pressure (yielding the activation volume) and the volume (yielding $(\partial p/\partial T)_V$ and the compressibility) are needed for a full description of the activation parameters.

1.4.4 Selected results

As an example we present results for some 4-(trans-4-alkylcyclohexyl)-benzonitriles (nPCH). They are typical representatives of rod-like liquid crystals displaying nematic phases, which have been synthesized and characterized by Eidenschink et al. [84–86]. Crystal and thermal properties are reported by Haase et al. [87, 88]. Comparison with other nematogens has been recently presented [89]. The phase diagrams , pVT data, and dielectric properties have been determined under pressure for various nPCHs, see Table 1.3. For shorter alkyl chain lengths monotropic nematic and smectic phases are observed. In the case of 4PCH a pressure-induced nematic phase (above a triple point of 320 K and 17 MPa) was detected by Friedrich [13, 90]. This finding was corroborated through pVT experiments by Shirakawa et al. [38] and discussed in the frame of the Pople-Karasz-Chandrasekhar theory [95]. Furthermore we note a high pressure NMR study by Emsley et al., who determined the pressure dependence of the orientational order of a biaxial solute dissolved in 7PCH [96].

Figure 1.37 compares the phase diagrams of the nPCHs, $n = 5 \ldots 8$. Evidently 6PCH has the smallest nematic range, whereas it is largest for 7PCH. The slopes of the transition lines are similar, being ~ 0.3 K/MPa for the melting (only smaller for 5PCH: ~ 0.25 K/MPa), ~ 0.44 K/MPa for the clearing line.

Table 1.3. Transition temperatures and initial slopes (in K/MPa) at 1 atm of selected nPCHs. *(N–I) monotropic, **Cr → Is transition

	Cr → N		N → Is		references for hp studies		
sample	T/K [84]	dT/dp	T/K [84]	dT/dp	DTA	pVT	diel.
2PCH	277*		313	0.373**	[90]		
3PCH	309	0.295	319	0.481	[13, 90]	[37, 42]	
4PCH	314*		313.5	0.426**	[13, 90]	[38]	
5PCH	303	0.246	328	0.440	[91]	[35, 42]	[91]
6PCH	315	0.298	320	0.456	[49]	[49]	[92]
7PCH	303	0.311	332	0.420	[60, 90]	[42]	[60]
8PCH	308 [87]	0.298	328 [87]	0.412	[50]	[50]	[93]
12PCH	332.5 [85]	0.295	334.3 [85]	0.361	[94]		

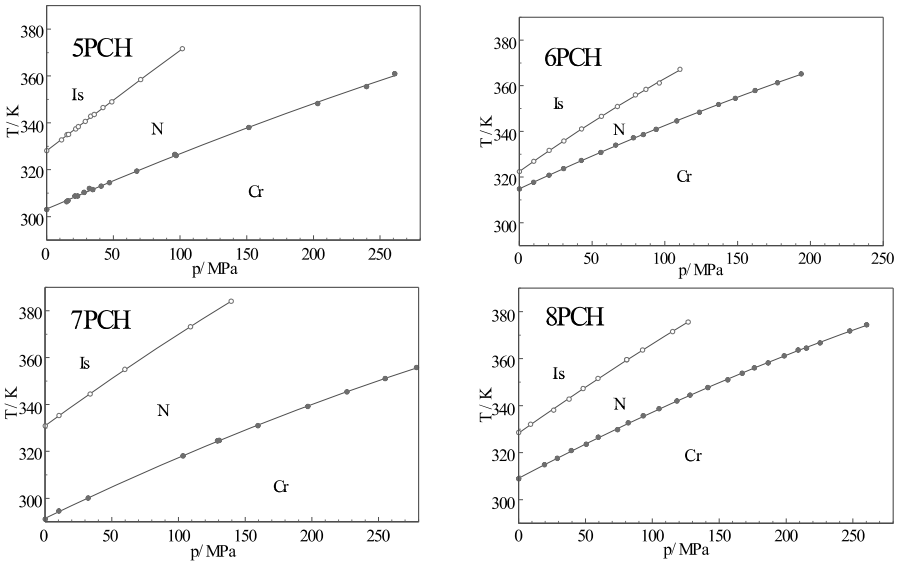

Fig. 1.37. Phase diagrams for nPCHs, $n = 5$–8, established with DTA

Figure 1.38 shows a typical dielectric spectrum of 8PCH at 346 K. Increasing pressure has the same effect as lowering the temperature: it shifts the loss curves to lower frequencies. From the frequency of maximum loss the relaxation time τ is derived that is plotted in Fig. 1.39 as $\ln \tau$ against pressure. Three different lines indicate the evaluation of the activation quantities: $\Delta^{\#}V$ (mean slope of the 340 K isotherm), $\Delta^{\#}H$ (vertical line at 80 MPa), and $\Delta^{\#}U$ (along the 312 $\mathrm{cm^3 mol^{-1}}$ isochore). Figure 1.39 shows that there is some bending in the isotherms that was also observed for alkylcyanobiphenyls. Particularly for 6PCH the corresponding plot exhibits a strong curvature in the isotherms that aggravated the evaluation of the activation quantities considerably. This is apparently due to the rather small nematic range. Using the slope at $\ln \tau = -17.5$ results in $\Delta^{\#}V \approx 80\,\mathrm{cm^3 mol^{-1}}$ in rough agreement with the other nPCHs.

In Figs. 1.40 and 1.41 the activation quantities are compared. $\Delta^{\#}V$ decreases with increasing temperature. There is some variation with the chain length. The activation enthalpy is practically independent of pressure, whereas the activation energy decreases a little bit with increasing volume. The most interesting result is the fact that $\Delta^{\#}U$ amounts to approximately half of the $\Delta^{\#}H$ value. This finding was first noted by Brückert et al. for alkylcyanobiphenyls [62]. Moreover, comparison of the dielectric relaxation times for the isotropic and nematic phase allow to calculate the nematic potential q and order parameter S [81]. Estimates for 8PCH show that q comprises only to 10–20 % of the total energy barrier [93].

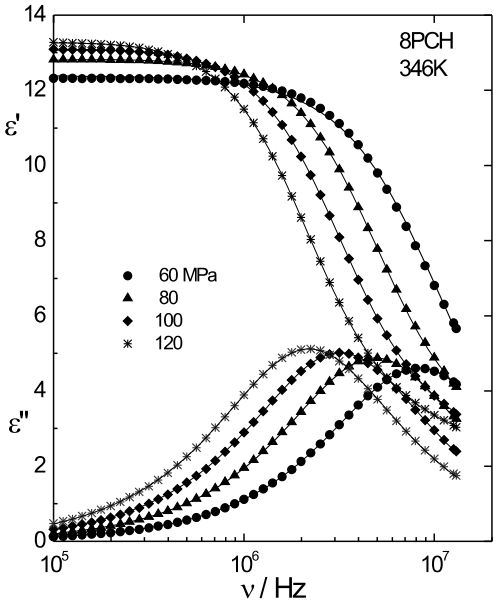

Fig. 1.38. Dielectric spectra, $\varepsilon'(\nu)$ and $\varepsilon''(\nu)$, for 8PCH at 346 K and various pressures

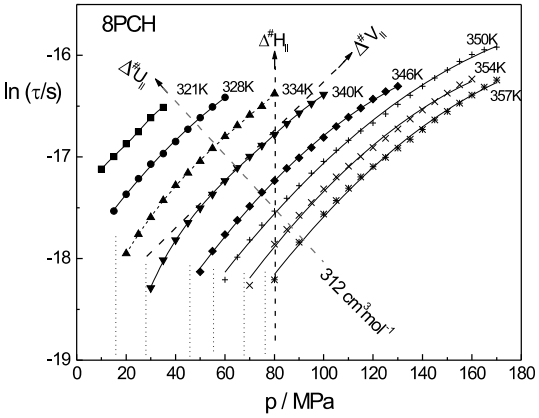

Fig. 1.39. Logarithm of the dielectric relaxation τ as a function of pressure for various temperatures. The three dashed lines show the different paths for the evaluation of the activation quantities: $\Delta^{\#}V$, $\Delta^{\#}H$, and $\Delta^{\#}U$

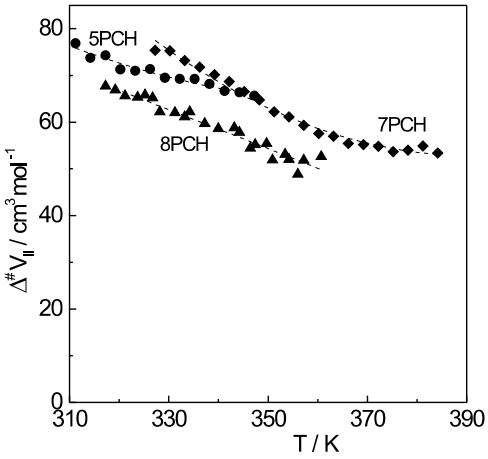

Fig. 1.40. Comparison of the activation volumes for 5PCH, 7PCH, and 8PCH

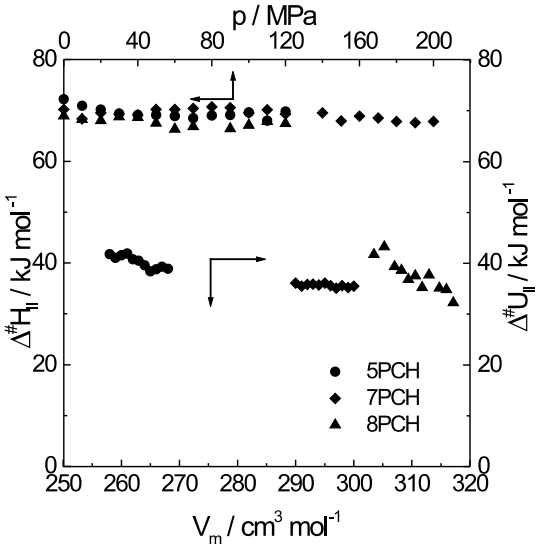

Fig. 1.41. Comparison of the energy parameters, $\Delta^{\#}H$ and $\Delta^{\#}U$, for 5PCH, 7PCH, and 8PCH

Finally, we would like to mention that the "inversed" nPCHs do not reveal nematic phases. Knowing that increasing pressure favours in general the occurrence of a nematic phase, we investigated recently 5HCP up to 300 MPa, without any indication of a pressure-induced phase [97]. Dunmur et al. have provided a detailed analysis of the relationships between molecular properties and different molecular cores of pentylcyano-mesogens [98]. They note that the lack of flexibility in the aromatic ring attached to the alkyl chain prevents the adoption of linear conformations, which would favour a nematic phase.

1.4.5 Summary

It was shown that the employment of pressure as an additional parameter is very useful for a better understanding of physical properties of liquid crystals, in particular, when pVT data are available. The experimental methods for dielectric and pVT measurements under pressure have been shortly described.

We repeat some important applications in the frame of high pressure investigations:

- Establishment of p-T phase diagrams.
- Isothermal, isobaric, and isochoric state changes can be distinguished.
- Splitting of the transition entropy into a constant-volume and a volumen-dependent part.
- Volume dependence of the clearing line enables to analyse the interaction potential.
- Evaluation of the activation volume and the (isochoric) activation energy.
- The difference between $\Delta^{\neq}H$ and $\Delta^{\neq}U$ amounts to $\sim 50\%$.

Some typical results are presented for nPCHs.

Acknowledgments. The authors appreciate a collaboration for many years between the Ruhr University of Bochum and the Jagiellonian University of Kraków. SU acknowledges financial support by the Polish Government KBN Grant No 2 P03B 052 22.

References

1. R.J. Hemley: *Effects of high pressure on molecules*, in: Ann Rev. Phys. Chem. **51**, 763 (2000); R.J. Hemley, P. Dera: *Molecular Crystals*, in: Rev. Min. Geochem. 41, 335 (2000)
2. P. Pollman: *High Pressure Investigations*, in: Handbook of Liquid Crystals, Vol. **1**, ed. by D. Demus, J. Goodby, G.W. Gray, H.W. Spiess, V. Vill (Wiley-VCH, Weinheim 1998) p. 355
3. G.R. Van Hecke: *Phase transitions and the effect of pressure*, in: Physical Properties of Liquid Crystals, Nematics, EMIS Datareview Series 25, ed. by D.A. Dunmur, A. Fukuda, G.R. Luckhurst (Institution of Electrical Engineers, London 2001) p. 127

4. P.E. Cladis, R.K. Bogardus, D. Aadsen: Phys. Rev. A **18**, 2292 (1978)
5. D.S.S. Rao, S.K. Prasad, S. Chandrasekhar, S. Mery, R. Shashidhar: Mol. Cryst. Liq. Cryst. Science & Technology Section A **292**, 301 (1997)
6. A. Anakkar, A. Daoudi, J.M. Buisine, N. Isaert, F. Bougrioua, Hat Nguyen: Liq. Cryst. **20**, 411 (1996); A. Anakkar, M. Ismaili, N. Isaert, Hat Nguyen: Mol. Cryst. Liq. Cryst. **362**, 269 (2001)
7. J. Przedmojski, S. Gierlotka, B. Pura, R. Wiśniewski: Cryst. Res. Technol. **23**, K72 (1988)
8. J. Thoen: *Thermal Methods*, in: Handbook of Liquid Crystals, Vol. **1**, ed. by D. Demus, J. Goodby, G.W. Gray, H.W. Spiess, V. Vill (Wiley-VCH, Weinheim 1998) p. 310
9. A. Würflinger: *Pure Component Phase Changes 1b, Liquid and Solid*, in: Experimental Thermodynamics Volume VII, Measurement of the thermodynamic properties of multiple phases, ed. By Th.W. de Loos, R.D. Weir (IUPAC upgrade, 2002)
10. S.L. Randzio: *Recent Developments in Calorimetry*, in: Annual Reports on the Progress of Chemistry, The Royal Society of Chemistry (1998) p. 433; J. Therm. Analysis **48**, 573 (1997); Chem. Soc. Rev. **25**, 383 (1996)
11. S. Chandrasekhar, R. Shashidhar: *High-pressure studies of liquid crystals*, in: Advances in Liquid Crystals, Vol. 4, ed. by G.H. Brown (Academic Press, London 1979) p. 84
12. Y. Maeda, D.S.S. Rao, S.K. Prasad, S. Chandrasekhar, S. Kumar: Liq. Cryst. **28**, 1679 (2001)
13. G.M. Schneider, A. Bartelt, J. Friedrich, H. Reisig, A. Rothert: Physica B **139** & **140**, 616 (1986)
14. M. Hartmann, M. Jenau, A. Würflinger, M. Godlewska, S. Urban: Z. Physik Chem. **177**, 195 (1992)
15. C. Schmidt, M. Rittmeier-Kettner, H. Becker, J. Ellert, R. Krombach, G.M. Schneider: Thermochim. Acta **238**, 321 (1994)
16. C. Schmidt, C. Ernst, S. Masberg, C. Meyer-Inci, H. Becker, G.M. Schneider: Polish J. Chem. **71**, 1742 (1997)
17. G.W.H. Höhne, W.F. Hemminger, H.J. Flammersheim: Differential Scanning Calorimetry (Springer, Berlin 1996)
18. J.M. Buisine, B. Soulestin, J. Billard: Mol. Cryst. Liq. Cryst. **97**, 397 (1983); **91**, 115
19. A. Daoudi, S. Longuemart, F. Roussel, C. Kolinsky, J.P. Bayle: Liq. Cryst. **28**, 291 (2001)
20. A. Würflinger, S. Urban: Phys. Chem. Chem. Phys. **3**, 3727 (2001)
21. S. Urban, A. Würflinger, A. Kocot: Liq. Cryst. **28**, 1331 (2001)
22. S. Urban, M. Massalska-Arodź, A. Würflinger, R. Dąbrowski: Liq. Cryst. **30**, in print (2003)
23. C. Ernst, G.M. Schneider, A. Würflinger, W. Weissflog: Ber. Bunsenges. Phys. Chem. **102**, 1870 (1998)
24. Y. Maeda, H. Furuya, A. Abe: Liq. Cryst. **21**, 365 (1996)
25. A. Würflinger, W. Weissflog: Z. Naturforsch. **55a**, 936 (2000)
26. S. Urban, A. Würflinger: Z. Naturforsch. **56a**, 489 (2001)
27. D. Guillon, J. Stamatoff, P.E. Cladis: J. Chem. Phys. **76**, 2056 (1982)
28. Y. Maeda, G.P. Cheng, S. Kutsumizu, S. Yano: Liq. Cryst. **28**, 1785 (2001)
29. W. Weissflog, I. Wirth, S. Diele, G. Pelzl, G. Schmalfuss, T. Schoss, A. Würflinger: Liq. Cryst. **28**, 1603 (2001)

30. D.S.S. Rao, S.K. Prasad, V. Prasad, S. Kumar: Phys. Rev. E **59**, 5572 (1999)
31. A. Würflinger, S. Urban: Liq. Cryst. **29**, 799 (2002)
32. W. Wedler: *Density*, in: Handbook of Liquid Crystals, Vol. 1, ed. by D. Demus, J. Goodby, G.W. Gray, H.W. Spiess, V. Vill (Wiley-VCH, Weinheim 1998) p. 334
33. A. Würflinger, M. Sandmann: *Equation of state for nematics*, in: Physical properties of liquid crystals, Nematics, EMIS Datareview Series, Vol. 25, ed. by D.A. Dunmur, A. Fukuda, G.R. Luckhurst (Institution of Electrical Engineers, London 2001), p. 151
34. A. Würflinger, M. Sandmann, W. Weissflog: Z. Naturforsch. **55a**, 823 (2000)
35. H. Ichimura, T. Shirakawa, T. Tokuda, T. Seimiya: Bull. Chem. Soc. Jpn. **56**, 2238 (1983)
36. T. Shirakawa, Y. Kikuchi, T. Seimiya: Thermochim. Acta **197**, 399 (1992); C. Hanawa, T. Shirakawa, T. Tokuda: Chem. Lett. Jpn. **10**, 1223 (1977)
37. T. Shirakawa, M. Arai, T. Tokuda: Mol. Cryst. Liq. Cryst. **104**, 131 (1984)
38. T. Shirakawa, H. Ichimura, I. Ikemoto: Mol. Cryst. Liq. Cryst. **142**, 101 (1987)
39. A. Abe, Su Y. Nam: Macromolecules **28**, 90 (1995); ibid. **29**, 3337 (1996); A. Abe, H. Furuya, R.N. Shimizu, Su Y. Nam: Macromolecules **28**, 96 (1995)
40. P.H. Keyes, W.B. Daniels: J. Phys. Colloq. **C3 40**, 380 (1979)
41. W.M. Lampe, P.J. Collings: Phys. Rev. A **34**, 524 (1986); C.S. Johnson, P.J. Collings: J. Chem. Phys. **79**, 4056 (1983); R.V. Tranfield, P.J. Collings: Phys. Rev. A **25**, 2744 (1982)
42. E. Kuss: Mol. Cryst. Liq. Cryst. **47**, 71 (1978); ibid **76**, 199 (1981)
43. R.G. Horn: J. Physique **39**, 167 (1978); R.G. Horn, T.E. Faber: Proc. Roy. Soc. London A **368**, 199 (1979)
44. G.M. Schneider: Thermochim. Acta **88**, 159 (1985)
45. R. Sandrock, G.M. Schneider: Ber. Bunsenges. Phys. Chem. **87**, 197 (1983)
46. A. Würflinger: Colloid Polymer Sci. **262**, 115 (1984); M. Jenau, J. Reuter, J.L. Tamarit, A. Würflinger: J. Chem. Soc. Faraday Trans. **92**, 1899 (1996)
47. F.E. Karasz, P.R. Couchman, D. Klempner: Macromolecules **10**, 88 (1977)
48. A. Abe, T. Takeda, T. Hiejima, H. Furuya: Macromolecules **34**, 6450 (2001)
49. M. Sandmann, F. Hamann, A. Würflinger: Z. Naturforsch. **54a**, 281 (1999)
50. M. Sandmann, F. Hamann, A. Würflinger: Z. Naturforsch. **52a**, 739 (1997)
51. M. Sandmann, A. Würflinger: Z. Naturforsch. **53a**, 233; 787 (1998)
52. R.A. Orwoll, V.J. Sullivan, G.C. Campbell: Mol. Cryst. Liq. Cryst. **149**, 121 (1987)
53. The Molecular Physics of Liquid Crystals, ed. by G.R. Luckhurst, G.W. Gray (Academic Press 1979); J.W. Emsley, G.R. Luckhurst, S.W. Smith: Mol. Phys. **70**, 967 (1990)
54. S. Urban, A. Würflinger: Adv. Chem. Phys. **98**, 143 (1997); S. Urban, H.G. Kreul, A. Würflinger: Liq. Cryst. **12**, 921 (1992)
55. J.R. McColl, C.S. Shih: Phys. Rev. Lett. **29**, 85 (1972); J.R. McColl: Phys. Lett. A **38**, 55 (1972)
56. W. Maier, A. Saupe: Z. Naturforsch. **14a**, 882 (1959); ibid **15a**, 287 (1960)
57. M.A. Bates, G.F. Luckhurst: Mol. Phys. **99**, 1365 (2001); Chem. Phys. Lett. **281**, 193 (1997)
58. A. Würflinger: Z. Naturforsch. **53a**, 141 (1998); A. Würflinger, S. Urban: ibid, 883 (1998)
59. S. Urban, A. Würflinger, B. Gestblom: Phys. Chem. Chem. Phys. **1**, 2787 (1999)

60. T. Brückert, D. Büsing, A. Würflinger, S. Urban: Z. Naturforsch. **50a**, 977 (1995); S. Urban, B. Gestblom, T. Brückert, A. Würflinger: Z. Naturforsch. **50a**, 984 (1995)
61. S. Urban, A. Würflinger, D. Büsing, T. Brückert, M. Sandmann, B. Gestblom: Polish J. Chem. **72**, 241 (1998)
62. T. Brückert, D. Büsing, S. Urban, A. Würflinger: Phys. Technol. Applic. Proceed. SPIE **3318**, 198 (1998)
63. Ph. Markwick, S. Urban, A. Würflinger: Z. Naturforsch. **54a**, 275 (1999)
64. N.E. Hill, W.E. Vaughan, A.H. Price, M. Davies: *Dielectric Properties and Molecular Behaviour*, ed. by T.M. Sugden (van Nostrand, London 1969)
65. S. Takashima: *Electrical Properties of Biopolymers and Membranes* (Adam Hilger, Bristol 1989); J.B. Hasted: *Aqueous Dielectrics* (Chapman & Hall, London 1973)
66. H. Kresse: Fortschr. Phys. **30**, 507 (1982)
67. S. Wróbel: this issue, Chap. 1.1
68. A. Würflinger: Int. Rev. Phys. Chem. **12**, 89 (1993)
69. S. Urban: Z. Naturforsch. **54a**, 365 (1999); S. Urban: Z. Naturforsch. **50a**, 826 (1995); S. Urban, A. Würflinger: Liq. Cryst. **27**, 1119 (2000)
70. M. Paluch, J. Zioło, S.J. Rzoska, P. Habdas: Phys. Rev. E **54**, 4008 (1996); M. Gorny, J. Zioło, S.J. Rzoska: Rev. Sci. Instrum. **67**, 4290 (1996)
71. W.G. Scaife, G. McMullin: Meas. Sci. Technol. **5**, 1576 (1994); High Press. Res. **13**, 77 (1994)
72. G.P. Johari, E. Whalley: J. Chem. Phys. **115**, 3274 (2001); and earlier papers
73. S.B. Lee, R.L. Smith, H. Inomata, K. Arai: Rev. Sci. Instrum. **71**, 4226 (2000)
74. S.P. Andersson, O. Andersson: Macromolecules **31**, 2999 (1998)
75. P. Czarnecki: Ferroelectr. Lett. Sect. **28**, 21 (2000)
76. S. Theobald, W. Pechhold, B. Stoll: Polymer **42**, 289 (2001)
77. A. Würflinger: Ber. Bunsenges. Phys. Chem. **82**, 1080 (1978); **84**, 653 (1980); U. Poser, A. Würflinger: Ber. Bunsenges. Phys. Chem. **92**, 765 (1988)
78. C.J.F. Böttcher, P. Bordewijk: Theory of Electric Polarisation II (Elsevier, Amsterdam 1978)
79. A. Würflinger: Ber. Bunsenges. Phys. Chem. **95**, 1040 (1991)
80. G. Williams: Trans. Faraday Soc. **60**, 1548 (1964)
81. S. Urban, A. Würflinger: this issue, Chap. 4.2
82. E. Whalley: in: Advances in High Pressure Research **1**, 43, ed. by R.S. Bradley (Academic, New York 1966)
83. H. Forsman, P. Andersson, G. Bäckström: J. Chem. Soc. Faraday Trans. 2, **82**, 857 (1986)
84. L. Pohl, R. Eidenschink, J. Krause, D. Erdmann: Phys. Lett. A **60**, 421 (1977); R. Eidenschink: Merck Kontakte **79**, 15 (1979)
85. R. Eidenschink, G.W. Gray, C. Hogg, A.R. Tajbakhsh: Mol. Cryst. Liq. Cryst. Lett. **112**, 181 (1984)
86. R. Eidenschink, D. Erdmann, J. Krause, L. Pohl: Angew. Chem. **89**, 103 (1977)
87. W. Haase, J. Loub, H. Paulus, M.A. Mokhles: Mol. Cryst. Liq. Cryst. **197**, 57 (1991); H. Paulus, W. Haase: Mol. Cryst. Liq. Cryst. Lett. **92**, 237 (1983)
88. W. Haase, R. Pendzialek: Mol. Cryst. Liq. Cryst. **97**, 209 (1983)
89. S. Urban, B. Gestblom, A. Würflinger: Mol. Cryst. Liq. Cryst. **331**, 113 (1999)
90. J. Friedrich: diplom thesis, Ruhr-University Bochum, Germany (1985)
91. T. Brückert, D. Büsing, A. Würflinger, S. Urban: Mol. Cryst. Liq. Cryst. **262**, 209 (1995)

92. Ph. Markwick, unpublished results
93. S. Urban, D. Büsing, A. Würflinger, B. Gestblom: Liq. Cryst. **25**, 253 (1998)
94. A. Bartelt, G.M. Schneider: Mol. Cryst. Liq. Cryst. **173**, 75 (1989); A. Bartelt: doctoral thesis, Ruhr-University Bochum, Germany (1988)
95. S. Chandrasekhar, R. Shashidhar: Ind. J. Pure Appl Phys. **9**, 975 (1971)
96. J.W. Emsley, G.R. Luckhurst, S.W. Smith: Mol. Phys. **70**, 967 (1990)
97. M. Massalska-Arodź, A. Würflinger, D. Büsing: Z. Naturforsch. **57a**, 233 (2002)
98. D.A. Dunmur, A.E. Tomes: Mol. Cryst. Liq. Cryst. **97**, 241 (1983)

2

Dynamic Susceptibility of Magnetic Systems

2.1 Dynamic susceptibility of paramagnetic and exchange-coupled spin systems

M. Bałanda

2.1.1 Introduction

Relaxation phenomena in magnetic materials cover a wide range of processes in which a new equilibrium state is reached after a change of the magnetic field. The relaxation effect is due to the exchange of energy between the spins and other degrees of freedom of the system. The process is usually characterized by its relaxation time τ, in which magnetization M_z will reach the equilibrium value M_0 after a change of the magnetic field from H to $H + \Delta H$, as follows:

$$\frac{dM_z}{dt} = \frac{M_0 - M_z}{\tau} \,. \tag{2.1}$$

The exchange of energy between the magnetic moments occurs with a speed of several orders higher than that between the spins and the crystal lattice. The spin-lattice relaxation is realized with the help of phonons and/or spin-waves. The relaxation course depends on the value of the applied magnetic field relative to the internal field H_i present in the substance. If $H \ll H_i$, there will be a small change in the directions of magnetic moments, which does not need interaction with the lattice. For $H \gg H_i$ a change in magnetization appears as a result of the change in the energy levels population and that change needs coupling to the lattice. Therefore, in order to investigate the spin-lattice relaxation, high constant magnetic fields parallel to the oscillating magnetic fields of low frequencies are needed to make the spin–spin relaxation negligible. On the other hand, fields of high frequencies and small amplitudes are necessary to study the spin–spin relaxation.

The inductive method of measurement the differential magnetic susceptibility $\chi_{\mathrm{AC}} = dM/dH$ is widely used for investigating the dynamic behavior

of the spin system. AC susceptibility is measured as a function of frequency of the alternating field, where static field, if any, is oriented parallel to the AC field. χ_{AC} is a complex value, with the imaginary component related to losses connected with the relaxation effects.

In this paper, basic ideas of the method will be presented. Next, a review will be given of the most important results on relaxation phenomena occurring both in paramagnetic, as well as in exchange-coupled magnetic systems, i.e. ferromagnets, spin–glasses and molecule–based magnets. The problems will be illustrated with the results obtained with the help of the AC susceptometer working in the frequency range of 5 Hz–10 kHz.

2.1.2 Magnetic susceptibility in alternating magnetic field

2.1.2.1 Real and imaginary components of χ_{AC}

Dynamic susceptibility, also called differential or AC susceptibility χ_{AC}, is defined as the response of the magnetization of the substance to a small change in the magnetic field, i.e. $\chi_{\mathrm{AC}} = dM/dH$. Let us consider a paramagnetic substance placed in an alternating magnetic field:

$$H(t) = H_0 + h\cos(\omega t)\ , \tag{2.2}$$

where H_0 is constant (may be zero), $\omega = 2\pi f$, f is frequency of the AC field, and h is the amplitude of the AC field. The amplitude is supposed to be small enough so that a linear response of the magnetization is obtained. Figure 2.1 (left) gives the general idea of the method. The magnetization related to $H(t)$ is given by the following equation:

$$\begin{aligned} M(t) &= M_0 + m\cos(\omega t - \theta) \\ &= M_0 + m\cos(\omega t)\cos\theta + m\sin(\omega t)\sin\theta\ . \end{aligned} \tag{2.3}$$

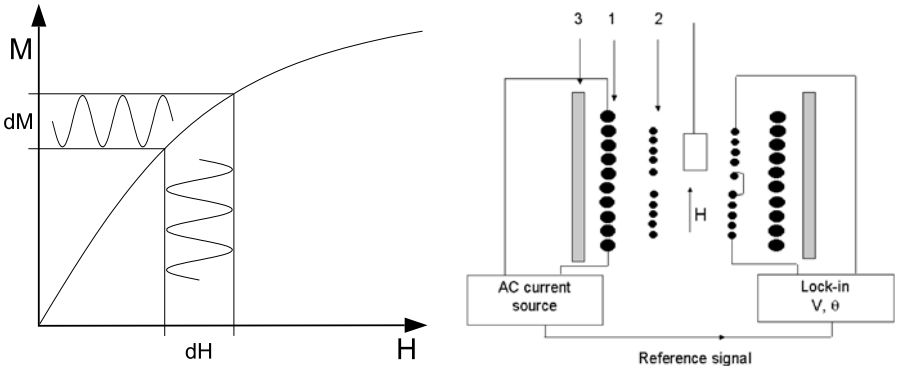

Fig. 2.1. *Left:* Variation of magnetization M upon alternating external field H. *Right:* Schematic picture of the AC susceptometer; 1 – primary coil, 2 – secondary coils, 3 – superconducting magnet

M_0 is the equilibrium magnetization due to the constant field H_0 and θ is the phase angle which describes the delay of $M(t)$ relative to $H(t)$. Taking

$$\chi' = \frac{m\cos\theta}{h} \quad \text{and} \quad \chi'' = \frac{m\sin\theta}{h} \tag{2.4}$$

one gets

$$M(t) = M_0 + \chi' h\cos(\omega t) + \chi'' h\sin(\omega t)\ . \tag{2.5}$$

The latter can be expressed [A] as $M_{\mathrm{AC}}(t) = M_0 + \chi_{\mathrm{AC}} h e^{i\omega t}$, where:

$$\chi_{\mathrm{AC}}(\omega) = \chi'(\omega) - i\chi''(\omega) = |\chi| e^{-i\theta}\ . \tag{2.6}$$

Thus, the AC magnetic susceptibility is a complex value with both real, χ', and imaginary, χ'', components dependent on ω and on H. The χ' component represents the response which is in phase with the driving field $H(t)$. The dependency of χ' on ω is called *magnetic dispersion*. The χ'' component is the out–of–phase component proportional to the energy absorbed from the field by the sample. The energy W absorbed per second per unit volume is given by:

$$W = \frac{\omega}{2\pi} \int\limits_{\text{cycle}} H\ dM = \frac{\omega}{2}\chi'' h^2\ . \tag{2.7}$$

This is why $\chi''(\omega)$ is often referred to as *magnetic absorption*. Magnetic absorption is caused by relaxation effects and leads to the phase shift θ between the magnetization and the field given by:

$$tg\theta = \chi''/\chi'\ . \tag{2.8}$$

For low frequencies of the oscillating field, χ' will be approximately equal to the static magnetic susceptibility χ_0, while χ'' will be equal to zero, which means that $M(t)$ will follow $H(t)$ without any phase shift. One should also remember that in general, χ' and χ'' are tensors, which are symmetric when $H_0 = 0$, but not so when $H_0 \neq 0$. (2.5) presents the linear response of the magnetic material to the applied alternating field given by (2.2). However, under certain conditions, the system may exhibit a nonlinear magnetic behavior, with $M = M_0 + \chi_1 H + \chi_2 H^2 + \chi_3 H^3 \ldots$, where χ_1 is the linear susceptibility, and χ_2, and χ_3 are the nonlinear susceptibilities. As a result, a sinusoidal field would induce non-sinusoidal oscillation of the magnetization. Expanding $M(t)$ (2.5) in frequency harmonics $n\omega t$ $(n = 1, 2, 3, \ldots)$ one gets

$$M(t) = M_0 + h\Sigma(\chi'_n\cos(n\omega t) + \chi''_n\sin(n\omega t))\ , \tag{2.9}$$

where χ'_n and χ''_n are the in–phase and out–of–phase components of the nth harmonic susceptibility. The nonlinear susceptibilities χ_2 and χ_3 are observed

in AC experiment as $\chi_2 h$ and $\frac{3}{4}\chi_3 h^2$, proportional to higher harmonic signals of frequencies 2ω and 3ω, respectively. Measurements of higher harmonics of the susceptibility is especially important for investigating phase transitions and critical behavior of the spin system [1], [2]. Due to symmetry properties of M, the second harmonic can be observed only if there is a spontaneous magnetization, e.g. in ferromagnets, while for spin glasses only odd harmonics are present [1].

2.1.2.2 AC susceptometer

In the apparatus designed for measuring χ_{AC}, the oscillating magnetic field is generated by the primary coil fed with the alternating current of frequency f and amplitude h. The reference signal is sent to the phase-sensitive detector tuned at the same frequency. The DC bias field can be generated by the superconducting magnet. The alternating field gives rise to the electromotive force induced in the secondary coil. In the case of two secondary coils wound oppositely (top- and bottom-coil) connected in a series (see Fig. 2.1(right)) the induced voltages are balanced and give the output signal equal to zero. When the sample is centered within one of the sensing coils, the voltage balance is disturbed and the resultant variation in flux gives a non-zero output signal measured by a phase-sensitive detector (lock-in). The measured voltage is proportional to the susceptibility of the sample, its volume V, and the frequency and amplitude of the alternating field [3]:

$$U = (1/\alpha) V f H \chi \,, \tag{2.10}$$

where U – measured root-mean-square (RMS) voltage, α – calibration coefficient of the system dependent on coil geometry, H – RMS magnetic field. In order to avoid the error connected with possible non-compensation of the secondary circuit, the signal is measured for the sample placed in the top-coil and in the bottom-coil in turn. For samples with large susceptibility, the demagnetization effect should be taken into account. In the case of measuring the higher harmonic susceptibilities, the output signal is registered with lock-in tuned at multiplies of the fundamental frequency, i.e. 2f, 3f, ... The most useful feature of the AC susceptometer is that both the in–phase and the out–of–phase components of susceptibility can be measured. In order to separate them, the phase difference between the sample signal and the reference to the phase-sensitive detector must be determined. The phasing procedure is performed using a test sample known to have $\chi'' = 0$.

2.1.3 Relaxation in oscillating magnetic field

The thermodynamic model for relaxation of a magnetic system in the presence of an oscillating magnetic field parallel to a constant field H_0 was derived by Casimir and du Pré. The geometry with the oscillating field parallel to the

static field is called longitudinal. The case of the orthogonal (transverse) geometry leads to spin resonance and will not be discussed here. In the Casimir–du Pré model [A, B], a magnetic sample is considered to consist of two parts, the spin system and the lattice system. When the entire crystal is in thermal equilibrium, the temperature T_s of the spin system and that of the lattice, T_l, are equal. As a result of a field change, the spin temperature will change from its equilibrium value and, subsequently, heat will be exchanged between the spin system and the lattice. In other words, spin-lattice relaxation will take place, and T_s will relax to T_l. In this process, the heat flow is proportional to the temperature difference:

$$dQ/dt = -\alpha(T_s - T_l) = -\alpha\Delta T \tag{2.11}$$

and the relaxation time is given by:

$$\tau = C_H/\alpha\,, \tag{2.12}$$

where C_H is the specific heat of the spin system in constant field. The relaxation time defined above has a general meaning and is used to describe any relaxation phenomena irrespective of the relaxation mechanism (see (2.1)). Considering the entropy change [B], one obtains the following expression for the complex susceptibility:

$$\chi(\omega) = \chi_S + \frac{\chi_T - \chi_S}{1 + i\omega\tau}\,. \tag{2.13}$$

The quantities χ_T and χ_S are the isothermal and the adiabatic susceptibility respectively. χ_T is the differential susceptibility in the limit of the lowest field frequencies for which the temperature equilibrium is obtained over the time scale of the experiment. On the other hand, if the oscillations of the AC field are fast compared to the time constant τ, $\omega \gg \tau^{-1}$, the magnetic system remains isolated from its surroundings and then the adiabatic susceptibility χ_S, lower than χ_T, is revealed. Splitting (2.13) into the real and imaginary parts, one gets:

$$\chi'(\omega) = \chi_S + \frac{\chi_T - \chi_S}{1 + \omega^2\tau^2} \tag{2.14}$$

$$\chi''(\omega) = (\chi_T - \chi_S)\frac{\omega\tau}{1 + \omega^2\tau^2}\,. \tag{2.15}$$

It follows from the above that the frequency–dependent in–phase susceptibility is always accompanied by an out–of–phase component. Figure 2.2 illustrates the frequency dependence of $\chi'(\omega)$ and $\chi''(\omega)$ given by (2.14) and (2.15) for the frequency range in which relaxation process occurs.

The plot of $\chi''(\omega)$ versus $\chi'(\omega)$ in a so-called Argand diagram [4] yields a semi–circle. Figure 2.3a presents a draft of the Argand diagram with $\chi = \chi_T$ (low ω) and $\chi = \chi_S$ (high ω) at the right-hand side and at the left-hand side

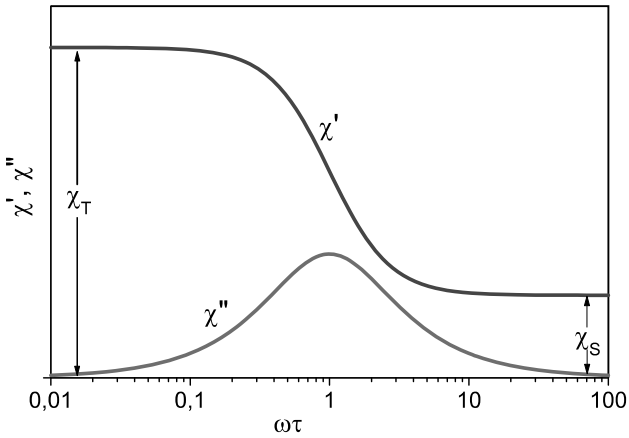

Fig. 2.2. Real and imaginary components of dynamic magnetic susceptibility for the frequency range close to the frequency of the relaxation process ($\omega_\tau \approx \tau^{-1}$); χ_T – isothermal susceptibility, χ_S – adiabatic susceptibility. The curves are given by (2.14) and (2.15) taking $\chi_S = \chi_T/4$

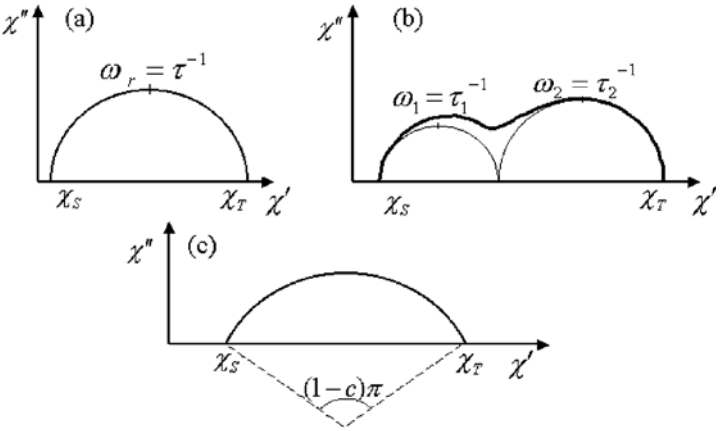

Fig. 2.3. $\chi''(\omega)$ vs $\chi'(\omega)$ (Argand plot) for: (**a**) relaxation process with a single time constant τ (Debye process); (**b**) relaxation process with two time constants τ_1 and τ_2; (**c**) distribution of relaxation time constants according to Cole–Cole equation (2.16)

of the semi-circle respectively. The frequency ω_τ, at which the absorption reaches its maximum $\chi_{\max} = \frac{1}{2}(\chi_T - \chi_S)$, determines the relaxation time τ of the relevant relaxation process: $\tau = \omega_r^{-1}$. If the component χ'' does not reach the $\chi''_{\max}$ value (the Argand plot is flattened), this means that more than one time constant is present (Fig. 2.3b) or one deals with the distribution of the relaxation times (Fig. 2.3c). In that case, $\chi(\omega)$ is modified to the Cole–Cole expression:

$$\chi(\omega) = \chi_S + \frac{\chi_T - \chi_S}{1 + (i\omega\tau)^{1-c}} , \tag{2.16}$$

where index c changes between 0 and 1. In the case of one relaxation process, characterized by single relaxation time (Debye process), parameter c is equal to zero, while for $c = 1$ no relaxation occurs. The Casimir – du Pré model deals with spin-lattice relaxation, however, it can be used to describe any relaxation process. The other possible process is the energy exchange between identical spins, i.e. the spin–spin relaxation or the cross-relaxation, with the energy exchange between different spins or spins subjected to various forces.

2.1.4 Relaxation processes in paramagnets

2.1.4.1 Spin-lattice relaxation

The energy exchange between magnetic moments and the lattice oscillations is enabled via the spin-orbit coupling. As can be expected for a phonon process, the spin-lattice relaxation time τ_{S-L} depends strongly on temperature. At low temperatures, $\tau_{S-L} \approx 1/T$, while at higher temperatures the decrease of τ_{S-L} with T gets more rapid. At the liquid helium temperature, τ_{S-L} is of the order of 10^{-2} s and at the liquid nitrogen temperature it is about 10^{-6}.

Figure 2.4 (upper part) presents the Argand plots for the common $CrK(SO_4)_2{\cdot}12H_2O$ alum at $T = 4.3$ K. The diagrams were obtained with the oscillating magnetic field of frequency between 5 Hz (highest χ', first points on the right) and 10000 Hz (smallest χ', last points on the left), for several values of the constant external field. The lower part of Fig. 2.4 compares the plots in fields 2.5, 5, 7.5 and 10 kOe for two temperatures, $T = 4.3$ K and $T = 10$ K. The plots obtained at $T = 4.3$ K are flattened, showing that more than one relaxation process occurs. One expects here three processes: the slowest process emerges starting from $H = 5$ kOe, the second process occurs with the average time constant and is the strongest one, the third process is expected on the left-hand side of the curves and is not accessible with our set-up. The relaxation time for the average relaxation process, given by the frequency of the highest χ'' value, does not change much as the field is increased: for $H = 2.5$ kOe $\tau \approx 10^{-3}$ s, while for $H = 20$ kOe $\tau \approx 5{\cdot}10^{-4}$ s. The main effect is the decrease of isothermal susceptibility; however, in order to determine χ_T(H) precisely, frequencies lower than 5 Hz should be used. The expected third process would probably be due to some type of spin–spin relaxation for crystal-field-resolved $S = 3/2$ Cr^{3+} multiplet [A]. Increasing the temperature to 10 K (see lower part of Fig. 2.4) weakens remarkably the field effect on relaxation. The plot gets more semicircular, with $\tau \approx 10^{-4}$ s for $H = 10$ kOe.

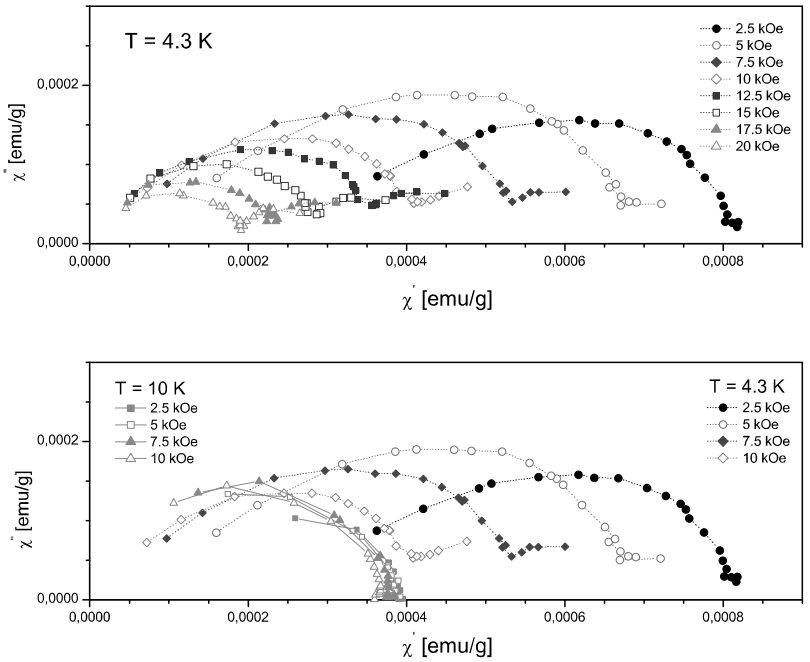

Fig. 2.4. Argand plots obtained for the $CrK(SO_4)_2{\cdot}12H_2O$ alum with frequency 5 Hz–10 000 Hz: (**a**) $T = 4.3$ K, applied DC field from 2.5 kOe up to 20 kOe; (**b**) applied DC field from 2.5 kOe up to 10 kOe, $T = 4.3$ K and $T = 10$ K

The extensive investigation of relaxation phenomena in paramagnetic salts, carried out mainly in Holland [5], [6], allowed one to distinguish three types of spin-lattice relaxation mechanisms:

(a) the direct process with the emission or absorption of one phonon
(b) the Raman process with the scattering of phonons on spins
(c) the Orbach process, including the excited state of the spin system.

In (b) and (c) two phonons of different energies are included. The relaxation times connected with (a), (b), and (c) reveal a different dependence on temperature (T^{-1}, T^{-7}, and $\exp(\Delta/k_BT)$ respectively), so the relative contribution of each of the three mechanisms varies with temperature. The external magnetic field influences mainly the direct process.

2.1.4.2 Spin–spin relaxation

When the frequency of the oscillating magnetic field increases, additional absorption appears besides the one due to the spin-lattice coupling. This additional absorption is connected with the relaxation within the spin system. The relevant spin–spin relaxation time, $\tau_{S,}$ is much lower than τ_{S-L} and does

not depend on temperature. Equations for $\chi'(\omega)$ and $\chi''(\omega)$ obtained with the method given above for $1/\tau_{S-L} \ll \omega$, are as follows:

$$\chi'(\omega) = \frac{\chi_S}{1+\omega^2\tau^2} \tag{2.17}$$

$$\chi''(\omega) = \chi_S \frac{\omega\tau}{1+\omega^2\tau^2}. \tag{2.18}$$

The basic mechanism for spin–spin relaxation is of magnetic dipolar type. As every magnetic dipole feels the resultant field coming from its neighbours randomly oriented in space, there is no specific frequency value of the precession in the field, but one deals with some distribution. The approximate relaxation time for this type of coupling is $\tau_S \approx 10^{-10}$ s [A, B]. It is understood as the time necessary for changing the direction of the precession axis.

Another possible mechanism for spin–spin relaxation is the exchange mechanism. It arises when paramagnetic ions, situated not far away from one another, are coupled by exchange interaction. As the exchange interaction favours parallel or antiparallel configuration, it is probable that adjacent spins will change their orientations. This type of coupling gives rise to the increase of τ_S [A].

2.1.5 Long-range ordered magnets

2.1.5.1 Dynamics of domain walls

In order to observe the spin-lattice relaxation in paramagnets, the non-zero external magnetic field is needed. In magnetically ordered materials (ferro-, ferri-, or antiferromagnets) strong internal magnetic fields are present due to the exchange coupling of the spins. It is known that below the Curie temperature T_c a ferromagnetic sample consists a number of domains. The transition region between domains constitutes a domain wall. The width of the domain wall is $d = (2JS^2/K_u a)^{1/2}$ [A], where J is the exchange constant, K_u is the anisotropy constant and a is the lattice parameter. The small width, $d \approx 10^{-8}$–10^{-7} cm, indicates that the walls are fixed to their positions, while for $d \approx 10^{-5}$ cm (as in most ferromagnets) walls are able to move reversibly around their equilibrium positions.

Applying AC magnetic field one measures the overall susceptibility of the spins in the domains and in the walls. It may be expected that the susceptibility coming from the total magnetization in a domain will be substantial rather at low frequencies. On the other hand, the wall spins should respond easily to the AC field even at high frequencies, as their subtle equilibrium state (a compromise between the energy of exchange, anisotropy and demagnetization effect) can be easily disturbed. In the external field, domains with **M** parallel to **H** will grow, and those with **M** antiparallel will diminish, so there will be a domain-wall displacement (DWD). In an AC field the walls will move back and forth. The situation will change if the domain walls are

pinned to lattice defects; it was indeed found [C] that domain walls will usually form at inclusions or impurities, as this lowers the wall energy. Anyhow, it is admitted that the first thing to happen in low fields is wall-displacement, while in high fields rotational processes take place.

Susceptibility resulting from the small amplitude motion of domain walls can be derived from the equation of motion, similar to that of a damped harmonic oscillator [C, A]:

$$m_w \ddot{y} + \beta_w \dot{y} + \alpha_w y = 2M_s h e^{i\omega t}, \tag{2.19}$$

where m_w denotes the "effective mass" of the wall, β_w is a damping parameter, α_w $(= 2\ K_u/d\ )$ is the stiffness parameter and M_s is magnetization of saturation. The term on the right-hand side of the equation represents the "pressure" on the wall due to the AC field. The equation yields a resonant behavior for $\beta_w^2 \ll m_w \alpha_w$, while in the limit for $\beta_w^2 \gg m_w \alpha_w$ a relaxation behavior with a relaxation time $\tau = \beta_w/\alpha_w$ is found. If D is the distance between two walls, the wall susceptibility [C], [4] is given by

$$\chi_w = \frac{4M_s^2}{\alpha_w D} \tag{2.20}$$

and can be determined by the experiment as the difference between the isothermal and adiabatic susceptibilities: $\chi_w = \chi_T - \chi_S$. Temperature dependence of wall susceptibility χ_w given by (2.20) is contained in two parameters, M_s and α_w, as the distance D between two domains stays almost constant up to temperatures very close to T_c. The stiffness parameter α_w is expected to decrease with increasing temperature because of the increase of the thermal energy of the domain wall, while $M_s(T)$ is nearly constant at low temperatures and goes to zero at T_c. In that way, one should observe an increase of χ_w with increasing temperature, but the behavior close to T_c may be complicated. Usually, values smaller than $1/N$, where N – demagnetization factor, are detected [4].

2.1.5.2 Loss mechanisms

As given above, the relaxation time increases with a damping parameter β_w responsible for losses connected with relaxation. The reason for damping is the change in the local magnetization at the movement of the domain wall. Several processes may contribute to β_w [A, C, D]. The most important process is the one associated with irreversible wall displacement or irreversible rotation magnetization, also called hysteresis loss. If the amplitude of magnetization is very small, the loss factor depends on the amplitude of the magnetic field. The hysteresis loss becomes less important in the high-frequency range. The next contribution to losses for ferromagnetic metals and alloys is the eddy current loss that grows as the square of frequency and plays an important role in the high-frequency range. The other process can be the diffusion of electrons like

that frequently observed for magnetite or other ferrites with Fe^{2+} and Fe^{3+} ions. A similar process is the induced relaxation of lattice defects. The last two processes yield an exponential (Arrhenius type) temperature dependence of the relaxation time:

$$\tau = \tau_0 \exp(E_a/k_B T), \tag{2.21}$$

where E_a is the energy involved in the transfer of electrons or defects.

At the end of this short paragraph let us note that in spite of the qualitative understanding of the domain dynamics it is generally very difficult to give a quantitative description of the phenomenon, which could relate the determined energy barriers to the specific parameters of the sample and domains. The above is due to the substantial complexity of the domain structure (stripe, bubble, branched domains) and of the local forces acting on the spins during non-equilibrium.

2.1.6 Some experimental results for ferro-, ferri- and antiferromagnets

2.1.6.1 Ferrites

The early reports on magnetic relaxation phenomena concern strong ferro- or ferrimagnets, mostly ferrites [E] with T_c up to 1000 K, crystallizing in the spinel- or garnet-type structure. The complex initial magnetic permeability $\mu = \mu_1 - i\mu_2$ ($\mu = 4\pi\chi + 1$) was measured by bridge and wave methods up to frequencies as high as 1 GHz. General characteristics of the spectra were similar to that presented in Fig. 2.2. The in-phase component μ_1 remained constant over a large frequency range and then, at $f \approx$ 1–100 MHz, after a small rise it dropped rapidly to a very small value; on the other hand, the losses, indicated by μ_2, showed their maximum at the frequencies of the μ_1 fall. The above relationship was explained by Snoek [E] with the help of ferromagnetic resonance in the anisotropy field. In addition to this high–frequency dispersion, another dispersion region was detected for many ferrites at considerably lower frequencies of $f \approx 100$ kHz. The temperature dependence of the relaxation time could be described by the Arrhenius law (2.21), with the activation energy of about 0.2 eV (19.3 kJ/mol). The small activation energy pointed to the electron diffusion process, which could be expected for ferrites containing iron ions in two valence states. Wijn and van der Heide [7] first noticed a relationship between the iron valence in a ferrite, the resistance of the material and the occurrence of the relevant losses. It was found that relaxation of that type could appear in the NiZn ferrite (containing only Fe^{3+} ions) after introducing Fe^{2+} ions of the order of 0.5 percent into the ferrite by means of high-temperature sintering.

Figure 2.5 presents the relaxation effect of the same type observed by us for a single crystalline sample of magnetite with small nonstoichiometry,

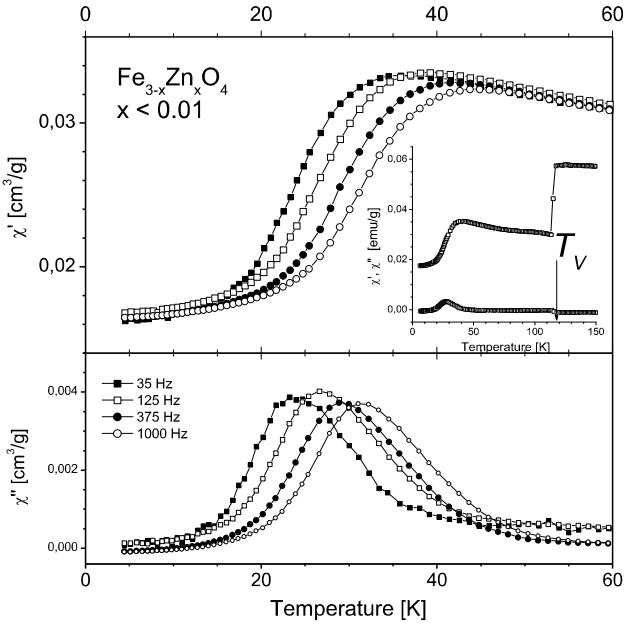

Fig. 2.5. Temperature dependence of χ' and χ'' of a magnetite single crystal measured at varied frequency (shown) in a field of 1 Oe parallel to [110] direction. Inset: Susceptibility jump at $T_V = 120$ K independent of frequency

$(Fe_{1-x}Zn_x)_3O_4$, $x < 0.01$. This relaxation effect shows up in the frequency dependence of the χ' inflection point and of the χ'' peak observed for $T =$ 10 K–50 K. Another anomaly is the sharp rise of χ' at the Verwey temperature $T_V = 120$ K (see inset), which does not depend on frequency. As it was established by an extensive investigation of magnetic after-effects [8], both transitions are driven by the anisotropy changes connected with the variations of the spin-orbit coupling associated with the extra electron of a Fe^{2+} ion. The orbital moment of Fe^{2+} ions is not completely quenched, thus giving rise to energy anisotropy, in contrast to Fe^{3+} ions, that do not contribute to the relaxation process due to their zero orbital moment. Below the Verwey temperature, the two types of ions are ordered; above T_V , the hopping of the sixth electron between the neighbouring ions takes place. The low temperature relaxation process presented in Fig. 2.5 should be due to the thermal activation of Fe^{2+} electrons [8]. One can assume that the relaxation time changes with temperature according to (2.21). Plotting the logarithm of the driving frequency versus the inverse of the χ'' peak temperature, we get $\tau_0 = 10^{-7}$ s and $E_a = 0.025$ eV. These values are comparable to the results obtained in [9] for the stoichiometric Fe_3O_4 crystal ($\tau_0 \approx 6 \cdot 10^{-9}$ s and $E_a \approx 0.04$ eV).

2.1.6.2 Hard magnets

Besides the investigations of the relaxation effects, measurements of the AC magnetic susceptibility are most often used for studying magnetic phase transitions occurring with the change of temperature or of the applied magnetic field (transition to the ordered state, spin reorientation or metamagnetic transition). The method can also help to analyse transitions caused by the change in anisotropy energy.

In [10] dealing with a $Nd_2Fe_{14}B$ spherical single crystal, extensive χ_{AC} studies provided detailed information on the anisotropy, domain structure and magnetization process of this important hard magnet. It has been agreed that at room temperature magnetic moments lie along the tetragonal c-axis, and with the decreasing temperature, at $T_{SR} \approx 135$ K, spin reorientation transition from easy axis to easy cone takes place. The observed susceptibility was in general due to the domain wall displacement (DWD) and to the domain magnetization rotation (DMR). A sharp peak for χ' and a sharp onset of χ'' were observed at T_{SR}, when the first anisotropy constant is equal to zero. The peak at T_{SR} was ascribed to the cooperation of thermally activated DWD and non-resistive DMR within a certain angle. The dependence on frequency of χ' and χ'' was explained as almost totally due to the magnetic relaxation processes important for low-field DWD. The authors derived also a set of formulas for initial susceptibility as a function of the anisotropy constants for DMR and DWD, as well as a formula for low-frequency eddy current contribution to χ''. However, as discussed in [11], AC susceptibility for a number of 3d-4f intermetallics ($Ho_2Fe_{14}B$, Er_2Co_{17}, Tm_2Fe_{17}) showed anomalies which could not be related to the behavior of anisotropy or magnetization. The two anomalies found for aligned bound Sm_2Fe_{17} [11] were explained as connected with the domain structure reconstruction with activation energy $E_a \approx 0.4$ eV and with the dynamic wall pinning and depinning with $E_a \approx 0.5$ eV. It was finally concluded that dynamic susceptibility is related to both the intrinsic crystal anisotropy constants and the extrinsic defect structure.

2.1.6.3 Rare earth metals

The results presented up to now concerned magnetic substances with strong exchange interactions, high temperatures of magnetic ordering and mostly metallic conductivity. AC susceptibility is very helpful in investigations of intermetallic compounds, for example binary or ternary compounds of rare earth metals with 3d, 4d or 5d elements. Usually, such compounds are complex ferrimagnets where competing ferro- and antiferromagnetic interactions lead to transitions between the phases with different magnetic structures. Frequency dependent and AC field-amplitude dependent measurements provide information on the temperatures and type of the transitions [12]. It is known that also in pure rare earth metals magnetic coupling between 4f shells

realized via the conduction electrons results in different orderings of the magnetic moments (ferromagnetic, complex sinusoidal or helical, modulated). The heavy rare earths (Gd, Tb, Dy, Ho, Er, Tm) display transitions from the low-temperature ferro-(ferri-)magnetic phase to the non-ferromagnetic (helical, modulated) phase below the Néel temperatue T_N [13]. In order to illustrate the cognitive possibilities of the AC susceptibility aimed at characterization of a magnetically ordered state, we present the results for Gd and Tm which are the first and the last element of the heavy rare earth magnets. Gadolinium is a simple ferromagnet with $T_c = 293.4$ K. At $T_{SR} = 225$ K the anisotropy constant changes sign and spin reorientation takes place with moments parallel to the c-axis for $T > T_{SR}$ and perpendicular to the c-axis for T below T_{SR}.
Thulium orders at $T_N = 56$ K with a sinusoidal modulation of the c-axis component of the magnetic moments. Below 38 K that modulation begins to square off and a system transforms to a ferrimagnetic structure with four moments up along c-axis followed by three moments down.

AC susceptibility data for a bulk sample of Gd measured at $f = 625$ Hz and $h = 1$ Oe as well as 10 Oe, are given in Fig. 2.6. In the inset χ' results, obtained with $f = 125$ Hz by the same h, are presented for the vicinity of T_c. The spin reorientation point T_{SR} is clearly seen as equal to the temperature at which χ' does not depend on h and at which χ'' component has

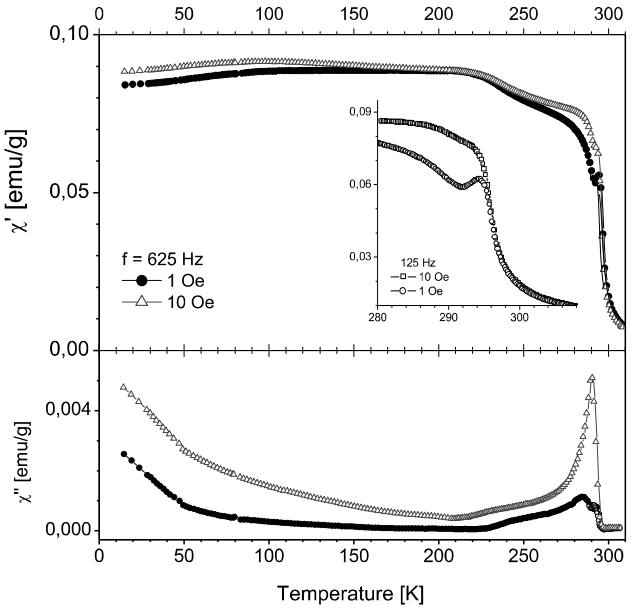

Fig. 2.6. AC susceptibility of bulk gadolinium sample measured at $f = 625$ Hz with two amplitudes of AC field (shown). Inset: χ' component in the vicinity of T_c for the same amplitudes of AC field and $f = 125$ Hz; maximum is seen for $h = 1$ Oe

minimum. The χ_{AC} results reported for Gd single crystals [14], [15] detect T_{SR} as a weak maximum and followed by a kink when measured with the AC field parallel to the c-axis ($\chi_{||}$) and as a maximum of χ' for AC field perpendicular to c-axis ($\chi_{\perp}$). Thus, it appears from Fig. 2.6 that T_{SR} may be determined with a good accuracy also for the polycrystalline bulk sample with the AC field-amplitude dependent measurement. For amplitudes small enough the distinct maximum of χ' is seen at $T \approx T_c$. That maximum resembles the Hopkinson effect in the initial permeability, frequently observed for ferrites [D]. For the same temperature, the single crystal data [15] reveal a sharp peak however its value is less than the demagnetizing-limited value. As the frequency effect is concerned, only a slight dependence of χ_{AC} on f was seen above 5 kHz for T close to T_c. in the literature one finds no much experimental evidence of frequency dependence (or independence) of T_c (or T_N) for magnetic materials which order at moderate temperatures, i.e at room temperature or below. It is known [A] that for strong ferromagnetic materials with T_c of several hundreds K or more, the frequency dependence of susceptibility was found only in the MHz range. On the other hand, relaxation effects were found for weak magnets (see the next paragraph). Thus, AC susceptibility measurements may still provide important information on transitions to the magnetically ordered state.

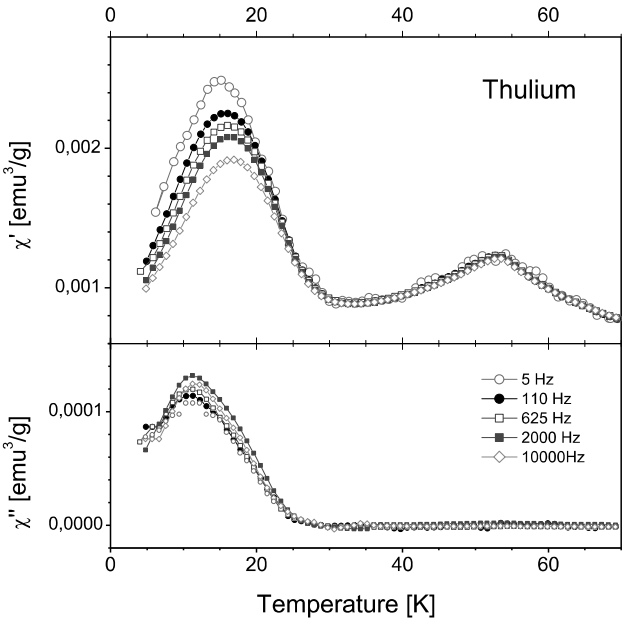

Fig. 2.7. AC susceptibility for thulium fillings measured at varied frequency (shown); below $T = 32$ K T_m is a ferrimagnet, the Néel point $T_N = 53$ K

Figure 2.7 shows χ_{AC} for thulium measured at varying frequency of the driving field. The maximum of χ' observed at $T_N = 53$ K reveals the AFM-PM (antiferromagnet-paramagnet) transition. It is seen that position of the maximum does not depend on frequency and that the χ'' component is absent, as it should be for a pure collinear antiferromagnet. There is, however, a strong frequency dependence of the low temperature anomaly seen for both components. The onset of χ'' is at $T = 32$ K, at which the complex ferrrimagnetic phase is known to arise. The frequency shift for the temperature of the χ' maximum is even higher than that observed for spin glasses (see Sect. 2.1.7). It appears that the formation of the combined antiphase ferrimagnetic arrangement of magnetic moments is the relaxation process. In opposite to gadolinium, results of the measurement with the varied amplitude were identical in the whole temperature range.

2.1.6.4 Weak magnets

An example of a wealth of information which can be obtained from the frequency and field–dependent AC susceptibility measurements is the paper of Groenendijk and van Duyneveldt [16] devoted to the quasi 1d Ising ferromagnet $Co[(CH_3)_3NH]Cl_3 \cdot 2H_2O$. The experiment, performed for a single crystalline sample, delivered the value of T_c, the value and direction of the moments, the intra- and interchain interactions, and the metamagnetic phase diagram. Three relaxation processes were found: (a) fast, of about 10^{-7} s –10^{-8} s, occurring near and above $T_c = 4.18$ K (b) intermediate, of about $2{\cdot}10^{-6}$ s, and (c) slow, of about $3{\cdot}10^{-4}$ s, present in the whole temperature range from 0 K up to T_c. The fast process was the spin–spin relaxation, for which the increase of the time constant was observed when the sample was cooled toward T_c. The effect was a critical slowing-down due to the decrease of the spin fluctuations in the ferromagnetically coupled chains. The intermediate process, which seems to be effective in low-dimensional systems, was suggested to arise due to the existence of solitons in the ferromagnetic chains. The third, slowest, relaxation process was entirely related to the movement of the domain walls. It appeared that values of both χ' and χ'' depended on the amplitude of the oscillating field and hence the Argand diagrams and the relaxation time constants were also h–dependent. When h was decreased, the average relaxation time increased. The effect was pronounced especially at lower temperatures. At T near to T_c, the amplitude dependence of χ could be no longer detected, and χ_T for all values of h used (up to 4 Oe) attained the expected value of $1/N$. The relaxation time τ extrapolated to zero field ($h = 0$) changed by four orders of magnitude across the magnetically ordered region, from 1 s at $T = 1$ K up to $5{\cdot}10^{-4}$ s at $T = T_c$.

Dynamic susceptibility in the frequency range of 5 Hz – 3 MHz was also used to study magnetic relaxation in $DyVO_4$ [17], which is an antiferromagnet with $T_N = 3.06$ K. It was found that relaxation was dominated by a spin–lattice Orbach process. Only at temperatures well within the ordered

state was spin–spin relaxation faster, and the relaxation time became temperature independent. Zero-field experiments showed significant deviations around T_N, while for $H_{\text{appl}} = 2$ kOe the Orbach process remained dominant over the entire temperature range.

Domain-wall dynamics close to the Curie temperature was investigated for the weakly uniaxial ferromagnet $GdCl_3$ in [18]. The relaxation time for $T < T_c$ showed the exponential behavior, but the observed speeding up of the relaxation rate with temperature in the close vicinity of T_c was ascribed to critical fluctuations rather than to thermal activation. This interpretation was based on the hypothetical linear walls, in which the magnitude of the local magnetization changes from $+M_s$ to $-M_s$. Such linear domain walls have been indeed found for the typical Ising ferromagnet $LiTbF_4$. Measurements of the complex susceptibility in the frequency range between 20 Hz and 50 MHz were carried out for the high–quality crystalline spheroids. The paper [18] presents the evidence for critical fluctuations and macroscopic-size effects on the domain-wall relaxation. It was found that on approaching T_c, the mean domain relaxation rate revealed a power-law speeding up and was dependent on the geometry of the sample.

2.1.7 Spin–glasses and spin–glass–like magnets

In the spin-glass phase [19, 20], magnetic moments are coupled by randomly distributed, both positive and negative, exchange interactions. Below the freezing temperature T_f the moments are blocked in a highly irreversible and metastable state characterized by the frustration of spins. The first spin–glasses discovered were metallic alloys consisting of magnetic ions in a matrix of a nonmagnetic host material (e.g. CuMn [21], AuFe [22]). The concentration of magnetic moments was low enough to ensure that no long-range magnetic order could appear; however, short-range interaction via the conduction electrons was possible. Insulating spin–glasses are compounds with a random-site occupancy of magnetic and nonmagnetic ions. The interactions between the nearest neighbors and the next-nearest neighbors are of opposite signs. The spin-glass phase appears at concentrations for which a symmetric distribution of the exchange coupling around zero can be assumed (e.g. $(Eu_{0.80}Sr_{0.20})S$ [23], $Rb_2Cu_{1-x}Co_xF_4$ [24]).

AC susceptibility measurement is an important technique for investigating spin-glasses, as no information on these systems can be extracted from neutron diffraction, with not many data to be gained from specific heat either. At freezing temperature, the in-phase component χ' exhibits a cusp-like anomaly, while χ'' shows a rapid onset followed by an inflection point and a weak maximum as the temperature is decreased. The main feature of the χ' anomaly is its frequency dependence observed already below 1kHz. This is in contrast to conventional ferromagnetic materials, where the frequency dependence of susceptibility was found only in the MHz range. It is assumed that in a spin-glass, clusters of short-range coupled spin exist, to each of which an

independent relaxation time can be assigned. A weak intercluster interaction modifies the expression for the relaxation time from the Arrhenius law (2.21) to the Vogel–Fulcher–Tammann formula

$$1/\tau = f_0 \exp[-E_a/k(T_f - T_0)], \tag{2.22}$$

with $f_0 = 10^{13}$ s and parameter T_0 arising from that inter-cluster coupling. Sometimes, the empirical parameter X is used to express the T_f vs f dependence, as following: $X = \Delta T_f/T_f \Delta(\ln f)$. The insulating spin-glasses show substantial T_f shift with frequency ($X \approx 0.01$) and χ'' equal to several % of χ'. For metallic spin-glasses, the frequency dependence is weaker and the related χ'' is less than 1% of χ'. It was found [22] that both components obey the following fundamental relation:

$$\chi''(\omega) = \frac{1}{2}\pi \frac{\partial \chi'(\omega)}{\partial \ln \omega}. \tag{2.23}$$

As already mentioned (See Sect. 2.1.3) the frequency dependence of χ' and the presence of χ'' signal are always a consequence of one or more relaxation processes with characteristic relaxation time constants. The highest χ'' (up to 50% of $(\chi_T - \chi_S)$) is reached when a relaxation process with one time constant takes place. Low values of χ'' in spin-glasses suggest a distribution of relaxation time constants. According to [25], the magnetic system can be considered to be an infinite number of subsystems, relaxing with characteristic time constant τ. In that case

$$\chi(\omega) = \chi_S + \int_0^\infty \frac{G(\tau)}{1 + j\omega\tau} d\tau = \chi_S + \int_{-\infty}^\infty \frac{\tau G(\tau)}{1 + j\omega\tau} d(\ln \tau), \tag{2.24}$$

where $G(\tau)$ is the weight factor of the relaxation process with time constant τ. When a function $\tau G(\tau)$ is symmetric around $\tau = \tau_c$ the curve given by (2.24) is identical to the Cole–Cole expression (2.16) and one derives [25]

$$\tau G(\tau) = \frac{\sin(c\pi)}{\pi[(\tau/\tau_c)^{1-c} + (\tau/\tau_c)^{c-1}] - \pi\cos(h\pi)}. \tag{2.25}$$

Parameters c and τ_c can be found experimentally from the Argand plot constructed for different temperatures. Knowing c and τ_c, one can evaluate the distribution function $\tau \mathrm{G}(\tau)$ for relaxation times as a function of $\log\tau$ for the investigated spin-glass. It appears that the half-width of $\tau G(\tau)$ remarkably increases upon cooling through T_f, for example, from 10^{12} s down to 10^{-3} s at $T = 1.2$ K for the (EuSr)S [25]. Such a wide distribution of relaxation times is characteristic for the spin–glass phase. The other feature is a dramatic slow-down of the most probable relaxation time τ_c: it was found [26] for the two-dimensional spin–glass $Rb_2Cu_{1-x}Co_xF_4$ that τ_c changes from 10^6 s at $T = 3$ K down to 10^{-10} s at $T = 7$ K.

The other systems with "frozen" disordered magnetic states are materials with significant local random anisotropy, such as amorphous alloys [26] of non-S-state ions with single-ion anisotropy axes distributed randomly in space. Random anisotropy magnets (RAM) [27] behave similarly to spin-glasses yet they are called spin–glass–like systems (or speromagnets) to distinguish them from spin–glasses, where the random distribution of moments results from the competing exchange interactions. A crucial parameter in the RAM–model is the constant second–order anisotropy parameter D representing local anisotropy, which, related to the exchange integral J_0, determines the properties of an amorphous magnet [28]. For weak random anisotropy, new magnetic states were predicted [29], namely the correlated speromagnet (CSM) and the ferromagnet with wandering axis (FWA), to which CSM is transformed by applying magnetic field. Both states are characterized by non-perfect ordering of their magnetic moments.

The molecule–based magnets [30], synthesized using wet chemistry methods, can be classified as spin-glass–like materials. The spinless solvent molecules, which are randomly distributed in the interstitial spaces, give rise to random anisotropy and spin–glass properties [31, 32], such as frequency–dependent susceptibility and irreversibility of magnetization. Figure 2.8 presents the temperature dependence of AC susceptibility for the manganese porphyrin salt $[Mn(CH_3)_4TPP][TCNE]$·solvent [33] measured for frequencies from 10 Hz up to 1000 Hz. One can notice a strong frequency dependence of $\chi'(X = 0.026)$, which is higher than that for ordinary spin–glasses, and

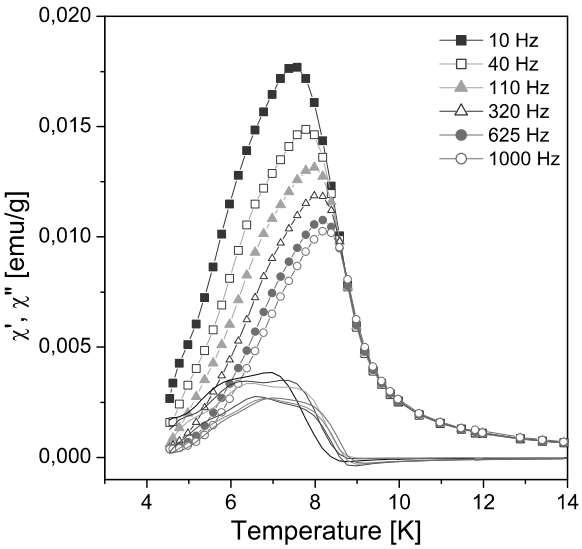

Fig. 2.8. Real (*symbols*) and imaginary (*lines*) components of χ_{AC} for Mn-porphyrin salt $[Mn(CH_3)_4TPP][TCNE]$·solvent measured at varied frequency (shown)

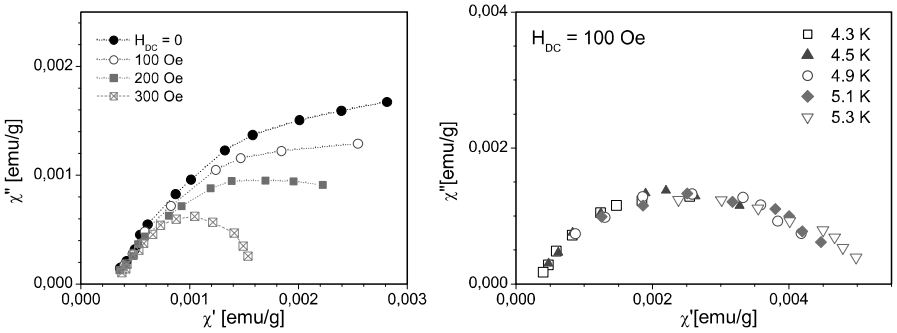

Fig. 2.9. Argand plots for Mn-porphyrin salt $[Mn(CH_3)_4TPP][TCNE]$·solvent measured at $f = 10$ Hz ÷ 1000 Hz: influence of the applied magnetic field at $T = 4.3$ K (*left*) and influence of temperature for $H = 100$ Oe (*right*)

the large out–of–phase component amounting to 20% of χ'. The relaxation effects are extremely strong for this organometallic compound. The Argand plot for $T = 4.3$ K is depicted in Fig. 2.9 (left, full circles). It can be seen that there is a broad distribution of relaxation times and the processes with $\tau > 10^{-1}$ s are beyond our experimental time window. By applying constant magnetic field we decrease the expected χ_T and narrow the distribution function. Figure 2.9 (right) illustrates the temperature effect on the relaxation processes in $H_{appl} = 100$ Oe. In the small temperature region between 4.3 K and 5.3 K, the time constants involved in the relaxation process move through our experimental time window ranging between $2{\cdot}10^{-1}$ s and 10^{-3} s.

2.1.8 Superparamagnetic particles and high–spin molecules

As predicted by Néel, a ferromagnetic particle becomes a monodomain if its size is reduced below the critical value ($d \approx 1$–100 nm), determined by the ratio of the exchange and dipole energy. Such monodomain particles can be viewed as large magnetic units, each having a magnetic moment of thousands of Bohr magnetons. At temperatures higher than the blocking temperature T_B, which depends on the volume of the particle and on the time-window of the experiment, a collection of monodomain particles behaves like a paramagnet (superparamagnet), because the moment of each particle rotates freely. Below T_B, the particles exhibit the single-domain ferromagnetic behavior, characterized by very slow relaxation and resonant spin tunnelling [34]. The relaxation time follows the exponential law given by (2.21), where τ_0^{-1} is the attempt frequency of the order of 10^{10} s^{-1}. AC susceptibility measurements enable probing different values of τ by varying the measurement frequency. A detailed experimental study on the magnetic relaxation of horse-spleen ferritin, which presents an example of natural nearly-monodisperse superparamagnetic particles, is reported in [35]. Above 30 K, χ' follows the Curie law and χ'' is nearly zero. Below 30 K, the blocking of progressively smaller magnetic

moments leads to the decrease of χ' and to the onset of a nonzero χ'' value. Both χ' and χ'' display frequency-dependent maxima. From the scaling of χ'' data, the distribution of relaxation times can be obtained. Information on possible interparticle interactions and on the distribution of particle sizes can be gained from the values of both components.

In the last decade, unusual magnetic relaxation properties were found for organometallic clusters in which spins of metal ions are coupled giving a high-spin ground state. The most prominent example here is the $Mn_{12}Ac$ complex [36], consisting of a core formed by eight $Mn^{III}(S = 2)$ and four $Mn^{IV}(S = 3/2)$ ions, and of the surrounding organic ligands. The ferrimagnetic coupling gives the total spin of a molecule $S = 10$. Magnetic interaction between $Mn_{12}Ac$ molecules is negligible. The characteristic feature of the cluster is a strong uniaxial anisotropy, expressed by the zero-field splitting parameter D. Anisotropy, combined with the high spin multiplicity gives rise to a large potential barrier DS^2 between the up- and down-spin states [37]. At low temperatures, such that $k_BT < D^2$, the free rotation of the magnetic moments is no longer possible. Only very slow magnetization change can occur.

The experimental evidence for the slow relaxation of high–spin molecules below T_B is a nonzero, frequency-dependent χ'' component. It was shown in Sect. 2.1.3 that conventional paramagnets display an out–of–phase susceptibility only in the presence of an external magnetic field. For high spin molecules, with the applied field set to zero, χ'' is indicative of slow relaxation of the magnetization, unable to keep in phase with the oscillating filed. The temperature behavior of χ' and χ'' for high-spin molecules is like that for superparamagnets: above T_B, $\chi' \propto 1/T$, while at $T = T_B$ χ' shows a frequency-dependent maximum; a peak in χ'' is observed just below T_B [36, 38, 39]. The relaxation times determined from $\chi''(\omega)$ follow the exponential law with τ_0 three orders of magnitude larger than that usually found in superparamagnets. It was found that at $T = 2$ K, τ is of the order of 2 months. Due to the remarkably large values of τ, the high-spin clusters are called single-molecule magnets. In single crystalline samples, the direction of the magnetic moment is common for all clusters due to the large anisotropy. For such systems, a coherent effect of the quantum tunnelling of molecular spins over the barrier height was observed, first by means of a "staircase" hysteresis loop [37–39] and then also with an applied DC–field–dependent dynamic susceptibility [40, 41]. In [40] the AC susceptibility of oriented $Mn_{12}Ac$ crystallites was measured in the external field applied at different angles to the sample easy axis. The χ' and χ'' peaks observed at $H_n = nH_1$ with $n = 0, 1, 2$, where $H_1 = 4.1$ kOe, gave evidence of field-tuned tunnelling between the excited magnetic states which are thermally populated. For another high-spin molecule, the Fe_8 cluster ($S = 10$), χ' also showed [41] three distinct maxima regularly spaced in the magnetic field. The maxima occurred for the same fields for which a strong decrease of the spin-lattice relaxation time was estimated from the frequency-dependent susceptibility measurements.

2.1.9 Summary

Measurements of AC magnetic susceptibility χ_{AC}, are essential for characterizing materials and for studying the dynamics of various types of magnetic systems. The low amplitude ($\sim$ 1 Oe) of the oscillating field probes the undisturbed ground state of the investigated system. Operating frequencies vary from several Hz (to compare with static susceptibility) up to the range of $\sim$ 100 kHz. χ_{AC} is a complex value with the real (in-phase) χ' and the imaginary (out–of–phase) χ'' component, where χ'' is related to losses due to energy absorbed from the field. These may be due to various relaxation processes, from spin-lattice relaxation in paramagnets to domain wall displacements in hard magnets. Relaxation time, or its distribution, can be determined from the relation between the intensities of both components (Argand plot). The paper gives the description of the spin-lattice and spin-spin relaxation in paramagnets and of the dynamics of domain walls in long-range ordered materials. Next, experimental χ_{AC} results are reviewed for the most representative magnetic substances. Literature data have been supplemented with own measurements. In particular, the following relaxation effects have been presented:

- low-temperature electron diffusion in the Zn-doped sample of magnetite $Fe_{3-x}Zn_xO_4$ ($x < 0.01$), for which activation energy and the relaxation time have been determined;
- reorientation of the magnetic moment in hard magnetic materials;
- magnetic phase-transitions in pure rare earth metals Gd and Tm;
- relaxation processes in some weakly coupled ferromagnets and in an antiferromagnet with low ordering temperatures;
- wide distribution of relaxation times in spin-glasses and spin-glass-like materials, illustrated with data for the novel molecular magnet $[Mn(CH_3)_4TPP][TCNE]\cdot$solvent;
- blocking phenomenon for superparamagnetic particles and quantum tunnelling effects in exotic high-spin molecules, e.g. $Mn_{12}Ac$ complex.

Relaxation effects in miscellaneous magnetic systems can be based on various mechanisms. The relatively well recognized from the relaxation point of view are paramagnets, superparamagnets and spin-glasses. On the other hand, relaxation effects in the long range ordered magnets depend on such factors as magnetic anisotropy, particular domain structure, macroscopic form or geometry of the sample, so systems of that type are less explored. Subsequent experimental studies, performed within the wide frequency range, would be desirable in order to get a more detailed knowledge on relaxation in magnetically ordered compounds.

References

A. A.H. Morrish: *The Physical Principles of Magnetism* (John Wiley & Sons, New York 1965)
B. R. Kubo, T. Nagamiya: *Solid State Physics* (McGraw-Hill, Inc. 1969)
C. C. Kittel, J.K. Galt: Solid State Physics **3**, 437 (1956)
D. S. Chikazumi: *Physics of Magnetism* (John Wiley & Sons, New York 1964)
E. J. Smit, H.P.J. Wijn: *Ferrites* (Philips Technical Library 1959)

1. T. Hashimoto, A. Sato, Y. Fujiwara: J. Phys. Soc. Japan **35**, 81 (1973)
2. S. Mukherjee, R. Ranganathan, S.B. Roy: Phys. Rev. B **50**, 1084 (1994)
3. Lake Shore Cryotronics, Inc., 7000 Series AC Susceptometer/DC Magnetometer – Users Manual, 1995
4. H.A. Groenendijk, A.J. van Duyneveldt, R.D. Willet: Physica **101**B, 320 (1980)
5. A.J. De Vries, D.A. Curtis, J.W.M. Livius, A.J. van Duyneveldt, C.J. Gorter: Physica **36**, 91 (1967)
6. J.A. van Duyneveldt. J. Soeteman, C.J. Gorter: Physica **47**, 1 (1970)
7. H.P.J. Wijn, H. van der Heide: Rev. Mod. Phys. **25**, 98 (1953)
8. F. Waltz, M. Weidner, H. Kronmüller: Phys. Stat. Sol. (a) **59**, 171 (1980)
9. V. Skumryev, H.J. Blythe, J. Cullen, J.M.D. Coey: J. Magn. Magn. Mater. **196**–**197**, 515 (1999)
10. D.-X. Chen, V. Skumryev, H. Kronmüller: Phys. Rev. B **46**, 3496 (1992)
11. D.-X. Chen, V. Skumryev, J.M.D. Coey: Phys. Rev. B **53**, 15014 (1996)
12. K. Łątka, R. Kmieć, A.W. Pacyna, R. Mishra, R. Pöttgen: Sol. State Sciences **3**, 545 (2001)
13. Ferromagnetic Materials, Vol. I, ed. by E.P. Wohlfarth (North-Holland, Amsterdam 1980)
14. S.Yu. Dan'kov, A.M. Tishin, V.K. Pecharsky, K.A. Gschneider, Jr.: Phys. Rev. B **57**, 3478 (1997)
15. J.M.D. Coey, V. Skumryev, K. Gallagher: Nature **401**, 35 (1999)
16. H.A. Groenendijk, A.J. van Duyneveldt: Physica **115** B+C, 41 (1982)
17. A. Kasten, P.H. Müller, M. Schenle: Physica **114** B+C, 77 (1982)
18. J. Kötzler, M. Grahl, I. Sessler: Phys. Rev. Lett. **64**, 2446 (1990)
19. H. Maletta, W. Zinn: *Spin Glasses*, in: Handbook on the Physics and Chemistry of Rare Earths, Vol. bf 12, ed. by K.A. Gschneider, L. Eyring (North-Holland, Amsterdam 1989)
20. J.A. Mydosh: *Spin Glasses: An Experimental Introduction* (Taylor & Francis, London 1993)
21. C.A.M. Mulder, A.J. van Duyneveldt, J.A. Mydosh: Phys. Rev. B **23**, 1384 (1981)
22. L. Lundgren, P. Svendlidh, O. Beckman: J. Phys. F. Met. Phys. **12**, 2663 (1982)
23. D.S. Fisher, D.A. Huse: Phys. Rev. Lett. **56**, 1601 (1986)
24. C. Dekker, A.F.M. Arts, H.W. de Wijn, A.J. van Duyneveldt, J.A. Mydosh: Phys. Rev. Lett. **61**, 1780 (1988)
25. J.J. Baalbergen, T.S. Ong, A.J. van Duyneveldt, J.C. Verstelle: J. de Physique **C8**, 1065 (1988)
26. J.M.D. Coey: J. Appl. Phys. **49**, 1646 (1978)
27. D.J. Sellmyer, S. Nafis: J. Appl. Phys. **57**, 3584 (1985)
28. R.I. Bewley, R. Cywinski: Phys. Rev. **54**, 15251 (1996)
29. E.M. Chudnovsky, W.M. Saslow, R.A. Serota: Phys. Rev. **B33**, 251 (1986)

30. J.S. Miller, A.J. Epstein: Angew. Chem. **106**, 399 (1994)
31. M.A. Gîrtu, C.M. Wynn, K.-I. Sugiura, J.S. Miller, A.J. Epstein: J. Appl. Phys. **81**, 4410 (1997)
32. M. Bałanda, K. Falk, K. Griesar, Z. Tomkowicz, W. Haase: J. Magn. Magn. Mater. **205**, 14 (1999)
33. K. Griesar, M. Athanassopoulou, E. Soto Bustamante, Z. Tomkowicz, A. Zaleski, W. Haase: Adv. Mater. **9**, 45 (1997)
34. J. Tejada, J.M. Hernández, E. del Barco: J. Magn. Magn. Mater. **196-197**, 552 (1999)
35. F. Luis, E. del Barco, J. M. Hernández, E. Remiro, J. Bartolomé, J. Tejada: Phys. Rev. **B59**, 11837 (1999)
36. A. Caneschi, D. Gatteschi, R. Sessoli, A.L. Barra, L.C. Brunel, M. Guillot: J. Am. Chem. Soc. **113**, 5873 (1991)
37. L. Thomas, F. Lionti, R. Ballou, D. Gatteschi, R. Sessoli, B. Barbara: Nature **383**, 145 (1996)
38. H.J. Eppley, H.-L. Tsai, N. de Vries, K. Foling, G. Christou, D.N. Hendrickson: J. Am. Chem. Soc. **117**, 301 (1995)
39. J.M. Hernández, X.X. Zhang, F. Luis, J. Tejada, J.R. Friedman, M.P. Sarachik, R. Ziolo: Phys. Rev. **B55**, 5858 (1997)
40. F. Luis, J. Bartolomé, J.F. Fernández, J. Tejada, J.M. Hernández, X.X. Zhang, R. Ziolo: Phys. Rev. **B55**, 11448 (1997)
41. F.L. Mettes, F. Luis, L.J. de Jongh: Phys. Rev. **B64**, 174411 (2001)

2.2 Dynamic susceptibility in heavy–fermion systems and related materials probed by electron spin resonance

H.-A. Krug von Nidda, M. Heinrich, and A. Loidl

2.2.1 Introduction

Heavy-fermion systems are intermetallic compounds, which contain ions with partially filled $4f$-(Ce, Yb) or $5f$-(U, Np) electron shells on regular lattice sites, but due to electronic correlations their paramagnetic moments become screened below a characteristic temperature $T^* \approx 10\,\mathrm{K}$ resulting in strongly enhanced effective masses m^* of the charge carriers [1, 2]. At low temperatures these compounds exhibit a Pauli susceptibility χ_P and Sommerfeld coefficient γ of the specific heat which are about 1000 times higher than in usual metals [3]. The electric resistivity shows a quadratic temperature dependence $\rho = AT^2$ indicating electron–electron scattering, which is not observable in normal metals, where its contribution is too weak in comparison with the phonon contributions. The low-temperature properties of such strongly correlated electron systems can be phenomenologically described in the framework of Landau's theory for Fermi liquids [4]. The Fermi-liquid state is characterized by the linear relation between χ_P and γ, the so called Wilson ratio R, which in appropriate normalization equals $R = 1$ for free electrons, but is slightly enhanced $R = 1 \ldots 2$ for heavy-fermion compounds [5]. A second important relation exists between resistivity and specific heat, where

$A/\gamma^2 = 10^{-5}$ (for A in $\mu\Omega\,\mathrm{cm\,K^{-2}}$ and γ in $\mathrm{mJ\,mol^{-1}\,K^{-2}}$) was empirically found by Kadowaki and Woods [6]. Both relations naturally follow from the mass enhancement of the heavy electrons $m^*/m_0 = T_\mathrm{F}/T^*$, which appears linearly in χ_P and γ, but squared in A. Here $T_\mathrm{F} \approx 10^4\,\mathrm{K}$ denotes the Fermi temperature for the Fermi gas of free electrons with mass m_0. The electronic correlations are caused by the scattering of the conduction electrons at the localized $4f$- or $5f$-electron shell, which is known as Kondo effect and results in the effective screening of the localized magnetic moments at low temperatures [7]. For this reason these compounds are also called Kondo lattices. Besides the Kondo effect, which favors a non magnetic ground state, the indirect exchange interaction of the localized moments via the conduction electrons (RKKY interaction [8]) promotes a magnetically ordered ground state. The final ground state depends on the hybridization strength $JN(E_\mathrm{F})$ of the local f moments with the conduction electrons which governs both interactions. Here J denotes the exchange coupling and $N(E_\mathrm{F})$ is the electronic density of states at the Fermi energy E_F. Following Doniach [9] one has to compare the energy gain due to the Kondo screening $T^* \propto \exp\left[-1/JN(E_\mathrm{F})\right]$ to the gain due to magnetic ordering $T_\mathrm{RKKY} \propto \left[JN(E_\mathrm{F})\right]^2$. In the case of weak hybridization, $T_\mathrm{RKKY} \gg T^*$, the localized moments remain stable down to lowest temperatures resulting in magnetic order ($T^* < 1\,\mathrm{K}$). In the case of strong hybridization, $T_\mathrm{RKKY} \ll T^*$, the ground state is a non magnetic metal with enhanced effective masses, so-called heavy fermions ($T^* \approx 10\,\mathrm{K}$), and with further increasing hybridization ($T^* > 100\,\mathrm{K}$) not only the magnetic moment but also the valence of the f shell becomes unstable resulting in intermediate valence [10]. If both energy scales are comparable $T_\mathrm{RKKY} \approx T^*$, one observes the highest effective masses and the competition of Kondo effect and RKKY interaction gives rise to interesting ground states like superconductivity [11], heavy-fermion band magnetism [12] or non Fermi-liquid behavior [13].

The dynamic susceptibility of the localized f moments contains important information on the microscopic situation at the Kondo ions. It can be probed by experiments, which are sensitive to the local electronic properties, like neutron scattering, nuclear magnetic resonance (NMR), and electron spin resonance (ESR). Indeed, a lot of Kondo-lattice systems have been investigated by NMR [14] and neutron scattering [15, 16], however only a few of the investigations were performed by means of ESR [17]. The reason may be the fact that the Kondo ion itself is not an appropriate ESR probe. Due to its strong hybridization with the conduction electrons, the spin of the Kondo ion relaxes too fast to give a measurable resonance signal. The expected linewidth is of the order of the characteristic temperature, i.e. several Tesla, and exceeds by far the field range of a typical ESR setup. Hence, it is necessary to dope small amounts of ions with stable magnetic moments into the compound under investigation. It turned out that Gd^{3+}, which itself belongs to the Lanthanides, usually fits very well onto the place of the f ions. Its half-filled $4f$ shell is very stable and therefore yields a measurable ESR signal.

The first Kondo-lattice compound, which was intensively studied by means of Gd-ESR, was intermediate valent $CePd_3$ [18]. Instead of an enhanced relaxation rate with respect to the non magnetic reference compound $LaPd_3$, a strong reduction of the relaxation rate was observed at low temperatures. This was explained by the opening of a pseudo gap in the conduction band due to coherence effects. A similar behavior was reported in intermediate valent $CeOs_2$ [19]. Later on, the heavy-fermion systems $CeCu_2Si_2$ [20] and $CeAl_3$ [20, 21] were investigated by Gd-ESR, which really exhibit an enhanced relaxation rate below the characteristic temperature T^* with respect to the reference compounds $LaCu_2Si_2$ and $LaAl_3$. However, the observed enhancement is by far not that large as expected from the bulk measurements. Again, it was assumed that the enhancement of the density of states is locally confined to the Ce ions, but the Kondo fluctuations of the Ce moments contribute to the relaxation of the Gd spin via the RKKY interaction. Similar results have been obtained in URu_2Si_2 [22], UPt_3 [23], $YbInCu_4$ [24] and $CeCu_6$ [25].

The aim of the present article is to work out a systematic pattern of the ESR in Kondo-lattice compounds in relation to NMR and neutron scattering and to review the recent developments in this field. After a short introduction into the peculiarities of ESR in metals and the dynamic susceptibility of Kondo ions, we review the systematic ESR investigation of CeM_2X_2, where M denotes a transition metal and X is Si or Ge. In these ternary compounds all possible ground states of a Kondo lattice are realized between magnetic order ($CeCu_2Ge_2$) and intermediate valence ($CeNi_2Si_2$). A separate section will be devoted to the Kondo insulator CeNiSn. Below its characteristic temperature $T^* = 20\,\mathrm{K}$, this compound reveals a coherence gap in the density of states resulting in semiconducting behavior. Finally, we give an outlook on electronic correlations in transition–metal oxides. Heavy-fermion formation has been observed by NMR e.g. in $Sr_{1-x}Ca_xRuO_3$ [26] and LiV_2O_4 [27, 28]. Recent ESR experiments in $Gd_{1-x}Sr_xTiO_3$ exhibit an appreciable enhancement of the electronic masses near the Mott–Hubbard metal-to-insulator transition as compared to free electrons.

2.2.2 ESR in metals

Detailed experimental reviews on this topic have been given by Taylor [29] and by Elschner and Loidl [17]. The theory has been summarized by Barnes [30]. Here, we shortly describe the basic features of Gd^{3+}-ESR spectra in metals. As a characteristic model system we present $CeCu_2Si_2$:Gd which belongs to the CeM_2X_2 series discussed below.

The electron spin resonance measures the power P_{abs} absorbed by the sample from the transverse magnetic microwave field $\mathbf{h}\cos(\omega t)$ with frequency $\nu = \omega/2\pi$ as a function of the static magnetic field $\mathbf{H} \perp \mathbf{h}$. To improve the signal-to-noise ratio one detects the field derivative dP_{abs}/dH by lock-in technique with field modulation. Figure 2.10 shows typical ESR spectra for $CeCu_2Si_2$:Gd together with the orientation dependence of resonance field H_{res}

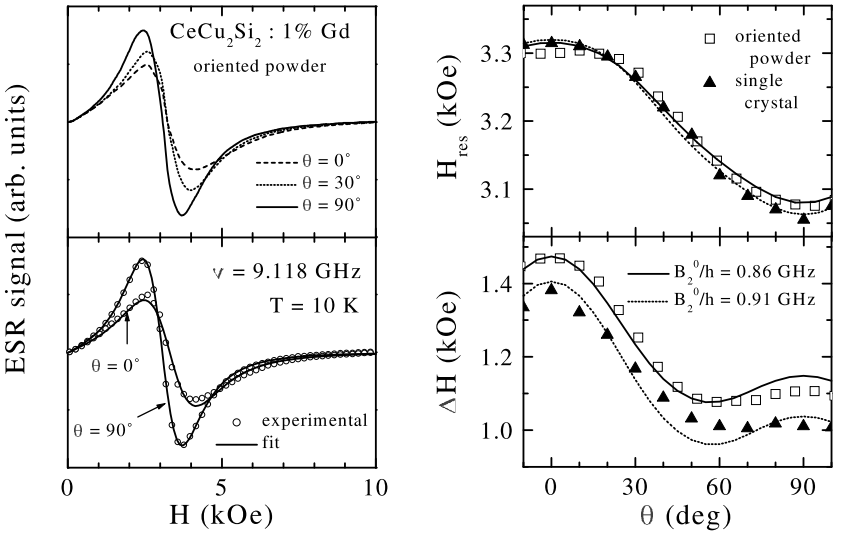

Fig. 2.10. *Left*: ESR spectra for an oriented powder sample $CeCu_2Si_2$:1%Gd at different orientations $\vartheta = \angle(c, H)$ (*upper frame*) fitted by the Dysonian line shape (*lower frame*). *Right*: Angular dependence of resonance field (*upper frame*) and linewidth (*lower frame*) for oriented powder compared to the single crystal results

and linewidth ΔH obtained from a fit with a Dysonian line shape

$$\frac{d}{dH}P_{\text{abs}} \propto \frac{d}{dH}\left\{\frac{\Delta H + \alpha\,(H - H_{\text{res}})}{(H - H_{\text{res}})^2 + \Delta H^2} + \frac{\Delta H + \alpha\,(H + H_{\text{res}})}{(H + H_{\text{res}})^2 + \Delta H^2}\right\}. \qquad (2.26)$$

This is a Lorentz curve which takes into account an admixture α of dispersion to the absorption signal. This admixture arises from the conductivity of the sample which drives electric and magnetic components of the microwave out of phase [31, 32] due to the skin effect. Because of the large linewidth, the resonance at $-H_{\text{res}}$ is included in (2.26) as well.

To explain the spectrum and its orientation dependence, one has to consider the following spin Hamiltonian:

$$\mathcal{H} = \mu_{\text{B}}\mathbf{HgS} + \frac{1}{3}B_2^0\left[3S_z^2 - S\,(S+1)\right] + J_{\text{Gd}}\mathbf{S}\cdot\boldsymbol{\sigma}. \qquad (2.27)$$

The first term describes the Zeeman interaction of the Gd-spin $\mathbf{S}$ with the static magnetic field $\mathbf{H}$ which splits the ${}^8S_{7/2}$-ground state of Gd^{3+} into eight equidistant energy levels $E_m = g\mu_{\text{B}}Hm\,(-7/2 \le m \le 7/2)$. The gyromagnetic tensor $\mathbf{g}$ for Gd^{3+} is approximately isotropic near $g = 2$. μ_{B} denotes the Bohr magneton. The microwave induces magnetic dipol transitions $\Delta m = \pm 1$, showing a single resonance absorption for $h\nu = g\mu_{\text{B}}H_{\text{res}}$, where h denotes the Planck constant.

The second term originates from the axial crystal-electric field (parameter B_2^0), which is dominant in all CeM_2X_2 compounds and yields a fine-structure splitting of the spectrum into seven resonance lines dependent on the polar angle ϑ between the crystallographic c-axis of the tetragonal structure and the magnetic field $\mathbf{H}$. For $B_2^0 \ll h\nu$ the resonance positions are approximated by

$$g\mu_B H_{m\to m+1} = h\nu - \frac{1}{2}B_2^0\,(2m+1)\left(3\cos^2\vartheta - 1\right). \tag{2.28}$$

The largest crystal-field splitting of the spectrum occurs at $\vartheta = 0°$ with a distance of $2B_2^0$ between neighboring resonances and it vanishes at the magic angle $\vartheta = 54.7°$. For larger values of B_2^0, one has to diagonalize the sum of Zeeman and crystal-field term and to determine the dipol transitions numerically. The angle of minimal splitting shifts for increasing B_2^0 to $\vartheta = 90°$.

The exchange interaction J_{Gd} between the conduction electrons (spin density σ) and the Gd spin, which is described by the third term in (2.27), leads to a coupling of the seven transitions and causes a narrowing of the ESR spectrum (comparable to the motional narrowing observed in NMR experiments) [33, 34]. In the case of strong exchange narrowing the spectrum again consists of one single Lorentz curve, whereby the crystal field remains visible in the orientation dependence of resonance field H_{res} and linewidth ΔH. The resonance field is given by the first moment of the fine structure, cf. (2.28). Its angular variation decreases with increasing temperature due to the Boltzmann factor. The linewidth contains an angular dependent contribution $\Delta H_{CF}(\vartheta) \propto M_2(\vartheta)/\Delta H_R$, proportional to the second moment M_2 of the fine structure divided by the relaxation ΔH_R via the exchange interaction, which will be discussed in the next section, cf. (2.30). $M_2(\vartheta)$ follows the angular dependence of the splitting showing a minimum at the magic angle.

2.2.3 Microscopic probes for the dynamic susceptibility

Now we focus on the resonance linewidth ΔH and its connection to the dynamic susceptibility of the Kondo lattice. In the following discussion, we use Ce^{3+} with electron configuration $4f^1$ as the Kondo ion, but the expressions can be analogously used for other Kondo ions, as e.g. Yb or U. The fluctuation-dissipation theorem provides the important relation between the imaginary part of the dynamic susceptibility $\chi_{Ce}(\mathbf{Q}, \omega, T)$ and the fluctuating magnetization $M_{Ce}(\mathbf{Q}, t)$ of the Kondo ions.

$$\frac{1}{2}\int_{-\infty}^{+\infty} < M_{Ce}(\mathbf{Q},0)M_{Ce}(\mathbf{Q},t) >_T \exp(i\omega t)dt = \frac{\mathrm{Im}\chi_{Ce}\,(\mathbf{Q},\omega,T)}{1-\exp\left(-\hbar\omega/k_B T\right)} \tag{2.29}$$

On the right-hand side, the term $1 - \exp\left(-\hbar\omega/k_B T\right)$ is the detailed–balance factor. The left-hand side is the Fourier-transformed thermal average of the

magnetization-correlation function $\langle \ldots \rangle_T$, which is proportional to the structure factor $S(\mathbf{Q}, \omega, T)$ measured by quasi-elastic neutron scattering (QNS) at momentum transfer $\mathbf{Q}$ and energy transfer ω [15, 16]. Hence, QNS directly measures the fluctuating magnetization of the Kondo ion.

Figure 2.11 illustrates, how the dynamic susceptibility is transferred to NMR and ESR probes by RKKY-like indirect exchange interactions via the conduction electrons. The NMR measures the spin-lattice relaxation rate $(1/T_1)_{\mathrm{NMR}}$ of the nuclear spin $\mathbf{I}$. The ESR measures the resonance linewidth ΔH_{ESR}, which represents the transversal spin-relaxation rate $(1/T_2)_{\mathrm{ESR}}$ of the Gd spin $\mathbf{S}$ and in metals equals the longitudinal or spin-lattice relaxation rate $(1/T_1)_{\mathrm{ESR}}$. For both NMR [35] and ESR [36] the relaxation rate $1/T_1$ consists of two contributions:

$$1/T_1 = (1/T_1)_{\mathrm{K}} + (1/T_1)_{\mathrm{Ce}} = b_{\mathrm{K}} T + b_{\mathrm{RKKY}} T \frac{\chi^0_{\mathrm{Ce}}}{\Gamma}. \tag{2.30}$$

The first term denotes the Korringa relaxation [37], which is typical for metals due to the direct exchange J_{Gd} (Gd-ESR) or hyperfine A (NMR) interaction with the conduction electrons (spin density σ). In usual metals, where the density of states $N(E)$ of the conduction electrons is approximately constant around the Fermi energy E_{F}, it increases linearly in temperature $(1/T_1)_{\mathrm{K}} = b_{\mathrm{K}} T$, with the slope $b_{\mathrm{K}} \propto N^2(E_{\mathrm{F}})$. The second term $(1/T_1)_{\mathrm{Ce}}$ is the contribution of the Kondo spins $\mathbf{s}$, which are strongly exchange coupled J_{Ce} with the conduction electrons. This contribution can be related to the dynamic structure factor $S(\mathbf{Q}, \omega, T)$ of QNS in the high-temperature approximation ($k_{\mathrm{B}} T \gg \hbar\omega$) and neglecting the $\mathbf{Q}$ dependence:

$$S(\omega, T) \propto \frac{T}{\omega} \mathrm{Im}\chi_{\mathrm{Ce}}(\omega, T) \propto (1/T_1)_{\mathrm{Ce,NMR}} \propto \Delta H_{\mathrm{Ce,ESR}}. \tag{2.31}$$

Using a purely relaxational ansatz for the correlation function in (2.29), the imaginary part of the dynamic susceptibility is of Lorentz shape centered at $\omega = 0$,

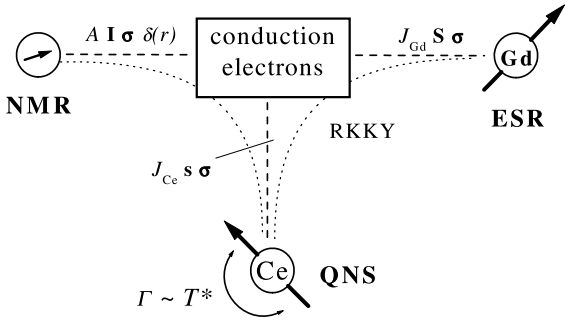

Fig. 2.11. Relaxation scheme for the Kondo ion (spin $\mathbf{s}$) to nuclear spin $\mathbf{I}$ and Gd spin $\mathbf{S}$

$$\mathrm{Im}\chi_{\mathrm{Ce}}(\omega,T)=\frac{\omega\Gamma}{\omega^2+\Gamma^2}\chi^0_{\mathrm{Ce}}\overset{\Gamma\gg\omega}{\longrightarrow}\frac{\omega}{\Gamma}\chi^0_{\mathrm{Ce}} \tag{2.32}$$

with the magnetic relaxation rate Γ (= quasi-elastic linewidth) and the static susceptibility χ^0_{Ce}. For NMR and ESR we are always working in the limit indicated on the right-hand side of (2.32), because our experimental frequencies are small compared to the quasi-elastic linewidth $\Gamma \approx T^*$. Figure 2.12 (left frame) shows different scenarios for the spin-lattice relaxation:

(a) heavy fermion with a characteristic temperature $T^* \approx 10\,\mathrm{K}$: At temperatures $T \ll T^*$, the Ce-4f momentum is completely screened by the conduction electrons; a large Pauli-like susceptibility χ^0_{Ce} and a large, temperature independent relaxation rate Γ yield a strongly enhanced Korringa-like increase in $1/T_1$. At temperatures $T > T^*$, the static susceptibility follows a Curie–Weiss law $\chi^0_{\mathrm{Ce}} = (T+\Theta)^{-1}$ with $\Theta = \sqrt{2}T^*$ [38, 39] and the relaxation rate Γ increases according to $\Gamma \propto \sqrt{T}$ [40]; therefore the Ce contribution $(1/T_1)_{\mathrm{Ce}}$ decreases with increasing temperature and for $T \gg T^*$ only the Korringa contribution $(1/T_1)_{\mathrm{K}}$ remains.

(b) Kondo insulator $T^* \approx 10\,\mathrm{K}$: At $T < T^*$ a gap of the order $\Delta \approx T^*$ opens in the density of states $N(E)$ at the Fermi energy so that $N(E_{\mathrm{F}}) \to 0$ for $T \to 0$. This strongly reduces the coupling coefficients b_{K} and b_{RKKY}, which both depend on $N(E_{\mathrm{F}})$. The gap can be approximately taken into account multiplying (2.30) by a factor $\exp(-\Delta/T)$.

(c) Intermediate valence $T^* \gg 10\,\mathrm{K}$: As T^* and Γ are very high, the second contribution can be neglected, yielding the linear metallic Korringa relaxation.

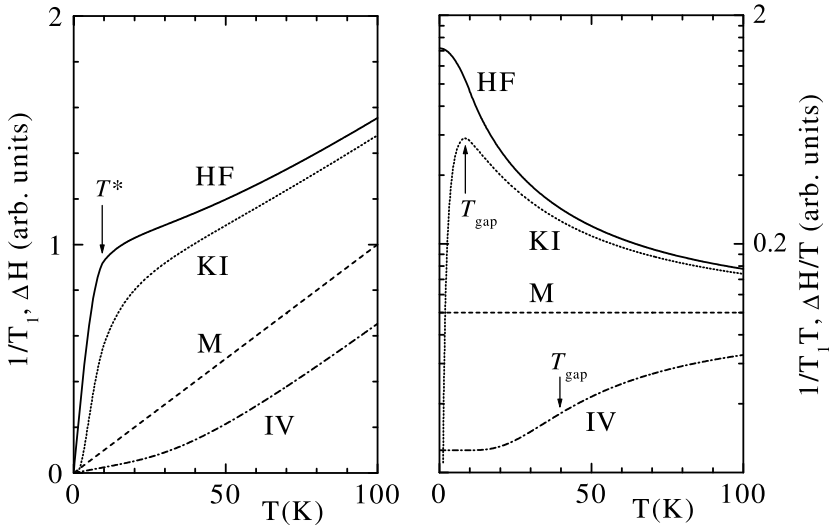

Fig. 2.12. Schematic temperature dependence of $1/T_1$ (*left*) and $1/T_1T$ (*right*) for heavy fermions (HF), Kondo insulator (KI), metal (M) and intermediate valence (IV)

Some of these systems (e.g. $CePd_3$, $CeOs_2$) exhibit a broad pseudo gap with a reduced density N_r of states around E_F on a range Δ of the order of T^*. This results in a reduced Korringa relaxation $b_r \propto N_r^2$ at low temperatures, an exponential intermediate regime and another linear regime with the normal Korringa slope b_K at high temperatures. For a rectangular pseudo gap (with E_F measured from the lower edge of the gap) the relaxation rate reads [19]

$$1/T_1 = Tb_K - T(b_K - b_r)\left(\frac{1}{e^{-E_F/T}+1} - \frac{1}{e^{(\Delta-E_F)/T}+1}\right). \tag{2.33}$$

As can be seen from (2.30), $1/T_1T$ corresponds to the imaginary part of the dynamic susceptibility plus a constant shift due to the Korringa slope b_K. This quantity is shown in the right frame of Fig. 2.12. Whereas normal metals reveal a constant behavior over the whole temperature range and heavy fermions saturate at a high value at low temperatures, Kondo insulators exhibit a maximum in $1/T_1T$ at a temperature T_{gap} which is a rough measure for the width of the gap.

Finally it is important to note that the ESR g value and NMR Knight shift are shifted from their insulator values by the polarization field of conduction electrons and Kondo ions, thereby reflecting the static susceptibility of the Kondo-lattice compound.

2.2.4 The Kondo lattices CeM_2X_2

The ternary compounds CeM_2X_2, where M denotes a d transition metal and X is Si or Ge, crystallize in the tetragonal $ThCr_2Si_2$ structure with space group I4/mmm [41]. The rare-earth ions occupy the corners $(0,0,0)$ and the center $(a/2, a/2, c/2)$ of the conventional unit cell. The transition-metal ions are found on the Cr places at $(0, a/2, c/4)$ and $(a/2, 0, c/4)$. Hence, the shortest distance between two Ce ions is a and the distance r between Ce and the next d ion is determined by $r^2 = (a/2)^2 + (c/4)^2$. Generally it is found that the smaller the value r, the stronger the hybridization and the larger the characteristic temperature T^*.

$CeCu_2Si_2$ is the most prominent member of these compounds ($r = 3.23\,\text{Å}$). With a characteristic temperature $T^* \approx 10\,\text{K}$ it represents the typical heavy-fermion behavior. Moreover, after the discovery of heavy-fermion superconductivity below $T_C = 0.65\,\text{K}$ [11], $CeCu_2Si_2$ became one of the most intensively studied Kondo lattices. Special attention has been devoted to the nature of the magnetically correlated A phase [42], which is found in the same temperature range as the superconductivity within an external magnetic field or for a slight Cu deficit. Gradual replacing of Cu by Ni decreases the unit cell and increases the hybridization [43]. The superconductivity is suppressed at 15% Ni and valence fluctuations start up for more than 30% Ni [44, 45]. $CeNi_2Si_2$ ($r = 3.13\,\text{Å}$) is a typical intermediate valent compound with a characteristic temperature $T^* \approx 600\,\text{K}$ [46].

Gradual replacing Si by Ge in $CeCu_2Si_2$ increases the unit cell and decreases the hybridization [47, 48]. Superconductivity is suppressed at 8% Ge and the magnetic phase directly evolves from the A phase. The ordering temperature monotonously increases with the Ge concentration. Pure $CeCu_2Ge_2$ ($r = 3.29\,\text{Å}$) is an antiferromagnetically ordered heavy-fermion system with $T^* = 6\,\text{K}$ and a Néel temperature $T_\text{N} = 4.1\,\text{K}$, where the Kondo screening and RKKY interaction are of nearly equal strength. It is important to note that applying hydrostatic pressure to $CeCu_2Ge_2$ yields a quite similar behavior like Si alloying. For pressures more than 70 kbar $CeCu_2Ge_2$ even becomes superconducting [49].

Alloying $CeCu_2Ge_2$ with Ni again increases the hybridization and yields a very rich phase diagram, which ends up at $CeNi_2Ge_2$ ($r = 3.22\,\text{Å}$), a non magnetic heavy-fermion compound with a characteristic temperature $T^* \approx 30\,\text{K}$ [50]. With increasing Ni concentration the first antiferromagnetic phase (T_N1), which is of local-moment type, is suppressed (at 15% Ni) and a second ordered phase develops, reaching a maximum ordering temperature $T_\text{N2} = 4.1\,\text{K}$ at 50% Ni. For higher Ni concentration the ordered moment strongly decreases, here the existence of heavy-fermion band magnetism [12] is suggested. For 80% Ni the magnetic order disappears and the occurrence of non Fermi-liquid behavior is discussed, as this compound is close to a magnetic instability [51, 52].

$CeRu_2Si_2$ ($r = 3.22\,\text{Å}$) is a heavy-fermion compound with a characteristic temperature $T^* \approx 15\,\text{K}$ [53]. It shows neither superconductivity nor magnetic order, but is close to a magnetic instability. Already a magnetic field of 7.7 T induces a metamagnetic phase transition [54]. Neutron scattering reveals increasing short-range antiferromagnetic correlations below 10 K [55].

2.2.4.1 Heavy Fermi liquid and intermediate valence

Most of the experiments presented here have been performed in oriented powder samples, because single crystals are hard to grow, but polycrystals are easily obtained from melting the starting elements in an argon-arc furnace. The polycrystalline ingots were ground to single-crystalline powder and – due to the uniaxial anisotropy of the magnetic susceptibility in CeM_2X_2 – aligned along the c-axis by a magnetic field and fixed with paraffin. As one can see from Fig. 2.10, the agreement between aligned powder and single-crystal data [56] is satisfactory.

Figure 2.13 shows the crystal-field parameter B_2^0 for the whole composition range between $CeCu_2Ge_2$ and $CeNi_2Si_2$, as determined from the angular dependence of the exchange narrowed ESR spectrum [57]. Only in the $CeNi_2(Si_{1-z}Ge_z)_2$ series, where we observe the largest values of B_2^0, the exchange narrowing is not strong enough at low temperatures, and B_2^0 was determined directly from the fine-structure splitting at $\vartheta = 0°$. In the isoelectronic series, where Si is replaced by Ge, only the volume is increased but the crystal field remains almost unchanged. Replacing Cu by Ni, which

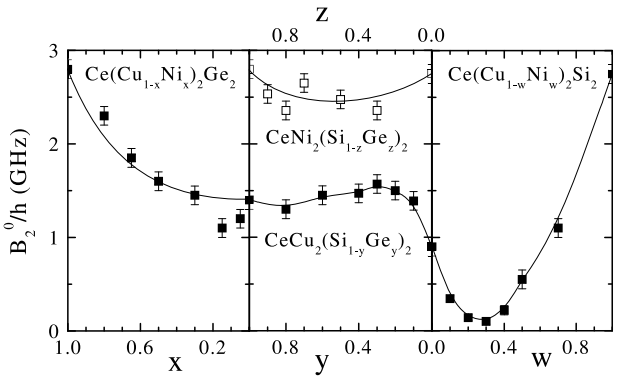

Fig. 2.13. The crystal-field parameter B_2^0 as a function of the composition for CeM_2X_2. In the *middle frame* the *open squares* belong to $CeNi_2(Si_{1-z}Ge_z)_2$

contains one electron less in its $3d$ shell, changes the electronic surrounding of the Gd^{3+} probe and results in a strong dependence of the crystal-field parameter on the Cu:Ni composition. Special attention should be devoted to the drastic decrease of the crystal-field parameter at the onset of valence fluctuations in $Ce(Cu_{1-w}Ni_w)_2Si_2$ at $w = 0.3$. As this decrease already starts in $CeCu_2(Si_{1-y}Ge_y)_2$, it cannot be explained by the Cu:Ni substitution alone, but it seems to be related to the onset of the valence fluctuations at $w = 0.3$ [43]. However at the same time, such a decrease is not observed in $CeNi_2(Si_{1-z}Ge_z)_2$. The reason is not clear, yet. Maybe, the local density of states in the copper compound provides a better coupling between Ce and Gd than in the nickel compound.

We start our discussion in the regime of strong hybridization, where the Kondo effect dominates and magnetic order is suppressed. Figure 2.14 shows the temperature dependence of the linewidth $\Delta H(T)$ for $Ce(Cu_{1-w}Ni_w)_2Si_2$ at the magic angle, at which the influence of the crystal field is smallest [57]. One clearly observes the two characteristic patterns for heavy fermions and intermediate valent compounds (cf. Fig. 2.12). In $CeCu_2Si_2$ (left frame) the linewidth $\Delta H(T)$ is dominated by the Ce-spin fluctuations, showing the typical negative curvature around T^*. For $w = 0$ and 0.1 the data are well fitted by (2.30), where a constant residual linewidth ΔH_0 was added to account for the contributions of crystal field and impurities. The characteristic temperatures were obtained from the fit as $T^* = 15\,\mathrm{K}$ and $56\,\mathrm{K}$ for $w = 0$ and 0.1, respectively. With increasing Ni concentration w the strong increase of T^* corresponds to a decrease in $\mathrm{Im}\chi_{\mathrm{Ce}}(\omega, T)$. For $w = 0.1$ the Ce contribution already weakens. At $w = 0.2$ we observe a nearly linear behavior like in a usual metal. The slight enhancement of the Korringa relaxation $b_{\mathrm{K}} = 7.5\,\mathrm{Oe/K}$ (with respect to $b_{\mathrm{K}} = 5\,\mathrm{Oe/K}$ at $w = 0$) reflects the change in the density of states due to the Ni doping. In the compounds $w = 0.3$ and $w = 0.4$ the Ce contribution is not visible any more, the linewidth even shows a positive

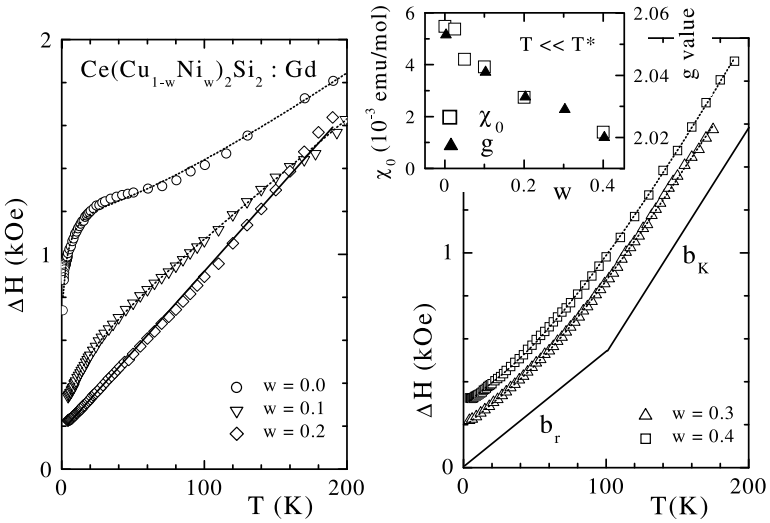

Fig. 2.14. Temperature dependence of the ESR linewidth for $Ce(Cu_{1-w}Ni_w)_2Si_2$, $0 \leq w \leq 0.4$. *Left frame*: The *dotted lines* are fit curves by (2.30): $w = 0; 0.1$: $T^* = 15; 56\,\mathrm{K}$, $b_\mathrm{K} = 5; 6\,\mathrm{Oe/K}$, $\Delta H_0 = 600; 140\,\mathrm{Oe}$, the *solid line* ($w = 0.2$) indicates a pure Korringa law. *Right frame:* The *dotted lines* are fitted by (2.33) for $w = 0.3; 0.4$: $\Delta = 380; 480\,\mathrm{K}$, $E_\mathrm{F} = 190; 350\,\mathrm{K}$, $b_\mathrm{r} = 5.6; 5.3\,\mathrm{Oe/K}$, $b_\mathrm{K} = 10.4; 12.1\,\mathrm{Oe/K}$, $\Delta H_0 = 186; 290\,\mathrm{Oe}$. The *solid lines* indicate reduced b_r and normal b_K Korringa slope. *Inset*: g value and static susceptibility [46] at $T \ll T^*$

curvature in its temperature dependence in accordance with the typical behavior of intermediate valent systems. The hybridization gap weakens the Korringa relaxation (b_r) at $T < T^*$ with respect to high temperatures (b_K) approximately by a factor 2. As $b_\mathrm{K} \propto N^2(E_\mathrm{F})$, the density of states in the gap is reduced by about $\sqrt{2}$. The half width $\Delta/2$ of the hybridization gap is a reasonable measure for the characteristic temperature. From the fit of $\Delta H(T)$ with (2.33), one obtains $T^* = 190\,\mathrm{K}$ and $240\,\mathrm{K}$ for $w = 0.3$ and 0.4, respectively. For higher Ni concentrations (not shown in Fig. 2.14) the increasing crystal field masks the signatures of the gap. The inset of Fig. 2.14 illustrates the correlation between the g value and static susceptibility χ_0 at low temperatures $T < T^*$, where both quantities saturate. As expected, the magnetic polarization of the Ce ions results in a comparable g shift for the Gd probe, which decreases with increasing hybridization. Due to the relatively small influence of the crystal field at Ni concentrations ($w < 0.5$), the compound $Ce(Cu_{1-w}Ni_w)_2Si_2$ turned out to be an ideal model system to study the onset of valence fluctuations by Gd-ESR.

2.2.4.2 Competition of magnetism and heavy Fermi liquid

Now we turn to the regime of weaker hybridization, where the influence of the RKKY interaction becomes comparable to the Kondo effect. In the left picture of Fig. 2.15 the temperature dependence of the resonance linewidth $\Delta H(T)$ is shown for $CeCu_2(Si_{1-y}Ge_y)_2$ at the orientation of minimum linewidth which corresponds to $\vartheta = 55°$ for $y = 0$ and $\vartheta = 90°$ for all other compositions due to the higher crystal field [58]. The solid lines were obtained by fitting the data at temperatures $T > T_N$ using (2.30), where again a constant residual linewidth was added to compensate approximately the crystal-field contribution. In the ordered regime $T < T_N$ the linewidth is governed by inhomogeneous broadening due to internal fields and therefore it does not represent the relaxation rate $1/T_1$ anymore. The fit curves nicely describe the experimental data and establish the typical scenario expected for heavy-fermion compounds. The contribution of the spin fluctuations is strongest for $CeCu_2Ge_2$ with the lowest characteristic temperature $T^* = 6\,\mathrm{K}$ and decreases with increasing Si content. At high temperatures all curves approximate the linear Korringa regime with $b_K \approx 5\,\mathrm{Oe/K}$ characteristic for the non magnetic reference compound $LaCu_2Si_2$ [20].

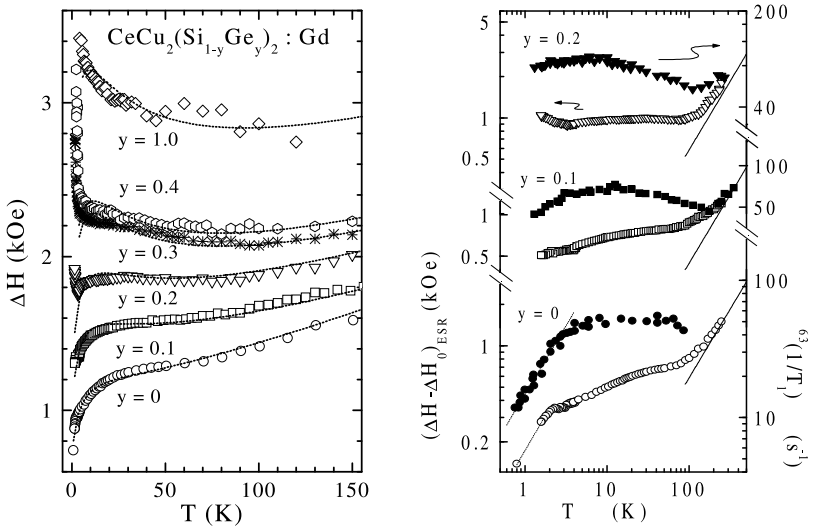

Fig. 2.15. *Left frame*: Temperature dependence of the ESR linewidth for $CeCu_2(Si_{1-y}Ge_y)_2$: The *solid lines* indicate the fit with (2.30), $0 \le y \le 1$: $15 \ge T^* \ge 6\,\mathrm{K}$, $0.6 < \Delta H_0 < 1.6\,\mathrm{kOe}$, $b_K = 5\,\mathrm{Oe/K}$. *Right frame*: Comparison of the ESR linewidth (*open symbols*) to the ^{63}Cu–NMR relaxation rate $1/T_1$ (*closed symbols*: $y = 0$ [59], $y = 0.1$; 0.2 [28, 60]). The *solid lines* indicate the high–temperature Korringa slope

The right picture in Fig. 2.15 compares the ESR linewidth to the ^{63}Cu-NMR spin-lattice relaxation rate [28, 59, 60]. Both quantities are normalized to the high-temperature regime, where the usual Korringa relaxation due to the delocalized conduction electrons dominates. Hence, the plot clearly reveals that the relative contribution of the Ce-spin fluctuations is higher in the NMR-relaxation rate than in the Gd linewidth. This fact proofs the local character of the Ce-4f hybridization and the relaxation mechanism via RKKY interaction: If the hybridization was spread over the whole conduction band, normal Korringa and 4f contribution should exhibit the same relative strength for both the ESR and the NMR probe. But the RKKY interaction strongly depends on the distance between the 4f moments and the respective probe. The corresponding squared matrix elements, which determine the relaxation rate, decrease proportional $1/R^6$ with increasing distance R of the probe to the Ce-4f momentum [61]. The nearest Cu neighbor of the Ce ion is located at only about 3/4 of the distance of the Ce–Ce (Gd) separation. Compared to the usual Korringa relaxation, this simple estimation yields a relative strength of the 4f contribution which is 5 times higher for the ^{63}Cu-NMR than for the Gd^{3+}-ESR. This estimate agrees well with the experimental result, where the 4f-contribution is more than 3 times larger for NMR than for ESR.

The temperature dependence of the ESR linewidth in the related compound $Ce(Cu_{1-x}Ni_x)_2Ge_2$ nicely reveals all peculiarities of the phase diagram, as it is shown in Fig. 2.16 (left frame) [62]. The logarithmic temperature scale better visualizes the low-temperature behavior. Both magnetic phases

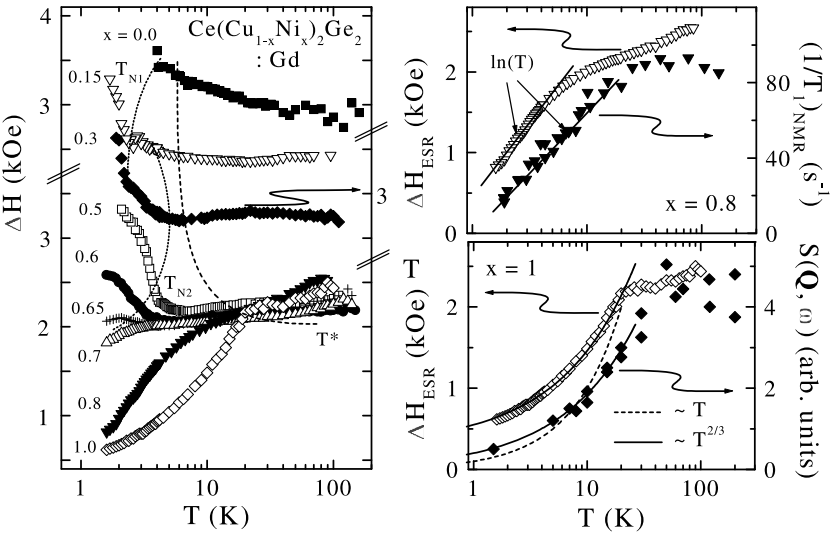

Fig. 2.16. Temperature dependence of the ESR linewidth for $Ce(Cu_{1-x}Ni_x)_2Ge_2$, $0 \leq x \leq 1$ at $\vartheta = 90°$ (*left*). Comparison to ^{63}Cu–NMR relaxation rate $1/T_1$ and structure factor $S(\mathbf{Q}, \omega)$ from neutron scattering [51] (*right*)

are indicated by a strong inhomogeneous line broadening below T_{N1} and T_{N2}, which can be taken as a measure for the ordered Ce moment. Especially for $0.5 < x < 0.8$ the strong reduction of the magnetic moment is accompanied by the decrease of the inhomogeneous contribution to the linewidth. A direct fit with (2.30) is omitted, because of the strong increase of the crystal-field parameter on increasing Ni concentration, which influences the temperature dependence, as well.

Nevertheless, the comparison to NMR ($x = 0.8$) and neutron-scattering ($x = 1.0$) data shows a quite satisfying agreement with the ESR linewidth, as one can see on the right-hand side of Fig. 2.16. At these Ni concentrations, it is interesting to focus on the non Fermi-liquid behavior near the quantum-critical point ($T_N = 0$), where magnetic order is suppressed. For $x = 0.8$ (upper frame) the NMR spin-lattice relaxation rate shows a clear deviation from the linear Fermi-liquid dependence at low temperatures [51]. But there is still a lack of theory concerning this point in a non Fermi-liquid. The logarithmic temperature scale suggests $1/T_1 \propto \ln(T)$ for $T < 15\,\mathrm{K}$. Further support was given by a logarithmic divergence in the Sommerfeld coefficient of the specific heat $C/T \propto \ln(T)$, in the temperature range $1 \leq T \leq 6\,\mathrm{K}$ [52], which is in accordance with theoretical predictions. The ESR linewidth seems to support the NMR data, however the logarithmic temperature dependence develops only for $T < 5\,\mathrm{K}$. For $CeNi_2Ge_2$ (lower frame) the typical kink, which marks the characteristic temperature T^*, appears near 20 K in the ESR linewidth and around 30 K in the neutron data [51]. This is not fully understood but possibly it is in part due to the influence of the relatively strong crystal field onto the ESR linewidth, which results in an only partially narrowed spectrum, where not all transitions are fully involved. However, it is interesting to note that ΔH as well as $S(\mathbf{Q}, \omega)$ decrease weaker than linearly. A Korringa behavior $1/T_1 \propto T$ is indicated as a dashed line. These deviations from a linear increase may still result from quantum-critical phenomena. But much more systematic work is needed to clarify this behavior in detail.

Another interesting effect is observed for $CeRu_2Si_2$, which is shown in Fig. 2.17 [57, 63]. The resonance linewidth (and CF parameter B_2^0) is of the same magnitude as in $CeNi_2Ge_2$ and also reveals the negative curvature near the characteristic temperature T^*, as it is typical for heavy-fermion compounds. However, below 8 K it becomes constant for 1% Gd doping and even increases for higher doping concentrations. At 0.5% Gd the signal is too weak to obtain additional information, because of the large linewidth. As can be seen in the inset of Fig. 2.17, doping of non-magnetic Y removes the plateau at low temperatures and restores the heavy-fermion behavior. It is important to note that the ^{29}Si-NMR relaxation rate in pure $CeRu_2Si_2$ [64] does not show any anomaly around 8 K, but exhibits a strongly enhanced Korringa rate below $T^* \approx 15\,\mathrm{K}$.

This comparison suggests that the Gd doping itself is responsible for the observed anomaly at low temperatures. Like the magnetic field of 7 T, which induces a metamagnetic transition in pure $CeRu_2Si_2$ [54], the presence of

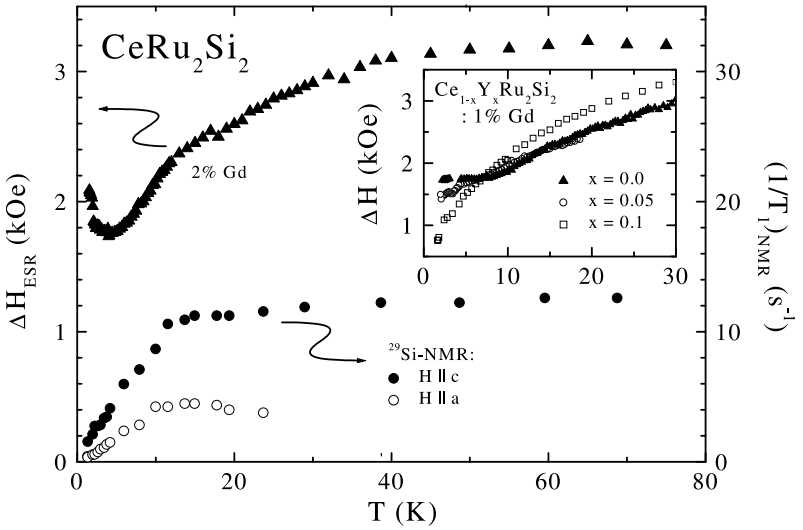

Fig. 2.17. Temperature dependence of the ESR linewidth for $CeRu_2Si_2$ at $\vartheta = 90°$ and comparison to ^{29}Si-NMR relaxation rate $1/T_1$ [64]. *Inset:* effect of Y doping

1% Gd spins may give rise to a magnetic transition. This was also supported by additional susceptibility measurements [65] at the doped sample which revealed a kink near 7 K after subtraction of the paramagnetic contribution of 1% Gd. The ordered moment of this induced ground state seems to be quite low, because there is no strong inhomogeneous line broadening as observed e.g. in $CeCu_2Ge_2$. The nature of this induced ground state may be related to the ground state observed in URu_2Si_2 ($T^* = 45$ K, $T_N = 17.5$ K), which was identified as a spin-density wave with extremely small ordered moments ($< 0.03\mu_B$) [66]. URu_2Si_2 was also intensively studied by Gd-ESR [22], and the Gd linewidth reveals a quite similar temperature dependence like $CeRu_2Si_2$. However, its absolute value is by far smaller, because the contribution of the crystal field is negligible in URu_2Si_2. In that compound it was possible to resolve an exponential decrease of the ESR linewidth below T_N related to the opening of an excitation gap due to the evolution of the spin-density wave, because there is no inhomogeneous broadening from large ordered moments. In $CeRu_2Si_2$ this behavior could be masked by the large contribution of the crystal field to the linewidth. Nevertheless the evolution of the plateau below 8 K could indicate some similar effect. In any case $CeRu_2Si_2$ is very close to a magnetic instability and a weak perturbation by additional magnetic ions probably induces magnetic order with highly itinerant character, which was also discussed for $Ce(Cu_{1-x}Ni_x)_2Ge_2$ at $x > 0.5$.

2.2.5 Kondo insulators

CeNiSn is a Kondo-lattice compound with $T^* \approx 20\,\mathrm{K}$. With decreasing temperature the electric resistance ρ shows a drastic increase below 7 K. This can be explained by the opening of an energy gap in the electronic density of states [67, 68]. Meanwhile, pure CeNiSn has been established as a semi metal with a small overlap of valence and conduction bands [69]. In this case the hybridization-matrix elements vanish at appropriate places of the Brillouin zone. Therefore, the density of states exhibits a very small but finite value in the hybridization gap at the Fermi energy. In agreement with NMR and neutron scattering [70, 71], ESR experiments show that the opening of a gap is an intrinsic property of CeNiSn and this gap can systematically be suppressed by substituting Co or Pt for Ni [72].

The anisotropy of the susceptibility allows to align the powdered CeNiSn along the a-axis of the monoclinic structure and to estimate the axial contribution B_2^0 from the orientation dependence of the exchange narrowed Gd-resonance line. For pure and all Co or Pt doped CeNiSn samples under investigation, the crystal field acting on the Gd probe $0.3 \lesssim B_2^0/h \lesssim 0.7\,\mathrm{GHz}$ is found by far smaller than in most CeM_2X_2 compounds and therefore of minor importance [72]. The temperature dependence of the resonance spectra was obtained for the field applied perpendicular to the aligned a-axis, where the minimum of the linewidth was identified.

In CeNiSn, both spin fluctuations and reduced density of states influence the Gd-ESR. Looking at the temperature dependence of the linewidth in pure CeNiSn:Gd (cf. Fig. 2.18, left frame), a Korringa behavior with a slope $b_\mathrm{K} \approx 18\,\mathrm{Oe/K}$ can be identified for temperatures above 25 K. At lower temperatures the slope increases yielding a gradient $b_\mathrm{K} \approx 34\,\mathrm{Oe/K}$ for $5 \leq T \leq 15\,\mathrm{K}$ and at the lowest temperatures, $T < 3\,\mathrm{K}$, the linewidth becomes almost constant. $\Delta H(T)$ of CeNiSn reveals good agreement with the model of a Kondo insulator as shown in Fig. 2.12. This becomes even more evident in the $1/T_1T$-plot for Gd-ESR and ^{119}Sn-NMR [70] in the left inset of Fig. 2.18, as this representation better pronounces the effect of the pseudo gap. Before dividing the ESR linewidth by the temperature, the constant value ΔH_0 at low temperatures was subtracted. The NMR-relaxation rate is shown for $H \parallel a$, because only for this direction data points are available down to 2 K. For the other orientations the data points exist above 4 K and reveal the same temperature dependence with up to 30% enhanced absolute values [70]. Both NMR and ESR show a parallel behavior, but the maximum in $1/T_1T$, which is a measure for the hybridization gap, is more pronounced in the NMR data. Again, this results from the smaller distance between Ce and Sn compared to the space between Ce and Gd, which is decisive for the relaxation mechanism via the RKKY interaction and underlines the local character of the hybridization.

To discuss the influence of the substitution of Ni by Co or Pt, we stay in the $1/T_1T$ representation (cf. right picture of Fig. 2.18). Focusing on the

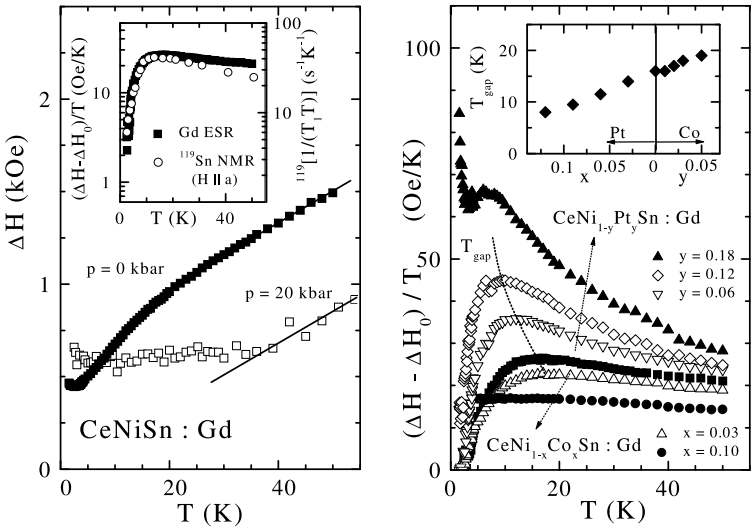

Fig. 2.18. *Left*: Temperature dependence of the ESR linewidth for CeNiSn:Gd for ambient pressure and at hydrostatic pressure of 20 kbar. *Solid lines* indicate the Korringa law. *Inset*: $(\Delta H - \Delta H_0)/T$ for CeNiSn:Gd in comparison to the ^{119}Sn–NMR relaxation rate $1/T_1T$ [70] of pure CeNiSn. *Right*: $(\Delta H - \Delta H_0)/T$ for CeNiSn:Gd for different Co (x) and Pt (y) doping. *Inset*: gap temperature $T_{\rm gap}$ dependent on the doping

$CeNi_{1-x}Co_xSn$ compounds, we recognize that the high-temperature Korringa slope decreases with increasing Co-concentration and also the transition region to an enhanced slope shifts to higher temperatures. The sample with 10% Co shows almost a pure Korringa behavior like a normal metal, indicating that the gap becomes smeared out at the Fermi energy. This may be connected to the fact that Co substitution does not change the size of the elementary-cell volume, but changes the band filling. Substitution of Ni by Pt increases the volume of the elementary cell and in turn decreases the hybridization. The gap is narrowed, as indicated by the shift of the maximum, and vanishes at 18% Pt, where $(\Delta H - \Delta H_0)/T$ maintains a high value for $T \to 0$, typical for a pure heavy-fermion system. The right inset in Fig. 2.18 illustrates the dependence of the hybridization gap on the Co and Pt doping, as determined from the temperature $T_{\rm gap}$ of the maximum in $(\Delta H - \Delta H_0)/T$. One observes a linear evolution of the gap, which is in very good agreement with the results from specific-heat measurements [73]: The maximum in the Sommerfeld coefficient, which is a measure for the hybridization gap as well, exhibits the same linear dependence on the doping scaled by a factor 1/3.

Now we turn back to the left picture of Fig. 2.18, which includes the effect of hydrostatic pressure on the Gd linewidth in CeNiSn [74]. The pressure experiment was performed in the same device which was used for $CeAl_3$ by

Schlott et al. [21]. A pressure of 20 kbar strongly increases the width of the hybridization gap. The linewidth remains nearly constant up to 30 K and exhibits the same Korringa rate at higher temperatures like at ambient pressure. Within the pressure cell the powder cannot be oriented and therefore the residual linewidth is somewhat larger. This behavior of $\Delta H(T)$ in CeNiSn under pressure strongly reminds on the typical pattern of intermediate valent compounds with vanishing $b_r \rightarrow 0$. This experiment shows the close relation between the gaps observed in Kondo insulators and intermediate-valence compounds in the electronic density of states: Both originate from the hybridization, but in the former case the gap is fully developed, whereas in the latter case the density of states is only partially reduced.

In this respect, it is important to mention the mixed-valent rare-earth compound SmB_6, a semiconductor with an extremely small band gap of 3–4 meV [75]. The nature of this gap has been under controversial discussion for a long time, but recently SmB_6 was also classified as a Kondo insulator [76]. The Gd-ESR linewidth observed in SmB_6 exhibits an analogous temperature dependence like in CeNiSn [77, 78] in agreement with the mentioned band gap. The intensive ESR studies, which have been performed in SmB_6 using Gd, Eu and Er as paramagnetic probes, are summarized in detail in the review article by Elschner and Loidl [17].

2.2.6 Summary and outlook

In conclusion we have shown that electron spin resonance is a well suited technique to study the dynamic susceptibility in heavy-fermion systems. Despite the fact that probe ions have to be doped into the material, the ESR linewidth contains valuable information on the local electronic properties like the spin-lattice relaxation of nuclear magnetic resonance and the dynamic structure factor of quasi-elastic neutron scattering. As model system we have chosen the CeM_2X_2 compounds which allow to tune widely the hybridization by the composition of transition metal M and silicon or germanium X.

The canonical heavy-fermion behavior was presented in $CeCu_2Si_2$, where the temperature dependence of the Gd linewidth is very well described by the two contributions of Ce-spin fluctuations and usual metallic Korringa relaxation, respectively. The simultaneous comparison with the Cu-NMR spin-lattice relaxation rate verifies the relaxation mechanism to the Ce spins via RKKY interaction and underlines the local character of the hybridization.

Gradual replacing Cu by Ni increases the hybridization up to intermediate valent $CeNi_2Si_2$. At the onset of valence fluctuations (30–40% Ni), the RKKY contribution vanishes and the Korringa rate becomes reduced at low temperatures due to the evolution of a hybridization gap at the Fermi energy. The linewidth data allow to determine the gap width and the concomitant reduction of the electronic density of states.

The competition of Kondo effect and magnetic order was presented in $CeRu_2Si_2$ and in the alloys $CeCu_2(Si_{1-y}Ge_y)_2$ and $Ce(Cu_{1-x}Ni_x)_2Ge_2$. The

temperature dependence of the Gd linewidth reflects all peculiarities of the respective phase diagrams. In the paramagnetic regime the Gd linewidth is dominated by the Ce-spin fluctuations like in $CeCu_2Si_2$. But the onset of magnetic order is characterized by a strong inhomogeneous line broadening to low temperatures, which can be taken as a measure for the ordered moment. Near the quantum-critical point, where magnetic order is suppressed, indications of non Fermi-liquid behavior are observed.

Finally we discussed the peculiarities of the Kondo insulator CeNiSn which does not belong to the CeM_2X_2 series. The nonlinear temperature dependence of the Gd linewidth clearly reveals the signatures of both relaxation via spin fluctuations and evolution of the hybridization gap. Doping Pt onto the Ni place narrows the gap and restores the pure heavy-fermion behavior, whereas hydrostatic pressure widens the gap and drives the system into intermediate valence.

These examples have shown that electron spin resonance is very sensitive to the various ground states in heavy-fermion systems. Meanwhile, in the field of strongly correlated electron systems the main interest shifts more and more from the traditional $4f$- and $5f$-based Kondo-lattice compounds to transition-metal oxides. E.g. the perovskite titanates $R_{1-x}A_xTiO_3$ (where R denotes Y^{3+}, La^{3+}, or some trivalent rare-earth ion, and A is a divalent alkali-earth ion like Ca^{2+} or Sr^{2+}) exhibit metallic conductivity due to a partial filling $3d^{1-x}$ of the Ti-$3d$ band and undergo a correlation-induced metal-to-insulator transition on approaching "half-filling" $x = 0$ (so-called Mott-insulator) [79]. A critical increase of the Sommerfeld coefficient γ of the specific heat has been observed in $La_{1-x}Sr_xTiO_3$ and $Y_{1-x}Ca_xTiO_3$ on approaching the metal-to-insulator transition from the metallic side, indicating an enhancement of the effective electron mass [80, 81]. Although these systems are ESR silent, probably because of the too fast relaxation of the Ti spins, the related compound $Gd_{1-x}Sr_xTiO_3$ [82], which exhibits a quite similar phase diagram (cf. Fig. 2.19), is well suited for ESR experiments, because it naturally contains Gd as ESR probe.

The left picture of Fig. 2.19 shows the temperature dependence of the Gd-resonance linewidth within the metallic regime $0.2 \leq x \leq 0.6$. Approaching the metal-to-insulator transition from above ($x \geq 0.2$), the prominent maximum in $\Delta H(T)$ increases and shifts to lower temperatures T^*. This behavior strongly reminds to the relaxation contribution of the Kondo ions in the typical heavy-fermion compounds. Instead of the Kondo f ions, the Ti^{3+} ($3d$) spin system exhibits fluctuations which are transferred to the Gd spin via super-exchange interactions. For an appropriate description of the dynamic susceptibility the itinerant character of the Ti electrons has to be taken into account, following Ishigaki and Moriya [83, 84]. For details of the fitting see [82]. The correlation of the linear slope b_{LT} at $T \ll T^*$ with the squared Sommerfeld coefficient γ^2 of the specific heat, as shown in the lower right frame of Fig. 2.19, underlines the enhancement of the electronic density of states

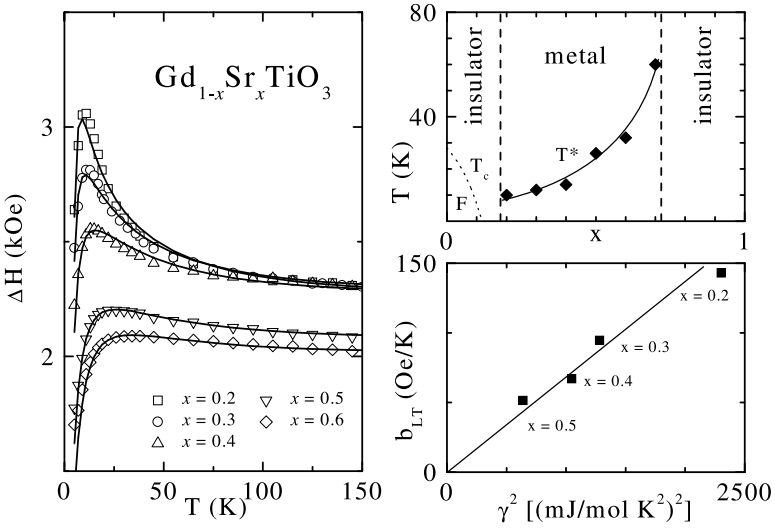

Fig. 2.19. *Left*: Temperature dependence of the ESR linewidth for $Gd_{1-x}Sr_xTiO_3$ in the metallic regime. *Solid lines* are fit curves following Moriya's spin-fluctuation theory [82]. *Right*: Phase diagram, T^* from maximum of the linewidth, F=ferrimagnetic phase with Curie temperature T_C (*upper frame*) and low-temperature Korringa slope b_{LT} vs. squared Sommerfeld coefficient γ of the specific heat (*lower frame*)

$N(E_F)$ which is visible by both macroscopic ($\gamma \propto N(E_F)$) and microscopic ($b_{LT} \propto N^2(E_F)$) probes. Similar results were obtained in $Gd_{1-x}Ca_xTiO_3$ [85].

All attempts to measure directly the ESR signal of the fluctuating spins, which are responsible for the heavy-fermion behavior in transition-metal oxides, failed up to now, as e.g. in the case of LiV_2O_4 [86]. As already mentioned above, its linewidth is probably too large like in the Kondo-lattice compounds. But there exists a lot of interesting problems in transition-metal oxides, where it is possible to detect the magnetic resonance of the *d*-electron spins of interest. In this case ESR gains an outstanding importance in the investigation of the microscopic degrees of freedom. To give only a few examples of recent ESR-research activities in this field, there is e.g. the orbital order in the colossal-magneto-resistance material $La_{1-x}Sr_xMnO_3$ [87] or the charge-order in the spin-ladder system NaV_2O_5 [88]. The spin-Peierls compound $CuGeO_3$ is intensively studied with magnetic resonance [89–91], and especially the influence of defects onto the dimerized ground state [92]. In related one-dimensional spin chains like in the telephone-number compound $La_{14-x}Ca_xCu_{24}O_{41}$ [93] or in the spinel $LiCuVO_4$ [94], the importance of the ring-exchange interaction is proven by means of ESR. Here we are just at the beginning of a large promising field for future investigations in paramagnetic resonance.

Acknowledgements. We have strongly benefited over the years from collaborations and discussions with many colleagues, especially with the members of the Sonderforschungsbereich SFB 252 "Elektronisch hochkorrelierte metallische Materialien", Darmstadt/Frankfurt/Mainz/Stuttgart and of the SFB 484 "Kooperative Phänomene im Festkörper: Metall-Isolator-Übergänge und Ordnung mikroskopischer Freiheitsgrade", Augsburg. In particular we want to mention our fruitful cooperations with several members of Kapitza Institute, Moscow, Kazan State University and Zavoisky Physical-Technical Institute, Kazan. We thank B. Elschner for his continuous support and many useful discussions and N. Büttgen for long lasting good teamwork with NMR and critical reading of the manuscript.

This work was partially supported by Deutsche Forschungsgemeinschaft (DFG) within SFB 252, SFB 484 and DFG project, grant no. LO 264/10-2, and by the Bundesministerium für Bildung und Forschung (BMBF) under the contract number VDI/EKM 13N6917.

References

1. G.R. Stewart: Rev. Mod. Phys. **56**, 755 (1984)
2. N. Grewe, F. Steglich: 'Heavy Fermions'. In: *Handbook on the Physics and Chemistry of Rare Earths, Vol. 14.* ed. by K.A. Gschneidner (Jr.), L. Eyring (Elsevier Science B. V., Amsterdam 1991)
3. H.R. Ott: Prog. Low Temp. Phys. **11**, 215 (1987)
4. P. Fulde, J. Keller, G. Zwicknagl: 'Theory of Heavy-Fermion Systems'. In: *Solid State Physics, Vol. 41.* ed. by H. Ehrenreich, D. Turnbull (Academic Press, San Diego 1988)
5. Z. Fisk, H.R. Ott, G. Aeppli: Jpn. J. Appl. Phys. **26**, Suppl. 26-3, 1882 (1987)
6. K. Kadowaki, S.B. Woods: Solid State Commun. **58**, 507 (1986)
7. J. Kondo: Prog. Theoret. Phys. **32**, 505 (1964)
8. M.A. Ruderman, C. Kittel: Phys. Rev. **96**, 99 (1994) T. Kasuya: Prog. Theoret. Phys. **16**, 45 (1956) K. Yosida: Phys. Rev. **106**, 681 (1957)
9. S. Doniach: Physica B **91**, 231 (1977)
10. J.M. Lawrence, P.S. Riseborough, R.D. Parks: Rep. Prog. Phys. **44**, 1 (1981)
11. F. Steglich, J. Aarts, C.D. Bredl, W. Lieke, D. Meschede, W. Franz, H. Schäfer: Phys. Rev. Lett. **43**, 1892 (1979)
12. B. Welslau, N. Grewe: Physica B **165** & **166**, 387 (1990)
13. M.B. Maple, M.C. de Andrade, J. Herrmann, Y. Dalichaouch, D.A. Gajewski, C.L. Seaman, R. Chau, R. Movshovish, M.C. Aronson, R. Osborn: J. low Temp. Phys. **99**, 223 (1995)
14. E. Dormann: 'NMR in intermetallic compounds'. In: *Handbook on the physics and chemistry of Rare Earth, Vol. 14.* ed. by K.A. Gschneidner (Jr.), L. Eyring (Elsevier Science B. V., Amsterdam 1991)
15. M. Löwenhaupt, K.H. Fischer: 'Valence-Fluctuation and Heavy-Fermion $4f$ systems'. In: *Handbook on the Physics and Chemistry of Rare Earths, Vol. 16.* ed. by K.A. Gschneidner (Jr.), L. Eyring (Elsevier Science B. V., Amsterdam 1993)

16. E. Holland-Moritz, G.H. Lander: 'Neutron Inelastic Scattering from Actinides and Anomalous Lanthanides'. In: *Handbook on the Physics and Chemistry of Rare Earths, Vol. 19*. ed. by K.A. Gschneidner (Jr.), L. Eyring (Elsevier Science B. V., Amsterdam 1994)
17. B. Elschner, A. Loidl: 'Electron-Spin Resonance on Localized Magnetic Moments in Metals'. In: *Handbook on the Physics and Chemistry of Rare Earth, Vol. 24*. ed. by K.A. Gschneidner (Jr.), L. Eyring (Elsevier Science B. V., Amsterdam 1997)
18. T. Gambke, B. Elschner, L.L. Hirst: Phys. Rev. Lett. **40**, 1290 (1978)
19. M. Schlott, H. Schäffer, B. Elschner: Z. Phys. B: Condens. Matter **63**, 427 (1986)
20. M. Schlott, B. Elschner, M. Herrmann, W. Aßmus: Z. Physik B: Condens. Matter **72**, 385 (1988)
21. M. Schlott, B. Elschner: Z. Phys. B: Condens. Matter **78**, 451 (1990)
22. R. Spitzfaden, A. Loidl, J.-G. Park, B.R. Coles: J. Phys. Condens. Matter **8**, 2857 (1996)
23. R. Spitzfaden, A. Schütz, H.-A. Krug von Nidda, B. Elschner, A. Loidl: Solid State Commun. **102**, 445 (1997)
24. T.S. Al'tschuler, M.S. Bresler, M. Schlott, B. Elschner, E. Gratz: Z. Phys. B: Condens. Matter **99**, 57 (1995)
25. T.S. Al'tschuler, S.G. L'vov, M.S. Bresler: Phys. Sol. State **40**, 543 (1998)
26. K. Yoshimura, T. Imai, T. Kiyama, K.R. Thurber, A.W. Hunt, K. Kosuge: Phys. Rev. Lett. **83**, 4397 (1999)
27. S. Kondo, D.C. Johnston, C.A. Swenson, F. Borsa, A.V. Mahajan, L.L. Miller, T. Gu, A.I. Goldman, M.B. Maple, D.A. Gajewski, E.J. Freeman, N.R. Dilley, R.P. Dickey, J. Merrin, K. Kojima, G.M. Luke, Y.J. Uemura, O. Chmaissem, J.D. Jorgensen: Phys. Rev. Lett. **78**, 3729 (1996)
28. N. Büttgen, H. Kaps, W. Trinkl, A. Loidl, M. Klemm, S. Horn: Can. J. Phys. **79**, 1487 (2001)
29. R.H. Taylor: Adv. Phys. **24**, 681 (1975)
30. S.E. Barnes: Adv. Phys. **30**, 801 (1981)
31. G. Feher, A.F. Kip: Phys. Rev. **98**, 337 (1955)
32. F.J. Dyson: Phys. Rev. **98**, 349 (1955)
33. T. Plefka: Phys. Stat. Sol. B **55**, 129 (1973)
34. S.E. Barnes: Phys. Rev. B **9**, 4789 (1974)
35. M.J. Lysak, D.E. MacLaughlin: Phys. Rev. B **31**, 6963 (1985)
36. M. Coldea, H. Schäffer, V. Weissenberger, B. Elschner: Z. Physik B: Condens. Matter **68**, 25 (1987)
37. J. Korringa: Physica **16**, 601 (1950)
38. J. Callaway: *Quantum Theory of the Solid State* (Academic Press, New York 1991) p. 448
39. A.C. Hewson: *The Kondo Problem to Heavy Fermions* (Cambridge University Press 1993)
40. D.L. Cox, N.E. Bickers, J.W. Wilkins: J. Appl. Phys. **57**, 3166 (1985)
41. P. Rogl: 'Phase Equilibria in Ternary and Higher Order Systems with Rare Earth Elements and Silicon'. In: *Handbook on the Physics and Chemistry of Rare Earth, Vol. 7*. ed. by K.A. Gschneidner (Jr.), L. Eyring (Elsevier Science B. V., Amsterdam 1984)
42. M. Lang, R. Modler, U. Ahlheim, R. Helfrich, P.H.P. Reinders, F. Steglich, W. Aßmus, W. Sun, G. Bruls, D. Weber, B. Lüthi: Physica Scripta (T) **39**, 135 (1991)

43. E.V. Sampathkumaran, R. Vijayaraghavan: Phys. Rev. Lett. **56**, 2861 (1986)
44. J. Ray, E.V. Sampathkumaran, G. Chandra: Phys. Rev. B **35**, 2095 (1987)
45. R. Kuentzler, Y. Dossmann, E.V. Sampathkumaran, S.K. Dhar, R. Vijayaraghavan: Phys. Rev. B **36**, 788 (1987)
46. M.A. Edwards, S. Horn, R.D. Parks: Solid State Commun. **61**, 65 (1987)
47. O. Trovarelli, M. Weiden, R. Müller-Reisner, M. Gómez-Berisso, J.G. Sereni, C. Geibel, F. Steglich: Physica B **223** & **224**, 295 (1995)
48. G. Knebel, C. Eggert, D. Engelmann, R. Viana, A. Krimmel, M. Dressel, A. Loidl: Phys. Rev. B **53**, 11586 (1996)
49. D. Jaccard, K. Behnia, J. Sierro: Phys. Lett. A **163**, 475 (1992)
50. A. Loidl, A. Krimmel, K. Knorr, G. Sparn, M. Lang, C. Geibel, S. Horn, A. Grauel, F. Steglich, B. Welslau, N. Grewe, H. Nakotte, F.R. de Boer, A. Murani: Ann. Physik (Germany) **1**, 78 (1992)
51. N. Büttgen, R. Böhmer, A. Krimmel, A. Loidl: Phys. Rev. B **53**, 5557 (1996)
52. F. Steglich, P. Gegenwart, C. Geibel, R. Helfrich, P. Hellmann, M. Lang, A. Link, R. Modler, G. Sparn, N. Büttgen, A. Loidl: Physica B **223** & **224**, 1 (1996)
53. R.A. Fisher, C. Marcenat, N.E. Phillips, P. Haen, F. Lapierre, P. Lejay, J. Flouquet, J. Voiron: J. Low Temp. Phys. **84**, 49 (1991)
54. P. Haen, J. Flouquet, F. Lapierre, P. Lejay, J.-M. Mignot, A. Ponchet, J. Voiron: J. Magn. Magn. Mat. **63** & **64**, 320 (1987)
55. J. Flouquet, S. Kambe, L.P. Regnault, P. Haen, J.P. Brison, F. Lapierre, P. Lejay: Physica B **215**, 77 (1995)
56. M. Schlott: Thesis, TH Darmstadt (1989)
57. H.-A. Krug von Nidda: Thesis, TU Darmstadt (1997)
58. H.-A. Krug von Nidda, A. Schütz, M. Heil, B. Elschner, A. Loidl: Appl. Magn. Reson. **12**, 287 (1997)
59. K. Asayama, Y. Kitaoka, Y. Kohori: J. Magn. Magn. Mat. **76** & **77**, 449 (1988)
60. N. Büttgen, H.-A. Krug von Nidda, A. Loidl: Physica B **230**, 590 (1997)
61. D.L. Cox: Phys. Rev. B **35**, 6504 (1987)
62. H.-A. Krug von Nidda, A. Schütz, M. Heil, B. Elschner, A. Loidl: Phys. Rev. B **57**, 14344 (1998)
63. A. Schütz: Diploma Thesis, TH Darmstadt (1996), unpublished
64. Y. Kitaoka, H. Arimoto, Y. Kohori, K. Asayama: J. Phys. Soc. Jpn. **54**, 3236 (1985)
65. G. Knebel: private communication (1997)
66. T.T.M. Palstra, A.A. Menovsky, J. van den Berg, A.J. Dirkmaat, P.H. Kes, G.J. Nieuwenhuys, J.A. Mydosh: Phys. Rev. Lett. **55**, 2727 (1985)
67. D.T. Adroja, B.D. Rainford, A.J. Neville, A.G.M. Jansen: Physica B **223** & **224**, 275 (1996)
68. T. Takabatake, G. Nakamoto, T. Yoshino, H. Fujii, K. Izawa, S. Nishigori, H. Goshima, T. Suzuki, T. Fujita, K. Maezawa, T. Hiraoka, Y. Okayama, I. Oguro, A.A. Menovsky, K. Neumaier, A. Brückl, K. Andres: Physica B **223** & **224**, 413 (1996)
69. P.S. Riseborough: Adv. Phys. **49**, 257 (2000)
70. T. Ohama, H. Yasuoka, Y. Isikawa: J. Phys. Soc. Jpn. **64**, 4566 (1995)
71. T.J. Sato, H. Kadowaki, H. Yoshizawa, T. Ekino, T. Takabatake, H. Fujii, L.P. Regnault, Y. Isikawa: J. Phys. Condens. Matter **7**, 8009 (1995)
72. S. Mair, H.-A. Krug von Nidda, M. Lohmann, A. Loidl: Phys. Rev. B **60**, 16409 (1999)

73. S. Nishigori, H. Goshima, T. Suzuki, T. Fujita, G. Nakamoto, H. Tanaka, T. Takabatake, H. Fujii: J. Phys. Soc. Jpn. **65**, 2618 (1996)
74. S. Mair: Diploma Thesis, University of Augsburg (1999), unpublished
75. S. von Molnar, T. Theis, A. Benoit, A. Briggs, J. Flouquet, J. Ravex, Z. Fisk: 'Study of the Energy Gap in Single Crystal SmB_6'. In: *Valence Instabilities*. ed. by P. Wachter, H. Boppart (North Holland, Amsterdam-New York 1982) p. 389
76. G. Aeppli, Z. Fisk: Comments Cond. Mat. Phys. **16**, 155 (1992)
77. K. Kojima, M. Kasaya, Y. Koi: J. Phys. Soc. Jpn. **44**, 1124 (1978)
78. T.S. Al'tschuler, G.G. Khaliullin, D.I. Khomskii: J. Exp. Theor. Phys. **63**, 1234 (1986)
79. M. Imada, A. Fujimori, Y. Tokura: Rev. Mod. Phys. **70**, 1040 (1998)
80. Y. Tokura, Y. Taguchi, Y. Okada, Y. Fujishima, T. Arima, K. Kumagai, Y. Iye: Phys. Rev. Lett. **70**, 2126 (1993)
81. Y. Taguchi, Y. Tokura, T. Arima, F. Inaba: Phys. Rev. B **48**, 511 (1993)
82. M. Heinrich, H.-A. Krug von Nidda, V. Fritsch, A. Loidl: Phys. Rev. B **63**, 193103 (2001)
83. A. Ishigaki, T. Moriya: J. Phys. Soc. Jpn. **65**, 3402 (1996)
84. T. Moriya: J. Magn. Magn. Mater. **14**, 1 (1979)
85. M. Heinrich, Diploma Thesis, University of Augsburg (2000), unpublished
86. M. Brando, N. Büttgen, V. Fritsch, J. Hemberger, H.-A. Krug von Nidda, M. Nicklas, K. Pucher, W. Trinkl, A. Loidl, E.W. Scheidt, M. Klemm, S. Horn: Eur. Phys. J. B **25**, 289 (2002)
87. J. Deisenhofer, M.V. Eremin, D.V. Zakharov, V.A. Ivanshin, R.M. Eremina, H.-A. Krug von Nidda, A.A. Mukhin, A.M. Balbashov, A. Loidl: Phys. Rev. B **65**, 104440 (2002)
88. M. Lohmann, H.-A. Krug von Nidda, M.V. Eremin, A. Loidl, G. Obermeier, S. Horn: Phys. Rev. Lett. **85**, 1742 (2000)
89. I. Yamada, M. Nishi, J. Akimitsu: J. Phys.: Condens. Matter **8**, 2625 (1996)
90. B. Pilawa: J. Phys.: Condens. Matter **9**, 3779 (1997)
91. A.I. Smirnov, V.N. Glazkov, L.I. Leonyuk, A.G. Vetkin, R.M. Eremina: J. Exp. Theor. Phys. **87**, 1019 (1998)
92. V.N. Glazkov, R.M. Eremina, A.I. Smirnov, G. Dhalenne, A. Revcolevschi: J. Exp. Theor. Phys. **93**, 143 (2001)
93. V. Kataev, K.-Y. Choi, M. Grüninger, U. Ammerahl, B. Büchner, A. Freimuth, A. Revcolevschi: Phys. Rev. Lett. **86**, 2882 (2001)
94. H.-A. Krug von Nidda, L.E. Svistov, M.V. Eremin, R.M. Eremina, A. Loidl, V. Kataev, A. Validov, A. Prokofiev, W. Aßmus: Phys. Rev. B **65**, 134445 (2002)

3

Relaxation Phenomena in High-T_c Superconductors: Experimental Methods and Results

A. Szytuła

3.1 Introduction

High temperature superconductors were discovered in 1986 [1] and up to now they are not fully understood. These materials exhibit a variety of unconventional features, which differ from typical metal or semiconductor properties.

High T_c-superconductors are complex compounds. In general, the crystal structures of these compounds have a layered character with CuO_2 planes and large unit cells in which point defects (oxygen vacancies) and substitution of elements strongly affect physical properties. The Cu ions carry a magnetic moment, which may play a dominant role in the appearance of the superconducting state. The superconducting compounds are derived from magnetic insulating compounds by appropriate doping of mobile charge carriers. In most cases, the charge carriers are holes (or electrons) located in the Cu-O planes, mainly in the oxygen p bands.

In this work properties of $La_{2-x}Sr_xCuO_4$, $YBa_2Cu_3O_{6+d}$ and $Y_{1-x}Ca_xBa_2Cu_3O_{6+d}$ are discussed. These compounds are four-or five-component systems with a complex crystal structure. In $La_{2-x}Sr_xCuO_4$ the copper atoms occupy only one crystal site, while in $YBa_2Cu_3O_{6+d}$ and $Y_{1-x}Ca_xBa_2Cu_3O_{6+d}$ two crystal sites with different atomic surroundings are occupied by the Cu atoms. With changing composition, changes in the physical properties from insulator to metal and from an antiferromagnetic to a superconducting state are observed.

In these complex systems fluctuations of different nature are possible. Magnetic relaxation connected with vortex dynamics is discussed in the chapter 11.2 of this book. In this chapter the spin relaxation connected with the microscopic (atomic) effects in high T_c superconductors is discussed.

The article is organized in such a way that initially a brief review is given about the basic concept of the experimental methods: Mössbauer and μ^+SR spectroscopy and neutron scattering. Then, the experimental results for three groups of high-T_c superconductors: $La_{2-x}Sr_xCuO_4$, $RBa_2Cu_3O_{6+d}$ and $Y_{1-x}Ca_xBa_2Cu_3O_{6+d}$ are presented.

3.2 Experimental techniques

Different experimental methods give different information on the properties of investigated materials. Thermodynamic measurements, such as magnetic susceptibility and specific heat, provide information averaged over time and space. Local probe techniques, for example: Mössbauer or muon spectroscopy, give evidence on local magnetic ordering. Each experimental technique utilizing hyperfine interactions measures local internal fields and their fluctuations in the time scale characteristic for the technique. For example, NMR using radio wave is a technique used to observe relatively slow dynamics in $10^{-2} \sim 10^{-4}$ s, whereas μ^+SR and Mössbauer effect cover faster fluctuations up to 10^{-10} s. Fluctuations in $10^{-3} - 10^{-6}$ s can be studied by ESR.

Fluctuations as fast as $10^{-10} - 10^{-14}$ s and coherence of $0.1 \sim 1$ nm can be studied by means of various neutron diffraction techniques. Higher energy resolution can be attained by neutron spin echo technique which allows to study the spin autocorrelation time of $10^{-9} - 10^{-12}$ s. Figure 3.1 provides a rough idea of the space-time characteristics of the above techniques.

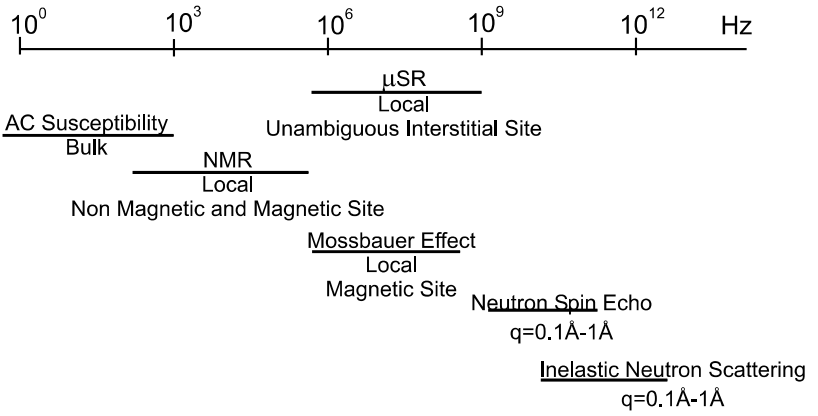

Fig. 3.1. Space-time characteristics of different experimental techniques

3.2.1 Mössbauer spectroscopy

In 1957 R.L. Mössbauer discovered that nuclei embedded in solids can show recoilless absorption and emission of radiation [2]. The Mössbauer effect offers a possibility of insight into the properties of a solid body on a microscopic scale. Parameters determining the shape of a Mössbauer spectrum are sensitive both to the electronic and magnetic environment of the resonantly scattering atom as well as to dynamical properties of the lattice.

The principle of the Mössbauer method is depicted in Fig. 3.2. The variation in Doppler velocity creates a spectrum of gamma energies and some of

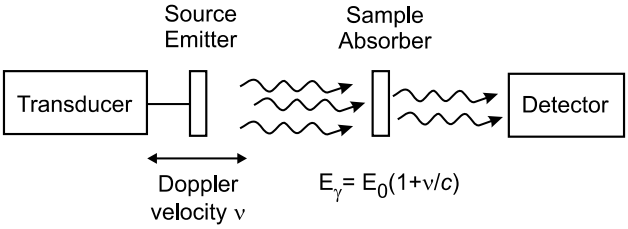

Fig. 3.2. Principle of Mössbauer spectroscopy

them are absorbed by the absorber. The recorded Mössbauer spectrum shows a number of absorption lines. Their specific energies are characteristic for the environment of the Mössbauer nuclei in the absorber. An example of a ^{57}Fe Mössbauer spectrum is presented in Fig. 3.3. From the number and position of the line the electronic charge density, the electric field gradient as well as the magnetic field at the nuclear site can be deduced.
The hyperfine Hamiltonian $\mathcal{H}_{hf}$ describing an interaction of the respective nuclear moments with the magnetic and electric fields at the nuclear site has the following elements:

$$\mathcal{H}_{hf} = \mathcal{H}_{EM} + \mathcal{H}_{EQ} + \mathcal{H}_{MD}, \tag{3.1}$$

where $\mathcal{H}_{EM}$ is monopole interaction, $\mathcal{H}_{EQ}$ is electric quadrupole interaction and $\mathcal{H}_{MD}$ is magnetic dipole interaction.

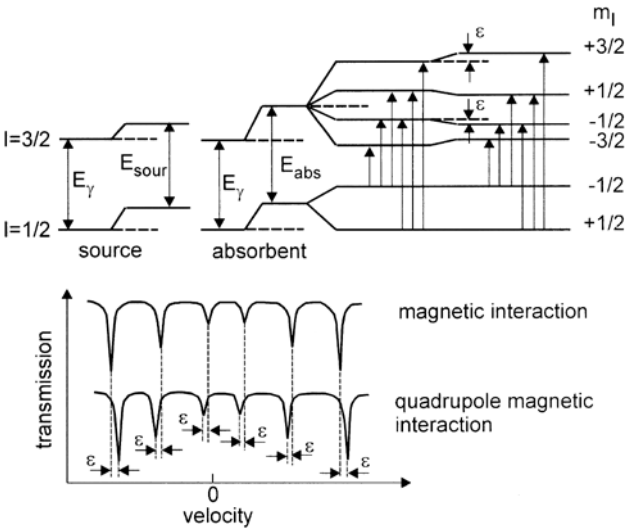

Fig. 3.3. Hyperfine structure of ^{57}Fe isotope in the nuclear energy levels and the γ transitions (not in scale)

3.2.1.1 Isomer shift

The electric monopole interaction between the nucleus and the penetrating electronic charge results in a shift of the nuclear energy. A simple expression for the energy shift of a nuclei level δE, due to the non zero s electron density at the nucleus, equals [3]:

$$\delta E = \frac{2\pi}{5} Z e^2 \left(R^2 - R_o^2\right) \left[\left|\Psi_a\left(0\right)\right|^2 - \left|\Psi_e\left(0\right)\right|^2\right], \tag{3.2}$$

where Z is the nuclear charge, $|\Psi_e(0)|^2$ and $|\Psi_a(0)|^2$ are the electron density at the nucleus of the emitter and absorber, and R_o and R are the nuclear radius in the ground and excited states, respectively. Due to a difference in the radius between the ground state and the excited (isometric) nucleus there is a difference $(\delta E_{ex} - \delta E_{gd})$ between the energy shift in the ground (δE_{gd}) and the excited (δE_{ex}) state. Consequently, the energy of the emitting or absorbing gamma ray of this nucleus is shifted by $(\delta E_{ex} - \delta E_{gd})$. The resonant energy between the source and the absorber is called the isomer shift (IS). IS is sensitive to changes in the s electron density and probes, for example, the valence of atoms.

3.2.1.2 Quadrupole splitting

The quadrupole moment of the nucleus interacts with the electric field gradient at the nuclear site via the quadrupolar interaction. This results in a splitting of nuclear energy levels with different $\pm m_I$. A discus like nucleus has a negative quadrupole moment and a cigar shaped nucleus a positive quadrupole moment Q. Nuclei with a spin $I = 0$ or $I = \frac{1}{2}$ are spherically symmetric and for this reason show no quadrupole splitting. The shift in the nuclear energy due to the quardupole interaction equals:

$$E_Q\left(m_I\right) = \frac{V_{zz}Q}{4I\left(2I-1\right)} \left|3m_I^2 - I\left(I+1\right)\right| \sqrt{1+\frac{1}{3}\eta^2}, \tag{3.3}$$

where $\eta = (V_{xx} - V_{yy})/V_{zz}$ (V_{ii} is an abbreviation of $\frac{\partial^2 V}{\partial i^2}$) is an axial component of the diagonalized electric gradient tensor. As for ^{57}Fe nuclei $I_{gd} = 1/2$ and $I_{ex} = 3/2$, the nuclear ground state does not show quadrupole splitting but the excited state has the energy splitting $\Delta E_Q = 1/2 V_{zz} Q$.

3.2.1.3 Magnetic hyperfine field

The magnetic dipole interaction with the magnetic flux density B_{hf} at the nucleus completely lifts the degeneracy with respect to the spin magnetic quantum number I_{zi},

$$\mathcal{H}_{MD} = -g_N \mu_N I_{zi} B_{hf}, \tag{3.4}$$

where g_N is the nuclear gyromagnetic ratio and $\mu_N = e\hbar/2m_p$ (m_p is the mass of the proton). This results in $2I_{gd}+1$ or $2I_{ex}+1$ equidistant energy levels for the nuclear ground or excited state, respectively. The maximum energy difference between the γ-transitions is related to the hyperfine field. By comparison of the measured hyperfine field with the free ion value (maximum moment size), the magnetic moment of the electronic shell can be deduced.

3.2.1.4 Relaxation phenomena

In the case of paramagnetic relaxation in the sample the shape of the Mössbauer spectra are described by the stochastic model of Blume and Tjon [4]. In this case the influence of the electric relaxation between the ground state and the higher energy levels are neglected.

The effective field is given by the relation

$$H(t) = H_o \frac{S_z(t)}{S}, \tag{3.5}$$

where H_o is independent on the time and S-spin. The fluctuation of the effective magnetic field is characterized by the time of relaxation of the spin. Detection of the relaxation behavior is possible in the case as their lifetime is longer or comparable to the lifetime τ_n of the nuclear excited state. $2{\cdot}10^{-8}$ s $< t < 10^{-6}$ s is the time window of the ^{57}Fe Mössbauer measurement the lifetime of the 14.4 keV level which is populated $1.3{\cdot}10^{-8}$ s. The relaxation effect caused the broadening of lines in Mössbauer spectrum.

In the case that the Mössbauer isotope belongs to a paramagnetic ion, for example ^{57}Fe, ^{157}Gd the sensitivity depends both on the Mössbauer properties of the isotope and on the static and dynamic properties of the paramagnetic spin. This spin may fluctuate under the influence of the exchange or dipole coupling with neighboring spins and/or coupling with the phonons. Two limiting cases are defined by the relative importance of τ_e, the spin fluctuation rate and τ_L the nuclear Larmor frequency ($\tau_L = \hbar/\omega_{nf}$ where ω_{nf} is of the hyperfine frequency of the Mössbauer atom). $\tau_e \ll \tau_L$, corresponds to the "fast paramagnetic relaxation" regime and $\tau_L \ll \tau_e$ corresponds to the "slow paramagnetic relaxation" regime.

For the case of fast paramagnetic relaxation, the hyperfine interaction involves the average value of the fluctuating electronic spin. In absence of any magnetic field this polarisation is zero. In presence of a field H_{loc} the Mössbauer line shapes depend on the ratio $g\mu_B H_{\mathrm{loc}}/2k_BT$. At very low temperatures where $\langle S\rangle_T$ approaches the full value of the sensitivity is relatively good but it decreases rapidly as the temperature increases.

For the case of slow paramagnetic relaxation, the fluctuation time of the electronic spin is longer than the characteristic nuclear Larmor time. In this case the hyperfine interaction involves the full value of the electronic spin and the three contributions correspond to the hyperfine interaction, the electronic and Zeeman interactions are included in the Hamiltonian. This Hamiltonian

is independent of temperature in as much as the electronic spin continues to fluctuate slowly and detection of any local field is possible only at low temperatures.

3.2.2 μ^+SR spectroscopy

Muon Spin Rotation Spectroscopy (μ^+SR) is a variant of other well-known hyperfine probe techniques such as Mössbauer spectroscopy [5].

The μ^+SR technique is based on two different experimental facts. Firstly, a muon is produces with its polarization antiparallel to its momentum and hence, the muon is naturally polarized. Secondly, the muon decay is anisotropic and its anisotropy is directly related to the μ^+ spin direction. The μ^+SR technique is a time differential method.

The muon (μ^+) is an elementary antiparticle. It is produced via colliding high energy protons (energy $\simeq$ 600 MeV–1 GeV) with a light target (C or Be) [6]. The muon beam (50–100 MeV) is directed onto the sample and the muons are implanted in the material. They are thermalized and come to rest after $\sim 10^{-9}$ s. Apart from ionizing the atoms of its host, they also produce vacancies during the first part of their path through the sample. This has no consequence for the experimental results since the area where they finally localize is unaffected. In a crystallographic environment, the muon localizes at sites near anions or interstitial sites. After localization, the muon spin interacts with the surrounding matter before it decays to a positron (which is the only particle recorded in the experiment), electron neutrino (ν_e) and muon antineutrino ($\overline{\nu}_\mu$):

$$\mu^+ \rightarrow e^+ + \nu_e + \overline{\nu}_\mu$$

The positron has enough energy to leave the sample and can be detected. Moreover, e^+ is emitted preferentially along the spin direction of the muon as a consequence of parity violation in the weak interactions. The angular distribution of the probability of positron emission, $N_{e^+}(\theta)$, is given by (see Fig. 3.4):

$$N_{e^+}(\theta) = 1 + A_0 \cos\theta \tag{3.6}$$

The asymmetry parameter A_0 is given by aP, where P is the beam polarization and a is an intrinsic parameter. Here θ is the angle between the direction of the emitted positron and the muon spin. The time evolution of polarization $P(t)$ can be followed recording the positron distribution as of elapsed lifetime of μ^+. It is sufficient to record the number of positrons emitted into a particular direction. In practice, this is done usually along the direction of the initial polarization $P(0)$ of the μ^+ beam.

Because of the limited life time of the muons (τ_μ) the number of detected positrons (N_{e^+}) equals:

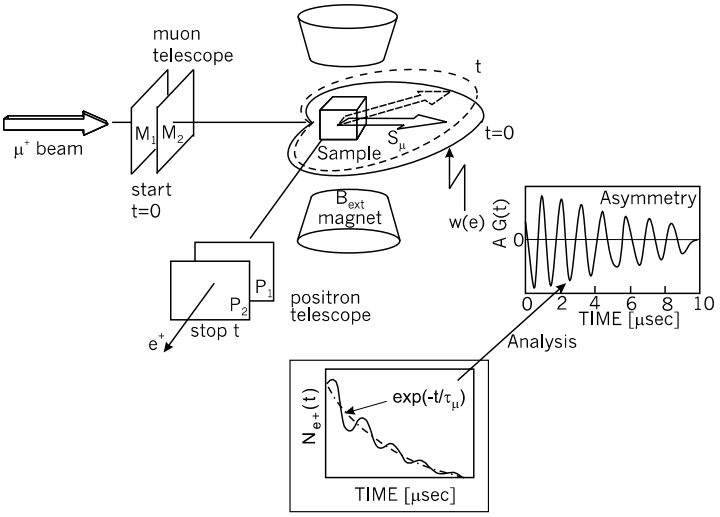

Fig. 3.4. Schematic representation of the μ^+SR technique. The polarized muons are implanted into the sample where they decay into a position and two neutrinos. The position is emitted preferentially along the muon spin direction ($N_{e^+}(\theta)$) and is energetically enough to leave the sample and to be detected. The *insets* show the μ^+SR histogram: the number of positrons detected in the function of the time and asymmetry function $AG(t)$

$$N_{e^+}(t) = N_{e^+}(0) \exp\left(\frac{-t}{\tau_\mu}\right). \tag{3.7}$$

Introducing the asymmetry of the number of positrons in the forward ($N_F(t)$) and backward ($N_B(t)$) direction we obtain:

$$N_F(t) = N_{e^+}(t)(1 + A(t)\cos\theta_F), \tag{3.8}$$

$$N_B(t) = N_{e^+}(t)(1 + A(t)\cos\theta_B). \tag{3.9}$$

The values of $\cos\theta_F$ and $\cos\theta_B$ are setup characteristics and are determined independently. $A(t)$ can be deduced from (3.8) and (3.9) as $A(t) = R(N_F - N_B)/(N_F + N_B)$ where R is a setup constant. $A(t)$ contains interesting information about the sample and, in general, equals:

$$A(t) = A(0)G(t)\cos(\varpi_\mu t). \tag{3.10}$$

If the sample exhibits long-range magnetic order, it is quite likely that the magnetic field at some type of stopping sites will be of the same magnitude and direction. Then in directions perpendicular to the direction of the local field one should observe oscillations superimposed on the experimental decay (see inset in Fig. 3.4). The local magnetic field experienced by the muon (B_μ) causes the muon spin to precess with a frequency $\varpi_\mu = \gamma_\mu B_\mu$, where γ_μ is the

gyromagnetic ratio of the muon. Because of (3.10) this frequency is directly observed in the μ^+SR spectrum (see inset in Fig. 3.4). The field B_μ is due to two contributions. The dominant contribution is produced by the classical dipolar interaction, the localized electronic dipole moments and the μ^+ spin. The second contribution is produced by the conductions at the muon site through the Fermi contact interaction. The μ^+SR method determine by the dipolar interaction, whereas Mössbauer effect and NMR techniques dominates the contact interaction. In the case of fast fluctuating fields with a correlation time τ_c, $G(t)$ equals:

$$G(t) = \exp(-\lambda t), \tag{3.11}$$

where λ is the damping rate and is give relation

$$\lambda = \gamma_\mu^2 \langle B_\mu \rangle \tau_c. \tag{3.12}$$

In this equation $1/\tau_c$ is the fluctuation rate of B_μ. Physically these field fluctuations may arise from two different mechanisms: diffusion of the muon through the material or changes in direction and magnitude of B_μ while the muon is localised. The latter is due to an electron spin relaxation process.

Summing up one should say that the main features of μSR are as follows:
–high sensitivity of magnetic ordering,
–wide measurable range of fluctuations,
–purely magnetic hyperfine interactions.

3.2.3 Neutron techniques

Neutrons are a useful tool for the study of condensed matter because they have no electric charge and their wavelengths as well as energies can be comparable with crystallographic dimensions and thermal vibrations, respectively. The magnetic moment of the neutron, $\mu_n = g_n \mu_N = 5.4 \cdot 10^{-4}\ \mu_B$ with $g_n = -1.91$ (the gyromagnetic ratio of the neutron) interacts with electronic magnetic moments of the material. The neutrons penetration depth is large so elastic and inelastic scattering of the neutrons reveal information about the nuclei and the magnetic moment of the electronic shells. The neutron cross section at thermal energy shows an irregular behavior throughout the periodic table [7], [8].

The energy of the neutron is in general between 2 meV (cold neutrons) and 200 meV (hot neutrons). Two laws determine the scattering process of a neutron with a sample: conservation of momentum and energy. The momentum and the energy transferred to the sample are:

$$\hbar \mathbf{q} = \hbar \mathbf{k}' - \hbar \mathbf{k}\ , \tag{3.13}$$

$$\hbar \varpi = \frac{\hbar^2}{2m_n} (\mathbf{k}^2 - \mathbf{k}'^2), \tag{3.14}$$

respectively, where k and k' denote the wave vectors of the neutron before and after the scattering process, and $\hbar\mathbf{q}$ and $\hbar\varpi$ are the momentum and energy transfer to the sample.

3.2.3.1 Neutron diffraction

Elastic scattering (only momentum transfer between neutrons and the material under study) of the neutrons gives structural or magnetic parameters of the compound. Constructive interference of the neutrons scattered by the crystal requires the condition:

$$\mathbf{q} = \mathbf{k} - \mathbf{k}' = \mathbf{G}_{hkl}\,, \tag{3.15}$$

where $\mathbf{G}_{hkl}$ is a reciprocal lattice vector which is to be associated with a particular set of crystal planes (hkl) in the direct space. If 2θ is the angle separating the incident and reflected beam, the equation results in Bragg's law:

$$\lambda_n = 2d_{hkl}\sin\theta\,, \tag{3.16}$$

where d_{hkl} is the distance between the (hkl) planes. Powder samples show all reflections as a function of 2θ because of the random orientation of the (hkl) planes. Single crystals allow to measure a map of reciprocal space. Contributions to the magnetic scattering cross-section are more complex.

For magnetic structures the magnetic unit cell contains multiple crystallographic unit cells. Such long-range magnetic ordering gives additional magnetic reflections at low Bragg angle on the neutron diffraction pattern.

3.2.3.2 Inelastic neutron scattering

Inelastic neutron scattering (INS) is characterized by energy transfer between the sample and the neutrons. The neutrons create or annihilate excitations, such as phonons or magnons, or change their momentum and the characteristic energy gain, or energy loss, of the neutrons ($\hbar\varpi$) is measured. The scattered neutron intensity is related to the response function $S(\mathbf{q}, \varpi)$ of the sample [7]:

$$\frac{d^2\sigma}{d\Omega dE'} = \left(\frac{g_n e^2}{m_e c^2}\right)^2 \frac{\mathbf{k}'}{\mathbf{k}} S\left(\mathbf{q}, \varpi\right), \tag{3.17}$$

where $\frac{d^2\sigma}{d\Omega dE'}$ is the differential cross section for scattering of neutrons in the solid angle $d\Omega$ with the energy $E' = (\hbar\mathbf{k}')^2/2m_n$.

The scattering law is possible to be also described by the relation

$$\frac{d^2\sigma}{d\Omega dE} \sim S\left(x,t\right)\mathbf{k}'/\mathbf{k} \tag{3.18}$$

where $S(x,t)$ is the correlation function gives by the formula

$$S(x,t) = \frac{1}{N}\int d^3x' \langle \rho(\mathbf{x}'t) \cdot \rho(\mathbf{x}-\mathbf{x}',0)\rangle \tag{3.19}$$

where ρ means the mass-, charge- or magnetization density depending on the sampling probe. $\langle\rangle$ stands for the thermal average over a canonical ensemble. The time dependent self- and pair- correlation contains the dynamics of the sample and implies inelastic scattering (spectroscopy).

The scattering function S($\mathbf{q}$,ω) is the spatial and temporal Fourier transform of a correlation function (3.19) in space and time. This leads to the following correspondence:

Excitations of internal degrees of freedom	$\longleftrightarrow$	Fluctuations in space and time

Energy Momentum	–	transfer	Life time, relaxation time, spatial solution

This correspondence between momentum transfer and correlation lengths on the one hand and energy transfer and relaxation times on the other hand is determined by means of the various experimental methods (coherent and incoherent inelastic scattering).

3.3 Experimental results

3.3.1 $La_{2-x}Sr_xCuO_4$ compounds

At high temperatures La_2CuO_4 compound crystallizes in the tetragonal K_2NiF_4-type structure (I4/mmm space group). The Cu atoms occupy 2(a) site: 0,0,0. La atoms are located at 4(e) site: 0,0,z and oxygen atoms are at two sites 4(e): 0,0,z and 4(c): 0,0.5,0.

At temperatures of about 500 K, this structure transforms to an orthorhombic structure with the space group *Cmca* and the following distribution of atoms: Cu at 4(a): 0,0,z; La at 8(f): 0,y,z; oxygen at 8(f): 0,y,z and 8(e): 0.25,0.25,z.

In these structures the Cu atom is located in the center of an oxygen octahedron. All the superconducting (p-type) $La_{2-x}Sr_xCuO_4$ systems have the same crystal structure. It is a common belief that holes located in the Cu-O planes, which are the charge carriers, are responsible for superconductivity. These holes, or missing electrons, are obtained by substitution of divalent Sr^{2+} ions for trivalent La^{3+}.

The phase diagram presented in Fig. 3.5 shows that pure La_2CuO_4 is an antiferromagnet with the Néel temperature $T_N = 300$ K. The values of T_N decrease with increasing concentration x. Then with increasing concentration

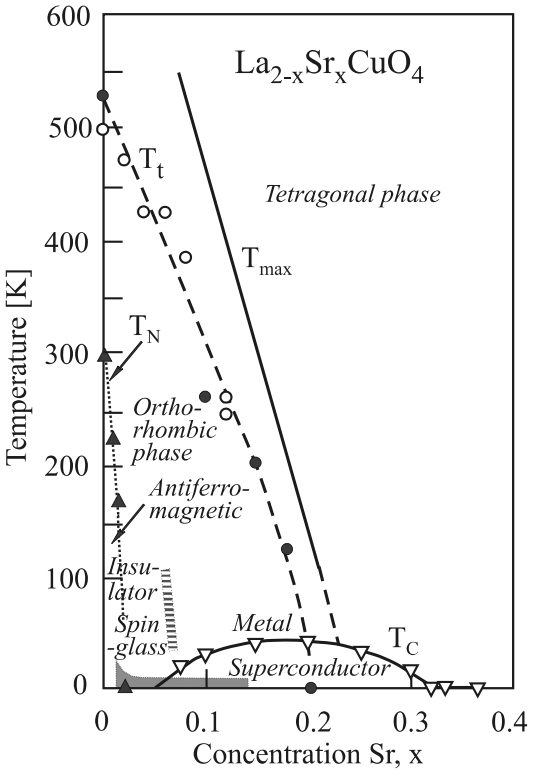

Fig. 3.5. Phase diagram of $La_{2-x}Sr_xCuO_4$ as a function of concentration x

at low temperatures, first spin-glass ($0.02 < x < 0.06$) and second the superconducting (for $0.05 < x < 0.25$) behavior was found. Magnetic data indicate that the properties of the samples with $x < 0.02$ are similar to the typical spin glass [10, 11] while in samples with $x > 0.02$ dynamical two-dimensional antiferromagnetic correlations exist at low temperatures. Simultaneously the critical temperature T_t of the structural phase transition from tetragonal to orthorhombic phase decreases with increasing Sr concentration. The dependence of $T_{\max}$ on the dilution parameter x is correlated with the above mentioned T_t variation. $T_{\max}$ is the temperature at which the susceptibility attains the maximum, below which the short-range spin fluctuations are stabilized. This is typical for two-dimensional spin systems. The above feature of the phase diagram indicates that in this system a change of the electronic band from a strong correlated system ($W < U$), for $x < 0.035$, to a weak correlated system ($W > U$), for $x > 0.27$, takes place. W is the width of the band of Cu atoms in CuO_2 plane and U is the energy of the Coulomb interaction between two holes in superconducting pairs. The change in the nature of the conduction from p to n near the concentration $x \approx 0.27$ [12] indicates that with increasing x the value of U decreases.

The antiferromagnetic ordering of the Cu spins was found in La_2CuO_4 below $T_N = 300$ K. The Cu magnetic moments form a simple antiferromagnetic structure. The Cu moments equal 0.5 μ_B, are parallel to the [110] direction [13, 14]. Neutron scattering on the single crystal La_2CuO_4 indicates the existence of a two-dimensional (2D) antiferromagnetic correlation below and above the Néel temperature [15, 16]. Magnetic interactions of the Cu magnetic moments ($s = 1/2$) in La_2CuO_4 could be described by the Heisenberg Hamiltonian:

$$\mathcal{H} = {}^1\!/_2 \sum_{ij} J_{ij} S_i S_j \tag{3.20}$$

with the exchange integrals of about 10^3 K in the basal plane and of 0.02 K between the planes. Also the energy anisotropy is of 0.03 K in the basal plane and of 0.1 K in the perpendicular direction. Quantum fluctuations play the deciding role in this quasi two-dimensional system. In $La_{2-x}Sr_xCuO_4$ the doping Sr atoms breaks the antiferromagnetic spin correlation on the Cu^{2+} ion site.

In $La_{2-x}Sr_xCuO_4$ system the antiferromagnetic ordering disappears with increasing x (Fig. 3.5). The inelastic neutron scattering gives evidence of the antiferromagnetic correlation, with the correlation length $\xi \approx \left(\frac{3.8}{\sqrt{x}}\right)$Å, corresponding to the average distance between holes in the CuO_2 planes [14], for the concentration $0.02 < x < 0.18$ in the metallic and the superconducting phases.

μ^+SR measurements of $La_{2-x}Sr_xCuO_4$ for $x = 0.01, 0.02$ and 0.05 indicate spin freezing below 4 K. These results suggest that a superconducting state exists for slow fluctuations of spin fluid [17].

The magnetic-superconducting phase diagram of $La_{2-x}Sr_xCuO_4$ (Fig. 3.5) [18] has been studied by Imbert et al. [19, 20] who used ^{57}Fe (0.5 at %) Mössbauer spectra to probe in detail the antiferromagnetic spin glass and superconducting phases. For La_2CuO_4, the Fe probe in the Cu site indicates the magnetic order with a hyperfine field of 400 kOe below $T_N = 220$ K. For $x = 0.02$, T_N is lower than 10 K. Mössbauer spectra for $La_{1.85}Sr_{0.15}CuO_4$ superconductor ($T_c = 20$ K) were collected. The spectrum from 4.1 K is interpreted as due to paramagnetic spin fluctuations of the diluted Fe atoms with a slow spin relaxation rate [21].

3.3.2 $RBa_2Cu_3O_{6+d}$ compounds (R = rare earth metals and Y)

The crystal structure of these compounds depends on the oxygen content. The oxygen parameter in the approximate range: $0.5 \leq d \leq 1$ determines the existence of the orthorhombic structure with *Pmmm* space group. The R atoms occupy the 1(h) site: 1/2,1/2,1/2; Ba 2(t) site: 1/2,1/2,0.1844 while Cu atoms occupy two non-equivalent positions 1(a): 0,0,0 and 2(q): 0,0,0.355. Oxygen atoms occupy four sites: O1 in 2(q) site 0,0,0.1588; O2 in 2(s) site:

0.5,0,0.3779; O3 in 2(r) site: 0,0.5,0.3780 and O4 in 1(e) site: 0,0.5,0. Except R = Ce,Tb,Pr, these compounds are superconductors with the critical temperature of about 92 K [22].

For $d < 0.5$, the systems become antiferromagnetic insulators with a tetragonal crystal structure (the space group $P4/mmm$). In this case the oxygen atoms occupy only three non-equivalent sites. The results of measurements of the $YBa_2Cu_3O_{6+d}$ system by different methods give the phase diagram shown in Fig. 3.6. Three kinds of phase transition are observed at the intermediate point $d = 0.5$: from a tetragonal to an orthorhombic crystal structure, from an insulator to a superconducting state and from an antiferromagnetic to a superconducting state. The change in the crystal structure with increasing oxygen content is illustrated in Fig. 3.7, where the unit cell in the three phases is shown. In the first phase (the tetragonal $YBa_2Cu_3O_6$) the oxygen is completely removed from the chain layer. In the second one (the tetragonal $YBa_2Cu_3O_{6+d}$) the chain layer sites are only partially occupied by oxygen. In the third one (the oxygenated orthorhombic $YBa_2Cu_3O_7$) the chain layer oxygen sites are fully occupied. Neutron diffraction measurements [23], [24] show that $YBa_2Cu_3O_6$ has an antiferromagnetic structure with the magnetic unit cell $(a\sqrt{2},a\sqrt{2},c)$. Below the Néel temperature $T_N = 415$ K, magnetic moments of Cu(2) atoms (equal 0.60(3.3) μ_B) are ordered within the basal plane. At low temperatures an additional ordering of the Cu(1) moments

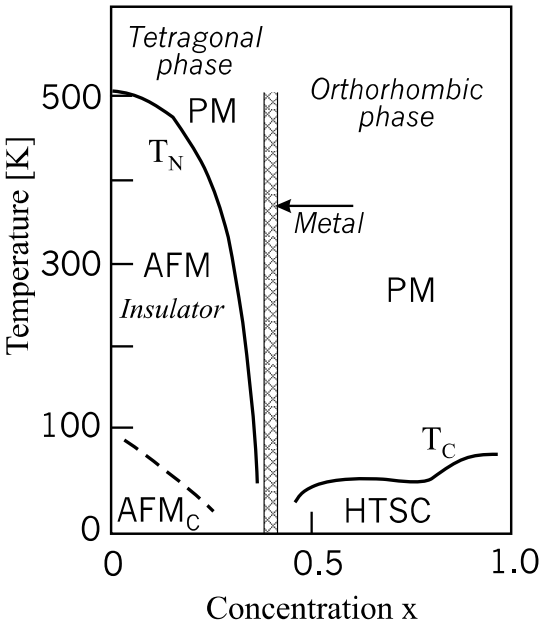

Fig. 3.6. Schematic phase diagram for $YBa_2Cu_3O_{6+d}$ as a function of oxygen concentration x

($\mu < 0.03\ \mu_B$) is observed (Fig. 3.8). With increasing oxygen content, the changes in the values of T_N and the magnetic moment μ are observed. The low temperature value of the ordered magnetic moment varies linearly with the Néel temperature.

For the oxygen concentration $d > 0.5$ in the CuO_2 layers a superconducting state is observed. The concentration dependence of the superconducting state

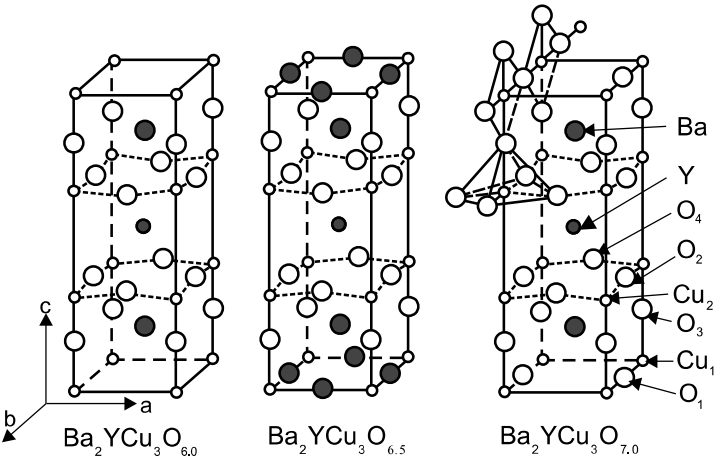

Fig. 3.7. Chemical unit cells for $YBa_2Cu_3O_6$ (*left*), $YBa_2Cu_3O_{6.5}$ (*center*) and $YBa_2Cu_3O_7$ (*right*)

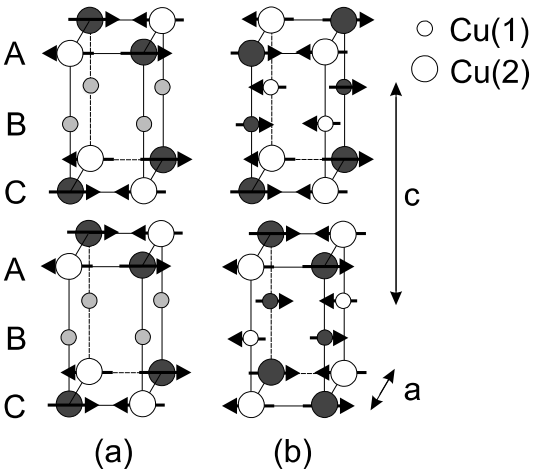

Fig. 3.8. Magnetic structure of $YBa_2Cu_3O_6$ at (**a**) high and (**b**) low temperatures

has two plateaux for $T_c \approx 90$ K and 60 K. These plateaux correspond to two structures: ortho-I and ortho-II characterized by different orderings of the oxygen vacancies.

The magnetic order, alike the crystal structure, has two-dimensional character. The magnetic interactions are described by an in-plane exchange interaction J and an interplanar coupling J'. The quasi two-dimensional character of magnetic structure results from $J' \ll J$ (J'/J of the order of 10^{-4}) [25].

The Néel temperature of $YBa_2Cu_3O_6$ compound is a very high ordering temperature, characteristic for a magnetic insulator. According to inelastic neutron scattering, above the Néel temperature T_N all these materials exhibit very strong spin correlations that persist within the Cu-O planes.

Because in these compounds the exchange interactions in the CuO_2 planes are much higher than the interactions between the planes, two-dimensional correlations exist above the Néel temperature. Because above $d = 0.5$ (in the superconducting state) magnetic moments exist, these correlations lead to enhanced fluctuations of magnetization.

Inelastic neutron scattering measurements give the following results for $YBa_2Cu_3O_{6+d}$:

- the spectra of the spin waves in AF state ($d < 0.5$, $T_N < 410$ K) have a two-dimensional character,
- for the sample with $d \simeq 0.37$ ($T_N = 180$ K) a strong renormalization of low-energy excitations is detected and spin fluctuations in the CuO_2 plane are stifled,
- in the superconducting state ($d \simeq 0.45$ ($T_c = 37$ K), $d = 0.51$ ($T_c = 47$ K), $d = 0.69$ ($T_c = 60$ K)) dynamic AF correlations between spin waves are observed. At low temperatures the magnetic excitations disappear [26].

The magnetic fluctuations in $YBa_2Cu_3O_{6+d}$ compounds are investigated by polarization analysis of the neutron scattering. Polarization analysis allows the unambiguous distinction of electronic magnetic fluctuations from all other excitations. These results give evidence for the existence of paramagnetic fluctuations in tetragonal non-superconducting phase ($d = 0.11$, 0.37) and small effect for the superconducting $d = 0.89$ sample [27].

A novel neutron scattering technique has been utilized to discover one-dimensional fluctuations with a very sharply defined modulation period of 16.65 Å along the b (or a) direction in $YBa_2Cu_3O_{6.93}$. The fluctuations are found to be absent in the reduced oxygen compound $YBa_2Cu_3O_{6.15}$. The wave vector of the fluctuations is consistent with accepted values of $2k_F$ for the Cu-O chains [28, 29].

The magnetic ordering in $YBa_2Cu_3O_{6+d}$ system was determined also by μ^+SR method [30]. In the ordered state the obtained results are similar to those obtained by neutron diffraction. The results for $YBa_2Cu_3O_{6.2}$ are shown in Fig. 3.9. The relaxation function $G_z(t)$ indicates magnetic ordering at 15 and 250 K and a paramagnetic state at $T = 315$ K. The μ^+SR measurements indicate that the three-dimensional static magnetic order disappears around

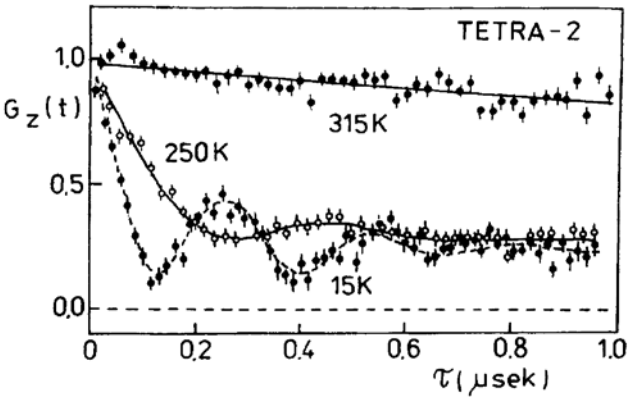

Fig. 3.9. Relaxation function $G_z(t)$ for $YBa_2Cu_3O_{6.2}$ at 15, 250 and 315 K [30]

$d = 0.4 \sim 0.5$ where the onset of superconductivity is observed. The muon spin precession frequency is almost constant for d between 0 and 0.35, indicating that the ordered moment of Cu does not depend on the d value. For $d \sim 0.4$, the authors of [30] observed spin glass behavior. This reflects an increasing random distribution of internal fields with increasing d.

The information on the relaxation phenomena in high temperature superconductors is obtained for the samples doped by the ^{57}Fe [31] or ^{170}Yb isotopes [32]. The analysis is based on the evolution of the line shapes between the paramagnetic region and the low temperature magnetically saturated state.

Substitution of Cu by Fe atoms in $YBa_2(Cu_{1-y}Fe_y)_3O_{6+d}$ results in an orthorhombic-tetragonal structure transition for $y = 0.02$–0.03. Neutron diffraction, EXAFS and Mössbauer measurements suggest that the majority (about 80 %) of the Fe atoms occupy the Cu(1) sites and the others occupy the Cu(2) site with the average population of 10–20 % [33]. Different results are given by electron microscopy, suggesting that the doped Fe atoms form clusters [34].

The value of the critical temperature of the onset of superconductivity decreases with increasing Fe content y. Upon increasing y above 0.13 the compounds are antiferromagnets with the magnetic order in the Cu(2) site with $T_N = 330$ and 380 K for $y = 0.17$ and 0.25, respectively. The superconducting-magnetic phase diagram of $YBa_2(Cu_{1-y}Fe_y)_3O_{6+d}$ (Fig. 3.10a) is similar to that obtained for $YBa_2Cu_3O_{6+d}$ (see Fig. 3.5). In the intermediate region $0.015 < y < 0.09$, the coexistence of the superconducting and magnetic phase is observed (Fig. 3.10b). The investigation of the $RBa_2Cu_3O_{6+d}$ compounds by Mössbauer spectroscopy is performed using ^{57}Fe probe or with R Mössbauer nuclei in sites which are intrinsically occupied by R atoms.

The ^{57}Fe Mössbauer spectrum gives very little information on superconductive properties, however, it contains much information on the magnetic state and reports on magnetic behavior of the Cu sublattices. The magnet-

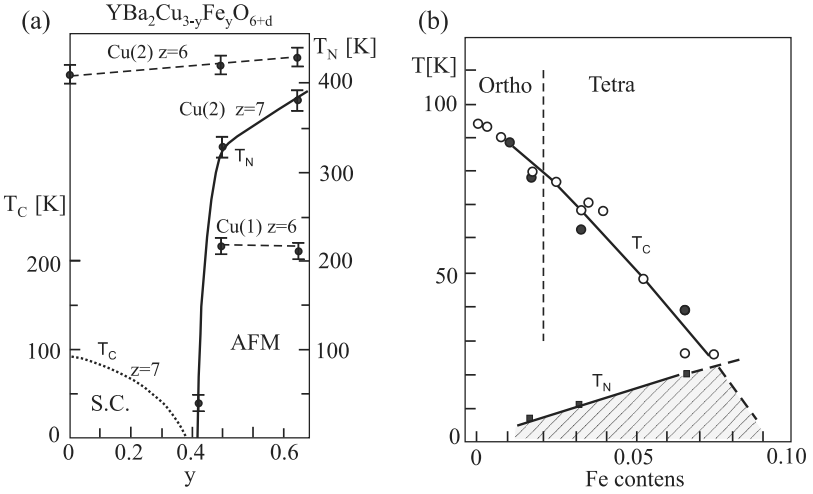

Fig. 3.10. (**a**) Superconducting-magnetic phase diagram of $YBa_2Cu_{3-y}Fe_yO_{6+d}$. z parameter define the number of the oxygen atoms on the chemical formula ($z = 6 + d$) (**b**) Part of the phase diagram presented in (a) for low concentration of Fe. Hatched area corresponds to the coexistence of the superconducting and magnetically ordered phases.

ically ordered Cu sublattice produces an exchange field at the iron ions located in the Cu sites. The analysis of the magnetic hyperfine splitting and quadrupole and isomer shift (a six-line pattern) gives information on the properties of the investigated sample.

The ^{57}Fe Mössbauer spectra of $YBa_2(Cu^{57}_{1-x}Fe_x)_3O_{6+d}$ compounds were investigated by different authors [31, 33, 35, 36]. In deoxygenated Fe doped 1:2:3 compounds the ^{57}Fe Mössbauer spectra at room temperature usually showed a well-defined sextuplet attributed to Fe spins in the Cu II sites, together with quadrupolar doublets related to fluctuating Fe spins in the Cu I (chain) sites. This result suggested that the antiferromagnetic order in the Cu(2) planes was not intrinsically modified by Fe doping, whereas frustration and disorder arise mainly from Fe clusters in the chain sites. Figure 3.11 shows the comparison of the experimental and theoretical Mössbauer spectra as a function of the longitudinal fluctuation rate of the temperature independent hyperfine field. The obtained results indicate that the average fluctuation rate decreases linearly as the temperature is lowered: from $5{\cdot}10^{10}$ s^{-1} for $T = 20$ K down to 10^7 s^{-1} for $T = 1.4$ K [35]. According to Dengler et al. [36] the broad lines can be interpreted in terms of distribution of hyperfine magnetic field or relaxation of the iron spins. Here we discuss the latter possibility. The problem is rather complex, because the relaxation of iron ions takes place in short-lived antiferromagnetic clusters of limited size located at different lattice sites. Dengler et al. [36] propose to analyze low temperature spectra in terms of two- or four-level relaxation model.

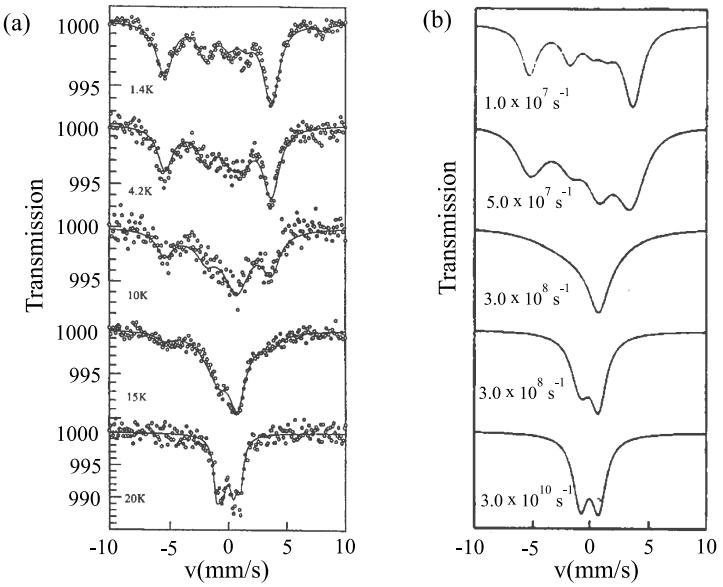

Fig. 3.11. Comparison of the (**a**) experimental ^{17}Fe Mössbauer absorption in $YBa_2(Cu_{0.95}Co_{0.04}Fe_{0.01})_3O_7$ as a function of temperature and (**b**) theoretical spectrum as a function of the longitudinal fluctuation rate [32]

For the two-level relaxation model the following assumptions were made:

i) the hyperfine field at the nucleus in the $a-b$ plane of the crystal unit cell fluctuates between $+H$ and $-H$ values,
ii) all the Fe atoms have the same relaxation time.

For $x = 0.03$, 0.06 and 0.10 the best agreement with the experimental results is obtained assuming that the relaxation rate has two components $\tau^{-1} = \tau_c^{-1} + \tau_i^{-1}$ and τ_c^{-1} is dominant at high temperatures while τ_i^{-1} at low ones.

In the four-level scheme the short-range order magnetization of the surrounding (cluster or magnetic domain around the Mössbauer atom) fluctuates between two easy directions ($\uparrow$ and $\downarrow$) of equal energy separated by a barrier proportional to the anisotropy energy density $K_c[\mathrm{J/m^3}]$. This fluctuation is of superparamagnetic character. The magnetic fluctuation rate w_c is described by the relation $w_c = w_c^0 \cdot \exp(-K_c V_c / k_B T)$, where V_c is the magnetic cluster volume.

The time of flight neutron spectrum of $YBa_2Cu_{3-x}Fe_xO_{6.5}$ consists of an elastic signal of nuclear origin and of an inelastic one due to phonons. When the temperature decreases, the elastic intensity slightly increases, whereas the phonon contribution decreases. Additionally we observe a quasielastic intensity arising from the fluctuations of the iron spin. The Fe spin relaxation is only of magnetic origin. The Mössbauer effect data for this sample agree

with the neutron observations: they show a freezing at low temperature of some paramagnetic Fe spins, whereas other spins appear static up to the Néel temperature. The difference between these two methods is that the Mössbauer technique is a local probe and is sensitive only to the magnetic order frozen on the time scale of about 10^{-9} s, whereas the neutron one is a global probe with a time scale of 10^{-11} s [37].

The ^{170}Yb Mössbauer spectra of $Y^{170}_{1-x}Yb_xBa_2Cu_3O_{6+d}$ ($x = 0.03$) indicate the influence of the paramagnetic relaxation. For the samples with $d \sim 1.0$ the thermal evolution of the paramagnetic relaxation rate is attributed partly to phonon driven processes and, possibly, partly to a coupling with magnetic fluctuations linked with the Cu(2)-O subsystem [38]. These fluctuations become quenched when the magnetic pseudo-gap opens near T_c. The spectra obtained for the deoxygenated $Y^{170}_{0.97}Yb_{0.03}Ba_2Cu_3O_{6.35}$ have different character. The analysis of those spectra indicate that all of the isolated Yb^{3+} ions have local magnetic (spin glass) behavior while for $d = 1.0$ all of the ions exhibit local non-magnetic behavior. The strong thermal variation of the sample averaged fluctuation frequency of the Yb^{3+} ions from $7{\cdot}10^8$ s^{-1} at $T = 1.4$ K to 10^{12} s^{-1} at $T = 30$ K is observed.

3.3.3 $Y_{1-x}Ca_xBa_2Cu_3O_{6+d}$ compounds

The calcium substitution has been investigated in both oxygenated [39, 40] and deoxygenated [41–43] $Y_{1-x}Ca_xBa_2Cu_3O_{6+d}$ systems. It is known that Ca is substituted mostly into the Y planes [40–44]. The increase in hole concentration is explained by the fact of substitution of divalent Ca for trivalent Y. While Ca is substituted to fully oxygenated Y-123 compound, the systems become overdoped and T_c decreases. In the deoxygenated samples Ca acts also as the donor of charge carriers and changes transport and magnetic properties of the system.

X-ray and neutron diffraction data show that $Y_{1-x}Ca_xBa_2Cu_3O_{6+d}$ ($d \simeq 0$) have a tetragonal crystal structure and Ca atoms prefer the Y position [44]. Temperature dependence of electrical resistivity indicates the insulator-metal transition [45]. The magnetic-superconducting phase diagram is shown in Fig. 3.12. For $0.175 < x < 0.25$ superconducting properties are observed.

Zero field muon spin rotation (ZF-μ^+SR) measurements give the following results [46]:

- for low Ca concentration ($x < 0.06$) three-dimensional antiferromagnetic order
- at low temperatures a spin-glass-like state is detected in the $0.03 < y < 0.18$ region
- for $x > 0.12$ the superconducting properties are observed.

Mössbauer effect measurements for deoxygenated $Y_{1-x}Ca_xBa_2(Cu_{0.992}{}^{57}Fe_{0.008})_3O_{6.7}$ compounds for $0.05 < x < 0.26$ are presented in [47, 48].

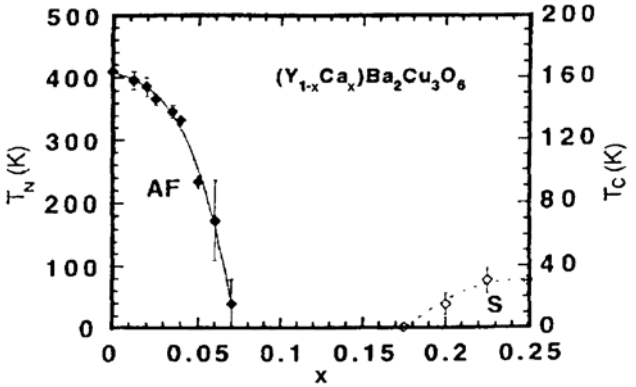

Fig. 3.12. Phase diagram for $Y_{1-x}Ca_xBa_2Cu_3O_6$ system. The Néel temperature and critical temperature are shown as a function of calcium content in the deoxygenated system

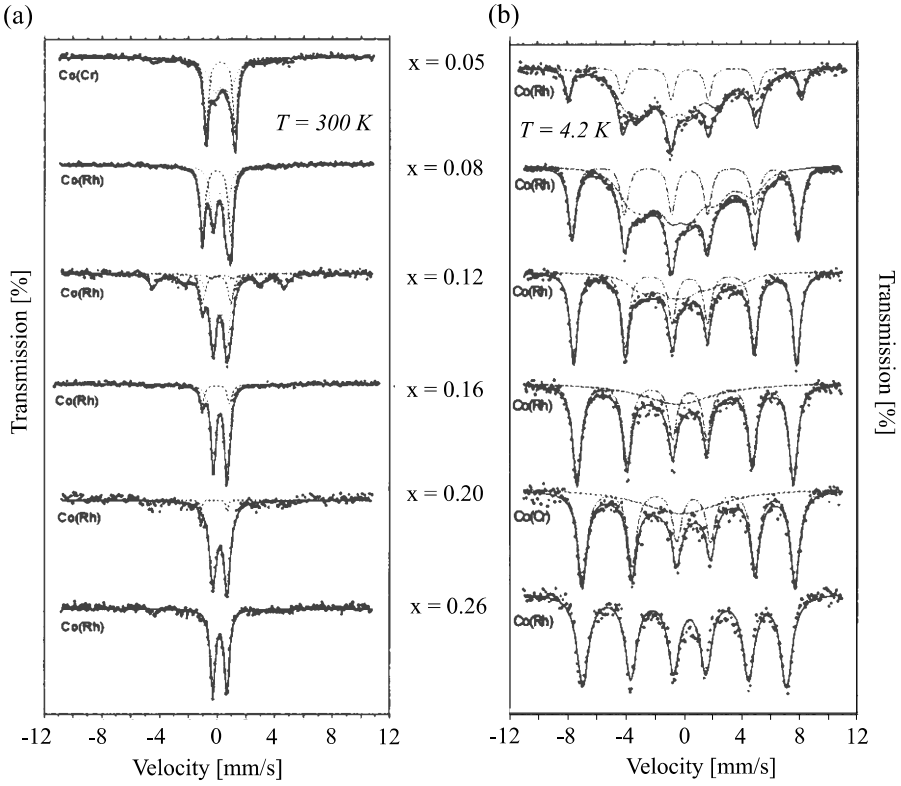

Fig. 3.13. Mössbauer spectra of $Y_{1-x}Ca_xBa_2(Cu^{57}_{0.992}Fe_{0.008})_3O_{6.1}$ compounds for xs = 0.05, 0.08, 0.12, 0.16, 0.20 and 0.26 at (**a**) room temperature and (**b**) at 4.2 K [47]

The Mössbauer spectra of $Y_{1-x}Ca_xBa_2(Cu^{57}_{0.992}Fe_{0.008})_3O_{6.1}$ collected for $0.05 \leq x \leq 0.26$ at room and liquid helium temperature are shown in Fig. 3.13. The spectra recorded at room temperature consist of two doublets with parameters similar to those observed for the oxygenated and deoxygenated $YBa_2Cu^{57}_{3-y}Fe_yO_{6+d}$ samples [31]. We can propose that one doublet can be identified with Fe^{2+} while the second one with Fe^{3+}. Their relative intensities change with hole doping (with increasing Ca content x). The low temperature spectra (at $T = 4.2$ K) consist of two Zeeman sextets: the first one is well distinguishable whereas the second one is much broadened. As we compare the intensities of doublets and sextets for different x, we can conclude that the first sextet may be attributed to Cu-O planes, as well defined antiferromagnetic order appears in these planes. The magnitude of the hyperfine magnetic field (from 435 to 500 kOe) suggests the high spin state of Fe^{3+} which interacts with magnetic moments of the surrounding Cu spins. The second sextet is associated probably with divalent Fe, with smaller magnetic moment, that is reflected in weaker magnetic hyperfine field (310 kOe). The analysis of the Mössbauer spectra at different temperatures indicate the existence of relaxation processes with the relaxation time slightly higher than the observation time of the method $\sim 10^{-7}$ s.

3.4 Summary

In the first part of this chapter a brief information on three experimental methods: Mössbauer and muon spectroscopy as well as neutron diffraction and the application of this methods to investigate relaxation phenomena in high-T_c superconductors is presented. The second part reports the experimental results concerning the relaxation phenomena for three groups of compounds: $La_{2-x}Sr_xCuO_4$, $YBa_2Cu_3O_{6+d}$ and $Y_{1-x}Ca_xBa_2Cu_3O_{6+d}$. They indicate that the high-T_c cuprates have various anomalous properties connected with the spin relaxation.

References

1. J.G. Bednorz, A. Müller: Z. Phys. B **64**, 189 (1986)
2. R.L. Mössbauer: Z. Physik **151**, 124 (1958); Z. Naturforsch **14**, 211 (1959)
3. G.K. Wertheim: *Mössbauer Effect: Principles and Applications* (Academic Press, New York 1964)
4. M. Blume, J.A. Tjon: Phys. Rev. **165**, 446 (1968)
5. *Muons and Pions in Materials Research*, ed. by J. Chappert, R.I. Grynszpan (Elsevier Science Publishers 1984)
6. A. Schenck: *Muon spin rotation spectroscopy: Principles and Applications in Solid State Physics* (Adam Hilger Ltd., Bristol and Boston 1985)
7. G.E. Bacon: *Neutron diffraction* (Clarendon Press, Oxford 1962)

8. S.W. Lovesey: *Theory of Neutron Scattering from Condensed Matter*, Vols. **1** and **2** (Clarendon Press, Oxford 1984)
9. M.Th. Rekveldt: Textures and Microstrctures **11**, 127 (1989)
10. F.C. Chon, N.R. Belk, M.A. Kastner, R.J. Birgenaux, A. Aharony: Phys. Rev. Lett. **75**, 2204 (1995)
11. D.C. Johnston: *Single-layer cuprate high-temperature superconductors*, in: Handbook of Magnetic Materials, Vol. **10**, ed. by K.H.J. Buschow (North Holland, Elsevier, Amsterdam 1997) p. 218
12. T. Tokagi, S. Ishibashi, M. Uota, S. Uchida, Y. Tokura: Phys. Rev. B **40**, 2254 (1989)
13. D. Vakain, S.K. Sinha, D.E. Moncton, D.C. Johnston, J.M. Newsam, C.R. Safinya, H.E. King Jr.: Phys. Rev. Lett. **58**, 2802 (1987)
14. T. Freltoft, J.P. Remeika, D.E. Moncton, A.S. Copper, J.E. Fischer, D. Harshman, G. Shirane, S.K. Sinha, D. Vakain: Phys. Rev. B **36**, 826 (1987)
15. G. Shirane, Y. Endoh, R.J. Birgeneau, M.A. Kastner, Y. Midaka, M. Oda, M. Suzuki, T. Murakani: Phys. Rev. Lett. **59**, 1613 (1987)
16. Y. Endoh, K. Yamada, R.J. Birgeneau, D.R. Gabbe, H.P. Jenssen, M.A. Kastner, C.J. Peters, P.J. Picone, T.R. Thurston, J.M. Tranquada, G. Shirane, Y. Hikada, M. Oda, Y. Enomoto, M. Suzuki, T. Murakami: Phys. Rev. B **37**, 7443 (1988)
17. D.R. Harshman, G. Aeppli, G.P. Espinosa, A.S. Copper, J.P. Remeika, E.J. Ansaldo, T.M. Riseman, D.L. Williams, D.R. Noakes, B. Ellman, T.F. Rosenbaum: Phys. Rev. B **38**, 852 (1988)
18. J.B. Goodenough, R.J. Birgeneaux, G. Shirane: in: *Physical properties of high temperature superconductors I*, ed. by D.M. Ginsberg (World Scientific, Singapore 1989) p. 151
19. P. Imbert, G. Jehanno, J.A. Hodges: Hyperfine Interactions **50**, 599 (1989)
20. P. Imbert, G. Jehanno: Hyperfine Interactions **55**, 1307 (1990)
21. I. Felner, U. Yaron, I. Nowik, E.R. Bauminger: Physica C **198**, 14 (1990)
22. M.K. Wu, J.R. Ashburn, C.J. Torn, P.F. Hor, R.L. Meng, L. Gao, Z.J. Huang, Y.Q. Wang, C.W. Chu: Phys. Rev. Lett. **56**, 908 (1986)
23. J.M. Tranquada, D.E. Cox, W. Kummann, H. Moudden, G. Shirane, M. Suenaga, P. Zolliker: Phys. Rev. Lett. **60**, 156 (1988)
24. P. Burlet, C. Vetteir, M.J. Jurgens, J.Y. Henry, J. Rossat-Mignod, H. Noël, M. Potel, P. Gougeon, J.C. Lavet: Physics C **153-155**, 1115 (1988)
25. J. Rossat-Mignod, P. Burlet, M.J. Jurgens, C. Vettier, L.P. Regnault, J.Y. Henry, C. Agache, L. Forro, H. Noël, M. Potel, P. Gougeon, J.C. Levet: J. de Phys. **49**, C8-2119 (1988)
26. J. Rossat-Mignod, L.P. Regnault, C. Vettier, P. Burlet, J.Y. Henry, G. Lapertoo: Physics B **169**, 69 (1991)
27. T.H. Brückel, K.U. Neumann, H. Capellmann, O. Schärpf, S. Kemmler-Sack, R. Kiemel, W. Schäfer: J. de Phys. **48** C8-21, 55 (1988)
28. H.A. Mook, P. Dai, K. Salama, D. Lee, F. Dogan, G. Aeppli, A.T. Boothvoyd, M.E. Mostoller: Phys. Rev. Lett. **77**, 370 (1996)
29. P. Dai, H.A. Mook, F. Dogan: Phys. Rev. Lett. **80**, 1738 (1998)
30. N. Nishida, H. Miyatake, D. Shimada, S. Okuma, M. Ishikawa, T. Tkabatake, Y. Nakazawa, Y. Kuno, R. Leitel, J.H. Brewer, T.M. Riseman, D.L. Williams, Y. Watanabe, T. Yamazaki, K. Nishiyama, K. Nagamine, E.J. Ansaldo, E. Torikai: Jpn. J. Appl. Phys. **26**, L1856 (1987)

31. I. Felner, I. Nowik: Supercond. Sci. Technol. **8**, 121 (1995)
32. J.A. Hodges, P. Imbert, G. Jehanno: Solid State Commun. **64**, 1209 (1987)
33. R.K. Siddique, S. Jha, W.C.H. Joiner, G.M. Julian: J. Phys.: Condens. Matter. **6**, 1019 (1994) and references therein
34. J.I. Bordet, P. Hodeau, M. Strobel, M. Marezio, A. Santoro: Solid State Commun. **66**, 435 (1988)
35. J.A. Hodges, P. Bonville, A. Forget: J. Magn. Magn. Mater. **204**, 49 (1999)
36. J. Dengler, L. Bottyán, Gy. Faigel, N.E. Kaner, D.L. Nagy, G. Ritter, U. Röhlich: Proc XXVIII Zakopane School of Physics, ed. by E.A. Görlich, K. Tomala (Institute of Physics, Jagiellonian Univeristy, Kraków 1993) p. 274
37. I. Mirebau, C. Bellouard, M. Henion, G. Jéhanno, V. Caignaret, A.J. Dianoux, T.E. Phillips, K. Moorjani: Physics C **184**, 299 (1991)
38. J.A. Hodges, P. Bonville, P. Imbert, G. Jéhanno, P. Debray: Physics C **184**, 270 (1991)
39. Y. Tokura, J.B. Torrance, T.C. Huang, A.I. Nazzal: Phys. Rev. B **38**, 7156 (1988)
40. R.G. Buckley, D.M. Pooke, J.L. Tallon, M.R. Presland, N.E Flower, M.P. Staines, H.L. Johnson, M. Meylan, G.V.M. Williams, M. Bowden: Physics C **174**, 383 (1991)
41. E.M. III McCarron, M.K. Crawford, J.B. Parise: J. Solid State Chem. **78**, 192 (1989)
42. H. Casalta, H. Alloul, J.F. Marucco: Physics C **204**, 331 (1993)
43. J.L. Tallon, C. Bernhard, H. Shaked, R.L. Hitterman, J.D. Jorgensen: Phys. Rev. B **51**, 12911 (1995)
44. P. Starowicz, S. Baran, A. Szytuła, V.F. Dong: Mol. Phys. Reports **15/16**, 237 (1996)
45. P. Starowicz, J. Sokołowski, M. Bałanda, A. Szytuła: Physics C **63**, 80 (2001)
46. Ch. Niedermayer, C. Bernhard, T. Blasius, A. Golnik, A. Moodenbaugh, J.I. Budnick: Phys. Rev. Lett. **80**, 3843 (1998)
47. P. Starowicz: Thesis (Jagiellonian University, Kraków 2000)
48. P. Starowicz, A. Szytuła, J. Żukrowski: Int. J. of Modern Phys. B **14**, 3685 (2000)

Part II

Relaxation Phenomena in Liquid Crystals

4

Non-chiral Calamitic Liquid Crystals

4.1 Introduction to dielectric relaxation in anisotropic fluids

D. A. Dunmur

4.1.1 Isotropic fluids

The absorption by matter of electromagnetic (EM) radiation pervades all natural phenomena, and in reality is the mechanism through which our knowledge of the natural world is obtained. The spectrum of radiation available to us ranges, in terms of frequencies, from 0 Hz to 10^{18} Hz corresponding to X-rays, with the visible region of light occupying a small range of frequencies from 10^{14} Hz to 10^{15} Hz. More than half of the electromagnetic spectrum (0 Hz to 10^{10} Hz) interacts with matter through its so-called dielectric response, and so the study of frequency dependent dielectric relaxation (energy absorption) in materials is a powerful technique to study the nature of matter. The necessary experiments can now be carried out with relative ease, but the interpretation of the results can be a challenge. In this section, we wish to give a brief introduction to the theoretical models available to extract information from measurements of dielectric relaxation, in particular from nematic liquid crystals. There are two problems to deal with: firstly we must have a suitable theory to describe the measured dielectric response as a function of frequency, or time if pulse techniques are being used. Secondly in order to use the results, we need a microscopic model to relate the parameters of the experimental results to molecular or atomic theories.

It was Debye who identified the contribution of molecular dipoles to the dielectric constant (ε) of insulating fluids. However his theory did not adequately describe the behaviour of dipolar liquids, and Onsager recognised that the reorienting field experienced by dipoles (the directing field) differed from the internal field by the reaction field. Thus the starting point for a microscopic theory of the dielectric properties of liquids is the Onsager equation (4.1), of which the Debye and Clausius-Mossotti equations are special cases.

$$(\varepsilon - 1) = \frac{N_0 F h}{\varepsilon_0}\left[\bar{\alpha} + \frac{\mu^2 F}{3k_B T}\right] . \tag{4.1}$$

Here N_0 is the number density, ε_0 is the permittivity of a vacuum, μ is the molecular dipole moment, $\bar{\alpha}$ is the mean polarisability, T the absolute temperature and the internal field factors for the reaction field (F) and the cavity field (h) are defined as:

$$F = \frac{(2\varepsilon + 1)\left(n^2 + 2\right)}{3\left(2\varepsilon + n^2\right)} , \tag{4.2a}$$

$$h = \frac{3\varepsilon}{(2\varepsilon + 1)} . \tag{4.2b}$$

This result is suitable for the interpretation of the static dielectric constant of isotropic non-associating dipolar liquids. However it needs to be modified to describe the dielectric properties of fluids in which there is correlation between the molecular dipoles, which may result in the enhancement or the reduction of the effective molecular dipole moment. The simplest way of accounting for short range dipole-dipole interactions is to introduce the Kirkwood correlation factor g_1. This can be written in a number of ways, but the most general is in terms of the spatial correlation function $G_1(\boldsymbol{r})$ for molecular dipoles, whose orientation is a function of position, as defined in (4.3):

$$g_1 = 1 + V^{-1}\int G_1(\boldsymbol{r}) d\boldsymbol{r} \text{ where } G_1(\boldsymbol{r}) = \frac{\langle \boldsymbol{\mu}(0) \bullet \boldsymbol{\mu}(\boldsymbol{r})\rangle}{\langle \boldsymbol{\mu}(0) \bullet \boldsymbol{\mu}(0)\rangle} . \tag{4.3}$$

V is the integration volume in (4.3) for the Kirkwood correlation factor. This factor is a useful measure of the local dipole organisation in fluids, and if $g_1 > 1$, there is local parallel ordering of dipoles, while if $g_1 < 1$, there is local antiparallel organisation of the dipoles.

So far it has been assumed that the dipolar molecules are rigid, or that there is only a single localised dipole in the molecule contributing to the dielectric properties. However if there are a number of dipolar groups present (μ_j), which are not rigidly connected, then they may make separate contributions to the dielectric constant. Thus the Onsager equation can be written as a sum of contributions from different molecular segments, see (4.4). Such a formulation is obviously of importance for understanding the dielectric properties of dipolar polymers, but it is also important when we come to consider the frequency dependent properties of flexible molecules.

$$\varepsilon(0) - \varepsilon(\infty) = \frac{F^2 h}{3\varepsilon_0 k_B T}\sum_j N_j \mu_j^2 . \tag{4.4}$$

In (4.4) and what follows, the high frequency contributions ($\omega = \infty$) to the electric permittivity have been subtracted off. These are the contributions from atomic and electronic polarisation, which are responsible for the infra-red and visible/uv refractive indices. For a non-absorbing dielectric, the polarisation

induced by an oscillating external potential is in phase with the applied field, but if the frequency of the applied field approaches a region of energy absorption or dielectric loss, the polarisation becomes out of phase with the applied field. In simple terms, if the frequency of the external field is less than or equal to the characteristic rotational frequency of the dipole, a rotating dipole will be perturbed by an external electric field. As the frequency of the external field approaches that of the rotating dipole, energy transfer occurs between the EM field and the dipole. For higher frequencies of the field, the dipole no longer contributes to the dielectric response, and the material becomes "transparent" i.e. non-absorbing and non-retarding to an external field. If a molecule contains a number of different dipolar groups, then the dipolar contributions to the dielectric response will disappear at different frequencies, as the frequency of an external field is changed.

To describe a frequency dependent dielectric response, for which the phase of the response and its amplitude may change, it is convenient to introduce a complex dielectric permittivity , defined as:

$$\varepsilon^{*}(\omega) = \varepsilon'(\omega) - i\varepsilon''(\omega) \ , \tag{4.5}$$

where ε' is a measure of the in-phase dielectric polarisation, and ε'' is a measure of the out-of-phase polarisation. For a single process which can be described by a single relaxation time (τ), the complex dielectric permittivity can be written, using (4.1) as:

$$\varepsilon^{*}(\omega) - \varepsilon(\infty) = (1 + i\omega\tau)^{-1} \frac{NF^2h}{3\varepsilon_0 k_B T} \ , \tag{4.6}$$

where the frequency ω is in radians s^{-1}. Rationalising this equation gives the real and imaginary parts of the permittivity as:

$$\varepsilon'(\omega) - \varepsilon(\infty) = \left(1 + \omega^2\tau^2\right)^{-1} \frac{NF^2h}{3\varepsilon_0 k_B T} \ , \tag{4.7a}$$

$$\varepsilon''(\omega) = \omega\tau \left(1 + \omega^2\tau^2\right)^{-1} \frac{NF^2h}{3\varepsilon_0 k_B T} \ . \tag{4.7b}$$

The quantity $\frac{NF^2h}{3\varepsilon_0 k_B T} = \varepsilon'(0) - \varepsilon'(\infty) = \delta\varepsilon'$ is the strength or dielectric increment for the relaxation. For a series of independent dipole relaxations occurring at different frequencies with corresponding relaxation times τ_j, the complex frequency dependent permittivity can be represented as a sum of terms, each of which corresponds to a particular relaxation process.

In general, for a single relaxation, the real and imaginary parts of the complex permittivity can be written as:

$$\varepsilon'(\omega) - \varepsilon'(\infty) = \frac{[\varepsilon'(0) - \varepsilon'(\infty)]}{[1 + \omega^2\tau^2]} \ , \tag{4.8a}$$

$$\varepsilon''(\omega) = \frac{\omega\tau\,[\varepsilon'(0) - \varepsilon'(\infty)]}{[1 + \omega^2\tau^2]} \ , \tag{4.8b}$$

which are sometimes more conveniently used in the form of the Debye–Pellat equations:

$$\varepsilon'(\omega) = \varepsilon'(\infty) + \frac{\varepsilon''(\omega)}{\omega\tau}\,, \tag{4.9a}$$

$$\varepsilon'(\omega) = \varepsilon'(0) - \omega\tau\varepsilon''(\omega)\ . \tag{4.9b}$$

A convenient way of presenting complex quantities is in the form of an Argand diagram, and the elimination of the variable $\omega\tau$ from (4.9a and 4.9b) gives the equation of a circle in the complex plane:

$$\varepsilon''(\omega)^2 + \left\{\varepsilon'(\omega) - \tfrac{1}{2}\left[\varepsilon'(0) + \varepsilon'(\infty)\right]\right\}^2 = \tfrac{1}{4}\left[\varepsilon'(0) - \varepsilon'(\infty)\right]^2\ . \tag{4.10}$$

The representation of the real and imaginary parts of the electric permittivity in the complex plane is known as a Cole–Cole plot, but it is not always a semi-circle for real fluids. A number of empirical descriptions of experimental Cole–Cole plots have been proposed, the first of which was introduced by Cole and Cole, and is known as Cole–Cole equation:

$$\varepsilon^*(\omega) - \varepsilon(\infty) = \frac{\left(\varepsilon'(0) - \varepsilon'(\infty)\right)}{1 + (i\omega\tau_0)^{1-\alpha}}\ . \tag{4.11}$$

This empirical equation in fact represents a relaxation process having a symmetrical distribution of relaxation times on a log scale about a critical time τ_0. Such a function may be appropriate for a single dipolar relaxation experiencing fluctuations in its local environment. The parameter α is a measure of the width of the distribution. Another empirical function used is the Cole–Davidson equation:

$$\varepsilon^*(\omega) - \varepsilon(\infty) = \frac{\left(\varepsilon'(0) - \varepsilon'(\infty)\right)}{(1 + i\omega\tau_0)^{\beta}}\ . \tag{4.12}$$

This can be used to fit an asymmetric or skewed Cole–Cole plot, and the parameter β is a measure of the width of an asymmetric distribution of relaxation times.

Both the Cole–Cole and Cole–Davidson equations are contained in the Havriliak–Negami equation,

$$\varepsilon^*(\omega) - \varepsilon(\infty) = \frac{\left(\varepsilon'(0) - \varepsilon'(\infty)\right)}{\left[1 + (i\omega\tau_0)^{1-\alpha}\right]^{\beta}}\,, \tag{4.13}$$

from which can be deduced a distribution of relaxation times $P(\ln\tau)$:

$$P(\ln\tau) = \frac{(\tau/\tau_0)^{\beta(1-\alpha)}\sin\beta\theta}{\pi\left[(\tau/\tau_0)^{2(1-\alpha)} + 2(\tau/\tau_0)^{1-\alpha}\cos\pi(1-\alpha) + 1\right]^{\beta/2}}\,, \tag{4.14}$$

where $\theta = \arctan\left[\sin\pi(1-\alpha)\,/\,\{(\tau\,/\tau_0\,) + \cos\pi(1-\alpha)\}\right]$.

There are a number of other empirical functions, which have been used to fit experimental results for real and imaginary permittivities, and for dielectric materials the Fuoss–Kirkwood and Jonscher descriptions have been frequently applied. The former involves an alternative parametrisation for the imaginary component of the permittivity given by the Debye–Pellat equations, such that:

$$\varepsilon''(\omega) = \tfrac{1}{2}\alpha_{FK}\left[\varepsilon'(0) - \varepsilon'(\infty)\right]\operatorname{sech}\left(\alpha_{FK}\ln\omega\tau\right) . \tag{4.15}$$

Like the Cole–Cole equation, this corresponds to a symmetrical distribution of relaxation times on a logarithmic scale, but the parameter α_{FK} is different. Finally the Jonscher approach has been to propose a universal power law for the imaginary part of the permittivity (4.16), characterised by two exponents, one each for the logarithmic decay of loss to high and low frequencies. While this approach can be useful to describe and compare the collective dielectric response of a wide range of materials, it is less useful in separating contributions from local modes which can be identified in molecular materials.

$$\varepsilon''(\omega) = \frac{\frac{1}{2}\alpha_J\left[\varepsilon'(0) - \varepsilon'(\infty)\right]}{(\omega/\omega_1)^{-m} + (\omega/\omega_2)^{1-n}} . \tag{4.16}$$

Most experimental techniques to measure dielectric relaxation operate in the frequency domain, but the interpretation of results for molecular materials is invariably done in terms of relaxation times. Direct methods to probe the time response to electric fields are available, as explained in Sect. 1.2, but it is also useful to be able to transform results obtained in the time domain to the frequency domain. The most general way to represent the motion of a dipole in the time domain is in terms of a dipole auto-correlation function. Strictly [1, 2] this should be the correlation function of a dipole interacting with a sphere of nearest neighbour dipoles, but if the Kirkwood correlation factor is assumed to be equal to unity, the appropriate correlation function can be defined as:

$$C(t) = \frac{\langle \boldsymbol{\mu}(0) \bullet \boldsymbol{\mu}(t)\rangle}{\langle \boldsymbol{\mu}(0) \bullet \boldsymbol{\mu}(0)\rangle} . \tag{4.17}$$

This can then be used to obtain the frequency dependence of the complex permittivity through the Laplace transform, such that:

$$\begin{aligned} \frac{(\varepsilon^*(\omega) - \varepsilon(\infty))}{(\varepsilon(0) - \varepsilon(\infty))}\left[\frac{(2\varepsilon^*(\omega) + \varepsilon(\infty))\,\varepsilon(0)}{(2\varepsilon(0) + \varepsilon(\infty))\,\varepsilon^*(\omega)}\right] &= 1 - i\omega\int_0^\infty C(t)\,\mathrm{e}^{i\omega t}dt \\ &\approx \frac{(\varepsilon^*(\omega) - \varepsilon(\infty))}{(\varepsilon(0) - \varepsilon(\infty))} . \end{aligned} \tag{4.18}$$

In developing molecular theories of dielectric relaxation it is easier to derive expressions for the molecular correlation functions than the dielectric spectrum directly. Furthermore the results of molecular dynamics simulations for the dielectric response of materials are most conveniently presented in terms

of appropriate dipole correlation functions. The correlation function may then be represented as an exponential function of time, or as a sum of exponentials, each of which can be characterised by a relaxation time. A correlation time can be defined for any correlation function as the time integral over the correlation function, but this requires that the function $C(t)$ goes to zero for infinite time. For condensed phases the interpretation of the correlation time or relaxation times depends on a microscopic model for the dipole dynamics, which is difficult enough for simple isotropic dipolar liquids, but is even more complicated for anisotropic fluids such as liquid crystals. Nevertheless much research has been done on the dielectric properties of liquid crystals, and in the following sections the dielectric relaxation for such systems will be considered.

4.1.2 Anisotropic fluids

The electric permittivity $\varepsilon_{\alpha\beta}$ is by definition a second rank tensor quantity, which relates the induced polarisation $\boldsymbol{P}$ to the macroscopic electric field $\boldsymbol{E}$.

$$P_\alpha = \varepsilon_0 \left(\varepsilon_{\alpha\beta} - \delta_{\alpha\beta}\right) E_\beta \,. \tag{4.19}$$

In general a symmetric second rank tensor has six independent components, which are reduced to three diagonal components if the tensor is defined with respect to a set of principal axes. For uniaxial symmetry there are only two independent components of the permittivity, parallel ($\varepsilon_\parallel$) and perpendicular ($\varepsilon_\perp$) to the single axis of symmetry. Under these circumstances, the electric permittivity tensor may be specified by its average value $\bar{\varepsilon}$ and anisotropy $\Delta\varepsilon$, defined as:

$$\bar{\varepsilon} = \tfrac{1}{3}\left(\varepsilon_\parallel + 2\varepsilon_\perp\right) \,, \tag{4.20a}$$

$$\Delta\varepsilon = \left(\varepsilon_\parallel - \varepsilon_\perp\right) \,. \tag{4.20b}$$

For isotropic materials the anisotropy $\Delta\varepsilon$ is zero, and the permittivity can be represented by a scalar quantity ε, which means that it is independent of the direction of measurement. For anisotropic materials, the measured permittivity will depend on direction, so it is necessary to define the direction of measurement in some way. With anisotropic solids, the directions of measurement are defined by the topology of the sample and where the electrodes are placed, but for fluids the directions are fixed by external constraints, such as surface or flow alignment or external electric and magnetic fields. The alignment of a uniaxial liquid crystal is determined by a single director, and this can be aligned parallel or perpendicular to electrode surfaces using suitable surface treatments. Such surface treatments interfere with high frequency measurements, and under these circumstances external fields are preferred. For biaxial liquid crystal phases, such as the smectic C phase, there are two directors, and in order to obtain a monodomain sample both directors must

be aligned. Furthermore biaxial materials require three independent components to specify their dielectric tensor, and such measurements are rare for liquid crystals.

In order to relate the dielectric properties of liquid crystals to the molecular properties of the constituent molecules, it is possible to develop an equivalent result to the Onsager equation, but for anisotropic fluids. This was first done by Maier and Meier [3] for uniaxial systems. In (4.21a–c) we give the corresponding equations taking full account of phase and molecular biaxiality [4];

$$\varepsilon'_{\parallel}(\omega) - \varepsilon_{\parallel}(\infty) = \frac{NF^2h}{3\varepsilon_0 k_B T}[\mu_z^2(1+2S) + \mu_y^2(1-S-D) + \mu_x^2(1-S+D)] , \tag{4.21a}$$

$$\varepsilon'_{\perp}(\omega) - \varepsilon_{\perp}(\infty) = \frac{NF^2h}{6\varepsilon_0 k_B T}[2\mu_z^2(1-S-P) + \mu_y^2(2+S+P+D+C) + \mu_x^2(2+S+P-D-C)] , \tag{4.21b}$$

$$\varepsilon'_{\perp'}(\omega) - \varepsilon_{\perp'}(\infty) = \frac{NF^2h}{6\varepsilon_0 k_B T}[2\mu_z^2(1-S+P) + \mu_y^2(2+S-P+D-C) + \mu_x^2(2+S-P-D+C)] . \tag{4.21c}$$

In these equations it has been assumed that the cavity and reaction field factors for anisotropic fluids can be replaced by their isotropic values. There is some justification for this, since the anisotropy of internal field factors reflects the long-range anisotropy in the radial distribution function for the molecules [5]. However a number of models have been developed for the anisotropic internal electric field in liquid crystals [6], and can be applied if desired. The fluid anisotropy enters into (4.21a–c), through the microscopic order parameters, S, D, P and C, which describe the degree of alignment of the molecules with respect to the symmetry axes of the phase. In defining these order parameters, it is assumed that the orientation of the molecular axes x, y, z can be related to the orthogonal symmetry axes of the aligned liquid crystal phase by the three Euler angles, θ, ϕ and ψ. The order parameters for the aligned liquid crystal can then be obtained by averaging over functions of θ, ϕ and ψ. The corresponding order parameters are [7]:

$$S = \left\langle \tfrac{1}{2}\left(3\cos^2\theta - 1\right)\right\rangle , \tag{4.22a}$$

$$D = \left\langle \tfrac{3}{2}\sin^2\theta\cos 2\psi\right\rangle , \tag{4.22b}$$

$$P = \left\langle \tfrac{3}{2}\sin^2\theta\cos 2\phi\right\rangle , \tag{4.22c}$$

$$C = \left\langle \tfrac{3}{2}\left[\left(1+\cos^2\theta\right)\cos 2\phi\cos 2\psi - 2\cos\theta\sin 2\phi\sin 2\psi\right]\right\rangle . \tag{4.22d}$$

The major order parameter is S, which describes the extent of the alignment of the molecular long axis with respect to the major director. If the molecules

of the liquid crystal are biaxial, but the phase is uniaxial, then the order parameter D must be included. For biaxial molecules the two transverse axes (x, y) perpendicular to the long molecular axis will differ. Thus the degree of order of these two axes with respect to the uniaxial director will also differ; the difference between these is D. For a perfectly ordered system $S = 1$, but $D = 0$, since both molecular transverse axes are perpendicular to the director. If the phase is macroscopically biaxial, then the alignment of the phase is determined by three orthogonal axes. As before, the major order parameter S describes the degree of order of the long molecular axis with respect to the major symmetry axis of the phase. However the order parameters of the long molecular axis with respect to the two minor symmetry axes of the phase will not be equal, and their difference is P. As for uniaxial phases, if $S = 1$, then $P = 0$. Finally the order parameter C is only non-zero if both the molecular and phase symmetries are biaxial. It represents the differences in the degrees of order of the two transverse molecular axes with respect to minor symmetry axes of the phase, and for perfect alignment, $C = 3$.

We now turn attention to the frequency dependence of the principal components of the dielectric permittivity tensor, as given in (4.21a–c). These equations contain no explicit dependence on translational order in the liquid crystal phases, and only describe the effects of orientational order and symmetry. Although the dynamics of dipolar molecules in layered smectic phases are largely determined by the orientational organisation of the molecules, translational order parameters will have some influence on the dielectric response. In particular for chiral and achiral biaxial smectic A and C phases, the microscopic dipole organisation results in characteristic collective relaxation modes. These are dealt with in Sect. 5.11.2. The different contributions of molecular dipole components to the electric permittivities separated in (4.21a–c), will all have different dynamical responses to an external electric field of variable frequency. Thus depending on the nature of the relaxation mode, the different terms on the right-hand sides of (4.21a–c) will relax at different frequencies giving rise to complex dielectric spectra. If the effects of phase biaxiality are ignored, the equations can be simplified to involve only the order parameters S and D. Furthermore it is usually assumed that contributions from the local biaxial ordering described by D are small and can be ignored, so with these simplifications, equations (4.21a) and (4.21b) become:

$$\varepsilon'_{\parallel}(\omega) - \varepsilon_{\parallel}(\infty) = \frac{NF^2h}{3\varepsilon_0 k_B T}\left[\mu_\ell^2 (1+2S)_{\omega_1} + \mu_t^2 (1-S)_{\omega_2}\right] , \tag{4.23a}$$

$$\varepsilon'_{\perp}(\omega) - \varepsilon_{\perp}(\infty) = \frac{NF^2h}{6\varepsilon_0 k_B T}\left[2\mu_\ell^2 (1-S)_{\omega_3} + \mu_t^2 (2+S)_{\omega_4}\right] , \tag{4.23b}$$

where the dipole components are written as μ_ℓ, parallel to the molecular long-axis, and μ_t, transverse to this axis. The subscripts ω_1, ω_2, ω_3 and ω_4 indicate the different frequencies at which the corresponding terms will relax, and the frequency dependence of these permittivity components is represented schematically in Fig. 4.1. Assuming that the experimental measure-

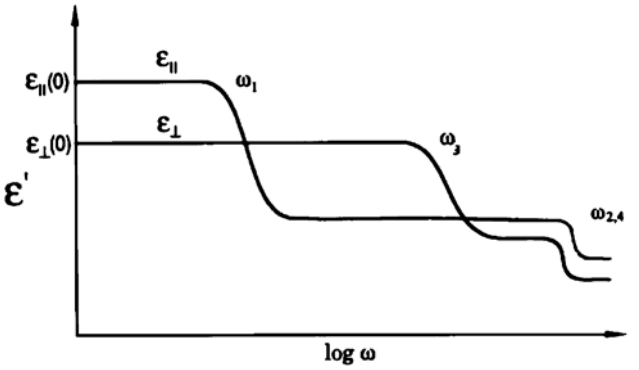

Fig. 4.1. Schematic plot of the real components of the permittivity as a function of frequency

ments for the real and imaginary parts of the permittivity components as a function of frequency can be separated into the different contributions identified in (4.23a , b), the corresponding strengths of the relaxations, or dielectric increments, are given by [8]:

$$\left(\delta\varepsilon'_{\parallel}\right)_1 = \frac{NF^2h}{3\varepsilon_0 k_B T}\,(1+2S)\,\mu_\ell^2\ , \tag{4.24a}$$

$$\left(\delta\varepsilon'_{\parallel}\right)_2 = \frac{NF^2h}{3\varepsilon_0 k_B T}\,(1-S)\,\mu_t^2\ , \tag{4.24b}$$

$$(\delta\varepsilon'_{\perp})_3 = \frac{NF^2h}{3\varepsilon_0 k_B T}\,(1-S)\,\mu_\ell^2\ , \tag{4.24c}$$

$$(\delta\varepsilon'_{\perp})_4 = \frac{NF^2h}{3\varepsilon_0 k_B T}\left(1+\tfrac{1}{2}S\right)\mu_t^2\ . \tag{4.24d}$$

The temperature dependences of these dielectric strengths are primarily determined by the variation of the principal order parameter S with temperature. To give an indication of the expected temperature dependence of the amplitudes of the dielectric relaxation, the appropriate functions of the order parameter are represented schematically as a function of temperature in Fig. 4.2. In order to obtain more information about the nature of the rotational dynamics of molecules in liquid crystals, it is necessary to formulate suitable microscopic models. First attempts to do this [9, 10] extended the Debye rotational diffusion model for a rigid dipolar molecule to nematic liquids by solving the rotational diffusion equation in the presence of an orienting nematic potential. This was subsequently generalised for molecules with off-axis dipoles by Nordio, Rigatti and Segre [11] to include the effects of an anisotropic rotational diffusion tensor, and their theory allows for various forms of an orienting potential. Their approach was based on the evaluation of time correlation functions of the fluctuating components of the molecular dipoles. The required correlation functions are for the components of the

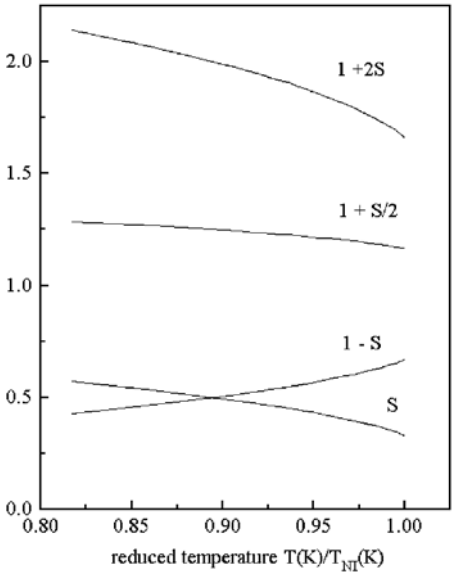

Fig. 4.2. Variation of functions of the order parameter with reduced temperature

molecular dipoles projected onto the alignment axes, or symmetry axes of the nematic phase, and these may be written as:

$$\left\langle \mu_{\parallel}(0) \bullet \mu_{\parallel}(t) \right\rangle = \tfrac{1}{3}(1+2S)\,\mu_{\ell}^{2}\Phi_{00}(t) + \tfrac{1}{3}(1-S)\,\mu_{t}^{2}\Phi_{01}(t)\ , \qquad (4.25a)$$

$$\left\langle \mu_{\perp}(0) \bullet \mu_{\perp}(t) \right\rangle = \tfrac{1}{3}(1-S)\,\mu_{\ell}^{2}\Phi_{10}(t) + \tfrac{1}{6}(2+S)\,\mu_{t}^{2}\Phi_{11}(t)\ . \qquad (4.25b)$$

The quantities $\Phi_{mn}(t)$ describe the time dependence of angular functions representing different relaxation modes for the molecular dipole in an anisotropic environment. Nordio et al. [11] have shown that for the rotational diffusion model, $\Phi_{mn}(t)$ may be written as a sum of exponentials:

$$\Phi_{mn}(t) = \sum_{k} A_{mn}^{k} \exp\left(-\frac{t}{\tau_{mn}}\right)\ . \qquad (4.26)$$

However numerical calculations led these authors to conclude that the expression (4.26) could be accurately represented by the first term, and this assumption has subsequently been substantiated by an analytical method due to Coffey et al. [12]. Thus the time dependence of each of the four separate contributions to the correlation functions in (4.25a, b) can be described by a single characteristic time (τ_{mn}) which depends on the parameters of the orienting potential, and the rotational diffusion coefficients. $\Phi_{00}(t)$ is connected to the relaxation of the longitudinal component of the molecular dipole by reorientation about a short axis. $\Phi_{01}(t)$ is the function which determines the rate of relaxation of the transverse molecular dipole component about the long molecular axis. $\Phi_{10}(t)$ is related to precessional motion of the long molecular axis about the director (the symmetry axis of the phase), while

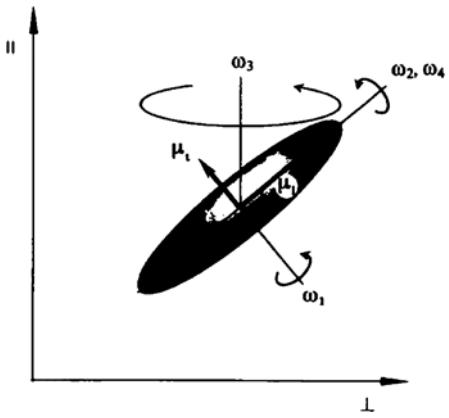

Fig. 4.3. Rotational relaxation modes for a molecule in a nematic potential

$\Phi_{11}(t)$ describes the rotational motion about the long axis of the precessing molecule. The modes of molecular motion represented by these correlation functions are illustrated in Fig. 4.3. Clearly, the absolute values for the characteristic relaxation times and frequencies depend on the parameters of the potential, however the predictions in terms of the relative values of the times are that $\tau_{00} \gg \tau_{11} \sim \tau_{10} > \tau_{01}$. A connection may now be established between the different contributions to the permittivity components given in (4.23a,b), and the different rotational modes, such that $(\omega_1)^{-1} \sim \tau_{00}$, $(\omega_2)^{-1} \sim \tau_{01}$, $(\omega_3)^{-1} \sim \tau_{10}$ and $(\omega_4)^{-1} \sim \tau_{11}$.

The temperature dependence of the magnitudes of the dielectric strengths associated with different rotational modes has already been considered, but the variation of the relaxation times with temperature is perhaps more interesting. There is at present no theory which describes the temperature variation of the dielectric relaxation frequencies of liquid crystals. Nordio et al. [11] calculated the variation of the characteristic frequencies of rotational modes as functions of the major orientational order parameter S. It is possible to predict from their results that τ_{00} should increase rapidly with decrease in temperature, while the relaxation times τ_{01} and τ_{10} should decrease slightly as the temperature falls. The frequency of mode τ_{11} is expected to be approximately independent of temperature.

Experimentally it is found that the dielectric relaxation frequencies for nematic liquid crystals usually exhibit an Arrhenius type of temperature dependence. The largest activation energy is found for relaxation modes of type ω_1, which are believed to be due to reorientation of the molecular dipoles about the short molecular axis. This motion is impeded by the ordering potential in the nematic phase, and it is possible to estimate the nematic potential parameters from the measured activation energies [13, 14]. The validity of this procedure has recently been considered in the light of results of molecular dynamics simulations, which were used to calculate dipole correlation functions for a model system of Gay–Berne particles [15].

4.1.3 Nematic liquid crystals

Although the dielectric spectra of liquid crystals span a large range of frequency, they are poorly resolved; that is the dielectric losses due to different relaxation processes do not occur at well-separated characteristic frequencies. Experimentally this is dealt with by using empirical fitting functions for the variation of the permittivities with frequency, however this does not provide any insight into the nature of the molecular processes responsible for the dielectric losses. For any dielectric loss spectrum there are two characteristics that have to be determined: the number of relaxation times or frequencies, and the width of the distributions associated with each of the relaxation times. A simple Debye relaxation can be represented by a single relaxation time, i.e. the dipole auto-correlation function is a single exponential. However it has been shown [16] that even a strongly non-Debye orientational relaxation may give rise to a single exponential correlation function if translational fluctuations in the polarization are included. The problem is compounded in dielectric studies of liquid crystals, because of their macroscopic anisotropy. Thus if the sample is not perfectly aligned, then relaxations characteristic of one component of the permittivity may be detected in measurements of the other.

The solution of the rotational diffusion equation for a rigid dipolar molecule in the presence of a nematic potential, as described above, predicts that the frequency dependence of each component of the electric permittivity can be characterised by two exponential decays. Rotation of the molecule about a short molecular axis in the presence of the nematic potential gives rise to the low frequency relaxation mode ω_1 detected in the parallel component of the permittivity. If the potential barrier is very high, then there may be an additional high frequency mode for the longitudinal component of the dipole due to librational relaxation within the wells of the potential [17]. Relaxation of the longitudinal component of the molecular dipole by precession about the director axis contributes to a high frequency mode ω_3 detected in the perpendicular component of the permittivity. The transverse component of the molecular dipole relaxes by rotation about the long molecular axis, a process which gives rise to high frequency dielectric relaxations in both the parallel ω_2 and perpendicular ω_4 components of the permittivity. Within the rotational diffusion model, if the anisotropy of the rotational diffusion coefficient is ignored, the relaxation times for modes 2 and 3 are equal i.e. $\tau_{01} = \tau_{10}$. Clearly the assumption of an isotropic rotational diffusion tensor for liquid crystal molecules is unrealistic, and allowing for the rod-like shape of the molecule causes τ_{01} to shift to relatively shorter times, and so causes the degeneracy τ_{01} and τ_{10} to be lifted. Furthermore the frequency of mode 4 for a rod-like molecule is also increased relative to that for a spherical molecule, resulting in a shorter time τ_{11}.

For a nematic potential assumed to be of the form:

$$\frac{u}{k_B T} = \sigma \cos^2 \theta \,, \tag{4.27}$$

where σ is proportional to the uniaxial order parameter S, approximate expressions for the relaxation times can be derived as [12, 18]:

$$\frac{\tau_{00}}{\tau_0} = \left(\frac{\mathrm{e}^{\sigma} - 1}{\sigma}\right)\left[\frac{2\sigma\sqrt{\sigma/\pi}}{1+\sigma} + 2^{-\sigma}\right]^{-1} \,, \tag{4.28a}$$

$$\frac{\tau_{01}}{\tau_0} = \frac{(1-S)(1+\Delta)}{1+\Delta(1-S)+\frac{1}{2}S} \,, \tag{4.28b}$$

$$\frac{\tau_{10}}{\tau_0} = \frac{1-S}{1+\frac{1}{2}S} \,, \tag{4.28c}$$

$$\frac{\tau_{11}}{\tau_0} = \frac{(2+S)(1+\Delta)}{2+\Delta(2+S)-\frac{1}{2}S} \,. \tag{4.28d}$$

The relaxation time τ_0 is that for rotational diffusion in the isotropic phase, and $\Delta = \frac{1}{2}\left[\frac{D_\parallel}{D_\perp} - 1\right]$ is a measure of the anisotropy of the rotational diffusion tensor. Clearly if it is assumed that $D_\parallel = D_\perp$, the relaxation times τ_{01} and τ_{10} are equal. The reduced relaxation times given by (4.28a–d) are plotted as a function of the order parameter S in Fig. 4.4, for $D_\parallel = D_\perp$ and $D_\parallel = 4D_\perp$. In solving the rotational diffusion equation, a uniaxial nematic potential has been assumed. This conceals a basic inconsistency, since molecules which have a dipole inclined to the long molecular axis are intrinsically biaxial. This

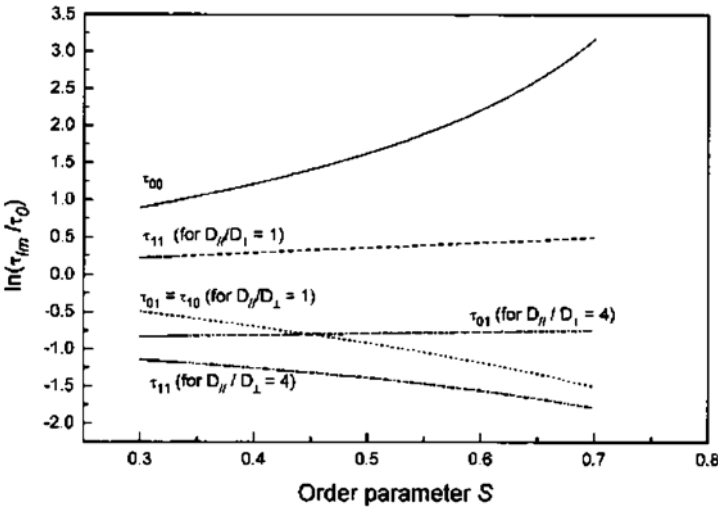

Fig. 4.4. Plot of the variation of the logarithm of reduced relaxation times as a function of order parameter for the rotational diffusion model

should be reflected in the nematic potential, but has so far been neglected in the dynamic theory. Furthermore it is assumed that in the isotropic phase a single dipole relaxation time is sufficient to describe the rotational dynamics of the rigid molecule.

The design of most dielectric relaxation experiments is such that the measuring electric field is either parallel or perpendicular to the director axis of the aligned sample. The detection of a low frequency relaxation in the perpendicular component of the permittivity can be used to identify misalignment in a sample. Measurements have been made [19] of dielectric spectra as a function of the angle between the aligning field, in this case a magnetic field, and the measuring electric field. This work showed that imperfect alignment can result in a small contribution from ω_1 to the measured perpendicular permittivity component, and a contribution from ω_3 to the measured parallel permittivity component.

Liquid crystals for applications are usually mixtures of a number of different components, so in order to understand their dielectric properties, some knowledge of the behaviour of mixtures is necessary. Many mixtures of polar isotropic liquids exhibit a single dielectric relaxation, even if the components individually have relaxations in different frequency ranges, and this behaviour is also often observed in liquid crystal mixtures. However in some mixtures of mesogens having significantly different structures, e.g. mixtures of two-ring and three-ring mesogens [20], two separated relaxations are sometimes detected.

The dielectric spectra measured in the isotropic phase of some simple liquid crystals can be analysed in terms of a symmetric distribution of relaxation times, which suggests the dominance of a single dipolar relaxation mechanism [21]. However many other liquid crystal molecules contain a number of dipolar groups, which are not rigidly connected, and these may give rise to dielectric spectra in the isotropic phase with separable relaxation regions. Thus internal motion in liquid crystal molecules will be expected to influence their molecular dynamics, and hence the dielectric relaxation spectra. A group of liquid crystalline materials in which internal flexibility plays an important role are so-called liquid crystal dimers. These compounds consist of two liquid crystal groups, flexibly linked by a methylene chain or a siloxane chain. The liquid crystal phases of such materials have been shown to have interesting transitional properties [22]. For example the nematic to isotropic transition temperatures strongly depend on the parity and length of the connecting chain. There is a strong odd-even effect, with even-membered chains having much higher transition temperatures than chains with an odd number of groups. This odd-even effect is also reflected in other liquid crystalline properties such as the transitional order parameter and entropy. Symmetric dimers are terminated by identical groups, while those compounds having different terminal groups are known as non-symmetric dimers. An understanding of the liquid crystal properties of liquid crystal dimers is expected to have rele-

vance for the description of the behaviour of liquid crystal polymers, to which they are structurally related.

In order to investigate the influence of internal flexibility on the dielectric properties of liquid crystals, we have measured the dielectric response of a number of liquid crystal dimers [23], and the structures of these are given in Table 4.1.

The dielectric properties of these materials are of interest from a number of aspects. In this section we will focus on their dielectric relaxation spectra. For the symmetric dimers, it was expected that they would have a zero longitudinal dipole moment, with negative dielectric anisotropy and no low frequency dielectric ω_1 relaxation. In fact we and others have found that the cyanobiphenyl dimers I and II have large positive dielectric anisotropy and a low frequency relaxation. Both are strongly temperature dependent, and we have interpreted this behaviour in terms of temperature-induced changes to the conformational distribution. Measurements on a non-symmetric dimer III, reveal two low frequency relaxations in the nematic phase. This dynamic dielectric response can be explained if two molecular species are proposed, one extended and one bent, for which the longitudinal dipole moments are similar, but which have significantly different ω_1 relaxation frequencies. The two terminating groups in compound III form liquid crystals, and a study has been made of their dielectric properties in a mixture [24]. In these mixtures, only a single low frequency relaxation was detected, and so we conclude that in

Table 4.1. Structures and transition temperatures
Cr – crystal; N – nematic; SmA – smectic A; I – isotropic

Compound	Phase behaviour and transition temperatures
I 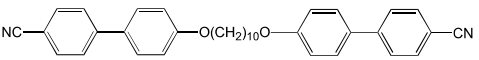 BCB.O10	Cr 90°C SmA 128°C N 185°C I
II 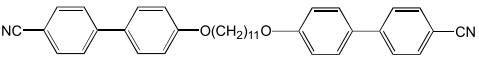 BCB.O11	Cr 122°C N 164°C I
III 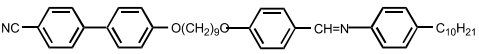 CB.O9O.10	Cr 92°C N 137°C I

the dimer, the linking chain constrains the relative orientation of the terminal groups in such a way to allow two distinct molecular configurations having separate low frequency dipole relaxations.

4.1.4 Conclusions

The frequency dependent dielectric properties of liquid crystals arise from the complex motion of dipolar groups of mesogenic molecules subjected to a local ordering potential. Thus the properties contain information both on the molecular properties of the mesogen and on the molecular organisation of the phase. Despite the complexity of the system, a mean field model is capable of explaining the principal features of the dielectric response. In this description of the dynamic dielectric properties of liquid crystals, we have chosen to use dimeric liquid crystals as examples. They show the main features of the dielectric response of nematic liquid crystals, as well as a new relaxation, which we believe is related to changes in molecular shape of the flexible mesogens.

According to the mean field theory outlined above, a rigid dipolar molecule in a uniaxial nematic phase will exhibit four relaxation regions in the dielectric spectra, two for the parallel component of the permittivity, and two for the perpendicular component of the permittivity. The end-over-end relaxation occurs at the lowest frequency, and is easily detected in the dielectric spectrum for the parallel permittivity component; this relaxation is very well-described by a Debye relaxation. Two other relaxations at higher frequencies are readily detected, one each in the parallel and perpendicular components of the permittivity. Fitting parameters for these relaxations indicate that they are non-Debye, and can be represented as a symmetric distribution of relaxation times about an average value. This in part reflects the fact that so far it has not been possible to separate clearly the high frequency modes that couple precessional motion and molecular rotation about the long molecular axis.

The main features of the dielectric response of a nematic liquid crystal can be identified in the Arrhenius plots (Fig. 4.5) of the logarithm of the relaxation frequencies against inverse absolute temperature. Thus for both dimers BCB.O11 and CB.O9O.10, broadened high frequency relaxations can be identified having a relatively low activation energy (see Table 4.2). In Fig. 4.5 results are given only for the parallel components of the permittivity, but there are similar high frequency relaxations in the dielectric response of the perpendicular components. Both dimers also show low frequency relaxations, which are due to end-over-end rotation of the molecular dipoles, and the corresponding activation energies are relatively high. The origin of the low frequency relaxation for the symmetric dimer BCB.O11 is of interest, since from its equilibrium structure it would not be expected to have a longitudinal dipole moment. Our explanation [23] is that the flexibility of the linking chain results in some conformers having a bent structure with a large longitudinal molecular dipole moment, and this exhibits a low frequency relaxation. Further evidence for this is provided by the fact that the non-symmetric dimer

Table 4.2. Havriliak–Negami fitting parameters and activation energies for relaxation modes†

	BCB.O11			CB.O9O.10	
Isotropic modes	$\alpha = 0, \beta = 0.5$			$\alpha = 0.1, \beta = 0.4$	
Nematic modes	high E_a= 14 kJmol^{-1}	$\parallel$	$\alpha = 0.4$, $\beta = 1$	high E_a = 17 kJmol^{-1}	$\alpha = 0.25$, $\beta = 1$
		$\perp$	$\alpha = 0.3$, $\beta = 1$		
	low E_a= 72 kJmol^{-1}	$\alpha = 0, \beta = 1$		intermediate E_a = 63 kJmol^{-1}	$\alpha = 0$, $\beta = 1$
				low E_a = 82 kJmol^{-1}	$\alpha = 0$, $\beta = 1$

†The fitting of the dielectric data is very sensitive to the chosen parameters, and it is difficult to determine the overall accuracy of the quantities derived from the fitted data. However we estimate that α and β are significant to $\pm$ 0.1, and the activation energies taken from the linear sections of the Arrhenius plots are reliable to $\pm$ 15%.

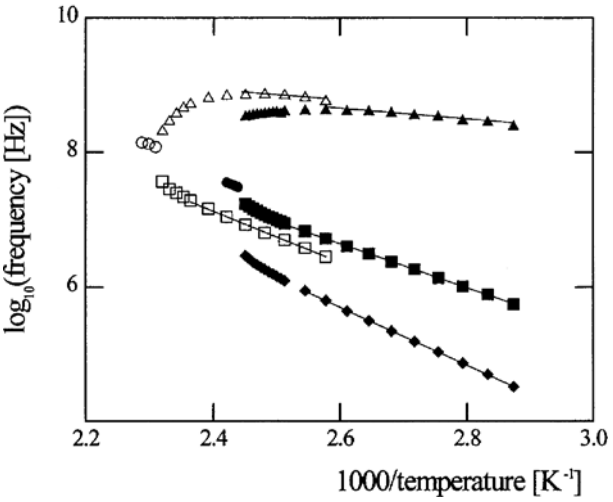

Fig. 4.5. Arrhenius plot of the logarithm of the frequency of relaxation modes for the parallel component of the permittivities for BCB.O11 (*open symbols*) and CB.O9O.10 (*closed symbols*) liquid crystal dimers. (◯): isotropic phase; (△, ▲): high frequency modes; (□): low frequency mode for BCB.O11; (⧫): low frequency mode for CB.O9O.10; (■): intermediate frequency mode for CB.O9O.10

CB.O9O.10 shows two low frequency relaxations. We attribute the lower of these to the end-over-end rotation of the extended form of the molecule, and the other to a more compact bent structure. The temperature dependence of the strengths of the low frequency relaxations is in accord with this model, and it is observed that for CB.O9O.10, there is a transfer of dielectric strength between the two low frequency relaxations as the temperature changes. Such behaviour would be expected if the molecule was changing its shape from bent to extended as the temperature is reduced. Thus dielectric studies can also reveal information on intramolecular effects in mesogenic molecules.

Acknowledgements. The author is pleased to acknowledge the collaborative research with the dielectrics group of the Department of Applied Physics, University of the Basque Country, Spain. In particular the author wishes to thank Professor Rosario de la Fuente, Professor Miguel Angel Perez Jubindo, and Sergio Diez, who carried out the measurements. Valuable discussions with Professor Geoffrey Luckhurst from the University of Southampton are also gratefully acknowledged. This project was supported by the European Commission through a Training and Mobility of Researchers Network, Contract No. FMRX CT970121.

References

1. S.H. Glarum: J. Chem. Phys. **33**, 1371 (1960)
2. E. Fatuzzo, P.R. Mason: Proc. Phys. Soc. **90**, 741 (1967)
3. W. Maier, G. Meier: Z. Naturforsch **16a**, 262 (1961)
4. K. Toriyama, D.A. Dunmur, S.E. Hunt: Liq. Cryst. **5**, 1001 (1988)
5. D.A. Dunmur, R.W. Munn: Chem. Phys. **76**, 249 (1983)
6. A.A Minko, V.S. Rachevich, S.Ye. Yakovenko: Liq. Cryst. **4**, 1 (1989)
7. D.A. Dunmur, K. Toriyama: In: D. Demus, J. Goodby, G.W. Gray, H-W. Spiess, V. Vill (eds.) *Physical properties of liquid crystals.* (Wiley-VCH, Weinheim 1999), p. 87
8. W. Otowski, W. Demol, W. van Dael: Mol. Cryst. Liq. Cryst. **226**, 103 (1993)
9. G. Meier, A. Saupe: Mol. Cryst. **1**, 515 (1966)
10. A.J. Martin, G. Meier, A. Saupe: Symp. Faraday Soc. **5**, 119 (1971)
11. P.L. Nordio, G. Rigatti, U. Segre: Mol. Phys. **25**, 129 (1973)
12. W.T. Coffey, Y.P. Kalmykov: Adv. Chem. Phys. **113**, 487 (2000)
13. A. Würflinger: Z. Naturforsch **53a**, 141 (1998)
14. S. Urban, A. Würflinger, B. Gestblom: Phys. Chem. Chem. Phys. **1**, 2787 (1999)
15. M.A. Bates, G.R. Luckhurst: Mol. Phys. **99**, 1365 (2001)
16. B. Bagchi, A. Chandra: Phys. Rev. Lett. **64**, 455 (1990)
17. A. Perico, R. Pratolongo, K.F. Freed, R.W. Pastor, A. Szabo: J. Chem. Phys. **98**, 564 (1993)
18. W.T. Coffey, Y.P. Kalmykov, J.T. Waldron: Liq. Cryst. **18**, 677 (1995)
19. J. Jadżyn, G. Czechowski, R. Douali, C. Legrand: Liq. Cryst. **26**, 1591 (1999)
20. S. Wróbel, M. Brodzik, R. Dąbrowski, B. Gestblom, W. Haase, S. Hiller: Mol. Cryst. Liq. Cryst. **302**, 1211 (1997)

21. S. Urban, B. Gestblom, T. Brückert, A. Würflinger: Z. Naturforsch **50a**, 984 (1995)
22. C.T. Imrie, G.R. Luckhurst: In: D. Demus, J. Goodby, G.W. Gray, H-W. Spiess, V. Vill (eds.) *Handbook of liquid crystals*, Vol. 2B, Chap. X. (Wiley-VCH, Weinheim 1999)
23. D.A. Dunmur, G.R. Luckhurst, M.R. de la Fuente, S. Diez, M.A. Peréz Jubindo: J. Chem. Phys. **115**, 8681 (2001)
24. A.H. Price, D. Davies: J. Chem. Soc. Faraday Trans. **93**, 1775 (1997)

4.2 Molecular rotations in liquid crystals as seen by the dielectric spectroscopy method

S. Urban and A. Würflinger

4.2.1 Introduction

Liquid crystalline (LC) phases are characterized by the orientational and/or positional arrangements of elongated molecules. In spite of that the rotational freedom of molecules has been observed in the liquid-like phases (nematic-N, smectic A and C – SmA, C) as well as in the solid-like phases (CrB, G, H,...) (e.g. [1–3]). The dielectric spectroscopy method is a powerful tool to study these stochastic motions if the molecules possess permanent dipole moments. The relaxation spectra reflect not only the rotational motions of molecules as a whole (reorientations around the principal inertia axes), but also some specific motions connected with the flexibility of molecular segments. Influence of a non-ideal ordering of molecules in a LC phase is observed as well.

In the present time the dielectric relaxation spectra, $\varepsilon^*(\omega) = \varepsilon'(\omega) - i\varepsilon''(\omega)$, $\omega = 2\pi\nu$, can be measured in a broad frequency range, from ca. 1 mHz up to ca. 10 GHz, using different experimental set-ups (compare Sects. 1.1 and 1.2). Thus, very slow as well as very fast relaxation processes can, in principle, be studied. In the case of so complex systems as liquid crystalline substances one can expect, however, that a measured spectrum may consist of several overlapping bands whose separation into elementary modes needs a knowledge of dipolar structure of molecules and the molecular arrangements in a given LC phase. In most cases the spectra are analyzed as a superposition of a few Cole–Cole formulas

$$\varepsilon^* - \varepsilon_\infty = \sum_k \frac{\delta_\mathrm{k}}{1 + (i\omega\tau_\mathrm{k})^{1-\alpha_\mathrm{k}}} \,, \tag{4.29}$$

where $\delta_\mathrm{k} = \varepsilon_\mathrm{sk} - \varepsilon_{\infty\mathrm{k}}$ is the dielectric strength (or dielectric increment) of the k-th relaxation process, ε_s and ε_∞ are the static and high frequency permittivities, respectively, α_k characterizes a distribution of the relaxation times τ_k. In the case of $\alpha_\mathrm{k} = 0$, the k-th relaxation process is described by a single relaxation time and the process is called the Debye-type process. In general,

Table 4.3. Chemical formulas, acronyms and phase sequences of the substances considered

Chemical formula	Acronym	Phase sequence
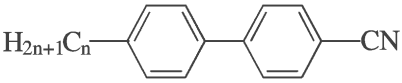	nCB	Is-N, $n = 5 \div 7$ Is-N-SmA$_d$, $n \geq 8$
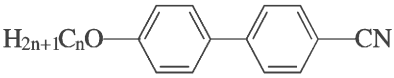	nOCB	Is-N, $n = 5 \div 7$ Is-N-SmA$_d$, $n \geq 8$
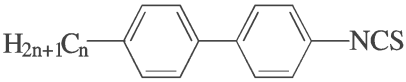	nBT	Is-CrE, $n \geq 2$
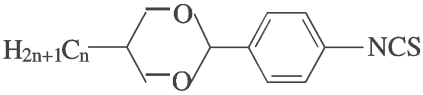	nDBT	Is-SmA$_1$, $n \geq 2$
	nPCH	Is-N, $n \geq 3$
	nCHBT	Is-N, $n \geq 6$
	3CCH	Is-N-SmB
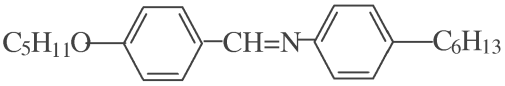	PBHA	Is-N-SmA-SmC- SmB-SmF-SmG
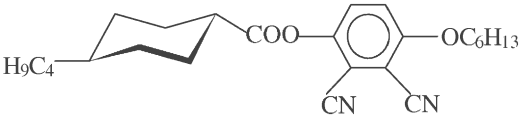	CNCN	Is-SmA
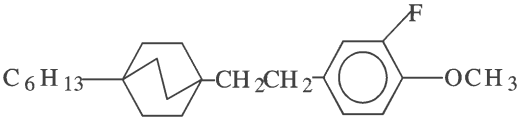	6BAP(F)	Is-N
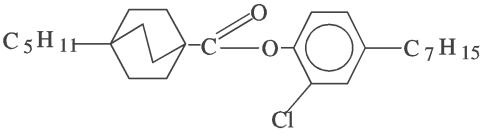	7CP5BOC	Is-N

the relaxation times characterizing the rotational dynamics of the molecules depend upon the temperature T, the pressure p, the density ρ (or molar volume V_{m}) and the specific interactions between molecules in a given state of matter. That can be expressed in terms of the activation parameters [4, 5] (see also Sect. 1.4)

$$\text{activation enthalpy} \qquad \Delta^{\#}H = R(\partial \ln \tau / \partial T^{-1})_p \tag{4.30}$$

$$\text{activation volume} \qquad \Delta^{\#}V = RT(\partial \ln \tau / \partial p)_T \tag{4.31}$$

$$\text{activation energy} \qquad \Delta^{\#}U = R(\partial \ln \tau / \partial T^{-1})_V \ . \tag{4.32}$$

All three parameters are interrelated: $\Delta^{\#}H = \Delta^{\#}U + (\alpha/\beta)T\Delta^{\#}V$, where α is the isobaric expansivity and β is the isothermal compressibility.

At the beginning of this chapter we shall consider a rigid rod-like dipolar molecule embedded into the nematic medium. Possible relaxation processes that may occur will be discussed. The model predictions will be confronted with the relaxation spectra measured for real substances. One special aspect of the molecular rotations in the N phase will be especially discussed: the rotations about the short axis and its relation to the nematic order parameter S. The substances consisting of molecules with strong longitudinal dipole moment are suitable for that purpose. Then we shall discuss and illustrate by the experimental results the motions of molecules around the long axes. In that case the molecules with a strong perpendicular dipole moment will be considered. Some examples of the relaxation spectra obtained for substances with flexible molecules will be presented. In the next part the main features of the relaxation processes observed in the isotropic phase, the liquid-like LC phases (N, SmA, SmC) and the crystal-like smectic phases (CrB, CrE) will be discussed. At the end the influence of pressure on the relaxation processes present in the LC phases will be shown. The behaviors of the longitudinal relaxation times at the isobaric, isothermal and isochoric conditions will be considered.

Here we use the acronyms instead of the full chemical names of LC substances discussed. Their chemical structures and information about phase sequences can be found in Table 4.3.

4.2.2 Rigid rod-like molecules in the nematic medium

The nematic phase is the simplest example of the anisotropic medium because the preferred orientation of the molecules along the director $\boldsymbol{n}$ is only distinguished. Let us first consider a rigid rod-like molecule embedded in the nematic medium. The dipole moment $\boldsymbol{\mu}$ is directed by an angle β in respect to the long axis which corresponds to the minimum of the momentum of inertia of the molecule. In such a case both the longitudinal μ_l and transverse μ_t components may contribute to the permittivity. By choosing an appropriate mutual orientation of the probing electric field $\boldsymbol{E}$ and the director $\boldsymbol{n}$ one

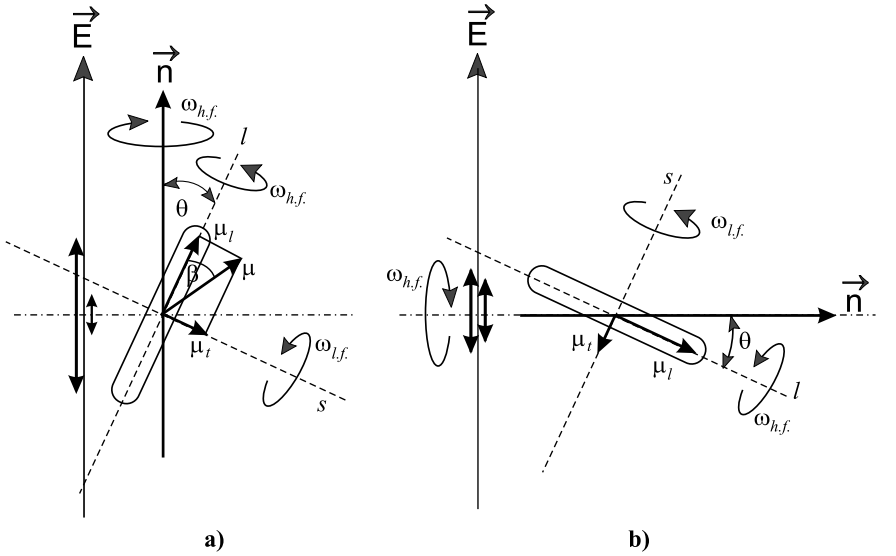

Fig. 4.6. Possible relaxation processes in the perfectly oriented nematic sample: (**a**) for parallel alignment, $\boldsymbol{E}||\boldsymbol{n}$, and (**b**) for perpendicular alignment, $\boldsymbol{E}\perp\boldsymbol{n}$. The dipole moment of the molecule is inclined from the long axis l by an angle β. Angle θ defines the order parameter S (see (4.37)). The *arrows* on the $\boldsymbol{E}$-axes indicate the projections of the dipole moments responsible for a given relaxation process. Three relaxation processes can be distinguished in both experimental geometries: *process 1* – flip-flop jumps of molecules around the short axes; *process 2* – precession of the long axis on a cone around the director $\boldsymbol{n}$; *process 3* – molecular rotations around the long axes. The first process gives contribution to the relaxation spectra at megahertz region (the l.f. process, marked as $\omega_{l.f}$), other processes are observed at hundreds MHz or in GHz frequencies (the h.f. processes, marked as $\omega_{h.f}$)

can measure the dielectric relaxation spectra for the parallel geometry, $\varepsilon^*_{||}(\omega)$, $\boldsymbol{E}||\boldsymbol{n}$, or for the perpendicular geometry, $\varepsilon^*_{\perp}(\omega)$, $\boldsymbol{E}\perp\boldsymbol{n}$ – Fig. 4.6.
Taking into account the fact that the order parameter S is considerably less than unity within the N phase, Nordio et al. [6] predicted four different modes of the molecular motions, two of which observed in $\varepsilon^*_{||}(\omega)$ spectrum, and other two in $\varepsilon^*_{\perp}(\omega)$ spectrum (compare Chap. 4.1). Recently Jadżyn et al. [7–9] have measured the broad band relaxation spectra for 6CHBT and 6CB. In order to account for all features of the spectra the authors had to assume yet another relaxation processes. They considered the molecules rotating around the three axes of symmetry – two of them concern the molecule itself (the long and short molecular axes) and the third axis is the director $\boldsymbol{n}$. They have found that the spectra measured in both geometries consist of three bands which can be explained by the fact that the molecular long axis l does not coincide with the axes corresponding to the minimum of the electric or magnetic polarizabilities which are responsible for the alignment of the

molecules in the external electric or magnetic fields, respectively. Usefulness of the model consideration was demonstrated by Jadżyn et al. in the analysis of the relaxation spectra measured for the isotropic and nematic phase of 6CHBT (Figs. 4.7 and 4.8). It should be mentioned, however, that the 6CHBT molecule can hardly be treated as a rigid body and other interpretation of particular processes (especially those with small increments) seems to be permissible.

4.2.3 Low frequency relaxation process in the nematic phase and the order parameter

The relaxation process observed at megahertz frequencies for $\boldsymbol{n} \parallel \boldsymbol{E}$ geometry (Fig. 4.6a) is connected with the molecular reorientations around the short axes and is called the low frequency, l.f., process. It contains information on the potential of mean torque responsible for the long range orientational order of the constituent molecules. The existing theories of the l.f. relaxation process [6, 10–12] are based on the model assuming that the symmetric top molecules perform rotational diffusion in the self-consistent mean field potential $U(\theta)$ proposed by Maier and Saupe [13]

$$U/k_{\mathrm{B}}T = -\sigma \cos^2 \theta \,, \tag{4.33}$$

where θ is the angle between the symmetry axis of the molecule and the director. The nematic potential barrier parameter is defined as $\sigma = q/RT$, where q is the height of the barrier separating two minima corresponding to $+\boldsymbol{n}$ and $-\boldsymbol{n}$ directions and R is the gas constant. This barrier hinders the molecular reorientations around the short axes and thus the longitudinal relaxation time $\tau_{\parallel}$ must be slowed down in comparison with the situation when the potential $q = 0$. In order to describe the reduction of the molecular rate Meier and Saupe [10] introduced the concept of a retardation factor $g_{\parallel} = \tau_{\parallel}/\tau_0$, where τ_0 corresponds to a hypothetical state with $q = 0$; it is usually extrapolated from the isotropic data assuming exponential dependence of τ_{is} upon T^{-1} or p [5, 10, 14, 15]. These authors have found a relation between $g_{\parallel}$ and q by considering the parallel relaxation process in the Maier–Saupe potential (4.33). Using several simplifications Meier and Saupe have derived the following formula

$$g_{\parallel} = \frac{\tau_{\parallel}}{\tau_0} = \frac{\exp(\sigma) - 1}{\sigma} \,. \tag{4.34}$$

The same problem was recently solved in a more rigorous mathematical way by Coffey et al. [12, 16]. The molecular rotation motion in the presence of the Maier–Saupe ordering potential was treated as the Brownian rotational diffusion. Using very sophisticated mathematical procedures the authors obtained the exact analytical solutions for the retardation factors $g_{\parallel}$ and $g_{\perp} = \tau_{\perp}/\tau_0$ in terms of σ. The following formula for the parallel retardation factor renders a close approximation to the exact solution for all σ

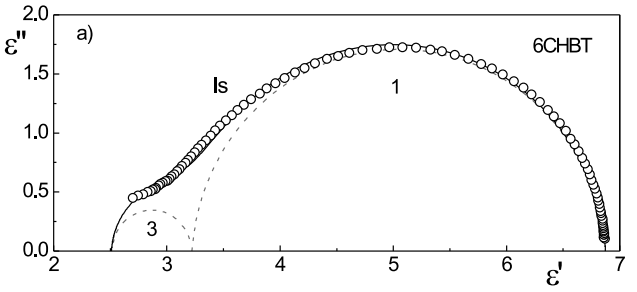

(**a**)

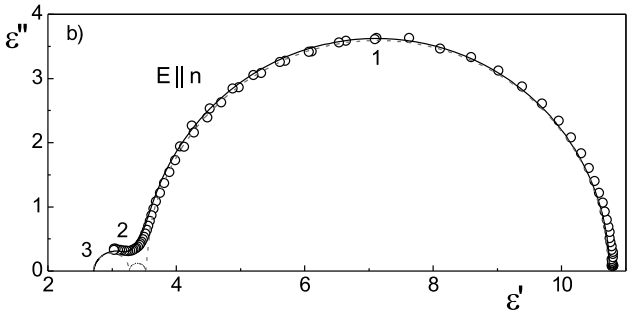

(**b**)

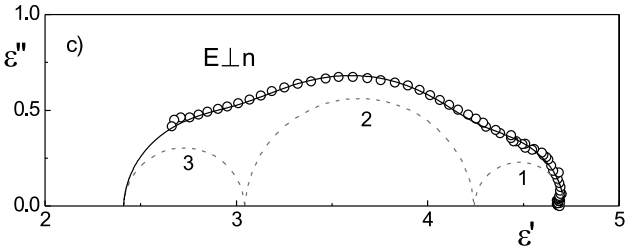

(**c**)

Fig. 4.7. Relaxation spectra for 6CHBT measured in the frequency range 10^5–10^9 Hz with the separation into elementary contributions corresponding to different modes depicted in Fig. 4.6

$$g_{\parallel} = \frac{\tau_{\parallel}}{\tau_0} = \frac{\exp(\sigma) - 1}{\sigma} \left(\frac{2}{1 + 1/\sigma} \sqrt{\sigma/\pi} + 2^{-\sigma} \right)^{-1} , \tag{4.35}$$

which is (4.34) with a correction term. For $\sigma > 1$ the Meier and Saupe formula considerably overestimates $g_{\parallel}$, which causes the q values calculated with the use of (4.35) to be approximately 25% greater than those obtained by (4.34). (Numerical data for both equations one can find in [17]).

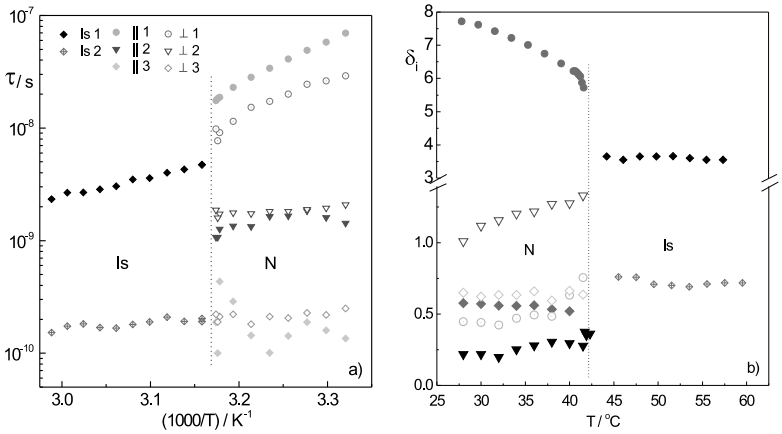

Fig. 4.8. The temperature dependence of the relaxation times (**a**) and the dielectric increments (**b**) obtained from the analysis of the relaxation spectra shown in Fig. 4.7

In the mean-field theory of the nematic state Maier and Saupe [13] assumed that the potential q is proportional to the order parameter S

$$q = \upsilon S \,, \tag{4.36}$$

where the strength parameter υ depends on the molar volume (e.g. [5] and references therein) and thus reflects the distance dependence of the interaction potential. The order parameter is defined as

$$S = \langle 3\cos^2\theta - 1\rangle/2 \,, \tag{4.37}$$

where θ is the angle between the molecular symmetry axis and the director $\boldsymbol{n}$. In order to perform averaging $\langle ...\rangle$ the distribution function of the nematic order, $f(\theta)$, must be known. The authors proposed the following simple form

$$f(\theta) = f(0)\exp\left(-\frac{q}{k_{\mathrm{B}}T}\sin^2\theta\right) = f(0)\exp\left(-\sigma\sin^2\theta\right) \,. \tag{4.38}$$

Thus, one has

$$\langle\cos^2\theta\rangle = \int_{-1}^{1} dx\, x^2 f(x) \Bigg/ \int_{-1}^{1} dx\, f(x) \quad , \tag{4.39}$$

with $x = \cos\theta$.

More recently Kalmykov and Coffey (K-C) [12] have derived the relation between S and σ in a more general way. Starting from the Maier and Saupe

interaction potential the authors applied the effective eigenvalue method and obtained a complex analytical equation which can well be approximated by the relation [12]

$$\sigma \approx \frac{3S(5-\pi S)}{2(1-S^2)} \ . \tag{4.40}$$

Combining the experimental σ-values as deduced from (4.34) and (4.35) respectively with (4.37)–(4.40) it is possible, in principle, to calculate the order parameter S for the nematic phase. However, in order to be in accord with the assumed approximations the following conditions should be fulfilled:

1. the molecules can be approximated by rigid rods;
2. the dipole moment should be directed along the long axis of the molecule;
3. the low frequency relaxation process can unambiguously be extracted from the spectra in both the isotropic and nematic phase;
4. the nematic range is sufficiently broad in order to avoid the pretransitional effects.

Thus, substances composed of two rings with a short wing and strong dipole group (-CN or -NCS) at the terminal positions should be especially well suited for that purpose [15, 18, 19]. As an example, let us present the results obtained for 5CB. The l.f. relaxation process in this substance was studied in our group at atmospheric as well as at elevated pressures [5, 15, 20–23].

Figure 4.9 presents the dispersion and absorption spectra for the isotropic, $\varepsilon^*_{\rm is}(\nu)$, and nematic, $\varepsilon^*_{\parallel}(\nu)$, phases of 5CB measured at atmospheric pressure. Similar pictures can be drawn when the measurements were performed for different pressures at T = const. It is well established that the absorption spectra in the nematic phase can be treated as the Debye processes. The spectra of the isotropic phase show a small distribution of the relaxation

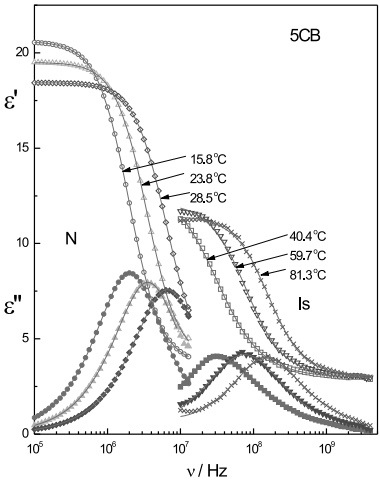

Fig. 4.9. Typical dispersion and absorption spectra for the nematic ($\boldsymbol{E} \parallel \boldsymbol{n}$) and isotropic phases of 5CB. The nematic sample was oriented by the electric field of ca. 3500 V/cm. The spectra of the isotropic phase come from the TDS measurements (compare Sect. 1.2). The *lines* are fits of the real and imaginary parts of the Cole–Cole formula (1) with $\alpha = 0$ in the nematic phase, and $\alpha \approx 0.10$–0.12 in the isotropic phase

times ($\alpha \approx 0.11$) for the main relaxation process which is connected with the rotations around the short axes. An additional high frequency process was also observed that can be ascribed to the fast molecular rotations around the long axes. Figure 4.10 shows the determined relaxation times for both phases. As it is seen the steps of τ at the clearing points are evident. The dashed lines show how the data for the isotropic phase were extrapolated to the nematic phase when τ_0 values were calculated. The potential q within the nematic phase of 5CB changes between ca. 6 and 9 kJ/mol according to the Meier–Saupe formula (4.34), and between ca. 7 and 12 kJ/mol according to Coffey et al. formula (4.35) [22]. Thus, it consists of ca. 10–18% of the total energy barrier hindering the molecular rotations around the short axes in the nematic phase of 5CB ($\Delta^{\#}H_{\|} = 66.3\,\mathrm{kJ/mol}$ [23]).

The order parameters calculated according to the equations derived by Meier and Saupe (MS) and Kalmykov and Coffey (KC) are shown in Fig. 4.11a (atmospheric pressure) and Fig. 4.12 (elevated pressures). They are presented together with other available data (for details see [15]). A large scatter of $S(T)$ can be noted for this as well as for other substances [15]. This arises from the fact that the order parameter is, in some sense, defined by the experimental technique used to measure it [15, 24–26]. As can be seen in Fig. 4.11a the Coffey et al. equations (4.35) and (4.30) lead to $S(T)$ values (marked as KC) which are more consistent with other results. The same was found for other substances as well [15]. The functional form of $S(T)$ is often approximated by the formula proposed by Haller [27]

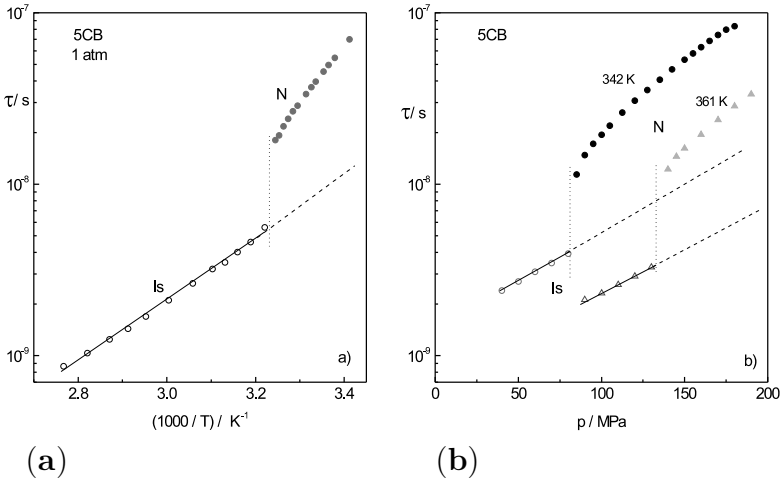

Fig. 4.10. Longitudinal relaxation times versus inverted temperature (**a**) and versus pressure (**b**) for the isotropic and nematic phases of 5CB. The *dashed lines* show how the isotropic relaxation times were extrapolated to the nematic phase in order to get the τ_0 values (see eqs. 4.34, 4.35)

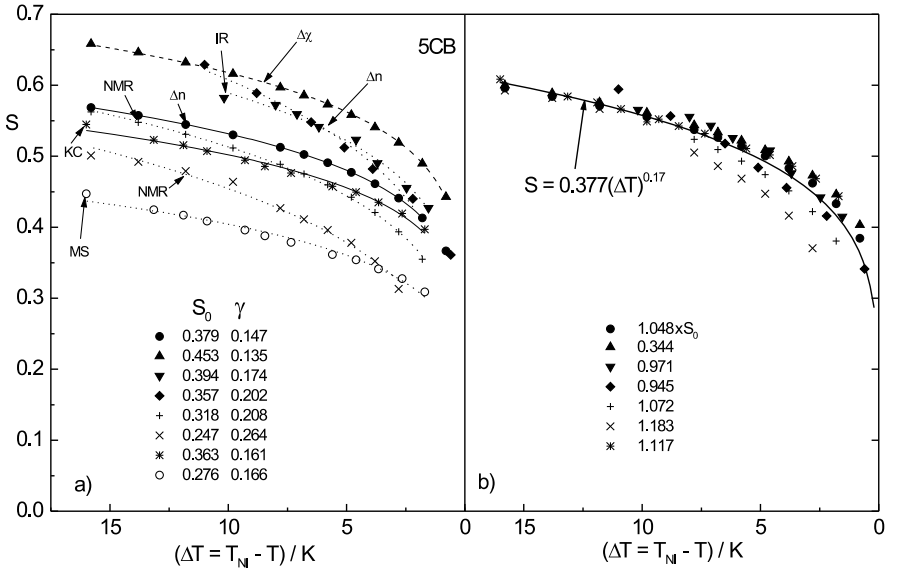

Fig. 4.11. Order parameter S for 5CB versus the reduced temperature $\Delta T = T_{NI} - T$. The results come from different experimental methods (infrared – IR, magnetic susceptibility – $\Delta\chi$, optical anisotropy – Δn, nuclear magnetic resonance – NMR). Present theoretical study: KC (Coffey et al.) and MS (Meier and Saupe). For details see [15]

$$S(T) = S_0(T_{NI} - T)^{\gamma} \tag{4.41}$$

with two adjustable parameters S_0 and γ. Let us try to check whether this scatter arises from different temperature variations of S as seen by particular methods or other factors. In the inset of Fig. 4.11a the values of S_0 and γ obtained by the fits of (4.41) to the experimental points are listed. The γ values strongly depend on the points close to T_{NI} and therefore the data closer than 3 K to the clearing point were neglected in fittings. The average value amounts $\gamma \approx 0.17$. Assuming this value we may try to shift all sets of the data to a common curve. It is supposed (e.g. [28, 29]) that S_0 is related to the clearing temperature: $S_0 = T_{NI}^{-\gamma} = (308.5)^{-0.17} = 0.377$. If so, one can use this as a reference value when choosing the normalization factors. Figure 4.11b presents the same points as in Fig. 4.11a multiplied by factors listed in the inset. It is clear that the majority of results, including the KC-values, exhibit similar temperature behavior. One may conclude therefore that different S_0 values arise from specific features of particular experimental techniques (local fields, coupling constants, etc.). The Kalmykov–Coffey approach was also used in calculations of the order parameter in 5CB as a function of pressure for several isotherms [15]. The way of obtaining the relaxation time τ_0 as a function of temperature and pressure is illustrated in Fig. 4.10b. Figure 4.12 presents the order parameters for several isotherms in the nematic phase of

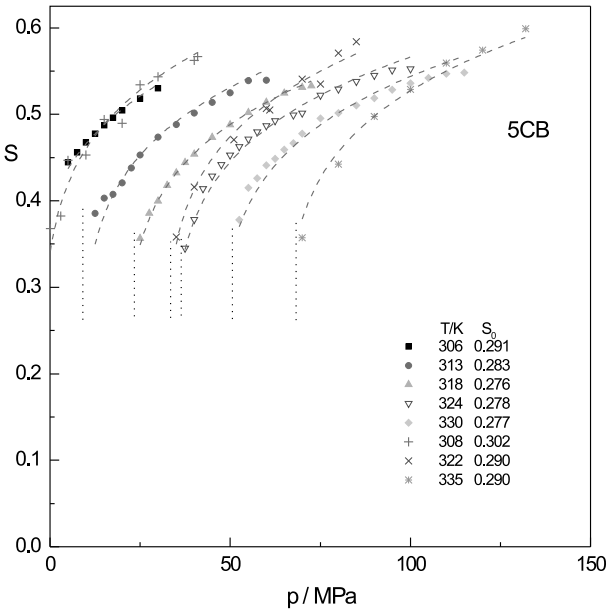

Fig. 4.12. Order parameter S versus pressure at several isotherms in the nematic phase of 5CB. Full points come from the relaxation times data (Coffey et al. approach); other symbols – from Raman scattering studies [27]. The *dashed lines* correspond to Horn's results [31] according to (4.42) with $b = 0.17$ and S_0 listed in the legend. *Vertical dotted lines* indicate the nematic-isotropic transition points

5CB. The comparison with other available data [30, 31] is given. The present results (full points) as well as the data obtained in the Raman experiment [30] can well be approximated by a formula closely related to the Haller formula (4.41)

$$S(p) = S_0(p - p_{NI})^b \tag{4.42}$$

where p_{NI} corresponds to the nematic-isotropic transition at given T (dotted vertical lines). The dashed lines are the fits of (4.42) with $b = 0.17$ taken from Horn's measurements [31]. The significant consistency of all results allow us to say that the method of calculation of the order parameter at high pressure leads to reasonable results as well. The same procedure was also applied to the relaxation data obtained as functions of T and p for 8PCH [14, 15]. The calculated order parameter was then used for the discussion of the pressure and temperature dependencies of the dielectric anisotropy of 8PCH [32].

It should be pointed out, however, that the method used here for the determination of S is indirect in comparison with other techniques based on a much more straightforward relations between the measured quantity and S [15, 24–26, 28, 29] (optical, magnetic and dielectric anisotropy, quadrupole splitting, Raman scattering, etc.). Bates and Luckhurst [26] have criticized this

way for the following reasons: the use of the dielectric relaxation times demands the validity not only of the Maier and Saupe potential of mean torque but also the diffusional model of reorientational motion in the presence of an ordering potential. Notwithstanding, the results of analysis of the dielectric relaxation times obtained recently for several LC substances at ambient and elevated pressure indicate that this can result in valuable data on the nematic order parameter S [14, 15, 18–22]. Especially the high pressure part of these studies is important because other experimental techniques are rather seldom used for this aim. Comparison of the present results with those coming from other methods allows us to conclude that the Coffey et al. theory [15, 17] better relates the relaxation times $\tau_{\parallel}$ and τ_{is} with the main parameters characterizing the nematic phase (nematic potential and order parameter). Further investigations of substances constituted of simple molecules (like 1OCB) with the aid of different experimental methods seem to be indispensable for a more conclusive opinion about the applicability of the described method of determination of the order parameter in the nematic phase (see also [54]).

4.2.4 Molecular rotations around the long axes. Influence of molecule flexibility

As can be deduced from Fig. 4.6 the molecular rotations around the long axes are much faster than those occurring around the short axes. The corresponding relaxation process falls onto hundreds MHz or even GHz frequencies, and is called the high frequency, h.f., relaxation process. One important factor is a much smaller inertia moment of molecules with respect to the long axis than around the other axes. Additionally, it is supposed that the nematic order facilitates this type of motions: the theories predict that the retardation factor $g_{\perp} = \tau_{\perp}/\tau_0$ is less than unity [11, 12, 16].

In order to illustrate the main differences between the l.f. and h.f. processes in the isotropic and nematic phases let us consider a molecule having a large dipole moment directed by an angle β close to $\pi/2$ with respect to the long axis. In the 6BAP(F) molecule (see Table 4.3) due to the fluorine atom at the *ortho*-position and the methoxy group at the *para*-position of the benzene ring the transverse component of the dipole moment is larger than the longitudinal component: $\mu_{\mathrm{l}}/\mu_{\mathrm{t}} \approx 0.40$ and $\beta \approx 68^{\circ}$ [33]. Such dipole structure is reflected in the dielectric relaxation spectra collected in both the isotropic and nematic phases of 6BAP(F) – Fig. 4.13. While in the isotropic phase both principal motions give overlapping relaxation bands, they could be detected separately in the nematic phase due to proper alignments of the sample. The calculated relaxation times are shown in Fig. 4.14.

As can be seen in Fig. 4.14, we have two sets of relaxation times characterizing the reorientations of molecules in the isotropic and nematic phase of 6BAP(F). τ_{l} and $\tau_{\parallel}$ correspond to the reorientations around the short axes in both phases, respectively, and are hindered by distinctly higher activation barriers than τ_{t} and $\tau_{\perp}$ ($\Delta^{\#}H_{\mathrm{l}} = 55.0\,\mathrm{kJ/mol}$, $\Delta^{\#}H_{\parallel} = 73.4\,\mathrm{kJ/mol}$

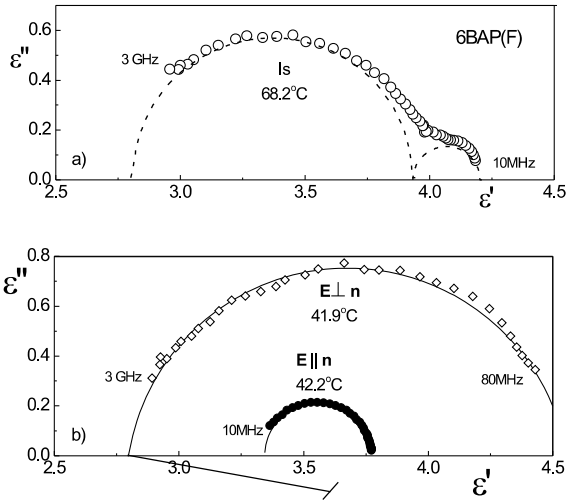

Fig. 4.13. Cole–Cole plots for the isotropic (**a**) and the nematic (**b**) phases of 6BAP(F). In (**a**) two Debye-type relaxation processes were assumed: the l.f. process corresponds to the molecular rotations around the short axes, and the h.f. process connected with the rotations around the long axes. These processes could be measured separately in the N phase due to the alignments of the sample in the magnetic field: $\boldsymbol{E} \parallel \boldsymbol{B}$ (l.f. process) and $\boldsymbol{E} \perp \boldsymbol{B}$ (h.f. process) [33]

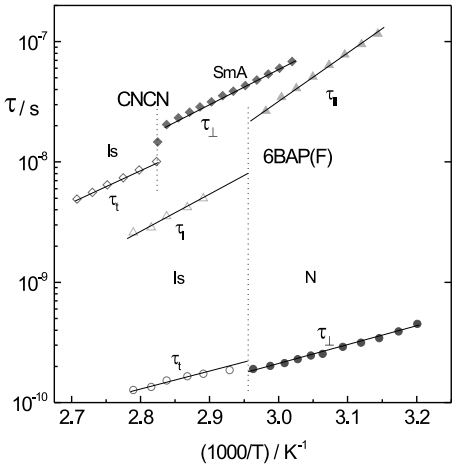

Fig. 4.14. Relaxation times for the isotropic and nematic phases of 6BAP(F) and the isotropic and SmA phases of CNCN

and $\Delta^{\#}H_{\mathrm{t}} = 23.6\,\mathrm{kJ/mol}$, $\Delta^{\#}H_{\perp} = 30.0$ kJ/mol) [33]. Additionally, at the Is-N transition point the first set of relaxation times undergoes a large jump, whereas the second one passes the clearing point rather smoothly. It is worth noting that the corresponding retardation factors are: $g_{\parallel} = 2.93$ and $g_{\perp} = 0.94$, in accord with the theoretical predictions.

The h.f. process is sensitive to different details of the molecular structures. The flexibility of the molecular tails leads usually to a distribution of the relaxation times $\tau_\perp$ which causes that the centre of the Cole–Cole arc is moved below the ε'-axis (compare Fig. 4.13b). Another possibility is that the molecular segments can reorientate independently which gives a more complicated relaxation spectra; that will be demonstrated below. Generally, a smooth passing of the transverse relaxation times through the clearing point as well as through the transition points separating the LC phases was commonly observed in the dielectric [33–36] as well as in the neutron scattering studies [37]. However, in the case of the CNCN molecule (Table 4.3) having two strongly polar-CN groups attached to the benzene ring at the lateral positions an opposite effect was observed [35, 38]. Due to steric constraints as well as a strong dipole-dipole interactions [39] the h.f. relaxation process is shifted below 100 MHz even in the isotropic phase, and the transversal relaxation time is in this case *slowed down* at the Is-SmA transition point with $g_\perp = 1.9$ (see Fig. 4.14). The activation barrier for the rotation motion around the long axes (52 and 54 kJ/mol in the Is and SmA phase, respectively) is rather typical for the values characterizing the l.f. process than the h.f. process in two-ring compounds [33, 34, 36].

The 7CP5BOC molecule (Table 4.3) has two polar groups: 2-chloro-4-heptylphenyl and the benzoate C(O)O bridging group. The dielectric relaxation spectra exhibit very weak increment for the l.f. process in the nematic phase, which was not noticeable in the isotropic phase [40]. Thus, the spectra $\varepsilon^*_{\rm is}(\omega)$

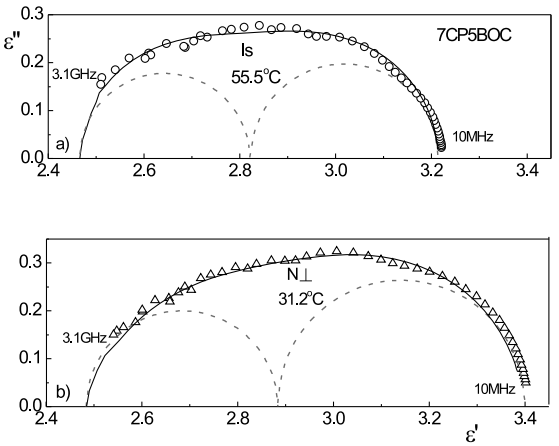

Fig. 4.15. Cole–Cole plots for the isotropic (**a**) and nematic (**b**) phases of 7CP5BOC. Complex relaxation spectra for the isotropic phase and for the perpendicular component in the nematic phase indicate that the molecular moieties rotate independently around the CO–∅ bond (∅ – benzene ring). The l.f. process was hardly observed due to very small dielectric increment ($\delta \approx 0.02$) and is not shown in the figure

and $\varepsilon^*_\perp(\omega)$ presented in Fig. 4.15 must be ascribed to the rotation motions around the long molecular axis. For both spectra two Debye-type semicircles could be consistently fitted. Taking into account the known dipole moments of both polar parts of the molecule, and the dielectric increments determined experimentally for both processes, it was possible to ascribe the slower process (with $\tau_1 \sim 10^{-9}$ s) to the 4-pentylbicyclo[2,2,2]octyl-1-carbonyl moiety, whereas the faster process (with $\tau_2 \sim 10^{-10}$ s) to the 4-heptyl-2-chlorophenyl moiety. The discussed processes must be distinguished from those observed for 6BAP(F) in the isotropic phase (Fig. 4.13a), that are connected with the whole molecule rotations around the two principal inertia axes.

4.2.5 Relaxation in the smectic phases

From the point of view of the molecular arrangements in mesophases one can distinguish the liquid-like phases (Is, N, SmA and SmC) and the crystal-like smectic phases (CrB, G, E, H...). As it was already mentioned the molecular rotations around the long axes are practically unchanged at each transition between the LC phases. However, the much more voluminous rotation around the short axes, and thus the l.f. process, must strongly be influenced by the actual packing of molecules in a mesophase. It is really the case, but the major changes concern the rate of the rotation, whereas the barriers hindering this process are weakly sensitive to the phase transitions! In order to demonstrate that let us consider the substances with both types of mesophases. Figure 4.16 shows the old results obtained by Kresse [1, 41] for PBHA (see Table 4.3). A small step is clearly seen of $\tau_\parallel$ at the transitions between the liquid-like phases, and a large step at the transitions to the crystal-like phases. However, the slopes of the lines fitted to the experimental points remain practically unchanged in all LC phases which means that the barrier for the l.f.

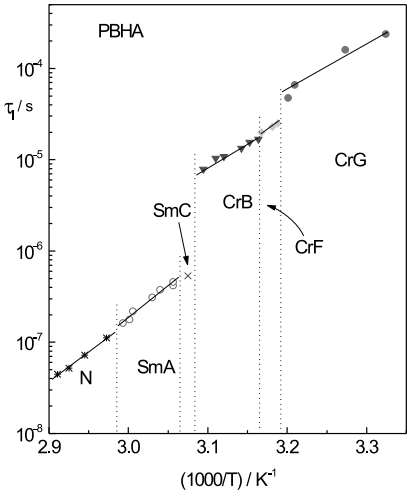

Fig. 4.16. Longitudinal relaxation time τ_1 of PBHA as a function of reciprocal temperature in different LC phases. *Vertical dashed lines* mark the phase transition points

process does not change markedly. Moreover, the dielectric experiments performed for several substances revealed that the barrier diminishes when the transition occurs between the N and SmA phase (e.g. [42–46]). A similar effect was also observed for the transition N-CrB [47].

In order to characterize the influence of molecular ordering on the l.f. process it would be desirable to observe the changes of the longitudinal relaxation times at the transitions between the isotropic and a given LC phase. For this aim one has to consider substances having similar chemical structures and preferably exhibiting a given phase sequence: Is-N, Is-SmA, Is-CrB, etc. Two-ring compounds having strong dipole moment created by the -CN or -NCS groups attached to the benzene ring at the *para*-position seem to be the best for that purpose. Additionally, several members of a given homologous series show the same phase sequences which enables one to observe the dependence of analyzed properties on the molecular length. All substances considered are listed in Table 4.3. The spectra of the isotropic phase were collected with the aid of the TDS method (see Sect. 1.2), whereas the LC phases were studied by means of a HP impedance analyzer (see Sect. 1.1) ([46] and references therein). It is characteristic that the relaxation spectra of the LC phases could well be described by the Debye equation in spite of the fact that the smectic phases could not be aligned neither by an electric nor magnetic fields.

Figure 4.17 presents the longitudinal relaxation times in a logarithmic scale versus inverted temperature for several substances representing different

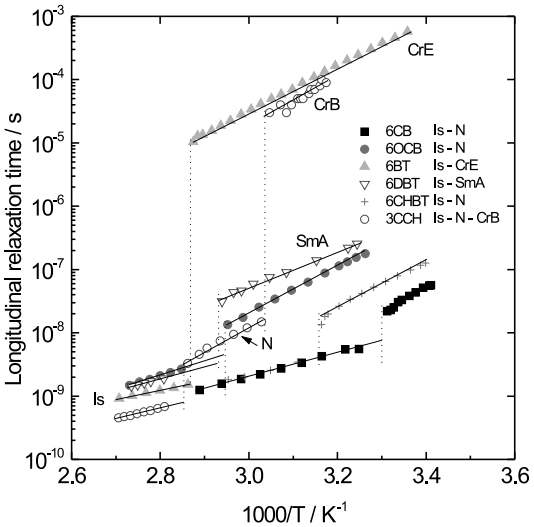

Fig. 4.17. Longitudinal relaxation times in the logarithmic scale versus inverted temperature for several substances in the isotropic and different LC phases. *Vertical lines* mark the transition points

homologous series. Two quantities characterizing the l.f. process in particular LC phases will be discussed: the retardation factor $g_{\mathrm{LC-Is}} = \tau_{\mathrm{LC}}/\tau_{\mathrm{Is}}$, where both relaxation times are taken at the transition point, and the activation enthalpy $\Delta^{\#}H_{\mathrm{l.f.}}$. The retardation factor reflects the change of the probability of flip-flop molecular rotations, due to molecular ordering in the LC phases, whereas $\Delta^{\#}H_{\mathrm{l.f.}}$ yields information about the actual energy barrier hindering the motion. Figures 4.18a and 4.18b show that the retardation of the molecular motions around the short axes when passing the clearing point strongly depends on the type of LC phase (note the logarithmic scale at the y-axis). The drop of the l.f. relaxation time is much greater in the case of crystal-like smectic B and E phases than for liquid-like phases (N, SmA). Such an effect should be expected – the more ordered the LC phase the less probable the molecular jumps between the potential minimums separated by 180°. On the other hand, the barriers hindering these motions (Fig. 4.18b) are close in the isotropic phase (ca. 25–35 kJ/mol) as well as in both types of LC phases (ca. 65–75 kJ/mol). Exceptions concern the SmA phase for which the barrier is always smaller than in the N phase [42–46]. One can conclude therefore that for two-ring compounds having a strongly polar group at one end and the alkyl tail at the second end the energy barrier hindering the molecular motions around the short axes is determined mainly by the side-by-side interactions. However, the probability of jumps, which is proportional to τ^{-1}, depends upon the degree of molecular order in LC phases. In order to perform a jump over 180° a molecule must have sufficient room created by the fluctuations of

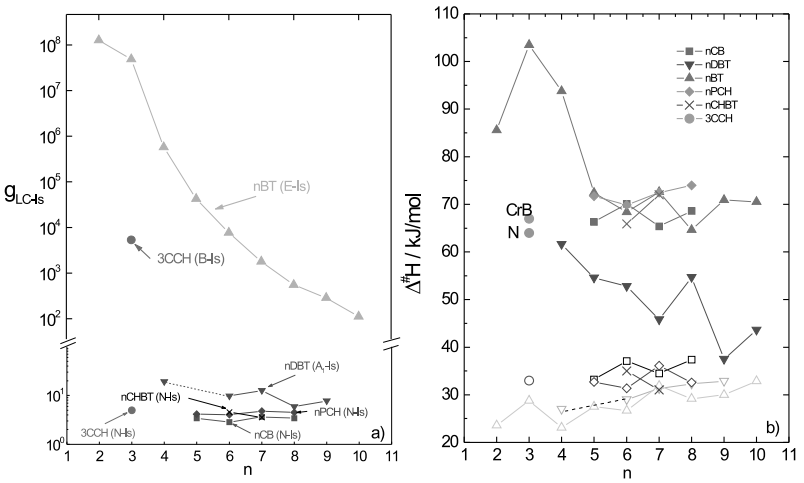

(a) **(b)**

Fig. 4.18. (**a**) Retardation factors for several two-ring homologous series as a function of the length of the alkyl chain. (**b**) The activation enthalpy in the isotropic (*open symbols*) and LC phases (*full symbols*) for the same substances

the positions of neighboring molecules which are markedly slowed down for the crystal-like phases. Considerable increase of the relaxation times and the height of the activation barriers observed for three shortest nBTs (compare Fig. 4.18) indicate how important role play the conformation motions of the alkyl tails in creating the room needed for the rotational jumps.

4.2.6 Influence of pressure on the relaxation processes in LC phases

Thermodynamic studies of LC substances under elevated pressures, reported in Sect 1.4, indicate a considerable sensitivity of their physical properties on the pressure. This arises from a great susceptibility of the intermolecular distances on the pressure in molecular systems. Also the relaxation processes occurring in the LC phases must be influenced by the external pressure. This was widely discussed in our previous review article [5]. Here we shall mention some recent results obtained for substances exhibiting the nematic, smectic A and CrE polymorphism.

In [22] the l.f. relaxation process in the N phase of 5CB was re-examined [20] using an improved experimental set-up. The data could be analyzed taking into account new pVT data. The dielectric properties of three other nematogens were investigated under high pressures: 8PCH [14, 32], 8CB [45] and 6OCB [49]. Three of the substances display the SmA phase: 8CB [45], 6DBT [50] and CNCN [38], and two other, 8BT [51, 52] and 6BT [53], exhibit the CrE polymorphism. Only in the case of CNCN the h.f. process connected with the molecular rotations around the long axes was studied, in other cases the l.f. process was examined.

Figure 4.19 presents the absorption and dispersion spectra collected (a) for the N phase of 5CB [22] and (b) for the CrE phase of 6BT [53], both measured at constant temperature and different pressures. Full analogy with the temperature dependence at 1 atm (see Fig. 4.9) can be noticed. The nematic state can easily be oriented by an electric or magnetic field, whereas these fields become ineffective in case of the smectic phases. In spite of that the measured relaxation spectra connected with the molecular rotations around the short axes can well be approximated by the Debye-type equation independently of the LC phase. For example, to the spectra in Fig. 4.19a purely Debye formula (4.29) with $\alpha = 0$ could be fitted, whereas the fits to the spectra in Fig. 4.19b give $\alpha \approx 0.02 \div 0.04$.

The longitudinal relaxation times determined as function of pressure at $T =$ constant are usually presented on semilogarithmic scale, as is shown in Fig. 4.20. As one can see in the figure, the points at given T can nicely be approximated by straight lines. However, the isotherms ending in the isotropic phase show some deviations of the points from the straight lines, which effect is especially pronounced in the N phase (compare Fig. 1.39). As it was explained in Sect. 1.4 the $\ln\tau$ vs. p plots yield the activation volume $\Delta^{\#}V_{\parallel}$, the activation enthalpy $\Delta^{\#}H_{\parallel}$ (see Fig. 1.39) and the activation energy $\Delta^{\#}U_{\parallel}$, if additionally pVT data are

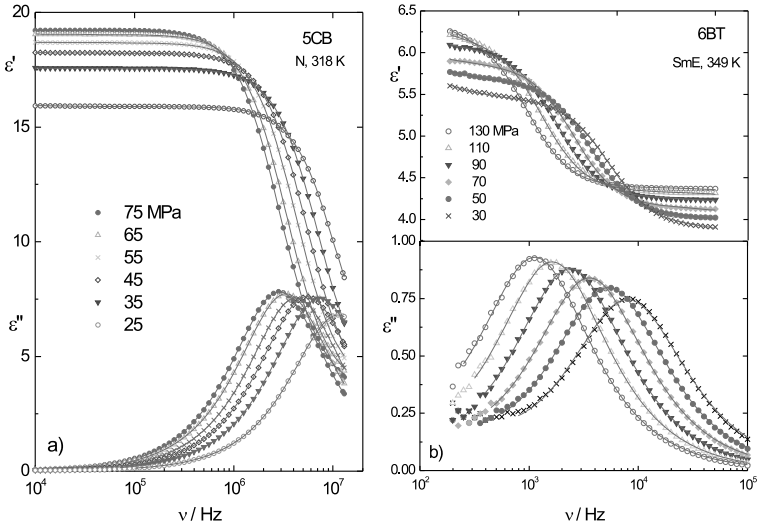

Fig. 4.19. The dispersion and absorption spectra collected for (**a**) the N phase of 5CB ($\boldsymbol{E} \parallel \boldsymbol{n}$) and (**b**) the CrE phase of 6BT (the sample could not be oriented)

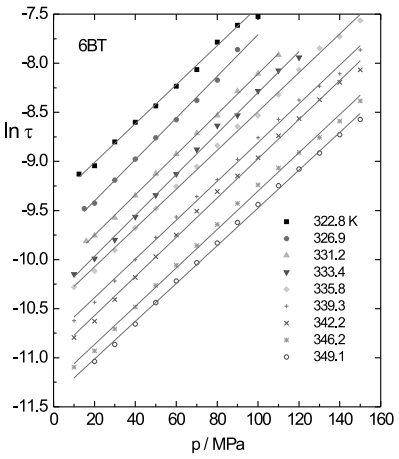

Fig. 4.20. Logarithm of the longitudinal relaxation time versus pressure in the CrE phase of 6BT. The slopes of the lines yield the activation volume $\Delta^{\#}V(T)$ which are presented in Fig. 4.22

available. The values of activation parameters obtained for all substances mentioned above are presented in Figs. 4.22 and 4.23. In spite of a scatter of points (this especially concerns the data for 8CB which is caused by the narrow ranges of the N and SmA phases) some characteristic features can be noted: (*i*) the largest values of $\Delta^{\#}V_{\parallel}$ and $\Delta^{\#}H_{\parallel}$ characterize the nematic phase, the lowest correspond to the SmA phases (SmA_1 or SmA_d); (*ii*) the values for the crystal-like CrE phase are close to those obtained for the N phase in spite of drastic change in the relaxation frequency $\nu_c = 1/(2\pi\tau_{\parallel})$ (compare the frequency scales in Fig. 4.19a,b; (*iii*) the $\Delta^{\#}V_{\parallel}$ values for the crystal-like E phase shows a slight

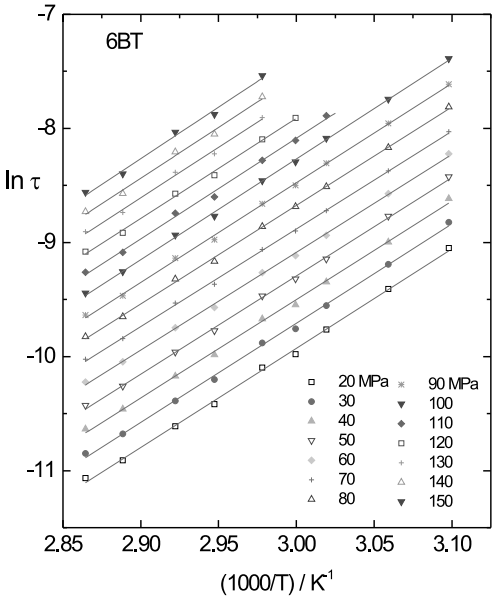

Fig. 4.21. Activation plots at different pressures within the CrE phase of 6BT. The data were taken from the plots in Fig. 4.20. The slopes of the lines yield the activation enthalpies $\Delta^{\#}H(p)$ which are presented in Fig. 4.23a

increase going away of the phase boundary, whereas they diminish with raising temperature for the liquid-like phases; the latter effect can be explained assuming that the increase of pressure leads to a breaking of the dipole-dipole associations because two monomers take less volume than the dimer; such associations are typical for compounds with the -CN group.

The most striking feature of the results presented in Fig. 4.23 is the fact that the activation energy $\Delta^{\#}U_{\|}$ consists ca. 50% of the activation enthalpy $\Delta^{\#}H_{\|}$ independently of the phase studied (nematic, smectic A_d or crystalline E). This indicates that both temperature and volume effects determine the molecular rotations around the short axes in LC phases to the same extent.

The pressure studies of CNCN in the smectic A phase indicate an unusual behavior of this substance. The attachment of two strongly polar -CN groups to the benzene ring at lateral positions results in a limited $p(T)$ range of the smectic A phase at relatively low pressure (compare Fig. 1.32b), and in a considerable slowing down of the rotation of molecules around the long axes (compare Fig. 4.14). Also the values the activation parameters $\Delta^{\#}V_{\perp}$ and $\Delta^{\#}H_{\perp}$, see Figs. 4.22 and 4.23a, are close to those characterizing the l.f. process in other related substances. This large hindrance of molecular rotations around the long (as well as around the short axes which was not observed in the dielectric experiments [35, 38], however) causes that by apply-

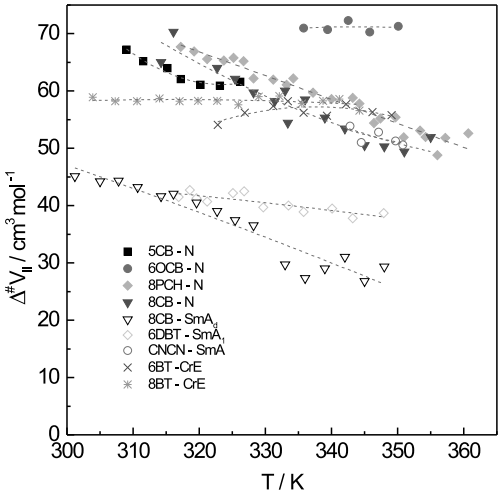

Fig. 4.22. Plots of the activation volumes versus temperature for several substances in different phases. *Full symbols* indicate the data for the nematic phase, other symbols concern the smectic phases. The *dashed lines* are guides for the eye only

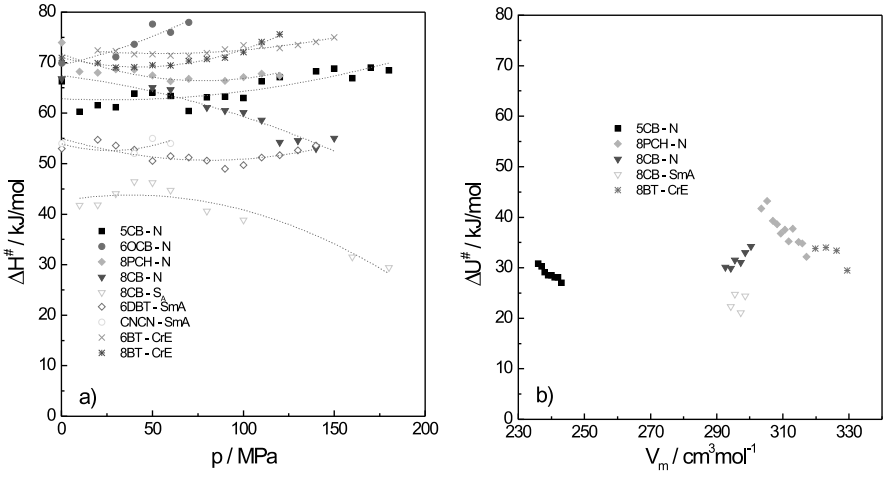

(**a**) (**b**)

Fig. 4.23. (**a**) Plots of the activation enthalpy versus pressure for the same substances as in Fig. 4.22. (**b**) Plots of the activation energy versus molar volume for four substances with known pVT data. The *dashed lines* are guides for the eye only

ing the hydrostatic pressure the space needed for molecular motions becomes strongly reduced, and finally the smectic phase disappears.

4.2.7 Summary

Dynamical properties of molecules in LC phases are determined by their chemical structures, deciding about the shape and flexibility of them, and by their arrangements in a given phase. The dielectric relaxation method is a powerful tool to study the molecular dynamics if the constituting molecules possess permanent dipolar group(s). Generally, two main relaxation processes have to be brought into prominence when a LC phase is studied: the low frequency relaxation process connected with the rotations around the short axes, and the high frequency process related mostly to the rotations around the long axes. However, other motions like internal rotations of polar parts and imperfect ordering of molecules in a given phase (especially in the nematic phase) contribute to the dielectric relaxation spectra. It is characteristic that so voluminous motion, as the rotation of molecules around the short axes, survives to the crystal-like phases. Unfortunately, the theoretical approaches to the dynamical properties consider the simplest cases only (nematic phase, rigid rod-like molecules). Application of the external pressure allow for a better understanding of the roles of the thermal and steric constraints determining the conditions in which the molecular rotations in different LC phases occur.

Acknowledgments. SU acknowledges a financial support by the Polish Government KBN Grant No 2 P03B 052 22.

References

1. H. Kresse: Adv. Liq. Cryst. **6**, 109 (1983)
2. S. Urban, K. Czupryński, R. Dąbrowski, B. Gestblom, J. Janik, H. Kresse, H. Schmalfuss: Liq. Cryst. **28**, 691 (2001)
3. J. Schacht, M. Buivydas, F. Gouda, L. Komitov, S. Stebler, S.T. Lagerwall, P. Zugenmaier, F. Horii: Liq. Cryst. **26**, 835 (1999)
4. G. Williams: Trans. Faraday. Soc. **60**, 1548 (1964)
5. S. Urban, A. Würflinger: Adv. Chem. Phys. **98**, 143 (1997)
6. P.L. Nordio, R. Rigatti, U. Segre: Mol. Phys. **25**, 129 (1973)
7. Jadżyn J., G. Czechowski, C. Legrand: Liq. Cryst. **26**, 1591 (1999)
8. J. Jadżyn, L. Hellemans, G. Czechowski, C. Legrand, R. Douali: Liq. Cryst. **27**, 613 (2000)
9. J. Jadżyn, G. Czechowski, D. Bauman: Z. Naturforsch. **55a**, 810 (2000)
10. G. Meier, A. Saupe: Mol. Cryst. **1**, 515 (1966)
11. A.J. Martin, G. Meier, A. Saupe: Symp. Faraday Soc. **5**, 119 (1971)
12. Y.P. Kalmykov, W.T. Coffey: Liq. Cryst. **25**, 329 (1998)
13. W. Maier, A. Saupe: Z. Naturforsch. **13a**, 564 (1959); Z. Naturforsch. **14a**, 882 (1958); Z. Naturforsch. **15a**, 287 (1960)
14. S. Urban, D. Büsing, A. Würflinger, B. Gestblom: Liq. Cryst. **25**, 253 (1998)

15. S. Urban, A. Würflinger, B. Gestblom: Phys. Chem. Chem. Phys. **1**, 2787 (1999)
16. W.T. Coffey, Yu.P. Kalmykov, J.T. Waldron: Liq. Cryst. **18**, 677 (1995)
17. A. Würflinger: Z. Naturforsch. **53a**, 141 (1998); A. Würflinger, S. Urban: Z. Naturforsch. **53a**, 883 (1998)
18. D. Bauman, P. Kędziora, C. Legrand, J. Jadżyn: Liq. Cryst. **21**, 389 (1996)
19. J. Jadżyn, C. Legrand, P. Kędziora, B. Żywucki, G. Czechowski, D. Bauman: Z. Naturforsch. **51a**, 933 (1996)
20. H.G. Kreul, S. Urban, A. Würflinger: Phys. Rev. A **45**, 8624 (1992)
21. S. Urban, H.G. Kreul, A. Würflinger: Liq. Cryst. **12**, 921 (1992)
22. S. Urban, A. Würflinger, D. Büsing, T. Brückert, M. Sandmann, B. Gestblom: Polish J. Chem. **72**, 241 (1998)
23. S. Urban, B. Gestblom, A. Würflinger: Mol. Cryst. Liq. Cryst. **331**, 113 (1999)
24. G.R. Luckhurst: in *The Molecular Physics of Liquid Crystals*, Chap. 4, ed. by G.R. Luckhurst, G.W. Gray (Academic Press, Oxford 1979)
25. C. Zannoni: in *The Molecular Dynamics of Liquid Crystals*, Chap. 2, ed. by G.R. Luckhurst, C.A. Veracini, NATO series, Vol. **431** (Kluwer Academic Publishers, Dordrecht 1994)
26. M.A. Bates, G.R. Luckhurst: Mol. Phys. **99**, 1365 (2001)
27. I.V. Haller: Prog. Solid State Chem. **10**, 103 (1975)
28. A. Buka, W.H. de Jeu: J. Phys. (Paris) **43**, 361 (1982)
29. W. Guo, B.M. Fung: J. Chem. Phys. **95**, 3917 (1991)
30. S.Ye. Yakovenko, M. Maiwald, A. Würflinger, J. Pelzl: Liq. Cryst. **26**, 23 (1999)
31. R.G. Horn: J. Phys. (Paris) **39**, 105, 137 (1978); R.G. Horn, T.E. Faber: Proc. Roy. Soc. **A368**, 199 (1979)
32. S. Urban, A. Würflinger: Liq. Cryst. **27**, 1119 (2000)
33. S. Urban, B. Gestblom, R. Dąbrowski, H. Kresse: Z. Naturforsch. **53a**, 134 (1998)
34. S. Urban, B. Gestblom, R. Dąbrowski: Liq. Cryst. **24**, 681 (1998)
35. S. Urban, B. Gestblom, R. Dąbrowski, J. Dziaduszek: Z. Naturforsch. **55a**, 733 (2000)
36. J. Chruściel, S. Wróbel, B. Gestblom, W. Haase: in *Modern Topics in Liquid Crystals*, ed. by A. Buka (World Scientific, Singapore, 1993) p. 31
37. F. Volino, A.J. Dianoux, J. Berges, H. Perrin: Mol. Cryst. Liq. Cryst. **142**, 107 (1987)
38. S. Urban, A. Würflinger: Z. Naturforsch. **56a**, 489 (2001)
39. D. Dunmur: Liquid Crystals: Chemistry, Physics and Applications, Eds. J. Rutkowska, S.J. Kłosowicz, J. Zieliński, Proceedings of SPIE **4759**, 196 (2002)
40. S. Urban, B. Gestblom, R. Dąbrowski: Z. Naturforsch. **54a**, 545 (1999)
41. H. Kresse, C. Selbmann, D. Demus, A. Buka, L. Bata: Cryst. Res. Technol. **16**, 1439 (1981)
42. C. Druon, J.M. Wacrenier: Ann. Phys. **3**, 199 (1978)
43. S. Urban, E. Novotna, H. Kresse, R. Dąbrowski: Mol. Cryst. Liq. Cryst. **262**, 257 (1995)
44. S. Urban, H. Kresse, R. Dąbrowski: Z. Naturforsch. **52a**, 403 (1997)
45. P. Markwick, S. Urban, A. Würflinger: Z. Naturforsch. **54a**, 275 (1999)
46. S. Urban, B. Gestblom, R. Dąbrowski: Polish J. Chem. **76** (2002)
47. T. Brückert, A. Würflinger: Z. Naturforsch. **51a**, 306 (1996)
48. S. Urban, K. Czupryński, R. Dąbrowski, B. Gestblom, J. Janik, H. Kresse, H. Schmalfuss: Liq. Cryst. **28**, 691 (2001)
49. S. Urban: Z. Naturforsch. **54a**, 365 (1999)

50. S. Urban, A. Würflinger: Z. Naturforsch. **54a**, 455 (1999)
51. S. Urban, A. Würflinger, A. Kocot: Liq. Cryst. **28**, 1331 (2001)
52. A. Würflinger, S. Urban: Liq. Cryst. **29**, 799 (2002)
53. S. Urban, A. Würflinger: Z. Naturforsch. **57a**, 233 (2002)
54. S. Urban, B. Gestblom, W. Kuczyński, S. Pawlus, A. Würflinger: Phys. Chem. Chem. Phys. **5**, 924 (2003)

4.3 Computer simulations of polar liquid crystals

L. Longa, H.-R. Trebin and G. Cholewiak

4.3.1 Introduction

Liquid crystals are condensed matter structures which occur quite frequently in nature [1, 2]. But the relationship between molecular interactions and relative stability of the corresponding liquid crystalline phases is still not fully understood. While it is widely accepted that the origin of liquid crystals rests in the elongated or flat or generally anisotropic shape of the molecules experiment and theory clearly show the importance of dispersive, induction and electrostatic interactions. Among them are the interactions between strong dipolar groups of particular interest. This has become evident soon after Gray et al. performed the synthesis of cyanobiphenyls [3, 4]. In these mesogens, a new class of phenomena known as reentrant phase transitions [5] was discovered and studied over the whole decade [6–8]. Also they appeared important in liquid crystal based display technology. Subsequently, strong dipoles were shown to affect not only the relative stability and the range of liquid crystalline phases, but also their symmetry [1, 9–11].

Interesting orderings can also be realized when dipole-dipole interactions are competing with entropy of packing as induced by molecular shape asymmetry. Such a situation is realized e.g. in the case of smectic phases formed by banana-shaped liquid crystalline molecules [12–14].

A direct and reliable way to account for structures that could be induced by dipolar forces is offered by computer simulations [15, 16]. They provide exact information about molecular ordering that results from particular molecular interactions. A purpose of this chapter is to discuss the effect of dipolar forces on mesophase formation and stability as derived from computer simulations. We are going to concentrate on effects that result from such forces by studying relatively simple models for which the case of a vanishing dipole is understood, too. In particular we shall be concerned with hard-rod and prolate Gay–Berne like molecules with embedded dipole moments for which many detailed simulations have been reported in the literature. The stability of various liquid crystals as function of position, orientation, molecular shape and strength of the dipole moment will be discussed whenever possible. Emphasis is put on the role that correlation functions play in a proper understanding of the structures and of their local, dipolar organization. Finally, an attempt

is made to make the chapter selfcontained by clarifying the essential points associated with the study of dipolar systems. However, we do not intend to give an exhaustive presentation of all known liquid crystalline phases with dipolar ordering. Our choice restricts to those cases that have been accessed in computer simulations, or are relevant to their understanding.

4.3.2 Liquid crystalline phases and dipolar ordering

Of all liquid crystalline phases the simplest one is the uniaxial nematic phase of calamitic liquid crystals. There the long range positional ordering of the centers of mass of the particles is absent and the correlations between the centers of mass of the molecules are similar to those existing in conventional liquids. The long axes of the molecules, on the other hand, lie on average parallel to each other defining a microscopically preferred direction, the *director*. Usually it is denoted by a unit vector $\hat{\boldsymbol{n}}$.

Though the constituent molecules may be polar, no ferroelectric nematics have been found experimentally so far in low molar mass liquid crystals. Microscopically this means that each molecule points *"up"* or *"down"* with equal probability and, consequently, the directions $\hat{\boldsymbol{n}}$ and $-\hat{\boldsymbol{n}}$ are equivalent. A typical snapshot of the molecular configuration is shown in Fig. 4.24a. However, the existence of a uniaxial polar nematic (which would be a ferroelectric fluid with a macroscopic dipole moment) is not forbidden by symmetry (see Fig. 4.24b). Actually it has been observed in computer simulations [17, 18] and in polymeric systems [19].

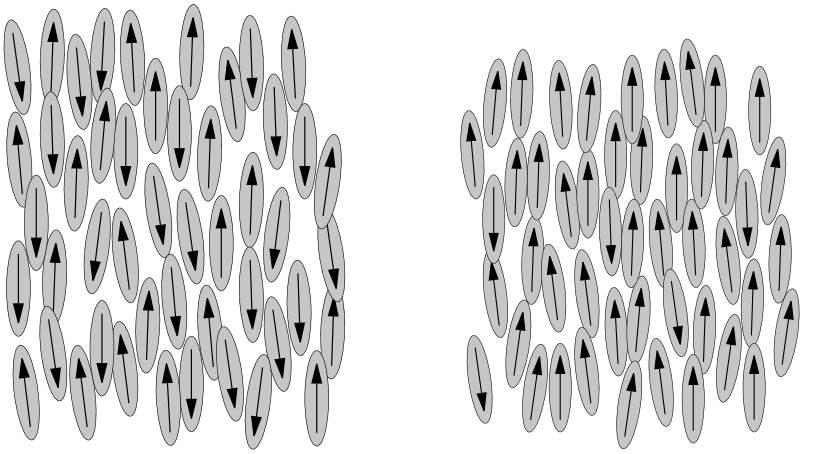

(**a**) (**b**)

Fig. 4.24. Snapshot of molecular arrangement in (**a**) uniaxial nematic phase composed of polar molecules and (**b**) uniaxial polar nematic phase of rod-like molecules. *Arrows* indicate orientation of dipole moments. In the case (**a**) the average performed over snapshots cancels out the dipole moment locally

More organized structures that could acquire some kind of polar ordering are smectics where the molecules are arranged in equidistant layers. Inside each layer the centers of mass may show no long-range positional order in which case each layer is a two-dimensional liquid. The molecules are, on the average, ordered perpendicular to the layer, as in the smectic A phase, or are tilted. In general, intra-layer diffusion of the molecules is easier than inter-layer. If an extra long-range positional order exists inside the layers such smectics are often referred to as crystal smectics.

The simplest of the smectic phases is the uniaxial smectic A phase of calamitics, which is shown in Fig. 4.25a. Note that the long molecular axes are, on the average, parallel to the layer normal and the dipoles (if present) are disordered to make the net macroscopic polarization vanish. The layer structure is rather weak and has a periodicity comparable to the length of a molecule in its fully extended configuration.

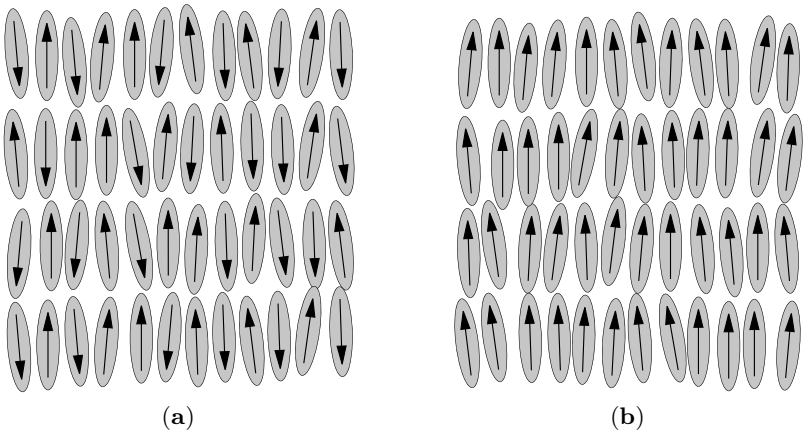

Fig. 4.25. Snapshot of the molecular arrangement in (**a**) a uniaxial, nonpolar smectic A phase and (**b**) a uniaxial polar smectic A phase of rod-like molecules. *Arrows* indicate the orientation of dipole moments. The average performed over snapshots (**a**) cancels out the dipole moment

As in the case of nematics the existence of a uniaxial polar smectic A phase (Fig. 4.25b) is not forbidden by symmetry and, indeed, was found in computer simulations of pear-shaped molecules with embedded axial dipole [18]. As far as we are aware of, it has not yet been detected in thermotropic or lyotropic liquid crystals, but films of more than a hundred layers stacked in a polar arrangement have been found to form by self-assembled mushroom shaped nanostructures of miniaturized triblock copolymers [20].

Another class of orthogonal smectic phases with polarized layers exists in liquid crystal compounds consisting of molecules with a strongly polar cyano- or NO_2 group at the one end of the aromatic core and only a single paraffin

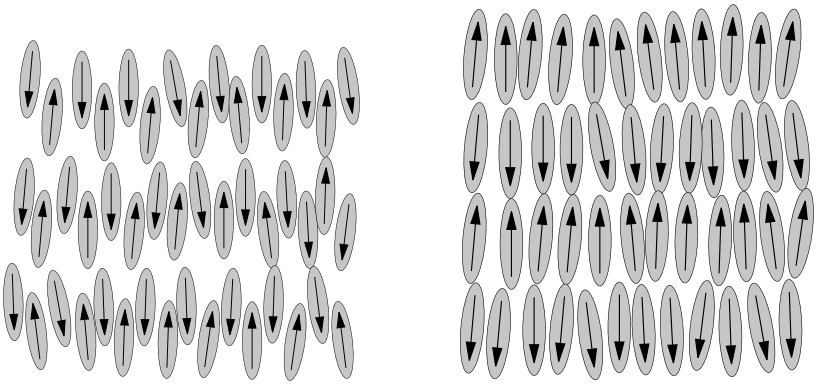

Fig. 4.26. (**a**) Molecular arrangement and dipolar ordering in the uniaxial, smectic A_d phase with cross section parallel to the layer normal. (**b**) Schematic representation of antiferroelectric order in the smectic A_2 phase with cross section parallel to the layer normal. *Arrows* indicate the orientation of dipole moments

tail at the other [1, 9, 10]. The smectic layers have a thickness ranging from one to two molecular lengths and one observes phase transitions between the optically identical smectic A phases. Out of these phases the so called smectic A_d, Fig. 4.26a, is similar to classical smectic A. One of the differences is that its periodicity is greater than the molecular length by a factor ranging from 1.1 to 1.6, with a typical value of 1.4. In the smectic A_2 phase, Fig. 4.26b, each layer has a periodicity comparable to the molecular length but, contrary to the layers of ordinary smectic A phases, it is ferroelectric. The ferroelectricity alternates on going from one layer to the next yielding an overall vanishing macroscopic polarization and antiferroelectric ordering (double layer structure).

A very interesting molecular arrangement is observed in the smectic $\tilde{A}$ phase, also known as 'antiphase', which has been detected both experimentally [10] and in computer simulations [18]. Locally the phase is similar to the smectic A_2, but globally antiferroelectric smectic A_2 domains are observed. They are arranged in a two-dimensional centered, rectangular lattice as shown in Fig. 4.27a. Thus the polarization of a single sublayer vanishes. If the lattice is assumed to be formed in the (x, z)-plane, the liquid character of the phase is maintained only in the y-direction.

Interestingly, the general rule that the lower temperature phases must display a greater degree of long range order does not always hold for this class of strongly polar liquid crystals. For example, the nematic state could be observed not only at temperatures above the domain of the smectic phase, but also below [5–8]. This behavior is now referred to as reentrant phase transition. Also one is able to observe phase transitions between the optically identical smectic A phases [8–11].

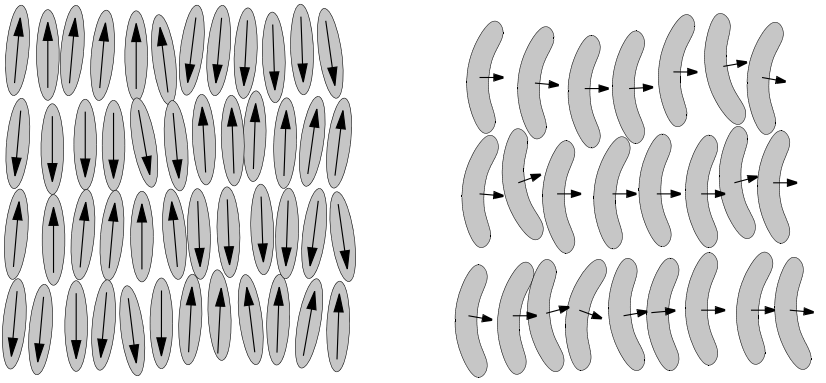

Fig. 4.27. (**a**) Molecular arrangement and dipolar ordering in the smectic $\tilde{A}$ phase with cross section parallel to the layer normal. (**b**) Schematic representation of ferroelectric order in the biaxial smectic A phase formed by banana-shaped molecules with cross section parallel to the layer normal. *Arrows* indicate orientation of dipole moments

A new type of (anti-) ferroelectric ordering could be predicted for systems where the entropy of packing of molecules within layers is competing strongly with dipolar interactions. This is exactly what we observe for systems of banana-like shaped molecules, where a biaxial, ferroelectric, smectic A phase is formed with spontaneous polarization perpendicular to the layer normal [21], Fig. 4.27b. On the other hand, discotic molecules with the dipole moments parallel to the rotation axis like to form polarized columns [22] or polar domains within the columns [23]. The overall resulting columnar structure is, however, nonpolar.

Finally, we mention that there exist tilted smectic phases of practical importance, with more complex types of polar ordering. They are not discussed here as we are not aware of any computer simulations relevant to them. Detailed information about their structure is given in [1, 24]. Interesting thoughts about liquid crystalline phases with polar order are found in an article by Blinov [25].

4.3.3 Models of interacting liquid crystalline molecules

It is obvious that the stability of a given liquid crystalline ordering is a direct consequence of intermolecular interactions. But it is also clear that the use of realistic many-body potentials in computer simulations at nonzero temperatures is an enormously complex computational problem. We therefore are forced to use relatively simple models, which only partly account for known properties of real liquid crystalline molecules. Fortunately, it proves satisfactory for studying gross features of liquid crystalline phases and of their

long-range organization. An advantage of such modelling is that it can pinpoint the molecular features that should be looked for in realistic systems to produce a given type of ordering. Our intention in this section is to introduce one of the most successful pair interaction potentials used to study mesophases by means of computer simulations, *the Gay–Berne potential*.

But before we are going to discuss properties of this model we summarize characteristic features of interactions between an arbitrarily shaped, but isolated, pair of molecules. The system is assumed to be in its quantum mechanical ground state. This approach promises a better understanding of what is actually disregarded in the original model and shows in which direction it could be generalized. Clearly, a restriction to pair interactions is already an approximation to more elaborated approaches in which the total electrostatic interaction between an ensemble of molecules is taken into account by use of the full apparatus of quantum statistical mechanics.

4.3.3.1 Pair potentials for liquid crystalline molecules

Under the restrictions discussed above the pair interaction for two isolated molecules can generally be written as the quantum mechanical average of the electrostatic interaction operator over the ground state of the system. However, a detailed analysis of such expression is quite complicated (if not impossible) and further simplifying assumptions are necessary (see e.g. [26] and references therein). One of them is that the flexibility of the molecules is of secondary importance. Then it simply follows that:

- at large intermolecular separations the potential must vanish;
- at short distances, the overlap of the electron clouds results in a strong repulsion. Though in general interactions at short distances are non-additive (due to electronic exchange effect) often a good approximation of the repulsive part is obtained by treating the molecules as hard bodies[1].

At short distances the hard body model introduces a simple characteristic of a molecular system, the so called *packing fraction*. It is defined as the ratio of the molecular ("Van der Waals") volume to the average volume per particle (as calculated from the density number). For example, cylinders closely packed in a hexagonal lattice yield a packing fraction $\frac{\pi}{2\sqrt{3}} \approx 0.906$. The experimentally found packing fraction for high temperature liquid crystalline phases is of the order of 0.66. For an ensemble of strongly elongated molecules it results in a tendency towards *parallel* ordering of long molecular axes (entropic excluded volume effects).

At another extreme, i.e. for large intermolecular separations, the overlapping of electronic clouds can be disregarded and thus the complete single-molecule bases can be used to decompose the ground state of the two molecules. The resulting expression yields three classes of terms

[1] By definition a hard body is impenetrable when in contact with another hard body but otherwise does not interact.

- **The electrostatic energy**. It is the electrostatic interaction between two separated, generally inhomogeneous, but in total neutral clouds of charges, where both molecules are assumed to be in the ground state. By performing multipole expansion of the charge densities the electrostatic energy can further be represented as an interaction energy between dipole-, quadrupole and higher multipole moments. In particular the dipole–dipole contribution relevant for us reads

$$V_{dipole-dipole} = \frac{\mu_1\mu_2}{r_{12}^3}[\hat{\boldsymbol{\mu}}_1 \cdot \hat{\boldsymbol{\mu}}_2 - 3(\hat{\boldsymbol{\mu}}_1 \cdot \hat{\boldsymbol{r}}_{12})(\hat{\boldsymbol{\mu}}_2 \cdot \hat{\boldsymbol{r}}_{12})]. \tag{4.43}$$

- **The induction energy**. It is obtained if one of the two molecules is in an excited state while the other is in the ground state. Such terms describe the distortion of the charge distribution of one molecule by fixed distribution of charges of the other, yielding what is known as dipole–induced dipole, quadrupole and multipole interactions. Again the leading term takes the form

$$V_{dipole-induced\,dipole} = -\frac{V_0\bar{\alpha}\mu^2}{r_{12}^6}\,[\,1 + P_2(\hat{\boldsymbol{\mu}}_1 \cdot \hat{\boldsymbol{a}}_2)P_2(\hat{\boldsymbol{a}}_2 \cdot \hat{\boldsymbol{r}}_{12}) + P_2(\hat{\boldsymbol{\mu}}_2 \cdot \hat{\boldsymbol{a}}_1)P_2(\hat{\boldsymbol{a}}_1 \cdot \hat{\boldsymbol{r}}_{12})\,]\,. \tag{4.44}$$

- **The dispersion energy**. It is obtained if both molecules are in excited states and can be thought of as an interaction between mutually excited charge distributions on both molecules. An example is provided by the standard induced dipole–induced dipole interaction

$$V_{dispersion} = -\frac{1}{r_{12}^6}\{V_1[\hat{\boldsymbol{a}}_1 \cdot \hat{\boldsymbol{a}}_2 - 3(\hat{\boldsymbol{a}}_1 \cdot \hat{\boldsymbol{r}}_{12})(\hat{\boldsymbol{a}}_2 \cdot \hat{\boldsymbol{r}}_{12})]^2 + V_2[(\hat{\boldsymbol{a}}_1 \cdot \hat{\boldsymbol{r}}_{12})^2 + (\hat{\boldsymbol{a}}_2 \cdot \hat{\boldsymbol{r}}_{12})^2]\}. \tag{4.45}$$

In the formulas above r_{12} is the distance between the (induced) dipole $(\boldsymbol{a}_1)$ $\boldsymbol{\mu}_1$ and the (induced) dipole $(\boldsymbol{a}_2)$ $\boldsymbol{\mu}_2$; $(\hat{\boldsymbol{a}}_\alpha)$ $\hat{\boldsymbol{\mu}}_\alpha$ is the unit vector parallel to the orientation of the (induced) dipole 'α'; $\hat{\boldsymbol{r}}_{12}$ is the unit vector pointing from the (induced) dipole "1" towards the (induced) dipole "2"; $\bar{\alpha}$ is the average molecular polarizability, and P_2 is the second-order Legendre polynomial.

Defined as above, the dispersive forces are expected to be strongly sensitive to the molecular electron distribution. Since the electron density defines the molecular shape the anisotropy of dispersive forces follows, in most cases, the molecular shape anisotropy. For "sufficiently" anisotropic molecules and for fixed distances between the centers of mass of the molecules the minimum of the dispersive part of the interaction is thus expected for parallel alignment of the long molecular axes.

Two different approaches are now possible. In the first one we may think of the interaction between *total* molecular multipole moments, referred to the center of mass of the molecule. An often used alternative approach divides each of the two molecules into "well localized" electronic units. If the localization of the units can indeed be justified the interaction between the molecules

can be viewed as interaction between each of the units. Hence, the molecule can be regarded as having a certain distribution of *localized* multiple moments (e.g. dipole moment associated with the cyano end group of cyanobiphenyles) as well as distribution of induction and dispersion contributions.

A few comments seem appropriate at this place:

- In our discussion we have disregarded three-body and, in general, many-body interactions, which may not necessarily be correct for dense systems. However, as far as we are aware of no systematic studies exist to date of many-body interactions on liquid crystalline properties.
- There are other contributions to pair interactions not discussed here like resonance and magnetic ones, but they are much weaker as compared to the ones already introduced. We may also think of modifications due to molecular flexibility or specific molecular shape.
- We have so far discussed some general features of pair interactions for anisotropic molecules. The approach as given, although very successful for an identification of relevant terms characterizing potential energy of two molecules, is not easily applicable for quantitative, ab initio predictions of liquid crystalline properties. One is often forced to use a series of additional simplifying assumptions thus making the final formulae severely limited.

Owing to the technical difficulties in ab initio modelling of real pair interactions between large molecules it is often more appropriate to use an alternative, semi-empirical description. In such approach the actual intermolecular interactions are approximated by functions depending on a number of adjustable parameters which, if necessary, can be fitted to experimental data. One commonly used form is the atom-atom Lennard–Jones interaction with attractive and repulsive parts that decay as 6th and 12th inverse powers of distance

$$V_{LJ} = \sum_{ab} 4\epsilon_{ab} \left[\left(\frac{\sigma_{ab}}{r_{ab}} \right)^{12} - \left(\frac{\sigma_{ab}}{r_{ab}} \right)^{6} \right], \tag{4.46}$$

where ϵ_{ab} is the potential well depth, and σ_{ab} is the shape parameter (i.e. distance at which the potential changes sign) for the interaction between atoms a on the molecule '1' and atoms b on the molecule '2'. Note that V_{LJ}, (4.46), includes part of attractive dispersion forces (4.45) and approximates repulsion at short distances. Terms that are normally added to (4.46) involve Coulomb, bond bending and torsional interactions. Detailed examples are discussed by Cook and Wilson in their atomistic simulations of liquid crystalline systems in the isotropic phase [27].

4.3.3.2 Gay–Berne pair potential

A difficulty in using realistic potentials like (4.46) for computer simulations is that they become computationally extremely expensive for large

molecules [27]. Alternatives that proved very successful in modelling the general behavior of liquid crystals are single site potentials that depend not only on the relative distance between the centers of mass of the molecules, but also on the mutual molecular orientations. One of the most popular pair interaction belonging to this class is a nonspherical version of the Lennard–Jones potential (4.46) as introduced by Gay and Berne [28]. For molecules of uniaxial symmetry it depends on the unit vectors $\hat{\boldsymbol{e}}_i$ and $\hat{\boldsymbol{e}}_j$ describing the orientations of a pair of molecules and on the separation vector $\boldsymbol{r} = \boldsymbol{r}_i - \boldsymbol{r}_j$ of their centers of mass $\boldsymbol{r}_i$ and $\boldsymbol{r}_j$. The detailed expressions are

$$V_{GB}(\hat{\boldsymbol{e}}_i, \hat{\boldsymbol{e}}_j, \boldsymbol{r}) = 4\,\epsilon(\hat{\boldsymbol{e}}_i, \hat{\boldsymbol{e}}_j, \hat{\boldsymbol{r}})\,\left(R^{-12} - R^{-6}\right), \tag{4.47}$$

where

$$R = \left[r - \sigma(\hat{\boldsymbol{e}}_i, \hat{\boldsymbol{e}}_j, \hat{\boldsymbol{r}}) + \sigma_0\right]/\sigma_0. \tag{4.48}$$

Here $r = |\boldsymbol{r}|$ is the length of the separation vector and $\hat{\boldsymbol{r}} = \boldsymbol{r}/r$ is the unit vector describing its orientation.

The Gay–Berne potential (4.47) is thus an anisotropic and shifted version of the potential (4.46). It differs from (4.46) in that both the potential well ϵ and the molecular shape parameter σ[2] are orientationally dependent. Originally the form of ϵ and σ was selected to give the best fit to the pair potential for a linear array of four equidistant point Lennard–Jones particles with a separation of $2\sigma_0$ between the first and fourth sites. The currently used definitions for the well and depth are

$$\sigma(\hat{\boldsymbol{e}}_i, \hat{\boldsymbol{e}}_j, \hat{\boldsymbol{r}}) = \sigma_0\,\left\{1 - \frac{1}{2}\,\chi\,\left[\frac{(\hat{\boldsymbol{r}}\cdot\hat{\boldsymbol{e}}_i + \hat{\boldsymbol{r}}\cdot\hat{\boldsymbol{e}}_j)^2}{1 + \chi\,(\hat{\boldsymbol{e}}_i\cdot\hat{\boldsymbol{e}}_j)} + \frac{(\hat{\boldsymbol{r}}\cdot\hat{\boldsymbol{e}}_i - \hat{\boldsymbol{r}}\cdot\hat{\boldsymbol{e}}_j)^2}{1 - \chi\,(\hat{\boldsymbol{e}}_i\cdot\hat{\boldsymbol{e}}_j)}\right]\right\}^{-1/2} \tag{4.49}$$

$$\epsilon(\hat{\boldsymbol{e}}_i, \hat{\boldsymbol{e}}_j, \hat{\boldsymbol{r}}) = \epsilon_0\,\epsilon^{\nu}(\hat{\boldsymbol{e}}_i, \hat{\boldsymbol{e}}_j)\,\epsilon'^{\mu}(\hat{\boldsymbol{e}}_i, \hat{\boldsymbol{e}}_j, \hat{\boldsymbol{r}}) \tag{4.50}$$

and

$$\epsilon(\hat{\boldsymbol{e}}_i, \hat{\boldsymbol{e}}_j) = \left[1 - \chi^2\,(\hat{\boldsymbol{e}}_i\cdot\hat{\boldsymbol{e}}_j)^2\right]^{-1/2} \tag{4.51}$$

$$\epsilon'(\hat{\boldsymbol{e}}_i, \hat{\boldsymbol{e}}_j, \hat{\boldsymbol{r}}) = 1 - \frac{1}{2}\,\chi'\,\left[\frac{(\hat{\boldsymbol{r}}\cdot\hat{\boldsymbol{e}}_i + \hat{\boldsymbol{r}}\cdot\hat{\boldsymbol{e}}_j)^2}{1 + \chi'\,(\hat{\boldsymbol{e}}_i\cdot\hat{\boldsymbol{e}}_j)} + \frac{(\hat{\boldsymbol{r}}\cdot\hat{\boldsymbol{e}}_i - \hat{\boldsymbol{r}}\cdot\hat{\boldsymbol{e}}_j)^2}{1 - \chi'\,(\hat{\boldsymbol{e}}_i\cdot\hat{\boldsymbol{e}}_j)}\right]. \tag{4.52}$$

The potential contains six parameters $(\kappa, \kappa', \mu, \nu)$ and (σ_0, ϵ_0). The first four determine the anisotropy of the repulsive and attractive forces while the other two introduce a natural length and energy scale. The parameters χ and χ' in (4.49–4.52) are related to the length-to-breadth ratio κ and potential well depths ratio κ' for the side-to-side and end-to-end molecular configurations

[2] Molecular shape is defined through the equipotential surface $V_{GB} = 0$, for which we have $r|_{V_{GB}=0} = \sigma$.

$$\chi = \frac{\kappa^2 - 1}{\kappa^2 + 1}\,, \tag{4.53a}$$

$$\chi' = \frac{\kappa'^{1/\mu} - 1}{\kappa'^{1/\mu} + 1}. \tag{4.53b}$$

They both vanish for spherical particles while χ is $+1$ for infinitely long rods and -1 for infinitely thin discs. The pair (σ_0, ϵ_0) corresponds to the shape parameter and well depth calculated for a configuration when all three molecular vectors $\hat{\boldsymbol{e}}_i$, $\hat{\boldsymbol{e}}_j$, and $\hat{\boldsymbol{r}}$ are mutually perpendicular (cross configuration). The last two parameters, μ and ν, tune the shape of the well depth in a more subtle way. In particular, the role of μ is comprehended, to a large extend, by relation (4.53b) while ν is connected to the well depth ratio κ'' for the side-to-side and cross configurations

$$\kappa'' = \frac{1}{(1 - \chi^2)^{\nu/2}}. \tag{4.54}$$

As already indicated before the parameters ϵ_0 and σ_0 of the Gay–Berne potential provide a natural length and energy scale. In terms of these constants all relevant physical quantities can be rendered dimensionless. The most often used (dimensionless) reduced quantities (denoted by a star) are listed below:

- length: $l^* = l/\sigma_0$
- time: $t^* = \sqrt{m\sigma_0^2/\epsilon_0}$
- density: $\rho^* = \rho\,\sigma_0^3$
- energy: $E^* = E/\epsilon_0$
- temperature: $T^* = kT/\epsilon_0$
- dipole moment: $\mu^* = \mu\,(\epsilon_0\sigma_0^3)^{-1/2}$.

Among the cases studied the original Gay–Berne model (OGB) [28], defined by $\kappa = 3$, $\kappa' = 5$, $\mu = 2$ and $\nu = 1$, is the one most thoroughly documented in the literature [29–31]. Its potential energy contours for the long molecular axes parallel to each other are shown in Fig. 4.28a.

Clearly, the OGB potential prefers a side-to-side arrangement of the pair of molecules which, in turn, promotes liquid crystallinity. The length-to-breadth ratio[3] is 3:1, as the value of κ suggests, and this seems to be the minimum value that is found experimentally for molecules forming liquid crystals. The complete phase diagram for this model is found in [31] and its sketch is shown in Fig. 4.28b. It is particularly simple, revealing only vapor, isotropic liquid, nematic and smectic B phases.

The Gay–Berne potential is very rich in predictions and remarkably successful in computer simulations of liquid crystalline phases. Using molecular dynamics and Monte Carlo techniques a phase behavior of the four-parameter

[3] It is defined as a ratio of distances corresponding to $V_{GB} = 0$ for end-to-end and side-to-side configurations.

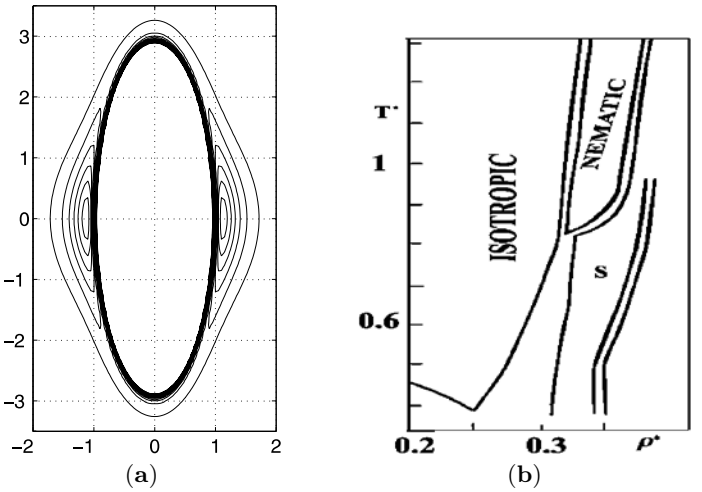

(**a**) (**b**)

Fig. 4.28. (**a**) The potential energy contours calculated for a pair of Gay–Berne particles. The molecules are assumed to be parallel to the z axis of the laboratory frame. The center of the reference molecule is located at the origin of laboratory frame. Owing to the cylindrical symmetry of the interactions only the $x - z$ cross section of the potential is shown. The contours are parameterized by the dimensionless potential energy (V_{GB}/ϵ_0). The innermost contours correspond to 2 and the other contours are for values of the scaled potential energy decreasing in steps of 0.25 until -5. In this figure and in all figures that follow quantities are given in reduced units. (**b**) Schematic representation of the corresponding phase diagram as determined from simulations by Miguel et al. [31]

Gay–Berne potential has been studied to prove that the model agrees well with what is observed for real mesogens [29–33].

In view of this success the original Gay–Berne potential has been developed further to include molecular biaxiality [34] (and to stabilize biaxial nematic phase [35]), flexibility [36], more complex molecules composed of a collection of Gay–Berne sites [37], dipolar forces [38–49], steric dipoles [18] and *zig-zag* shaped molecules [50].

Extension of the Gay–Berne potential to include dipole–dipole interactions due to a permanent dipole moment is straightforward. In this case the pair potential energy (4.47) should be supplemented by the contribution (4.43)

$$V = V_{GB} + V_{dipole-dipole}. \tag{4.55}$$

Just to have an impression what the potential energy for a pair of dipolar Gay–Berne particles looks like we sketch the energy contours in Fig. 4.29 for the OGB potential with a single longitudinal dipole moment per molecule. Note changes of the contours on going from central to terminal dipoles.

As the OGB with longitudinal dipole moments is one of the most frequently studied polar version of the Gay–Berne potential we are going to

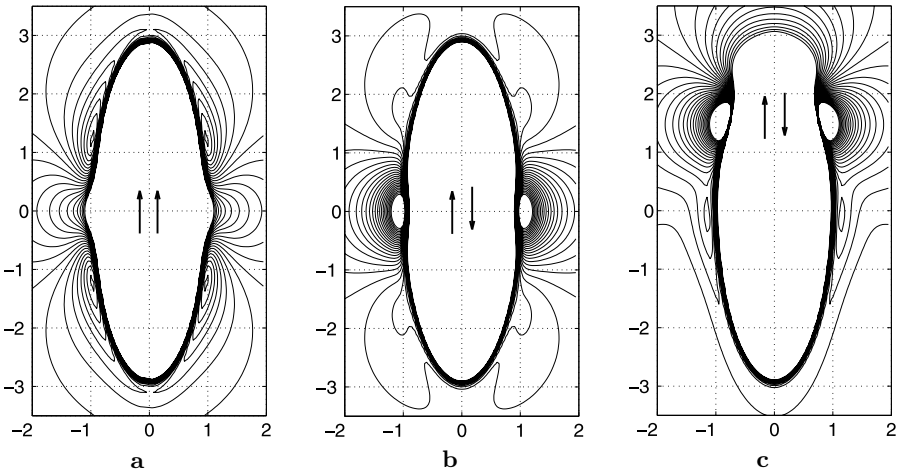

Fig. 4.29. The potential energy contours calculated for a pair of Gay–Berne particles with embedded longitudinal dipole moment. The molecules and the dipole moments are taken parallel to the z axis of the laboratory frame. The center of the reference molecule is located at the origin of the laboratory frame. The contours are parameterized by the dimensionless total potential energy (V/ϵ_0). The innermost contours correspond to 2 and the other contours are for values of the scaled potential energy decreasing in steps of 0.25 until -5. Orientation and localization of the dipole moments along the molecules is indicated by arrows. The position $d^* = 2 \times$ *(actual position from molecular center)*$/\sigma_0$ of the dipoles is: (**a**) d^* arbitrary, (**b**) $d^* = 0$, (**c**) $d^* = 0.75$. In all cases the value of the dipole moment is $\mu^* = 2.5$

discuss in detail the relation between the strength and position of the longitudinal dipole moment on the formation of mesophases. Not only central and terminal, but also intermediate positions of the dipoles are considered. The discussion will be illustrated with the results obtained for an ideally oriented polar version of the OGB system with longitudinal dipoles [48], here referred to as IOGB. In the IOGB model the translational degrees of freedom of the molecules are unrestricted but their orientations are fixed parallel to the z axis of the laboratory frame. That is the dipoles can be oriented either parallel or antiparallel to the positive z axis and are given by $\boldsymbol{\mu}_i = \mu\, s_i \hat{\mathbf{z}}$, where $s_i = \pm 1$. Their location on the molecular axis is given by a parameter d^* (see Fig. 4.29), which denotes the distance of the dipole from the molecular center.

At high temperatures, the IOGB model exhibits an ideally oriented nematic phase, which is the reference state of the system. In the limit of vanishing dipole moment nematic[4], smectic A and smectic B phases are stable.

[4] Nematic phase of perfectly oriented Gay–Berne model without dipoles has been studied by Wagner [51, 52].

The simplification of the ideal nematic order is reasonable whenever structures with strong alignment are expected, which is the case for smectic- and crystalline phases of the polar OGB system.

4.3.4 Computer simulations with dipoles

Simulations of a system can be done at many different levels of fidelity. The simulations dealt with here are Molecular Dynamics (MD) and Monte Carlo (MC) simulations for a classical system of molecules interacting through a potential like (4.55). Our goal is to extract information about equilibrium bulk properties for given temperature and pressure (or density). We do not intend to discuss here specific MD or MC algorithms used in simulations, which are well presented in [15, 16], but rather describe essential details specific to the analysis of phase behavior of polar mesogens.

Usually a simulation for a system with dipoles is carried out for an ensemble of a few hundred to a few thousand of molecules. Though the number depends strongly on actual computational resources available and on the problem studied a system size dependence was observed when the number of particles was less than 500 (see e.g. simulation for dipolar hard-core system [53]). This dependence may result from a combination of the long-range nature of dipolar (or generally electrostatic) interactions, approximations used to calculate them and the structure analyzed. Importantly, the system size sets up the limit for the allowed wavelengths of fluctuations. Hence the correlation length in the system that we simulate should actually be smaller than the system size. In studying systems close to a second- or weakly first order phase transition, where usually the correlation length exceeds the system size, a finite size scaling analysis of quantities looked for is necessary. As a rule, it is always important to carry out tests with larger systems for possible finite size effects, especially for systems with long-range interactions.

Assume now that our collection of molecules is restricted to a rectangular volume $L_x \times L_y \times L_z$. With a small system size we cannot simulate correctly bulk properties as a considerable number of particles resides on its surface (about 49% for a cubic box of 1000 molecules). To overcome this difficulty one usually introduces periodic boundary conditions where the system of interest, called central box, is surrounded by identical systems i.e. with exactly the same configuration of molecules at any moment of simulations [15]. As a particle moves through a boundary its image from a neighboring box enters and hence the constant density is maintained in every box as well as in the whole system. It is assumed that the behavior of a real, infinite system is most similar to that composed of periodic images of the central box. The interaction potential of the real system can now be approximated by an interaction between any two particles i and j of the central box and their images. It is thus given by the following expression

$$V = \frac{1}{2} \sum_{i \neq j} V_{PBC}(\boldsymbol{r}_i, \boldsymbol{r}_j, \ldots) + \sum_i V_{PBC}(\boldsymbol{r}_i, \boldsymbol{r}_i, \ldots) \tag{4.56}$$

where

$$V_{PBC}(\boldsymbol{r}_i, \boldsymbol{r}_j, \ldots) = \sum_{\boldsymbol{m}}{}' V\left(\boldsymbol{r}_i - \boldsymbol{r}_j + \sum_{\alpha=x,y,z} \boldsymbol{L}_\alpha\, m_\alpha, \ldots\right). \tag{4.57}$$

The sum in (4.57) runs over all vectors $\boldsymbol{m}$ with integer coefficients m_α, and $\boldsymbol{L}_\alpha$ are the vectors of length L_α parallel to the edges of the box. The prime indicates that for $\boldsymbol{m} = \boldsymbol{0}$ the terms with $i = j$ are to be omitted. Note that $\boldsymbol{r}_j - \sum_{\alpha=x,y,z} \boldsymbol{L}_\alpha m_\alpha$ are image particles of the particle 'j' and that the second term in (4.56) represents interaction of the particle 'i' with all its images. Clearly, only positions and orientations of the molecules in the central box are to be stored during simulations.

Usually special techniques, discussed in the next subsections, are needed to have a credible estimate of the infinite sum (4.56) for the electrostatic part of the interactions. The trouble, in particular with the dipole–dipole interaction, is due to its long range. The sum (4.56) is only conditionally convergent in this case, which means that the result depends on the way in which we add up the terms. It also means that the straight truncation of the dipole–dipole interaction at a given (spherical) cutoff (so that the interactions beyond cutoff are neglected) is generally not acceptable at the cutoff distances commonly used for simulations[5]. Such straight truncation is known to yield wrong predictions for energetic, dynamical and dielectric properties of the system. We should add that the proper treatment of the dipolar forces is the most time consuming part of the simulations and it is this part of the code that limits the system size in practice.

The available methods fall into two categories, the explicit molecule–molecule description and the molecule–continuum description. Two most commonly used representatives of these methods are the Ewald summation technique [15, 16, 54–64] and the Onsager reaction-field [15, 62–66] method, respectively. The Ewald summation technique treats essentially in an exact manner the interaction between the dipoles in the central box and its periodic replicas, whereas the Onsager reaction field replaces "uninteresting" dipole moments, located beyond the cutoff radius from a given dipole, by a dielectric continuum. Recently, some improvements over the original techniques also have been proposed [67–70].

4.3.4.1 Ewald summation technique for dipolar interactions

The Ewald summation technique for the calculation of the dipole–dipole part in the sum (4.57) is probably the most reliable one available today. It could

[5] A standard potential cutoff, which we utilize for the Gay–Bernie part of (4.57) is $r^*_{cut} = 4.0$, i.e. $V_{GB} = 0$ for $r > r_{cut}$. Correspondingly, the system size $L_{\min} = \min(L_x, L_y, L_z)$ must be taken greater than $2\,r_{cut}$. Choosing $L_{\min}$ we must be aware of finite size effects when the actual correlation length in the system is comparable with $L_{\min}$.

be introduced using a few equivalent formulations but from a mathematical point of view it amounts in multiplying each m-dependent term in (4.57) by a convergence factor, usually of the Gaussian form $\exp(-s|\boldsymbol{m}|^2)$, which makes (4.57) absolutely convergent. If we then calculate the so modified lattice sum by any correct method and take the limit of $s \to 0$ afterwards, we obtain a finite result. It becomes equivalent to performing a conditional summation (4.57) over spherical shells. The dipole–dipole part of the potential energy (4.56) so calculated splits itself into rapidly converging real- and Fourier-space lattice sums. More specifically, it is being reduced to four different terms: *(a)* a real term arising from the short-range interaction in the real space; *(b)* a reciprocal term arising from the long-range interaction in the reciprocal space; *(c)* a self-energy term correcting the contribution in the reciprocal space, and *(d)* a surface term connected with the continuum surrounding the replicated sample. They read [64, 71]

$$\begin{aligned} V_{dd} = \frac{1}{2} \sum_{i \neq j} (\boldsymbol{\mu}_i \cdot \boldsymbol{\mu}_j)\, B(r_{ij}) - (\boldsymbol{\mu}_i \cdot \boldsymbol{r}_{ij})\, (\boldsymbol{\mu}_j \cdot \boldsymbol{r}_{ij})\, C(r_{ij}) \\ + \frac{2\pi}{V} \sum_{\boldsymbol{k}} \neq 0 \frac{\exp(-k^2/4\gamma^2)}{k^2} |F(\boldsymbol{k})|^2 - \frac{2\gamma^3}{3\sqrt{\pi}} \sum_{i=1}^{N} \boldsymbol{\mu}_i^2 \\ + \frac{2\pi}{(2\epsilon_{surr} + 1)\, V} \left(\sum_{i=1} \boldsymbol{\mu}_i \right)^2 . \end{aligned} \tag{4.58}$$

In the expression above $\boldsymbol{k}$ denotes the reciprocal lattice vector given by $\boldsymbol{k} = (2\pi n_x/L_x, 2\pi n_y/L_y, 2\pi n_z/L_z)$ with $n_x,\ n_y,\ n_z = 0, .., n_{\max}$ and γ is the convergence parameter. The functions $B(r_{ij})$ and $C(r_{ij})$ are defined as

$$B(r_{ij}) = \frac{\operatorname{erfc}(\gamma r_{ij})}{r_{ij}^3} + 2\, \frac{\gamma}{\sqrt{\pi}}\, \frac{\exp(-\gamma^2\, r_{ij}^2)}{r_{ij}^2} \tag{4.59}$$

and

$$C(r_{ij}) = 3\, \frac{\operatorname{erfc}(\gamma r_{ij})}{r_{ij}^5} + 2\, \frac{\gamma}{\sqrt{\pi}} \left(2\gamma^2 + \frac{3}{r_{ij}^2} \right) \frac{\exp(-\gamma^2\, r_{ij}^2)}{r_{ij}^2}, \tag{4.60}$$

whereas the so-called dipole structure factor $|F(\boldsymbol{k})|^2$ is given by

$$F(\boldsymbol{k}) = \sum_{i=1}^{N} (\boldsymbol{\mu}_i \cdot \boldsymbol{k})\, \exp(i\, \boldsymbol{k} \cdot \boldsymbol{r}_i); \tag{4.61}$$

$\operatorname{erfc}(x) = \frac{2}{\sqrt{\pi}} \int_x^\infty dt\, e^{-t^2}$ is the complementary error function. Finally, the surface term acts as a depolarization field and is due to the total dipole moment of the central box confined in the volume V. The parameter ϵ_{surr} that enters the surface term is the dielectric constant of the continuum surrounding the whole

system i.e. central box plus all its replicas. Actually it is not clear what is the best choice for ϵ_{surr}. Assuming that the surrounding medium is the same as the bulk one this parameter should be found selfconsistently so that the bulk dielectric constant is equal to the surface one. However, this would considerably slow down simulation so the standard choice for ϵ_{surr} is an a priori value taken to be either infinity (tinfoil or metal boundary conditions) or 1 (vacuum boundary conditions). For dipolar systems the first extreme value would be most desirable because it makes the surface term vanish. Indeed when the net polarization in the simulation cell could be disregarded ($\sum_{i=1}^{N} \boldsymbol{\mu}_i/N \approx 0$), as e.g. for structures with no net polarization, adopting tinfoil boundaries seems legitimate[6] as there is no considerable polarization effects coming from the bulk. But this term is not necessarily negligible when there is a net dipole moment in the simulation cell and it may modify the internal energy in an essential way. Thus, in general, the choice of the boundary conditions may have an influence on the results of simulations [71–73].

The infinite Ewald sum, (4.58), is independent of the convergence parameter γ. In the calculations, however, when only a finite number of terms can be considered, γ and the number of $\boldsymbol{k}$ vectors are adjustable parameters and are typically chosen to optimize computations. In particular γ is usually chosen large so that the sum in real space disregards pairs separated more than $L_{\min}/2$, where $L_{\min} = \min(L_x, L_y, L_z)$. Typically, one uses $\gamma \cong 5/L_{\min}$ and includes about 100–500 wavevectors in the sum over reciprocal space. An analysis of the errors resulting from such truncation of both series has been reported by Neumann et al. [58], Kolafa et al. [59], Fincham [60] and Hummer [61]. In particular Hummer [61] has proposed an empirical rule allowing to achieve the same accuracy for the Fourier sum with two different values of γ. The rule states that the corresponding $\boldsymbol{k}$-space cutoff distances have to be chosen according to $|\boldsymbol{n}_{1,\max}|/|\boldsymbol{n}_{2,\max}| = \gamma_1/\gamma_2$.

In our simulations of the IOGB systems [48] at densities of the order of 0.3 we found that the optimal value for the parameter γ is $5.75/L_{\min}$. With this choice of γ the real space part of the Ewald sum could indeed be limited to the central box and the Fourier space part restricted to vectors $\boldsymbol{k} = (2\pi n_x/L_x,\, 2\pi n_y/L_y,\, 2\pi n_z/L_z)$, such that $|\boldsymbol{n}| = \sqrt{n_x^2 + n_y^2 + n_z^2} \leq 6$.

4.3.4.2 Reaction field method

A direct use of the Ewald summation technique is computationally very expensive, especially for large systems. Another widely used approach, which stays relatively cheap, is the Onsager reaction field method [65, 66]. In this method each particle "i" interacts with other particles confined within a sphere S_i of radius r^*_{cut}. The medium outside the cutoff sphere of each molecule is replaced by a uniform dielectric continuum with a static dielectric constant ϵ_{RF}.

[6] Exception here could be a calculation of the dielectric constant, which may depend on the boundaries adopted.

It gives rise to a reaction field $\boldsymbol{E}_{RF,i}$ on the dipole "i". The solution of the Maxwell equations adequate to the above approximation yields an electric field at the center of the sphere given by

$$\boldsymbol{E}_{RF,i} = \frac{2(\epsilon_{RF}-1)}{(2\epsilon_{RF}+1)r_{cut}^3}\boldsymbol{M}_i, \tag{4.62}$$

where $\boldsymbol{M}_i$ is the total dipole moment of the sphere S_i. A dipole $\boldsymbol{\mu}_i$ immersed in the field (4.62) has a potential energy

$$V_{RF,i} = -\frac{2(\epsilon_{RF}-1)}{(2\epsilon_{RF}+1)}\frac{\boldsymbol{M}_i\cdot\boldsymbol{\mu}_i}{r_{cut}^3}. \tag{4.63}$$

Consequently, the dipole–dipole energy of the whole system is

$$V_{dd} = \frac{1}{2}\sum_{i\neq j}\left[V_{dipole-dipole}(\boldsymbol{r}_{ij}) - \frac{2(\epsilon_{RF}-1)}{(2\epsilon_{RF}+1)}\frac{\boldsymbol{\mu}_i\cdot\boldsymbol{\mu}_j}{r_{cut}^3}\right]\theta(r_{cut}-r_{ij}), \tag{4.64}$$

where θ is the theta Heaviside function. As expected, the reaction field vanishes for vacuum ($\epsilon_{RF}=1$) whereas it is maximal for metallic ($\epsilon_{RF}=\infty$) surroundings. Its action on the system is to polarize molecules in the central box. Hence the direct antiferroelectric ordering between the dipole moments is weakened. As ϵ_{surr} for the Ewald method the true ϵ_{RF} should be calculated selfconsistently so that the average dielectric constant of the central box agrees with ϵ_{RF}. But in practice, as in the case of the Ewald summation, the simulations are often carried out with a fixed value of $\epsilon_{RF} \gg 1$. For example, in the case of the structures with vanishing *average* dipole moment of the central box, a substitution $\epsilon_{RF}=\infty$ is usually a satisfactory choice. The detailed value of ϵ_{RF}, given it is large, does not affect significantly calculated thermodynamic properties and correlation functions in this case. This has been explicitly demonstrated for the Stockmayer fluid [74] in liquid and vapor phases, and for the dipolar Gay–Berne with longitudinal dipole moments where both selfconsistent and tin-foil values of ϵ_{RF} have been used [48, 49, 62, 63].

To complete this subsection we note that the Ewald summation and the approximate reaction field method are not equivalent. This is quite clear if we compare the respective formulas (4.58) and (4.64). While the Ewald technique correctly accounts for long-range nature of the dipolar forces the reaction field method turns the dipole–dipole interaction into a spherically symmetric, relatively short-ranged effective potential, like the Gay–Berne one[7]. However, for many cases studied in the literature concerned with polar Gay–Berne systems [48, 49, 62–64] the differences between the use of the Ewald summation and the reaction field with conducting boundary conditions ($\epsilon_{RF}=\infty$) appear to be of secondary importance. This holds true both for nonpolar liquid

[7] A generalization of the reaction field to include a possible anisotropy of the dielectric continuum also is possible although we are not aware of such analysis.

phases like nematic and isotropic liquids and for nonpolar crystalline phases. The proper use of the reaction field requires, however, the use of a selfconsistently calculated averaged dielectric constant ϵ_{RF}.

4.3.4.3 Further computational details

Simulations of model polar liquid crystalline systems can be carried out using either classical Molecular Dynamics (MD) or Monte Carlo (MC) methods. They allow to find a direct connection between pair interactions and the corresponding structural, dynamic and energetic properties of the system. Simulations are usually performed in the NVT (constant number of molecules N, volume V and temperature T) or NPT (constant number of molecules N, pressure P and temperature T) ensemble as described in [15, 16]. In order to investigate the phase behavior of mesogenic systems constant pressure simulations (NPT) seem more suitable, especially for small systems. By allowing the central box dimensions to change the natural smectic and crystal structures can easily fit the dimensions of the simulation box, which is harder to achieve in the NVT ensemble.

But when dipolar interactions are calculated using the Ewald summation technique, the NPT simulations are computationally much more expensive than the NVT simulations. The reason is the necessity of recalculating tabulated earlier wave vectors and consequently also wave vector dependent terms $\exp(-k^2/4\gamma^2)/k^2$ in (4.58) when the box dimensions are changed.

A typical time step taken in MD simulations for the integration of the equations of motion is $\delta t^* \simeq 0.001 t^*$. Usually about 10^4–10^6 timesteps are needed to equilibrate the system of more than 500 molecules. Quantities of interest are calculated and averaged over 10^4–10^6 additional timesteps. Large runs are needed especially close to a phase transition.

A single time step in a MD run corresponds to one cycle of MC simulation, where one cycle represents N trial displacements and reorientations of the molecules at constant volume followed by one attempted box length move. The last step applies, of course, only when NPT simulations are carried out. The parameters controlling maximal increment of the displacements, the orientations and of the box dimensions are chosen such that the acceptance ratio for attempted moves is between 20% and 50%.

4.3.5 Structure analysis

The structures of liquid crystalline phases identified in simulations are characterized in terms of the probability densities for finding groups of one, two, or more molecules at specified positions and orientations in phase space [76–78]. The most important of these are the singlet and the pair distributions. They can be used to calculate some of the equilibrium properties of mesophases, like the total average potential energy, pressure, specific heat, etc. [76–78].

In this section we are going to discuss in detail various singlet, pair and three-body distribution functions and the way in which they can be extracted from the simulation data. We demonstrate, by referring to an ideally oriented system of Gay–Berne molecules with embedded longitudinal dipole moments [48], that all these functions are necessary to elucidate the short-range and long-range organization in liquid crystalline phases formed by polar systems. In particular, the importance of triplet correlations for a proper understanding of the structures and of their local, dipolar organization is demonstrated. In order to simplify the notation we assume that the model mesogenic molecules are axially symmetric with inversion symmetry, i.e. only longitudinal components of the dipole moments are considered. Generalization to the biaxial case, as induced e.g. by transversal dipoles, is straightforward [76].

4.3.5.1 Singlet distribution functions and order parameters

The simplest of the distribution functions is the one-particle density distribution function. For liquid crystals composed of uniaxial molecules it is defined as

$$P^{(1)}(\boldsymbol{r},\hat{\boldsymbol{\Omega}}) = \frac{1}{N}\left\langle \sum_{i=1}^{N} \delta(\boldsymbol{r}-\boldsymbol{r}_i')\,\delta(\hat{\boldsymbol{\Omega}}-\hat{\boldsymbol{\Omega}}_i')\right\rangle, \tag{4.65}$$

where δ is the Dirac delta function and the ensemble average $\langle ... \rangle$ is performed over primed variables representing the molecular positions and orientations. Clearly, $P^{(1)}(\boldsymbol{r},\hat{\boldsymbol{\Omega}})\,d^3\boldsymbol{r}\,d\hat{\boldsymbol{\Omega}}$ gives the probability of finding a mesogenic molecule within the range $[\,\boldsymbol{r},\boldsymbol{r}+d\boldsymbol{r}\,]$ of positions and the range $[\,\hat{\boldsymbol{\Omega}},\hat{\boldsymbol{\Omega}}+d\hat{\boldsymbol{\Omega}}]$ of orientations, where the latter being represented by the unit vector $\hat{\boldsymbol{\Omega}}$. Integration of $P^{(1)}$ over positions and orientations yields the normalization condition: $\int d^3\boldsymbol{r}\,d\hat{\boldsymbol{\Omega}}\; P^{(1)}(\boldsymbol{r},\hat{\boldsymbol{\Omega}}) = 1$.

Associated with the distribution function (4.65) are the order parameters. They can be introduced by referring to the Fourier integral representation of the spatial Dirac delta function: $\delta(\boldsymbol{r}) = \frac{1}{V}\sum_{\boldsymbol{k}} e^{i\,\boldsymbol{k}\cdot\boldsymbol{r}}$ and the representation of the angular delta: $\delta(\hat{\boldsymbol{\Omega}}-\hat{\boldsymbol{\Omega}}') = \sum_{L,m} Y_m^L(\hat{\boldsymbol{\Omega}})\,Y_m^L(\hat{\boldsymbol{\Omega}}')^*$, where $k_i = \frac{2\pi m_i}{L_i}$; $m_i = 0,\pm1,...$; $i = x,y,z$, and where the functions Y_m^L are the spherical harmonics [79]. Substitution of these representations into (4.65) yields

$$P^{(1)}(\boldsymbol{r},\hat{\boldsymbol{\Omega}}) = \frac{1}{V}\sum_{\boldsymbol{k},L,m} P_{\boldsymbol{k}Lm}\,e^{i\,\boldsymbol{k}\cdot\boldsymbol{r}}\,Y_m^L(\hat{\boldsymbol{\Omega}})\,, \tag{4.66a}$$

$$P_{\boldsymbol{k}Lm} = \frac{1}{N}\left\langle \sum_{i=1}^{N} e^{-i\,\boldsymbol{k}\cdot\boldsymbol{r}_i'}\; Y_m^L(\hat{\boldsymbol{\Omega}}_i')^*\right\rangle. \tag{4.66b}$$

The averages $P_{\boldsymbol{k}Lm}$ are just the order parameters and many of them vanish in practice. In general, the set of indices $\{\boldsymbol{k},L,m\}$ giving nonzero values for

$P_{\boldsymbol{k}Lm}$ can be selected by referring to irreducible representations of the space group associated with the structure. Identification of nonzero $\{\boldsymbol{k}, L, m\}$ is particularly simple for uniaxial nematics and for orthogonal uniaxial smectics with one dimensional density modulation [76, 81]. In the former case there is no dependence on positions in (4.66a), due to the translational symmetry of the nematics. That is, only $P_{\mathbf{0}Lm} = \langle P_L \rangle Y_m^L(\hat{\boldsymbol{n}})^*$ order parameters, with $\langle P_L \rangle$ being the average value of the L-th order Legendre polynomial, are nonzero [79]. It yields

$$P^{(1)}(\boldsymbol{r}, \hat{\boldsymbol{\Omega}}) = P^{(1)}(\hat{\boldsymbol{\Omega}}) = \frac{1}{V} \sum_L \langle P_L \rangle \sum_{m=-L}^{L} Y_m^L(\hat{\boldsymbol{\Omega}})\, Y_m^L(\hat{\boldsymbol{n}})^*$$
$$= \frac{1}{V} \sum_L \frac{2L+1}{4\pi} \langle P_L \rangle P_L(\hat{\boldsymbol{\Omega}} \cdot \hat{\boldsymbol{n}}) = P^{(1)}(\hat{\boldsymbol{\Omega}} \cdot \hat{\boldsymbol{n}}). \tag{4.67}$$

The director dependence of $P_{\mathbf{0}Lm}$ follows from the fact that in the nematic state the global $O(3)$ symmetry is broken to its uniaxial subgroup. In simulations $\hat{\boldsymbol{n}}$ could be identified with the direction maximizing the expression $\langle P_L \rangle = \max_{\hat{\mathbf{n}}:|\hat{\boldsymbol{n}}|=1} \frac{1}{N} \langle \sum_{i=1}^N P_L(\hat{\boldsymbol{\Omega}}'_i \cdot \hat{\boldsymbol{n}}) \rangle$ or, equivalently, with an eigenvector of the alignment tensor [80] $\mathbf{Q} = \frac{1}{2N} \left\langle \sum_{i=1}^N (3\hat{\boldsymbol{\Omega}}'_i \otimes \hat{\boldsymbol{\Omega}}'_i - 1) \right\rangle$, corresponding to a nondegenerate eigenvalue.

For nonpolar nematics the states $\hat{\boldsymbol{n}}$ and $-\hat{\boldsymbol{n}}$ of the director are equivalent and only terms with even Ls are nonzero in (4.67). For polar nematics [17, 18] both even and odd Ls must be retained. In particular, $\langle P_1 \rangle$ is the average polarization of the phase. Typical forms of the one-particle distribution function (4.67) for a nematic phase formed in Gay–Berne system along with some values of $\langle P_2 \rangle$ and $\langle P_4 \rangle$ are given by Bates and Luckhurst [32].

Our exemplary simulations of polar liquid crystals are restricted to the IOGB model, where $\langle P_{2L} \rangle = 1$. In this case the general formulas (4.65, 4.66a) become much simpler, especially for orthogonal smectics. More specifically, for smectic ordering along the director the one-particle distribution function reduces to $P^{(1)}(s, z)$ given by [48]

$$P^{(1)}(s, z) = \frac{1}{N} \left\langle \sum_{i=1}^{N} \delta_{s,s'_i}\, \delta(z - z'_i) \right\rangle$$
$$= \frac{1}{2L_z} \left[1 + 2 \sum_{n=0}^{\infty} \zeta_{2n+1}\, s \cos\left[(2n+1)qz\right] + 2 \sum_{n=1}^{\infty} \tau_{2n} \cos\left(2nqz\right) \right], \tag{4.68}$$

where we introduced smectic (τ_{2n}) and dipolar (ζ_{2n+1}) order parameters. Their definitions follow from the Fourier expansion of $P(s, z)$ under normalization condition: $\sum_{s=\pm 1} \int_0^{L_z} dz P^{(1)}(s, z) = 1$, with $q = \frac{\pi}{l}$ being the wavelength

of the smectic structure and l being the layer spacing. The leading amplitudes ζ_1 and τ_2 are given by

$$\zeta_1 = \underset{\{l\}}{\mathrm{Max}} \left| \frac{1}{N} \left\langle \sum_{j=1}^{N} s'_j \, \exp\left(i\,\pi z'_j / l\right) \right\rangle \right| \tag{4.69}$$

$$\tau_2 = \underset{\{l\}}{\mathrm{Max}} \left| \frac{1}{N} \left\langle \sum_{j=1}^{N} \exp\left(2\,i\,\pi z'_j / l\right) \right\rangle \right|. \tag{4.70}$$

The same procedure can be used to find higher order amplitudes of the singlet distribution function (4.68).

4.3.5.2 Pair distribution functions

The one-particle properties of uniaxial nematics and smectics are well understood. But a similar analysis for pair and higher order distribution functions is still far from being complete. A reason for that becomes clear if we write the definition of the simplest of these functions, namely that of the pair distribution [76, 77]

$$P^{(2)}(\boldsymbol{r}_1, \hat{\boldsymbol{\Omega}}_1, \boldsymbol{r}_2, \hat{\boldsymbol{\Omega}}_2) = \left\langle \sum_{i,j,i\neq j}^{N} \delta(\boldsymbol{r}_1 - \boldsymbol{r}'_i)\, \delta(\hat{\boldsymbol{\Omega}}_1 - \hat{\boldsymbol{\Omega}}'_i)\, \delta(\boldsymbol{r}_2 - \boldsymbol{r}'_j)\, \delta(\hat{\boldsymbol{\Omega}}_2 - \hat{\boldsymbol{\Omega}}'_j) \right\rangle. \tag{4.71}$$

Though (4.71) seems a straightforward generalization of the formula (4.65), in practice it appears to be a complex quantity, both to calculate and to represent graphically. Even for uniaxial nematics composed of uniaxial, rigid molecules we need to analyze a function depending on seven variables. Only recently this issue has been resolved by studying a complete set of rotational invariants [82]. Interestingly, it has been shown that the seemingly large group of these invariants can be divided into classes having the same asymptotic behavior at large distances and at high orientational order.

The analysis of pair correlations becomes much easier for the ideal nematic order as present in the IOGB model. In this case a simpler version of $P^{(2)}$ can be introduced through the relation [48]

$$\begin{aligned} P^{(2)} \equiv P^{(2)}(\boldsymbol{r}, s_1\hat{\boldsymbol{z}}, s_2\hat{\boldsymbol{z}}) &= \frac{V}{N^2} \left\langle \sum_i \sum_{j\neq i} \delta_{s_1 s_i} \delta_{s_2 s_j} \delta(\boldsymbol{r} - \boldsymbol{r}_i + \boldsymbol{r}_j) \right\rangle \\ &= P^{(2)}(r, \hat{\boldsymbol{r}}\cdot\hat{\boldsymbol{z}}, s_1 s_2) = \sum_L \frac{2L+1}{2}\, P_L^{(2)}(r, s_1 s_2)\, P_L(\cos\theta), \end{aligned} \tag{4.72}$$

where θ is the angle between the unit intermolecular vector and $\hat{\boldsymbol{z}}$. $P^{(2)}$ gives the probability that one particle with dipole orientation s_1 is separated by

a distance $\boldsymbol{r}$ from another with dipole s_2 (irrespective of their absolute positions), relative to the probability expected for a completely random distribution at the same density. It represents pair correlations of translationally invariant phases and is an approximation of the correlations for crystalline structures.

There are two pair distribution functions that can be derived from $P^{(2)}$, which are of particular interest for layered structures. One is the axial pair distribution function, $P_{\parallel}^{(2)}(z, s_1 s_2)$, defined as

$$P_{\parallel}^{(2)}(z, s_1 s_2) = \frac{L_z}{2N^2} \left\langle \sum_i \sum_{j \neq i} \delta_{s_1 s_i}\, \delta_{s_2 s_j}\, \delta(z - |z_i - z_j|) \right\rangle . \tag{4.73}$$

It gives the probability of finding centers of mass of two particles at a resolved, relative distance of z along the director, and with orientations s_1, s_2 of the molecular dipoles relative to the same probability calculated for an ideal gas of particles at the same density. We calculate $P_{\parallel}^{(2)}(z, \uparrow\uparrow)$ for pairs of molecules with the same dipolar orientations and $P_{\parallel}^{(2)}(z, \uparrow\downarrow)$ for pairs of molecules with their dipoles oriented in opposite directions, where $s = 1 \equiv \uparrow$ and $s = -1 \equiv \downarrow$. From these two functions we then obtain $P_{\parallel}^{(2)}(z)$ for arbitrary orientation of the dipoles by summing over s_1 and s_2.

The structure perpendicular to the director can be probed with the transversal pair distribution function, $P_{\perp}^{(2)}(r_\perp, s_1 s_2)$, where $r_\perp$ is the distance between the centers of mass of particles projected onto a plane orthogonal to $\hat{\boldsymbol{z}}$. It is defined by [48]

$$P_{\perp}^{(2)}(r_\perp, s_1 s_2) = \frac{1}{4\pi D} \int_0^{2\pi} d\phi \int_{-D}^{D} dz\; P^{(2)}(r_\perp, \phi, z, s_1 s_2) = \frac{V}{4\pi r_\perp D N^2}$$
$$\times \left\langle \sum_i \sum_{j \neq i} \delta_{s_1 s_i}\, \delta_{s_2 s_j}\, \delta(r_\perp - |\boldsymbol{r}_i - \boldsymbol{r}_j|_\perp)\, \Theta(D - |z_i - z_j|) \right\rangle . \tag{4.74}$$

Here $\Theta(x)$ denotes the Heaviside step function and D is a small parameter ($D^* \approx 0.5$) defining what is meant in simulations by saying that molecules belong to the same plane normal to $\hat{\boldsymbol{z}}$. Note that regarding $\boldsymbol{r}_i$ and $\boldsymbol{r}_j$ in (4.72) as positions of the dipole moments yields another interesting pair distribution function. It shows the tendency for the dipoles to gather in the plane.

In analogy to the case of longitudinal correlations (4.73), we can introduce transversal correlations $P_{\perp}^{(2)}(r_\perp, \uparrow\uparrow)$ and $P_{\perp}^{(2)}(r_\perp, \uparrow\downarrow)$, for parallel and antiparallel dipolar orientations, respectively, and $P_{\perp}^{(2)}(r_\perp)$, for arbitrary orientation of the dipoles. Also, by expanding the general $g_\perp(\boldsymbol{r}_\perp)$ into angular Fourier series we can introduce tetratic, hexatic etc. order parameters measuring the degree of angular correlations between the clusters of molecules. For example, the hexatic order is given by the hexatic order parameters $\Psi_{6n}(\overline{r}_\perp)$ defined as

$$P_{\perp}^{(2)}(\boldsymbol{r}_{\perp}) \equiv \frac{1}{2D}\sum_{s_1 s_2}\int_{-D}^{D} P^{(2)}(\boldsymbol{r}, s_1\hat{\boldsymbol{z}}, s_2\hat{\boldsymbol{z}})\,dz$$
$$= P_{\perp}(\overline{r}_{\perp})\sum_{n}\Psi_{6n}(\overline{r}_{\perp})\,\exp\left(i\,6n\phi_{jk}\right), \tag{4.75}$$

where $\overline{r}_{\perp}$ is the average in-plane nearest neighbor separation (position of the leading peak of $g_{\perp}(r_{\perp})$) and ϕ_{jk} is the angle that the separation vector $\boldsymbol{r}_j - \boldsymbol{r}_k$ between neighboring molecules j and k makes with the x-axis. The dominant hexatic order parameter corresponds to $n = 1$ in the formula (4.75). In selecting the nearest neighbors we can consider molecules separated e.g. between $\overline{r}_{\perp} \pm \delta$ with δ being the distance from $\overline{r}_{\perp}$, where the magnitude of the leading peak of $g_{\perp}(r_{\perp})$ halves. For ideal triangular lattice $\Psi_6 = 1$.

4.3.5.3 Three-body distribution functions

Structural properties of a system could further be characterized using higher order distributions. Of them, the triplet distribution function is of particular importance, especially for strongly polar liquid crystals where frustration plays an important rôle [5–7]. Although correlations higher than two-body are straightforward to evaluate in simulations [77] the results for liquid crystals are scarce [48]. This is probably due to the fact that the general parametrization of the three-body distribution in terms of spherical invariants is quite complicated and the calculation of averages time consuming. Even for a relatively small system of $N = 648$ IOGB molecules which we have studied the number of triplet configurations to be analyzed in one cycle is gigantic and equals $N(N-1)(N-2)/6 = 45\,139\,896$. Also visualization of the correlations, even if we manage to count triplets, is a nontrivial task.

For ideally oriented dipolar systems the task is manageable as the triplet distribution function $P^{(3)}$ considerably simplifies [48]. Actually, we are going to concentrate only on the translationally invariant part of the in plane three-body correlations which reads

$$P_{\perp}^{(3)}(r_{\perp}, \theta, s_1 s_2 s_3) = \frac{V^2}{8\pi r_{\perp}^2 D^2 N^3}\Big\langle \sum_i \sum_{j\neq i}\sum_{k\neq j\neq i} \delta_{s_1 s_i}\delta_{s_2 s_j}\delta_{s_3 s_k}$$
$$\delta(r_{\perp} - |\boldsymbol{r}_j + \boldsymbol{r}_i|_{\perp})\,\delta(r_{\perp} - |\boldsymbol{r}_k + \boldsymbol{r}_i|_{\perp})\,\Theta(D - |z_j - z_i|)$$
$$\Theta(D - |z_k - z_i|)\,\delta(\theta - Min(|\phi_j - \phi_k|, 2\pi - |\phi_j - \phi_k|))\Big\rangle. \tag{4.76}$$

By definition $P_{\perp}^{(3)}$ counts only those triplets that lie in planes perpendicular to the director and form isosceles triangles with two of the three sides being r and the angle between them being θ.

Owing to the symmetry of the IOGB model we think that other configurations do not contribute in an essential way to a quantitative understanding of the three-body correlations. As for the pair distribution two cases are considered. In the first case the vectors $\boldsymbol{r}_i$, $\boldsymbol{r}_j$, and $\boldsymbol{r}_k$ in (4.76) are assumed to

refer to the centers of mass of the molecules. In the second case these vectors parameterize positions of the dipole moments. Thus $P_{\perp}^{(3)}$ accounts for tendency of the three centers of mass or, in the second case, of the three dipole moments to gather in planes perpendicular to the director.

Moreover we will distinguish three nonequivalent dipole configurations: $s_1 s_2 s_3 = \uparrow\uparrow\uparrow$, $\uparrow\uparrow\downarrow$ and $\uparrow\downarrow\downarrow$, and determine corresponding distribution functions $P_{\perp}^{(3)}(r_{\perp}, \theta, \uparrow\uparrow\uparrow)$, $P_{\perp}^{(3)}(r_{\perp}, \theta, \uparrow\uparrow\downarrow)$ and $P_{\perp}^{(3)}(r_{\perp}, \theta, \uparrow\downarrow\downarrow)$, where the dipole moment s_1 refers to the nonequivalent vertex of isosceles triangles. Summing up over all possible orientations of $s_1 s_2 s_3$ yields the total distribution $P_{\perp}^{(3)}(r_{\perp}, \theta)$. All technical details concerned with the calculations of $P_{\perp}^{(3)}$ are given in our publication [48].

4.3.6 Hard particles with dipoles

Zarragoicoechea and coworkers were the first to examine by means of computer simulations the effect of the dipole moment immersed into several hard body molecules (cut-spheres [83–85], ellipsoids of revolution [86], spherocylinders [85, 87, 88]) on phase equilibria. They concluded that the dipolar forces are of minor importance to the formation of mesogenic phases.

By re-examining the hard spherocylinder case McGrother and coworkers [62, 89–92] only partly supported these observations. Their detailed simulations refer to the case of the spherocylinders with length to diameter ratio equal to 5, for which the system of vanishing dipole moment is well documented and exhibits isotropic, nematic and smectic A phases [75]. They found that central longitudinal dipole moments tend to destabilize the nematic phase relative to the isotropic and the smectic A phases as compared to the non-polar system. This is due to the strong enhancement of the molecular side-by-side in-plane antiparallel correlations which are responsible for the formation of the smectic layers. It is also found that an isotropic-nematic-smectic A triple point exists below which the nematic phase disappears.

The nematic phase is also destabilized relative to the smectic A phase (but not to the isotropic phase) for systems with a central transverse dipole moment. In this case the enhanced tendency to form layers is due to strong nose-to-tail interaction of the transverse dipoles. These interactions cause that the dipoles can form chain and ring domain structures within smectic layers. The terminal longitudinal dipoles, on the other hand, destabilize smectic A relative to nematic, where the latter phase becomes stable only at high densities.

4.3.7 Dipolar Gay–Berne systems

Although the dipolar interactions added to anisotropic repulsion yield an interesting model system with rich liquid crystalline phase behavior, the anisotropic attraction is by no means negligible in the stabilization of orientationally ordered phases. A model that takes all the three elements into

account i.e. repulsion at short distances, dispersive interactions at large distances and dipolar forces is the Gay–Berne system with embedded dipole moments. Here we discuss the results of computer simulations for this model. The discussion is illustrated with our NVT Monte Carlo simulations for the IOGB system composed of $N = 648$ polar molecules with longitudinal dipole moments (some tests being performed for $N = 2592$) [48]. The dipolar energy is calculated with the help of both, Ewald summation technique and reaction field. We investigate the influence of the dipole strength and the dipole location in the molecule on the formation of the smectic A phase and of higher ordered phases. Studied are also dipolar correlations in these phases.

4.3.7.1 Central dipole moments

For central, longitudinal dipole moments ($d^* = 0$) Satoh et al. [38] have shown that the isotropic liquid-nematic phase transition is not sensitive to the value of the dipole moment. Contrary to that the nematic-smectic A phase transition is shown to depend on the strength of the dipole moment. Moreover the stability range of the smectic phase for strong dipoles is wider compared to that in nonpolar systems. That is the central dipole moments enhance stability of smectic layers, which agrees qualitatively with what is reported for dipolar hard spherocylinders. Similar conclusions can be drawn for the IOGB model. We illustrate this with simulations performed for $T^* = 2.8$ and $\rho^* = 0.335$. Starting from the nematic reference state we find that an increase of the central dipole moment from $\mu^* = 0$ to $\mu^* = 1.5$ (the average dipole–dipole energy $\langle V_{dd}\rangle/\langle V\rangle$ being 23% of the total energy) yields a (weak) dipole–induced smectic A structure. The structure is characterized by $\tau_2 = 0.11$ ($\zeta_{2n+1} = 0$), and the layer spacing, $l^* \approx 2.7$, indicating that the layers are slightly interdigitated.

The pair distributions, Figs. 4.30a and 4.30b, are fluid-like and similar to what is observed in the nematic phase. As deduced from Figs. 4.30a and 4.30b the dipoles are distributed randomly within the layers, with no track of long-range ordering. The short-range, in-plane correlations are dominated by the antiparallel molecular arrangement (Fig. 4.30b). The 'fine structure' of these correlations, as displayed by the triplet in-plane distribution function, shows local hexagonal structure and linear correlations of the triplets. The leading peak of these correlations is dominated by the triplets occupying equilateral triangles as seen from Figs. 4.31a and 4.31b. Figures 4.31a and 4.31b also show that the peak at 60° is due to the triplets with one dipole moment being oriented in the opposite direction than the other two. The contribution from linear triplets, where the middle dipole has different orientation than the terminal ones, is equally important (see peak at 180° in Fig. 4.31b). The distribution function where all three dipoles are oriented in the same direction is negligible.

Further increase of magnitude of the central dipole to $\mu^* = 2.0$ ($\langle V_{dd}\rangle/\langle V\rangle \approx 37\%$) leads to a new structure which, most likely, is a crys-

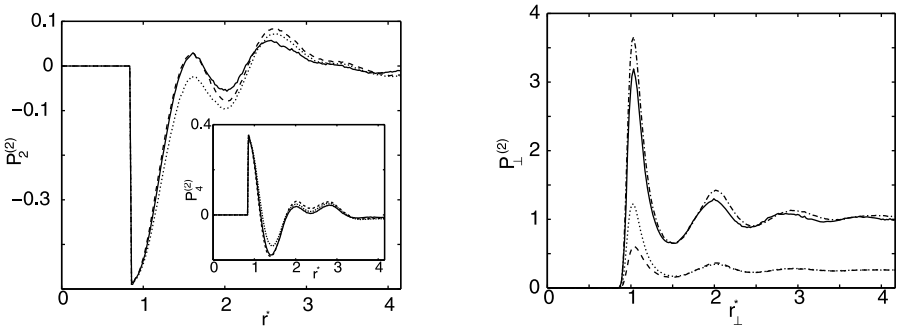

(**a**) (**b**)

Fig. 4.30. (**a**) The pair distribution functions $P_L^{(2)}(r^*)$ for $L = 2$ and $L = 4$ (*inset*) in the nematic phase of nonpolar molecules (*continuous line*) and $P_L^{(2)}(r^*, s_1 s_2)$ in the smectic A phase of the IOGB model with central dipole moment $\mu^* = 1.5$. The *dotted line* represents the $s_1 s_2 = \uparrow\downarrow$ while the *dashed one* corresponds to $s_1 s_2 = \uparrow\uparrow$ dipole configurations. (**b**) The transversal pair distribution functions $P_\perp^{(2)}(r_\perp^*)$ for the same cases as in (**a**). Additionally, the *dash-dotted line* represents the total distribution function, $P_\perp^{(2)}(r_\perp^*)$

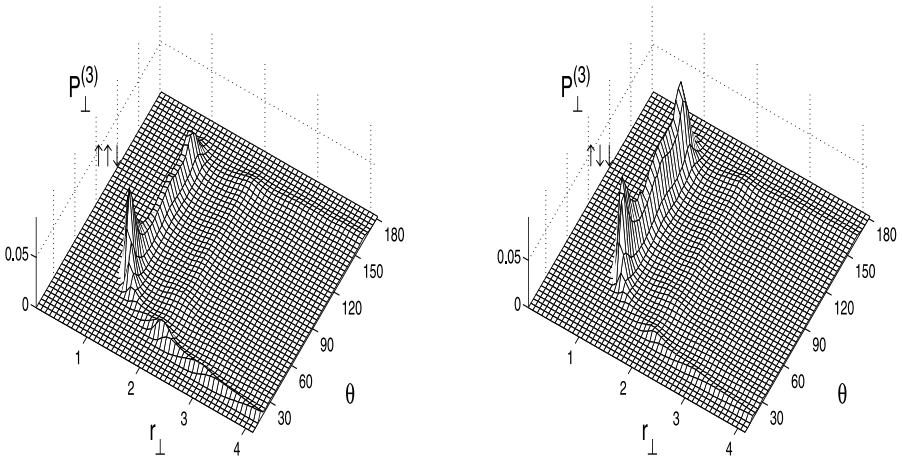

(**a**) (**b**)

Fig. 4.31. The triplet distribution function $P_\perp^{(3)}(r_\perp^*, \theta, s_1 s_2 s_3)$ for the IOGB model with central dipole moments of $\mu^* = 1.5$ in the smectic A phase: (**a**) $s_1 s_2 s_3 = \uparrow\uparrow\downarrow$; (**b**)$s_1 s_2 s_3 = \uparrow\downarrow\downarrow$

talline S_B with ABAB stacking. Again no long-range dipolar order across the layers (Fig. 4.32a) or within the layers is observed even though the smectic order parameter τ_2 of 0.8 is close to its saturation value of 1. Inspection of $P_\perp^{(2)}$ (Fig. 4.32b) shows that the system has developed hexagonal type of

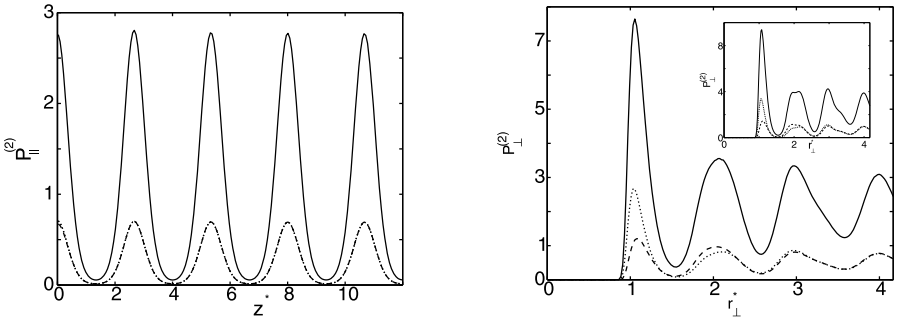

Fig. 4.32. (**a**) The axial pair distribution function $P_{\parallel}^{(2)}(z^*, s_1 s_2)$ and (**b**) the transversal pair distribution function, $P_{\perp}^{(2)}(r_{\perp}^*, s_1 s_2)$ in the smectic B phase. The dipolar strength of the central dipole is $\mu^* = 2$. The *solid lines* represent dipole-averaged total distribution functions and the *dashed lines* are for the $s_1 s_2 = \uparrow\uparrow$ distribution. The *dotted lines* give the $s_1 s_2 = \uparrow\downarrow$ distributions. The *inset* in (**b**) shows the transversal distribution in the same phase, but for $T^* = 2$

correlations with the hexatic order parameter Ψ_6, (4.75), of 0.69. The hexagonal in-plane arrangement becomes even more apparent by looking at the triplet correlations. They follow the same trends as previously observed ones for $\mu^* = 1.5$ with one exception that the corresponding peaks are now much better resolved and with higher amplitudes. A similar structure also exists for an even higher central dipole moment ($\mu^* = 2.5$) or lower temperatures. This is in line with the very recent MC NPT simulations by Houssa et al. [63], who also observe a stable dipolar S_B phase, most probably of AA or AB stacking, although this aspect of the ordering has not been studied.

Simulations of Houssa et al. [63] additionally allow interesting conclusions to be drawn about the stability of the nematic phase. Namely they show that for sufficiently strong dipole moments ($\mu^* = 2.5$) added to the OGB potential the nematic phase could be eliminated forcing the system to evolve directly from the isotropic phase to smectic B phase. Again most of the results obtained for the dipolar Gay–Berne systems are in qualitative agreement with those of equivalent dipolar hard spherocylinders.

Central dipole moments perpendicular to the long molecular axis of the OGB molecules also have been considered [41, 46], and the results appear somewhat controversial. Namely in the paper [41] the dipoles were found to have no impact on the liquid crystalline transitions, in contrast to an equivalent hard spherocylinders system, where transverse dipoles enhance the stability of the smectic A phase [90]. On the other hand, similar studies performed by Berardi et al. [46] demonstrate enhanced layering and formation of chains and rings of dipoles in smectic planes, consistent with the results for dipolar hard spherocylinders [90]. One possible explanation of this discrepancy is that in the paper [41] the long-range dipole–dipole interactions have been treated

in the same way as the Gay–Berne part, i.e. without referring to the Ewald- or reaction field methods.

4.3.7.2 Intermediate and terminal dipole moments

Simulations with noncentral locations of the dipole moments also were performed. In particular, terminal longitudinal dipoles were studied by Satoh et al. [39]. They found that the isotropic liquid-nematic transition temperature is shifted towards higher temperatures and the temperature range of the stability of the nematic phase is enhanced with increasing value of the dipole moment. Additionally, the strong terminal dipoles form at low temperatures a crystalline structure with tetragonal order within layers [42]. Berardi et al. [40] concentrated on the smectic phases and they found smectic $\tilde{\text{A}}$ phase for the OGB system with terminal dipoles.

Simulations carried out for the equivalent IOGB model are consistent with those findings although our system was too small to observe modulated anti-ferroelectric bilayer stripe domains characteristic of smectic $\tilde{\text{A}}$. Two cases were considered: *(a)* nearly terminal dipoles ($d^* = 0.75$) and *(b)* the dipoles localized at molecular end ($d^* = 1$).

One of the structures found for $d^* \approx 0.75$ and for moderate dipole moments ($\mu^* \approx 1.5$) is, with high probability, the smectic A_d. Such identification is supported by the small value of the translational order parameter τ_2 ($\tau_2 \approx 0.35$) and by properties of the correlation functions. Indeed, we observe that the relative distance between the positions of the molecular centers along the z direction is about 1.7, which means that the layers are strongly interdigitated. Analysis of transversal distributions of the molecules within a single layer and within the planes of the dipole moments additionally shows that the strongest transversal pair correlations (and hence also the triplet ones) are for in-plane antiparallel dipole moments with the corresponding centers of mass of the molecules being separated by $l \approx 1.7$ (see Figs. 4.33a and 4.33b). The leading peak of $P_\perp^{(2)}$ at $r_\perp^* \approx 0.9$, Fig. 4.33a comes from molecular pairs that compensate their dipole moments (*weak dimers*) and is much stronger than the peak at $r_\perp^* \approx 1.06$ of the in-layer correlations (inset in Fig. 4.33a). The total triplet dipole correlations, calculated in the plane of the dipoles, are practically dominated by the $s_1 s_2 s_3 = \uparrow\downarrow\downarrow$ triplet correlations, which we show in Fig. 4.33b. These correlations have essentially two broad peaks at 90° and 180°. Although this phase could also be a crystalline phase with interdigitated, tetragonal layers (S_{crT}) the apparently very small probability to have in-plane molecules with parallel dipole moments at reduced distance of $0.9 \times \sqrt{2}$ suggests that the structure is more likely of smectic A_d-type. The smectic layers could be viewed as being supported by correlated dimers with the layer spacing $2l^*$ of approximately 3.4. Interestingly, the local hexagonal ordering of central dipoles is transformed into a tetragonal one.

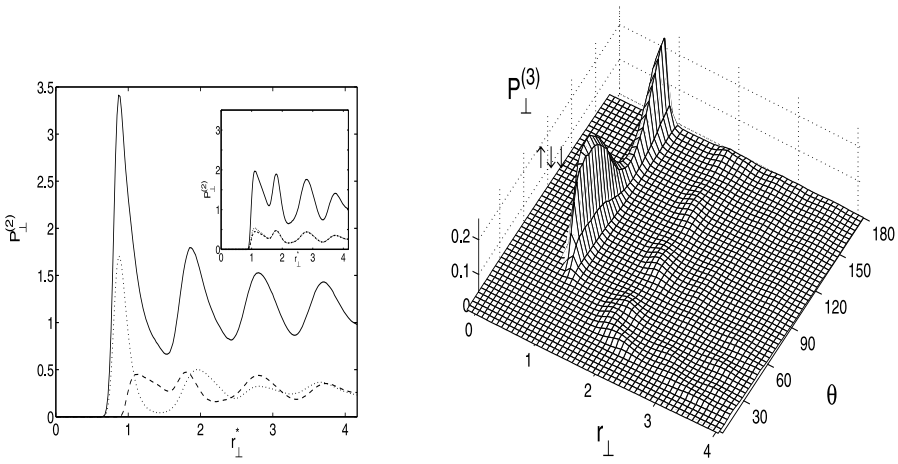

(**a**) (**b**)

Fig. 4.33. (**a**) The transversal pair distribution function, $P_\perp^{(2)}(r_\perp^*, s_1 s_2)$ for the in-plane dipole moments, in the smectic A_d phase of the IOGB model. The dipole moment μ^* of 1.5 is located at $d^* = 0.75$. The molecular centers are localized in the neighboring layers. The *continuous line* represents the total distribution function, $P_\perp^{(2)}(r_\perp^*)$; *dotted* and *dashed lines* correspond to $s_1 s_2 = \uparrow\downarrow$ and $s_1 s_2 = \uparrow\uparrow$, respectively. The *inset* shows the corresponding transversal distribution viewed from smectic plane of molecular centers. (**b**) The triplet distribution function $P_\perp^{(3)}(r_\perp^*, \theta, s_1 s_2 s_3)$ for the case (**a**) in the plane of $\uparrow\downarrow\downarrow$-oriented dipole moments (the centers of mass of the molecules with oppositely oriented dipoles are located in the neighboring layers). This case shows the strongest dipolar correlations between the dipoles

For dipole moments of magnitude $\mu^* = 2$ the peaks of the distribution functions become sharper and their fine structure could be resolved indicating that the structure is of S_{crT} type, similar to that reported by Satoh [42]. But even now with relatively strong dipolar interactions, no long-range dipolar order has been found. We observe, however, a strong enhancement of the $\uparrow\uparrow\uparrow$ triplet correlations indicating that for stronger dipoles we should detect a crystalline phase with polarized layers. Indeed, for very strong dipoles ($\mu^* = 2.5$) a bilayer crystalline structure with tetragonal in-plane ordering is stabilized. Now both order parameters ζ_1 and τ_2 are nonzero and high ($\zeta_1 = 0.89$, $\tau_2 = 0.75$), which indicates that the antiferroelectric dipolar order is even stronger than the smectic ordering. The crystalline structure thus has dipolar ordering similar to that observed for the antiferroelectric smectic A_2 phase. Interestingly, the axial *up–up* correlations are stronger than the *up–down* correlations. The *up–down* correlations within one smectic layer are almost negligible.

For large shifts in the dipole location ($d^* = 1$) and for $\mu^* = 2$ we recovered planar domains very similar to those reported by Berardi et al. [40], but present systems were too small for a quantitative analysis of the ordering.

4.3.8 Towards realistic simulations

Computer simulations based on detailed atomistic interactions between liquid crystalline molecules are still quite rare (see e.g. [27, 93, 94] and references therein). The reason for that is the computational complexity of interactions, which causes that only small systems are manageable so far (up to 144 molecules). Consequently, studies are restricted to the isotropic, nematic and, sometimes, crystalline phases for which the system size is not a severe obstacle.

As concerning simulations of realistic polar liquid crystals the molecular systems considered so far were those with terminal dipoles (PCH5, PCH5-Cl, 5CB, 5OCB). Of these the most accurate atomistic studies are by Cook and Wilson [27]. Their comparison with experiment of densities and of dipolar properties of PCH5 and PCH5-Cl molecules in the isotropic phase is quite encouraging. It shows that atomistic simulations indeed may have predictive power for bulk properties of mesogens. We expect that within the next few years a determination of liquid crystalline behavior from molecular modelling prior to synthesis should be possible.

Acknowledgments. This work was supported by the Polish project (KBN) No. 5 P03B 052 20 and by the project C12 of Collaborative Research Centre 382 of the Deutsche Forschungsgemeinschaft (DFG).

References

1. P. G. de Gennes and J. Prost: *The Physics of Liquid Crystals*, 2nd ed. (Clarendon Press, Oxford 1993)
2. G. W. Gray and J. W. Goodby: *Smectic liquid crystals. Textures and structures*, (Leonard Hill, Glasgow 1984)
3. G. W. Gray, K. J. Harrison, and J. A. Nash: Electron. Lett. **37**, 18 (1973)
4. G. W. Gray and J. E. Lydon: Nature **252**, 221 (1974)
5. P. E. Cladis: Phys. Rev. Lett. **35**, 48 (1981)
6. A. N. Berker and J. S. Walker: Phys. Rev. Lett. **47**, 1469 (1981)
7. L. Longa and W. H. de Jeu: Phys. Rev. **A** 26, 1632 (1982)
8. L. Longa: "Models of high-temperature liquid crystalline phases and of related phase transitions", Institute of Nuclear Physics, Kraków, Raport No 1454/PH (1989)
9. A. M. Levelut, R. J. Tarento, F. Hardouin, M. F. Achard, and G. Sigaud: Phys. Rev. **A 24**, 2180 (1981)
10. F. Hardouin, A. M. Levelut, M. F. Achard, and G. Sigaud: J. Chim. Phys. **80**, 53 (1983)
11. L. Longa and W. H. de Jeu: Phys. Rev. **A** 28, 2380 (1983)
12. Y. Matsunaga, and S. Miyamoto: Mol. Cryst. Liq. Cryst. **237**, 311 (1993)
13. H. Matsuzaki and Y. Matsunaga: Liq. Cryst. **14**, 105 (1993)
14. G. Pelzl, S. Diele, and W. Weissflog: Adv. Mater. **11**, 707 (1999)

15. M. P. Allen, D. J. Tildesley: *Computer Simulation of Liquids* (Clarendon Press, Oxford 1987)
16. D. Frenkel and B. Smit: *Understanding molecular simulation: from algorithms to applications*, 2nd ed. (Academic Press, San Diego 2001)
17. F. Biscarini, C. Zannoni, C. Chiccoli, and P. Pasini: Mol. Phys. **73**, 439 (1991)
18. R. Berardi, M. Ricci, and C. Zannoni: Chem. Phys. Chem. **7**, 444 (2001)
19. T. Watanabe, S. Miyata, T. Furukawa, H. Takezoe, T. Nishi, M. Sone, A. Migita, and J. Watanabe: Jpn. J. Appl. Phys. **35**, L505 (1996)
20. S. I. Stupp, V. LeBonheur, K. Walker, L. S. Li, K. E. Huggins, M. Keser, and A. Amstutz: Science **276**, 384 (1997)
21. T. Niori, T. Sekine, J. Watanabe, T. Furukawa, and H. Takezoe: J. Mater. Chem. **6**, 1231 (1996)
22. J. J. Weis, D. Levesque, and G. J. Zarragoicoechea: Phys. Rev. Lett. **69**, 913 (1992)
23. R. Berardi, S. Orlandi, and C. Zannoni: J. Chem. Soc., Faraday Trans. **93**, 1493 (1997)
24. S. Singh: Phys. Reports **324**, 107 (2000)
25. L. M. Blinov: Liq. Cryst. **24**, 143 (1998)
26. A. J. Stone: in *The Molecular Physics of Liquid Crystals*, ed. by G. R. Luckhurst and G. W. Gray (Academic Press, London 1981)
27. M. J. Cook and M. R. Wilson: Liq. Cryst. **27**, 1573 (2000)
28. J. G. Gay and B. J. Berne: J. Chem. Phys. **74**, 3316 (1981)
29. E. de Miguel, L. F. Rull, M. K. Chalam, and K. E. Gubbins: Mol. Phys. **71**, 1223 (1990)
30. E. de Miguel, L. F. Rull, M. K. Chalam, K. E. Gubbins and F. van Swol: Mol. Phys. **72**, 593 (1991)
31. E. de Miguel, L. F. Rull, M. K. Chalam, and K. E. Gubbins: Mol. Phys. **74**, 405 (1991)
32. M. A. Bates and G. R. Luckhurst: J. Chem. Phys. **110**, 7087 (1999)
33. J. T. Brown, M. P. Allen, E. M. del Río, and E. de Miguel: Phys. Rev. E **57**, 6685 (1998)
34. R. Berardi, C. Fava, and C. Zannoni: Chem. Phys. Lett. **236**, 462 (1995)
35. R. Berardi and C. Zannoni: J. Chem. Phys. **113**, 5971 (2000)
36. G. La Penna, D. Catalino, and C. A. Veracini: J. Chem. Phys. **105**, 7097 (1996)
37. M. P. Neal, A. J. Parker, and C. M. Care: Mol. Phys. **91**, 603 (1997)
38. K. Satoh, S. Mita, and S. Kondo: Liq. Cryst. **20**, 757 (1996)
39. K. Satoh, S. Mita, and S. Kondo: Chem. Phys. Lett. **255**, 99 (1996)
40. R. Berardi, S. Orlandi, and C. Zannoni: Chem. Phys. Lett. **261**, 357 (1996)
41. E. Gwóźdź, A. Bródka, and K. Pasterny: Chem. Phys. Lett. **267**, 557 (1997)
42. K. Satoh, S. Mita, and S. Kondo: Mol. Cryst. Liq. Cryst. **300**, 143 (1997)
43. G. Ayton, D. Q. Wei, and G. N. Patey: Phys. Rev. E **55**, 447 (1997)
44. R. Berardi, S. Orlandi, and C. Zannoni: J. Chem. Soc., Faraday Trans. **93**, 1493 (1997)
45. M. Houssa, L. F. Rull, and S. C. McGrother: J. Chem. Phys. **109**, 9529 (1998)
46. R. Berardi, S. Orlandi, and C. Zannoni: Int. J. Mod. Phys. C **10**, 477 (1999)
47. G. Cholewiak, J. Stelzer and L. Longa: SPIE Int. Soc. Opt. Eng. **3318**, 179 (1998)
48. L. Longa, G. Cholewiak, and J. Stelzer: A. Phys. Pol. B **31**, 801 (2000)
49. G. Cholewiak: PhD thesis (Jagellonian University, M. Smoluchowski Institute of Physics, Kraków 2002)

50. I. M. Withers, C. M. Care, and D. J. Cleaver: J. Chem. Phys. **113**, 5078 (2000)
51. W. L. Wagner: Mol. Cryst. Liq. Cryst. **299**, 33 (1997)
52. W. L. Wagner and L. Bennett: Mol. Phys. **94**, 571 (1998)
53. S. C. McGrother and G. Jackson: Phys. Rev. Lett. **76**, 4183 (1996)
54. S. W. de Leeuw, J. W. Perram, and E. R. Smith: Proc. R. Soc. Lond. A **373**, 27 (1980)
55. J. W. Perram, H. G. Petersen, and S. W. de Leeuw: Mol. Phys. **65**, 875 (1988)
56. M. Sprik: in *Observation, Prediction and Simulation of Phase Transitions in Complex Fluids*, ed. by M. Baus, L. F. Rull and J. P. Ryckaert (Kluwer, Dordrecht 1995)
57. V. Lobaskin and P. Linse: J. Chem. Phys. **109**, 3530 (1998)
58. M. Neumann and O. Steinhauser: Chem. Phys. Lett. **95**, 417 (1983)
59. J. Kolafa and J. W. Perram: Mol. Simul. **9**, 351 (1992)
60. D. Fincham: Mol. Simul. **13**, 1 (1994)
61. G. Hummer: Chem. Phys. Lett. **235**, 297 (1995)
62. A. Gil-Villegas, S. C. McGrother, and G. Jackson: Mol. Phys. **92**, 723 (1997)
63. M. Houssa, A. Qualid, and L. F. Rull: Mol. Phys. **94**, 439 (1998)
64. T. M. Nymand and P. Linse: J. Chem. Phys. **112**, 6152 (2000)
65. L. Onsager: J. Am. Chem. Soc. **58**, 1486 (1936)
66. J. A. Barker and O. R. Watts: Chem. Phys. Lett. **3**, 144 (1969)
67. I. G. Tironi, R. Sperb, P. E. Smith, and W. F. van Gunsteren: J. Chem. Phys. **102**, 5451 (1995)
68. P. H. Hünenberger and W. F. van Gunsteren: J. Chem. Phys. **108**, 6117 (1998)
69. S. L. Marshall: J. Phys.: Cond. Mat., **12**, 4575 (2000)
70. P. Demontis, S. Spanu, and G. B. Suffritti: J. Chem. Phys. **114**, 7980 (2001)
71. J. J. Weis and D. Levesque: Phys. Rev. E **48**, 3728 (1993)
72. J. E. Roberts and J. Schnitker: J. Chem. Phys. **101**, 5024 (1994)
73. J. E. Roberts and J. Schnitker: J. Phys. Chem. **99**, 1322 (1995)
74. B. Garzón, S. Lago, and C. Vega: Chem. Phys. Lett. **231**, 366 (1994)
75. P. Bolhuis and D. Frenkel: J. Chem. Phys. **106**, 666 (1997)
76. C. Zannoni: in *The Molecular Physics of Liquid Crystals*, ed. by G. R. Luckhurst and G. W. Gray (Academic Press, London 1981)
77. J. P. Hansen and I. R. McDonald: *Theory of Simple Liquids* 2nd ed. (Academic Press, London 1986)
78. J. P. Hansen: in *Observation, Prediction and Simulation of Phase Transitions in Complex Fluids*, ed. by M. Baus, L. F. Rull, and J. P. Ryckaert (Kluwer, Dordrecht 1995)
79. A. Lindner: in *Drehimpulse in der Quantenmechanik* (B. G. Teubner, Stuttgart 1984)
80. J. Vieillard-Baron: Mol. Phys. **28**, 809 (1974)
81. P. J. Wojtowicz: in *Introduction to Liquid Crystals*, ed. by E. B. Priestley, P. J. Wojtowicz, and P. Sheng (Plenum Press, New York and London 1975)
82. L. Longa, G. Cholewiak, H.-R. Trebin, and G. R. Luckhurst: Eur. Jour. Phys. E **4**, 51 (2001)
83. G. Z. Zarragoicoechea, D. Levesque, and J. J. Weis: Mol. Phys. **74**, 629 (1991)
84. G. Z. Zarragoicoechea, D. Levesque, and J. J. Weis: Mol. Phys. **75**, 989 (1992)
85. J. J. Weis, D. Levesque, and G. J. Zarragoicoechea: Phys. Rev. Lett. **69**, 913 (1992)
86. J. J. Weis, D. Levesque, and G. J. Zarragoicoechea: Phys. Rev. A, **46**, 7783 (1992)

87. D. Levesque, J. J. Weis, and G. Z. Zarragoicoechea: Phys. Rev. E **47**, 496 (1993)
88. G. Z. Zarragoicoechea, D. Levesque, and J. J. Weis: Mol. Phys. **78**, 1475 (1993)
89. S. C. McGrother, A. Gil-Villegas, and G. Jackson: J. Phys. Cond. Matt. **8**, 9649 (1996)
90. A. Gil-Villegas, S. C. McGrother, and G. Jackson: Chem. Phys. Lett. **269**, 441 (1997)
91. S. C. McGrother, G. Jackson, and D. J. Photinos: Mol. Phys. **91**, 751 (1997)
92. S. C. McGrother, A. Gil-Villegas, and G. Jackson: Mol. Phys. **95**, 657 (1998)
93. S. Hauptmann, T. Mosell, S. Reiling, and J. Brickmann: Chem. Phys. **208**, 57 (1996)
94. B. Stevensson, A. V. Komolkin, D. Sandström, and A. Maliniak: J. Chem. Phys. **114**, 2332 (2001)

4.4 Dielectric properties of liquid crystalline polysiloxane doped with dichroic dye

D. Bauman and E. Wolarz

4.4.1 Introduction

Among the various new trends developed in the last twenty-five years in modern polymer science, the design and investigation of liquid crystalline polymers (LCPs) have been the ones growing most rapidly and fruitfully [1–11].

Similarly as low molar weight liquid crystals (LCs), these polymers fall into two general classes. The first one consists of fairly rigid, anisotropic and highly polarizable mesogenic units, which can be rod-shaped, disc-shaped or lath-shaped (thermotropic LCPs). The second class of monomers causing liquid crystallinity in polymers are amphiphilic groups (lyotropic LCPs). Taking into account the location of the mesogenic groups one can distinguish between three kinds of polymers (Fig. 4.34):

a) polymers with mesogenic groups in the main chain (main-chain LCPs),
b) polymers with side mesogenic groups attached to the polymer chain (side-chain or comb-shaped polymers),
c) polymers with mixed structure.

In the following, we restrict our attention to the thermotropic liquid crystalline side-chain polymers only.

Side-chain LCPs consist of two more or less incompatible parts, a polymer backbone, which may adopt a coil conformation and mesogenic units, which are free to form liquid crystalline phases. Both parts are joined by a flexible segment, a so-called spacer. Due to much lower viscosity compared to main-chain LCPs, side-chain LCPs have electro-optical characteristics similar to those of low molar weight LCs and, due to the decoupling of the mesogenic groups, similar relation between the structure and properties is found. On the other hand, side-chain LCPs display good mechanical and film-forming properties inherent to polymers. This gives opportunity of many applications, both

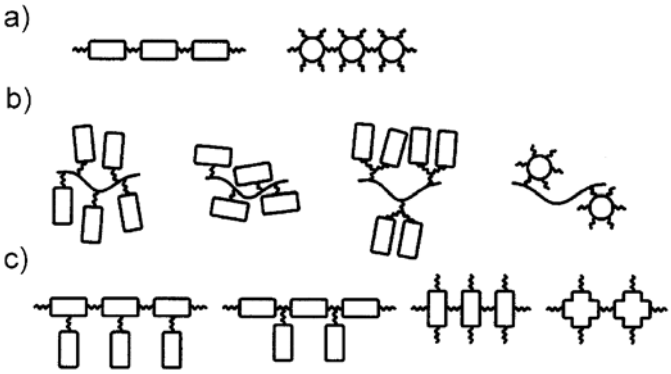

Fig. 4.34. Schema of the thermotropic LCPs: (**a**) main-chain LCPs, (**b**) side-chain LCPs, (**c**) LCPs with mixed structure

in basic science and technology. For the most of side-chain LCPs the absence of the melting transition is observed, instead, the transition to the glassy state takes place [10]. Therefore, one of the very interesting features of side-chain LCPs is the memory effect occurring because of the possibility to freeze in the LC-structure and its orientational order unchanged below the glass transition temperature. This is not the case for most LCs, where the LC-order cannot be transferred into a glassy state because it is destroyed by crystallization upon cooling. Thus, LCPs can be successfully used in optical memory devices. Applications of these substances to various other fields, such as display devices, aligned films, non-linear optics, wave-guides, optical compensators, selective optical filters and reflectors have been also proposed and demonstrated [5]. Moreover, side-chain LCPs can be utilized as the well-orienting solvents to study the direction-dependent molecular properties of the dissolved guest molecules [12] ("guest-host" effect [13]). On the other hand, the guest molecules can be used as probes to reflect the orientational properties and dynamics of polymeric host media [14–16].

Further, some dopant molecules oriented in side-chain LCPs give possibility to use such systems in nonlinear optics. It is known that for second order nonlinear processes, such as second harmonic generation or the nonlinear electro-optical effect, it is necessary to operate with a medium with some degree of order [17]. Side-chain LCPs fulfill this requirement. If, additionally, the dopant with high value of the second order hyperpolarizability is chosen, one is able to obtain the system with nonlinear coefficients (at optical frequencies) much larger than those found in inorganic single crystals. The compounds with high second order hyperpolarizability should be searched among the molecules exhibiting large changes of the dipole moment at $\pi \rightarrow \pi^{\star}$ electronic transition from the ground state to the excited state [17]. Molecules fulfilling this condition are the so-called charge transfer (CT) molecules. Typical examples of such CT-molecules are azo-dye molecules. They possess delocalized electrons

in conjugated π-electron system and the absorption of the visible light by these dyes results from a $\pi \rightarrow \pi^{\star}$ charge transfer transition, the direction of which is mostly parallel to the molecular plane [18]. Therefore, azo-dyes dissolved in side-chain LCPs seem to be ideal nonlinear media. It is also possible to synthesize copolymers containing both mesogenic and azo-dye units in their side chains [17]. This gives the possibility of greater dye concentrations in the liquid crystalline polymeric material to be used and higher optical contrast ratio to be achieved.

Finally, it should be noted that irradiation of the photoresponsive azo-dye molecules can cause the reversible *trans-cis* isomerization of the photochromic group simultaneously inducing a local phase transition. Therefore, azo-dye molecules dissolved in LCPs or attached as the side groups to the backbone in LC copolymers may act as a convenient probe of the polymer conformation, both in bulk and in solution [19].

Because of so many applications of the dye–LCP mixtures it seems to be necessary to carry out the investigation of the basic properties of such mixtures in order to obtain more information about the nature of the intermolecular interaction between dye molecules and mesogenic groups, their dynamics and packing in the mesomorphic phase. Dielectric spectroscopy is one of the methods which can be recommended to realize this purpose. This method was already widely used for study of pure side-chain LCPs [20–28], copolymers [29] and oligomers [30] containing mesogenic groups with permanent electric dipole moment. However, up to now little is known about the dielectric properties of the LCPs doped with low molecular weight mesogenic [31–33] or non-mesogenic [34, 35] substance.

In this section we intend to show the possibility of utilizing the dielectric spectroscopy technique for mixtures of LCP and a small amount of a dichroic dye. The chosen host polymer is one of the mesogenic side-chain polysiloxanes with weak polar groups and the dopants are two selected azo-dyes with relatively large electric dipole moment. LCPs with siloxane backbone are very convenient for investigations because they have very broad mesophase range [36] and some of them are mesogenic already below room temperature. The selected azo-dyes, however, are characterized by very good solubility which provides the driving force for penetration of the polymer and enables carrying out investigations at different dopant concentrations.

4.4.2 Probe preparation and thermodynamical data

The chosen mesogenic side-chain polymer (PS6) having the chemical structure presented in Fig. 4.35a was synthesized at the Warsaw Academy of Agriculture (Department of General Chemistry), Poland, as described in the literature [37], via hydroxylation of an alkene-type mesogen 4-(5-hexenyloxy)-benzoic acid 4′-methoxyphenyl ester with poly(methylhydrogensiloxane) in the presence of a catalytic amount of hexachloroplatinic (IV) acid. PS6

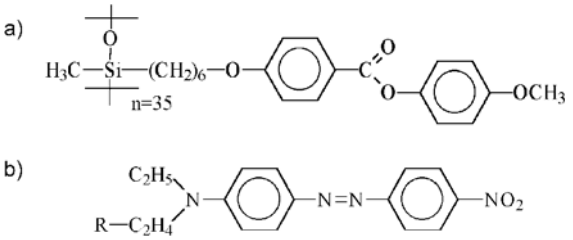

Fig. 4.35. Side-chain polymer (PS6) (**a**) and non-mesogenic dichroic azo-dyes (**b**): R = H (**1**), R = phenyl ring (**2**)

shows smectic A and nematic phases between solid and isotropic states.

The two non-mesogenic dichroic azo-dyes (**1** and **2**) with the structure shown in Fig. 4.35b were synthesized and chromatographically purified in the Institute of Dyes, Łódź University of Technology, Poland. The dyes were dissolved in the polymer matrix at concentrations up to 0.08 molar fraction (taking the molar mass of the dye molecule and the monomer unit of the polymer). Mixtures containing higher amount of the dye were prepared also, but they were not investigated further because of a strong destructive effect of the dye on the mesophase range. The mixtures were prepared by stirring the two components at a temperature of about 400 K (above the clearing point of pure PS6). The solubility of the dyes was checked by means of a UV–Vis spectrometer Varian Cary 17 and by using a polarizing microscope. Figure 4.36 shows, as an example, the polarized components of the absorption spectrum, $A_{\parallel}$ and $A_{\perp}$ for dye **1** in PS6 in the smectic A ($T = 301\,\mathrm{K}$) and nematic

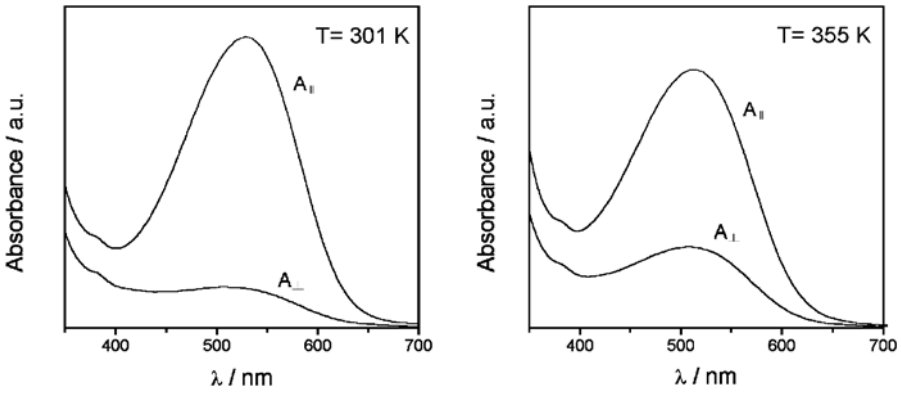

Fig. 4.36. Polarized components of the absorption spectra of dye **1** in PS6 at $T = 301\,\mathrm{K}$ (smectic A phase) and $T = 355\,\mathrm{K}$ (nematic phase). A_i ($i = \parallel, \perp$) are absorbances of the light polarized, respectively, parallel and perpendicular to the optical axis. From [38], slightly modified

($T = 355\,\mathrm{K}$) phases [38]. Such absorption curves are typical of both azo dyes investigated – only one absorption band without vibronic structure in the visible spectral region is observed. This band is related to the CT transition. The position of the band maximum, $\lambda_{\max}$, is different for the dyes, it is equal to 525 nm for **1** and 510 nm for **2**. The half-widths of the optical absorption band for both mixtures had comparable values, equal to 150 nm. The significant difference in the absorbance values of both polarized components indicates that the dyes investigated can be oriented in PS6 to a high extent.

The DSC scans were done using a Perkin–Elmer DSC–2C Differential Scanning Calorimeter with an interfaced computer for data collection and evaluation. The samples were heated and cooled with rate equal to 5 K/min in a temperature range between 280 K and 400 K. The transition enthalpies were determined with accuracy equal to 0.1 J/g, whereas the precision of the transition temperatures evaluation was determined by the width of the transition region. The observation of the mesophase type and estimation of the clearing point were carried out using a polarizing microscope Leitz Orthoplan Pol equipped with Mettler hot-stage FP82.

One comment should be made here about the phase transitions in polymers. Owing to the specific features associated with the procedures of polymer synthesis (chain polymerization, polycondensation) polymer samples always contain polymer molecules with varying numbers of monomers, i.e., strictly speaking, they are multicomponent systems. Therefore, the temperature at which a phase transition takes place is not as precisely defined as for single-component substances. The macromolecules with different numbers of monomers do not behave identically when the temperature is changed and as a result the phase transition is spread over a temperature range. In the temperature interval of the phase transition the coexistence of two phases is usually observed, which is in agreement with the thermodynamic law for first order phase transition [39].

Figure 4.37 shows the nematic-isotropic phase transition temperatures of PS6–**1** and PS6–**2** mixtures as a function of the molar fraction of the dyes, obtained from observation under a polarizing microscope.

Because of the presence of the two-phase region, the phase transition temperatures were calculated as mean values of the down and up limits of this region. The experimental points were fitted using a linear regression procedure, giving the slope coefficients, dT/dc, equal to $-219 \pm 3\,\mathrm{K}$ and $-297 \pm 6\,\mathrm{K}$ for PS6–**1** and PS6–**2** mixtures, respectively. This indicates a destructive influence of both dyes on the mesophase region, more efficient in the case of dye **2**. The stronger destabilization of the mesophase after addition of **2** is probably connected with repulsive steric interactions among the dye molecules and surrounding liquid crystal matrix due to the additional phenyl ring attached to the terminal group. It should be noticed that all the experimental points fit very well to the straight lines, which confirms a good solubility of the dyes investigated up to the molar fraction equal to 0.08.

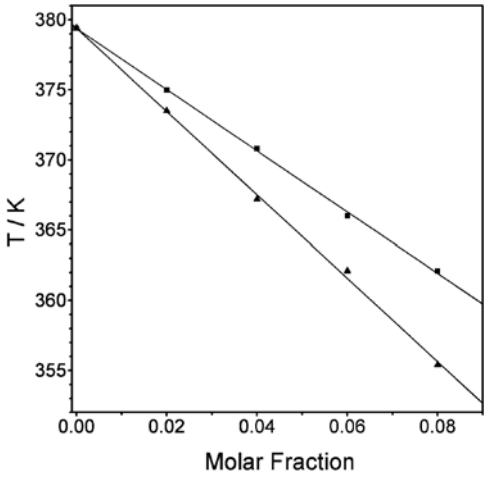

Fig. 4.37. Nematic–isotropic phase transition temperature as a function of dye molar fraction for PS6–**1** (*squares*) and PS6–**2** (*triangles*) mixtures. From [35], slightly modified

Figure 4.38 presents the DSC scans for pure PS6 and the PS6–**1** and PS6–**2** mixtures (molar fraction = 0.08) in the vicinity of the nematic–isotropic phase transition, obtained during heating the samples. It is seen, that the addition of the dye not only lowers the clearing temperature but causes also the broadening of the two-phase region, especially in the case of **2**. Analogous behaviour had been observed in the case of mixtures composed of low molecular mass

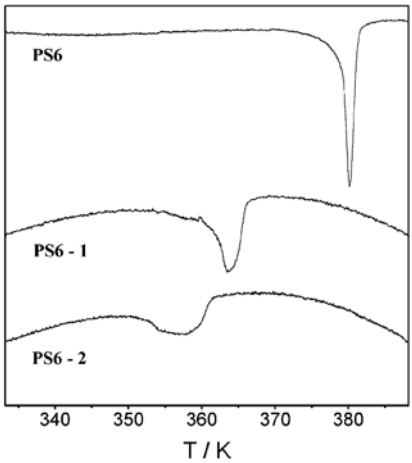

Fig. 4.38. DSC plots for pure PS6 and for PS6–**1** and PS6–**2** mixtures (molar fraction = 0.08) in the vicinity of the nematic–isotropic phase transition. From [35], slightly modified

Table 4.4. DSC data for pure PS6 and PS6–**1** and PS6–**2** mixtures (0.04 and 0.08 molar fraction)

Substance	T_{SN} (K)	ΔT_{SN} (K)	T_{NI} (K)	ΔT_{NI} (K)	ΔH_{SN} (J/g)	ΔH_{NI} (J/g)
PS6	312 (307)	2 (3)	380 (378)	1.5 (1)	0.2	2.3
PS6–**1** (0.04)	308	2.5	372 (369)	2 (2)	0.2	2.0
PS6–**1** (0.08)	303	3	364 (361)	3 (3)	0.2	1.7
PS6–**2** (0.04)	304	2.5	368 (366)	3 (3)	0.2	1.8
PS6–**2** (0.08)	297	3	357 (354)	5 (5)	0.2	1.6

liquid crystals and non-mesogenic dopants [40–48]. In Table 4.4 the DSC data for pure PS6 and its mixtures with the dyes are gathered. Because the smectic A–nematic and the nematic–isotropic phase transitions are relatively broad, the half-height widths of the respective DSC curve peaks, ΔT_{SN} and ΔT_{NI}, are given in the table apart from the mean transition temperatures, T_{SN} and T_{NI}. The transition enthalpies, ΔH_{SN} and ΔH_{NI}, are also presented. The values in the table were obtained during the heating and cooling (in parentheses) processes.

For mixtures, the nematic–smectic A transition temperature during the cooling process was very difficult to determine because of the low value of the enthalpy change. The transition temperatures for pure PS6, given here, are in good agreement with data found in the literature [1]. In the presence of the dye, not only the nematic–isotropic and the smectic A–nematic phase transition temperatures, but also the nematic–isotropic phase transition enthalpies decrease.

4.4.3 Dielectric relaxation

4.4.3.1 Experimental technique

The complex dielectric permittivity, $\varepsilon^* = \varepsilon' - i\varepsilon''$, was measured using a Hewlett–Packard 4192A self-balancing bridge controlled by a modified Atari Mega STII computer. The measurements were carried out in the frequency range from 100 Hz to 13 MHz at different temperatures between 295 K and 400 K. The temperature was stabilized by means of Eurotherm 818 with an accuracy better than ±0.05 K. The capacitor used in the dielectric experiments was constructed of two gold-coated glass plates separated by 100 µm spacers. The active area of the capacitor was 78 mm^2. The capacitor was filled with the test substance simply by placing it on one hot electrode and then squeezing it with the other one. Before starting the measurement of the frequency characteristics, the capacitor containing the polymer or the polymer doped with the dye was heated to 400 K and cooled down under action of

1 T magnetic field to orient macroscopically the sample homeotropically with respect to the electrodes and to stabilize the thickness of the spacers.

In order to obtain the values of the permittivity components of the oriented samples, the filled capacitor was placed in an electromagnet first in a position where the magnetic field $\boldsymbol{B}$ was parallel to the measuring electric field $\boldsymbol{E}$ ($\varepsilon_{\parallel}$) and then rotated so that $\boldsymbol{B}$ and $\boldsymbol{E}$ were orthogonal ($\varepsilon_{\perp}$). It was estimated that the overall uncertainty was 2 % for ε' and better than 5 % for ε''.

The imaginary parts of the electric permittivity were fitted by means of an interactive computer program with Fuoss–Kirkwood functions [49]

$$\varepsilon''(f) = \frac{\varepsilon''_{\max}}{\cosh[b \ln(f/f_R)]} , \tag{4.77}$$

where $\varepsilon''_{\max}$ is the amplitude of maximum loss, f_R is the frequency of maximum loss, and b is the parameter related to curve width, Δ, by $b = 1.14/\Delta$ (for Debye function $b = 1$). The conductivity term

$$\varepsilon''(f) = \sigma_0 f^{-n} \tag{4.78}$$

was incorporated in the fitting procedure ($n \approx 1$) too.

Figure 4.39 shows the three-dimensional plots of the dielectric loss of pure PS6 versus frequency and temperature for the cases $\boldsymbol{E} \parallel \boldsymbol{B}$ and $\boldsymbol{E} \perp \boldsymbol{B}$.

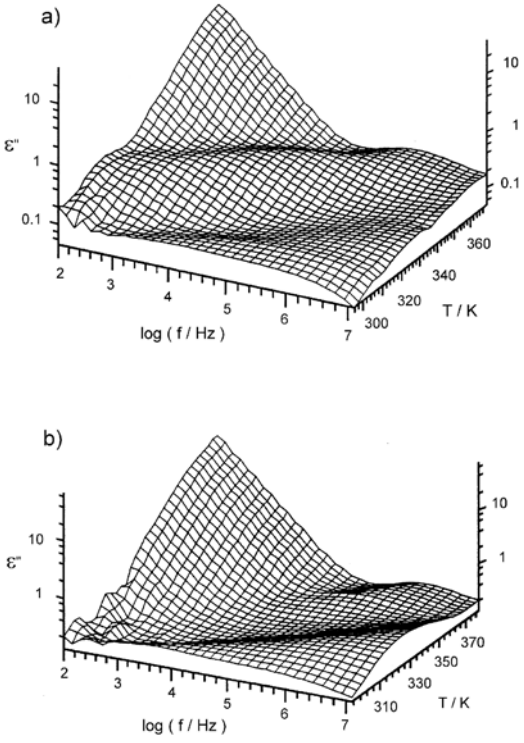

Fig. 4.39. Three dimensional plots of ε'' versus frequency and temperature for PS6: (**a**) $\boldsymbol{E} \parallel \boldsymbol{B}$ and (**b**) $\boldsymbol{E} \perp \boldsymbol{B}$. From [34], slightly modified

A pronounced difference in the relaxation behaviour for the parallel and perpendicular components of the dielectric permittivity can be seen from these plots indicating the good orientation of PS6 in the magnetic field used.

4.4.3.2 Dielectric relaxation in pure PS6

The dielectric spectra of liquid crystalline side-chain polymers appear to be more complex than those for low molecular weight mesogens. Apart from the relaxation processes due to the motions of the dipole moment of the mesogenic groups, the dielectric spectra typically contain two or more dispersion regions connected with the dynamics of the polymer main chain [10, 24]. According to the Nordio–Rigatti–Segre theory [50] as well as theory proposed by Araki et al. [23] and generalized by Kozak et al. [51], for low molecular weight calamitic LC four relaxation processes should be expected in the dielectric spectra. Two of them may be observed in the parallel component of the electric permittivity, $\varepsilon_{\parallel}$ and two in the perpendicular one, $\varepsilon_{\perp}$. Bormuth and Haase [22, 24, 26] proposed that in the case of side-chain LCPs the theoretical equations given in [23, 50, 51] need to be supplemented by a third term, which describes the backbone motions. Then, the dipole time correlation functions for directions parallel and perpendicular to the optical axis, which is parallel to $\boldsymbol{B}$, should be written as follows:

$$\langle \mu_{\parallel}(0)\mu_{\parallel}(t)\rangle = \frac{1}{3}[\mu_l^2(1+2S)\Phi_{00}(t) + \mu_t^2(1-S)\Phi_{01}(t) + \mu_h^2 f_{\parallel}(S)\Phi_h(t)], \tag{4.79a}$$

$$\langle \mu_{\perp}(0)\mu_{\perp}(t)\rangle = \frac{1}{3}[\mu_l^2(1-S)\Phi_{10}(t) + \mu_t^2\left(1+\frac{S}{2}\right)\Phi_{11}(t) + \mu_h^2 f_{\perp}(S)\Phi_h(t)], \tag{4.79b}$$

where μ_l and μ_t are, respectively, longitudinal and transverse components of the mesogenic group dipole moment, μ_h is the dipole moment of the backbone unit, S is the order parameter [52], $\Phi_{ij}(t)$ $(ij = 00, 01, 10, 11)$ describe the time dependence of different angular functions representing different relaxation modes, which involve the motions of the mesogenic group molecular axes in the Euler space [20, 25, 51], Φ_h is the correlation function arising from the main chain contributions [22, 24]. The third term with μ_h depends only slightly on S because the backbone is aligned rather randomly.

In the experiment, for pure side-chain LCPs, the δ-, α- and β-relaxation processes were observed [10, 20, 21, 25, 29]. The main relaxation process found in $\varepsilon_{\parallel}$ is δ-process [25], which is connected with 180° jumps on the long molecular axes of the mesogenic groups. Thus, it is due to motions of $\mu_{\parallel}$ and is described by the first term in (4.79a) (mode 00). The α-relaxation process is usually revealed both in the parallel and perpendicular components of ε and is assigned as the appropriate combinations of the processes described by the other terms in (4.79a) and (4.79b), differently weighted in the two orientations

with respect to $\boldsymbol{B}$ [26]. It is interpreted as superposition of the rotation of the mesogenic groups around their long molecular axes and the segmental motions of the main chain [21, 26]. The β-relaxation process is usually concerned with the intramolecular movement of the dipolar groups.

For the parallel component of the dielectric permittivity, $\varepsilon_{\parallel}$ of PS6 the numerically stable results were obtained at temperatures above 330 K, i.e. in the nematic and isotropic phases only. At lower temperatures the maximum loss frequency of the observed relaxation process was less than 1 kHz, and the amplitude was comparable to the apparatus noise in this region. Therefore, only the δ- and α-relaxation processes gave significant contributions to the relaxation observed in $\varepsilon_{\parallel}$ of PS6 in the frequency and temperature regions under consideration. As a consequence, the dielectric loss spectra of PS6 were fitted by taking a superposition of two Fuoss–Kirkwood functions, and an additional term for low frequency conductivity. The example at $T = 350$ K (nematic phase) is presented in Fig. 4.40. It is seen that the δ-relaxation process occurs at the frequency of two–three decades smaller than the adequate relaxation process in low molecular weight LCs [53]. Similar results were previously obtained for other LCPs [20–28]. This is of course connected with the higher viscosity of LCPs with respect to LCs, but an additional factor must be also taken into account. δ-Relaxation process cannot be, namely, described as a single particle process. Since the side chains are linked via flexible spac-

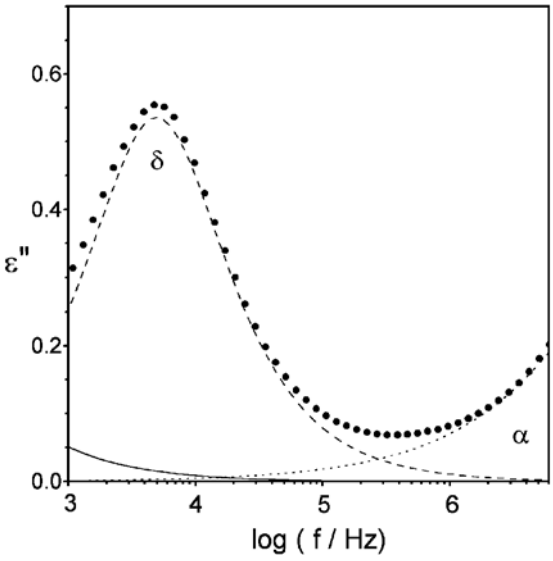

Fig. 4.40. Parallel component ($\boldsymbol{E} \parallel \boldsymbol{B}$) of the dielectric loss spectra of PS6 at $T = 350$ K. *Dashed* and *dotted curves* represent resolved δ- and α-relaxation processes, respectively, and *solid curve* is the conductivity component. From [35], slightly modified

ers to the backbone, the motions of the neighbouring chains are more or less correlated. The strong influence of the motions of the backbone itself should also not be neglected.

The δ-relaxation process is observed both in the nematic and isotropic phases, but the significant differences in the relaxation frequency (thus in the relaxation time) in these two states occur, similarly as it was found in the case of low molecular weight LCs [53]. Therefore the δ-process can be analyzed in terms of theory given by Martin, Meier and Saupe [54, 55]. They extended the Debye theory [56] of dielectric relaxation in isotropic liquids to the nematic LCs and showed that the relaxation time corresponding to the rotation around the short molecular axis in the presence of the nematic potential, $\tau(Q)$ is larger than that in the absence of the nematic potential, τ_0 by a factor:

$$g = \frac{\tau(Q)}{\tau_0} \,, \tag{4.80}$$

called the retardation factor. Here Q is the height of the potential barrier, and τ_0 is a hypothetical time, which can be obtained by extrapolation of temperature dependence of the rotational relaxation time in the isotropic phase ($Q = 0$) to a given temperature in the nematic phase. According to the Maier–Saupe mean field theory of nematics [57], the nematic potential has the following form:

$$U(\theta) = -QP_2(\cos\theta) \,, \tag{4.81}$$

where $P_2(\cos\theta)$ is the second Legendre polynomial and θ is the angle between the molecular long axis of LC and the direction of the orientation.

The intermolecular forces, leading to the potential barrier, cause the orientation of the LC molecules, and thus it is clear that there is a relationship between Q and the order parameter S. This order parameter is defined by [52]:

$$S = \langle P_2 \rangle = \frac{1}{2}\left(3\langle\cos^2\theta\rangle - 1\right) = \frac{\int_0^\pi [\frac{1}{2}(3\cos^2\theta - 1)] f(\theta)\sin\theta d\theta}{\int_0^\pi f(\theta)\sin\theta d\theta} \,, \tag{4.82}$$

where the angular brackets mean averaging over all possible orientations of the molecules in space. Here $f(\theta)$ is the undisturbed distribution function of the nematic order and can be presented in the form [54, 55]:

$$f(\theta) = f(0)\exp\left(-\frac{Q'}{k_B T}\sin^2\theta\right) \,. \tag{4.83}$$

On the basis of the retardation factor, g, calculated from the experimental data for PS6, the height of the potential barrier, Q ($Q' = 3/2\,Q$) and next $\langle P_2 \rangle$ as a function of temperature were determined. Figure 4.41 presents the dependence of $\langle P_2 \rangle$ on the reduced temperature $T^* = T/T_{NI}$.

In opposition to the parallel component, the fitting procedure for the perpendicular one was successful only at low temperatures (up to 310 K) giving

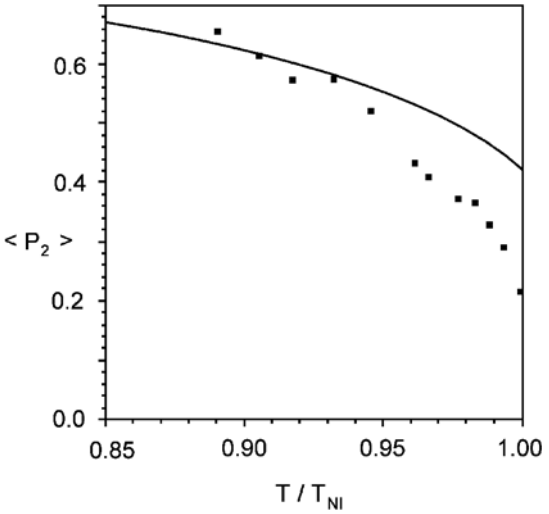

Fig. 4.41. Order parameter $\langle P_2 \rangle$ for PS6 versus reduced temperature. *Solid curve* represents $\langle P_2 \rangle$ from Maier–Saupe theory [57]. From [34], slightly modified

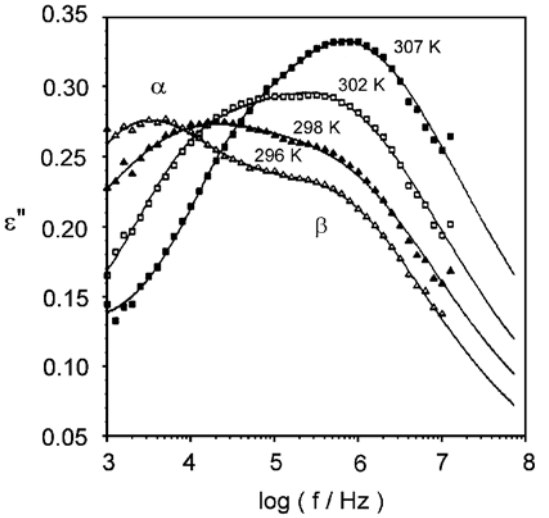

Fig. 4.42. Perpendicular component ($\boldsymbol{E} \perp \boldsymbol{B}$) of the dielectric loss spectra of PS6 between $T = 296\,\mathrm{K}$ and $T = 307\,\mathrm{K}$. Resolved α- and β-relaxation processes can be observed. From [34], slightly modified

the possibility to observe well-resolved α- and β-processes (Fig. 4.42). At higher temperatures (both in the liquid crystalline and isotropic phases) the fitting of the loss curve gave numerical instabilities in the values of the maximum frequency and the strength of the relevant relaxation processes.

4.4.3.3 Dielectric relaxation of PS6 doped with dichroic dye

The dielectric spectra of PS6 doped with dyes **1** or **2** could be analyzed only for the case $\boldsymbol{E} \parallel \boldsymbol{B}$ in the nematic phase. In the isotropic phase and in the case $\boldsymbol{E} \perp \boldsymbol{B}$ reasonable fitting was not possible because broad and asymmetric dielectric loss curves were obtained.

Figure 4.43 shows the dielectric loss spectra of two mixtures, PS6–**1** and PS6–**2** (molar fraction = 0.04) at $T = 350\,\mathrm{K}$.

An additional band with relaxation frequency of about one order of magnitude higher than the relevant frequency for the mesogenic groups of polymer is seen. The two separated processes were also observed by Kresse et al. [31, 32] in binary mixtures of side-chain LCP with low molecular weight LC. Because molecules of **1** and **2** are elongated in form and contain strongly polar terminal -NO_2 group, in analogy to low molecular weight LCs [53], one can suggest that the observed additional relaxation process is connected with the rotation of the dye molecules around their short axes. The azo dyes used are doped to PS6 at relatively small concentration, but reveal a pronounced relaxation strength in $\varepsilon_{\parallel}$ due to the strong contribution of the -NO_2 group to $\mu_{\parallel}$. However, the contributions of the -COO and -CH_3O groups of PS6 to $\mu_{\parallel}$ are small and therefore the dye relaxation dominates the spectrum. Moreover, the re-orientational motion of the dye molecules is not limited by the existence of chemical linkages to the polymer backbone. Thus, the relaxation

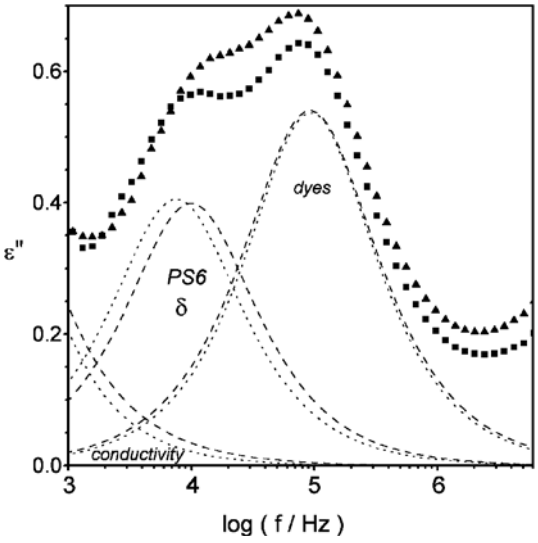

Fig. 4.43. Parallel components of the dielectric loss at $T = 350\,\mathrm{K}$ and the fitted with Fuoss–Kirkwood and conductivity curves for PS6–**1** (*squares, dotted curves*) and PS6–**2** (*triangles, dashed curves*) mixtures. The molar fraction of the dyes was equal to 0.04. From [35], slightly modified

of this process is only about one order of magnitude lower than the frequency of relaxation process connected with the rotation around the short axis in low molecular weight LCs [53].

From the results presented in Fig. 4.43 it is seen that both **1** and **2** influence the orientational order of the PS6 matrix: the shift of the relaxation frequency of δ-process towards higher values is observed, which means that **1** and **2** perturb the orientation of PS6. The shift of the relaxation frequency is greater in the case of PS6–**2** than PS6–**1**, which can be a result of an additional destructive influence of the terminal phenyl ring, linked to the stiff part of the molecule **2** via a flexible ethyl chain, on the ordering of the side groups of PS6. The same sequence of the destructive influence of **1** and **2** on the mesophase range was also observed in thermal behaviour, described in the previous section.

The relaxation frequencies and the amplitudes of the relaxation process related to **1** and **2** molecules in PS6 are almost identical. Similar values of amplitude result from the fact that the end phenyl ring in **2** does not contribute to the dipole moment, which originates mainly from the -NO_2 group.

The influence of concentration changes of **2** in PS6 on the parallel component of the dielectric loss spectra is presented in Fig. 4.44. The increase of the dye concentration from 0.04 to 0.08 molar fraction shifts both the relaxation frequency of the δ-process of the mesogenic groups and that connected with the rotation of the dye dipole moment to higher values. The amplitude of the dye dielectric loss rises about two times after doubling the molar fraction of the dopant. The increase of the relaxation frequency for both processes are at least a result of the perturbation of the nematic order, caused by the addi-

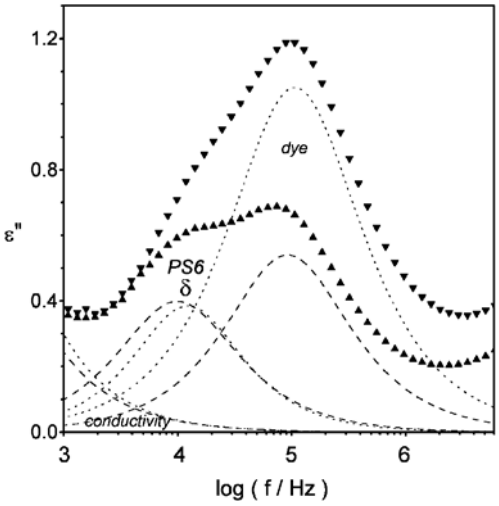

Fig. 4.44. Parallel components of the dielectric loss and the fitting curves for PS6–**2** mixtures at $T = 350$ K. The molar fraction of the dye were equal to 0.04 (*up triangles, dashed curves*) and 0.08 (*down triangles, dotted curves*). From [35], slightly modified

tional amount of dye molecules in the mixture. The decrease of the viscosity of the mixture due to an additional amount of the low molecular weight dopant should be also taken into account.

4.4.3.4 Dielectric relaxation parameters

Figure 4.45 presents temperature dependencies of the fitting parameters obtained by using (4.77).

The data were obtained for pure PS6 in the nematic and isotropic phases and for mixtures: PS6–**1** (molar fraction = 0.04) and PS6–**2** (molar fractions = 0.04 and 0.08) in the nematic phase. All the data are related to the parallel orientation of the samples $\boldsymbol{E} \parallel \boldsymbol{B}$. Also the intensity, described by the area under the fitting curve, equal to $\pi\varepsilon''_{\max}/b$, could be analyzed, but in the case when the half-height widths of the fitting curves are similar to each other, the temperature dependencies of the amplitude and intensity differ only by a constant factor. This is so in the present case.

The relation between $\log f_R$ and T^{-1}, given in Fig. 4.45a, is in agreement with the Arrhenius law:

$$f_R = h \exp\left(-\frac{W}{k_B T}\right) , \tag{4.84}$$

where W is the energy barrier for the dipole relaxation (activation energy) and h is the constant parameter characteristic for a particular relaxation process. The Arrhenius-like behaviour is typical for dielectric relaxation processes in the nematic phase. The reorientation around the short axis of the dye molecules in PS6 is also described by the Arrhenius formula. The activation energies of the relaxation processes are given in Table 4.5.

Table 4.5. Activation energy of the dielectric relaxation processes observed in parallel geometry of experiment for pure PS6 and PS6–**1** and PS6–**2** mixtures ($\Delta W = \pm 2$ kJ/mol)

Substance	W (kJ/mol)		
	Isotropic Phase	Nematic Phase	
		δ-Relaxation	Relaxation of Dye
PS6	72	113	–
PS6–**1** (0.04)	–	112	97
PS6–**2** (0.04)	–	113	108
PS6–**2** (0.08)	–	112	105

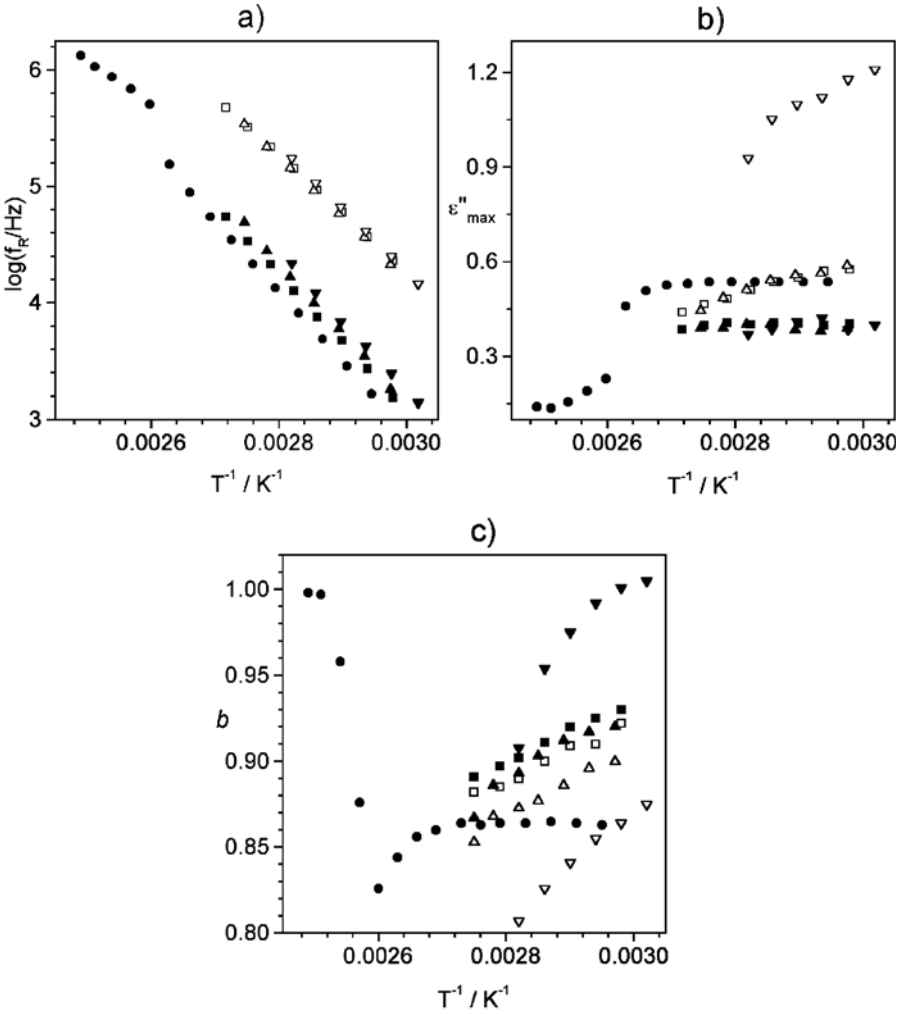

Fig. 4.45. Logarithm of frequency of the maximum loss (**a**), amplitude of the maximum loss (**b**), and b parameter (**c**) as a function of reciprocal temperature calculated for the Fuoss–Kirkwood functions for pure PS6 (*circles*), PS6–**1**–0.04 (*squares*), PS6–**2**–0.08 (*up triangles*), and PS6–**2**–0.08 (*down triangles*) mixtures. *Solid symbols* describe δ-relaxation process, the *open symbols* – relaxation of dye around the short molecular axis. The errors do not exceed the following values: $\Delta \log f_R / \log f_R = 0.01$, $\Delta\varepsilon''_{\max}/\varepsilon''_{\max} = 0.05$, $\Delta b/b = 0.05$. From [35], slightly modified

It is seen that the activation energy of the δ-relaxation process for pure PS6 remains almost unchangeable after addition of the dye to the matrix. The activation energy of the dye relaxation process depends on the type of the terminal group, and is slightly larger for **2** than for **1**.

Figures 4.45b and 4.45c present, respectively, the amplitudes and b parameters, describing the shape of the fitted Fuoss–Kirkwood curves. It can be seen that for the δ-relaxation process in pure PS6 in the nematic phase these parameters are independent of temperature. Such a behaviour was also observed previously for the low-frequency relaxation in aligned side-chain LCPs [20]. The reduction of the amplitude and the increase of the b parameter up to the values comparable to 1 (Debye-type relaxation), observed for PS6 above clearing temperature, are also typical for the isotropic phase.

In PS6–**1** and PS6–**2** mixtures, a weak tendency of broadening the absorption band describing the δ-process with an increase of temperature is observed. As for pure PS6, the amplitude of δ-relaxation in PS6–**1** and PS6–**2** mixtures is constant in the mesophase. Moreover, the amplitude of this process is less in mixtures than in pure PS6, and, at concentrations used, it is almost independent of the type of the dye terminal group and the concentration of the dopant. Contrary to the amplitude, the b parameter increases with dye concentration, and a tendency towards Debye-type absorption is observed.

Both the amplitude and b parameter calculated for the dye dielectric loss band decrease with the increase of temperature. This effect is typical for low molecular weight LCs [53]. The amplitude and the width of the dye relaxation band depend not only on the temperature but also on the concentration of the dye. On the other hand, these parameters are practically independent on the terminal group (hydrogen atom or phenyl ring).

4.4.4 Summary and conclusions

In this section, the dielectric properties of a liquid crystalline siloxane polymer with weak electric dipole moment and the mixture of this polymer with azo dyes having strong dipole moment connected with the terminal -NO_2 group were described. The dye molecules were similar in size and geometrical shape to the mesogenic side groups of the polymer. The flexible ethyl chains attached at the end of the dye molecules allowed good solubility of these compounds into the polymer matrix. Introduction of the non-mesogenic dyes into the liquid crystalline polymer resulted in decreasing the phase transition temperatures and broadening the two-phase region between the nematic and isotropic phases.

Magnetic field of about $1\,T$ gave good homeotropic alignment of both the mesogenic groups and the dye molecules with respect to the capacitor electrodes. This was reflected in the dielectric spectra obtained for two different geometries of the experiment ($\boldsymbol{E} \parallel \boldsymbol{B}$ and $\boldsymbol{E} \perp \boldsymbol{B}$). The spectra of the mixtures, measured in parallel geometry, were composed of three relaxation bands, but the relaxation frequency of the dielectric loss maximum was observed in the frequency range of the measurement only for two of them. The process with the lowest relaxation frequency was attributed to the δ-relaxation process of the mesogenic groups. The second process, separated from the previous one by about one decade, was interpreted as reorientation of the dye permanent

electric dipole moment around the short molecular axis. The α-relaxation process was only partially observed near the upper frequency limit of the bridge used, and it was not possible to be analyzed.

The relation between the frequency of the maximum dielectric loss, measured for parallel geometry, and the reciprocal temperature satisfies the Arrhenius law both for the δ-process and the relaxation process of the dye. At a given temperature, the relaxation frequency of the δ-process was increased in the presence of the dissolved dye. The relaxation frequency of the dye dipole moment was independent of the terminal group. The amplitude of the δ-process in pure PS6 and PS6–**1** and PS6–**2** mixtures in the mesophase was found to be independent of temperature, whereas for the dye relaxation process, the amplitude decreased with an increasing temperature. A good separation of the bands indicated that the dye molecules and the mesogenic groups relaxed separately. On the other hand, the dye molecules were well oriented in the polymer matrix, which indicates the sensitivity of these non-mesogenic dopants to the nematic potential.

The authors wish to thank Professor Dr. Wolfgang Haase for the opportunity to record dielectric spectra in the Institute of Physical Chemistry, Darmstadt University of Technology, Germany and for fruitful discussion.

References

1. H. Finkelmann, G. Rehage: Adv. Polym. Sci. **60/61**, 99 (1984)
2. V.P. Shibaev, N.A. Plate: Adv. Polym. Sci. **60/61**, 173 (1984)
3. L.L. Chapoy: *Recent Advances in Liquid Crystalline Polymers* (Elsevier, London 1985)
4. A. Blumstein: *Polymeric Liquid Crystals* (Plenum, New York 1985)
5. C.B. McArdle: *Side-Chain Liquid Crystal Polymers* (Blackie, Glasgow 1989)
6. P.J. Collings: *Liquid Crystals*, Chap. 9 (Princeton University Press, Princeton, New Jersay 1990)
7. A. Ciferri: *Liquid Crystallinity in Polymers. Principal and Fundamental Properties* (VCH, Weinheim 1991)
8. A.M. Donald, A.H. Windle: *Liquid Crystalline Polymers* (Cambridge University Press, Cambridge 1992)
9. N.A. Plate: *Liquid Crystal Polymers* (Plenum, New York 1993)
10. R. Zentel: 'Liquid Crystalline Polymers'. In: *Liquid Crystals*, ed. by H. Stegemeyer (Steinkopff, Darmstadt, Springer, New York 1994) pp. 103–141
11. V.P. Shibaev, L. Lam: *Liquid Crystalline and Mesomorphic Polymers* (Springer, New York 1994)
12. V.D. Neff: 'Infrared, Raman, Visible and Ultraviolet Spectroscopy of Liquid Crystals'. In: *Liquid Crystals and Plastic Crystals*, Vol. 2, ed. by G.W. Gray, P.A. Winsor (Ellis Horwood Ltd., Chichester 1974) pp. 231–253
13. G.H. Heilmeier, L.A. Zanoni: Appl. Phys. Lett. A **13**, 91 (1968)
14. D. Bauman, E. Wolarz: Mol. Cryst. Liq. Cryst. Lett. **7**, 161 (1990)
15. E. Wolarz, D. Bauman: J. Polym. Sci. Polym. Phys. **31**, 383 (1993)
16. E. Wolarz, D. Bauman: Liq. Cryst. **19**, 221 (1995)

17. G.R. Möhlmann, C.P.J.M. van der Vorst: 'Side Chain Liquid Crystal Polymers as Optically Nonlinear Media'. In: *Side-Chain Liquid Crystal Polymers*, ed. by C.B. McArdle (Blackie, Glasgow 1989) pp. 330–356
18. J. Cognard, T. Hieu Phan: Mol. Cryst. Liq. Cryst. **68**, 207 (1981)
19. F. Ciardelli, C. Carlini, R. Solaro, A. Altomare, O. Pieroni, J.L. Houben, A. Fissi: Pure Appl. Chem. **56**, 329 (1984)
20. G.S. Attard: Mol. Phys. **58**, 1087 (1986)
21. G.S. Attard, G. Williams: Liq. Cryst. **1**, 253 (1986)
22. F.-J. Bormuth, W. Haase: Mol. Cryst. Liq. Cryst. **153**, 207 (1987)
23. K. Araki, G.S. Attard, A. Kozak, G. Wiliams, G.W. Gray, D. Lacey, G. Nestor: J. Chem. Soc., Faraday Trans. II **84**, 1067 (1988)
24. F.-J. Bormuth, W. Haase: Liq. Cryst. **5**, 1849 (1989)
25. C.M. Haws, M.G. Clark, G.S. Attard: 'Dielectric Relaxation Spectroscopy of Liquid Crystalline Side Chain Polymers'. In: *Side-Chain Liquid Crystal Polymers*, ed. by C.B. McArdle (Blackie, Glasgow 1989) pp. 196–223
26. W. Haase, F.-J. Bormuth: 'The Significance of Dielectric Relaxation Processes and Switching Properties for Data Storage in Liquid Crystal Polymer Media'. In: *Polymers in Information Storage Technology*, ed. by K.L. Mittal (Plenum Press, New York 1990) pp. 51–65
27. W. Haase, F.-J. Bormuth, M. Pfeiffer, E. Jakob: Ber. Bunsenges. Phys. Chem. **95**, 1050 (1991)
28. G. Williams: 'Dielectric Relaxation of Liquid Crystals'. In: *The Molecular Dynamics of Liquid Crystals*. ed. by G.R. Luckhurst, C.A. Veracini (Kluver Academic Publishers, Dordrecht 1994) pp. 431–450
29. H. Pranoto, F.-J. Bormuth, W. Haase, U. Kiechle, H. Finkelmann: Makromol. Chem. **187**, 2453 (1986)
30. E. Jakob, F.-H. Kreuzer, N. Haeberle, D. Kilian, W. Haase: J. Mater. Chem. **6**, 935 (1996)
31. H. Kresse, S.G. Kostromin, V.P. Shibaev: Liq. Cryst. **6**, 333 (1989)
32. H. Kresse, H. Stettin, S.G. Kostromin, V.P. Shibaev: Mol. Cryst. Liq. Cryst. **178**, 1 (1990)
33. H. Seiberle, W. Stille, G. Strobl: Macromolecules **23**, 2008 (1990)
34. E. Jakob, E. Wolarz, E. Białecka-Florjańczyk, D. Bauman, W. Haase: Mol. Cryst. Liq. Cryst. **258**, 253 (1995)
35. E. Wolarz, D. Kilian, W. Haase, D. Bauman: J. Polym. Sci. Polym. Phys. **37**, 369 (1999)
36. V.P. Shibaev, Ya.S. Freidzon, S.G. Kostromin: 'Molecular Architecture and Structure of Thermotropic Liquid Crystal Polymers with Mesogenic Side Groups'. In: *Liquid Crystalline and Mesomorphic Polymers*, ed. by V.P. Shibaev, L. Lam (Springer, New York 1994) pp. 77–120
37. H. Finkelmann, G. Rehage: Makromol. Chem. Rapid Commun. **1**, 31 (1980)
38. E. Chrzumnicka, D. Bauman, J. Jadżyn: Acta Phys. Polon. A **102**, 767 (2002)
39. D.E. Martiré: 'Thermodynamics of Phase Transitions'. In: *The Molecular Physics of Liquid Crystals*, ed. by G.R. Luckhurst, G.W. Gray (Academic Press, London 1979) pp. 221–261
40. G.A. Oweimreen, D.E. Martiré: J. Chem. Phys. **72**, 2500 (1980)
41. P. Diot, J.K. Foitzik, W. Haase: Phys. Rev. Appl. **20**, 121 (1985)
42. W. Haase, O. Trinquet, U. Quotschalla, J.K. Foitzik: Mol. Cryst. Liq. Cryst. **148**, 15 (1987)

43. D. Bauman: Mol. Cryst. Liq. Cryst. **159**, 197 (1988)
44. D. Bauman: Mol. Cryst. Liq. Cryst. **174**, 1 (1989)
45. D. Bauman, H. Moryson, J. Jadżyn: Acta Phys. Polon. A **85**, 553 (1994)
46. D. Bauman, T. Martyński, E. Mykowska: Liq. Cryst. **18**, 607 (1995)
47. D. Bauman, A. Wąsik, J. Jadżyn: Liq. Cryst. **20**, 195 (1996)
48. D. Bauman, J. Solczyński, E. Chrzumnicka: Acta Phys. Polon. A **92**, 1151 (1997)
49. F.M. Fuoss, J.G. Kirkwood: J. Am. Chem. Soc. **63**, 385 (1941)
50. P.L. Nordio, R. Rigatti, U. Segre: Mol. Phys. **25**, 129 (1973)
51. A. Kozak, J.K. Mościcki, G. Williams: Mol. Cryst. Liq. Cryst. **201**, 1 (1991)
52. V. Zwetkoff: Acta Phys. USSR **10**, 557 (1939)
53. H. Kresse: 'Dielectric Behavior of Liquid Crystals'. In: *Advances of Liquid Crystals*, ed. by G.H. Brown (Academic Press, New York 1983) pp. 109–172
54. A.J. Martin, G. Meier, A. Saupe: Symp. Faraday Soc. **5**, 119 (1971)
55. G. Meier, A. Saupe: 'Dielectric Relaxation in Nematic Liquid Crystals'. In: *Liquid Crystals*, ed. by G.H. Brown, G.J. Dienes, M.M. Labes (Gordon and Breach Science Publishers, New York 1967) pp. 195–205
56. P. Debye: *Polar Molecules* (Chemical Catalogue Co., New York 1929)
57. W. Maier, A. Saupe: Z. Naturforsch. A **14**, 882 (1960); **15**, 287 (1960)

5

Ferro- and Antiferroelectric Liquid Crystals

5.1 Modeling of ferroelectric and antiferroelectric liquid crystals

B. Žekš and M. Čepič

5.1.1 Introduction

In this section a historical overview will be presented of the development of phenomenological theoretical models of ferroelectric and antiferroelectric liquid crystals. In Sect. 5.1.2 the two order parameters of ferroelectric smectic C* (Sm C*) liquid crystals will be introduced, which are the tilt of long axes of molecules from the normal to the smectic layers and the in-plane electric polarization, that corresponds to the ordering of molecules transverse to their long axes. The phenomenological models of ferroelectric liquid crystals (FLC) will be presented, that correspond to the Landau expansion of the free-energy density in the tilt and the polarization order parameters. An extension of the phenomenological model of FLC will also be demonstrated, that includes as the additional order parameter the transverse quadrupolar ordering and that describes some anomalies of FLC's, that cannot be accounted by the model with only two order parameters. In these models the layered structure of smectic liquid crystals is not explicitly taken into account and the same is true for the phenomenological models of antiferroelectric liquid crystals (AFLC), that are presented and described in Sect. 5.1.3. Such models cannot describe all existing phases in AFLC and therefore discrete models of AFLC's were introduced, which take explicitly smectic layers into account and assume some inter-layer interactions , which must have longer range then only between nearest neighboring layers. Discrete models are described in Sect. 5.1.4 , while in Sect. 5.1.5 the nature and the structure of the inter-layer interactions is presented together with possible phases predicted by such models.

5.1.2 Phenomenological models of ferroelectric liquid crystals

Ferroelectric smectic liquid crystals were discovered by R.B. Meyer and coworkers [1, 2] in 1975. This discovery was theoretically predicted by using symmetry arguments. In the high temperature paraelectric phase, which is the smectic A (Sm A) phase the elongated molecules are arranged in smectic layers and are on the average oriented with their long axes perpendicular to the smectic layers. There is no head-to-tail ordering of molecules, which means that the same number of molecules are pointing in both directions perpendicular to the smectic layers and consequently there is no longitudinal polarization (i.e. perpendicular to smectic layers). As the molecules are in axially symmetric position, there is also no transverse polarization and the Sm A phase is apolar, for chiral as well as for achiral molecules. By lowering the temperature, at the transition temperature T_c the molecules tilt with their long axes away from the normal to the smectic layers and the Sm A phase transforms into the tilted smectic C (Sm C, for achiral molecules) or to the chiral smectic C* phase (Sm C*, for chiral molecules). For achiral molecules, in the Sm C phase, the tilt breaks the axial symmetry around the long axis of the molecule, but the tilt plane (the plane formed by the normal to the smectic layers and the long axes of the tilted molecules) remains the mirror symmetry plane. Consequently, the symmetry is apolar and the transverse polarization does not exist. Or in other words: The tilt in the Sm C phase does not induce polarization. In the chiral system, i.e. in the Sm C* phase, the tilt breaks the mirror plane symmetry of the tilt plane, the two directions perpendicular to the tilt plane are not equivalent and the transverse polarization exists. In the Sm C* phase, the tilt induces the polarization and the phase is ferroelectric. It is an improper ferroelectric, because the primary order parameter of the Sm A↔Sm C* phase transition is the tilt, that only induces the secondary order parameter – the polarization. In the achiral Sm C phase the tilt is homogeneous, while in the chiral Sm C* phase the direction of the tilt changes a little from one smectic layer to another and a helicoidal tilted structure is obtained. Locally, in each smectic layer the polarization is perpendicular to the tilt and it also forms a helix.

The tilt order parameter must give the magnitude and the direction of the tilt and is therefore a two-component order parameter

$$\boldsymbol{\xi} = (\xi_x, \xi_y). \tag{5.1}$$

The tilt vector $\boldsymbol{\xi}$ is the projection of the local average unit vector $\boldsymbol{n}$ that points along the long molecular axis, to the plane of smectic layers, i.e. on the xy plane if the z-axis of the coordinate system is perpendicular to the smectic layers. ξ_x and ξ_y are the components of the tilt vector in the x- and y-direction, respectively and are related to the magnitude of the tilt vector (θ), and to the phase of the tilt (ϕ) as (Fig. 5.1):

$$\xi_x = \theta \cos\phi, \tag{5.2a}$$

$$\xi_y = \theta \sin\phi. \tag{5.2b}$$

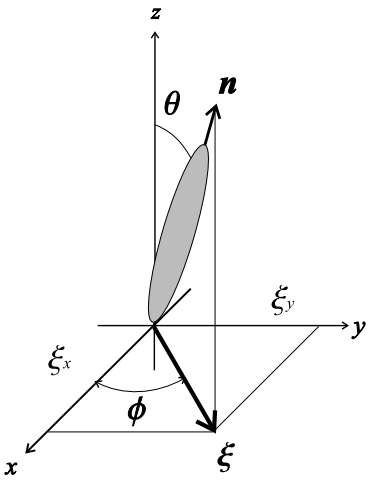

Fig. 5.1. The tilt order parameter $\boldsymbol{\xi} = (\xi_x, \xi_y)$ is the projection of the director given by the unit vector $\boldsymbol{n}$ along the long molecular axis on the xy plane. The $\boldsymbol{n}$ associated with the "average" molecule on the picture schematically represents the director

These expressions are valid for small tilt angles, when $\sin\theta \approx \theta$. The secondary order parameter, i.e. the transverse polarization, is also a two-component vector with the components in x and y directions

$$\boldsymbol{P} = (P_x, P_y). \tag{5.3}$$

In the vicinity of the Sm A↔Sm C* phase transition, the non-equilibrium free energy density G can be expanded in terms of the invariants of the symmetry operations of the chiral Sm A phase [3, 4].

$$\begin{aligned} G = G_A &+ \frac{1}{2}a\left(\xi_x^2 + \xi_y^2\right) + \frac{1}{4}b\left(\xi_x^2 + \xi_y^2\right)^2 \\ &- \Lambda\left(\xi_x\frac{d\xi_y}{dz} - \xi_y\frac{d\xi_x}{dz}\right) + \frac{1}{2}K_3\left[\left(\frac{d\xi_x}{dz}\right)^2 + \left(\frac{d\xi_y}{dz}\right)^2\right] \\ &+ \frac{1}{2\epsilon}\left(P_x^2 + P_y^2\right) + c_p\left(P_x\xi_y - P_y\xi_x\right) - \mu_c\left(P_x\frac{d\xi_x}{dz} + P_y\frac{d\xi_y}{dz}\right). \end{aligned} \tag{5.4}$$

Here G_A is the free energy density of the Sm A phase. The system is considered to be homogeneous in the xy plane and the two order parameters $\boldsymbol{\xi}$ and $\boldsymbol{P}$ can be different in different smectic layers and therefore depend on the coordinate z. The coefficient a is temperature dependent ($a = \alpha(T - T_0)$) as the tilt $\boldsymbol{\xi}$ is the primary order parameter.

At higher temperatures T, a is positive and the minimum of G corresponds to $\boldsymbol{\xi} = 0$, i.e. to the Sm A phase. At lower T the Sm A phase becomes unstable with respect to $\boldsymbol{\xi}$ and the system transforms into the tilted phase. The Lifshitz term Λ, that is different from zero only in chiral systems, tends to distort the homogeneously tilted structure and produces a helicoidal deformation, that is stabilized by the elastic term K_3. The harmonic term in the polarization

$(1/\epsilon)$ is always positive, as $\boldsymbol{P}$ is the secondary order parameter that does not cause the instability. There are two bilinear coupling terms between the tilt and the polarization. The c_p-term is the piezoelectric coupling that produces the polarization perpendicular to the tilt plane. The coefficient c_p is chiral, i.e. it is different from zero only in chiral systems. The flexoelectric coupling term (μ_c) is achiral and describes the coupling of polarization and tilt that changes when going from one smectic layer to another. For simplicity, the above expansion does not include derivative terms in the polarization, which seems to be consistent with the secondary order parameter role of the polarization. But with this assumption one neglects the polarization inter-layer interactions, which can be important in some cases, as it will be shown later.

Minimization of the free energy (5.4) with respect to the two order parameters – the tilt $\boldsymbol{\xi}$ and the polarization $\boldsymbol{P}$ – leads to the second order phase transition between the high temperature Sm A phase ($\boldsymbol{\xi} = 0, \boldsymbol{P} = 0$) and the low temperature helicoidal ferroelectric Sm C* phase with

$$\xi_x = \theta \cos(q_c z), \qquad \xi_y = \theta \sin(q_c z), \tag{5.5a}$$

$$P_x = -P \sin(q_c z), \qquad P_y = P \cos(q_c z), \tag{5.5b}$$

where the critical wave vector of the instability of the Sm A phase is temperature independent

$$q_c = \frac{\Lambda + \epsilon \mu_c c_p}{K_3 - \epsilon \mu_c^2}, \tag{5.6}$$

while the transition temperature T_c is given as

$$T_c = T_0 + \frac{1}{\alpha} \left[\epsilon c_p^2 + (K_3 - \epsilon \mu_c^2) q_c^2 \right] \tag{5.7}$$

and the magnitudes of the polarization P and of the tilt θ are strictly proportional

$$P = \epsilon \left(c_p + \mu_c q_c \right) \theta, \tag{5.8}$$

where the temperature dependence of the tilt θ is given simply as

$$\theta = \sqrt{\frac{\alpha}{b} (T_c - T)}. \tag{5.9}$$

In the limit of achiral systems, Λ and c_p go to zero and therefore $q_c \to 0$ (5.6), i.e. the helicoidal structure unwinds into homogeneously tilted one without polarization ($P = 0$ from (5.8)).

The obtained relations and temperature dependencies qualitatively agree with experimental data. But there are some systematic discrepancies [5].

- The ratio P/θ is not temperature independent (as predicted by (5.8)) but has been found to be strongly temperature dependent in a 1 K temperature interval below T_c.
- The period of the helix $2\pi/q_c$ is not temperature independent (as predicted by (5.6)) but shows a strong temperature dependence in a 1 K temperature interval below T_c.
- The electric susceptibility is expected to be small and constant below T_c, but experiments reveal a large dielectric susceptibility and a strong temperature dependence.

Such relatively narrow cross-over effects in the interval of 1 K close to the transition cannot be described by simply adding higher order terms in the free energy density expansion (5.4) and must be related to the existence of two physically different regimes. It has been shown [6] that the quadrupolar transverse ordering can account for these cross-over effects. Quadrupolar transverse ordering is not a chiral property of the system, because the tilt induces quadrupolar transverse ordering also in achiral systems and the magnitude of the ordering is not small and is proportional to θ^2. Comparing this to the dipolar order, which is proportional to θ, one can see that close to T_c (small θ) the quadrupolar order is negligible, but already relatively near to T_c ($\sim$ 1 K away) quadrupolar order becomes significant and the effects of chiral coupling, that produces the polarization, are stronger.

5.1.3 Phenomenological models of antiferroelectric liquid crystals

The antiferroelectric order in liquid crystals was first observed in MHPOBC in 1989 [7], although the first antiferroelectric liquid crystalline material was synthesized already in 1983 [8]. The antiferroelectric chiral smectic phase (Sm C^*_A) is a tilted smectic phase, where the tilt directions alternate from one layer to another between two opposite directions. Consequently, also the induced in-plane polarization alternates between two opposite directions and two neighboring layers form therefore an antiferroelectric unit cell (Fig. 5.2). Because of chirality there is a small deviation from the 180° alteration in the tilt (and in the polarization) between the consecutive layers and a modulated, helicoidal structure appears, formed by two ferroelectric helices gearing into each other antiferroelectrically.

The antiferroelectric Sm C^*_A phase is only one phase in a temperature sequence of phases in materials like MHPOBC which are therefore called antiferroelectric liquid crystals (AFLCs). In MHPOBC, for example, the sequence observed[7, 9] by lowering temperature was Sm A$\leftrightarrow$Sm $C^*_\alpha\leftrightarrow$Sm $C^*\leftrightarrow$Sm C^*_γ $\leftrightarrow$Sm C^*_A. Here we see between the Sm A phase and the ferroelectric Sm C^* phase and between the Sm C^* phase and the antiferroelectric Sm C^*_A phase intermediate phases Sm C^*_α and Sm C^*_γ, the structure of which was not known in 1989 at the time of discovery of antiferroelectricity in liquid crystals. It was only evident that they display neither ferroelectric nor antiferroelectric

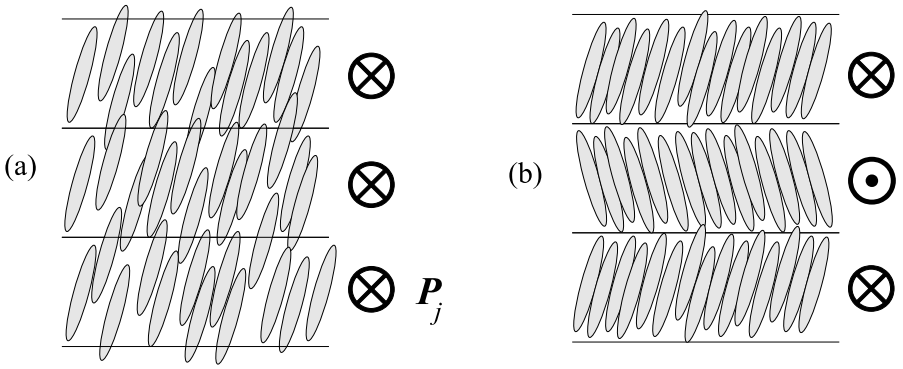

Fig. 5.2. Tilt and polarization in the (**a**) ferroelectric Sm C* and (**b**) in the antiferroelectric Sm C$^*_A$ phase (neglecting a helicoidal modulation)

properties but a combination of both, i.e. they are ferrielectric. Because the largest unit cell of known structures in the above phase sequence was composed of two smectic layers also the first theoretical attempts to describe antiferroelectric liquid crystals started with the supposition that all AFLC structures are bilayer structures. Orihara and Ishibashi [10] have defined the ferroelectric order parameter

$$\boldsymbol{\xi}_f = \frac{1}{2}\left(\boldsymbol{\xi}_j + \boldsymbol{\xi}_{j+1}\right) \tag{5.10}$$

and the antiferroelectric order parameter

$$\boldsymbol{\xi}_a = \frac{1}{2}\left(\boldsymbol{\xi}_j - \boldsymbol{\xi}_{j+1}\right), \tag{5.11}$$

which are the sum and the difference of the tilt vectors in the two neighboring smectic layers. Analogously, the ferroelectric polarization

$$\boldsymbol{P}_f = \frac{1}{2}\left(\boldsymbol{P}_j + \boldsymbol{P}_{j+1}\right) \tag{5.12}$$

and the antiferroelectric polarization

$$\boldsymbol{P}_a = \frac{1}{2}\left(\boldsymbol{P}_j - \boldsymbol{P}_{j+1}\right) \tag{5.13}$$

were introduced as a secondary order parameters, where $\boldsymbol{P}_j$ is the in-plane polarization of the j-th layer.

The free energy density of antiferroelectric liquid crystals can be obtained within this approximation of bilayer structures as an expansion in scalar invariants formed by the above order parameters

$$
\begin{aligned}
G = G_A &+ \frac{1}{2}a_a\boldsymbol{\xi}_a^2 + \frac{1}{4}b_a\boldsymbol{\xi}_a^4 + \Lambda_a\left(\xi_{ax}\frac{d\xi_{ay}}{dz} - \xi_{ay}\frac{d\xi_{ax}}{dz}\right) + \frac{1}{2}K_{3a}\left(\frac{d\boldsymbol{\xi}_a}{dz}\right)^2 \\
&+ \frac{1}{2}a_f\boldsymbol{\xi}_f^2 + \frac{1}{4}b_f\boldsymbol{\xi}_f^4 + \Lambda_f\left(\xi_{fx}\frac{d\xi_{fy}}{dz} - \xi_{fy}\frac{d\xi_{fx}}{dz}\right) + \frac{1}{2}K_{3f}\left(\frac{d\boldsymbol{\xi}_f}{dz}\right)^2 \\
&+ \frac{1}{2}\gamma_1\,\xi_a^2\xi_f^2 + \frac{1}{2}\gamma_2\,(\boldsymbol{\xi}_a\cdot\boldsymbol{\xi}_f)^2 \\
&+ \frac{1}{2\epsilon_a}P_a^2 + C_a\,(P_{ax}\xi_{ay} - P_{ay}\xi_{ax}) - \mu_a\left(P_a\cdot\frac{d\boldsymbol{\xi}_a}{dz}\right) \\
&+ \frac{1}{2\epsilon_f}P_f^2 + C_f\,(P_{fx}\xi_{fy} - P_{fy}\xi_{fx}) - \mu\left(P_f\cdot\frac{d\boldsymbol{\xi}_f}{dz}\right),
\end{aligned}
\tag{5.14}
$$

which is a simple generalization of the (5.4). Here it is assumed, that only the coefficients a_a and a_f are temperature dependent as

$$a_f = \alpha_f(T - T_f^0), \tag{5.15a}$$

$$a_a = \alpha_a(T - T_a^0). \tag{5.15b}$$

Here T_f^0 and T_a^0 are the transition temperatures from the Sm A phase to the homogeneous ferroelectric and antiferroelectric phase, respectively.

Possible phases obtained by the minimization of the above free energy include the helicoidal ferroelectric phase Sm C*, where $\boldsymbol{\xi}_a = 0, \boldsymbol{P}_a = 0$ and $\boldsymbol{\xi}_f \neq 0, \boldsymbol{P}_f \neq 0$, and the helicoidal antiferroelectric phase Sm C$_A^*$, where $\boldsymbol{\xi}_f = 0, \boldsymbol{P}_f = 0$ and $\boldsymbol{\xi}_a \neq 0, \boldsymbol{P}_a \neq 0$. The model predicted other two phases, where all order parameters are different from zero and the phases are therefore ferrielectric distorted bilayer structures [11, 12]. These phases were for some time possible candidates for the observed intermediate phases between Sm A, Sm C* and Sm C$_A^*$: Sm C$_\alpha^*$, Sm C$_\gamma^*$, Sm C$_{AF}^*$, Sm C$_{FIH}^*$, Sm C$_{FIL}^*$, but it was shown later [13] by the resonant X-ray scattering technique that the intermediate phases have larger periodicity (3-, 4- or more smectic layers) and therefore cannot be described by bilayer models.

5.1.4 Discrete models

In systems where a tilt direction changes from the smectic layer to the neighboring smectic layer significantly, the continuous descriptions is no more correct. In these systems also macroscopic properties like elastic constants cannot be understood as a measure of the energy cost for deviations of order parameter from the homogeneous orientation. In the synclinic Sm C phase the molecular long axes are tilted with respect to the smectic layer normal, Fig. 5.2. A direction of the tilt does not vary from layer to layer. Any changes of tilt directions that are not homogeneous increase the free energy of the system and can be treated as elastic deformations as long as changes are small. On the other hand, in the anticlinic Sm C$_A$ phase, tilts in neighboring layers have opposite directions. The order parameters changes are abrupt since the tilt direction changes from layer to layer for 180°. Therefore the elastic

energy in such structure cannot be directly connected with the changes of tilt directions.

In order to describe such a system continuously it is necessary to introduce new order parameters which allow also for a bilayer structure of the Sm C_A^* phase. Introduction of two order parameters, where one reflects the synclinic properties and the other anticlinic properties of the phases including influences of one order to another, results in a complicated expression for the free energy (5.14). As the size of the primitive cell increases to three and more layers, as found by X-ray scattering [13], more and more order parameters enter the expression for the free energy. In general, as many layers form the basic structure, as many 2D order parameters are necessary to describe the structure and consequently their scalar invariants in the free energy. As shown by Pikin et al. [14] the number of 2D order parameters can be reduced by the use of the short pitch modes, although many of them enter the expression for the free energy.

Alternatively, the system with a complex unit cell can be described within a discrete modeling where interactions between molecules from different layers i.e. inter-layer interactions are separated from interactions between molecules in the same smectic layer, i.e. intra-layer interactions. The separation is appropriate for systems where smectic order is high and smectic layers are well formed (Fig. 5.2b). Intermolecular interactions between molecules, which are large in comparison to intermolecular distances, originate in van der Waals interactions which include repelling part or steric interactions as well as their attractive part. If molecules possess dipolar moments, the interactions are also electrostatic. Detailed calculation of inter-molecular interactions is extremely complicated since the calculations have to consider interactions of different parts of different molecules and various molecular conformations for complex molecules that consists of more then hundred atoms. Therefore we model intermolecular interactions by phenomenological approximations based on symmetry considerations. Here we will focus on the most general liquid crystalline system formed from chiral polar molecules where smectic layers are already well defined. We will consider all interactions which might influence the structure of tilted smectic phases according to our opinion. The most important interactions in these systems are intra-layer interactions, which induce molecular tilts in smectic layers. Interactions between nearest layers define basic macroscopic properties such as ferroelectricity and antiferroelectricity or basic structural properties as synclinicity and anticlinicity. Since in general these materials exhibit transition from the synclinic to the anticlinic phase, close to the transition temperatures, where interactions between nearest layers must be small, interactions of longer range become important. In chiral systems also electrostatic dipolar interactions which are of longer range might be important. In the following we will describe the origin of these interactions as well as their phenomenological description.

5.1.5 Discrete phenomenological model of antiferroelectric liquid crystals

In a discrete model of antiferroelectric liquid crystal both model parameters are the smectic layer properties, i.e. the order within the j-th smectic layer is described with the tilt order parameter $\boldsymbol{\xi}_j$ and the polarization order parameter $\boldsymbol{P}_j$. Both parameters can vary from layer to layer but in the continuation we assume that their magnitudes remain constant and only their direction changes.

5.1.5.1 Intra-layer interactions

The main contribution to the free energy of the system comes from van der Waals interactions within the smectic layer. Since intermolecular distances are shorter than molecular dimensions, molecules are arranged in the structure where parts of different molecules are as close as possible. This leads first to the alignment of long molecular axes, and then with lowering of the temperature and decreasing of the entropic part of the free energy, to layer ordering and finally molecules become tilted.

Interactions that lead to the tilt can be expressed in tilt order parameters as

$$\frac{1}{2}a\boldsymbol{\xi}_j^2 + \frac{1}{4}b\boldsymbol{\xi}_j^4 + \frac{1}{6}c\boldsymbol{\xi}_j^6. \tag{5.16}$$

Here only the first parameter $a = \alpha(T - T_0)$ is temperature dependent. Molecules in a single isolated layer become tilted at the temperature T_0 if only van der Waals interactions between molecules in the layer are present. In materials where b is positive, the transition to the tilted phase is continuous. Since the transition to the tilted phase is either continuous or discontinuous the last term in (5.16) with c positive has to be considered [15].

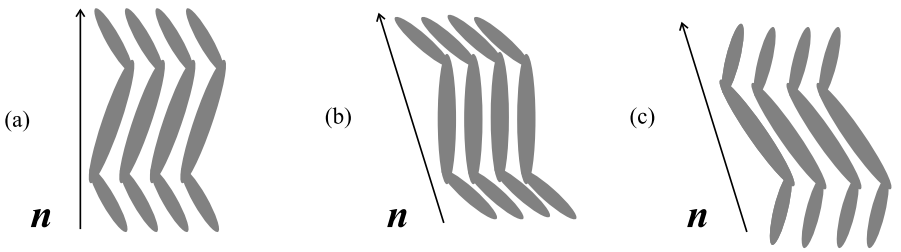

Fig. 5.3. (**a**) Non-tilted S-shaped molecules, (**b**) Tilted S-shaped molecules. Distances between parts of the adjacent molecules are greater in the non-tilted phase (**a**) than in the tilted phase (**b**), van der Waals interactions between tilted molecules with different orientation (**b**) and (**c**) differ although the tilt is the same

When molecules tilt, the rotation around molecular axis becomes hindered. Let us demonstrate this for the case of S-shaped molecules although the argument is general. In Fig. 5.3 it is clearly seen that attractive van der Waals forces differ in two molecular orientations (b) and (c). The time averaged molecular orientation is therefore in the direction where attractive interactions are the strongest and the tilt therefore induces the polar ordering. If molecules are achiral, polar ordering still exists but cannot be observed since the molecules do not possess an observable property connected with the polar ordering. The coupling of the tilt and polarization can be expressed as

$$c_p(\boldsymbol{\xi}_j \times \boldsymbol{P}_j)_z, \tag{5.17}$$

where c_p is called the piezoelectric coupling due to historical reasons. The coupling was for the first time predicted by symmetry considerations for ferroelectric liquid crystals[1] and only recently has been recognized, that such interactions exist also in achiral systems [16]. Since chiral systems become polar when molecules become tilted and tilt is always connected with a decrease of the layer thickness, the coupling was called "piezoelectric" in a more general meaning. Layer polarization is directly proportional to the polar order parameter as $\boldsymbol{P}_j = P_0 \cdot \boldsymbol{\eta}_j$, where P_0 is the polarization of the completely polarly ordered layer and $\boldsymbol{\eta}_j$ gives the polar order in the j-th layer. Therefore polar order parameter can also be called shortly polarization.

Polar ordering of chiral molecules which possess at least some component of the dipole moment perpendicular to the tilt, results in effective layer polarization and leads also to electrostatic interactions within a layer,

$$\frac{1}{2\epsilon}\boldsymbol{P}_j^2 \rightarrow \frac{1}{2} b_0 \boldsymbol{\eta}_j^2. \tag{5.18}$$

On the left side of (5.18) only strict electrostatic interactions between dipoles are given but in the right expression also van der Waals interactions between molecules with polar structure can be included into the parameter b_0 in addition. Parameter b_0 is always positive since polar ordering is never critical in chiral polar smectics.

5.1.5.2 Interactions between nearest layers (NN)

In layered systems where molecules are of the same length as the layer thickness, they do not interact only within a layer but also parts of the molecules interact with parts of the molecules from neighboring layers. In systems where smectic order is low the fraction of the molecules which are found between the layers is relatively high (Fig. 5.4). Tilted molecules which interpenetrate through layers promote the homogeneous tilt since the molecular bending is energetically not favored (Fig. 5.4, dark molecule). On the other hand, in systems where smectic order is high, changes in the tilt direction from layer to layer can be large, since the fraction of interpenetrating molecules

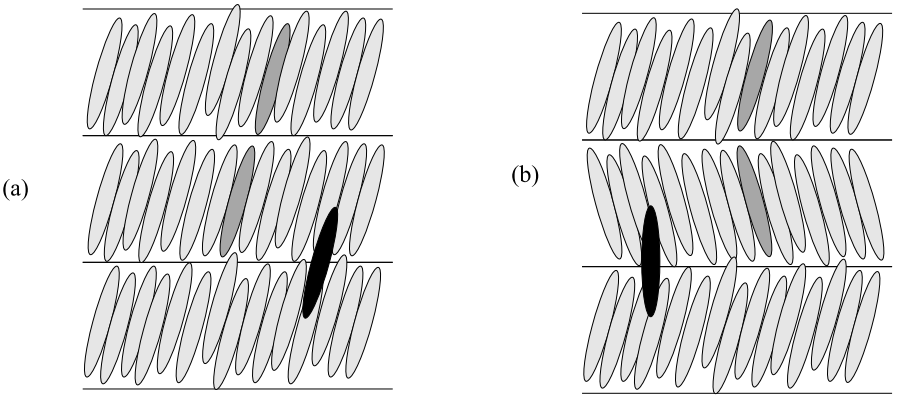

Fig. 5.4. (**a**) Interpenetrating molecules (*dark*) are energetically not disfavored in synclinic order, (**b**) In anticlinic order interpenetrating molecules (*dark*) are energetically strongly disfavored. Distances between parts of molecules in neighboring layers are larger in synclinic order ((a)-*gray pair*) than in the anticlinic order ((b)-*gray pair*)

is small and therefore also the energy cost is low (Fig. 5.4, dark molecule). Molecules which are found in neighboring layers interact through attractive part of van der Waals forces. Van der Waals interactions exist only when positional correlations exist [17]. Positional correlations between molecules in neighboring layers are weak but cannot be treated as negligible since molecular tails from neighboring layers are found in the same layer interfaces. Comparing shaded molecules in neighboring layers, distances between parts of the correlated molecules in the synclinically ordered layers (Fig. 5.4a) are greater than distances in the anticlinically ordered layers (Fig. 5.4b). That leads to the preferable anticlinic structure when the layer order is high. Since varying the temperature also smectic order varies, in some systems might happen that at higher temperature where diffusion is favored, the synclinic order is preferred, but at lower temperature, where smectic order is higher, the anticlinic order appears. Described interactions are expressed in tilt order parameters from neighboring layers.

$$\frac{1}{2}a_1(T)(\boldsymbol{\xi}_j \cdot \boldsymbol{\xi}_j). \tag{5.19}$$

Parameter a_1 can be either negative or positive. For negative values of parameter a_1 the term is minimal when tilts in neighboring layers are parallel or synclinic. For positive values the anticlinic arrangement minimizes the free energy. Temperature dependence of the parameter a_1 takes into account that with decreasing temperature inter-layer interactions change. The parameter a_1 always becomes less negative or even positive since it is expected that inter-layer diffusion decreases with lowering the temperature when it is not influenced by some other effects.

Inter-layer interactions lead in continuous models, in addition to the renormalization of the transition temperature, to elastic terms which are given by

$$\frac{1}{2}K_3\left(\frac{d\boldsymbol{\xi}(z)}{dz}\right)^2 \qquad \text{where} \qquad K_3 = \frac{1}{2}\,a_1\,d^2. \tag{5.20}$$

In addition to attractive van der Waals forces between elongated molecules also interactions between parts of the molecules which account for chiral molecular structures have to be considered. Although a chiral intra-layer results in the polar ordering of the layer expressed in the piezoelectric coupling, the chiral part of inter-layer interactions cause that neither ideal synclinic nor ideal anticlinic order is energetically favorable. The interactions are expressed by the chiral term

$$\frac{1}{2}f_1\left(\boldsymbol{\xi}_j \cdot \boldsymbol{\xi}_{j+1}\right)_z, \tag{5.21}$$

that favors perpendicular alignment of tilts in neighboring layers and results in a distortion of the synclinic or anticlinic structures. It also results in the opposite handedness of the helices in synclinic and anticlinic chiral phases. Chiral parameter f_1 can be either positive or negative and has opposite signs in left and right handed systems. The term in the continuous limit for systems with long helicoidal modulations corresponds to the Lifshitz term

$$\frac{1}{2}\Lambda\left(\xi_x\frac{d\xi_y}{dz} - \xi_y\frac{d\xi_x}{dz}\right) \qquad \text{where} \qquad \Lambda = f_1\,d, \tag{5.22}$$

where Λ gives chiral parameter and is related to the discrete chiral parameter f_1.

In tilted systems additional quadrupolar ordering might become important at higher tilts, i.e. lower temperatures. It has to be distinguished between the electrostatic quadrupolar moment [18], which is always present in molecules with more polar groups, and the geometrical quadrupolar moment which resumes the lath-like molecular structure [6, 19]. Interactions lead to the biquadratic coupling of the nearest layers and can be expressed in tilts as

$$\frac{1}{4}b_Q\left(\boldsymbol{\xi}_j \cdot \boldsymbol{\xi}_{j+1}\right)^2. \tag{5.23}$$

Electrostatic quadrupolar moments favor perpendicular tilts in nearest layers and are given by the positive contribution to the parameter b_Q. On the other hand, increasing quadrupolar ordering (Fig. 5.6) favors both, i.e. synclinic and anticlinic tilts. The inter-layer molecular diffusion is encouraged in quadrupolarly ordered systems and simultaneously anticlinic tilts are favored because of attractive van der Waals interactions. It results in the negative value of the parameter b_Q.

Flexoelectric effect or flexoelectric coupling is the common name for the property of the system where polarization is induced due to the spatial variation of molecular order in the material. In tilted chiral smectics, the polarization is induced by the variation of the tilt, since molecular rotation hindrance

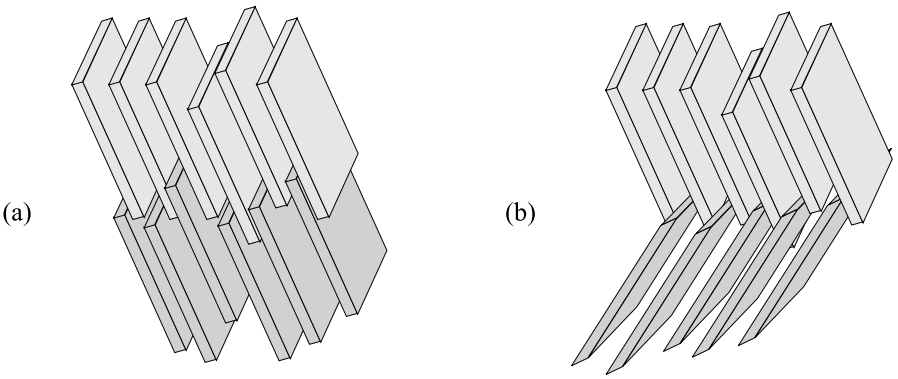

Fig. 5.5. Geometrical quadrupolar ordering of lath-like molecules. Both, (**a**) synclinic and (**b**) anticlinic order is favored

is affected due to different interactions with molecules above and below the layer. It therefore results in the change of the polar order. Recently it was found that in some systems flexoelectrically induced polarization can be comparable to the piezoelectrically induced polarization [20]. The coupling is given as

$$\frac{1}{2}\mu\left(\boldsymbol{\xi}_{j+1}-\boldsymbol{\xi}_{j-1}\right)\cdot\boldsymbol{\eta}_j, \tag{5.24}$$

where μ is the flexoelectric parameter. From the expression (5.24) can be seen that the flexoelectrical part of the polarization is the most important in systems where next nearest layers are anticlinic. Therefore it can be expected that phenomena related to the flexoelectric coupling can be best studied in systems with very short modulations. In continuous description the term is equivalent to the flexoelectric term expressed in derivative of the tilt order parameter

$$\frac{1}{2}\mu_c\left(\boldsymbol{P}\cdot\frac{d\boldsymbol{\xi}}{dz}\right) \qquad \text{where} \qquad \mu_c=\mu\, d, \tag{5.25}$$

where μ_c stands for the flexoelectric parameter used in continuous models.

Among inter-layer interactions between nearest layers, electrostatic interactions between induced dipoles are also one of the most important interactions in systems with significant polarization. To account for electrostatic interactions we have to consider some positional correlations between molecules from neighboring layers, since two layers without positional correlations do not interact electrostatically [17]. Considering hexatic cylindrically symmetric correlations of elongated molecules in two neighboring layers (Fig. 5.5), it can be shown that antiferroelectric ordering of dipoles is favored for elongated molecules [18]. Since the polarization is proportional to the polar ordering, interactions can be given by

$$\frac{1}{2} b_1 \left(\boldsymbol{\eta}_j \cdot \boldsymbol{\eta}_{j+1} \right), \tag{5.26}$$

where b_1 includes polarization, correlations and intermolecular distances and is therefore smaller than b_0. Due to the favored antiferroelectric polar ordering the parameter b_1 is always positive.

Couplings with neighboring layers lead to elastic contributions to the free energy of the system and can be given by derivatives of order parameters, the corresponding term in continuous models gives the spatial variation of the polarization. Influences of this term, to our knowledge, have not been considered yet.

5.1.5.3 Interactions with next nearest layers (NNN)

Positional correlations exist to a certain degree also between molecules in next nearest neighboring layers. Assumed positional correlation in nearest layers leads to a higher probability for a molecule in the next nearest layer to be found directly above or below the interacting molecule (Fig. 5.6). It was shown that also these interactions always favor antiferroelectric ordering in interacting layers [18], and therefore they always compete with achiral NN interactions but enhance the effect of chiral NN interactions. Since NN interactions can under some circumstances cancel out, these interactions might become very important. The free energy contribution is given by

$$\frac{1}{2} b_2 \left(\boldsymbol{\eta}_j \cdot \boldsymbol{\eta}_{j+2} \right), \tag{5.27}$$

where b_2 is always positive and gives effective dipole-dipole interactions between next-nearest layers. Also this term would in continuous models lead to the elastic term connected with space variation of the polar ordering.

We did not find any other interactions which could be of non-negligible importance and of longer range than next nearest layers.

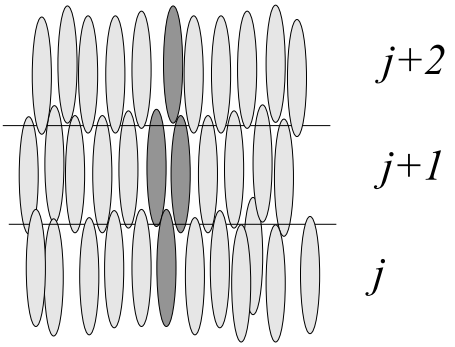

Fig. 5.6. Due to the partial interpenetration of molecules from the j-th to the $(j+1)$-st layer, it is more probable to find molecules in the marked positions

5.1.5.4 Free energy

The free energy of a smectic system that consists of chiral molecules is therefore

$$
\begin{aligned}
G = \alpha \sum_{j=1}^{N} & \frac{1}{2}\,(T - T_0)\,\boldsymbol{\xi}_j^2 + \frac{1}{4}\,b\,\boldsymbol{\xi}_j^4 + \frac{1}{6}\,c\,\boldsymbol{\xi}_j^6 \\
& + \frac{1}{2}\,a_1(T)\;(\boldsymbol{\xi}_j \cdot \boldsymbol{\xi}_{j+1}) + \frac{1}{2}\,f_1\;(\boldsymbol{\xi}_j \times \boldsymbol{\xi}_{j+1})_z \\
& + \frac{1}{2}\,b_0\,\boldsymbol{\eta}_j^2 + \frac{1}{2}\,b_1\;(\boldsymbol{\eta}_j \cdot \boldsymbol{\eta}_{j+1}) + \frac{1}{8}\,b_2\;(\boldsymbol{\eta}_j \cdot \boldsymbol{\eta}_{j+2}) + \frac{1}{4}\,b_Q\;(\boldsymbol{\xi}_j \cdot \boldsymbol{\xi}_{j+1})^2 \\
& + c_p\,(\boldsymbol{\eta}_j \times \boldsymbol{\xi}_j)_z + \frac{1}{2}\,\mu\;(\boldsymbol{\xi}_{j+1} - \boldsymbol{\xi}_{j-1}) \cdot \boldsymbol{\eta}_j,
\end{aligned}
\tag{5.28}
$$

where besides the leading parameter $a = \alpha(T - T_0)$ also a_1 depends on the temperature as explained before. The elimination of the polarization η leads to effective inter-layer interactions expressed in tilts [21]. Achiral interactions are non-negligible to the fourth neighboring layers and chiral interactions are important to third neighboring layers. The inter-layer part of the free energy, which defines the modulations of tilt directions, is than

$$
\begin{aligned}
G_{\text{int}} = \frac{1}{2} \sum_{j=1}^{N} & \left(\sum_{k=1}^{4} \tilde{a}_k\;(\boldsymbol{\xi}_j \cdot \boldsymbol{\xi}_{j+k}) + \sum_{k=1}^{3} \tilde{f}_k\;(\boldsymbol{\xi}_j \times \boldsymbol{\xi}_{j+k})_z \right) \\
& + \frac{1}{4}\,b_Q\;(\boldsymbol{\xi}_j \cdot \boldsymbol{\xi}_{j+1})\,.
\end{aligned}
\tag{5.29}
$$

The parameters a_i and f_i are defined by microscopic interactions and cannot vary arbitrarily. They are

$$
\begin{aligned}
\tilde{a}_1 &= a_1 + \left(\frac{c_p^2}{b_0} + \frac{1}{4}\,\frac{\mu^2}{b_0} \right)\,\left(\frac{b_1}{b_0} \right) \\
\tilde{a}_2 &= \frac{1}{2}\,\frac{c_p^2}{b_0} \left[\frac{1}{2} \left(\frac{b_2}{b_0} \right) - \left(\frac{b_1}{b_0} \right)^2 \right] + \frac{1}{2}\,\frac{\mu^2}{b_0} \left[1 + \frac{1}{4} \left(\frac{b_2}{b_0} \right) \right] \\
\tilde{a}_3 &= -\frac{1}{4}\,\frac{\mu^2}{b_0}\,\left(\frac{b_1}{b_0} \right) \\
\tilde{a}_4 &= \frac{1}{8}\,\frac{\mu^2}{b_0}\,\left[\left(\frac{b_1}{b_0} \right)^2 - \frac{1}{2}\,\left(\frac{b_2}{b_0} \right) \right] \\
\tilde{f}_1 &= f_1 - \frac{2\,c_p\,\mu}{b_0}\,\left[1 + \frac{1}{4}\,\left(\frac{b_1}{b_0} \right)^2 + \frac{1}{8}\,\left(\frac{b_2}{b_0} \right) \right] \\
\tilde{f}_2 &= \frac{c_p\,\mu}{b_0}\,\left(\frac{b_1}{b_0} \right) \\
\tilde{f}_3 &= \frac{1}{2}\,\frac{c_p\,\mu}{b_0}\,\left[-\left(\frac{b_1}{b_0} \right)^2 + \frac{1}{2}\,\left(\frac{b_2}{b_0} \right) \right].
\end{aligned}
\tag{5.30}
$$

5.1.5.5 Structures and phase sequences

To get possible structures that are stable in the AFLC, the free energy has to be minimized with respect to all tilt order parameters $\boldsymbol{\xi}_j$. Experimental evidences have shown that the magnitude of the tilt can be taken as constant, therefore only tilt directions have to be found. Detailed minimization procedure is described in the Sect. 5.4 of this book, where also comparison with experimental observation is presented. Here we only quote some of the most important results.

Let us assume that a behavior of the microscopic interactions in AFLC is general: steric NN interactions prevail at higher temperatures and van der Waals attractive NN interactions prevail at lower temperatures, therefore the sign of a_1 changes from negative to positive. Geometrical quadrupolar interactions are more important than electrostatic quadrupolar interactions which results in the negative sign of the parameter b_Q. All the rest of parameters have the signs as discussed before and are temperature independent. Minimization of the free energy with a proper choice of model parameters leads to the most general observed phase sequence Sm A$\leftrightarrow$Sm C$^*_\alpha\leftrightarrow$Sm C$^*\leftrightarrow$Sm C$^*_{FI2}$ $\leftrightarrow$Sm C$^*_{FI1}\leftrightarrow$Sm C$^*_A$, where historically called Sm C$^*_\beta$ phase has later been recognized as the Sm C$^*_{FI2}$ phase [22] although it has been long considered as a normal Sm C* phase. The Sm C$^*_\gamma$ phase is also believed that it is the Sm C$^*_{FI1}$ phase.

The schematic structure of all six different tilted phases are given in Fig. 5.7. The Sm C$^*_\alpha$ phase is helicoidally modulated with the length of a few smectic layers. The Sm C* phase is also helicoidally modulated but the period of the modulations extends over a few hundred layers. The basic difference between both phases probably arises in the nature of interactions that cause the helicoidal modulation. In the Sm C$^*_\alpha$ phase the short pitch modulation arises due to the competition between NN adn NNN interactions but in the Sm C* phase the NN interactions prevail over NNN interactions and the helicoidal modulation is a consequence of chiral NN interactions. In the Sm C$^*_{FI2}$ phase the basic unit consists of four layers. The structure can also be described as two antiferroelectric helices geared into each other for a general angle. On the other hand the basic unit of the Sm C$^*_{FI1}$ phase consists

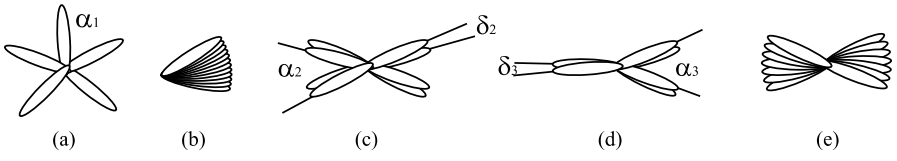

Fig. 5.7. Structures of phases, given as projections onto the smectic layer, appearing with lowering the temperature in antiferroelectric liquid crystals. (**a**) the Sm C$^*_\alpha$ phase, (**b**) the Sm C* phase, (**c**) the Sm C$^*_{FI2}$ phase, (**d**) the Sm C$^*_{FI1}$ phase and (**e**) the Sm C$^*_A$ phase

three layers which gives rise to its ferrielectric properties. The lowest temperature phase, the Sm C_A^* phase appears in the region where anticlinic tilts are favored. Two ferroelectric helices gear into each other forming a double antiferroelectric helix. The order of the phases appearing in the phase sequence is always the same but some them can be missing. In AFLC the Sm C_A^* phase is always present and has given them the name.

5.1.6 Summary

A short historical overview of the development of phenomenological models of ferroelectric and antiferroelectric liquid crystals is given. For a theoretical modeling of the ferroelectric liquid crystals the tilt order parameter and the polarization order parameter are needed. The free energy is expressed in both order parameters and only small changes of both order parameters from the layer to the layer are allowed. Description is therefore sometimes also called continuous. After discovery of the antiferroelectric liquid crystals, the phenomenological model for the ferroelectric liquid crystals has been extended to systems with a double layer periodical structures by introduction of the ferroelectric and antiferroelectric tilts and polarizations. The model allow for some of the phases but fails to predict phases with periodical structures with periods longer than two layers.

Discrete models where inter-layer interactions are taken into account explicitly, allow for more complex structures with three-, four- and more layer in general incommensurate periodicities. Various microscopic interactions and their phenomenological description as well as the link between the terms in the continuous and discrete description is discussed. The general free energy for a smectic liquid crystal that consists of chiral molecules is presented, and the typical phase sequence including the structures of the stable phases is briefly analyzed.

References

1. R. B. Meyer, L. Liebert, L. Strzelecki, P. Keller: J. de Phys. Lett. **36**, L69 (1975)
2. I. Muševič, R. Blinc, B. Žekš: *The Physics of Ferroelectric and Antiferroelectric Liquid Crystals* (World Scientific, Singapore 2000)
3. V. L. Indebom, S. A. Pikin, E. B. Loginov: Sov. Phys. Crystallogr. **21**, 632 (1976)
4. R. Blinc, B. Žekš: Phys. Rev. A **18**, 740 (1978)
5. B. Žekš, T. Carlsson, C. Filipič, B. Urbanc: Ferroelectrics **84**, 3 (1988)
6. B. Žekš: Mol. Cryst. Liq. Cryst. **114**, 259 (1984)
7. A. D. L. Chandani, E. Górecka, Y. Ouchi, H. Takezoe, and A. Fukuda: Jpn. J. Appl. Phys., Part 2 **28**, L1265 (1989)
8. A. M. Levelut, C. Germain, P. Keller, L. Lebert, J. Billard: J. Physique **44**, 623 (1983)

9. An extensive overview of experimental observations is given in M. Čepič, E. Gorecka, D. Pociecha, N. Vaupotič, in Sect. 5.4 of this book
10. H. Orihara, Y. Ishibashi: Jpn. J. Appl. Phys. **30**, L1819 (1990)
11. B. Žekš, M. Čepič: Liq. Cryst. **14**, 445 (1993)
12. V. L. Lorman, A. A. Bulbitch, P. Toledano: Phys. Rev. **E49** 1367 (1994)
13. P. Mach, R. Pindak, A. M. Levelut, P. Barois, H. T. Nguyen, C. C. Huang, and L. Furenlid: Phys. Rev. Lett. **81**, 1015 (1998)
14. S. Pikin, M. Gorkunov, D. Kilian, W. Haase: Liq. Cryst. **26**, 1107 (1999); S. Pikin, M. Gorkunov, D. Kilian, W. Haase: Liq. Cryst. **26**, 1115 (1999); S. Pikin, D. Kilian, M. Gorkunov, W. Haase: Liq. Cryst. **26**, 1123 (1999)
15. M. Škarabot, M. Čepič, B. Žekš, R. Blinc, G. Heppke, A. V. Kityk, and I. Muševič: Phys. Rev. **E58**, 575 (1998)
16. D. J. Photinos, E. T. Samulski: Science **270**, 783 (1995)
17. R. Bruinsma, J. Prost: J. Phys. II France **4**, 1209 (1994)
18. M. Čepič, B. Žekš: Mol. Cryst. Liq. Cryst. **301**, 221 (1997)
19. D. Pociecha, E. Górecka, M. Čepič, N. Vaupotič, B. Žekš, D. Kardas, and J. Mieczkowski: Phys. Rev. Lett. **86**, 3048 (2001)
20. P. O. Andreeva, V. K. Dolganov, C. Gors, R. Fouret, E. I. Kats: Phys. Rev. **E59**, 4143 (1999)
21. M.Čepič, B.Žekš, Phys. Rev. Lett. **87**, 085501 (2001)
22. E. Górecka, D. Pociecha, M. Čepič, R. Dabrowski, B. Žekš: Phys. Rev. **E65**, 061703 (2002)
23. M. Čepič, E. Górecka, D. Pociecha, B. Žekš, H. T. Nguyen: Jou. Chem. Phys. **117**, 1817 (2002).

5.2 Switching processes in ferroelectric liquid crystals: Theoretical aspects

S. A. Pikin

5.2.1 Introduction

The switching of polarization in ferroelectric liquid crystals (FLCs) is of great physical interest and practical application [1–12]. Such a switching process is related to many specific features of FLCs, such as molecular properties, boundary conditions, defective structure, ionic conductivity. For example, the peculiarity of a FLC consists in the inclination of smectic planes with respect to the domain surface normal, which results in the spontaneous polarization divergence at the dislocation walls existing near interfaces. The structure and properties of ferroelectric smectic-C domains at various interfaces are different in dependence on the effects of surface tension. The motion of the volume electric charge is of importance in such a situation. The switching in an alternating electric field is inevitably related with several relaxation processes, such as an orientational relaxation near the cell surface and the charge relaxation which are always present during the polarization reversal. Many characteristics of the FLC devices are directly connected with these physical properties of the cells.

In this paper, the properties of ferroelectric smectic-C domains are considered in the framework of a model for the polarization and director surface anchoring. The formation of ferroelectric domain structures in conventional electro-optical cells is described. The influence of the interface conditions, cell thickness, concentration and mobility of free ions on the spatial director and polarization distributions as well as on the dielectric response and relaxation processes is shown. The surface orientational relaxation in the ferroelectric smectic is discussed. The monostability and bistability of electro-optical states in ferroelectric films are considered in dependence on anchoring conditions at the cell boundaries and domain walls. It is shown that the effect of bistability occurs under a certain critical condition which strongly depends on the polarization and anchoring strength. All these properties are shown to effect on the phenomenon of the V-shaped electro-optical switching. Solutions of the problem of hysteresis-free and thresholdless electro-optical switching are given for the case of the action of alternating electric fields. The qualitative relations between the frequency of applied field, rise time in the field and various relaxation frequencies are found to explain and predict such a switching in real FLC materials.

5.2.2 Polarization reversal in thick films

5.2.2.1 Non-stationary solution for applied dc electric field

The electro-optical switching is closely related to the processes of polarization reversal, that is why the questions concerning the relations between the vector of spontaneous polarization $\boldsymbol{P}$, electric field $\boldsymbol{E}$, constants of surface anchoring, internal parameters of an FLC arise when we want to describe the electro-optical behavior of these materials. In a simplest case, when the interaction of $\boldsymbol{P}$ and $\boldsymbol{E}$ only is taken into account, the equation describing the azimuth motion of director $\boldsymbol{n}$ and polarization $\boldsymbol{P}$ takes the form

$$PE \sin \varphi = \gamma \Theta^2 \frac{\partial \varphi}{\partial t} \tag{5.31}$$

where γ is the viscosity coefficient for the azimuth motion of director, Θ is the tilt angle of director with respect to the axis z which is normal to smectic layers in the chiral smectic C* phase. It is assumed that vector $\boldsymbol{E}$ is perpendicular to the FLC cell and directed along axis y, the smectic layers are perpendicular to the cell surface, the motion of vector $\boldsymbol{P}$ occurs in plane XY, i.e., we have the so called "book shelf" geometry [1] (see Fig. 5.8). As a rule, below, we shall use the simple relationship between magnitudes P and Θ, $P = \mu\Theta$, where μ is the "piezo-modulus" of a FLC, the sign of μ depends on the molecular chirality. The latter equation is dictated by the symmetry of the smectic C* phase [13]. Equation (5.31) does not take into account an orientational elasticity of this phase, the boundary conditions at the surface of smectic layer, a possible ionic current and other factors, the polarizational helix is assumed to be

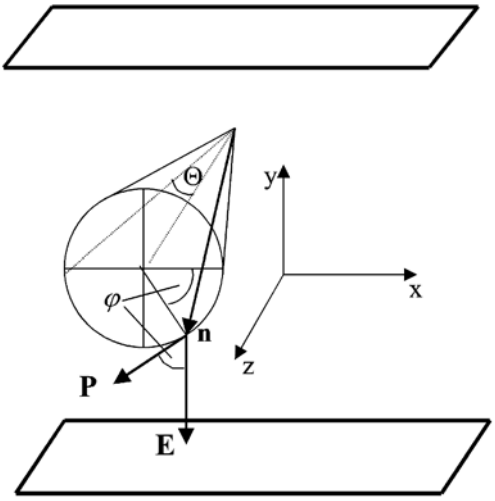

Fig. 5.8. Director motion in the case of the book-shelf geometry of the FLC layer

unwound. The term in the left side of (5.31) is due to the term $-\boldsymbol{P}\cdot\boldsymbol{E}$ which is present in the free energy of this phase, variation of which with respect to angle φ results in torque $PE\sin\varphi$. It is assumed here and below that director $\boldsymbol{n}$ is rotating on the surface of the tilt cone of the molecules (see Fig. 5.8).

Equation (5.31) has a simple solution [14, 15] which has the form

$$\varphi = \arccos\frac{(1+\cos\varphi_0)\exp(-2at)-(1-\cos\varphi_0)}{(1+\cos\varphi_0)\exp(-2at)+(1-\cos\varphi_0)} \tag{5.32}$$

where φ_0 is an initial value of the angle between vectors $\boldsymbol{E}$ and $\boldsymbol{P}$, and a is the characteristic parameter of the problem,

$$a \equiv \frac{1}{\tau_E} = \frac{PE}{\gamma\Theta^2}\,, \tag{5.33}$$

magnitude $1/|a|$ is the so-called rise time τ_E which is necessary for the effective polarization reversal. The polarizational current $i_{p,y} = \partial P_y/\partial t$ has a maximum in absolute value, $|i_{p,y}|_{\max} = aP$, at the moment of time $t_m = (2a)^{-1}\ln[(1+\cos\varphi_0)/(1-\cos\varphi_0)]$. Though the assumptions made above are sufficiently rough, and the φ_0 value is not well determined in (5.32), the observed magnitudes of the rise time and maximum of polarizational current are in a qualitative accordance with the characteristics estimated above. Expression (5.33) will be used below for estimations.

5.2.2.2 Non-stationary solutions for applied ac electric field

Unlike the non-stationary solution for a dc electric field discussed above, the behavior of the φ distribution changes when the alternating field $E = E_0\cos\omega t$ is applied. In this case, (5.31) takes the form

$$PE_0 \cos\omega t \sin\varphi = \gamma\Theta^2 \frac{\partial\varphi}{\partial t} \,. \tag{5.34}$$

The solution of (5.34) is [16, 17]

$$\varphi(t) = \arctan \frac{1}{\sinh\left(\text{const} - a/\omega \sin\omega t\right)} \tag{5.35}$$

with a given by (5.33), where E_0 substitutes for E, const determines an initial value φ_0. This solution shows that angle φ can be close to values 0 or π for small values of the rise time τ_E, but at certain moments of time φ is close to $\pi/2$. If a is less than ω then angle φ cannot reach values 0 and π, and it takes an intermediate value. A constant in (5.35) can be in general a function of coordinates, for instance a function of the distance y from the cell surface along the normal to the surface. The homogeneous distribution of φ, depending on time accordingly to (5.35), is not valid for a finite anchoring energy and corresponding boundary conditions for the angle φ at values $y = 0$ and $y = d$, where d is the layer (cell) thickness.

To take into account a possible heterogeneity in the spatial distribution of φ, we should add into (5.34) a term related to the orientational deformations and elasticity. Besides, in the absence of external charges, a certain perturbation Ξ_y of the electric field $E_y = E_0 \cos\omega t + \Xi_y$ can be present in the cell, which is related to polarization P_y and opposite to P_y in sign, i.e., $\Xi_y = -\varsigma P_y = -\varsigma P \cos\varphi$, where ς is a positive constant. Taking into account such a depolarization effect, we obtain the equation

$$\gamma\Theta^2 \frac{\partial\varphi}{\partial t} = K\Theta^2 \frac{\partial^2\varphi}{\partial y^2} + P\left(E_0 \cos\omega t - \varsigma P \cos\varphi\right) \sin\varphi \,, \tag{5.36}$$

where K is the modulus of orientational elasticity. We find the following solution of (5.36) in the bulk of the cell [16, 17]:

$$\varphi = \arctan \frac{1}{\sinh\left(\text{const} \pm \frac{y}{\xi_P} - \frac{a}{\omega} \sin\omega t\right)} \,, \tag{5.37}$$

where

$$\xi_P = \sqrt{\frac{K\Theta^2}{\varsigma P^2}} \,. \tag{5.38}$$

Solution (5.37) describes the motion of orientational kinks of width ξ_P along the y axis with velocity $v = \pm a\xi_P \cos\omega t$ which is equal to magnitude $\pm a\xi_P$ in the limit $\omega \to 0$ [18]. Such a situation is possible when orientational perturbations may arise somewhere in the cell in areas of size ξ_P which is much less than the cell thickness d. Then these perturbations as kinks are traveling through the cell and result in the polarization reversal (see Fig. 5.9). The solution, shown in Fig. 5.9, correspond to zero values of φ at the boundaries if ratio a/ω is much less than ratio d/ξ_p. For very high frequencies ω, such a motion represents fast oscillations with the small amplitude $a\xi_P/\omega$ near a certain point in the cell. The kink motion was observed experimentally [19].

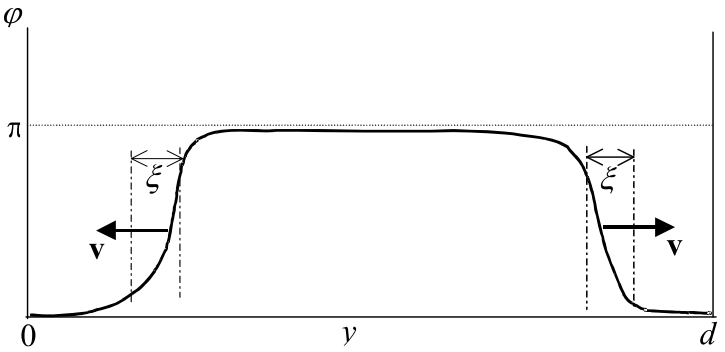

Fig. 5.9. Kink motion through the FLC layer along axis y

5.2.3 High frequency switching of the ferroelectric with a deformed helix

The thresholdless switching considered above had no connection with the helical orientational structure of the smectic C* phase, i.e., it was assumed that such a helix is unwound due to some boundary conditions for not very thick smectic films. For thicker cells, when d is sufficiently larger than the pitch of helix h, we should consider the effects of the director twisting along axis z on the electro-optical switching. Under the action of a dc field E, the helix of director and polarization is unwound under a certain threshold condition. This process is described by equation

$$K\Theta^2 \frac{\partial^2 \varphi}{\partial z^2} + PE \sin \varphi = 0 \tag{5.39}$$

which assumes that $\varphi(z) = q_H z$ for $E = 0$, where $q_H = 2\pi/h$ is the initial wave number of the helix, no boundary conditions are taken into account. The threshold value of field E_{unw}, which has to be overcome for the helix unwinding, is well known [20]:

$$E_{unw} = \frac{\pi^2}{16} \frac{K\Theta^2 q_H^2}{P} \,. \tag{5.40}$$

For an ac electric field applied to the helix, we should find for the solution of equation of the type (5.36) instead of (5.39), and it is a rather hard problem. It is clear that the increase in frequency of applied field has to lead to the corresponding increase in value $E_{unw}(\omega)$ that is observed in experiments [21]. Below such a threshold, the helix is strongly deformed: it contains relatively wide intervals of the untwisted FLC structure and very narrow intervals of the twisted orientation for both directions of electric field, E_+ (solid line represents this distribution in Fig. 5.10) and E_- (dotted line in Fig. 5.10) [22]. The larger E, the smaller is the interval Δz where the director azimuth angle φ changes on the π value, the tilt angle Θ stays practically constant during the

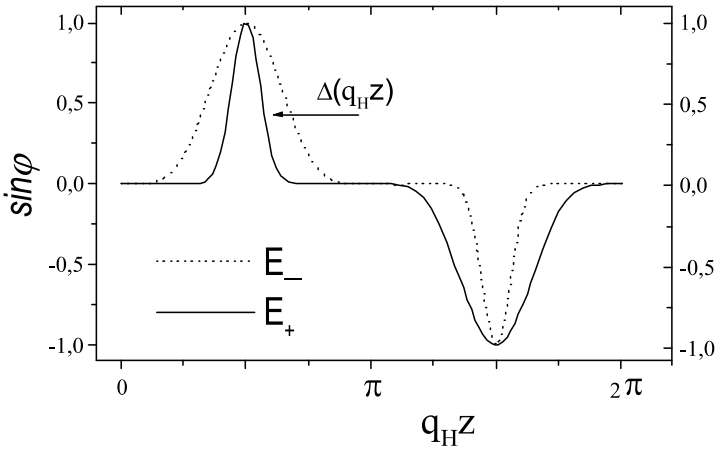

Fig. 5.10. Schematic representation of the φ angle distribution along axis z, when the helix is strongly deformed in ac electric field [22]

process. Such a structure was confirmed by numerical calculations for applied dc field [20]. In the latter case, the response time τ_E of strong perturbations of the helix is determined by (5.33), i.e., it becomes comparable with the conventional orientational relaxation time $\tau_{\rm or} = \gamma/Kq_H^2$. It should be noted that, for $E <\sim E_{unw}$, the Δz interval is of the order of $\Delta z \sim \xi_E = \left(K\Theta^2/PE_{unw}\right)^{1/2} \sim q_H^{-1}$, i.e., it is comparable with the helix pitch.

For the ac field with amplitude $E <\sim E_{unw}$, we can conclude that if frequency ω becomes larger than magnitude τ_E^{-1}, the Δz interval becomes dependent on $\omega = 2\pi f$. In such a case, $\Delta z\,(\omega)$ is less than q_H^{-1}, since the helix follows the changing field with a great delay: the total unwinding does not occur, wide parts of the helix are not disturbed, but, at small distances $\Delta z\,(\omega)$ from the walls as induced defects of the helix, the helix deformation is large. A transformation of the "solid" distribution in Fig. 5.10 to the "dotted" one, accompanied by a change in interval Δz without the total helix unwinding, can be considered as a rough illustration of an orientational diffusion. It occurs after the change in the sign of field E.

Thus, instead of (5.36), we shall use the model which assumes most essential orientational changes at small distances $\Delta z\,(\omega)$ for which a relation of the type of (5.40) is valid, where $\Delta z\,(\omega)$ substitutes for q_H^{-1}. The model is taking into account the rotational Brownian movement of molecules about a fixed axis. It is like the first model, in which Debye [23] considered such a movement in two dimensions of a rigid rotator subjected to an external time varying electric field. The distribution function $\rho_{\rm or}(\varphi, t)$, used by Debye, is defined as follows: $\rho_{\rm or}(\varphi, t)d\varphi$ is the number of molecules, whose axes lie in an element of angle $d\varphi$, in the circumference of a circle. The function $\rho_{\rm or}$ depends both on the time and the angle φ, which is the azimuth angle in our

case. The Smoluchowski equation for the problem can be written simply by replacing the spatial coordinate by the angular coordinate φ. The angle φ in a diffusion equation is actually an ensemble average of angles φ, and the equation has the form:

$$D_{\text{or}}\frac{\partial^2\rho_{\text{or}}}{\partial\varphi^2} = \frac{D_{\text{or}}}{q_H^2}\frac{\partial^2\rho_{\text{or}}}{\partial z^2} = \frac{\partial\rho_{\text{or}}}{\partial t}\,, \tag{5.41}$$

where D_{or} is the orientational diffusion coefficient. Physically, the diffusion corresponds to the change in director orientation $\Delta\varphi$ at distance $\Delta z \approx q_H^{-1}\Delta\varphi$ during time $\Delta t \sim f^{-1}$, when the φ values are given at the borders between the mentioned wide and narrow zones (see Fig. 5.10) of the deformed helix. Thus, accordingly to the diffusion equation (5.41), we obtain the estimate

$$\Delta z^2(\omega) \sim \frac{D_{\text{or}}}{q_H^2\omega}\,. \tag{5.42}$$

Correspondingly, we obtain the estimate of response time τ_E^{-1} for the case of a high-frequency electric field with the amplitude

$$E <\sim E_{unw} \propto (K\Theta^2/\Delta z^2(\omega)P) \propto \omega\ :$$
$$\tau_E(\omega) \sim \frac{\gamma\Theta^2}{PE_{unw}} \sim \frac{\gamma D_{\text{or}}}{Kq_H^2\omega}\,. \tag{5.43}$$

Equation (5.43) describes the characteristic time of orientation perturbations, which coincides with the relaxation time of these perturbations at the diffusion lengths $\Delta z(\omega)$ decreasing as $\omega^{-1/2}$ with increasing ω accordingly to (5.42). Thus, the response time of such helix deformations is inversely proportional to the frequency ω. The temperature dependence of this response time is also of great importance. If, accordingly to the Stokes–Einstein – like relation, $D_{\text{or}} \propto k_BT/\gamma$, where k_B is the Boltzmann constant, T is the temperature, we should expect the dependence $\tau_E \propto 1/\omega$ with not an essential temperature change. This means that the low-temperature behavior of $\tau_E(\omega)$ may be sufficiently smooth when the frequency is not very high and the field-linear effects take place (in a broad frequency range $\sim 1\,\text{kHz}$). For very high frequencies ω, the field – squared effect related to the dielectric anisotropy plays the main role, and the described helix response has to change. In a low frequency region, the response time is practically independent of frequency. The described peculiar features of the electrooptical response time were observed experimentally for the so called high frequency – high voltage mode of deformed helix in FLCs (DHF mode) in a broad temperature range [22].

5.2.4 Bistability in confined ferroelectric films

In reality, boundary conditions play an essential role for many processes of electro-optical switching and, therefore, these conditions should be taken into

account for the solutions of corresponding tasks. The problem of surface tension in FLCs is sufficiently complicated because of polar interactions of the molecules, and polar and azimuth director deviations at an interface. First, we shall consider the case of strong azimuth anchoring conditions at the cell surface when the surface tension W has an elemental form as an expansion in terms of tilt (polar) angle Θ stopped to the second power [24, 25], i.e.:

$$W = \mu\Phi\Theta_{surf} + \upsilon\Theta_{surf}^2 \,, \tag{5.44}$$

where $\mu\Theta_{surf} = P_{surf}$ is the interface polarization, Φ is the effective electric potential of the smectic film surface, and υ is the parameter of Van der Waals interactions. The first term in (5.44) describes the interaction of the polarization with an interface, the second term describes interactions of induced electric dipoles. We shall show further that this simple form for the surface tension can be useful for the explanation of many phenomena in FLCs. Magnitude W leads to the heterogeneity of director and polarization distributions in the electro-optical cell when only function $\Theta(\boldsymbol{r})$ is of importance. For the book-shelf geometry of the cell and for a fixed temperature, the boundary conditions may be conjugated to the orientation of director and polarization in the bulk, for instance the tilt angle distribution may be homogeneous in the cell. However, the azimuth angle can be heterogeneous in such a case.

Let us consider, as an example, the case of a strong polar anchoring at the interface when the first term in surface tension (5.44) is much larger than the second term. We shall assume that the tilt angle is homogeneous, and, therefore, the boundary problem for the azimuth director motion can be formulated in the following way [15, 26–28]: the equation of motion is

$$PE\sin\varphi + K\Theta^2\frac{\partial^2\varphi}{\partial y^2} = \gamma\Theta^2\frac{\partial\varphi}{\partial t} \,, \tag{5.45}$$

and the boundary conditions for the film are

$$\mu\left|\Phi\right|\sin\varphi_s = \pm K\Theta\left(\frac{\partial\varphi}{\partial y}\right)_s \,, \tag{5.46}$$

where the signs $\pm$ correspond to $y = 0$ and $y = d$. For the lack of electric field, the stationary solutions of the problem are $\varphi = 0$ and $\varphi = \pi$ if magnitude $\mu\left|\Phi\right| d$ is much less than $K\Theta$. A weak electric field can induce the transitions to both the states, i.e., we have the bistabilty situation in this case. For the opposite inequality (a very strong polar anchoring), the stationary state is

$$\varphi(y) \approx \frac{\pi K\Theta}{\mu\left|\Phi\right| d} + \left(\pi - \frac{2\pi K\Theta}{\mu\left|\Phi\right| d}\right)\frac{y}{d} \,, \tag{5.47}$$

distribution (5.47) is weakly perturbed by a weak field and it is restored after switching off this field. Thus, we have the effect of mono-stability in such a case. The bistability effect exists for a strong anchoring too if the initially

applied field is strong enough. A physical reason for this effect is following. If E is sufficiently large to overcome the anchoring forces, the azimuth angle distribution becomes homogeneous ($\varphi = \pi$). In this case, the energy of electric interaction $\mu\Theta\xi_E E$ is larger than the energy of elastic azimuth perturbations $K\Theta^2/\xi_E$, the initial distribution of φ is homogeneous: $\varphi(z) = 0$. In the latter case, the applied field must be larger than a small threshold value of the order of $E_c \approx (\pi/d)^2 \left(K\Theta^2/P\right)$ to induce a heterogeneous distribution $\varphi(z) \propto \sin(\pi z/d)$. For a not very strong field above this threshold, we have the mono-stability situation.

It was shown [15, 26] that the parameter

$$\xi_E = \sqrt{\frac{K\Theta}{\mu E}} \tag{5.48}$$

is the scale of the heterogeneity near the film surface. After the field is switched off, the state $\varphi = \pi$ is stored if the surface tension $\mu\Theta\Phi$ is less than the indicated potential barrier which is to be overcome in order to return the film to the initial state. Thus, the effect of bistability occurs under a certain critical condition which can be qualitatively written as

$$\mu\,|\Phi| \sim \mu\xi_E E \sim (K\mu\Theta E)^{1/2}\ , \quad \log\left(\mu\,|\Phi|\right) = \text{const} + \frac{1}{2}\log E\ . \tag{5.49}$$

The analytic solution of the problem can be given for the more complicated boundary conditions for the azimuth angle (as compared with (5.46)) [28], which have the form

$$\mu\,|\Phi|\sin\varphi_s + \upsilon\Theta\sin 2\varphi_s = \pm K\Theta\left(\frac{\partial\varphi}{\partial y}\right)_s\ . \tag{5.50}$$

The stationary solution of (5.45) is well known:

$$\varphi(y) = 2\arcsin\left[k\cdot\mathrm{sn}\left(\frac{y}{\xi_E} - \frac{c}{\sqrt{2}}; k\right)\right] \tag{5.51}$$

with $|k| < 1$, k is modulus of the Jacobi elliptical function $\mathrm{sn}(x, k)$, c is a constant, k and c should be found by substitution of (5.51) into (5.50). The transition to the state $\varphi = \pi$ in a sufficiently high field corresponds to the limit $k \to 1$. From (5.50) and (5.51) we find

$$\varphi(y) = 2\arcsin\left[\tanh\left(\beta + \frac{y}{\xi_E}\right)\right]\ , \tag{5.52}$$

where β is the solution of the equation

$$4\frac{\upsilon}{K}\tanh^3\beta - \frac{1}{K}\left(\frac{\mu\,|\Phi|}{\Theta} + 2\upsilon\right)\tanh\beta + \frac{1}{\xi_E} = 0\ . \tag{5.53}$$

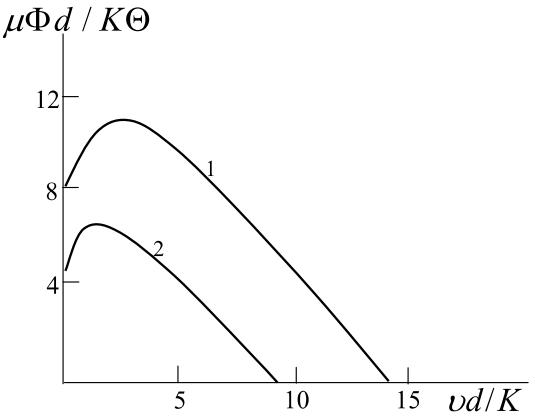

Fig. 5.11. Bistability range in the plane $(\mu\Phi d/K\Theta, \upsilon d/K)$ for the different values of parameter $(PEd^2/K\Theta^2)$, which are equal to 60 (*curve 1*) and 20 (*curve 2*) [28]. The range corresponds to the areas under the curves

For $\upsilon = 0$ and $(K\Theta/\xi_E\mu\,|\Phi|) < 1$, from (5.53) we obtain $\tanh\beta = (K\Theta/\xi_E\mu\,|\Phi|)$; for $(K\Theta/\xi_E\mu\,|\Phi|) > 1$, we get $\varphi = \pi$ everywhere in the cell. The latter condition coincides with (5.48) and (5.49) which are necessary for the bistability effect. From (5.53) the area of values of parameters υ and Φ, in which the bistability occurs, was determined (see Fig. 5.11), and the relaxation time τ_{off} was calculated numerically for the situation when field E is switched off [28]. The time τ_{off} decreased with increasing parameters υ and Φ, i.e., it is difficult to reach the bistability effect in such a case. Equation (5.49) also show that large values of modulus μ are not favorable for the effect, since the field E must be respectively large. Thus, analytic and numerical solutions of this problem [26–28] confirm the existence of the critical field value

$$E_{\text{bist}} \approx \frac{\mu\Phi^2}{K\Theta} \,. \tag{5.54}$$

The numerical calculations show that the bistability can be achieved for various initial director distributions provided the applied field exceeds the critical value.

5.2.5 Inclinations of smectic planes and dislocation walls

Let $\boldsymbol{o}$ denote a spatial orientation of smectic crystalline axis z, $\boldsymbol{e}$ denote the normal to the film surface (see Fig. 5.12), ϑ $(\vartheta_1, \vartheta_2)$ denote the two-component order parameter in a smectic C*, where

$$\vartheta_1 = n_z n_y \,, \quad \vartheta_2 = n_z n_x \,, \vartheta^2 \approx \Theta^2 \,, \tag{5.55}$$

XY is the smectic plane, polarization $\boldsymbol{P}$ is related to order parameter ϑ by

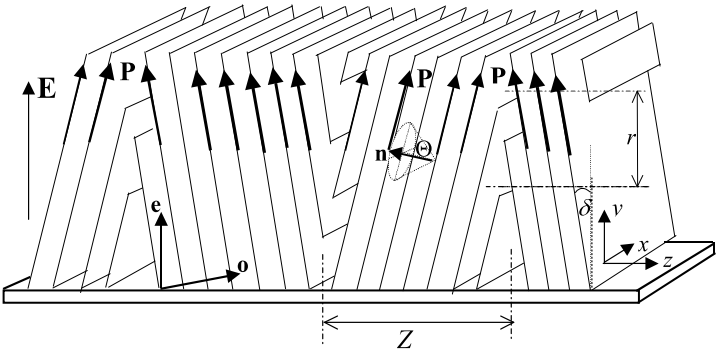

Fig. 5.12. The model of surface-induced $\delta-$ inclinations of smectic planes and dislocation walls. Formation of ferroelectric domains (only one half of the cell is shown)

equations [29]

$$P_x = \mu\vartheta_1 \ , \quad P_y = -\mu\vartheta_2 \ . \tag{5.56}$$

In fact, the terms $\mu\Theta\Phi$ and $\upsilon\Theta^2$ in surface tension W (see (5.44)) exhibit the invariants $\boldsymbol{P}\cdot\boldsymbol{e}$ and $(\vartheta\times\boldsymbol{e})^2$ respectively, vector $\boldsymbol{P}$ is assumed to be perpendicular to the film surface and vector ϑ is assumed to be parallel to the film surface in the case under consideration, i.e., here, the azimuth angle $\varphi(0)$ is equal to zero. It is correct for sufficiently strong interactions at the interface (large constants Φ and υ). Generally speaking, the invariant $(\vartheta\cdot\boldsymbol{e})^2$ is also allowable, which is non-zero for non-zero values of φ. It should be noted that vectors $\boldsymbol{o}$ and $\boldsymbol{e}$ are fixed in the case of interface chiral smectic C*-anisotropic solid, but vector $\boldsymbol{P}$ can change its azimuth orientation under the electric field action. The two mentioned invariants in W, which are Θ-squared, can be larger than the first term for sufficiently large values of Θ in a wide range of angles φ, i.e., in the case of a weak total anchoring at the interface.

Assuming that the boundary problem is solved, i.e., the $\Theta(y)$ distribution is found, we can apply (5.44) for some qualitative estimations concerning a concurrence of orientational and positional perturbations near the film surface under the influence of temperature and other factors. For instance, below the smectic A–smectic C* phase transition temperature, the surface anchoring energy W interferes with rotations of the director and polarization vectors, which must occur in the C* phase with decreasing temperature to adjust the thermodynamically equilibrium tilt angle and spontaneous polarization values. The similar problem occurs for the polarization reversal. In all such cases, the corresponding orientational perturbations must result in an accumulation of the elastic orientational energy in a certain thin sub-surface layer (in thickness ξ). We can make some qualitative conclusions [24, 25] concerning this sub-surface layer by the following estimations.

If elastic deformations of the tilt angle distribution are characterized by modulus K (the term $K(\partial\Theta/\partial y)^2$ in the free energy), and elastic deformations of the azimuth angle distribution are characterized by modulus $K\Theta^2$ (this approximation is usually applied), then, for both of these accumulated energies, we have the estimates

$$K\left(\frac{\Theta}{\xi}\right)^2 \xi \approx |W| \tag{5.57}$$

and, respectively,

$$\xi \approx \frac{K\Theta^2}{|W|}\,. \tag{5.58}$$

Thus, the accumulated elastic energy density for the heterogeneous director orientation is of the order of

$$F_{\rm or} \approx K\left(\frac{\Theta}{\xi}\right)^2 \approx \frac{W^2}{K\Theta^2}\,. \tag{5.59}$$

To release stresses in the sub-surface layer, smectic planes must bend towards proper directions from normal $\boldsymbol{e}$ in the case of the initial book-shelf geometry. But such a bending of crystalline planes can only occur if a grid of dislocations appears in the sub-surface layer. Let dislocations have characteristic core energy u per unit length and average distance r between them, the core radius is equal to molecular length l (the smectic mono-layer thickness as the Burgers vector). Then the excess in the free energy density, related to this grid of dislocations, is a magnitude of the order of

$$F_{\rm disl} \approx \frac{u}{r^2}\,. \tag{5.60}$$

The grid of dislocations turns out to be more favorable than the orientational distortion when $F_{\rm disl}$ becomes less than $F_{\rm or}$. As a result, the dislocation walls can arise with average distance $r \propto l/\delta$ between dislocations and with angle $\delta \propto l/r$ between crystalline planes in neighboring smectic parts separated by the walls. This corresponds to the appearance of smectic planes inclined in reference to the interface normal through angle δ (see Fig. 5.12). Thus, (5.57)–(5.60) lead to the expression

$$\delta \approx \pm\frac{lW}{\Theta\sqrt{Ku}} \tag{5.61}$$

in accordance with the relation $F_{\rm disl} \approx F_{\rm or}$. If surface potential enhances a polarization ($\Phi < 0$), but Van der Waals' forces do not interfere with the appearance of a finite tilt angle ($\upsilon > 0$), then, in accordance with (5.44) and (5.61), inclination angle δ admits the following estimate [24, 25]:

$$\delta \approx \pm \frac{l\,(\mu\,|W| - \upsilon\Theta)}{\sqrt{Ku}}\ . \tag{5.62}$$

Equation (5.62) shows that the δ angle is the linear function of piezo-modulus μ and tilt angle Θ. For fixed values of Θ, i.e., at fixed temperatures, the inclination angle reduces to zero for a certain value of modulus μ. In the case of the second order phase transition between smectic A and smectic C*, inclination δ is practically independent of temperature in vicinity of the phase transition point $T_{\rm AC}$, where magnitude Θ is small. On the contrary, in the case of first order transitions (for instance, chiral smectic C* – chiral nematic) as well as in the case of second order transitions and low temperatures, the inclination angle is practically proportional to the tilt angle.

In the presence of mentioned inclinations of smectic planes, which are of both signs and related to dislocation walls, the system of ferroelectric domains can arise in a thin smectic film placed between solid electrodes. It is the case of strong anchoring at the interface, and, in such a case, the inclinations occur along crystalline axis z, the sign of these inclinations periodically changes. The experimental evidence of the existence of such inclinations was given for the FLCs with a sufficiently strong spontaneous polarization by X-ray diffraction measurements [24] which show that the smectic layer inclination is almost proportional to polarization. Besides, δ changes under an external field treatment, probably due to the Φ change caused by a redistribution of ions. The measurements also show the well-pronounced transition from the domain structure to the book-shelf orientation of smectic layers when the voltage amplitude exceeds a certain threshold.

5.2.6 Ferroelectric domains in the smectic-C* films

The system of ferroelectric domains shown in Fig. 5.12 arises, as a rule, when a field treatment is applied, which is necessary for the formation of a quasi-equilibrium number of dislocation walls distributed more or less regularly along axis z, the number of walls per unit length is of the order of $1/Z$, where Z is the domain width. The problem of optimization of the domain width is strongly nonlinear because of big disturbances related to the wall formation. But we can make some qualitative conclusions concerning the start of such a formation when small orientation perturbations arise in inclined smectic planes for the lack of the effects of free charges and internal fields. We shall show that inclination δ provokes the appearance of weak modulations $\tilde{\Theta}(z)$ and $\varphi(z)$, where $\tilde{\Theta} = \Theta - \Theta_0$, Θ_0 is the thermodynamically equilibrium tilt angle, since the free energy density contains, in such a case, an additional term of the flexoelectric type [30]:

$$\mu_f \Theta^2 \mathrm{div}\boldsymbol{P} \Rightarrow \mu_f \Theta_0^2 \delta\tilde{\Theta}\frac{\partial\varphi}{\partial z}\ , \tag{5.63}$$

where $\mathrm{div}\boldsymbol{P} \approx \partial P_z/\partial z \approx \mu_f \Theta_0 \delta(\partial\varphi/\partial z)$, μ_f is a flexoelectric coefficient. Taking into account conventional corrections

$$K\Theta_0^2\left(\frac{\partial\varphi}{\partial z}\right)^2 + K\left(\frac{\partial\tilde{\Theta}}{\partial z}\right)^2 + b\Theta_0^2\tilde{\Theta}^2 \tag{5.64}$$

with positive constant b in the free energy density and assuming the harmonic dependence

$$\tilde{\Theta} \propto A\cos qz\,, \quad \varphi \propto B\sin qz\,, \tag{5.65}$$

we conclude that non-zero solutions of the corresponding linear equations for amplitudes A and B exist under the condition

$$q^2 \propto \frac{\Theta_0^2}{K^2}\left(\mu^2\mu_f^2\delta^2 - bK\right)\,. \tag{5.66}$$

From the problem (5.63)–(5.66) we see that the infinitesimal harmonic perturbations can arise if the inclination of smectic planes really occurs ($\delta \neq 0$) and the piezo- and flexoelectric constants (μ and μ_f) are reasonably large. However, it is a hard problem to calculate finite amplitudes A and B because of nonlinear processes including the appearance of dislocations and interactions of polarization charges (with density $\rho_P = -\mathrm{div}\boldsymbol{P}$) with free charges as well as because of electric currents. A qualitative solution of the problem was proposed [30] in the assumption that, for a certain level of dissipation during a finite time, one can find for a minimum of energy density

$$F = -\frac{1}{Z}(\mathrm{div}\boldsymbol{P})^2 + \left(\frac{1}{Z}\right)^2\Theta^2 - \boldsymbol{P}\cdot\boldsymbol{E}\,. \tag{5.67}$$

In the right side of (5.67), the first term describes an energy gain due to the presence of dislocation walls in which polarization charges are neutralized by free charge carriers with the same density but of the opposite sign. The second term describes an increase in the elastic energy due to a repulsion of the walls. If the domain structure is organized in such a way that vector $\boldsymbol{P}$ is in the $\{\boldsymbol{eo}\}$ plane (see Fig. 5.12), then $\mathrm{div}\boldsymbol{P} \sim (\mu\Theta\delta/\Delta z)$, where Δz is the wall width (of the order of l), and, therefore, the minimization of F with respect to Z results in the relation

$$Z \propto \left(\frac{\Delta z}{\mu\delta}\right)^2 \tag{5.68}$$

with δ given by (5.62).

We notice from this relation that the domain width is inversely proportional to the spontaneous polarization squared at low temperatures, i.e., $Z(T) \propto (T_{\mathrm{AC}} - T)^{-1}$ when $\delta \sim \Theta$, but it is finite at the phase transition temperature because of a finite value of δ for positive values of Φ. Namely such a temperature behavior of the domain width was observed experimentally [31]. The width of the domains practically does not depend on the film

thickness in accordance with (5.68), but two systems of domains were observed: the so-called "surface" and "bulk" domains. The width of surface domains is larger. The dielectric spectroscopy also shows the existence of two different modes, so-called "bulk" and "surface" modes, which have different properties. For instance, the relaxation frequency of bulk mode depends on the electric conductivity σ, but the relaxation frequency of surface mode is only dependent on the ionic concentration c_{ion}. The suppression of relaxation strengths of these modes by the bias field has a quasi-threshold character; the corresponding "threshold" field has the dependence on conductivity for the bulk mode, but it is only dependent on the ionic concentration for the surface mode.

5.2.7 Relaxation frequencies and strengths of the domain modes

5.2.7.1 Relaxation frequencies of the bulk and surface modes

In reality, both the electrochemical and diffusion processes are of importance near the electrodes. These processes change the electric potential distribution near the cell boundaries, where a volume electric charge exists in a sub-layer which has the thickness of the order of the Debye screening radius $r_D \approx (\varepsilon\varepsilon_0 k_B T/2e_{\text{ion}}^2 c_{\text{ion}})^{1/2}$, where ε is an average dielectric constant, e_{ion} is the ion charge. Due to this effect, the boundary conditions should be changed, and the ionic distribution $c_{\text{ion}}(y,t)$ as a result of the diffusion-electrical processes should be taken into account. To simplify the problem, a certain effective electric field $\tilde{E}_i$ at distances of the order of r_D from the electrodes can be considered and included into the equations written above. The simplest form of $\tilde{E}_i$ is

$$\tilde{E}_i = -\frac{\partial \Phi_i}{\partial y} = \frac{E_i r_D^2}{r_D^2 + z\,(d-y)}\,,$$

$$\Phi_i = -E_i \frac{r_D^2}{\sqrt{4r_D^2 + d^2}} \ln \frac{\sqrt{4r_D^2 + d^2} - d + 2y}{\sqrt{4r_D^2 + d^2} + d - 2y}\,, \tag{5.69}$$

where r_D is much less than d. Equations (5.69) show that $\tilde{E}_i \approx E_i$ if y and $d-y$ are less than r_D, but $\Phi_i \approx 0$ and $\tilde{E}_i \approx 0$ at the middle of the cell, i.e., when y and $d-y$ are of the order of $d/2$. The diffusion can be neglected in the bulk of a FLC if Debye length r_D is much less than d, since in this case magnitude D_{ion}/d^2 is much less than magnitude $\sigma/\varepsilon_0\varepsilon = D_{\text{ion}}/r_D^2$ in the equation of conservation of charge, where D_{ion} is an average diffusion coefficient for ionic mass (the diffusion coefficient for electric charge is $e_{\text{ion}} D_{\text{ion}}$).

It should be noted that potential Φ_i from (5.69) is much less than the applied voltage V when r_D is much less than d, therefore it can be neglected in the boundary conditions for the electric potential, but field $\tilde{E}_i$ should be taken into account in the equations of the director motion, since this field

determines the director behavior at small distances ξ from the electrodes. In general, length ξ is a result of the competition between electric and elastic forces arising near the electrodes. In the presence of field E_i, from (5.48) we obtain that $\xi = \xi_E = (K\Theta/\mu E_i)^{1/2}$. Length ξ can be of the order of r_D which is, roughly speaking, of the order of Φ_i/E_i, when r_D is much less than other lengths.

Since many facts and physical arguments indicate essential effects of free ions on the formation and behavior of the domains [30], it is reasonable to consider the bulk mode relaxation time as the space charge relaxation time τ_e,

$$\frac{1}{\tau_e} \approx \frac{\sigma}{\varepsilon\varepsilon_0} \approx \frac{D_{\text{ion}}}{r_D^2} \,. \tag{5.70}$$

Specific features of the domains near the cell boundaries allow to suppose that the surface mode relaxation time can be considered as the director deviation relaxation time τ_{or},

$$\frac{1}{\tau_{\text{or}}} \approx \frac{K}{\gamma r_{\text{ion}}^2} \approx \frac{e_{\text{ion}}^2 c_{\text{ion}} K}{\varepsilon\varepsilon_0 \gamma k_B T} \,. \tag{5.71}$$

The experimental data [30, 32] confirm that characteristic scale r_D may be essential for the relaxation processes under consideration. It should be noted that ratio $\tau_e/\tau_{\text{or}} \sim (K/\gamma D_{\text{ion}})$ is a material constant in accordance with the experimental data [30].

5.2.7.2 Relaxation strengths of the bulk and surface modes

The BIAS field effects on the relaxation strength of the considered modes, and this reflects a general suppression of the perturbations of charge and polarization, which responds to the action of a weak field. For the bulk mode, such a suppression can have a quasi-threshold character because of the dissipation processes: when the dissipation energy exceeds a certain level the thermal noise obscures the expected signal of charge density oscillations. This level is reached when, roughly speaking, the energy dissipation during time t per unit volume $\sigma E_{e,th}^2 t$ exceeds the free energy gain $\propto -Z^{-1}(\text{div}\boldsymbol{P})^2 \propto -\Theta^{-2}(\text{div}\boldsymbol{P})^4$ related to the bulk mode. Thus, a "threshold BIAS" is estimated as [30]

$$E_{e,th} \propto \mu^2 \Theta^3 \left(\frac{1}{\sigma t}\right)^{1/2} \,. \tag{5.72}$$

This threshold is independent of the cell thickness in accordance with experiments [30, 33]. It is seen also that the threshold must depend on temperature proportionally to $\Theta^3 \propto (T - T_{\text{AC}})^{3/2}$. A noticeable shift of such a threshold to lower values, when T approaches T_{AC}, was shown experimentally [30]. This dissipation process does not suppress orientation oscillations totally,

i.e., the director and polarization reorientation processes take place in high fields. The suppression of the corresponding mode demands for a different "threshold" condition. The rough estimation of the latter one, when the strong field-polarization interaction occurs, results in

$$E_{\mathrm{or},th} \propto \frac{K\Theta}{\mu r_D^2} \,. \tag{5.73}$$

This expression shows that the threshold can be considerably higher than the previous one due to a small double layer thickness r_D, and it also decreases near the T_{AC} temperature [30].

Accordingly to (5.70) and (5.71), the relaxation frequencies τ_e^{-1} and τ_{or}^{-1} have the qualitative proportionality $\tau_e^{-1} \sim c_{\mathrm{ion}} D_{\mathrm{ion}} \sim c_{\mathrm{ion}}/\alpha_{\mathrm{ion}}$ and $\tau_{\mathrm{or}}^{-1} \sim c_{\mathrm{ion}}$, where α_{ion} is the viscosity coefficient for the ion motion. Accordingly to (5.72) and (5.73), the corresponding relaxation strengths have the suppression quasi-thresholds $E_{e,th}$ and $E_{\mathrm{or},th}$ which possess proportionality $E_{e,th} \sim (\alpha_{\mathrm{ion}}/c_{\mathrm{ion}})^{1/2}$ and $E_{\mathrm{or},th} \sim c_{\mathrm{ion}}$. Because of the different dissipation processes under consideration, the discussed modes demonstrate different dependencies on the concentration and mobility of free ions. For example, the relaxation frequency and relaxation strength of the surface mode only depend on the ion concentration, they are proportional to magnitude c_{ion}. For the bulk mode, these characteristics depend on the concentration and mobility of ions, the relaxation frequency is directly proportional to the electric conductivity, and the suppression threshold squared is inversely proportional to the concentration and mobility of ions.

The effect of ionic dopants was confirmed experimentally [32] by the investigations of relaxation frequencies and relaxation strengths for various concentrations and diffusion properties of free ions. The experimental data [32] on the influence of conductive dopants on the surface mode had shown a systematical increase in the relaxation frequencies when the concentration of ionic dopants increased. The corresponding relaxation strength also shifted to higher values under these conditions, i.e., the quasi-threshold increases also. The relaxation frequency of the bulk mode had shown a different behavior for different dopants: large molecules of dopant 1,4-bis(dicyane-methylene)-2,5-cyclohexadiene (TCNQ) with low mobility overpowered the increase in the ion concentration, i.e., the conductivity decreased due to such dopants and, correspondingly, the relaxation frequency decreased; the dopant tetrabutyleammoniumiodide (TBAI) increased this frequency due to a higher mobility of ions. A clear correspondence between these data and the concentration dependence of the relaxation strengths was observed: the TBAI dopant shifted the relaxation strength as a function of the applied BIAS to smaller values of the voltage, but the TCNQ dopant shifted the corresponding curve to larger values of the voltage. Thus, these experiments had shown substantial effects of free charges on the existence of the ferroelectric domain structure in compounds with high spontaneous polarization.

5.2.7.3 Elimination of the ferroelectric domains by a strong field

The third term in (5.67) describing the interaction between external field and polarization can induce the transition of inclined smectic planes to the book-shelf state if E exceeds a certain threshold value $E_{\rm sat}$. Equation (5.67) allows to estimate qualitatively $E_{\rm sat}$ when the polarization and director orientations occupy optimum positions under the action of strong field (see Fig. 5.12). In such a case, a further increase in E will induce a rotation of the director cones and smectic planes towards new positions with smaller inclination angle δ, the polarization saturation occurs for $\delta = 0$. Accordingly to (5.67), for finite values of δ, the energy gain, due to the presence of dislocation walls, is of the order of $-\mu^4\Theta^2\delta^4$, but the energy loss because of a mismatch between vectors $\boldsymbol{P}$ and $\boldsymbol{E}$ is of the order of $\mu E\Theta\delta^2$. Therefore, such a mismatch is not essential for sufficiently large values of δ and for small values of E, but it leads to a general unsuitability of this domain structure if E exceeds a saturation value of the order of

$$E_{\rm sat} \propto \mu^3\delta^2\Theta\ . \tag{5.74}$$

Thus, this rough estimate shows that the domain walls can be eliminated by relatively strong fields, and the saturation field value has a strong nonlinear dependence on piezo-modulus μ in accordance with experimental data [25].

5.2.7.4 Surface orientational relaxation in the ferroelectric smectic

In general, a surface orientation relaxation can also exist in the absence of the domain structure (for instance, for a weak spontaneous polarization), but in the presence of surface tension of the type (5.44). As an example, the observed surface mode with relaxation frequency $1/\tau_{\rm or}$ in the chiral C* phase with the initial homeotropic alignment should be mentioned [34, 35]. This phenomenon was studied in a FLC possessing the first order phase transition chiral smectic C*–chiral nematic N*. The surface relaxation appeared at the temperature T_{th}, nearly 10 K below the transition temperature T_{NC}. At this temperature, a change in the texture was observed: the homeotropic alignment disappeared and a partial planar alignment became visible.

To explain this effect, let us apply (5.44), where, now, the first term describes the gain in energy when the polarization vector is parallel to the film surface (for the homeotropic director orientation), and the second term describes an increase in the surface energy when director $\boldsymbol{n}$ deviates from surface normal $\boldsymbol{e}$ (in the C* phase, the director takes a position at the cone surface at an angle of the order of Θ to the surface normal). We shall assume that there is an internal field E_i near the film surface in a sub-layer (in thickness r_D). It is apparent that, by analogy with the consideration of bistability effects, the internal field tends to change the polarization and director orientations to new states if interaction $PE_i = \mu\Theta E_i$ overcomes a potential barrier (within

the sub-layer) of the order of $F_{\rm or}$ (see (5.59)). A new orientation state arises (and it is stored) if the applied field (here, E_i) is larger than the threshold field value

$$E_{th} \approx \frac{K\Theta}{\mu\xi^2} \approx \frac{W^2}{K\mu\Theta^3} \tag{5.75}$$

which coincides with the estimate of $E_{\rm bist}$ (see (5.54)). For a weak homeotropic anchoring at the interface, we can consider a limit case when $\mu|\Phi|$ is much larger than $\upsilon\Theta$. In this case, we notice from (5.75) that, for a given value of field E_i, the condition $E_i \geq E_{th}$ is only fulfilled for sufficiently large values of Θ. Therefore, we can estimate a threshold (minimum) value of Θ (Θ_{th}) as a function of E_i:

$$\xi \approx \frac{K\Theta}{\mu\,|\Phi|}\,, \Theta_{th} \approx \frac{\mu\Phi^2}{KE_i}\,, \xi_{th} \approx \frac{|\Phi|}{E_i}\,. \tag{5.76}$$

Thus, Θ_{th} is finite and, therefore, the effect is only possible at temperatures below the corresponding threshold temperature T_{th} which is less than T_{NC}. This effect is more probable for first order phase transitions than for second order ones since the tilt angle can be sufficiently large near the first order transition point. For intermediate temperatures below T_{NC}, we shall use the dependence $\Theta(T) \sim \sqrt{(b^*/\alpha^*)(T_{NC}-T)}$, where α^* and b^* are coefficients in an ordinary expansion for the free energy. Thus, a rough estimate for T_{th} is

$$(T_{NC} - T_{th}) \approx \frac{b^*}{\alpha^*}\Theta_{th}^2\,. \tag{5.77}$$

Correspondingly, an estimate for relaxation frequency $\omega_{\rm or}$ at $T \approx T_{th}$ is

$$\omega_{\rm or} = \frac{1}{\tau_{\rm or}} \approx \frac{K}{\gamma\xi^2} \approx \frac{K}{\gamma}\left(\frac{E_i}{\Phi}\right)^2\,. \tag{5.78}$$

For estimations, we shall use typical data
$\alpha^* \sim 10^3\,\mathrm{J\cdot m^{-3}\cdot K^{-1}}$, $b^* \sim 10^6\,\mathrm{J\cdot m^{-3}}$, $(T_{NC}-T_{th}) \sim 10\,\mathrm{K}$, $\omega_{\rm or} \sim 10^4\,\mathrm{s^{-1}}$, $\mu \sim 10^{-4}\,\mathrm{C\cdot m^{-2}}$, $K \approx 10^{-11}\,\mathrm{N}$, $\gamma \approx 10^{-1}\,\mathrm{Pa\cdot s}$,
then (5.75)–(5.78) lead us towards the values:

$$\xi \sim 0.1\,\mu\mathrm{m}\,, \quad |\Phi| \sim 0.1\,\mathrm{V}\,, \quad E_i \sim 10^6\,\mathrm{V\cdot m^{-1}}\,. \tag{5.79}$$

We would like to emphasize here that the parameters (5.79) were determined from the measured magnitudes $\omega_{\rm or}$ and T_{th}. Taking into account a probable "electric" nature of the ξ scale, we can conclude that ξ represents a typical estimate ($0.1\,\mu$m) for the electric screening radius r_D which is related to surface potential Φ and internal field E_i by a reasonable relation: $r_D \sim |\Phi|/E_i$. Thus, we conclude that the described relaxation process near the interface is really explained, in the framework of the present approach, by the deformation of homeotropic alignment in the smectic C* phase.

5.2.8 Problem of hysteresis-free electro-optical switching

5.2.8.1 Observations and models of the V-shaped electro-optical switching

The V-shaped switching takes place in a certain part of the temperature interval of existence of the ferrielectric and SmC* phases [12, 36, 37]. In some substances, the formation of a striped texture along the normal to smectic layers was observed during the switching when the smectic layers were approximately normal to a substrate [38]. The domains were visible optically in the absence of an applied electric field. It was discussed [38] that the surface effect plays a crucial role in the V-shaped switching. In the rubbing cell, the width of the domains was much narrower than in the temperature gradient cell. The domains [38] were quite similar to the domains observed in the FLCs [24, 30, 39]. The light transmittance at zero voltage was quite low in the rubbing cell.

In other substances, the mentioned striped texture and domains were not observed [40] but the X-ray diffraction investigations had shown the inclinations of smectic planes from the normal to a substrate on large angles δ (a chevron angle $\sim \pi/10$). It was suggested [41] that in the cell bulk the director distribution is homogeneous, while there is a director twisting in a thin sub-surface layer near the substrate. It was shown [42, 43] that the increase in amount of charged impurities resulted in a change of V-shape and in hysteresis phenomena.

The reported experimental data allow to make the conclusion that, in the AFLC mixtures, the charged dislocation walls are related to the inclinations of smectic planes, as in the case of a SSFLC [30], and they may play the role of importance for the observed phenomena. Really, the chevron angle δ is an inevitable consequence of the effects at the interface FLC/substrate [24, 39]. It was noted above that the inclinations of both signs are equivalent, and they inevitably result in the appearance of dislocation walls possessing the polarization charges (see Fig. 5.12). The polarization charges are favorable if the amount of free ions is enough to neutralize them.

When the ion mobility is high, but the ion concentration is low, and the field change is slow, then the ions succeed the field change and the dislocation walls become unfavorable because of non-compensated polarization charges. Contrary, a low ion mobility, a high ion concentration, and a fast field change promote the preservation of the dislocation walls since, in such a case, they are partially neutralized. The existence of the bulk domains results, in general, in a poor reversibility and hysteresis phenomena.

A fairly high light transmittance in the temperature gradient cell with respect to the rubbing cell [38] is related to a smaller value of the δ inclination (because of a weaker surface anchoring) and, as a consequence, to a larger disturbance of the optical axis orientation in the bulk of the cell. A larger frequency (~ 1 Hz) of ac field results in a hysteresis in the V-shaped

switching at low temperatures that can be explained by the presence of the bulk dislocation walls which possess large polarization charges only partially compensated during the polarization reversal.

The V-shaped switching was also observed in AFLCs in the absence of the bulk domains [37]. It should be underlined that the bulk domains are not necessary for the reversible V-shaped switching. Contrary, such domains trouble the reversible rotation of the polarization vector by an ac field. However, the surface dislocation walls and ferroelectric domains must obviously appear because of the surface tension effects.

The reasons why the reversible V-shaped switching is observed in the new AFLC mixtures may be the following. Large values of the δ angle, which increases with the increase in piezomodulus μ and anchoring constant W [24], may result in large polarization charges, related to the surface dislocation walls, and in small domain widths. In FLCs, this width is about several μm, while in the studied AFLC [38] it was much less, for instance in the rubbing cell. The measured δ angles [24, 40] drastically differ: in the AFLCs, δ is several times larger than in the FLCs.

The amount of free ions must not be large to avoid the bulk domains. The polarization charges related to the surface walls are stronger than the charges which appear due to polarization twisting along the normal to a substrate in such a sub-layer. The surface walls promote to the reversibility of azimuth rotations in weak electric fields. The reversibility in weak fields may be related to a large value of the dc field E_{bist} for the effect of bistability, since the bistability threshold, related to the existing walls, strongly depends on the δ value [24],

$$E_{\text{bist}} \propto \frac{\delta^4 \mu^3 \Theta}{K} \,. \tag{5.80}$$

Equation (5.80) is the consequence of equations of type (5.44) and (5.54) when the domain wall surface tension W_{dw} of the order of $W_{dw} \sim (\text{div}\boldsymbol{P})^2 l^3 \sim l\delta^2 P^2$ is taken into account.

The bulk domains and dislocation walls must be absent for high values of δ and low concentrations of ions, since, in this case, free ions do not compensate a large polarization charge, but the surface walls must be present. In such a case, the distribution of the polarization vector and director in the cell is shown in Fig. 5.13. The polarization vector is parallel to the film surface for zero field value to avoid the appearance of a non-compensated polarization charge in the bulk of the film. Here, a hysteresis phenomenon is less probable.

When the applied field and ionic motion, as it was noted above, promote to the preservation of the bulk walls, the polarization vectors on the inclined director cones are parallel to the film surface for zero field value, as in the previous case, because of the same reasons. But, here a hysteresis phenomenon can take place. Figure 5.14 shows the corresponding distribution of the bulk walls and director orientations.

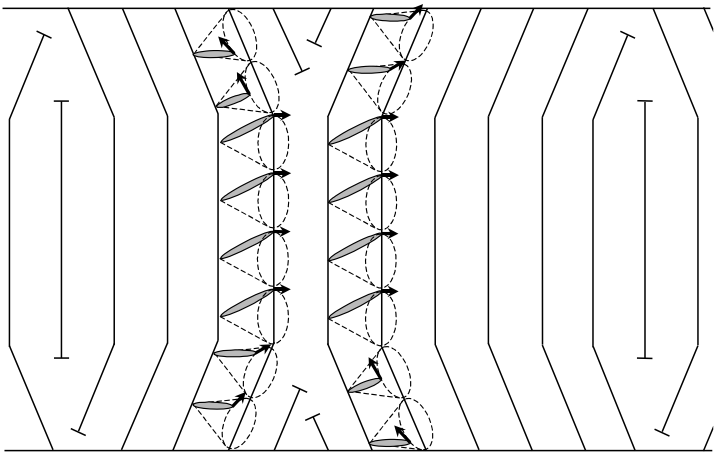

Fig. 5.13. The distribution of director orientations for a sufficiently high ac field may eliminate the bulk walls at low frequencies. The surface dislocation walls are present

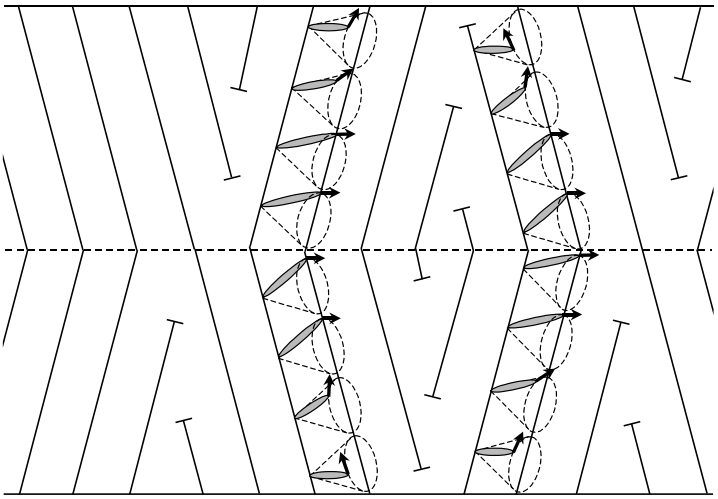

Fig. 5.14. The distribution of the bulk walls and director orientations for a low ac field may preserve the bulk walls at high frequencies during the process of polarization reversal in the cell bulk

Thus, from the comparative analysis of switching data on FLCs and AFLCs, it can be concluded that the reversible V-shaped switching is due to a relatively strong anchoring at the cell surface, a large piezoelectric effect, a low content of free ions, and due to the existence of narrow surface domains. Hysteresis phenomena arise during the switching due to the increasing content of free ions and appearance of the bulk domains.

5.2.8.2 Basic equations and assumptions

We shall consider the problem of hysteresis-free switching for the cell with the book-shelf geometry (see Fig. 5.8) assuming the absence of the bulk domains, the surface domains are assumed to create strong anchoring conditions at the surface of the FLC layer. For the description of the switching process in alternating electric fields, we should take into account in general the following system of equations: the equation for the distribution of director azimuth orientation $\varphi(y,t)$ arising under the influence of electric field $E_y(y,t)$ inside the cell; the equation for distribution $E_y(y,t) = -\partial\Phi(y,t)/\partial y$ (electric potential $\Phi(y,t)$ may be a more convenient variable for numerical calculations) which follows from the law of conservation of external charge with density ρ_{ion} and the Maxwell equation $\partial D_y/\partial y = \rho_{\text{ion}}$, where electric induction $D_y = \varepsilon_0 E_y + P_y$; the equation of the motion of medium, in the presence of the external charge, with velocity v_y; the equation of continuity for concentration c_{ion} reflecting the mass conservation law which transforms into the diffusion equation in the absence of an electric current and a macroscopic fluid motion. Thus, this problem is very complicated. It is possible to simplify it under certain assumptions.

Since velocity v_y has the order of value of $\tau_m E_y \rho_{\text{ion}}$, where τ_m is the characteristic relaxation time L^2/α, L is the characteristic size on which v_y changes, α is the fluid viscosity, $E_y\rho_{\text{ion}}$ is the volume force, magnitude v_y $\partial\rho_{\text{ion}}/\partial y$ in the charge conservation law can be neglected, as a second order term, if the external charge density ρ_{ion} is sufficiently small. The diffusion can be also neglected in the bulk of a FLC if Debye length r_D is much less than d as it was discussed above. In this case, the mentioned law has the form

$$\frac{\partial\rho_{\text{ion}}}{\partial t} + \frac{\partial}{\partial y}(\sigma E_y) = 0\,. \tag{5.81}$$

Taking into account the Maxwell equation, from (5.81) we obtain the equation

$$\frac{\partial}{\partial y}\left[-\sigma\frac{\partial\Phi}{\partial y} + \frac{\partial}{\partial t}\left(-\varepsilon_0\frac{\partial\Phi}{\partial y} + P_y\right)\right] = 0 \tag{5.82}$$

which can be rewritten, for $P_y = P\cos\varphi$, in the form

$$\varepsilon_0\frac{\partial^2\Phi}{\partial y\partial t} + \sigma\frac{\partial\Phi}{\partial y} + P\sin\varphi\frac{\partial\varphi}{\partial t} = 0\,. \tag{5.83}$$

The second assumption is related to the equation of the motion of medium, in which the estimate $v_y \sim \tau_m E_y \rho_{\rm ion}$ was used above. This motion interacts with director deviations, namely torque $\left(\tilde{\alpha}\Theta^2/L\right) v_y$ is acting on the director, $\tilde{\alpha}$ being a specific small viscosity coefficient which is similar to the Lesli coefficient α_3 for nematics. Thus, the term $\left(\tilde{\alpha}\Theta^2 L/\alpha\right) E_y \rho_{\rm ion}$ could be included into the equation of the director azimuth change in the spatial range of size L, but it is small because magnitude $(\tilde{\alpha}\Theta^2/\alpha)$ is much less than unity. Due to these assumptions, the equation for director motion has the form

$$\gamma\Theta^2 \frac{\partial\varphi}{\partial t} = K\Theta^2 \frac{\partial^2\varphi}{\partial y^2} - P\frac{\partial\Phi}{\partial y}\sin\varphi \,. \tag{5.84}$$

The boundary conditions for variables φ and Φ at the cell surface are simple for a strong anchoring and when diffusion phenomena are neglected:

$$\varphi = 0 \text{ at } y = 0 \text{ and } y = d\,; \;\; \Phi = 0 \text{ at } y = 0\,, \quad \Phi = -V\cos\omega t \text{ at } y = d\,. \tag{5.85}$$

Thus, accordingly to (5.83) and (5.84) and made assumptions, the final form of two equations for the two variables $\varphi(y,t)$ and $\Phi(y,t)$ is

$$\gamma\Theta^2 \frac{\partial\varphi}{\partial t} = K\Theta^2 \frac{\partial^2\varphi}{\partial y^2} - P\sin\varphi\frac{\partial(\Phi+\Phi_i)}{\partial y}\,, \tag{5.86}$$

$$\varepsilon_0 \frac{\partial^2(\Phi+\Phi_i)}{\partial y\partial t} + \sigma\frac{\partial(\Phi+\Phi_i)}{\partial y} + P\sin\varphi\frac{\partial\varphi}{\partial t} = 0 \tag{5.87}$$

with boundary conditions (5.85) and magnitude Φ_i presented in form (5.69). The system of equations (5.86)–(5.87) can be used for numerical calculations.

For an analytic approach and estimates, it is convenient to use an approximation in the form $E_y(y,t) = E_0\cos\omega t + \Xi(y,t)$, where perturbation $\Xi(y,t)$ is small if polarization P is not large, this case is of interest for applications. Besides, magnitude Φ_i can be omitted for certain estimates. Below, we shall consider equations

$$\gamma\Theta^2 \frac{\partial\varphi}{\partial t} = K\Theta^2 \frac{\partial^2\varphi}{\partial y^2} + P\left(E_0\cos\omega t + \Xi\right)\sin\varphi\,, \tag{5.88}$$

$$\frac{\partial\Xi}{\partial t} + \frac{\sigma}{\varepsilon_0}\Xi - \frac{P}{\varepsilon_0}\sin\varphi\frac{\partial\varphi}{\partial t} = 0\,, \tag{5.89}$$

and show that the phase shift in distributions $E_y(y,t)$ and $\varphi(y,t)$ is responsible for hysteresis phenomena during the switching process. It will be seen that the hysteresis-free electro-optical switching demands a certain correspondence between the characteristic frequencies which are: ω, space charge relaxation frequency $\sigma/\varepsilon_0\varepsilon$, orientational relaxation frequency $\omega_{\rm or} \sim (Kq^2/\gamma)$, inverse switching time $a = (PE/\gamma\Theta^2)$, inverse switching time due to P itself $\tau^{-1} \sim (P^2/\varepsilon_0\gamma\Theta^2)$.

5.2.8.3 Switching of the cell with a low conductivity FLC and an additional low resistance

First, we shall consider the case of very small conductivity of a FLC. In this case, we obtain from (5.88) and (5.89) that $\Xi \approx -(P/\varepsilon_0)\cos\varphi$, and for qualitative estimations, the φ distribution is described in the bulk of the cell by equation

$$\gamma\Theta^2\frac{\partial\varphi}{\partial t} = K\Theta^2\frac{\partial^2\varphi}{\partial y^2} + P\left(E_0\cos\omega t - \frac{P}{\varepsilon_0}\cos\varphi\right)\sin\varphi\,, \tag{5.90}$$

which has solutions

$$\varphi = \arctan\left\{1/\left[\sinh\left(\text{const} \pm \frac{y}{\xi_P} - \frac{a}{\omega}\sin\omega t\right)\right]\right\}\,, \tag{5.91}$$

where $\xi_P = (\varepsilon_0 K\Theta^2/P^2)^{1/2}$, values of y are larger than distances ξ and $d-\xi$ from the cell surface. Equations (5.90) and (5.91) are similar to (5.36)–(5.38). The choice of the solution form in (5.91) depends on boundary conditions. For example, for symmetric conditions (5.85), we can write

$$\varphi = \arctan\left\{1/\left[\sinh\left(-\frac{y}{\xi_P} - \frac{a}{\omega}\sin\omega t\right)\right]\right\} \quad \text{if } y < d/2\,, \tag{5.92a}$$

$$\varphi = \arctan\left\{1/\left[\sinh\left(\frac{y-d}{\xi_P} - \frac{a}{\omega}\sin\omega t\right)\right]\right\} \quad \text{if } y > d/2\,. \tag{5.92b}$$

At $y \sim \xi_P$ and $\sim (d-\xi_P)$, φ is close to 1, but for larger values of y, i.e., in the cell bulk, φ is close to π when a is less than ω. If the velocity of kinks $v = \pm a\xi_P$ (see Sect. 5.2.2.2 and Fig. 5.9) is high enough, then such a kink is travelling through the whole cell during the time d/v which is shorter than period $2\pi/\omega$. In the latter case, we can consider the φ distribution as a slightly heterogeneous in the cell (the characteristic length is about d) except the narrow layers of width q^{-1} near the FLC layer boundaries.

Near the cell boundaries, the φ value can be estimated by using the expansion

$$\varphi(y,t) = Bqy + (qy)^3\, g_1(t) + (qy)^5\, g_2(t) + \ldots \tag{5.93}$$

which shows that $\varphi = 0$ at $y = 0$ for strong anchoring conditions. Here, B is a constant, q^{-1} is a characteristic length determined by the sub-surface behavior of a FLC (see Sect. 5.2.7.1). The substitution of expression (5.93) into (5.88) results in magnitudes

$$g_1 = -\frac{Ba}{6\omega_{\text{or}}}\cos\omega t\,,\, g_2 = \frac{Ba}{120\omega_{\text{or}}^2}(\omega\sin\omega t - a\cos^2\omega t)\,, \tag{5.94}$$

where $\omega_{\text{or}} \approx Kq^2/\gamma$.

In the static situation and in the presence of field E_i, from (5.90) we obtain that $\varphi = 2\arcsin[\tanh(qy)]$, where $q = (PE_i/K\Theta^2)^{1/2} \sim \xi_E^{-1}$ with ξ_E given by (5.48), i.e., φ is equal to zero at $y = 0$, but $\varphi = \pi$ if q^{-1} is much less than y. It was mentioned above that length q^{-1} can be of the order of r_D when r_D is much less than other characteristic lengths. For a sufficiently large value of P, magnitude q^{-1} may be of the order of the kink width ξ_P. In the latter case, expressions (5.92) and (5.93) should be comparable at $y \sim \xi_P$ and $\sim (d-\xi_P)$, and this leads to some conditions for B, $\omega_{\rm or}$, ω, and a, which correspond to the existence of the considered solutions. For example, distribution (5.92) with maximum values of angle $\varphi \approx \pi$ in the bulk occurs if ω is much less than a. In general, due to boundary conditions and arbitrary values of a, ω, and $\omega_{\rm or}$, values of φ in the bulk can be less than such a maximum. We suppose that magnitudes B and $\omega_{\rm or}$ can be obtained, for instance numerically, for the problem with the mentioned boundary conditions. Further, we shall discuss mainly the bulk behavior of distribution $\varphi(y,t)$.

The analytic estimation of light transmittance $I(t)$ through the cell with the crossed polarizers and with distribution $\varphi(y,t)$ inside can be done for small tilt angles Θ and a corresponding weak change in the director orientation in the cell plane (see Fig. 5.15). In this case, for an average value of this change squared, we have

$$I(t) \propto \frac{1}{d}\int_0^d \sin^2(2\psi)\mathrm{d}y \approx 4\Theta^2 \cdot \frac{1}{d}\int_0^d \cos^2\varphi \mathrm{d}y\ , \tag{5.95}$$

where $\psi \approx \Theta\cos\varphi$ is the angle between the polarization vector of incident light and the director orientation in the cell plane. Here, an ordinary phase retardation multiplier is not written. The integration in (5.95) (taking into account (5.92)) results in the estimate

$$I(t) \propto \left\{1 - \frac{2\xi_P}{d}\left[\tanh\left(\frac{d}{2\xi_P} + \frac{a}{\omega}\sin\omega t\right) - \tanh\left(\frac{a}{\omega}\sin\omega t\right)\right]\right\} \tag{5.96}$$

which shows that the transmittance has a minimum

$$I_{\min} \propto \left\{1 - \frac{2\xi_P}{d}\left[\tanh\left(\frac{d}{2\xi_P} - \frac{a}{\omega}\right) + \tanh\left(\frac{a}{\omega}\right)\right]\right\} \tag{5.97}$$

at $\omega t = 3\pi/2$ when the magnitude a is less than ω. Contrary, $I(t)$ has its maximum

$$I_{\max} \propto \left\{1 - \frac{2\xi_P}{d}\left[\tanh\left(\frac{d}{2\xi_P} + \frac{a}{\omega}\right) - \tanh\left(\frac{a}{\omega}\right)\right]\right\} \tag{5.98}$$

at $\omega t = \pi/2$ in the latter case.

If we consider the transmittance as a function of the applied field E, then (5.96) shows large hysteresis if a is less than ω, since the increase and

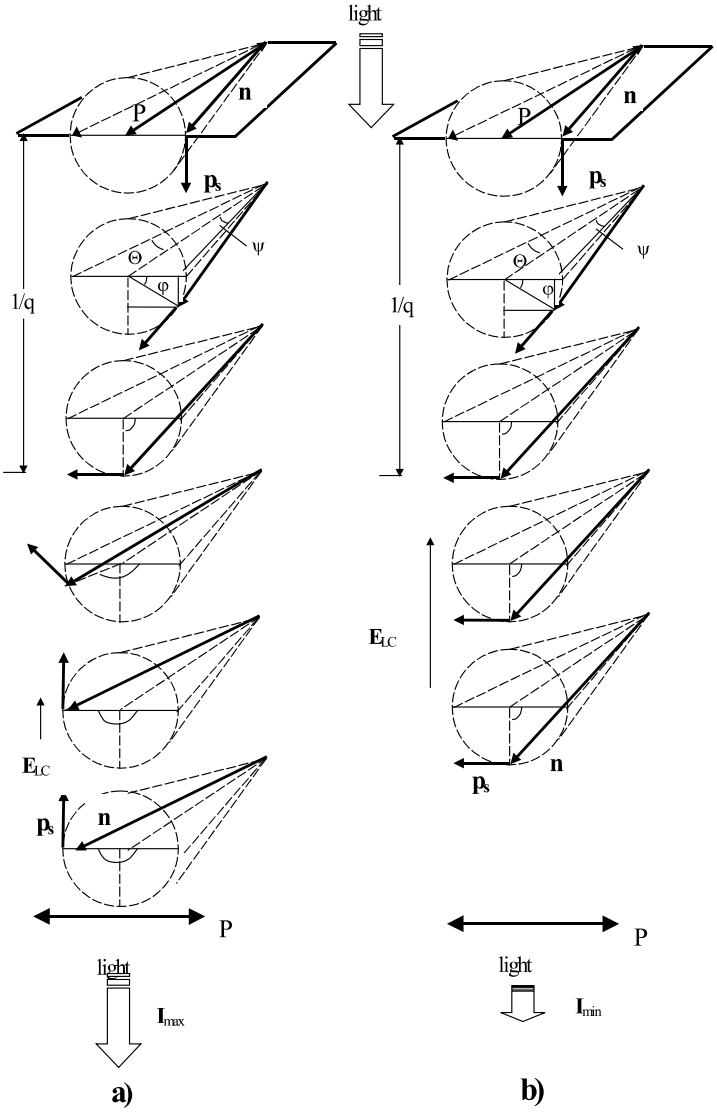

Fig. 5.15. A sketch of the director distribution over the cell thickness in the absence of hysteresis in the optical transmittance (only upper half of the cell with crossed polarizers P is shown). (**a**) case $U = U_0$, $E_{\mathrm{LC}} \approx 0, \varphi$ in the bulk $\approx \pi, \psi$ is finite everywhere throughout the cell, and the optical transmission is maximum; (**b**) case $U = 0, E_{\mathrm{LC}}$ is finite, φ in the bulk $\approx \pi/2$, therefore $\psi \approx 0$, and the optical transmission is minimum

decrease in E during the two halfs of period $2\pi/\omega$ results in the minimum and maximum of $I(t)$ for $E = 0$. This means that, for a finite frequency of the field applied to the FLC layer with a high electric resistance, field hysteresis obviously exists. But, when frequency ω is much less than a, the hysteresis can be avoided with respect to the alternating voltage $U = U_0 \sin \omega t$ applied to whole electric circuit, where a resistor (with very small resistance R_1) is connected in parallel with the FLC layer, and a capacitor (with not large capacitance C_2) is connected in series with the FLC layer. In the latter case, if the voltage across the FLC layer is equal to $V \cos \omega t \approx \omega R_1 C_2 U_0 \cos \omega t$, then $U = -U_0 \sin(\omega t - \delta)$, where $\delta \approx \omega R_1 (C_{\mathrm{LC}} + C_2)$. In reality, capacitance C_2 is the capacitance C_p of the aligning polymer layer of thickness d_p which is less than the FLC layer thickness d.

Thus, for $a \gg \omega$, from (5.96), where $a = \omega R_1 C_2 U_0 P/\gamma \Theta^2 d$, we obtain that the hysteresis with respect to voltage $U = -U_0 \sin(\omega t - \delta)$ takes place, but it could be small if δ is small. The latter conditions are fulfilled if $a \gg R_1^{-1}(C_{\mathrm{LC}} + C_2)^{-1} \gg \omega$, and, in this case, from (5.96) we have

$$I_{\min} \propto \left[1 - \frac{2\xi_P}{d} \tanh\left(\frac{d}{2\xi_P}\right)\right] \text{ for } \omega t = 0\,, \quad \pi\,;$$
$$I_{\max} \propto \left[1 - \cosh^{-2}\left(\frac{a}{\omega}\right)\right] \text{ for } \omega t = \pi/2\,, \quad 3\pi/2\,. \tag{5.99}$$

Equations (5.97)–(5.99) show a thickness dependence of the transmittance which is high for small values of the ξ_P/d ratio because, in such a case, only a narrow range of the FLC layer has the director orientation $\varphi \sim \pi/2$ which almost coincides with the orientation of one of the polarizers (see Fig. 5.15).

It should be noted that (5.99) could determine the relations for a weak hysteresis of light transmittance of the FLC layer with respect to the voltage acting in an electric circuit when the following conditions are fulfilled: the FLC layer possesses a relatively small resistance $R_1 = R_{\mathrm{LC}} = (d/S\sigma)$, where S is the electrode area; the external capacitor and the FLC layer have not large capacitance $C_2 = C_p$ and $C_1 = C_{\mathrm{LC}}$ respectively. But this situation of sufficiently high conductivity demands taking into account the conductivity term in (5.89) that changes the director and polarization distributions and gives a possibility for the hysteresis-free behavior of light transmittance with respect to the external voltage U.

5.2.8.4 Hysteresis-free switching for high frequency voltage applied to the cell

To take into account the FLC conductivity, we should find the solutions of the complete equations (5.86) and (5.87) with proper boundary conditions. In general, this problem demands computer calculations. To get some qualitative analytic results, we shall analyze (5.88) and (5.89), where the approximation $E_y(y,t) = E_0 \cos \omega t + \Xi(y,t)$ is used, Ξ being less than E_0, but it seems that qualitative results are valid for $\Xi \sim E_0$. Perturbation Ξ is found from (5.89)

into which magnitude φ as a solution of (5.88) is substituted. For estimations, we assume that parameter a is larger than frequency ω and, correspondingly, function $\varphi(y,t)$ smoothly changes along axis y during period $2\pi/\omega$, i.e., $\partial\varphi/\partial y \sim 1/d$ inside the FLC layer except narrow sub-surface layers. Then the solution of (5.88), where term $(\partial\varphi/\partial y)^2$ is neglected, takes the form

$$\varphi(y,t) \approx \arctan\left[\sinh\left(\text{const} \pm \frac{y}{d} - \frac{a}{\omega}\sin\omega t\right)\right]^{-1} . \tag{5.100}$$

Respectively, magnitude Ξ takes the form

$$\Xi \approx \frac{aP}{\varepsilon_0}\exp\left(-\frac{\sigma}{\varepsilon_0}t\right)\int^{t}\exp\left(\frac{\sigma}{\varepsilon_0}t'\right)\cosh^{-2}Y(y,t')\cos\omega t'\,\mathrm{d}t' , \tag{5.101}$$

where $Y(y,t) = -(a/\omega)\sin\omega t \pm (y/d) + \text{const} \approx -at \pm (y/d) + \text{const}$ in the bulk of the FLC layer for time t less than $1/a$. Near the layer boundaries, at distances of the order of q^{-1} from them, function $\varphi(y,t)$ is described by (5.93). Thus, in the approximation under consideration, from (5.93), (5.100) and (5.101) we obtain the estimate of Ξ for the bulk:

$$\Xi \approx \frac{4aP}{\varepsilon_0[(\sigma\varepsilon_0^{-1}-2a)^2+\omega^2]}\exp(2Y_0)\left[\left(\sigma\varepsilon_0^{-1}-2a\right)\cos\omega t + \omega\sin\omega t\right] , \tag{5.102}$$

with magnitude $Y_0 \approx \pm(y/d) + \text{const}$ which is about $1/2$ in the center of the layer; and the value of Ξ near the surface:

$$\Xi \approx \frac{BaP\omega(qy)^4}{6\varepsilon_0\omega_{\mathrm{or}}(\sigma^2\varepsilon_0^{-2}+\omega^2)}\left(\sigma\varepsilon_0^{-1}\sin\omega t - \omega\cos\omega t\right) \tag{5.103}$$

with magnitude $\omega_{\mathrm{or}} \sim Kq^2/\gamma$. Equation (5.102) shows that, for small values of σ, the perturbation Ξ can be opposite in sign to field $E_0\cos\omega t$ when σ/ε_0 is much less than ω, since, in this case, free ions have no time to compensate the polarizational charges near the electrodes during the zero-field relaxation time $\varepsilon_0\sigma^{-1}$. If ω is much less than σ/ε_0 and a, then free ions have time to compensate the polarizational charges when σ/ε_0 is large than $2a$, and field Ξ can coincide in sign with field $E_0\cos\omega t$ in this case, but, if σ/ε_0 is less than $2a$, the signs of these fields can be opposite.

We see from (5.103) that Ξ is the rapidly increasing function of y. For $qy \sim 1$, values (5.102) and (5.103) should be approximately equal. Thus, we get the following conditions for characteristic frequencies:

$$\frac{B\sigma\varepsilon_0^{-1}}{6\omega_{\mathrm{or}}(\sigma^2\varepsilon_0^{-2}+\omega^2)} \approx \frac{4}{(\sigma\varepsilon_0^{-1}-2a)^2+\omega^2} ; \quad \omega^2 \approx \sigma\varepsilon_0^{-1}\left(2a-\sigma\varepsilon_0^{-1}\right) . \tag{5.104}$$

If magnitudes B and $\omega_{\rm or}$ are known from the solutions (5.93) and (5.100) of the problem with $\Xi = 0$, then conditions (5.104) are necessary for the existence of solutions (5.102), (5.103) and a corrected solution for angle φ with maximum values $\varphi \sim \pi$ in the bulk. In general, B and $\omega_{\rm or}$ should be obtained for such a corrected function $\varphi(y,t)$.

To calculate function $\varphi(y,t)$, we should substitute magnitude Ξ into (5.88) and solve this latter for a new field value E. This leads us to substitution of term $-(a/\omega)\sin\omega t$ in Y by term $-(a/\omega)\sin\omega t - (P/\gamma\Theta^2)\int \Xi {\rm d}t$. In this case, the transmittance depends mainly on the bulk behavior of φ, and, therefore, $I(t)$ is approximately determined by the equation of type (5.95),

$$I(t) \propto \left\{ 1 - \frac{2}{d} \int\limits_0^{d/2} \frac{{\rm d}y}{\cosh^2\left(\frac{y}{d} + \frac{a}{\omega}\sin\omega t + \frac{P}{\gamma\Theta^2}\int\limits^t \Xi(y,t'){\rm d}t' \right)} \right\} , \qquad (5.105)$$

with magnitude Ξ given by (5.102). It is seen from (5.105) that the transmittance has a minimum

$$I_{\rm min} \propto \left(1 - \frac{2\omega}{a\sin\omega t} \right) , \qquad (5.106)$$

with $0 < \omega t < \pi/2$, when

$$\frac{a}{\omega}\sin\omega t + \frac{P}{\gamma\Theta^2}\int\limits^t \Xi(y,t'){\rm d}t' = 0 , \qquad (5.107)$$

i.e., under condition

$$\tan\omega t = \tan\delta \approx \frac{\omega}{\left(\sigma\varepsilon_0^{-1} - 2a\right) + \tau\left[\left(\sigma\varepsilon_0^{-1} - 2a\right)^2 + \omega^2\right]} . \qquad (5.108)$$

with $\tau^{-1} \equiv (4P^2/\varepsilon_0\gamma\Theta^2)$.

Conditions (5.104) do not change qualitatively if the solution of (5.84) has no spatial dependence in the bulk, i.e., if

$$\varphi(y,t) \approx \arctan\frac{1}{\sinh\left(-\frac{a}{\omega}\sin\omega t\right)} . \qquad (5.109)$$

In this case, magnitude $I(t)$ is approximately equal to

$$I(t) \propto 4\Theta^2\cos^2\varphi \propto \tanh^2\left[\frac{a}{\omega}\sin(\omega t - \delta)\right] , \qquad (5.110)$$

and the minimum $I_{\rm min} = 0$ takes place under the same conditions (5.108).

Equations (5.106)–(5.110) correspond to the phase shift in transmittance $I(t)$, which can be written as a function $I\,[\sin(\omega t - \delta)]$ in vicinity of minimum, if voltage $V\cos\omega t$ is applied to the FLC layer. Therefore, the absence of field hysteresis in the optical transmittance, with respect to the total voltage $U = -U_0\sin(\omega t - \delta^*)$, with $\tan\delta^* = \omega R_{\rm LC}(C_p + C_{\rm LC})$, applied to the cell, occurs when $\tan\delta = \tan\delta^*$. Here, $R_{\rm LC}$ and $C_{\rm LC}$ are the resistance and capacitance of the FLC layer, and U_0 is connected with V by the relation

$$U_0 = V\frac{\sqrt{1+\omega^2 R_{\rm LC}^2(C_{\rm LC}+C_p)^2}}{\omega R_{\rm LC}C_p}\,. \tag{5.111}$$

For small values of magnitude $\omega R_{\rm LC}(C_p + C_{\rm LC})$, from (5.111) we obtain the approximate relation $V \approx U_0\omega R_{\rm LC}C_p$, and $\delta^* \approx \omega R_{\rm LC}(C_p+C_{\rm LC})$. In fact, due to a small but finite resistance of an FLC, the phase shift of the field in the bulk $E_{\rm LC}(t) = (V/d_{\rm LC})\cos\omega t + \Xi$ with respect to the external voltage $U(t)$ is less than $\pi/2$ on a small magnitude δ, but the phase shift of the φ distribution in the bulk with respect to the field $E_{\rm LC}(t)$ is larger than $\pi/2$ on magnitude δ, and thus the absence of hysteresis in the optical transmittance (5.105) and (5.110) with respect to the total voltage U is possible. Since, in the absence of hysteresis, we have $U \propto \sin(\omega t - \delta)$ and $E_{\rm LC} \propto \cos(\omega t - \delta)$, the field in the bulk $E_{\rm LC} = 0$ when the total applied voltage is maximum and, contrary, $E_{\rm LC}$ is finite when $U = 0$. The situation is illustrated by Fig. 5.15.

It should be noted that, in this case, the perturbation Ξ is opposite in sign to field $E_0\cos\omega t$ accordingly to (5.102) and (5.104) when ω is much less than σ/ε_0 and a. We should note also that the mentioned characteristic length q^{-1} can be dependent on frequency ω at large values of ω when the orientational diffusion becomes essential, i.e., when frequency ω becomes larger than magnitude $a = \frac{PE}{\gamma\Theta^2}$, where E is the electric field inside the cell (see Section 5.2.3). The obtained results show that this field is less than $E_0\cos\omega t$ because of the opposite sign of perturbation Ξ which is large enough at the V-shaped switching conditions. In this case, the relaxation time of the orientation perturbations $\tau_E\,(\omega)$ is inversely proportional to frequency ω and, therefore, it can be small at high frequencies.

Equations (5.104) and (5.108) determine the magnitude ω_{inv}, i.e., the frequency value for which the hysteresis inversion has to be observed, and we obtain

$$\omega_{inv}^2 \approx \frac{1}{2}\left[\frac{\sigma^2}{\varepsilon_0^2}\left(\frac{\varepsilon_0}{\tau\sigma}-1\right) + \sqrt{\frac{\sigma^4}{\varepsilon_0^4}\left(\frac{\varepsilon_0}{\tau\sigma}-1\right)^2 + \frac{4\sigma^2}{\varepsilon_0^2\tau R_{\rm LC}(C_{\rm LC}+C_p)}}\right] \tag{5.112}$$

For the case: $\tau\sigma/\varepsilon_0 \gg 1$ and C_p being not large, from (5.104) and (5.112), we obtain the following relationships:

$$a_{inv} \approx \frac{\sigma}{2\varepsilon_0}\,, \quad \frac{a_{inv}}{\omega_{inv}} \propto \sqrt{\frac{\tau\sigma}{\varepsilon_0}} \gg 1\,, \quad \varepsilon_0 V(U_{0,inv})/d \propto \tau\sigma P/\varepsilon_0\,,$$
$$\omega_{inv} \approx \sqrt{\frac{1}{\tau R_{\rm LC}(C_{\rm LC}+C_p)}}\,, \quad U_{0,inv} \approx \frac{d\sigma}{2\varepsilon_0}\frac{\gamma\Theta^2}{PC_p}\sqrt{\frac{\tau(C_{\rm LC}+C_p)}{R_{\rm LC}}} \qquad (5.113)$$
$$\delta \approx \sqrt{\frac{R_{\rm LC}(C_{\rm LC}+C_p)}{\tau}} \ll 1\,.$$

Results (5.113) are qualitatively valid for values $\tau\sigma/\varepsilon_0$ of the order of unity under the assumptions considered. Thus, we see that, in order to have hysteresis-free electro-optical switching, the characteristic frequencies mentioned above must be tightly related to each other. The hysteresis inversion frequency is an increasing function of the decreasing resistance of the LC layer. It is seen that an increase in capacitance C_p results in a decrease in the inversion frequency. Besides, (5.113) show that, in general, the hysteresis-free situation only occurs when the frequency and amplitude of the external voltage have unique values at given parameters of a FLC and of an alignment layer (or external circuit elements). In fact, (5.113) describe the most suitable conditions for the effect observation, but deviations from them, for example a change in U_0, must lead to a worse pronounced V-shaped switching. The obtained distribution $\varphi(y,t)$ corresponding to the assumption $a \gg \omega$ has a qualitative character. However, the discussed qualitative conclusions are of interest when compared with the experimental data.

For relatively large conductivity and not large capacitance C_p, as in the experiments [44], (5.113) describe the observed qualitative dependence of ω_{inv} and $U_{0,inv}$ on the values of resistance $R_{\rm LC}$ and capacitance C_p. The observed dependence of $f_i = \omega_{inv}/2\pi$ on the applied voltage U_0 at a fixed temperature for different values of C_p had shown the existence of maximum on such curves, which correspond to the values $U_{0,inv}$ for given parameters of the cell. An increase in C_p resulted in a decrease in values of f_i and $U_{0,inv}$ in accordance with (5.113). For typical values $\gamma \sim 10^{-1}\,\mathrm{Pa\cdot s}$, $K \sim 10^{-11}\,\mathrm{N}$, $\mathrm{P} \sim 10^{-4}\,\mathrm{C\cdot m^{-2}}$, $\sigma/\varepsilon_0 \sim 10^3\,\mathrm{s^{-1}}$, $\varepsilon_p d/d_p \sim 10$, $R_{\rm LC}(C_p + C_{\rm LC}) \sim 10\varepsilon_0/\sigma$, and $\Theta \sim 1$, we obtain estimates $\omega_{inv} \sim 10^3\,\mathrm{s^{-1}}$ ($f_i \sim 10^2\,\mathrm{Hz}$) and $U_{0,inv} \sim 1\,\mathrm{V}$ which are in accordance with experimental data [44]. Experiments also show a thickness dependence of the observed transmittance. This may be explained by a relation

$$I_{\min} \propto \left(1 - \frac{4d_p}{\varepsilon d_p + \varepsilon_p d}\right) \qquad (5.114)$$

which occurs according to (5.106) under conditions (5.113). Besides, an ordinary phase retardation multiplier in $I(t)$ also has the oscillating thickness dependence. We also recall that the obtained results are valid for a FLC with relatively low spontaneous polarization useful for many applications.

In the case of very large values of C_p (very thin alignment layer), the total voltage applied to the cell is almost equal to the voltage on the FLC layer,

$\delta \approx \pi/2$ and $U_{\mathrm{LC}} \approx U_0$, i.e., we could find the conditions of hysteresis-free switching for the LC layer with applied field $E_0 \cos \omega t$. In this case, magnitude $\mathrm{tg}\delta$ determined by (5.108) would be very large and the corresponding solution $\omega = \omega^*$ would be given by the equation

$$\omega^{*2} \approx -\left(\frac{\sigma}{\varepsilon_0} - 2a\right)^2 + \frac{1}{\tau}\left(2a - \frac{\sigma}{\varepsilon_0}\right) \tag{5.115}$$

if $\tau^{-1} > (2a - \sigma\varepsilon_0^{-1})$. Respectively, since $a \approx 1/2\tau$, from (5.104) and (5.115) we obtain

$$\omega^{*2} \approx \frac{\sigma}{\varepsilon_0}\left(\frac{1}{\tau} - \frac{\sigma}{\varepsilon_0}\right) \tag{5.116}$$

where inequality $\tau\sigma/\varepsilon_0 < 1$ should be fulfilled. However, this inequality contradicts the made assumption $E_0 > P/\varepsilon_0$, so we can only say about a general tendency: an increase in weak polarization P leads to an increase in ω_{inv} (see (5.113)); the inversion frequency ω_{inv}, if it exists, is low for $\tau\sigma/\varepsilon_0 \approx 1$ correspondingly to (5.116).

If $\tau^{-1} < (2a - \sigma\varepsilon_0^{-1})$, then we obtain from the condition of maximum of $\tan \omega t$ in expression (5.108):

$$a^* \approx \frac{\sigma}{\varepsilon_0} + \frac{1}{2\tau}\,, \quad \omega^{*2} \approx \frac{\sigma}{\varepsilon_0}\left(\frac{1}{\tau} + \frac{\sigma}{\varepsilon_0}\right)\,,$$
$$(\tan \omega t)_{\max} \approx \frac{1}{2\tau\sqrt{\frac{\sigma}{\varepsilon_0}\left(\frac{\sigma}{\varepsilon_0} + \frac{1}{\tau}\right)}} \tag{5.117}$$

These relations also show that ω_{inv} has to increase with increasing polarization, i.e., with increase in τ^{-1}, but (5.117) are not valid when magnitude $\tau\sigma/\varepsilon_0$ becomes less than unity.

Magnitude ω_{inv} cannot be found in the framework of the assumptions under consideration if the electric conductivity is low and the polarization is large, this problem requires numerical calculations. The problem can be more complicated at low conductivity, i.e., at low concentration of free ions, since, in such a case, the r_D length becomes larger than the LC layer thickness, and the ion diffusion becomes essential in the whole LC layer. The latter situation was analyzed recently in a certain approximation [45], and the conditions were numerically found, under which the V-shaped electro-optical response can be realized in the FLC layers with alignment layer. It was assumed that slow, zero-field diffusion of ions through a FLC cell plays the main role in the effect, the polarization is large and the electric torque is zero. The ionic free carriers make the internal electric field in the FLC inhomogeneous and modify the director distribution and the optical properties of a cell, the found value of f_i was very low. Numerical calculations [46] have also shown a positive role of a thick (1 μm) polymer layer in contact with a conductive FLC layer in promoting the V-shape electro-optical response, however, no experimental data

have been presented to verify these calculations. The influence of the thickness and polarization charges on the electro-optical behavior of twisted smectic C* cells was studied by the method of de Vries eigenmodes [47], however, only the static case in the absence of alignment layers was considered.

The experiments [44] with a number of FLCs have shown that the V-shaped switching is only observed just at the hysteresis inversion frequency, which is mainly determined by parameters of a voltage divider formed by the aligning (or/and dielectric) layer and the FLC layer. Except the impedance, other properties of a FLC (P, Θ, γ, anchoring conditions, etc) are also important influencing both f_i and the shape of the V-shaped response.

5.2.9 Conclusions

The shown examples of an analytic consideration of the electro-optical switching problem give useful qualitative conclusions about the polarization reversal in the FLC cell under the action of ac electric fields. These examples clearly point out the essential role of ionic impurities in the process, which effect very much the behavior of a FLC in a sub-electrode area and in the bulk of the cell. The polymer alignment layers are of importance not only for the anchoring conditions, but also for the functioning of the electric circuit as a whole. It was shown in [48] that the proposed theoretical consideration qualitatively explains the observed phenomenon.

Unfortunately, the obtained results, concerning some limit cases for the characteristic frequencies and lengths, cannot describe the full picture of the cell behavior, for example for a small conductivity, a large polarization, a very thin alignment layer, and a chevron structure of a FLC. The study of these effects requires computer simulations. The light transmission through the cell, especially for large tilt angles in the FLC layer and spatially dependent azimuth angles in the bulk of the cell, also require numerical calculations, for example by the de Vries method, to take into account the eigenmodes with different elliptical polarizations and propagation indices depending upon the local refractive indices of the deformed FLC. The work in these directions is in progress. Recent numerical calculations of the optical transmittance of FLC cells [48] made for operation in the V-shape regime show excellent agreement with experimental data. It was concluded that the cell conductivity must be tuned very precisely to get V-shape switching at a particular frequency.

Acknowledgments. I thank W. Haase, L. Blinov, E. Pozhidayev, F. Podgornov, A. Sinha for many fruitful discussions and Ye. Loginov for technical assistance. Financial support from the Alexander von Humboldt-Stiftung and Russian Foundation for Basic Research (Grant 00-02-17801) is acknowledged.

References

1. N.A. Clark, S.T. Lagerwall: Appl. Phys. Lett. **36**, 899 (1980)
2. M.A. Handschy, N.A. Clark, S.T. Lagerwall: Phys. Rev. Lett. **51**, 471 (1983)
3. J.E. Maclennan, N.A. Clark, M.A. Handschy: In: Lam. L., Prost. J. (eds.) *Solitons in Liquid Crystals*. Springer, New York, p. 151 (1992)
4. J.S. Patel: Appl. Phys. Lett. **60**, 151 (1991)
5. M.A. Handschy, N.A. Clark: Ferroelectrics **59**, 69 (1984)
6. B. Park, S.S. Seomun, M. Nakata, M. Takahashi, Y. Takanishi, H. Takezoe: Jpn. J. Appl. Phys. Part. I **38**, 1474 (1999)
7. S. Inui, N. Iimura, T. Suzuki, H. Iwane, K. Miyachi, Y. Takanishi, A. Fukuda: J. Mater. Chem. **6**, 671 (1996)
8. S.T. Lagerwall: In: Ferroelectric and Antiferroelectric Liquid Crystals. VCH, Weinheim, p. 390 (1999)
9. A. Chandani, Y. Cui, S.S. Seomun, Y. Takanishi, K. Ishikawa, H. Takezoe, A. Fukuda: Liq. Cryst. **26**, 151, **26**, 167 (1999)
10. M. Takeuchi, K. Chao, T. Ando, T. Matsumoto, A. Fukuda, M. Yamashita: Ferroelectrics **246**, 1 (2000)
11. B. Park, M. Nakata, S.S. Seomun, Y. Takanishi, K. Ishikawa, H. Takezoe: Phys. Rev. E. 59:R3815 (1999)
12. P. Rudquist, J.P.F. Lagerwall, M. Buivydas, F. Gouda, S.T. Lagerwall, N.A. Clark, J.E. Maclennan, R. Shao, D.A. Coleman, S. Bardon, D.R. Link, G. Natale, M.A. Glaser, D.M. Walba, M.D. Wang, X.H. Chen: J. Mater. Chem. **9**, 1257 (1999)
13. R.B. Meyer, L. Liebert, L. Strzeleski, P. Keller: J. Phys. Lett. **30**, 69 (1975)
14. S.A. Pikin: Mol. Cryst. Liq. Cryst. **179**, 201 (1990)
15. S.A. Pikin: Ferroelectrics **117**, 197 (1991)
16. E.I. Demikhov, S.A. Pikin, E.S. Pikina: Phys. Rev. E. **52**, 6250 (1995)
17. E.I. Demikhov, S.A. Pikin, E.S. Pikina: J. Phys. II France **6**, 75 (1996)
18. P. Schiller, G. Pelzl, D. Demus: Liq. Cryst. **2**, 21 (1987)
19. C. Langer, R. Stannarius: Ferroelectrics **244**, 647 (2000)
20. B.I. Ostrovski, S.A. Pikin, V.G. Chigrinov: Zh. Eksp. Theor. Fiz. **77**, 1615 (1979)
21. Yu. Panarin, E. Pozhidaev, V. Chigrinov: Ferroelectrics **114**, 181 (1991)
22. E. Pozhidaev, S. Pikin, D. Ganzke, S. Shevtchenko, W. Haase: Ferroelectrics **246**, 235 (2000)
23. P. Debye: Phys. Z. **35**, 101 (1934)
24. L.A. Beresnev, E. Schumacher, S.A. Pikin, Z. Fan, B.I. Ostrovsky, S. Hiller, A.P. Onokhov, W. Haase: Jpn. J. Appl. Phys. **34**, 2404 (1995)
25. S.A. Pikin, L.M. Blinov, L.A. Beresnev, S. Hiller, E. Schumacher, B.I. Ostrovsky, W. Haase: Ferroelectrics **178**, 111 (1996)
26. S.A. Pikin: Nuovo. Cimento. D. **10**, 1281 (1988)
27. A.I. Allagulov, S.A. Pikin, V.G. Chigrinov: Liq. Cryst. **5**, 1099 (1989)
28. A.I. Allagulov, V.G. Chigrinov, S.A. Pikin: Kristallografiya **35**, 1537 (1991)
29. S.A. Pikin: In: *Structural Transformations in Liquid Crystals*. Gordon & Breach Science Publishers, New York (1991)
30. S.A. Pikin, L.A. Beresnev, S. Hiller, M. Pfeiffer, W. Haase: Mol. Mat. **3**, 1 (1993)
31. L.A. Beresnev, M.V. Loseva, N.I. Chernova, S.G. Kononov, P.V. Adomenas, E.P. Pozhidaev: JETP Lett. **51**, 516 (1990)

32. S. Hiller, S.A. Pikin, W. Haase: Ferroelectrics **166**, 119 (1995)
33. M. Pfeiffer: PhD thesis, TH Darmstadt (1993)
34. A.M. Biradar, S. Hiller, S.A. Pikin, W. Haase: Liq. Cryst. **20**, 247 (1996)
35. A.M. Biradar, S. Hiller, S.A. Pikin, W. Haase: Ferroelectrics **180**, 589 (1996)
36. A. Fukuda: (ed) Antiferroelectricity and thresholdless antiferroelectricity in liquid crystals. Tokyo Institute of Technology (1997)
37. M. Takahashi, B. Park, M. Nakata, Y. Takanishi, K. Ishikawa, H. Takezoe: Conference Summaries. 7^{th} International Conference on Ferroelectric Liquid Crystals. Darmstadt, Germany, p. 340 (1999)
38. S.S. Seomun, T. Gouda, T. Takanishi, K. Ishikawa, H. Takezoe, A. Fukuda, C. Tanaka, T. Fujiyama, T. Maruyama, S. Nishiyama: In: A. Fukuda (ed) Antiferroelectricity and thresholdless antiferroelectricity in liquid crystals. Tokyo Institute of Technology, p. 214 (1997)
39. L. Beresnev, A. Iida, T. Noma, H. Miyata, W. Haase: Abstracts. 6^{th} International Conference on Ferroelectric Liquid Crystals. Brest, France, p. 226 (1997)
40. Y. Takanishi, K. Ishikawa, H. Takezoe, A. Iida: Conference Summaries. 7^{th} International Conference on Ferroelectric Liquid Crystals. Darmstadt, Germany, p. 352 (1999)
41. T. Ogasawara, Y. Takanishi, K. Ishikawa, H. Takezoe: Conference Summaries. 7^{th} International Conference on Ferroelectric Liquid Crystals. (1999) Darmstadt, Germany, p. 342
42. S.T. Lagerwall, P. Rudquist: Conference Summaries. 7^{th} International Conference on Ferroelectric Liquid Crystals. Darmstadt, Germany, p. 100 (1999)
43. A.D.L. Chandani, Y. Cui, S.S. Seomun, Y. Takanishi, K. Ishikawa, H. Takezoe: Liq. Cryst. **26**, 167 (1999)
44. L.M. Blinov, E.P. Pozhidayev, F.V. Podgornov, A. Sinha, W. Haase: Ferroelectrics **277**, 3 (2002)
45. M. Čopič, J.E. Maclennan, N. Clark: Phys. Rev. E. **63**, 1703 (2001)
46. Yu. Panarin, V. Panov, O.E. Kalinovskaya, J.K. Vij: Ferroelectrics (2000) **246**, 35
47. M. Ismaili, G. Joly, N. Isaert, A. Anakkar: Liquid Crystals **28**, 253 (2001)
48. L.M. Blinov, E.P. Pozhidaev, F.V. Podgornov, S.A. Pikin, S.P. Palto, A. Sinha, A. Yasuda, S. Hashimoto and W. Haase: Phys. Rev. E **66**, 021701-10 (2002)

5.3 Dielectric properties of ferroelectric liquid crystals in finite samples and near the transitions to the hexatic phases

M. Glogarová and I. Rychetský

5.3.1 Introduction

Dielectric properties of ferroelectric liquid crystals in the ideal unbounded sample are nowadays well understood. The dielectric dispersion is essentially dominated by the dynamics of the soft-mode, responsible for the phase transition from the paraelectric SmA phase to the ferroelectric SmC^* phase, and

the Goldstone mode connected with the helicoidal structure in the ferroelectric SmC^* phase [1]. This subject is already compiled in monographs [2, 3].

Anchoring of polar molecules at the surfaces embarrasses that simple picture due to the strong effect of boundary conditions. In planar samples the polarity of anchoring produces an additional modulation, director twist-bend along the axis perpendicular to the axis of the helix [4]. Such a structure differs significantly from the ideal helix and its dielectric response is strongly dependent on the sample thickness.

In a thin enough sample when the sample thickness becomes comparable with the pitch of the helix, the entire structure is helix-free. The director twist-bend fixed by the surface polar anchoring can still exist as well as in the helicoidal samples. This space modulation is called a twisted structure [4].

In Sect. 5.3.2 we will describe in detail the dielectric response of both structures (helicoidal and twisted), which can exist in real samples. The depolarization field existing due to the spontaneous polarization and its partial charge compensation is taken into account in quantitative considerations.

In Sect. 5.3.3 behavior of polar modes in the vicinity of the phase transitions from the ferroelectric SmC^* or antiferroelectric SmC^*_A phase to the hexatic ferroelectric (SmI^*, SmF^*) phases or hexatic antiferroelectric (SmI^*_A, SmF^*_A) phases, respectively, are studied. It is shown that the main relaxation process can be attributed to the bond orientational order mode coupled to the molecular tilt and polarization.

5.3.2 Dielectric response of SmC^* phase in planar samples

In real dielectric measurements the liquid crystal is confined between two glass plates forming a thin layer of a few micrometers up to several tens of micrometers. Due to the strong planar anchoring the helix free layers occur at the glass plates. As the surface anchoring is strongly polar, which is usually the case of chiral smectics, the long molecular axes at the opposite surfaces make an angle $2\theta_0$ (θ_0 is the tilt angle) and spontaneous polarization, $\boldsymbol{P}_S$, vectors are anti-parallel. This configuration results in a director twist-bend and $\boldsymbol{P}_S$ vector splay between both sample surfaces. The resulting structure is a superposition of the helix along the smectic layer normal parallel to the sample surfaces and the director twist-bend [4]. The surface unwound layers and the helix in the bulk are incompatible structures and their combination is inevitably accompanied by a periodic array of dechiralization lines [4, 5]. The scheme of this structure is shown in Fig. 5.16a.

In thin enough samples, the entire structure is helix-free with the director twist-bend within the smectic layer and $\boldsymbol{P}_S$ vector splay along the x-axis perpendicular to the surfaces. This space modulation (*twisted structure*) is shown in Fig. 5.16b.

5.3.2.1 Phenomenological description of helicoidal and twisted structures

The equilibrium structures are derived from the minimum of the free energy allowed by the symmetry of the SmA − SmC* phase transition, with the gradient terms [6–8]:

$$f = \frac{a}{2}\left(\xi_1^2 + \xi_2^2\right) + \frac{b}{4}\left(\xi_1^2 + \xi_2^2\right)^2 - \Lambda\left(\xi_1\frac{\partial\xi_2}{\partial z} - \xi_2\frac{\partial\xi_1}{\partial z}\right) - P_x E_x + \frac{K_3}{2}\left\{\left(\frac{\partial\xi_1}{\partial z}\right)^2 + \left(\frac{\partial\xi_2}{\partial z}\right)^2\right\} + \frac{K'}{2}\left(\frac{\partial\xi_1}{\partial x} + \frac{\partial\xi_2}{\partial y}\right)^2 + \frac{K''}{2}\left(\frac{\partial\xi_1}{\partial y} - \frac{\partial\xi_2}{\partial x}\right)^2 \tag{5.118}$$

where $a = \alpha(T - T_0)$. The temperature T_0, the Lifshitz constant Λ and the elastic constants K_3, K', K'' are assumed being renormalized by virtue of a coupling of the director ξ and the polarization $\boldsymbol{P}$ [1]. For simplicity, in the following, we take $K' = K'' = K$. The director and the polarization in polar coordinates read:

$$(\xi_1, \xi_2) = (\theta_0 \cos\phi, \theta_0 \sin\phi) \tag{5.119a}$$

$$(P_x, P_y) = (-P_0 \sin\phi, P_0 \cos\phi)\,, \tag{5.119b}$$

where P_0 and θ_0 are equilibrium values, ϕ is the angle between the director ξ and the x-axis (plate-sample normal) and $\phi + \pi/2$ is the angle between $\boldsymbol{P}$ and the x-axis. In the unbounded SmC* phase below the temperature T_C the helicoidal structure appears with the pitch p:

$$\theta_0 = \sqrt{\frac{\alpha}{b}(T_C - T)}\,, \quad \phi_0 = -\frac{\pi}{2} + qz\,, \quad q = \frac{\Lambda}{K_3}\,, \quad p = \frac{2\pi}{q}\,. \tag{5.120}$$

In a plate-like sample of the thickness d the boundary conditions at the surfaces should be considered:

$$\phi(x = 0) = -\pi/2\,, \quad \phi(x = d) = \pi/2\,. \tag{5.121}$$

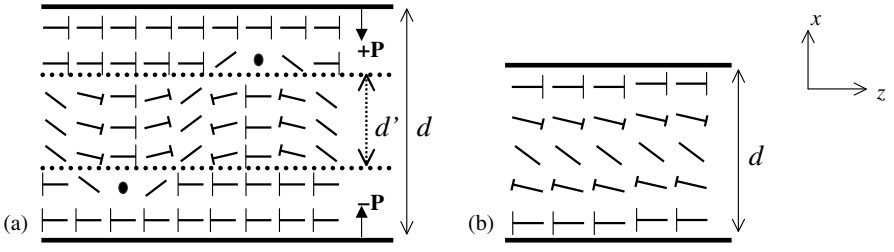

Fig. 5.16. (a) helicoidal structure with dechiralization lines (*dots*); *full lines* – glass plates; *dotted lines* – effective surfaces for pinning of the helix; *bold arrows* – polarization at the surfaces. **(b)** twisted structure.
Molecules are represented by nails, the tips of which point towards the observer

It implies the polarization near the surfaces is parallel with the inner normals of the plates: $\boldsymbol{P}(x = 0, d) = (\pm P_0, 0, 0)$. Then in the thin enough sample ($d \approx p$) the twisted structure appears below T_{C}^*:

$$\theta_0 = \sqrt{\frac{\alpha}{b}(T_{\mathrm{C}}^* - T)}\,, \quad \phi_0 = \frac{\pi}{d}x - \frac{\pi}{2}\,, \quad 0 \le x \le d\,. \tag{5.122}$$

Due to the surface anchoring, the phase transition from the SmA to the SmC* twisted structure takes place at a thickness dependent temperature [8, 9]

$$T_{\mathrm{C}}^* = T_0 - \frac{K\pi^2}{\alpha d^2} < T_0 < T_{\mathrm{C}} = T_0 + \frac{2\pi\Lambda}{\alpha p}\,, \tag{5.123}$$

where T_{C} is the $\mathrm{SmA} - \mathrm{SmC}^*$ transition temperature of the bulk crystal. When the sample is thick ($d \gg p$) the helicoidal structure (5.120) is well developed in the sample, and it can be approximately considered as the helix (5.120) pinned at the new surfaces (effective surfaces in Fig. 5.16a). This structure is further called as *pinned helix*.

The polarization of the inhomogeneous structure is spatially dependent and the density of induced charges $\rho = -\mathrm{div}\boldsymbol{P}$ would create a depolarization field inside the sample. In the static structure these charges are compensated by electronic and ionic conductivity (screening process) and henceforth the depolarization field has not been considered. On the other hand the depolarization field plays an important role in the dynamics when the characteristic time of the charge screening is comparable or longer than the experimental time-scale (typically below 1 MHz).

5.3.2.2 Dynamic dielectric response

The dynamic dielectric response of the planar sample can be obtained from the Landau–Khalatnikov relaxation equation constructed on the basis of the free energy (5.118) (see [10]):

$$\gamma\theta_0^2\frac{\partial\phi}{\partial t} = \theta_0^2\left(K\frac{\partial^2\phi}{\partial x^2} + K_3\frac{\partial^2\phi}{\partial z^2}\right) - P_0E_x(t)\sin\left(\phi + \frac{\pi}{2}\right)\,, \tag{5.124}$$

It was assumed that θ_0 is temporally and spatially independent, γ is the rotational viscosity and the homogeneous electric field is directed along the x-axis. The macroscopic electric field $\boldsymbol{E}(t)$ in general differs form the applied external electric field $\mathcal{E}(t)$.

Inserting the oscillating homogeneous electric field $\mathcal{E}_x(t) = \mathcal{E}\exp(\mathrm{i}\omega t)$ the equilibrium (*twisted* or *helicoidal structure*) is perturbed, so that

$$\phi(x, z, t) = \phi_0(x, z) + \delta(x, z)\exp(\mathrm{i}\omega t)\,, \tag{5.125}$$

where $\delta(x, z)$ is a small perturbation. Considering the pinning of the structure at the surfaces the boundary conditions are:

$$\delta(x=0,z)=\delta(x=d,z)=0 \tag{5.126}$$

The polarisation deviates from its equilibrium value as $(\delta P_x, \delta P_y, 0)$, where

$$\delta P_x=-P_0\delta(x,z)\cos[\phi_0(x,z)]\,,\quad \delta P_y=-P_0\delta(x,z)\sin[\phi_0(x,z)] \tag{5.127}$$

Assuming that the temporal evolution of polarization is faster than the screening process the depolarization field has to be considered

$$\mathrm{div}\varepsilon_0\boldsymbol{E}=\mathrm{div}\varepsilon_0(\mathcal{E}+\boldsymbol{E}_{\mathrm{dep}})=\mathrm{div}\varepsilon_0\boldsymbol{E}_{\mathrm{dep}}=\varrho+\varrho_{\mathrm{free}}\approx -L\mathrm{div}\delta\boldsymbol{P}\,, \tag{5.128}$$

where $\varrho=-\mathrm{div}\delta\boldsymbol{P}$ is the charge induced by the polarization fluctuations and the free screening charge is approximated as $\varrho_{\mathrm{free}}\approx -(1-L)\mathrm{div}\delta\boldsymbol{P}$. Depolarization factor L is a measure of the charge screening. In case that the problem depends on the x-axis only, the macroscopic electric field can be written as $E_x(t)=\mathcal{E}_x(t)+E_{\mathrm{dep},x}(t)$.

Twisted structure

The equilibrium twisted structure (see Fig. 5.16b) is described by (5.122). Since all quantities are x-dependent only, the depolarization field can be calculated from (5.128) as:

$$\varepsilon_0 E_{\mathrm{dep}}(x)=-L\delta P_x(x)\,, \tag{5.129}$$

where the depolarization factor L expresses the extent of the charge compensation: $L=0$ corresponds to the total compensation, while $L=1$ represents no compensation and the highest depolarization field. Substituting (5.125), (5.127) and (5.129) into (5.124) the dynamic equation becomes:

$$\left[\mathrm{i}\omega\gamma d^2+\frac{L\mu^2}{\varepsilon_0}\sin^2\left(\phi+\frac{\pi}{2}\right)\right]\delta(x)-\frac{K}{d^2}\frac{\partial^2\delta(x)}{\partial x^2}+\frac{\mu^2\mathcal{E}}{P_0}\sin\left(\phi+\frac{\pi}{2}\right)=0\,, \tag{5.130}$$

where $\mu=P_0/\theta_0$. For simplicity the positive definite function $\sin^2(x)$ is approximated by its average value over the sample: $\langle\sin^2(x)\rangle=1/2$. Then the dynamic equation reads:

$$\left(\mathrm{i}\omega\gamma d^2+\frac{L\mu^2}{2\varepsilon_0}\right)\delta(x)-\frac{K}{d^2}\frac{\partial^2\delta(x)}{\partial x^2}+\frac{\mu^2\mathcal{E}}{P_0}\sin\left(\phi+\frac{\pi}{2}\right)=0\,. \tag{5.131}$$

The solution of (5.131) with the boundary conditions (5.126) can be easily found:

$$\delta(x)=-\frac{\mathcal{E}P_0}{(K\pi^2/d^2+\varepsilon_0^{-1}L\mu^2/2+\mathrm{i}\omega\gamma)\theta_0^2}\sin\frac{\pi x}{d} \tag{5.132}$$

Inserting the solution (5.132) into the variation of polarization (5.127), the local susceptibility is calculated

$$\chi(x) = \frac{\partial P_x}{\partial \varepsilon_0 \mathcal{E}_x} = \frac{\varepsilon_0^{-1}\mu^2 \sin^2(\pi x/d)}{(K\pi^2/d^2 + \varepsilon_0^{-1} L\mu^2/2 + \mathrm{i}\omega\gamma)} \,, \tag{5.133}$$

and finally, the average susceptibility reads

$$\chi_{\mathrm{av}} = \frac{1}{d}\int_0^d \chi(x)\mathrm{d}x = \frac{\chi_0}{1 + \mathrm{i}\omega\tau} \,, \tag{5.134}$$

with the static susceptibility χ_0:

$$\chi_0 = \frac{\mu^2 d^2}{2\varepsilon_0(\pi^2 K + d^2\varepsilon_0^{-1} L\mu^2/2)} \tag{5.135}$$

and the relaxation frequency f_{r}:

$$f_{\mathrm{r}} = (2\pi\tau)^{-1} = \frac{1}{2\pi\gamma}\left(\frac{K\pi^2}{d^2} + \frac{\varepsilon_0^{-1} L\mu^2}{2}\right) \,. \tag{5.136}$$

Using dimensionless quantities: $\tilde{L} = L\varepsilon_0^{-1}\mu^2/(2Kq^2)$, $\Omega = \gamma\omega/Kq^2$, and $A = \mu^2/2\varepsilon_0 Kq^2$, the total susceptibility is rewritten as

$$\chi_{\mathrm{av}} = \frac{A}{\pi^2/(qd)^2 + \tilde{L} + \mathrm{i}\Omega} \,. \tag{5.137}$$

In Sect. 5.3.2.5 we use $L = L_t$ for the twisted structure.

Pinned helix

The equilibrium helicoidal structure in real planar samples is shown in Fig. 5.16a. For calculation of the dynamic dielectric response we use a simplified model of this structure. We consider that the thickness of the unwound surface layers is much lower compared to the sample thickness and thus their contribution to the sample permittivity is negligible. Therefore we cut off the surface layers together with the disclinations and consider new "effective surfaces" as are shown by dotted lines in Fig. 5.16a, at which the helicoidal structure is assumed being pinned [10].

We calculate the response only for the sample bulk, where the helix is independent of x-axis and thus it is described by $\phi_0 = -\pi/2 + qz$. The dynamics will be calculated on the assumption of pinning at the "effective surfaces", $\delta(x = -d/2) = \delta(x = +d/2) = 0$.

The solution is a mode, which can be called a *pinned Goldstone mode*, and can be searched in the form: $\delta(x, z) = G(x)\sin(qz)$. Equation (5.128) is rewritten as

$$\mathrm{div}\varepsilon_0 \boldsymbol{E}_{\mathrm{dep}} = LP_0 \sin^2(qz)\partial G(x)/\partial x \approx (1/2)LP_0\partial G(x)/\partial x \,, \tag{5.138}$$

where an average along the z-axis was performed for simplification. Equation (5.124) is reduced to:

$$K\frac{\partial^2 G}{\partial x^2} - (\mathrm{i}\gamma\omega + K_3 q^2)G - P_0 E_x(t)/\theta_0^2 = 0 \,, \tag{5.139}$$

where the depolarization field should be encountered in $E_x(t)$. The solution of (5.139) gives

$$G(x) = \frac{P_0\mathcal{E}}{\theta_0^2}\frac{1}{D(\omega)}\left(\frac{\cosh(x\sqrt{D(\omega)/K})}{\cosh(\frac{d}{2}\sqrt{D(\omega)/K})} - 1\right) \,, \tag{5.140}$$

where $D(\omega) = \mathrm{i}\gamma\omega + K_3 q^2 + (1/2)\varepsilon_0^{-1}L\mu^2$. From the solution the local dielectric susceptibility is calculated

$$\chi(x,z) = \frac{\partial P_x}{\partial\varepsilon_0\mathcal{E}_x} = -\frac{\delta}{\varepsilon_0\mathcal{E}}P_0\sin(\phi_0 + \pi/2) = -\frac{G(x)}{\varepsilon_0\mathcal{E}}P_0\sin^2(qz) \,, \tag{5.141}$$

and by averaging of (5.141) one gets the total susceptibility as

$$\chi_{\mathrm{av}} = \frac{1}{pd}\int_0^p\int_0^d \chi\,\mathrm{d}x\mathrm{d}z = A\left(1 - \frac{\tanh\left(\frac{1}{2}qd\sqrt{\tilde{D}(\Omega)}\right)}{\frac{1}{2}qd\sqrt{\tilde{D}(\Omega)}}\right)\frac{1}{\tilde{D}(\Omega)} \,, \tag{5.142}$$

where $\tilde{D}(\Omega) = D(\omega)/Kq^2 = \mathrm{i}\Omega + \tilde{L} + K_3/K$ and dimensionless quantities A, Ω and $\tilde{L}$ were defined above. The multiple modes with the relaxation frequencies

$$1/\tau_n = \left(K_3 q^2 + \varepsilon_0^{-1}L\mu^2/2 + K(\pi/d)^2(1+2n)^2\right)\gamma^{-1}, \; n = 0, 1, \ldots \tag{5.143}$$

contribute to the susceptibility, but there is only small deviation from a single Debye relaxation. One should realize that the depolarization factor can be different for helicoidal and twisted structures. When comparing the susceptibilities of both structures in Sect. 5.3.2.5, we use $L = L_t$ in (5.137) and $L = L_h$ in (5.142).

5.3.2.3 Pinned SmA phase

The relaxation equation for the SmA paraelectric phase is

$$\gamma_\theta\frac{\partial\delta\theta_0}{\partial t} = -a\delta\theta_0 + K\frac{\partial^2\delta\theta_0}{\partial x^2} - \mu E_x(t) \,. \tag{5.144}$$

Assuming pinning of the tilt at the surfaces: $\delta\theta_0(x = \pm d/2) = 0$, and taking into account relation between fluctuations of polarization and the tilt $\delta P_x = \mu\delta\theta_0$, the dynamic susceptibility can be obtained:

$$\chi_{\mathrm{av}} = \left\{ 1 - \frac{\tanh\left[\frac{1}{2}d\sqrt{D'(\omega)/K}\right]}{\frac{1}{2}d\sqrt{D'(\omega)/K}} \right\} \frac{\varepsilon_0^{-1}\mu^2}{D'(\omega)}, \tag{5.145}$$

where $D'(\omega) \equiv \mathrm{i}\gamma_\theta\omega + a + \varepsilon_0^{-1}L\mu^2$. Multiple modes with the temperature and thickness dependent relaxation frequencies ($T > T_{\mathrm{C}} > T_0$):

$$1/\tau_n = \left[\alpha(T - T_0) + \varepsilon_0^{-1}L\mu^2 + K(\pi/d)^2(1+2n)^2\right]\gamma_\theta^{-1},\ n = 0, 1, \ldots \tag{5.146}$$

contribute to the response, but there is only slight deviation from the Debye-like shape. The mode $1/\tau_0$ possesses the highest dielectric strength.

5.3.2.4 Experimental results

The results derived from the free energy for the dielectric response in previous paragraphs are confirmed for several materials by experimental studies of both twisted samples and samples with the helicoidal structure. Namely, dielectric strength and relaxation frequency of the mode detected in the SmC* phase and the transition temperature between the SmA and SmC* phases have been found strongly thickness dependent [8, 11–15]. The sample structure is easily established by microscope observations. The presence of dechiralization lines in the sample texture confirms the existence of the helicoidal structure. If no lines are seen in the texture the sample structure is twisted. In principle the completely homogeneous SmC structure can occur in ultra thin planar samples [16]. Such a structure usually can happen only in the case when a special surface treatment ensures that the surface anchoring is not strongly polar. Dielectric properties of this structure are not treated in this contribution.

Generally, it is considered that the twisted structure occurs in thin samples, when sample thickness is comparable to or smaller than the helicoidal pitch. This conclusion is often far from reality and the twisted structure appears even in much thicker samples. The reason is that under a definite surface the anchoring energy gained by establishing the helicoidal structure in thick samples is rather small and additionally lowered by the inevitable presence of dechiralization lines. Moreover, the energy barrier that has to be overcome during the transition from one structure to the other is rather high. From this reason the structure existing in the real sample may be non-equilibrium and depending on the sample history.

In the following the thickness dependence of the relaxation frequency and dielectric strength is reported for modes existing in the SmC* phase of materials of different structures to compare their dielectric responses.

Helicoidal structure

In Fig. 5.17 the temperature dependences of the relaxation frequencies, f_{r}, and the dielectric strength, $\Delta\varepsilon$, are shown for the mode detected in the SmC*

phase of 10AL studied in samples of denoted thickness [15]. The microscope observation established the helicoidal structure in all samples in the whole temperature range of the SmC* phase existence. One can see that when increasing the thickness from 6 μm to 100 μm the relaxation frequency of the pinned Goldstone mode is decreased about 6 times and its dielectric strength increased about 10 times. Analysing (5.142) and (5.143) one can see that the theory qualitatively agree with these experimental results. The temperature changes seen on $\Delta\varepsilon(T)$ and $f_{\mathrm{r}}(T)$ on the upper limit of the SmC* phase are due to the changes of helicoidal pitch, the decrease of f_{r} on cooling are due to the increase of viscosity [15].

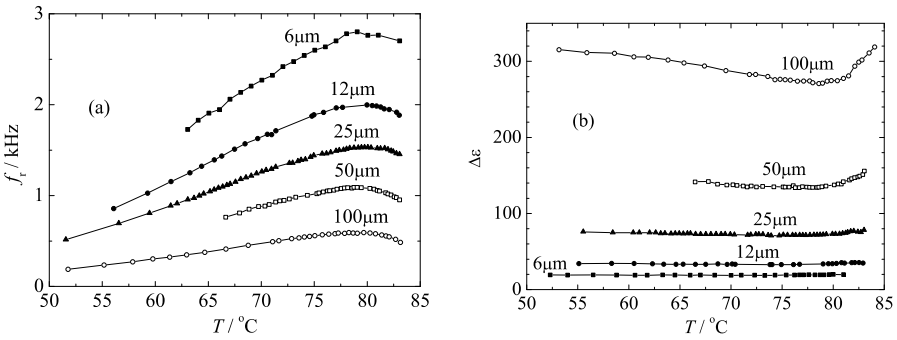

Fig. 5.17. Temperature dependence of **(a)** relaxation frequencies and **(b)** dielectric strength of the pinned Goldstone mode for 10AL samples of indicated thickness [15]

Twisted structure

In Fig. 5.18 similar results are presented for the twisted structure for material denoted as BCl8/3 [17]. In contrast to 10AL in this material the twisted structure existed for all studied sample thickness. In this case the mode detected in the SmC* phase is the thickness mode. Its relaxation frequency is significantly decreasing and its dielectric strength increasing when increasing the sample thickness. The thickness dependences of both quantities are also shown in Fig. 5.19 showing qualitative agreement with the theoretical results (5.135), (5.136) derived for the twisted structure. In Figs. 5.18 and 5.19 one can also see that the phase transition temperature between the SmC* and SmA phases is shifted to higher temperatures on the increase of the sample thickness, which confirms the validity of (5.123) derived for the twisted structure. The effect of the sample thickness on the behavior of the soft-mode in the paraelectric SmA phase (which is also seen in Fig. 5.18) is realized only via the shift of T_{C}, the slope of f_{r} remaining unaffected (see (5.146)). However, in [18] a change of the slope with the thickness was reported.

Comparison of helicoidal and twisted structures

A difference between the dielectric response of twisted and helicoidal structure can be documented when both structures occur in the same sample. This has been tested with a material denoted as H6/9, which exhibits a spontaneous unwinding of the helicoidal structure below 114 °C [15]. In Fig. 5.20a,b, f_r and $\Delta\varepsilon$ are shown respectively, in dependence of temperature for samples of denoted thickness. Just below the transition to the SmC* phase, where the helicoidal structure is present, high values of $\Delta\varepsilon$ are detected for all sample thickness (see Fig. 5.20b). When approaching the unwinding temperature on cooling, $\Delta\varepsilon$ decreases steeply. This fact agrees with the microscope observation showing that the sample area with the helicoidal structure decreases. The 12 μm thick sample becomes completely unwound even below 117 °C, which is reflected in the drop in $\Delta\varepsilon$ below this temperature. As for f_r, its increase on cooling just below the transition to the SmC* phase can be explained by a gradual extinction of the helicoidal structure because of the helix unwind-

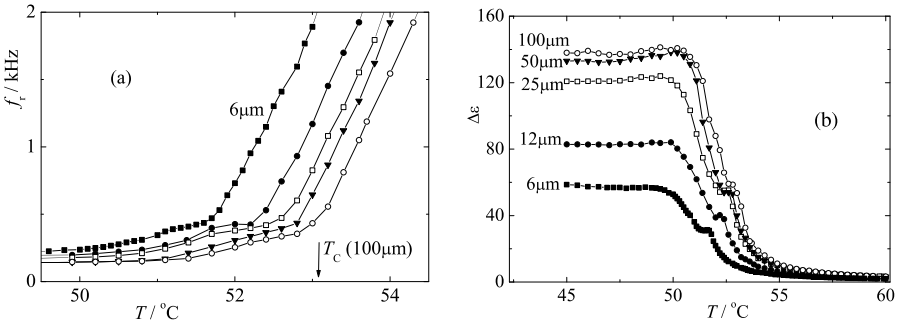

Fig. 5.18. Temperature dependence of **(a)** relaxation frequencies and **(b)** dielectric strength for BCl8/3 samples of indicated thickness. Symbols for definite thickness are the same in both (a) and (b). T_C for 100 μm sample is shown [17]

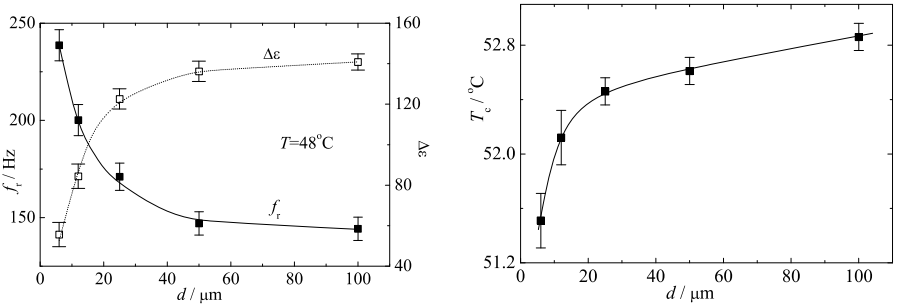

Fig. 5.19. The thickness dependence of the dielectric strength, relaxation frequency and phase transition temperature for BCl8/3 [17]. The lines are guides for eyes

ing on cooling. The low temperature decrease of f_r might be caused by an increase of viscosity (see Fig. 5.20a).

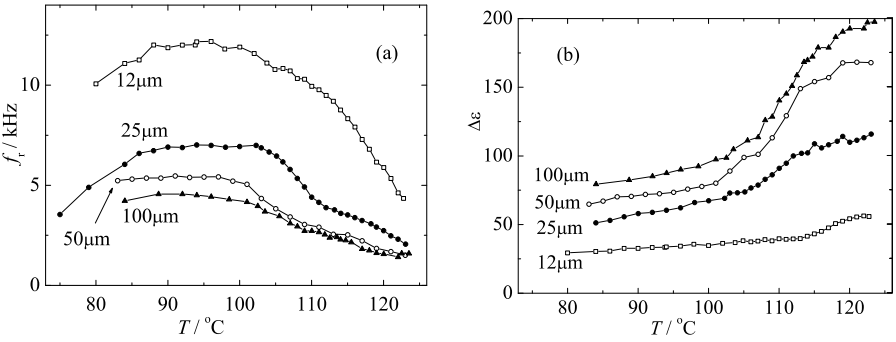

Fig. 5.20. Temperature dependences of **(a)** relaxation frequencies, and **(b)** dielectric strength in the SmC* phase for H6/9 samples of denoted thickness [15]

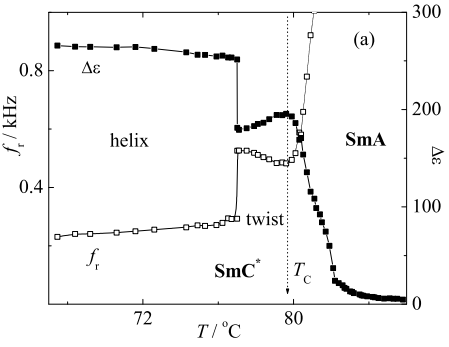

Fig. 5.21. Temperature dependence of the relaxation frequency and dielectric strength for 6 μm thick 9AL sample in both SmA and SmC* phases. The jump in the SmC* phase corresponds to the change of the structure from twisted to the helicoidal one. T_C is the phase transition temperature [19]

A quantitative difference between properties of the thickness mode and the pinned Goldstone mode has been found with a material denoted as 9AL [19]. With this compound the twisted structure spontaneously appears when entering the SmC* phase on cooling in samples of the thickness lower than 20 μm, but the helix can be generated by application of a weak a.c. field. A jump down in f_r and jump up in $\Delta\varepsilon$, when the structure is transformed from the twisted to the helicoidal one, is seen in Fig. 5.21 for a sample 6 μm thick. On further cooling the helix is stable and no changes in both f_r and $\Delta\varepsilon$ are observed [19].

5.3.2.5 Conclusions

(i) Dielectric response of the *twisted structure* exhibits Debye-like character (5.134). A nearly Debye-like response for the pinned helicoidal structure is confirmed by numerical inspection of (5.142), though generally this response is multi-relaxational [10]. The relaxation frequency and dielectric strength of both the *thickness mode in the twisted structure* and the *pinned Goldstone mode in the pinned helicoidal structure* are strongly dependent on the sample thickness.
(ii) With the increase of the sample thickness the permittivity of both structures significantly increases. Non-zero depolarization factors L_{t} and L_{h} ensure that both permittivities (5.134) and (5.142) tend to saturation for thick enough samples.
(iii) From quantitative comparison made for 9 AL a reasonable agreement between the permittivity values measured with twisted sample 6μm thick and the result given by the theory is obtained if $L_{\mathrm{t}} \approx 0.01 \ll 1$, which means that only 0.01 of the internal field remains non-compensated [19]. For the helicoidal structure a similar comparison yields $L_{\mathrm{h}} < 0.001$. For the calculation the following values have been used: $\theta_0 = 15\,\mathrm{deg}$, $p = 1$ μm, $K_3 = 5 * 10^{-12}$ N, $P_0 = 50\ \mathrm{nCcm}^{-2}$. Strong anisotropy of the smectic structure implies $K_3 \ll K$, we consider $K = 50K_3$.
(iv) Experimentally observed higher relaxation frequency of the twisted structure as compared with that of the helicoidal structure requires $L_{\mathrm{t}} > L_{\mathrm{h}}$ in the model expressions (5.137) and (5.142). This relation was checked numerically [10, 19] since the analytical form of the relaxation frequency of the helicoidal structure is not available. This relation qualitatively agrees with estimation of depolarization factors obtained in (iii) on the basis of comparison of permittivities of both structures.

The presented theory describes reasonably the dielectric response of finite SmC^* samples exhibiting helicoidal or twisted structure. The results derived for both relaxation frequency and dielectric strength are very sensitive to depolarization fields. A comparison with experiment shows that these fields must be almost compensated by internal charges, but not completely.

5.3.3 Dielectric behavior of ferroelectric and antiferroelectric liquid crystals near the transition to the hexatic phases

During the last years hexatic smectic phases have been intensively studied and understanding of their structures has been increased considerably. It is known that the hexatic smectic liquid crystalline phases exhibit a long-range three-dimensional bond orientational order (BOO) and a short-range translational order. The nature of these phases is confirmed by X-ray diffraction, which shows a diffuse six-fold pattern [20].

In this contribution the interest is paid to the transition from SmC^* phases to the tilted hexatic phases, both can exhibit either ferroelectric or antiferroelectric properties. In tilted hexatic phases the tilt-bond coupling constrains

the local tilt to point either along the local bond directions (SmI) or between them (SmF). The centers of gravity of molecules exhibit the 6-fold alignment, but 6-fold symmetry axis is lost in hexatic SmI and SmF phases due to the tilt of molecules. Thus the symmetry of these tilted phases becomes C_{2h} or, for chiral substances C_2, the same as that of the SmC phase or chiral SmC* phase, respectively. For this reason the hexatic order exists also in the SmC or SmC* phases, and increases discontinuously at the first order phase transition to the hexatic phase. The first mean field approaches [21, 22] considered the molecular tilt and BOO for order parameters. To describe the static and dynamic dielectric behavior the coupling of BOO to polarization has to be taken into account.

The first theoretical predictions of the behavior of dielectric relaxation modes in such coupled system have been done in [23]. That approach has been successful to explain the behavior in the vicinity of the phase transition from the smectic to the hexatic phases in both ferroelectric and antiferroelectric liquid crystals under a condition of saturated spontaneous tilt angle at this transition [23–25]. If this condition is not fulfilled and the spontaneous tilt angle exhibits an anomaly at the transition to the hexatic phase the theory must be extended, taking into account the space modulation of the BOO parameter.

5.3.3.1 Simple phenomenological description

Free energy and order parameters

The full phase sequence SmA–SmC*–SmI* or (SmF*) can be described by a free energy with the tilt angle θ as the order parameter, which becomes soft at the phase transition SmA–SmC* and BOO parameter A, which is soft at the phase transition to the hexatic phase. Polarization P is introduced as a hard parameter to describe the dielectric properties. These order parameters are introduced as complex functions [21, 26]:

$$\begin{aligned} \text{tilt} \quad & \theta = \theta_0 \exp[\mathrm{i}(\phi_\theta + \pi/2)], \\ \text{bond orientation} \quad & A = A_0 \exp[\mathrm{i}6\phi_A], \\ \text{polarization} \quad & P = P_0 \exp[\mathrm{i}\phi_P], \end{aligned} \tag{5.147}$$

where θ_0 is the tilt angle with respect to the smectic layer normal (z-axis) and the director projection to the xy-plane makes an angle ϕ_θ with the x-axis. The polarization of the amplitude P_0 lies in the smectic layer making an angle ϕ_P with the x-axis. The amplitude A_0 represents a measure of the hexatic order and the bond of two adjacent molecules makes an angle ϕ_A with the x-axis. The six-fold axis is a symmetry element of the bond orientation order A. Phases and amplitudes of tilt, bond and polarization will be derived from the free energy minimization in the next paragraph. In the SmC* phase the polarization is perpendicular to the tilt plane, i.e. $\phi_P = \phi_\theta - \frac{\pi}{2}$ or $\phi_P = \phi_\theta + \frac{\pi}{2}$. In the SmI* phase the molecules are inclined along hexagon diagonals, i.e.

$\phi_A = \phi_\theta$, while in the SmF* phase they are tilted against the center of hexagon edges, $\phi_A = \phi_\theta + \frac{\pi}{6}$.

The free energy density constructed of the order parameters (5.147) is composed of 4 parts:

$$F = F_\theta + F_P + F_A + F_{int}, \tag{5.148}$$

where

$$F_\theta = \frac{1}{2}a(\theta\theta^*) + \frac{1}{4}b(\theta\theta^*)^2 + \frac{\mathrm{i}}{2}\lambda(\theta\dot{\theta}^* - \dot{\theta}\theta^*) + \frac{1}{2}\kappa(\dot{\theta}\dot{\theta}^*) \tag{5.149a}$$

$$F_P = \frac{1}{2}\chi^{-1}PP^* \tag{5.149b}$$

$$F_A = \frac{1}{2}\alpha AA^* + \frac{1}{4}\beta(AA^*)^2 + \frac{1}{6}\gamma(AA^*)^2 + \left(\frac{\mathrm{i}}{2}\right)\Lambda(A\dot{A}^* - \dot{A}A^*) \tag{5.149c}$$

$$+ \frac{1}{2}K(\dot{A}\dot{A}^*) \tag{5.149d}$$

$$F_{int} = \frac{c}{2}(P\theta^* + P^*\theta) + \frac{f}{2}(\theta^6 A^* + \theta^{*6}A) + \frac{g}{2}(\theta^5 PA^* + \theta^{*5}P^*A), \tag{5.149e}$$

where $a = a_0(T - T_1)$, $\alpha = \alpha_0(T - T_2)$, $T_2 \ll T_1$. The dot stands for the derivative with respect to z. The coefficients c, f and g could be positive or negative and will be discussed below. The inequality $T_2 \ll T_1$ anticipates occurrence of the SmC* phase at higher temperatures than the hexatic phase. In the following the gradient terms in P and A are neglected for simplicity ($\Lambda = K = 0$). This simplification is equivalent to presumption that both P and A adopt the modulation of θ. In the interaction part we keep only bilinear interaction between P and θ, and the interaction of P with A and θ, which determines the dielectric properties near the SmC*–SmI* (or SmF*) phase transition. The invariants $\theta^4P^2A^* + \theta^{*4}P^{*2}A$, $\theta^3P^3A^* + \theta^{*3}P^{*3}A$, ..., $P^6A^* + P^{*6}A$, which are of the same order as the terms g and f, would not change the picture qualitatively, and they are also neglected for simplicity.

Structure of tilted phases and phase transitions

Conditions for the free energy extreme give for the bond orientation amplitude A_0 an equation that cannot be solved analytically, but it shows that when θ_0 becomes non-zero, A_0 is also non-zero:

$$A_0(\alpha - \chi g^2\theta_0^{10} + \beta A_0^2 + \gamma A_0^4) = (\chi gc - f)\theta_0^6, \tag{5.150}$$

For phase ϕ_A there are two solutions depending on c, f and g:
(i) The condition $\chi gc - f < 0$ gives $\phi_A = \phi_\theta$, which corresponds to the SmI* phase.
(ii) For $\chi gc - f > 0$ we get $\phi_A = \phi_\theta + \frac{\pi}{6}$, which corresponds to the SmF* phase.

The sign of c determines the sign of polarization: for $c < 0$, $\phi_P = \phi_\theta + \pi/2$ and for $c > 0$, $\phi_P = \phi_\theta - \pi/2$. We shall further study the SmI* phase only with the negative polarization ($c < 0$). For the polarization vector magnitude the free energy extreme gives

$$P_0 = -\chi c\theta_0 + \chi g\theta_0^5 A_0. \tag{5.151}$$

Then the spontaneous tilt is (higher order corrections being neglected):

$$\begin{aligned} \theta_{\mathrm{S}}(z) &= \theta_0 \exp[\mathrm{i}(\phi_\theta(z) + \pi/2)], \\ \theta_0^2 &= \frac{a_0}{b}(T_{\mathrm{C}} - T), \quad T_{\mathrm{C}} = T_1 + (\chi c^2 + \lambda^2/\kappa)/a_0, \\ \phi_\theta &= qz + \phi_0, \quad q = -\lambda/\kappa, \end{aligned} \tag{5.152}$$

where ϕ_0 is an arbitrary phase shift and T_{C} is the temperature of the SmA-SmC* phase transition.

Cooling the system from high temperatures, the SmC* phase appears below T_{C}. The tilt of molecules by θ_0 effectively acts as a 'field' which induces nonzero value of the bond orientation order A also in the SmC* phase (see (5.150)). This is in agreement with the lack of symmetry difference between the SmC* and SmI* phases, and the only distinction between these phases lies in the magnitude of the bond order. The hexatic order, even if allowed by symmetry, is generally not observed in the SmC* phase, which indicates small value of A_0 in this phase. However, weak bond-orientational order in the SmC phase evolving continuously into the SmI phase was observed in a freely suspended film [27].

When we suppose that the tilt is saturated (temperature independent) in the vicinity of the phase transition temperature T_{I} to the hexatic phase, the temperature dependence of the amplitude of BOO above T_{I} can be expressed as

$$A_0(T) = (f - \chi gc)\theta_0^6/\alpha_0(T - T_2), \quad T \geq T_{\mathrm{I}}(\geq T_2), \tag{5.153}$$

and slightly below T_{I} the expansion of $A_0(T)^2$ in $T_{\mathrm{I}} - T$ gives:

$$A_0(T)^2 = A_0(T_{\mathrm{I}}^{-0})^2 + \frac{2\alpha_0}{-\beta}(T_{\mathrm{I}} - T) = -3\beta/4\gamma + \frac{2\alpha_0}{-\beta}(T_{\mathrm{I}} - T), \tag{5.154}$$

where $T_{\mathrm{I}} = T_2 + 3\beta^2/16\gamma\alpha_0$, $A_0(T_{\mathrm{I}}^{-0})$ is the bond order at T_{I} in the SmI* phase, which is supposed to be much higher than that at T_{I} in the SmC* phase. Due to the coupling A with P the change in BOO induces a jump of polarization ΔP when crossing T_{I} from the SmC* to the SmI* phase

$$\Delta P \equiv P(T_{\mathrm{I}}^{-0}) - P(T_{\mathrm{I}}^{+0}) = \chi g\theta_0^5[A(T_{\mathrm{I}}^{-0}) - A(T_{\mathrm{I}}^{+0})] \approx \chi g\theta_0^5 A(T_{\mathrm{I}}^{-0}). \tag{5.155}$$

At the SmC*–hexatic phase transition the polarization can abruptly increase or decrease below T_{I} depending on the sign of g. A typical temperature dependence of the spontaneous polarization and spontaneous tilt angle in the vicinity of the transition to the hexatic phase is shown in Fig. 5.22. While θ_0 exhibits no anomaly at this transition, P_0 increases in the hexatic phase showing $g > 0$.

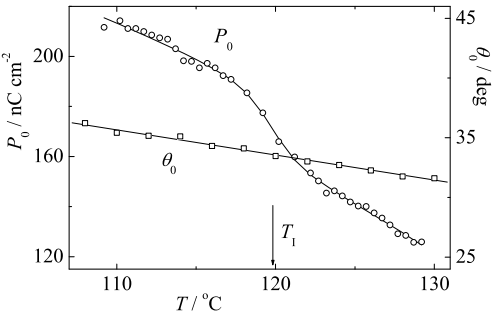

Fig. 5.22. Temperature dependences of spontaneous tilt angle and spontaneous polarization for compound C8OCOOC6. $T_{\rm I}$ indicates the SmC*–SmI* phase transition [25]. The lines are guides for eyes

Dynamic dielectric response

The description of the dynamic behavior in the vicinity of the transition to the hexatic phase is described in detail in [23]. It is based on the free energy density (5.148), where, for simplicity, we put $f = 0$. This simplification will not change the qualitative picture of the dynamics studied. It means that the term g represents the only interaction between the tilt θ and the bond orientation A. At the same time this term represents the coupling between the bond orientation A and polarization P, which is crucial for the dielectric properties near the SmC*–SmI* transition.

For the dynamic dielectric response we shall proceed in the usual way [28]. First we need the variation of the free energy F caused by small fluctuations around an equilibrium state: $P = P_{\rm S} + p, \theta = \theta_{\rm S} + \vartheta, A = A_{\rm S} + e$, where

$$\begin{aligned} p &= \delta(P_0 \exp(\mathrm{i}\phi_P)) = (\delta P_0 + \mathrm{i}\delta\phi_P P_0) \exp[\mathrm{i}\phi_P] = (p_1 + \mathrm{i}p_2) \exp[\mathrm{i}\phi_P] \\ \vartheta &= (\vartheta_1 + \mathrm{i}\vartheta_2) \exp[\mathrm{i}(\phi_\theta + \pi/2)] \\ e &= (e_1 + \mathrm{i}e_2) \exp[\mathrm{i}6\phi_A], \end{aligned} \tag{5.156}$$

p_1 is fluctuation of the amplitude (amplitudon) and p_2 is the fluctuation of the phase (phason) of the polarization. Likewise we have amplitudon ϑ_1 and phason ϑ_2 of the tilt, and amplitudon e_1 and phason e_2 of the bond orientation. Introducing the viscosity for amplitudons and phasons, γ_{p1}, $\gamma_{\vartheta 1}$, γ_{e1}, and γ_{p2}, $\gamma_{\vartheta 2}$, γ_{e2}, respectively, the Landau-Khalatnikov relaxation equations can be constructed and solved in the form:

$$\begin{aligned} &p_1 = p_{10} \sin q\,x, \quad \vartheta_1 = \vartheta_{10} \sin q\,x, \quad e_1 = e_{10} \sin q\,x, \\ &p_2 = p_{20} \cos q\,x, \quad \vartheta_2 = \vartheta_{20} \cos q\,x, \quad e_2 = e_{20} \cos q\,x\,. \end{aligned} \tag{5.157}$$

An applied homogeneous electric field $E_x = E_0 \exp \mathrm{i}\omega t$, which is perpendicular to the z-axis (layer normal), interacts with the induced polarization $\delta P_x = \frac{1}{2}(p + p^*)$ as $-E_x \delta P_x$. The total susceptibility $\chi_{\rm tot}(\omega) = \partial\langle P_x\rangle/\partial E_x = -(p_{10} +$

$p_{20})/2E_0$, where brackets mean spatial average. For 6 unknown amplitudes p_{10}, p_{20}, ϑ_{10}, ϑ_{20}, e_{10}, e_{20}, 6 dynamical equations are finally obtained:

$$\begin{pmatrix} \chi_{p1}^{-1} & -c & g\theta_0^5 & 0 & 0 & 0 \\ -c & \chi_{\vartheta 1}^{-1} & 0 & 0 & 0 & 0 \\ g\theta_0^5 & 0 & \chi_{e1}^{-1} & 0 & 0 & 0 \\ 0 & 0 & 0 & \chi_{e2}^{-1} & 0 & g\theta_0^5 \\ 0 & 0 & 0 & 0 & \chi_{\vartheta 2}^{-1} & -c \\ 0 & 0 & 0 & g\theta_0^5 & -c & \chi_{p2}^{-1} \end{pmatrix} \begin{pmatrix} p_{10} \\ \vartheta_{10} \\ e_{10} \\ e_{20} \\ \vartheta_{20} \\ p_{20} \end{pmatrix} = \begin{pmatrix} -E_0 \\ 0 \\ 0 \\ 0 \\ 0 \\ -E_0 \end{pmatrix} \tag{5.158}$$

where $\chi_{e1}^{-1} \equiv \mathrm{i}\omega\gamma_{e1} + \alpha + 3\beta A_0^2 + 5\gamma A_0^4$, $\chi_{e2}^{-1} \equiv \mathrm{i}\omega\gamma_{e2} + \alpha + \beta A_0^2 + \gamma A_0^4$, $\chi_{\vartheta 1}^{-1} \equiv \mathrm{i}\omega\gamma_{\vartheta 1} + a + 3b\theta_0^2$, $\chi_{\vartheta 2}^{-1} \equiv \mathrm{i}\omega\gamma_{\vartheta 2} + a + b\theta_0^2$ and $\chi_{p1}^{-1} \equiv \mathrm{i}\omega\gamma_{p1} + \chi^{-1}$, $\chi_{p2}^{-1} \equiv \mathrm{i}\omega\gamma_{p2} + \chi^{-1}$. One can get eigenmodes and their relaxation frequencies for $E_0 = 0$. The equations describe 3 coupled amplitudons and 3 coupled phasons, the amplitudons and phasons do not mutually influence. The bare polarization is connected with the fast rotations of molecules around their axes, while the tilt and the bond orientation are connected with much slower molecular motions ($\gamma_{pi} \ll \gamma_{\vartheta i},\ \gamma_{ei},\ i = 1, 2$). From it follows that in the high frequency range only the bare polarization modes (amplitudon and phason) with the relaxation times $\tau_{pi} \equiv \chi\gamma_{pi},\ i = 1, 2$, contribute to the response. At a considerable lower frequency range where $\omega\tau_{p1} \ll 1$ and $\omega\tau_{p2} \ll 1$, the pure polarization susceptibility approaches its static value χ and the coupled slower modes of the tilt and of the bond orientation come into play. To obtain transparent enough expressions for relaxation frequency of these modes we make several reasonable assumptions. We suppose that in the SmC* phase but far below the SmA–SmC* transition, the relaxation times of both amplitudon and phason of the bare tilt $\tau_{\vartheta 1}$, $\tau_{\vartheta 2}$ are temperature independent, the tilt θ_0 being saturated. The phasons are assumed considerably slower than the amplitudons, e.g. $\tau_{e1}/\tau_{e2} \ll 1$, and also e-modes are slower than ϑ-modes, i.e. $\tau_{\vartheta 1}/\tau_{e1} \ll 1$. $\tau_{\vartheta 2}/\tau_{e2} \ll 1$. The last relations are reasonable at least near the transition to the hexatic phase due to the softening of the e-modes and the saturation of the ϑ-modes. Under these assumptions the eigenfrequencies of mixed tilt-bond amplitudon and phason modes can be calculated from (5.158) (for details see [23]). In the calculation expansion with respect to small quantities is used. The eigenfrequencies of mixed modes are increased compared to the frequencies of the pure tilt or bond modes. Near T_I the ϑ-like modes are temperature independent (since θ_0 is saturated) and e-like modes vary with temperature (since A_0 depends on the temperature). The approximate relaxation frequencies of the e-modes near above the phase transition to the hexatic phase read (for amplitudon and phason):

$$\begin{aligned} &(\tau_{-1})^{-1} \propto \alpha_0[T - (T_2 + 2\chi_{\vartheta 1}^0 g^2\theta_0^{10}/\alpha_0)], \\ &(\tau_{-2})^{-1} \propto \alpha_0[T - (T_2 + 2\chi_{\vartheta 2}^0 g^2\theta_0^{10}/\alpha_0)], \quad T > T_\mathrm{I}(> T_2) \end{aligned} \tag{5.159}$$

Switching the coupling between e- and ϑ-modes off (e.g. $g = 0$), both frequencies (5.159) are equal and the single e-mode exists in the SmC* phase. Switch-

ing the coupling on and taking into account the relation $\chi^0_{\vartheta 1} < \chi^0_{\vartheta 2}$ (since the susceptibility of pure tilt phason $\chi^0_{\vartheta 2}$ is larger than that of amplitudon $\chi^0_{\vartheta 1}$), mode splitting into the amplitudon and phason appears, and $(\tau_{-1})^{-1} > (\tau_{-2})^{-1}$. Nevertheless, the frequency difference $(\tau_{-1})^{-1} - (\tau_{-2})^{-1} \propto \theta_0^{10}$ is small in the SmC* phase. Temperature dependence of the relaxation frequencies $(\tau_{-1})^{-1} \approx (\tau_{-2})^{-1}$ above T_{I} is shown in Fig. 5.23. Below T_{I} in the hexatic

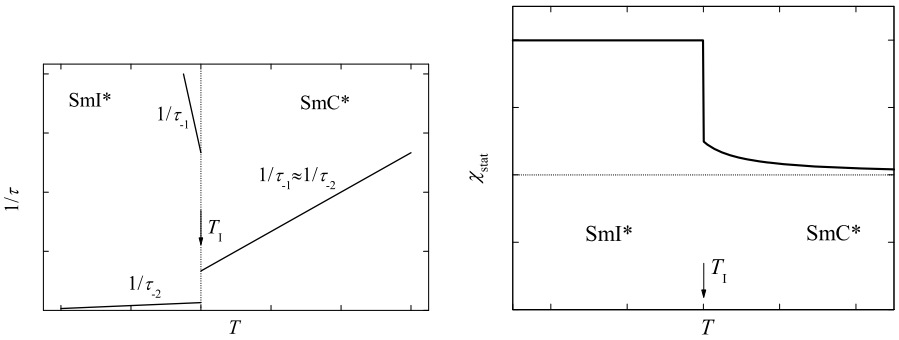

Fig. 5.23. Theoretical temperature dependence of the relaxation frequencies $1/\tau_{-1}$, $1/\tau_{-2}$ for renormalized mixed *e*-like modes (*left*), and the static susceptibility (*right*). T_{I} indicates the SmC*–SmI* phase transition [23]

phase the bond order becomes abruptly large, (see (5.154)). Then the respective amplitudon and phason frequencies of renormalized *e*-modes, up to the lowest order of $T_{\mathrm{I}} - T$ are:

$$(\tau_{-1})^{-1}(T) \propto 3\beta^2/4\gamma + 8\alpha_0(T_{\mathrm{I}} - T), \tag{5.160}$$

$$(\tau_{-2})^{-1}(T) \propto \frac{-\chi gc\theta_0^6}{A_0(T_{\mathrm{I}}^{-0})}\left(1 - \frac{\frac{\alpha_0}{-\beta}(T_{\mathrm{I}} - T)}{A_0(T_{\mathrm{I}}^{-0})^2}\right) \approx \frac{-\chi gc\theta_0^6}{A_0(T_{\mathrm{I}}^{-0})}, \quad T \le T_{\mathrm{I}}.$$

Comparing (5.159) and (5.160) one can conclude that at the transition to the hexatic phase there is a jump up of amplitudon frequency and a strong linear increase on decreasing temperature (see Fig. 5.23). On the other hand, the *e*-phason frequency strongly drops at T_{I} as:

$$\frac{(\tau_{-2})^{-1}(T_{\mathrm{I}}^{-0})}{(\tau_{-2})^{-1}(T_{\mathrm{I}}^{+0})} \doteq -\frac{32}{3}\chi gc\sqrt{\frac{-\gamma^3}{3\beta^5}}\theta_0^6 = \frac{A_0(T_{\mathrm{I}}^{+0})}{A_0(T_{\mathrm{I}}^{-0})} \ll 1, \tag{5.161}$$

where $A_0(T_{\mathrm{I}}^{+0})$ and $A_0(T_{\mathrm{I}}^{-0})$ are amplitudes of the bond order at T_{I} in the SmC* and the hexatic phases, respectively. The formula (5.160) predicts further frequency decrease of *e*-like phason on cooling below T_{I} (see Fig. 5.23).

The dynamic susceptibility can be determined as a superposition of four relaxators, amplitudons and phasons of both tilt-like and bond-like modes. Under the conditions used for determination of relaxation frequencies, it is

inferred that the main contribution to the susceptibility comes from e-phason with the frequency $(\tau_{-2})^{-1}$. The result of the calculation [23], the temperature dependence of the static susceptibility in the vicinity of the transition to the hexatic phase is shown in Fig. 5.23.

5.3.3.2 Properties of modes found experimentally in ferroelectric materials

In both SmC* and hexatic phases only a single mode has been detected in dielectric spectroscopy. Temperature dependences of f_r and $\Delta\varepsilon$ of this mode in the vicinity of the phase transition SmC*-SmI* are shown in Fig. 5.24 for a substance denoted as C8OCOOC5 [23]. One can see a remarkable decrease of the relaxation frequency and increase of dielectric strength when approaching the phase transition from the SmC* to the SmI* phase. This mode can be identified with the τ_{-2} mode defined in (5.160), which is the e-like phason (phase fluctuations in the bond orientation) renormalized due to coupling with P and θ. The relaxation frequency $f_\mathrm{r} = (\tau_{-2})^{-1}/2\pi$ of the observed e-like phason decreases nearly linearly in the SmC* phase when approaching the SmI* phase. This dependence is in accordance with (5.159) and Fig. 5.23. The jump in f_r around T_I, is not as sharp as it is forecast by the theory (Fig. 5.23). The smearing out of this jump is due to a coexistence of phases, which occurs typically within the temperature interval 2 to 3 K. In the SmI* phase f_r is one order lower than that in the SmC* phase, and further slightly decreases on cooling. The drop of $(\tau_{-2})^{-1}$ at T_I gives a ratio of the amplitudes of the bond order of both phases that meet at T_I. For the substance C8OCOOC5 it was calculated according to relation (5.161) that the amplitude of the bond order is increased 48 times when entering the hexatic phase [23]. The e-like amplitudon has nearly the same relaxation frequency in the SmC* phase as the e-like phason (Fig. 5.23), but just below T_I its relaxation frequency abruptly increases and continues in a linear increase on further cooling (see (5.160)). This amplitudon mode is weak and cannot be distinguished from the corresponding stronger phason mode.

Comparing the static permittivity calculated from the theory (see Fig. 5.23) with the experimental results obtained one has in mind that only the e-like phason gives a substantial contribution to the static permittivity. Then we can hold its dielectric strength $\Delta\varepsilon$ as the static permittivity. Let us compare the $\Delta\varepsilon(T)$ dependence found for C8OCOOC5 (Fig. 5.24) with the static permittivity calculated from the model and shown in Fig. 5.23. A qualitative agreement is seen in the SmC* phase where both dependences exhibit an increase on cooling. The jump at the SmC*-SmI* phase transition is not observed in experiment because of the coexistence of both phases in the temperature range 2–3 K, which smears the sharp jump upwards into a continuous increase. An increase in permittivity is observed even behind the temperature range of coexistence of phases instead of a constant predicted by the model for the SmI* phase. The experiment shows that the permittivity behavior in the

SmI* phase is more complicated than predicted by the presented theory, and it may substantially differ for various materials [23]. Moreover, experimental studies well below the SmC*-SmI* phase transition are limited due to very low relaxation frequency of the observed mode.

In some compounds (e.g., see Fig. 5.25), in contrast to the effects discussed so far, an increase of the relaxation frequency and decrease of permittivity occur at T_I. At the same time tilt decreases and there is also change of the pitch p of the helix. This can be explained considering also gradient terms of BOO in the free energy [29, 30].

5.3.3.3 Transition to the hexatic phase in antiferroelectric liquid crystals

In antiferroelectric smectic C, SmC^*_A, phase the molecules in the adjacent layers are tilted in average in opposite directions and the direction of the in-plane spontaneous polarization differs by 180 degrees. In such a phase only two modes can be dielectrically active [3]. It is the vibration of the director tilt in the next layers in the same direction changing its amplitude (acoustic amplitudon) and the vibrations of the director azimuthal orientation in the opposite direction keeping constant tilt angle (optical phason, or antiphase mode). The first mode can be visible in dielectric spectroscopy only near the upper border of the smectic C* phase, where it is soft and quickly becomes hard on temperature lowering, the other can be active within the whole antiferroelctric phase.

Because of chirality the structure is spatially modulated to a double helix, in which the directions of the spontaneous tilt and the polarization slowly precess along the layer normal. As a result, polarization of the adjacent layers is not fully compensated. Vibration of the non-zero local polarization can give an additional mode in the dielectric response. Assuming discreteness of

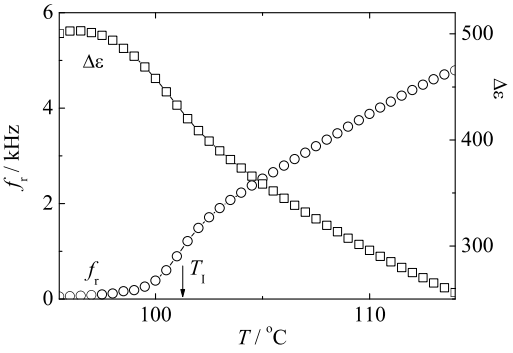

Fig. 5.24. Temperature dependence of the relaxation frequency and dielectric strength of compound C8OCOOC5. The arrow indicates the temperature T_I of the SmC*–SmI* phase transition as determined from DSC [23]

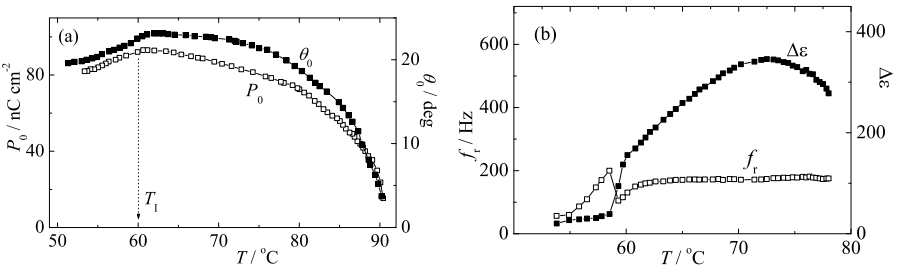

Fig. 5.25. Temperature dependence **(a)** of the tilt and polarization and **(b)** of the relaxation frequency and dielectric strength of compound ZLL7/6. The arrow indicates the temperature T_I of the SmC*–SmI* phase transition [29, 30]

the structure it is convenient to define the ferroelectric (FE) and antiferroelectric (AF) order parameters as $\boldsymbol{P}_\mathrm{F} = (\boldsymbol{P}_1 + \boldsymbol{P}_2)/2$, and $\boldsymbol{P}_\mathrm{A} = (\boldsymbol{P}_1 - \boldsymbol{P}_2)/2$, where $\boldsymbol{P}_1$ and $\boldsymbol{P}_2$ are polarizations of the next layers. Similar expressions can be defined for θ_F and θ_A. The non-compensated polarization in the AF helicoidal structure, P_x, existing along the in-plane electric field direction can be expressed as [25]

$$P_x = -d\,\partial P_{\mathrm{A},x}/\partial z \tag{5.162}$$

z being the helicoidal axis and d the smectic layer thickness. To describe the phase transition to the hexatic phase in AF liquid crystals one can write a free energy expansion based on (5.148), where the terms in P and θ parameters are written in both FE and AF version with the same functional form. The lowest coupling of the polarization P_F and the bond order parameter A is $P_\mathrm{F}\theta_\mathrm{F}^5 A$ and the equilibrium value $\theta_\mathrm{F} = 0$. The optical phason and acoustic amplitudon are not sensitive to the appearance of the hexatic order. On the opposite, the fluctuation of the AF order parameters amplitudon and phason of θ_A and P_A are not dielectrically active in continuum [3], but they become active assuming discreteness of the sample because of non-zero polarization (5.162). Since the equilibrium tilt θ_A is nonzero in the SmC$^*_\mathrm{A}$ phase, the main coupling term $P_\mathrm{A}\theta_\mathrm{A}^5 A$ between P_A and A is also nonzero and consequently the transition to the hexatic phase should be reflected in these modes. Then for the dielectric susceptibility in the vicinity of the SmC$^*_\mathrm{A}$ – SmI$^*_\mathrm{A}$ (or SmF$^*_\mathrm{A}$) phase transition one can get [25]

$$\chi_\mathrm{A}(\omega) = \chi_1(\omega) + \frac{\pi d}{p}\chi_\mathrm{h}(\omega) \tag{5.163}$$

where $p \gg d$ is the helicoidal pitch and $\chi_1(\omega)$ is temperature independent contribution to $\chi_\mathrm{A}(\omega)$ from P_F fluctuations. The last term, being the contribution of the P_A fluctuations due to the existence of the helix in the discrete lattice, is increasing when approaching the transition because of the softening of BOO amplitudon and may become visible in the dielectric spectrum near the transition to the hexatic phase.

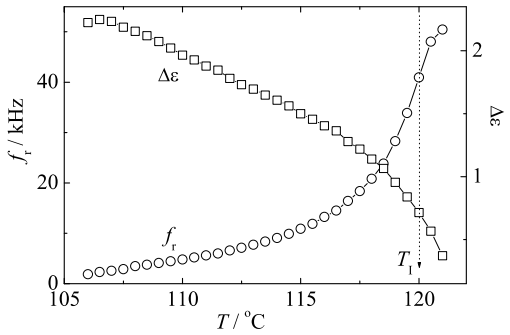

Fig. 5.26. Temperature dependence of the relaxation frequency and dielectric strength of compound C8OCOOC6. The arrow indicates the temperature T_I of the SmC^*_A–SmI^*_A phase transition [25]. The lines are guides for eyes

In the AF hexatic phase rather strong BOO phason may appear, similarly as in the FE hexatic phase. Typical behavior of modes found in the vicinity of the $SmC^*_A - SmI^*_A$ phase transition is shown in Fig. 5.26 [25]. This behavior is in accordance with the above picture. In the SmC^*_A no mode is detected except a close vicinity of this phase transition where a very weak BOO amplitudon is seen. In the phase transition a jump of the relaxation frequency is observed similarly as for the transition in the FE materials. In the hexatic phase rather strong BOO phason is detected.

5.3.4 Summary

The first part concerns the effect of the anchoring of molecules at the surfaces on the structure of the ferroelectric liquid crystals in finite samples. Due to this anchoring the structure in planar samples significantly differs from the ideal helix. In thin enough samples the helix is unwound but the anchoring produces a director twist-bend along the sample normal. Fluctuations of this structure – *thickness mode* – bring the main contribution to the dielectric response. In thick samples the director twist-bend still exists and is completed with the helix along the layer normal, which is clamped at the surfaces. The vibration of such a complicated structure – *pinned Goldstone mode* – is generally multimode, but there is only slight deviation from a single Debye relaxation. Theory and experiment show that permittivity of both structures increases and relaxation frequency decreases with increased sample thickness. For high enough thickness these dependences are saturated due to compensation of depolarization field by ionic conductivity. A comparison of theory and experiment shows that less than 1% of this field remains non-compensated. The surfaces pin also the soft mode in the SmA phase. This effect does not change the slopes of the temperature dependences of permittivity and relaxation frequency, only the SmA–SmC^* phase transition temperature is shifted to higher temperatures with increased sample thickness.

In the second part a model of ferroelectric hexatics and its comparison with experimental results were presented. The phase transition from the ferroelectric SmC* phase to the hexatic phase is of the first order without symmetry change. It is characterized by a spontaneous appearance of macroscopic values of bond orientation order (BOO) below this transition. A nonzero but very small hexatic order is present even in the SmC* phase. Orientation of intermolecular bonds and molecular tilt are coupled resulting in SmI* or SmF* structures. The coupling of polarization with BOO can cause a change of polarization when the hexatic order appears. The tilt angle does not change at the transition region. Dynamic dielectric response is contributed by 3 coupled amplitudons and 3 coupled phasons of polarization, molecular tilt and BOO. The strongest part of the dielectric response is attributed to the phasons, in particular those of the tilt and BOO. The model gives partial softening of the BOO phason above the hexatic transition, and substantial decrease of its relaxation frequency and increase of the permittivity in the hexatic phase. Recently, anomalous behavior of the tilt angle has been observed in some hexatics, which requires generalization of the model presented here.

References

1. R. Blinc, B. Žekš: Phys. Rev. **18**, 740 (1978)
2. J.W. Goodby et al.: *Ferroelectric Liquid Crystals: Principles, Properties and Applications*. (Gordon and Breach Science Publishers 1991)
3. I. Muševič, R. Blinc, B. Žekš: *The Physics of Ferroelectric and Antiferroelectric Liquid Crystals*. (World Scientific 2000)
4. M. Glogarová, J. Pavel: Mol. Cryst. Liq. Cryst. **114**, 249 (1984)
5. M. Brunet, C. Williams: Ann. Physique **3**, 237 (1978)
6. S.A. Pikin, V.L. Indenbom: Usp. Fiz. Nauk **125**, 251 (1978)
7. A. Levstik, Z. Kutnjak, C. Filipič, I. Levstik, Z. Bregar, B. Žekš, T. Carlson: Phys. Rev. A **42**, 2204 (1990)
8. I. Rychetský, M. Glogarová, A.M. Bubnov: Ferroelectrics **212**, 21 (1998)
9. S.A. Pikin, K. Yoshino: Jap. J. Appl. Phys. **20**, L-557 (1981)
10. I. Rychetský, V. Novotná, M. Glogarová: J. Phys. IV France **10**, Pr.7-119 (2000)
11. M. Glogarová, H. Sverenyák, J. Holakovský, H.T. Nguyen, C. Destrade: Mol. Cryst. Liq. Cryst. **263**, 245 (1995)
12. Yu. Panarin, Yu. Kalmykov, S.T. MacLughadha, H. Xu, J.K. Vij: Phys. Rev. E **50**, 4763 (1994)
13. H. Miyata, M. Maeda, I. Suzuki: Liquid Crystals **20**, 303 (1996)
14. V. Novotná, M. Glogarová, H. Sverenyák, A.M. Bubnov: Mol. Cryst. Liq. Cryst. **303**, 219 (1996)
15. V. Novotná, M. Glogarová, A.M. Bubnov, H. Sverenyák: Liquid Crystals **23**, 511 (1997)
16. N.A. Clark, S.T. Lagerwall: Appl. Phys. Lett. **36**, 899 (1980)
17. V. Novotná, O. Tsyganenko, M. Glogarová, I. Rychetský, V. Hamplová, M. Kašpar: Ferroelectrics **241**, 239 (2000)

18. J. Schadt, F. Giesselmann, P. Zugenmaier, W. Kuczynski: Ferroelectrics **173**, 157 (1995)
19. M. Glogarová, V. Novotná, I. Rychetský, M. Kašpar, V. Hamplová: Mol. Cryst. Liq. Cryst. **364**, 353 (2001)
20. J.J. Benattar, J. Doucet, A.M. Lambert: Phys. Rev. A **20**, 2505 (1979)
E. Gorecka, Li Chen, O. Lavrentovich, W. Pyzuk: Europhys. Lett. **27**, 507 (1994)
21. R. Bruinsma, D.R. Nelson: Phys. Rev. B **23**, 402 (1980)
22. D.R. Nelson, B.I. Halperin: Phys. Rev. B **21**, 5312 (1980)
23. I. Rychetský, D. Pociecha, V. Dvořák, J. Mieczkowski, E. Gorecka, M. Glogarová: J. Chem. Phys. **111**, 1541 (1999)
24. D. Pociecha, M. Glogarová, E. Gorecka, I. Rychetský, J. Mieczkowski, V. Dvořák: Mol. Cryst. Liq. Cryst. **328**, 275 (1999)
25. M. Glogarová, D. Pociecha, E. Gorecka, I. Rychetský, J. Mieczkowski: Ferroelectrics **245**, 43 (2000)
26. The director projection $\xi = (\xi_1, \xi_2) = (\theta_0 \cos(\phi_\theta + \pi/2), \theta_0 \sin(\phi_\theta + \pi/2))$ can be expressed as a complex function $\theta = \theta_0 \exp[\mathrm{i}(\phi_\theta + \pi/2)]$.
27. J.D. Brock, A. Aharony, R.J. Birgenau, K.W. Evans-Lutterodt, J.D. Litster, P.M. Horn, G.B. Stephenson, A.R. Tajbakhsh: Phys. Rev. Lett. **57**, 98 (1986)
28. See for example T. Carlson, B. Žekš, C. Filipič, A. Levstik, R. Blinc: Mol. Cryst. Liq. Cryst. **163**, 11 (1988)
29. M. Glogarová, V. Novotná, I. Rychetský, M. Kašpar, V. Hamplová: Ferroelectrics **277**, 209 (2002)
30. I. Rychetský, M. Glogarová, V. Novotná: Phys. Rev. E **67**, 021704 (2003)

5.4 Systems with competing synclinic-anticlinic interactions

M. Čepič, E. Gorecka, D. Pociecha and N. Vaupotič

5.4.1 Introduction

It seems that in order to obtain ferroelectricity at least some positional order in the system is necessary [1], as until now no liquid ferroelectric phase has been found. The least ordered phases with ferroelectric properties are smectics. The smectic layer can have non-zero spontaneous electric polarisation P_s if built of chiral molecules that are tilted from the layer normal. The value of the P_s is proportional to the transversal dipole of the molecule placed at or close to the chiral centre and to degree of hindered rotation around the molecular long axes. Both factors could be controlled by careful molecular designing. The alternative approach for obtaining ferroelectric smectic layers requires using strongly bent-shaped molecules.

Apart from the structure that is stack of the layers with the same direction of tilt vector (synclinic Sm C) more complex phases exist, differing in arrangement of tilt in consecutive smectic layers. Among them, the simplest one is that with the anticlinic tilt in neighboring layers (anticlinic Sm C_A). For the

rod-like compounds the bilinear coupling between tilt and polarisation leads to the straightforward relation: synclicnic structure is ferroelectric (Sm C^*) while the anticlinic structure is antiferroelectric (Sm C^*_A). Both types of polar phases were confirmed experimentally for numerous compounds [2]. However, it is still difficult to predict which molecular factors determine the tilt thus polar structure. The anticlinic phase is only rarely reported for compounds with non-branched molecular tails, i.e. it is more frequent for materials showing weak layer intercalation. On the other hand to observe anticlinic phase, the materials with at least three aromatic rings in the mesogenic core are usually necessary. These might point, that in order to obtain anticlinic structure the strong interlayer van der Waals interactions between molecular cores accompanied by weak molecular tails interdigitation are necessary. Contrary, the strong interdigitation between molecular tails locks the tilt between the layers, and promotes the synclinic structure. However, it seems that for many materials free energy of the synclinic and the anticlinic structure is similar and the type of the polar phase that actually appears, depends on the very subtle factors, e.g. in some homologoues series, extending the molecular tails by just one carbon atom is sufficient to reverse polarity of the phase [3]. For such systems it was also observed that bulk antiferroelectric phase might become ferroelectric in a thin sample due to the interactions with the sample surfaces [4]. On the other hand, the ferroelectric phase might become antiferroelectric upon doping with a small amount of bent-shaped molecules [5].

Competition between syclinic and anticlinic arrangement have also other important consequences and some of them will be discussed in this section. We will consider the systems in which the phase sequence become more complex. In chiral materials besides fundamental Sm C^* and Sm C^*_A structures, intermediate phases may appear. There are known three such phases, Sm C^*_α, Sm C^*_{FI1} and Sm C^*_{FI2}, not always correctly, but for historical reason, called 'ferrielectric' phases [6, 7]. The most general phase sequence upon lowering temperature is: Sm A $\leftrightarrow$ Sm C^*_α $\leftrightarrow$ Sm C^* $\leftrightarrow$ Sm C^*_{FI2} $\leftrightarrow$ Sm C^*_{FI1} $\leftrightarrow$ Sm C^*_A. In different materials or upon changing enantiomeric excess some of these phases are missing, but if they exist they always appear in the same temperature sequence.

5.4.2 Theoretical modelling

In order to describe the structure of polar smectics, besides the nematic and the smectic order parameters, two additional parameters are necessary. The two-dimensional tilt order parameter is a vector $\boldsymbol{\xi} = \{n_x n_z, n_y n_z\}$ which gives the average tilt of molecular long axes with respect to the layer normal (Fig. 5.27). Its definition takes into account also the up-down symmetry. The two-dimensional polar order parameter is a vector $\boldsymbol{P} = \{P_x, P_y\}$ which gives the polarisation obtained from averaging of the molecular dipoles. Two different approaches have been used for the theoretical analysis of the tilted polar smectics. In continuous models [8–13] it has been assumed that spa-

tial variation of order parameters is continuous. Model parameters express macroscopic properties like elastic constants or piezoelectricity. Continuous models successfully reproduced structures and properties of the ferroelectric Sm C* phase and the antiferroelectric Sm C$^*_A$ phase, but failed to reproduce more complex phases like the Sm C$^*_\alpha$, Sm C$^*_{FI2}$ and Sm C$^*_{FI1}$ [2, 6].

A discrete model was introduced for the first time in [14]. In discrete models the tilt and polar orders are given for each smectic layer. In general the structure of the system with N layers is given by N tilt vectors $\boldsymbol{\xi}_j$ and N polarisation vectors $\boldsymbol{P}_j$. Contributions of intralayer and interlayer interactions are considered separately. The advantage of the discrete models are that intensive spatial changes of both order parameters are allowed. Within the framework of such models, the structure of the Sm C$^*_\alpha$ phase has been proposed in [15], few years before it was confirmed by resonant X-ray measurements [16]. Recently also structures of Sm C$^*_{FI2}$ and Sm C$^*_{FI1}$, consistent with experiment were reproduced, as well as the correct phase sequence in dependence of the enantiomeric excess. In the following we will consider in detail the most general free energy for the chiral polar smectics which can reproduce structures of all chiral smectic C phases and the observed phase sequences.

5.4.2.1 Free energy

In chiral polar smectics we consider various, sometimes competing intralayer and interlayer interactions. A delicate balance between these forces slightly changes with temperature and results in a number of phases, being stable in a narrow temperature region. Considering arguments in [17] we introduce order parameter $\boldsymbol{\eta}$, which describes degree of hindered molecular rotation around long axes. This leads for the chiral molecules to an asymmetric distribution of the molecular transverse dipole moments in the smectic layer. A layer polarisation is $\boldsymbol{P}_j = P_0\,\boldsymbol{\eta}_j$, where P_0 is the maximal polarisation for system with restricted molecular rotation. The free energy expressed in terms of both order parameters $\boldsymbol{\xi}_j$ and $\boldsymbol{\eta}_j$ is

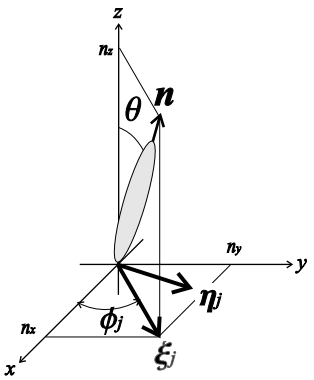

Fig. 5.27. Definitions of the tilt order parameter $\boldsymbol{\xi}_j$ and the polar order parameter $\boldsymbol{\eta}_j$, which are not perpendicular in general

$$
\begin{aligned}
G = a \sum_{j=1}^{N} \quad & \frac{1}{2}\,(T - T_0)\,\boldsymbol{\xi}_j^2 + \frac{1}{4}\,b\,\boldsymbol{\xi}_j^4 + \frac{1}{2}\,a_{10}\;(\boldsymbol{\xi}_j \cdot \boldsymbol{\xi}_{j+1}) \\
& + \frac{1}{2}\,a_{11}\,\boldsymbol{\xi}_j^2\,(\boldsymbol{\xi}_j \cdot \boldsymbol{\xi}_{j+1}) + \frac{1}{2}\,f_1\;(\boldsymbol{\xi}_j \times \boldsymbol{\xi}_{j+1})_z \\
& + \frac{1}{2}\,b_0\,\boldsymbol{\eta}_j^2 + \frac{1}{2}\,b_1\;(\boldsymbol{\eta}_j \cdot \boldsymbol{\eta}_{j+1}) + \frac{1}{8}\,b_2\;(\boldsymbol{\eta}_j \cdot \boldsymbol{\eta}_{j+2}) \\
& + c_p\,(\boldsymbol{\eta}_j \times \boldsymbol{\xi}_j)_z + \frac{1}{2}\,\mu\;(\boldsymbol{\xi}_{j+1} - \boldsymbol{\xi}_{j-1}) \cdot \boldsymbol{\eta}_j \\
& + \frac{1}{2}\,b_Q\,(\boldsymbol{\xi}_j \cdot \boldsymbol{\xi}_{j+1})^2 .
\end{aligned}
\tag{5.164}
$$

The first two terms resume intralayer steric and attractive van der Waals interactions expressed in tilt angles. The phase transition from orthogonal to the tilted phase in an isolated racemic smectic layer occurs at the temperature T_0. The parameter a_{10} is due to the achiral part of van der Waals interactions between nearest neighbouring layers (NN) and parameter a_{11} gives the affect of the tilt on the these interactions. Parameter f_1 resumes chiral part of NN van der Waals interactions. It is proportional to the enantiomeric excess $x = c_L - c_R$ where c_L and c_R are concentrations of left- and right-handed enantiomers respectively, thus $f_1 = f_{10}x$ where f_{10} is valid for optically pure sample. Parameter b_0 gives the intralayer polar interaction and parameters b_1, b_2 give electrostatic interactions between nearest and between next nearest neighbouring layers (NNN). Since the polar order parameter is not a primary one for the SmA-SmC phase transition the b_0 constant is always positive. Electrostatic NN and NNN interactions always favour antiferroelectric order in interacting layers thus b_1 and b_2 are always positive. Interlayer electrostatic interactions exist only when positional correlations between molecules in different layers are present [18]. These correlations decrease exponentially with distance and therefore we assume that $b_0 \gg b_1 \gg b_2$. The parameter $c_p = c_{p0}\;x$ gives the piezoelectric coupling between the tilt and the polarisation. It exists in chiral samples, its magnitude is c_{p0} in optically pure samples, it has opposite signs in enantiomers and is zero in racemic mixture. The parameter μ gives the flexoelectric coupling since it couples the space variation of the tilt and the polarisation. The parameter b_Q gives the quadrupolar coupling between nearest layers. For a negative value, b_Q favours uniplanar tilts in nearest layers, it does not distinguish between the synclinic and the anticlinic structures [19]. All parameters in (5.165) are expressed in temperature units (K), except the parameter a which is expressed in J m^{-3}K^{-1}. Elimination of the polarisation [20] leads to the free energy expressed only in tilt vectors, in which indirect, polarisation mediated, interlayer interactions, extend up to the fourth nearest layers. The interlayer part of the free energy is

$$
G_{int} = \sum_j \frac{1}{2}\left(\sum_{i=1}^{4} \tilde{a}_i(\boldsymbol{\xi}_j \cdot \boldsymbol{\xi}_{j+i}) + \sum_{i=1}^{3} \tilde{f}_i(\boldsymbol{\xi}_j \times \boldsymbol{\xi}_{j+i})_z + b_Q\;(\boldsymbol{\xi}_j \cdot \boldsymbol{\xi}_{j+1})^2\right).
\tag{5.165}
$$

where the values of parameters $\tilde{a}_i$ and $\tilde{f}_i$ depend on the values of the parameters in (5.165). The detailed derivation of the parameters is given in [20] and they are quoted in ([21], see Eq.(5.30)). Parameters $\tilde{a}_i$ have an achiral character and, depending on their sign, favour the synclinic ($\tilde{a}_i < 0$) or the anticlinic ($\tilde{a}_i > 0$) arrangement of molecules in interacting layers. The chiral interactions are given by the parameters $\tilde{f}_i$. They favour a perpendicular tilt directions $+90°$ or $-90°$ in interacting layers depending on the sign of the corresponding $\tilde{f}_i$. Parameters $\tilde{f}_i$ include direct van der Waals interactions f_1 and combined piezoelectric and flexoelectric interactions, thus their value can be comparable to that of achiral NN interactions.

5.4.2.2 Stable phases and their structures

In order to find possible structures, as the first approximation, we analyse only the interlayer part of the free energy, assuming the constant magnitude of the tilt angle in each smectic layer. Later we extend the analysis also to the influence of the interlayer interactions on the magnitude of the tilt and polarisation vector. We assign α_j to the phase difference between tilt directions in neighbouring layers: $\alpha_j = \phi_{j+1} - \phi_j$, where ϕ_j gives the tilt direction in the j-th smectic layer. The structure of the phase is determined by all differences α_j and the magnitude of the tilt θ. It can be given as a sequence of the phase differences $\{\ldots \alpha_{j-1}, \alpha_j, \alpha_{j+1}, \ldots\}$, where in general all the phase differences can differ. The interlayer part of the free energy is given as

$$G_{int} = \frac{1}{2}\theta^2 \sum_j \Big(\tilde{a}_1 \cos\alpha_j + \tilde{a}_2 \cos(\alpha_j + \alpha_{j+1}) + \tilde{a}_3 \cos(\alpha_j + \alpha_{j+1} + \alpha_{j+2}) + \tilde{a}_4 \cos(\alpha_j + \alpha_{j+1} + \alpha_{j+2} + \alpha_{j+3}) + \tilde{f}_1 \sin\alpha_j + \tilde{f}_2 \sin(\alpha_j + \alpha_{j+1}) + \tilde{f}_3 \sin(\alpha_j + \alpha_{j+1} + \alpha_{j+2}) + b_Q\, \theta^2 \cos^2\alpha_j \Big). \quad (5.166)$$

A systematic search for possible solutions that minimise the free energy assumes array of M phase differences as a basic repetitive unit. It should be noticed that in general the periodic structure of M phase differences is incommensurate with the layer structure.

Solutions $M = 1$. The simplest solution of (5.166) is an array of equal phase differences α_1. To find the possible minimum, the constant value of $\alpha_j = \alpha_1$ is inserted into (5.166) and unimportant constants are abandoned

$$G_{int} = \Big(\tilde{a}_1 \cos(\alpha_1)_j + \tilde{a}_2 \cos(2\alpha_1) + \tilde{a}_3 \cos(3\alpha_1) + \tilde{a}_4 \cos(4\alpha_1) + \tilde{f}_1 \sin(\alpha_1) + \tilde{f}_2 \sin(2\alpha_1) + \tilde{f}_3 \sin(3\alpha_1) + b_Q\, \theta^2 \cos^2(\alpha_1) \Big). \quad (5.167)$$

The phase difference α_1 can have any value between $-\pi$ and π. If b_Q is small and negative and the effective parameter $\tilde{a}_1$ is large and negative in

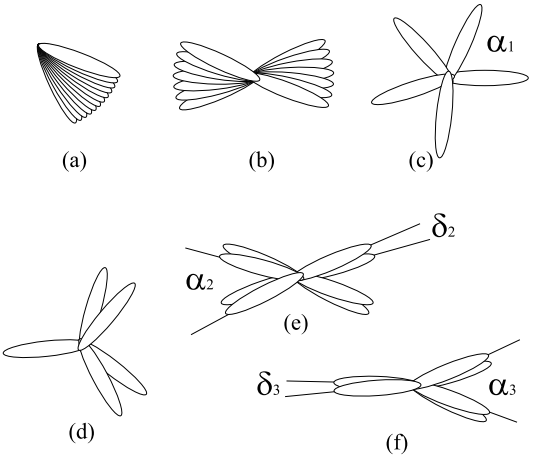

Fig. 5.28. Projections of phase structures onto the smectic plane. (**a**) The Sm C* phase with $\alpha_1 = 4^\circ$ (**b**) The Sm C^*_A phase with $\alpha_1 = 176^\circ$ (**c**) The Sm C^*_α phase with $\alpha_1 = 66^\circ$ (**d**) The Sm C^*_α phase with $\alpha_1 = 134^\circ$ (**e**) The Sm C^*_{FI2} phase with $\alpha_2 = 42^\circ$ and $\delta_2 = 8^\circ$ (**f**) The Sm C^*_{FI1} phase with $\alpha_3 = 44^\circ$ and $\delta_3 = 12^\circ$

comparison with the rest of effective parameters, than $\alpha_1 \to 0$. Also strong quadrupolar coupling b_Q can stabilise this solution if effective $\tilde{a}_1$ is negative. The structure corresponds to the Sm C* phase shown in Fig. 5.28a. The polar properties of the phase are defined by the single layer polarisation $\boldsymbol{P}_j$. Due to the nonzero phase difference α_1, the long, helically modulated structure is formed. The helically modulated phase is optically uniaxial because of space averaging of the dielectric permittivity tensor. As the period of helical modulation is usually comparable with the light wavelengths, pronounced optical rotatory power (ORP) is expected in this phase [22].

On the other hand, for the small negative b_Q but $\tilde{a}_1$ positive and large in comparison with the rest of the effective parameters, the $\alpha_1 \approx \pi$. Also this structure could be stabilised by large negative quadrupolar coupling b_Q. The structure corresponds to the SmC^*_A phase shown in Fig. 5.28b. For this phase the basic structural unit consists of two smectic layers, in which electric polarisation is canceled out, giving rise to antiferroelectric properties. Since α_1 is slightly different than π, the helix is formed. If the chiral NN interactions have the same sign in the SmC^*_A and the Sm C* phases the helix twist sign is opposite in these phases. The space averaging of the dielectric permittivity tensor over the period of the helix gives the uniaxial optical properties of the phase. Pronounced ORP is expected as the length of the helix is usually comparable to the light wavelength.

General value of α_1 is obtained for a small b_Q and $\tilde{a}_1$ comparable to the rest of effective parameters. Both $\tilde{f}_1$ and $\tilde{a}_2$ parameters are significant in systems with large piezoelectric c_p and flexoelectric μ parameters. The structure corresponds to the Sm C^*_α phase.

In systems with negative $\tilde{a}_1$, $\alpha_1 < \pi/2$ (Fig. 5.28c). This situation is typical for the system in which the Sm C^*_α phase exists between SmA and Sm C^* or the Sm C^*_{FI2} phases. For system with positive $\tilde{a}_1$, $\alpha_1 > \pi/2$. The Sm C^*_α with $\alpha_1 > \pi/2$ is formed between Sm A and Sm C^*_A phases (Fig. 5.28d). To our best knowledge no structure studies for such system were conducted.

The Sm C^*_α phase has hellicoidaly modulated structure with periods of a few layers i.e. much shorter than the light wavelength, thus for this phase zero ORP is expected.

Summarising, although all three phases Sm C^*_α, Sm C^*_A, Sm C^* can be described by clock structure, given by the single phase difference α_1, they have substantially different macroscopic properties.

Solutions $M = 2$. The next simplest possible solution corresponds to two interchanging phase differences α and β. The average free energy for two smectic layers is expressed similarly as in (5.167)

$$\begin{aligned} G_{int} = & \frac{1}{2}\tilde{a}_1\left(\cos\alpha + \cos\beta\right) + \tilde{a}_2\cos(\alpha+\beta) \\ & + \frac{1}{2}\tilde{a}_3\left(\cos(\alpha+2\beta) + \cos(2\alpha+\beta)\right) + \tilde{a}_4\cos(2\alpha+2\beta) \\ & + \frac{1}{2}\tilde{f}_1\left(\sin\alpha + \sin\beta\right) + \tilde{f}_2\sin(\alpha+\beta) \\ & + \frac{1}{2}\tilde{f}_3(\sin(\alpha+2\beta) + \sin(2\alpha+\beta)) + \frac{1}{2}b_Q\,\theta^2\left(\cos^2\alpha + \cos^2\beta\right). \quad (5.168) \end{aligned}$$

The Ansatz represents a structure that, in general, is incommensurate with the layer spacing. Only if $\beta = \pi - \alpha$, the structure is commensurate. Minimization with respect to both phase differences α and β results in a structure where β is close to $\pi - \alpha$. The slight incommensurability $\delta = 2\pi - 2\alpha - 2\beta$ leads to helical structure. The complete structure is given by two angles α_2, δ_2 thus $2\beta = 2\pi - 2\alpha_2 - \delta_2$. The solution represents the Sm C^*_{FI2} phase with the basic structural unit of four layers (Fig. 5.28e). This unit is characterized by the dielectric permitivitty tensor with three different diagonal values, two of them being dependent on the angle α_2. Thus in general the tensor is biaxial, it becomes uniaxial for the special case $\alpha_2 = 90°$. Due to the helical structure of the phase the ORP is expected, that is stronger the smaller is α_2. The space averaged polarisation in the basic structural unit is nearly cancelled out, thus the phase has antiferroelectric properties. The tiny non-compensated P_s results from incommensurability δ_2. The structure of Sm C^*_{FI2} phase is stable for $\tilde{a}_1 \approx 0$ and significant quadrupolar coupling b_Q, but the stability limits cannot be given as a simple algebraic expression.

Solutions $M = 3$. Next, we search for the solution where three phase differences interchange. Due to the up and down symmetry we restrict the search only to the sequences $\{\beta, \alpha, \beta\}$. The free energy averaged over three layers is than

$$\begin{aligned} G_{int} = & \frac{1}{3}\,\tilde{a}_1\,(\cos\alpha + 2\cos\beta) + \frac{1}{3}\,\tilde{a}_2\,(2\cos(\alpha+\beta) + \cos(2\beta)) \\ & + \tilde{a}_3\,\cos(\alpha+2\beta) + \frac{1}{3}\,\tilde{a}_4\,(\cos(2\alpha+2\beta) + \cos(\alpha+3\beta)) \\ & + \frac{1}{3}\,\tilde{f}_1\,(\sin\alpha + 2\sin\beta) + \frac{1}{3}\,\tilde{f}_2\,(\sin(\alpha+2\beta) + \sin(2\beta)) \\ & + \tilde{f}_3\sin(\alpha+2\beta) + \frac{1}{3}\,b_Q\,\theta^2\left(\cos^2\alpha + 2\cos^2\beta\right). \end{aligned} \tag{5.169}$$

Solution presents nearly commensurate structure when $(2\beta + \alpha) \approx 2\pi$. Such a structure can be recognised as the Sm C^*_{FI1} phase with the three-layer basic unit (Fig. 5.28f). The unit is polar and the dielectric permittivity tensor for this unit is biaxial. The small incommensurability $\delta_3 = 2\pi - \alpha - 2\beta$ results in the helix formation, thus the phase is optically active. The complete structure is given by two different angles α_3, δ_3 thus $2\beta = 2\pi - \alpha_3 - \delta_3$. It is stable for small negative $\tilde{a}_1$ and significant quadrupolar coupling b_Q, although stability limits cannot be given as a simple algebraic expression.

We can search also for more complex solutions but it seems that presented ones, Sm C^*, Sm C^*_A, Sm C^*_α, Sm C^*_{FI2} and Sm C^*_{FI1}, can consistently explain macroscopic properties of all stable phases in antiferroelectric liquid crystals.

Phase transitions between tilted phases. Whenever symmetries of subphases are different the second or first order phase transition is possible. In studied systems, in a broad range of parameter values, the phase transitions between subphases are of first order with discontinues change of the basic structural unit. The phase transition between the Sm C^*_α and the Sm C^* phases that are of the same symmetry should be of first order [23]. This is observed indeed in the system with strong chiral interactions. However, as the enantiomeric purity is lowered the Sm $C^*_\alpha \leftrightarrow$ Sm C^* transition line on temperature-concentration phase diagram, might end up in a critical end point and above critical concentration the continuous evolution between both structures takes place.

The magnitude of the tilt θ. Finally, we also discuss, how the interlayer interactions influence the magnitude of the tilt θ. In the free energy (5.164) the main tilt dependence is hidden in the first two terms that resume intralayer steric and attractive van der Waals interactions. It has been shown that in some antiferroelectric liquid crystals also sixth order terms in tilt are necessary to describe the proper, continuous temperature dependence of the tilt. Here we will restrict the analysis to the fourth order terms and will give hints how to address the problem of discontinuous orthogonal-tilted phase transition. An assumption of the constant tilt in all smectic layers satisfy symmetry

considerations in all phases except of the three-layer Sm C^*_{FI1} phase. However, also in this phase the Ansatz can be treated as a good approximation as long as we can expect that effective parameters that give interlayer interactions are small in comparison with the value of $(T - T_0)$. Since the Sm C^*_{FI1} phase appears at lower temperatures, the approximation is reasonable.

The procedure to find the magnitude of the tilt is similar for all structures, therefore let us use as an example the analysis of the structure of the Sm C^*_α phase. To the free energy (5.167), the intralayer part

$$\frac{1}{2}\,\tilde{a}_0\,\theta^2 + \frac{1}{4}\,b\,\theta^4\,, \tag{5.170}$$

where

$$\tilde{a}_0 = (T - T_0) - \frac{c_p^2}{b_0}\left[1 + \frac{1}{2}\left(\frac{b_1}{b_2}\right)^2\right] - \frac{1}{4}\frac{\mu^2}{b_0}\left[1 + \frac{1}{4}\left(\frac{b_1}{b_2}\right)^2 + \frac{1}{2}\left(\frac{b_2}{b_0}\right)\right] \tag{5.171}$$

is added. In order to find the magnitude of the tilt for given model parameters, the free energy is minimized with respect to the magnitude of the tilt θ. The solution is

$$\theta^2 = -\frac{A(\alpha_1)}{B(\alpha_1)}\,, \tag{5.172}$$

where

$$A(\alpha_1) = a_0(T) + \tilde{a}_{10}\cos(\alpha_1) + \sum_{i=2}^{4}\tilde{a}_i\ \cos(i\ \alpha_1) + \sum_{i=1}^{3}\tilde{f}_i\ \sin(i\ \alpha_1) \tag{5.173a}$$

$$B(\alpha_1) = b + \tilde{a}_{11}\cos\alpha_1 + 2\ b_Q.\cos^2(\alpha_1)\,. \tag{5.173b}$$

It is clearly seen from (5.172) that also interlayer interaction influence the magnitude of the tilt especially in the temperature region where $\tilde{a}_0 < \tilde{a}_i$ or $\tilde{f}_i$. So, within the temperature region close to the transition temperature to the tilted phase, which is defined by the magnitudes of the interlayer effective parameters, the search for a stable solution have to take into account the influences on the magnitude of the tilt. We insert $\theta^2(T, \alpha)$ into the free energy (5.166) and obtain

$$F = -\frac{1}{4}\frac{A(\alpha_1)^2}{B(\alpha_1)} \tag{5.174}$$

and minimize the expression with respect to the phase difference α_1 in the region where θ^2 given by (5.172) is positive. When α_1 is found, the tilt θ is also known from (5.172).

Using the same procedure also the structure of the Sm C^*_{FI2} can be found providing that the average values over two layers of interlayer contributions

are used. The free energy have to be minimized with respect to two phase differences α_2 and δ_2. On the other hand, in the three-layer structure of the Sm C^*_{FI1} phase, tilt thus P_s should not be equal in all layers. However, when studying the structure far from the transition temperature to the tilted phase, the assumption of constant tilt is reasonable. But exact structure can be obtained only by simultaneous minimization of the free energy with respect to two phase differences and two magnitudes of the tilt.

If in the intralayer part of the free energy (5.170) the sixth order term, $c\theta^6$, is important i.e. the phase transition to the tilted phase can be of the first or second order with tilt depending as $\sim (T - T_c)^{1/4}$ than θ^2 is found as a solution of the minimization of the free energy

$$A(\alpha_1) + B(\alpha_1)\theta^2 + c\,\theta^4 = 0\,. \tag{5.175}$$

The continuation of the procedure is the same as before, only calculation of the stable solution becomes more complicated and in some cases additional metastable solutions appear.

5.4.3 Experiment

In order to verify the proposed model, its predictions have to be compared with experimental results. Below we will discuss the evidences for the structures and properties of the intermediate phases found in various materials Table 5.1 and briefly mention some techniques that have been used in these studies.

Table 5.1. Molecular structures of materials

MHPOBC

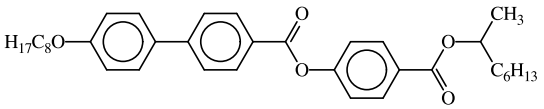

10OTBBB1M7

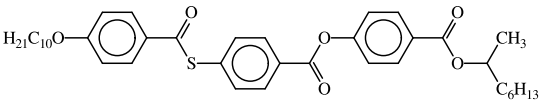

As620

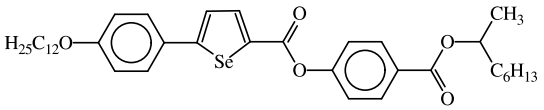

MHDOPTCOB

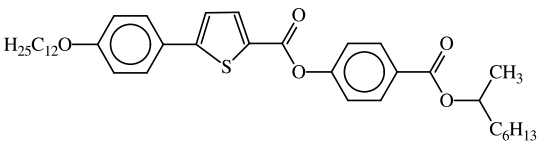

5.4.3.1 Phase transitions

The most commonly used technique for determining phase transitions is Differential Scanning Calorimetry (DSC). In this method a difference in a heat flow between a sample and a standard is measured, which both are kept at the same temperature or heated (cooled) at the same rate. Additional amount of energy (heat) is absorbed or released by a sample as the substance undergoes the phase transition with non-zero enthalpy and/or heat capacity (c_p) changes. However, this method does not allow to distinguish unambiguously between the first order transition in which both, a transition enthalpy and heat capacity changes, are observed and the second order transition with zero transition enthalpy change. In order to obtain reliable data about the order of the phase transition and critical behavior of heat capacity changes, an AC calorimetry method should be applied [24]. In this method the sample is exposed to a small oscillating heat input. The resulting amplitude of the sample temperature oscillations enables obtaining c_p data, while the phase difference between the input and output signals enables determining the phase transition order.

By careful adjusting of measurement conditions, e.g. scanning rate and the sample weight, up to five phase transitions could be observed by DSC in the narrow temperature region between SmA and Sm C^*_A phases (Fig. 5.29).

The enthalpy changes at these phase transitions are usually about $0.01\,\mathrm{Jg}^{-1}$. More detailed data about the nature of the phase transitions were obtained in

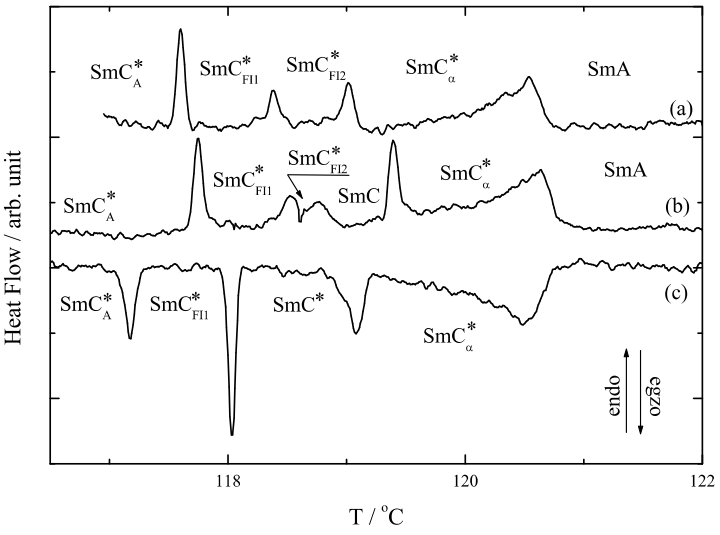

Fig. 5.29. DSC scans ($1\,\mathrm{Kmin}^{-1}$) for MHPOBC mixtures: (**a**) heating of pure S-MHPOBC, (**b**) heating of mixture with 1.5% of R-enantiomer, (**c**) cooling of mixture with 1.5% of R-enantiomer. Note, that for pure enantiomer the ferroelectric Sm C^* is not observed – see paragraph about the phase diagram

the ac-calorimetry studies. The most thorough measurements were performed for the MHPOBC system, as a function of chiral purity [25]. In this system the phase transition between orthogonal SmA phase and the Sm C^*_α phase, in the whole concentration range in which the Sm C^*_α exists, is of the second order with pronounced heat capacity anomalies. All transitions between the tilted phases are of the first order.

5.4.3.2 Structure and properties

Magnitude of tilt. The tilt magnitude in the polar smectics is usually measured by determining the angle difference between extinction directions in an homogeneously oriented (planar) sample placed between crossed polarisers and exposed to an electric field with reversing polarity. This method gives accurate values of the tilt only far from the orthogonal-tilted phase transition. Near the phase transition the tilt order parameter becomes more susceptible, and the external electric field, due to the tilt-polarisation coupling can induce deviation from the thermodynamic equilibrium tilt value. Moreover, this method also implies that the phase during the measurement is switched into the synclinic state, so the actual structure of more complex phases is destroyed.

The other method of the tilt angle studies is based on the birefringence measurements. At first order approximation, the difference between birefringence of the orthogonal SmA phase and tilted phase is proportional to the squared magnitude of the tilt angle [26]. However, this approximation is valid only if the length of the optical helix assures the uniaxial optical properties of the phase. The method allows obtaining the high resolution information about the tilt magnitude of the non-perturbated phase structure, as birefringence measurements do not require sample switching.

As the transition from the orthogonal SmA phase to the tilted phase is usually of the second order, the tilt angle increases continuously from zero with decreasing temperature as $(T - T_0)^\beta$. The critical exponent β describing the tilt changes may vary for different materials, moreover it can change for a given sample with temperature. The second order Sm A-Sm C^*_α phase transition with temperature crossover of the exponent has been confirmed for MHPOBC (Fig. 5.30) and MHPOCBC materials [26]. Close to the SmA-Sm C^*_α phase transition the critical exponent is nearly 0.5, further it changes to ~ 0.25. A small discontinuous change of tilt of $\sim 1^\circ$ at SmC^*_α-Sm C^* in MHPOBC and $\sim 0.2^\circ$ at Sm C^*_α-SmC_A in MHPOCBC was observed.

Basic structural unit. The basic period of the electron density modulation along the smectic layer normal can be detected by conventional X-ray diffraction. If the phase additionally has the uniplanar or close to uniplanar periodic structure of few syclinic and anticlinic layers, besides diffraction related to the layer thickness, additional signals should be recorded, as the electron density at synclinic and anticlinic boundaries is not identical [27]. These signals should weaken as the difference between boundaries diminish, and finally

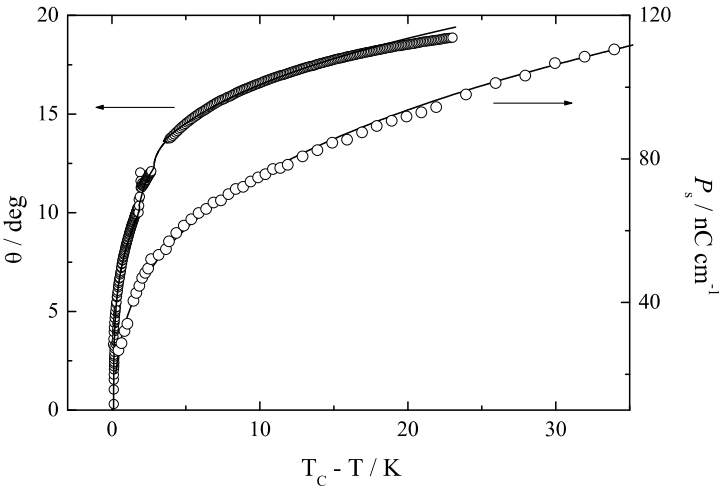

Fig. 5.30. Magnitude of tilt angle and value of Ps vs. temperature for mixture of S-MHPOBC with $\sim$ 2% of R-enantiomer. The tilt variation, taken from [26], was determined from the birefringence measurements

should disappear for the clock-like structure. On the other hand, if the short periodic structures are helical or strongly distorted from uniplanar, the resonant X-ray method is useful. This method is limited only to the materials having an edge of an absorption band at the wavelength of used X-ray beam. The method tests orientational ordering of molecules, because the diffracted intensity depends on the orientation of an asymmetric bonds around the resonant atoms relative to the polarization of the incident X-ray beam [28].

The resonant X-ray method was used for structure studies of three compounds 10OTBBB1M7, As620 and MHDDOPTCOB [16, 29, 30] exhibiting intermediate phases. It has been deduced that periods of short wavelength modulations are: one layer in the Sm C* phase, two layers in the Sm C$^*_A$ phase, three layers in the Sm C$^*_{FI1}$ phase, four layers in the Sm C$^*_{FI2}$ phase and five or more layers in the Sm C$^*_\alpha$ phase. It is commonly believed that the modulation periods in the Sm C$^*_{FI2}$ and Sm C$^*_{FI1}$ phases are universal, but that of the Sm C$^*_\alpha$ phase varies depending on material and moreover, it changes with temperature. Among intermediate phases only the Sm C$^*_\alpha$ phase has the clock structure. Both phases, Sm C$^*_{FI2}$ and Sm C$^*_{FI1}$, have distorted clock structures. The position and the polarisation of the observed resonant X-ray signals excluded the uniplanar structure.

Helical structure. In all Sm C* subphases there is a long wavelength modulation of tilt direction along the layer normal. The period p of the helical structure varies usually from 10^{-7} to 10^{-5} m. Depending on its value different methods are used to determine it. If the pitch length is comparable to the light wavelength, for homeotropically oriented samples selective reflection is

observed [31]. The selective reflection can be easily measured by spectroscopic methods in the visible and near IR range. Apart from the half-pitch band observed in all helical phases, for the phases with the polar basic structural unit (Sm C*, Sm C$^*_{FI1}$), the full pitch band is additionally observed [6, 22]. When the modulation period is in the micron range, it can be estimated from the periodicity of line defects, so-called dechiralization lines, that are formed in thick planar cells in order to meet the conditions of the unwound structure at the glass surfaces and helical structure in the sample bulk [32]. The defects periodicity could be measured by laser diffraction or by direct microscopic observations. The periodicity of the lines should be related to full pitch length in case of phases with polar basic unit, and to half of the pitch when the unit cell is non-polar (Sm C$^*_A$ or Sm C$^*_{FI2}$) [33].

The sign of the helical structure can be determined observing the sign of the optical activity. If the pitch is longer than the wavelength of the measuring light, the sense of the helical twisting and optical rotatory power is the same [31].

The helix pitch length in Sm C$^*_{FI1}$ and Sm C$^*_{FI2}$ phases is usually in the micron range and generally it is longer that in the Sm C* and Sm C$^*_A$ phases. For instance for MHPOBC the pitch is ~ 630 nm in the Sm C$^*_A$ and $\sim 4.5\,\mu$m in the Sm C$^*_{FI2}$ phase. In 10OTBBB1M7 strong temperature dependence of the optical pitch within the Sm C$^*_{FI2}$ temperature range was observed, the helix unwinds and reverses its twist [34, 35]. The pitch length in the Sm C$^*_{FI1}$ phase was estimated to be also in the micron range, however precise measurement could not be performed. The system of line defects gives only weak light diffraction and moreover it is frequently observed that the periodicity of the lines varies substantially from sample to sample [36]. It suggests some dynamic behavior that is strongly influenced by surface interactions, thus most probably the periodicity of the dechiralization lines is not in a simple relation with the helix pitch length [34].

In all materials exhibiting synclinic and anticlinic structures, the helix twist sense in the Sm C* phase is opposite to that in the Sm C$^*_A$ phase. Moreover, helix handedness reverses between Sm C$^*_{FI1}$ and Sm C$^*_{FI2}$ phases [37].

Spontaneous electric polarisation. The value of spontaneous electric polarisation $\boldsymbol{P}_s$ can be measured by two methods, from hysteresis loop or switching current. In the first method a potential difference on the capacitor connected to the sample is recorded vs. applied electric field. This allows to determine a surface charge that flows during the polarisation reversal, thus value of $\boldsymbol{P}_s$. In the latter method a current is plotted vs. time as the sample is switched, and the $\boldsymbol{P}_s$ is determined by the integration of observed peaks. The methods imply that during the measurement, the sample is switched between synclinic states. The actual structure of more complex phases is destroyed and therefore the flexoelectric part of the spontaneous polarisation related to the spatial variation of tilt direction is lost. Only the piezoelectric part of the electric polarisation in the smectic layer $\boldsymbol{P}_j$ is measured.

Due to bilinear coupling between tilt and polarisation, in the first approximation, the magnitude of $\boldsymbol{P}_s$ should follow the temperature variation of tilt angle. Indeed, it increases critically from zero, (Fig. 5.30), however, the critical exponents for tilt and $\boldsymbol{P}_s$ temperature dependence are usually different. In materials forming antiferroelectric phases the value of spontaneous polarisation is rather high, and reaches a few hundreds nC cm^{-2}. No discontinuities are observed for P_s at phase transitions between SmC subphases.

Dielectric response. Dielectric spectroscopy allows measurment of the frequency dependent complex dielectric permittivity of liquid crystalline materials. This method provides information about movements of molecules that change the electric polarisation of the sample. In most cases it is possible to distinguish between phases with polar and non-polar structures. The studied material is usually placed into a cell built of two glass sheets with ITO electrodes. For high frequency studies cells with gold electrodes are used for their higher electric conductivity. The capacity c and the resistance R of the sample, measured as a function of applied electric field frequency with impedance analyser, allow to determine the real and imaginary part of the dielectric constant: $\epsilon' = \frac{c}{c_0}$, $\epsilon'' = \frac{1}{R\omega c_0}$, where c_0 is the capacity of an empty cell. The dielectric dispersion data are usually analysed by the Cole–Cole formula [38]: $\epsilon^* - \epsilon_\infty = \sum_m \frac{\Delta\epsilon_m}{1+(if/f_{rm})^{(1-\alpha_m)}} - i\frac{\sigma}{2\pi\epsilon_0 f}$ where $\Delta\epsilon_m$, f_{rm} and α_m are the dielectric strengths, relaxation frequencies and distribution parameters of the different active modes, labelled by m. For a single Debye type relaxation parameter $\alpha_m = 0$ indicating a well-defined relaxation time. In case of more complex relaxation behavior of a system also Davidson-Cole [39] or Havriliak-Negami [40] equations are used. The last term in the Cole-Cole equation accounts for ionic conductivity, σ, of the sample. However, presence of mobile ionic impurities in the sample, besides lowering the sample resistance can also be the origin of additional low frequency modes, through the formation of charged layers at the electrodes [42].

The phase transition from the orthogonal to the tilted phase is signified by the appearance of fluctuations of the tilt. The dielectric mode due to the fluctuations of the tilt magnitude (*soft mode*) is present in both phases (Figs. 5.31 , 5.32). In the Sm C* or Sm C$^*_\alpha$ phase it coexists with much stronger mode due to fluctuations of the tilt direction, that deform the phase helielectric structure (*Goldstone-like mode*) [41]. In the Sm C* phase the Goldstone mode frequency is lower and its strength higher the longer the pitch is [43] and the higher the spontaneous polarisation. The dielectric response depends also on the cell thickness [44].

Interpretation of relaxation processes in the intermediate phases is still ambiguous. It seems that in the Sm C$^*_\alpha$ phase the main contribution to dielectric response is due to the distortion of its helical structure [45]. The mode is observed at frequency $\sim 10^5$–10^6 Hz, much higher than the Goldstone mode in the ferroelectric SmC* phase.

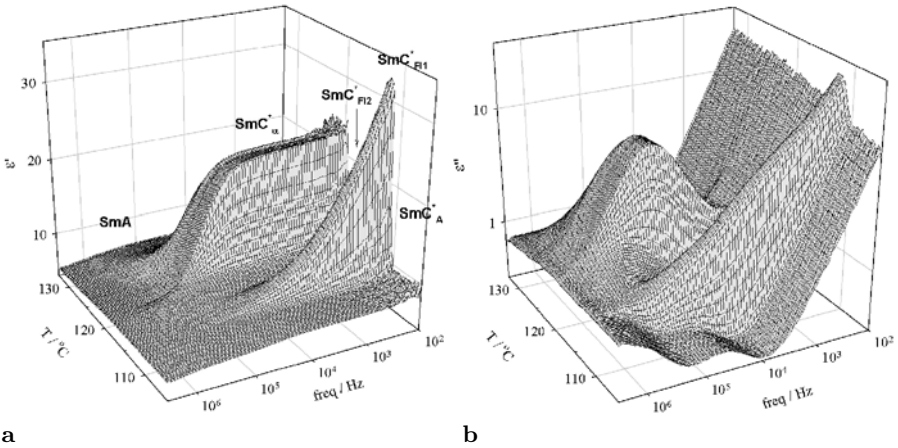

Fig. 5.31. Temperature-frequency dependence of real and imaginary parts of complex dielectric permittivity for 10OTBBB1M7 compound. Note, that a logarithmic scale was used in the figure with an imaginary part to make weak modes well visible

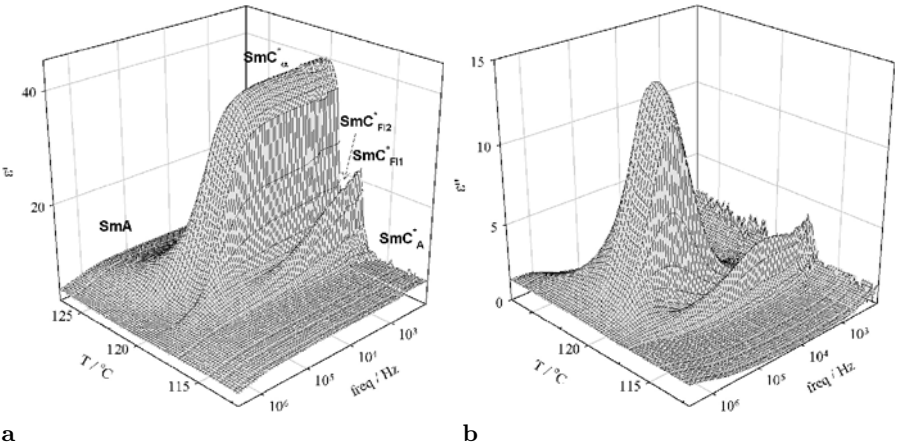

Fig. 5.32. Temperature-frequency dependence of real and imaginary parts of complex dielectric permittivity for optically pure S-MHPOBC compound

In phases that have compensated spontaneous electric polarisation in their basic structural unit, SmC^*_A and SmC^*_{FI2}, dielectrically active modes are weak [45]. Their dielectric strength ($\Delta\varepsilon \sim 1$–5) is orders of magnitude lower and the relaxation frequency higher than observed in the ferroelectric phase. Three or two modes have been found in the SmC^*_A and SmC^*_{FI2} phases in the frequency range up to 10^9 Hz, which is accessible in standard dielectric measurements [45, 46]. The highest frequency mode, observed above 10^8 Hz, changes continuously through all tilted phases, Sm A and isotropic phase, thus it originates in non-collective motions of molecules, most probably rota-

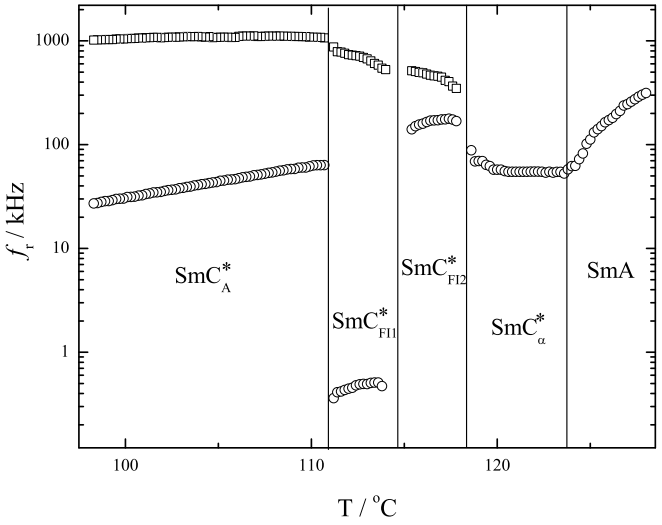

Fig. 5.33. Relaxation frequency of collective modes obtained from fitting the complex dielectric permittivity in 10OTBBB1M7 compound to Cole-Cole formula

tion around one of the main molecular axis. The other modes have relaxation frequencies usually in the range of 10^4–10^6 Hz (Fig. 5.33). The higher frequency mode is believed to be polar due to the antiphase azimuthal motions of molecules in neighboring layers, fluctuations that distort the basic unit. The lower frequency relaxation process, is commonly interpreted as *helical (phason) mode* – the mode due to the distortion of the helix. This mode could be dielectrically active because of tiny non-compensated polarisation resulting from non-commensurability of the tilt structure with the 2- or 4-layer basic unit structure. Also molecular rotations around the long molecular axis have been suggested for the origin of this process [47].

It is believed that in the SmC^*_{FI1} phase dominating dielectric mode is due to the helix distortion (ferrielectric Goldstone mode). The phase has a polar basic structural unit, thus it is observed that the dielectric response in SmC^*_{FI1} phase is much stronger than in the SmC^*_A and SmC^*_{FI2} phases, however usually weaker than in SmC^* phase. The analysis with Cole-Cole formula shows that the mode relaxation frequency is in the range 100 Hz–1 kHz, but with very broad distribution of relaxation frequencies – the distribution parameter α_m is typically about 0.3–0.5. This might suggest the presence of other fluctuations in the same frequency window. It was speculated that due to the interactions with surfaces, domains with opposite orientations of the three layer basic structural units are formed, with defect walls separating them. In each domain $\boldsymbol{P}_s$ is nearly uniform. For such structures the dielectrically active relaxation process could be movement of boundaries between domains. The related mode should be observed at low frequency as it requires the reorien-

tation of molecules only in some smectic layers, thus it needs low activation energy. Probably in the Sm C^*_{FI1} phase the movement of the domain walls and ferrielectric helical modes coexist in the same frequency window, and can not be separated. It is commonly observed that applying a relatively weak bias electric field in the Sm C^*_{FI1} phase increases the dielectric mode strength and moves the mode to higher frequency. This might be because weak bias field stabilises large domains in which the helical mode takes over. Under higher bias field the mode is quenched resulting in a non-monotonic dependence of $\Delta\varepsilon$ on applied dc voltage [48]. In the Sm C^*_{FI1} phase there is also present the mode at higher frequency, that is probably due to the distortion of the basic structural units, similarly as in antiferroelectric phases.

Birefringence. Precise measurements of phase birefringence were performed using transmission ellipsometry method [49]. In this method the light propagates through the sample usually at oblique (45°) incidence, and phase difference δ and amplitude ratio ϕ between the *p*-component of light polarisation, that is in the plane of incidence, and *s*-component that is normal to the plane of incidence, are measured. Alternatively, conoscopic observation [50] has been applied. In conoscopy the light from the point source propagates through the thick homeotropically oriented sample, and the pattern due the interference between extraordinary and ordinary rays is observed.

Because of the helical structure, the smectic C subphases are uniaxial despite the biaxility of the dielectric permittivity tensor for their basic structural units. In order to avoid the spatial averaging effects, film samples of thickness much below the length of the helical pitch have to be used in ellipsometry. In conoscopy the electric field is applied to unwind the helical structure.

Ellipsometry confirmed that the Sm C^*_α phase has clock structure with helical pitch up to ten layers [51, 52]. Additionally, both methods, ellipsometry [53] and conoscopy [4], undoubtfully proved that the Sm C^*_{FI1} and Sm C^*_{FI2} phases have biaxial structural units. Basing on the ellipsometry results the distortion angles α_2 and α_3, describing the basic structural unit, have been analysed. For the Sm C^*_{FI1} $\alpha_3 = 56°$ in MHPBC has been given. For Sm C^*_{FI2} $\alpha_2 = 7°$ in MHPBC and $\alpha_2 = 18°$ in MHDD6PTCOB have been found. However, these results could have large errors. The birefringence of the thin film is strongly affected by the surface layers, that are synclinic or anticlinic, thus different than the sample bulk. It has been proved that the anticlinic surface layers exist also in the Sm C^*_α temperature range, leading to weak birefringence of the free standing films drawn in this phase [51]. Moreover the magnitude of the tilt can differ in surface and bulk layers [54].

In order to diminish the influence of surfaces, thick free-standing film samples should be studied, but with unwound helix e.g. materials showing spontaneous helix twist inversion have to be used. The only known compound showing this phenomenon, within the temperature range of the Sm C^*_{FI2} phase, is 10OTBBB1M7. Around the inversion temperature the strongly birefringent, schlieren texture with numerous disclination lines is observed for the surface free sample proving directly the biaxiality of the phase (Fig. 5.34).

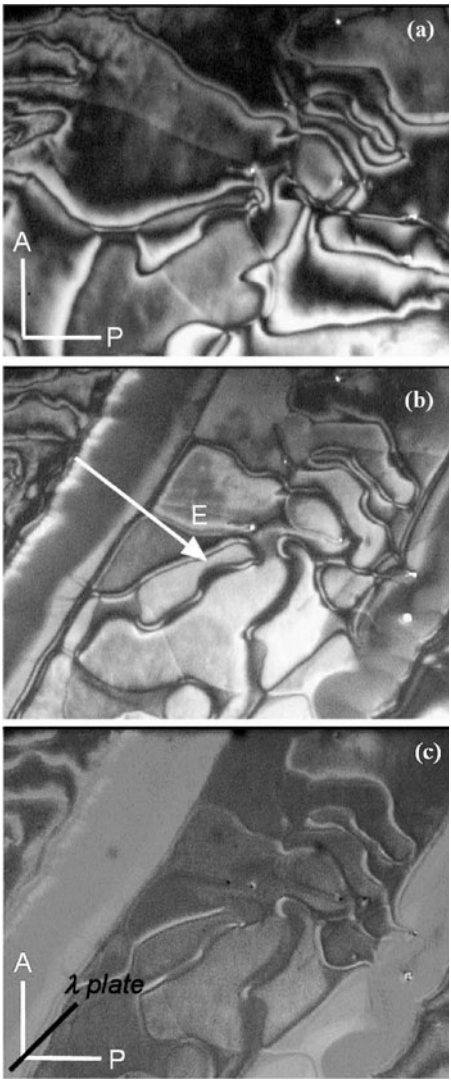

Fig. 5.34. (**a**) Schlieren texture of the Sm C^*_{FI2} phase in freely suspended ~ 10 μm thick film at the helix inversion temperature observed between crossed polarizers (P, A). (**b**) Electric field E is applied within the film plane. The boundary between region with π walls and region with 2π walls, is clearly seen between crossed polarizers. (**c**) The λ plate is inserted into the optical pathway between the sample and analyser. Inserting of λ plate increases/decreases birefringence, thus shifts the interference colours to the blue/red, if the long axis of optical indicatrix of the liquid crystal and λ plate are parallel/perpendicular. Dielectrically switched regions where the long axis of optical indicatrix (the average tilt plane) is parallel to the field, are blue. Ferroelectrically switched regions where the tilt plane is perpendicular to the field, are red

If electric field is applied in the smectic plane, dielectric switching is observed, that evidences compensated $\boldsymbol{P}_s$ within the unit cell. As the field strength increases above the threshold value E_c, the layer coupling is broken and ferroelectric switching is observed.

Optical rotatory power. In order to measure ORP the homeotropically oriented sample is placed between crossed polarisers with the layers perpendicular to the incident light beam. The input polarisation given by polariser is rotated in the sample and the magnitude of the rotation is controlled by the analyser, which is turned to obtain a minimum of transmitted light intensity. The angle of analyser rotation divided by sample thickness gives the ORP value.

According to the de Vries formula [55] the optical rotatory power depends on the helix pitch length p and anisotropy ϵ of the dielectric permittivity tensor for the basic structural unit, along the direction perpendicular to the layer normal ORP $\sim (2\pi/p)\ (\epsilon/\epsilon_o)^2\ (8\lambda^2\ (1-\lambda^2))^{-1}$ where $\lambda = \lambda_0/np$; λ_0, ϵ_o and n being wavelength of the light, the mean dielectric permittivity and the mean refractive index, respectively. The simple geometrical calculations, in which the dielectric tensors of each layer in the crystallographic unit cell are summed up and normalised for the value of one layer, show that effective ϵ for Sm C^*_{FI2} phase is $\epsilon_{FI2} = \epsilon_{is}(2\cos^2(\alpha_2/2) - 1)$ and for the Sm C^*_{FI1} phase is $\epsilon_{FI1} = \frac{1}{3}\epsilon_{is}(4\cos^2(\alpha_3/2) - 1)$, where $\epsilon_{is} = (\epsilon_2 - \epsilon_1) + (\epsilon_3 - \epsilon_2)\sin^2\theta$ is the dielectric anisotropy of the uniplanar structure, ϵ_i are the components of the dielectric tensor of a single, θ tilted, smectic layer. The ϵ_{is} is a good approximation of dielectric anisotropy in SmC^* and SmC^*_A phases. The ORP, and thus the dielectric anisotropy is always negligible in Sm C^*_α phase due to its clock structure. The other intermediate phases have non-zero optical activity (Fig. 5.35) [35].

Comparing ORP for the phases with uniplanar structure (Sm C^* and Sm C^*_A) and phases with distorted structure (Sm C^*_{FI1} and Sm C^*_{FI2}), knowing the helical pitch p and tilt θ temperature dependence, distortion angles α_2 and α_3 can be obtained. The angles were estimated [34] for 10OTBBB1M7 to be: $\alpha_3 \approx 46^\circ$ in the Sm C^*_{FI1} and $\alpha_2 \approx 26^\circ$ in Sm C^*_{FI2} phase. The upper limit for the deviation from uniplanar geometry in Sm C^*_{FI2}, $\alpha_2 \approx 40^\circ$ is obtained, if we assume that the tilt does not change between Sm C^*_A and Sm C^*_{FI2}.

If a similar analysis is applied for MHPOBC the distortion $\alpha_3 \approx 42^\circ$ is obtained in Sm C^*_{FI1}. In Sm C^*_{FI2}, the maximal distortion (when assuming that tilt is the same as in the Sm C^*_A phase) is $\alpha_2 \approx 62^\circ$. Including the small changes in the tilt provides $\alpha_2 \approx 48^\circ$. As a comparison, the value obtained by Akizuki et al. [56] for the Sm C^*_{FI2} phase of MHPBC, based on optical activity simulations using the 4×4 matrix method, was $\alpha_2 \approx 50^\circ$.

It should be mentioned that accuracy of distortion angles determination by ORP method is greatly limited by the pitch length and tilt angle measurements. An advantage of the method is that since thick free suspended film samples are studied, the influence of surface structures is minimized.

5.4.3.3 General phase diagram for the antiferroelectric system

The phase diagrams for various mixtures of compounds that showed intermediate phases, have been studied [2, 57]. However, surprisingly rarely the phase diagrams in which R and S forms of the same compound, thus system in which only the chiral part of interactions is changed, are reported. Here we present results acquired for MHPOBC compound, a prototype antiferroelectric material. For high optical purity compounds, the sequence of tilted phases Sm $C^*_\alpha \leftrightarrow$ Sm $C^*_\beta \leftrightarrow$ Sm $C^*_\gamma \leftrightarrow$Sm C^*_A was reported with decreasing temperature. The smectic Sm C^*_γ phase is the same as Sm C^*_{FI1}, while the majority of authors accept that the Sm C^*_β phase is a ferroelectric Sm C^* phase. However, there are some reports that this phase has antiferroelectric properties [58]. As recently shown, the controversy arises due to the slightly different optical purity of investigated materials [59]. In extremely high optical purity samples of S-MHPOBC enantiomer four tilted Sm C phases appear, but dielectric spectroscopy measurements clearly exclude the presence of the ferroelectric Sm C^* phase (Fig. 5.32). No Goldstone mode that is inherent to the Sm C^* phase was detected. In the Sm C^*_β phase only weak mode at high frequency (~ 350 kHz) is present, typical for the phase with an antiferroelectric order. Thus it was concluded that the Sm C^*_β phase is the Sm C^*_{FI2} phase. For samples with a slightly lower optical purity five SmC subphases could be identified below the Sm A phase (Fig. 5.36). An additional phase appears between the Sm C^*_α and Sm C^*_{FI2} phases. The dielectric permittivity in this phase is an order of magnitude higher than in all other phases, thus typical for the ferroelectric Sm C^* phase. As the optical purity decreases fur-

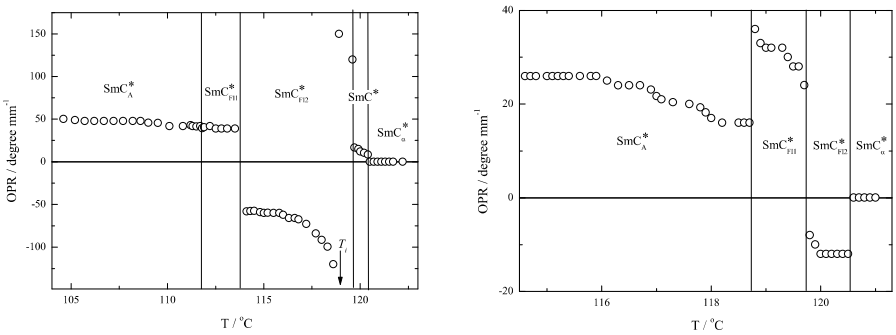

a **b**

Fig. 5.35. Optical rotatory power measured with red light ($\lambda = 632$ nm) for (**a**) 10OTBBB1M7 compound, T_i is the helix twist inversion temperature. Note that the phase sequence is diffrent than observed in e.g. dielectric measuremets. This compound has metastable Sm C^* phase that is observed in freshly prepared samples and disappears if the sample is kept at elevated temperature [34]. In the Sm C^* phase $pn < \lambda$, thus the sign of the ORP is opposite to the helix twist sense. In other phases the sign of the ORP follows the helix twist sense. (**b**) MHPOBC compounds

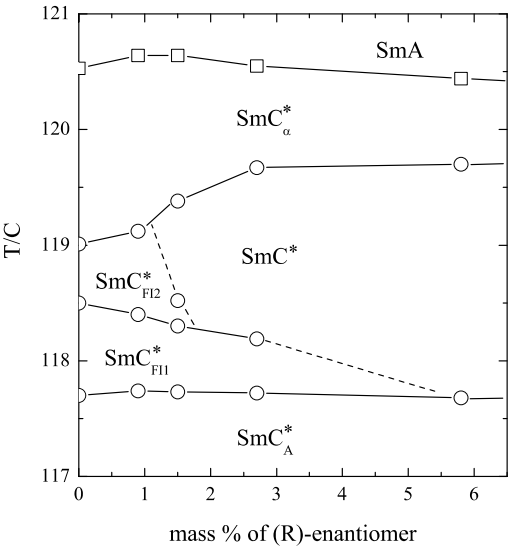

Fig. 5.36. Temperature-optical purity phase diagram for the MHPOBC system

ther, Sm C^*_{FI2} phase disappears and in the concentration range $\sim$ 1.5–6% of R-MHPOBC the phase sequence Sm $C^*_\alpha \leftrightarrow$ Sm $C^* \leftrightarrow$ Sm $C^*_{FI1} \leftrightarrow$Sm C^*_A is observed, that is the phase sequence incorrectly reported in the literature for the pure enantiomeric MHPOBC compound [6]. In mixtures with a concentration of R-MHPOBC higher than 6% the Sm C^*_{FI1} phase is also missing. As the optical purity is further reduced (above $\sim$ 25% concentration of R enantiomer) the Sm C^*_α phase disappears, and direct Sm A$\leftrightarrow$ Sm C^* phase transition is observed. In racemic mixtures only synclinic and anticlinic structures are stable.

The temperature-optical purity phase diagram observed for the MHPOBC system seems to be rather general. However, some variations were observed, e.g. for TFMHPOCBC in pure enantiomer direct Sm A $\leftrightarrow$ Sm C^*_A phase transition is observed while the Sm C^*_α phase is induced as the optical purity decreases [60].

5.4.4 Comparison of theoretical results and experimental observations

Within the presented model, assuming typical values of parameters it is possible to account for the observed temperature sequence and properties of Sm C subphases. As examples, two systems: 10OTBBB1M7 and MHPOBC were analysed, as for these materials most complete sets of experimental data were acquired. We show that for chosen model parameters, upon lowering the temperature, the phase sequence Sm A $\leftrightarrow$ Sm $C^*_\alpha \leftrightarrow$ Sm $C^*_{FI2} \leftrightarrow$ Sm $C^*_{FI1} \leftrightarrow$ Sm C^*_A, is predicted, the same that has been

observed experimentally for both enantiomerically pure compounds. In addition, the same set of model parameters accounts for more detailed phase properties, e.g. helical pitch of a few layers in the Sm C^*_α phase and the distortion angles α_2 and α_3 about 40° in the Sm C^*_{FI2} and the Sm C^*_{FI1} phases. The model allowed also for the correct temperature behavior of the helical structure including helix twist reversal within the temperature range of the Sm C^*_{FI2} phase, as well as the change of helix handedness at the transition from the Sm C^*_{FI2} to the Sm C^*_{FI1} phase. We also show that for the obtained structures the simulated dielectric response was in qualitative agreement with experiment.

We assumed that θ^2 is proportional to $(T-T_c)$, T_c being the transition temperature to the tilted phase, thus temperature affects interlayer interactions by influencing the achiral NN interactions $a_1 = a_{10} + a_{11}\theta^2$ and NN quadrupolar interactions $\tilde{b}_Q = b_Q\theta^2$. The other six parameters $b_0, b_1, b_2, f_1, c_p, \mu$, thus corresponding interactions, are temperature independent. The approximate values of some parameters could be deduced from the experimental data. Parameter b_0 gives intralayer interactions and its order of magnitude can be estimated from the difference of the transition temperatures between the synclinic Sm C^* and the anticlinic Sm C^*_A phase in enantiomeric and racemic samples. We assumed the value of 2 K. Next, parameters $b_1$and b_2 are strongly influenced by the positional correlations which decrease exponentially, therefore we estimated $b_0/b_1 = 5$ and $b_0/b_2 = 100$. The parameter f_1, which gives the chiral part of van der Waals NN interactions is presumably small and therefore taken as zero. For the rest of parameters we assumed the order of magnitude of a degree Kelvin. Precise values used for the analysis for the two compounds 10OTBBB1M7 and MHPOBC are given in the Table 5.2.

The temperature range for the stability of each phase was obtained by comparison of the minimal free energies for various structures. The temperature dependence of the phase difference α_1 and distortion angles α_2 and α_3 found for 10OTBBB1M7 are shown in Fig. 5.37. The direction of the tilt vector in consecutive layers is twisted in a unique sense for both four-layer and three-layer basic structural units (Fig. 5.37), and the sign of the twist is determined exclusively by the chiral NN interactions. The incommensurability of the structure, that defines the long wavelength helix, for the three low temperature phases Sm C^*_{FI2}, Sm C^*_{FI1} and Sm C^*_A is given by δ (Fig. 5.37, below). The angle δ, thus the length of the pitch, is influenced not only by NN but

Table 5.2. Model parameters used in the theoretical modelling

	$a_{10} + a_{11}(T - T_c)$	μ	c_p	b_Q
MHPOBC	$-4.1 - 2.3(T - T_c)$	0.77	0.6	$0.25(T - T_c)$
10OTBBB1M7	$-4.0 - 0.6(T - T_c)$	2.1	1.2	$0.3(T - T_c)$

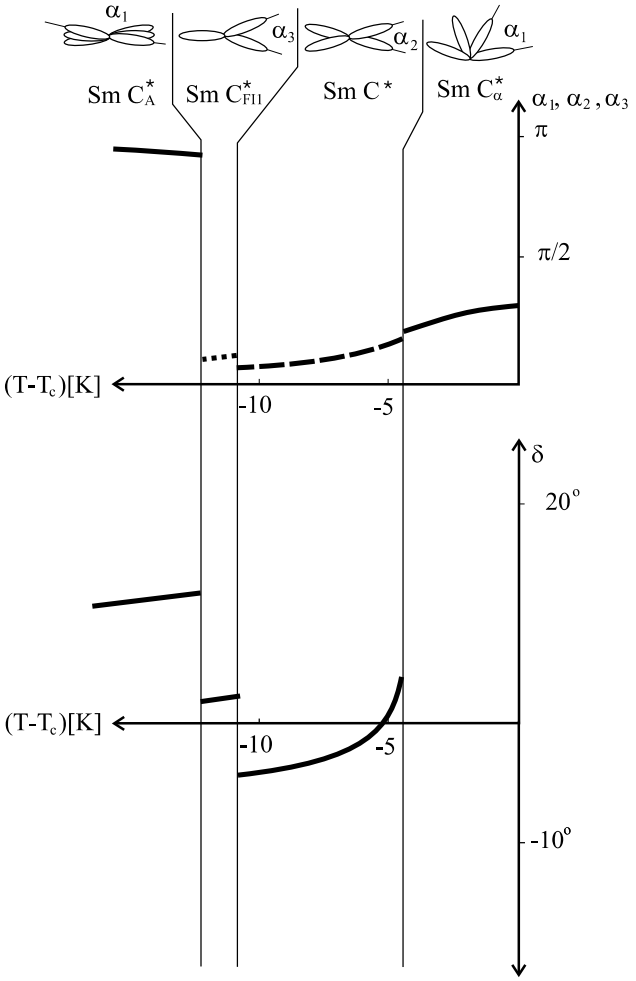

Fig. 5.37. *Above*: the phase difference in dependence of the temperature for a clock structure (α_1) - solid line, for the four-layer distorted clock structure (α_2)- dashed line and for the three layer distorted clock structure (α_3)- dotted line. Temperature stability regions obtained by the free energy minimization are marked as well as schematic structures of corresponding phases. Model parameters are given in Table 5.2. *Below*: corresponding temperature dependence of the deviation from commensurate structures, δ, obtained by the free energy minimization. The sign of δ defines also the handedness of the helix

also by chiral interactions to more distant layers. The strength of these interactions is affected by temperature dependence of quadrupolar interactions [**?**], and their competition may lead to infinite pitch at certain temperatures in the Sm C^*_{FI2} phase.

Analysing the dielectric response of the system, the fluctuations that change electric polarisation have to be found. The polar fluctuations are tested by applying a small electric field, which deforms the stable structure. Only small changes of the structure are expected thus the order parameters can be written as

$$\begin{aligned}\boldsymbol{\xi}_j &= \boldsymbol{\xi}_{j,0} + \delta\boldsymbol{\xi}_{j,||} + \delta\boldsymbol{\xi}_{j,\perp} \\ \boldsymbol{\eta}_j &= \boldsymbol{\eta}_{j,0} + \delta\boldsymbol{\eta}_{j,||} + \delta\boldsymbol{\eta}_{j,\perp}\end{aligned} \tag{5.176}$$

Here $\boldsymbol{\xi}_{j,0}$ and $\boldsymbol{\eta}_{j,0}$ are the equilibrium order parameters in the j-th layer in the absence of the external field. Variations in magnitudes of both order parameters due to the external electric field are given by $\delta\boldsymbol{\xi}_{j,||}, \delta\boldsymbol{\eta}_{j,||}$ and variation of their directions in respect to the direction of the electric filed are given by $\delta\boldsymbol{\xi}_{j,\perp}, \delta\boldsymbol{\eta}_{j,\perp}$. To find the dielectric response of the system, which is due to the coupling between the external electric field at frequency ω and the layer polarisation, a term $-\sum_j P_0 \boldsymbol{E}\cdot\boldsymbol{\eta}_j$ is added to the free energy. The phase and the magnitude changes of order parameters are expressed as a linear combination of plane waves with the wave vector k in the helicoidal coordinate system:

$$\begin{aligned}\delta\xi_{j,||} &= \sum_k \delta\xi_{k,||} \exp\{ikdj + i\omega t\}, \quad \delta\xi_{j,\perp} = \sum_k \delta\xi_{k,\perp} \exp\{ikdj + i\omega t\} \\ \delta\eta_{j,||} &= \sum_k \delta\eta_{k,||} \exp\{ikdj + i\omega t\}, \quad \delta\eta_{j,\perp} = \sum_k \delta\eta_{k,\perp} \exp\{ikdj + i\omega t\}\end{aligned}$$

The free energy then splits into two parts: the equilibrium free energy in the absence of the external electric field (G_0) and the part containing the variation in the free energy due to the external field (δG). The variation δG consists of the elastic (G_{el}) and electric (G_E) contributions. The elastic deviation can be expressed as

$$G_{el} = \frac{1}{2}\sum_k \left(\delta\xi_{i,-k,||}, \delta\xi_{i,-k,\perp}, \delta\eta_{i,-k,||}, \delta\eta_{i,-k,\perp}\right) \underline{G_2}(k) \begin{pmatrix} \delta\xi_{i,k,||} \\ \delta\xi_{i,k,\perp} \\ \delta\eta_{i,k,||} \\ \delta\eta_{i,k,\perp} \end{pmatrix}. \tag{5.177}$$

The $\underline{G_2}(k)$ gives a dynamical matrix which is a 4×4 matrix for the phases with clock structure Sm C*, Sm C$^*_A$ and Sm C$^*_\alpha$. In the more complex Sm C$^*_{FI2}$ and Sm C$^*_{FI1}$ phases, the basic periodicity of phase differences has to be considered. Therefore in the Sm C$^*_{FI2}$ phase the 8×8 matrix, while in the Sm C$^*_{FI1}$ 12×12 matrix has to be analysed. The matrix elements give the contributions of intralayer and interlayer interactions when small deviations are induced via the external electric field. To find the dielectric response, the Landau-Khalatnikov equations have to be solved including the time dependent external field. The detailed procedure for determining the frequency and the dielectric strength of modes can be found in [61]. The modes, in

some phases, can be related to the simple molecular motions. It has been found, as expected, that the *tilt amplitudon mode* related to the changes of the amplitude of the molecular tilt is strong only in a narrow temperature range, close to the transition from the SmA phase. In the Sm C^* phase the strongest mode is the *phason (Goldstone) mode* due to the deformation of the helix. In the Sm C^*_α phase the dielectric response has similar origin, it is *phason mode* due to the deformation of the short helically modulated structure. However, for the set of parameters given in Table 5.2, in the Sm C^*_α phase, in the same frequency window also *polarisation mode* exists. This is the mode related to the fluctuations in which the polarisation in the smectic layer is changed without changing the tilt direction or magnitude. The fluctuations are due to the collective movements of the molecules in which the distribution of dipole moments is changed without changing the average tilt of molecules. In the Sm C^*_A phase the lowest energy mode is *phason mode*, the mode is due to the fluctuations that deform the helix but only weakly distort the two layer basic structural units. The *polarization mode* is also present, its strength is comparable but frequency is higher than that of the *phason mode*. At still higher frequency the *structural unit distortion mode* appears. For more complex phases, generally the modes can not be related to simple molecular movements. However, it seems that also in Sm C^*_{FI2} and Sm C^*_{FI1} phases the dielectrically active are these modes that are mainly due to the helix distortion and changes of polarization in the smectic layers, thus *phason-like* and *polarisation-like modes*. As the unit cell Sm C^*_{FI1} has higher non-compensated $\boldsymbol{P}_s$ the dielectric response due to the *phason mode* in this phase is much stronger than in Sm C^*_{FI2} phase. *The structural unit distortion modes* could be observed at high frequencies.

Generally, in the system with one layer basic structural unit, the number of modes coincide with the number of degrees of freedom (the magnitude and the phase of both tilt and polarisation vectors). In systems with a more complex basic unit, the number of modes is multiplied with the number of layers forming the basic unit. Therefore, in the Sm C^*_{FI2} phase 16, while in Sm C^*_{FI1} phase 12, modes should be present, respectively, but some of them can be degenerated. At present it is difficult to tell which of these modes has the lowest frequency.

The advantage of the presented model is that it can also account for the influence of the enantiomeric excess on the phase diagram. In the racemic mixture the synclinic NN interactions given by the negative $\tilde{a}_1$ are stronger than anticlinic NNN interactions (positive $\tilde{a}_2$), and the synclinic Sm C phase appears directly below the Sm A phase. Upon decreasing temperature, $\tilde{a}_1$ increases and changes sign at a temperature where quadrupolar interactions ($\tilde{b}_Q$) are already significant. Since quadrupolar interactions favor both synclinic and anticlinic tilts in NN layers, intermediate phases are not formed and direct transition from the Sm C phase to the Sm C_A phases is obtained. As the enantiomeric excess in the sample increases, the temperature where the $\tilde{a}_1$ changes sign, increases. Therefore the influence of quadrupolar interac-

tions is weaker and cannot prevent the appearance of the modulated phases. Directly below the Sm A phase, the parameter $\tilde{a}_1$ becomes comparable, by its absolute value, to the parameter $\tilde{a}_2$ [**?**] and the Sm C^*_α phase is formed. Upon decreasing temperature it evolves into the Sm C^* phase due to increasing quadrupolar interactions. In the temperature region where $\tilde{a}_1 \approx 0$ the structure with two interchanging phase differences α and β, i.e. Sm C^*_{FI2} is formed. Decreasing the temperature further, the parameter $\tilde{a}_1$ becomes positive and thus simultaneously with the $\tilde{a}_3$ parameter encourages the structure where tilts in third neighboring layers are synclinic. This structure corresponds to the Sm C^*_{FI1} phase. With optical purification the temperature range of modulated phases increases. In enatiomerically pure samples the temperature range of the intermediate phases are sufficiently broad to prevent appearance of the Sm C^* phase. The direct phase transition between the Sm C^*_α phase and the Sm C^*_{FI2} phase is observed.

5.4.5 Conclusions

The origin and the structure of the intermediate Sm C phases have been widely discussed over the last decade. Recent results obtained with few complementary techniques show that the phases have structures modulated over few smectic layers, the Sm C^*_α phase has the clock-like, while the Sm C^*_{FI2} and the Sm C^*_{FI1} phases have distorted clock-like structures. The presented model accounts for the Sm C subphases due to the presence of chiral and achiral NN and NNN interactions as well as quadrupolar interlayer interactions. In systems in which the NN and NNN interactions are competing and quadrupolar order is weak the Sm C^*_α phase appears while the growing strength of quadrupolar ordering leads to Sm C^*_{FI2} and Sm C^*_{FI1} phases. The distorted clock-like structure of the later phases is due to the chiral NN interactions, that include not only relatively weak direct van der Waals, but also combined piezoelectric and flexoelectric interactions. As some interactions strongly depend on enantiomeric excess the presented model reproduces the experimental temperature–optical purity phase diagram.

References

1. R. G. Petschek and K. M. Wiefling: Phys. Rev. Lett. **59**, 343 (1987)
2. A. Fukuda, Y. Takanishi, T. Isozaki, K. Ishikawa and H. Takezoe: J. Mater. Chem. **4**, 997 (1994)
3. D. Kardas, J. Mieczkowski, D. Pociecha, J. Szydlowska, E. Gorecka: J. Mater. Chem. **11**, 741 (2001)
4. E. Gorecka, D. Pociecha, M. Glogarova, J. Mieczkowski: Phys. Rev. Lett. **5**, 2946 (1998)
5. E. Gorecka, D. Pociecha, E. Araoka, D. Link, M. Nakata, J. Thisayukta, Y. Takanishi, K. Ishikawa, J. Watanabe, H. Takezoe: Phys. Rev. E **62**, R4524 (2000)

6. A. D. L. Chandani, E. Gorecka, Y. Ouchi, H. Takezoe, and A. Fukuda: Jpn. J. Appl. Phys., Part 2 **28**, L1265 (1989)
7. E. Gorecka, A. D. L. Chandani, Y. Ouchi, H. Takezoe, and A. Fukuda: Jpn. J. Appl. Phys., Part 1 **29**, 131 (1990)
8. V. L. Indebom, S. A. Pikin, E. B. Loginov: Sov. Phys. Crystallogr. **21**, 632 (1976); S. A. Pikin, V. L. Indebom: Ferroelectrics **20** 151 (1978)
9. R. Blinc, B. Žekš: Phys. Rev. A **18**, 740 (1978)
10. B. Žekš: Mol. Cryst. Liq. Cryst. **114**, 259 (1984)
11. H. Orihara, Y. Ishibashi: Jpn. J. Appl. Phys. **30**, L1819 (1990)
12. B. Žekš, M. Čepič: Liq. Cryst. **14**, 445 (1993)
13. V. L. Lorman, A. A. Bulbitch, P. Toledano: Phys. Rev. E **49**, 1367 (1994)
14. H. Sun, H. Orihara, Y. Ishibashi: J. Phys. Soc. J. **62**, 2706 (1993)
15. M. Čepič, B. Žekš: Mol. Cryst. Liq. Cryst. **63**, 61 (1995)
16. P. Mach, R. Pindak, A. M. Levelut, P. Barois, H. T. Nguyen, C. C. Huang, and L. Furenlid: Phys. Rev. Lett. **81**, 1015 (1998); P. Mach, R. Pindak, A. M. Levelut, P. Barois, H. T. Nguyen, H. Baltes, M. Hird, K. Toyne, A. Seed, J. W. Goodby, C. C. Huang, and L. Furenlid: Phys. Rev. E **60**, 6793 (1999)
17. D. J. Photinos and E. T. Samulski: Science **270**, 783 (1995); P. K. Karahalious, A. G. Vanakaras and D. J. Photinos: Phys. Rev. E **65**, 031712 (2002)
18. R. Bruinsma, J. Prost: J. Phys. II France **4**, 1209 (1994)
19. D. Pociecha, E. Gorecka, M. Čepič, N. Vaupotič, B. Žekš, D. Kardas and J. Mieczkowski: Phys. Rev. Lett. **86**, 3048 (2001)
20. M. Čepič, B. Žekš: Phys. Rev. Lett. **87**, 5501 (2001)
21. B. Žekš, M. Čepič: Sect. 5.1 in this volume
22. I. Muševič, R. Blinc, B. Žekš: *The Physics of Ferroelectric and Antiferroelectric Liquid Crystals* (World Scientific, Singapore 2000)
23. P. M. Chaikin and T. C. Lubensky: *Principles of condensed matter physics* (Cambridge University Press, Cambridge 1995)
24. C. W. Garland: Termochim. Acta **88**, 127 (1985)
25. K. Ema, M. Kanai, H. Yao, Y. Takanishi and H. Takezoe: Phys. Rev. E **61**, 1585 (2000)
26. M. Škarabot, M. Čepič, B. Žekš, R. Blinc, G. Heppke, A. V. Kityk, and I. Muševič: Phys. Rev. E **58**, 575 (1998)
27. Private communication from Y. Takanishi. Three layer and two layer periodicuty was observed in X-ray synchrotron diffraction experiment for SmC_{FI1} and SmC_{FI2} phases, respectively
28. A. M. Levelut and B. Pansu: Phys. Rev. E **60**, 6803 (1999)
29. L. S. Matkin, H. F. Gleeson, P. Mach, C. C. Huang, R. Pindak, G. Srajer, J. Pollmann, J. W. Goodby, M. Hird, and A. Seed: Appl. Phys. Lett. **76**, 1863 (2000)
30. A. Cady, J. A. Pitney, R. Pindak, L. S. Matkin, S. J. Watson, H. F. Gleeson, P. Cluzeau, P. Barois, A.-M. Levelut, W. Caliebe, J. W. Goodby, M. Hird, and C. C. Huang: Phys. Rev. E **64**, 050702 (2001)
31. P. G. de Gennes and J. Prost: *The Physics of Liquid Crystals* (Oxford University Press, Oxford 1993)
32. M. Glogarova, J. Fousek, L. Lejcek, J. Pavel: Ferroelectrics **58**, 161 (1984)
33. K. Miyachi, Y. Takanishi, K. Ishikawa, H. Takezoe and A. Fukuda: Ferroelectrics **149**, 61 (1993)
34. M. Čepič, E. Gorecka, D. Pociecha, B. Žekš, H. T. Nguyen: J. Chem. Phys. **117**, 1817 (2002)

35. I. Musevic and M. Skarabot, Phys. Rev. E **64**, 051706 (2001)
36. K. Miyachi, M. Kabe, K. Ishikawa, H. Takezoe, A. Fukuda: Ferroelectrics **147**, 147 (1994)
37. F. Beaubois, J. P. Marcerou, H. T. Nguyen and J. C. Rouillo: Eur. Phys. J. **3**, 273 (2000)
38. K. S. Cole and R. H. Cole: J. Chem. Phys. **9**, 341 (1941); K. S. Cole and R. H. Cole: J. Chem. Phys. **10**, 98 (1942)
39. D. W. Davidson and R. H. Cole: J. Chem. Phys. **18**, 1417 (1951); D. W. Davidson and R. H. Cole: J. Chem. Phys. **19**, 1484 (1951)
40. S. J. Havriliak: *Dielectric and Mechanical Relaxation in Materials* (Hanser, Munich 1997)
41. A. Levstik, T. Carlsson, C. Filipič, I. Levstik and B. Žekš: Phys. Rev. A **35**, 3527 (1987)
42. K. W. Wigner: Archiv. Elektrotechnik **2**, 371 (1914)
43. J. Szydlowska, D. Pociecha, J. Matraszek, J. Mieckowski: Liq. Cryst. **26**, 1787 (1999)
44. M. Glogarova et al.: Sect. 5.3 in this volume
45. Yu.P. Panarin, O. Kalinovskaya and J. K. Vij: Liq. Cryst. **25**, 241, (1998)
46. S. Merino, M. R. de la Fuente, Y. Gonzalez, M. A. Perez Jubindo, B. Ros, and J. A. Puertolas: Phys. Rev. E **54**, 5169 (1996); Yu.P. Panarin, O. Kalinovskaya, J. K. Vij and J. W. Goodby: Phys. Rev. E **55**, 4245 (1997); M. Čepič, G. Heppke, J. M. Hollidt, D. Loetzsch and B. Žekš: Ferroelectrics **147**, 43 (1993); M. Glogarova, H. Sverenyuk, H. T. Nguyen and C. Destrade: Ferroelectrics **147**, 159 (1993)
47. H. S. Urban, A. Würflinger: Sect. 4.2 in this volume
48. J. Hou, J. Schacht, F. Giesselmann and P. Zugenmaier: Liq. Cryst. **22**, 409 (1997)
49. S. Heinekamp, R. A. Pelcovits, E. Fontes, E. Y. Chen, R. Pindak, and R. B. Meyer: Phys. Rev. Lett. **52**, 1017 (1984)
50. T. Fujikawa, K. Hiraoka, T. Isozaki, K. Kajikawa, H. Takezoe and A. Fukuda: Jap. J. Appl. Phys. **32**, 186, (1993)
51. D. A. Olson, S. Pankratz, P. M. Johnson, A. Cady, H. T. Nguyen, and C. C. Huang: Phys. Rev. E **63**, 061711 (2001)
52. Ch. Bahr, D. Fliegner, C. J. Booth, J. W. Goodby: Phys. Rev. **51**, R3823 (1995); B. Rovšek, M. Čepič, B. Žekš: Phys. Rev. **54**, R3113 (1996)
53. P. M. Johnson, D. A. Olson, S. Pankratz, T. Nguyen, J. Goodby, M. Hird, and C. C. Huang: Phys. Rev. Lett. **84**, 4870 (2000)
54. B. Rovšek, M. Čepič, B. Žekš: Mol. Cryst. Liq. Cryst. **328**, 997 (1997)
55. H. P. de Vries: Acta Crystallographica **4**, 219 (1951)
56. T. Akizuki, K. Miyachi, Y. Takanishi, K. Ishikawa, H. Takezoe and A. Fukuda: Jpn. J. Appl. Phys. **38**, 4832 (1999)
57. Y. Takanishi and H. Takezoe: in *Chirality in Liquid Crystals* ed. H. S. Kitzerow, C. Bahr (Springer Verlag 2001)
58. J. F. Li, E. A. Shack, Y. K. Yu, X. Y. Wang, C. Rosenblatt, M. E. Neubert, S. S. Keast and H. Gleeson: Jap. J. Appl. Phys. 2 **35**, L1608 (1996); T. Sako, Y. Kimura, R. Hoyakawa, N. Okabe, Y. Suuki: Jap. J. Appl. Phys. **235**, L114 (1996); A. Jakli: J. Appl. Phys. **85**, 1101 (1999)
59. E. Gorecka, D. Pociecha, M. Čepič, B. Žekš and R. Dabrowski: Phys. Rev. E. **65**, 061703 (2002)

60. S. Inui, T. Suzuki, N. Iimura, H. Iwane and H. Nohira: Ferroelectrics **148**, 79 (1993)
61. N. Vaupotič, M. Čepič, B. Žekš: Ferroelectrics, **245**, 175 (2000)

5.5 Dielectric study of collective and molecular dynamics in glass-forming chiral low-molecular-weight liquid crystals

M. R. de la Fuente, M. A. Pérez Jubindo, B. Ros, and J. L. Serrano

5.5.1 Introduction

A glass can be defined as an amorphous solid that possesses no long-range order but only a short-range order comparable to that of a liquid. However, for those systems that undergo a glass transition upon cooling from a liquid crystalline state, there is a higher-order degree, different depending on the mesophase that is undercooled. Low-molar-mass glass-forming liquid crystals have emerged as a class of materials with considerable technological interest due to their potential applications in the field of information storage [1]; the information can be transferred to a mesophase at temperatures above the glass transition temperature, T_g, and can be stored in the glassy state for a long time. Among them, those with a SmC* phase capable of being vitrified are the most interesting due to the non-centrosymmetry (possibility of non-linear optical phenomena) and ferroelectricity of this phase [2–5].

Very few structural requirements have been clearly proposed for the formation of a glassy state for low-molecular-weight liquid crystals [6, 7]. Nevertheless, compounds with bulky structures have provided most of the examples of mesomorphic glassy phases reported so far. Unfortunately, these structural characteristics cause a loss in mesomorphism due to the lowering of the length-to-breadth ratio. Thus, a suitable balance between these factors must be reached in order to obtain a glassy liquid crystal phase. The compounds reported here represent further examples of how wider structures and polar substituents favor glassy state transitions. Such structures increase both the free volume and the polar molecular interactions responsible for the formation of these phases.

In this work we deal with three compounds belonging to different series. They formed part of a deep study related to the molecular structures that promote antiferroelectricity [5]. The aim of these studies was to use the naphthalene unit as an alternative to the biphenyl core and to incorporate an ester group directly linked to the stereogenic center. However, some of the synthesized compounds do not show antiferroelectric or ferrielectric behavior but have the peculiarity of showing glassy mesophases. Compound **1** (Table 5.3) has a glassy SmC* phase. The analogous compound but with the common

Table 5.3. Phase transition sequence

Compound		Phasetransitiontemperature
1	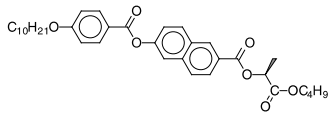	I 65.9°C N* 65.3°C SmA 35°C SmC* -31.2°C glass
2	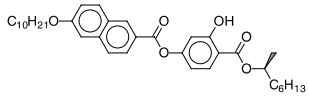	I 29°C SmA -43°C glass
3	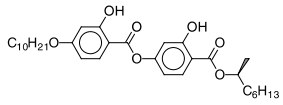	I -25°C N* -40. 5°C glass

chiral terminal chain derived from 2-octanol [8] show ferro, ferri and antiferroelectric mesophases but no glass transition [5, 8]. The two other compounds that will be presented in this work have the naphthalene group and/or lateral –OH substituent, compounds **2** and **3**, being a SmA and a N* phase, respectively, that vitrifies.

These compounds were previously characterized by DSC and optical microscopy [5]. Here we only present the dielectric studies.

Broadband dielectric spectroscopy is a very useful technique to analyze the freezing-in-process of motions related to the vitrification, above all in liquid crystals, where many collective and molecular reorientational processes are dielectrically active: rotation around long and short molecular axes, precession around director (see Sect. 4.1 in this book) and, in ferroelectric mesophases, Goldstone mode and soft mode (see Sect. 5.3 in this book). Our study reveals that some of these modes are affected by the glass transition. The temperature dependence of their frequencies follows the Vogel–Fulcher–Tammann law (VFT). This law was first introduced as an empirical law followed by the viscosity, the dielectric relaxation frequencies, etc., in polymers and glass-forming liquids [9]. However, it is also followed by some molecular relaxations in glass-forming low-molecular-mass liquid crystals [10, 11]. For one of our studied compounds, this is the case not only of the molecular modes related to rotations around the long and short axes but also of the collective Goldstone mode.

5.5.2 Experimental

The synthetic pathways followed to obtain these compounds together with DSC studies can be found in [5].

The complex dielectric permittivity, $\varepsilon(\omega)$, was measured over 11 decades of frequency (10^{-2}–10^{9} Hz) using three different measuring systems: a frequency

response analyzer (Schlumberger 1260) equipped with a high-impedance preamplifier of variable gain (Novocontrol dielectric interface) and two impedance analyzers, the HP 4191A and the HP 4192A. The cell consisted of two gold-plated brass electrodes (diameter 5 mm) separated by 50 µm thick silica spacers. We did not treat the electrodes and the samples were misaligned but mostly planar. For compound **1** we also measured the tilt angle, θ, and the spontaneous polarization, P_S, in the ferroelectric SmC* phase (for these measurements we used commercially available cells purchased from Linkam). P_S was measured using the triangular wave method, which also allowed us to determine the rotational viscosity of the C-director, γ_C [12].

5.5.3 Results and discussion

In general several processes contribute to the complex dielectric permittivity. One of the major difficulties in the analysis of the dielectric relaxation spectra of liquid crystals is the fact that the different relaxation modes often occur closely spaced in the frequency domain, so the dielectric loss peaks appear partially superposed. To know the amplitudes, frequencies and activation energies of every process, the experimental data were fitted in each phase to:

$$\varepsilon(\omega) = \sum_k \Delta\varepsilon_k(\omega) + \varepsilon_\infty - i\sigma_{dc}/\omega\varepsilon_0 \tag{5.178}$$

where $\Delta\varepsilon_k(\omega)$ accounts for the contribution of each mode, σ_{dc} for the dc conductivity, and ε_∞ for the high frequency permittivity. For $\Delta\varepsilon_k(\omega)$ we used the Havriliak–Negami (H-N) function:

$$\Delta\varepsilon_k(\omega) = \frac{\Delta\varepsilon_k}{(1 + (i\omega\tau)^\alpha)^\beta} \tag{5.179}$$

where $\Delta\varepsilon_k$ is the dielectric amplitude, τ the relaxation time and α, β control the shape of the relaxation. $\alpha = \beta = 1$ is the Debye function; $\beta = 1\,, 0 < \alpha \leq 1$ is the Cole–Cole function; $\alpha = 1\,,\ 0 < \beta \leq 1$ is the Cole–Davidson function. In general all these parameters are temperature dependent.

From the fitted parameters, τ, α and β, the relaxation frequencies, f_k, were calculated as:

$$f_k = \frac{1}{2\pi\tau}\left[\tan\left(\frac{\pi}{2(\beta+1)}\right)\right]^{1/\alpha} \tag{5.180}$$

Now, let us present the results for each compound. We will start with compound **1**.

We studied the optically pure compound and the racemic mixture. For this latter case the helical structure of the tilted smectic mesophase and the modes associated to the ferroelectricity are suppressed allowing a better study of the molecular modes.

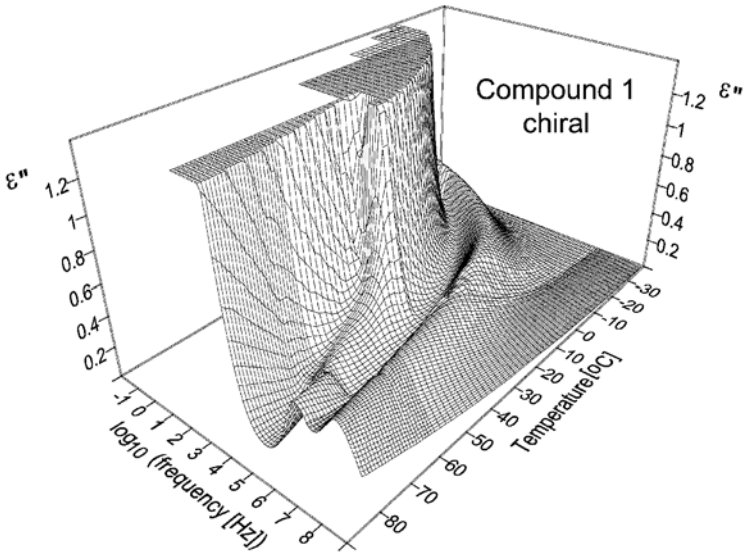

Fig. 5.38. Three-dimensional plot of the dielectric losses vs. temperature and frequency for compound **1** (optically pure). (Reproduced from [4]. Copyright 1997 Taylor&Francis)

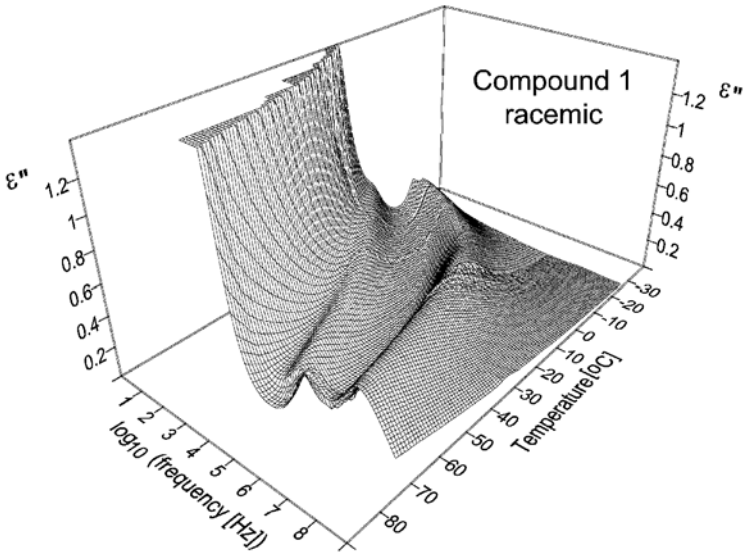

Fig. 5.39. Three-dimensional plot of the dielectric losses vs. temperature and frequency for compound **1** (racemic mixture). (Reproduced from [4]. Copyright 1997 Taylor&Francis)

Figures 5.38 and 5.39 are three-dimensional plots of the losses, ε'', versus temperature and frequency (10^2–10^9 Hz), for the chiral compound and the racemic mixture, respectively. In the I and N* (N) phases they exhibit two different relaxation processes, which are clearly seen as two maxima in $\varepsilon''(\omega)$ for each temperature. The high frequency process is mainly related to the rotation around the molecular long axis (hereafter called mode t, where t means transverse dipole moment) and the low frequency one to the rotation around the molecular short axis (hereafter called mode l, where l means longitudinal dipole moment). In the SmA phase also two peaks were found, but a more detailed study shows that in the chiral compound, the peak with the lower frequency is a superposition of two different processes, the soft mode (collective amplitude fluctuations of the tilt angle) and mode l. The behavior in the SmC phase of the racemic mixture is as in the SmA phase. For the chiral compound the low frequency side is dominated by the Goldstone mode (azimuthal fluctuations of the director around layer normal) whose amplitude hides both, mode l and soft mode. A dc bias field in general can suppress the Goldstone mode but for this compound the available voltage (10 V for the Solartrom Schlumberger or 35 V for the Hewlett–Packard) is not enough and we could not study the soft mode in this phase.

Figures 5.40, 5.41 and 5.42 are typical plots of the complex permittivity versus the logarithm of the frequency at 46 °C (SmA phase) for the chiral compound, at 30 °C (SmC phase) for the racemic mixture and 30 °C (SmC* phase) for the chiral compound, respectively. The figures show the relaxations mentioned above. For the SmA phase: mode t, soft mode and mode l; for the SmC phase: mode t and mode l; for the SmC* phase: mode t and Goldstone

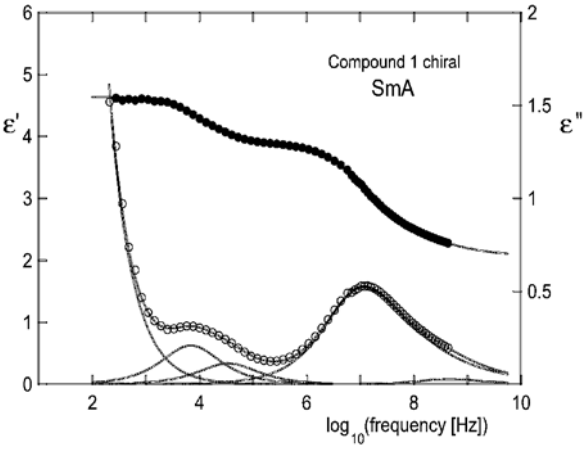

Fig. 5.40. Complex permittivity vs. frequency in the SmA phase (chiral, compound **1**): ε' (•), ε'' (○). The *solid lines* are fit curves using (5.178) and (5.179): (from high to low frequency) mode x, mode t, soft mode, mode l and conductivity contribution. (Reproduced from [4]. Copyright 1997 Taylor&Francis)

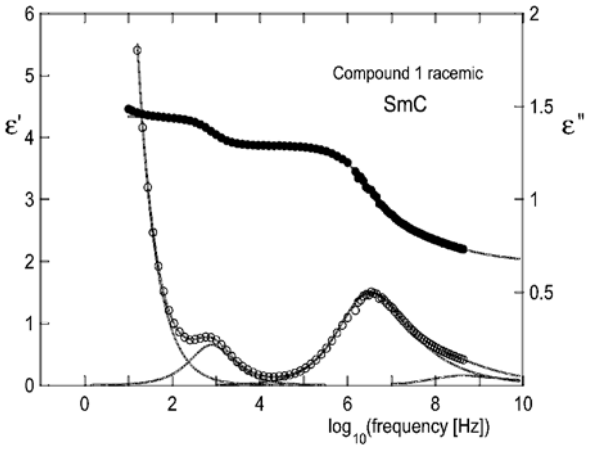

Fig. 5.41. Complex permittivity vs. frequency in the SmC phase (racemic mixture, compound **1**): ε' (•), ε'' (○). The *solid lines* are fit curves using (5.178) and (5.179): (from high to low frequency) mode x, mode t, mode l and conductivity contribution. (Reproduced from [4]. Copyright 1997 Taylor&Francis)

mode. In the three cases the solid lines are the fittings to (5.178) and (5.179). However, in the high frequency side another relaxation with very small amplitude is needed to fit the data. We will call this mode x and it might be related to some internal degree of freedom of the molecule associated with a polar group. Figure 5.43 shows the dielectric amplitude of the different modes versus temperature for the chiral compound. For the racemic mixture the behavior is similar. The squares correspond to mode l, which was determined (mainly) in the racemic mixture. Figure 5.44 shows the frequencies with the same criterion as in Fig. 5.43. The solid lines represent the fits to the Arrhenius law:

$$f_{\mathrm{k}} = f_{\infty \mathrm{k}} \exp\left(-\frac{E_a}{k_{\mathrm{B}} T}\right) \tag{5.181}$$

for mode l in the I and SmA phase and mode x, or to the VFT:

$$f_{\mathrm{k}} = f_{\infty \mathrm{k}} \exp\left(-\frac{A}{T - T_0}\right) \tag{5.182}$$

for mode l in the SmC phase and mode t and Goldstone mode in the SmC* phase. E_{a} is the activation energy, T_0 is the so-called Vogel or ideal glass transition temperature (30–50 K below the calorimetric glass transition T_{g}), and A is a constant.

Dielectric data for low-molar-mass liquid crystals are in general well described assuming the small step rotational diffusion model for the molecular dynamics (see Sect. 3.1 in this book). In this theory each molecule is assumed to act independently of its neighbors, which just contribute to a mean potential. The frequencies of the modes related to rotation around molecular short

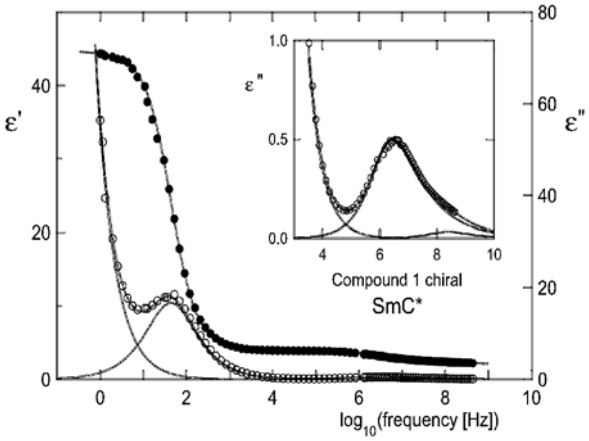

Fig. 5.42. Complex permittivity vs. frequency in the SmC* phase (chiral, compound **1**): ε' (•), ε'' (○). The *solid lines* are fit curves using (5.178) and (5.179): (from high to low frequency) mode x, mode t, Goldstone mode and conductivity contribution. The inset shows the high frequency range in an enlarged scale. (Reproduced from [4]. Copyright 1997 Taylor&Francis)

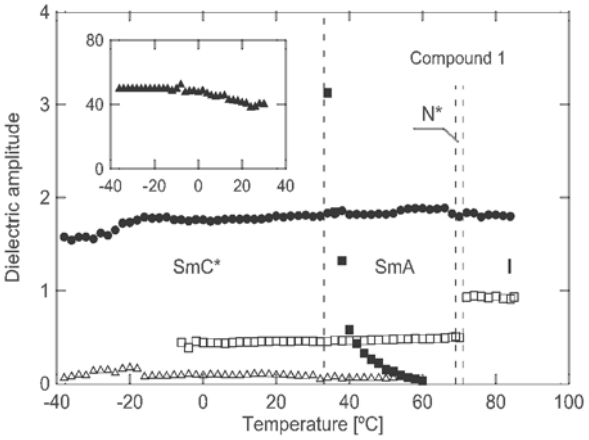

Fig. 5.43. Dielectric amplitudes of the different modes vs. temperature (compound **1**): (△) mode x, (□) mode l, (■) soft mode, (▲) Goldstone mode, (•) mode t. (Reproduced from [4]. Copyright 1997 Taylor&Francis)

and long axes, called in this work l and t, respectively, follow the Arrhenius law in each mesophase being allowed jumps at the I-N or I-Sm phase transitions due to the onset of order of the molecular director and also changes in the activation energy from one phase to other due to changes in the rotation barriers.

In our compound the relaxation frequency of mode l can be fitted to the Arrhenius law in the isotropic ($E_a = 80\,\mathrm{kJ\,mol^{-1}}$) and SmA ($E_a = 98\,\mathrm{kJ\,mol^{-1}}$) phases with a jump at the phase transition. However, the relaxation frequency of mode t does not show any jump at the phase transitions but only continuous non-Arrhenius temperature dependence, typical of molecular processes when approaching a glass transition [16]. It is hard to explain that it represents the no spatially correlated reorientation motion of one molecule (molecular motion) due to the high values of the apparent activation energy near T_g (from $29\,\mathrm{kJ\,mol^{-1}}$ in the isotropic phase to $132\,\mathrm{kJ\,mol^{-1}}$ in the SmC* phase near T_g). It should be more appropriate to discuss it in terms of cooperative regions of groups of molecules. As mentioned before, our data fit well to the VFT law (5.182), that is the most general one among those empirical laws proposed to describe the non-Arrhenius behavior in glass-forming liquids. We fit our data for the frequency of mode t using this equation covering a broad frequency and temperature range from the isotropic phase till under the calorimetric glass transition temperature (see Fig. 5.44). The values of the fit parameters are listed in Table 5.4. $T_0 = 207\,\mathrm{K}$ is 35 K below the calorimetric T_g in agreement with the predictions. Far away from T_g we should expect an Arrhenius behavior; however, and contrary to the results reported in the literature for glass-forming liquids [17], we did not find a crossover temperature T_A defined by the intersection of the Arrhenius with the VFT law. Following the kinetic approach of Adam and Gibbs [18] T_0 can be interpreted as the temperature where the cooperatively rearranging region, defined as the smallest volume element that can relax to a new configuration independently, diverges. There-

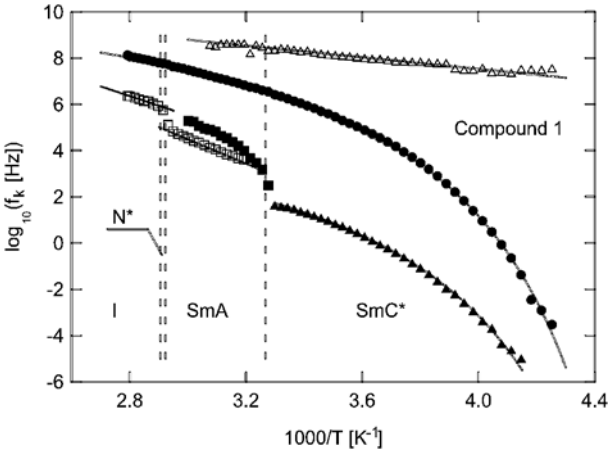

Fig. 5.44. Frequency of the different modes vs. temperature (compound **1**): (△) mode x, (□) mode l, (■) soft mode, (▲) Goldstone mode, (•) mode t. The *solid lines* are fit curves to the Arrhenius law, (5.181), for mode l in the I and SmA phase and mode x, and to the VFT law, (5.182), for mode l in the SmC phase and for mode t and Goldstone mode. (Reproduced from [4]. Copyright 1997 Taylor&Francis)

Table 5.4. Parameters of the fittings to the Vogel–Fulcher–Tammann law

N*	T_0[K]	process	f_∞[Hz]	γ_∞[Pa s]	A[K]
1	207	Rotation around molecular long axis	5.9×10^{10}		414
1	207	Goldstone mode	4.7×10^{5}		380
1	241	Goldstone mode		0.29	195
1	207	Rotation around molecular short axis	7.6×10^{7}		480
2	196	Rotation around molecular long axis	3.36×10^{10}		462
2	196	Rotation around molecular short axis	1.4×10^{9}		1107
2	196	Soft mode	2.2×10^{8}		500
3	187	Rotation around molecular long axis	1.5×10^{17}		856
3	187	Rotation around molecular short axis	1.5×10^{15}		848

*N is the number of compound

fore, we can assume that even in the range of isotropic phase measured, the rotation around the molecular long axis is in our case a cooperative process. Now let us comment the spectral shape of this mode (H-N, (5.180)) In the isotropic and N* (N) phases the α parameter increases smoothly from 0.78 to 0.81, it jumps in the SmA phase up to 0.85. This value remains in the SmC* (SmC) phase and only decreases when the temperature is close to the glass transition. The behavior of the β parameter is different. The value of this parameter decreases continuously from values around 0.77 in the isotropic phase, 0.66 in the N* phase and from 0.63 to 0.41 in the SmA phase. The same tendency is observed in the SmC* phase where this parameter reaches values around 0.31 at temperatures close to the glass transition. The β parameter shows clearly the tendency of this relaxation to become broader upon cooling towards T_g. In the literature of glass forming systems the relaxation affected by the glass transition is usually called α relaxation. The shape of this relaxation is usually described by means of the Kohlrausch-Williams-Watts (KWW) or stretched relaxation function [9]:

$$\phi(t) = \exp\left(-\left(t/\tau\right)^{\mathrm{n}}\right) \tag{5.183}$$

The n index could be related to the α, β parameters of the Havriliak-Negami functions through [19]:

$$n = (\alpha\beta)^{1/1.23} \tag{5.184}$$

On approaching the glass transition a decrease of n, related to a broadening of the relaxation, is observed. Several approaches have been proposed to account for this strong non-Debye character of the relaxation. For example Matsuoka et al. [20] assumed that this is due to co-operative rearranging regions of different size. In the case of liquid crystals the behavior is more complex because even very far from the glass transition or with no glass transition, the shape of mode t is broad, strongly non-Debye [8, 13, 14]. However it is clear that the β parameter of this mode, and then n, suffers an important decrease on approaching T_g.

The frequency of the other molecular mode, mode l, related to the rotation around the molecular short axis, also fits well to the VFT law in the SmC phase, with the same value for the Vogel temperature, T_0, as the mode t. However, the spectral shape of this mode is near-Debye in the whole studied temperature range. Note that our analysis stop at temperatures higher than in the case of mode t, due to its mixing with the dc conductivity contribution for low temperatures.

For the chiral compound not only the molecular modes were characterized but also the two collective modes related to the ferroelectric character of the SmC* phase. The soft mode, related to amplitude fluctuations of the molecular director with respect to the layer normal, was only studied in the SmA phase. As mentioned before, our low frequency experimental set-up has a limit of 10 V for the bias voltage, which is not enough to unwind the helix and quench the Goldstone mode in the SmC* phase, then it was not possible to study the soft mode in this phase. Its spectral shape is Cole–Cole ($\alpha = 0.91$). The dielectric amplitude obeys the Curie–Weiss law and the frequency decreases on approaching the SmA-SmC* phase transition, as usual for this mode. Regarding the Goldstone mode, which is related to the phase fluctuation of the helical structure, in general its frequency is practically temperature independent (see Sect. 3.2.3 in this book). However, for our compound the frequency of the maximum losses decreases from 10^2 to 10^{-2} Hz over a temperature difference of 40 K with high local activation energies growing from 96 to 154 kJ mol^{-1} upon cooling. It can also be fitted with the VFT law (see Table 5.4). We obtained the same Vogel temperature ($T_0 = 207$ K) as for the molecular modes. Its dielectric amplitude reaches a value of around 50 and the temperature dependence is as usual for this mode.

The frequencies of the modes are directly related to the viscosities. For the case of the Goldstone mode we could obtain the corresponding rotational viscosity, γ_G, through measurement of the spontaneous polarization (using the triangular wave method) and the tilt angle, θ [12]. It should be pointed out that due to the great increase of the viscosity we were not able to measure P_S below 4 °C because the signal did not saturate even with fields as strong as 80 Vμm^{-1}. The values obtained for the rotational viscosity of the C-director, γ_C, ($\gamma_G = \gamma_C / \sin^2\theta$) were above 10 Pa·s. Figure 5.45 is an Arrhenius plot of γ_G. Except in the vicinity of the transition temperature SmA-SmC*, these γ_G values fit well to the VFT law (see Table 5.4). The Vogel temperature ($T_0 = 241$ K) value coincides for this magnitude with the calorimetric glass transition temperature, T_g, although this has no precise meaning because it depends on the cooling rate. At this temperature γ_G becomes infinitely large. This result explains the strong temperature dependence of the frequency of the Goldstone mode. According to the results of the generalized model [21] the Goldstone mode relaxation frequency, f_G, can be written in terms of the P_S, θ, γ_G and the Goldstone mode dielectric strength, $\Delta\varepsilon_G$ by the relation:

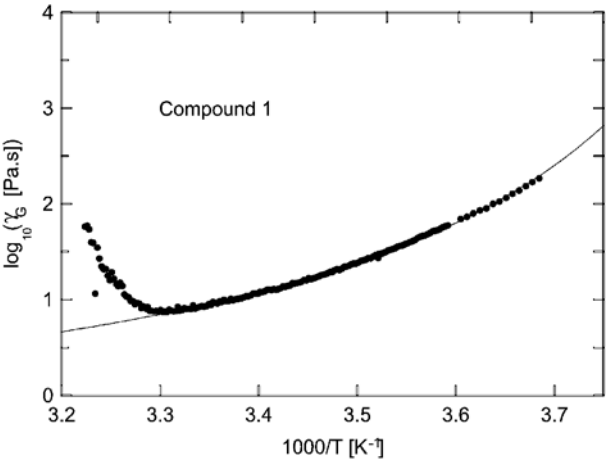

Fig. 5.45. Arrhenius plot of the Goldstone mode rotational viscosity (compound **1**). The *solid line* represents the fit curve using the VFT law. (Reproduced from [3]. Copyright 1995 The American Physical Society)

$$f_{\mathrm{G}} = \frac{P_{\mathrm{S}}^2}{4\pi\varepsilon_0\theta^2\Delta\varepsilon_{\mathrm{G}}\gamma_{\mathrm{G}}}. \tag{5.185}$$

Assuming that the ratio P_{S}/θ and $\Delta\varepsilon_{\mathrm{G}}$ are nearly temperature independent, the unusual behavior of the frequency found here will be due to the fast growth of the viscosity on cooling down towards the glass transition. However, $\Delta\varepsilon_{\mathrm{G}}$ (see Fig. 5.43) also depends on temperature, which would explain the different temperature behavior of f_{G} and $1/\gamma_{\mathrm{G}}$(T_0 is different for both magnitudes, see Table 5.4).

Now we briefly describe the results with the two other compounds.

Figure 5.46 is a three-dimensional plot of the dielectric losses versus temperature and frequency (10^2–10^6 Hz) for compound **2**. In the isotropic phase two relaxation processes were observed: mode t and mode l. Figure 5.47 is a typical plot of the complex permittivity versus the logarithm of the frequency at 18 °C in the SmA phase. There three clear peaks are observed. The frequencies are plotted in Fig. 5.48 versus temperature. We assume that the one with the lowest frequency corresponds to l mode, showing the typical behavior predicted by the rotational diffusion theory at the I–N or I–Sm phase transition: a jump of the frequency due to the onset of order for the molecular long axis due to the nematic or smectic potential. Although compound **2** does not have a SmC* phase prior to the formation of the glass state, it is possible that it could show in the SmA phase a pretransitional behavior typical of compounds showing this phase transition (as compound **1**). Then, for the intermediate mode we suggest collective amplitude tilt fluctuations, a soft mode. In fact, this compound shows a clear electroclinic effect under a strong ac field of low frequency. The three modes follow the VFT law (see Table 5.4).

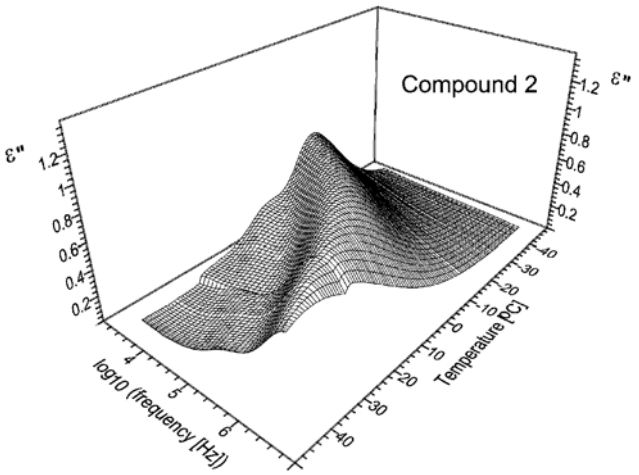

Fig. 5.46. Three-dimensional plot of the dielectric losses vs. temperature and frequency for compound **2**. (Reproduced from [5]. Copyright 1997 American Chemical Society)

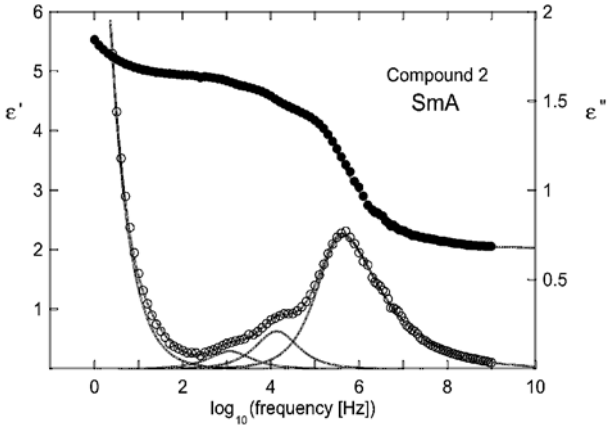

Fig. 5.47. Complex permittivity vs. frequency in the SmA phase (compound **2**): ε' (•), ε'' (○). The solid lines are fit curves using (5.178) and (5.179): (from high to low frequency) mode t, soft mode, mode l and conductivity contribution. (Reproduced from [5]. Copyright 1997 American Chemical Society)

Figure 5.49 is a three-dimensional plot of the dielectric losses versus temperature and frequency (10^2–10^6 Hz) for compound **3**. In the isotropic phase we only observed one peak and in the N* two. In most nematogens in the isotropic phase only one broad relaxation is obtained (see Sect. 3.1 in this book). However, in smectogens two well-separated peaks are usually observed [8, 13, 14]. Figure 5.50 is a typical plot of the complex permittivity versus the logarithm of the frequency at −32 °C in the N* phase. There two

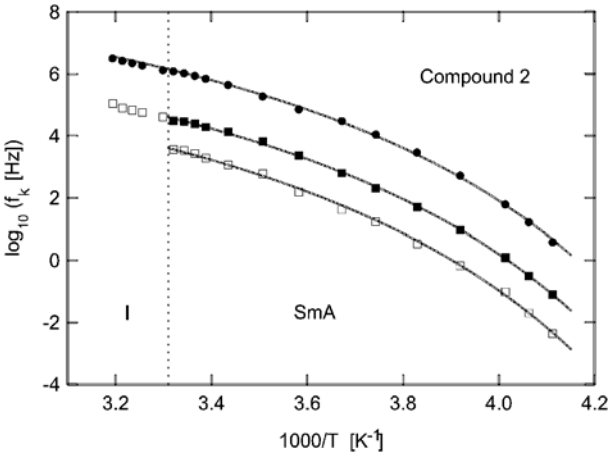

Fig. 5.48. Frequency of the different modes vs. temperature (compound **2**): (□) mode l, (■) soft mode and (•) mode t. The *solid lines* are fit curves to the VFT law, (5.182). (Reproduced from [5]. Copyright 1997 American Chemical Society)

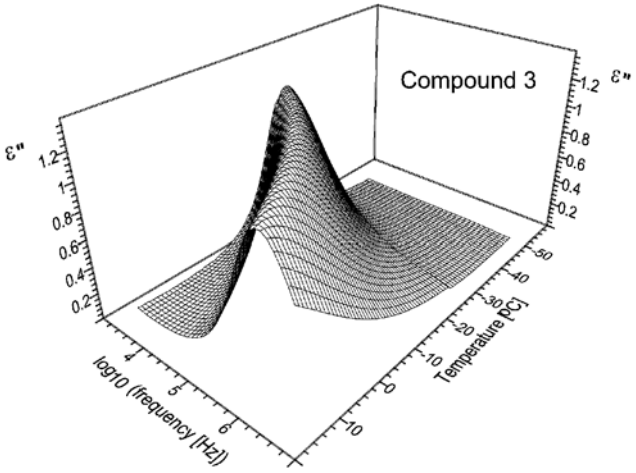

Fig. 5.49. Three-dimensional plot of the dielectric losses vs. temperature and frequency for compound **3**. (Reproduced from [5]. Copyright 1997 American Chemical Society)

clear peaks are observed. The frequencies are plotted in Fig. 5.51 versus temperature. The one with the lowest frequency corresponds to l mode, and the other to mode t. Both follow the VFT law (see Table 5.4).

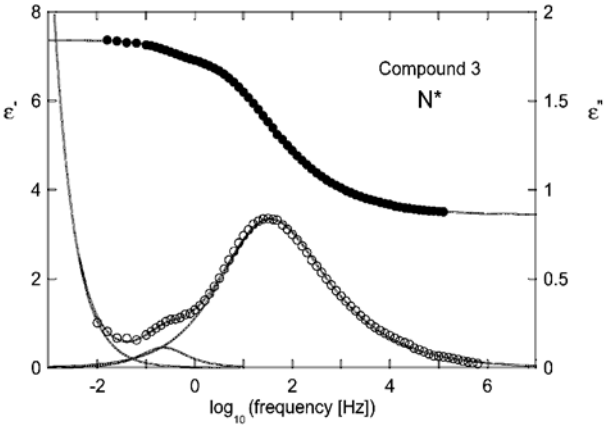

Fig. 5.50. Complex permittivity vs. frequency in the N* phase (compound **3**): ε' (•), ε" (○). The *solid lines* are fit curves using (5.178) and (5.179): (from high to low frequency) mode t, mode l and conductivity contribution. (Reproduced from [5]. Copyright 1997 American Chemical Society)

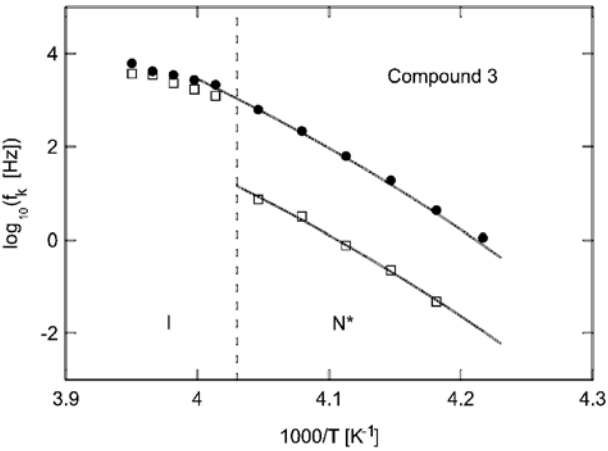

Fig. 5.51. Frequency of the different modes vs. temperature (compound **3**): (□) mode l and (•) mode t. The *solid lines* are fit curves to the VFT law, (5.182). (Reproduced from [5]. Copyright 1997 American Chemical Society)

5.5.4 Summary and conclusions

Three chiral low-mass liquid crystals with a varied physical behavior have been reported. The presence of the naphthalene group in the central core together with the voluminous chiral tail [-COO*CH(CH_3)COOC_4H_9] or the –OH lateral substituent appear to promote the formation of glassy mesophases. The glassy mesophases are SmC* for compound **1**, SmA for compound **2** and N* for compound **3**. Broadband dielectric spectroscopy is a very

useful tool to analyze the polar motions in liquid crystals and particularly to study the dynamical properties when a glass transition takes place. The broad time-scale covered by our experimental set-up (11 decades) using the same cell allowed us to follow several relaxation modes during a broad temperature range that include several phase transitions and the vitrification process. The most interesting was compound **1**. It shows a SmC* phase that vitrifies. We observed three modes whose frequency follow the VFT law: the rotation around the molecular long and short axes and the Goldstone mode. The ideal glass transition temperature or Vogel temperature, temperature where the frequency becomes zero, is the same for the three modes. The frequencies of the modes are related to certain viscosities, then the viscosities should become infinitely large. In particular we have obtained the one related with the Goldstone mode and it suffers an enormous increase when approaching the glass transition.

Acknowledgments. This work was supported by the Spanish Government, Project No. CICYT. MAT 2000-1293-C02-(01and 02) and the Universidad del País Vasco, Projects No. UPV060.310-G16/98 and No. 9/UPV00060.310-13562/2001.

References

1. G.S. Attard, C.T. Imrie, F.E. Karasz: Chem. Mater. **4**, 1246 (1992)
2. M. Loddoch, G. Marowsky, H. Schmid, G. Heppke: Appl. Phys. B. **59**, 591 (1994)
3. Y. González, B. Palacios, M.A. Pérez Jubindo, M.R. de la Fuente, J.L. Serrano: Phys. Rev. E. **52**, R5764 (1995)
4. B. Palacios, M.R. de la Fuente, M.A. Pérez Jubindo, M.B. Ros: Liq. Cryst. **23**, 349 (1997)
5. Y. González, M.B. Ros, J.L. Serrano, B. Palacios, M.R. de la Fuente, M.A. Pérez Jubindo: Chem. Mater. **9**, 2786 (1997)
6. W. Wedler, P. Hartmann, U. Bakowsky, S. Diele, D. Demus: J. Mater. Chem. **2**, 1195 (1992)
7. W. Wedler, D. Demus, H. Zaschke, K. Mohr, W. Schäfer, W. Weissflog: J. Mater. Chem. **1**, 347 (1991)
8. S. Merino, M.R. de la Fuente, Y. González, M.A. Pérez Jubindo, M.B. Ros, J.A. Puértolas: Phys. Rev. E. **54**, 5169 (1996)
9. K.L. Ngai, E. Riande, G.B. Wright: (eds) Proceedings of the Second International Discussion Meeting on Relaxations in Complex Systems, Alicante, J. Non-Cryst. Solids. **172–174** (1994)
10. H. Kresse, S. Ernst, W. Wedler, D. Demus: Ber. Bunsenges. Phys. Chem. **94**, 1478 (1990)
11. H.R. Zeller: Phys. Rev. Lett. **48**, 334 (1982)
12. M.R. de la Fuente, A. Ezcurra, M.A. Pérez Jubindo, J. Zubia: Liq. Cryst. **7**, 51 (1990)

13. M.R. de la Fuente, M.A. Pérez Jubindo, J. Zubia, T. Pérez Iglesias, A. Seoane: Liq. Cryst. **16**, 1051 (1994)
14. M.R. de la Fuente, S. Merino, M.A. Pérez Jubindo, M.T. Sierra: Mol. Cryst. Liq. Cryst. **259**, 1 (1995)
15. H. Kresse, S. Tschierske, A. Hohmuth, C. Stützer, W. Weissflog: Liq. Cryst. **20**, 715 (1996)
16. A. Schönhals, F. Kremer, A. Hofmann, E.W. Fischer, E. Schlosser: Phys. Rev. Lett. **70**, 3459 (1993)
17. A. Schönhals, F. Kremer: J. Non-Cryst. Solids. **172–174**, 336 (1994)
18. G. Adam, J.H. Gibbs: J. Chem. Phys. **43**, 139 (1965)
19. A. Alegría, E. Guerrica-Echevarría, L. Goitiandía, L. Tellería, J. Colmenero: Macromolecules **28**, 1516 (1995)
20. S. Matsuoka, X. Quan X: Macromolecules **24**, 2770 (1991)
21. T. Carlsson, B. Zeks, C. Filipic, A. Levstik: Phys. Rev. A **42**, 877 (1990)

5.6 Dielectric properties and switching processes in ferroelectric liquid crystals based composites

E. Pozhidaev and W. Haase

5.6.1 Introduction

Ferroelectric liquid crystal (FLC) based composites, which are under development and investigation in recent years, are polymer dispersed ferroelectric liquid crystals (PDFLC) and microconfined FLC's (MFLC). Generally PDFLC's are a bunch of polymer dispersed liquid crystal (PDLC) films, which are prospective electrooptic materials due to utilizing of electrically controlled light scattering, the ease of fabrication, the reliability in work and the flexibility [1]. The PDFLC material present a planar-oriented polymer film with FLC droplets dispersed therein. The FLC director in all droplets is aligned on average in the same direction parallel to the film plane [2–4]. PDFLC's are of interest due to a combination of advantages of composite polymer liquid crystalline materials such as PDLC, mentioned above, with the fast electrooptical response which is an inherent property of FLC's [5, 6].

However, there are problems, which impede with the progress of application of PDFLC films in display devices. These are a high value of driving voltage, low light modulation depth, low optical transmission and low contrast ratio of PDFLC cells [2, 3, 7]. On the other hand, there are many scientific ideas of how to overcome these problems. We will focus in our contribution on those points.

During recent years, the study of liquid crystals in confined geometry has been an active area of research. While PDLC's based on nematic liquid crystals have been investigated extensively [8, 9], FLC's in confinements [10–13] evoke new questions. Even in mesoporous submicrometer systems, which are actually different from PDFLC composites, striking deviations from bulk behavior are found [14, 15]. An influence of geometrical restrictions on collective

modes of FLC's is already evident. The origin of this influence is not clear yet, and is under discussion in this paper for both basic types of the confinement in FLC composites: PDFLC and MFLC.

5.6.2 Microstructures of FLC based composites

5.6.2.1 Structures and preparation of MFLC

Two porous structures for the microconfinement of ferroelectric liquid crystals have been described [13, 16]:

The first type of a microstructure is an (organic) nitro-cellulose Synpor membrane (Pragochem) with interconnected cavities having diameters between 0.23 and 0.85 µm (see Fig. 5.52). The second type is an (inorganic) aluminium oxide Anopore membrane (Anotech) with regular separated cylindrical pores of 0.2 µm diameter. The thickness of the filter sheets is about 60 µm (see Fig. 5.53). Membranes must be heated before filling with FLC during 48 hours in vacuum in order to remove adsorbed water. The empty Synpor as well as Anpore membranes are dielectrically inactive, the real part of the dielectric permittivity is constant in the measured frequency range, and accordingly no loss peak can be observed. For the dielectric experiments, the samples are cut to disks of about 1 cm diameter and filled with the FLC material in its isotropic phase. The excess liquid crystal material from the outer surfaces is carefully removed by pressing the samples between filter paper. For the measurements, the sample disks are covered on both sides with thin aluminum foil to ensure good electrical contact and to avoid electrode polarization effects in the low frequency range.

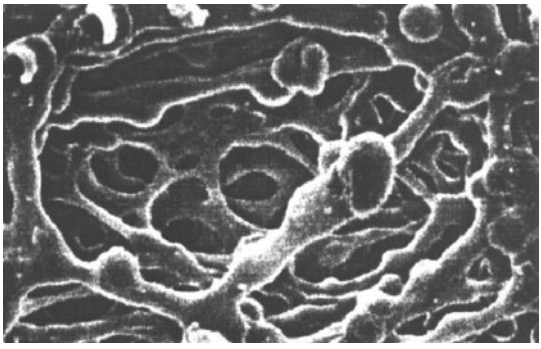

Fig. 5.52. Scanning electron microscope image of a Synpor membrane with a pore diameter of 0.6 µm. The image size is 20×13 µm. From [13]

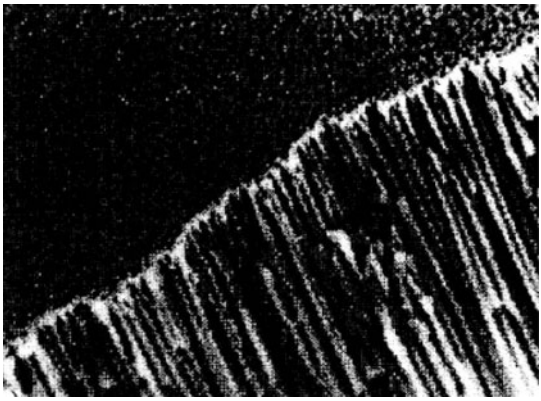

Fig. 5.53. Scanning electron microscope image of an Anopore membrane with a pore diameter of 0.2 µm. From [13]

5.6.2.2 Preparation of PDFLC films and structures of FLC droplets

Many PDFLC films had been produced by the thermally induced phase separation (TIPS) method [1] from a suspension of a ferroelectric liquid crystal and a polymer. Polyvinylbutyral was used often as the polymer [2–4]. Uniaxial alignment of the samples had been achieved by shear deformation during the cooling process. The average droplet size in the film plane depends on the concentrations of the FLC and the polymer, on the cooling velocity and the shear deformation amplitude. Epoxy compounds had been used also as polymer matrices in polymerization induced phase separation (PIPS) method [1, 17] of PDFLC film preparation, and FLC's had been dispersed therein also from mixtures of epoxy compounds and FLC's [7, 18, 19]. Usually Norland optical Adhesive (NOA 65) have been used as a pre-polymer for manufacturing of PDFLC films [18, 19] by the PIPS method. Formation of FLC droplets occur via the PIPS method because mixtures of NOA 65 with FLC's were slowly cooled down from the isotropic state simultaneously under UV curing.

For studying the texture of the droplets the samples were placed in a hot stage of a polarizing microscope. The observation was carried out under crossed polarizers on one side and only with one polarizer on the other side. Microphotos of PDFLC layer textures [20, 21], see Fig. 5.54, show the existence of two basic types of FLC structures inside the droplets. These are disclinations of first a concentric type forming so-called single focal conic domains and second of a faint wavy type of disclinations, see also Fig. 5.55. Studies [20, 21] with FLC mixtures possessing disclinations along the smectic layers (see Fig. 5.55) showed concentric spheres around the point defects (Fig. 5.55 a,c). This structure is more characteristic for small droplets (less than 6 µm). For droplets of a larger size, a formation of several focal-conic domains is possible (Fig. 5.56 c,d). It should be noted that the variation of

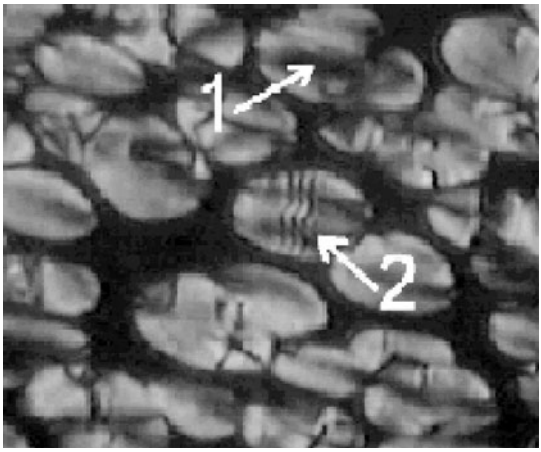

Fig. 5.54. Microphoto of a PDFLC film texture, shown in polyvinylbutyral film using the TIPS method. The image size is 35×30 μm^2. Two basic types of FLC droplets are presented: 1 – disclinations of a concentric type (single focal conic domain) and 2 – wavy type. From [20]

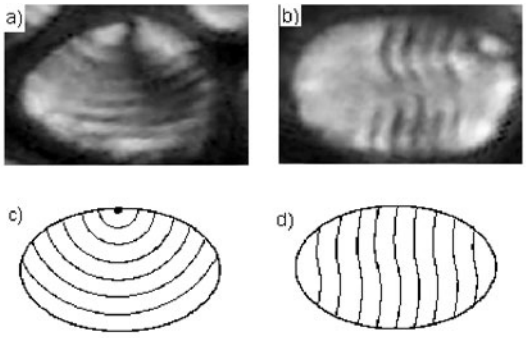

Fig. 5.55. Microphotos of FLC droplets, shown in a polyvinylbutyral film using the TIPS method. The image size is 7.5×10 μm^2 with disclinations of (**a**) - concentric type (single focal conic domain) and (**b**) - wavy type. (**c**) and (**d**) are the corresponding alignments of smectic layers inside the droplets. From [20]

the brightness of these droplets in dependence on the sample rotation is negligible. The textures of three different configurations of the FLC director inside the droplets are presented in Fig. 5.56. In case of a single focal-conic domain (Fig. 5.56 a,b), one can see two dark lines with the origin in point defects located near the interface. The lines are parallel to the polarizers and turn if the stage with the sample turn. Consequently, if the PDFLC films contain such a type of droplets no considerable anisotropy of macroscopic optical properties is possible. The high anisotropy was achieved only for the case of samples with the droplets possessing a wavy type structure (Fig. 5.55 b,d). If

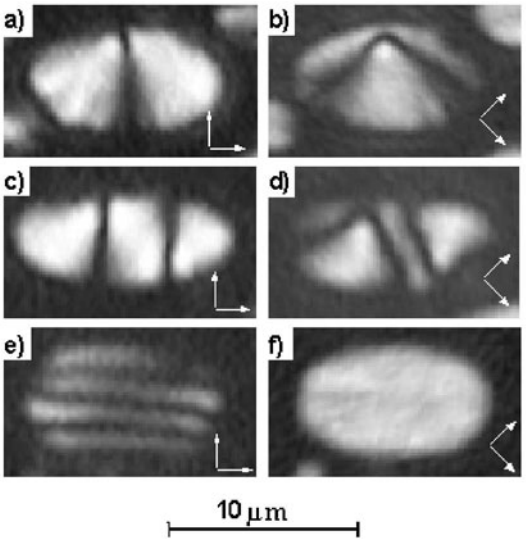

Fig. 5.56. FLC droplets between crossed polarizers. (**a**), (**b**) Droplet with a single focal-conic domain; (**c**), (**d**) Droplet with two focal-conic domains; (**e**), (**f**) Droplet with wavy-deformed smectic layers. *Arrows* show the orientation of the polarizers axes. From [22]

the long axis of such a droplet is aligned along one polarizer, the brightness of the droplets is minimal and the texture presents several dark lines which are oriented nearly parallel to the long axis (Fig. 5.56 e). The droplets become very bright if their long axes form an angle of 45 ° with the axis of the polarizers (Fig. 5.56 f) [22]. So, to achieve high efficiency of light modulation in PDFLC cells, it is necessary to optimize the composition and preparation technique in such a way that all droplets would have the internal structure of the wavy type (Fig. 5.55 d). Unfortunately, it is not clear how to achieve this, because such structures can be obtained in experiment only accidentally.

As for a shape and size of droplets, there are possibilities of their variations due to the technological process of PDFLC film preparation. Using the same PIPS method, the authors of [18] developed a PDFLC film with FLC droplets size of about 0.6 µm but in [19] it is reported about strongly oblate droplets which are 80 to 300 µm in length and 8 to 20 µm in width (see Fig. 5.57). This result was obtained when a FLC was mixed thoroughly with an epoxy resin and the curing agent NOA 65 in a ratio 4:5:1. The uniaxial structure of the PDFLC film was formed by shearing deformation during the curing process. In [18] the curing agent NOA 65 and the FLC ZLI 4655-100 (Merck) were mixed in 1:1 weight ratio. The temperature of the mixture was raised to isotropic state so that a homogeneous PDFLC mixture was formed. The mixture was filled into a planar aligned ITO coated cell of a thickness of 10 µm, heated to isotropic state, and cooled down followed by UV curing.

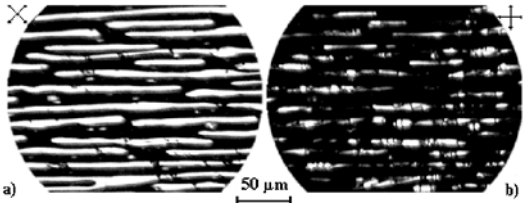

Fig. 5.57. Optical microscope picture of a PDFLC sample prepared by PIPS method under crossed polarizers. The polarizer and the composite film long axes of droplets are parallel (*right*) or under an angle 45 ° (*left*). From [19]

TIPS method with the polyvinylbutyral and shear alignment during cooling provides droplets of elliptical shape with an average value of axes 5 µm and 10 µm, respectively, as shown (Figs. 5.54–5.56).

Here, one can see a variety of sizes and shapes of FLC droplets in PDFLC films. Such a situation is a good chance for investigating simultaneously both electrooptical and dielectric properties of FLC's in confined geometry. Just this comparative analysis of dielectric and electrooptical data is impossible for the case of MFLC structures described in [13, 14, 16]. That is why we shall consider first the electrooptics of PDFLC.

5.6.3 Electrooptics of PDFLC films

5.6.3.1 Electrooptical modulation due to electrically controlled light scattering effect

There are two basic ways to modulate the light beam by using PDFLC films:

First, the PDFLC film can be used as an electrically controlled phase retarder placed between two polarizers [3, 7], similar to the Clark-Lagerwall cell [6].

The second method is based on the light scattering effect [2, 4, 23]. The light scattering PDFLC modulators can be designed both with a single polarizer [2, 4, 23, 24] and polarizer-free [25–27]. The PDFLC modulator with a single polarizer (see Fig. 5.58) consists of two glass substrates covered with transparent ITO electrodes on the internal surfaces and a planar-aligned PDFLC film between them. The light polarizer can be placed before or after the sandwich. The angle α determines the angle between the polarizer axis and the long axes of the FLC droplets. The components of PDFLC's are chosen so that the refractive index of the polymer is equal to one of the refractive indices of the liquid crystal, namely to $n_{\perp}$ [25]. Owing to this, the light passes through the cell without scattering if the polarizer is oriented perpendicular to the director inside the FLC droplets (Fig. 5.58 b). If $\alpha = \theta = 45\,^{\circ}$, an opposite pulse of the driving electric field reorients the director just parallel to the light polarization (Fig. 5.58 a) resulting in an intensive scattering due to the high gradient of the refractive index at the droplet interface. Usually

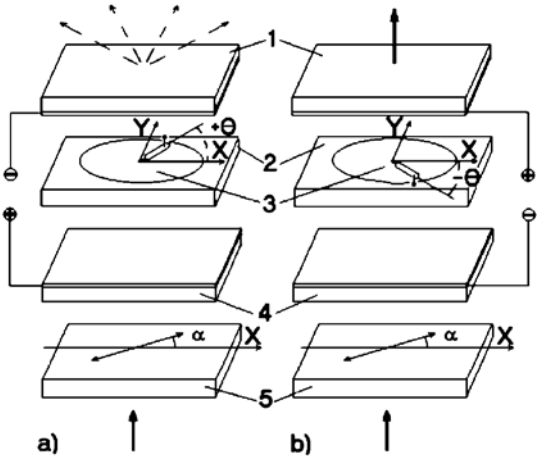

Fig. 5.58. The design and the principle of the operation of a single-polarizer PDFLC light modulator. 1, 4, substrates with transparent electrodes; 2, polymer; 3, FLC droplet; 5, polarizer

the tilt angle θ of commercially available FLC mixtures is less than 45 °, therefore it is impossible to obtain maximal efficiency of the light scattering. Illustrations of phenomena described above are given in Fig. 5.59. Here all photos were made in the geometry of just one polarizer. The interface of the droplets with wavy type structure is seen as a solid line (Fig. 5.59 e), if the long axis is oriented parallel to the polarization of light. It means that there is a high gradient of refractive index on the droplets boundary corresponding to an intensive scattering of the transmitted light. For the perpendicular orientation of light polarization (Fig. 5.59 f), the interfacial line vanishes due to the optical homogeneity of the structure. In this case, the light passes through the film without scattering. For the focal-conic domain structure, there is no high anisotropy of the scattering efficiency (Fig. 5.59 a–d). So, to achieve high efficiency of light modulation in a single-polarizer PDFLC cell, it is necessary to have the internal structure of just wavy type.

Theoretical and experimental considerations of light modulation characteristics of PDFLC films possessing an internal structure of wavy type of PDFLC droplets were done in [22, 28, 29]. The brightness of PDFLC cells can be determined with T_1 being the high level of the optical signal corresponding to a positive electric pulse and T_2 denoting the lower level of a response to a negative electric pulse. The light transmission T_1 was evaluated as:

$$T_1 = T_\perp \left[1 + \left(\frac{T_{||}}{T_\perp} - 1 \right) \cos^2(\alpha + \theta) \right] . \tag{5.186}$$

The light modulation amplitude is given by the relationship:

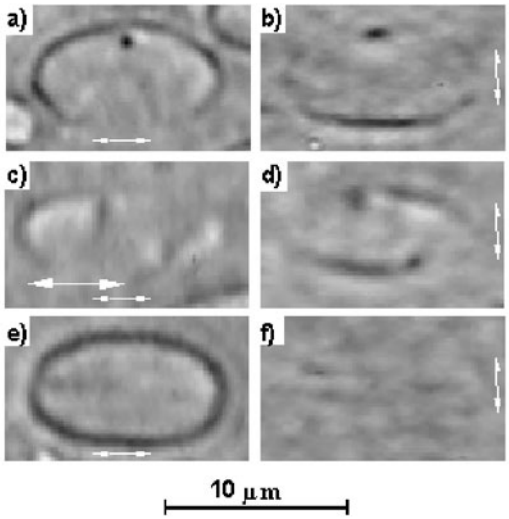

Fig. 5.59. Microphotos of the FLC droplets in a linear polarized light. (**a**), (**b**) Droplet with a single focal-conic domain; (**c**), (**d**) Droplet with two focal-conic domains; (**e**), (**f**) Droplet with wavy-deformed smectic layers. *Arrows* show the orientation of the polarizer. From [22]

$$\Delta T = T_1 - T_2 = T_\perp \left(1 - \frac{T_{||}}{T_\perp}\right) \sin 2\alpha \sin 2\theta, \tag{5.187}$$

and the contrast ratio is:

$$C = \frac{T_1}{T_2} = \frac{1 + \left(\frac{T_{||}}{T_\perp} - 1\right) \cos^2(\alpha + \theta)}{1 + \left(\frac{T_{||}}{T_\perp} - 1\right) \cos^2(\alpha - \theta)}. \tag{5.188}$$

Here $T_\perp = I_\perp / I_0$, $T_{||} = I_{||} / I_0$ are the light transmission components of the polarization which is either perpendicular or parallel to the FLC director, respectively, I_0 is the intensity of incident light, $I_\perp$, $I_{||}$ are the polarized components of the radiation passed through the cell.

As a result of (5.186), the light transmission T_1 reaches its maximum at $\alpha + \theta = 90\,^\circ$ or at $\alpha = 90\,^\circ - \theta$, which is equal to $T_\perp$. The maximum of the modulation amplitude ΔT (see (5.187)) occurs at $\alpha = 45\,^\circ$ and is independent on the angle θ. A more complicated situation is observed for the contrast ratio. Following from (5.188), the contrast ratio reaches his maximum value at the angle:

$$\alpha_m = \frac{1}{2} \arccos \left(\frac{T_\perp - T_{||}}{T_\perp + T_{||}} \cos 2\theta\right) \tag{5.189}$$

It should be noted that α_m depends not only on the tilt angle θ but also on the light transmission anisotropy $T_{||}/T_\perp$. As a consequence the maximum

contrast ratio, as follows from (5.188), can be estimated by using the approximate formula:

$$C_m \cong 1 + \left(\frac{T_\perp}{T_{||}} - 1\right) \sin^2 2\theta \cong \frac{T_\perp}{T_{||}} \sin^2 2\theta \,. \tag{5.190}$$

The highest contrast ratio, as it follows from (5.190), equals to $\theta = 45\,^\circ$, and for this case the angle α does not play a role because the PDFLC become insensitive to any orientation of the light polarizing plane regarding to the long droplets axes. Let us note that the maximal values of T_1, ΔT and C coincide only for FLC with $\theta = 45\,^\circ$ in the geometry $\alpha = 45\,^\circ$, as it follows from theoretical consideration [28, 29]. Unfortunately, PDFLC's based on FLC's with $\theta = 45\,^\circ$ never had been developed, thus theoretical predictions given by (5.188) and (5.190) could not been checked experimentally. In a general case ($0 < \theta < 45\,^\circ$), the design should be chosen to provide optimal combination of the light modulation parameters. Calculations of the contrast ratio in dependence of the ratio $T_{||}/T_\perp$ and the angle α for the general case [22, 28, 29] according to (5.188) are presented in a 3D-graph in Fig. 5.60. Here $\theta = 26\,^\circ$ which is the real tilt angle for many FLC mixtures at room temperature. An experimental verification of the relationship (5.188) had been carried out also [22]. PDFLC films were produced by the TIPS method from the mixture of 40 wt.% ferroelectric liquid crystal ZhKS-285 (P. N. Lebedev Institute of Russian Academy of Sciences) with the tilt angle $\theta = 26\,^\circ$ and the helix pith $p_o = 0.4\,\mu$m and 60 wt.% polyvinylbutyral. The average droplet size in the film plane was $6 \times 10\,\mu$m. The film thickness was about 9 μm. Figure 5.61

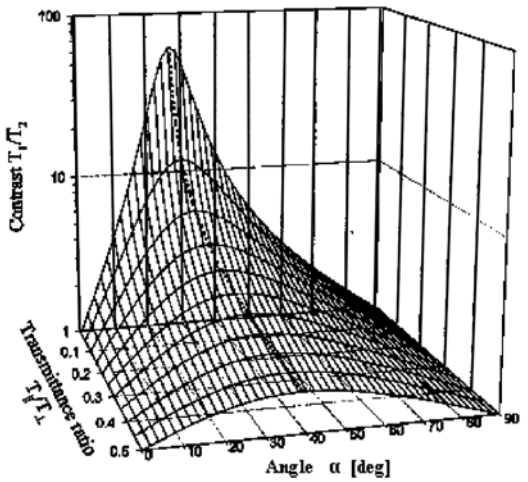

Fig. 5.60. Contrast ratio of a single-polarizer PDFLC cell as a function of the angle α and the transmittance ratio $T_{||}/T_\perp$ according to (5.188). Maximal values of the contrast are plotted by a *dotted line*. The tilt angle $\theta = 26\,^\circ$. From [29]

shows both evaluated and measured dependencies of the contrast ratio, the light modulation amplitude and the transmittance T_1 of a single-polarizer PDFLC cell on the angle α. As we can see, the theoretical and experimental dependencies are in good agreement with each other. The contrast ratio of more than 40:1, the light transmittance and the modulation depth of about 40% for polarized light can be provided even for the tilt angle $\theta = 26°$, as it is shown in Fig. 5.61. These parameters of light modulation are comparable with corresponding parameters of ordinary FLC cells, but PDFLC films are more steady.

Non-polarized light can be modulated by a double PDFLC cell, which consists of two PDFLC cells arranged in series [25, 26]. The idea based on the fact that any PDFLC cell possessing mismatching of refractive indices of the polymer matrix n_P and $n_{||}$ of the FLC dispersed therein, can be considered as a light scattering polarizer. The parameter $T_{||}/T_{\perp}$ proposed above just show polarizing capability of any PDFLC cell themselves. Under this approach, any cell in a pairwise PDFLC construction operates in the same manner as the one polarizer cell described previously. The external polarizer stand for another cell of the pair. Both PDFLC cells are identical, but for opposite directions of supplied electric field. It means, that under the electric field applied to both cells as shown in Fig. 5.62 a, the long molecular axes in both cells are parallel to each other and lie in the XY plane, along the X axis. For this case the light with the polarization plane along the Y axis is not scattered when passing through the device because of the actual absence of the refractive index gradient on the polymer FLC droplet interface. The phenomenon occurs as a consequence of the condition $n_P = n_{\perp}$ which is satisfied in experiment with rather high accuracy of about 2 to 3% [25]. The described arrangement is

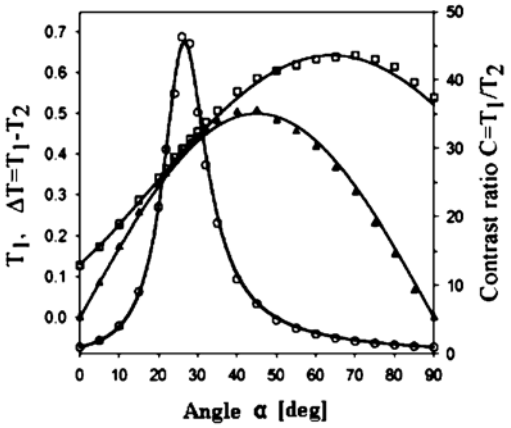

Fig. 5.61. Calculated and experimental dependencies of the transmittance T_1 (□), modulation depth (△) and contrast ratio C (O) on the angle α. $T_{\perp} = 0.643$. $T_{||}/T_{\perp} = 0.014$ according to (5.186), (5.187), (5.188). From [22]

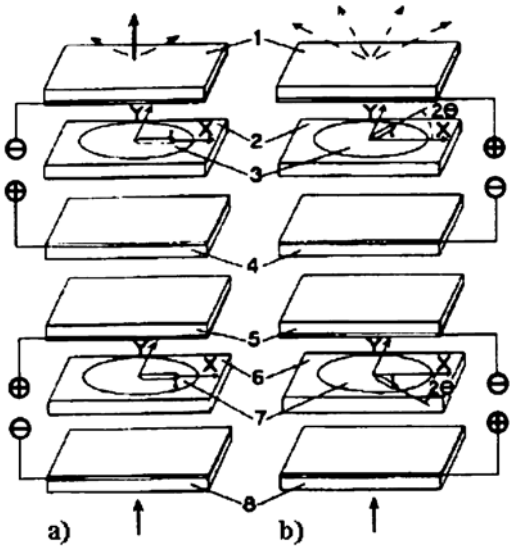

Fig. 5.62. Scheme of the double PDFLC cell: 1, 4, 5, 8 – conducting transparent substrates, 2, 6 – polymer films, 3, 7 – FLC droplets

essentially a system of scattering polarizers oriented in a parallel fashion. FLC molecules in droplets turn at an angle $2\theta = 45\,^\circ$ under changing the electric field polarity, but still remain in the XY plane (Fig. 5.62 b). Molecules in upper and lower films turn in the opposite directions to the X axis, and the angle between them reached to $4\theta = 90\,^\circ$. The PDFLC device scatters the light of any polarization in this geometry, like a PDLC based on a nematic liquid crystal. The maximal value T_{1D} of the optical transmission, which determines the brightness of the device, depends on the angle α_D between the orientations of PDFLC droplets long axes as [27]:

$$T_{1D} = (T_\perp - T_{||})^2 \cos^2(\alpha_D - 2\theta) + 2T_\perp T_{||}\,, \tag{5.191}$$

where $T_\perp$, $T_{||}$ are the same parameters each of a pair of identical cells. Those have been defined already by discussing the one polarizer PDFLC cell. The optical transmission reaches the maximal value $T_{1D} = T_\perp^2 + T_{||}^2$, if $\alpha_D = 2\theta$.

The light modulation depth ΔT_D of the double PDFLC cell

$$\Delta T_D = (T_\perp - T_{||})^2 \cdot \sin 2\alpha_D \cdot \sin 4\theta \tag{5.192}$$

reveals the maximum value $\Delta T_D = (T_\perp - T_{||})^2$ at $\alpha_D = 45\,^\circ$ and $\theta = 22.5\,^\circ$.

The contrast ratio C_D of the double PDFLC modulator is evaluated as:

$$C_D = \frac{(T_\perp - T_{||})^2 \cos^2(\alpha_D - 2\theta) + 2T_\perp T_{||}}{(T_\perp - T_{||})^2 \cos^2(\alpha_D + 2\theta) + 2T_\perp T_{||}}\,. \tag{5.193}$$

It follows from this that the value C_D reaches its maximal magnitude at the angle α_{mD}:

$$\alpha_{mD} = \frac{1}{2} \arccos \left(-\frac{(T_\perp - T_{||})^2}{(T_\perp + T_{||})^2} \cdot \cos 4\theta \right) . \tag{5.194}$$

The value α_{mD} depends not only on the tilt angle θ but also on the light transmission anisotropy $(T_\perp - T_{||})$ of the cells. In the case of $T_\perp \gg T_{||}$, the angle $\alpha_{mD} \approx 90$–20. Then the maximum contrast ratio C_{mD}, as follows from (5.193), can be estimated by using the approximation:

$$C_{mD} \cong \frac{1}{2} \frac{T_\perp}{T_{||}} \sin^2 4\theta . \tag{5.195}$$

Thus, changing the geometry of the PDFLC device (angle α_D) leads to the variation of its light modulation characteristics. The optimized parameters for the polarizer-free PDFLC modulator are $\alpha_D = 45\,^\circ$, $\theta = 22.5\,^\circ$, $T_\perp \to 1$ and $T_{||} \to 0$. The maximum light transmission T_{1D}, modulation depth ΔT_D and contrast ratio C_D at different values of these parameters can be estimated from the equations (5.191) to (5.195).

5.6.3.2 Saturation voltage of PDFLC films

There is a problem, which hinders progress in application of PDFLC films in display devices, namely the high driving voltage. The high voltage causes not only a large energy of surface interaction, but also a redistribution of the electric field in a dielectrically inhomogeneous medium. As was discussed earlier [17], the electric field inside the LC droplets of composite films is not the same as the applied electric field $E = U/D$, where U is the applied voltage and D the total thickness of the PDLC layer. In the case of an isolated spherical droplet in a polymer matrix, the electric field inside the LC droplet is expressed by:

$$E_{\mathrm{LC}} = \frac{U}{D} \cdot \frac{3}{(\varepsilon_{\mathrm{LC}}/\varepsilon_p + 2)} , \tag{5.196}$$

where $\varepsilon_{\mathrm{LC}}$ and ε_p are the dielectric constants of the liquid crystal and polymer, respectively. Usually, $\varepsilon_{\mathrm{LC}} > \varepsilon_p$, for example, a parallel component of dielectric constant of LC 5CB [30] at low frequency is equal to 18, ε_p of polyvinylbutyral is equal to 6. Consequently, the electric field inside 5CB droplets will be $E_{\mathrm{LC}} = 0.6 \cdot U/D$. There is only one way to increase the value of E_{LC} up to U/D, namely to choose the composition so, that $\varepsilon_{\mathrm{LC}} = \varepsilon_p$. The problem is more actual for the PDFLC's, since a value of proper FLC dielectric constant in this case may reach 100 and more. For example, in the case of a spherical droplet of a FLC with $\varepsilon_{\mathrm{LC}} = 300$ dispersed in polyvinylbutyral

matrix, $E_{\mathrm{LC}} = 0.058 \cdot U/D$, as it follows from (5.196). Therefore the saturation voltage of PDFLC films is much more usually than corresponding FLC cells, as it was measured experimentally [31] (see Fig. 5.63). The morphology of planar oriented PDFLC films [3, 4, 20] differs substantially from the structure of PDLC prepared in the traditional way [17]. A strong deviation of droplets shape from a sphere is characteristic of the PDFLC films [19], as is illustrated in Fig. 5.57, and just this feature allows to solve the problem of the saturation voltage diminishing. In practice, the droplet cavities become very flattened during the fabrication of the planar oriented structure. The large droplets (with size strongly exceeding the thickness of PDFLC film) have more disk-like than ellipsoidal shape (see Fig. 5.64). The in-plane size of such droplets is much more than the lateral one. The requirement of the continuity of the $\varepsilon \boldsymbol{E}$ vector in dielectric multilayer structure yields the electric field E_{LC} in LC droplet as [19]:

$$E_{\mathrm{LC}} = \frac{U}{D} \cdot \frac{1 + \frac{d_p}{d_{\mathrm{LC}}}}{1 + \frac{\varepsilon_{\mathrm{LC}}}{\varepsilon_p} \cdot \frac{d_p}{d_{\mathrm{LC}}}}, \tag{5.197}$$

where d_{LC} is the thickness of LC droplets, $d_P = d_{P1} + d_{P2}$ is the thickness of polymer (see Fig. 5.64), $D = d_P + d_{\mathrm{LC}}$. Similar to the case (5.196), E_{LC}

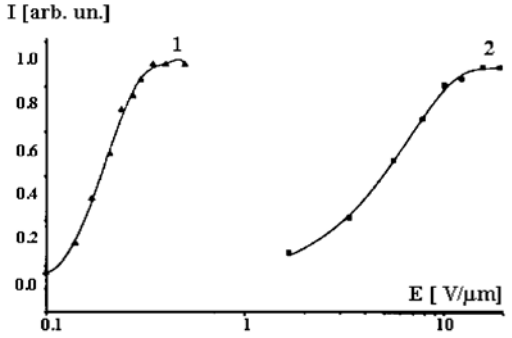

Fig. 5.63. Electric field – optical transmittance characteristics of a FLC cell (*curve 1*) and a PDFLC cell based on the same FLC (*curve 2*). The FLC cell layer thickness is 5.8 μm, the film thickness is 9 μm, the averaged droplet size is 3 μm, droplets have almost spherical shape. From [31]

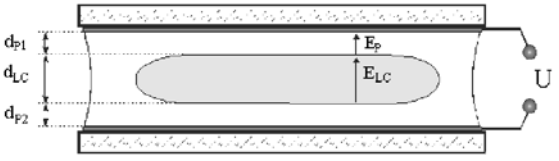

Fig. 5.64. Scheme of a cross-section of the planar oriented PDFLC film with strongly oblate droplets

is equal to the applied electric field U/D, if components with $\varepsilon_{\rm LC} = \varepsilon_P$ are chosen. As a result of (5.197), there is another way to increase $E_{\rm LC}$ up to U/D. It occurs at any ratio $\varepsilon_{\rm LC}/\varepsilon_P$, if we reduce the total thickness d_P of the polymer layers relative to the lateral size $d_{\rm LC}$ of the LC droplet. Then $d_P/d_{\rm LC} \Rightarrow 0$, and $E_{\rm LC} \Rightarrow U/D$. For example, in the case of strongly oblate FLC droplets with $\varepsilon_{\rm LC} = 300$, dispersed in a polyvinylbutyral matrix, $E_{\rm LC} = 0.04 \cdot U/D$ according to (5.197), if $d_P = d_{\rm LC}$, but the electric field tension $E_{\rm LC} = 0.51 \cdot U/D$, if $d_P = 0.02 d_{\rm LC}$.

An experimental observation of the discussed phenomenon has been carried out [19, 32] with PDFLC's possessing a droplet structure as it is shown in Fig. 5.57. Most of the droplets are isolated, but some of them are connected with each other. It was found from observation of cross-sections of PDFLC film that polymer layers separated the FLC droplets from conductive substrates are either very thin ($\ll 1\,\mu$m) or quite absent [19]. It means according to (5.197), that the saturation voltage must be low, what was indeed observed experimentally (see Fig. 5.65). Comparing the experimental data of Fig. 5.63 and Fig. 5.65 and taking into account relationships (5.196) and (5.197), one can conclude that for almost spherical droplets $E_{\rm LC} = 0.03 \cdot U/D$ as it follows from Fig. 5.63, but for the case of strongly oblate droplets $E_{\rm LC} = 0.5 \cdot U/D$.

Decreasing of the FLC elastic energy themselves results in diminishing of the saturation field of PDFLC films [32]. Additionally, the saturation field depends on dynamics of FLC molecules reorientation [31], because it results in dynamics of dielectric permittivity $\varepsilon_{\rm LC}(t)$, or in dielectric dispersion $\varepsilon_{\rm LC}(f)$ (here t and f are time and frequency, respectively). Actually, relationships (5.196) and (5.197) are valid for the static case but dielectric dispersion

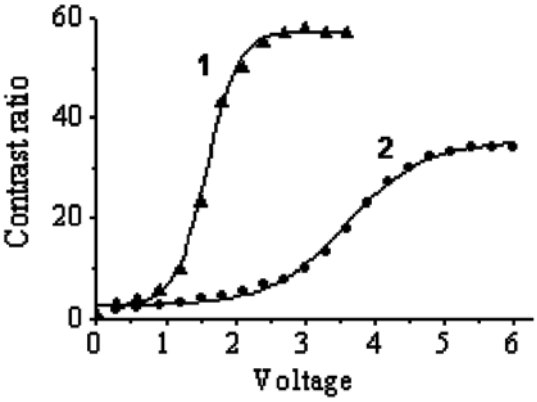

Fig. 5.65. Electric voltage – contrast ratio characteristics of a FLC cell (*curve 1*) and a PDFLC cell based on the same FLC (*curve 2*). The FLC cell layer thickness is 4.0 µm, the PDFLC film thickness is 4.0 µm, strongly oblate droplets typical sizes are $80 \div 300\,\mu$m in length and $8 \div 20\,\mu$m in width, polymer layers separating the FLC droplets from conductive substrates are very thin ($\ll 1\,\mu$m)

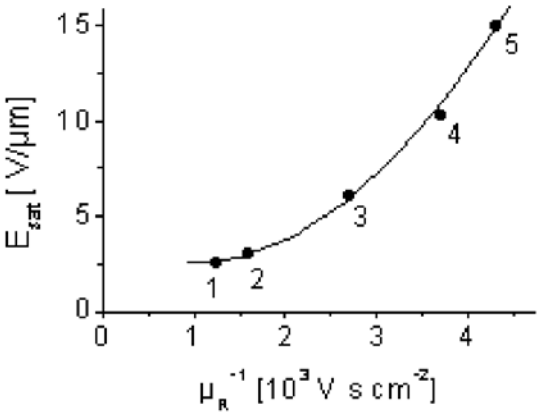

Fig. 5.66. Dependence of the saturation field on inverse charge mobility for PDFLC's which were obtained due to variation both γ_ϕ/P_S and d_0. Experimental points correspond to: 1 – FLC-313B, $d_0 = 3\,\mu$m, 2 – FLC-309C, $d_0 = 5\,\mu$m, 3 – FLC-309C, $d_0 = 3\,\mu$m, 4 – FLC-340, $d_0 = 3\,\mu$m, 5 – FLC-178, $d_0 = 2.5\,\mu$m. All FLC's were developed in P. N. Lebedev Physical Institute of RAS. From [31]

strongly affects on redistribution of electric field in dielectrically inhomogeneous medium, and on $E_{\rm LC}$ magnitude consequently. This effect can be taken into account through a parameter of mobility of charge transferred in PDFLC droplets with the polarization reversal current caused by FLC molecules reorientation under the external electric field. This specific parameter of charge mobility μ_R was grounded in [31]:

$$\mu_R = P_S d_0/\gamma_\phi \tag{5.198}$$

where P_S is the spontaneous polarization, d_0 is droplets diameter, γ_ϕ is the rotational viscosity. It was found experimentally, that the saturation field is inversely proportional to μ_R [31] (see Fig. 5.66). Finally, the problem of the saturation voltage diminishing is solved principally with creation of PDFLC films operating at saturation at 5 V (see Fig. 5.65).

5.6.3.3 Dynamics of electrooptic response of PDFLC films

PDFLC films exhibit the same shape of electrooptic response under the action of ac rectangular voltage, as ordinary FLC cells (see Fig. 5.67). An ordinary bistable operation of PDFLC cells in the same manner as FLC cells [6] had been reported also [7, 33]. On the contrary, some kind of memory in optical transmittance of PDFLC films instead of truth bistability had been discussed in [34, 35] (see Fig. 5.68). This short time memory differs from true bistability. After a rectangular driving voltage pulse switched off, electrodes of a PDFLC cell are electrically shorted through internal resistance of a generator (top curve in Fig. 5.68), but the light transmittance jumps to its opposite state

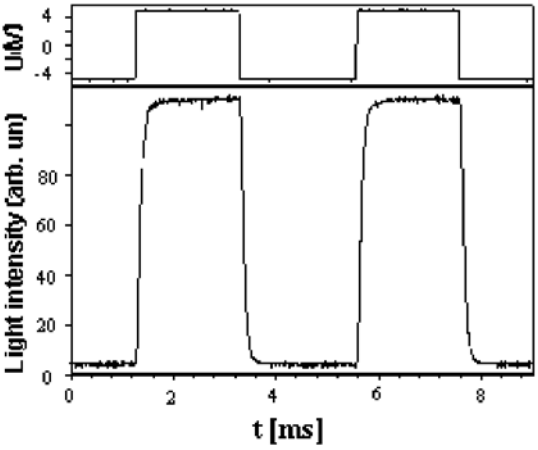

Fig. 5.67. Typical electrooptical response of a low voltage composite PDFLC film (*bottom*) under the action of ac rectangular voltage (*top*). From [19]

(see Fig. 5.68, bottom curve). During a pause between pulses, when the voltage is not applied to the PDFLC cell, the light transmittance relaxes slowly to the opposite state also. Relaxation of the light transmittance occurs after any such jumps caused by electric pulses switching on or switching off, even at the electric pulse duration. The situation looks like a manifestation of an elec-

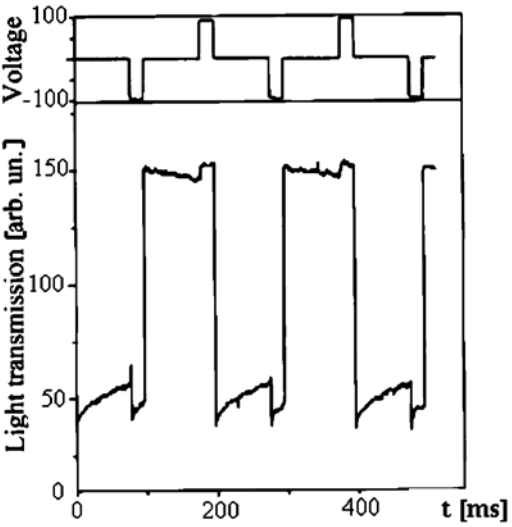

Fig. 5.68. Electrooptical response of a PDFLC film (*bottom*) under the action of ac rectangular voltage (*top*). The PDFLC layer thickness is 10 µm, droplets as they shown in Fig. 5.54

trical charge memory, when electrical capacitance of polymeric matrix plays a role of a voltage source for FLC droplets, if the external driving voltage is switched off.

The electrooptic response time $\tau_{0.1-0.9}$ of PDFLC films is faster, and its temperature dependence is much smoother in comparison with corresponding FLC cells under the action of the same electric field tension [18, 31, 35]. The electrooptic response time of PDFLC cells can be even almost independent of temperature, (see Fig. 5.69). The very strong difference between temperature dependencies of $\tau_{0.1-0.9}$ at switching of molecules in FLC and PDFLC cells indicates really a new type of molecular dynamics of FLC's in droplets. Probably, the dynamics of molecular reorientation in FLC droplets is quite different from the ordinary uniform reorientation of molecules on the smectic cone, which principally provides strong temperature dependence of the electrooptic response time. The main reason of this dependence, as it is known, is an activation process, resulting in the Arrhenius law for the rotational viscosity. A comparison of temperature dependencies of $\tau_{0.1-0.9}$ for FLC and PDFLC illustrates a possibility to avoid the activation process in FLC molecular dynamics. The same temperature independent electrooptic response time already had been reported [36] for a case of Deformed Helix Ferroelectric (DHF) liquid crystal [37]. A model of orientation diffusion of strongly deformed space distribution of FLC molecules orientations in DHF liquid crystals under the action of the electric field had been proposed for explanation of the phenomenon [36]. The space distribution of FLC molecule orientation is essentially non-uniform in droplets of FLC's also (see Figs. 5.54 to 5.56). That is why non-Arrhenius switching processes occur, probably, in FLC droplets. Temperature dependencies of rotational viscosity in FLC droplets of PDFLC films are much more smooth in comparison with those in ordinary FLC cells.

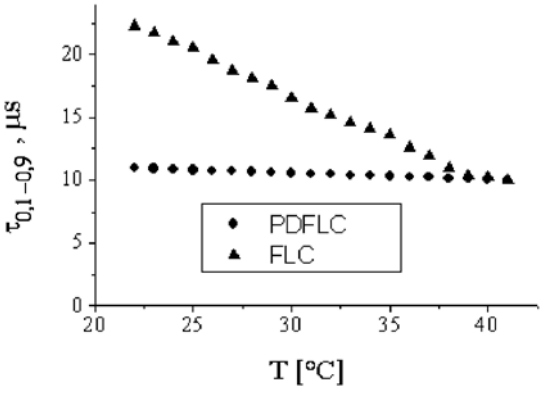

Fig. 5.69. Temperature dependencies of electrooptic response time of 1.8 μm FLC cell and 10 μm PDFLC cell based on the same FLC. The electric field tension $E = 10$ V/μm, $f = 500$ Hz both for FLC and PDFLC

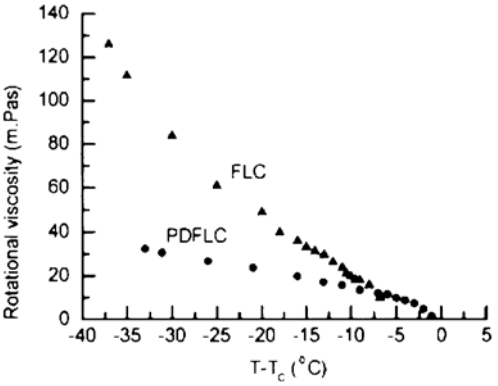

Fig. 5.70. Temperature dependencies of rotational viscosity for both FLC ZLI 4655-100 and PDFLC based on the same FLC. From [18]

Here an ordinary bulk switching of the FLC director takes place [18], (see Fig. 5.70). A smoother temperature dependence of the rotational viscosity of PDFLC in comparison with the FLC one means, most probably, partial suppression of activation energy influence the switching processes of FLC molecules under the applied field. Maybe, it is coupled with an influence of a restricted geometry of FLC droplets.

5.6.4 Effects of confined geometry in MFLC and PDFLC

5.6.4.1 Dielectric properties of MFLC, PDFLC and bulk FLC.

The dynamics of ferroelectric liquid crystals confined in porous nitro-cellulose membrane has been investigated by broadband dielectric spectroscopy [13, 16]. The complex inner membrane structure (Figs. 5.52 and 5.53) of random interconnected voids can be treated as a frozen random defect disorder in the mesophases. The dielectric effect of the Goldstone and soft modes of the FLC DOBAMBC [5] are suppressed by the confinement, may be because of relatively small dielectric strength $\Delta\varepsilon = 12$ even in bulk of this liquid crystal. If the dielectric strength of the Goldstone mode of a FLC is quite high $\Delta\varepsilon = 1000$, for instance, in the smectic C* phase of 4-(3-methyl-2-chloropentanoyloxy)-4′-heptyloxybiphenyl (called C7) [38], then the dielectric effect of the Goldstone mode is clearly present, although with almost two orders

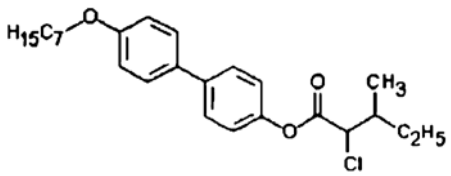

C7

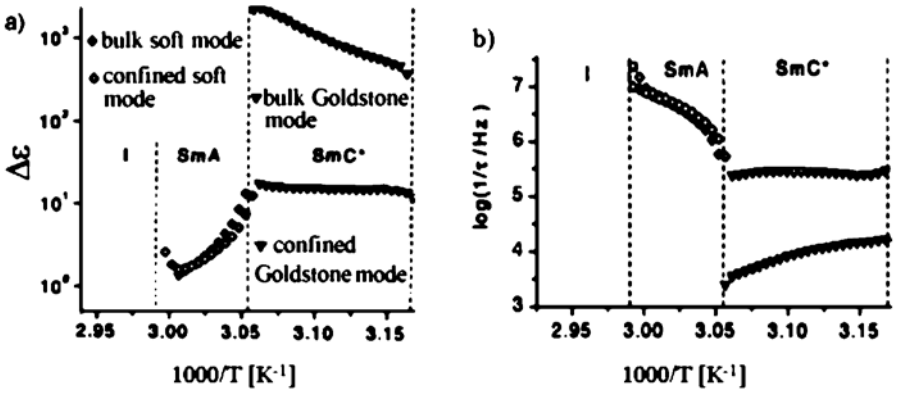

Fig. 5.71. Temperature dependencies of dielectric strengths (**a**) and relaxation frequencies (**b**) observed in the bulk and microconfined porous of nitro-cellulose liquid crystal FLC-C7. From [8] modified

of magnitude reduced strength (see Fig. 5.71 a). The Goldstone mode effect under the confinement shifts to higher frequencies by more than one decade, Fig. 5.71 b, while the confinement has a minor influence on the soft mode.

PDFLC's supply quite different conditions of liquid crystal confinement in comparison with MFLC systems based on nitro-cellulose membranes, as it follows from a comparison of photos in Figs. 5.52 and 5.53 and Figs. 5.54 to 5.57. Typical sizes of FLC droplets in PDFLC films are one to two orders larger in porous nitro-cellulose. Nevertheless, dielectric manifestations of the confinement in PDFLC's are the same, as was shown in [35, 39, 40] with a PDFLC based on polyvinylbutyral with droplets of FLC-309C dispersed therein. The PDFLC film thickness was 10 μm, FLC droplet structure is shown in Figs. 5.54 to 5.56. The collective processes have been studied by dielectric relaxation spectroscopy in the frequency range 10 Hz up to 13 MHz.

In the C* phase the bulk of the FLC-309C shows a pronounced Goldstone mode effect with a dielectric strength $\Delta\varepsilon = 200$ but this is suppressed in the PDFLC by more than one decade (see Fig. 5.72). The Goldstone mode effect of the PDFLC film based on the FLC-309C shifts to higher relaxation frequencies by more than one decade in comparison with the bulk of the same FLC (see Fig. 5.73).

It is not so evident that the increase of the relaxation frequency and the decrease of the dielectric strength can be explained by existing approaches. For the dielectric strength and relaxation frequency of the Goldstone mode one obtains [41]:

$$\Delta\varepsilon_G = \frac{1}{2\varepsilon_0 K_\phi q^2}\left(\frac{P_S}{\theta}\right)^2 \tag{5.199}$$

$$\nu_G = \frac{K_\phi q^2}{2\pi\gamma_\phi}, \tag{5.200}$$

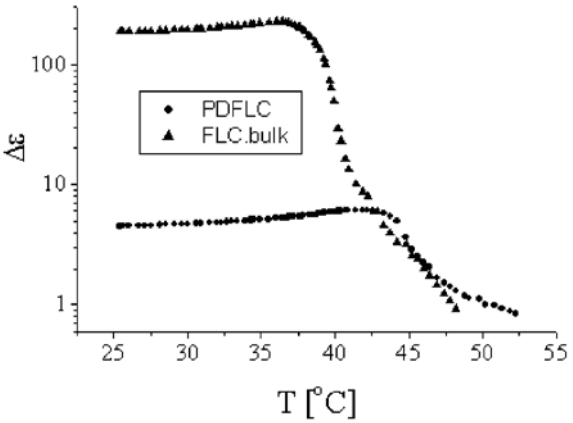

Fig. 5.72. Temperature dependencies of the dielectric strength observed in the FLC-309C bulk and in the PDFLC based on the same FLC

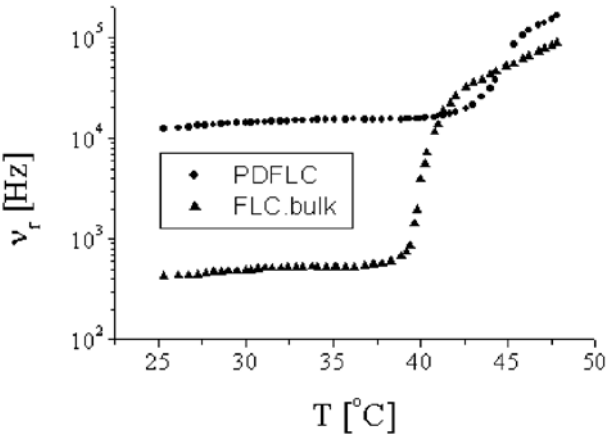

Fig. 5.73. Temperature dependencies of the relaxation frequency observed in the FLC-309C bulk and in the PDFLC based on the same FLC

where γ_ϕ is the rotational viscosity , q is the wavevector and K_ϕ the effective elastic constant.

For a bulk sample with an undistorted helix of pitch p one can define an elastic energy [32]:

$$W_{el} = \frac{1}{2} K_\phi q^2 = \frac{1}{2} K_\phi \left(\frac{2\pi}{p} \right)^2 , \tag{5.201}$$

but in restricted geometry, when the helix is suppressed, the elastic energy relates mainly to twisting of molecular distribution in smectic layers [10–12], and can be expressed as:

$$W_{el} \sim K_{\phi} \left(\frac{2\pi}{d} \right)^2 , \tag{5.202}$$

where d is typical size of confined geometry. A lower dielectric strength (or larger relaxation frequency) could occur as a result of an increase of the elastic energy according to (5.198) to (5.202). Principally, it could be if the FLC wave vector q increases (or the pitch p decreases), a result of the confinement. Nevertheless, experiments show smoother deformations just in PDFLC droplets in comparison with the bulk of FLC, possessing helical twisting [22]. For instance, Fig. 5.55 illustrates a typical pitch (about 1 to 1.5 μm) of deformations in FLC droplets, while in the bulk of the same FLC-309C the helix pitch is about 0.4 μm [21, 39]. Consequently, the wave vector q in PDFLC droplets is smaller in comparison with the FLC bulk one (probably, because of partial helix unwinding due to surface anchoring). Equations (5.198)–(5.202) result in estimations, which are quite opposite to the experimental results, presented in Figs. 5.72 and 5.73. On the other hand, in experiments with MFLC based on nitro-cellulose membrane [13, 16], the helix pitch $p = 0.3$ μm of the FLC-C7 [42] is comparable with the typical porous diameter, but the shift of dielectric strength and relaxation frequency of almost two decades takes place (see Fig. 5.71). Surface anchoring for explaining the shifts discussed above seems to be not so promising because the shifts in PDFLC and MFLC are practically the same, but the surface conditions of the confinement and sizes of FLC droplets are quite different.

5.6.4.2 Basic parameters of confined FLC's

Many measurements have been made in order to compare the basic physical properties of ferroelectric liquid crystals in their bulk and in composite PDFLC films [18, 31, 32, 35, 36, 39, 40, 43–45]. A strong decrease of the spontaneous polarization, the pyroelectric and piezoelectric coefficients are found in PDFLC's in comparison with the bulk of corresponding FLC's, while the apparent tilt angle decreases by 25% at the saturation voltage [39, 40, 45], Fig. 5.74b. The encapsulation of the FLC-309C in the polymer matrix (polyvinylbutyral) decreases the spontaneous polarization P_s about 5 times (see Fig. 5.74a). This value is larger as expected because only 40% of the PDFLC consist of the ferroelectric liquid crystal which contribute to the spontaneous polarization. Taking into account this ratio, the expected P_s of the PDFLC film should be 2.5 times less in comparison with an ordinary FLC cell.

The decrease of the dielectric strength (Fig. 5.72) cannot be explained by the decrease of the spontaneous polarization to the tilt angle ratio only. So, a ratio $\left(\frac{P_S}{\theta}\right)^2$ is 16 times smaller in the PDFLC in comparison with the FLC, as follows from Fig. 5.74. Then, according to (5.198), the expected decrease of $\Delta\varepsilon$ is just by a factor 16, but the real decrease is by a factor 50 (see Fig. 5.72). The same situation is with the increase of the relaxation frequency. It means that the relation-

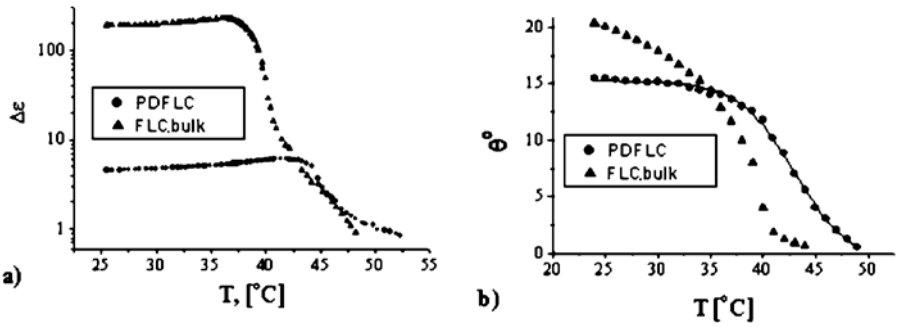

Fig. 5.74. Temperature dependencies of (**a**) the dielectric strength and (**b**) the tilt angle of the FLC-309C in the bulk and the PDFLC based on the same FLC

ships (5.198) and (5.200), valid for the FLC bulk, are not applicable for PDFLC composites.

The phase transition temperature from SmC* to SmA* phase of the PDFLC is about 4 °C larger in comparison with the FLC 309C mixture (Fig. 5.74). It indicates clearly an increase of the free energy density under the confinement in comparison with the same FLC in its bulk, which could relate to a larger elastic energy or to larger piezoelectric and flexoelectric contributions to the free energy of the PDFLC.

5.6.5 Summary

The effects of confined geometry manifest clearly in the same manner in dielectric properties of two basic types of ferroelectric liquid crystal based composites: PDFLC's and MFLC's. The last one are e.g. FLC's dispersed in nitro-cellulose membranes. The effect is independent of the conditions of the confinement and of the typical sizes of FLC droplets. An increase of the free energy density of FLC's because of the confinement is evident in experiments but there is no theory of the confinement yet.

A structure of smectic layers inside FLC droplets of PDFLC films have been investigated experimentally and described carefully as a base for theoretical description of optical properties of PDFLC composite films. The developed theory of the light modulation in PDFLC's by means of electrically controlled anisotropic light scattering is in good agreement with experimental data. One polarizer and polarizer-free PDFLC light shutter had been developed as a result of the FLC composites optimization.

Switching processes in PDFLC films have been analyzed both from the point of view of the electrooptic response dynamics and the electric field redistribution between the polymer matrix and the FLC inside droplets. Advantages of PDFLC films as very steady and fast switching electrooptic light shutters have been discussed.

Acknowledgement. Numerous contributions of co-workers of the authors to the development and investigation of ferroelectric liquid crystal based composites are gratefully acknowledged. V. Ya. Zyryanov and S. L. Smorgon were actually first, who developed polymer dispersed ferroelectric liquid crystals and initiated according research both experimentally and theoretically, D. Ganzke and A. L. Andreev performed dielectric measurements. Part of the work was supported by INTAS grant N° 97-1923 and by the Deutsche Forschungsgemeinschaft (Ha 782/49) via the German-Russian cooperation.

References

1. G. P. Crawford, S. Zumer: *Liquid Crystals in Complex Geometries* (Taylor&Francis Publ., London, Bristol, 1996)
2. V. Ya. Zyryanov, S. L. Smorgon, V. F. Shabanov: In *Abstracts of 4th. International Meeting on Optics of Liquid Crystals*, p. 70, Florida, USA (1991); in *Abstracts of First Summer European Liquid Crystal Conference*, p. 141, Vilnius, Lithuania (1991)
3. H. S. Kitzerov, H. Molsen, G. Heppke: Appl. Phys. Lett. **60**, 3093 (1992)
4. V. Ya. Zyryanov, S. L. Smorgon and V. F. Shabanov: SID 92 Digest **23**, 776 (1992)
5. R. B. Meyer, L. Libert, L. Strzelecki, P. Keller: J. Phys. Lett. **36**, L-69 (1975)
6. N. A. Clark, S. T. Lagerwall: J. Appl. Phys. **36**, 899 (1980)
7. P. Patel, D. Chu, J. L. West, S. Kumar: SID 94 Digest **25**, 845 (1994)
8. S. A. Rozanski, R. Stannarius, H. Groothues, F. Kremer: Liq. Cryst. **20**, 59 (1996)
9. S. A. Rozanski, R. Stannarius, F. Kremer: Zeitschrift für Phys. Chem. **211**, 147 (1999)
10. Yu. P. Panarin, Yu. P. Kalmykov, S. T. Mac Lughadna, H. Hu, J. K. Vij: Phys. Rev. E **50**, 4763 (1994)
11. M. Glogarova, H. Sverenyak, J. Holakovsky, H. T. Nguen, C. Destrade: Mol. Cryst. Liq. Cryst. **263**, 245 (1995)
12. V. Novotna, M. Glogarova, A. M. Bubnov, H. Sverenyak: Liq. Cryst. **23**, 511 (1997)
13. S. A. Rozanski, R. Stannarius, F. Kremer: IEEE Transactions on Dielectric and Electrical Insulation **8**, 488 (2001)
14. S. A. Rozanski, F. Kremer, R. Stannarius: Mol. Cryst. Liq. Cryst. **329**, 483 (1999)
15. L. Naji, F. Kremer, R. Stannarius: Liquid Crystals **25**, 363 (1998)
16. S. A. Rozanski, R. Stannarius, F. Kremer, S. Diele: Liq. Cryst. **28**, 1071 (2001)
17. J. W. Doane, *Liquid Crystals, Applications and Uses*: by B. Bahadur, World Scientific Publ., 1, Chapt. 14 (1990)
18. S. Kundu, S. Sinha Roy, T. Pal Majumder, S. K. Roy: Ferroelectrics **243**, 197 (2000)
19. S. L. Smorgon, A. V. Barannik, V. Ya. Zyryanov, E. P. Pozhidaev, A. L. Andreev, I. N. Kompanets, D. Ganzke, W. Haase: Mol. Cryst. Liq. Cryst. **368**, 207 (2001)

20. V. Ya. Zyryanov, S. L. Smorgon, V. F. Shabanov, E. P. Pozhidaev: Mol. Mat. **9**, 139 (1998)
21. E. P. Pozhidaev, S. L. Smorgon, A. L. Andreev, I. N. Kompanets, V. Ya. Zyryanov, S. I. Kompanets: Ferroelectrics **212**, 153 (1998)
22. V. Ya. Zyryanov, E. P. Pozhidaev, S. L. Smorgon, V. A. Barannik, V. V. Prasnjakov, A. L. Andreev, I. N. Kompanets, S. A. Shevchenko, D. Ganzke, W. Haase: Ferroelectrics **243**, 179 (2000)
23. V. Ya. Zyryanov, S. L. Smorgon and V. F. Shabanov: JETP Lett. (Rus.) **57**, 15 (1993)
24. V. Ya. Zyryanov, S. L. Smorgon and V. F. Shabanov: Ferroelectrics **143**, 271 (1993)
25. V. Ya. Zyryanov, S. L. Smorgon, V. F. Shabanov, E. P. Pozhidaev: SID 94 Digest **25**, 605 (1994)
26. V. Ya. Zyryanov, S. L. Smorgon, V. F. Shabanov, E. P. Pozhidaev: Proceedings SPIE **2731**, 188 (1996)
27. V. Ya. Zyryanov, S. L. Smorgon, V. F. Shabanov, E. P. Pozhidaev, A. L. Andreev, I. N. Kompanets, P. Maltese, W. Haase: Proceedings SPIE **2972**, 107 (2001)
28. V. Ya. Zyryanov, S. L. Smorgon, V. F. Shabanov, E. P. Pozhidaev, A. L. Andreev, I. N. Kompanets, S. T. Shin: Proceedings SID "Asia Display '98", 1037, Seoul, Korea (1998)
29. V. Ya. Zyryanov, S. L. Smorgon, A. V. Shabanov, E. P. Pozhidaev, A. L. Andreev, I. N. Kompanets: J. of Optical Technology (Rus.) **66**, 121 (1999)
30. S. Chandrasekhar, *Liquid Crystals* (Cambridge University Press, 1977)
31. E. P. Pozhidaev, S. L. Smorgon, A. L. Andreev, I. N. Kompanets, V. Ya. Zyryanov, S. Shin: Trends in Optics and Photonics Series (TOPS) **14**, 94 (1997)
32. A. L. Andreev, E. P. Pozhidaev, I. N. Kompanets, T. V. Fedosenkova, V. Ya. Zyryanov, S. L. Smorgon, T. Weyrauch, W. Haase: Ferroelectrics **243**, 189 (2000)
33. H. Molsen, H. S. Kitzerov: J. Appl. Phys. **75**, 710 (1994)
34. V. Ya. Zyryanov, S. L. Smorgon, A. V. Shabanov, A. L. Andreev, E. P. Pozhidaev, I. N. Kompanets: 16^{th} *Intern. Liquid Crystal Conf., Kent, USA,* Abstracts, 168 (1996)
35. E. P. Pozhidaev, D. Ganzke, A. L. Andreev, A. P. Chervonkin, W. Haase: 5^{th} *Intern. Symposium on Relaxation Phenomena in Dielectric and Magnetic Systems*, Darmstadt, Germany, Abstracts, O-36 (2002)
36. E. P. Pozhidaev, S. A. Pikin, D. Ganzke, S. A. Shevtchenko, W. Haase: Ferroelectrics **246**, 235 (2000)
37. L. A. Beresnev, V. G. Chigrinov, D. I. Dergachev, E. P. Pozhidaev, J. Fünfschilling, M. Schadt: Liquid crystals **5**, 1171 (1989)
38. C. Bahr, G. Heppke: Mol. Cryst. Liq. Cryst. Lett. **4**, 31 (1986)
39. D. Ganzke: Ph.D thesis, Technische Universität Darmstadt, Deutschland (2002)
40. E. P. Pozhidaev, D. Ganzke, V. Ya. Zyryanov, S. L. Smorgon, W. Haase: Liquid Crystals **29**, 1305 (2002)
41. T. Carlsson, B. Zeks, C. Filipic, A. Levstik: Phys. Rev. A **42**, 877 (1990)
42. E. Demikhov: Europhys. Lett. **25**, 259 (1994)

43. H. S. Kitzerow: Liq. Cryst. **16**, 1 (1994)
44. R. Bartolino, N. Scaramuzza, E. S. Barna, A. Th. Ionescu, L. A. Beresnev, L. M. Blinov: J. Appl. Phys. **84**, 2835 (1998)
45. F. Dubois, A. Daoudi, C. Legrand, J. M. Buisine, V. Laux: 5^{th} *Intern. Symposium on Relaxation Phenomena in Dielectric and Magnetic Systems*, Darmstadt, Germany, Abstracts, P-3 (2002)

5.7 Dielectric behavior of phases formed by bent-shaped molecules

H. Kresse

5.7.1 Introduction

5.7.1.1 General remarks

The ferroelectricity of liquid crystalline samples as presented by M. Glogarova (Sect. 5.3) of this book and the related theoretical description by B. Zeks in Sect. 5.1 is based on a reduction of the symmetry in tilted liquid crystalline phases of optically active molecules [1, 2]. Contrary to it banana-phases B can be formed by non-chiral bent-shaped molecules as result of steric interactions [3]. In order to discuss this problem more general, the reorientation of molecules will be briefly described. Figure 5.75 shows the reorientation of an ideal rod-like molecule about its short axis in a nematic phase. The selected molecule is surrounded by the grey painted additional potential barrier U(θ) which describes the influence of other molecules in the nematic phase and results during reorientation in a partial parallel orientation of the rods. The dependence of U(θ) on the rotation angle θ with respect to a second molecule

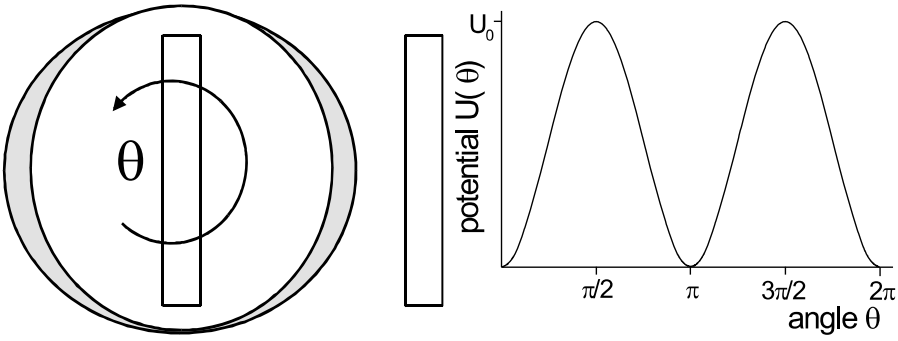

Fig. 5.75. (**a**) Potential of a rod-like molecule during reorientation about the short molecular axes. The potential is grey illustrated. (**b**) Potential according to Maier and Saupe [4]

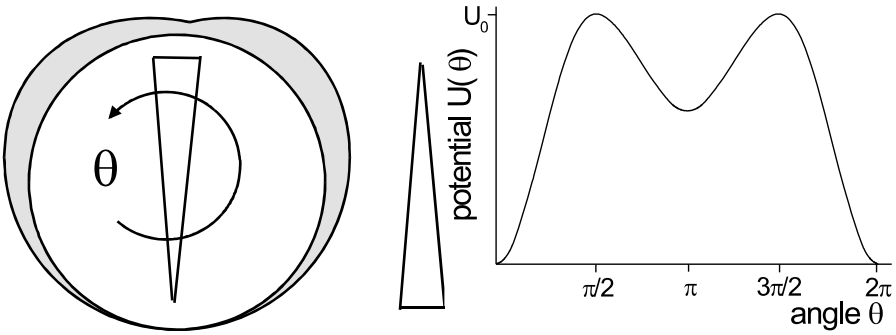

Fig. 5.76. Potential of a wedge-like molecule during rotation about the short molecular axes. The situation for $\theta = 0$ is illustrated in (**a**)

oriented in direction of the main axes is given at the right side of the picture according to the model by Martin et al. [4]. It reflects the uniaxial character of the nematic phase.

If now the molecule under consideration is wedge-like shaped, the barrier during rotation changes, specially in such a way that the positions at $\theta = 0$ and $\theta = \pi$ are not equivalent as shown in Fig. 5.76. Thus, a preferred antiparallel orientation of the long axes of the molecules can be expected in the short range order which results in a compensation of the longitudinal molecular dipole components (antiparallel dipole correlation). Due to this a decrease of the static dielectric constant in direction of the main axis ($\varepsilon_{||0}$) is measured [5]. Optically the sample still can be regarded as a uniaxial system. The second problem is related to the reorientation of the molecules about their long axis.

If now the molecules are bent-shaped an additional barrier $U(\varphi)$ during reorientation about the angle φ can appear which can look like that given in

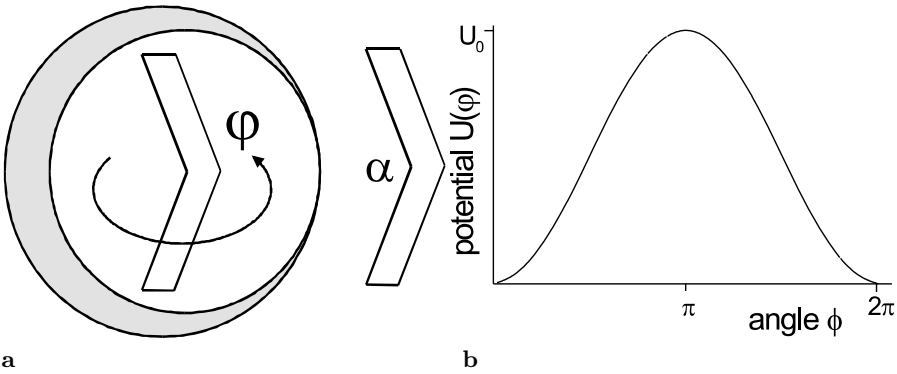

Fig. 5.77. Potential of a bent-shaped molecule during rotation about the long molecular axes with respect to a neighboring molecule. α - bent angle

Table 5.5. X-ray pattern and structure models of different B phases according to Diele and Wirth [8]

phase	X-ray non-oriented	X-ray oriented	structural model	remarks
B_1	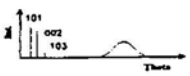			2D structure, tilt of the molecules; mosaic texture; order parameter: S: 0.82..0.85
B_2	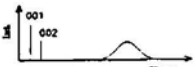	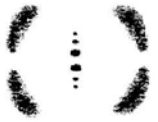	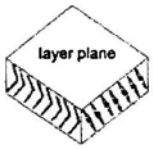	tilt of the molecules, chiral smectic layers; antiferroelectric structure; fan-shaped or schlieren texture; S: ~ 0.8
B_5	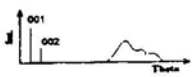	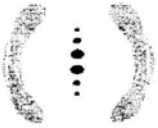	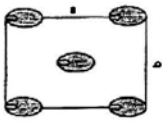	tilt of the molecules, chiral smectic layers; antiferroelectric structure; fan-shaped or schlieren texture; S: ~ 0.82
B_6				tilt of the molecules, intercalated structure; fan-shaped or schlieren texture; S: ~ 0.8
B_7	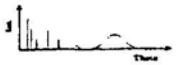	up to now no orientation with common methods		probably 2D structure; screw-like growth of nuclei and texture features indicate a helical superstructure

a **b**

Fig. 5.78. Possible arrangements of two bent-shaped molecules: (**a**) ferroelectric short range order, (**b**) compensation of the perpendicular dipole components

Fig. 5.77. A possible analytical expression could be $U(\varphi) = U_0 \ \sin^2(\varphi/2)$. In the case where the thermal energy $U_{th} \propto k_B T$ is smaller than $U(\varphi)$ one can expect two types of preferred lateral order of the molecules as presented in Fig. 5.78. This again results in a lot of possible arrangements of the molecules in B phases [6, 7] and in different order of ferroelectric sub-units within one phase. The last problem is discussed in Sect. 5.4 of this book written by M. Čepič et al. Structure models of some of the phases deduced by S. Diele at al. from X-ray pattern of bent-shaped molecules and the electro-optic behavior [8] are shown in Table 5.5. This Table contains the X-ray pattern of a non-oriented sample and a sketch of an oriented one. Specially the outside reflections give a good impression of the fluctuations of the lateral distances. A structure model deduced from the pattern is given in the next column. S in the last column means the degree of order. This Table will be discussed later together with the results of dielectric investigations. $U(\varphi)$ has to be also a function of the bent angle α. The simple analytical expression $U(\varphi, \alpha) = U_0 \cdot \sin^2(\varphi/2) \cdot \sin^2(3\alpha/4)$ agrees in first approximation well with the experimental finding that stable phases are obtained at about $\alpha = 2\pi/3$ and the above discussed limiting case for $\alpha = 0 (U(\varphi, \alpha) = 0)$. From the side of chemical structure and its dynamics we have to consider deviations from this simplified model of the molecular shape and to regard α as a function of temperature due to conformation changes.

5.7.1.2 Dielectric measurements

How are all of these effects reflected in the dielectric behavior? First of all, that part of the molecule which is strongly affected by the influence of the surrounding must exhibit a permanent dipole moment. Thus, it can be used as a sensor for the dipolar order and dynamics. To relate the observed dielectric effects to the molecular structure it is also important to orient the sample [9]. This possibility could not be used (exception [10]) for characterization of the different B phases because of experimental problems (no orientation in low magnetic or electric fields, and too long orientation time in relation to chemical stability).

Furthermore measurements in different phases are needed to see the change of the parameters at the phase transitions. In most of the cases a description of the measured complex dielectric function $\varepsilon^*(\omega) = \varepsilon'(\omega) - \mathrm{i}\varepsilon''(\omega)$ by two Cole–Cole mechanisms (terms 1–3), a conductivity contribution (term 4) and term 5 for the capacitance of the double layer at low frequencies, is useful:

$$\varepsilon^*(\omega) = \varepsilon_2 + \frac{\varepsilon_0 - \varepsilon_1}{1 + (i\omega\tau_1)^{1-\alpha_1}} + \frac{\varepsilon_1 - \varepsilon_2}{1 + (i\omega\tau_2)^{1-\alpha_2}} - \frac{iA}{f^M} + \frac{B}{f^N} \tag{5.203}$$

Here ε_i are low and high frequency limits of the dielectric constant, $\omega = 2\pi f$ (f = frequency), $i = \sqrt{-1}$, τ_1, τ_2 are the relaxation times, α_1, α_2 = Cole–Cole distribution parameters of the related relaxation process and A ($\kappa = 2{\cdot}A{\cdot}\pi{\cdot}\varepsilon^0$, if $N = 1$; $\varepsilon^0 = 8.85 \cdot 10^{-12}$ F/m) the conductivity term as well as M, B and N as further fitting parameters responsible for the slope of conductivity and capacity of the double layer. A superposition of the last three terms can be observed in some cases at low frequencies. Furthermore effects related to ion mobility can occur at frequencies between 10^{-3} and 10^{-2} Hz. In all of these cases the results of the fitting procedure were critically analyzed with respect of the standard deviation of the related fitting parameters.

5.7.2 The B_1 phase

Results of dielectric measurements in the isotropic and the B_1 phase of sample **1** (Cr 343 B_1 403 I) are presented in Fig. 5.79 [11]. In the isotropic phase

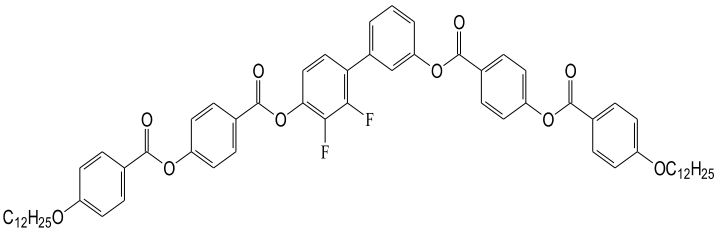

1

only one relaxation range at about 1 MHz can be seen which is super-imposed by the formation of a standing wave in the metallic measuring cell. The high frequency limit permittivity of this relaxation process was calculated to be about 5. Thus, there must exist a second dielectric relaxation process at frequencies $f > 10$ MHz which reduces the dielectric constant to less than 3. This should be related to the fast motions of the terminal –OR dipoles and libration of dipoles in the central part of the molecule **1**. In the B_1 phase two relaxation ranges were detected, the first at high frequencies (0.3 MHz) and the second at 1 kHz. The low frequency absorption can also be observed in samples consisting of symmetrical molecules [12]. Thus, this motion should

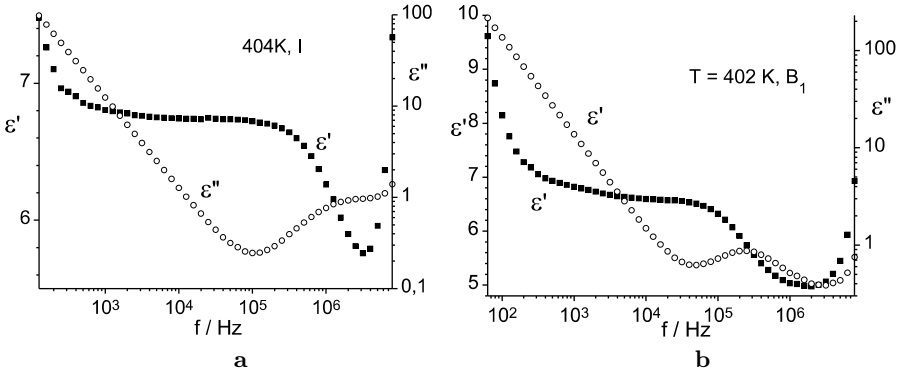

Fig. 5.79. Dielectric function (dispersion ε' and absorption ε'') curves of sample **1** in the isotropic (**a**) and the B_1 (**b**) phases

not be related to the reorientation about the two short molecular axes. The high frequency process is caused by the reorientation around the long axes because molecule **1** mainly shows dipole moments perpendicular to the long axes. In relation to other samples, where this process is observed in the GHz range [13], it is shifted to lower frequencies due to the extended shape of molecule **1**. This problem will be discussed in the next chapter related to the B_2 phase.

In order to see the change of the dielectric losses measurements in the pretransition range were performed. They are shown in Fig. 5.80. Three conclusions can be made:

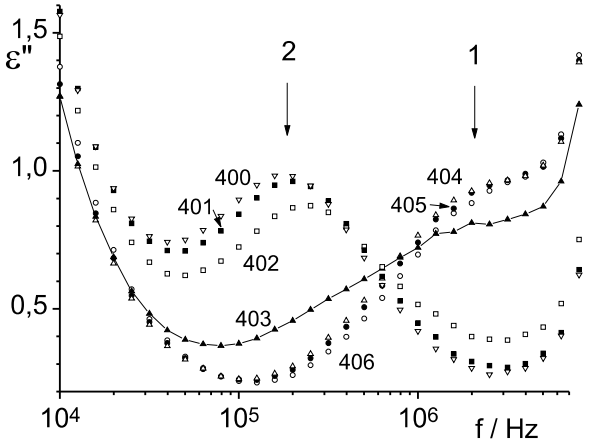

Fig. 5.80. Dielectric loss at temperatures near to the I/B_1 transition. The numbers indicate the temperatures in K

- at first a stepwise decrease of the relaxation frequency at the phase transition I/B_1 can be seen,
- secondly, there is no big step of the absorption intensity at this phase transition,
- and thirdly in the same way in which the absorption intensity in the isotropic phase decreases (arrow 1, data are superimposed by the standing wave) that of the B_1 phase increases (arrow 2, see $T = 403$ K, line graph).

Specially the last observation confirms that the mechanism is the same in both phases, namely the reorientation around the long axes. The relaxation times and the limits of the dielectric constants calculated according to (5.203) are presented in Fig. 5.81a and b. The strong increase of the relaxation time at the I/B_1 transition is accompanied by a relatively small change of the dielectric constants. If we consider the high frequency mechanism as reorientation of the longitudinal dipoles we can regard ε_1 as a limit of the dielectric constant which can be compared to that of the isotropic phase. The small decrease of ε_1 at the phase transition points to the antiparallel arrangement of the dipoles as given in Fig. 5.78b. This is in agreement with the results from X-ray investigations. Small units of 2–3 molecules build up a columnar rectangular order [8] as shown in the model structure of Table 5.5.

Differences of the dielectric constants between the two experimental runs may be related to different orientations of the sample. The low frequency relaxation which can be also observed in symmetrical molecules [12] may be an effect of the super-structure.

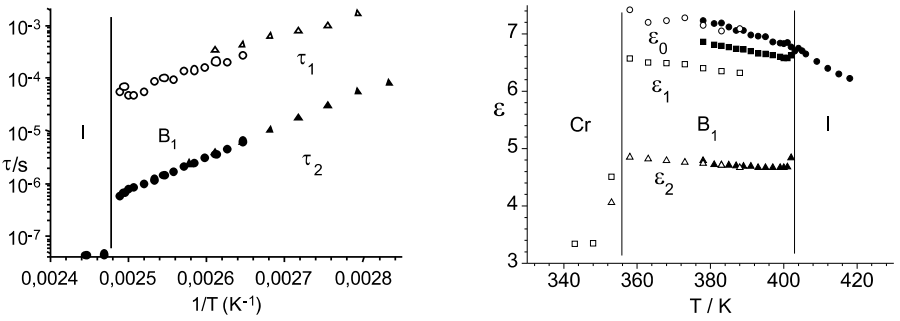

Fig. 5.81. (**a**) Dielectric relaxation times of sample **1**. The data were obtained from two experimental runs. For every run the sample was heated into the isotropic state and cooled down. The errors of τ_1 were calculated to $\pm 50\%$, that of τ_2 in the B_1 phase to $\pm 10\%$ and in the isotropic state to $\pm 30\%$.
(**b**) Limits of the dielectric constants of sample **1** obtained from two different cooling runs. There are strong deviations of the ε_1 data (*open* and *closed squares*) and small of ε_2 (*open* and *closed triangles*), but the related relaxation times τ_2 (*crosses* and *closed triangles*) agree within the error. This effect may indicate different orientations of the sample

5.7.3 The B_2 phase

As seen in Table 5.5 the molecules are tilted in the classical B_2 phase. The arrangement of the molecules is ferroelectric in the short range within one layer as presented in Fig. 5.78a. The question is now, how the molecules are ordered to each other in different layers? This problem is discussed and experimentally proved by Link et al. [6]. The data which will be presented now are obtained from statistically distributed samples, because the bias voltage of 36 V of our dielectric equipment was not high enough to orient the samples in a 50 µm cell. To our knowledge there exist only one dielectric measurement on an oriented sample in an ITO-cell [10]. In this case the resistance of the ITO-layer did not allow to measure at higher frequencies. Furthermore Górecka et al. [14] have shown that the absorption intensity of chiral bent-shaped molecules in very thin ITO-cells behaves like the Goldstone mode. We were unable to observe such effects in non-chiral samples.

Results based on comparative measurements on the two homologous **2** and **3** [15] will be presented in the following part. Sample **2** is shown below together with the main relaxation mechanism as discussed in the introduction. Sample **3** contains only an additional Cl-atom in 6-position which makes the molecule symmetric. This means one cannot see the reorientation around the *a* axis for sample **3** using the dielectric method. Only the reorientation about the long molecular axis (*b*) can be detected. Sample **3** could be well

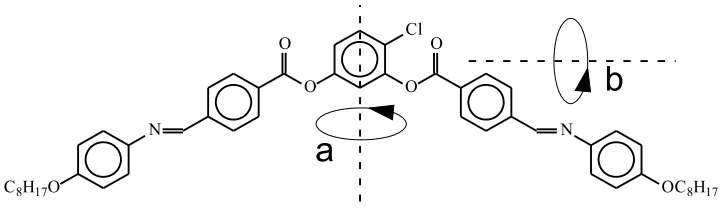

sample **2**: Cr 393 B_2 406 I
sample **3**: Cr 399 N 421 I (I 421 N 370 S_C 350 Cr)
(The S_C phase is a modulated bilayer [15])

oriented in the nematic phase and shows a negative dielectric anisotropy [15]. Perpendicular to the nematic director an intensive dielectric absorption was observed. No relaxation related to the reorientation around the short axes of the molecules in both the isotropic and the nematic phase was found. The dielectric constants of sample **3** show no deviation from that observed in other nematic samples [9].

Dielectric data of sample **2** for a selected frequency range are given in Fig. 5.82. The intensity of the dielectric absorption and the low frequency limit of the dielectric constants increase considerably at the phase transition from the isotropic to the B_2 phase. The increase of the real part ε'

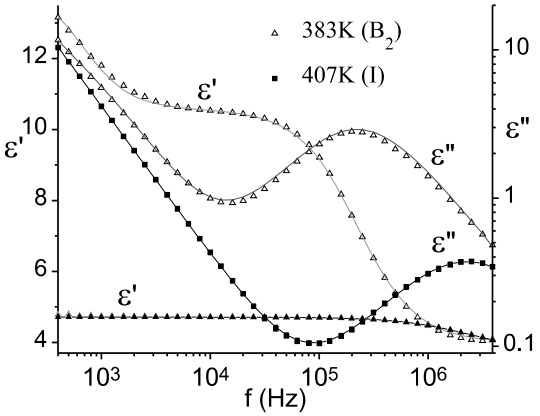

Fig. 5.82. Dielectric function of sample **2** shown in a selected frequency range

of the complex dielectric permittivity ε^* in the B_2 phase is caused by an additional absorption mechanism at lower frequencies and an intensive relaxation in the MHz-range. The separation of the low-frequency absorption due to conductivity and double layer from the complex dielectric spectrum is difficult to do in a lot of cases. The data analysis according to (5.203) results in the limits of dielectric constants presented in Fig. 5.83. The low frequency process was detected only in theB_2 state and not in the SmC phase of sample **3**. For comparative considerations the relaxation frequencies of the high frequency process ($f_{R2} = 1/2\pi\tau_2$) and the related dielectric increments $\Delta\varepsilon_2 = \varepsilon_1 - \varepsilon_2$ of sample **2** as well as $\Delta\varepsilon_\perp = \varepsilon_{0\perp} - \varepsilon_{1\perp}$ of sample **3** (there exists only one mechanism seen perpendicular to the ne-

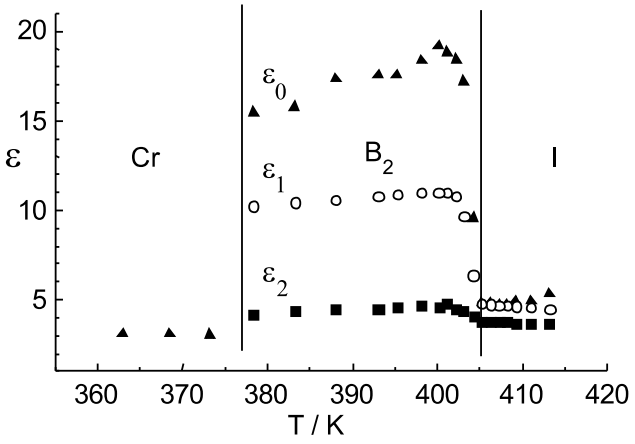

Fig. 5.83. Limits of the dielectric constant of sample **2** in the isotropic and the B_2 phase

matic director) in the mesophases are compared with each other in Fig. 5.84. The increments of sample **3** could not be estimated in the isotropic state due to its high relaxation frequency. It should be noted that the relaxation times of both compounds are in the same order of magnitude and the increments of the statistically oriented B_2 phase are much higher than those of the oriented nematic sample. These are the reasons why we are discussing as mechanism the reorientation about the long axes and why we assume in the lateral direction a strong positive dipole correlation in the B_2 phase. The relaxation frequency of sample **2** shows the expected behavior: a pronounced step at the I/B_2 transition. The higher relaxation frequency of sample **3** should also be caused by a lower bent angle (see Fig. 5.77).

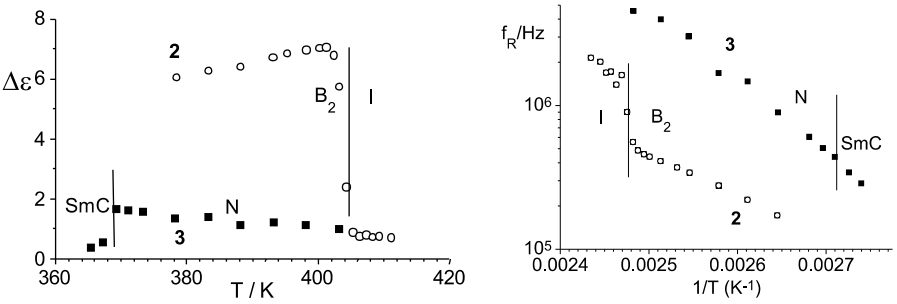

Fig. 5.84. (**a**) Dielectric increments of the high frequency process of sample **2** and of the only relaxation seen in the perpendicular direction of sample **3**. (**b**) Relaxation frequencies of the absorption at high frequencies of the samples **2** and **3**

The next part gives answer to the question of the molecular origin of the increase of ε_1 at the I/B_2 transition. For discussion of this problem sample **4** with the polymorphism Cr 341 B_2 400 I [16] was synthesized and investigated in a wide frequency range. Experimental data of the dielectric function are shown in Fig. 5.85. The low conductivity of sample **4** did allow to calculate the relaxation data of both mechanisms with high accuracy. Relaxation times and related activation energies are given in Fig. 5.86a. The activation energies of the high and low frequency mechanisms agree within the error with each other. Comparative considerations of results on symmetrical samples [17], of the relaxation times [16], of the surface structure by atomic force microscopy [18] and of theoretical models [19] leads us to the preliminary conclusion that the low frequency relaxation results from a collective motion in the B_2 phase, and not from the hindered reorientation of molecules around the short axes (see also [20]). The limits of the dielectric permittivity computed according to (5.203) are presented in Fig. 5.86b. They are smaller than those of sample **2**. A remarkable step of the dielectric incre-

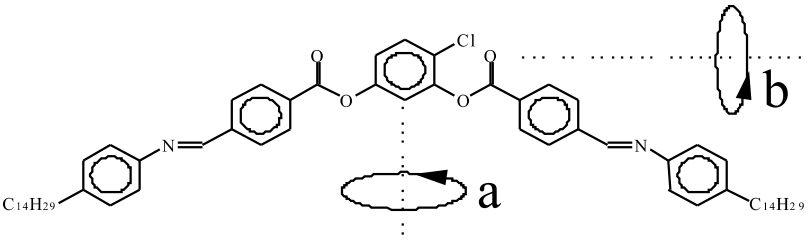

4

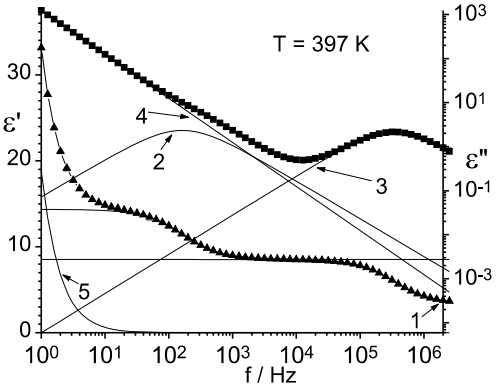

Fig. 5.85. Measured dielectric function of sample **4** according to [16]. The numbers are related to the different terms of (5.203). The points are giving the sum of these terms

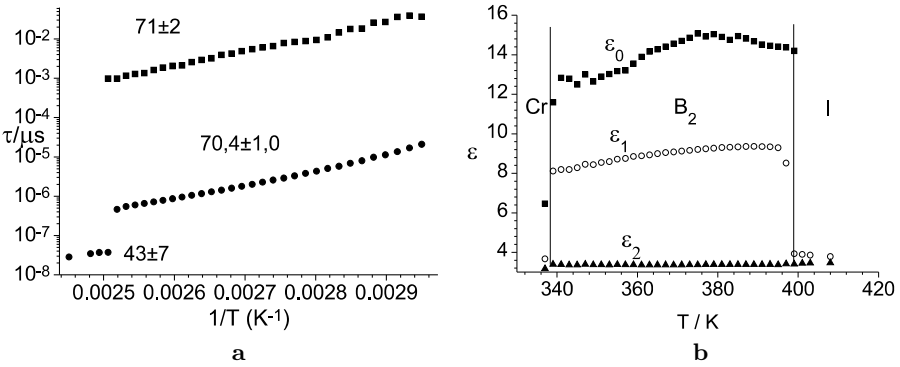

Fig. 5.86. (**a**) Relaxation times of sample **4** in different phases. The numbers given are the activation energies in kJmol^{-1}. (**b**) Calculated limits of the dielectric constants of sample **4**

ment $\Delta\varepsilon_2 = \varepsilon_1 - \varepsilon_2$ appears for the reorientation about the long molecular axis from 5 in B_2 to less than 0.4 in the isotropic state to about 6 in the B_2 state. Furthermore the ε_2 data of sample **4** are much lower than those of

sample **2**. This effect can be explained by the fast reorientation of the alkyloxy groups of sample **2** ($\tau < 10^{-8}$ s which is not seen in our experiments). If the terminal dipoles show a separate relaxation range these groups cannot be responsible for the strong increase of the dielectric increment at the I/B_2 transition. Therefore the appearance of the ferroelectric short range order is mainly connected with the chemical structure of the stiff main part of the molecule.

An additional evidence for the importance of the stiff part of the molecule can be obtained by changing the dipole moment. Therefore the below given homologs were synthesized and characterized by the dielectric method [21]. The difference of the increments $\Delta\varepsilon_2$ of sample **5** and **6** results from the fluorine-dipole in the biphenyl part situated at different positions. Thus, the fluorine dipole in position 4 (sample **6**) gives always a dipole component in direction of the bend and due to this the perpendicular dipole moment increases. In sample **5**, having the fluorine in position 1, directly besides the carboxyl group, the dipole moment is partially compensated by the neighboring carbonyl group and decreases the perpendicular dipole moment. This results in a much smaller increment. For sample **6** an increment between that of **4** and **5** was found. The class of fluorinated samples is stable at higher temperatures and shows relatively low clearing temperatures. Therefore dielectric measurements in the isotropic phase were done. The dielec-

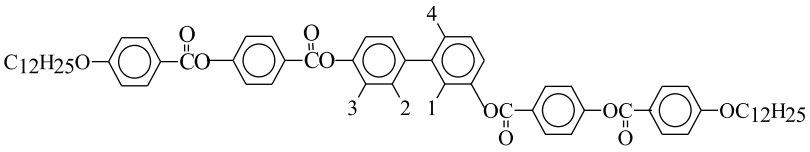

Sample **5**: 1=F; 2, 3, 4 = H Cr 393 B_2 421 I
Sample **6**: 4=F; 1, 2, 3 = H Cr 388 B_2 426 I
Sample **7** 2=F; 1, 3, 4 = H Cr 376 B_2 418 (415 B_2 321 Cr)

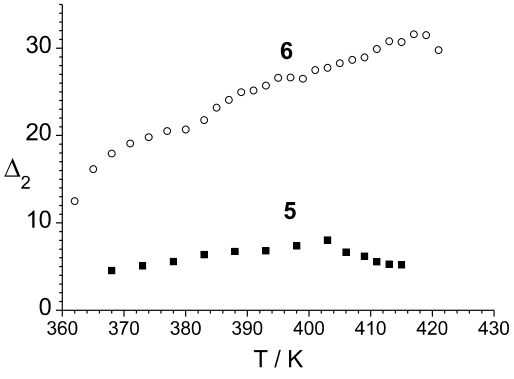

Fig. 5.87. Dielectric increments of the high frequency relaxation of samples **5** and **6**

tric constants presented in [21] show a clear tendency of stronger increase by approaching the phase transition into the B_2 phase at 415 K. They give evidence for the formation of ferroelectric clusters within the isotropic phase, too.

5.7.4 The CP_A phase

Till now only sample **8** is known which exibits the CP_A [22] or the orthogonal achiral biaxial smectic A phase and a classical SmA modification. Such phase transitions will be discussed later in Sect. 5.7.6. The only difference between the CP_A and the B_2 phase is that in the first case the bent-shaped molecules are ordered orthogonally within the layers whereas in the B_2 modification the molecules are tilted. There exist no in-plane order in both phases. The

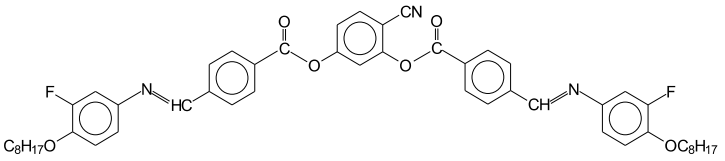

8

Cr 346 CP_A 418 SmA 453 I

sample with the CP_A modification shows antiferroelectric switching like the B_2 phase. The real part of the dielectric function in the isotropic and the CP_A phase is presented in Fig. 5.88.

These experimental data show that the dielectric function increases by about one decade on going from the isotropic to the CP_A state. The dielectric

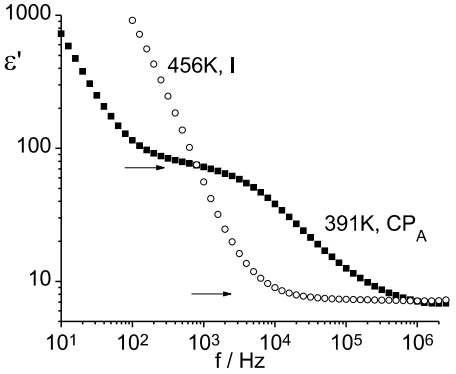

Fig. 5.88. Dielectric dispersion as function of frequency of sample **8** in the isotropic and the CP_A phases. The *arrows* are related to the low frequency limits of the dielectric constants

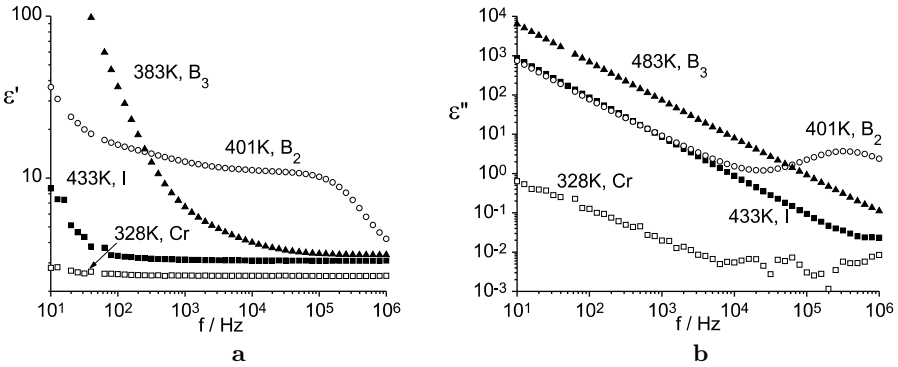

Fig. 5.89. (**a**) Real part of the dielectric function of sample **9** in different phases. (**b**) Imaginary part of dielectric function of of sample **9**

constant of sample **8** is much higher than that of sample **4** (see Fig. 5.89) due to the strong dipole moment in the central part of the molecule. For comparison with other data it should be noted that the dielectric constants by arrows marked in Fig. 5.88 can be regarded as ε_1 and ε_2, respectively. In contradiction to sample **4** no low frequency absorption in sample **8** could be separated. Whether this is a typical effect or only a result of the high conductivity super-imposing the low-frequency relaxation is not clear at the moment. In any case Fig. 5.88 gives clear evidence of a ferroelectric short range order in the CP_A phase. This underlines the difference from the classical SmA phase.

5.7.5 The B_3 phase

First dielectric investigations on the B_3 phase were carried out on sample **9**. Due to a lot of different sharp X-ray reflections this phase was classified as being a solid state [23]. The components of the complex dielectric permittivity shown in Fig. 5.89a show the expected behavior for the isotropic and the B_2 phases, but a strong increase of ε' at low frequencies and a high frequency limit which is higher than that of the isotropic phase. The related absorption data are shown in Fig. 5.89b. The B_3 phase shows the highest ε''-values in

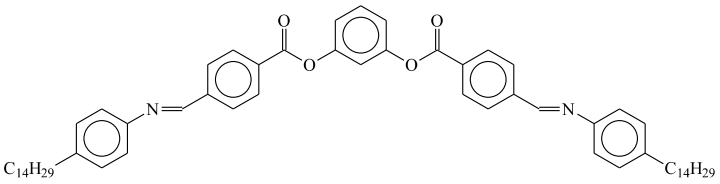

9

Cr 94.6 B_3 132.8 B_2 156.3 I; I 150.2 B_2 122.7 B_3 56.6 Cr

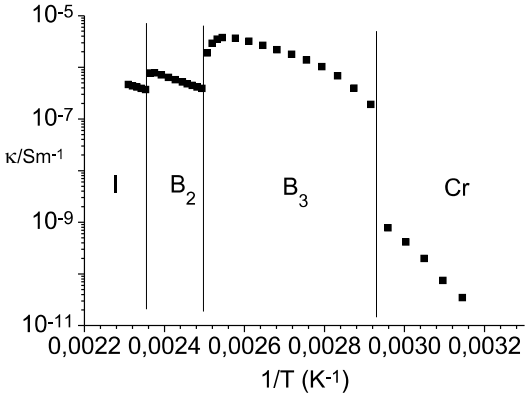

Fig. 5.90. Conductivity of sample **9** versus the reciprocal temperature

relation to those of other modifications. Measurements down to 1 mHz gave no evidence for a maximum related to a low-frequency absorption. Thus, two reasons can be discussed for this anomaly: a very intensive low frequency dielectric absorption of Debye-type with a relaxation frequency below 10^{-3} Hz or an increase of the conductivity. Both effects are also in agreement with the increase of the real part of the dielectric permittivity at low frequencies shown in Fig. 5.89a. The interpretation as conductivity is presented in Fig. 5.90.

5.7.6 The B_4 phase

Sample **10** showing the B_2/B_4 transition is given below [24]. For the B_4 phase several diffuse X-ray reflections in the wide angle region were found [25]. Thus, it may be a phase with higher order within the layers or a disordered solid modification. Figure 5.91a shows only the high frequency limits of dielectric constant ε_2 as calculated from measurements in the MHz range [26]. The B_2 phase exhibits the two expected relaxation ranges. The limits of the dielectric function in the B_2 phase were calculated to $\varepsilon_0 = 18$ and $\varepsilon_1 = 12$ and surprisingly, in the B_4 phase to 6 at low frequencies. The difference between the

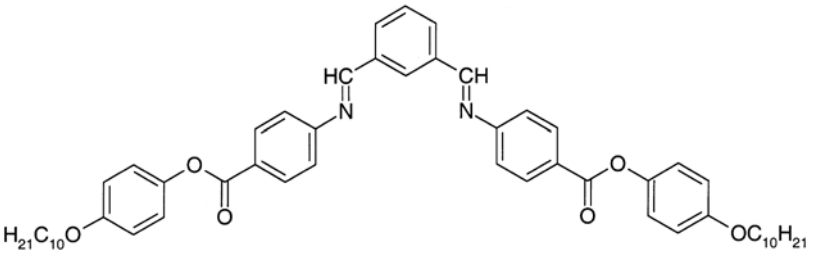

10

Cr 397 B_4 420 B_2 426 (heating); I 424 B_2 406 B_4 (cooling)

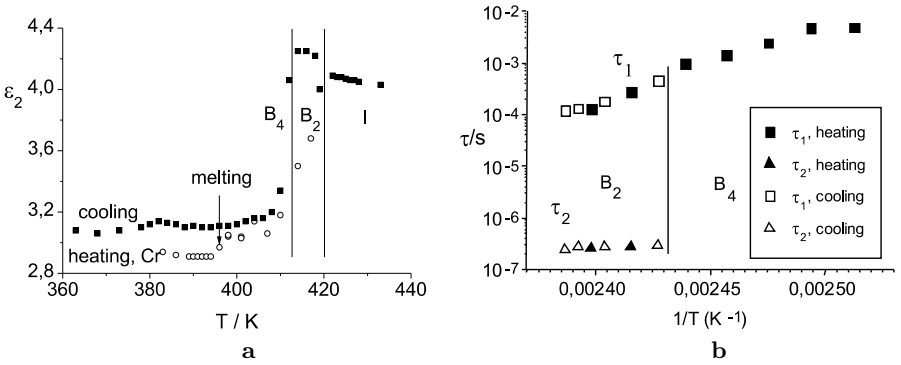

Fig. 5.91. (**a**) High frequency limits of the dielectric constant of sample **10**. (**b**) Relaxation times of sample **10** obtained by heating and cooling according to [24]

high frequency limits of dielectric permittivities obtained at 390 K during cooling and heating (see Fig. 5.91a) indicates that there is also dynamics in the B_4 phase at higher frequencies. The only relaxation process found in the B_4 phase on cooling and heating seems to be a continuation of the low-frequency relaxation in the B_2 phase. Therefore it should be related to the dynamics of the super-structure seen also in the AFM measurements [26]. From the dynamical point of view the B_4 phase may be a low temperature phase with a higher order within the layers. Further investigations are necessary to solve this problem.

5.7.7 The B_5 phase

Only sample **11** containing the B_5 phase was investigated by the dielectric method [27]: The structure of the B_5 phase is similar to that of the B_2 modification. The only difference is that the B_5 phase is characterized by the beginning of a positional order within the layers.

For the given sample **11** three different phases of B_2 type, the B_5 phase and a low temperature phase were detected. Experimental data obtained in the B_2' and the B_5 phases are shown in Fig. 5.92. A low frequency absorption at about 100 Hz can be seen in the B_2' phase. Contrary to it the separation of a low frequency mechanism in the dispersion curve the B_5 phase is not significant.

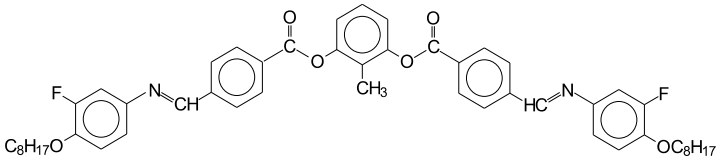

11

I 426 B_2 420 B_2' 415 B_2'' 409 B_5 385 B_X 376 Cr

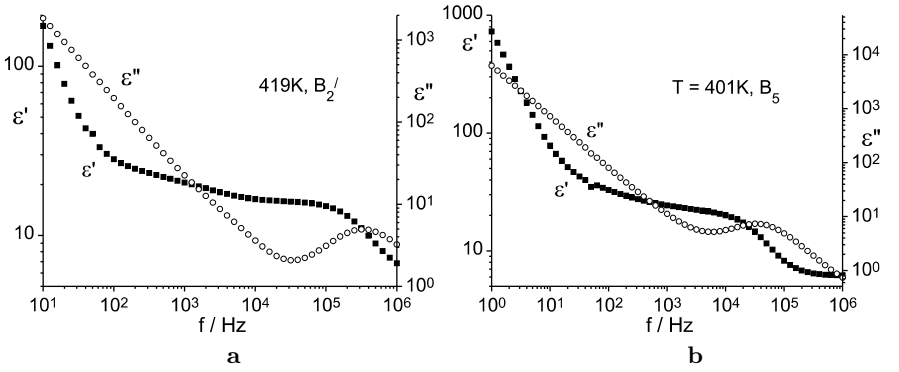

Fig. 5.92. Dielectric functions of sample **11** measured in the B_2' (**a**) and the B_5 (**b**) phases

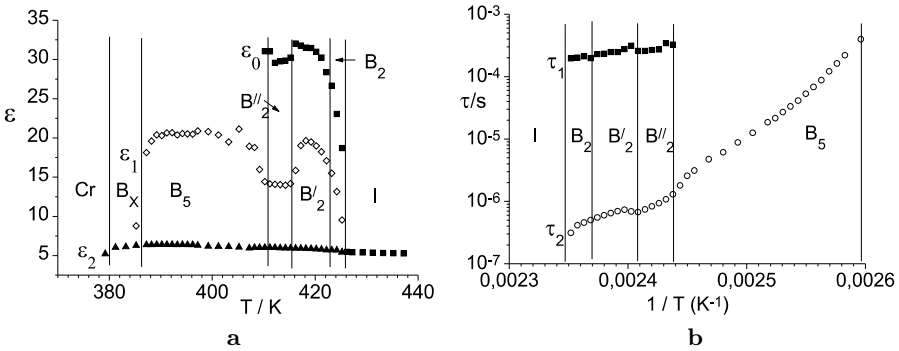

Fig. 5.93. (**a**) Limits of the dielectric constant of sample **11**. (**b**) Relaxation times of sample **11** in different phases

Therefore the existence of this mechanism is still open. An absorption process at 0.1 MHz can be seen in both phases. The related limits of the dielectric constants are shown in Fig. 5.93a. There is no difference between the ε_1 data of the B_2' and the B_5 phases. This indicates that the dipoles show generally a ferroelectric short range order in both modifications. Also the relaxation times for the high frequency process τ_2 changes not remarkably at the B_2''/B_5 transition (Fig. 5.93b). Thus, B_5 can be regarded from the dynamical point of view as a modified B_2 phase.

5.7.8 The B_6 phase

As shown in Table 5.5 the tilted molecules are intercalated in the B_6 phase. Therefore the B_6 phase can be regarded as a high temperature phase of the B_1 modification. Dielectric measurements were performed on sample **12** [28]. There could be found only one relaxation mechanism related to the re-

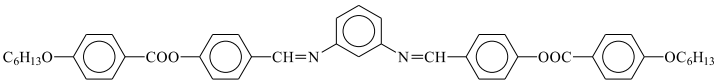

12

Cr 407 B_1 415 B_6 421 I.

orientation around the long axis. The limits of the dielectric constants in Fig. 5.94a and the relaxation times in Fig. 5.94b show no significant difference between the B_1 and the B_6 phases. The high conductivity of sample **11** did not allow to separate well the low-frequency absorption. The dielectric constant ε_1 shows a clear decrease at the I/B_6 and no change at the B_6/B_1 transition pointing to the discussed antiparallel order of the molecular dipoles.

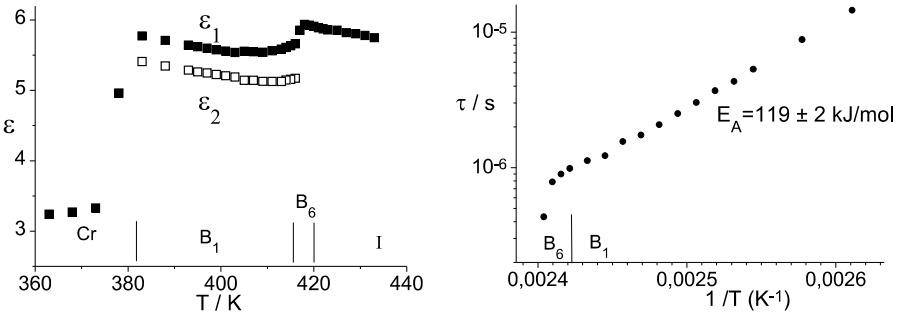

Fig. 5.94. (**a**) Dielectric constants of sample **12** according to [28]. (**b**) Relaxation times of sample **12**. The lowest value is influenced by the transition into the isotropic phase

5.7.9 The B_7 phase

The structure of the B_7 phase is not clear at the moment because no alignment of the samples was possible. An interesting observation is the screw-like growth of the nuclei at the I/B_7 transition which points to a helical superstructure. This could also be seen in AFM pictures [29]. Dielectric measurements on sample **13** [30] show an increase of the dielectric constant at the transition into the B_7 phase and also values of $\varepsilon_1 > 3$ in the low temperature phase B_X (see Fig. 5.95a). The error of the relaxation times in the isotropic phase is about 50% because of the very small increment and the influence of conductivity. It is obvious that a strong hindrance of the reorientation around the long axis takes place at the transition into the B_7 phase (Fig. 5.95b). The high values of the dielectric increment in the B_7 phase may be related to a collective motion of ferroelectric aggregates with a higher relaxation time.

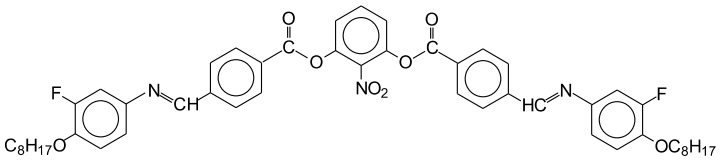

13

B_X 415 K B_7 440 K I; I 436 K B_7 403 K B_X

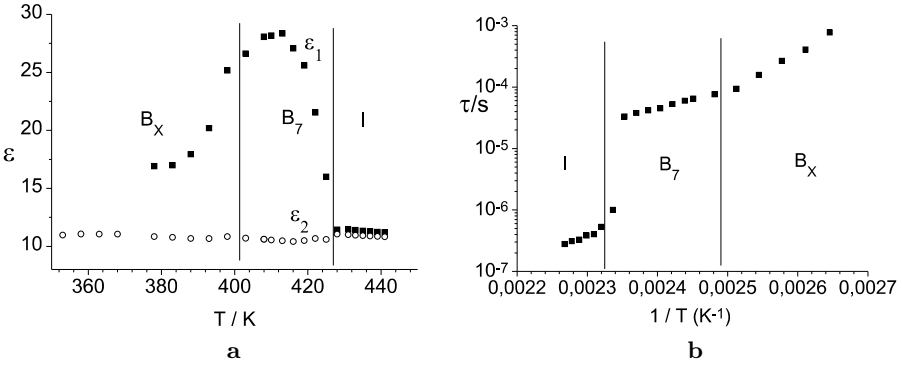

Fig. 5.95. (**a**) Dielectric constants of sample **13**. (**b**) Relaxation times of sample **13**

This points to a higher order within the layers which exist also in the B_X phase. At the transition into the B_X phase a reduction of the dielectric constant takes place pointing to changes in the super-structure. The same effect was detected in another sample. In this case the low temperature phase was named B_8 , a phase [29] showing an X-ray pattern different from that of the discussed B_X modification.

5.7.10 The transition between classical and banana phases

The general behavior for the reorientation of a bent-shaped molecule around the long molecular axis is demonstrated in Fig. 5.77. If now the potential for the hindrance of this motion is in the same order of magnitude as the thermal energy one should observe the interesting transition between classical phases without hindrance of this motion into banana phases. This situation can be realized in two ways: by lowering the thermal energy (temperature) and by increasing or decreasing of the tilt angle.

The first sample showing this exotic polymorphism was synthesized by Weissflog et al. [31]. The chemical structure of sample **14** is given below. It is interesting that the dielectric constant increases continuously from the SmA to the SmC phase and splits into two values (ε_0, ε_1) in the B_2 state (Fig. 5.96b). The strong increase of the dielectric constant specially in the SmC phase indicates the step by step formation of the ferroelectric short range order of the transversal dipoles (positive dipole correlation) as result of the more and

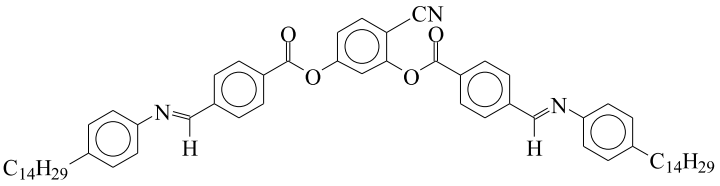

14

Cr 361 B_2 399 SmC 413 SmA 437 I

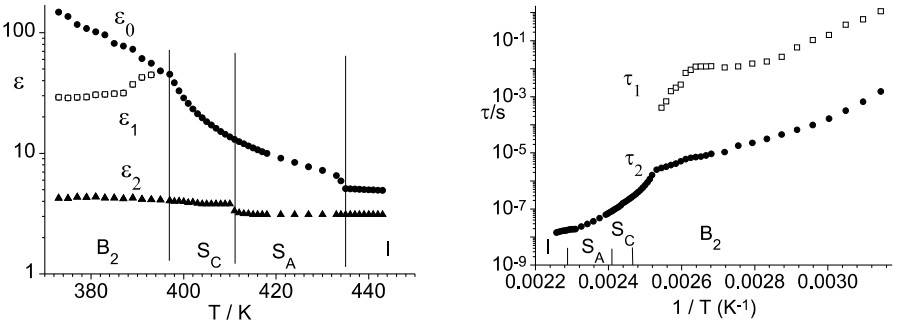

Fig. 5.96. (**a**) Limits of the dielectric constant of sample **14**. The error of the ε_0 in the B_2 phase is 50% due to the strong conductivity of the sample. (**b**) Relaxation times of sample **14**. The error of τ_1 in the B_2 phase is about 30% due the high conductivity

more stronger hindrance for the reorientation around the long molecular axis. In contradiction to the I/B_2 transition where this change takes place mainly at the phase transition temperature one can see here a continuous transition with respect to the lateral order. This means that the short range structure shown in Fig. 5.78a forms continuously. Consequently, the relaxation time τ_2 related to the reorientation about the long axes changes also continuously from the isotropic to the B_2 phase (Fig. 5.96b). The same behavior was found at the transition between the SmA and the CP_A phase [20].

Very interesting results were obtained recently on sample **15** showing the polymorphism Cr 390 (B_2 344 SmC 364 SmA 377 N 382 I): Sample 15 did allow at the first time the orientation in the nematic phase [32]. The disadvantage are the metastable liquid crystalline phases which results in crystal-

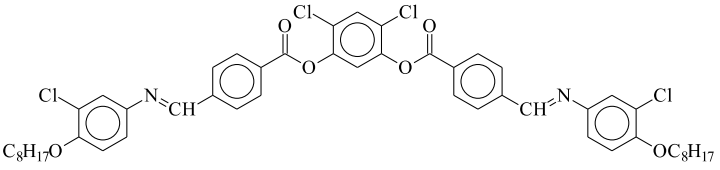

15

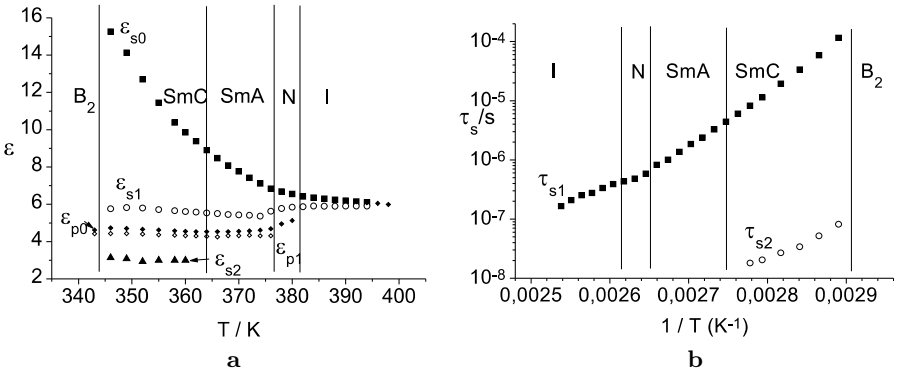

Fig. 5.97. (**a**) Limits of the dielectric constants parallel (p) and perpendicular (s) to an orienting magnetic field of sample **15**. (**b**) Dielectric relaxation times of sample **15**

lization just at the SmC/B_2 transition. From Fig. 5.97a it is obvious that the strong increase of the dielectric constant in the oriented smectic phases with decreasing temperature results from the dipole components perpendicular to the long axis. This effect develops also continuously with decreasing temperature like shown in Fig. 5.96a. Thus, the conclusions that τ_1 is related to the reorientation about the long axes and the increase of the dielectric constants at the I/B_2 results mainly from the dipole-dipole correlation are confirmed (Note that the high frequency process denoted in the B_2 phase as τ_2 was named here τ_1 in accordance with (5.203).). The second relaxation in the perpendicular direction seen at much shorter relaxation times may be caused by a local dynamics of the terminal alkyloxy-groups and librations. In the parallel direction only one absorption with small intensity and practically the same relaxation times as the τ_{1s} was observed. This relaxation should result from the fluctuations of the direction of the individual molecules (degree of order) and non-complete alignment of the sample. A reorientation about the short axis could not be seen, probably due to the symmetry of the molecule **15**.

5.7.11 Summary

Generally it can be concluded that the dielectric method is a valuable tool to study phase transitions and the behavior of the different phases formed by bent-shaped molecules. The reason for it is that dielectric investigations are sensitive to changes in the short range order and the dynamics of single molecules as well as to that of super-structures.

Acknowledgment. The author is grateful to his colleagues Dr. Diele, Dr. Hauser, Prof. Pelzl, Dr. Schlacken, Prof. Tschierske and Prof. Weissflog for discussions, Dr. Schmalfuss and Dr. Salfetnikova for experimental help as well as the DFG and the state of Sachsen-Anhalt for financial support.

References

1. S.T. Lagerwall: Ferroelectric Liquid Crystals. In: *Handbook of Liquid Crystals*, p. 515, D. Demus, J. Goodby, G.W. Gray, H.-W. Spiess, V. Vill, Eds. (Wiley-VCH, Weinheim, 1998)
2. K. Miyachi, A. Fukuda: Antiferroelectric Liquid Crystals. In: *Handbook of Liquid Crystals*, D. Demus, J. Goodby, G.W. Gray, H.-W. Spiess, V. Vill, Eds. (Wiley-VCH Weinheim p. 665, 1998)
3. T. Niori, T. Sekine, J. Watanabe, H. Takezoe: J. Mater. Chem. **6**, 1231 (1996)
4. A.J. Martin, G. Meier, A. Saupe: Symp. Faraday. Soc. **5**, 119 (1971)
5. H. Kresse, P. Rabenstein: Phys. Stat. Sol. A. **100**, 83 (1987)
6. D.R. Link, G. Natale, R. Shao, J.E. McLennan, N.A. Chlark, E. Körblova, D.M. Walba: Science **278**, 1924 (1997)
7. H.B. Brand, P.E. Cladis, H. Pleiner: Macromolecules **25**, 7723 (1992)
8. G. Pelzl, S. Diele, W. Weissflog: Adv. Mater **11**, 707 (1999)
9. H. Kresse: Dielectric Behaviour of Liquid Crystals. In: *Advances in Liquid Crystals*, G.H. Brown, Ed. (Academic Press New York, 1983) p. 109
10. G. Heppke, A. Jakli, S. Rauch, H. Sawade: Phys. Rev. E. **60**, 5575 (1999)
11. H. Kresse, C. Tschierske, G. Dantlgraber, unpublished results
12. H. Schmalfuss, D. Shen, C. Tschierske, H. Kresse: Liq. Cryst. **27**, 1235 (2000)
13. A. Axmann: Z. Naturforsch. **21A**, 290 (1965)
14. E. Gorecka, D. Pochiecha, F. Araoka, D.R. Link, M. Nakata, J. Thisayukta, Y. Takanashi, K. Ishikawa, J. Watanabe, H. Takezoe: Phys. Rev. E. **62**, 4524 (2000)
15. W. Weissflog, Chr. Lischka, S. Diele, G. Pelzl, I. Wirth, S. Grande, H. Kresse, H. Schmalfuss, H. Hartung, A. Stettler: Mol. Cryst. Liq. Cryst. **333**, 203 (1999)
16. H. Schmalfuss, W. Weissflog, A. Hauser, H. Kresse: Proc. SPIE **4147**, 109 (2000)
17. J. Salfetnikova, H. Schmalfuss, H. Nadasi, W. Weissflog, A. Hauser, H. Kresse: Liq. Cryst. **27**, 1663 (2000)
18. A. Hauser, H. Schmalfuss, H. Kresse: Liq. Cryst. **27**, 629 (2000)
19. H. Schlacken, P. Schiller, H. Kresse: Liq. Cryst. **28**, 1235 (2001)
20. S. Wróbel, W. Haase, D. Kilian, L.-C. Chien: Ferroelectrics **243**, 277 (2000)
21. J. Salfetnikova, T. Zhuchkova, G. Dantlgraber, C. Tschierske, H. Kresse: Liq. Cryst. **29**, 155 (2002)
22. A. Eremin, S. Diele, G. Pelzl, H. Nadasi, W. Weissflog, J. Salfetnikova, H. Kresse: Phys. Rev. E **64**, 51707 (2001)
23. J. Salfetnikova, H. Kresse, H. Schmalfuss, H. Nadasi, W. Weissflog: Liq. Cryst. **27**, 1663 (2000)
24. H. Kresse, H. Schmalfuss, W. Weissflog, C. Tschierske, A. Hauser: Mol. Cryst. Liq. Cryst. **366**, 505 (2001)
25. S. Diele, G. Pelzl, W. Weissflog: Liquid Crystals Today **9**, 8 (1999)
26. H. Kresse, J. Salfetnikova, H. Nadasi, W. Weissflog, A. Hauser: Liq. Cryst. **28**, 1017 (2001)
27. A. Eremin, I. Wirth, S. Diele, G. Pelzl, H. Schmalfuss, H. Kresse, H. Nadasi, K. Fodor-Csorba, E. Gacs-Baitz, W. Weissflog: Liq. Cryst. **29**, 775 (2002)
28. H. Kresse, H. Schmalfuss, W. Weissflog: Liq. Cryst. **28**, 799 (2001)
29. H. Schmalfuss, A. Hauser, H. Kresse: Mol. Cryst. Liq. Cryst. **351**, 221 (1999)
30. J. Salfetnikova, H. Nadasi, W. Weissflog, A. Hauser, H. Kresse: Liq. Cryst. **29**, 115 (2002)

31. W. Weissflog, L. Kovalenko, I. Wirth, S. Diele, G. Pelzl, H. Schmalfuss, H. Kresse: Liq. Cryst. **27**, 677 (2000)
32. H. Kresse, H. Schlacken, U. Dunemann, M.W. Schröder, G. Pelzl, W. Weissflog: Liq. Cryst. **29**, 1509 (2002)

5.8 Electrooptical studies of relaxation processes in ferroelectric liquid crystals

W. Kuczyński

5.8.1 Introduction

Electrooptic effects in liquid crystals possessing polar order have been investigated since the discovery of ferroelectricity [1]. Actually, the opposite is true: the existence of ferroelectricity in a chiral smectic liquid crystal was first demonstrated using electrooptic (EO) effects. A similar statement is valid for antiferroelectric liquid crystals. In the first papers reporting the observation of antiferroelectric behavior in smectic liquid crystals [2, 3] the electrooptic effects were used for demonstrating antiferroelectricity and for determining phase structures. The electroclinic effect was discovered by observation of electrooptic phenomena also [4].

The electrooptic effects consist in changes of optical properties due to the influence of an electric field. In liquid crystals this influence arises due to the coupling of the electric field with either the spontaneous polarization (linear effect) or the dielectric anisotropy (quadratic effect). The linear effect is dominating in ferroelectric liquid crystals. In these materials the second order dielectric effect is much weaker and is significant at higher fields only [5]. In antiferroelectric liquid crystals, the spontaneous polarization exists inside of each smectic layer [6] but in the bulk, it is almost canceled due to the nearly anti-parallel tilt directions of molecules in adjacent layers. The small residual polarization being a consequence of the helical structure usually does not exceed a few percent of the single layer's polarization and rotates around an axis perpendicular to the smectic layers plane with the same period, as the tilt direction does. For this reason, in antiferroelectric liquid crystals both electrooptic effects – linear and quadratic – appear with comparable intensity.

Investigations of polarization effects in chiral liquid crystals are usually performed using dielectric methods. Electrooptic investigations, however, can be also very useful and may deliver information inaccessible with other methods. This statement concerns, in particular, nonlinear effects, which in antiferroelectric phases (due to the mentioned compensation of polarization in each couple of smectic layers) might be even stronger than linear effects. Investigations of higher harmonics with electrooptical methods are much easier than using dielectric methods. Electrooptic investigations reveal also some modes, which are not active in dielectric experiments, as they do not introduce any change in polarization. Of special interest is the unique feature,

Table 5.6. Application of electrooptic phenomena

Field strength	*Applications*	*Physics*
strong	Displays Light switches	Tilt angle Polarization Viscosity
weak	Analog devices Light modulation Gray scale	Collective modes Elasticity, viscosity Flexoelectric polarization

offered by the electrooptic method – the possibility of performing measurements of material properties in various directions in the aligned liquid crystal sample. EO methods offer also the possibility of performing low frequency or even zero-frequency (DC) measurements. The electrooptic methods are very sensitive – as low changes in the position of the optic axis of 10^{-7} radian can be detected. Furthermore, the non-collective processes, for instance rotations around axes of molecules, do not contribute to the electrooptic effects and thus do not screen the collective modes, as usually the case in dielectric experiments.

On the other hand, the electrooptic phenomena establish the basis for almost all applications of tilted chiral smectics. In this case, however, mostly strong fields are used. Strong field effects are based on the switching phenomena. Thus, the applications of electrooptic effects can be divided into two groups: small field effects and strong field effects (Table 5.6). Both groups are of great importance for both physics and technology. Because of their technical importance, the electrooptic effects in strong fields have been described comprehensively in many papers and handbooks (see e.g. [5, 7] and references therein). Therefore in this paper we will concentrate our attention on small field effects.

5.8.2 The coupling between the electric field and the spontaneous polarization

Dipolar ordering can appear in tilted smectic liquid crystals either consisting of chiral molecules with transverse dipoles [1] or containing a chiral admixture [8]. It follows from the symmetry properties that in such a case the spontaneous polarization may emerge in each smectic layer. The polarization vector is then perpendicular to the tilt plane and parallel to the smectic layer plane.

When the tilt direction in adjacent layers is the same or almost the same (Fig. 5.98a) we are dealing with a ferroelectric liquid crystal (FLC) and when it is opposite (or nearly so) – with an antiferroelectric liquid crystal (AFLC, Fig. 5.98b). Other combinations of the tilt directions are considered as the antiferroelectric subphases [9].

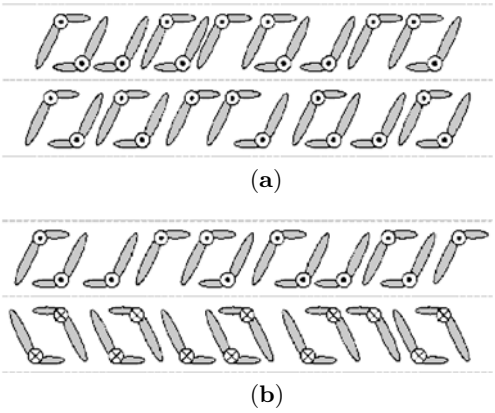

Fig. 5.98. Arrangement of chiral molecules (represented by *hockey sticks*) in ferroelectric (**a**) and antiferroelectric (**b**) phases. The dipoles (located at the *stick edge*) are directed perpendicular to the figure plane, either towards the reader (*points*) or outwards (*crosses*). In the ferroelectric phase the molecules are tilted in one direction (*synclinic*) and average dipole moments of adjacent smectic layers are parallel to each other (**a**). In the antiferroelectric phase the tilt directions in adjacent layers are opposite (*anticlinic*) and dipole moments are anti-parallel (**b**)

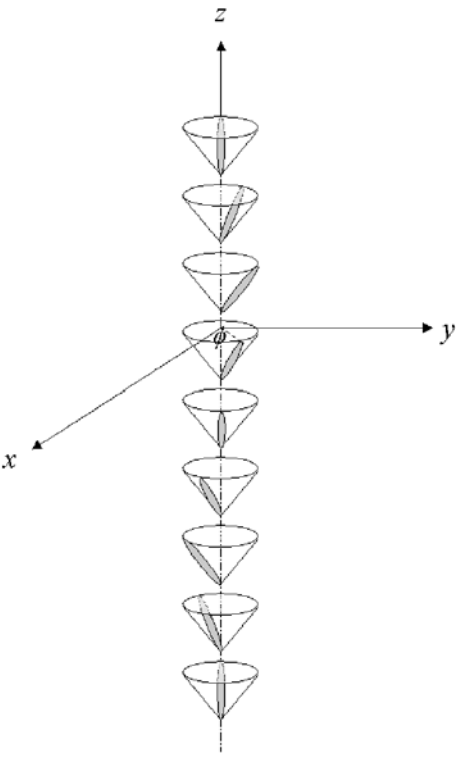

Fig. 5.99. The structure of helical smectic C*. The average tilt plane of molecules in a given smectic layer rotates around the layer normal creating a helix (right handed in the figure). The tilt angle Θ is kept constant while the azimuthal angle ϕ is varying according to the form $\phi = 2\pi z/p$ (p is the helical pitch)

An important structural complication appears due to the presence of the molecular chirality. The chirality not only removes the mirror plane from the group of symmetry elements of the smectic phase making the existence of spontaneous polarization possible, but also causes the creation of a macroscopic helical superstructure (Fig. 5.99). The helix, in turn, causes vanishing of the net spontaneous polarization in bulk samples of ferroelectric liquid crystals. In antiferroelectric liquid crystals, due to the anticlinic arrangement of every pair of smectic layers actually two helices are present, one for each tilt direction, shifted mutually by half of the helical pitch p [6].

5.8.2.1 Deformation of a helical smectic liquid crystal

When an electric field is applied in the smectic layer plane, all dipole moments of smectic layers tend to align in the field direction. This process causes the change in the position of the tilt plane, which in turn changes the optical properties of the sample. Figure 5.100 shows schematically the changes of the azimuthal angle ϕ.

In bulk samples, the electrooptic effects are mainly connected with either the deformation or unwinding of the helix. In weak fields we then observe the fluctuations of the ϕ angle called Goldstone mode which may exist only in the tilted smectic phases. We observe also the changes in the amplitude of the order parameter (the value of the tilt angle Θ), caused by the coupling of the molecular tilt with the spontaneous polarization (electroclinic effect). These changes of the Θ angle called "soft mode" are present in both ferroelectric and paraelectric phase. In thin samples whose thickness does not exceed considerably the helical pitch the helix is removed due to the surface interactions and the sample adopts the so-called SSFLC (surface stabilized ferroelectric liquid crystal) geometry [10]. This structure is bistable in the case of ferroelec-

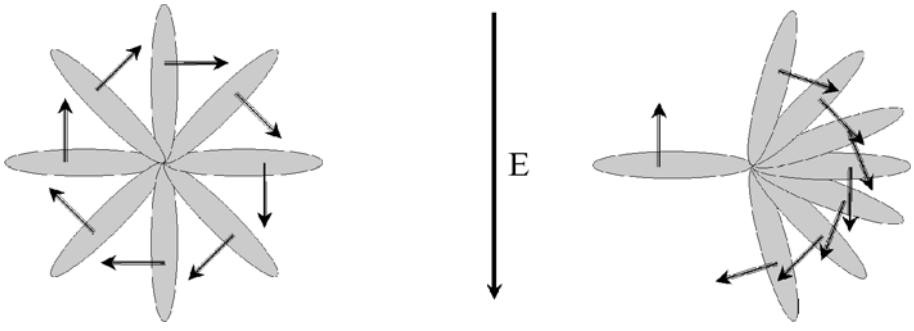

Fig. 5.100. Projections of the average molecular directions on the plane parallel to the smectic layers. The *arrows* represent net dipole moments of smectic layers without electric field (**a**) and in the presence of electric field $\boldsymbol{E}$ (**b**)

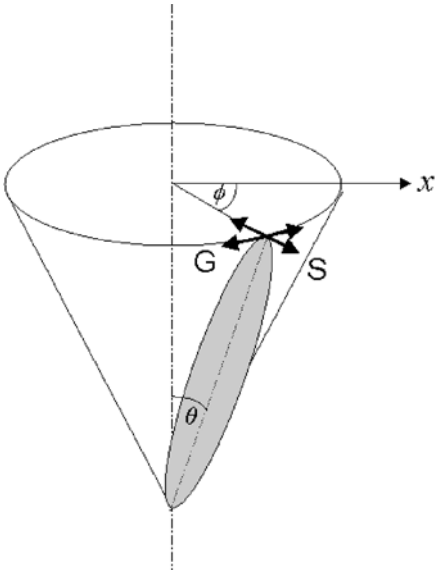

Fig. 5.101. The Goldstone (G) and soft (S) modes in a ferroelectric liquid crystal. The *cone* represents possible directions of long molecular axes in the smectic C*-phase and the *arrows* – the directions of collective excitations

tric liquid crystals and mostly tristable in the case of antiferroelectric liquid crystals.

Thus, the application of a week electric field changes both the amplitude and phase of the complex order parameter Ψ [11]:

$$\Psi = \Theta \cdot \exp(i\phi) \; . \tag{5.204}$$

In other words, the field influences both the azimuth angle ϕ (the Goldstone mode) and the tilt angle Θ (the soft mode, see Fig. 5.101). Both modes cause changes in the optic axis position. If the sample is placed between two polarizers, the change in the optic axis position causes the change in the intensity of light passing the system polarizer – sample – analyzer.

Electrooptic phenomena rely on changing *macroscopic* optical properties due to interactions of the electric field with permanent or induced dipole moments on the *microscopic* scale. To make use of electrooptic measurements and find the connection between the microscopic properties of a molecule and macroscopic properties of the sample one has to calculate:

(i) the electric field effect on molecules on the microscopic scale,
(ii) the effect of the changes of the molecular properties on the macroscopic properties of the medium, and
(iii) the appearance of the changes of phenomenological properties in a given detection method.

In our case step (iii) means that we have to find the changes in light intensity caused by the changes in the indicatrix' position and/or shape.

Let us consider first the simpler case of a helicoidal material with local spontaneous polarization, i.e. a ferroelectric liquid crystal.

5.8.3 Ferroelectric liquid crystals in weak electric fields

To find the electric field effect on the molecule (see Fig. 5.100) we have to solve the equation of motion [11–14] of tilted smectic molecules:

$$B_3 \frac{\partial^2 \phi}{\partial z^2} + \gamma \frac{\partial \phi}{\partial t} = |\boldsymbol{P}_0 \times \boldsymbol{E}| \ , \tag{5.205}$$

where B_3 is an elastic constant (for the movement on the cone), γ – the twist viscosity coefficient, ϕ – the azimuthal angle of the director, i.e. the angle between the tilt plane and an arbitrary chosen axis in the layer plane, P_0 – the polarization of the unit volume of a smectic layer (i.e. the spontaneous polarization of the smectic layer) and E – the electric field vector. The solution to the equation of motion in the case of small deformations is [12–14]:

$$\phi = qz + \phi_0 \cdot \sin qz \cdot \cos(\omega t - \beta) \ , \tag{5.206}$$

with

$$\phi_0 = \frac{P_0 \cdot E}{B_3 q^2 \sqrt{1 + \omega^2 \tau_G^2}} \ . \tag{5.207}$$

In (5.206) and (5.207) q denotes the wave vector of the helix ($q = 2\pi/p$, p is the helical pitch), $\beta = \arctan(\omega \cdot \tau_G)$ – the phase lag between the applied field and the deformation, τ_G – the relaxation time of the Goldstone mode ($\tau_G = \gamma \cdot B_3/q^2$). The angle ϕ_0 has the meaning of the amplitude of helix deformation and is still a microscopic quantity. Equation (5.206) presents the solution to the first task mentioned in the former section. To solve the second task, i.e. to find the changes of macroscopic optical properties, one has to average ϕ_0 over the whole sample volume. After some tensorial calculations [12, 14] we find for the change in the optic axis position:

$$\Delta\alpha = \frac{1}{2} \phi_0 \cdot \Theta \ . \tag{5.208}$$

This result allows us to find the dielectric and electrooptic responses.

5.8.3.1 Dielectric response

The Goldstone mode dielectric susceptibility χ_G is:

$$\chi_G = \varepsilon_G - 1 = \frac{P_E}{\varepsilon_0 \cdot E} = |\boldsymbol{P}_0| \, \frac{\langle \cos \phi \rangle}{\varepsilon_0 E} \ , \tag{5.209}$$

where E is the strength of the electric field applied parallel to the smectic layer plane, ϕ is the angle between E and the normal to the tilt plane of molecules, P_0 – the polarization of unit volume of a smectic layer (i.e. the spontaneous polarization) and P_E is the projection of P_0 on the field direction.

The mean value $\langle \cos\phi \rangle$ can be calculated from (5.206). The result is:

$$\langle \cos\phi \rangle = \phi_0/2 \; . \tag{5.210}$$

After inserting into (5.209) we obtain:

$$\chi_G = \frac{P_0^2}{2\,\varepsilon_0\, B_3\, q^2 \cdot \sqrt{1+\omega^2 \cdot \tau_G^2}} \; . \tag{5.211}$$

The dielectric susceptibility χ_S describing the soft mode can be calculated in a similar way:

$$\chi_S = \frac{C \cdot \Theta}{\varepsilon_0 \cdot E} \; . \tag{5.212}$$

The product $C \cdot \Theta$ denotes the polarization induced by tilting of molecules by angle Θ, C is the constant describing coupling of the polarization and the tilt within the smectic layers in the SmA phase. The amplitude of the induced tilt angle Θ can be found by solving the corresponding equation of motion. Garoff and Meyer [4] obtained the following result:

$$\Theta = \frac{C \cdot E}{A \cdot \sqrt{1+\omega^2 \cdot \tau_S^2}} \; , \tag{5.213}$$

where A is a generalized susceptibility and $\tau_S = G/A$ (G – viscosity) is the soft mode relaxation time. Thus, the dielectric susceptibility attributed to the soft mode is given by:

$$\chi_S = \frac{C^2}{A \cdot \varepsilon_0 \cdot \sqrt{1+\omega^2 \cdot \tau_S^2}} \; . \tag{5.214}$$

5.8.3.2 Optical response

In optical methods of measurement the changes in optical properties of the sample caused by external fields are registered. In most cases an electric field is applied, although other fields, e.g. a flow field [12] can be used as well.

As the optical biaxiality of smectic C* samples is usually very small [15], the homogeneously aligned liquid crystal sample can be considered as a birefringent plate made of a uniaxial crystal. When such a sample is placed between the polarizer and analyzer which polarization directions make the angle γ, the intensity of light transmitted by the system is [16]:

$$I = I_0 \cdot \left(\cos^2\gamma - \sin(2\alpha) \cdot \sin(2\beta) \cdot \sin^2\frac{\rho}{2} \right) \; , \tag{5.215}$$

where I_0 is the light intensity on entering the crystal, α and β – angles between optic axis of the sample and the polarization directions of polarizer

and analyzer, respectively. The angle ρ denotes the phase lag between the ordinary and extraordinary rays after passing the sample:

$$\rho = \frac{2\pi \cdot \Delta n \cdot d}{\lambda} , \tag{5.216}$$

where Δn denotes the birefringence, d – the sample thickness and λ – the wavelength of light. When the polarizer and the analyzer are crossed then $\gamma = \pi/2$ and (5.215) simplifies:

$$I = I_0 \cdot \sin^2(2\alpha) \cdot \sin^2 \frac{\rho}{2} , \tag{5.217}$$

where α is the azimuthal angle, made by the optic axis (in our case the helix axis, parallel to the smectic layers normal) with the polarization plane of the polarizer or analyzer.

Depending on the orientation of molecules in the sample two cases can be specified:

i) homeotropic orientation (smectic planes parallel to the walls of the cell) and
ii) planar orientation (smectic layers perpendicular to the walls).

Homeotropic orientation

The geometry of the experiment performed for measurements of the electrooptic response in a homeotropically oriented sample is schematically shown in Fig. 5.102.

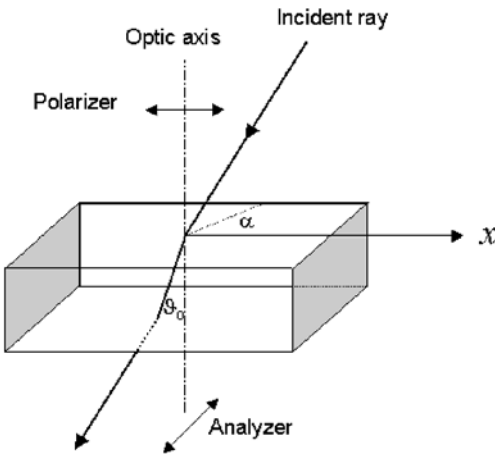

Fig. 5.102. The geometry of electrooptical experiments with use of homeotropically aligned samples. The *shadowed planes* represent the electrodes

The intensity of light after passing the analyzer is described with (5.217). If the angle ϑ between the light ray inside the crystal and the optic axis is small, then the phase shift ρ is [17]:

$$\rho \approx \frac{2\pi \Delta n\, d}{\lambda \cos \vartheta} \cdot \sin^2 \vartheta \ . \tag{5.218}$$

If an electric field of strength E is applied parallel to the smectic layers, the optic axis changes its position. Thus, the ϑ angle will be affected and, consequently, the light intensity $I(\rho)$ will vary. The ratio of the amplitudes of the light modulation and the field strength can be calculated by differentiation of (5.217):

$$A_H \equiv dI(\vartheta)/dE = B_H \cdot d\vartheta/dE \ . \tag{5.219}$$

Making use of (5.218) we get

$$A_H = \frac{2\pi\, d\, \Delta n}{\lambda \cos \vartheta_0}\, I_0 \sin^2 (2\alpha) \sin \left(\frac{2\pi\, d\, \Delta n}{\lambda \cos \vartheta_0} \sin^2 \vartheta \right) \sin \vartheta \cos \vartheta \frac{d\vartheta}{dE} \ , \tag{5.220}$$

where ϑ_0 denotes the value of ϑ angle for $E = 0$. If changes of the angle ϑ are small, the proportionality constant B_H, dependent on the experimental conditions, reads:

$$B_H = (2\pi/\lambda) \cdot I_0\, d\, \Delta n \cdot \sin^2 (2\alpha) \cdot \sin \rho_0 \cdot \sin \vartheta_0 \ , \tag{5.221}$$

where ρ_0 is given by (5.218) with $\vartheta = \vartheta_0$.

The constant B_H can be calculated from (5.221) if all parameters in this equation are known. An alternative way to get this quantity is a calibration procedure. This procedure consists in measuring the light intensity changes caused by variation of the ϑ_0 angle, i.e. by mechanical tilting of the sample.

It is obvious from (5.221) that the method will be most sensitive when $\alpha = \pi/4$ and $\varrho_0 = (2k + 1) \cdot \pi/2$ (k – integer). The second condition means that the angle of initial tilting of the sample ϑ_0 should be adjusted to get about half the light intensity behind the analyzer ($I/I_0 \approx 1/2$).

The value of the derivative $d\vartheta/dE$ for a given mode can be calculated using (5.207) or (5.213). For the Goldstone mode we have [12]:

$$\vartheta = \vartheta_0 + 1/2\phi_0(E) \cdot \Theta \ , \tag{5.222}$$

and the amplitude of light intensity modulation is

$$A_G = \frac{B \cdot P_0 \cdot \Theta}{2\, B_3\, q^2 \cdot \sqrt{1 + \omega^2 \cdot \tau_G^2}} \ , \tag{5.223}$$

with $B = B_H$ from (5.221). Similarly, for the soft mode we have:

$$\vartheta = \vartheta_0 + \Theta(E) \ , \tag{5.224}$$

and after differentiation of (5.213) we get for the light intensity modulation amplitude:

$$A_S = \frac{B \cdot C}{A \cdot \sqrt{1 + \omega^2 \cdot \tau_S^2}} , \tag{5.225}$$

with $B = B_H$ (5.221).

Planar orientation

The planar geometry is schematically shown in Fig. 5.103. The optic axis of the sample is perpendicular to the observation direction and parallel to the glass plates, which are covered with a conducting layer (e.g. indium tin oxide layer). Because the sample is placed between crossed polarizers, the light intensity is also described by (5.217).

The electric field applied to the electrodes (parallel to the light ray) forces the dipole moments of the smectic layers to gather in its direction, i.e. perpendicular to the glass walls. Thus, a change in the optic axis position takes place in the plane parallel to the glass walls and only the α angle will be affected:

$$\alpha = \alpha_0 + \alpha(E) . \tag{5.226}$$

The changes in the light intensity will be described by:

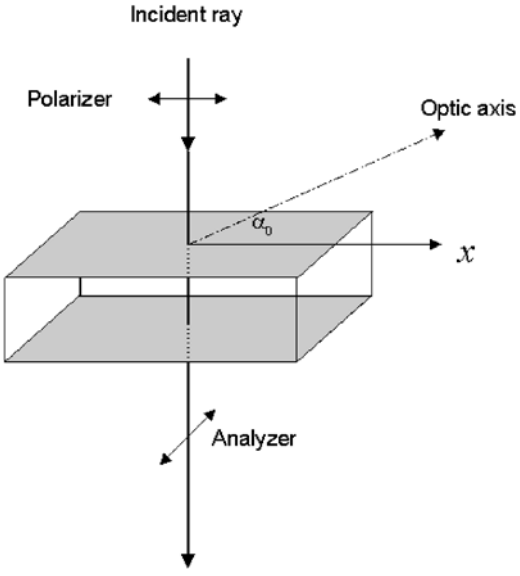

Fig. 5.103. Geometry of electrooptic experiments with use of planar orientation. The *shadowed planes* represent the semitransparent electrodes

$$A_p \equiv dI/dE = B_p \cdot d\alpha/dE \ . \tag{5.227}$$

Differentiation of (5.217) gives

$$A_p = 2I_0 \sin^2 \frac{\varrho}{2} \sin 4\alpha \frac{\mathrm{d}\alpha}{\mathrm{d}E} \ . \tag{5.228}$$

If the changes of α angle are small, then

$$B_p = 4I \cdot ctg\,(2\,\alpha_0) \ . \tag{5.229}$$

The constant B_p can be easily determined either from measurements of the light intensity changes while rotating the sample around the normal of incidence or by measuring the light intensity I in the absence of the electric field. It follows from (5.228) that the light modulation amplitude A_p is maximum when $\alpha_o = 22.5\,^\circ$ and then the calibration constant $B_p = 4I$ [18]. Putting (5.227) and (5.207) or (5.213) together we got for the Goldstone and soft modes results similar to those we have obtained in the case of the homeotropic orientation ((5.223) and (5.225)), but now $B = B_p$, (5.229).

Thus, in both geometries (homeotropic and planar) we got similar results (they differ by a constant factor only).

5.8.3.3 Correlation between the dielectric and electrooptic responses

As demonstrated in Sect. 3.2, both dielectric and optical methods deliver similar information on the ferroelectric modes. Comparing (5.211) with (5.223) and (5.214) with (5.225) we see that the forms describing dielectric and electrooptical responses of the Goldstone and the soft mode, respectively, are similar. The correlation between dielectric and optical data occurred to be especially good for the soft mode [17]. The analogous correlation for the Goldstone mode is less pronounced. The weaker correlation observed for the Goldstone mode is mainly caused by the fact, that the helical structure of the SmC^* phase in planar oriented samples is not perfect. The helical structure is not compatible with the planar boundary conditions [19] and the ideal helical structure assumed in calculations presented in Sects. 3.1 and 3.2 is not fulfilled in the experiments. The assumption concerning the helical structure is better fulfilled in the case of the homeotropic orientation; however, in this geometry the simultaneous measurement of dielectric and optical properties is hardly possible.

The correlation between ferroelectric modes follows from the performed calculations, (5.211) and (5.223). The ratio of electric susceptibility and optical response for the Goldstone mode is:

$$\frac{\chi_G}{A_G} = \frac{1}{B} \cdot \frac{P_0}{\varepsilon_0\,\Theta} \ . \tag{5.230}$$

Similarly, combination of (5.214) and (5.225) gives for the soft mode:

$$\frac{\chi_S}{A_S} = \frac{1}{B} \cdot \frac{C}{\varepsilon_0} \,. \tag{5.231}$$

B denotes here the proportionality coefficient B_H (5.221) or B_p (5.229), depending on the experimental geometry. Equations (5.230) and (5.231) are in a way similar – both give the value of the coupling constant tilt – polarization (P_0/Θ or C). This constant can be obtained using forms (5.230) and (5.231) without actually measuring the tilt or the polarization. When the tilt angle Θ in the ferroelectric phase is known, (5.230) gives the unique possibility to calculate the local spontaneous polarization of a single smectic layer. This value of polarization is obtained using electric field of a small strength, which causes only small deformation of the helix. Thus, one can assume that – if the surface interactions do not significantly modify the helical structure – this polarization is determined in the presence of the nearly unperturbed helix and, consequently, contains both the ferroelectric and flexoelectric [20] components. This situation is completely different from that usually taking place during measurements of the spontaneous polarization using polarization reversal (e.g. with bridge methods or integrating the polarization reversal current). As the polarization measured using strong fields does not contain the flexoelectric component, it may differ from that obtained from (5.230). Hence, the simultaneous measurement of the spontaneous polarization using both these methods gives a rather rare possibility to separate the ferroelectric and flexoelectric components [21].

5.8.4 Antiferroelectric liquid crystals in the electric field

In general, the dependence of light intensity on electric field strength can be realized in two ways: through the dependence $\alpha(E)$ or $\rho(E)$, see (5.217). In the case of ferroelectric liquid crystals the $\rho(E)$ dependence is weak and therefore it was neglected in our previous considerations. In antiferroelectric liquid crystals, however, stronger fields are used and the $\rho(E)$ dependence must also be taken into account. The dependence $\alpha(E)$ means that the position of the optic axis changes under the electric field influence. In chiral liquid crystals this change is caused by helix deformation due to the linear coupling of the spontaneous polarization of a smectic layer with the electric field [22], i.e.

$$\alpha = \alpha_0 + bE \,, \tag{5.232}$$

where α_o describes the position of the optic axis with respect to the light polarization plane in the absence of an external field, and b is a constant. On the other hand, the change of ρ occurs due to the change of birefringence Δn.

This change results from the modification of the indicatrix shape, mainly caused by quadratic coupling of the dielectric anisotropy $\Delta\varepsilon$ with the electric field [23]:

$$\rho = \rho_o + cE^2 \,, \tag{5.233}$$

where ρ_o is the phase lag without the field (5.216) and c is a constant.

5.8.4.1 Optical response

The change of the electric field strength by ΔE causes the change of the light intensity by ΔI, which can be expressed as:

$$\Delta I = \frac{dI}{dE}\Delta E \,. \tag{5.234}$$

The calculation of the electrooptic effect is then reduced to calculation of the derivative *dI/dE:*

$$\begin{aligned} dI/dE = {} & 2I_0 b \left(\sin 4\alpha_0 \cos 4bE + \cos 4\alpha_0 \sin 4bE\right) \sin \varrho/2 \\ & + I_0 cE \left(\sin 2\alpha_0 \cos 2bE + cos2\alpha_0 \sin 2bE\right)^2 \sin \varrho \,. \end{aligned} \tag{5.235}$$

In the case of small deformations ($bE \ll 1$, $cE^2 \ll 1$) the functions occurring in (5.235) can be expanded in series. If, additionally, $|\sin\rho| \gg |\rho - \rho_o|$, then taking into account terms up to the second order in E, we obtain:

$$\frac{1}{I_0}\frac{dI}{dE} = 2b\sin(4\alpha_0)\sin^2\frac{\rho_0}{2} + E\left[8b^2\cos(4\alpha_0)\sin^2\frac{\rho_0}{2} + c\sin^2(2\alpha_0)\sin\rho_0\right]. \tag{5.236}$$

Taking into account (5.234) we see that the first term in (5.236)

$$H_1 = 2b\sin 4\alpha_0 \sin^2 \varrho_0/2 \,, \tag{5.237}$$

describes the linear electrooptic effect and the second term

$$H_2 = E\left[8b^2\cos 4\alpha_0 \sin^2 \varrho_0/2 + c\sin^2(2\alpha_0)\sin\varrho_0\right] \,, \tag{5.238}$$

describes the quadratic electrooptic effect. The second order response H_2 consists of two terms:

$$H_{2b} = E\left[8b^2\cos(4\alpha_0)\sin^2(\varrho_0/2)\right] \,, \tag{5.239}$$

and

$$H_{2c} = E\left[c\sin^2(2\alpha_0)\sin\varrho_0\right] \,. \tag{5.240}$$

If the external electric field is sinusoidal, then the first term describes the light modulation with the fundamental frequency f_0 and the second one – the

modulation at the doubled frequency $2f_0$ (second harmonic). The modulation with fundamental frequency depends solely on the coefficient b, describing the linear deviation of the optic axis in the electric field (see (5.237)). On the other hand, the second harmonic (double frequency) modulation depends on both b and c coefficients ((5.239) and (5.240)) describing the linear and quadratic changes of the indicatrix.

The results of calculations presented in this Section are valid for both ferroelectric and antiferroelectric liquid crystals, with different values of b and c coefficients. These calculations are also applicable to the paraelectric smectic A phase. Experiments confirmed the predicted characteristic behavior of the linear and quadratic electrooptic responses in all mentioned phases (see Fig. 5.104).

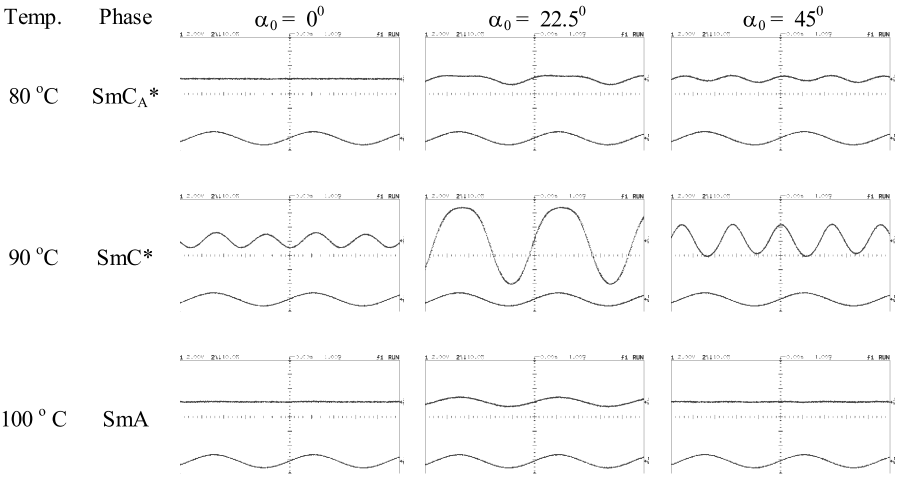

Fig. 5.104. Oscilloscope pictures of the electrooptic response (*upper lines*) of a 5 μm thick sample of the mixture W106c [24]. The *lower lines* present the applied AC voltage 1.4 V rms. of 120 Hz frequency. The pictures were taken in different phases and at different azimuthal angles α_0 between the optic axis and polarization direction (indicated in the Figure, after Dardas [25])

In all cases presented in Fig. 5.104 the same voltage (1.4 V rms., 120 Hz) was applied (the lower curve). The electrooptic response is presented in the upper part of the oscilloscope pictures. In the antiferroelectric SmC^*_A phase in the usual geometry ($\alpha_0 = 22.5°$) both first and second harmonics contribute to the electrooptic response with comparable intensity. The second harmonic alone appears at $\alpha_0 = 45°$ and no electrooptic signal is observed at $\alpha_0 = 0°$. In the ferroelectric SmC* phase strong signals of both fundamental and second harmonic frequency are present, however, at $\alpha_0 = 0°$ and $\alpha_0 = 45°$ the first harmonic response vanishes. The amplitudes and phases of the second harmonic measured at these angles are different, in agreement with (5.236) and

Table 5.7. First and second harmonic intensities

Harmonics	Term		$\alpha_0 = 0$	$\alpha_0 = 22.5°$	$\alpha_0 = 45°$
1-st	$H_1(\Delta\alpha)$	$2b \sin 4\alpha_0 \sin^2 \varrho_0/2$	0	$2b$	0
2-nd	$H_{2b}\left[(\Delta\alpha)^2\right]$	$8b^2 \cos 4\alpha_0 \sin^2 \varrho_0/2$	$8b^2$	0	$-8b^2$
2-nd	$H_{2c}(\Delta\varrho)$	$2c \sin 2\alpha_0 \sin^2 \varrho_0$	0	c	$2c$

Table 5.7. The second harmonic response is not observable in the paraelectric SmA phase at any α_0.

5.8.4.2 Angular dependence

Figure 5.105 shows an example of the first and second harmonic intensities calculated using (5.237) and (5.238).

On changing the α_0, e.g. through the rotation of the microscope stage, the modulation amplitude changes with the period $\pi/2$ for both the fundamental and second harmonic frequency ((5.237) and (5.238)). The intensities of light modulation for the fundamental f_0 and second harmonic $2f_0$ frequencies predicted for some characteristic azimuthal ϕ_0 angles are summarized in Table 5.7. The linear term H_1 is maximum at $\alpha_0 = (2k-1)\pi/4$, (where $k = 0, 1, 2...$) and vanishes when $\alpha_0 = 2k\pi/4$. The amplitude of the fundamental frequency modulation H_1 is symmetric with respect to the α_0 axis. By contrast, the second harmonic modulation H_2 is, in general not symmetric relative to the α_0 axis. The term H_{2b} dependent on b is symmetric with respect to the α_0-axis, whereas the second term H_{2c}, dependent on the birefringence changes, contains a component independent of α_0. The

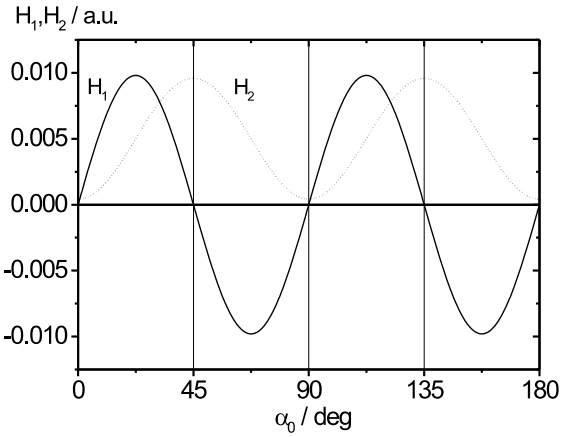

Fig. 5.105. Angular dependence of the linear and quadratic electrooptic responses calculated using forms (5.237) and (5.238) with $b = 0.01$ and $c = 0.005$

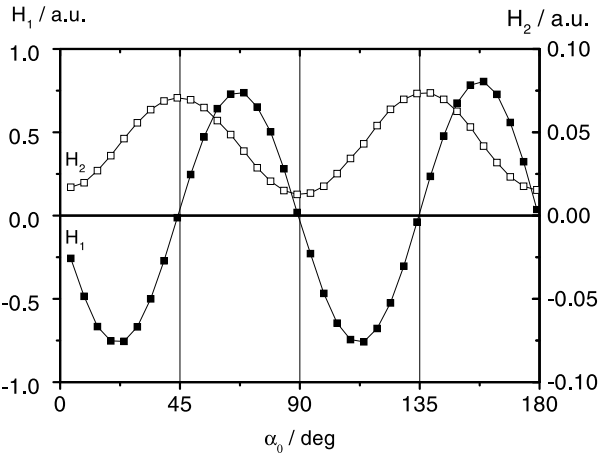

Fig. 5.106. Angular dependence of the first and second harmonic electrooptic responses measured for 4-(1-methylheptyloxycarbonyl)phenyl-4′-(3-butanoyloxy prop-1-oxy)biphenyl-4-carboxylate in the antiferroelectric SmC^*_A phase at 75 °C and 120 Hz (after Dardas [25])

first component vanishes at $\alpha_0 = 22.5°$ and the second one at $\alpha_0 = 0$. These predictions are confirmed by the experiment. Figure 5.106 shows the results obtained for 4-(1-methylheptyloxycarbonyl)phenyl-4′-(3-butanoyloxy prop-1-oxy)biphenyl-4-carboxylate (D11) in the antiferroelectric phase.

5.8.4.3 Separation of the second harmonic components

In practice, both components of the second harmonic are observed simultaneously and their sum is registered. An example of this sum calculated from (5.238) is shown in Fig. 5.107. In this example the sum is not symmetric with respect to the azimuth axis and never vanishes. To better see the H_2 on α_0 dependence, let us transform the sum to the another shape.

$$\frac{H_2}{E} = A + (B - 2A) \cdot \sin^2 2\alpha_0 \,, \tag{5.241}$$

with $A = 8b^2 \cdot \sin^2(\rho_0/2)$ and $B = c \cdot \sin \rho_0$.

As we see, the angular dependence can be divided into two parts: one independent of α_0 and the second, which follows the dependence of $\sin^2(2\alpha_0)$ with the amplitude $B - 2A$ (see Fig. 5.107). This observation creates an easy way to separate components A and B dependent on $(\Delta\alpha)^2$ and on Δn, respectively. The predicted behavior is confirmed by experiments. As an example, the azimuth angle dependence of the first and second harmonic response for the material D11 in the antiferroelectric phase is shown in Fig. 5.106. In the second harmonic response a constant background and a part modulated with

the period of 90° are present. Using data from the presented figure, one can calculate the coefficients b and c and, in turn, some molecular parameters using a molecular model (see, e.g. [26]).

5.8.5 Frequency dependence

Both the Goldstone and soft modes show distinct frequency dependence. This dependence is most frequently studied using dielectric methods (see, e.g. [27]). It follows, however, from (5.223) and (5.225) that the relaxation phenomena, described by equations of Debye type, appear in electrooptic investigations as well. Indeed, these phenomena have been observed experimentally (see e.g. [17, 27–29]). The advantages of electrooptic methods are especially distinct at low frequencies. Dielectric experiments performed at frequencies below about 100 Hz are difficult, first of all because of ionic contaminations, which can cause the electrode polarization, double layers creation and, especially when orienting or insulating layers are used, the Maxwell–Wagner effect (see, e.g. [30]). The presence of ions can also be a source of another relaxation process observed at low frequencies, see e.g. [31]. In dielectric experiments the ac current flowing through the sample is measured directly, hence the presence of ions screens the capacitive current under study and thus strongly influences the measurement of the complex electric permittivity.

The situation in electrooptic experiments is quite different. In these experiments the changes in optical properties caused by applied electric voltage are measured instead of the alternating current. The influence of ions might only appear as the change in the distribution of electric potential between electrodes (the dielectric method, as well, is not free from this inconvenience). To illustrate the discussed problems the results of investigations of a ferroelectric

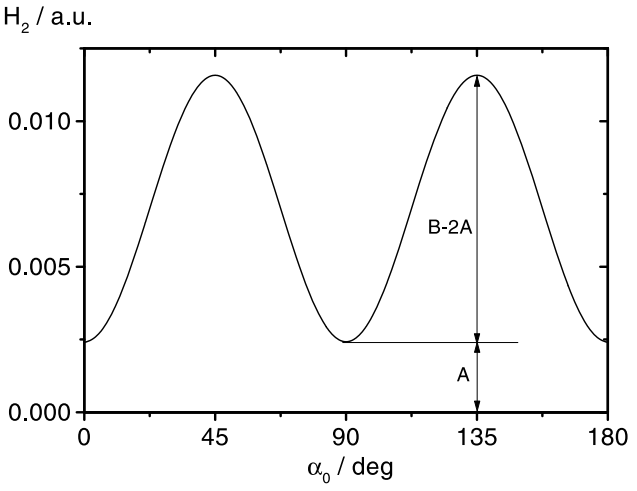

Fig. 5.107. The components of the second harmonic electrooptic response

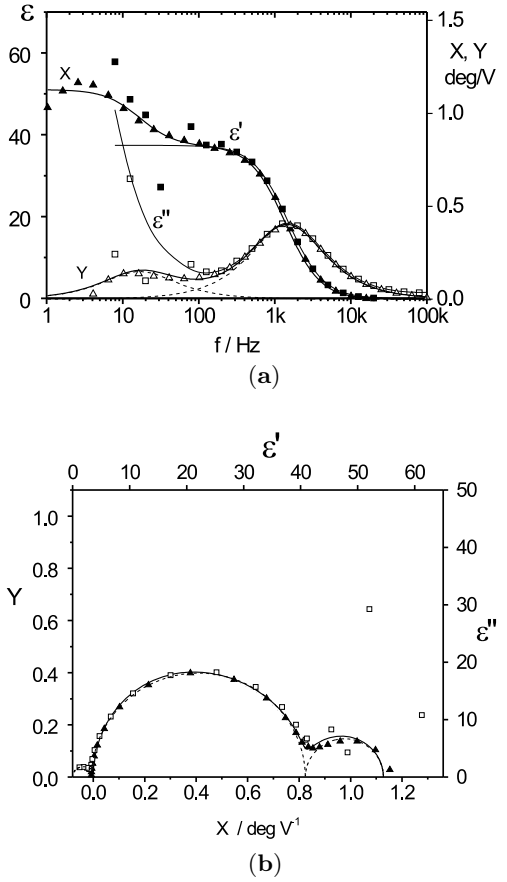

Fig. 5.108. Results of dispersion investigations in the mixture Felix 15-100 performed using the dielectric (*squares*) and electrooptic (*triangles*) method. Full symbols present the real components and the open symbols – the imaginary components of the complex responses. (**a**) frequency dependence (**b**) Cole – Cole plots

mixture FELIX 15-100 (Hoechst) performed using both methods are shown in Fig. 5.108.

It is evident that below the frequency 80 Hz the results of dielectric measurements become very inaccurate. The scattering of experimental data is so large, that no reasonable frequency dependence is possible to infer. Similar effects were observed for other ferroelectric and antiferroelectric liquid crystals. However, in low frequency range the electrooptic measurements still can be performed and give accurate results. The measurements presented in Fig. 5.108 allow identification of an additional relaxation band. Relaxation of surface layers [32] or defects [19] probably cause this band. Due to experimen-

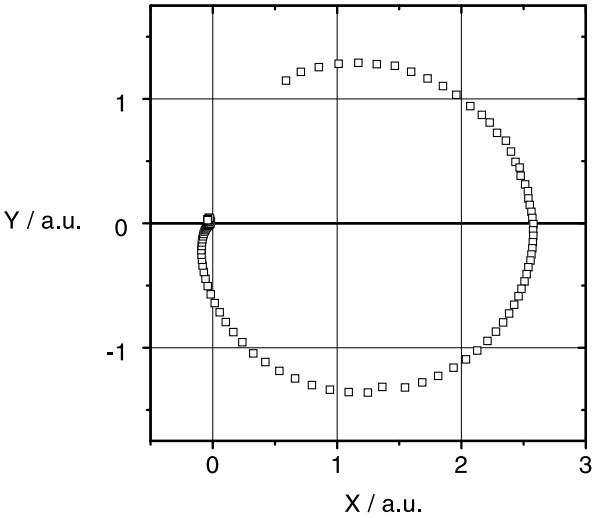

Fig. 5.109. Cole-Cole-like plot of the electrooptic response obtained for terephthalydene-bis(p-n-decylaniline) in the smectic C* phase in the frequency range 1 Hz–100 kHz (after Pavel et al. [29])

tal problems when using dielectric methods, the investigation of this effect was up to now only rarely performed [33].

Figure 5.109 illustrates the results of low-frequency electrooptic investigations in the ferroelectric phase of terephthalydene-bis(p-n-decylaniline). To describe the presented results using a sum of Debye-type components one has to assume that some of the components possess negative amplitude [29]. This situation is without any analogy in dielectric experiments. In dielectric experiments the electric permittivity is always positive and never decreases with falling frequency (except the abnormal dispersion observed in some materials at optical frequencies). In electrooptic experiments the amplitudes of some modes might have opposite signs. This effect has a simple explanation: the optical properties connected with some modes might cause e.g. opposite deviations of the optic axis of the sample or opposite changes of Δn at different frequencies. Thanks to this property, the relaxation bands can be easier separated.

5.8.6 Experimental procedures

Experimental investigations of the phenomena described in the former paragraphs are most frequently carried out using either a polarizing microscope equipped with a light detector or an optic bench and a laser as the light source. A lock-in amplifier measures the amplitude of the ac photoelectric signal from the photodiode. The lock-in amplifier performs the selection of signals with the fundamental f and the second harmonic $2f$ frequencies. The

cells walls produce either planar or homeotropic alignment. In the case of planar alignment the glass plates possess semitransparent electrodes, coated with orienting layers that secure good orientation. The electric field is applied using either the semitransparent electrodes (in the case of planar alignment) or two stripes of metal foil (in the case of homeotropic alignment). The samples are placed inside the hot stage. Electrooptic experiments might be carried out simultaneously with the dielectric experiments. In this case the measuring voltage of the dielectric bridge or impedance meter serves as the voltage causing the electrooptic phenomena.

5.8.7 Comparison of dielectric and electrooptic methods

It has been shown above that the results obtained with optical and dielectric methods are consistent. Both methods, having their advantages and disadvantages, are complementary.

The most important advantage of the dielectric method is its simplicity. Further, it is very convenient, as various commercial instruments for easy and precise measurements of electric impedance are available. On the other hand, there are no commercially available instruments for electrooptical measurements. Nevertheless, it could pay to set up the apparatus for optical measurements because of numerous advantages of this method. The most striking of them are listed below.

i) The depth of light intensity modulation is proportional to the intensity of the *collective* modes. Here, there is practically *no background* caused by phenomena, not connected with either ferroelectricity or antiferroelectricity (which are always contributing to the dielectric response). The electrooptic Kerr effect for instance, is expected to be 10^6 times less than the noise limit for electric field strengths used. Other mechanisms of dielectric polarization (e.g. molecular rotations) do not influence the optical properties of the sample. The observed effect of the orientation of molecules is predominantly due to the coupling of the electric field with the spontaneous polarization. This fact enables an unambiguous separation of collective and non-collective responses. It simplifies e.g. the investigation of critical phenomena at phase transitions and makes it possible to determine the critical exponents univocally.

ii) The *sensitivity* of optical methods is about 3 orders of magnitude higher than that of the dielectric method. As small changes in the optic axis position as 10^{-7} radian ($\sim 0.02°$), which correspond to equivalent changes in dielectric permittivity of about 10^{-5}, are possible to detect. Due to this extreme sensitivity the measuring e.g. of the electroclinic effect is possible up to much higher temperatures, more than 20 K over the temperature of transition from the SmC* to SmA phase [37]. Usually, dielectric measurements of the soft mode are effective only at a few degrees above the transition to the paraelectric phase. Due to the high sensitivity, optical measurements may be performed using extremely low electric fields.

This makes it possible to avoid nonlinear effects, which are of particular importance close to phase transitions. The high sensitivity is especially important in investigations of antiferroelectric liquid crystals, because the optical (and also dielectric) response of collective modes in these materials is weaker as compared with ferroelectric liquid crystals due to the compensation of the spontaneous polarization in each pair of smectic layers.

iii) The *frequency range* is not limited from below – even measurements at static electric field (nearly zero frequency) are possible [17]. This follows from the fact that the influence of DC electric conductivity on optical properties is small. The high limit of measuring frequency depends first on the lock-in amplifier used and may be situated in the MHz region. The so-called "low pass effect", which disturbs the dielectric measurements when ITO electrodes are used, is here of less importance.

iv) The optical method enables one to make observations in an *arbitrary direction* – not only in the direction of the electric field, as it is always done in the dielectric measurements. Since the vector of the spontaneous polarization lies in the smectic layers plane, only planar orientation is useful in dielectric investigations of ferroelectric modes. This restriction is not valid when optical methods are used – the angle between the light ray and the field direction can be arbitrary. Moreover, if we use polarized light, the angle between polarization plane and optic axis plane can be treated as a second independent variable. Thus, we have actually two independent, adjustable angles: between the optic axis of the sample and the incident ray and between the optic axis and the polarization plane. The use of other geometries may deliver additional information on the investigated material. The homeotropic orientation may be used as well. Homeotropically oriented samples have at least one important advantage: they can be prepared without defects, whereas a planar sample cannot [19] as the helical structure and planar orientation are not compatible. Thus, the investigation of homeotropic samples deliver information on *bulk properties* of the sample, whereas the results obtained for planar samples reflect not only the material properties but also the properties of the measuring cell.

v) Using optical methods the changes in both the azimuthal and tilt *angles can be measured directly* (supposing the calibration procedure has been done). In the dielectric method these angles can be calculated in same cases only [35], when the dielectric anisotropy is known.

vi) The combination of the dielectric and the optical responses gives a unique possibility to determine the spontaneous polarization of a smectic layer in the presence of (quasi)-undisturbed helical structure, what in turn enables the determination of e.g. some flexoelectric coefficients, elastic and viscosity constants.

vii) The optical method offers an easy way for investigation of higher order response (harmonics). This is especially important in investigations of antiferroelectric liquid crystals, where some modes are not active at the

fundamental frequency. For example, in the so-called in-phase mode [27] the changes in the polarization caused by the changes in the position of molecules on the cone of constant tilt angle compensate in each two successive smectic layers and do not contribute to the electric permittivity. However, this mode can produce polarization of higher orders, which could be observed in dielectric experiments performed at three times higher frequency [23, 36, 37]. Such dielectric experiments are, however, quite difficult to perform. Measurements of higher harmonics of the electrooptic response could be a convenient solution to this problem.

Thus, the investigations of collective modes in liquid crystals can be performed using either the dielectric or optical method. The information provided by both methods is equivalent. However, there are many experiments which can be performed only using electrooptic methods.

5.8.8 Summary

Electric fields applied to a liquid crystal sample cause changes in its optical properties. These effects are especially pronounced in chiral tilted smectic liquid crystals due to the coupling of the electric field with the spontaneous polarization of smectic layers. In ferroelectric liquid crystals linear effects are dominating. In antiferroelectric liquid crystals both linear and second order electrooptic effects are of comparable magnitude. The electric field causes changes in the position of the optic axis and the changes in the shape of the indicatrix. The first effect is responsible for the electrooptic modulation at fundamental frequency. Both mentioned effects influence the second harmonic response. Separation of both contributions can deliver information on the molecular properties of smectic materials. Electrooptic effects can also be applied for investigation of relaxation processes. The electrooptic investigations are particularly useful at low frequencies.

References

1. R.B. Meyer, L. Liebert, L. Strzelecki, P. Keller: J. Phys. Lett. (Paris) **36**, L-69 (1975)
2. A.P. L Chandani, E. Górecka, Y. Ouchi, H. Takezoe, A. Fukuda: Jap. J. Appl. Phys. **28**, L1265 (1989)
3. Y. Galerne, L. Liebert: Phys. Rev. Lett. **64**, 906 (1990)
4. S. Garoff, R.B. Meyer: Phys. Rev. Lett. **38**, 848 (1977)
5. S.T. Lagerwall: *Ferroelectric and antiferroelectric liquid crystals.* (Wiley-VCH, Weinheim, 1999)
6. A. Fukuda, Y. Takanishi, T. Isozaki, K. Ishikawa, H. Takezoe: J. Mater. Chem. **4**, 997 (1994)
7. L.M. Blinov, V.G. Chigrinov: *Electrooptic effects in liquid crystal materials.* (Springer, New York, 1996)

8. W. Kuczyński, H. Stegemeyer: Chem. Phys. Lett. **70**, 123 (1980)
9. T. Matsumoto, A. Fukuda: Liq. Cryst. Today **8**, 6 (1998)
10. N.A. Clark, S.T. Lagerwall: Appl. Phys. Lett. **36**, 899 (1980)
11. P.G. de Gennes: *The Physics of Liquid Crystals.* (Oxford University Press, New York, 1974)
12. P. Pierański, E. Guyon, P. Keller, L. Liebert, W. Kuczyński, P. Pierański: Mol. Cryst. Liq. Cryst. **38**, 275 (1977)
13. P. Pierański, E. Guyon, P. Keller: J. Phys. (Paris) **36**, 1005 (1975)
14. J. Hoffmann, W. Kuczyński, J. Małecki, J. Pavel: Ferroelectrics **76**, 61 (1987)
15. S.A. Różański, W. Kuczyński, J. Małecki: Phys. Stat. Sol. A **112**, 617 (1989)
16. M. Born, E. Wolf: *Principles of Optics.* (Pergamon Press, London, 1959) p. 693
17. W. Kuczyński, J. Hoffmann, J. Małecki: Ferroelectrics **150**, 279 (1993)
18. G. Anderson, I. Dahl, P. Keller, W. Kuczyński, S.T. Lagerwall, K. Skarp, B. Stebler: Appl. Phys. Lett. **51(9)**, 640 (1987)
19. M. Glogarova, J. Fousek, L. Lejcek, J. Pavel: Ferroelectrics **58**, 161 (1984)
20. I. Dahl, S.T. Lagerwall: Ferroelectrics **58**, 215 (1984)
21. W. Kuczyński, J. Hoffmann: In: Proc. 25. Freiburger Arbeitstagung Flüssigkristalle p. 34 (1996)
22. K. Hiraoka, H. Takezoe, A. Fukuda: Ferroelectrics **147**, 13 (1993)
23. H. Orihara, Y. Ishibashi: J. Phys. Soc. Jap. **64(10)**, 3775 (1995)
24. R. Dąbrowski: Private communication (1999)
25. D. Dardas: Diploma Thesis, University of Technology, Poznan (1999)
26. Y.P. Panarin, O. Kalinovskaya, J.K. Vij, J.W. Goodby: Phys. Rev. E **55**, 4345 (1997)
27. M. Buivydas, F. Gouda, S.T. Lagerwall, B. Stebler: Liq. Cryst. **18**, 886 (1995)
28. S. Garoff, B.B. Meyer: Phys. Rev. A **19**, 338 (1979)
29. J. Pavel, M. Sidir, M. Glogarova, M. Boschmans, H. Sverenyak: Mol. Cryst. Liq. Cryst. **263**, 149 (1995)
30. B. Hilczer, J. Małecki: *Electrets.* (Elsevier, Amsterdam, Oxford, New York, Tokyo, 1986)
31. S. Sarmento, P. Simeao Carvalho, M. Glogarova, M.R. Chaves, H.T. Nguyen, M.J. Ribeiro: Liq. Cryst. **25**, 375 (1998)
32. V. Bourny, J. Pavel, V. Lorman, H. T Nguyen: Ferroelectrics **244**, 303 (2000)
33. V. Bourny, J. Pavel, P. Gisse, H.T. Nguyen: Ferroelectrics **241**, 247 (2000)
34. W. Kuczyński, J. Hoffmann, B. Stryła, J. Małecki: Ferroelectrics **114**, 319 (1991)
35. F. Gouda, W. Kuczyński, S.T. Lagerwall, M. Matuszczyk, T. Matuszczyk, K. Skarp: Phys. Rev. A 46 **2**, 951 (1992)
36. H. Orihara, K. Kawada, N. Yamada, Y. Ishibashi: Mol. Cryst. Liq. Cryst. **303**, 159 (1997)
37. K. Obayashi, H. Orihara, Y. Ishibashi: J. Phys. Soc. Japan **64**, 3188 (1995)

5.9 Infrared studies of the orientational order and dynamics of molecules in ferroelectric and antiferroelectric liquid crystals

A. Kocot and R. Wrzalik

5.9.1 Introduction

It is commonly accepted that in both antiferro- (SmC^*_A) and ferroelectric (SmC^*) phases of liquid crystals, the transversal permanent dipoles located near the chiral center play an essential role in the appearance of ferroelectricity and/or antiferroelectricity [1, 2].

The anisotropic intermolecular dispersion interactions between the cores, as well as between the end groups of the molecules and the packing consideration, favor parallel arrangement of the molecules within a layer. This gives rise to a strong ferroelectric coupling within the layers. For the molecules in neighboring layers, however, the interaction is mainly transmitted via the end groups of molecules that is through long range interactions, which should be relatively weak. Nowadays the main postulated model for this is the pairing of the transverse dipole moments localized on the end chains of the molecules [3, 4]. It would be quite interesting to understand from the molecular point of view why such antiferroelectric and ferrielectric phases exist in liquid crystals and how they are stabilized. A number of methods have been recently used to study the structure and macroscopic properties of various ferro-, ferri- and antiferroelectric phases. However, in spite of a great number of studies, it is far from a clear understanding of the molecular origin of these mesophases.

Infrared spectroscopy has been found to be very useful in obtaining orientational information about the molecular groups and particularly microscopic examination of the rotational motion of the dipoles around the long molecular axis. Polarized Fourier transform infrared (FT-IR) spectroscopy can be used to study the orientational distribution and rotation of the selected transition dipoles in antiferro-, ferroelectric and paraelectric phases of homogeneously oriented liquid crystal samples [3–16]. An electric field applied to the sample in the SmC^* phase rotates the absorbance profiles by a degree close to the optical tilt angle either clockwise or anticlockwise depending on the polarity of the electric field. Similar rotation of the absorption profiles can be observed in the SmC^*_A phase as an effect of the transition between two induced ferroelectric (F(+) or F(−)) states, when an electric field higher than the threshold value is applied. The absorbance profiles for several IR bands as a function of the rotation angle of the polarizer and rotation angle of the sample can be measured and quantitatively analyzed in terms of the orientational distribution function parameters using general formulas derived for polarized IR absorption.

FT-IR time resolved spectroscopy (FT-IR TRS) with simultaneous temporal and spectral resolution has emerged as a powerful technique to ex-

plore dynamics and segmental information concerning both structural and orientational changes of molecules in transient systems [17, 18]. The FT-IR TRS technique applied to the analysis of the dynamics of liquid crystals have revealed new information that enables us to penetrate into detailed sub-molecular mechanisms of the electrically induced liquid crystal reorientation [3, 6, 10–12, 16]. The step-scan vibrational spectroscopy with polarized light was used to study the dynamics of molecular orientation and the conformational changes accompanying electro-optic switching in the chiral SmA phase [19], as well the antiferro-, ferri- and ferroelectric phases of the non-polymeric and polymeric liquid crystals [10–12, 16]. FT-IR TRS has been used here to observe the dynamics of the AFLC molecules, following the field induced switching. The results are compared with the observation of the dynamics obtained by electro-optical method in the time domain and with the dielectric response in the frequency domain.

5.9.2 Determination of the absorbance profile and the segmental tilt angle of the molecule

The experimental arrangement for the study of the effect of the electric field on IR absorbance of FLC material [5, 8] is shown in Fig. 5.110. IR polarized measurements were performed in transmission mode at normal and oblique incidence of the IR beam. In the transmission mode, at normal incidence, Fig. 5.110(a), the absorbance was recorded for the polarizer angle varied in the range from 0 to 180° with the angular step of 10°. At oblique incidence case, Fig. 5.110(b), the absorbance was recorded for a sample tilt varied in the range from $\sim -60°$ to $+60°$, in reference to the normal incidence angle but only for two polarizer angles 0° and 90° [8]. A BioRad FTS-6000 FTIR

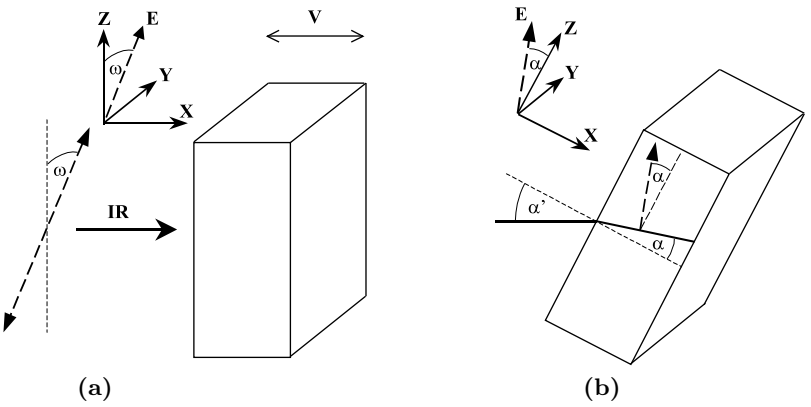

Fig. 5.110. Geometries for polarized IR measurements of homogeneously aligned samples: (**a**) the normal incidence mode at various polarizer orientations, (**b**) the oblique incidence mode-sample is rotated around the ***Y*** axis

spectrometer with a liquid-nitrogen cooled MCT detector was used to record the spectra in the wave number range from 450 to 4000 cm^{-1} with a resolution of 1 cm^{-1}. A total of 64 scans were co-added to increase the signal-to-noise ratio. The samples investigated are the ferroelectric mixture-ZLI-3654 and one antiferroelectric compound: (S)-12OBBB8, see Fig. 5.111.

(a) Chiral components of ZLI-3654 mixture

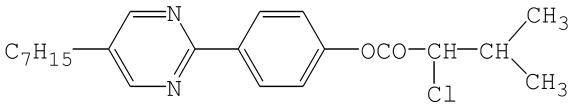

-30 S_C* 62 S_A 76 N* 86 I*

(b) (S)-12OBBB8,

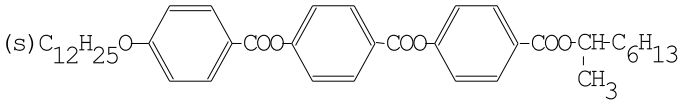

Cr 69 SmC_A* 99 SmCγ* 99.3 FiLC 101 SmC* 121 SmA 130 I

Fig. 5.111. Structural formulas and phase diagrams for the LC samples studied: (**a**) chiral component of ZLI-3654 mixture; phase digram below is given for the mixture, (**b**) (S)-12OBBB8. Transition temperatures are in °C. FiLC denotes FI2 (or SmC^*_γ) phase

In the SmA phase, the absorbance of the bands with transition dipole moments along the long molecular axis is maximal for the polarizer parallel to the smectic layer normal and consequently the absorbance of the perpendicular bands has maxima rotated by 90°. When an electric field is applied to the sample in SmC* phase the maxima of absorbance rotate through approximately the optical tilt angle either clockwise or anticlockwise (with respect to their position in the SmA phase) depending on the polarity of the electric field. The angular dependence of the peak absorbance and the effect of the electric field on this dependence can be conveniently represented in the form of a polar plot (circular graphs). The distance from the centre represents the peak absorbance at the polarizer position ω. The results of the absorbance profile vs. polarization angle for ZLI-3654 sample are given in Fig. 5.112. As seen from these figures, the maximum absorbance for different bands give quite different angles of rotation following the polarity changes of the DC field. In order to obtain a precise value of the rotation angle of the particular dipole moment, the absorbance profile is fitted to the following formula [7, 9, 15]

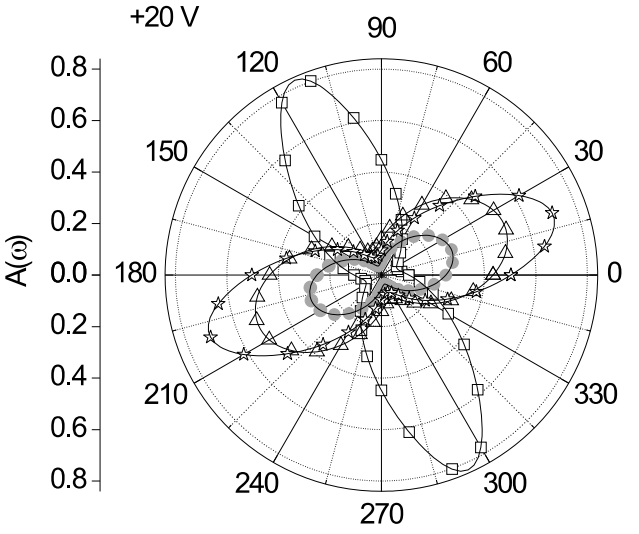

a

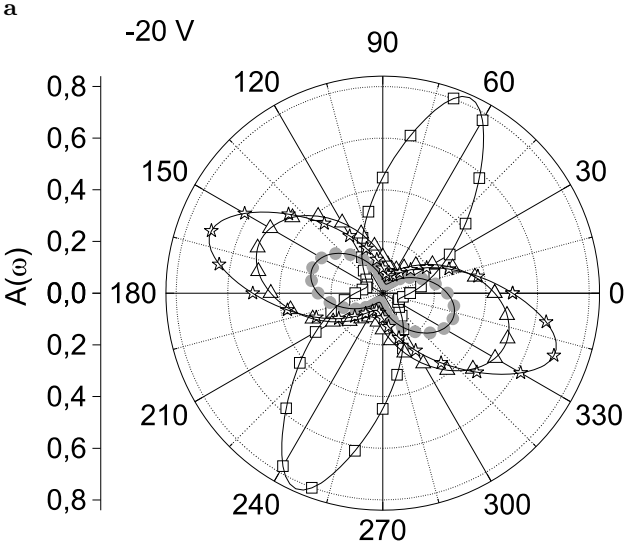

b

Fig. 5.112. Polar plot of the absorbance vs. the polarizer rotation angle for four representative bands in the SmC* phase of homogeneously aligned ZLI-3654 mixture. *Symbols* represent the experimental data; *solid lines* are fits to (5.242). ● – 653 cm^{-1}; △ – 798 cm^{-1}; ★ – 1607 cm^{-1}; □ – 1772 cm^{-1}

$$A(\omega) = -\log\left[10^{-A_{||}} + \left(10^{-A_{\perp}} - 10^{-A_{||}}\right) \cdot \sin^2(\omega - \omega_0)\right], \tag{5.242}$$

where $A_{||}$ and $A_{\perp}$ are the maximal and minimal values of absorbance, ω is the polarizing angle and ω_0 is the angle for which a maximal absorbance is obtained. $A_{||}$ and $A_{\perp}$ can be related to the main components in laboratory frame in the following way:

$$\begin{aligned} A_Z &= A_{||}\cos^2(\omega_0) + A_{\perp}\sin^2(\omega_0), \\ A_Y &= A_{||}\sin^2(\omega_0) + A_{\perp}\cos^2(\omega_0), \\ A_{YZ} &= 2(A_{||} - A_{\perp})\sin(\omega_0)\cos(\omega_0). \end{aligned} \tag{5.243}$$

In order to complete the information about the distribution of the transition dipole absorbance measurements were carried out for the oblique angles of incidence of the radiation. For a homogeneously aligned sample this can be realized both by the rotation of the sample around the axis lying in the ***Y-Z*** plane either parallel or perpendicular to the optical axis. As a result another two absorbance profiles, $A(\alpha)$, are recorded for each dipole [13]. Since light is refracted when going through the material of different refractive indices, the angle α between electric vector and the ***Y-Z*** plane in the LC film, is related to the tilt angle of the sample, α', through Snell's law

$$n_1 \sin\alpha' = n_2 \sin\alpha, \tag{5.244}$$

where: n_1 is the refractive index of the first medium, n_2 is the refractive index of the second medium, α is the angle of refraction in the second medium. One usually can ignore the influence of the window on the refraction angle in LC material regarding the first medium as air and the second as the LC layer itself. The optical path is dependent on the tilt angle of the sample so the measured absorbance $A'(\alpha)$ must be scaled to the same sample thickness through which the IR beam travels (usually the path for the normal incidence). The scaled absorbance is equal $A(\alpha) = A'(\alpha)\cos(\alpha)$, where α can be found from (5.244) if the refractive index of the sample, n_2, and the tilt angle of the sample are known. Unfortunately n_2 is also α-dependent. Therefore, it is convenient to make additional absorbance measurements for the incident IR beam being polarized in parallel way to the tilt axis. In such a case the absorbance depends only on the beam path and the scaling factor can be simply obtained from ratio of the absorbances as $\cos(\alpha) = A'(\alpha)/A(0)$.

5.9.3 Effect of electric field in the SmC* phase

For the ZLI-3654 sample it was found that 20 V is sufficient to obtain the saturated value of the switching angle. The angles are as follows: 21.8° – 1772 cm^{-1}, 25° – 1607 cm^{-1}, 24° – 1584 cm^{-1}, 20.5° – 1543 cm^{-1}, 20° – 822 cm^{-1}, 19° – 798 cm^{-1}, 23.2° – 722 cm^{-1}, and 18.6° – 653 cm^{-1} [13]. It has to been noted that the angles for the dipoles parallel to the phenyl

ring are significantly higher than for the perpendicular ones. These results for switching angles can be explained in terms of the non-isotropic rotation around the long molecular axis and shall be discussed in details later. Such a non-isotropic rotation can be considered as a reason for the existence of ferroelectricity in the chiral systems [3, 4, 7]. Figure 5.113 shows distributions of absorbance for several transverse dipoles versus the tilt angle of the sample (in the plane that contains the layer normal and the DC field). Although the angle, through which the cell rotates, is limited ($\sim -60°$ to $+60°$) in this method, a non-cylindrical symmetry of the distribution of transversal dipoles can be clearly seen. CH_2 rocking dipole in the tail lies in the window plane, the out-of-plane dipole of the phenyl group is inclined at a small angle with respect to the window plane while the other dipoles are rather far from this. Particularly the Cl-C chiral group dipole is at big angle to the window plane.

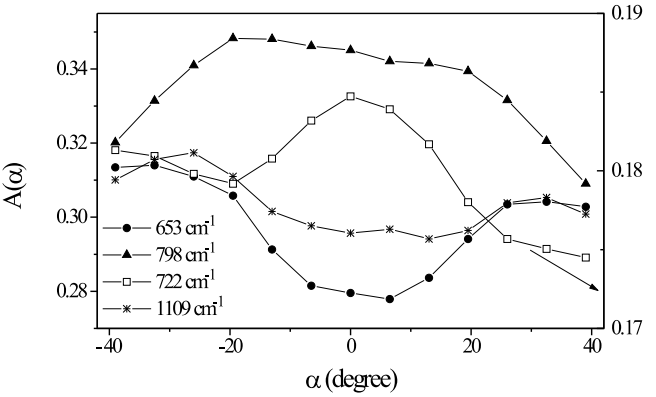

Fig. 5.113. Dependence of the absorbance on the sample rotation angle for ZLI-3654. Wave numbers: • – 653 cm^{-1}; ▲ – 798 cm^{-1}; ○ – 722 cm^{-1}; × – 1109 cm^{-1}

Similar results were obtained for a homogenously aligned sample using the attenuated total reflection method (ATR). This method enables one to reproduce full absorbance profile, Fig. 5.114, in the plane normal to the director (despite some difficulties with this method in the precise calculation of the penetration depth) [14]. There is a clear evidence, that the distribution of the transition dipole moments around the long molecular axis is not uniform. The preferred direction of the chiral Cl-C dipole and phenyl transversal dipole (in phenyl plane) are close to the $\boldsymbol{X}$ axis ($\boldsymbol{X}$ axis is in the direction of DC field) while phenyl C-H out-of-plane dipole is close to the $\boldsymbol{Y}$ axis. This proves that the rotation of the molecule around its long axis is biased.

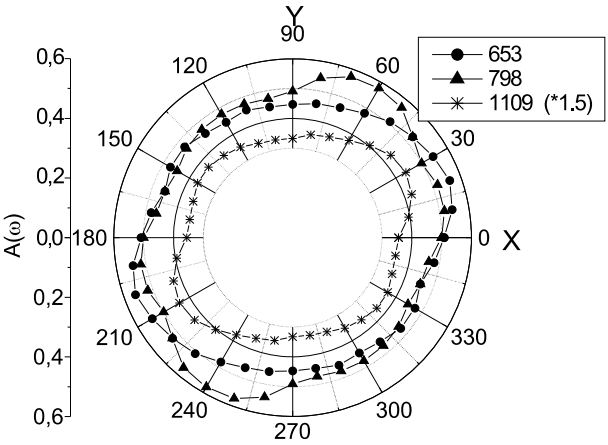

Fig. 5.114. Angular dependence of the absorbance on the polarizer orientation for homogeneously aligned ZLI-3654 under DC field ($\boldsymbol{X}$ and $\boldsymbol{Y}$ axis correspond to p and s polarization in ATR experiments): • – 653 cm^{-1}; ▲ – 798 cm^{-1}; ✳ – 1109 cm^{-1}

5.9.4 Calculations of the absorbance components and of the distribution function

Considering the well-oriented sample of a domain, the natural frame of reference is determined by the anisotropy of the material. The orientation of the molecule in the laboratory, frame of reference can be described by the three Eulerian angles (θ, ϕ, ψ). Denoting the unit vectors of the laboratory frame by $\boldsymbol{e}_X$, $\boldsymbol{e}_Y$, $\boldsymbol{e}_Z$ and those of the molecular frame of reference by $\boldsymbol{e}_x$, $\boldsymbol{e}_y$, $\boldsymbol{e}_z$, the relations between the unit vectors and the Eulerian angles can be express using the formulas as in [20, 21]. $\cos\,\theta = (\boldsymbol{e}_Z\ \boldsymbol{e}_z)$ where θ denotes the angle between $\boldsymbol{e}_Z$ and $\boldsymbol{e}_z$. The vector $\boldsymbol{n}$, which is normal to the plane is defined by $\boldsymbol{e}_Z$ and $\boldsymbol{e}_z$ and the angle ϕ with $\boldsymbol{e}_X$ thus $\boldsymbol{n} = [\boldsymbol{e}_Z \times \boldsymbol{e}_z]/\sin\theta$ and $(\boldsymbol{n}\ \boldsymbol{e}_X) = \cos\phi$. Angles θ and ϕ define the $\boldsymbol{z}$ axis of the molecular frame of reference: usually the axis of highest symmetry of the molecule is chosen as $\boldsymbol{z}$ axis which for rod-like molecules is the molecular long axis. Angle ψ describes the rotation of the molecule around the axis $\boldsymbol{e}_Z$. This is the angle that $\boldsymbol{e}_x$ makes with $\boldsymbol{n}$ so $(\boldsymbol{n}\ \boldsymbol{e}_x) = \cos\,\psi$.

Any vector defined with respect to the molecular frame can be transformed into the laboratory frame of reference by matrices M

$$(p_x,\ p_y,\ p_z) \underset{M}{\Rightarrow} (p_X,\ p_Y,\ p_Z)$$

$$M = \tag{5.245}$$

$$\begin{bmatrix} \cos\phi\cos\psi - \cos\theta\sin\phi\sin\psi & \cos\phi\sin\psi + \cos\theta\sin\phi\cos\psi & \sin\theta\sin\phi \\ -\sin\phi\cos\psi - \cos\theta\cos\phi\sin\psi & -\sin\phi\sin\psi + \cos\theta\cos\phi\cos\psi & \sin\theta\cos\phi \\ \sin\theta\sin\psi & -\sin\theta\cos\psi & \cos\theta \end{bmatrix}$$

The probability of a certain orientation of a molecule is described by the orientational distribution function $f(\theta, \phi, \psi)$. When the molecule is rod-shaped or when any orientation around its axis is equally probable then f does not depend on ψ. In the case of a SmA or nematic phase, the material is uniaxial, that is the distribution function does not depend on ϕ. For such conditions, the orientational order in the material is described by a single order parameter

$$S = 0.5\langle 3\cos^2\theta - 1\rangle\,, \tag{5.246}$$

where the bracket means the ensemble average for all of the molecules in the system. In general, however, the rotation around the molecular long axis is not free. Then distribution function depends on ψ, and the axes $\boldsymbol{x}$ and $\boldsymbol{y}$ have different average inclinations to the $\boldsymbol{Z}$ axis. This biaxiality of the molecule is characterized by a parameter called dispersion and denoted by D [20, 21]

$$D = 3/2\langle(\boldsymbol{e}_{xZ})^2 - (\boldsymbol{e}_{yZ})^2\rangle = 3/2\langle\sin^2\theta\cos 2\psi\rangle. \tag{5.247}$$

5.9.4.1 Uniaxial phase

If the $\boldsymbol{Z}$ axis of the laboratory frame of reference is parallel to the director of the sample, then the permittivity tensor becomes diagonal, and $\varepsilon_{XX} = \varepsilon_{YY} \neq \varepsilon_{ZZ}$ if the material is uniaxial. Let the sample have either a homogeneous or homeotropic orientation then $\boldsymbol{Z}$ axis is either parallel to the sample surface in the former case or normal to it in the latter case. If the light beam falls perpendicularly to the sample and its electric field is parallel to one of the optical axes then the light beam behaves as an ordinary ray. Propagation and absorption are determined by the corresponding diagonal element of the permittivity tensor ε, that is by ε_{YY}, if $\boldsymbol{E}$ is perpendicular to the director and by ε_{ZZ}, if $\boldsymbol{E}$ is parallel to it. The absorption is governed by the imaginary part of the permittivity, which is in turn, proportional to (p_Y^2) and (p_Z^2), respectively [20, 21]. Assume that the direction of the transition moment is given by the polar angles β and γ in the molecular frame of reference that is, its components are:

$$\boldsymbol{p} = |\boldsymbol{p}|(\sin\beta\cos\gamma, \sin\beta\sin\gamma, \cos\beta)\,,$$

Absorbance components are determined by the components of the transition moment and by the order parameters S and D. Vector $\boldsymbol{p}$ has to be transformed from the molecular system into the laboratory frame of reference using the transformation matrix M, and then the averages of the components have to be determined. Assuming that the distribution function f does not depend on ϕ (the material is uniaxial) we get

$$\begin{aligned} A_Y &= 0.5\,k\,\left\{\sin^2\beta\,\left[1 - \left\langle\sin^2\theta\right\rangle\,\left\langle\sin^2(\psi-\gamma)\right\rangle\right] + \cos^2\beta\,\left\langle\sin^2\theta\right\rangle\right\} \\ A_Z &= k\,\left\{\sin^2\beta\,\left\langle\sin^2\theta\right\rangle\,\left\langle\sin^2(\psi-\gamma)\right\rangle + \cos^2\beta\,\left\langle\cos^2\theta\right\rangle\right\}\,, \end{aligned} \tag{5.248}$$

where: $k = (2A_X + A_Z)/3$.

Assuming that the distribution function with respect to ψ has at least C_2 symmetry, the average values of absorbance components A_Y and A_Z will be the following:

$$\begin{aligned} A_Y &= {}^{A}\!/_{6}\left\{2(1-S) + \sin^2\beta\ (3\ S + D\cos 2\gamma)\right\} \\ A_Z &= {}^{A}\!/_{3}\left\{2\ S + 1 - \sin^2\beta\ (3S + D\cos 2\gamma)\right\}\ . \end{aligned} \tag{5.249}$$

5.9.4.2 Ferroelectric phase – a model with the tilt fluctuation

Lets assume that azimuthal fluctuation can be ignored in the ferroelectric phase. Then the absorbancies A_Z, A_Y and A_{YZ} can be expressed in terms of $\langle\sin\psi\rangle$ and $\langle\sin^2\psi\rangle$ as follows [7]:

$$\begin{aligned} A_Z = k\ \{&\cos^2\beta\ \left\langle\cos^2\theta\right\rangle - 2\sin\beta\ \cos\beta\ \langle\sin\theta\ \cos\theta\rangle\ \langle\sin\psi\rangle \\ &+ \sin^2\beta\ \left\langle\sin^2\theta\right\rangle\left\langle\sin^2\psi\right\rangle\} \\ A_Y = k\ \{&\cos^2\beta\ \left\langle\sin^2\theta\right\rangle + 2\sin\beta\ \cos\beta\ \langle\sin\theta\ \cos\theta\rangle\ \langle\sin\psi\rangle \\ &+ \sin^2\beta\ \left\langle\cos^2\theta\right\rangle\left\langle\sin^2\psi\right\rangle\} \\ A_{YZ} = k\ \{&\langle\sin\theta\ \cos\theta\rangle\ \left[\cos^2\beta - \sin^2\beta\ \left\langle\sin^2\psi\right\rangle\right] \\ &+ \sin\beta\ \cos\beta\ \left[\left\langle\cos^2\theta\right\rangle - \sin^2\theta\right]\ \langle\sin\psi\rangle\} \end{aligned} \tag{5.250}$$

The polar angles β describing the orientation of the transition dipoles in the molecular system are widely reported in the literature [23, 24]. Since the angle θ describes the orientation of the molecular long axis ($\boldsymbol{z}$ axis) in the laboratory system, the averages $\langle\cos^2\theta\rangle$ and $\langle\sin\theta\cos\theta\rangle$ provide information about the distribution of the long molecular axis. In order to reduce the number of unknown variables in (5.250) the averages $\langle\sin\psi\rangle$ and $\langle\sin^2\psi\rangle$ can be expressed in terms of the following approximation for the azimuthal distribution function $f(\psi)$ [7]

$$f(\psi) = \frac{1}{2\pi} + a\cos(\psi - \psi_0) + b\cos\ [2(\psi - \psi_0)]\ , \tag{5.251}$$

$$\langle\sin\psi\rangle = \int_0^{2\pi} \sin(\psi)\ f(\psi)\ d\psi = \pi\, a\sin(\psi_0),$$

$$\left\langle\sin^2\psi\right\rangle = \int_0^{2\pi} \sin^2(\psi)\ f(\psi)\ d\psi = \frac{1}{2}\left[1 - \pi\, b\cos(2\psi_0)\right],$$

where: a, b indicate the degree of polar and quadrupolar biasing and ψ_0 is the angle of biasing. The overall distribution for all molecules is generally a linear combination of $[f(\psi) + f(-\psi)]/2$ and $[f(\pi - \psi) + f(-\psi + \pi)]/2$. For positive polarization the first term is predominant while for the negative polarization the second one.

5.9.4.3 Biased rotation of the 12OBBB8 molecule in in the SmC^*_A and SmC^* phases

Calculations of the absorbance components have been carried out for the 12OBBB8 sample [15] of the structure shown in Fig. 5.111(b). The absorbance profiles, $A(\omega)$, have been obtained in SmA (395 K), SmC^* (380 K) and SmC^*_A phase (345 K), see Fig. 5.115. Results for angular shift of different bands are given in Table 5.8. The absorbance profiles for three bands were used simultaneously for the calculation of the rotational distribution around the long

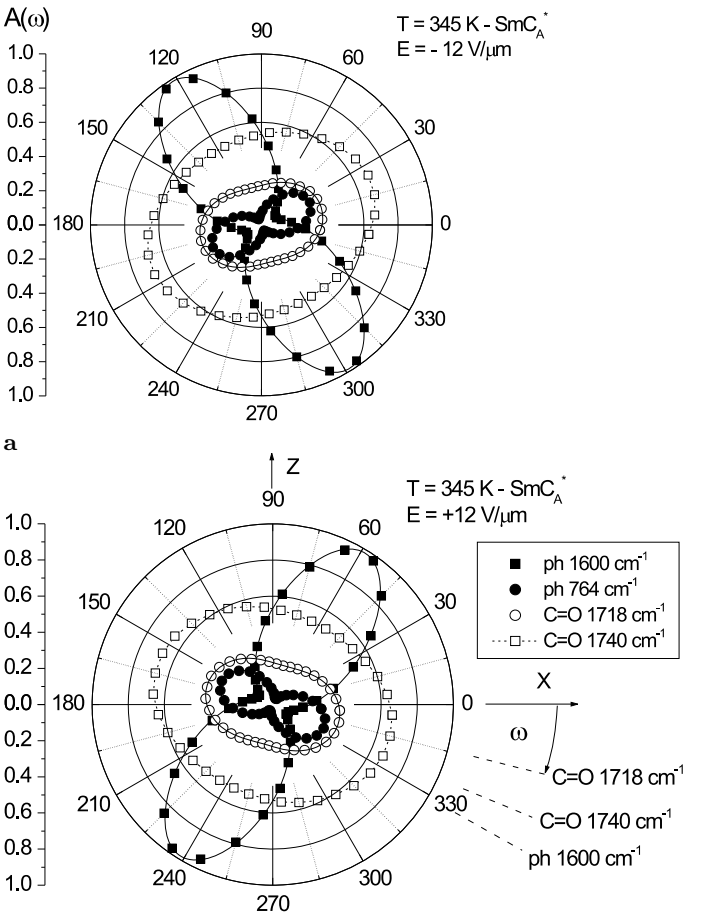

Fig. 5.115. Absorbance profiles vs. the polarizer rotation angle for representative bands in the SmC^*_A phase of the homogeneously aligned 12OBBB8 sample at 345 K: (**a**) for $E = -12\,\mathrm{V/\mu m}$, (**b**) for $E = 12\,\mathrm{V/\mu m}$. *Symbols* represent the experimental data; *solid lines* are fits to (5.242). • – 764 $\mathrm{cm^{-1}}$; ■ – 1600 $\mathrm{cm^{-1}}$; ○ – 1718 $\mathrm{cm^{-1}}$; □ – 1740 $\mathrm{cm^{-1}}$

Table 5.8. Angular shift ω_o/deg of peak profiles with applied electric field for (S)-12OBBB8

T/ phase	phenyl 1600 cm^{-1}	phenyl 764 cm^{-1}	CH_2 sym 2928 cm^{-1}	CH_2 as 2928 cm^{-1}	CH_3 sym 1380 cm^{-1}	C=O core 1740 cm^{-1}	C=O chiral 1718 cm^{-1}
SmC^*_A F(+)	−30.57	−25.18	−22.58	−26.75	−30.19	−23.34	−14.05
345 K F(−)	31.30	24.69	22.08	26.56	29.43	21.94	15.67
SmC^* F(+)	−25.70	−20.31	−18.61	−23.17	−24.95	−18.86	−13.63
380 K F(−)	25.29	20.85	17.95	23.94	25.11	19.26	13.11

SmC^*_A – E = 12 V/μm, SmC^* – E = 6 V/μm

molecular axis; phenyl ring stretching (∼1600 cm^{-1}), phenyl out-of-plane deformation (764 cm^{-1}) and C=O stretching (∼1718 cm^{-1}). Factors k, for each dipole, were obtained from the band profile in the SmA phase using formula (5.248). Possible conformations of the molecule have been carefully studied with the use of quantum orbital calculations in order to establish realistic geometry of the molecule. The torsional angles C_k-O-C_{ph}-C_{ph} (k-carbonyl, ph-phenyl) and C_{ph}-C_{ph}-C_k=O were 55° and 5°, respectively. They agree well with the values reported for similar structures [25, 26]. Therefore, the structure of the core has been considered not planar – particularly the planes of phenyl rings form angles of about 50° to 60° with respect to each other. The following polar angles of the dipoles were taken: $\beta = 24.4°$ for the phenyl stretching vibration (1600 cm^{-1}), $\beta = 10°$ for C-C out-of-plane vibration (764 cm^{-1}) and $\beta = 61.4°$ for the carbonyl C=O stretching vibration.

In the SmA phase it is commonly assumed that molecules rotate freely around their long axis ($\langle \sin \psi \rangle = 0$ and $\langle \sin^2 \psi \rangle = 0.5$). In such a case the transition dipole is uniformly distributed around the long molecular axis and the order parameter S, for different transition dipole moments, can be simply determined by formula (5.248) and (5.249). However, it was found that values S obtained for different bands are not consistent with each other. Therefore we postulate that the rotation around the long molecular axis is not isotropic, i.e. $\langle \sin^2 \psi \rangle \neq 0.5$. To find the true value of the average one can make use of the structural information e.g. that the azimuthal angles γ, of the C-C phenyl stretching dipole and the out of plane (764 cm^{-1}) vibration dipole moment differ by 90° in the molecular frame. The calculated fluctuations of the long molecular axis were $\langle \cos^2 \theta \rangle = 0.74$ and $\langle \sin^2 \psi \rangle = 0.48$ using the experimental absorbance for the C-C phenyl stretching peak and the formulas (5.248). The same value $\langle \sin^2 \psi \rangle = 0.48$ has also been obtained for the carbonyl dipole near the chiral carbon, see Table 5.9. Next, k factors for each band were obtained from the absorbance components in the SmA phase using (5.250). Non isotropic rotation of the short axis has also been reported by Lalanne et al. [28] for a FLC dynamic studies. They observed pretransitional

Table 5.9. The calculated rotational bias parameters for (S)-12OBBB8

T/K	phase	a	b	$\lvert\psi_0\rvert$	$\lvert\langle\sin\psi\rangle\rvert$	$\langle\sin^2\psi\rangle$
345	SmC^*_A F(+)	0.039	0.052	41	0.081	0.486
	F(−)	0.036	0.065	39	0.072	0.479
380	SmC^* F(+)	0.031	0.055	38	0.050	0.478
	F(−)	0.032	0.047	37	0.049	0.479
395	SmA	–	–	–	–	0.480

slowing down far above the SmC^*-SmA phase transition temperature using the degenerate four wave mixing investigation for chiral compounds. This effect appears to be directly linked to the ψ privileged direction evidenced by IR experiments.

In order to solve this problem in SmC^*_A and SmC^* phase, a simultaneous calculation were carried out for three transition dipole moments located in the molecular core. These are the phenyl stretching vibration (1600 cm^{-1}), the C-C out of plane vibration (764 cm^{-1}) and the carbonyl C=O stretching vibration near the chiral center. The molecular core was assumed to be rigid hence the biasing parameters for the constituents of the core were calculated as an entity. The averages $\langle\sin\psi\rangle$ and $\langle\sin^2\psi\rangle$ were substituted in (5.250) using the approximation for the azimuthal distribution function (5.251). It was reasonable to assume that the transition dipole moments under consideration must have the same degree of biasing (a and b) but with different biasing angles. For simplicity reasons the azimuthal angle γ for chiral carboxyl dipole in the molecular system was chosen to be zero. So, the biasing angle, ψ_0, directly indicates the privileged orientation of the chiral carboxyl dipole. Consequently, privileged orientations of other dipoles can be found from torsional angles between the corresponding dipoles in the molecule. The overall distribution for all molecules was taken as a linear combination of $[f(\psi) + f(-\psi)]/2$ and $[f(\pi - \psi) + f(\pi + \psi)]/2$.

The results of calculations are listed in Table 5.9 in terms of rotational bias parameters. Values of $\langle\sin\psi\rangle$, $\langle\sin^2\psi\rangle$ and ψ_0 are related to the chiral carbonyl dipole for the positive electric field. For the negative field, the angle ψ_0 turns into $\psi_0 + 180°$. In all the above cases the calculated parameters reproduce the experimental profile extremely well (see Fig. 5.115). The fitting parameters; $\langle\cos^2\theta\rangle$ and $\langle\sin\theta\cos\theta\rangle$ and a, b, can be used for reproducing the absorbance profiles of the remaining carbonyl group centered at 1740 cm^{-1} and the symmetrical stretching CH_3 band 1380 cm^{-1}. The absorbance profile of the 1740 cm^{-1} band (Fig. 5.115) was found to be a superposition of the two profiles, one with an angle $\omega_0 = 13.5°$, the other with the angle $\omega_0 = 9°$ in the SmC^*_A phase. This reflects the fact that one of the C=O dipole moments is rotated with respect to the second one by a torsional angle of $\sim 55°$ so they have a different privileged orientation. The calculated profile reproduces the experimental data quite well. For the CH_3 group, the polar angle was taken to be 109° and the best fit to the experimental data is obtained when

$\psi_0 = 222°$. This is in good accordance with the torsional angle between the carbonyl group and CH_3 group, of about 220°, which is quite a reasonable value for the most probable conformation [25]. From our calculations, we obtain tilt angle of 25.0° for SmC* and 29.8° for SmC^*_A phase. These are in good agreement with the experimental values for the SmC* phase.

These results show a slightly higher angle and degree of biasing for the C=O transition dipole moment in the SmC_A* phase than in SmC*, although angles of biasing are very similar to those reported for the Ajinomoto compound [7]. The degree of polar biasing, factor a, was found to be significantly lower than factor b of the quadrupolar biasing of the distribution function in contrast to the result for the Ajinomoto compound.

5.9.4.4 Antiferroelectric and ferroelectric phase – a model with tilt and phase fluctuation

The analytical formulas (5.249) proposed by Jang et al. [7] are very convenient in use, nevertheless, the assumptions made for the model are not realistic in most cases. Fluctuations of the tilt angle are restricted in the model to a single plane and therefore formula (5.249) does not transform into formulas (5.248) on entering the SmA phase. It is clear that in SmA phase fluctuations of the tilt are twice degenerated and in such a case a model assumption cannot be used. On the other hand fluctuations of the azimuthal angle are known to be quite strong in all tilted phases, even more important than the tilt angle fluctuations. It would also be difficult to analyze the absorbance profile, obtained as a function of a sample rotation, in an oblique incidence mode. Such a profile cannot be reproduced if azimuthal fluctuations are ignored. Therefore an attempt has been made to calculate absorbance components for a general case, i.e. in the presence of both the tilt angle and azimuthal angle fluctuations. A similar calculation procedure was used as previously: transition dipole components were transformed from molecular to the laboratory frame of reference. It is worth noting, that the resulting formulas are quite complicated and they are expressed in terms of many averages, which are dependent basically on the orientational distribution function $f(\theta, \phi, \psi)$ and some approximations need to be done in order to simplify the problem. For small tilt fluctuations it is reasonable to assume that $f(\theta, \phi, \psi) = f(\psi)$ $f(\theta, \phi)$, where $f(\psi)$ has a similar form as previously (5.251), and $f(\theta, \phi)$ is approximated by the functions:

$$f(\theta, \phi) = g(\theta)\ h(\phi)/C,$$

where: $g(\theta) = \exp(-\ln(5.243)\sin^2(\theta - \theta_0)/\delta\theta^2)$,

$$h(\phi) = \exp(-4\ln(5.243)\sin^2(\tfrac{1}{2}(\phi - \phi_0))/\delta\phi^2),$$

$$C = \int g(\theta)\ h(\phi)\, d\phi\ \sin\theta\, d\theta. \tag{5.252}$$

Distribution functions $g(\theta)$ and $h(\phi)$ have a π and 2π periodicity, respectively, and they become normal (gaussian) distributions for small half widths, $\delta\theta$ and $\delta\phi$, respectively.

Using the above distribution function we can simulate the angular dependence of the IR absorbance for any experimental geometry applied in the experiment, i.e. vs. polarization angle, $A(\omega)$, in the normal transmission mode and vs. sample rotation, $A(\alpha)$, in the oblique incidence mode for both homogeneous and homeotropic alignment. It was possible to reproduce absorbance components for a number of bands. As a result of the fitting procedure both were obtained: the parameters of biasing, for the rotation around the long molecular axis, as well as the fluctuations of the azimuthal angle, $\delta\phi$, and the tilt angle, $\delta\theta$, of the long molecular axis.

Calculation has been carried out for the AFLC sample, (S)12OBBB8 using the same structural parameters as in the last paragraph. Absorbance profile $A(\omega)$ and $A(\alpha)$ have been simulated for major bands:) phenyl ring stretching ($\sim$ 1600 cm^{-1}) peak, phenyl out-of-plane deformation (764 cm^{-1}) and C=O stretching ($\sim$ 1718 cm^{-1}) in order to find the most appropriate parameters of the orientational distribution function. Qualitative information about the orientation and fluctuation of the long molecular axis ($\boldsymbol{z}$ axis of the molecular system) can be preliminarly achieved by analyzing $A(\omega)$ and $A(\alpha)$ profiles of the phenyl ring stretching peak.

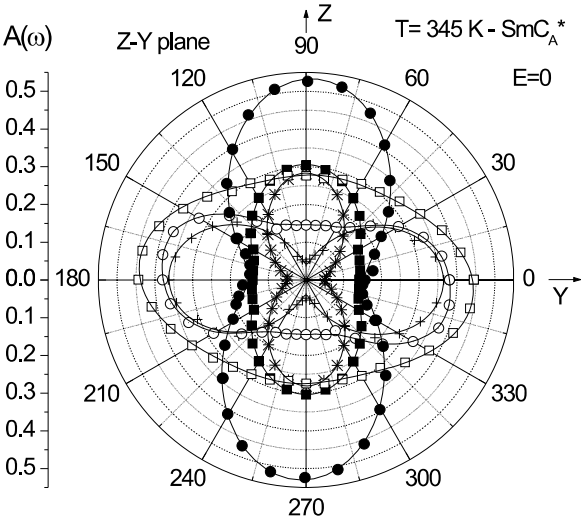

Fig. 5.116. Absorbance profiles vs. the polariser rotation angle for representative bands in unwound SmC$_A$* phase of the homogeneously aligned 12OBBB8 sample at 345 K. *Symbols* represent the experimental data; *solid lines* are fits to (1) : • – 756 cm^{-1}, + – 764 cm^{-1}; ∗ – 1600 cm^{-1}; ■ – 1610 cm^{-1}; ○ – 1729 cm^{-1}; □ – 1735 cm^{-1}. Absorbance for 1735 cm^{-1}is multiplied by factor 0.5

In the SmC^*_A phase an alternating field of the frequency 1 kHz and of the amplitude of 5 V/μm was applied in order to unwound the helical structure. The amplitude was not sufficient to switch the sample into the ferroelectric state, hence the unwound AF structure was achieved. Figure 5.116 and Fig. 5.117(a) show $A(\omega)$ and $A(\alpha)$ profiles, respectively. $A(\omega)$ profiles obtained for the phenyl bands show high dichroism with the maximum in the plane perpendicular to the smectic layer for the phenyl stretching band

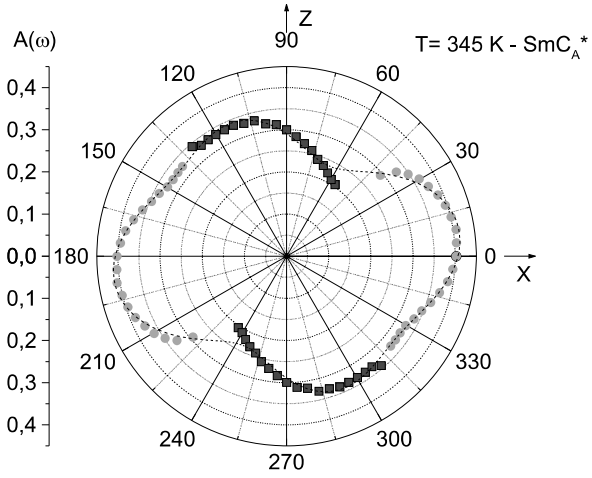

a

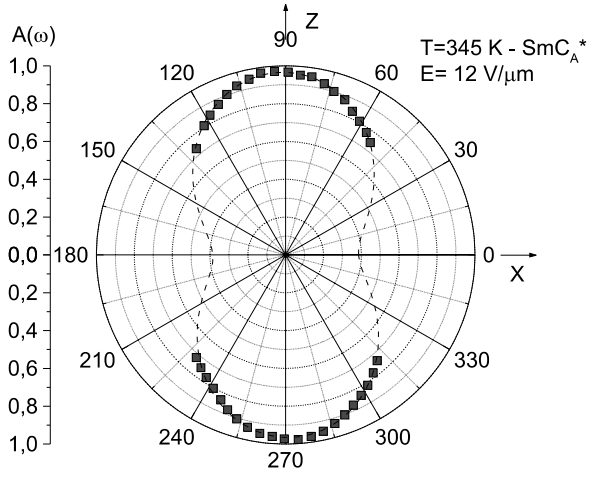

b

Fig. 5.117. Absorbance profiles, $A(\alpha)$, for phenyl bands of (S)-12OBBB8 compound obtained in oblique incidence mode. (**a**) unwound SmC^*_A phase at 345 K, (**b**) electrically induced ferroelectric state at 345 K. *Symbols* represent the experimental data: ● – 764 cm^{-1}, ■ – 1600 cm^{-1}

(1600 cm^{-1}) and in the plane of the smectic layer for the out-of-plane phenyl band (764 cm^{-1}). The oblique angle profile, which is presented in Fig. 5.117(a) as a combination of 1600 cm^{-1} and 764 cm^{-1} peak profiles $A(\alpha)$, shows two distinct maxima for the phenyl band. Here, the phenyl 1600 cm^{-1} peak profile was rotated 90° in order to display (together with 764 cm^{-1} profiles) the

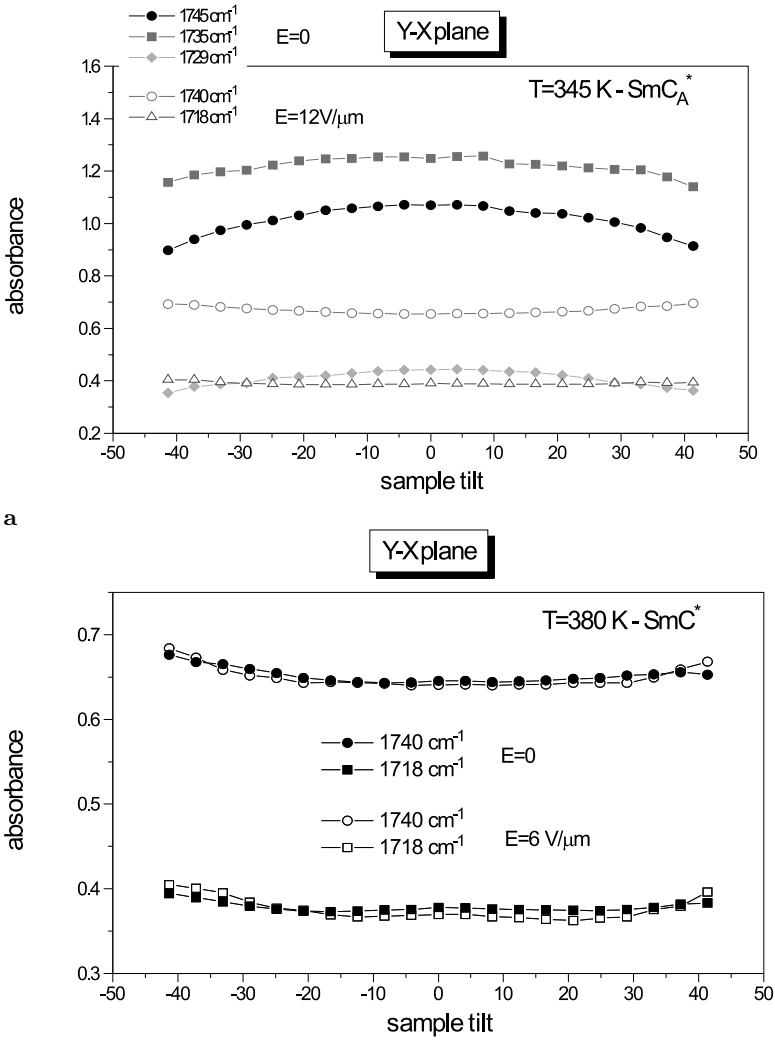

Fig. 5.118. Absorbance dependence, $A(\alpha)$, for carbonyl bands of (S)-12OBBB8 obtained in oblique incidence mode. (**a**) unwound AF : 1729 cm^{-1}(◆), 1735 cm^{-1}(■), 1745 cm^{-1}(●), and induced ferroelectric structure 1718 cm^{-1}(△), 1740 cm^{-1}(○) in SmC^*_A phase at 345 K: (**b**) SmC^* phase at 380 K: 1718 cm^{-1}(□), 1740 cm^{-1}(○)

angular distribution of the long molecular axis. It is likely that these two maxima correspond to the anticlinic AF structure with the director tilt in the ***X-Z*** plane. They are separated by 70°, which is approximately double the tilt angle at this temperature. Oblique angle dependence, $A(\alpha)$, obtained for the carboxyl C=O stretching ($\sim$1718 cm^{-1}) (see Fig. 5.118a) shows maximum at $\alpha \cong 0$ which suggests that C=O dipole is close to the ***Y*** axis in the unwound SmC$^*_A$ phase. In the SmC* phase and induced F+ and F− states of the SmC$_A$* phase the absorbance shows minimum at $\alpha \cong 0$ so the chiral C=O dipole is rather close to the ***X*** axis.

In the SmC* phase two ferroelectric states F+ and F− were induced following the application of the electric field, +12V/μm and −12V/μm, respectively. Figure 5.115 shows that the peak maxima rotate clockwise for +12V/μm (or anticlockwise for −12V/μm) with respect to the position in SmA phase. The $A(\alpha)$ profile for the phenyl stretching band (1600 cm^{-1}) indicates that the long molecular axes align close to the ***Z-Y*** plane. So it is reasonable to initially assume the most probable azimuthal angle, $\phi_0 \cong 0°$, that coincide with the tilt plane, and the tilt angle, θ_0, to be equal to the phenyl switching angle $\theta_0 \cong 31°$. Since the phenyl stretching dipole nearly coincides with the long

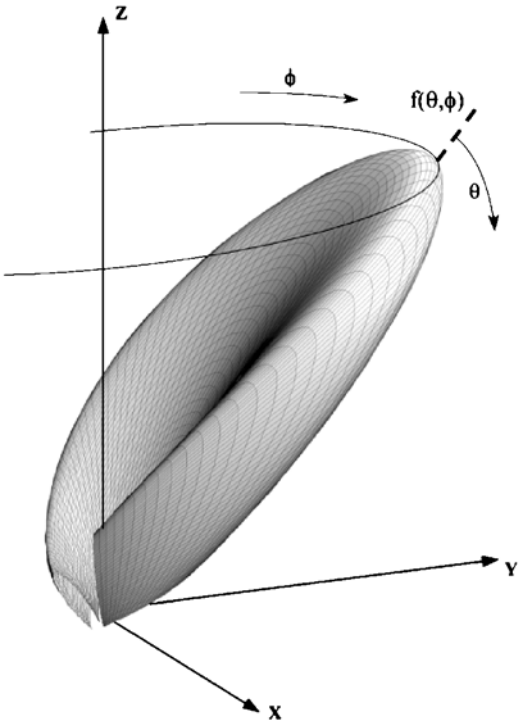

Fig. 5.119. Orientational distribution function $f(\theta, \phi)$ for long molecular axis in electrically induced F(+) state of SmC$^*_A$ phase at 345 K of (S)-12OBBB8

molecular axis we can expect that $A(\omega)$ profile displays their distribution in the tilt plane, that is described by $\delta\theta$, Fig. 5.117(b). On the other hand, $A(\alpha)$ profile for the phenyl ring, which is a cross section of the absorbance perpendicular to the tilt plane, display the azimuthal angle fluctuations $\delta\phi$. Undoubtedly the angular width of the $A(\omega)$ profile is narrower than the $A(\alpha)$ profile therefore we can conclude that the tilt angle fluctuations are smaller than the azimuthal fluctuations. Quantitative comparison of the simulated and experimental absorbance profiles (done for 1600 cm^{-1}, 764 cm^{-1} and 1718 cm^{-1} band) deliver the following parameters of the distribution function, $f(\theta, \phi)$: $\theta_0 = 34°$, $\delta\theta = 12°$, $\phi_0 = 0°$, $\delta\phi = 47°$, see Fig. 5.119. It might be slightly surprising that the fitted value of the tilt angle, θ_0, is significantly higher than the apparent tilt for the phenyl stretching dipole. This is, however, explained by the broad azimuthal distribution of the long molecular axes. A significant contribution from transition dipoles far from $\phi_0 = 0°$ plane makes the apparent tilt angle lower than the true tilt angle. The biasing angle, $\psi_0 = 33°$ is similar to the one found with the use of formulas (5.250), (5.251) while the biasing degree parameters, $a = 0.14$, $b = 0.18$, are almost four times higher than the ones obtained previously.

5.9.5 Dynamics of the electric field induced molecular reorientation

TRS may be categorized into two types: time-domain experiments and frequency-domain experiments. The output from the time-domain experiments is a stack of time-resolved spectra; the structural and orientational changes of the sample can be analyzed in terms of spectral changes. In the frequency domain experiments, a frequency correlation analysis is applied to the time resolved spectra to yield a spectrum defined by two independent infrared wave numbers. Thus information about the dynamic orientational correlation between different parts of the molecule can be obtained. The main idea of the step-scan interferometry lies in fact that the optical retardation of the interferogram is held constant during sampling of the time dependence of the signal. Consequently the spectral multiplexing is decoupled from the time dependence of the data collection. Interferogram elements are finally sorted out and rearranged into a family of interferograms attributed to the relevant lag of the time scale. The output from the experiment is a stack of time-resolved spectra, that are obtained as Fourier transforms of the interferograms, Fig. 5.120.

The experiment was carried out at temperature of 345 K on the mono-domain (S)-12OBBB8 sample of the homogeneous orientation. A square wave electric field, with amplitude of 10 V/μm was applied across the sample and this produced a director reorientation between 30° and –30° with respect to the layer normal. The response times of 4.9 μs for (S)-12OBBB8 were determined from the observed rotation of the optic axis in visible range. The IR spectra in the wave number range from 500 to 4000 cm^{-1} were determined and analyzed for principal bands.

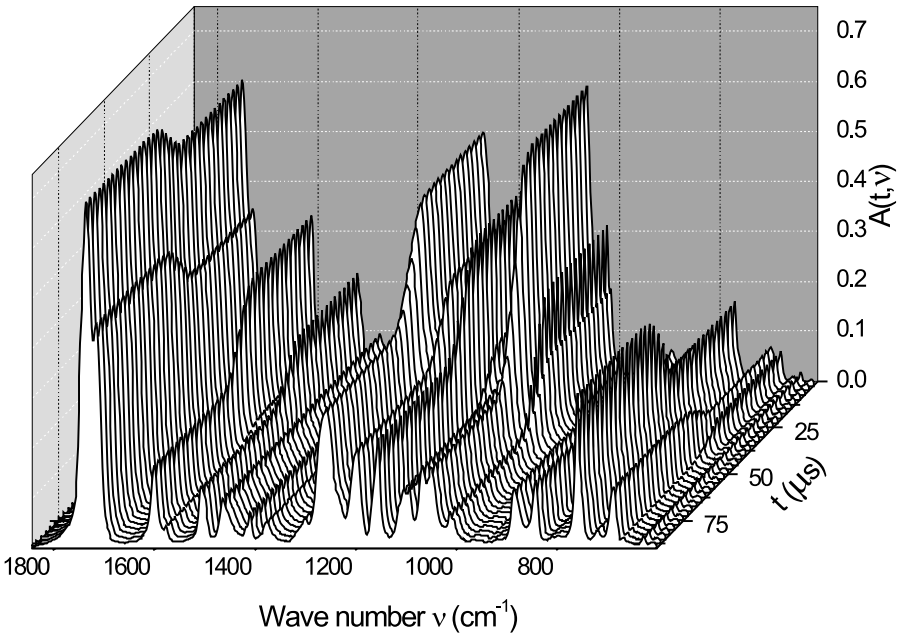

Fig. 5.120. Water fall plot of absorbance vs. wavenumber and time in its response to a square shape of the applied external field for (S)-12OBBB8 sample

It is unreasonable to directly compare the time dependence of the absorbance for different bands. The absorbance is not a simple function of the polarization angle and in general it is not easy to get information about the reorientational motion from absorbance measurements taken at an arbitrary polarization angle. In principle, it is better (however more time consumable) to follow the orientational dynamics of different molecular segments by carrying out the time-resolved experiment for different angles of the polarizer. The absorbance profiles $A(\omega)$ were obtained for selected molecular segments at each lag of time, Fig. 5.121. The apparent tilt angles for particular segments were taken as positions of maximal absorbance and are shown as a function of time in Fig. 5.122.

As expected the absorbance profiles recorded for most prominent bands in the SmA* phase, clearly show the C 2mm symmetry about the normal to the smectic layer plane, $\omega = 0$, with the mirror planes perpendicular and along the layer normal. Effect of the electric field in the SmC$^*_A$ phase is shown on Fig. 5.121, and it presents a temporal evolution of absorbance profiles induced by switching the electric field from -20 to 20 V/μm at $t = 0$. As noted before for the apparent angle measurements, here it is also clear that the core transition dipoles rotate through a larger angle than the tail transition dipoles. This indicates that in equilibrium under the applied field the tails are less tilted than the cores with respect to the layer normal.

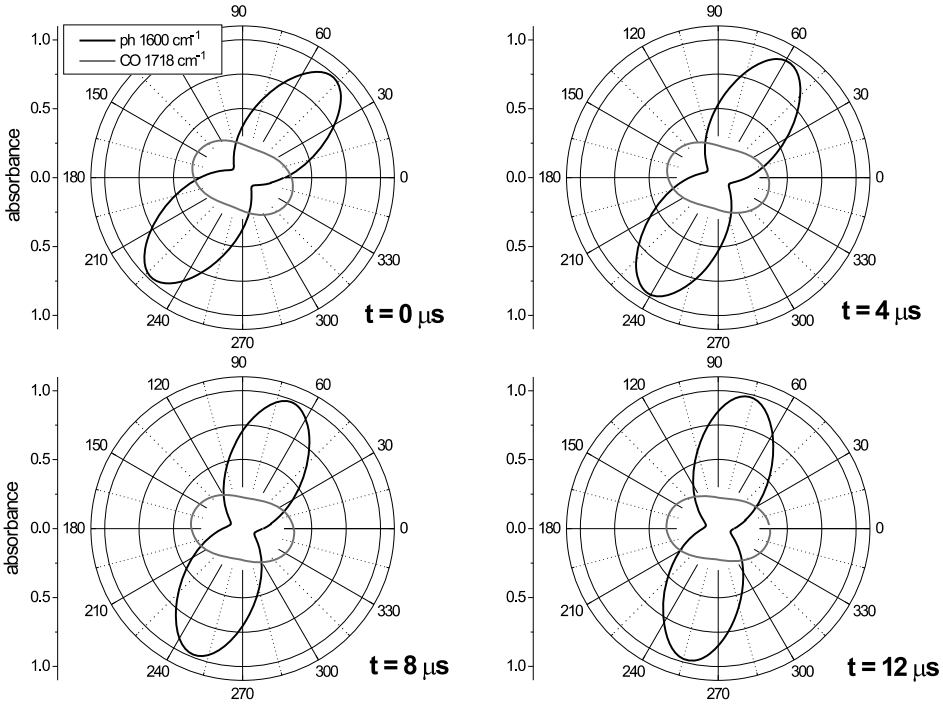

Fig. 5.121. Absorbance profiles for (S)-12OBBB8 samples during electrically induced transition from F− to F+ state

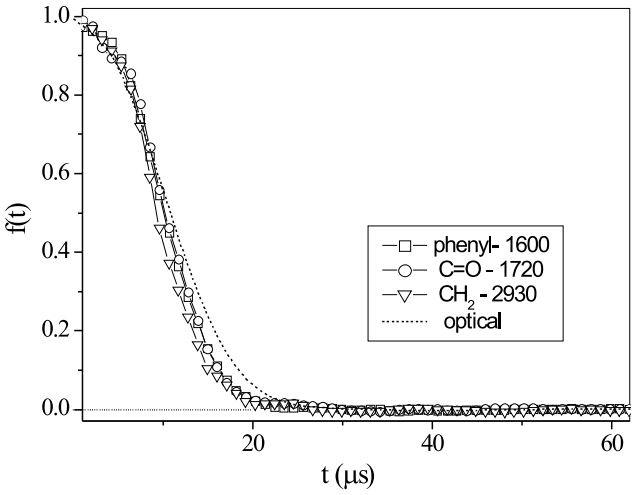

Fig. 5.122. Time dependence of the apparent tilt angle for the 1600 cm^{-1} (□), 1720 cm^{-1} (○), 2930 cm^{-1} (∇), and the optical tilt angle (· · ·) for (S)-12OBBB8 sample

Despite the differences in angular velocities for different absorbance profiles the final (equilibrium) position is reached at approximately the same time. This fact can be clearly shown by plotting the fractional evolutions, $f(t) = (\omega(t) - \omega_{\min})/(\omega_{\max} - \omega_{\min})$. They exhibit a similar reorientation rate as the one found from the optical switching, see Fig. 5.122 for (S)-12OBBB8. Nevertheless, there are some significant differences observed for different transition dipoles in the character of the temporal evolution, $f(t)$. In contrast to the monotonic decay found for the phenyl stretching dipole the other two dipoles, i.e. carboxyl C=O and CH_2 symmetric stretching show significant overshooting before they reach equilibrium position. Some characteristic oscillation of the $f(t)$ dependence can also be seen in the case of C=O and CH_2 bands. It would be quite interesting to understand the molecular mechanisms of such behavior. The main process that occurs for all dipoles and is described by the switching time of the order 5 μs, is due to the collective reorientation of the long molecular axis. The other process, seen only for transversal dipoles, is probably related to collective changes of the biasing angle. It is useful to apply Fourier analysis to separate those two processes. Figure 5.123 shows the imaginary part of Fourier transform of $f(t)$. The main peak at the low frequency of about 30 kHz occurs for all dipoles and a quite weak one (at about $1.8 \cdot 10^5$ Hz) is visible for C=O dipole and similarly for the dipole of CH_2 bands. For comparison we also measured the dynamic dielectric response using the similar driving voltage as in the dynamic IR response in the frequency domain.

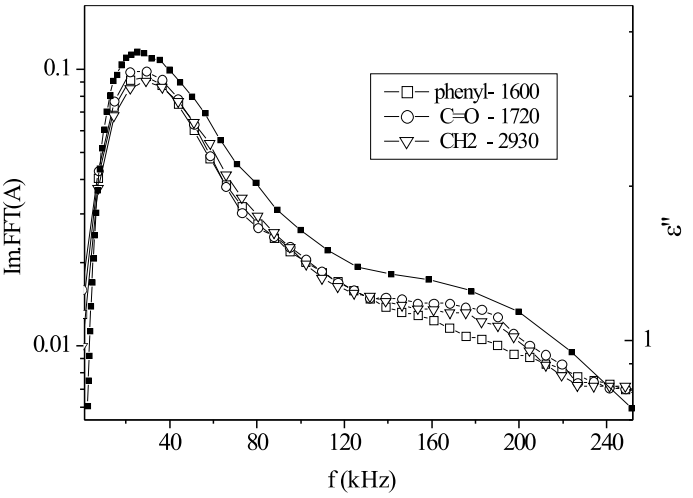

Fig. 5.123. Imaginary part of the FFT of the IR response obtained for the 1600 cm^{-1} (□), 1720 cm^{-1} (○), 2930 cm^{-1} (▽) , and (■) dielectric response for (S)-12OBBB8 compound

The problem of finding the mechanisms governing the various relaxation processes in the antiferroelectric phase is not straightforward, and a combination of dielectric, electro-optic and photon correlation spectroscopy was already used to study these phenomena. Four possible physical mechanisms are suggested to exist in SmC_A^* phase. These are: 1) anti-phase motion or the distortion of the antiferroelectric order caused by the change of azimuthal angle in the opposite sense for the two adjacent layers; 2) in phase fluctuation of the tilt angle or the antiferroelectric soft mode; 3) non-cancellation mode due to the fluctuation of the net polarization in the antiferroelectric phase, which is caused either by the anti-phase fluctuations of the tilt angle or helical fluctuations of the azimuthal angle (Goldstone mode) according to other authors; and 4) disturbance of antiferroelectric helix owing to the dielectric anisotropy. It has to be noted however that the above mechanisms are typical for low value of driving voltage. In order to get the measurable effect in time resolved IR spectroscopy, however, we use rather high value of driving voltage, which possibly switches sample directly from one induced ferroelectric state to another. Therefore, we can rule out those mechanisms, which are due to the antiferroelectric polarization. On the other hand, the fact of non-appearance of the high frequency mode for the phenyl stretching dipole might suggest that this process is due to the collective rotation around long molecular axes. Hence, this process is probably related to changes of the biasing angle or the biasing amplitude [7, 15] in the rotation around the long molecular axis. It is reasonable to compare the dynamic IR response in frequency domain with dielectric response for the similar driving voltage. Interestingly dielectric response also consist of two peaks of about similar frequencies as was observed for the C=O band. The low frequency peak seems to have the same origin as suggested for IR dynamic response but the high frequency one has been usually assigned to the deviation from antiferroelectric ordering [29]. It is possible that use of time resolved IR spectroscopy, with different geometry or combined with other experimental methods, will help to clarify the origin of this mode.

5.9.6 Summary

Absorbance profiles of different molecular segments have been analyzed in SmA, unwound SmC^* and the two states (AF and F) of SmC_A* phase. It was shown that the absorbances of the different bands attain their maxima at different angles of polarization. This gives clear evidence of biasing rotation of almost all molecular segments, hence of the whole molecule, around its long axis.

Two models have been used for calculation of the IR absorbances in the ferroelectric phase. In the first approach analytical formulas have been obtained for absorbance vs. polarizer angle dependence considering tilt angle fluctuation while the azimuthal fluctuations were ignored. For the second model general formulas have been obtained that include both the tilt angle and the azimuthal fluctuations. The absorbance profiles have been simulated for the

model and orientational distribution function parameters have been obtained. Tilt angle fluctuations have been found to be much smaller than the azimuthal ones. It has been proved that AFLC molecules as a whole perform biasing rotation around the molecular long axis. The biasing orientation for the chiral carboxyl dipole is found close to the normal to the ***X-Z*** plane in ferroelectric phase or close to the ***Y-Z*** plane in the AF phase.

Despite the differences in the temporal evolution of the orientations of different absorbance profiles the equilibrium position is reached at approximately the same time. The main process, which is described by switching time of the order 5 μs, occurs for all dipoles and is assigned to the reorientation of the long molecular axis. The other process, which is observed only for transversal dipoles, is probably related to the change of the biasing angle. The results are found to be consistent with the dynamic observations obtained by electrooptical and dielectric methods.

Acknowledgments. Support from the Committee for Scientific Research (KBN): Grant No 2P03B 09817 is gratefully acknowledged.

References

1. R.B. Meyer, L. Liebert, L. Strzelecki, P. Keller: J. Phys.(Paris) **36**, L69 (1975)
2. R.B. Meyer: Mol. Cryst. Liq. Cryst. **40**, 33 (1977)
3. K.H. Kim, K. Ishikawa, H. Takezoe, A. Fukuda: Phys. Rev. E **51**, 2156 (1995)
4. K. Miyachi, J. Matsushima, Y. Takanishi, K. Ishikawa, H. Takozoe, A. Fukuda: Phys. Rev. E **52**, R2153 (1995)
5. A. Kocot, G. Kruk, R. Wrzalik, J.K. Vij: Liquid Crystals **12**, 1005 (1992)
6. S.V. Shilov, S. Okretic, H.W. Siesler, R. Zentel, T. Öge: Macromol. Rapid Commun. **16**, 125 (1995)
7. W.G. Jang, C.S. Park, J.E. Maclennan, K.H. Kim, N.A. Clark: Ferroelectrics **180**, 213 (1996)
8. T. Perova, A. Kocot, J.K. Vij, R. Zentel: SPIE **2731**, 107 (1996)
9. A. Kocot, R. Wrzalik, J.K. Vij: Liquid Crystals **21**, 147 (1996)
10. S.V. Shilov, H. Skupin, F. Kremer, T. Wittig, R. Zentel: Phys. Rev. Lett. **79**, 1686 (1997)
11. S.V. Shilov, H. Skupin, F. Kremer, F. Gebhard, R. Zentel: Liquid Crystals **22**, 203 (1997)
12. A.L. Verma, B. Zhao, S.M. Jiang, J.C. Sheng, Y. Ozaki: Phys. Rev. E **56**, 3053 (1997)
13. T. Perova. A. Kocot, J.K. Vij: Ferroelectrics **214**, 83 (1998)
14. A. Kocot, T. Perova, J.K. Vij, R. Wrzalik: Ferroelectrics **214**, 1 (1998)
15. A. Kocot, R. Wrzalik, B. Orgasińska, T. Perova, J.K. Vij, H.T. Nguyen: Phys. Rev. E, **59**, 551 (1999)
16. A.L. Verma, B. Zhao, H. Terauchi, Y. Ozaki: Phys. Rev. E **59**, 1868 (1999)
17. T. Nakano, T. Yokoyama, H. Toriumi: Appl. Spectrosc. **47**, 1354 (1993)
18. R.E. Murphy, F.H. Cook, H. Sakai: J. Opt. Soc. Am. **65**, 600 (1975)
19. F. Hide, N.A. Clark, K. Kito, A. Yasuda, D.M. Walba: Phys. Rev. Lett. **75**, 2344 (1995)

20. W.H. de Jeu: *Physical properties of Liquid crystalline Materials* (Gordon & Brach, 1980)
21. E. Hild, A. Kocot, J.K. Vij, R. Zentel: Liquid Crystals **16**, 783 (1994)
22. G. Turrell: Infrared and Raman Spectra of Crystals (Academic Press, 1972) p. 153
23. J.P. Hummel, P.J. Flory: Macromolecules **13**, 479 (1980)
24. P. Coulter, A. Windle: Macromolecules **22**, 1129 (1989)
25. K. Tishiro, J. Hao, M. Kobayashi, T. Inoue: J. Am. Chem. Soc. **112**, 8273 (1990)
26. R. Centore, A. Tuzi: Acta Cryst. **C45**, 107 (1998)
27. H. Toriumi, H. Sugisawa, H. Watanabe: Mol. Cryst. Liq. Crys. **214**, 11 (1992)
28. J.R. Lalanne, J. Buchert, S. Kielich: *Modern Nonlinear Optics*, Advances in Chemical Physics LXXXV, 159 (1993), ed. by I. Prigogine, S.A. Rice, J. Wiley
29. K. Hiraoka, H. Takazoe, A. Fukuda: Ferroelectrics **147**, 13 (1993)

5.10 On the dielectric relaxation in the antiferroelectric phase and sub-phase Alpha

Ch. Legrand, R. Douali, F. Dubois and H.T. Nguyen

5.10.1 Introduction

It is well known that the polymorphism of antiferroelectric liquid crystals is very rich. Indeed, these materials exhibit smectic phases (paraelectric – noted as SmA^*, ferroelectric phase – SmC^*, sub-phase alpha – SmC^*_α, ferrielectric phase – SmC^*_{FI}, and antiferroelectric phase – SmC^*_A) with paraelectric, ferroelectric, ferrielectric or antiferroelectric like properties, respectively [1–3]. A good understanding of the structure and the dynamics of these phases is important from a theoretical point of view and for applications (displays, telecommunications ...) [4, 5]. This explains why a large number of theoretical and experimental studies were devoted to these materials.

Dielectric spectroscopy is one of the techniques used to investigate the molecular dynamics in liquid crystals [6]. The aim of this paper is to report new experimental data on dielectric properties of an antiferroelectric liquid crystal. The discussion is focused on the dielectric behaviors of the SmC^*_α and SmC^*_A phases. In the SmC^*_α phase, without superimposition of a D.C. bias, one relaxation process is detected with a linear temperature dependence of the reversed dielectric strength and of the critical frequency. The SmC^*_α phase is detected since a break in slopes is observed at the SmA^* – SmC^*_α and the SmC^*_α – SmC^* phase transitions. This relaxation process is strongly modified under bias. At high bias, the behavior of the observed process is similar to that of the soft mode at a SmA^* – SmC^* phase transition. Using simulations based on the clock model, the temperature evolutions of the *Goldstone* and soft modes in the SmC^*_α phase are studied. Two different behaviors are evidenced depending on the azimuthal angle difference $\Delta\phi$ between two adjacent

layers. A good agreement is obtained with experimental results by considering the influence of the azimuthal angle ϕ and its temperature evolution. In the SmC^*_A phase, the dielectric spectra show the existence of two relaxation processes denoted L.F. (Low Frequency) and H.F. (High Frequency) with relatively low dielectric strengths. The physical origin of these relaxation processes is discussed. In particular, using dielectric results on *nematic* liquid crystals, we show that the attribution of the L.F. relaxation process to the molecular reorientation around the short axis is possible. The substance investigated shows an interesting polymorphism, so one can use the dielectric data obtained for verification of the discrete model developed recently (see Sect. 5.1 by Žekš and Čepič and Sect. 5.4 by Gorecka et al.).

5.10.2 Experimental

The studied compound is the homologue $n = 11$ (denoted as 11FF) of the following benzoate series (Fig. 5.124) [7]. The mesomorphic properties have been analyzed by optical microscopy on pure enantiomeric and racemic compounds and on mixtures, by means of D.S.C. and electro-optic measurements.

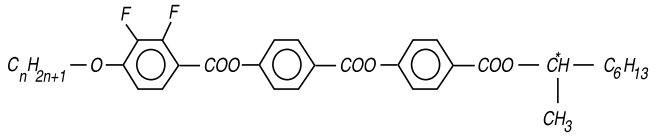

Fig. 5.124. Chemical formula and transition temperatures (in °C) of the 11FF compound

Dielectric measurements have been performed in the homogeneous orientation (helical axis in the preparation plane) on cooling and on heating. The experimental set-up is made of an HP4284A impedance analyzer (20 Hz–1 MHz) and a measuring cell. This set-up and the sample preparation were described in a previous paper [8]. The sample thickness was about 22 µm (much higher than the helical pitch). The homogeneous orientation was obtained with P.V.A. coating and rubbing. The sample orientation was optically checked with a polarizing microscope. To analyze the results, the dielectric spectra were fitted with the following formula using Mathcad software (one relaxation process case):

$$\varepsilon^* = \varepsilon' - i\varepsilon'' = \varepsilon_\infty + \frac{\Delta\varepsilon}{1 + i(F/F_C)^{(1-\alpha)}} - i\frac{\sigma}{2\pi F \varepsilon_0}\,, \tag{5.253}$$

where $i = \sqrt{-1}$, ε_∞ is the permittivity at a high frequency, $\Delta\varepsilon$, F_C and α are respectively the dielectric strength, the critical frequency and the distribution

factor of the relaxation process, σ and ε_0 are the conductivity and the vacuum permittivity. In the SmC^*_α phase, the effect of a D.C. bias superimposed to the measuring field was also studied.

5.10.3 Dielectric studies

5.10.3.1 Static dielectric permittivity

In this section, we discuss the temperature evolution of the static permittivity and attribute the different parts of the plot $\varepsilon_s(T)$ to the different phases exhibited by the compound. The temperature evolution of the measured real part permittivity at low frequency (100 Hz) is reported in Fig. 5.125.

On cooling from the SmA^* phase, the static permittivity ε'_s is first increasing. This increase is more pronounced in the SmC^*_α and SmC^* phases up to a maximum ($\varepsilon'_s \approx 240$) detected at 107.5 °C. This maximum is followed by a strong decrease and a weak increase until 78 °C where a second maximum ($\varepsilon'_s \approx 180$) is observed. At lower temperatures ($T < 78$ °C), we can distinguish two plateaus corresponding to the ferrielectric and the antiferroelectric phases. Let us notice that it is difficult to distinguish the two ferrielectric phases (SmC^*_{FI1} and SmC^*_{FI2}). The lowest value of ε'_s ($T < 65$ °C, $\varepsilon'_s \approx 10$) is obtained for the SmC^*_A antiferroelectric phase. On heating, the general evolution is similar to the one observed on cooling but with a strong temperature shift. Such a shift, more pronounced at low temperatures, has already been reported for other compounds with the same phase sequence [9, 10]. The temperature range attributed to the SmC^*_A antiferroelectric phase is much larger (until 80 °C). As shown in Fig. 5.126, the shift disappears at 108.5 °C. We believe that this temperature corresponds to the SmA^* – SmC^*_α phase transition.

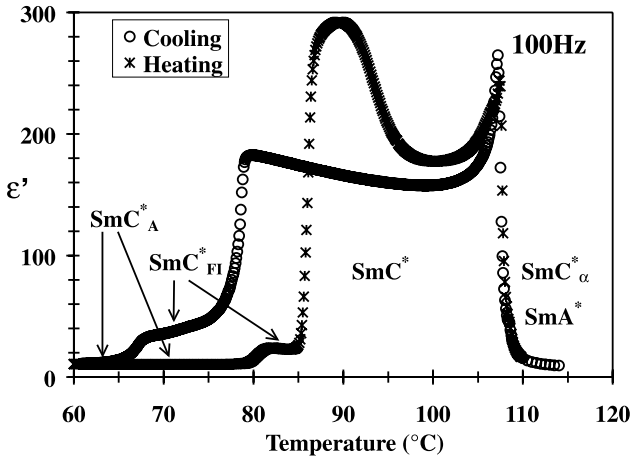

Fig. 5.125. Static permittivity versus temperature

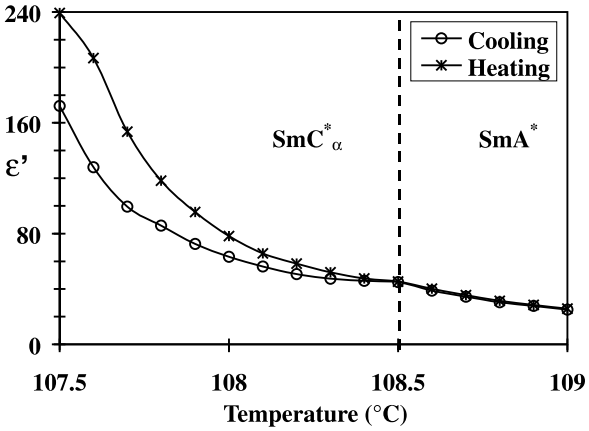

Fig. 5.126. Static permittivity near the SmA^* – SmC^*_α phase transition

The second characteristic of the plot on heating is the high value of ε'_s observed at 89.5 °C ($\varepsilon'_s \approx 290$). Some authors attributed this behavior to an anti-phase dielectric mode in the SmC^*_{FI} ferrielectric phase [10, 11]. In our case, this interpretation is difficult to verify because the dielectric spectra in the SmC^*_{FI} phases are highly polydispersive (contribution of several relaxation processes in the dielectric response) [12]. Due to a low frequency contribution in this temperature range, the real permittivity at 100 Hz is lower than the static value.

5.10.3.2 Evidence of SmA*, SmC* and SmC^*_α phases

Dielectric studies without D.C. bias

Without D.C. bias, except the previously mentioned temperature shift, similar dielectric behavior are obtained on cooling and on heating in the SmA^*, SmC^*_α and SmC^* phases. For this reason, we will present only experimental data on cooling. Examples of dielectric spectra in the different phases are given in Fig. 5.127. In a first approximation, the frequency dependence of ε' and ε'' shows the existence of only one relaxation process. The distribution factor is lower than 0.15, which is in agreement with dielectric spectra dominated by one relaxation process.

Figure 5.128 shows the temperature evolutions of $\Delta\varepsilon$, $1/\Delta\varepsilon$ and F_C. In the SmA^* and SmC^* phases, we find again the dielectric behavior connected respectively with the classical soft mode and *Goldstone* mode [6]. In the SmA^* phase, at $T_C + 2\,°C$ (110.2 °C), the dielectric strength and the critical frequency are respectively 7.5 ($1/\Delta\varepsilon \approx 0.13$) and 120 kHz. The dielectric strength increases up to 30 at the SmA^* – SmC^*_α phase transition whereas the critical frequency decreases up to 20 kHz. The reversed dielectric strength and

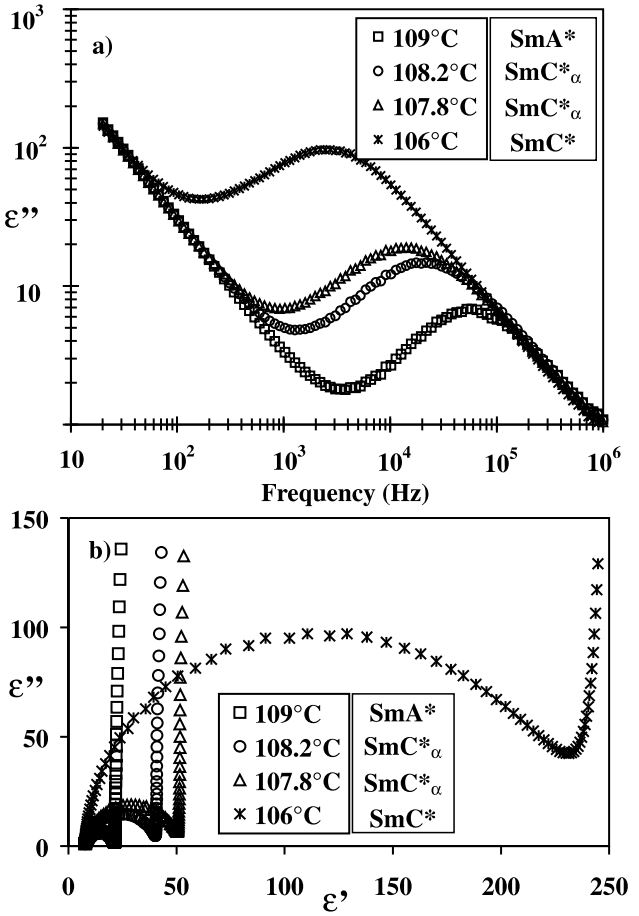

Fig. 5.127. Dielectric spectra and *Cole–Cole* plots in the SmA*, SmC$^*_\alpha$ and SmC* phases without D.C. bias

the critical frequency linearly depend on temperature with slopes of respectively 0.05/ °C and 50 kHz/ °C. In the SmC* phase, the relaxation process presents a high dielectric strength ($\Delta\varepsilon \geq 200$) and a relatively low critical frequency ($F_C \approx 2$ kHz). These two parameters slightly depend on the temperature. The plots $1/\Delta\varepsilon(T)$ and $F_C(T)$ present breaks in slopes (0.02/ °C and 15 kHz/ °C) over a temperature range of 1.2 °C (108.5 °C–107.3 °C). The change of the behavior at 108.5 °C is also observed on static permittivity (Fig. 5.126). The temperature range of 1.2 °C is in agreement with that previously mentioned for the SmC$^*_\alpha$ phase and determined from D.S.C. measurements and optical observations [7]. We attribute the temperatures at which breaks in slopes are observed to the SmA* – SmC$^*_\alpha$ and SmC$^*_\alpha$ – SmC* phase transitions. Let us notice that the SmA* – SmC$^*_\alpha$ transition temperature dif-

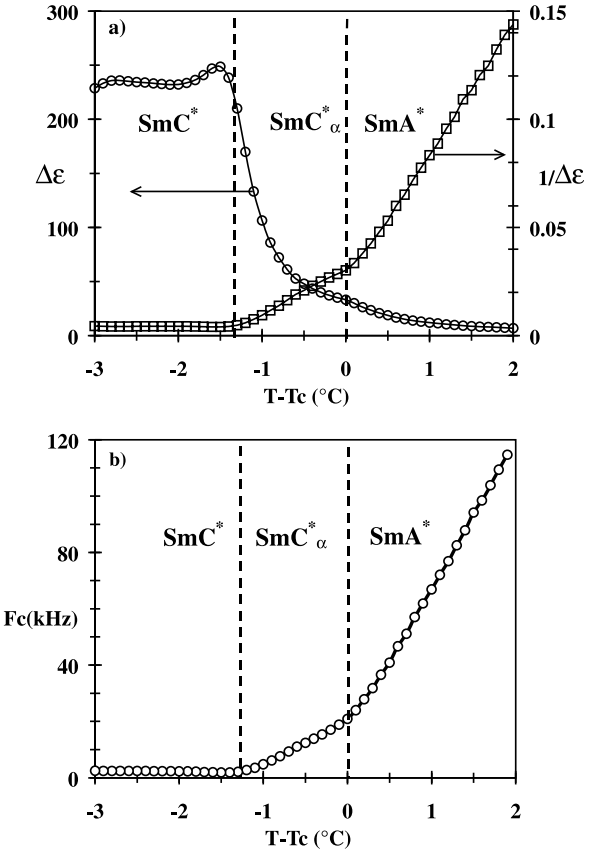

Fig. 5.128. $\Delta\varepsilon$ (**a**), $1/\Delta\varepsilon$ (**a**) and F_C (**b**) evolutions versus temperature in the SmA^*, SmC^*_α and SmC^* phases without D.C. bias

fers from that obtained with the high frequency $\varepsilon'(T)$ curve (Fig. 5.129) and usually used to determine this transition temperature [13]. This last temperature is higher and depends on the selected high frequency. The process observed in the SmC^*_α phase without D.C. bias goes continuously from the SmA^* soft mode to the SmC^* *Goldstone* mode with linear temperature dependencies of the reversed dielectric strength and of the critical frequency. Such an evolution of the dielectric response is in agreement with second order SmA^* – SmC^*_α and SmC^*_α – SmC^* phase transitions as detected with D.S.C. measurements and has already been reported on other compounds [10, 14].

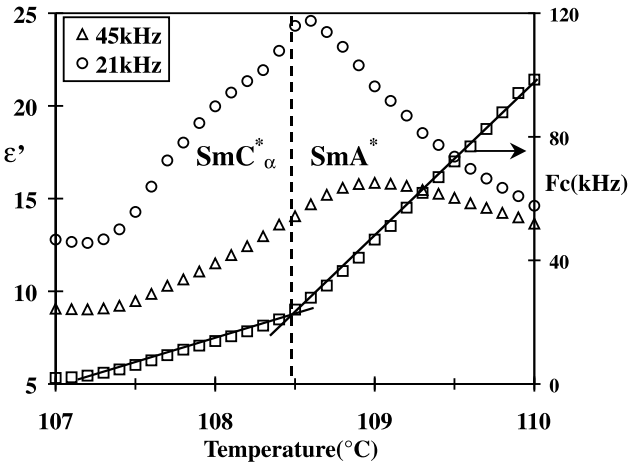

Fig. 5.129. High frequency real permittivity evolution *versus* temperature in the SmA^* and SmC^*_α phases without D.C. bias: comparison with the temperature evolution of the critical frequency $F_C(T)$

Dielectric studies with D.C. bias

To have a better understanding of the origin of the relaxation process observed in the SmC^*_α phase, we have studied the effect of a D.C. bias as a function of temperature.

Figure 5.130 shows the influence on the dielectric spectra of a D.C. bias varying from 0 V to 40 V. Up to 11 V (0.5 V/μm electric field), the dielectric spectra are slightly modified. At higher bias values, the relaxation process shifts at high frequency and its dielectric strength is strongly decreased. This behavior is confirmed in Fig. 5.131 where the bias dependence of these parameters in the SmC^*_α and SmA^* phases is reported for different temperatures. Only weak variations are obtained in the SmA^* phase. Let us notice that only a slight effect of the D.C. bias was observed in the SmC^*_α phase of a compound with similar chemical formula [14]. Our results show that the relaxation process observed in the SmC^*_α phase without bias is connected with the helicity of this phase (*Goldstone* mode).

In Fig. 5.132, the results at high D.C. bias (40 V) are compared to these without D.C. bias. Without D.C. bias, we find again the previously described behavior (Fig. 5.128). Under high D.C. bias, the dielectric strength and the critical frequency present respectively a maximum and a minimum at the SmA^* – SmC^*_α phase transition. Linear temperature dependencies of the reversed dielectric strength and of the critical frequency are also observed from one part to the other of this transition. This behavior [6] is a characteristic of the soft mode at the SmA^* – SmC^* phase transition, usually evidenced with measurements under bias. The relaxation process under bias could be attributed to the soft mode at the SmA^* – SmC^*_α phase transition.

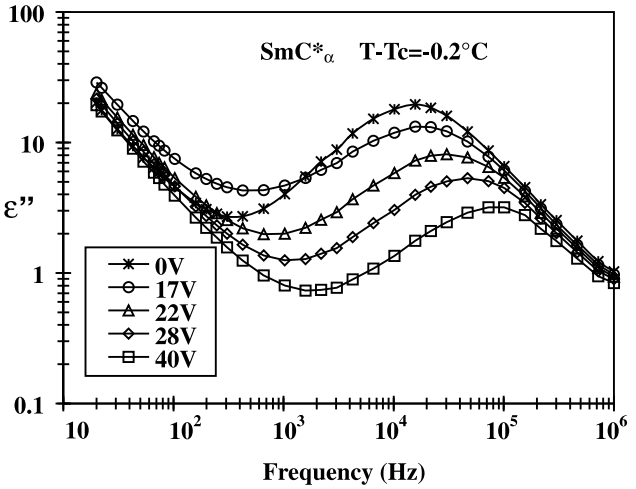

Fig. 5.130. D.C. bias effect on dielectric spectra in the SmC^*_α phase

Confrontation with theoretical predictions

We discuss our experimental results without D.C. bias on the basis of the clock model recently extended to dielectric properties prediction [15–19]. This discrete model takes into account ferroelectric or antiferroelectric interactions of one *smectic* layer with the nearest and next nearest layers respectively via two parameters a_1 and a_2. The azimuthal angle difference between two adjacent layers is linked to these two parameters:

$$\Delta\phi \approx \arccos\left(\frac{-a_1}{a_2}\right) .$$

The model predicts the existence of two relaxation processes connected with the soft mode and the *Goldstone* mode in the SmC^*_α phase. In Fig. 5.133, we present simulations of the dielectric strength ($\Delta\varepsilon_S$, $\Delta\varepsilon_G$) of these processes for two values of the azimuthal angle ϕ. The azimuthal angle is modified with the parameter a_1. The other parameters have been chosen equal to those previously used [19]. For a limited value of the angle ϕ (e.g. 30 °), the amplitude of the *Goldstone* mode is much higher than the soft mode in all the SmC^*_α phase temperature range. So, the soft mode is masked and cannot be detected. When the azimuthal angle is larger (e.g. 150 °), we observe two different dielectric behavior versus temperature. Near the SmA^* – SmC^*_α phase transition, the soft mode is predominant and its amplitude decreases on cooling contrary to the *Goldstone* mode. At lower temperatures, the *Goldstone* mode becomes larger than the soft mode.

The homologue 11FF presents a monotone evolution of dielectric properties. This behavior corresponds to the case of a limited value of the azimuthal angle ϕ. In this case, the relaxation process without D.C. bias is

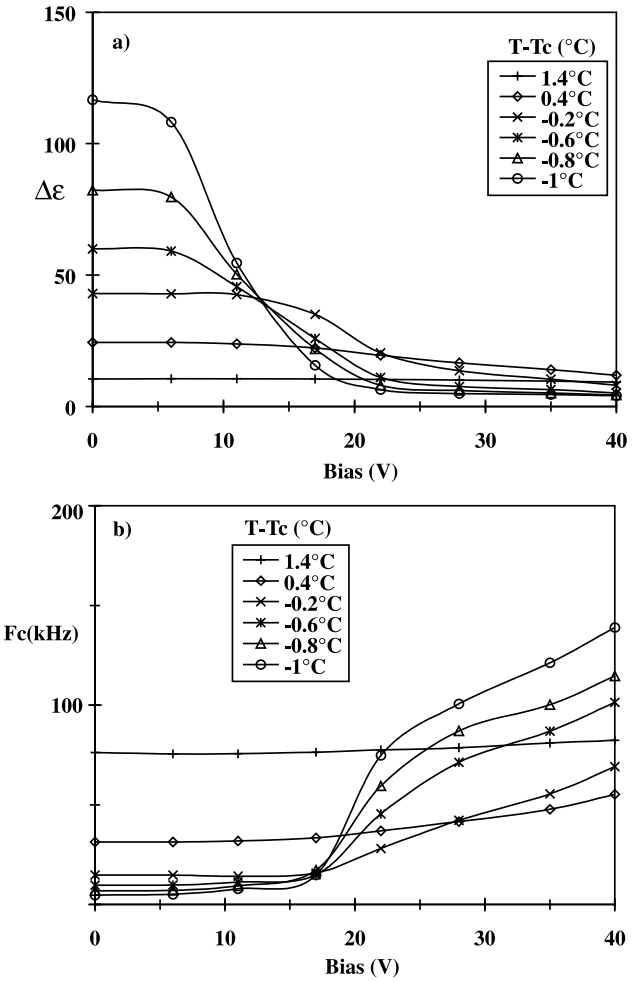

Fig. 5.131. D.C. bias effect on the dielectric strength and the critical frequency in the SmA^* and SmC^*_α phases

linked to the *Goldstone* mode. The dielectric strength increase and the critical frequency decrease observed on cooling can be explained by a decrease of ϕ with temperature. The evolution of the azimuthal angle ϕ experimentally deduced from optical measurements confirms this interpretation: the pitch was found to increase (when ϕ decreases) with temperature in the SmC^*_α phase of the compound [20, 21]. The low dielectric strength and the high frequency of the *Goldstone* mode in the SmC^*_α phase is connected with the very short helical pitch in this phase. Under D.C. bias, the SmC^*_α phase is progressively unwound, the *Goldstone* mode disappears and the soft mode can be detected. Such an interpretation is in agreement with experimental data.

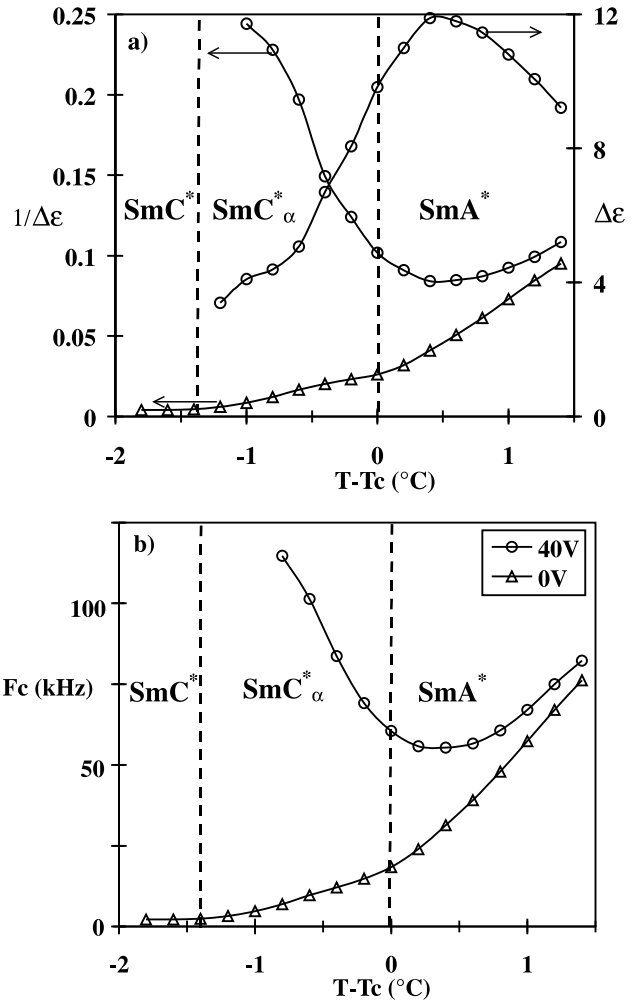

Fig. 5.132. Temperature dependencies of $\Delta\varepsilon$, $1/\Delta\varepsilon$ and F_C without (Δ) and with (O) a D.C. bias of 40 V in the SmC* and SmA* phases

Let us notice that a dielectric behavior corresponding to the second case (high azimuthal angle) has been observed for another homologue of the same series [22].

5.10.3.3 Substantiation of the SmC^*_A phase

Dielectric spectra

The dielectric losses versus frequency $\varepsilon''(F)$ in the antiferroelectric SmC^*_A phase are presented in Fig. 5.134 at different temperatures. They show the

existence of two dielectric relaxation processes with a relatively low dielectric strength. These relaxation processes slightly depend on temperature. They present critical frequencies of about a few kilohertz and a few hundreds kilohertz and are denoted respectively L.F. (Low Frequency) and H.F. (High Frequency). The ionic conductivity ($\varepsilon''_\sigma \propto 1/F$ at low frequencies) is sufficiently weak and does not mask the relaxation at low frequencies.

These two relaxation processes seem to be a characteristic of the antiferroelectric SmC^*_A phase and have been previously observed on other compounds [23, 24]. Different interpretations have been proposed for the molecular dynamics corresponding to these relaxations. To discuss these relaxation processes and their evolution versus temperature, the spectra have been fitted using the previous formula (5.253). A second relaxation process was added:

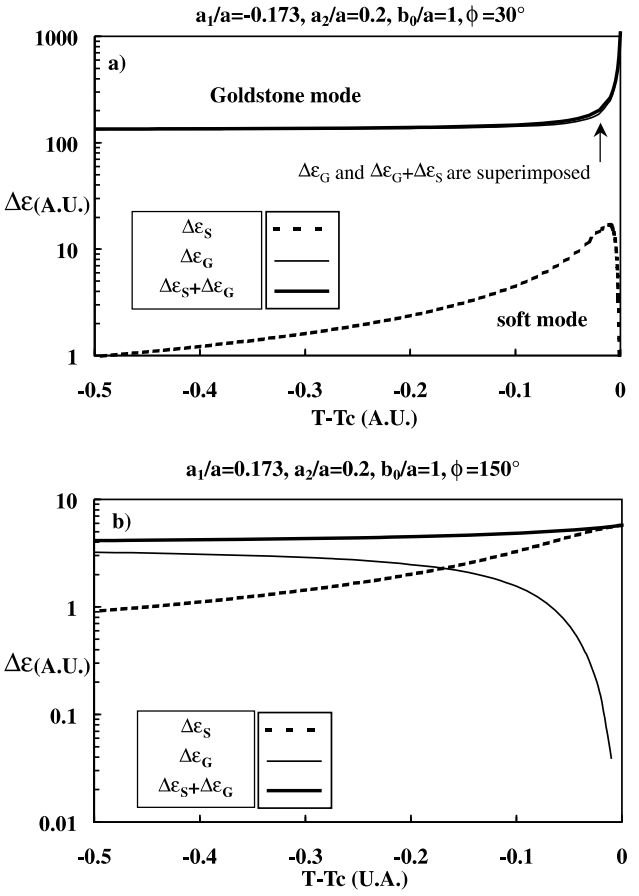

Fig. 5.133. Dielectric strength evolution versus temperature in the SmC^*_ϕ phase (soft and *Goldstone* modes)

$$\varepsilon^*(\omega) = \varepsilon'(\omega) - i\varepsilon''(\omega)$$
$$= \varepsilon_\infty + \frac{\Delta\varepsilon_1}{1 + (i\omega\tau_1)^{(1-\alpha_1)}} + \frac{\Delta\varepsilon_2}{1 + (i\omega\tau_2)^{(1-\alpha_2)}} - i\frac{\sigma}{2\pi F\varepsilon_0}\,.$$

High frequency relaxation processes

Two different interpretations have been reported in the literature for the H.F. process.

Soft mode in the SmC^*_A phase

Some authors have attributed the H.F. process to the soft mode of the SmC^*_A phase [24]. The critical frequency of the H.F. process decreases with temperature (Fig. 5.135). The dielectric strength has a reversed behavior. This is not in agreement with theoretical predictions for the soft mode. For this reason, this attribution has to be rejected for 11FF compound. A second argument is that the soft mode is observable (sufficiently high dielectric strength) only near the transition to the paraelectric phase (SmA^* – SmC^*, SmA^* – SmC^*_α and SmA^* – SmC^*_A phase transitions). In our case, the temperature range between the paraelectric SmA^* phase and the antiferroelectric SmC^*_A phase is large (39 °C).

Anti-phase reorientation

Due to the helicoidal structure of the SmC^*_A phase, the angle α between the macroscopic polarizations in two adjacent layers j and $j+1$ is slightly

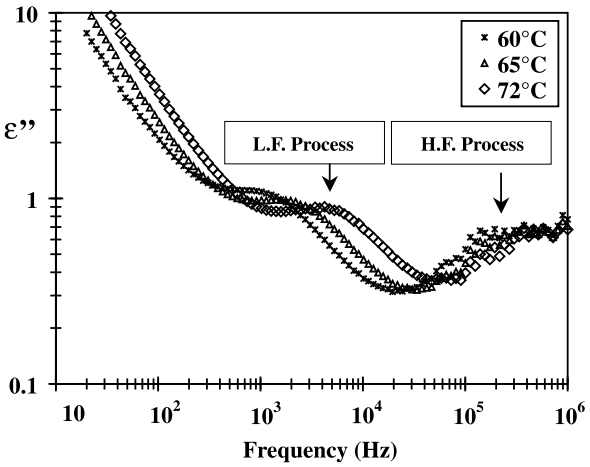

Fig. 5.134. Dielectric losses at different temperatures in the SmC^*_A phase of the 11FF compound

different from 180° and a weak resultant polarization $\boldsymbol{\delta P}$ exists without applying an electric field (Fig. 5.136a). The second motion which can correspond to the H.F. dielectric relaxation process is the so-called *non-cancellation* mode (N.C.M.) linked to the anti-phase reorientation of the molecules [25, 26] (Fig. 5.136 b). This mode induces fluctuations of the resultant polarization $\boldsymbol{\delta P}$ detectable from dielectric measurements when the measuring field is in the layer's plane (homogeneous orientation). The high critical frequency of this process can be explained by the high elastic and restoring torques of such a motion.

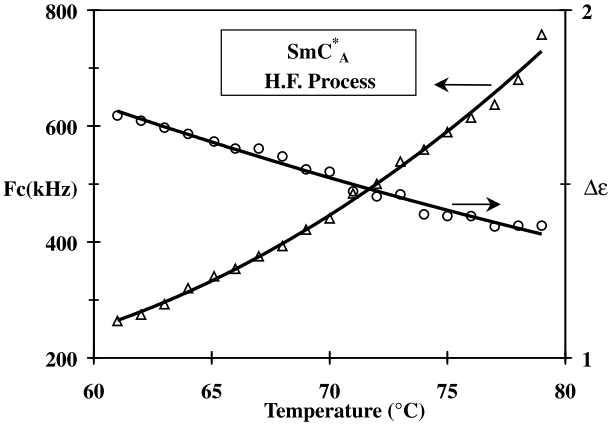

Fig. 5.135. Critical frequency and dielectric strength of the H.F. process versus temperature

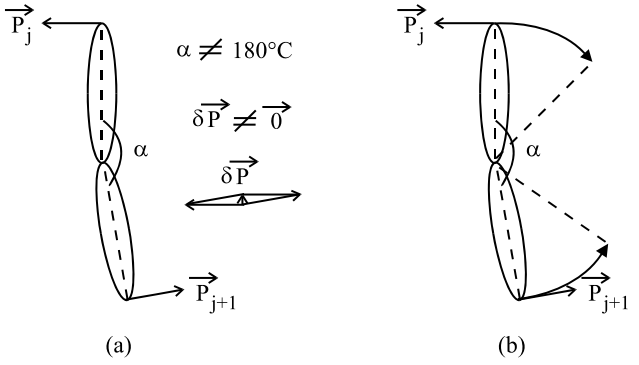

Fig. 5.136. (**a**) Small local polarization in the SmC^*_A phase. (**b**) The anti-phase reorientation of molecules

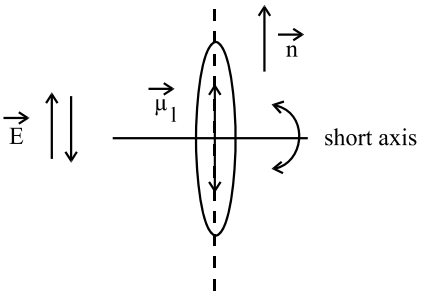

Fig. 5.137. Rotation around the short axis

Low frequency relaxation processes

Two possible interpretations have also been proposed in the literature to explain the L.F. process.

Rotation around the short axis

The rotation around the short axis illustrated below (Fig. 5.137) is a non collective mode. This so-called *flip-flop* reorientation process is well known and has been widely studied in *nematic* and *smectic* phases [27, 28]. This process appears when the measuring electric field excites the longitudinal part μ_l of the permanent dipolar moment of molecules. An homeotropic orientation ($\boldsymbol{E} \parallel \boldsymbol{n}$) is the best configuration to observe this process. The dielectric relaxation process connected with the rotation around the short axis is thermally activated and the critical frequency presents an *Arrhenius*-type behavior versus temperature ($F_C \propto \exp(-W/k_BT)$), where W is the activation energy connected with the orientating potential barrier of liquid crystal phase, T the absolute temperature and k_B the Boltzmann's constant.

As reported by some authors, we obtain such a behavior with the 11FF compound (Fig. 5.138). The activation energy is about 1.15 eV and similar to the one obtained with another material [29].

Some authors rejected this attribution arguing that the rotation around the short axis is not observable in a homogeneous orientation (configuration of our measurements). We think that this argument is only valid for *nematic* or non tilted *smectic* phase. In case of the SmC^*_A phase in homogeneous orientation, the helical axis is perpendicular (and the *smectic* planes are parallel) to the measuring electric field. The molecules are tilted to the layer normal and their average direction is not perpendicular to the electric field. As a result, their longitudinal dipolar moments and the rotation around the short axis can be excited during dielectric measurements and the corresponding dielectric relaxation process observed. Such an interpretation is in good agreement with recent results obtained on *nematic* liquid crystals [30]. J. Jadzyn et al. studied the dielectric response of *nematic* liquid crystals by varying the angle $\beta = (\boldsymbol{E}, \boldsymbol{n})$ between the *nematic* director and the measuring electric field. Let

us notice that, for *nematic* liquid crystals, the director orientation is fixed by applying a high magnetic field (typically 1 Tesla). The results obtained for the relaxation process connected with rotation around the short axis as a function of the angle β are reported in Fig. 5.139. We observe that the dielectric strength $\Delta\varepsilon$ of this process is maximal in a homeotropic orientation ($\beta = 0\,^\circ$) and decreases when β increases to become weak for $\beta = 90\,^\circ$. The critical frequency presents a reversed behavior.

In pseudo-homeotropic orientation, the helical axis is perpendicular to the electrodes surface and the average angle between the molecular axis and the measuring electric field is the tilt angle θ. The dielectric strength should be higher than this obtained in homogeneous orientation whereas the critical frequency should be lower (Fig. 5.139). This is in agreement with experimental results of some authors who compared the dielectric properties of the SmC^*_A phase aligned in homogeneous and pseudo-homeotropic orientations [25].

In-phase reorientation

As discussed before, a weak resultant polarization $\boldsymbol{\delta P}$ exists between two adjacent layers of the SmC^*_A phase. When the molecules in two adjacent layers rotate in the same sense (in-phase reorientation), the resultant polarization vector $\boldsymbol{\delta P}$ also rotates (Fig. 5.140). These fluctuations of $\boldsymbol{\delta P}$ can be detected dielectrically. The critical frequency of the corresponding relaxation process will be lower than in the case of the anti-phase reorientation because there is no restoring torque. However, to better understand the nature of such a mode, more than two layers should be taken into account. In conclusion, it is not possible to conclude on the origin of the L.F. relaxation process of the SmC^*_A phase.

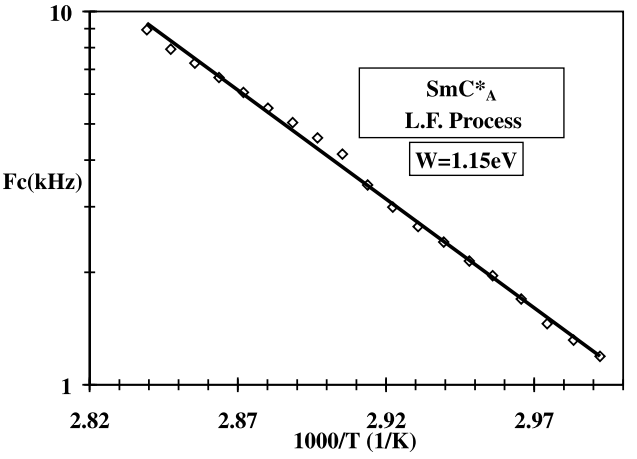

Fig. 5.138. *Arrhenius*-type behavior of the L.F. process in the SmC^*_A phase

5.10.4 Conclusions

We have performed dielectric measurements in the different phases of an antiferroelectric liquid crystal. In the sub-phase alpha, SmC^*_α, using simulations based on the clock model, we have shown the influence of the azimuthal angle α on the dielectric properties of the SmC^*_α phase. A good agreement is obtained with experimental results by considering a limited value of this angle and by taking into account its temperature evolution confirmed with optical period measurements [21]. The relaxation process observed without D.C. bias goes continuously from the SmA^* phase soft mode to the SmC^* phase *Goldstone* mode. This process is strongly modified under bias and is attributed to the SmC^*_α phase *Goldstone* mode. At high bias, the observed relaxation process has the same behavior as that of the soft mode at a SmA^*

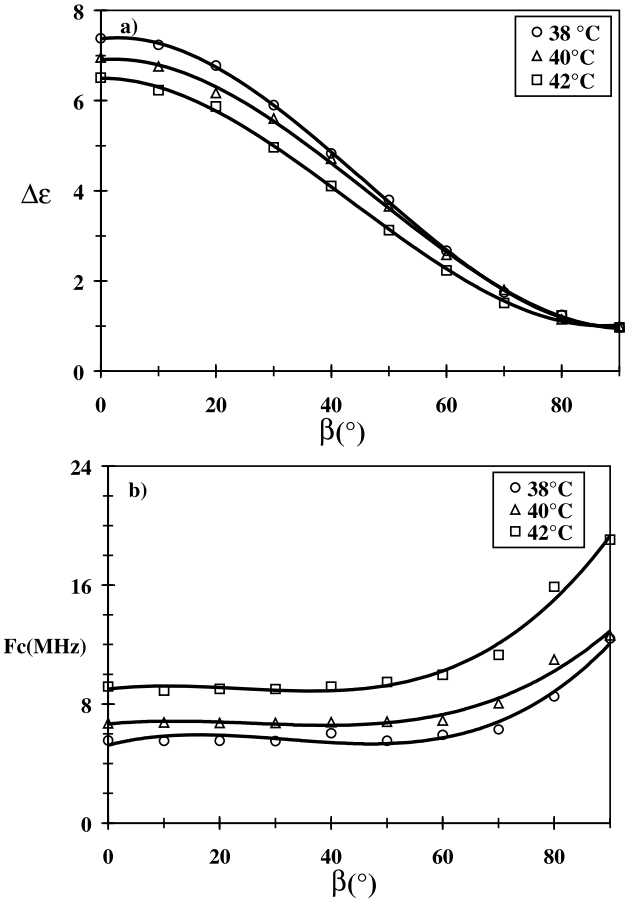

Fig. 5.139. Rotation around the short axis versus the angle between the measuring field and the molecular director in a *nematic* liquid crystal (6CHBT)

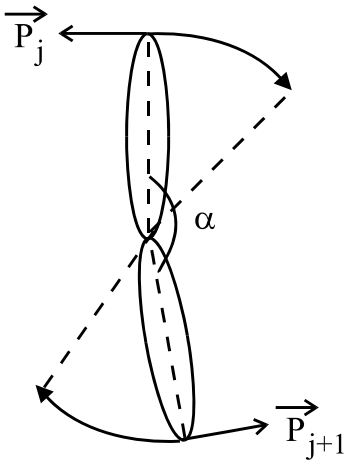

Fig. 5.140. In-phase reorientation corresponding to the L.F. relaxation process in the SmC^*_A phase

– SmC^* phase transition. It is attributed to the soft mode of the SmA^* – SmC^*_α phase transition. The dielectric study of the 11FF compound confirms the existence of two relaxation processes in the SmC^*_A phase. The H.F. relaxation process is attributed to the anti-phase reorientation of the molecules. Two interpretations are possible for the molecular dynamics corresponding to the L.F. process: rotation around the short axis or in-phase reorientation of the molecules. We have shown that the rotation around the short axis can occur in homogeneously orientated samples. The characteristic parameters (dielectric strength and critical frequency) are different from those of pseudo-homeotropic orientation.

References

1. A. D. L. Chandani, Y. Ouchi, H. Takezoe, A. Fukuda, K. Terashima, K. Furukawa, A. Kishi: Jpn. J. Appl. Phys. **28(7)**, L1261 (1989)
2. N. Okabe, Y. Suzuki, I. Kawamura, T. Isozaki, H. Takezoe, A. Fukuda: Jpn. J. Appl. Phys. **31**, L793 (1992)
3. H. T. Nguyen, J. C. Rouillon, P. Cluzeau, G. Sigaud, C. Destrade, N. Isaert: Liq. Cryst. **17**, 571 (1994)
4. T. Matsumoto, A. Fukuda, M. Johno, Y. Motoyama, T. Yui, S. Seomun, M. Yamashita: J. Mater. Chem. **9**, 2051 (1999)
5. J. L. de Bougrenet de la Tocnaye: In: *FLC99,7th International Conference on Ferroelectric Liquid Crystals at Darmstadt, Germany, August 29–September 3, 1999*
6. F. Gouda, K. Skarp, S. T. Lagerwall: Ferroelectrics **113**, 165 (1991)
7. V. Faye, J. C. Rouillon, C. Destrade, H. T. Nguyen: Liq. Cryst. **19(1)**, 47 (1995)
8. R. Douali, C. Legrand, V. Faye, H. T. Nguyen: Mol. Cryst. Liq. Cryst. **328**, 209 (1999)

9. P. Gisse, J. Pavel, H. T. Nguyen, V. L. Lorman: Ferroelectrics **147**, 43 (1993)
10. P. Simeao Carvalho, M. Glogarova, M. R. Chaves, H. T. Nguyen, C. Destrade, J. C. Rouillon, S. Sarmento, M. J. Ribeiro: Liq. Cryst. **21(4)**, 511 (1996)
11. V. L. Lorman, A. A. Bulbitch, P. Toledano: Phys. Rev. E **49(2)**, 1367 (1994)
12. S. Sarmento, P. Simeao Carvalho, M. R. Chaves, F. Pinto, H. T. Nguyen: Liq. Cryst. **28(5)**, 673 (2001)
13. V. Bourny, J. Pavel, V. Lorman, H. T. Nguyen: Liq. Cryst. **27(5)**, 559 (2000)
14. F. Bibonne, J. P. Parneix, H. T. Nguyen: Eur. Phys. J. AP **3**, 237 (1998)
15. B. Žekš, M. Čepič: Liq. Cryst. **14(2)**, 445 (1993)
16. M. Čepič, B. Žekš: Mol. Cryst. Liq. Cryst. **61**, 263 (1995)
17. M. Čepič, B. Žekš: Liq. Cryst. **20(1)**, 29 (1996)
18. M. Škarabot, M. Čepič, B. Žekš, R. Blinc, G. Heppke, A. V. Kytik, I. Muševič: Phys. Rev. E **58(1)**, 575 (1998)
19. N. Vaupotič, M. Čepič, B. Žekš: Ferroelectrics **245**, 185 (2000)
20. V. Laux, N. Isaert, G. Joly, H. T. Nguyen: Liq. Cryst. **26(3)**, 361 (1999)
21. V. Laux, N. Isaert, V. Faye, H. T. Nguyen: Liq. Cryst. **27(1)**, 81 (2000)
22. R. Douali, C. Legrand, H. T. Nguyen: Ferroelectrics **245**, 101 (2000)
23. S. Hiller, S. A. Pikin, W. Haase, J. W. Goodby, I. Nishiyama: Jpn. J. Appl. Phys. **33**, L1170 (1994)
24. F. Bibonne, H. Fredon, J. P. Parneix, V. Faye, H. T. Nguyen: Ferroelectrics **215**, 87 (1998)
25. M. Buivydas, F. Gouda, S. T. Lagerwall, B. Stebler: Liq. Cryst. **18(6)**, 879 (1995)
26. A. Fąfara, M. Marzec, S. Wróbel, R. Dąbrowski, W. Haase: IEEE Transactions on Dielectrics and Electrical Insulation **8(3)**, 477 (2001)
27. J. Jadżyn, J. P. Parneix, C. Legrand, R. Njeumo, R. Dąbrowski: Acta Physica Polonica A **71**, 53 (1987)
28. C. Druon, J. M. Wacrenier: Mol. Cryst. Liq. Cryst. **98**, 201 (1983)
29. J. P. F. Lagerwall, T. Fütterer, D. Moro, G. Heppke: Ferroelectrics **244**, 223 (2000)
30. J. Jadżyn, G. Czechowski, R. Douali, C. Legrand: Liq. Cryst. **26(11)**, 1591 (1999)

5.11 Dielectric and electrooptic studies of MHPOBC analogues

S. Wróbel, W. Haase, A. Fąfara and M. Marzec

5.11.1 Introduction

Since the discovery of the liquid crystalline antiferroelectric SmC^*_A phase [1–4] for MHPOBC (4-(1-methylheptyl-oxycarbonyl)phenyl-4′-octyloxybiphenyl-4-carboxylate) compound much experimental and theoretical work has been done on antiferroelectric liquid crystals (AFLCs) because of their tri-stable switching useful for display applications. A few interesting review articles [4–6] extended papers [7, 8] and book editions [9, 10] have been devoted to this exciting new subject in the physics and chemistry of liquid crystals. One

can not speak only of AFLCs without referring to ferroelectric liquid crystals (FLCs) because the compounds exhibiting the antiferroelectric SmC_A^* phase usually display a ferroelectric phase (sometimes in a narrow temperature gap) as well as other phases and/or sub-phases. Up to now it has been proved that ferroelectricity and antiferroelectricity in calamitic liquid crystals are of molecular origin (chirality and polarity of molecules) as well as of the point symmetry of the tilted smectic structures. The tilt breaks the point symmetry from ∞/m for orthogonal SmA to $2/m$ for tilted SmC phase whereas chirality of molecules further reduces the local symmetry to 2 (twofold polar axis) allowing for ferroelectricity as it has been proved in the papers by Meyer et al. [11, 12].

One of the models of the antiferroelectric liquid crystalline phase is presented in Fig. 5.141a. Locally in the j-th layer there is a ferroelectric like order (Fig. 5.141b) of polar molecules which can be described [13–16] by the two-dimensional primary order parameter $\boldsymbol{\xi}_j$,

$$\boldsymbol{\xi}_j = (\sin\theta_o \cos\phi_j, \sin\theta_o \sin\phi_j) \equiv (\xi_{j1}, \xi_{j2}) \tag{5.254}$$

where θ_o is the tilt angle of the molecules and ϕ is the phase of the director in the laboratory frame (X, Y, Z). In the antiferroelectric phase the tilt angle changes its sign upon going from one layer to another (Fig. 5.141a). One can define a unit cell for AFLCs which consists of two neighboring layers having anticlinic order of molecules.

In the SmC_A^* phase there are in-plane polarization vectors $(\boldsymbol{P}_j)$ that change their direction practically by 180° on going between the two neighboring layers. To describe polymorphism and dynamics of the antiferroelectric phases two order primary parameters [17] were introduced:

$$\boldsymbol{\xi}_f = 0.5(\boldsymbol{\xi}_j + \boldsymbol{\xi}_{j+1}) \,, \tag{5.255a}$$

$$\boldsymbol{\xi}_a = 0.5(\boldsymbol{\xi}_j - \boldsymbol{\xi}_{j+1}) \,. \tag{5.255b}$$

The secondary ferroelectric and antiferroelectric (Fig. 5.141c) order parameters are defined [17], respectively, as a sum and difference of two polarization vectors in the neighboring layers:

$$\boldsymbol{P}_f = \frac{1}{2}(\boldsymbol{P}_j + \boldsymbol{P}_{j+1}) \,, \tag{5.256a}$$

$$\boldsymbol{P}_a = \frac{1}{2}(\boldsymbol{P}_j - \boldsymbol{P}_{j+1}) \,. \tag{5.256b}$$

In the antiferroelectric phase they are not completely compensated due to the helicoidal structure of two sub-lattices. A theoretical description of dielectric and electrooptic properties of ferroelectric liquid crystals has been developed by Blinc & Žekš [13–15], Pikin & Indenboom [16], and Carlsson et al. [18]. Theoretical approaches to AFLCs are being developed by Žekš et al. [19–21], Skarabot et al. [22], Madhusudana et al. [23], Toledano et al. [24], Čepič et al. [25] and Pikin et al. [26–29] analyzing different Landau expansions of the free energy expressed in terms of the primary $(\boldsymbol{\xi}_f, \boldsymbol{\xi}_a)$

and secondary ($\boldsymbol{P}_f, \boldsymbol{P}a$) order parameters. The so-called clock (or discrete) model allows one to describe phases and sub-phases showing up on the phase diagrams (see Sect. 5.1 by Žekš et al. and Sect. 5.4 by Čepič et al.). The dielectric behavior of AFLCs was theoretically described in a paper by Voupotič et al. [30].

Dielectric spectroscopy is a useful tool to study molecular dynamics, phase transitions as well as collective processes showing up due to the fluctuations of the order parameters. Some of the fluctuations are dielectrically active giving mostly a non-Arrhenius type of dielectric relaxation processes. There are many papers about the dielectric behavior in the transition region between antiferroelectric and ferroelectric phases [31–58]. For the liquid crystalline phases of these materials dielectric spectroscopy reveals rich dielectric spectra between 10 Hz and 10 GHz. There are several dielectrically active modes observed in the antiferroelectric SmC^*_A phase which can be planar aligned using a low frequency AC electric field and/or surface effects.

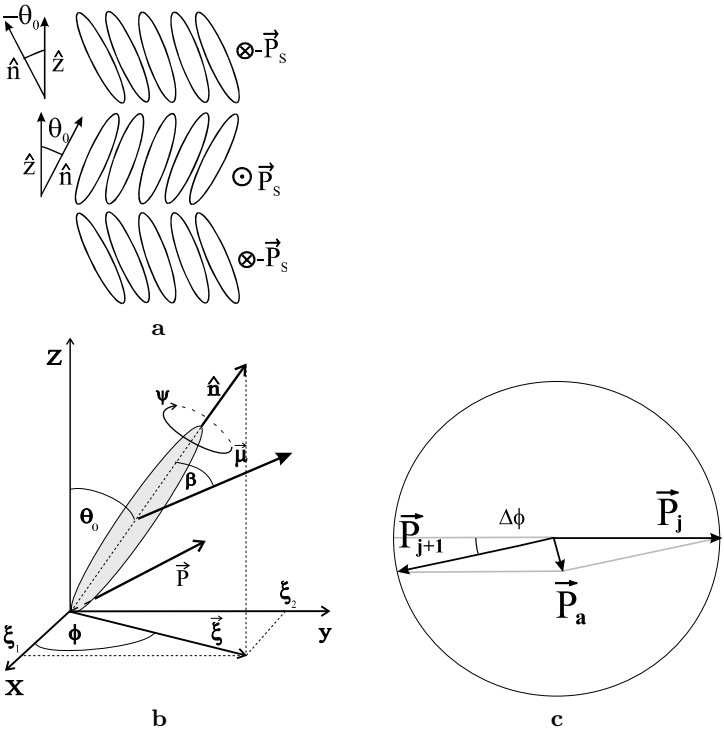

Fig. 5.141. (**a**) Local order of molecules in three neighboring layers, (**b**) ferroelectric primary order parameter of the j-th layer (**c**) antiferroelectric secondary order parameter

By applying external electric fields one can modify dielectric and electrooptic properties of para-, ferro-, ferri- and antiferroelectric phases. The most pronounced effect has been observed for the Goldstone mode (GM) in the SmC^* phase. In this case rather weak bias voltage of 10 V applied across a 30 μm-cell suppresses the GM. It is interesting from the physical standpoint that the GM suppression, i.e. the suppression of the high dielectric permittivity state, is in some sense analogous to suppressing the state of superconductivity by a magnetic field. Both states of ferroelectricity and superconductivity (see Sect. 11.1 by Tomkowicz and Bałanda) can also be suppressed by changing the composition of the materials.

The aim of this work is to present studies on the polymorphism, electrooptic and dielectric properties of a few MHPOBC analogues having on one hand slightly different molecular structures and showing both ferroelectric and antiferroelectric phases as well as sub-phases. On the other hand, partially fluorinated compounds are investigated that show new electrooptic properties. It is interesting that by changing the structure of an achiral chain one can distinctly modify the dielectric and electrooptic behavior. New MHPOBC analogues (Fig. 5.142, Table 5.10) exhibiting ferroelectric and antiferroelectric phases, have been studied by means of frequency domain dielectric spectroscopy (FDDS), time domain spectroscopy (TDS) and electrooptic methods to evaluate such parameters as: 1. Dielectric relaxation times, 2. Dielectric strengths, 3. Activation energies for the molecular and collective processes, 4. Spontaneous polarization $P_s(T)$, 5. Tilt angle and 6. Threshold voltages $E_c(T)$. Most of these studies have been performed on mono-domains aligned in electrooptic cells by employing strong AC fields. The substances investigated were synthesized by Dąbrowski et al. [59–61] and they possess the following molecular structure:

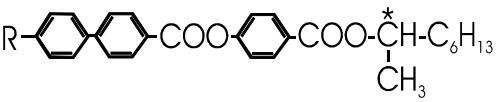

Fig. 5.142. General molecular structures of the compounds studied. For MHPOBC R=$OC_{10}H_{21}$ (see Čepič et al., Sect. 5.4 of this book). *R* has been modified (see Tables 5.10) as to obtain different dielectric and electrooptic behavior

The phase diagrams of the compounds studied are shown in Table 5.10 where some compounds possess partially fluorinated end group R. Some of the substances studied – in addition to ferroelectric and antiferroelectric phases – show the sub-phases like: SmC^*_α, $SmC^*\gamma$ (or SmC^*_{FI1}) and SmC^*_β (or SmC^*_{FI2}) (see Čepič et al., Sect. 5.4 of this book) that are not indicated in Table 5.10.

Table 5.10. Transition temperatures and abbreviations of the compounds discussed in this section

Substances

Group R, see Fig. 5.142	Phase diagram	Abbreviation
$H_3CCOO(CH_2)_3$-O-	Cr.1 55.8 °C Cr. 60 °C SmI_A^* (56 °C) SmA* 130 °C Is.	MHPEPBC
$H_7C_3COO(CH_2)_3$-O-	Cr. 67 °C SmI_A^* (41.6 °C) SmC_A* 92.3 °C SmA* 116.9 °C Is.	MHPBPBC
$H_{15}C_7COO(CH_2)_3$-O-	Cr. 49 °C SmI_A^* (22 °C) SmC_A* 88.7 °C SmC* 91.5 °C SmA* 105.3 °C Is.	MHPOPBC
$H_7C_3COO(CH_2)_4$-O-	Cr. 69.4 °C SmC_A^* 89.7 °C SmC*100.6 °C SmA* 111 °C Is.	MHPBBBC
$F_3CCOO(CH_2)_3$-O-	Cr. 82 °C SmC_A* 120.4 °C SmC* 124.5 °C SmA* 130 °C Is.	MHPE(F)PBC
$F_7C_3COO(CH_2)_3$-O-	Cr. 84 °C SmI_A^* (54 °C) SmC_A*120 °C SmC* 124 °C SmA* 129 °C Is.	MHPB(F)PBC
$F_{15}C_7COO(CH_2)_3$-O-	Cr. 69 °C SmC_A^* 100 °C SmC* 125°C SmA* 154 °C Is.	MHPO(F)PBC
$F_7C_3COO(CH_2)_4$-O-	Cr. 70 °C SmC_A^* 121 °C SmC* 126 °C Is.	MHPB(F)BBC
F_3C-$CH_2CH_2COO(CH_2)_3$O-	Cr. 99 °C SmC_A^* 110 °C SmC* 123°C SmA* 127 °C Is.	MHPB(3F)PBC
F_3C-$CH_2CH_2COO(CH_2)_4$O-	Cr. 88 °C SmC_A^* 112 °C SmC* 115.6°C SmA* 117 °C Is.	MHPB(3F)BBC

5.11.2 Calorimetric and dielectric studies

Below one can find the most representative calorimetric and dielectric data obtained for the substances shown in Fig. 5.142 and Table 5.10.

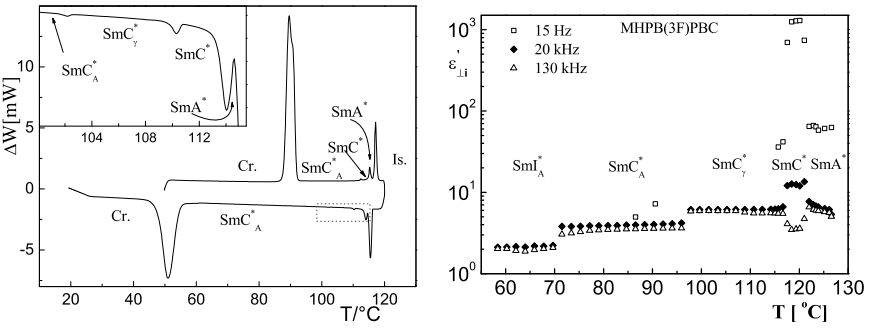

Fig. 5.143. (**a**) Selected DSC thermograms obtained for MHPB(3F)BBC. (**b**) Temperature dependencies of dielectric permittivities obtained at different frequencies for MHPB(3F)PBC

5.11.2.1 Phase transitions

Thermal properties of the substances shown in Table 5.10 were studied using the differential scanning calorimetry (DSC) method. The measurements were performed both on heating and cooling of the samples. Transition temperatures and enthalpies were studied by using Perkin Elmer PYRIS 1 DSC calorimeter. The calorimetric measurements were performed in a wide temperature range using heating and cooling rates between 1 °C/min to 50 °C/min as to better expose weak second order phase transitions.

The temperature scale of the instrument was calibrated by means of the melting points of indium and water and the melting point of indium was used for energy calibration. Samples having a mass of a few milligrams were placed in aluminum crucibles. An empty aluminum crucible was used as a reference. All substances studied in this work are characterized by a complex polymorphism.

The transition from the liquid crystalline to the crystalline state showed significant hysteresis for all substances studied. Polarizing microscopy observation was used as a complementary method to identify liquid crystalline phases. Examples of textures are shown in Fig. 5.144a,b,c,d. In most cases texture observations were done on the samples being under electric field to assure better circumstances for identification of different phases and sub-phases as well.

The DSC runs obtained for MHPB(3F)BBC on heating and cooling of the sample are presented in Fig. 5.143a. Four anomalies are present on the DSC heating curve. They are also seen on the cooling curve, but in most cases shifted towards lower temperatures due to a hysteresis effect. After subtracting a linear background the enthalpy changes, connected with the observed phase transitions, were calculated by numerical integration of the DSC anomalies. The peak temperatures of anomalies are given with an accuracy

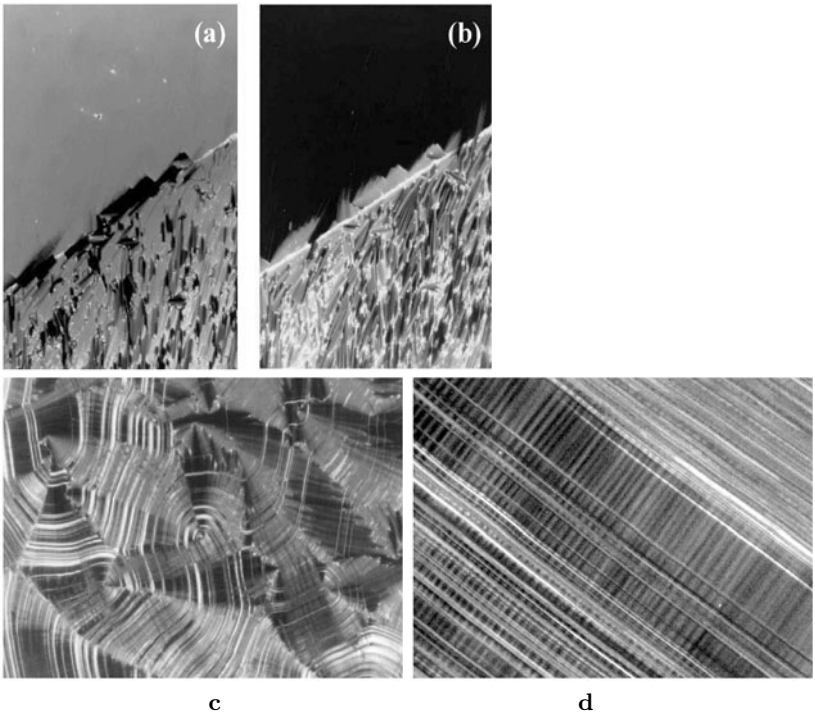

Fig. 5.144. (**a**) Bright and (**b**) dark states observed during electrooptic switching in the SmC* phase of MHPBBBC. Exemplary textures of non-aligned (**c**) and aligned (**d**) antiferroelectric phase of MHPOPBC

of ±0.1 °C and the enthalpy changes at the transitions with an accuracy of about 5%. Phase transitions are detected in dielectric measurements as well (Fig. 5.143b) what will be discussed below.

As seen in Fig. 5.143a the melting enthalpy (100.3 kJ/mol) for the substance under investigation is significantly higher than those of the other phase transitions. This is due to the fact that at least two translational and the rotational degrees of freedom are released at the melting point of these materials. The clearing point shows higher enthalpy change (9.2 kJ/mol) than the transitions between the liquid crystalline phases (SmC*–SmA*: 0.66 kJ/mol, Sm^*_A–SmC*: 0.06 kJ/mol) because it is a transition from partially ordered liquid crystal to the liquid state. In the case of MHPOBC analogues the clearing points are transitions from one of the smectic phases (SmA* or SmC*) directly to the isotropic phase which is connected with bigger enthalpy and entropy changes than, for instance, in the case of the cholesteric-isotropic transition. On the other hand, transitions between liquid crystalline phases cause much smaller thermal anomalies (SmC* – SmC^*_γ or SmA* – SmC*). This can be explained by very small changes of ordering between the phases in the

latter case. Employing very small heating and cooling rates one can detect transitions between sub-phase alpha and neighboring phases (see Čepič et al. Sect. 5.4).

Releasing the hindrance for the rotational degrees of freedom at different phase transitions triggers stochastic reorientational motions of molecules which in case of polar molecules lead to dielectric absorption in a particular frequency range. For instance, the spontaneous polarization vector $\boldsymbol{P}_S$ comes from a non-uniform reorientation of molecules around their long axes and it can be expressed by:

$$\boldsymbol{P}_S = \sum_j \boldsymbol{\mu}_j = N\,\boldsymbol{\mu}_\perp\,\langle\cos\psi\rangle \tag{5.257}$$

where the angle ψ is the Euler angle describing the molecular reorientation around the long axis and N is the number of molecules per unit volume.

Liquid crystals are strongly anharmonic systems in which the molecules can jump (or reorient) between shallow potential wells. For calamitic liquid crystals with elongated rod like molecules there is a possibility of different molecular reorientations leading to a complex dielectric spectrum in a wide frequency range (see Urban & Würflinger in Sect. 4.2 and Dunmur in Sect. 4.1). Translational stochastic motions of ions, released at the melting point and at other phase transitions cause a pronounced contribution to the low frequency part of the dielectric spectrum due to the sub-hertz frequency range relaxation as studied thoroughly by Biradar et al. [62].

Dielectric spectroscopy is a complementary method for studying phase transitions. Figure 5.143b presents low frequency dielectric permittivity obtained for one of the MHPOBC analogues. Some of the phase transitions are very well evidenced. One can see two sharp changes corresponding to the transition between paraelectric SmA* and ferroelectric SmC* phases (at a temperature of about 122 °C) and the transition between ferroelectric SmC* and ferrielectric SmC^*_γ phase takes place at about 117 °C. These temperatures agree well with those obtained from spontaneous polarization measurements [55]. The anomalies in $\varepsilon'_\perp$ vs. temperature curves seen especially at frequencies of 20 kHz and 130 kHz (Fig. 5.143b) show that there are transitions between the ferro-, ferri- and antiferroelectric phases. The transitions are also evident in the three-dimensional plot of the dispersion and absorption curves presented in Fig. 5.145 for MHPBPBC and in Fig. 5.146 for MHPB(3F)PBC.

5.11.2.2 Dielectric properties

Frequency domain dielectric spectroscopy (FDDS) measurements in the frequency range from 10 Hz to 13 MHz have been performed using HP 4192A impedance analyzer controlled by PC (see Sect. 1.1). A gold-coated cell having a capillary gap of 23 μm between the gold electrodes was used for measuring dielectric spectra. In a few cases ITO cells were also employed. However, the

dielectric data obtained by using thin ITO cells give qualitatively different results. In the case of FLCs and AFLCs measurements of the perpendicular component of the complex dielectric permittivity are of great interest because the order parameter fluctuations active in dielectric spectroscopy can be detected for planar alignment only, i.e. when the helix axis is parallel to the electrodes. Theoretically, for homeotropic alignment only the molecular processes contribute to the dielectric spectrum. To obtain planar alignment a low frequency electric field up to 200 Vp-p was used. The field was first applied in the

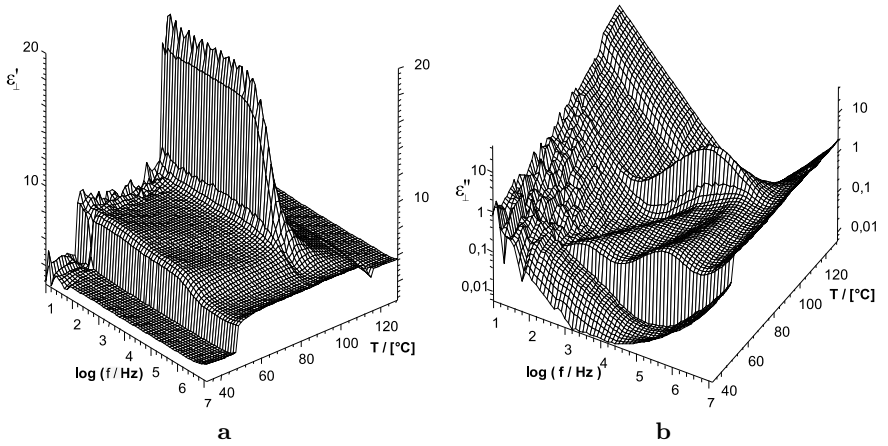

Fig. 5.145. 3-D dielectric spectra for MHPBPBC: (**a**) dispersion curves, (**b**) absorption curves

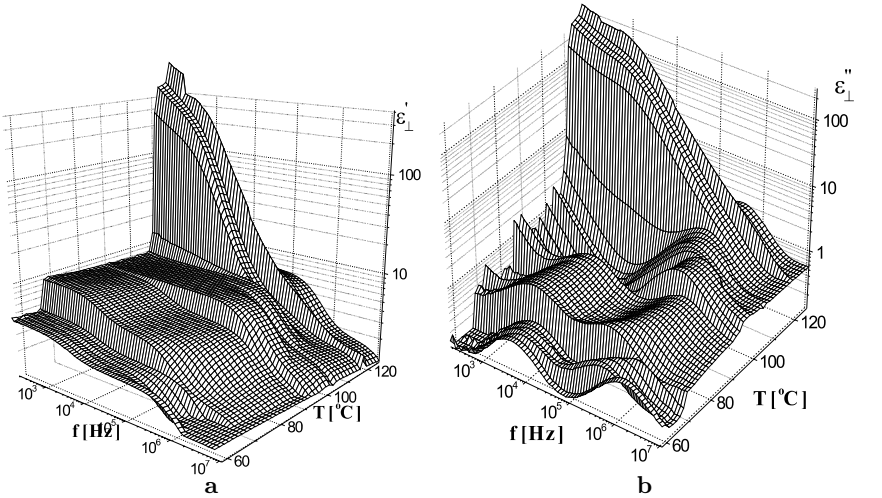

Fig. 5.146. 3-D dielectric spectra for MHPB(3F)PBC: (**a**) dispersion curves, (**b**) absorption curves

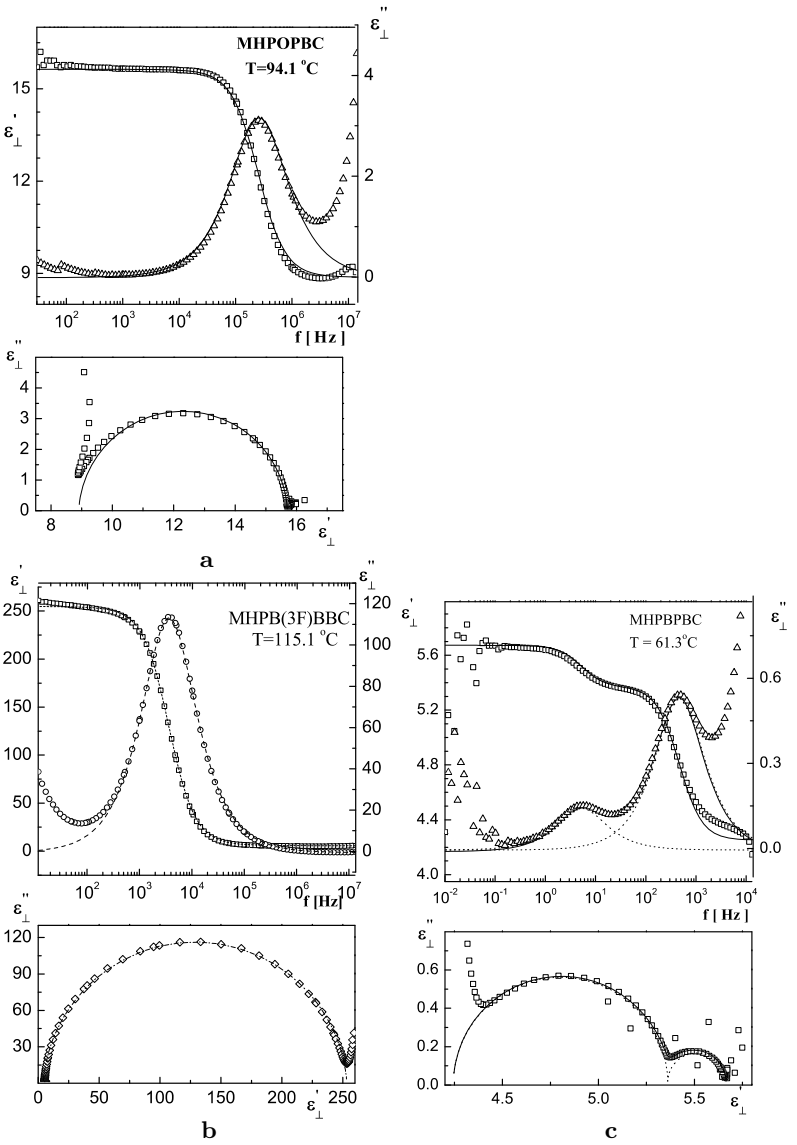

Fig. 5.147. Dielectric spectra acquired for (**a**) the paraelectric SmA* phase of MHPOPBC ($\varepsilon(0) = 15.6$, $\varepsilon(\infty) = 8.8$, $\tau = 6.6 \cdot 10^{-7}\,s$, $\alpha = 0.04$), (**b**) the ferroelectric SmC* phase of MHPB(3F)BBC ($\varepsilon(0) = 254$, $\varepsilon(\infty) = 5.4$, $\tau = 4.7 \cdot 10^{-5}\,s$, $\alpha = 0.0$) and (**c**) the antiferroelectric SmC_A^* of MHPBPBC ($\varepsilon(0) = 5.66$, $\tau_1 = 3.1 \cdot 10^{-5}\,s$, $\alpha_1 = 0.02$, $\varepsilon(0)_1 = 5.36$, $\tau_2 = 5.3 \cdot 10^{-7}\,s$, $\alpha_2 = 0.02$, $\varepsilon(\infty) = 4.24$). *Solid* and *dashed lines* are obtained by fitting (5.258) to the experimental data

SmA* phase and then upon slowly cooling a uniformly aligned mono-domain of the SmC* or SmC_A^* phase was obtained (see photos in Fig. 5.144). To study

the soft mode below the SmA*-SmC* transition, the bias voltages between –35 V and +35 V were applied to suppress the GM in the SmC* phase.

TDS was employed to study molecular relaxation processes which are presented between 10 MHz and 10 GHz. In this method a pulse is reflected from the sample placed at the end of the coaxial line. Both incident and reflected pulses are recorded by using a fast digital scope and analyzed by a computer program to obtain a dielectric spectrum (see Sect. 1.2 by Gestblom).

In Figs. 5.145a and 5.145b one can see 3-D plots of the dielectric spectra obtained for MHPBPBC. In the SmA* phase there is a nice soft mode SM contribution. In the SmC^*_A phase two dielectric modes are observed. Figures 5.146a and b present 3-D spectra for the fluorinated compound MHPB(3F)PBC which exhibits very high dielectric permittivity in the SmC* phase. In addition to the antiferroelectric SmC^*_A this substance exhibits also a highly ordered SmI^*_A phase with two low-frequency dielectric modes. Exemplary dielectric spectra for different phases are seen in Figs. 5.147a,b,c.

5.11.2.3 Bias field influence on the dielectric spectra

Application of an external electric field can modify dielectric properties of all phases mentioned above. Bias field dependencies of the SM above T_c for MHPBPBC (Fig. 5.148a) show that for small voltages its intensity slightly increases and then remains constant. It was found that for small bias fields one observes a linear dependence of the SM dielectric absorption (Marzec [63]).

The most pronounced effect has been observed in the SmC* phase of MHPOBC (Fig. 5.149) for the Goldstone mode contribution. As seen in this case a rather weak bias voltage of 10 V applied across a 30 µm cell suppresses this low frequency relaxation process. The dielectric absorption tends practically to zero whereas the dielectric permittivity approaches the $\varepsilon(\infty)$ value characteristic for molecular contributions. Comparing the dielectric spectra in ferroelectric (Fig. 5.149) and paraelectric phases (Fig. 5.148a) it is seen that the influence of the bias field on the soft mode, observed in the paraelectric SmA* phase, is much weaker.

The influence of the bias field on the dielectric spectra in the SmC^*_A phase is presented in Figs. 5.150a and b, respectively, for MHPO(F)PBC and MHPBPBC. One can see that for MHPO(F)PBC the low frequency absorption peak is being suppressed at high bias voltages (Fig. 5.150a) whereas for MHPBPBC the dielectric spectrum is being enhanced (Fig. 5.150b). It is surprising that in the case of MHPO(F)PBC the bias field suppresses only the low-frequency part of the dielectric spectrum [55].

Stressing again MHPO(F)PBC exhibits in comparison with MHPBPBC quite the opposite bias field dependence of the dielectric spectrum in the antiferroelectric phase, i.e. it becomes suppressed under bias field. Maybe it is due to the existence of two kinds of antiferroelectric phases observed by us dielectrically (Kilian et al. [36] Fąfara et al. [51, 55]). Furthermore the influence of the measuring electric field on the GM dielectric spectrum studied by

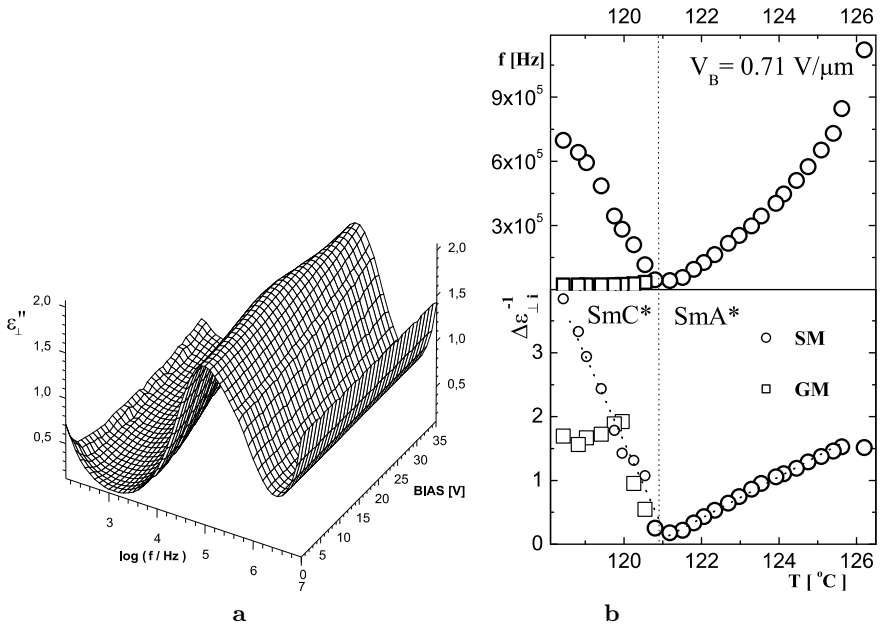

Fig. 5.148. (**a**) Bias field dependence of the soft mode absorption measured for MHPBPBC at $T = 84.8\,^{\circ}\mathrm{C}$ (**b**) Soft mode dielectric parameters vs. temperature obtained for MHPO(F)PBC in the vicinity of the critical temperature. SM and GM contributions are seen

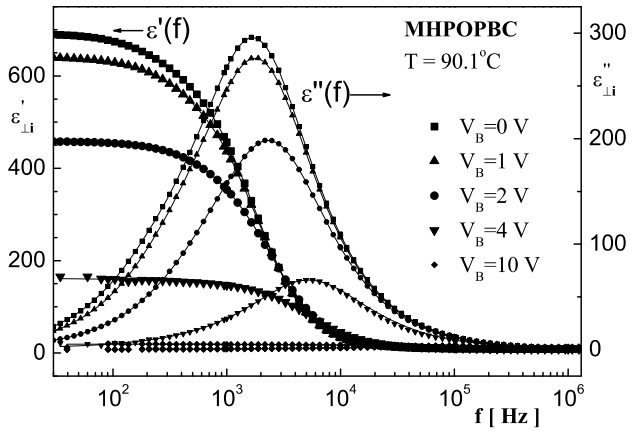

Fig. 5.149. Bias field dependence of the Goldstone mode dielectric spectrum acquired for the SmC* ferroelectric phase of MHPOPBC. Real ($\varepsilon'_{\perp}$) and imaginary ($\varepsilon''_{\perp}$) parts of the dielectric permittivity

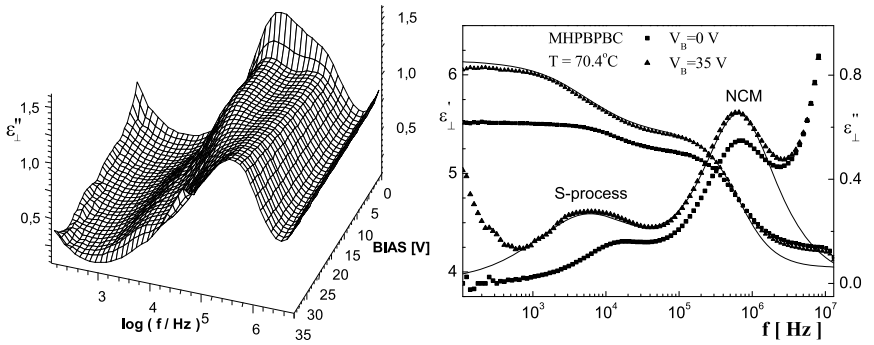

Fig. 5.150. (**a**) MHPO(F)PBC bias field dependence of the antiferroelectric modes absorption measured at $T = 80.0\,^{\circ}\mathrm{C}$, (**b**) MHPBPBC bias field dependence of the antiferroelectric modes absorption measured at $T = 70.4\,^{\circ}\mathrm{C}$

Kilian et al. [36, 64] leads to a splitting of the dielectric modes in a ferrielectric phase.

5.11.2.4 Data processing of the dielectric spectra and discussion

As seen above the dielectric spectra of para-, ferro-, ferri- and antiferroelectric phases are much different. Each phase exhibits a characteristic dielectric spectrum (see Fig. 5.147). For instance, for the antiferroelectric phase in planar alignment a sum of two Cole–Cole functions (5.258), which includes conductivity term, was fitted to the experimental spectra using least-square method:

$$\varepsilon^{*}(\omega) = \varepsilon^{'}(\omega) - i\varepsilon^{''}(\omega) = \varepsilon(\infty) + \frac{\varepsilon(0)_1 - \varepsilon(\infty)}{1 + (i\omega\tau_1)^{1-\alpha_1}} + \frac{\varepsilon(0) - \varepsilon(0)_1}{1 + (i\omega\tau_2)^{1-\alpha_2}} + \frac{\sigma}{i\varepsilon_o\omega} \tag{5.258}$$

where $\varepsilon(0)$, $\varepsilon(0)_1$ and $\varepsilon(\infty)$ are respectively the static, quasi-static and high frequency limit dielectric permittivities, α_1 and α_2 are parameters accounting for distribution of the relaxation times, τ_1 and τ_2 are the most probable relaxation times for the processes observed, σ is a quasi-static conductivity of the sample under investigations and ε_o is dielectric permittivity of the free space.

In the SmA* phase a characteristic Curie-Weiss behavior for the soft mode (SM) is observed (Fig. 5.148b). This mode is connected with amplitude fluctuations of polarization (known also as amplitudon [10]). It shows up at the transition temperature to one of the tilted phases (SmC*, SmC^*_A or SmC^*_{FI2}).

In the SmC* phase a large Goldstone mode (GM) absorption peak (Fig. 5.149) is observed with its characteristic behavior, i.e. the dielectric increments and relaxation frequencies are temperature independent (Figs. 5.151a

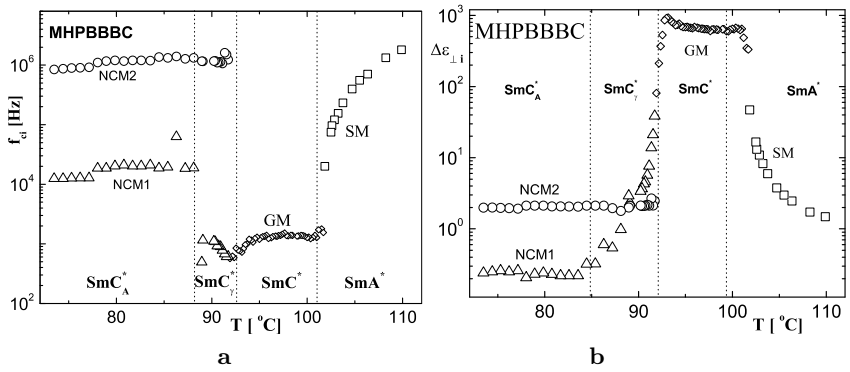

Fig. 5.151. Relaxation frequencies (**a**) and dielectric increments (**b**) for dielectric relaxation processes observed in different phases of MHPBBBC studied by Fąfara et al. [48]

and b). GM is due to the phase fluctuations of polarization vector $\boldsymbol{P}_S$ and it is sometimes called phason [10].

In the SmC^*_A phase of materials studied there is a dielectric spectrum incorporating contributions from at least two relaxation processes (Fig. 5.147c) in the frequency window of the dielectric spectrometer used. The respective absorption peaks become better resolved upon lowering of temperature. The dielectric increments of these modes obtained for MHPBBBC are almost temperature independent (see Fig. 5.151).

Usually the higher frequency process (NCM2) known from literature as a Non-Cancellation Mode (NCM) is connected with antiferroelectricity. This process is not a single relaxation process ($\alpha \approx 0.3$) and the temperature dependence of the relaxation time for it is rather complicated. According to the model NCM may be due to out-of-phase fluctuations of the polarization vectors in neighboring smectic layers. The low frequency mode (NCM1) found for MHPBBBC in its antiferroelectric phase is not a molecular process. It seems that both processes NCM1 and NCM2 are connected with the order parameter fluctuations illustrated later on.

Theoretically, in the SmC^*_A phase the anti-parallel order of spontaneous polarization vectors of the neighboring smectic layers should cancel out the macroscopic polarization, and as a consequence no contribution to the dielectric spectrum from collective modes is present. However, due to the helicoidal order of polarization vectors they are not collinear and there is always a non-compensated antiferroelectric polarization vector (Fig. 5.141c) having phase and amplitude dependent on the differences of phases and amplitudes in the two neighboring layers. There are some hints that one of the collective modes giving contribution to dielectric permittivity is the in-phase azimuthal mode.

On the other hand the low frequency relaxation process in the SmC^*_A phase of MHPBPBC seems to be connected with the reorientation around the short molecular axis (S-process, see Fig. 5.152a). It is an Arrhenius type process with the activation energy of about 110 kJ/mol which is a characteristic value for the reorientation of molecules around the short axis. Contrary the processes: SM, GM and NCM are collective ones and they display a non-Arrhenius type behavior (Figs. 5.151a and 5.151b). In the case of MHPB(3F)PBC these two relaxation processes (NCM and S-process) observed in the antiferroelectric SmC^*_A phase survive to the highly ordered SmI^*_A phase (Fig. 5.146) which is also antiferroelectric.

In the literature for some MHPOBC like compounds three low frequency dielectric relaxation modes are observed in the SmC^*_A phase (de la Fuente et al. [41], Panarin et al. [44], Makrenek et al. [53], Wojciechowski et al. [54] and many others). Usually the third process appears in the low temperature range of the antiferroelectric SmC^*_A phase showing a tendency to form a glassy state.

Interesting temperature dependencies of the relaxation frequencies and dielectric increments for each process observed in the dielectric spectrum for MHPBBBC are presented in Fig. 5.151. As was mentioned above in the paraelectric SmA* phase typical SM is observed. The strong Goldstone Mode is observed in the SmC* phase with its characteristic behavior in this phase. The relaxation frequencies of the GM and the NCM are practically temperature independent contrary to what is seen in Fig. 5.152 for the NCM of MHPBPBC and MHPB(3F)PBC.

It is interesting that for some substances the dielectric increments and relaxation frequencies of the antiferroelctric modes are temperature independent (after Fąfara [55]), i.e. they behave like GM dielectric parameters. As

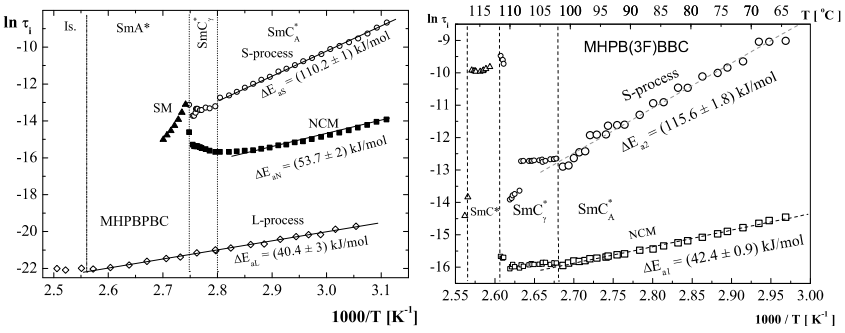

Fig. 5.152. (**a**) Arrhenius plots for different relaxation processes observed in the isotropic, SmA*, SmC* and SmC^*_A phases of MHPBPBC (SM, S-process, L-process, and NCM) (**b**) Arrhenius plots of molecular and collective relaxation processes observed in different phases of MHPB(3F)BBC

seen from Figs. 5.151 and 5.152 between the SmC^* and SmC^*_A phases there is a ferrielectric SmC^*_γ (or FI1) phase which exhibits strong anomalies of the dielectric increments and relaxation frequencies.

In Fig. 5.152b Arrhenius plots are presented for the antiferroelectric phase of MHPB(3F)BBC. One can see that for the substance under investigation two modes: S-process and NCM with activation energies equal to 116 kJ/mol and 42 kJ/mol, respectively, have been observed in antiferroelectric SmC^*_A phase.

As mentioned before TDS was used to study molecular relaxation processes arising between 10 MHz and 10 GHz. The TDS dielectric spectra are broad and contain contributions from the molecular reorientation around the long molecular axis (L-process) and from some intramolecular motions as well. The activation energies computed are equal to (40 ± 3) kJ/mole (Fig. 5.152a) and typical for the L-process found in many ferroelectric and non-ferroelectric liquid crystals as well.

5.11.3 Discussion of collective and molecular processes

The relaxation times and activation energies have been computed for five relaxation processes: 1) soft mode (SM), 2) Goldstone mode (GM), 3) NCM, which are collective ones, and 4) S-process and 5) L-process, which are of molecular origin. The SM apparent activation energies and Curie temperatures are compiled in Table 5.11 for selected compounds. The activation energies are too high for any molecular process and they change sign upon the SmC^*–SmC^*_A transition (Fig. 5.148b). In this sense SM is not an Arrhenius process.

It is very interesting that S-process is observed for both homeotropic and homogenous alignments of the antiferroelectric phase. The activation energies calculated from the data obtained for both alignments are the same within the experimental error limits [55].

As shown above the Goldstone mode, soft mode and S-process appear to be Debye-type processes characterized by single relaxation times. On the other

Table 5.11. Curie temperatures and apparent activation energies for the SM in paraelectric phases

Substance	T_C [°C]	E_a [kJ/mol]
MHPEPBC	(55.5 ± 0.4)	(124 ± 2)
MHPBPBC	(90.65 ± 0.04)	(383 ± 22)
MHPOPBC	(91.02 ± 0.07)	(253 ± 10)
MHPBBBC	(101.79 ± 0.08)	(681 ± 48)
MHPB(F)PBC	(116.9 ± 1.1)	(133 ± 14)
MHPO(F)PBC	(121.77 ± 0.05)	(776 ± 84)

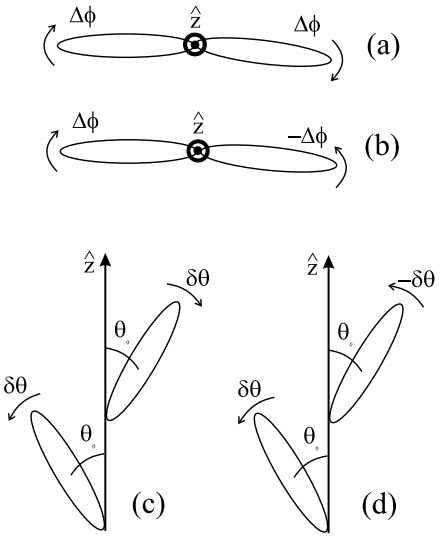

Fig. 5.153. A model of collective modes in AFLC discussed by Žekš and Čepič [19–21]. (**a**) in-phase and (**b**) anti-phase fluctuations of phase, (**c**) anti-phase and (**d**) in-phase fluctuations of amplitude

hand, NCM, and especially denoted by us the molecular L-process exhibit a distribution of the relaxation times.

The ferroelectric (SM and GM) and antiferroelctric modes (NCM) are sensitive to phase transitions. The S-process is seen for planar alignment of the SmC^*_A phase due to the tilt of molecules (see Legrand et al., Sect. 5.10). For homeotropic alignment only this process is observed in the paraelectric SmA^* and antiferroelctric SmC^*_A phase.

The modes observed dielectrically for AFLCs are illustrated in Fig. 5.153. In-phase and out-of-phase fluctuation of ϕ and θ_0 lead to the fluctuations of the secondary order parameter $\boldsymbol{P}_a$ (see Fig 5.141c). This might be an explanation for NCM dielectrically active mode.

5.11.4 Some aspects of electrical and optical behavior

Electrooptic measurements of spontaneous polarization $P_S(T)$, tilt angle θ_o and critical field $E_c(T)$ were performed using Mettler – Toledo FP82 hot stage driven by FP90 controlling processor. LINKAM – 7 μm and EHC – 10 μm cells were used. The measurements of $P_S(T)$ were done by means of a reversal current method employing a digital HP scope with IEEE488.2 interface controlled by HP 54653A Scope Link program. Temperature dependence of spontaneous polarization $P_S(T)$ was measured for different frequencies of driving triangular wave. The amplitude of voltage applied was up to 200 $Vp-p$. To this end an Agilent 33120A wave form generator and a F20A FLC Electronics voltage amplifier has been employed. $P_S(T)$ has been studied as a function of the achiral chain structure. The critical field ($E_c(T)$) has been determined by polarizing microscopy observations of arising or vanishing of dechiralization lines under DC electric field.

The samples were aligned by applying a low frequency AC field between 5 and 20 V/μm. Texture observations and electrooptic measurements were performed using ITO cells with a thickness from 6 to 10 μm.

5.11.4.1 Reversal current method

The reversal current method was used to perform measurements of spontaneous polarization. Exemplary current response spectra are presented in Figs. 5.154a,b,c. It is worth to note that at lower frequencies, namely 1 Hz, 5.5 Hz and 10 Hz, the response current spectrum measured for the antiferroelectric phase consists of two separated peaks (Fig. 5.154b) whereas at higher frequencies, i.e. 50, 200 and 500 Hz, only one peak is observed. This means that at higher frequencies there is a direct switching between the two ferroelectric states. Figure 5.154c presents polarization response currents versus temperature obtained for ferroelectric and antiferroelectric phases at 10 Hz. For some materials a current peak was observed due to the ionic conductivity (Fig. 5.154c). This peak survives even to the SmA* and isotropic phases. In this study the ionic conductivity contribution was not taken into account during integration procedure.

The current response spectrum changes with temperature: for the ferroelectric SmC* phase only one peak is observed whereas for the low temperature range of the antiferroelectric SmC^*_A phase the response pulses consist of two well-separated peaks. The position of the second peak shifts towards higher fields with decreasing temperature. Such behavior was found in other AFLCs for example by Fukuda et al. [4] and Hou et al. [45].

5.11.4.2 Spontaneous polarization

Temperature dependencies of spontaneous polarization are presented in Figs. 5.155a and b for two selected compounds. The values of the spontaneous polarization were calculated as a total integrated area of the current peaks (A) with respect to the baseline:

$$P_S = \frac{A}{2S} = \frac{1}{2S} \int I_{re}(t) dt \,, \tag{5.259}$$

where S is the surface of ITO electrode.

Temperature behavior of spontaneous polarization for AFLC is similar to that for FLC systems. According to the extended mean-field theory of the second order transition [9, 10, 13, 16] the spontaneous polarization P_S should obey the square root law with the critical exponent $\beta = 0.5$. It is seen from Figs. 5.155a,b that the SmA* - SmC* transition is almost a continuous one, but the β parameter is equal to 0.27 for MHP(3F)PBC and 0.23 for MHPBBBC. The fluorinated compound displays much larger spontaneous polarization which according to Dąbrowski [61] is caused by increased stiffness of the molecules due to fluorination of the achiral chain.

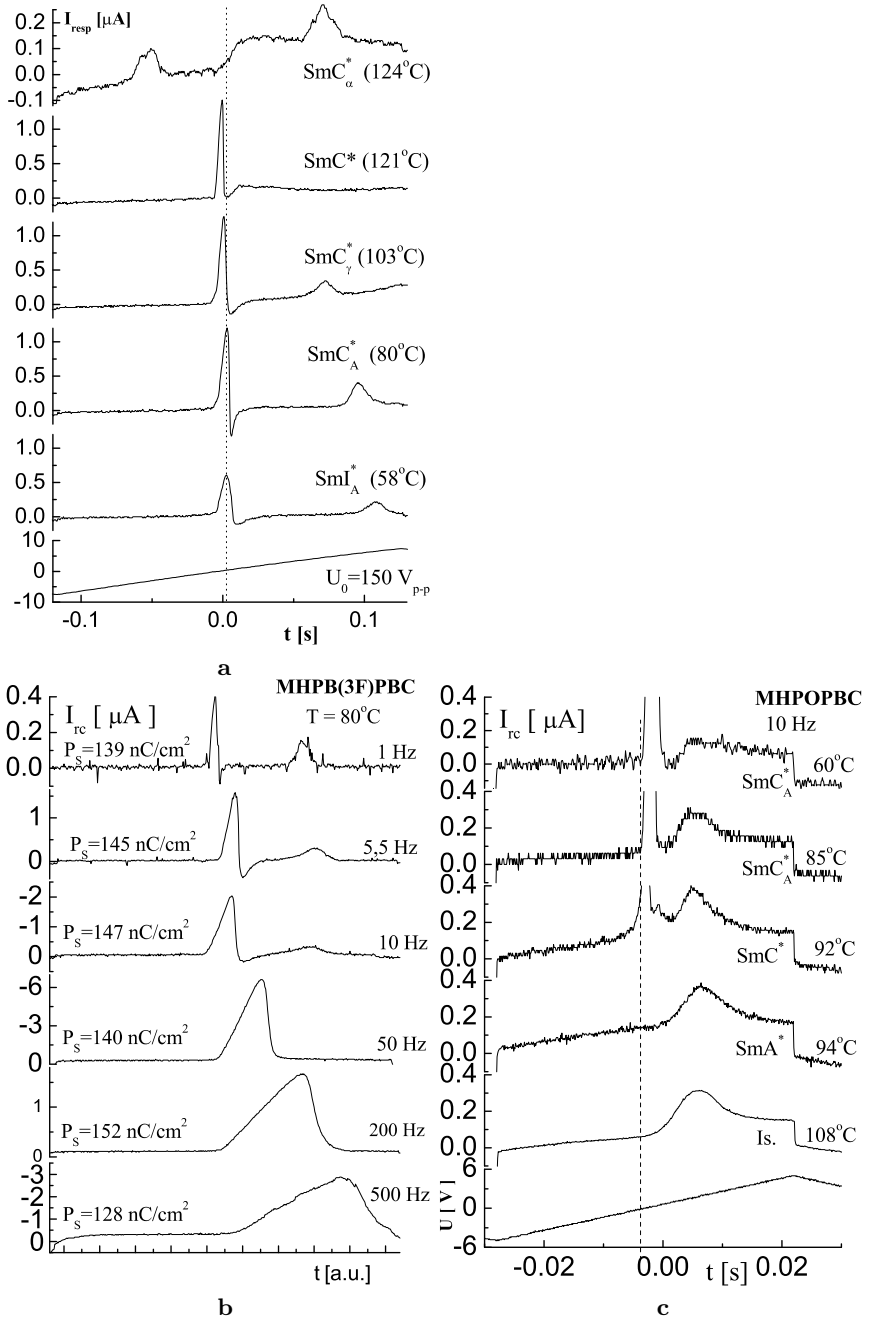

Fig. 5.154. Reversal current peaks obtained for: (**a**) different phases of MHPB(F)PBC, (**b**) antiferroelectric SmC^*_A phase of MHPB(3F)PBC using different frequencies, (**c**) influence of temperature on the current peak related to the ionic conductivity contribution for MHPOPBC

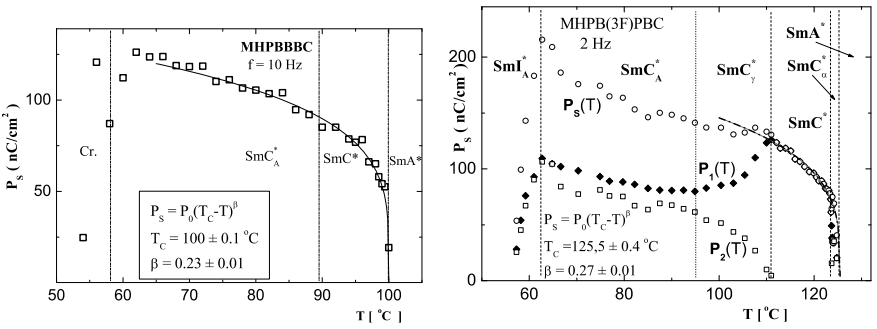

Fig. 5.155. Spontaneous polarization vs. temperature obtained for (**a**) MHPBBBC and (**b**) MHPB(3F)PBC. In (**b**) two components of P_S are shown for ferri- and antiferoelectric phases

Temperature dependencies of spontaneous polarization have been studied as a function of the chain structure (Fig. 5.156a). As seen the spontaneous polarization is distinctly higher for fluorinated compounds what may

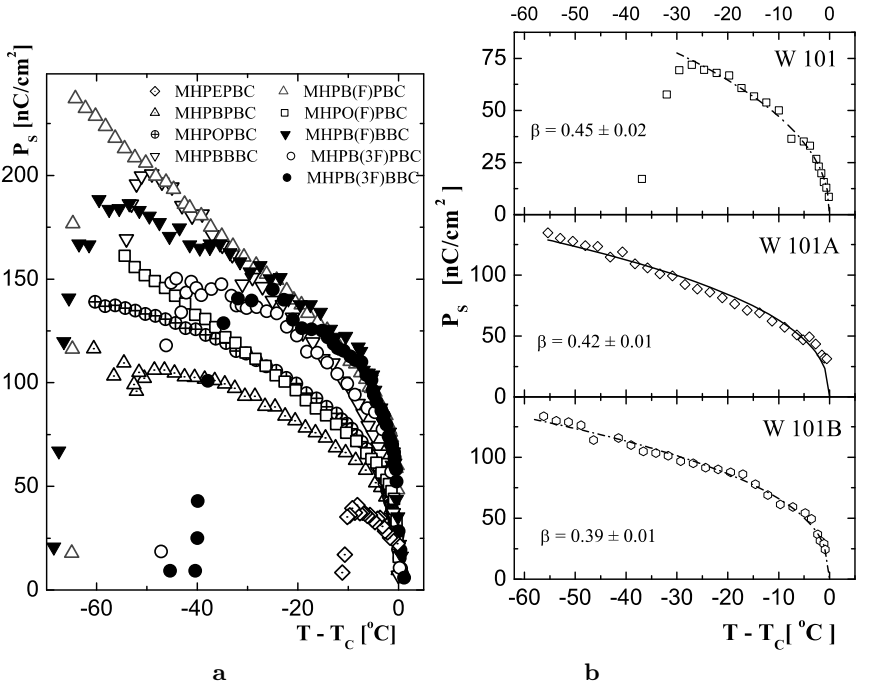

Fig. 5.156. $P_S(T)$ for the substances studied (**a**) and for three mixtures: W101, W101A and W101B (**b**) [61]

be connected with an increased stiffness of the end achiral chain and/or an increased hindering of the L-process. As seen for single component the mean-field model describes temperature dependencies of P_S only qualitatively. On the other hand the antiferroelectric phases of the mixtures studied [61] exhibit mean-field behavior of spontaneous polarization (Fig. 5.156b). It seems that the transition between orthogonal and tilted phases for mixtures studied is of the second order type. At high fields the $P_S(T)$ changes smoothly upon the SmC*-SmC$^*_A$ transition.

5.11.4.3 Tilt angle

Measurements of the tilt angle have been carried out on aligned samples. Exemplary temperature dependence of the tilt angle is shown in Fig. 5.157a for MHPBPBC. The temperature dependence of θ_o follows the mean-field behavior in the antiferroelectric phase. However, close to the SmC$^*_A$-SmI$^*_A$ transition and especially in the hexatic phase the tilt angle decreases with decreasing temperature. Similar effects have been found by Glogarová et al. [66] and Jägemalm et al. [67]. On the other hand, $P_S(T)$ does not go down (Fig. 5.156a) which is consistent with the model predicting that $\langle \cos \psi \rangle$ (5.257) increases with decreasing temperature.

Some of the substances studied exhibit a large electroclinic effect in the SmA* phase (see Fig. 5.157a) just above T_c. This effect was thoroughly studied by Fąfara [55] and it is even comparable with that known as giant surface electroclinic effect reported recently by Shao et al. [68]. Temperature dependencies of the spontaneous polarization and the tilt angle show that the SmA*-SmC$^*_A$ transition is of the second order, whereas the SmC$^*_A$-SmC* is of the first order type. Fig. 5.157b illustrates how far the mean-filed model [65] is

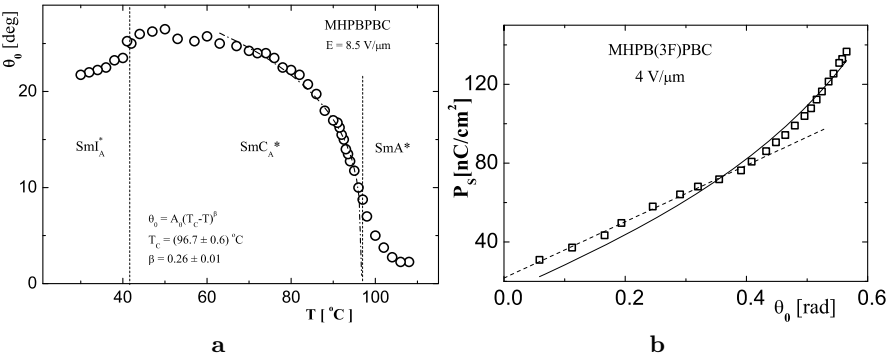

Fig. 5.157. (**a**) Tilt angle vs. temperature for MHPBPBC showing two antiferroelectric phases: SmC$^*_A$ and highly ordered SmI$^*_A$. (**b**) P_S versus θ_o for MHPB(3F)PBC. Exemplary fit of the mean-field model [65] to the experimental points; *dashed line* – linear behavior for small angles, *solid line* – a fit with quadratic term)

good for description of the relation between the secondary ($\boldsymbol{P}_j$) and primary ($\boldsymbol{\xi}_j$) order parameters.

5.11.4.4 Critical voltage

The critical (or threshold) voltages were measured by observation of the dechiralization lines (see Fig. 5.144d) under the polarizing microscope. The measurements were done on both increasing and decreasing of the voltage applied across the electrooptic cell. One should note that the threshold voltages measured in the antiferroelectric phase are significantly higher than those in the ferroelectric phase and they increase tremendously in the highly ordered SmI^*_A phase (Fig. 5.158a). As seen the critical voltage changes discontinuously at the SmC^*_A - SmC^* transition. From the practical standpoint it is not good that the threshold voltages become so high at low temperatures. This is especially seen in the case of hexatic, highly ordered SmI^*_A phase. Practical applications of the latter are doubtful, especially due to the fact that the tilt angle becomes smaller upon decreasing temperature in this phase.

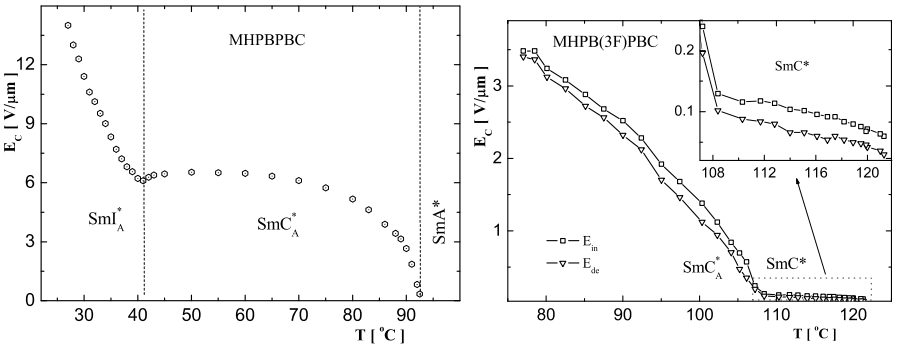

Fig. 5.158. (**a**) Critical voltage vs. temperature for liquid like (SmC^*_A) and highly ordered (SmI^*_A) antiferroelectric phases of MHPBPBC and (**b**) Threshold voltage vs. temperature in the vicinity of the SmC^*_A - SmC^* transition for MHPB(3F)PBC

5.11.5 Summary

1. DSC heating and cooling runs, as well as measurements of static dielectric permittivity show rich polymorphism of the substances studied.
2. Using FDDS and TDS spectroscopy three collective non-Arrhenius dielectric relaxation processes (Soft Mode, Goldstone Mode and non-Cancellation Mode) and two molecular Arrhenius-type dielectric relaxation processes (reorientation around the short and long axes) have been found

for the materials studied. Goldstone Mode, Soft Mode as well as the S-process, connected with reorientation around the short molecular axis, appear to be Debye-type processes characterized by single relaxation times. On the other hand, the NCM, and the L-process exhibit distribution of the relaxation times. The S-process is seen for planar alignment of the SmC^*_A phase due to the tilt of molecules.

3. Two sub-phases: SmC^*_α SmC^*_γ were found for MHPOBC analogues in addition to classical ferroelectric and antiferroelectric phases.
4. It has been found that the spontaneous polarization depends on the structure of the achiral chain of MHPOBC analogues studied and is distinctly higher for fluorinated compounds compared to nonfluorinated ones. It also depends strongly on the spacer length between the molecular core and the end chain bearing the polar group.
5. The SmA^* - SmC^* (or SmC^*_A) transitions exhibit a mean-field tri-critical point behavior. This effect is observed in non-linear dielectric measurements, i.e., in spontaneous polarization measurements. FDDS measurements show that the mean-field transition parameters depend on the bias voltage.
6. The SmA^* - SmC^*_A transition for mixtures studied in this work is of the second order type.
7. Using the current response method two characteristic well-separated peaks for the low temperature range of the antiferroelectric SmC^*_A phase have been revealed. The reversal current spectrum depends on the type of phase and it could be used as a first step in phase identifications.
8. Last but not least, the substances studied in scope of this contribution are components of the mixtures, showing interesting V-shape switching, thoroughly studied recently by Goc et al. [69, 70].

Acknowledgments. The authors would like to thank Professor Roman Dąbrowski and co-workers for providing single compounds as well as mixtures for our investigations. One of the authors (W.H.) would like to thank the DFG for financial assistance. S.W., W.H. and M.M. are grateful to the DLR Büro in Bonn and KBN in Warsaw for financial support of our workshops organized in scope of the German-Polish Project (Pol-N-85-94 and Pol 99-022). Fruitful discussions with Drs. L. Beresnev, L. Blinov, I. Dierking, W. Kuczyński, S. Pikin, and E. Pozhidaev are gratefully acknowledged.

References

1. A.D.L. Chandani, Y. Ouchi, H. Takezoe, A. Fukuda, K. Terashima, K. Furukawa, A. Kishi: Jpn. J. Appl. Phys. **28**, L1261–L1264 (1989)
2. A.D.L. Chandani, E. Górecka, Y. Ouchi, H. Takezoe, A. Fukuda: Jpn. J. Appl. Phys. **28**, L1265–L1268 (1989)

3. A.L.D. Chandani, Y. Ouchi, H. Takezoe: Jpn. J. Appl. Phys. **28**, L1261–L1264 (1989)
4. A. Fukuda, Y. Takanishi, T. Isozaki, K. Ishikawa, H. Takezoe: J. Mater. Chem. **4**, 997(1994)
5. K. Miyachi, A. Fukuda: "Antiferroelectric Liquid Crystals". In: Handbook of Liquid Crystals, Vol. 2B. ed. By D. Demus, J. Goodby, G.W. Gray, H.-W. Spiess, V. Vill (Wiley-VCH, Weinheim – New York – Chichester – Brisbane – Singapore – Toronto 1998), pp. 665–691
6. H. Takezoe, K. Hiraoka, T. Isozaki. K. Miyachi, H. Aoki, A. Fukuda: "Dielectric Properties in Antiferroelectric Liquid Crystals". In: *Modern Topics in Liquid Crystals. From Neutron Scattering to Ferroelectricity.* Ed. by A. Buka (World Scientific, Singapore – New Jersey – London – Hong Kong 1993) pp. 319–336
7. M. Glogarova, H. Sverenyak, H.T. Nguyen, Ch. Destrade: Ferroelectrics **147**, 43 (1993)
8. P. Gisse, J. Pawel, H.T. Nguyen, V.L. Lorman: Ferroelectrics **147**, 27 (1993)
9. S.T. Lagerwall: "Ferroelectric and Antiferoelectric Liquid Crystals" (Wiley-VCH, Weinheim – New York – Chichester – Brisbane – Singapore – Toronto 1999)
10. I. Muševič, R. Blinc, B. Žekš: "The Physics of Ferroelectric and Antiferroelectric Liquid Crystals" (World Scientific, Singapore – New Jersey – London – Hong Kong 2000)
11. R.B. Meyer: The 5^{th} International Liquid Crystal Conference, Stockholm 1974
12. R.B. Meyer, L. Liebert, L. Strzelecki, P. Keller: J. Phys. Lett. (Paris) **36**, L69–71 (1975)
13. R. Blinc, B. Žekš: Phys. Rev. A **18**, 740 (1978)
14. B. Žekš, A. Levstic, R. Blinc, J. Phys. (Paris) Colloque C3, supplement No. 4, **40**, pp. C3409-C3312 (1979)
15. R. Blinc: "Models for Phase Transitions in Ferroelectric Liquid Crystals: Theory and Experimental Results". In: *Phase Transitions in Liquid Crystals.* Ed. by S. Martellucci and A.N. Chester (New York, Plenum Press 1992) pp. 343–363
16. S.A. Pikin, V.L. Indenboom: Uspiekhi Fiz. Nauk **125**, 251 (1978)
17. H. Orihara, Y. Ishibashi: Jpn. J. Appl. Phys. **29**, L115 (1990)
18. T. Carlsson, B. Žekš, C. Filipič, R. Blinc: Mol. Cryst. Liq. Cryst. **163**, 11 (1988)
19. M. Čepič, B. Žekš: Mol. Cryst. Liq. Cryst. **263**, 61 (1995)
20. B. Žekš, M. Čepič: SPIE **3318**, 68 (1997)
21. M. Čepič, B. Rovšek, B. Žekš: Mol. Cryst. Liq. Cryst. **351**, 209 (2000)
22. M. Škarabot, M. Čepič, B. Žekš, R. Blinc, G. Heppke, A.V. Kityk, I. Muševič: Phys. Rev. E **58**, 575 (1998)
23. A. Roy, N.V. Madhusudana: Europhysics Letters **36**, 221 (1996)
24. P. Toledano, A.M. Figueiredo Neto, A.A. Boulbitch, A. Roy: Phys. Rev. E **59**, 6785 (1999)
25. M. Čepič, G. Heppke, J.-M. Hollidt, D. Lötzsch, B. Žekš: Ferroelectrics **147**, 150 (1993)
26. S.A. Pikin, S. Hiller, W. Haase: Mol. Cryst. Liq. Cryst. **262**, 424 (1995)
27. S. Pikin, M. Gorkunov, D. Kilian, W. Haase: Liq. Crystals **26**, 1107 (1999)
28. S. Pikin, M. Gorkunov, D. Kilian, W. Haase: Liq. Crystals **26,** 1115 (1999)
29. S. Pikin, D. Kilian, M. Gorkunov, W. Haase: Liq. Crystals **26**, 1123 (1999)
30. N. Voupotič, M. Čepič, B. Žekš: Ferroelectrics **245**, 185 (2000)
31. K. Hiraoka, A. Taguchi, Y. Ouchi, H. Takezoe, A. Fukuda: Jpn J. Appl. Phys. **29**, L103 (1990)

32. K. Hiraoka, H. Takezoe, A. Fukuda: Ferroelectrics **147**, 13 (1993)
33. H. Moritake, Y. Uchiyama, K. Myojin, M. Ozaki, K. Yoshino: Ferroelectrics **147**, 53 (1993)
34. S. Hiller, S.A. Pikin, W. Haase, J.W. Goodby, I. Nishiyama: Jpn. J. Appl. Phys. **33**, L1096 (1994)
35. S. Hiller, S.A. Pikin, W. Haase, J.W. Goodby, I. Nishiyama: Jpn. J. Appl. Physics **33**, L1170 (1994)
36. D. Kilian: PhD Thesis, Darmstadt University of Technology, Darmstadt (1999)
37. J. Hatano, Y. Hanakai, H. Furue, H. Uehara, S. Saito, K. Murashiro: Jpn. J. Appl. Phys. **33**, 5498 (1994)
38. H. Uehara, Y. Hanakai, J. Hatano, S. Saito and K. Murashiro: Jpn. J. Appl. Phys. **34**, 5424 (1995)
39. M. Buivydas, F. Gouda, S.T. Lagerwall, B. Stebler: Liq. Crystals **18**, 879 (1995)
40. P. Simeão Carvalho, M.R. Chaves, C. Destrade, H.T. Nguyen, M. Glogarova: Liq. Crystals **21**, 31 (1996)
41. S. Merino, M.R. de la Fuente, Y. Gonzalez, M.A. Perez Jubindo, B. Ros, J.A. Puertolas: Phys. Rev. E **54**, 5169 (1996)
42. D. Kilian, S. Hiller, W. Haase, J.-M. Hollidt, G. Heppke: Ferroelectrics **180**, 137 (1996)
43. M. Buivydas, F. Gouda, G. Andersson, S.T. Lagerwall, J. Bömelburg, G. Heppke and B. Gestblom: Liq. Crystals, **23**, 723 (1997)
44. Yu.P. Panarin, O. Kalinovskaya, J.K. Vij, J.M. Goodby: Phys. Rev. E **55**, 4345 (1997)
45. J. Hou, J. Schacht, F. Gießelmann, P. Zugenmaier: Liquid Crystals **22**, 401 (1997)
46. J. W. O'Sullivan, J.K. Vij, H.T. Nguyen: Liquid Crystals **23**, 77 (1997)
47. M. Buivydas, S.T. Lagerwall, F. Gouda, R. Dübal, A. Takeichi: Ferroelectrics **212**, 55 (1998)
48. A. Fąfara, B. Gestblom, S. Wróbel, R. Dąbrowski, W. Drzewiński, D. Kilian and W. Haase: Ferroelectrics **212**, 79 (1998)
49. A. Fąfara, M. Marzec, S. Wróbel, R. Dąbrowski, K. Czupryński: Proceedings of SPIE Vol. **4147**, pp. 71–74 (2000)
50. M. Marzec, A. Fąfara, S. Wróbel, M. Godlewska, R. Dąbrowski, K. Czupryński, W. Haase: Proceedings of SPIE Vol. **4147**, pp. 89–94 (2000)
51. A. Fąfara, M. Marzec, W. Haase, S. Wróbel, D. Kilian, M. Godlewska, K. Czupryński, R. Dąbrowski: Ferroelectrics **245**, pp. 81–89 (2000)
52. M. Marzec, D. Ganzke, W. Haase, R. Dąbrowski, K. Czupryński, A. Fąfara, S. Wróbel: Mol. Cryst. Liq. Cryst. **366**, pp. 583–591 (2001)
53. M. Makrenek, D. Ganzke, W. Haase, S. Wróbel, R. Dąbrowski: Mol. Cryst. Liq. Cryst. **366**, pp. 573–581 (2001)
54. M. Wojciechowski, A.L. Gromiec, G.W. Bąk: Sci. Bull. Lodz Tech. Univ. Phys. **19**, 51 (1999)
55. A. Fąfara: PhD Thesis, Jagiellonian University, Kraków 2001
56. A. Fąfara, D. Ganzke, W. Haase, M. Marzec, S. Wróbel, C. Czapczyński, R. Dąbrowski: Ferroelectrics **276**, pp. 41–48 (2002)
57. S. Wróbel, W. Haase, D. Kilian, L.-C. Chien, L. Chong-Kwang: Ferroelectrics **243**, pp. 277–289 (2000)
58. M. Marzec, E. Gondek, S. Wróbel, R. Dąbrowski: accepted for Mol. Cryst. Liq. Cryst.

59. W. Drzewiński, R. Dąbrowski, K. Czupryński, J. Przedmojski, M. Neubert: Ferroelectrics **212**, 281 (1998)
60. W. Drzewiński, K. Czupryński, R. Dąbrowski, J. Przedmojski, M. Neubert, S. Yakovenko, A. Muravski: Mol. Cryst. Liq. Cryst. **351**, 297 (2000)
61. R. Dąbrowski: Ferroelectrics **243**, 1 (2000)
62. A.M. Biradar, D. Kilian, S. Wróbel, W. Haase: Liq. Cryst. **27**, 509 (2000)
63. M. Marzec: PhD Thesis, Jagiellonian University, Kraków 1997
64. D. Kilian, M. Marzec, S. Wróbel, R. Dąbrowski, W. Drzewiński and W. Haase, Mol. Cryst. Liq. Cryst. **328**, 131 (1999)
65. F. Giesselmann: 'Landau Description of the SmA* - SmC* Phase Transition in Ferroelectric Liquid Crystals'. In: *Selforganisation in Chiral Liquid Crystals*. ed. by W. Kuczyński (Scientific Publishers OWN, Poznań 1997) pp. 7–33
66. M. Glogarová, V. Novotná, M. Kašpar, V. Hamplová: SPIE Proceedings Vol. **4759**, 106 (2002)
67. P. Jägemalm, J.P.F. Lagerwall, A. Dahlgren, L. Komitov, A.S. Matharu, C. Grover, F. Gouda, A.A. Kutub: Ferroelectrics **244**, 147 (2000)
68. R.-F. Shao, J.E. Maclennan, N.A. Clark, D.J. Dyer, D.M. Walba: Liq. Crystals **28**, 117 (2001)
69. F. Goc: PhD Thesis, Institute of Molecular Physics of Polish Academy of Sciences, Poznań 2002
70. F. Goc, W. Kuczyński, R. Dąbrowski, SPIE Proceedings **4147**, 75 (2000)

6

Calamitic and Discotic Metallomesogens

6.1 Dielectric study of smectic and columnar ferroelectric metallomesogens

M.R. de la Fuente, M.Á. Pérez Jubindo, T. Sierra, and J.L. Serrano

6.1.1 Introduction

Over the past few years some interest has been devoted to the study of mesogenic metal-containing compounds [1]. One of the aspects that makes them different from typical organic liquid crystals is the great variety of molecular geometries that can be obtained by introducing metals into the chemical structure: rod-like, disc-like, brick-like, open-book or K shapes among others [2–6]. Similar to organic mesogens, these compounds exhibit either calamitic or discotic mesophases. In this work we will present mainly dielectric studies on some metallomesogenic compounds, both chiral and non-chiral with special emphasis in those that show ferroelectric behavior. Metal-containing liquid crystals open this field not only to a significant number of new structures but also add to the ferroelectric behavior other properties inherent to the presence of metals in the structure, such as magnetism, as well as the use of new methods of characterization (for example EPR [7]).

The first group of target compounds is made of mesogenic dimers consisting of two organic ligands bridged through transition metal centers showing smectic mesomorphism [8, 9]. The chiral compounds show the ferroelectric SmC* phase [10, 11]. The molecules are highly biaxial with a brick-like shape. Although with some peculiarities due to their shape, the ferroelectric and dielectric behavior can be understood in the same way as for the most conventional organic molecules. For example, the mode related to rotation around the molecular long axis, the soft mode and the Goldstone mode have been characterized (the metal centers were Cu, Pd and VO but we will stress on the VO compounds with some reference to other cases as necessary).

The second group of target compounds consists of chiral disc-shaped molecules. Disc-shaped molecules can form columnar mesophases [12] when

Table 6.1. Phase transition sequence

	Compound	Phase transition temperature
1	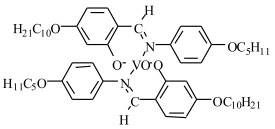	I 178 °C SmA 156 °C SmC
2	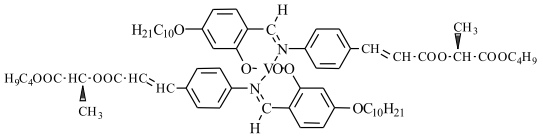	I 170 °C SmA 125 °C SmC* 100 °C ODIC
3	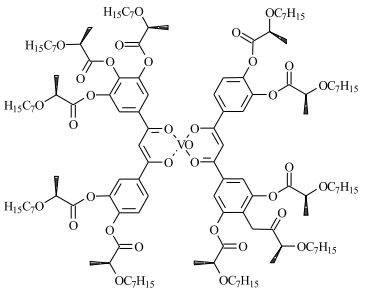	I 143 °C Col_r* −70 °C glass

the molecules are suitably substituted with flexible side chains. The cores stack to form columns surrounded by the disordered aliphatic side chains. The centers of the cores form a rectangular (ordered or disordered) or hexagonal (ordered or disordered) lattice in the plane normal to the columnar axis. The occurrence of ferroelectricity in columnar phases was predicted by Prost in 1982 [13] and experimentally detected first in 1992 by Bock and Helfrich [14–19]. To show this phenomenon the disc-shaped molecules have to be chiral and lie tilted with respect to the column axis. The macroscopic polarization is perpendicular to the column axis and the tilt plane and is due to the tilt-induced dipole moment of the chiral molecules. However, many questions regarding the molecular organization within the mesophase and the switching mechanism remain unanswered [20]. Our compounds consist of two penta-substituted organic ligands bridged through transition metal centers given rise to a disc-like core surrounded by ten flexible tails derived from L(-)-lactic acid. They show a columnar rectangular tilted mesophase within a wide temperature range. This phase is switchable and shows a Goldstone-like mode similar to that present in the most usual ferroelectric SmC* phase, which suggests the presence of a helical structure. The metal centers were Cu, Pd and VO but we will stress on the VO compounds with some references to the other cases when necessary. (See Table 6.1 for formulas and phase transition sequences) [21–23].

We will treat and discuss separately the calamitic and the columnar compounds.

6.1.2 Experimental

The synthetic pathways followed to obtain these compounds together with DSC studies can be found in [8] for compound **1**, [10] for compound **2** and [21] for compound **3**.

The complex dielectric permittivity, $\varepsilon(\omega)$, was measured over 11 decades of frequency (10^{-2}–10^{9}Hz) using three different measuring systems: a frequency response analyzer (Schlumberger 1260) equipped with a high-impedance preamplifier of variable gain (Novocontrol dielectric interface) and two impedance analyzers, the HP 4191A and the HP 4192A. The cell consisted of two gold-plated brass electrodes (diameter 5 mm) separated by 50 μm thick silica spacers. We did not treat the electrodes and the samples were misaligned but mostly planar. For ferroelectric compounds we also measured the spontaneous polarization, P_S (for these measurements we used commercially available cells purchased from Linkam). P_S was measured using the triangular wave method, which also allowed us to determine the switching time [24]. Other studies, such as X-ray, circular dichroism or electrooptic switching studies can be found in [21–23] for the second group of compounds.

6.1.3 Results and discussion

6.1.3.1 Calamitic compounds

Non-chiral systems Let us start with compound **1** which shows SmA and SmC phases. It has a brick-like molecular shape (see Fig. 6.1) with two different short axes, and, due to the squared pyramidal geometry of the oxovanadyl group, has a net electric dipole moment along the C_2 symmetry axis (x in Fig. 6.1 , the shortest axis), which is perpendicular to the plane that contains the two rings of the 2,4-salicylaldimine. The symmetrical arrangement of the alkyl chains makes the dipole moment along the z and y axes zero, then the only possible dielectric relaxations should be related to the above-mentioned dipole moment, μ_t. To be sure about the alignment of the material, the low frequency measurements were also performed with another sample holder that allows the application of a magnetic field. The anisotropy of the paramagnetic contribution [25] favors the V-O bond being perpendicular to the magnetic field and the molecules tend to align with their longest axis, z, perpendicular to the magnetic field. To achieve planar alignment the magnetic field was applied parallel to the electrodes. We could not obtain the homeotropic alignment.

The dielectric spectrum shows only one relaxation, which is thermally activated. Its frequency is around 30 MHz in the isotropic phase and 1 MHz in the SmC phase.

To know the strength, frequency and activation energy of this mode, the experimental data were fitted in each phase to:

$$\varepsilon(\omega) = \Delta\varepsilon_e(\omega) + \sum_k \Delta\varepsilon_k(\omega) + \varepsilon_\infty - i\sigma_{dc}/\omega\varepsilon_0 \,, \tag{6.1}$$

where $\Delta\varepsilon_e(\omega)$ accounts for a spurious contribution on the low frequency side of the spectrum due to the electrode polarization, $\Delta\varepsilon_k(\omega)$ accounts for the contribution of each mode (for this compound only one mode), σ_{dc} for the dc

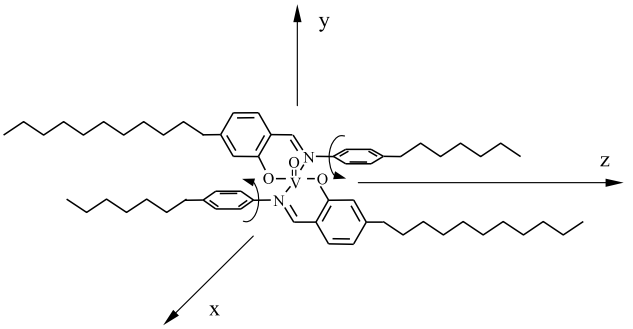

Fig. 6.1. Sketch of the molecular structure of compound **1** showing the three mean axes

conductivity, and ε_∞ for the high frequency permittivity. For $\Delta\varepsilon_k(\omega)$ we used the Havriliak–Negami (H-N) function:

$$\Delta\varepsilon_k(\omega) = \frac{\Delta\varepsilon_k}{(1 + (i\omega\tau)^\alpha)^\beta} \,, \tag{6.2}$$

where $\Delta\varepsilon_k$ is the dielectric strength, τ the relaxation time and α, β control the shape of the relaxation. From the fitted parameters, τ, α and β, the relaxation frequencies, f_k, were calculated as:

$$f_k = \frac{1}{2\pi\tau} \left\{ \tan\left(\frac{\pi}{2(\beta+1)} \right) \right\}^{1/\alpha} \,. \tag{6.3}$$

Figure 6.2 is an Arrhenius plot of the frequency versus temperature. It shows an important jump at the I-SmA phase transition and a change in the activation energy, from around 70 kJ mol^{-1} in the isotropic phase to around 90 kJ mol^{-1} in both smectic mesophases.

Figure 6.3 shows the dielectric strength versus temperature. It is around 0.5 everywhere with a small increase at the I-SmA phase transition and a continuous but small decrease in the SmC mesophase. In the SmC phase the shape of the relaxation is near-Debye ($\alpha = \beta = 1$) and in the isotropic phase and on the high temperature side of the SmA phase it is broader ($\alpha = 0.9$ and β ranging between 0.6 and 0.8).

Most of the relaxation studies in liquid crystals have been performed on compounds with more-or-less rod-like symmetry and theories for molecular motion have also been proposed for this type of liquid crystals. These theories are based on the small step rotational diffusion model for the molecular dynamics (see Sect. 4.1 in this book). Each molecule is assumed to act independently of its neighbors, which just contribute to a mean potential. The

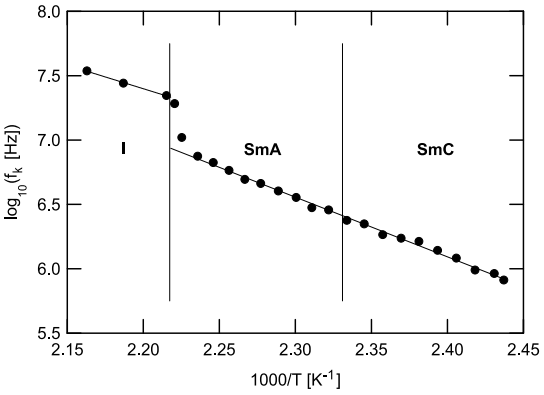

Fig. 6.2. Arrhenius plot of the frequency of the relaxation vs. temperature (compound **1**). The *solid lines* are fit curves to the Arrhenius law (Reproduced from [9], copyright 1994 WILEY-VCH)

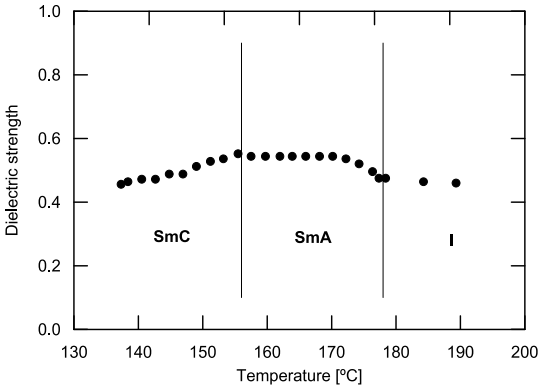

Fig. 6.3. Dielectric strength versus temperature (compound **1**) (Reproduced from [9], copyright 1994 WILEY-VCH)

frequencies of the modes related to rotation around molecular short and long axes follow the Arrhenius law in each mesophase. These activation energies could vary from one phase to other due to changes in the rotation barriers. The frequency of the mode related to the rotation around short axis jumps-down at the I-N or I-Sm phase transitions due to the onset of order of the molecular director. For the rotation around long axis one usually obtains a small jump (up) or no jumps at the I-N or I-Sm phase transitions. In our case, the alignment conditions together with the molecular structure allow us to assign the observed relaxation to the rotation around molecular long axis that involve reorientations of the dipole moment transverse to the long molecular axis. However, the temperature behavior of the frequency is not as expected because we obtain a jump (down) on going from the isotropic to the SmA mesophase. To interpret this behavior we will take into account the results of a previous EPR study [26], which showed that the order parameter of the long axis is high and that there is also a high in plane local order of the short axes. Then, one can assume that the motion around the long axis is a diffusion in a hard potential (for example a potential that includes a quadrupolar term that tend to maintain the shortest axes parallel). If this is so, the above-mentioned jump could be understood as the result of a sudden increase of the orientational order parameter of the short axes, in the same way as happens at the I-N phase transition when the frequency of the reorientation of the molecular long axis decreases due to the order induced by the nematic potential. We also measured a similar compound but being Cu the metal that joined the two ligands. In this case the coordination around the metal is square and there is no dipole moment associated to this group and hence not net dipole moment associated to the whole molecule. The dielectric response was completely flat as expected.

Chiral systems The following step in this study was devoted to chiral metallo-organic compounds showing calamitic mesophases (compound **2** (VO) and its homologous with Cu and Pd, see Table 6.1).

The presented results are part of a deeper study devoted to explain the molecular origin of the spontaneous polarization in SmC* phases of metallomesogens: salicylideneamine complexes, open-book dinuclear palladium complexes, H-shaped chloro-bridged dinuclear palladium complexes, and K-shaped benzylideneamine β-diketone palladium complexes [10]. In this work the target compounds are salicylideneamine metal complexes (see Table 6.1). The three compounds show similar phase transition sequence I-SmA-SmC*-X (X = orientationally disordered crystalline phase for VO, glassy SmC* for Cu and crystal for Pd), with a noticeable spontaneous polarization in the SmC* phase: 30 nC cm^{-2} for VO, 50 nC cm^{-2} for Cu, and 55 nC cm^{-2} for Pd. In all cases the fields needed for the switching process were quite high. The switching times were also very high; comparable to those obtained in polymeric ferroelectric liquid crystal materials, $\tau\,\mathrm{E} \approx 10\,\mathrm{ms\,V\,\mu m^{-1}}$. In an attempt to establish the origin of the polar order of these materials, it is essential to be aware of two main characteristics inherent in their molecular structure. They deviate considerably from the conventional rod-like shape; they are biaxial brick-like with three different axes: a longitudinal axis and two transverse axes. To better understand the molecular structure let us look at the synthetic step in which the complex is formed. During the chelation process, two salicylidenaniline ligands must face each other in such a way that all four chelating heteroatoms together with the metal are in the same plane. Thus, one of the ligands must be rotated by 180 ° with respect to the other ligand. As a result of this, a C_2 symmetry axis perpendicular to the plane that contains the metal and the coordination atoms is the only symmetry element of the molecule provided that one stereogenic center is present in one of the tails of each ligand. Thus, on average, a net dipole moment for these molecules can only be found parallel to their C_2 axis, the shortest axis. To explain the P_S measured values in the SmC* phase, molecules must be on average tilted with the molecular C_2 symmetry axis in the direction of the polar axis, so that the shortest axis is perpendicular to the tilt plane, as shown in Fig. 6.4. At this point let us take into account the role of the oxovanadium group in the ferroelectric behavior of these compounds. Because the vanadyl ion is lopsided, the square-pyramidal geometry of the vanadium complex is noncentrosymmetric. This means that when the complex is obtained from achiral salicylideneaniline ligands a racemic mixture must result. However, if ligands are chiral the subsequent optically active diasteromeric mixture is obtained. As a consequence, a preferred direction either toward or away from the molecular tilt plane of the oxovanadium group should be expected. Thus, the dipole associated with this group will contribute either negatively (as it would be in our case to explain the lower P_S value for VO than for Cu or Pd compounds) or positively to the effective molecular dipole in the P_S values.

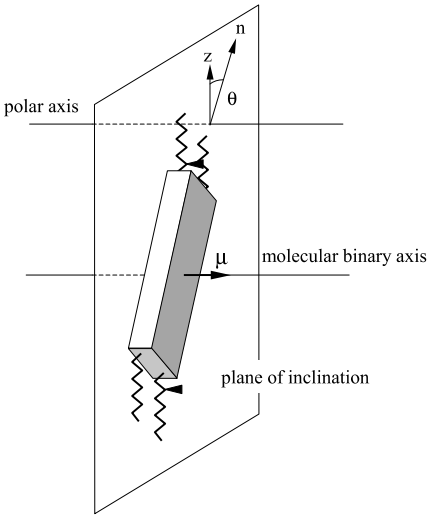

Fig. 6.4. Schematic diagram of the molecular structure showing the tilt of the long molecular axis. The longest transverse axis lies, in average, on the tilt plane. n, molecular director; z layer normal; θ, tilt angle (compound **2**) (Reproduced from [10], copyright 1996 American Chemical Society)

Now let us start with the dielectric results. We only present the results for the VO compound. Figure 6.5 is a three-dimensional plot of ε' vs. temperature and frequency. The different dielectric modes are not very clearly seen due to the high spurious contributions related to the dc conductivity and electrode polarization contributions (see (6.1)). At the low frequency side and on going down in temperature, the first decrease is related to the decrease of these spurious effects on going from the I to the SmA phase; the following increase is related to the appearance of a low frequency mode in the SmC* phase and the following increase occurs when the compound enters into the solid rotatory phase (or orientationally disordered crystal, ODIC). When analyzing the spectra more carefully in the isotropic phase we observe two thermally activated relaxations. The high frequency one is in the MHz region and the low frequency one in the kHz region. The molecules only have a net dipole moment along the shortest axis. Both relaxations should be related to it. The high frequency one could be related to the rotation around the molecular long axis and the low frequency one to the rotation around the intermediate axis. Both relaxations were also observed in the SmA and SmC* phases. Figures 6.6 and 6.7 show the complex dielectric permittivity versus the logarithm of the frequency at 128 °C (SmA) and 120 °C (SmC*), respectively. In both figures we have subtracted previously the spurious contributions due to dc conductivity and electrode polarization. We have chosen for the SmA a temperature near the para-ferroelectric phase transition where together with the two modes above mentioned there is another mode that

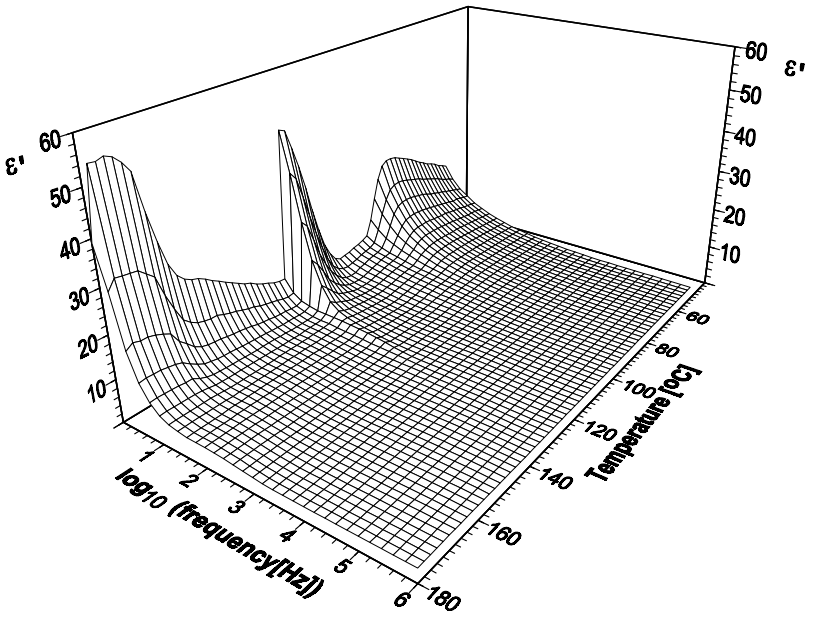

Fig. 6.5. Three-dimensional plot of ε' vs. temperature and frequency (compound **2**)

we have assigned to the soft mode due to the temperature dependence of its strength and frequency. In the SmC* phase we observed another mode in the low frequency side, the Goldstone mode. Its strength is larger than the strength of the other modes and its frequency goes quickly down a few degrees below the SmA-SmC* phase transition temperature. A dc field produced a decrease in its dielectric strength. However, we could not suppress it due to the low maximum dc value or our experimental set-up (10V).

In each phase the dielectric results have been fitted to (6.1) and (6.2). The Goldstone mode, the soft mode and the mode related to rotations around the longest transverse axis are near Debye. The mode related to rotations around the long axis is broader with the α parameter around 0.8 and $\beta = 1$ (Cole–Cole). From the fittings of the complex dielectric permittivity (continuous lines in Figs. 6.6 and 6.7) we deduced the strengths and frequencies of all mentioned modes. Figures 6.8 and 6.9 show the temperature dependence of the frequencies and strengths. The behavior of the soft mode frequency is as is usually found in the SmA phases of compounds with second order SmA-SmC* phase transition [13]. The strength of this mode is very weak, except for the temperature range near the transition, where it reaches 1.5. We could not study this mode in the SmC* phase because of the high dielectric strength of the Goldstone mode (around 40) that cannot be quenched by the dc bias voltage of our low frequency set-up (10 V). The Goldstone mode frequency is very low, 3 Hz near the SmA phase and goes quickly down on decreasing

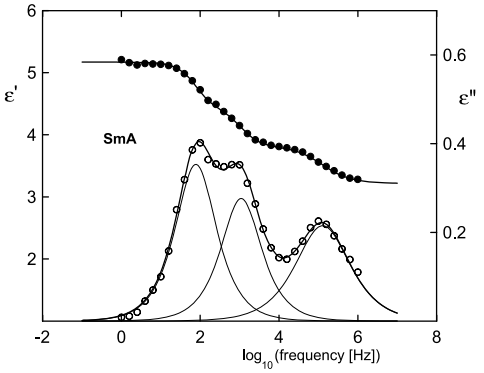

Fig. 6.6. Complex permittivity vs. frequency in the SmA phase (compound **2**): ε' (•), ε'' (○). The *solid lines* are fit curves using (6.1) and (6.2): (from high to low frequency) mode h, soft mode and mode l (Reproduced from [11], copyright 1996 WILEY-VCH)

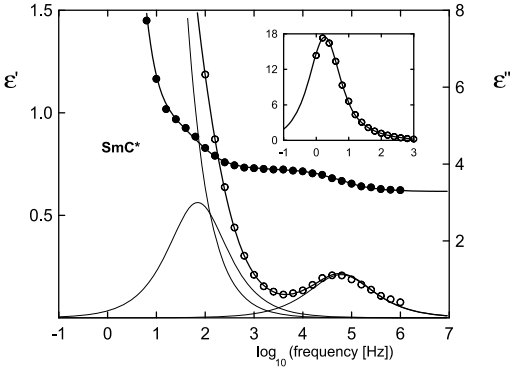

Fig. 6.7. Complex permittivity vs. frequency in the SmC* phase (compound **2**): ε' (•), ε'' (○). The *solid lines* are fit curves using (6.1) and (6.2): (from high to low frequency) mode h, mode l and Goldstone mode. The *inset* shows the Goldstone mode contribution (only the imaginary component; the real component is off scale) (Reproduced from [11], copyright 1996 WILEY-VCH)

the temperature. This is in accordance with the large values obtained for the switching time (milliseconds at 1 V μm^{-1} [12]) and is a consequence of the high rotational viscosity. The frequencies of the modes related to rotations around molecular axes have thermal activation. The high frequency one, hereafter called mode h, exhibits a small step at the I-SmA phase transition. In the smectic mesophases follows an Arrhenius law, being the activation energy 103 kJ mol^{-1} in the paraelectric phase and 144 kJ mol^{-1} in the ferroelectric one. The low frequency one, hereafter called mode l, also follows the Arrhenius law in the I and SmA phases being the activation energy 20 kJ mol^{-1} and 63 kJ mol^{-1}, respectively. Note that these values are lower than those

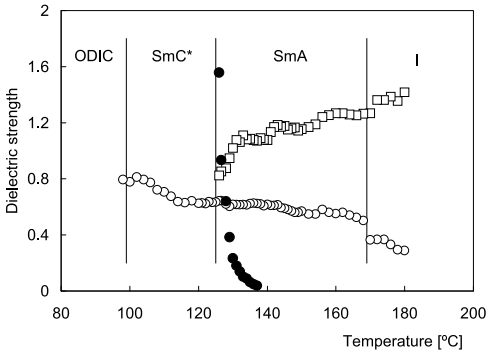

Fig. 6.8. Dielectric strength of the different modes vs. temperature (compound **2**): (○) mode h, related to rotation around molecular long axis; (□) mode l, related to rotation around the longest transverse axis; (●) soft mode (Goldstone mode is around 40)

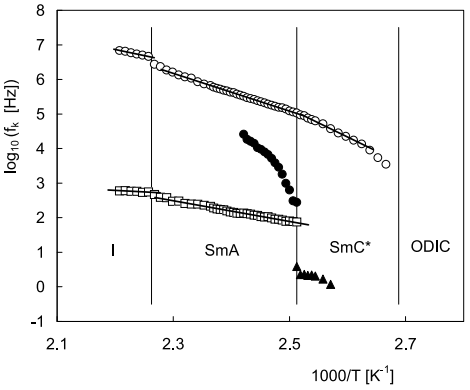

Fig. 6.9. Arrhenius plot of the frequency of the different modes vs. temperature (compound **2**): (○) mode h, (□) mode l, (●) soft mode, (▲) Goldstone mode. The *solid lines* are fit curves to the Arrhenius law (Reproduced from [11], copyright 1996 WILEY-VCH)

corresponding to the high frequency mode. The dielectric strength of mode l decreases continuously upon cooling down. In the SmC* phase it is difficult to analyze it due to the appearance of the Goldstone mode. The dielectric strength of mode h has a jump-up at the I-SmA phase transition and increases continuously upon cooling down. Below the SmC* phase the compound has a solid rotatory phase with a very low frequency and high strength dielectric mode that covers all other possible active modes. For example we could not determine if mode h was just hidden or frozen.

At this point, let us compare the results for this compound with the results for compound **1**. For the non-chiral compound the net dipole moment is fully related to the VO center and only one mode appears in the dielectric response.

The temperature dependence of the strength of this mode is similar to that of the mode we called h. Moreover its frequency also showed a jump at the I-SmA phase transition that was explained as due to the onset of some in-plane order (at least local) of the transverse axes. In the chiral compound at the SmA-SmC* phase transition an important change in the activation energy occurs: from 103 kJ mol^{-1} in the SmA phase to 144 kJ mol^{-1} in the SmC*, that does not happen neither in the non-chiral compound at the SmA-SmC phase transition, nor in other ferroelectric liquid crystals. This change could be explained in the context of the model of Urbanc and Zeks [27] as due to an important increase of the quadrupolar order of transverse axes when molecules are tilted (note that to guarantee the existence of a non-vanishing spontaneous polarization, the molecules should tilt as indicated in Fig. 6.4 and not with their longer transverse axis perpendicular to the tilt plane, as it was expected according to excluded volume effects). However, to explain the jump of the frequency at the I-SmA (for both compounds **1** and **2**) this quadrupolar ordering of transverse axes should also be important in the SmA phase. This phase is uniaxial, and then this order should be local.

Now let us come back to mode l. The behavior of its frequency is quite unusual. Its activation energy in the SmA phase is lower than that of the high frequency mode by a factor of two, which is unlikely; this would mean less hindrance to rotate around a transversal axis than around the longitudinal axis or that the order parameter of the long axis is smaller than that of the intermediate axis, this having a tendency to point along the director. Probably the molecules in our study cannot be described as flat, and then it is not justified to talk of overall motions. To finish, note that this mode is not present in the spectra of the previous non-chiral compound.

6.1.3.2 Discotic compounds

Our last group of compounds consists of metal-containing chiral disc-shaped molecules. They have ten chiral peripheral chains. Details of the chemistry of these compounds together with results from X-ray, circular dichroism, differential scanning calorimetry (DSC) and electrooptic switching studies can be found in [21–23]. These studies show that, upon cooling from their isotropic phases, these compounds have a wide temperature range of columnar phase, identified as Col_r* by X-ray, in which molecular cores form a rectangular lattice ($P2_1$) in the plane normal to the columnar axis. These mesophases vitrify. The glass transitions have been calorimetrically found at around –70 °C. On cooling from the isotropic liquid the mesophases display dendritic textures. When the mesophases are allowed to form at a very slow rate or annealed at 100 °C for several hours, a texture with Maltese crosses often appears. The extinction brushes are tilted at high angle with respect to the direction of the crossed polarizers, indicating a high tilt angle of the molecules with respect to the columnar axis. Circular dichroism studies have allowed deducing the existence of a helical order within the column (see Fig. 6.10). Only

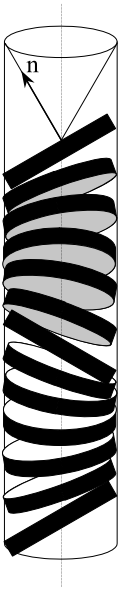

Fig. 6.10. Molecular orientation in a column showing the helical structure (Reproduced from [22], copyright 1998 Taylor & Francis)

a non-parallel arrangement of the molecules within the column, together with the rotation of the molecular director along the column axis describing a helix, can account for the appearance of a positive exciton coupling corresponding to the $\pi - \pi^*$ transition. Col_r^* phases are electro-optically switchable but we could not measure the spontaneous polarization using the triangular wave method, probably because of the high value of the conductivity of the compounds at high temperatures and the high fields needed to invert the polarization at low temperatures. In these compounds the origin of the spontaneous polarization lies in the tilt induced molecular dipole moment within the columnar phase. Tilt, promoted by repulsion between tails and attraction between rigid cores, mainly affects the cores, whereas the peripheral tails maintain an orientation almost perpendicular to the column axis. In this conformation a deflection point appears in the molecule. If the stereogenic center is located at the position where the tails and core deflects, dipole moments contained at these sites tend to align along a preferred direction, and hence a net polarization perpendicular to the column axis appears. Only when tilting is directed either in the same direction in all the columns or alternates in such a way that columnar polarizations do not cancel out can a macroscopic polarization be obtained that can be switched by an electric field. These conditions are fulfilled by rectangular phases with C_2 and $P2_1$ symmetries. For our compounds the symmetry was $P2_1$ (see Fig. 6.11 , where the ellipses mean the tilted discs).

Dielectric spectra are quite similar for the three compounds (hereafter, unless necessary, we only mention the VO compound). Figures 6.12 and 6.13

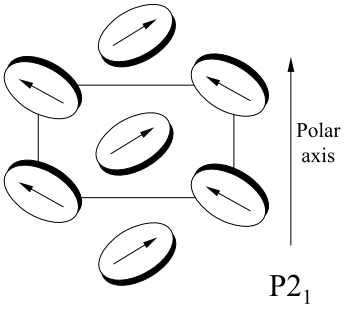

Fig. 6.11. Rectangular structure of the Col$_r$* phase. The ellipses mean the tilted discs

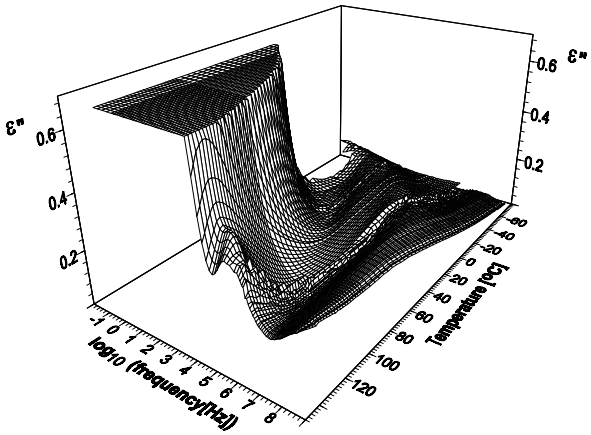

Fig. 6.12. Three-dimensional plot of the dielectric losses, ε'', vs. temperature and frequency for compound **3**

are three-dimensional plots of the imaginary and real parts of the dielectric permittivity, respectively, versus temperature and frequency (note the different frequency axis). In the isotropic phase (Fig. 6.12) two clear peaks can be observed. Upon cooling into the Col$_r$*, the one with the highest frequency is clearly observed; its frequency is quickly reduced when decreasing the temperature. In this plot the high temperature and low frequency part in the Col$_r$* phase is not so clear due to the important value of the dc conductivity contribution. Figure 6.13 (real component) can help us to better understand the spectrum. The low frequency relaxation in the isotropic phase is still present in the columnar phase (around $10^{4.5}$ Hz) and another relaxation appears. Note the increase in the low frequency side of the real component at the I-Col$_r$* phase transition. Now let us analyze more carefully these relaxations.

Figure 6.14 is a plot of the complex dielectric permittivity versus the logarithm of the frequency in the isotropic phase. The two relaxations above mentioned are clearly seen. One at frequencies around 10^6 Hz (hereafter called mode l) and the other around 10^9 Hz (hereafter called mode h). In the Col$_r$* phase, together with modes h and l, a new mode (hereafter called columnar

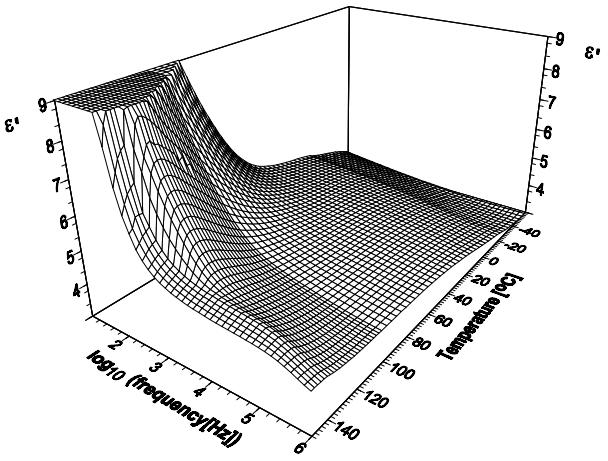

Fig. 6.13. Three-dimensional plot of the real part of the dielectric permittivity, ε', vs. temperature and frequency for compound **3**

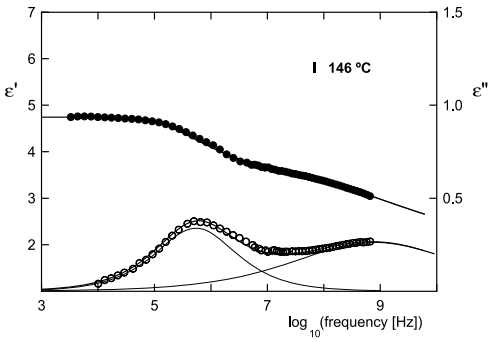

Fig. 6.14. Complex permittivity vs. frequency in the isotropic phase (compound **3**): ε' (•), ε'' (○). The *solid lines* are fit curves using (6.1) and (6.2): (from high to low frequency) mode h and mode l (Reproduced from [22], copyright 1998 Taylor & Francis)

mode) appears (see Fig. 6.15). To find the strengths, frequencies and activation energies of every process, the experimental data were fitted for each phase to (6.1) and (6.2). In the two last figures we have subtracted from the experimental points the spurious contributions due to the electrode polarization and also the dc conductivity contribution. The continuous lines are fits to (6.1) and (6.2). In the isotropic phase, modes h and l are almost Cole–Cole (β =1) with $\alpha = 0.5$ (0.6 for Pd compound and 0.7 for Cu compound) for mode h and $\alpha = 0.9$ for mode l. In the columnar phase the spectra are more complex. Modes h and l broaden continuously with decreasing temperature. For example at –40 °C mode h has $\alpha = 0.3$. Moreover, the appearance of a mode with a much larger strength makes the analysis, above all of mode l, very

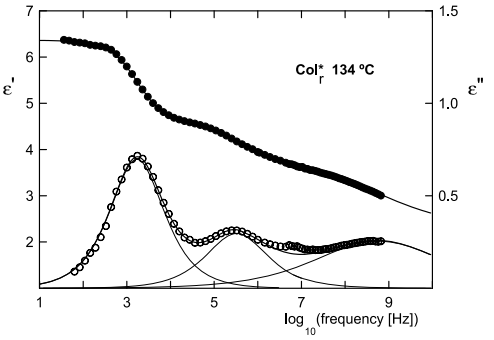

Fig. 6.15. Complex permittivity vs. frequency in the Col$_r$* phase (compound **3**): ε' (•), ε'' (○). The *solid lines* are fit curves using (6.1) and (6.2): (from high to low frequency) mode h, mode l and columnar mode (Reproduced from [22], copyright 1998 Taylor & Francis)

difficult. However, due to the different thermal activation we can confirm that at –80 °C mode h is still active and at –20 °C mode l. Figures 6.16 and 6.17 show, respectively, the temperature dependence of the dielectric strength and the frequency of the three modes. The analysis of modes h and l for the Pd and Cu compounds is more difficult than for the VO compound due to their smaller strength and also to the larger value for the columnar mode (3 for VO, 4 for Pd and 6 for Cu).

The frequency of mode h falls continuously on cooling and does not show any jump at the I-Col$_r$* transition. In the isotropic phase and in the high temperature side of the Col$_r$*, it follows the Arrhenius law being the activation energy 52 kJ mol^{-1}. However, for lower temperatures the process becomes more activated with temperature and shows a non-Arrhenius behavior. This temperature dependence can be well described by the empirical

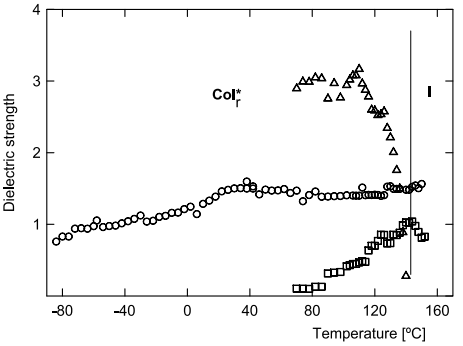

Fig. 6.16. Dielectric strength of the different modes vs. temperature (compound **3**): (○) mode h, (•) mode l, (△) columnar mode (Reproduced from [22], copyright 1998 Taylor & Francis)

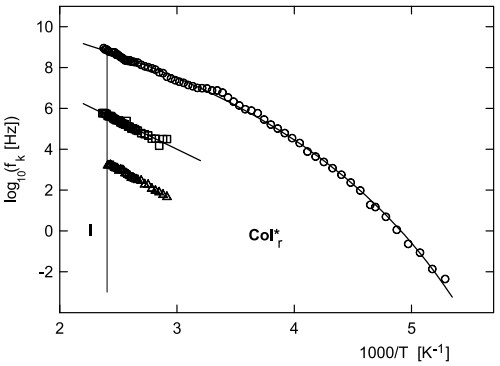

Fig. 6.17. Arrhenius plot of the frequency of the different modes vs. temperature (compound **3**): (○) mode h, (●) mode l, (△) columnar mode. The *solid lines* are fit curves to the VFT law (mode h) or to the Arrhenius law (mode l) (Reproduced from [22], copyright 1998 Taylor & Francis)

Vogel–Fulcher–Tammann (VFT) law, $f_h = f_{h\infty} \exp\{(-A/(T - T_0)\}$, during more than eleven decades of frequency as it is shown by the continuous line in Fig. 6.5. In this expression T_0 is the so-called Vogel or ideal glass transition temperature (in general between 30 and 50 K below the calorimetric glass transition T_g) and A is a constant. In our case, T_0= 121 K, $A = 2235$ K and $f_{h\infty} = 6{\times}10^{11}$ Hz (see Sect. 5.5.3 in this book for a deeper discussion about this law).

The frequency of mode l does not show any jump at the I-Col$_r$* phase transition and follows the Arrhenius law with activation energy of 56 kJ mol^{-1} in both phases. Note that we could obtain this frequency only till 65 °C, which opens the possibility of non-Arrhenius behavior for lower temperatures.

The frequency of the columnar mode decreases with temperature, being around 10^3 Hz near the I-Col$_r$* transition. We could only characterize this mode properly till 60 °C because at this temperature the conductivity is still high and the relaxation frequency low.

Now let us discuss the possible origin of each mode. Modes h and l are present in the I and Col$_r$* phases, then they are not directly related to the columnar structure. Dielectric studies, both in chiral [28, 29] and achiral [30, 31] discotics, forming columnar non-tilted mesophases, show also these two modes. They assigned mode 1 to a motion of the discs around the column axis (that coincides with the molecular director for non-tilted columns). We think that the same explanation is valid in our case: a rotation around the molecular director (normal to the plane of the discs). In the Col$_r$* phase there is a tilt induced dipole moment in the plane of the discs, perpendicular to the tilt direction and to the column axis, so a rotation around the disc axis should contribute to the dielectric permittivity. The molecules have a symmetric structure, similar to one of the cases in [29, 30]; then they do not necessarily have a net molecular dipole moment in the plane of the molecule

in the isotropic phase. Hence, the conformation of the carbonyl groups must be disordered leading to a mean square dipole moment in the plane of the molecule. Another possibility to explain the presence of mode l in the isotropic phase is the existence of a local order, similar to that present in the columnar phase, producing a dipole moment lying in the disc plane in the same manner as in the Col_r* phase. This last explanation will justify the increase of the dielectric strength in the isotropic phase on cooling (see Fig. 6.16). We think that mode h should be related to motions of the side groups of the discs. The side groups contain an ester linkage and a branch, which provide an important degree of rigidity for the chain from the point of attachment to the phenyl ring to the oxygen atoms bonded to the stereogenic carbon. These motions should be small angle (librations). They are observed in the dielectric response over a wide range of temperature. It becomes broader and broader on cooling and shows non-Arrhenius behavior, typical of a α process related to a glass transition. Moreover, in other cases, such lateral motions are explained as β relaxations also actives in the glassy state [28–30, 32, 33]. In our case the slowing down of the relaxation could be explained due to the proximity of part of the side group to the rigid part of the disc.

The so-called columnar mode was observed neither in achiral nor in chiral non-tilted columnar mesophases by other authors [28–30, 32, 33]. We think that is related to the chiral and tilted character of the Col_r* phase. It appears at the I-Col_r* phase transition, its strength is larger and its frequency smaller than those of the other modes. These facts suggest that it could be similar to the Goldstone mode in SmC* phase. The Goldstone mode is a collective mode related to the azimuthal fluctuations of the director around the helical axis. We think that in our case the same explanation is possible if a helical structure, consisting in tilted molecules whose tilt direction rotates along the columnar axis, is present (see Fig. 6.10). The columnar mode should be related to azimuthal fluctuations of the director around the helix axis that coincides with the columnar axis. The higher strength of this mode is due to the direct coupling of the macroscopic polarization and the field. As we have above mentioned the presence of a helix is also confirmed by circular dichroism studies [21, 23]. The strength of the Goldstone mode in SmC* phases can be reduced by applying a bias field. This effect is due to the unwinding of the helix. We could not study the effect of a bias field over the strength of this mode because our low frequency set-up can only supply 10 V and the cells are thick (50 μm).

6.1.4 Summary and conclusions

In the design of new molecular structures to show known properties of liquid crystals, such as ferroelectricity, metallomesogens have appeared as a promising alternative to organic mesogens. The great variety of molecular shapes that can be achieved allows analyzing many theoretical and experimental aspects mostly introduce to explain phenomena in the most conventional

rod-like organic liquid crystals. Our brick-like complexes show ferroelectric properties in the SmC* phase and their dielectric response shows some peculiarities related to their biaxial molecular shape. In the specific case of columnar liquid crystals, our metal complexes of organic ligands show also ferroelectric switching. This response is only possible because a polar organization can be achieved because of the nature of stacking of the disc-like complexes. The dielectric studies show that one of the modes in the Col_r* phase could be a Goldstone-like mode, similar to that present in SmC* phases, whose existence needs a helical arrangement. This helix was confirmed by circular dichroism studies.

Acknowledgments

This work was supported by the Spanish Government, Project No. CICYT. MAT 2000-1293-C02- (01 and 02) and the Universidad del País Vasco, Projects No. UPV060.310-G16/98 and No. 9/UPV00060.310-13562/2001.

References

1. J.L. Serrano (ed.): *Metallomesogenes. Synthesis, Properties and Applications* (VCH, Weinheim 1996)
2. M. Marcos, J.L. Serrano, T. Sierra, M.J. Giménez: Angew. Chem. Int. Ed. Eng. **31**, 1471 (1992)
3. M.A. Athanassopoulou, S. Hiller, L.A. Beresnev, Y.G. Galyametdinov, M. Schweissguth, W. Haase: Mol. Cryst. Liq. Cryst. **261**, 29 (1995)
4. M. Ghedini, D. Pucci, N. Scaramuzza, L. Komitov, S.T. Lagerwall: Adv. Mater. **7**, 659 (1995)
5. P. Espinet, J. Etxebarria, M. Marcos, J. Pérez, A. Remón, J.L. Serrano: Angew. Chem. Int. Ed. Eng. **28**, 1065 (1989)
6. J. Baena, P. Espinet, M.B. Ros, J.L. Serrano, A. Ezcurra: Angew. Chem. Int. Ed. Eng. **32**, 1203 (1993)
7. P.J. Alonso, M. Marcos, V.M. Orera, M.L. Sanjuan, J.L. Serrano: Liq. Cryst. **13**, 585 (1993)
8. J.L. Serrano, P. Romero, M. Marcos, P.J. Alonso: J. Chem. Soc. Chem. Commun. 859 (1990)
9. M.A. Pérez Jubindo, M.R. de la Fuente, M. Marcos: Adv. Mater. **6**, 941 (1994)
10. R. Iglesias, M. Marcos, J.L. Serrano, T. Sierra, M.A. Pérez Jubindo: Chem. Mat. **8**, 2611 (1996)
11. S. Merino, F. de Daran, M.R. de la Fuente, M.A. Pérez Jubindo, R. Iglesias, M. Marcos: Adv. Mat. **8**, 644 (1996)
12. C. Destrade, P. Foucher, H. Gasparoux, N.H. Tinh, A.M. Levelut, J. Malthete: Mol. Cryst. Liq. Cryst. **10**, 759 (1984)
13. J. Prost: *Symmetries and Broken Symmetries. Comptes Rendus du Colloque Pierre Curie,* ed. by N. Boccara (Inst. Dev. Sci. Educ. Technol., Paris 1982)
14. H. Bock, W. Helfrich: Liq. Cryst. **12**, 697 (1992)
15. H. Bock, W. Helfrich: Liq. Cryst. **18**, 387 (1995)

16. H. Bock, W. Helfrich: Liq. Cryst. **18**, 707 (1995)
17. G. Heppke, D. Krüerke, M. Müller, H. Bock: Ferroelectrics **179**, 203 (1996)
18. G. Scheroswsky, X.H. Chem: J. Mater. Chem. **5**, 417 (1995)
19. G. Scheroswsky, X.H. Chem: Liq. Cryst. **17**, 803 (1994)
20. A. Jákli, M. Müller, D. Krüerke, G. Heppke: Liq. Cryst. **24**, 467 (1998)
21. J. Barberá, R. Iglesias, J.L. Serrano, T. Sierra, M.R. de la Fuente, B. Palacios, M.A. Pérez Jubindo: J. Am. Chem. Soc. **120**, 2908 (1998)
22. B. Palacios, M.R. de la Fuente, M.A. Pérez Jubindo, R. Iglesias, J.L. Serrano, T. Sierra: Liq. Cryst. **4**, 481 (1998)
23. J.L. Serrano, T. Sierra: Chem. Eur. J. **6**, 759 (2000)
24. M.R. de la Fuente, A. Ezcurra, M.A. Pérez Jubindo, J. Zubia: Liq. Cryst. **7**, 51 (1990)
25. E. Campillos, M. Marcos, J.L. Serrano, J. Barberá, P.J. Alonso, J.I. Martínez: Chem. Mater. **5**, 1525 (1993)
26. J.I. Martínez: Resonancia paramagnética electrónica de metalomesógenos de cobre y vanadio. Aspectos dinámicos y estructurales. PhD Thesis, University of Zaragoza, Zaragoza 1994
27. B. Kutnjak-Urbanc, B. Zeks: Liq. Cryst. **18**, 483 (1995)
28. S.U. Vallerien, M. Werth, F. Kremer, W. Spiess: Liq. Cryst. **8**, 889 (1990)
29. M. Werth, S.U. Vallerien, W. Spiess: Liq. Cryst. **10**, 759 (1991)
30. H. Groothues, F. Kremer, D. Collar, C. Lillya: Liq. Cryst. **18**, 117 (1995)
31. D. Kilian, D. Knawby, M.A. Athanassopoulou, S.T. Trzaska, T.M. Swager, S. Wrobel, W. Haase: Liq. Cryst. **27**, 509 (2000)
32. U. Dahn, C. Erdelen, H. Ringsdorf, R. Festag, J.H. Wendorff, P.A. Heiney, N.C. Maliszewskyj: Liq. Cryst. **6**, 759 (1995)
33. B. Glüsen, W. Heitz, A. Kettner, J.H. Wendorff: Liq. Cryst. **20**, 627 (1996)

6.2 Relaxation processes in columnar phases of vanadyl complexes

W. Haase, M.A. Athanassopoulou, D. Kilian, T.M. Swager, and S. Wróbel

6.2.1 Introduction

Discotic liquid crystals were discovered in 1977 by Chandrasekhar et al. [1], but little attention was paid to their physical properties until the late 1980s. Markovitsi et al. [2] described the one-dimensional energy migration in a columnar phase based on fluorescence experiments. Since then several fluorescence experiments were outlined [3] including those directed at OLED applications [4]. Electrical conductivity and photoconductivity were measured for different compounds [3, 5]. Moreover, ferroelectric switching in columnar phases [6] and lyomesophases [7] were described.

Within this contribution we will focus on the physical properties of columnar metallomesogens. Columnar phases of some metallomesogens show large electrical conductivity of the order of semiconductors [3]. Recently strong photoluminescence and photoconductivity were reported for rare-earth phthalocyanins [8]. In comparison, not much attention has been paid in order to investigate the magnetic properties of columnar arrangements in paramagnetic

metallomesogens. The columnar liquid crystalline state of Mn(III)-TCNE system [9] is one of the examples investigated. Here a ferrimagnetic chain -Mn(III)-TCNE-Mn(III)- with the spins $S_{\mathrm{Mn}} = 2$, $S_{\mathrm{TCNE}} = 1/2$ exists. For the columnar structure of a copper-complex, Eastman et al. [10] basing on ESR investigations came up with a model of an antiferromagnetic coupling within the chain. Dielectric and electrooptic studies on columnar mesophases of complex vanadyl compounds were presented in [11] by de la Fuente et al. The usefulness of dielectric relaxation spectroscopy in order to characterize chiral and nonchiral metallomesogens has been already demonstrated for nematics and for smectics [11, 12].

Swager and coworkers presented liquid crystalline materials containing vanadyloxo-linear chains forming one-dimensional polymers, in solid phases and the low temperature columnar mesophases [13–16]. A model of V=O· − ·V=O chain in the solid state is presented schematically in Fig. 6.18.

In addition to the evidence based on the crystal structure data, the polymer structure has been proved using the frequency of the V=O stretching modes that vary from 854 to 868 cm^{-1}, depending on the kind of phase. In the isotropic state the polar oligomers disassemble showing higher wave number V=O stretching frequencies between 992 and 994 cm^{-1}, indicating the presence of monomers. It should be stressed that the vanadyl complexes described by Swager et al. and those studied in this work do not exhibit an ideal disk-like shape of molecules which is generally required for columnar liquid crystalline phases. According to Swager's model [13–16] the columnar phases of these substances have short range intermolecular correlations along the column wherein neighbor pairs assemble forming disc-like entities.

Recently DSC, polarizing microscopy, X-ray diffraction and dielectric studies [17–20] were described for three of these compounds [13–16]. The molecular structures of three samples discussed in this contribution are shown in Fig. 6.19.

In this contribution we shall review our studies on vanadyl complexes and discuss X-ray data in more detail. DC magnetic susceptibility measurements [18], outlined for some compounds shown in Fig. 6.19 , will be presented. For the compounds **2**(14) and **3**(12) only the magnetic data are presented in this contribution.

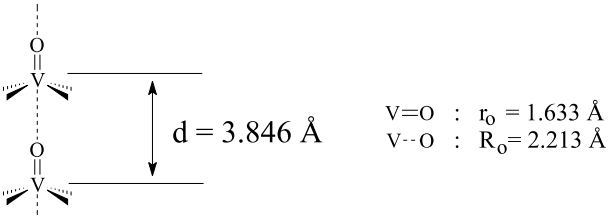

Fig. 6.18. V=O· − ·V=O chain structure of vanadyl complexes in the solid state. r_{o} is the length of the V=O bond and R_{o} is the length of the V···O bond

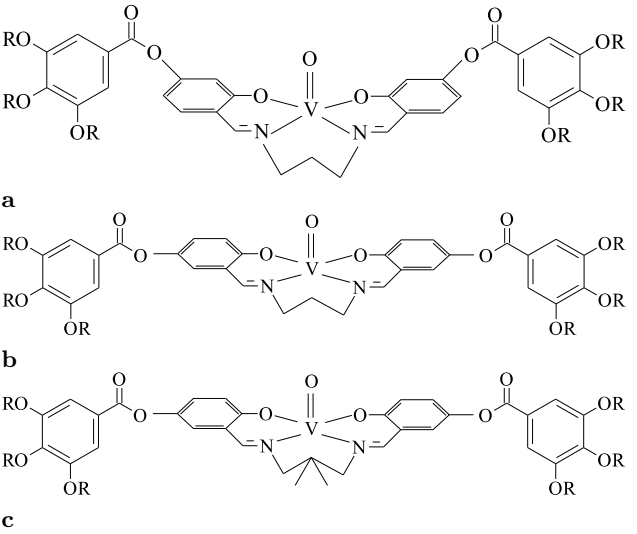

Fig. 6.19. Molecular structure of compounds investigated: **(a)** **1**(10) - $R = C_{10}H_{21}$, **1**(12) - $R = C_{12}H_{25}$ and **1**(14) - $R = C_{14}H_{29}$; **(b)** **2**(14) - $R = C_{14}H_{29}$; **(c)** **3**(12) - $R = C_{12}H_{25}$; there are two methyl groups attached to the central C-atom of the chelate ring

6.2.2 Thermoanalytical, structural and magnetic investigations

6.2.2.1 DSC and polarizing optical microscopy

The studies of phase transitions were performed using a Perkin Elmer DSC 2 with a home-made interface for data acquisition. A Leitz Orthoplan Pol microscope, equipped with video system (Sony video camera, video printer, video tape recorder and monitor) and the Mettler hot stage FP 82 with FP 80 controller, was used. The phase transition data shown in Table 6.2 for the compounds **1**(10), **1**(12), and **1**(14) were obtained by DSC calorimetry on heating the samples.

All three samples show a sequence of up to three columnar mesophases and the so-called ODIC phase (orientationally disordered crystal) at lower

Table 6.2. Transition temperatures in [°C] and phases obtained on heating

Complex	Transition temperatures and phases
1(10)	**Cr** 85 **ODIC** 120 **Col**$_{ro}$ 153 **Col**$_{rd}$ 172 **Col** $_{hd}$ 181 Is
1(12)	**Cr**$_1$ 48.5 **Cr**$_2$ 68 **ODIC** 97.1 **Col**$_{ro}$ 140.9 **Col**$_{rd}$ 157.6 **Col**$_{hd}$ 182.2 **Is**
1(14)	**Cr**$_1$ 68 **Cr**$_2$ 82 **ODIC** 89.6 **Col**$_{ro}$ 134.9 **Col**$_{hd}$ 187.9 Is

temperatures and one or two solid phases. The DCS traces of all the compounds investigated are presented in Fig. 6.20.

Upon increasing the chain length the clearing point increases slightly. The Col_{hd} phase of **1**(10) is rather narrow compared to those of **1**(12) and **1**(14). The transition Col_{ro} to Col_{rd} for **1**(10) and **1**(12) can be observed upon heating under the polarizing microscope at ca. 7 degrees below the DSC peak maximum. The transition Col_{rd} - Col_{hd} found for **1**(10) is rather sharp. The phase transition, which starts at lower temperatures, could be interpreted as a pretransition effect accompanying the transformation between the ordered and disordered rectangular phase.

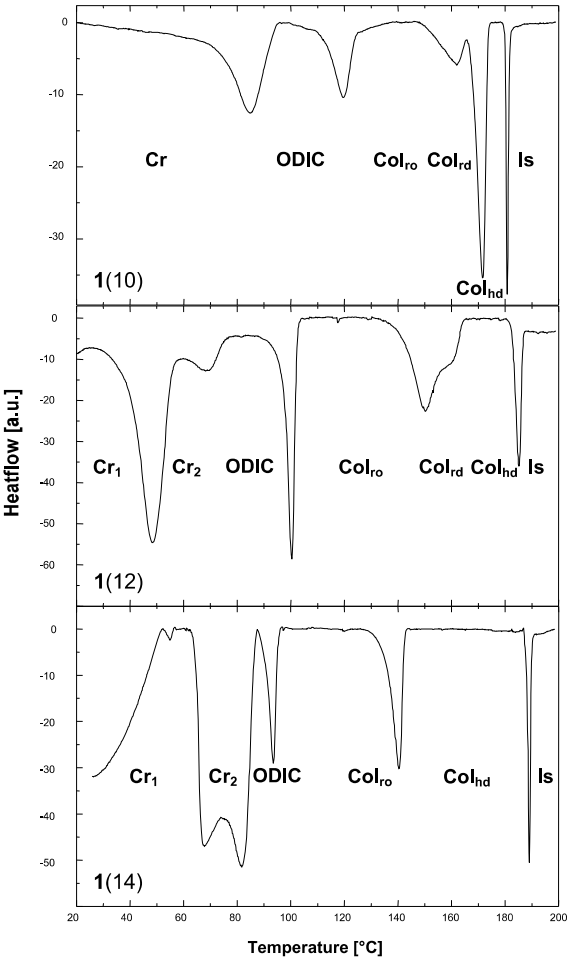

Fig. 6.20. DSC thermograms obtained for three vanadyl complexes of type **1**

6.2.2.2 X-ray diffractometry

The X-ray measurements were performed on a focusing horizontal two-circle diffractometer (Stoe Stadi 2). The oven used was home made. The CuK_α radiation was focused on a curved Ge (110) monochromator. A linear position sensitive detector (Stoe Mini PSD) allowed for fast scanning of the diffraction pattern. All three compounds **1**(10), **1**(12) and **1**(14) were investigated at several temperatures. The aim of such studies was to characterize the mesophases in order to obtain related structural parameters. The X-ray data of **1**(12) and **1**(14) were presented in detail in [18, 19]. Here some of the data obtained for **1**(10) (Fig. 6.21) are reported.

The X-ray diffraction data displays the following characteristic features:

- At $2\theta \sim 24°$ there is an intense and broad reflex indicating that the V=O· – ·V=O distance is ∼ 3.7–3.8 Å (see Table 6.3);
- For all temperatures a broad peak at 4.6 Å is visible indicating the molten alkyl chains;
- Table 6.3 shows for the Col_{ro} phase of **1**(10) a comparison of the computed (comp.) and experimental (exp.) *d*-values as well as the suggested indexing. As one can see there are only (hk0)-reflexes and the (001)-reflex present.

In Table 6.4 the lattice parameters for the Col_{ro} and the Col_{hd} phases of **1**(10), **1**(12) and **1**(14) are presented.

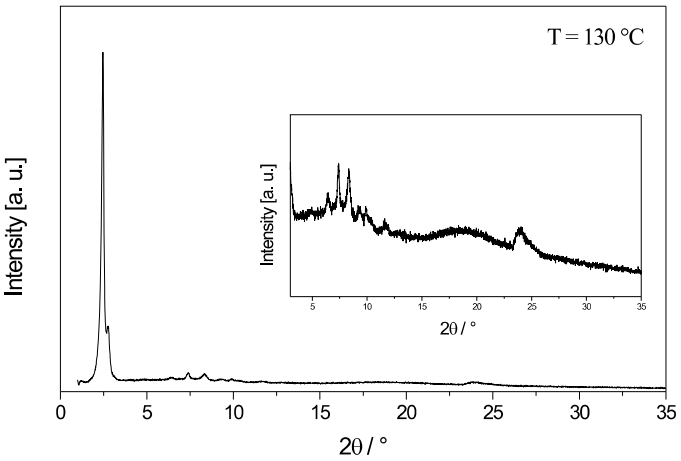

Fig. 6.21. X-ray diffraction pattern obtained for **1**(10) at 130 °C representing the Col_{ro} phase

Table 6.3. $d_{exp.}$, $d_{comp.}$ and reflex indices of Col_{ro} - phase for **1**(10) at $T = 130\,^{\circ}C$

$2\theta/^{\circ}$ **exp.**	$2\theta/^{\circ}$ **comp.**	d/Å **exp.**	d/Å **comp.**	(hkl)	**Results**
2.471	2.471	35.73	35.73	1 1 0	a: 63.50 Å
2.780	2.780	31.75	31.75	2 0 0	b: 43.22 Å
4.090	4.086	21.58	21.61	0 2 0	c : 3.71 Å
4.920	4.942	17.94	17.86	2 2 0	V: 10181 $Å^3$
6.450	6.286	13.70	14.05	1 3 0	$\rho = 1.01 g/cm^3$
7.400	7.417	11.93	11.91	3 3 0	Z = 4
8.350	8.347	10.58	10.58	6 0 0	
9.330	9.297	9.47	9.50	6 2 0	
9.900	9.894	8.93	8.93	4 4 0	
11.630	11.648	7.60	7.68	7 3 0	
		4.6 (diffuse	reflex)		
23.960	23.960	3.71	3.71	0 0 1	

Table 6.4. Lattice parameters for Col_{ro} and Col_{hd}-phases of **1**(10), **1**(12) and **1**(14)

Compound	Col_{ro}-phase			Col_{hd}-phase
1(10)	$a = 63.5$ Å	$b = 43.2$ Å	$c = 3.7$ Å	$a = 35.4$ Å
1(12)	60.3	49.5	3.7	36.5
1(14)	63.9	51.8	3.7	37.2

6.2.2.3 Magnetic properties

The magnetic susceptibilties were measured by using two Faraday balance set-ups [21, 22]: one of them could cover the data from 4 K to room temperature and the other one from room temperature up to ca. 460 K, where the samples start to decompose. The high temperature set-up uses home-made electrical heating equipment [22]. The temperature range covered spreads over the entire liquid crystalline range. The susceptibility data obtained and the derived magnetic moment are presented in Fig. 6.22.

The magnetic moment, for all three compounds **1**(10), **2**(14), **3**(12), starting from about 460 K down to ca. 75 K, is constant and equals 1.8 μ_B which is close to the spin only value (1.73 μ_B for $S = 1/2$ system) of one unpaired electron. At 75 K down to 5.6 K the magnetic moment increases upon decreasing the temperature indicating clearly a ferromagnetic coupling within the one-dimensional chains. In order to fit the data to a theoretical equation

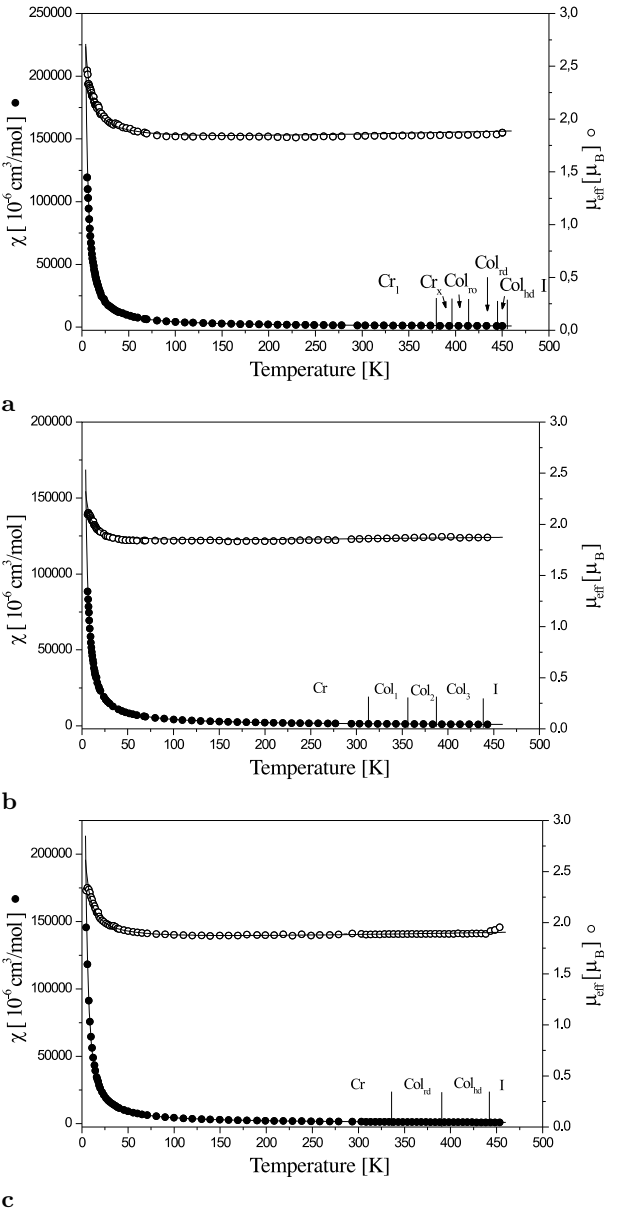

Fig. 6.22. Magnetic susceptibilities χ and effective magnetic moments μ_{eff} vs. temperature for compounds: **(a) 1**(10), **(b) 2**(14) and **(c) 3**(12) (see Fig. 6.19). *Solid lines* were obtained by fitting (1) to the experimental points

Table 6.5. Magnetic parameters obtained due to fitting procedure

Compound	g	$J(\mathrm{cm}^{-1})$	$x_p(\%)$
1(10)	2.04	4.6(5)	2.7
2(14)	2.04	3.6(9)	2.9
3(12)	2.04	2.5(9)	2.8

for ferromagnetically coupled linear chains the model given by Baker et al. [23] was used. Only the exchange interaction inside the chain between neighbored spins is taken into account. Beside the chain structure V=O· − ·V=O, the uncoupled VO-centers were also taken into consideration using (6.4),

$$\chi = (1 - x_p)\chi^{chain} + x_p C/T + N_\alpha. \tag{6.4}$$

Here x_p is the percentage of uncoupled VO-units, C is the Curie constant and N_α is the temperature independent paramagnetism (here $100 \cdot 10^{-6}$ cm^3/mole was taken). The Curie constant holds:

$$C = \frac{N_L g^2 \mu_B^2}{3k_B} S(S+1), \tag{6.5}$$

where N_L is Avogadro's number, g is Lande's splitting factor, k_B is Boltzmann's constant, S is the spin quantum number, here $S = 1/2$.

Fitting (6.4) to the experimental data and using the Hamiltonian:

$$\hat{H} = -2J \sum_{i=1}^{\infty} (\hat{S}_i \cdot \hat{S}_{i+1}) \tag{6.6}$$

one can receive the data presented in Table 6.5 (g-values are always fixed).

The results presented in Table 6.5 are very interesting. At first they show there is a weak ferromagnetic coupling along the 1d-chain. Moreover, because for three different compounds the magnetic behavior is comparable, one can conclude there is really a one-dimensional chain at least in the solid and highly ordered discotic phases. Hence this can be considered as additional structural evidence for the polymer structure.

6.2.3 Dielectric and electrooptical investigation

6.2.3.1 Experimental

Dielectric spectroscopy

For dielectric studies the sample capacitors were prepared from two plane parallel gold electrodes deposited on quartz glass plates providing small surface resistance ($< 5\,\Omega$) with an area of 7×13 mm^2 separated by 23 µm mica

spacers to obtain a stable capillary gap between the gold electrodes at high temperatures. Practically no deviation from linear behavior of the capacitance of empty cell over a large temperature range has been detected. As a reference substance for calibration of the cells toluene (purified for spectroscopy) was used and the cell calibration was done for it between 20 and 50 °C.

To fill the sample capacitors a portion of the substance was first put on a microscope slide and slowly melted under vacuum into the isotropic phase. Upon reaching the clearing point the substance generally expelled entrapped gases and residual solvents from synthesis and purification. These conditions were maintained for one hour and then the substance was cooled to room temperature under vacuum. The recrystallized droplet was then cut into stripes and transferred onto the slot of the sample capacitor which was vertically mounted in the vacuum hot stage.

The capacitor was filled with the sample under vacuum by a combination of capillary action flow and gravity at a temperature slightly above the clearing point of the substance studied. The filling process was monitored by an HP 4192A self-balancing impedance analyzer set to a frequency of 100 kHz. Upon saturation of the dielectric permittivity, the sample was slowly cooled under vacuum to room temperature. The filling was accomplished within two hours. It appeared from these procedures that the sample is stable at ambient atmosphere as long as the temperature is kept well below the clearing point. It was also apparent that after keeping the substances at high temperatures even under vacuum for a very long time, i.e. from a few days to weeks, some signs of degradation as indicated by the color and texture changes occurred.

Frequency domain dielectric spectroscopy (FDDS) has been applied to study the dielectric spectra of the three vanadyl complexes **1**(10), **1**(12) and **1**(14) over the frequency range from 10 mHz to 13 MHz. The computer controlled apparatus consists of a HP4192A impedance analyzer and a Schlumberger Solartron 1250 FRA in conjunction with a self-constructed amplifier based on the principle of the so-called *Chelsea Dielectric Interface* [17, 24] and a EUROTHERM 818 controller. Those systems allow us to do dielectric measurements between room temperature and 200 °C. The dielectric spectra were measured over the frequency range from 10 Hz to 10 MHz with 15 experimental points per decade.

Electrooptical measurements

The Leitz Wetzlar Orthoplan polarizing optical microscope equipped with a Mettler FP 82 hot stage driven by a FP 80 central processor was used for electrooptical experiments. The voltage signal was applied to a thick EHC cell employing a HP 33120A waveform generator and the FLC Electronic F20A voltage amplifier. To measure the polarization currents, an HP54603B digital oscilloscope was attached. The oscilloscope recorded the voltage drop on a 100 kΩ resistor being in series with the EHC cell.

6.2.3.2 Results and discussion

Conductivity

In Fig. 6.23 the temperature dependence of the conductivity at 10 Hz for **1**(10) taken from [20] is presented.

Similar behavior was reported for **1**(12) and **1**(14) [19]. At lower temperatures the conductivity is rather low, namely 10^{-9} S/m, what agrees with properties of good insulators being of the order of 10^{-9} – 10^{-10} S/m. Within the ODIC phase the conductivity starts to increase with a small step at the phase transition ODIC-Col$_{ro}$. In the broad range of the Col$_{ro}$ phase the conductivity increases but at higher temperatures it behaves in a non-Arrhenius like fashion being more or less temperature independent. In the Col$_{hd}$ phase up to the isotropic phase the conductivity grows tremendously reaching values of 10^{-5} S/m thereby indicating semiconducting properties. As discussed for the X-ray data in [18], [19] and [20] the disordered phases do not show a strong wide angle peak at 3.8 Å indicating breaking of the V=O· – ·V=O units. It is interesting to note that at low temperatures the low frequency part of the dielectric spectrum (Fig. 6.24) show some similar trends as the conductivity. This behavior was explained as being due to ionic diffusion processes for our compounds [19, 20].

Dielectric relaxation processes

The characterization of the dielectric spectra is complicated. In Fig. 6.24 the dielectric permittivity $\varepsilon'(f,\ T)$ and $\tan\delta(f,\ T)$-data are presented for compound **1**(10). Note Figs. 6.24a and b show the dielectric data up to 200 °C, i.e. deeply into the isotropic phase (the clearing point for **1**(10) is 181 °C, see Table 6.2), whereas for **1**(14) the data in Fig. 6.25 are only presented until 175 °C (the clearing point for **1**(14) is 188 °C, see Table 6.5).

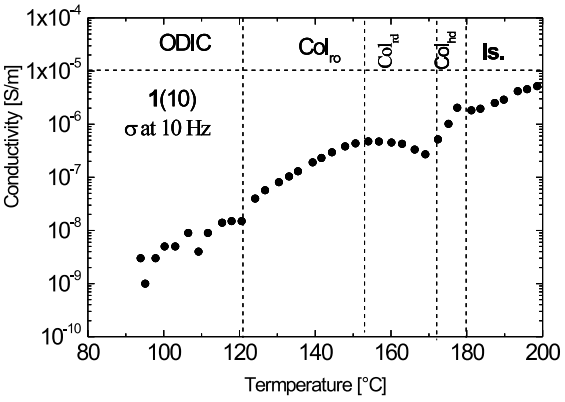

Fig. 6.23. Temperature dependence of conductivity for **1**(10)

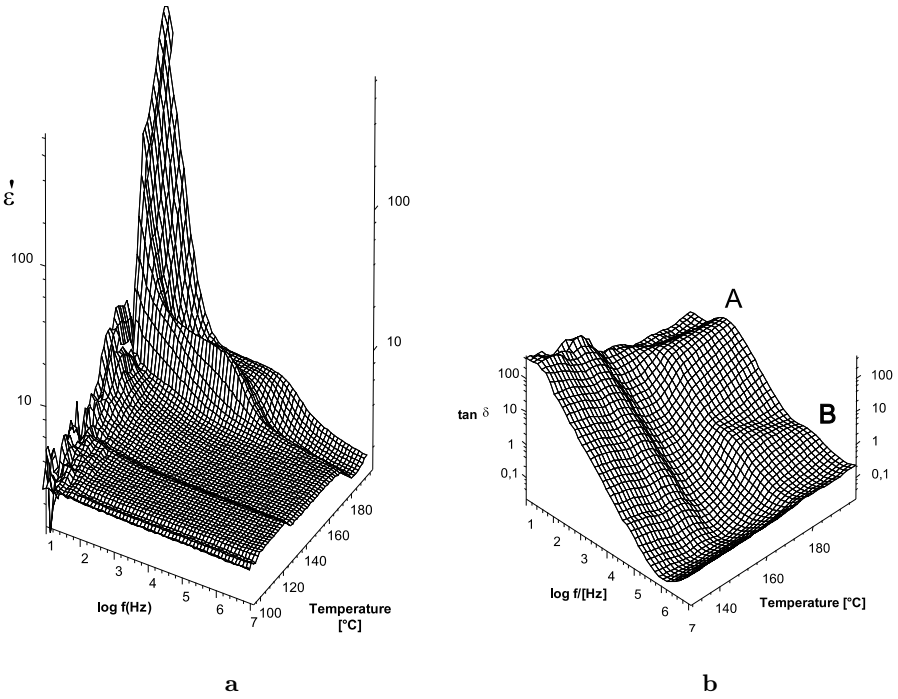

Fig. 6.24. **(a)** 3-D plot of the real part of dielectric permittivity $\varepsilon'(f,T)$ for **1**(10), **(b)** $\tan\delta(f,T)$ obtained for different columnar phases of **1**(10)

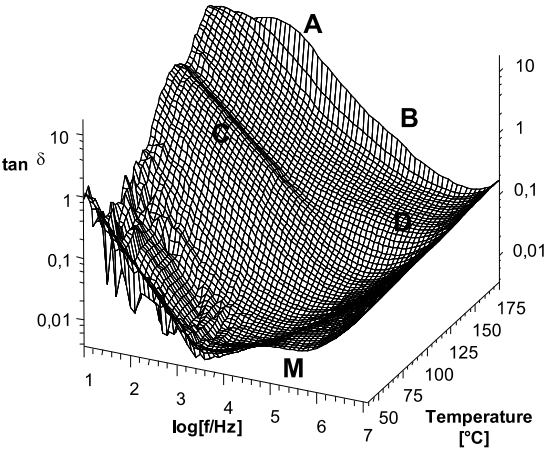

Fig. 6.25. 3-D plot of the $\tan\delta$ (f,T) dielectric spectra obtained for different columnar phases of **1**(14)

In the high temperature Col_{hd} phase and in the isotropic phase two processes can be separated. The broad process **A** (Figs. 6.24b and 6.25) is clearly evident in the data below 1 Hz taken by the Schlumberger-Solartron and HP4192A equipment (Fig. 6.26a). This process displays a high intensity and can be interpreted due to ionic interfacial polarization which was described in a similar fashion for other LC-materials by Biradar et al. [25]. The bias field dependence is shown in Fig. 6.26b.

The higher frequency process **B**, present at about 10 kHz and observable only in the Col_{rd} and isotropic phases, can be interpreted due to reorientation of the isolated monomers around their short axis after breaking the $V{=}O\cdot - \cdot V{=}O$ bond within the high temperature phases. In these phases the columns are now liquid-like with a great reorientational mobility of the molecules. It is surprising this process can only be seen inside the upper Col_{hd} and isotropic phases (Fig. 6.24b and 6.25) indicating clearly its molecular origin. Using an Arrhenius type plot (see Fig. 6.27) the activation energy for the process **B** was computed as 194 ± 5 kJ/mole that could be connected with the breaking of the oligomeric structures. This value is very high as compared with the energy barrier for most probably molecular reorientation around the long axis observed dielectrically even in hexatic phases of calamitic liquid crystals (see Sect. 4.2 and our former assignment in [19, 20]).

The other process **C** presented in Figs. 6.25 and 6.28 is typical for the Col_{ro} phase and shows up at about 100 Hz. One can assume this process is connected with relaxations of the chain structure inside the column.

Inside the liquid crystalline phase there exists a weakly activated process **D** (see Fig. 6.25) at about 100 kHz. This process exists in the Col_{rd} phase, where the columns are disordered but still some $V{=}O\cdot - \cdot V{=}O$ units exist. Therefore this weakly intense process is assigned as rotational relaxation of the molecules inside the columns.

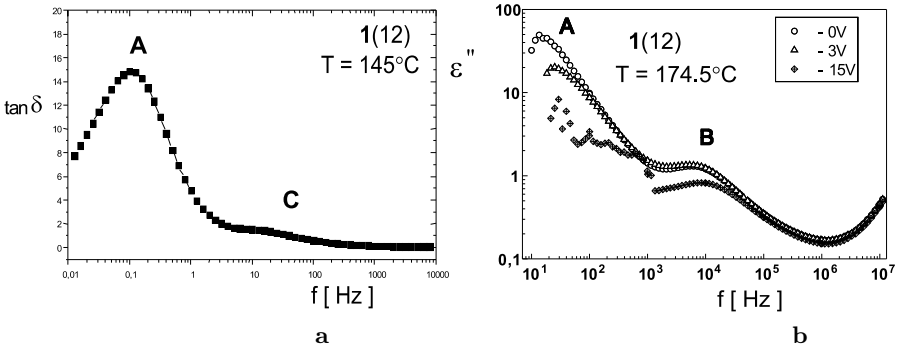

a **b**

Fig. 6.26. (a) Sub-hertz dielectric spectrum (relaxation modes **A** and **C**) acquired for **1**(10) using Schlumberger-Solartron equipment, **(b)** Bias field influence on the low frequency dielectric relaxation spectrum obtained for **1**(12)

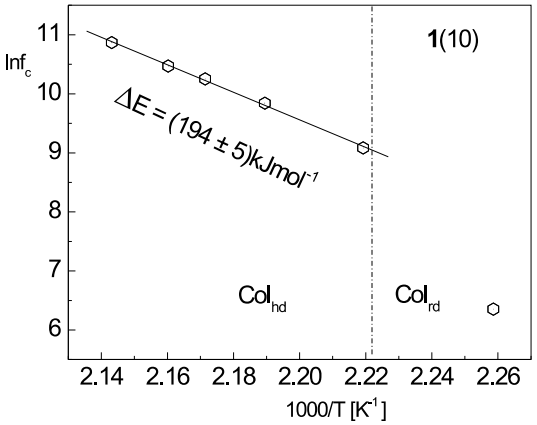

Fig. 6.27. Arrhenius plot for the **B**-process found for **1**(10)

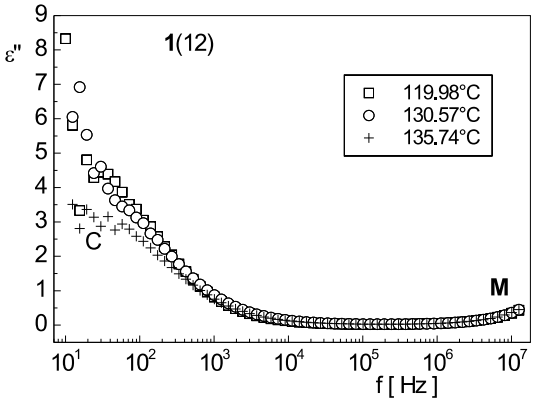

Fig. 6.28. Process **C** for **1**(12) due to chain relaxation

Finally there is the process **M** (see Fig. 6.25) which exists in the frequency range from 10 kHz to 1 MHz but only in the ODIC phase and in the crystalline Cr_2 and Cr_1 phases. This process is similar to the β-process showing WLF-behavior of glass forming materials like polymers. Therefore we assumed this process is due to glass forming behavior in the metastable phases Cr_1 and Cr_2.

In paper [20] the temperature hysteresis in dielectric permittivity is presented for **1**(10) indicating a change in the alignment from planar to homeotropic. This transition was even observed under the polarizing microscope on cooling from the Col_{hd} to Col_{rd} phase. As a consequence of the transition to the planar alignment the $\varepsilon_{\parallel}$ component was measured on cooling.

Reversal current and switching experiments

Investigations under polarizing microscope indicate that the dielectric response of the materials doesn't create a reorientation of the optic axis and no switching behavior could be detected within the temperature range of interest. But the lack of an electro-optical response was not necessarily unexpected and the absence of such an effect is not a basis for concluding that these systems are not ferroelectric, because an inversion of the polarization along the column's axis does not result in a change in the optic axis. On the other hand, reversal current measurements gave some very interesting results.

By applying a triangular waveform, voltage reversal current peaks could be detected as demonstrated in Fig. 6.29. By numerical integration of the reversal current peaks the apparent spontaneous polarization was calculated to 70 nC cm^{-2} at maximum [19].

Now the question arises does such behavior indicate ferroelectric switching? For a comparison we [26] measured reversal current spectra on a truly nonchiral compound, 4-n-pentyl-N-(4-pentyloxy-2-hydroxy-benzyliden)-aniline (in short SA5), in the smectic C, nematic and isotropic phases (Fig. 6.30).

At the same frequency of 2 Hz and layer thickness of 2 μm similar behavior for such achiral material as for **1**(10), **1**(12) and **1**(14) compounds was found. This result can be explained as being due to charge accumulation as in the case reported by Biradar et al. [25]. Considering the data we can not assume there is improper ferroelectricity like in ferroelectric liquid crystal, but we can not clearly exclude the possibility of improper ferroelectricity at all. Therefore we shall make a list of the points which prevent us from speaking of a truly liquid crystalline ferroelectric property:

1. As demonstrated in Figs. 6.29 and 6.30 the apparent spontaneous polarization can be seen for non-chiral compounds even in their isotropic phase provided the substances exhibit enhanced conductivity;

2. Reversal current peaks appear only at low frequencies of about 1 Hz and we believe this is due to the enhanced ionic conductivity within the columnar phase;

3. The temperature dependence of the apparent spontaneous polarization is atypical for FLCs because P_s goes down upon decreasing the temperature within the columnar mesophase;

4. There was no optical switching at all which could be observed between crossed polarizers (see our remarks above).

6.2.4 Summary

Optical microscopy, DSC and X-ray were used to characterize the three homologous compounds **1**(10), **1**(12), **1**(14) (Fig. 6.19). Up to two crystalline phases, one orientally disordered crystal (ODIC) phase and up to three columnar phases (Col_{ro}, Col_{rd}, Col_{hd}) as well the isotropic phase could be detected.

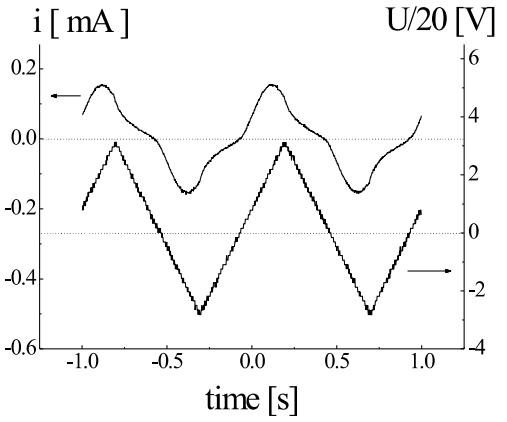

(a)

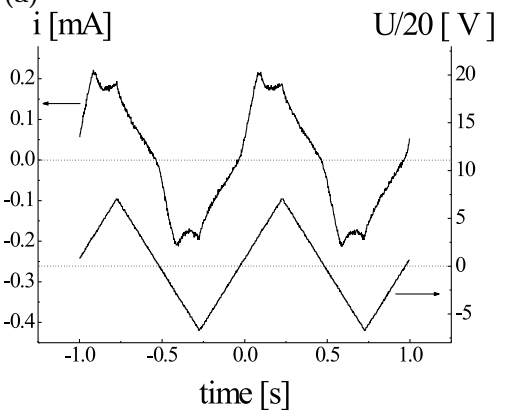

(b)

Fig. 6.29. Polarization reversal current peaks (*top curves*) and driving voltage (*bottom curves*) for **1**(10). Measurements done on heating up the sample at two the temperatures: **(a)** $T = 120\,^{\circ}\mathrm{C}$ and **(b)** $T = 130\,^{\circ}\mathrm{C}$; driving voltage frequency $f = 1$ Hz, amplitude ± 50 V, LC layer thickness 10 μm

Magnetic susceptibility measurements between 5.6 K and 460 K clearly showed the existence of ferromagnetic coupling in three different compounds **1**(10), **2**(14) and **3**(12) visible as increase of the magnetic moment (μ_{eff}) on going down to lower temperatures. The exchange coupling constant J was calculated for the compound **1**(10) to be 4.64(5) cm^{-1} and similar for the other two compounds. This is in accord with the existence of weakly ferromagnetically coupled one-dimensional V=O· − ·V=O chains.

The conductivity measurements showed insulator behavior at low temperatures but a strong increase of conductance on increasing the temperature. As a consequence, the high temperature columnar phase and the isotropic phase show semiconducting properties, i.e. conductivity of the order of 10^{-5} S/m.

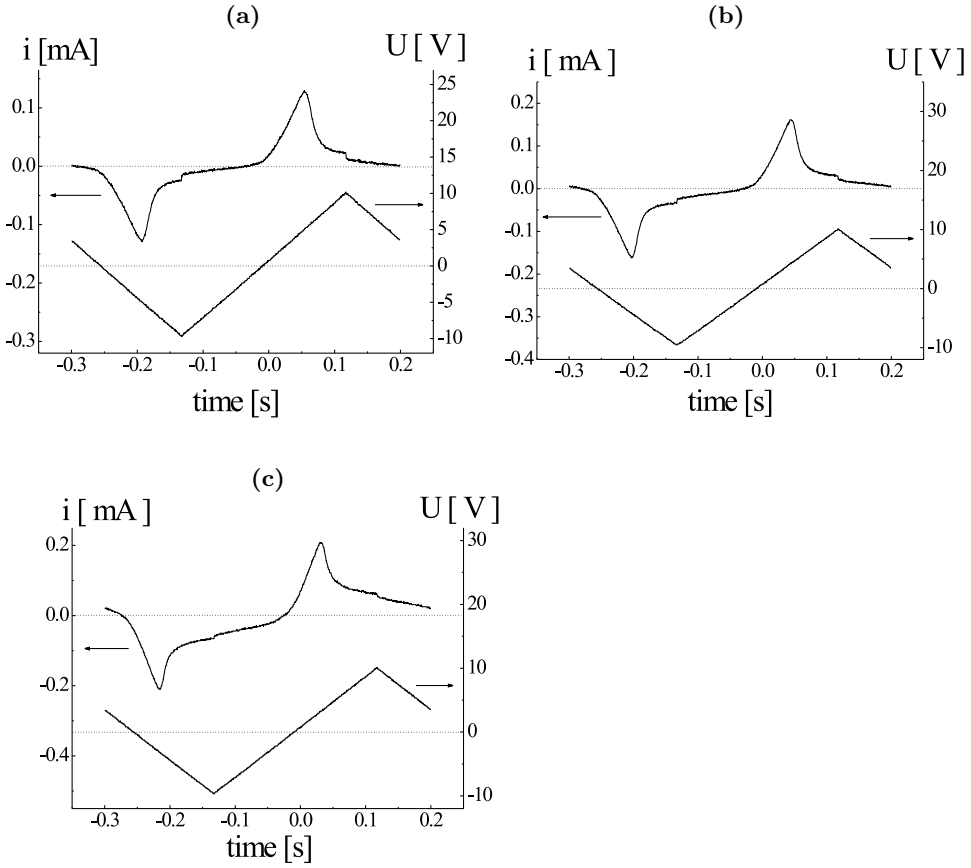

Fig. 6.30. Polarization reversal current peaks (*top curves*) and driving voltage (*bottom curves*) measured for two liquid crystalline and isotropic phase of SA5 [26]. Measurements done on heating up at temperatures: **(a)** $T = 55\,^{\circ}\mathrm{C}$ (SmC phase), **(b)** $T = 75\,^{\circ}\mathrm{C}$ (N phase) and **(c)** $T = 98\,^{\circ}\mathrm{C}$ (**Is.** phase); driving voltage frequency $f = 2$ Hz, amplitude $\pm\,10$ V, LC layer thickness 2 μm

Four relaxation processes could be detected in the columnar phases of vanadyl complexes. The process **A** exists in their high temperature Col_{hd} phase and in the isotropic phase. This process is due to ionic interfacial processes. The process **B** at about 10 kHz exists only at high temperatures and characterizes the relaxation most probably around the molecule's long axes. The weak process **C** exists in the Col_{rd} phase and it can be explained as columnar relaxation of the polar chains. Finally the process **D** can be explained due to columnar relaxations. The process **M** exists mainly in the OIDC phase, representing WLF-like β-relaxations of the side chain units.

Switching has not been detected under the optical microscope. The measured apparent spontaneous polarization allows one to calculate an apparent

hysteresis. But the apparent spontaneous polarization show atypical properties for ferroelectric liquid crystals. Therefore we do not believe, our materials can be considered as a non-chiral ferroelectric liquid crystals.

Acknowledgments

Two of us (W.H. and S.W.) would like to thank Dr. Eugene Pozhidaev for his help in reversal currents experiments and fruitful discussions.

References

1. S. Chandrasekhar, B.K. Sadashiva, K.A. Suresk: Pramana **7**, 471 (1977)
2. D. Markovitsi, F. Rigaut, M. Mouallem: Chem. Phys. Lett. **135**, 236 (1987)
3. S. Chandrasekhar: *Handbook of Liquid Crystals*, Vol. 2B, ed. by D. Demus, J. Goodby, G.W. Gray, H.-W. Spiess, V. Vill (Willey – VCH 1998), p. 749
4. S. Benning, H.-S. Kitzerow, H. Bock, M.-F. Achard: Liquid Crystals **27**, 901 (2000)
5. Y. Shimizu, T. Fuchita, T. Higashiyama, T. Sugino: Mol. Cryst. Liq. Cryst. **331**, 575 (1999)
6. H. Bock, W. Helfrich: Liquid Crystals **18**, 387 (1995)
7. D. Krüerke, P. Rudquist, S.T. Lagerwall, H. Sawade, G. Heppke: Ferroelectrics **243**, 207 (2000)
8. K. Yoshino, S.B. Lee, T. Sonda, H. Kawagishi, R. Hidayat, K. Nakayama, M. Ozaki, K. Ban, K. Nishizawa, K. Ohta, H. Shirai: J. Appl. Phys. **88**, 7137 (2000)
9. Z. Tomkowicz, M. Balanda, K. Falk, W. Haase: Chap. 8 of this book
10. M.P. Eastman, M.L. Horng, B. Frieha, K.W. Shen: Liquid Crystals **2**, 223 (1987)
11. M.R. de la Fuente, M.A. Perez Jubindo, T. Sierra, J.L. Serrano: Sect. 6.1 of this book
12. M.A. Athanassopoulou, S. Hiller, L.A. Beresnev, Y.G. Galyametdinov, M. Schweißgut, W. Haase: Mol. Cryst. Liq. Cryst. **261**, 29 (1995)
13. A.G. Serette, P.J. Carroll, T.M. Swager: J. Am. Chem. Soc. **114**, 1887 (1992)
14. A.G. Serette, T.M. Swager: J. Am. Chem. Soc. **115**, 8879 (1993)
15. H. Zhang, P.J. Carroll, T.M. Swager: Liquid Crystals **14**, 1421 (1993)
16. A. G. Serette: Ph.D. Thesis, University of Pennsylvania, USA (1994)
17. D. Kilian: Ph.D. Thesis, Darmstadt University of Technology, Germany (1999)
18. M.A. Athanassopoulou: Ph.D. Thesis, Darmstadt University of Technology, Germany (1999)
19. D. Kilian, D. Knawby, M.A. Athanassopoulou, T.M. Swager, S. Wróbel, W. Haase: Liquid Crystals **27**, 509 (2000)
20. W. Haase, D. Kilian, M.A. Athanassopoulou, D. Knawby, T.M. Swager, S. Wróbel: Liquid Crystals **29**, 133 (2002)
21. L. Merz, W. Haase: J. Chem. Soc. Dalton Trans. 875 (1980)
22. S. Gehring, P. Fleischhauer, H.Paulus, W. Haase: Inorg. Chem. **32**, 54 (1993)
23. G.A. Baker, Jr.G.S. Rushbrooke, H.E. Gilbert: Phys. Rev. A **135**, 1272 (1964)
24. J. Pugh: 'Automate Digital Dielectric Measurements', IEE-Conference on Dielectric Materials, Measurements and Application, Aston (1979)
25. A.M. Biradar, D. Kilian, S. Wróbel, W. Haase: Liquid Crystals **27**, 225 (2000)
26. E. Pozhidaev, S. Wróbel, W. Haase: unpublished results

Part III

Special Aspects of Relaxation Phenomena in Magnetic Systems

7

Magnetic Properties and ESR Behavior of Some Molecular Compounds Containing Copper(II) Trimers with the Quartet Spin Ground State

Z. Tomkowicz and W. Haase

7.1 Introduction

Trinuclear copper(II) complexes seem to be grateful objects for magnetic studies because they contain spin trimers being sufficiently small units, which allow for fundamental treatment. On the other hand they can reveal a reach variety of behavior, particularly when they interact magnetically. The compounds described here contain ferromagnetically inner coupled trimers, what makes them exceptionally attractive, because trimers with antiferromagnetic coupling are most frequently encountered. The formulas and used abbreviations of studied compounds are: $Cu_3(C_6H_5CO_2)_4\{(C_2H_5)_2NC_2H_4O\}_2(CH_3OH)_2$, abbr. Cu_3EtBz·2MeOH; $Cu_3(C_{11}H_9CO_2)_4\{(C_4H_9)_2NC_2H_4O\}_2(CH_3OH)_2$, abbr. Cu_3BuNaEs·2MeOH; $Cu_3(C_6H_5CO_2)_4\{(C_4H_9)_2NC_2H_4O\}_2(C_2H_5OH)_2$, abbr. Cu_3BuBz·2EtOH; $Cu_3(C_6H_5CO_2)_4\{(C_2H_5)_2NC_2H_4O\}_2(H_2O)$, abbr. Cu_3EtBz·H_2O and $Cu_3(C_6H_5CO_2)_4\{(C_4H_9)_2NC_2H_4O\}_2(H_2O)$, abbr. Cu_3BuBz·H_2O. The first three compounds contain linear trimers, but the last two contain triangle trimers. The triangles in Cu_3EtBz·H_2O are isosceles. In Cu_3BuBz·H_2O they are a little distorted. Structural characterization of studied compounds can be found in [1–4]. The first two compounds belong to the triclinic crystallographic system, the last three to the monoclinic system. Here, in Fig. 7.1, only the molecular structures of Cu_3BuNaEs·2MeOH and of Cu_3EtBz·H_2O are shown for reader guidance. The two trimers in the unit cell of Cu_3BuNaEs·2MeOH are not crystallographically equivalent. The shortest intermolecular Cu-Cu distance in Cu_3EtBz·2MeOH is 8.01 Å, in Cu_3BuBz·2EtOH 8.08 Å, in Cu_3BuNaEs·2MeOH 11.7 Å, in Cu_3EtBz·H_2O 6.76 Å and in Cu_3BuBz·H_2O 7.05 Å. The substances with linear trimers are paramagnetic and show intriguing ESR behavior, namely their resonance line exhibits an unexpectedly large shift with temperature. Instead, the substances with angled trimers show spin glass-like properties below $\sim$ 10 K. Their ESR spectra show no resonance shift, however, they drastically change at about 10 K [5]. This chapter is a review of magnetic, structural, far-infrared absorp-

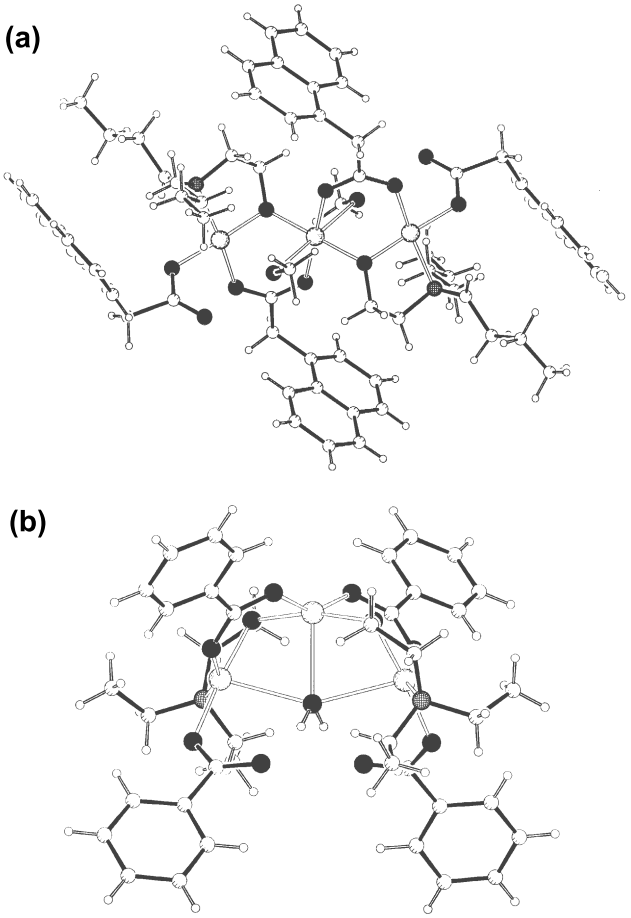

Fig. 7.1. (**a**) – Molecular structure of $Cu_3BuNaEs{\cdot}2MeOH$, (**b**) – molecular structure of $Cu_3EtBz{\cdot}H_2O$. *Large white circles* are copper atoms, *black circles* are oxygen atoms, *globe-like circles* are nitrogen atoms, *smaller circles* are carbon atoms and the *smallest circles* are hydrogen atoms

tion and ESR (including ESR under high pressure) studies of these substances. It is based on several papers [5–8] and should be useful as systematized description of rich diversity of behavior of the studied substances.

7.2 Review of used experimental methods

The syntheses of the studied compounds are described in [1–4]. All measurements were performed on powder samples.

AC susceptibility data were obtained [5] using a Lake Shore susceptometer (model 7225) equipped with a superconducting magnet. Both components χ' and χ'' of the complex susceptibility $\chi^* = \chi' - \mathrm{i}\,\chi''$ were measured in a heating mode. DC magnetization data were obtained [5] with a Quantum Design SQUID magnetometer. The data were corrected for underlying diamagnetism as well as for the contribution of the temperature independent Van Vleck paramagnetism.

ESR spectra were taken [8] with a Bruker ESP300E X-band spectrometer ($\nu = 9.428$ GHz) using a flow liquid helium cryostat. The first derivative of the absorption lines was recorded. High pressure X-band ESR ($\nu = 9.4$ Ghz) spectra were obtained by means of an apparatus described in [9]. With this apparatus the measurements in the pressure range $0 \div 700$ MPa are possible above liquid nitrogen temperature.

X-ray powder diffraction patterns were obtained [8] with a Siemens diffractometer equipped with a low temperature attachment. CuK_α radiation was used.

Far-infrared absorption measurements were made [8] in the 80–500 cm^{-1} wavenumber range using a Digilab FTS-14 Fourier transform spectrometer set at 2 cm^{-1} resolution. Polyethylene and Si windows and Apiezon L grease as a suspension agent were used.

7.3 Results and discussion

7.3.1 Magnetic studies

7.3.1.1 Linear trimers

Temperature dependence $\chi(T)$, typical for studied compounds with linear trimers, is shown in Fig. 7.2 for $\mathrm{Cu_3BuNaEs{\cdot}2MeOH}$. The inset shows the reciprocal dependence. The high temperature part of the $\chi^{-1}(T)$ curve was fitted according to the Curie–Weiss formula

$$\chi^{-1} = (T - \theta)/C\,, \tag{7.1}$$

where $C = N\mu^2/3k$, θ is a paramagnetic Curie temperature and μ is a paramagnetic moment of the trimer. The other symbols have their conventional meaning. The value of θ, obtained from fit, equals +25 K and the value of magnetic moment, calculated per Cu-ion, equals $1.79 \pm 0.05\mu_B$ in a good agreement with the free ion value of $1.73\mu_B$. The obtained values of θ for other compounds are given in Table 7.1.

In Fig. 7.3 DC magnetic susceptibility results in the form of $\mu_{\mathrm{eff}} = 2.282\sqrt{\chi T}$ are compared for all compounds with linear trimers. These data were analyzed in the whole temperature range with the following form of anisotropic spin Hamiltonian written in the axial symmetry approximation

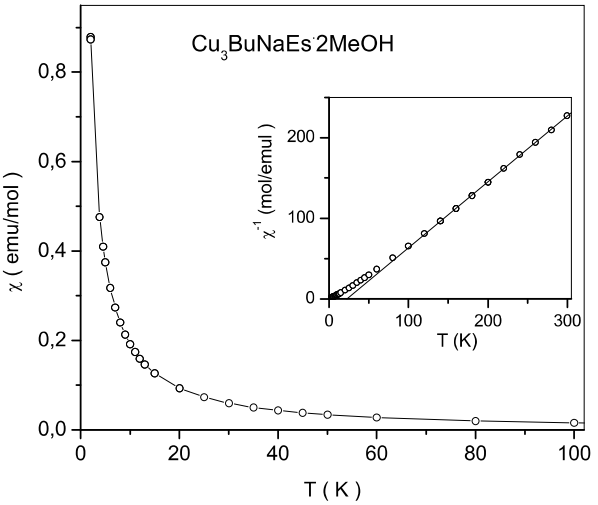

Fig. 7.2. Temperature dependence of DC magnetic susceptibility χ for Cu_3BuNaEs·2MeOH measured in magnetic field of 2000 Oe. *Solid line* is a guide for the eye. *Inset* shows $\chi^{-1}(T)$ dependence in the extended temperature range. *Solid line* in the *inset* is a fit to the Curie–Weiss law

Table 7.1. Magnetic parameters as obtained from magnetic measurements. In the case when two values of $|D|$ are given the lower one comes from $M(H)$ and higher one from $\chi(T)$ fits

Compound	J_{12} (cm^{-1})	J_{13} (cm^{-1})	g	$\lvert D\rvert$ (cm^{-1})	θ_{inter} (K)	θ (K)
Cu_3EtBz·2MeOH	19.3 ±1	−2.2 ±1	2.07 ±0.01	1 2	0	+13.7 ±1
Cu_3BuBz·2EtOH	22 ±1	0 ±1	2.05 ±0.02	1.6 3	0	+19.5 ±2
Cu_3BuNaEs·2MeOH	47 ±7	−6 ±4	2.02 ±0.01	1.2 1.3	0	+25.0 ±2
Cu_3EtBz·H_2O	36 ±3	−7 ±4	2.08 ±0.03	0 ±0.5	+1.5 ±1	+19.3 ±3
Cu_3BuBz·H_2O	46 ±5	−5.5 ±5	2.06 ±0.03	0 ±0.5	+0.9 ±0.5	+28.6 ±2

$$H_{3s} = -2 \sum_{j>i=1}^{3} \{J_{ij}^z s_i^z s_j^z + J_{ij}^{xy}(s_i^x s_j^x + s_i^y s_j^y)\} + \sum_{i=1}^{3} \mu_B \mathbf{H} \cdot \mathbf{g} \cdot \mathbf{s_i} \quad , \quad (7.2)$$

where s_1, s_3 are spins of the terminal Cu-ions and s_2 is the spin of the central Cu-ion. J_{12} is the exchange integral operating between nearest neighbors and J_{13} is the exchange integral operating between the terminal Cu-ions, H is magnetic field, μ_B is the Bohr magneton and g is a tensor of the spectroscopic factor, here assumed to be isotropic. Also J_{13} was assumed to be isotropic. Let us call the anisotropic components of J_{12} as J^{xy} and J^z. The anisotropy of exchange interaction leads to zero field splitting $2D$ of the spin ground state, which can be expressed as

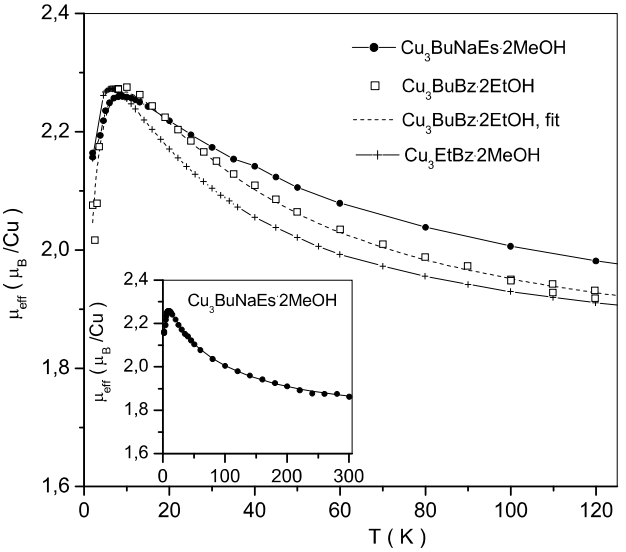

Fig. 7.3. Comparison of experimental results for $\mu_{\text{eff}} = 2.828\sqrt{\chi T}$. The *dashed line* is the fit. *Inset*: $\mu_{\text{eff}}(T)$ for $Cu_3BuNaEs{\cdot}2MeOH$ in the temperature range up to 300 K. *Solid line* in the *inset* is a fit

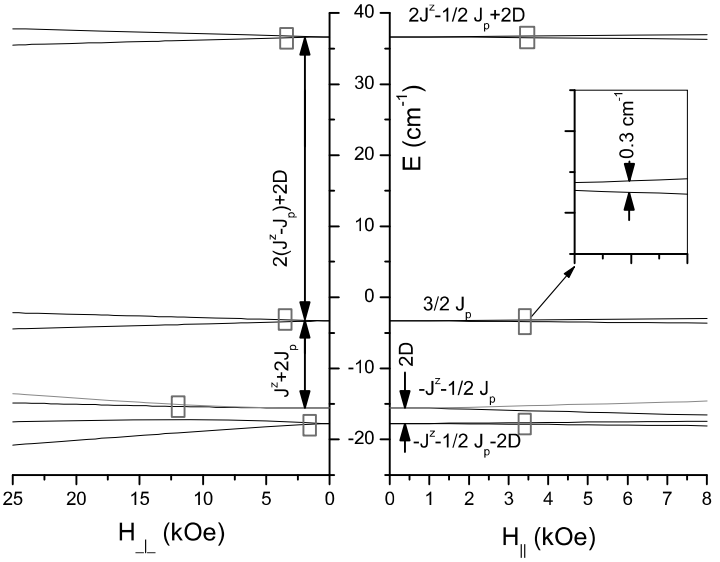

Fig. 7.4. Diagram of the spin levels for ferromagnetically coupled Cu-trimer plotted as a function of magnetic field H for the direction of field parallel and perpendicular to the crystal field axis. For this plot the zero field splitting parameter D is greater than 0. For $D < 0$ the sequence of the two lowest levels should be reversed. The expressions for the energy levels (written on the right diagram) refer to the case $H = 0$; $J_p \equiv J_{13}$. See text. *Small rectangulars* denote allowed ESR transitions. From [8]

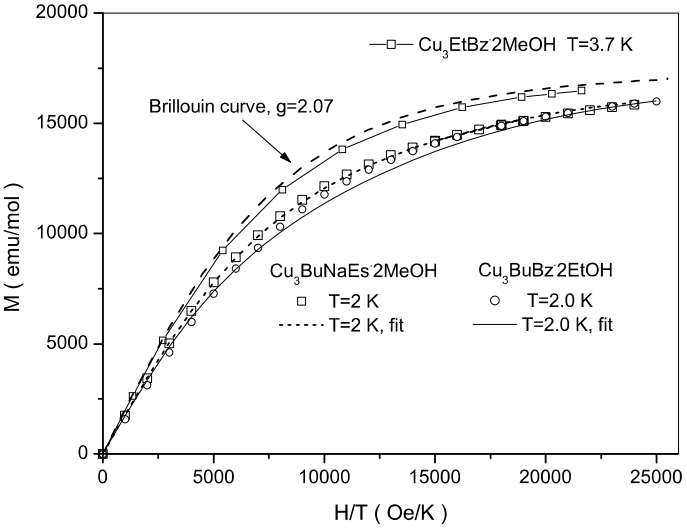

Fig. 7.5. Magnetization vs. H/T dependences for compounds with linear trimers

$$2D = -\frac{3}{2}J^z + \frac{1}{2}\sqrt{8(J^{xy})^2 + (J^z)^2} \tag{7.3}$$

or 2D $\cong -4\Delta/3$ for small $\Delta \equiv J^z - J^{xy}$. In the case of ferromagnetic coupling, i.e., when $J_{12} > 0$, D is greater than 0 when $J^{xy} > J^z$. The diagram of spin levels resulting from Hamiltonian (7.2) is shown in Fig. 7.4. The parameters obtained from fitting with the use of Hamiltonian (7.2) are given in Table 7.1. For $Cu_3BuNaEs{\cdot}2MeOH$ the two crystallographically different trimers were considered as magnetically equivalent. In Fig. 7.5 magnetization vs. H/T plots are presented. They were well fitted with Hamiltonian (7.2), however the obtained values of D parameter were a little lower than those obtained from the susceptibility data, see Table 7.1.

Good fits obtained with Hamiltonian (2) prove that linear trimers in studied compounds behave as superparamagnetic units with spin 3/2 at low temperatures.

7.3.1.2 Nonlinear trimers

In Fig. 7.6(a) and Fig. 7.6(b) temperature dependences of the AC and DC susceptibility, respectively, are shown for $Cu_3EtBz{\cdot}H_2O$. The corresponding plots for $Cu_3BuBz{\cdot}H_2O$ are quite similar. For both compounds the anomalies of χ' and χ'' components of AC susceptibility are observed in the vicinity of 10 K. The transition point determined at the half height of steep part of χ'' peak is 9.3 K for $Cu_3BuBz{\cdot}H_2O$ and 10.0 K for $Cu_3EtBz{\cdot}H_2O$. These anomalies can be suppressed by a static magnetic field. They are also weakly dependent on frequency. In Fig. 7.6(b) DC susceptibility curves $\chi(T)$ obtained

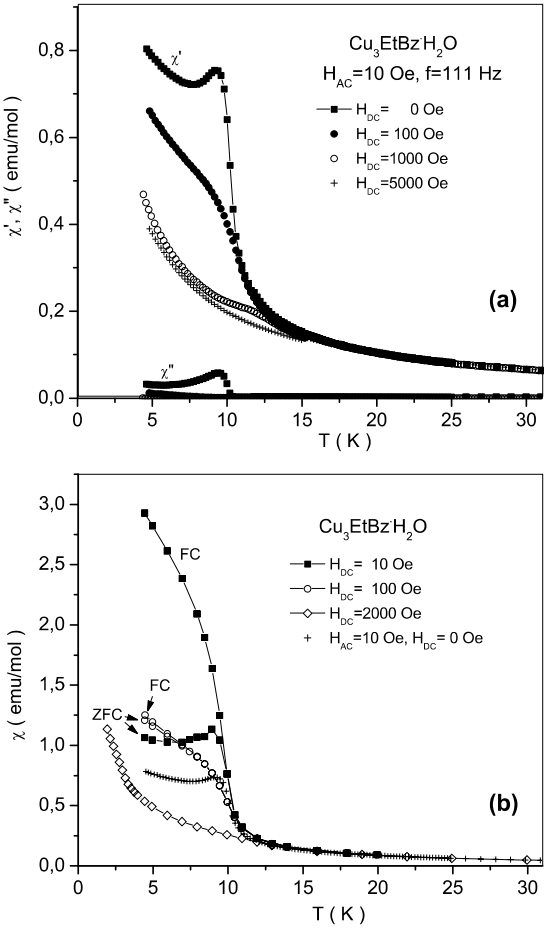

Fig. 7.6. Magnetic susceptibility vs. temperature for $Cu_3EtBz{\cdot}H_2O$ measured in different static magnetic fields; (**a**) – AC susceptibility; (**b**) – DC susceptibility obtained by means of the SQUID magnetometer. FC – field cooling, ZFC – zero field cooling. *Crosses* in (**b**) represent the *black square* χ' *curve* from (**a**)

in the field cooling (FC) and zero field cooling (ZFC) regime are shown. In the ZFC regime the sample was cooled in zero magnetic field then a field was switched on in which $\chi(T)$ was measured with increasing temperature. Next in the FC regime the sample was cooled in the same field and $\chi(T)$ was measured with decreasing temperature. It is seen that the difference between ZFC and FC curves disappears for higher magnetic fields. Both ZFC and FC susceptibilities approach some high field limit. In Fig. 7.6(b) also one AC curve was included for comparison. It is seen that it agrees with ZFC DC susceptibility. The observed behavior can point at the spin-glass character

of investigated compounds. In such a case an anomaly at ~ 10 K would be a freezing point.

In Fig. 7.7 the $\mu_{\text{eff}}(T)$ dependences are shown for $Cu_3EtBz{\cdot}H_2O$ and $Cu_3BuBz{\cdot}H_2O$ together with temperature dependences of the DC reciprocal susceptibility. In the inset of Fig. 7.7 the low temperature part of $\mu_{\text{eff}}(T)$ dependences is shown in an enlargement. The origin of an additional anomaly at ~ 2.8 K is unknown. The high temperature part of $\chi^{-1}(T)$ curves was fitted to the Curie–Weiss law. From fits θ parameter was determined. The data were also fitted with the total spin Hamiltonian (7.1) of [5] in a more extended temperature range. In the case of $Cu_3BuBz{\cdot}H_2O$ an approximation $J_{12} = J_{23}$ was assumed (Cu-Cu-Cu triangles are not exactly isosceles). The intertrimer interaction was taken into account as a mean field correction. Because of omitting the lowest temperature part of the plot the parameter D could not be determined, however, the quality of fits was a little bit better with D equal zero. The parameters obtained from fits are given in Table 7.1. The parameter θ_{inter} is a measure of intertrimer interaction. Result $D = 0$ agrees with $M(H)$ dependences, which are shown in Fig. 7.8. These dependences could be well fitted with the Brillouin function even for such low temperature as 2 K, where a decrease of M due to zero field splitting was expected.

Spin glass-like properties of nonlinear trimers can be understood with the help of Fig. 7.9. It is seen in the figure that every trimer is connected with its 4 neighbors by 8 exchange interactions. Because of symmetry only two interactions J_1 and J_2 are different. When they are of comparable magnitude but of opposite sign then a frustration may appear. Such cases of spin glass

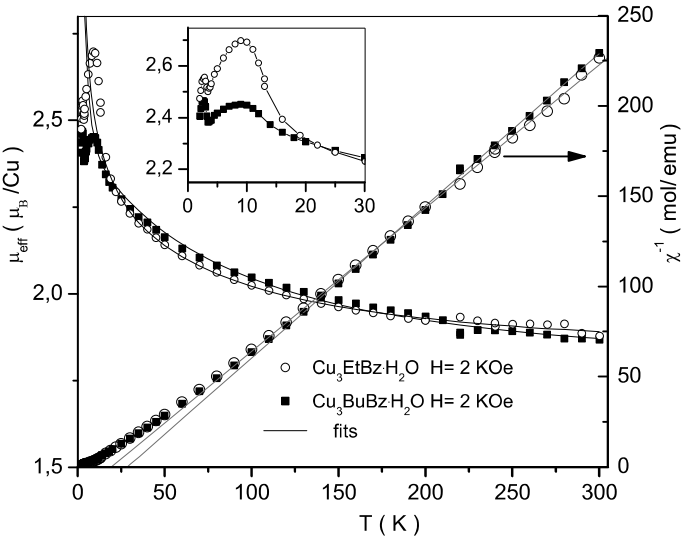

Fig. 7.7. Temperature dependences of μ_{eff} and reciprocal magnetic susceptibility. *Inset* is the low temperature part of $\mu_{\text{eff}}(T)$ dependences in an enlargement. From [5]

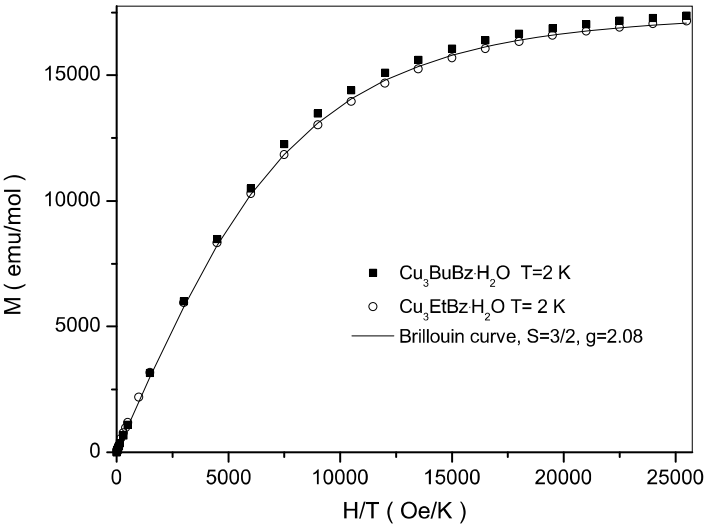

Fig. 7.8. Magnetization curve for $Cu_3BuBz{\cdot}H_2O$ and $Cu_3EtBz{\cdot}H_2O$. *Solid line* is the fit with the Brillouin function

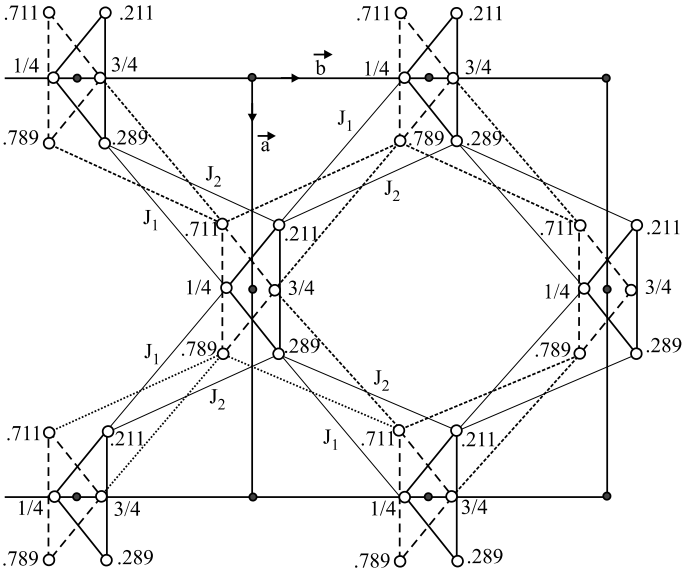

Fig. 7.9. Trimers arrangement in the crystal structure of $Cu_3EtBz{\cdot}H_2O$ in the projection on the *ab*-plane ($a = 14.549$ Å, $b = 12.456$ Å, $c = 24.368$ Å, $\beta = 90.14°$ [4]). Black points are the inversion centers. Two layers parallel to the *ab* plane are shown. Intertrimer magnetic interactions (J_1, J_2) are shown by *solid* or *dashed lines*, depending on the layer. The numbers given present *z*-coordinates

behavior without chemical disorder were reported in the literature, see [10] and were called topological spin glasses. One of the reasons that the nonlinear trimers show the transition into the frozen state, but linear trimers do not, can be the shorter intermolecular Cu-Cu distances in compounds with nonlinear trimers (see Introduction).

7.3.2 ESR studies of compounds with linear trimers

X band ESR spectra of powdered Cu_3EtBz·2MeOH and Cu_3BuNaEs·2MeOH are presented in Fig. 7.10 for different temperatures. The spectra of Cu_3BuBz·2EtOH show similar character to the spectra of Cu_3EtBz·2MeOH. The low temperature spectra can be interpreted assuming approximately a uniaxial symmetry and a value of D much higher than $h\nu$. The dominant component of these spectra then corresponds to $g_\perp$. It is seen in the figure that the resonance line exhibits a shift with temperature. Such shift was also observed for the unique line in single crystal X-band ESR spectra of Cu_3EtBz·2MeOH [3, 6]. The shift is smooth for Cu_3EtBz·2MeOH and Cu_3BuBz·2EtOH, but for Cu_3BuNaEs·2MeOH it shows some discontinuity. Temperature dependences of the resonance field H_{res} are shown in Fig. 7.11. The shift was interpreted by Fleischhauer et al. [6, 7] as a result of thermal averaging of signals from different spin multiplets. This thermal averaging seems to be quite analogous to the dynamic averaging of lines well known in ESR spectroscopy [11]. When the rate of transition between multiplets is very fast the signals merge into one line, whose position depends on the occupation of the excited levels.

The rate of transitions between multiplets needed for the merger of signals can be estimated in the following way. Let the number of molecules in the ground state be N_g and the number of molecules in the excited state be N_e, with the ratio N_g/N_e given by the Boltzmann distribution. Let the probabilities for upward and downward transitions be w_{ge} and w_{eg}. In the thermal equilibrium the numbers of transitions up and down between two levels should be equal, i.e., $N_g w_{ge} = N_e w_{eg}$. Let us define the mean interconversion rate $w_0 = (w_{ge} + w_{eg})/2$. The value $\tau = 1/(2w_0)$ is then the relaxation time, which reflects the measure of interaction of spin system with the lattice. When τ is very long, ESR signals from both levels are separately observed, their separation is ΔH_{res0}. The signals coalesce into one line when τ is so low, that $\tau^{-1} > \gamma_e \Delta H_{res0}$, where γ_e is the free electron magnetogyric ratio. In our case $\gamma_e \Delta H_{res0} \approx \gamma_e(1\text{ kOe}) = 1.76{\cdot}10^{10}\text{ s}^{-1}$, thus $\tau < 5.5{\cdot}10^{-11}$ s.

The convincing experiment that the thermal averaging of lines is responsible for the thermal shift of H_{res} can be ESR at high frequency. Separation of lines ΔH_{res0} in the high frequency spectrum in the absence of thermal averaging will be much higher than in the X-band spectrum. Then the lines, which merged in the X-band experiment ($h\nu = 0.3\text{ cm}^{-1}$), can be separately observed in a high frequency experiment. Such experiment was performed for Cu_3EtBz·2MeOH at the frequency $\nu = 245$ GHz ($h\nu = 8.17\text{ cm}^{-1}$) [6]. Predicted value of ΔH_{res0} in this experiment is ∼26.6 kOe. In fact, the line

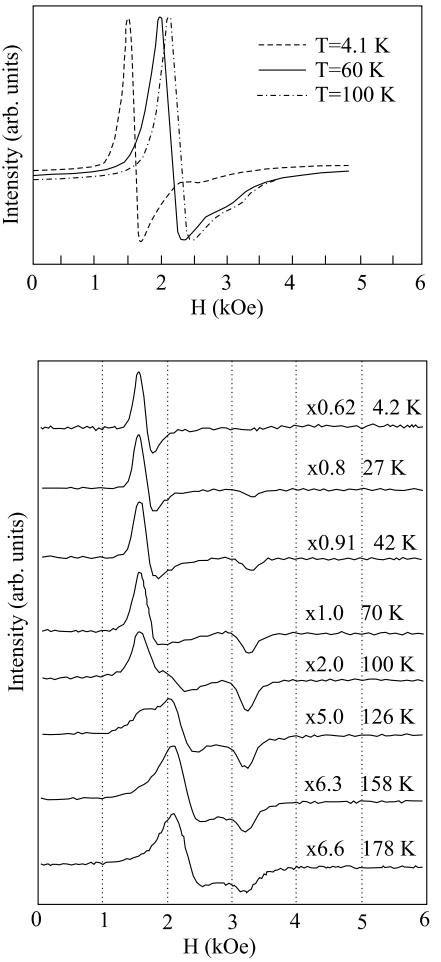

Fig. 7.10. Temperature evolution of ESR spectra of Cu_3EtBz·2MeOH (*upper diagram*) and Cu_3BuNaEs·2MeOH (*lower diagram*). The notation, e.g., ×0.62 means the multiplication factor for the intensity. From [8]

positions did not change with temperature (at least up to 30 K) confirming the interpretation of the H_{res} shift in the X-band as result of a merger of lines. This imposes the limits on τ, namely $2{\cdot}10^{-12}\text{s} \leq \tau \leq 55{\cdot}10^{-12}\text{s}$. The experimental high frequency spectrum is shown in Fig. 7.12. This spectrum was taken at 4 K in the magnetic field range of $6 \div 9$ T.

The mechanism of the resonance shift seems to be essentially an intramolecular property, which, however, can depend on external factors. It is very interesting to learn which factors modify the process of thermal averaging, so that the difference in ESR behavior is observed between Cu_3EtBz ·2MeOH and Cu_3BuBz·2EtOH on the one hand and Cu_3BuNaEs·2MeOH on

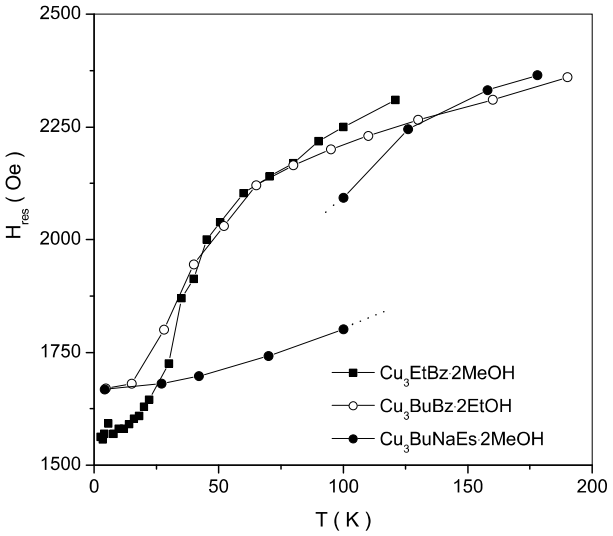

Fig. 7.11. Temperature dependences of resonance field for compounds with linear trimers. The *solid lines* are guides to the eye. From [5]

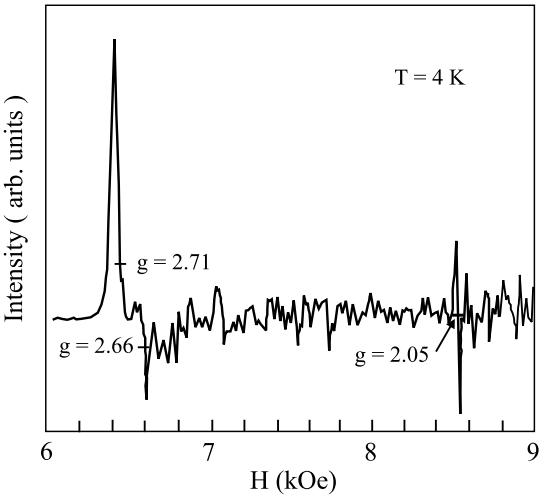

Fig. 7.12. High frequency ESR spectrum of Cu_3EtBz·2MeOH ($\nu_{res} = 245$ GHz) at 4 K. Reprinted from [6] with permission from Elsevier Science

the other hand. It seems, that the step change of H_{res} for Cu_3BuNaEs·2MeOH is caused by a crystallographic phase transition. When this transition involves a change of molecular packing only it would mean that intermolecular interactions play a role. An ESR experiment, performed under high pressure, addresses this question because the pressure, first of all, should influence intermolecular distances. Therefore high pressure ESR studies were performed as well as X-ray powder diffraction studies at low temperatures and far-infrared absorption measurements for one or both of compounds Cu_3EtBz·2MeOH and Cu_3BuNaEs·2MeOH.

X-band high pressure-low temperature ESR spectra were taken for Cu_3EtBz·2MeOH. It is seen in Fig. 7.13 that the effect of pressure is to increase g_{eff} ($h\nu = g_{\text{eff}}\mu_B H_{res}$), what is also accompanied by the increase of the linewidth ΔH_w. In order to shed light on the step change of H_{res} for Cu_3BuNaEs·2MeOH at ∼100 K X-ray powder diffraction measurements were performed for this substance. The obtained diffraction patterns are shown in Fig. 7.14. The pattern for 120 K practically does not differ from that obtained at room temperature. An apparent difference comes from a smaller amount of the substance in the case of measurement at room temperature and from the temperature shift of line positions. The diffraction pattern essentially changes at lower temperatures between 80 and 120 K. This means that a crystallographic phase transition occurs somewhere in this temperature range.

In order to decide whether the observed phase transition involves a change of intramolecular structure or a change of intermolecular packing only the far-infrared absorption measurements were undertaken. The spectra, which were obtained at different temperatures, are shown in Fig. 7.15 for Cu_3EtBz·2MeOH and Cu_3BuNaEs·2MeOH. The bands on the spectra originate mainly from intramolecular vibrations of the ligands. A tentative assignment of these bands could reasonably be given with the aid of the literature data for similar compounds [12, 13]. However, some bands can be interpreted as skeletal modes of the four planar – six octahedral – four planar coordination sequence of the Cu-trimer. The band of Cu_3EtBz·2MeOH at 307 cm^{-1} and the doublet band of Cu_3BuNaEs·2MeOH at 294 and 318 cm^{-1} were assigned to the T_{1u} skeletal mode of the CuO_6 coordination complex [14–16]. The splitting of ca. 6 cm^{-1} of the 307 cm^{-1} and 24 cm^{-1} of the second band may be caused by an axial deformation of the O_h copper complex due to a vibration coupling with the square planar coordination complex of the Cu-trimer. It is seen that this deformation is much stronger for the Cu_3BuNaEs·2MeOH coordination compound. The doublet intensity for this compound decreases smoothly under heating, which may point at an intratrimer charge transfer.

One can conclude that because no significant change of spectra with temperature is observed, it means that no change of molecular structure occurs. Thus, the phase transition observed by X-ray diffraction for Cu_3BuNaEs·2MeOH refers to the change of intermolecular packing. It follows thereby that the mechanism of the resonance shift is related with intermolecular interactions.

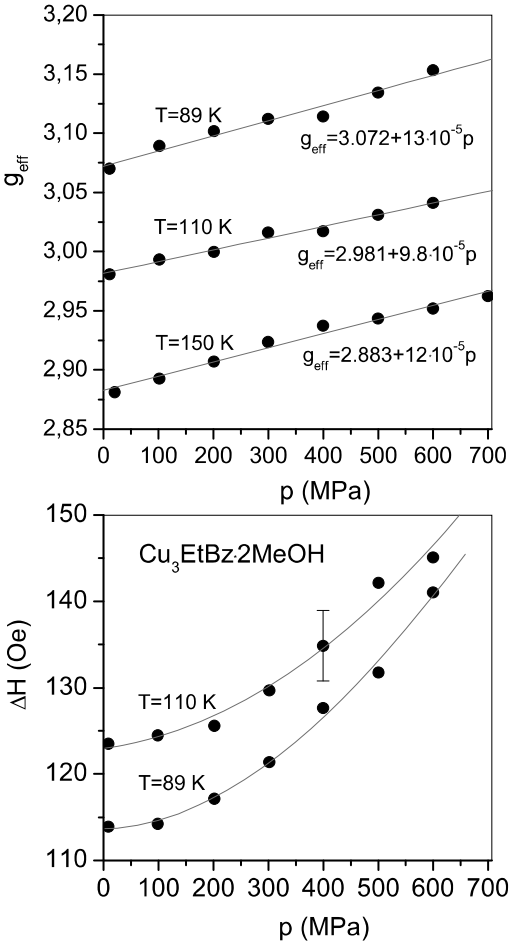

Fig. 7.13. Pressure dependences of g_{eff} and the linewidth ΔH_{res} for Cu_3EtBz·2MeOH measured at different temperatures. The *solid lines* in the *upper diagram* are linear fits, and the *solid lines* in the *lower diagram* are guides to the eye. A typical error bar is shown in the lower diagram. From [8]

Relaxations between multiplets generally occurs due to thermal vibrations, which modulate the exchange integral. The intramolecular vibrations are expected to have an energy higher than the energy distances between spin multiplets of our system, so they cannot induce direct transitions between spin multiplets. However, the transitions can be induced by two-phonon processes. The two-phonon processes are usually very rapid, particularly when they involve phonons, which come from a densely populated part of the phonon spectrum. The transitions between multiplets are allowed for our system because of mix-

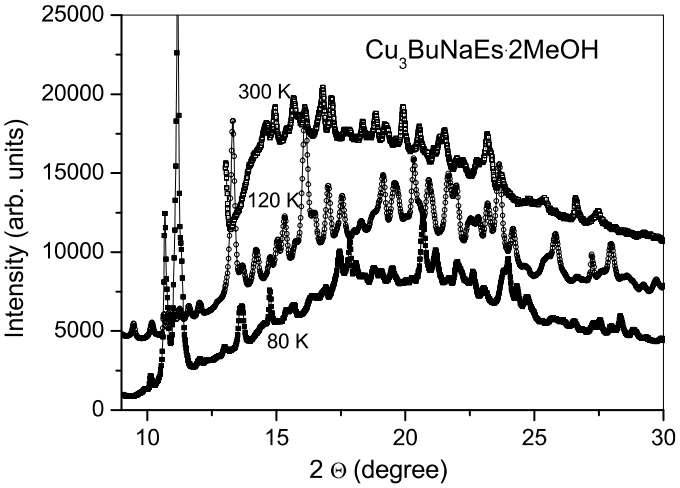

Fig. 7.14. X-ray powder diffraction patterns for $Cu_3BuNaEs{\cdot}2MeOH$. The pattern for 300 K (of worse quality) was obtained with a smaller amount of the sample. From [8]

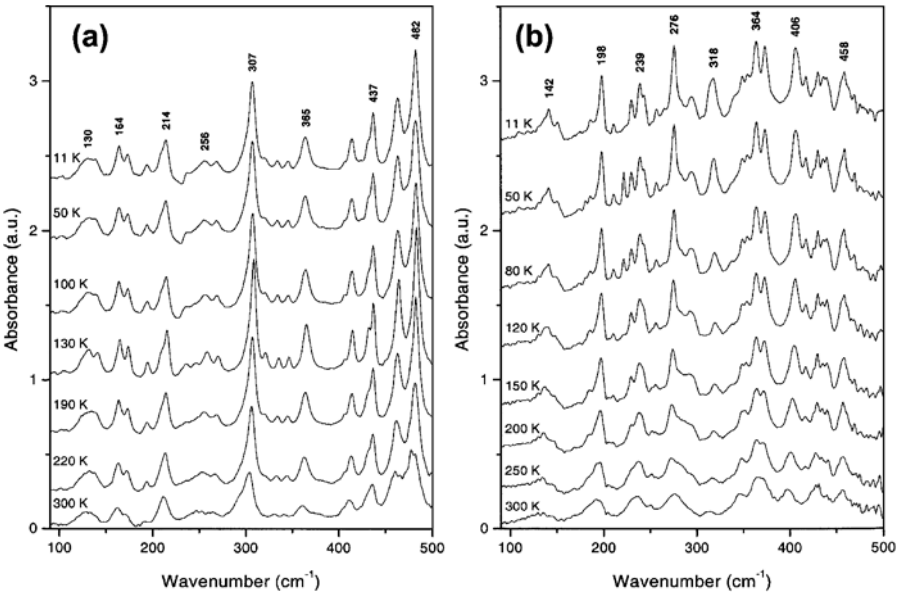

Fig. 7.15. Far-infrared spectra for $Cu_3EtBz{\cdot}2MeOH$ (**a**) and for $Cu_3BuNaEs{\cdot}2MeOH$ (**b**) obtained at different temperatures. From [8]

ing states of different total spin. The question, whether these processes give sufficiently short relaxation time requires, however, a quantitative analysis.

Fleischhauer et al. [7] were able to reproduce well the temperature dependence of H_{res} by taking the thermal average of H_{res} and varying the energy distances between spin multiplets. However, the obtained values of energy levels did not agree with those resulting from exchange integrals obtained from magnetic measurements. This is probably because of not taking into account details of multiplets relaxation.

The temperature evolution of ESR spectra for Cu_3BuNaEs·2MeOH in Fig. 7.10 can now be understood in the following way. At the lowest temperature only $g_\perp$ component is seen, but with increasing temperature the line at $g = 2.06$ appears. It looks like $g_\perp$ component from the higher spin doublet (see Fig. 7.4). As is seen no thermal averaging as yet takes place. At about 100 K the phase transition occurs, which involves a change of spectrum with temperature. This change can be interpreted by assumption that the mechanism of thermal averaging is switched on at about 100 K and that the transition is of the first order (because the change occurs in some temperature range). The absence of averaging at low temperature may originate from the drastic decrease of intermolecular distances below 100 K in agreement with results of the high pressure experiment for Cu_3EtBz·2MeOH, where such decrease should occur but in lower degree. Therefore in the high pressure experiment the line broadens only, while for Cu_3BuNaEs·2MeOH the lines become sharp at low temperatures. It means that τ^{-1} becomes much lower than $\gamma_e \Delta H_{res0}$ below 100 K, being one of the two extreme cases of [11]. It is worth to remark that Cu_3BuNaEs·2MeOH differs from other two linear trimeric complexes in that the nearest inter-trimer distance at room temperature is significantly greater for this compound and the exchange intratrimer interaction J_{12} is about two times greater. Let us finally recall that the compounds containing nonlinear trimers have shorter intertrimer distances (6.76 or 7.05 Å). Consistently, they show no resonance shift.

It should be noted that the observed shift of H_{res} would be not possible without anisotropy of exchange interactions. Unfortunately, no detailed information about this anisotropy can be obtained from the X-band ESR spectra. Instead, nearly full information can, in principle, be obtained from high frequency ESR spectra even for powder samples. To this end the high frequency ESR spectrum of Cu_3EtBz·2MeOH from Fig. 7.12 was analyzed. Numerical simulations of the spectrum were performed using the Hamiltonian (7.2). Temperature factors and a partial ordering of microcrystallites by the large magnetic field were not taken into account. The spectrum could be qualitatively described with anisotropic exchange parameters, but two sets of parameters were possible: (i) $J^{xy} \approx 16.7$ cm^{-1}, $J^z \approx 20$ cm^{-1}, corresponding to $2D \approx -4.35$ cm^{-1} and (ii) $J^{xy} \approx 18.3$ cm^{-1}, $J^z \approx 16.7$ cm^{-1}, corresponding to $2D \approx 2.14$ cm^{-1}. The simulated spectra are presented in Fig. 7.16(a) and Fig. 7.16(b) respectively. In both cases the mean value of J_{12} (~ 17.8 cm^{-1}) is close to the value obtained from magnetic susceptibility

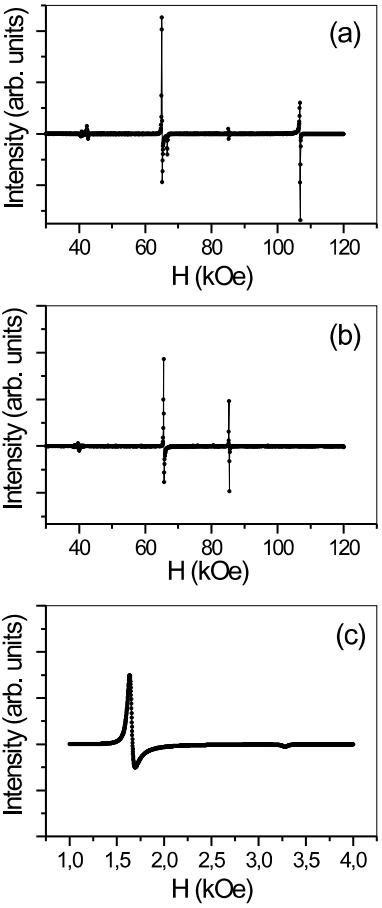

Fig. 7.16. ESR spectra simulated for the frequency $\nu = 245$ GHz (**a**) $D < 0$, (**b**) $D > 0$ and for the X-band experiment (**c**), see text. From [8]

measurements (~ 19.3 cm^{-1}). In Fig. 7.16(a) a weak negative line is seen on ESR spectrum at 66 kOe. This line could be reproduced in the case (i), only with J_{13} different from zero. The value $2|D| \approx 4.35$ cm^{-1} of the case (i) is a little outside the limits $2 \div 4$ cm^{-1} of magnetic measurements [5], instead, the value $2D \approx 2.14$ cm^{-1} of the case (ii) better agrees with magnetic data. In spite of numerous trials it was impossible to reproduce the line at 66 kOe with Hamiltonian (7.2) for $D > 0$. It is not excluded, however, that it would be possible with a more general form of Hamiltonian. An additional difference between the case (i) and (ii) is a line at about 107 kOe, seen in Fig. 7.16(a), but absent in Fig. 7.16(b). Unfortunately, this line is outside the experimental range of magnetic field. New high frequency ESR measurement, performed in more extended range of magnetic field, is necessary in order to decide between both two cases.

As mentioned above, the line positions in the high frequency spectrum of Cu_3EtBz·2MeOH do not change with temperature (at least up to 30 K). It

means that exchange integrals and the exchange anisotropy do not change with temperature. Nevertheless, it is worth to be aware what kind of resonance shift is caused by decreasing of the exchange anisotropy. To this end we simulated a powder averaged X-band spectra. The typical spectrum obtained for parameters of case (i) or (ii) is shown in Fig. 7.16(c). As follows from the simulations, a shift of H_{res} can in fact be obtained when $|D|$ is decreasing. This is, however, possible only in some limited range of D values. For the value of $|D|$ greater than some upper limit, H_{res} is not sensitive on D and for the value of $|D|$ a little smaller than some lower limit, an X-band ESR spectrum would drastically change, which is not observed. These simulations are consistent with the conclusion that the exchange anisotropy does not remarkably change with temperature, and cannot be responsible for the resonance shift with temperature. Thus, our results agree with the interpretation of Fleischhauer et al. [7] that this shift appears as an effect of thermal averaging of lines belonging to the different quickly relaxing spin multiplets.

7.4 Summary

Magnetic, structural and ESR (also under high pressure) studies of five substances containing spin copper trimers were reviewed. The studied substances were: Cu_3EtBz·2MeOH, Cu_3BuBz·2EtOH, Cu_3BuNaEs·2MeOH, Cu_3EtBz ·H_2O and Cu_3BuBz·H_2O. All trimers are ferromagnetically inner coupled having a quartet as a spin ground state. The first three substances contain linear trimers and are paramagnetic with an appreciable value of zero field splitting D about 2 cm^{-1} originating from the anisotropy of the nearest neighbors exchange interaction. The last two substances contain triangle trimers and show spin glass-like properties below a transition point of ∼10 K. Inter-trimer magnetic coupling correlates with lower inter-trimer distances for these substances in comparison with substances containing linear trimers.

The substances with linear trimers show unusual ESR behavior. Their resonance field H_{res} exhibits a large temperature shift. This shift is a smooth function of temperature for Cu_3EtBz·2MeOH and Cu_3BuBz·2EtOH but it is a stepwise function for Cu_3BuNaEs·2MeOH. It was shown by means of X-ray diffraction that the step change of H_{res} is associated with a crystallographic phase transition. It was also shown using far infra-red spectroscopy that this phase transition involves a change of molecular packing only.

ESR studies were performed under high pressure for Cu_3EtBz·2MeOH. It was shown that H_{res} decreases with pressure but the line width increases.

The observed resonance shift was interpreted as originating from thermal averaging of quickly relaxing spin multiplets. The mechanism of relaxation depends on inter-trimer distances and is most probably connected with spin-phonon coupling.

Acknowledgements. We are grateful to Elsevier Science publisher and the authors who kindly agreed for the reproduction of figures.

References

1. W. Haase, S. Gehring: J. Chem. Soc. Dalton Trans. **1985**, p. 2609
2. H. Muhonen, A. Pajunen, R. Hämäläinen: Acta Crystallogr. **36**, Sect. B, 2790 (1980)
3. P. Fleischhauer: Ph.D. Thesis, Darmstadt University of Technology, Darmstadt (1994)
4. S. Gehring, P. Fleischhauer, H. Paulus, W. Haase: Inorg. Chem. **32**, 54 (1993)
5. Z. Tomkowicz, P. Fleischhauer, W. Haase, M. Baran, R. Szymczak, A.J. Zaleski, R. Jabłoński: J. Magn. Magn. Mater. **172**, 128 (1997)
6. P. Fleischauer, S. Gehring, C. Saal, W. Haase, Z. Tomkowicz, C. Zanchini, D. Gatteschi, D. Davidov, A.L. Bara: J. Magn. Magn. Mater. **159**, 111 (1996)
7. P. Fleischhauer, S. Gehring, W. Haase: Ber. Bunsenges. Phys. Chem. **96**, 1701 (1992)
8. Z. Tomkowicz, W. Haase, P. Fleischhauer, M. Krupski, H. Micklitz, O. Friedt, E. Ściesińska, J. Ściesiński, P. Sczaniecki: J. Magn. Magn. Mater. **236**, 347 (2001)
9. M. Krupski: Rev. Sci. Instrum. **67**, 2894 (1996)
10. J.N. Reimers, J.E. Greedan, R.K. Kremer, E. Gmelin, M.A. Subramanian: Phys. Rev. B **43**, 3387 (1991)
11. J.A. Weil, J.R. Bolton, J.E. Wertz: *Electron Paramagnetic Resonance – Elementary Theory and Practical Applications* (Wiley, New York 1994), p. 304
12. E.L. Bokhenov, I. Natkaniec, E.F. Sheka: Phys. Stat. Sol. B **75**, 105 (1976)
13. V. Volovsek, L. Colombo, K. Furic: J. Raman Spectrosc. **14**, 347 (1983)
14. K. Nakamoto: *Infrared Spectra of Inorganic and Coordination Compounds* (Russian translation, MIR, Moscow 1966)
15. T. Grzybek, J.A. Janik, J.M. Janik, A. Kulczycki, G. Pytasz, E. Ściesińska, J. Ściesiński: J. Raman Spectrosc. **1**, 185 (1973)
16. J.R. Ferraro, L.J. Bassile, L.R. Garcia-Ineguez, P. Paoletti, L. Fabrizzi: Inorg. Chem. **15**, 2342 (1976)

8

Magnetic Properties and Relaxation Processes in Manganese(III)-Porphyrin-TCNE-Systems

Z. Tomkowicz, M. Bałanda, K. Falk and W. Haase

8.1 Introduction

One-dimensional magnetic systems aroused always a great interest. It has been known for a long time that magnetic chains cannot magnetically order at temperatures above 0 K. Finite critical temperatures of transition into the ordered state were usually interpreted as a result of weak interchain magnetic interactions. Porphyrin based molecular magnets [MnR_4TPP][TCNE]·solvent have a chain structure composed of manganese(III) porphyrin discs MnTPP (TPP = tetraphenylporphyrin) alternating with $TCNE^-$ radical (tetracyanoethylene), being the bridge between two Mn^{III}-ions, see Fig. 8.1. Substituents R are attached at the disc peripheries, while solvent molecules are located in free space between chains. Up to date only a few substances of this family have been structurally characterized (with R = H or Cl) [1, 2]. A number of members of the porphyrin family were for the first time synthesized in our group with the following R: OCH_3, $OC_{10}H_{21}$, $OC_{12}H_{25}$, $OC_{14}H_{29}$, ortho-F, para-F, CN, CF_3 [3] (ortho and para differentiate place of attachment). Hereafter the abbreviation Mn-R-TCNE for their chemical formula will be used. It is known from X-ray investigations at room and higher temperatures that the substances Mn-$OC_{10}H_{21}$-TCNE, Mn-$OC_{12}H_{25}$-TCNE and Mn-$OC_{14}H_{29}$-TCNE form a hexagonal columnar liquid crystalline phase [4], in which the MnR_4TPP-group and the TCNE-radical are only partially ordered. With decreasing symmetry there is a phase transition into the crystalline phase, and the lattice symmetry is expected to underlie a distortion.

The studied substances of porphyrin family acquire significant magnetic properties with decreasing temperature. There are two carriers of magnetic moments in the chains: Mn^{III}-ions, with the spin value $S = 2$, and $TCNE^-$ radicals with the delocalized spin $s = 1/2$. Both are strongly antiparallelly coupled creating a ferrimagnetic system. While the intra-chain Mn-TCNE distance is $\sim$ 5 Å the shortest interchain distance is very large, 17–30 Å depending on the kind of substituents. In such a case magnetic exchange interactions between the chains are impossible.

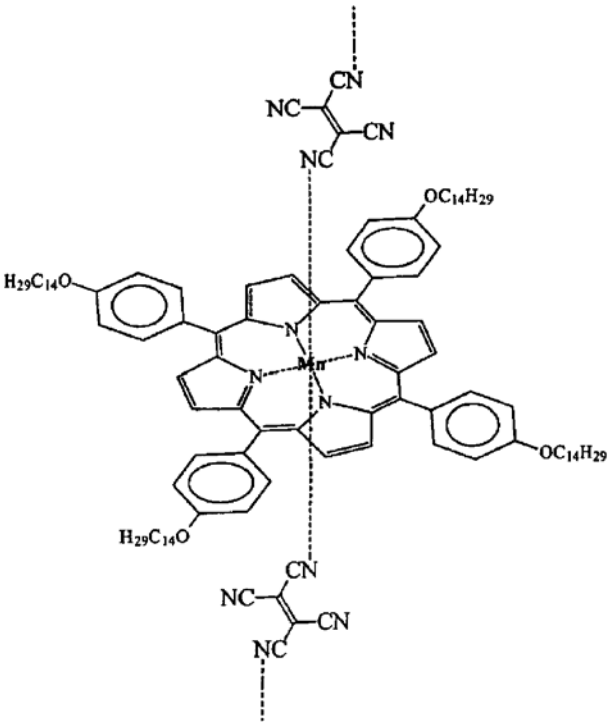

Fig. 8.1. Chemical structure of the Mn-$OC_{14}H_{29}$-TCNE complex

Bałanda et al. extensively studied the magnetic properties of manganese(III) porphyrin-TCNE complexes with R = $OC_{12}H_{25}$, F, CN using AC and DC magnetic susceptibility techniques [5]. The strong maximum of AC susceptibility χ_{AC}, observed at $\sim$ 20 K, they interpreted as a phase transition into the ferromagnetic state. In Fig. 8.2 their results are plotted as the effective magnetic moment $\mu_{\mathrm{eff}} = 2.828(\chi_{\mathrm{AC}}T)^{1/2}$ in dependence on temperature. The low temperature values of μ_{eff} depend strongly on the applied DC magnetic field. The results for $\mu_{\mathrm{eff}} = 2.828(\chi_{\mathrm{DC}}T)^{1/2}$, obtained in DC measurements [4] by means of a magnetic balance in the temperature range up to 460 K, are also shown in Fig. 8.2. The high temperature value of μ_{eff}, equal 5.2 μ_B, and a shallow minimum (at $\sim$ 320 K, not seen in the scale of the figure) agree with the theoretical prediction for 1-d ferrimagnetic chains. It is worth to note that both AC and DC results shown in Fig. 8.2 are similar to DC SQUID results for [MnTTP][TCNE] obtained by Winter et al. [6]. By applying a static magnetic field Bałanda et al. [5] observed also a second AC susceptibility anomaly, which emerged on the low temperature wing of the above-mentioned maximum. By analogy with the behavior of other systems it was proposed, that this anomaly manifests a reentrant spin glass transition [7–11]. Such transition is expected when the width of the distribution of

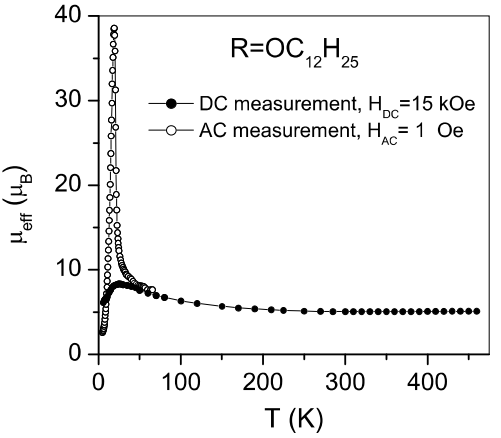

Fig. 8.2. Temperature dependences of the effective magnetic moment for Mn-$OC_{12}H_{25}$-TCNE. See text

interchain interactions is comparable but smaller than the average interchain interaction.

The only known magnetic interactions, which could be operating between so distant chains are dipolar ones. Ostrovsky et al. [11] showed in a theoretical way that dipolar interactions in a system of parallel chains with anisotropy are able to give such high critical temperature T_c as 20 K. On the other hand Gambardella et al. [12] have recently shown that monoatomic Co chains on a Pt substrate exhibit ferromagnetic behavior below the blocking temperature $T_B = 15 \pm 5$ K of their spin segments, although no sign of interchain coupling was found.

In order to confirm whether the high temperature anomaly at $T_c \sim 20$ K is consistent with dipolar interactions, measurements of pressure dependence of T_c was undertaken by Mascarenhas et al. [13]. The studied substance was Mn-$OC_{14}H_{29}$-TCNE. It was observed that T_c initially decreased with pressure showing a minimum at $p = 1.5$ kbar and further increased with pressure reaching 37 K at 21 kbar. No clear explanation of this interesting effect exists for now, although several possibilities are analyzed.

In this work we show the results of recent studies aiming at further explanation of the nature of magnetism of the manganese(III)-porphyrin-TCNE complexes. The newly studied substances are Mn-$OC_{10}H_{21}$-TCNE, Mn-$OC_{14}H_{29}$-TCNE and Mn-ortho-F-TCNE. The earlier studied substance Mn-$OC_{12}H_{25}$-TCNE, for which some completing results were obtained is also included in this work. As indicated, exact details of crystal structure are not known, but from the magnetic point of view we are dealing with systems of distant parallel ferrimagnetic chains. Some disorder is introduced to this system by a statistical distribution of solvent molecules in space between chains. Magnetic properties of such systems are not fully understood.

8.2 Experimental

The metal-free porphyrin was synthesized according to Adler et al. [14]. The metallation and the bridging reaction are described by Jones et al. [15] and Summerville et al. [16].

0.1 mol of the corresponding benzaldehyde was solved in 300 ml boiling propionic acid, then 0.1 mol pyrrol was dropped slowly to this mixture. After refluxing the solution for one hour the precipitated violet product was filtered and washed with acetone and water.

After drying the porphyrin was solved in 300 ml hot DMF and 0.05 mol manganese(II) acetate tetrahydrate was added to the mixture. After refluxing for one hour the precipitating green product was filtered and washed with water, dried in air and dissolved in 150 ml of hot methanol. The same volume of half-concentrated hydrochloric acid was added to this solution and the precipitating green product was filtered, washed with water and dried in air.

The bridging reaction with tetracyanoethylene (TCNE) was done in Schlenk-type glassware under an argon atmosphere. 0.5 mmol of the green manganese(III) chloride was dissolved in 20 ml methanol and 20 ml pyridine, next 10 mmol sodium boronhydride was then added and the stirred mixture was refluxed for one hour. After that procedure the purple product was filtered, washed with methanol and dried in vacuum. A solution of 1.5 mmol TCNE in 15 ml toluene was added then to the compound. After stirring the mixture for one hour at room temperature the precipitating dark green product was filtered, washed with toluene and dried in vacuum for several hours.

The success of the bridging reaction with TCNE was proved via the typical shift of the ν_{CN} wagging bands in the IR spectroscopy ($\nu_{CN}(1) = 2258$ cm^{-1}, $\nu_{CN}(2) = 2219$ cm^{-1} for free TCNE). Table 8.1 summarizes the results of the synthesis.

Table 8.1. Synthesized substances and results of analysis

Substance	Formula	$\nu_{CN}(1)$	$\nu_{CN}(2)$	Remaining solvent	Yield [%]*
Mn-OCH_3-TCNE	$MnC_{54}H_{36}N_8O_4$	2193	2143	2 toluene	63
Mn-$OC_{10}H_{21}$-TCNE	$MnC_{90}H_{108}N_8O_4$	2196	2144	2 pyridin, 1 methanol	68
Mn-$OC_{12}H_{25}$-TCNE	$MnC_{98}H_{124}N_8O_4$	2193	2143	2 toluene	34
Mn-$OC_{14}H_{29}$-TCNE	$MnC_{106}H_{140}N_8O_4$	2198	2144	1 methanol	39
Mn-ortho-F-TCNE	$MnC_{50}H_{24}N_8F_4$	2197	2142	3 methanol	68
Mn-para-F-TCNE	$MnC_{50}H_{24}N_8F_4$	2196	2138	1/2 methanol	62
Mn-CN-TCNE	$MnC_{54}H_{24}N_{12}$	2225	2132	1/2 toluene, 1 methanol	47
Mn-CF_3-TCNE	$MnC_{54}H_{24}N_8F_{12}$	2202	2161	1 toluene, 2 methanol	44

* The yield is based on the amount of metal-free porphyrin used for the synthesis.

AC magnetic susceptibility χ_{AC} measurements were performed using a Lake Shore susceptometer, model 7225. Measurements of both components of $\chi_{AC} = \chi' - i\chi''$ were carried out as a function of temperature, frequency f, oscillating field amplitude H_{AC} and static magnetic field H_{DC}. Besides the fundamental susceptibility, higher harmonic signals χ_2 and χ_3 were detected at frequencies $2f$ and $3f$, respectively. DC magnetization measurements were obtained with the extraction method using the same instrument. In zero field cooling (ZFC) regime the sample was cooled in zero magnetic field, the field was switched on and the sample was measured on heating in this field. In field cooling (FC) regime the sample was cooled in field and measured in this field on heating.

A transmission electron microscope was used to inspect grains of the Mn-$OC_{14}H_{29}$-TCNE sample. Only shadows were observed but it was possible to state that grains had the form of thin bars with rounded edges. Typical dimensions were: 0.6 μm × 0.1 μm and thickness < 0.1 μm.

8.3 Results

Mn-$OC_{12}H_{25}$-TCNE is one of the substances earlier studied [5]. Studies of this substance were continued for a new sample. Figure 8.3a presents the temperature dependences of AC susceptibility obtained at zero static magnetic field H_{DC}. The maxima of χ' and χ'' components, observed at $T_c \approx 20$ K, are strongly frequency dependent, however, there is no frequency dependence from their right hand side. This feature is common for all substances studied in this work, which show the maximum of χ_{AC} near 20 K. The dependence on H_{AC} was also measured and appeared to be small (not shown). While χ' component decreased, the loss component χ'' increased with increasing H_{AC}. This H_{AC} dependence was observed mainly in the temperature region of the susceptibility maximum, as checked in the H_{AC} range of 1–20 Oe. According to this dependence the harmonics of the fundamental susceptibility are expected. They were, in fact, observed and are presented below for Mn-$OC_{10}H_{21}$-TCNE (see Fig. 8.11).

Figure 8.3b presents χ_{AC} vs. T plots obtained in a static magnetic field of 100 Oe. It is seen that both components of χ_{AC} decrease in the field approximately one order of magnitude and, what is most interesting, χ_{AC} shows the double structure. The upper part of the χ' peak near T_c is not more frequency dependent, however a frequency dependent anomaly emerges at lower temperatures, which is accompanied with a well separated χ'' component. This frequency dependence means that some relaxations occur in the sample, the nature of which is to be clarified in this work. The maximum of χ' shifts a little to higher temperatures together with its χ'' component as compared with the case of $H_{DC} = 0$. With increasing static field both anomalies separate further. The situation in H_{DC} of 5 kOe is similar to that of Mn-$OC_{10}H_{21}$-TCNE, see Fig. 8.4b.

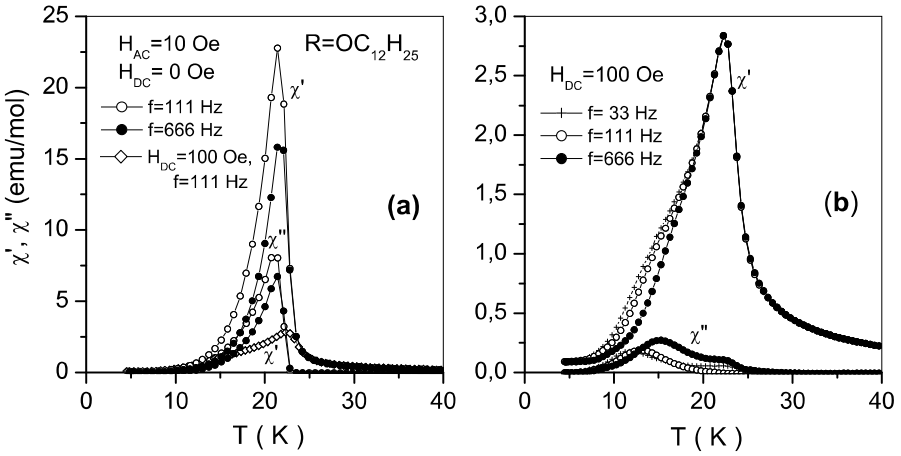

Fig. 8.3. Temperature dependences of AC susceptibility for Mn-$OC_{12}H_{25}$-TCNE at different frequencies in DC magnetic field equal zero (**a**) and 100 Oe (**b**)

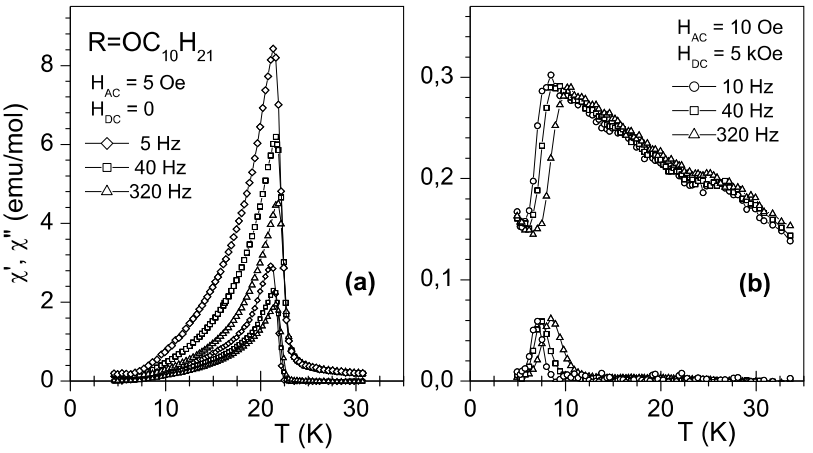

Fig. 8.4. Temperature dependences of AC susceptibility for Mn-$OC_{10}H_{21}$-TCNE at different frequencies in DC magnetic field equal zero (**a**) and 5 kOe (**b**). *Lower size curves* are χ''

In Fig. 8.4a the temperature dependences of AC susceptibility are shown for Mn-$OC_{10}H_{21}$-TCNE at zero H_{DC} and at three different frequencies. In Fig. 8.4b the same is shown for H_{DC} of 5 kOe. In Fig. 8.5 the temperature dependences of χ_{AC} are shown for several DC magnetic fields. It is seen that the peak of χ' splits (splitting of χ'' is hardly seen in the scale of figure) in static magnetic fields. Its right component shifts to higher temperatures, decreases with increasing H_{DC} and finally almost disappears in the scale of figure. The

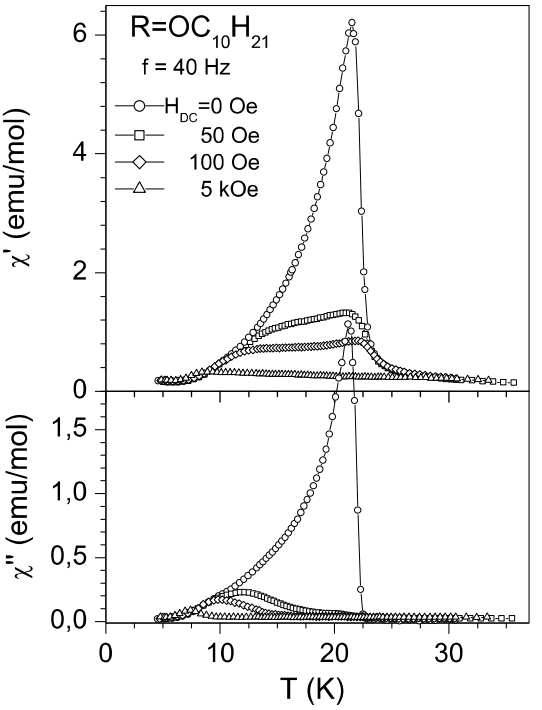

Fig. 8.5. Temperature dependences of AC susceptibility for Mn-$OC_{10}H_{21}$-TCNE at the frequency of 40 Hz in different DC magnetic field

left component also decreases but in lower degree and shifts to lower temperatures. This behavior is analogical to that observed for Mn-$OC_{12}H_{25}$-TCNE.

Such shifts in opposite directions with increasing static field were observed for many systems with ferromagnetic and spin glass transition, which was established, e.g., for $Eu_{0.54}Sr_{0.46}S$, by neutron diffraction, susceptibility and specific heat measurements [17]. Generally, the double maxima of AC susceptibility for these reentrant systems were observed at zero DC field but for $(Fe_{0.17}Ni_{0.83})_{75}P_{16}B_6Al_3$ [7] two peaks appeared only by the application of a small field.

In Fig. 8.6a the temperature dependences of AC susceptibility for Mn-$OC_{14}H_{29}$-TCNE are shown for different frequencies at $H_{DC} = 0$ and in Fig. 8.6b the same is shown for $H_{DC} = 50$ Oe. Here the double structure of AC susceptibility maximum is well seen already at $H_{DC} = 0$. Apart from the main anomaly at ~ 19 K a small anomaly occurs at ~ 8 K. However, on applying a DC field of 50 Oe the third anomaly emerges on the low temperature wing of the susceptibility maximum, as is seen from $\chi'(T)$ and $\chi''(T)$ dependences at different frequencies in Fig. 8.6b. With higher static magnetic field the frequency dependence near the maximum disappears, similarly as for

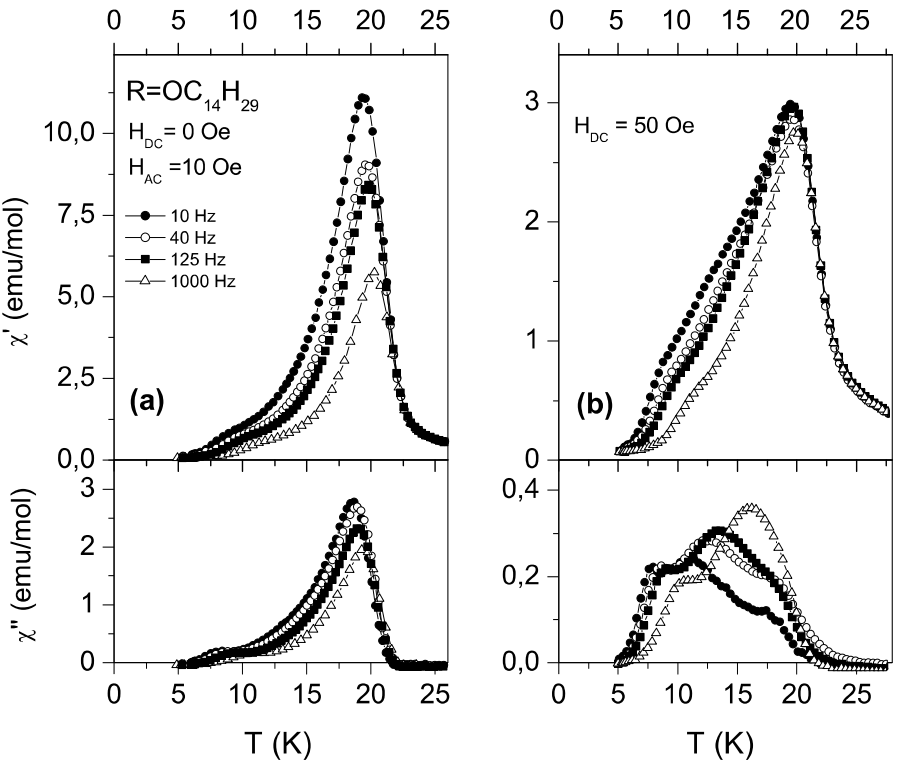

Fig. 8.6. Temperature dependences of AC susceptibility for Mn-$OC_{14}H_{29}$-TCNE at different frequencies in DC magnetic field equal zero (**a**) and 50 Oe (**b**)

Mn-$OC_{12}H_{25}$-TCNE, see Fig. 8.3b. The evolution of the susceptibility with DC magnetic field is shown in Fig. 8.7 for a frequency of 40 Hz. While the higher temperature susceptibility peak moves to the right, decreases in amplitude and finally almost disappears with increasing DC field, the anomaly, which appears in DC field, moves in opposite direction, similarly as observed for Mn-$OC_{10}H_{21}$-TCNE and Mn-$OC_{12}H_{25}$-TCNE. In DC field of 5 kOe two low temperature anomalies overlap and temperature dependence of AC susceptibility (see inset in Fig. 8.7) is nearly the same as shown in Fig. 8.4b for Mn-$OC_{10}H_{21}$-TCNE. Thus, the temperature dependences of AC susceptibility in applied DC magnetic field of 5 kOe are similar for Mn-$OC_{10}H_{21}$-TCNE, Mn-$OC_{12}H_{25}$-TCNE and Mn-$OC_{14}H_{29}$-TCNE. It should be noted, that these $\chi_{AC}(T)$ dependences, obtained on heating in DC field of 5 kOe do not differ, independently, whether they were obtained in zero field cooling (ZFC) or field cooling (FC) conditions.

In order to clarify the nature of the observed anomalies additional measurements were performed. In Fig. 8.8 temperature dependence of low field magnetization $M(T)$ for Mn-$OC_{14}H_{29}$-TCNE is shown. It was obtained dur-

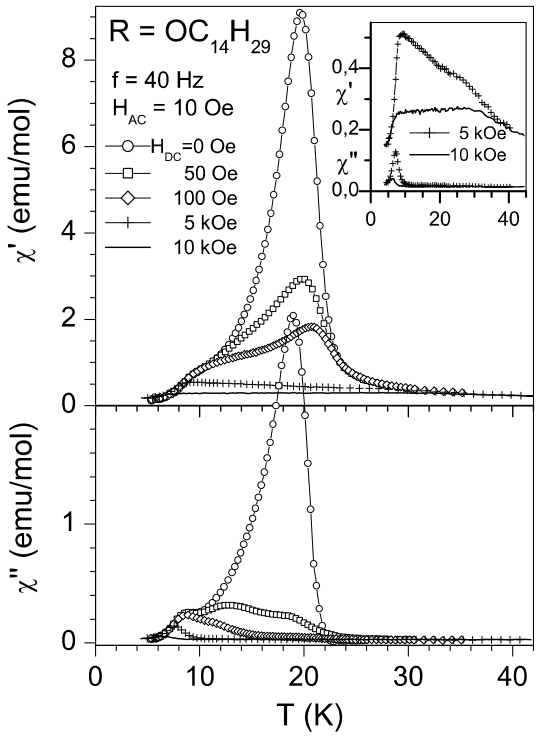

Fig. 8.7. Temperature dependences of AC susceptibility for Mn-$OC_{14}H_{29}$-TCNE at the frequency of 40 Hz in different DC magnetic field. *Inset* shows dependences for 5 and 10 kOe in magnification

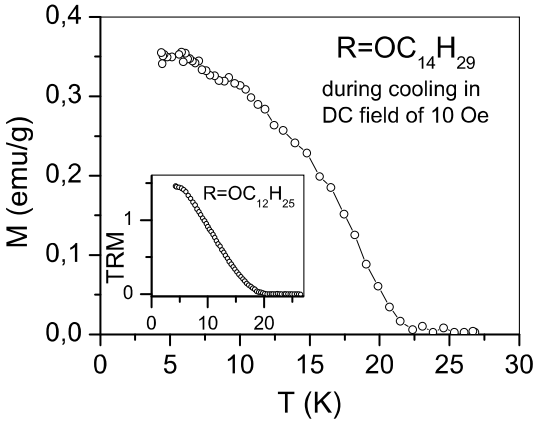

Fig. 8.8. Temperature dependence of magnetization for Mn-$OC_{14}H_{29}$-TCNE obtained by cooling in DC field of 10 Oe. *Inset* shows thermoremanent magnetization for Mn-$OC_{12}H_{25}$-TCNE obtained in zero DC field after cooling the sample in field of 200 Oe

ing cooling in DC field of 10 Oe. Similar, but noisy dependence was obtained in a smaller remanence field of the superconducting magnet of the experimental setup. As is seen in Fig. 8.8, a finite magnetization suddenly appears at 22 K indicating a phase transition but no another anomaly occurs at lower temperatures. Some anomaly at about 8 K was, however, expected from AC studies. It is recalled that an analogical $M(T)$ dependence was obtained from Mn-$OC_{12}H_{25}$-TCNE [5]. In the inset thermoremanent magnetization (TRM) vs. temperature is shown for this substance. It was obtained on heating the sample in zero DC field after cooling in field of 200 Oe. Measurements were performed at a rate of 1.5 K/min and 0.5 K/min, but no difference was observed and TRM persisted up to $T_c \approx 20$ K.

Measurements of magnetization vs. magnetic field were performed at different temperatures for all studied substances. It is already known from magnetization measurements in [5] that $M(H)$ dependences, obtained at low temperatures, show a hysteresis loop. Nevertheless, in order to be sure that substances are not antiferromagnetic in their ground state, it was purposeful to check whether magnetization is irreversible also at much smaller magnetic fields. To this end $M(H)$ dependence was measured for Mn-$OC_{12}H_{25}$-TCNE at 4.3 K with field increasing and decreasing in both directions in some small H range up to $H_{\max}$, then after heating the sample above 30 K the next $M(H)$ dependence was measured at 4.3 K in the increased H range and so on. The obtained product of coercive field H_c and remanent magnetization M_r is shown in Fig. 8.9. With small $H_{\max}$ the obtained loops are very thin, but their area is not equal zero. With increasing $H_{\max}$, the loops dramatically open at about 4 kOe becoming very wide. It is in agreement with the spin flop suggested in [18], which occurs in field $\sim$ 4 kOe at 4.2 K.

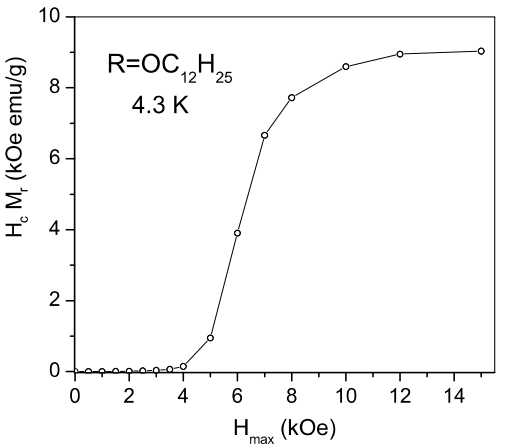

Fig. 8.9. Product of the coercive field and remanent magnetization as a function of the maximum value of magnetic field by measurements of hysteresis loops (see text)

The hysteresis loops were observed nearly up to T_c. In Fig. 8.10 a hysteresis loop, obtained at 16 K, is shown for Mn-$OC_{12}H_{25}$-TCNE. It is seen that magnetization at 16 K becomes reversible at fields somewhat greater than 0.5 kOe. Coercive field at 16 K equals 20 ± 1 Oe. The loop is narrowed in the middle. This means that magnetic field supports the ferromagnetic state near T_c in agreement with the earlier observation that T_c is enhanced by magnetic field.

It should be at last recalled, what concerns magnetization, that it is time dependent in magnetic field [18] and shows difference dependent on that whether the samples were measured in ZFC or FC conditions [5]. Such property can point at spin glass or ferromagnetic state with domain freezing. However, superparamagnetism with a blocking temperature at the maximum of ZFC magnetization is also possible.

Temperature dependences of AC susceptibility harmonics were measured and results for $H_{DC} = 0$ are shown in Fig. 8.11. In this figure fundamental, second and third harmonics, obtained for Mn-$OC_{10}H_{21}$-TCNE, are compared as a function of temperature. The interesting point is that the second harmonic is much greater than the third. This means that a spontaneous magnetization exists in the sample what is in agreement with the low field magnetization result (similar to that shown in Fig. 8.8.) Measurements of harmonics in small DC magnetic fields of 0, 46 and 200 Oe were performed for Mn-$OC_{12}H_{25}$-TCNE and for Mn-$OC_{14}H_{29}$-TCNE in DC field of 8 Oe. The magnitudes of harmonics strongly decrease with increasing DC field, but in 200 Oe the second harmonic for Mn-$OC_{12}H_{25}$-TCNE is still discernible. The forms of temperature dependences of harmonics signals are similar for all three substances with the second harmonic much greater than the third. No distinct anomalies of the second and third harmonic accompanied the anomaly of the fundamental

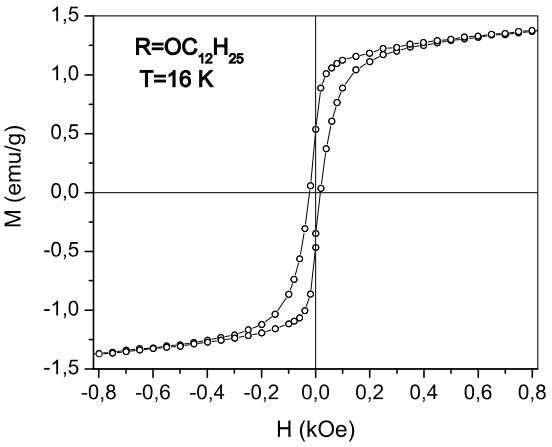

Fig. 8.10. Hysteresis loop of magnetization for Mn-$OC_{12}H_{25}$-TCNE obtained at 16 K

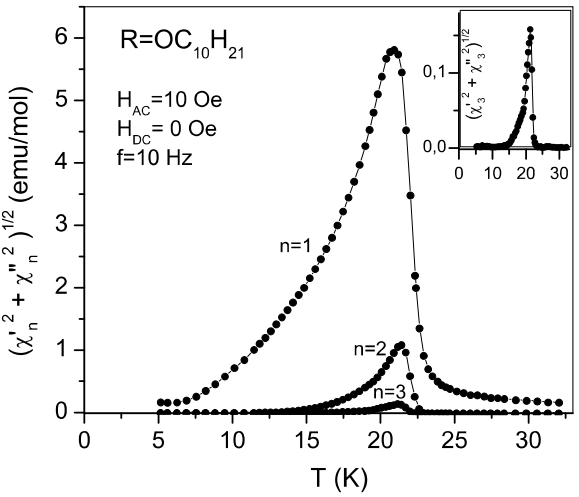

Fig. 8.11. Temperature dependences of magnitude of AC susceptibility harmonics for Mn-$OC_{10}H_{21}$-TCNE obtained without static magnetic field. $n = 1$ – fundamental, $n = 2$ – second, $n = 3$ – third harmonic. *Inset* shows the magnitude of third harmonic in magnification

AC susceptibility, which emerged in static magnetic fields. The lack of third harmonic anomaly questions the interpretation that reentrant spin glass transition takes place, because an appearance of such anomaly is expected by that transition [19, 20]. No harmonics at all were observed for Mn-$OC_{14}H_{29}$-TCNE at the anomaly of $\sim$ 8 K in zero DC field.

It was interesting to check whether a significant anomaly of AC susceptibility, observed at $\sim$ 8 K in a relatively strong magnetic field of 5 kOe (see Fig. 8.4b), is accompanied by harmonics. To this end measurements for Mn-$OC_{14}H_{29}$-TCNE were performed. However, no harmonics of fundamental AC susceptibility were found in DC field of 5 kOe in the whole temperature range.

The substance Mn-ortho-F-TCNE shows quite another behavior. Temperature dependences of χ_{AC}, obtained at $H_{DC} = 0$, are presented in Fig. 8.12. Here an anomaly appears at $\sim$ 8 K. This anomaly is strongly frequency dependent and the peak of χ'' moves as a whole with frequency on the temperature scale. Such frequency dependence is not characteristic for spin glass freezing but rather points at superparamagnetic relaxations. Nothing changes in static applied magnetic field, as checked for 10 Oe. It was also checked that the observed anomaly is not accompanied by harmonics. Presented $\chi_{AC}(T)$ plots, corresponding to $H_{DC} = 0$, are similar to that shown in Fig. 8.4b for Mn-$OC_{10}H_{21}$-TCNE, corresponding to $H_{DC} = 5$ kOe, except that no ferromagnetic transition is seen in Fig. 8.12. Also the weak anomaly of AC susceptibility for Mn-$OC_{14}H_{29}$-TCNE, observed at $\sim$ 8 K in $H_{DC} = 0$

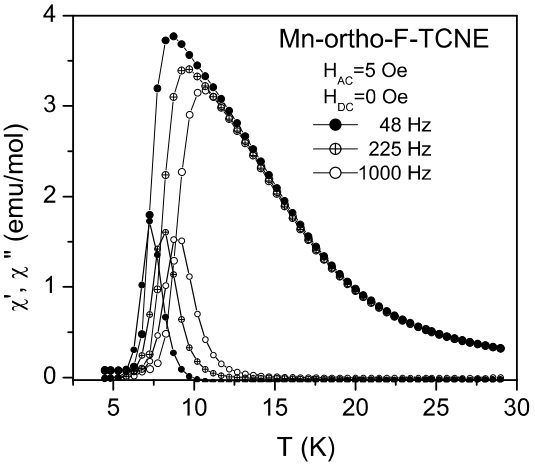

Fig. 8.12. Temperature dependences of AC susceptibility for Mn-ortho-F-TCNE at different frequencies and zero static magnetic field

(see Fig. 8.6) seems to be of the same kind. Magnetization, measured for Mn-ortho-F-TCNE in remanent field of the superconducting magnet, showed no anomaly as a function of temperature. However, at 4.2 K a $M(H)$ loop was observed. The hysteresis loop obtained at $T = 1.7$ K exhibits step at $H = 0$ on both branches, see [21]. Such steps are characteristic for magnetization tunneling and for polycrystalline material only at $H = 0$ can be observed. It can be concluded that all described behavior of Mn-ortho-F-TCNE originates from blocking of superparamagnetic segments of spin chains. The blocking phenomenon of such segments was reported by Gambardella et al. [12] as mentioned in the Introduction.

8.4 Discussion

The obtained results allow for construction of the model, which explains magnetic properties of the studied substances at low temperatures. The anomaly at $T_c \approx 20$ K is most likely the ferromagnetic transition, however, its strong frequency dependence may point both at partially glassy character of the ferromagnetic state and/or the presence of domains. Observation of harmonics in the vicinity of transition seems to be connected with multidomain structure of grains. In superposed static magnetic field greater than 200 Oe harmonics disappear, what can mean that grains become one-domain particles.

The AC susceptibility anomalies, which emerged in magnetic field seem to be connected with blocking of relaxing magnetic moments of some centers. The relaxing centers can be clusters, whose presence originates from disorder brought about by solvent molecules. In this disorder the local changes

of anisotropy direction (spin canting) occur. By dipolar interchain interactions this can cause ferromagnetism [22], which because of randomly canted spins would have partially glassy character. Because many spins would be unfavorably oriented the presence of frustrated spin segments of chains is expected. The ferromagnetic state created in this way would consist of an infinite percolating cluster with smaller clusters and spin segments of single chains being apart. While the infinite cluster would be responsible for the phase transition at $T_c \sim 20$ K, the smaller superparamagnetically relaxing clusters would show the blocking anomaly at lower temperature. This blocking seems to be signaled by the anomaly of AC susceptibility and also by a maximum of ZFC magnetization, as shown together in Fig. 6 of [5]. In stronger magnetic field, when the anisotropy barrier decreases, the blocking temperature also decreases. Moreover, magnetic chains become effectively decoupled, because interchain magnetic coupling energy is very small. Thus, $\chi_{\mathrm{AC}}(T)$ dependence approaches in the limit of high fields the blocking temperature for spin segments of single chains. To be sure, such FC and ZFC behavior as observed here could be explained by the presence of domains [23, 24], however, for Mn-CN-TCNE, which seems to show no ferromagnetic transition [5] also similar behavior was observed.

For Mn-ortho-F-TCNE there is no ferromagnetic transition, so only the blocking anomaly due to spin segments of single chains is observed at ~ 8 K. Instead, the anomaly observed at ~ 8 K for Mn-$OC_{14}H_{29}$-TCNE can originate from spin segments of uncoupled chains whose presence can result from a glassy character of material.

It should be noted that without canting the ferromagnetic state would be impossible in the discussed chain systems because dipolar interactions usually lead to antiferromagnetic structure. In fact, the substance [MnOEP][HCBD] (OEP = octaethylporphyrinato, HCBD = hexacyanobutadiene) having similar chain structure but no solvent (thereby without disorder) is antiferromagnetic with the Néel temperature $T_N = 20.5$ K [25].

The spin canted magnetic structure resulting from disorder corresponds to many axis anisotropy. However, a quite regular FM structure is also possible when two axis anisotropy is present. Such magnetic structure is shown in Fig. 8.13 in projection onto the plane perpendicular to the chains. This is an optimum structure for the ferromagnetism appearance, as obtained by Monte Carlo simulations [13] using a program based on Metropolis algorithm [26]. In these simulations the energy of anisotropy was assumed to be much greater than that of dipolar interactions between two nearest neighbor spins belonging to two nearest neighbor chains. The black circles in Fig. 8.13 denote the chains belonging to the smallest cluster with which such structure can be obtained. The optimum conditions for ferromagnetism are when both anisotropy axes are perpendicular to each other and to the chain axis. It does not play a role whether chains are in registry or out of registry or whether there is some distortion. A lattice distortion is even necessary as a reason for two axis anisotropy and is anticipated at low temperatures. The role of disorder in

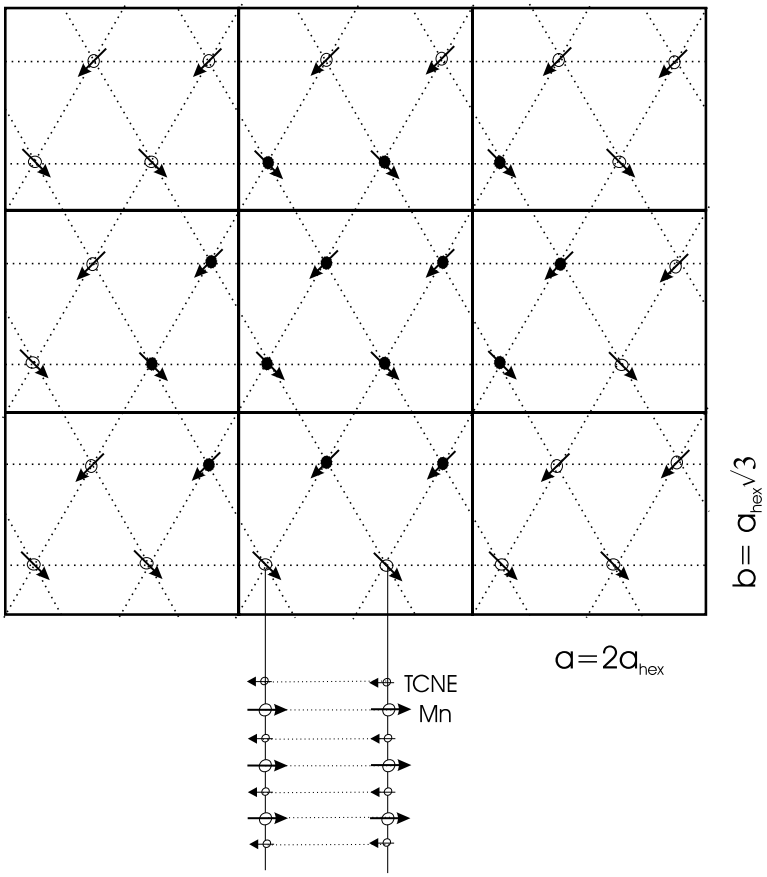

Fig. 8.13. Two-axis magnetic structure proposed for investigated substances shown in projection along chains. In the *bottom* an alignment of spins along chains is shown. See text

such structure would be to introduce some glassy character. The magnetic structure with two axis anisotropy is in agreement with theoretical predictions of Ostrovsky et al. [11] who estimates $T_c \sim 20$ K for a similar stripe-domain canted structure.

8.5 Summary

A number of porphyrin based molecular magnets $[MnR_4TPP][TCNE]\cdot$solvent with different substituents R was synthesized. The obtained substances have chain structure, in which the magnetic moments of Mn^{III}-ions are strongly antiparallelly coupled with magnetic moments of TCNE radicals creating one-dimensional ferrimagnetic systems. Magnetic properties of these sub-

stances were studied using magnetic AC and DC susceptibility technique. The substances with R = $OC_{10}H_{21}$, $OC_{12}H_{25}$ and $OC_{14}H_{29}$ showed one AC susceptibility anomaly in the form of a strong maximum at $T_c \sim 20$ K, but with superposed DC field the second anomaly emerged from this maximum on its low temperature side. Both anomalies showed different magnetic relaxations. This allowed to interpret the first anomaly as ferromagnetic phase transition and the second one as being a result of blocking of some clusters. The substance Mn-ortho-F-TCNE does not show the ferromagnetic transition (not knowing for the present why), thus only the low temperature anomaly is seen for this substance, even without the externally applied DC magnetic field. The blocking clusters in Mn-ortho-F- TCNE were identified as spin segments of chains.

Clusters as well as the glassy character of studied substances are due to disorder caused by solvent molecules. This disorder can simultaneously be a source of ferromagnetism, which arises by dipolar interchain interactions.

The second mechanism of ferromagnetism was proposed as originating by dipolar interchain interactions and two axis anisotropy. This mechanism leads to a regular magnetic structure, in which, however, some disorder is also present because of solvent molecules.

References

1. J.S. Miller, J.C. Calabrese, R.S. McLean, A.J. Epstein: Adv. Mater **4**, 498 (1992)
2. E.J. Brandon, D.K. Rittenberg, A.M. Arif, J.S. Miller: Inorg. Chem. **37**, 3376 (1998)
3. K. Falk: Ph.D. Thesis, Darmstadt University of Technology, Darmstadt (2002)
4. K. Griesar, M.A. Athanassopoulou, A. Soto Bustamante, Z. Tomkowicz, A.J. Zaleski, W. Haase: Adv. Mater. **9**, 45 (1997)
5. M. Bałanda, K. Falk, K. Griesar, Z. Tomkowicz, W. Haase: J. Magn. Magn. Mater. **205**, 14 (1999)
6. H. Winter, M. Keleman, E. Dormann: Mol. Cryst. Liq. Cryst. **273**, 111 (1995)
7. M.B. Salamon, K.V. Rao, Y. Yeshurun: J. Appl. Phys. **52**, 1687 (1981)
8. S.M. Bhagat, J.A. Geohegan, M.L. Spano: J. Appl. Phys. **52**, 1741 (1981)
9. J. Nogués, K.V. Rao: J. Magn. Magn. Mater. **135**, L11 (1994)
10. B.H. Verbeek, G.J. Nieuvenhuys, H. Stocker, J.A. Mydosh: Phys. Rev. Lett. **40**, 586 (1978)
11. S. Ostrovsky, W. Haase, M. Drillon, P. Panissod: Phys. Rev. B **64**, 134418 (2001) and Chap. 4 in this book
12. P. Gambardella, A. Dallmeyer, K. Maiti, M.C. Malagoli, W. Eberhardt, K. Kern, C. Carbone: Nature **416,** 301 (2002)
13. F. Mascarenhas, K. Falk, P. Klavins, J.S. Schilling, Z. Tomkowicz, W. Haase: J. Magn. Magn. Mater. **231**, 172 (2001)
14. A.D. Adler, F.R. Longo, R.D. Finarelli, J. Goldmacher, J. Assour, L. Korsakoff: J. Org. Chem. **32**, 476 (1967)
15. R.D. Jones, D.A. Summerville, F. Basolo: J. Am. Chem. Soc. **100**, 4416 (1978)

16. D.A. Summerville, T.W. Cape, E.D. Johnson, F. Basolo: Inorg. Chem. **17**, 3297 (1978)
17. H. Maletta: J. Appl. Phys. **50**, 7312 (1979)
18. M. Bałanda, K. Falk, K. Griesar, Z. Tomkowicz, T. Wasiutyński, W. Haase: Mol. Cryst. Liq. Cryst. **335**, 133 (1999)
19. A. Gencer, I. Ercan: Int. J. Mod. Phys. B **12**, 143 (1998)
20. S. Mukherjee, R. Ranganathan, S.B. Roy: Phys. Rev. **50**, 1084 (1994)
21. K. Falk, M. Bałanda, Z. Tomkowicz, F. Mascarenhas, J.S. Schilling, P. Klavins, W. Haase: Polyhedron **20**, 1521 (2001)
22. C.M. Wynn, M.A. Girtu, K-I. Sugiura, E.J. Brandon, J.L. Manson, J.S. Miller, A.J. Epstein: Synth. Met. **85**, 1695 (1997)
23. P.A. Joy, S.K. Date: J. Magn. Magn. Mater. **218**, 229 (2000)
24. P.S.A. Kumar, P.A. Joy, S.K. Date: Physica B **269**, 356 (1999)
25. A.J. Epstein, J.S. Miller: Synth. Met. **80**, 231 (1996)
26. P. Lacorre, J. Pannetier: J. Magn. Magn. Mater. **71**, 63 (1987)

9

Dipolar Interaction and Three-dimensional Magnetic Ordering of some Chain and Layered Compounds

S. Ostrovsky, W. Haase, M. Drillon and P. Panissod

9.1 Introduction

The field of molecule-based magnets involves the design and complex study of molecular compounds that exhibit a spontaneous magnetic ordering below a critical temperature. During the last two decades there is an increasing interest in the synthesis and investigation of this type of complexes as shown by a growing number of publications and review articles (see for example [1, 2]). As a class, molecule-based magnets possess many properties of organic polymeric compounds combined with the magnetic properties of classical bulk magnets that includes low specific density, flexibility, optical transparency, compatibility with polymers for composites, solubility, biocompatibility, high magnetic susceptibility etc. Many of these nonmagnetic characteristics are not available with conventional metal oxide-based magnets but are very important technological attributes. Therefore molecular magnetism is one of the most challenging research areas in the development of new technologies. For example, among the possible applications there are high-density information storage, magneto-optical devices, magnetic switches etc. Research interest in this field is motivated by the need for a better understanding of the fundamental principles that govern magnetic behavior. To synthesize new improved molecular magnetic materials with specific magnetic and electronic properties a deeper insight into the relation between the molecular structures and the macroscopic physical properties is required.

Magnetic ordering is not an intrinsic property of isolated molecules, and it requires cooperativity over the whole 2D or 3D system. To achieve bulk magnetic behavior for a molecular system some intermolecular interactions must be present in at least two (but preferably three) directions. The nature and paths of this coupling and their dependence on structural modifications of compounds are the subject of much investigations. Molecule-based magnets exhibit a wide variety of bonding and structural motifs. These include isolated molecules (zero dimensional, 0D), and compounds showing extended bonding within chains (1D), within layers (2D) and within 3D network structures. If

spins of the neighboring ions in these motifs occupy orthogonal orbitals it results in ferromagnetic coupling and can lead to ferromagnetic ordering with a large value of bulk magnetic moment. However such configurations leading to ferromagnetism are rather difficult to obtain. It is even more difficult to realize it along the three directions of space. Because of such strong tendency for spins on adjacent sites to couple antiferromagnetically the common way to obtain materials with a net moment and high critical temperature T_C values is to build ferrimagnetic arrays, chains or planes, with at least two uncompensated spin sub-networks. However, within the crystal, built from these arrays, it is still quite seldom to obtain ferromagnetic coupling between the motifs themselves so that the 3D system is usually antiferromagnetic. This is why an alternative way to prepare bulk magnets has been suggested: by introducing long organic ligands between the motifs the antiferromagnetic interchain or interlayer exchange can be made negligible, leading to the coupling being dominated by the weaker – but potentially ferromagnetic – dipole-dipole interactions in order to achieve bulk magnetic ordering. Even if the dipolar interaction leads to antiferromagnetic coupling between the motifs it is still possible to tailor the single ion anisotropy so that the net moments of the motifs are not collinear [3]. In such a way a canted antiferromagnet can be synthesized with a net bulk moment that can be up to 0.7 times that of the motifs if a 90° canting angle is achieved. As will be seen, by incorporating large exchange in one or two directions, sizeable T_C's can be achieved despite the weakness of the dipole-dipole interactions between chains or layers.

Thus, in most cases, 3D magnetic ordering in molecule-based magnets is a result of more than one mechanism: ferro- or ferrimagnetic spin coupling within a chain or magnetic layer and dipolar interactions between these motifs. From the practical application viewpoint, the pure dipolar interaction is essentially an academic problem as long as only ionic/atomic moments are involved. Even for rare earth compounds with the largest ionic moment the expected dipolar ordering temperature does not exceed a few Kelvin. The situation changes when interacting subunits involve not individual atomic moments but magnetic assemblies comprising a large number of strongly exchange coupled atomic moments. The magnetic ordering temperature for such systems can be much higher than in the case of isolated ions. Indeed Villain and Loveluck [4] suggested early that, for weakly coupled chains or layers, the long-range ordering is achieved when the thermal energy is comparable to the interaction energy between correlated spin blocks of size $\eta(T)$ $(= \xi$ for chains and ξ^2 for layers), where $\xi(T)$ is the correlation length resulting from the exchange interaction within the motifs. Consequently the expected ordering temperature is η times larger than would be deduced from the value of the mere dipolar interaction between single spins.

In this chapter we demonstrate that dipolar interaction can indeed be responsible for the 3D ordering in magnetic chain and layered compounds at rather high critical temperature. Since a review on the research on molecular magnets is out of the scope of the paper, we shall only present two selected

examples of chain and layered compounds in Sect. 9.2. Then, in Sect. 9.3, we shall describe the modified molecular field model that has been used to calculate successfully the critical temperature of these compounds.

9.2 Selected experimental results

9.2.1 Mn-porphyrin based charge-transfer complexes

A large number of already known molecule-based magnets comprising different types of chains have been reported so far. In 1D compounds, the ferrimagnetic chains represent probably the most promising systems, since they are characterized by a net magnetization and may exhibit strong short-range spin correlations. An important class of chain systems is the family of Mn-porphyrin based charge-transfer complexes, [Mn^{III}(TPP)][TCNE] (TPP is tetraphenylporphyrin, TCNE is tetracyanoethylene) [5]. The schematic structure of the chain is presented in Fig. 9.1. Detailed investigations [6] identified an alternating chain structure with Mn^{III}-porphyrin cations bound to TCNE anions and solvent molecules per chain unit. Magnetic moments of cations ($S_{Mn} = 2$) and anions ($S = 1/2$) are strongly antiferromagnetically coupled. Recently, a large number of papers appeared focusing on the magnetic properties of Mn-porphyrin based complexes showing similar magnetic behaviors [7–9]. Over a wide temperature range the magnetic properties are well dominated by the antiferromagnetic interaction between Mn^{III} and $[TCNE]^-$ radical giving 1D ferrimagnetism (Fig. 9.2). The temperature T_m, at which the characteristic minimum of χT occurs, indicates that the exchange interaction along the chain is very strong, typically of the order of $k_B T_m$. Upon decreasing temperature, magnetic properties deviate from the ferrimagnetic

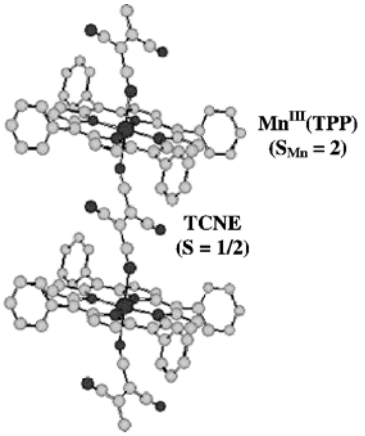

Fig. 9.1. Schematic structure of [Mn^{III}(TPP)][TCNE]

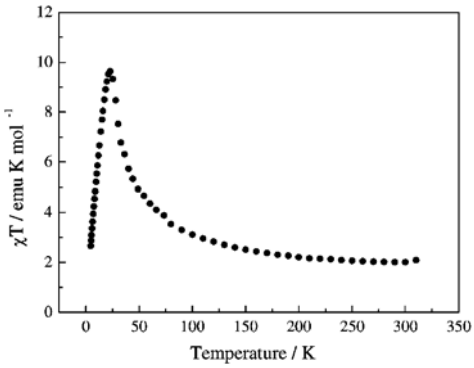

Fig. 9.2. Magnetic properties of Mn-OC_{10}-TCNE (reproduced from [10])

chain model, and at some temperature a sudden drop in χT occurs. It is well known that an isolated linear chain will not order by itself above absolute zero. Besides the intra-chain, some coupling between the chains should be present to provide 3D ordering at a finite temperature. To minimize the inter-chain exchange interactions the long alkoxy chains R=OC_nH_{2n+1} (with $n = 10$–14) in para-position of the phenyl groups of porphyrin were used [11–15]. Although the distance between magnetic chains is increased up to 31 Å, the ordering temperature is not significantly affected, T_C varying from 21.7 for $n = 10$ to 20.5 for $n = 14$. The AC susceptibility data, showing an out-of-phase signal (Fig. 9.3), and the large coercive fields observed at low temperature confirm the stabilization of a ferromagnetic state. The nature and paths of this ordering are of great interest. Because of large inter-chain distances (more than 20 Å) the superexchange interaction can be discarded. The electrostatic exchange interaction is well known to vanish extremely rapidly with the distance between metal centers, crudely as $J \sim r^{-n}$ with $n = 10$ to 12 [16, 17]. So

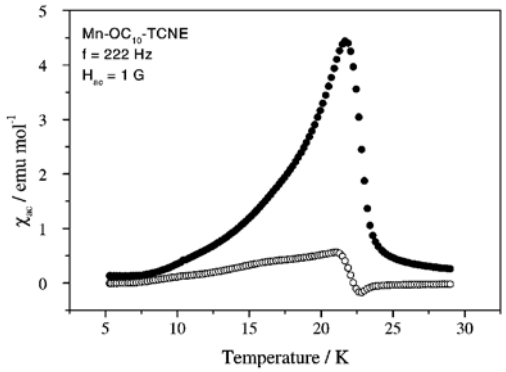

Fig. 9.3. A.C. susceptibility of Mn-OC_{10}-TCNE (reproduced from [10])

for molecule-based compounds the intermolecular exchange interactions are shown to be tenuous for distances larger than 10 Å, except when π-electron ligands are involved in the exchange process [18, 19].

Therefore, in the absence of obvious inter-chain exchange pathways, the classical dipolar interaction together with the single-ion anisotropy were proposed to be responsible for the bulk magnetic ordering in this class of compounds [20–22]. Due to the presence of two inter-chain separations, Wynn and coworkers deduced that the interaction is ferromagnetic (F) in one direction (along the shortest inter-chain distance) and antiferromagnetic (AF) in the second direction. Hence, in the absence of local anisotropy, the resulting system would be antiferromagnetic. In order to explain the existence of a net magnetic moment in the system the presence of single ion anisotropy is needed. The authors invoked a canting of the spins due to the presence of Mn^{III} single ion anisotropy resulting in a *canted antiferromagnet* (or *weak ferromagnet*) [3]. The strength of the inter-chain dipolar interaction was estimated from the point dipole model with spins in registry between neighboring chains. The interaction strength is typically a few mK for the most favorable cases. In order to explain the much higher observed T_C the authors have used the relationship developed for anisotropic exchange interaction [23]:

$$k_B T_C = 4S\,(S+1)\,[J_{intra} J_{inter}]^{1/2}\,, \tag{9.1}$$

where J_{intra} is the strong in-chain exchange interaction and J_{inter} the weak dipolar interaction along the transversal directions. The resulting T_C's ($\sim$ 8 K) compare favorably with those observed experimentally. This crude model clearly emphasizes that bulk magnetic ordering with substantial critical temperature can be achieved in chain systems due to dipolar interactions. However one can question the applicability of a quantitative approach developed for an exchange interaction between chains to the case of the dipolar interaction. Indeed, in this latter case, the strength of the inter-chain coupling is not that computed for individual spins but between correlated spin blocks. Moreover this strength depends on the temperature as does the in-chain correlation length.

9.2.2 Hydroxide-based layered compounds

The hydroxides $M(OH)_2$ (M = Co, Ni or Fe) may be viewed as prototypes of layer-like systems. They consist of regular 2D triangular arrays of metal ions co-ordinated by hydroxyl ligands, which form a sandwich structure. The parent compounds $M_2(OH)_3X$ (M = Co, Ni, Cu) where the exchanged species $X = NO_3^-$ or OAc^- is linked to the metal ion, exhibit a similar structure [24]. This structure can be described as $[M_2(OH)_3]$ layers held together through hydrogen bonds involving the exchanged anion X^-. The in-plane metal-metal distances are very similar for the different compounds (about 3.15 Å). The distance between metal-based layers can be controlled by the extension of

the organic anions which play the role of spacers. For example for very large ligands, such as alkyl sulfate or carboxylate, the interlayer spacing is determined by the length of the alkyl chain of the organic anion and is in the range 9 to 40 Å [25, 26]. The schematic layer structure of this class compounds is shown in Fig. 9.4.

The magnitude and the F or AF nature of the in-plain coupling are shown to depend closely on the organic radical and the structure of the hydroxide layer. For instance, the compounds $Cu_2(OH)_3(C_mH_{2m+1}CO_2) \cdot zH_2O$ exhibit two structural varieties α and β which only differ by the thickness of the inorganic layer [27, 28]. The β polymorphs order ferromagnetically, even for very large basal spacing, while α ones show the classical features of 2D antiferromagnets. Antiferromagnetic in-plane correlations result in an AF 2D short range order and no 3D order is observed. In the case of F in-plane correlations, the situation depends on the interlayer spacing. For small spacing (less than 10 Å) the interlayer interactions, dominated by superexchange through hydrogen bonds, stabilize an AF 3D order between layers. For large spacing, the compounds exhibit a spontaneous magnetization in zero field below an ordering temperature ranging from 21.2 to 19 K for interlayer distances varying from 28.8 Å to 40.4 Å. Such large F ordering temperatures and their weak dependence on the interlayer spacing cannot be explained by superexchange interaction between the layers.

The magnetic behavior of Cu(II) alkyl carboxylate complexes is representative for the long spacer compounds. Figure 9.5 illustrates variable temperature DC measurements for $m = 10$. The magnetization curve increases strongly on decreasing temperature. The occurrence of a long-range magnetic state is confirmed by an out-of-phase (χ'') signal, and a hysteretic effect at low temperature ($H_C = 1500$ Oe at 2 K). Both the magnitude of the net magnetization and its variation in high fields point towards a ferrimagnetic or a non-collinear configuration of the Cu(II) spins. Another characteristic feature is the presence of a broad minimum in the temperature dependence of $\chi T\,(T)$, well above T_C. This thermal behavior is very well approximated by

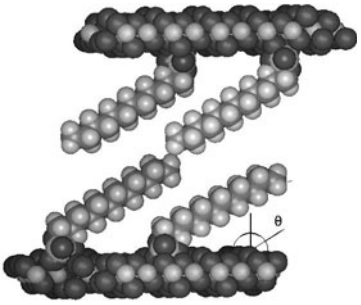

Fig. 9.4. Schematic layer structure of hydroxide-based compounds (reproduced from [30])

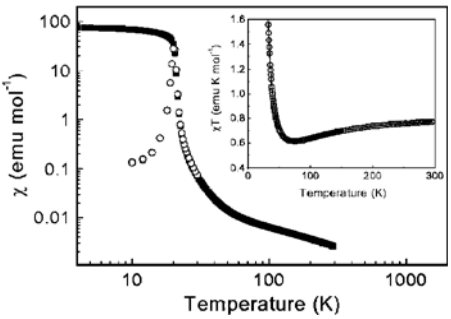

Fig. 9.5. Magnetic behavior of the Cu(II) alkyl carboxylate complex for $m = 10$ (reproduced from [30])

a double exponential law $C_1 \exp(\alpha J/k_B T) + C_2 \exp(\beta J/k_B T)$ [28]. The driving interaction, responsible for the initial decay of χT is antiferromagnetic one ($\alpha J/k_B = -40.47\,\mathrm{K}$). It is attributed to the dominant in-plane interaction. Conversely, the low temperature behavior of χT is dominated by the second term ($\beta J/k_B = 126.8\,\mathrm{K}$) that is appropriate for a 2D Heisenberg ferromagnet [29]. Note that the sum $C_1 + C_2 = 0.807$ is the high temperature Curie constant for two Cu(II) ions.

It was already pointed out that, for such large spacing, the direct exchange between unpaired electrons in adjacent layers becomes negligible. Due to the nature of the chains the spin polarization effect is also negligible. Nevertheless, the compounds exhibit a spontaneous magnetization and a characteristic hysteresis cycle that indicate long-range magnetic order. Unlike in case of chain compounds, for which 1D ordering is not allowed above 0 K, the question arises in layered compounds of the dimensionality of this magnetic order. Indeed, Ising-like anisotropy may promote 2D long-range ordering, and the weak dependence of the critical temperature on the layer spacing could be considered as an evidence for 2D rather than 3D ordering. However, owing to the large hysteretic effects, characteristic of bulk magnets, 3D ordering has to be considered. In order to know more about the nature of the phase transition, these systems have been studied in the framework of a "generalized scaling" theory [30]. A spectacular crossover of the F component to the susceptibility from a 2D to a 3D regime is evidenced by the Arrhenius plot $\log(\chi T)$ vs. $1/T$ (Fig. 9.6). At high temperature the exponential regime $C_2 \exp(\beta J/k_B T)$, characteristic of a 2D Heisenberg system, is evidenced by a straight line down to $T \sim 30\,\mathrm{K}$. Upon further reduction of the temperature a sudden departure from linearity occurs and the system obeys the power law $\chi T = 0.40\,(1 - 21.05/T)^{-1.36}$ with a critical exponent characteristic of a 3D regime and $T_C = 21.05\,\mathrm{K}$. Therefore, in order to explain the occurrence of this 3D magnetic ordering in the layer compounds with very large interlayer spacing the influence of through space dipolar interaction has to be considered.

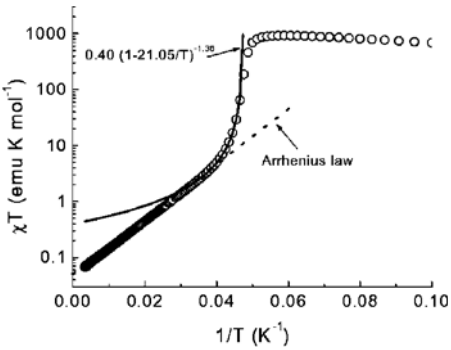

Fig. 9.6. Magnetic data for Cu(II) alkyl carboxylate complex ($m = 10$) as χT vs. $1/T$ (reproduced from [30])

9.3 Model for the dipolar interaction between ferrimagnetic chains or layers

As mentioned above the presence of exchange interaction within the chains or the layers implies that the spins are correlated to some extent and behave as spin blocks the size of which increases with decreasing temperature. Basically the dipolar energy reads as $\langle\mu\rangle^2/r^3$ where $\langle\mu\rangle$ is the thermal average of the individual moment and r the average distance between the moments. When the spins are correlated in blocks containing η individual spins the dipolar energy between the spin blocks becomes $\langle\eta\mu\rangle^2/\eta r^3$ i.e. η times larger than between individual spins. Following the remark of Villain and Loveluck [4] the 3D ordering temperature due to the dipolar interaction between the motifs can be estimated as

$$k_B T_C \approx \eta\,(T_C)\,|e_{dip}\,(T_C)|\ , \tag{9.2}$$

where e_{dip} is the dipolar energy computed for the most stable spin configuration and using the thermal average value of the individual moments at T_C, while η is the number of correlated spins at T_C. Note that (9.2) involves the same intra-motif exchange interaction (through η) and inter-motif interaction (through e_{dip}) as (9.1), but the second approach takes now explicitly the correlation effects into account.

This simple estimation of the ordering temperature due to dipolar interaction between chains has been first used for the ferrimagnetic chain compound $\mathrm{Mn}^{II}(\mathrm{hfac})_2\mathrm{NITR}$ built of spin-5/2 manganese alternating with spin-1/2 radicals along the chains [31]. However the authors did not attempt to solve the implicit equation for T_C: presumably they used the experimental T_C value to estimate the second term. Considering the crude nature of the model a quite good agreement between theoretical and experimental T_C value was obtained.

In the more realistic approach proposed here after for chain and layer compounds the implicit equation (9.2) for T_C is solved within a molecular field

approximation to compute e_{dip} and using the relevant theoretical expressions for the correlation length in an isolated chain or an isolated layer (see also [32, 33]). The main idea of the model is that, within the 1D or the 2D motifs where exchange coupling dominates, the correlation length diverges exponentially at $T = 0$ and so does the actual dipolar interaction between the motifs. Consequently the condition for magnetic ordering (9.2) is met at a much higher temperature than could be postulated from the mere Curie law increase of the average paramagnetic moments. This remark holds in all cases except for chains where the exchange coupling is purely isotropic (Heisenberg like): in this case the divergence of the correlation length follows a much slower power law.

9.3.1 Chain compounds with very large interchain spacing

We consider an assembly of 1D ferrimagnetic chains. Each chain is composed of alternating spins $S_A = 2$ and $S_B = 1/2$ coupled by AF exchange interaction between nearest neighbors only. All chains are assumed to be parallel and equally spaced, resulting in a 3D lattice with a hexagonal (triangular) structure (Fig. 9.7). The distance between the neighboring chains is large enough to neglect any superexchange mechanism between spins of adjacent chains.

The magnetic behavior of the 3D assembly of chains is considered in two steps. (i) We regard the isolated ferrimagnetic chain as dominated by the exchange interaction. The behavior of this chain at a given temperature can be described using a correlation length ξ that diverges at $T = 0$ K. We assume that this correlation length is determined by the large in-chain exchange only and takes the same value and the same temperature dependence for the chain assembly as for the isolated chain. (ii) The critical temperature of the possible 3D ordering as well as its ground state configuration are determined by dipole–dipole interactions between blocks of correlated spins (superspins) from different chains.

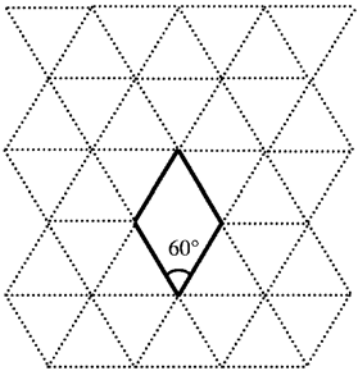

Fig. 9.7. Hexagonal structure of Mn-Porphyrin-based magnets (section perpendicular to the chain direction)

If the single-ion anisotropy is negligibly small, the isolated ferrimagnetic chain is described by the isotropic exchange hamiltonian

$$H = -J \sum_i (\mathbf{S}_{2i-1}\mathbf{S}_{2i} + \mathbf{S}_{2i}\mathbf{S}_{2i+1}), \tag{9.3}$$

where J (< 0) is the exchange constant between nearest neighbors and the spin operators $\mathbf{S}_i$ with odd and even subscripts refer to S_A and S_B respectively. The approach for solving such a one-dimensional linear chain is to consider a ring with a limited number of spin pairs, n. The magnetic behavior of this system can be computed from the matrix diagonalization technique. To simulate the magnetic behavior of the infinite chain, one has to increase the number of links n and to extrapolate the calculated susceptibility curve to $n \to \infty$ [34]. After such extrapolation, it is shown that the behavior of the – (1/2–2) – ferrimagnetic Heisenberg chain can be well described by the simple expression [35]

$$\chi T = P_1 \left(\frac{|J|}{k_{\mathrm{B}} T} \right)^a + 3.375 \exp \left(\frac{P_2 |J|}{k_{\mathrm{B}} T} \right), \tag{9.4}$$

where $P_1 = 1.812$, $P_2 = -0.948$, and $a = 1.78$. In the high-temperature limit, the system behaves as a paramagnetic mixture of spins $S_A = 2$ and $S_B = 1/2$, as pointed out by the prefactor of the exponential, corresponding to the sum of the Curie constants. With temperature decreasing, the χT product passes through a minimum and then diverges. At low temperature, the chain can be regarded as an assembly of correlated pairs ($S_A - S_B$), where, within the correlation length ξ, all S_A spins are oriented in one direction and all S_B in the opposite one. Upon decreasing temperature, the number of correlated pairs becomes larger and larger. For the $(1/2 - 2)$ ferrimagnetic chain under consideration, this number and the magnetic susceptibility are related through

$$n = \frac{32}{9g^2} \chi T \,, \tag{9.5}$$

where g is the Lande factor and χT is given by (9.4). Hence, the correlation length eventually becomes infinity only at $T = 0$.

Equations (9.4) and (9.5) allow us to fully describe the behavior of the isolated $(1/2 - 2)$ ferrimagnetic Heisenberg chain in terms of correlation length at some given temperature. The exchange parameter J is obtained from the high-temperature magnetic data where the system is well described by the isolated chain model. Assuming that this parameter is temperature independent, one can compute the magnetic properties of the single chain as well as the correlation length ξ at low temperature where 3D ordering occurs. Accordingly, each chain is considered as a set of spatially distributed superspins, the neighboring superspins being oppositely directed (Fig. 9.8). In the 3D assembly of chains, each superspin interacts with all other superspins through the dipolar interaction. The energy of this interaction can be calculated as follows

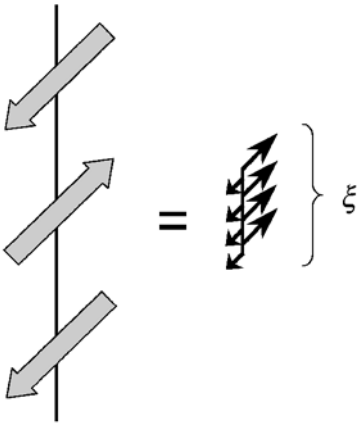

Fig. 9.8. Ferrimagnetic chain as a set of spatially distributed superspins

$$E_{dip} = \mu_B^2 g^2 \sum_{i \in CS} \sum_{j \in OS} \frac{1}{r_{ij}^3} \left[\mathbf{S}_i \mathbf{S}_j - \frac{3\left(\mathbf{S}_i \mathbf{r}_{ij}\right)\left(\mathbf{S}_j \mathbf{r}_{ij}\right)}{r_{ij}^2} \right] , \tag{9.6}$$

which takes into account the spatial extension of the spin blocks that are assumed to be of equal length ξ. The summation on i extends over all individual spins in the central superspin (i.e. E_{dip} takes the value of ηe_{dip} in (9.2)). The summation on j includes all moments in other superspins. Because of the long range of dipolar interactions this summation is performed over distances proportional to ξ, such that the value of the calculated energy has converged within 0.001%.

The energy in (9.6) depends upon the correlation length (hence on temperature) and on the spatial orientation of the interacting spins. The ground state spin configuration for a given correlation length can be obtained by energy minimization. The perfect spin alignment corresponding to this ground configuration occurs only at $T = 0$. At finite temperature other configurations acquire some nonzero probability but a predominant orientation exists. So, in order to get a picture of the critical region where the transition to long-range order takes place, we use a molecular-field approach where orientation and spatial fluctuations are taken into account through the thermal average of the moments. It must be noted that this approach differs from the usual molecular-field approximation in the fact that correlations along the chains are taken into account. As a consequence, the temperature dependence of the molecular field arises not only from the Curie-low variation of the magnetization but also from the coupling factor (the double sum in (9.6)) that varies coarsely as $\xi(T)$.

The expected variation of the spontaneous magnetization $\langle \mu \rangle / \mu$ as a function of temperature can be computed by solving a self-consistent set of equations. The molecular field is given by the dipolar energy (9.6) as a function of the thermal average of the superspin moment, while the thermal variation of this last is given by the classical Langevin function

$$\frac{\langle\mu\rangle}{\mu} = \left[\coth(x) - \frac{1}{x}\right], \tag{9.7}$$

where

$$x = \frac{\langle\mu\rangle}{\mu}\frac{E_{dip}(T)}{k_{\mathrm{B}}T}.$$

E_{dip} in (9.6) is calculated for the full moment at 0 K, therefore the thermal dependence of the moments is introduced as $\langle\mu\rangle/\mu$ in the expression of x. By solving numerically (9.6) and (9.7) the ground configuration and the thermal variation of the spontaneous magnetization can be found. If one is interested only in the critical temperature at which 3D ordering occurs, (9.7) can be linearized around $\langle\mu\rangle = 0$, which results in the implicit equation

$$T_{\mathrm{C}} = \frac{E_{dip}(T_{\mathrm{C}})}{3k_{\mathrm{B}}}. \tag{9.8}$$

Consider now a strong local anisotropy, with an easy axis normal to the chain direction, so that the behavior of the ferrimagnetic chain system may be described by the Ising hamiltonian. The properties of this ferrimagnetic chain have been solved by the transfer-matrix technique [36]. The final expression for the $(1/2-2)$ chain can be very well approximated from the sum of two Arrhenius-like contributions

$$\chi T = P_1 \exp\left(\frac{P_2|J|}{k_{\mathrm{B}}T}\right) + (3.375 - P_1)\exp\left(\frac{P_3|J|}{k_{\mathrm{B}}T}\right), \tag{9.9}$$

where $P_1 = 0.4837$, $P_2 = 2.14146$, and $P_3 = -1.36585$. The number of correlated pairs in a superspin as a function of temperature can be calculated as before using (9.5) where χT is now given by (9.9). The thermal average of the superspin moment in the case of Ising chain behaves as hyperbolic tangent, so that the final expression for T_C differs from (9.8) and has the following form:

$$T_{\mathrm{C}} = \frac{E_{dip}(T_{\mathrm{C}})}{k_{\mathrm{B}}}. \tag{9.10}$$

In the next step the proposed model of quantum chains coupled through dipolar interactions has been compared to experimental results by focusing on the Mn-porphyrin-based magnets with very large interchain spacing [11–15]. The crystal structure of all investigated compounds indicates a hexagonal packing of the chains. The in-chain distance between Mn and the center of the neighboring $[\mathrm{TCNE}]^-$ radical is about 5 Å for all complexes. The interchain spacing d, ordering temperatures and exchange parameters obtained from high temperature magnetic data are summarized in Table 9.1.

For a simple description of these systems, we consider in what follows the picture of the chain projections whose base is a rhombus with an angle of 60°.

Table 9.1. Experimental data of Mn-porphyrin-based magnets (reproduced from [32])

Complex	d (Å)	T_C(K)	J (cm^{-1})	
			Heisenberg	Ising
Mn-OC_{10}-TCNE	21.1	21.7	−81	−46
Mn-OC_{12}-TCNE	30.8	22.0	−123	−70
Mn-OC_{14}-TCNE	31.2	20.5	−103	−58

The 3D hexagonal lattice is obtained by translation of this unit cell in two directions normal to the chains (Fig. 9.7). Depending on the periodicity of the spin configuration, we have to include different number of chains in this unit cell. In the simplest case the magnetic unit cell involves only four chains, so the whole crystal lattice consists of four different types of superspins with different orientations. In the case where any single-ion anisotropy is neglected, these spins can rotate freely and the energy of dipolar interactions (9.6) is a function of eight spatial angles. The ground state configuration has been obtained by energy minimization against these eight parameters. At low temperature when the dipolar energy becomes significant and can produce the 3D magnetic ordering, the energy minimum corresponds to an antiferromagnetic (AF) spin alignment between the chains. All spins are oriented perpendicular to the chains, forming lines along the small diagonal of the rhombus. Within these directions, all moments are parallel, while moments from two neighboring lines are antiparallel to each other (Fig. 9.9). The ordering temperature calculated for this AF spin configuration is very low for all investigated compounds (about 2–3 K). So, the experimental ordering temperatures cannot be explained by the dipolar interaction in the framework of the isotropic chain model.

We shall now consider the case where single-ion anisotropy of Mn is present, as suggested by the fact that the coercive field measured in the ordered state is large (about 0.5 T at 4 K). This is understood as arising

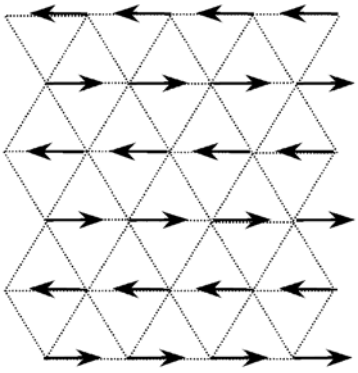

Fig. 9.9. Antiferromagnetic spin alignment (section perpendicular to the chain direction)

from the very strong Jahn–Teller effect for manganese(III). The total structure of the regarded complexes is hexagonal but each Mn ion is square-planar coordinated by the porphyrin disc. This local symmetry can result in some preferential orientation (easy axis) for each metal center in the plane perpendicular to the chain direction, and at low temperature the magnetic behavior of the isolated chain would be strongly anisotropic as is observed in the 3D ferromagnetic state. All previous calculations are repeated in the limit of the 1D Ising model. As for the isotropic case, the energy minimum corresponds to AF spin alignment, all spins being oriented along the easy axis direction. The ordering temperatures are 15.4 K, 21.0 K and 17.7 K for Mn-OC_{10}-TCNE, Mn-OC_{12}-TCNE and Mn-OC_{14}-TCNE, respectively, in good agreement with the experiment. It must be noted that the large increase of the calculated temperature in the anisotropic case is not due to the reduction of the number of degrees of freedom as could be quickly inferred by comparing (9.8) and (9.10): using (9.10) (1 degree of freedom) and the Heisenberg coupling scheme increases the calculated ordering temperature by 10% only. The most important difference between the two cases (isotropic and anisotropic coupling) is the fact that the correlation length and the dipolar energy in the chains diverges according to an exponential law in the latter case rather than a power law in the former one. One can then conclude that the anisotropy of the coupling is needed to explain the relatively high critical temperature observed in the regarded compounds.

In order to check how the results depend on the relative position of Mn and $[TCNE]^-$ in different chains we compared the results of calculations for the following situations: (i) all Mn ions (and $[TCNE]^-$ radicals respectively) are arranged in registry in planes perpendicular to the chain directions; (ii) Mn ion in one chain alternates with $[TCNE]^-$ radical in the neighboring chain; (iii) the magnetic species of neighboring chains are shifted by half a repeat unit along the chains. In all cases the energy minimum corresponds to the AF spin alignment, the ordering temperature being practically the same.

It should be noted that in the case of a 2D triangular lattice of point dipoles lying in the plane the ground state was shown to be ferromagnetic [37]. The difference between the case of a plane of point dipoles and the present network of chains is obviously the existence of a lateral surface where magnetic charges are created. Therefore, unlike for the infinitely thin plane, there is a non zero demagnetizing field in the latter, which eventually destabilizes the uniform ferromagnetic state. As is well known, the demagnetizing energy can be released by forming magnetic domains within the ferromagnetic system. In order to investigate the possibility that the actual ground state of the system be a multidomain ferromagnet, we extended the calculations by increasing the number of chains in the magnetic unit cell. As in the previous case, the AF spin alignment lies lower in energy than the uniform ferromagnetic one. But the energy minimum corresponds to a stripe structure. Within each stripe all Mn spins are oriented parallel giving rise to a large uncompensated magnetic moment. Moments of the neighboring stripes are oppositely directed (Fig. 9.10). The

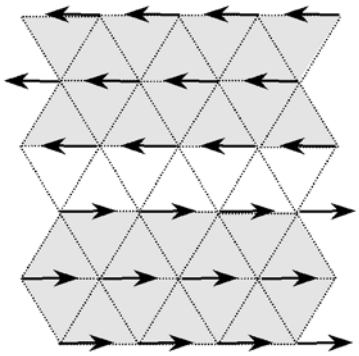

Fig. 9.10. Stripes spin alignment (section perpendicular to the chain direction)

lowest energy corresponds to a configuration with stripe width of about 30 lines. The critical temperature calculated for this spin configuration slightly increases as compared to the case of AF spin alignment (about 0.4 K for all investigated complexes).

It is then clear that the destabilization of the uniform ferromagnetic order with respect to the AF one is mainly due to the surface demagnetizing energy and a multidomain ferromagnetic ground state is expected. The calculated stripes can be regarded as one example of these domains. Of course, the particular shape of the domains appears only due to initial assumptions of the model. Usually nature prefers more complicated types of surfaces. An estimate based in the low magnetic density, commonly exhibited in molecular systems, gives a domain size of about 10^3 Å [38]. The obtained ferromagnetic stripes have comparable width.

Until now, we have stated that the easy axes of Mn ions are rigorously parallel. Alternatively non collinear spin configurations may be considered, which would promote weak ferromagnetism. Considering the local fourfold symmetry we performed the calculations for easy axes of different Mn ions

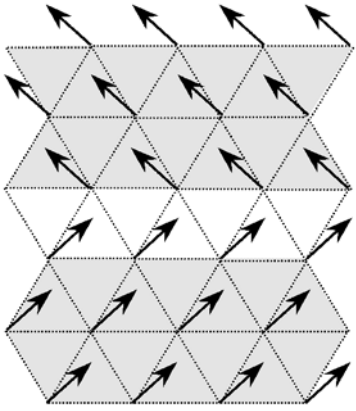

Fig. 9.11. Canted stripes spin alignment (section perpendicular to the chain direction)

Table 9.2. Ordering temperatures calculated for different spin configurations (reproduced from [32])

	Ordering temperature (K)			
Complex	Exp	AF	Stripes	Canted
Mn-OC_{10}-TCNE	21.7	15.4	15.7	14.8
Mn-OC_{12}-TCNE	22.0	21.0	21.4	20.1
Mn-OC_{14}-TCNE	20.5	17.7	18.1	16.9

perpendicular to each other. Like in the previous case, the energy minimum corresponds to a stripe structure (Fig. 9.11). Within each stripe the spin moments are parallel, while those of neighboring stripes are canted. The critical temperatures for these canted-stripe configurations are about 0.8 K lower than the ones for AF spin alignment in the corresponding system (all calculated results are summarized in Table 9.2).

It should be noted that the ordering temperatures calculated in the framework of the dipolar model are a bit lower than the experimentally observed ones. A possible reason is that, at low enough temperature, the correlation length ξ is of the order of the particle size. As a result, all spins within a chain are correlated in a single superspin, and there is no antiparallel neighboring superspin at all. This results in an enhancement of the dipolar energy, and accordingly in a slight increase of the ordering temperature.

9.3.2 Layered compounds with very large interlayer spacing

Like in the case of chain compounds the magnetic behavior of layered compounds is considered in two steps: an isolated 2D square lattice dominated by in-plane exchange interaction and dipolar interaction between blocks of correlated spins from different layers. Therefore is assumed that (i) the in-plane correlation length is driven by the in-plane exchange interaction only, (ii) any exchange interaction between layers is negligible because of very large interlayer distance c and only through-space dipole coupling is available between moments located in different layers. In addition, a small local anisotropy is assumed to favors the spin orientation normal to the layers, in order to get the observed ferromagnetic behavior (in plane magnetization would result in an AF coupling between the planes.

Let us start from the isolated 2D square lattice of spins $S = 1/2$, coupled by ferromagnetic exchange interaction to their nearest neighbors. At absolute zero, the magnetic layer exhibits a ferromagnetic alignment of the spins due to exchange coupling, and the ground state corresponds to the higher spin multiplicity. Upon increasing temperature, the spins become only correlated on a finite distance ξ. For a 2D Heisenberg ferromagnet, ξ is related to the exchange constant J and the spin value S by the relationship [39]

$$\xi^2 = \frac{JS}{k_B T} \exp\left(\frac{4\pi J S^2}{k_B T}\right) . \tag{9.11}$$

And the magnetic susceptibility reads

$$\chi = \frac{1}{3\pi JS} \exp\left(\frac{4\pi JS^2}{k_{\mathrm{B}}T}\right) . \tag{9.12}$$

It is assumed that this in-plane correlation length is determined by the in-plane exchange interaction only and takes the same value and the same temperature dependence as for an isolated magnetic layer. So using the exchange parameter J obtained from the high-temperature magnetic data one can compute the magnetic properties of an isolated layer as well as the corresponding correlation length at any temperature. To introduce the in-plane correlation length, each layer is considered as a set of spatially distributed superspins. For the sake of simplicity each superspin is assumed to be a square, the side length of this square is set equal to ξ. In order to model its spin block structure each plane is considered at a non-zero temperature as a checkerboard made of square blocks containing ξ^2 parallel – correlated – spins S. The net moment of each spin block is $\xi^2 g S \mu_B = \xi^2 \mu$ and is assumed oriented anti-parallel to its neighbors thus prefiguring a multidomain structure in the 3D ordered state (Fig. 9.12). It must be emphasized that the finite size of these domains is essential since the dipole–dipole interaction between uniformly magnetized infinite planes is virtually zero. Accordingly, the expected transition is not towards a uniform ferromagnet but a multidomain one (unless the size of the sample grains is small). This is somehow similar to the most stable state found above for the chain compound.

The magnetic planes are stacked in registry so as to minimize the dipolar energy, i.e. the squares form columns of spin-up (down) in the direction perpendicular to the magnetic layers.

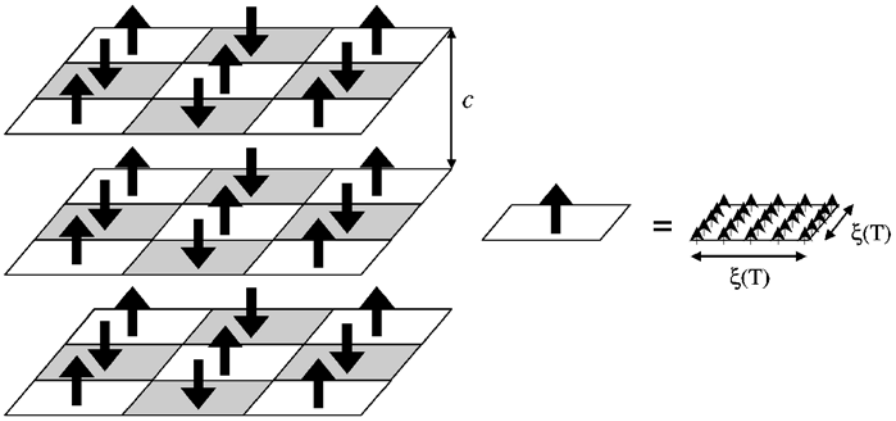

Fig. 9.12. Model of spin arrangement in ferromagnetic layers at non-zero temperature

The energy of dipolar interaction between superspins from different magnetic layers can be calculated as before using (9.6). Now the summation on i extends over all individual spins in the central square, which build up the superspin in the central layer. The summation on j includes all moments in other layers within a radius r from the origin in the layers and for L layers on each side of the central one.

Because of the long range of dipolar interactions, we have performed trial calculations for increasing values of r and L. The calculation is shown to converge rapidly for r values of the order of ξ, most probably because of the alternating spin-up and spin-down arrangement at this length scale. Along the direction perpendicular to the layers the calculation converges also for a number of layers $2L$ such that $Lc \approx \xi$. Therefore, in the following calculations, the summation was limited to a parallepipedon of side length 3ξ in-plane, i.e. over $L = \xi/c$ layers above and below the central one and nine squares in every layer.

With the knowledge of μ, $\xi(T)$ and the numerical calculation of dipolar energy, the expected variation of the spontaneous magnetization as a function of temperature can be computed as before by solving the self-consistent set of (9.6) and (9.7) or the implicit (9.8).

Now the present model can be compared with the experimental observations. The $m = 7$ alkyl copper(II) compound with $c = 28.8\,\text{Å}$ exhibits a long-range magnetic ordering below $T_C = 21.2$ K (m is a number of carbon atoms in alkyl chain). The moment density obtained by fitting the magnetization curves to Langevin functions in paramagnetic regime yield a moment value of 4.7 ± 0.3 emu/g (1600 emu/mol). Taking into account the basal surface area of the actual unit cell, this yields a value of $0.03\,\mu_B/\text{Å}^2$ for the moment density in the layer. Therefore, we have used an equivalent square lattice of spin $S = 1/2$ ($\mu = 1\mu_B$) with a lattice parameter a equal to 5.7 Å.

Using the magnetization data obtained for the $m = 7$ copper(II) compound, in the paramagnetic range above T_C, the rate of divergence of $\xi(T)$ has been determined by a fit to (9.11) of the thermal variation of the effective paramagnetic moment $\xi^2 g\mu_{BS}$ (Fig. 9.13). The value of J/k_B was obtained in the range 44–47 K. A similar value was obtained by fitting the thermal dependence of the susceptibility to (9.12). Note that this value of J is an effective exchange interaction for the equivalent square lattice used in the model. As far as the actual exchange constant between copper(II) ions is concerned, this value should be renormalized to take into account the trigonal symmetry and the bound density of the real compound.

Figure 9.14 displays the temperature dependence of the spontaneous magnetization computed within present model for a square lattice with $S = 1/2$, $a = 5.7\,\text{Å}$, $J/k_B = 45\,\text{K}$ at different values c/a. The critical temperature at which spontaneous magnetization occurs is found to be 19.4 K for $c/a = 5$ which compares well with the experimental value $T_C = 21.2$ K observed in the regarded compound. Large changes of the c/a ratio do not modify dramati-

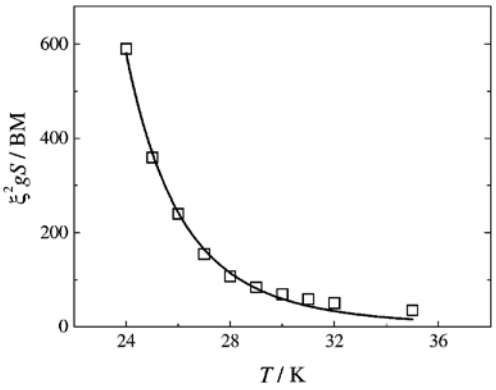

Fig. 9.13. Variation of the effective paramagnetic moment of the $m = 7$ alkyl copper(II) compound, theoretical fit using (9.11) is plotted in *solid line* (reproduced from [33])

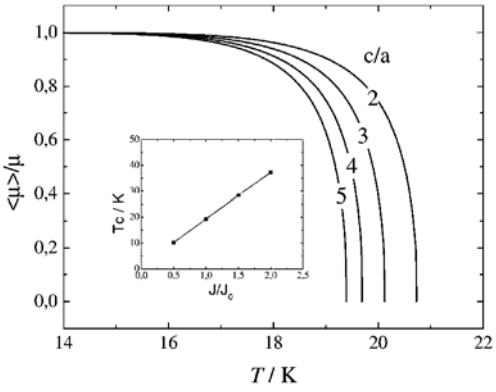

Fig. 9.14. Influence of the c/a ratio on the theoretical thermal variation of the spontaneous magnetization (reproduced from [33])

cally the critical temperature, as observed experimentally. This is explained by the fact that the dipolar interaction between magnetic layers leads to 3D ordering as soon as the in-plane correlation length ξ reaches a threshold value. Because of the exponential divergence of $\xi\,(T)$, the temperature for which the threshold is reached depends only weakly on interlayer distance. By the contrast, modifications of the in-plane exchange interaction J that affects directly the thermal dependence of ξ, induce significant variations of the long-range ordering temperature.

The calculation has been performed for a preferred orientation of the moments perpendicular to the layers, which corresponds to the lowest dipolar energy and favors a ferromagnetic order. In case of an in-plane preferred orientation, due to single ion anisotropy, the ordered state is antiferromagnetic,

the dipolar energy is coarsely divided by 2 but the ordering temperature is reduced by less than 10 %.

9.3.3 Conclusions about the model

Despite the crudeness of the molecular field approximation, it has been shown here that, in both cases of chain and layer compounds, the critical temperature for dipolar induced 3D magnetic ordering can be reasonably well predicted when taking into account the spin correlation length within the chains or the layers. It may be argued that the molecular-field approximation usually overestimates the transition temperature because it neglects spatial fluctuations. This would place the calculated temperatures as upper bounds. However, in the present model, the critical temperature is determined essentially by the correlation length reaching a threshold value, i.e. by the in-chain (in-plane) exchange interaction. Actually, changing by a factor 3 the strength of the base dipolar interaction, by modifying either the interchain spacing or the moment values, leads only to weak differences of the calculated critical temperature (about 10 %). This remark applies also to the change in the number of degrees of freedom from 3 to 1 between freely rotating and uniaxial moments respectively. The reason is the exponential divergence of $\xi(T)$, which results in an exponential increase of the net moment of the spin blocks and accordingly of the dipolar energy. As compared to this rapid thermal variation any change of the preexponential factor – base dipolar energy and the way it is estimated – induces only a logarithmic correction. We thus believe that more sophisticated approaches – using renormalization techniques for instance – would basically yield very similar results. One exception to this rule is the case of chains of isotropically coupled spins because the power-law variation of the correlation length is much slower and similar to that of the thermal average of the moment.

9.4 Summary

The design of new molecular based magnets requires a deep understanding of all relevant processes responsible for the bulk magnetic properties. It is common practice to use suitable bridging ligands for optimization of the overlap between magnetic properties and thus the exchange interaction. However, the choice of the bridging ligands may be dictated by other consideration than the optimization of the magnetic properties. A good alternative way is to use a combination of the exchange interaction and a through space dipolar coupling. Though the dipolar interaction is usually ignored as exchange coupling usually dominates it is shown in this contribution that it may have a key role in the nature of the 3D magnetic ordering in some chain and layered magnetic materials. Due to long-range effect this interaction is present even for very large intercenter distances where the exchange coupling can be

neglected. In the case when dipolar interaction takes place not between individual spins but between strongly correlated spin blocks – which results from the large exchange interaction within the chains or the layers – 3D ordering is expected (and observed) at substantial critical temperatures. In this respect, this alternative way for the design of molecular ferromagnets may appear very promising in the future.

References

1. E. Coronado, P. Delhaes, D. Gatteschi, J. S. Miller (eds.): *Molecular magnetism: from molecular assemblies to the devices*, vol. 321 of NATO ASI Series (Kluwer Academic, Dordrecht 1996)
2. J. S. Miller, M. Drillon (eds.): *Magnetism: molecules to materials*, vol. 1 (Wiley VCH, Weinheim 2001)
3. C. M. Wynn, M. A. Girtu, K.-I. Sugiura, E. J. Brandon, J. L. Manson, J. S. Miller, A. J. Epstein: Synth. Metals **85**, 1695 (1997)
4. J. Villain, J. M. Loveluck: J. Phys. Lett. (Paris) **38**, 77 (1997)
5. R. D. Jones, D. A. Summerville, F. Basolo: J. Am. Chem. Soc. **100**, 4416 (1978)
6. J. S. Miller, J. C. Calabrese, R. S. McLean, A. J. Epstein: Adv. Mater. **4**, 490 (1992)
7. A. J. Epstein, C. M. Wynn, M. A. Girtu, W. B. Brinckerhoff, K.-I. Sugiura, J. S. Miller: Mol. Cryst. Liq. Cryst. **305**, 321 (1997)
8. M. Kelemen, C. Wachter, H. Winter, E. Dormann, R. Gompper, D. Hermann: Mol. Phys. **90**, 407 (1997)
9. K. Griesar, M. Athanassopoulou, E. Soto Bustamante, Z. Tomkowicz, A. Zaleski, W. Haase: Adv. Mater. **9**, 45 (1997)
10. K. Falk: PhD thesis, Darmstadt University of Technology, Darmstadt (2002)
11. K. Falk, R. Werner, Z. Tomkowicz, M. Bałanda, W. Haase: J. Magn. Magn. Mater. **196–197**, 564 (1999)
12. M. Bałanda, K. Falk, K. Griesar, Z. Tomkowicz, W. Haase: J. Magn. Magn. Mater. **205**, 14 (1999)
13. M. Bałanda, K. Falk, K. Griesar, Z. Tomkowicz, T. Wasiutyński, W. Haase: Mol. Cryst. Liq. Cryst. **335**, 133 (1999)
14. F. Mascarenhas, K. Falk, P. Klavins, J. S. Schilling, Z. Tomkowicz, W. Haase: J. Magn. Magn. Mater. **231**, 172 (2001)
15. K. Falk, M. Bałanda, Z. Tomkowicz, F. Mascarenhas, J. Schilling, P. Klavins, W. Haase: Polyhedron **20**, 1521 (2001)
16. D. Bloch: J. Phys. Chem. Solids **27**, 881 (1963)
17. L. J. De Jongh, R. Block: Physica **79B**, 568 (1975)
18. D. Gatteschi, O. Kahn, J. S. Miller, F. Palacio (eds.): *Magnetic molecular materials*, vol. 198 of NATO ASI Series (Kluwer Academic, Dordrecht 1991)
19. R. E. Coffman, G. R. Buettner: J. Phys. Chem. **83**, 2387 (1979)
20. C. M. Wynn, M. A. Girtu, J. S. Miller, A. J. Epstein: Phys. Rev. B **56**, 315 (1997)
21. M. A. Girtu, C. M. Wynn, K.-I. Sugiura, J. S. Miller, A. J. Epstein: J. Appl. Phys. **81**, 1 (1997)
22. C. M. Wynn, M. A. Girtu, W. B. Brinckerhoff, K.-I. Sugiura, J. S. Miller, A. J. Epstein: Chem. Mat. **9**, 2156 (1997)

23. P. M. Richards: Phys. Rev. B **10**, 4687 (1974)
24. R. L. Carlin: *Magnetochemistry* (Springer, New York 1986)
25. S. Yamanaka, T. Sako, K. Seki, M. Hattori: Solid State Ionics **53**, 527 (1992)
26. V. Laget, P. Rabu, C. Hornick, F. Romero, R. Ziessel, P. Turek, M. Drillon: Mol. Cryst. Liq. Cryst. **305**, 291 (1997)
27. V. Laget, C. Hornich, P. Rabu, M. Drillon, R. Ziessel: Coord. Chem. Rev. **178–180**, 1533 (1998)
28. P. Rabu, S. Rouba, V. Laget, C. Hornich, M. Drillon: Chem. Commun. 1107 (1996)
29. V. Laget, C. Hornich, P. Rabu, M. Drillon: J. Mat. Chem. **9**, 169 (1999)
30. M. Drillon, P. Panissod, P. Rabu, J. Souletie, V. Ksenofontov, P. Gütlich: Phys. Rev. B **65**, 104404 (2002)
31. A. Caneschi, D. Gatteschi, P. Rey, R. Sessoli: Inorg. Chem. **30**, 3936 (1991)
32. S. Ostrovsky, W. Haase, M. Drillon, P. Panissod: Phys. Rev. B **64**, 134418 (2001)
33. M. Drillon, P. Panissod: J. Magn. Magn. Mater. **188**, 93 (1998)
34. F. Suzuki, N. Shibata, C. Ishii: J. Phys. Soc. Jpn. **63**, 1539 (1994)
35. M. Drillon, E. Coronado, R. Georges, J. C. Gianduzzo, J. Curely: Phys. Rev. B **40**, 10992 (1989)
36. R. Georges, J. Curely, M. Drillon: J. Appl. Phys. **58**, 914 (1985)
37. P. I. Belobrov, R. S. Gekht, V. A. Ignatchenko: Sov. Phys. JETP **57**, 636 (1983)
38. F. Palacio, F. J. Lazaro, A. J. van Duyneveldt: Mol. Cryst. Liq. Cryst. **176**, 289 (1989)
39. M. Takahashi: Phys. Rev. Lett. **58**, 168 (1987)

10

Electron Delocalization in Dimeric Mixed-Valence Systems

S. Ostrovsky

10.1 Introduction

Mixed-valence (MV) transition metal clusters contain two or more metal ion centers in different oxidation states between which an itinerant extra electron can transfer. These kind of compounds are of great interest because of their unusual spectral and magnetic properties and the possibility to use these properties for studying the intramolecular electron transfer process in many biologically important systems [1, 2]. For instance, valence delocalized $[Fe_2S_2]^+$ pairs where iron is in the formal oxidation state +2.5 were found in a variety of iron-sulfur clusters in ferredoxins. Because of this, a growing interest in the characterization, the modeling and in the theoretical description of such compounds exists [3–6]. MV dimers are very convenient systems for better understanding of the electron delocalization process because of the possibility to take into account all relevant interactions. In this contribution we briefly discuss some of these interactions and their influence on the properties of the dimeric MV compounds. As a final step the investigation of a MV iron dimer in the generalized vibronic model is presented.

10.2 Electronic interactions

The conception of double exchange was first suggested by Zener [7] for explanation of ferromagnetism observed in the MV manganites of perovskite structure. The process involves the coupling of two localized magnetic moments through the migration of the extra electron between these magnetic centers. This extra electron cannot be attributed to a single center, it behaves as an itinerant. According to the Hund rule, the migrating electron forms a high-spin configuration at each metal ion. Since the itinerant electron holds the orientation of its spin during process of migration, double exchange results in a strong spin polarization effect which favors a ferromagnetic spin alignment.

A general solution of the double exchange problem for a MV dimer was suggested by Anderson and Hasegawa [8]. It was shown that the energies of the MV dimer are:

$$E(S) = \pm t \frac{S + 1/2}{2S_0 + 1} , \tag{10.1}$$

where t is the transfer integral between the different center orbitals occupied by the itinerant electron, S is the total spin of the system and S_0 is the spin core without extra electron. The energy splitting due to double exchange is linear in S and maximal for the maximal total spin value. So the double exchange in dimeric systems always results in ferromagnetic ground state independently of the sign of the transfer integral.

Along with the double exchange interaction the magnetic exchange is presented in MV systems as well. Energies of a MV dimer in presence of both interactions are the following:

$$E_{\pm}(S) = -JS(S+1) \pm B(S+1/2) , \tag{10.2}$$

where J is the isotropic exchange parameter and $B = t/(2S_0 + 1)$ is the double exchange parameter for the regarded complex. The behavior of the MV system is determined by the interplay between these two type of interactions. When magnetic exchange is ferromagnetic ($J > 0$) both interactions favor the stabilization of state with maximal total spin value. In the case of antiferromagnetic exchange interaction ($J < 0$) the combined effect of magnetic exchange and double exchange leads to some interesting results. Figure 10.1 represents the $E_{\pm}(S)/|J|$ as a function of $B/|J|$ for the Fe(II)-Fe(III) system in presence of an antiferromagnetic exchange. Because the diagram

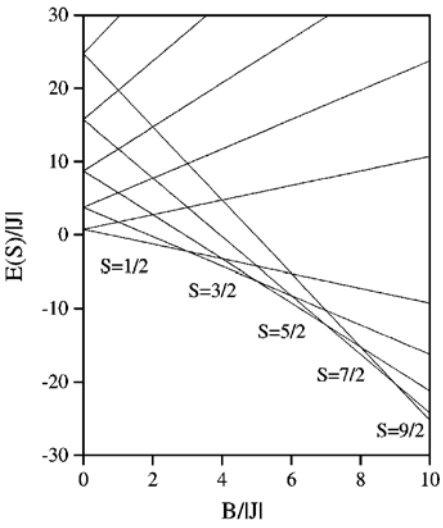

Fig. 10.1. Correlation energy diagram of the MV iron dimer in the presence of double exchange and antiferromagnetic Heisenberg exchange

is symmetric about the change of sign of the double exchange parameter the part for the positive value is presented only. When double exchange is weak enough the magnetic exchange dominates and the ground state is $S = 1/2$. With the increasing of the $B/|J|$ absolute value the ground state becomes successively 3/2, 5/2, 7/2, and finally 9/2 for the strong double exchange. From (10.2) it is easy to obtain the ratio between the magnetic exchange and double exchange parameters where ground state changes from S to $S + 1$:

$$B/|J| = 2(S+1) \ . \tag{10.3}$$

So when B is larger than $9|J|$ state with $S = 9/2$ is the lowest in energy. Since in real systems double exchange exceeds the magnetic exchange significantly the electron delocalization results in ferromagnetic ground state.

10.3 Vibronic interactions: PKS model

The moving electron strongly perturbs the ligand environment so the vibronic coupling plays a considerable role in MV systems along with isotropic and double exchange interactions. The background for the consideration of the vibronic effects in this kind of systems was suggested by Piepho, Krausz and Schatz and became well-known as the PKS model [9–11]. It is assumed that the subunits have the same point group symmetry in both oxidation states (with and without extra electron) so only totally symmetric normal coordinates q_{A} and q_{B} associated with each subunits are regarded. It is introduced new collective coordinates:

$$q_{\pm} = \frac{1}{\sqrt{2}}\left(q_{\mathrm{A}} \pm q_{\mathrm{B}}\right) \ . \tag{10.4}$$

The "in-phase" q_+ mode decreases and increases the potential energy of both subunits at the same time. So it does not affect the extra electron migration and can be excluded from the consideration. On the contrary, the "out-of-phase" q_- mode is relevant to the electron transfer process. Depending on the sign of q_- the nuclear displacements stimulate the location of the extra electron on one of the ions (A or B). The opposite sign of q_- mode promotes the location of the extra electron on another subunit. Vibrational coordinate $q_- \equiv q$ for two coupled centers is shown in Fig. 10.2.

The adiabatic potentials relating to a given full spin S of the system have the following form:

$$U_{\pm}^{S}(q) = -JS(S+1) + \omega q^2/2 \pm \left[\left(B\left(S+1/2\right)\right)^2 + v^2 q^2\right]^{1/2} \ , \tag{10.5}$$

where ω is the frequency of PKS out-of-phase mode, v is the vibronic coupling parameter. Depending on the relationship between double exchange parameter and vibronic coupling with the PKS out-of-phase mode there

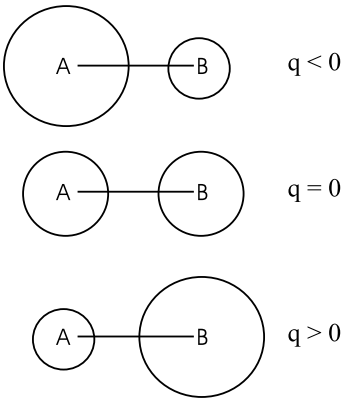

Fig. 10.2. Schematic representation of the out-of-phase vibrational mode

are three principal types of the adiabatic curves (Fig. 10.3). When the double exchange is negligibly small compared with the vibronic interaction $\left(B\left(S+1/2\right) \ll v^2/\omega\right)$ the potential curve U_{-}^{S} has two well separated minima (Fig. 10.3a). The wave functions in these minima correspond to a localization of the extra electron on one of the subunits. The system is fully localized (class I in Robin and Day classification scheme [12]). With the increasing of the double exchange interaction the barrier between these minima becomes lower. In the case when $B\left(S+1/2\right) < v^2/\omega$ the electron transfer process is possible but requires an activation energy. This situation is shown in Fig. 10.3b and corresponds to the class II in Robin and Day scheme. And finally, in the case of weak vibronic interaction (or strong double exchange) when $B\left(S+1/2\right) > v^2/\omega$ the potential curve U_{-}^{S} has one minimum at the position $q = 0$ and the extra electron is fully delocalized (class III system). So the PKS interaction produces a localization effect.

In many-electron MV dimers the states with different total spin values are present. The vibronic coupling with PKS out-of-phase mode is spin independent whereas the double exchange is maximal for the highest spin state and decreases with the total spin decreasing. As a result the extra electron may be localized for the low spin states and delocalized for the high spin ones. This

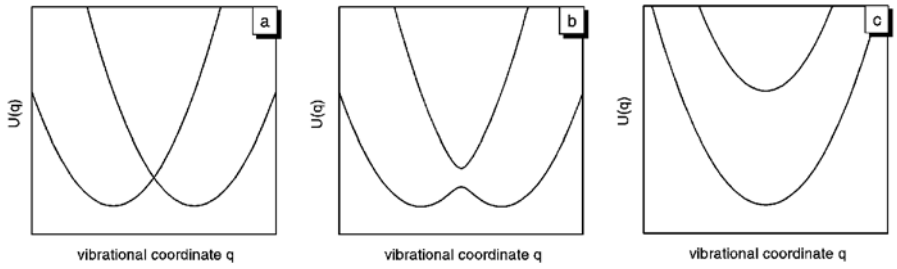

Fig. 10.3. The adiabatic potentials for a MV dimer with diamagnetic cores

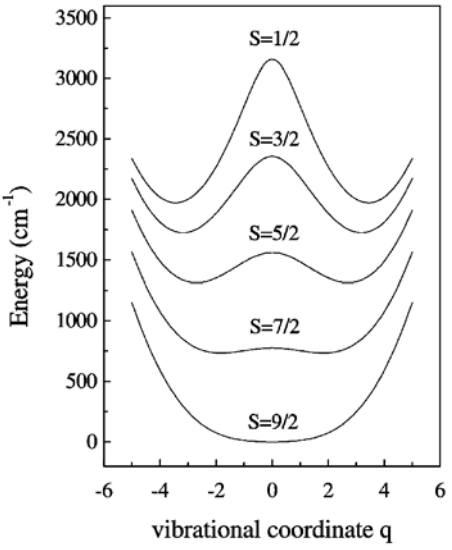

Fig. 10.4. The adiabatic potentials (low-lying group) for symmetric MV iron dimer: $B = 820\,\mathrm{cm}^{-1}$, $\omega = 310\,\mathrm{cm}^{-1}$, $v = 3.5\,\omega$ (reproduced from [13])

situation is illustrated in Fig. 10.4. The adiabatic curve for $S = 9/2$ possesses a single minimum with fully delocalized itinerant electron while the $S = 1/2$ adiabatic curve has two well separated deep minima which correspond to the trapped states.

In real systems some additional electron trapping could occur due to asymmetry of the compound. The electron configurations with an itinerant electron trapped at ion A and B have now different energies and it leads to preferable localization of the extra electron on the ion with the less energy. Figure 10.5 presents adiabatic potentials for $[L^1Fe_2(\mu\text{-OBz})(Obz)(H_2O)](ClO_4)$ analyzed in [13]. Strong double exchange results in the ferromagnetic ground state. The corresponding adiabatic curve possesses one minimum however, for asymmetric iron dimer this minimum corresponds to the extra electron localization on one of the Fe sites. The system is partially localized.

One of the most striking features of MV systems is the occurrence in the visible or near-infrared region of a new absorption band not characteristic of the separate subunits. This is the so-called intervalence absorption band. It results from the transitions between the states of different parity with the same spin value. In the framework of the PKS model for a fully delocalized system the intervalence absorption band is expected to be narrow and intense. The position and the shape of this band depend only slightly on temperature. With the increase of the degree of localization the intervalence band becomes broader and less intense. For class I system the PKS model predicts the broad optical band in the high energy region. This band has low intensity and depends strongly on temperature.

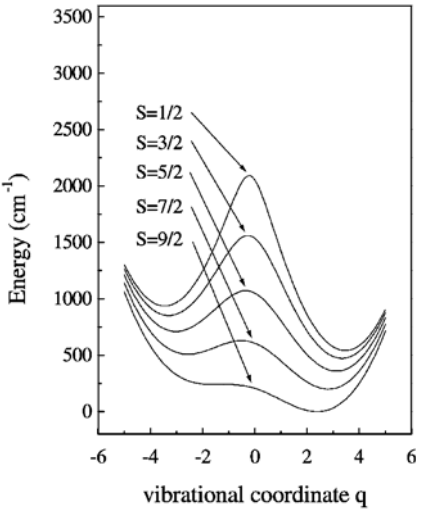

Fig. 10.5. The adiabatic potentials (low-lying group) for non-symmetric MV iron dimer: $B = 600\,\mathrm{cm}^{-1}$, $\omega = 310\,\mathrm{cm}^{-1}$, $v = 3.5\,\omega$, $W = 400\,\mathrm{cm}^{-1}$ (reproduced from [13])

10.4 Vibronic interactions: Piepho type of vibrations

Piepho [14, 15] suggested a new vibronic model for these type of compounds. Piepho type vibrations change the metal-metal distances and result thus in the modulation of the value of the transfer integral. One can expand the double exchange parameter in the Taylor series and obtain in the first approximation:

$$B(r) = B(r_0) + \left(\frac{\partial B}{\partial r}\right)_{r=r_0} Q\,, \tag{10.6}$$

where r is the metal-metal distance, r_0 is the metal-metal distance for the system without the itinerant extra electron, $Q = r - r_0$ is the vibrational coordinate in the Piepho model, $\lambda_0 = -\left(\partial B/\partial r\right)_{r=r_0}$ is the vibronic coupling parameter with the P-vibrations. It should be mentioned that the effective (multielectron) P-coupling parameter $\lambda(S) = \lambda_0 (S + 1/2)$ possesses the same spin dependence as the double exchange parameter.

The problem of localization-delocalization in the dimeric MV clusters in the presence of both type of vibrations (PKS and Piepho) was studied in [16]. In the framework of semiclassical adiabatic approach the potential surfaces were analyzed. Depending on the relationship between the key parameters of the dimeric MV system several qualitatively different types of the adiabatic surfaces were found (in the following consideration Ω is the frequency of Piepho type of vibrations):

1. PKS coupling exceeds Piepho coupling $\left(v^2/\omega > \lambda^2 (S + 1/2)^2 /\Omega\right)$. The behavior of the system as well as the shape of lower sheet of the adiabatic surface depend on the value of the double exchange parameter. If double exchange is weak $\left(B(S + 1/2) \ll v^2/\omega - \lambda^2 (S + 1/2)^2 /\Omega\right)$ the extra electron

is strongly localized and the system belongs to class I. The corresponding adiabatic potential possesses two equivalent minima in qQ-plane. These minima are symmetric in the q-subspace and shifted along the Q axis in the negative direction. With the increasing of the double exchange these two minima move toward the Q axis, the barrier between them becoming lower. The extra electron becomes more and more delocalized (class II). Under the condition $\left(B\left(S+1/2\right)=v^2/\omega-\lambda^2\left(S+1/2\right)^2/\Omega\right)$ the minima are transformed into one minimum in which the extra electron is fully delocalized (class III). So in the case of strong PKS coupling depending on the magnitude of the double exchange MV dimer can belong to class I, II or III.

2. Piepho coupling exceeds PKS coupling $\left(v^2/\omega<\lambda^2\left(S+1/2\right)^2/\Omega\right)$. Under this condition the system is fully delocalized independently of the relative value of the double exchange parameter. The MV dimer belongs to class III even providing small magnitude of the double exchange. The molecular vibrations effectively enhance the double exchange giving rise to a strong ferromagnetic contribution.

3. Both types of vibrations are equal in magnitude. The situation is similar to the case 2. The extra electron is fully delocalized.

The intervalence absorption in the generalized vibronic model was considered by Piepho [14, 15]. The correlation between the degree of delocalization and parameters of this band (position, width and intensity) in the presence of both type of vibrations differs from that for PKS model. As it was already mentioned, in the PKS model the class III system exhibits strong but narrow intervalence band and as a consequence the optical properties of some real compounds cannot be explained in the framework of this model. In the case of taking into account both types of vibrations the fully delocalized system can exhibit strong broad intervalence band if Piepho coupling is dominant. This broad band arises from the transitions between fully delocalized states.

10.5 MV iron dimer in the presence of both types of vibrations

10.5.1 Model

Let us consider a dimeric MV system with one itinerant extra electron delocalized over two spin cores $S_{\mathrm{A}}=S_{\mathrm{B}}=S_0$. To explain the behavior of the regarded compound we use a hamiltonian that includes isotropic exchange interaction, double exchange and vibronic coupling with PKS and Piepho type of vibrations. All of these interactions cannot mix states of the system belonging to the different values of the total spin S. As a consequence, we have for each value of the total spin S the following block of the full hamiltonian matrix (reduced Planck constant $\hbar=1$):

$$\mathbf{H}(S)=\left[-JS\left(S+1\right)+\frac{\omega}{2}\left(q^2-\frac{\partial^2}{\partial q^2}\right)+\frac{\Omega}{2}\left(Q^2-\frac{\partial^2}{\partial Q^2}\right)\right]\begin{array}{c}\begin{matrix}\psi_+^{SM} & \psi_-^{SM}\end{matrix}\\ \begin{pmatrix}1 & 0\\ 0 & 1\end{pmatrix}\end{array}$$
$$+\begin{array}{c}\begin{matrix}\psi_+^{SM} & \psi_-^{SM}\end{matrix}\\ \begin{pmatrix}B\left(S+\frac{1}{2}\right)-\lambda\left(S\right)Q & vq+\frac{1}{2}W\\ vq+\frac{1}{2}W & -\left(B\left(S+\frac{1}{2}\right)-\lambda\left(S\right)Q\right)\end{pmatrix}\end{array} \tag{10.7}$$

where all parameters are determined as earlier. If sites A and B are non equivalent the states corresponding to localization of the extra electron on these spin cores have different energies. In (10.7) this energy difference is denoted as W. The basis set in (10.7) is the following:

$$\psi_{\pm}^{SM}\left(r\right)=\frac{1}{\sqrt{2}}\left(\psi_A^{SM}\left(r\right)\pm\psi_B^{SM}\left(r\right)\right)\ , \tag{10.8}$$

where $\psi_{\mathrm{A(B)}}^{SM}\left(r\right)$ means the electronic wave function of the system with the extra electron localized on center A(B). M is the magnetic quantum number.

The eigenfunctions of (10.7) can be found in the following form:

$$\Phi_\nu^{SM}\left(r,q,Q\right)=\sum_{n=0}^{\infty}\sum_{m=0}^{\infty}\quad\left(\psi_+^{SM}\left(r\right)C_{\nu nm}^{+(S)}\chi_n\left(q\right)\chi_m\left(Q\right)\right.$$
$$\left.+\psi_-^{SM}\left(r\right)C_{\nu nm}^{-(S)}\chi_n\left(q\right)\chi_m\left(Q\right)\right)\ . \tag{10.9}$$

Here $\chi_n\left(q\right)$ and $\chi_m\left(Q\right)$ are harmonic oscillator functions.

The secular equations corresponding to (10.9) are:

$$\sum_{n=0}^{\infty}\sum_{m=0}^{\infty}C_{\nu nm}^{+(S)}\left(H_{(n'm'|nm)}^{(S)}-\delta_{n'n}\delta_{m'm}E_\nu\right)$$
$$+\sum_{n=0}^{\infty}\sum_{m=0}^{\infty}C_{\nu nm}^{-(S)}H_{(n'm'|nm)}^{\prime\prime(S)}=0\ ,$$
$$\sum_{n=0}^{\infty}\sum_{m=0}^{\infty}C_{\nu nm}^{-(S)}\left(H_{(n'm'|nm)}^{'(S)}-\delta_{n'n}\delta_{m'm}E_\nu\right)$$
$$+\sum_{n=0}^{\infty}\sum_{m=0}^{\infty}C_{\nu nm}^{+(S)}H_{(n'm'|nm)}^{\prime\prime(S)}=0\ , \tag{10.10}$$

where

$$H^{(S)}_{(n'm'|nm)} = \left[\omega\left(n+\tfrac{1}{2}\right)+\Omega\left(m+\tfrac{1}{2}\right)+B\left(S+\tfrac{1}{2}\right)-JS\left(S+1\right)\right]\ \delta_{n'n}\delta_{m'm}$$
$$-\lambda\left(S\right)\left(\sqrt{\tfrac{m}{2}}\delta_{m,m'+1}+\sqrt{\tfrac{m+1}{2}}\delta_{m,m'-1}\right)\ \delta_{n'n}\,,$$
$$H'^{(S)}_{(n'm'|nm)} = \left[\omega\left(n+\tfrac{1}{2}\right)+\Omega\left(m+\tfrac{1}{2}\right)-B\left(S+\tfrac{1}{2}\right)-JS\left(S+1\right)\right]\ \delta_{n'n}\delta_{m'm}$$
$$+\lambda\left(S\right)\left(\sqrt{\tfrac{m}{2}}\delta_{m,m'+1}+\sqrt{\tfrac{m+1}{2}}\delta_{m,m'-1}\right)\ \delta_{n'n}\,,$$

$$H''^{(S)}_{(n'm'|nm)} = v\left(\sqrt{\tfrac{n}{2}}\delta_{n,n'+1}+\sqrt{\tfrac{n+1}{2}}\delta_{n,n'-1}\right)\ \delta_{m'm}+\tfrac{1}{2}W\delta_{n'n}\delta_{m'm}\,. \tag{10.11}$$

Diagonalization of this matrix gives eigenvalues and eigenfunctions (10.9) of the system. In general the dimension of this block is infinite, but in practical calculations for moderate vibronic coupling it is enough to take into account in (10.9) and (10.10) the upper limit in the summations equal to 50 without significant loss of accuracy. In this case the dimension of the matrix for each value of the total spin is equal to 5000 and the problem can be easily solved.

To obtain the profile of the intervalence absorption band we calculate the dipole intensity of each vibronic line:

$$D\left(\nu'S'M'\rightarrow\nu SM\right) =$$
$$\delta_{\mathrm{S'S}}\delta_{\mathrm{M'M}}\sum_{\gamma=x,y,z}\frac{N^{SM}_{\nu'}-N^{SM}_{\nu}}{N}\left|\left\langle\Phi^{SM}_{\nu'}\right|m_\gamma\left|\Phi^{SM}_{\nu}\right\rangle\right|^2\,, \tag{10.12}$$

where m_γ is the γ-th component of the electric dipole operator ($\boldsymbol{m}=\sum e_i\boldsymbol{r}_i$) and

$$N^{SM}_{\nu}=\exp\left(-E^{S}_{\nu}/k_BT\right)\,. \tag{10.13}$$

These electronic transitions are z polarized [11, 14]. Following the Franck–Condon approximation one can obtain the expression:

$$D\left(\nu'SM\rightarrow\nu SM\right)=\left(\frac{N^{SM}_{\nu'}-N^{SM}_{\nu}}{N}\right)\Delta^2_{\nu'\nu}\left|\left\langle\psi^{SM}_{+}\ |m_\gamma|\ \psi^{SM}_{-}\right\rangle^0\right|^2\,, \tag{10.14}$$

where the matrix element $\left\langle\psi^{SM}_{+}\,|m_\gamma|\,\psi^{SM}_{-}\right\rangle^0$ is evaluated at $q=0$ and $Q=0$, and $\Delta_{\nu'\nu}$ is given by:

$$\Delta_{\nu'\nu}=\sum_{n,m}\left(C^{+(S)}_{\nu'nm}C^{-(S)}_{\nu nm}+C^{-(S)}_{\nu'nm}C^{+(S)}_{\nu nm}\right)\,. \tag{10.15}$$

The intervalence absorption band is the totality of transitions ($\nu'SM\rightarrow\nu SM$) with different spin S and magnetic quantum number M. Each of these transitions can be replaced by Gaussians and thus one can calculate the envelope of theoretical intervalence band contour.

A significant information about the localization (delocalization) of the extra electron can be obtained from the probability distribution in the configuration (qQ) space. Using eigenfunctions (10.9) of the hamiltonian (10.7) one can obtain the following expression: $P_\nu^{SM}(qQ) = \int \left|\Phi_\nu^{SM}\right|^2 \mathrm{d}\tau_{\mathrm{el}}$ – the probability to find the system at configuration qQ in state Φ_ν^{SM}. This probability is independent of the magnetic quantum number M and has the following form:

$$P_\nu^S(qQ) = \sum_{n,n'} \sum_{m,m'} \chi_n(q)\ \chi_{n'}(q)\, \chi_m(Q)\, \chi_{m'}(Q) \times \left(C_{\nu nm}^{+(S)} C_{\nu n'm'}^{+(S)} + C_{\nu nm}^{-(S)} C_{\nu n'm'}^{-(S)} \right) . \tag{10.16}$$

For obtaining the probability to find the system at configuration qQ in any state one has to summarize (10.16) over all total spin values, its projections and vibronic levels using corresponding Boltzmann distribution:

$$P(qQ) = \frac{\sum_\nu \sum_S (2S+1)\, P_\nu^S(qQ) \exp\left(-E_\nu^S/k_BT\right)}{\sum_\nu \sum_S (2S+1) \exp\left(-E_\nu^S/k_BT\right)} . \tag{10.17}$$

Another important value for estimation of the extent of valence trapping is a degree of delocalization of the itinerant extra electron. According to [11] we define:

$$P_\nu^{SM}(el) = \int\int \left|\Phi_\nu^{SM}\right|^2 \mathrm{d}q\mathrm{d}Q . \tag{10.18}$$

This value consists of three parts and specifies the relative contributions of $\left|\psi_A^{SM}\right|^2$, $\left|\psi_B^{SM}\right|^2$ and $\psi_A^{SM}\psi_B^{SM}$. Since $\psi_A^{SM}\psi_B^{SM}$ is a measure of delocalization, we define the degree of delocalization of the extra electron in state Φ_ν^{SM} by the square of its coefficient as was suggested in [11]. Substituting (10.9) in (10.18) one obtains:

$$\left(\beta_d^S(\nu)\right)^2 = \left\{ \sum_n \sum_m \left[\left(C_{\nu nm}^{+(S)}\right)^2 - \left(C_{\nu nm}^{-(S)}\right)^2 \right] \right\}^2 . \tag{10.19}$$

The degree of delocalization of the extra electron for the whole system is given by the thermal averages:

$$\overline{\beta_d^2} = \frac{\sum_\nu \sum_S (2S+1) \left(\beta_d^S(\nu)\right)^2 \exp\left(-E_\nu^S/k_BT\right)}{\sum_\nu \sum_S (2S+1) \exp\left(-E_\nu^S/k_BT\right)} . \tag{10.20}$$

Equation (10.20) gives us a quantitative description of the degree of delocalization and together with the probability distribution in configuration space (10.17) provides an important information about the behavior of the MV dimer at given temperature.

10.5.2 Analysis. Intervalence absorption band

Here the presented model is proved for one example. The synthesis, crystal structure and Mössbauer data of the mixed-valence iron dimer $[L^1Fe_2(\mu\text{-}OAc)_2](ClO_4)$ were described elsewhere [17]. The schematic structure of the investigated compound is presented in Fig. 10.6. The complex has a centrosymmetric geometry with an Fe–Fe distance of 2.74 Å. Mössbauer data show that the regarded compound is completely delocalized over the whole temperature range. The previously reported intervalence absorption band of the investigated dimer [17, 18] was measured for the compound dissolved in different solvents. To avoid the influence of solvents the near infrared absorption was remeasured for the complex pressed in potassium bromide (1 mg sample mixed with 100 mg KBr and pressed with 10 t) [19]. The investigated compound demonstrates a broad intervalence absorption band in the near infrared region at about $8900\,cm^{-1}$ which differs from the data obtained in solvents (about $9400\,cm^{-1}$). With the temperature increasing this band becomes slightly broader. The position of the maximum of the intervalence absorption band is practically independent of the temperature which is typical for class III compounds. As it was already mentioned in the framework of the pure PKS model the fully delocalized system (class III) exhibits strong narrow intervalence absorption band. But the investigated complex shows a broad intervalence band and can be explained in the model with two different types of vibrations only [13, 16].

The vibronic model dealing with the multicenter and local vibrations can be considered as more or less good approximation reflecting the reality occuring in MV systems. When the whole system consists of well isolated subunits the relevant vibrational modes can be found easily. In the case of MV cluster consisting of strongly coupled subunits (like the present case) the multicenter and local vibrations are mixed and some simplification is required. The core of the complex consists of two iron ions and two bridging oxygen atoms. Let us assume that the main contributions to the vibrational spectrum are due to the

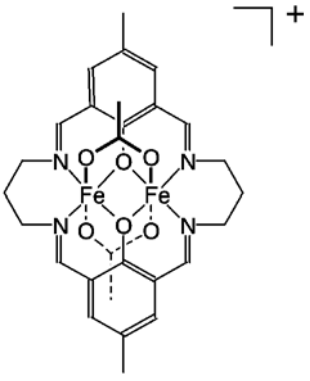

Fig. 10.6. Schematic structure of $[L^1Fe_2(\mu\text{-}OAc)_2](ClO_4)$

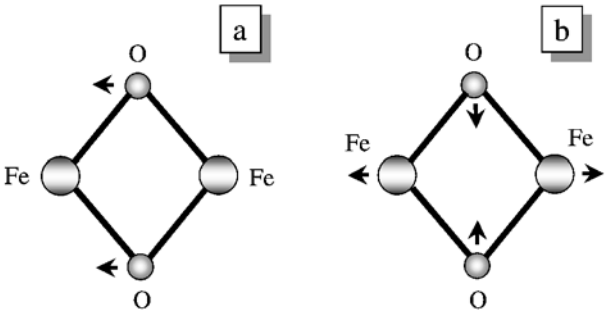

Fig. 10.7. Normal modes associated with (**a**) PKS vibrations and (**b**) Piepho vibrations (the *arrows* show relative nuclear displacement)

core vibrations. Four atoms result in the 6 metal-ligand vibrational degrees of freedom. Figure 10.7 shows two of these 6 normal modes which can be associated as PKS and Piepho types. Vibrations presented in Fig. 10.7a change metal-ligand distances while the metal-metal distance is constant. The situation in Fig. 10.7b is just the opposite: the metal-ligand distances are constant and the modulation of metal-metal distance occurs. Using standard normal coordinate analysis program with force constant from [5, 6] we obtained the following frequencies of vibrations: 310 cm^{-1} for the mode presented in Fig. 10.7a and 125 cm^{-1} for the mode presented in Fig. 10.7b. In our preliminary Raman scattering investigations several low-frequency absorption lines in the region 100–400 cm^{-1} were detected. To indicate the relevant absorption bands a resonance Raman spectroscopic studies will be performed in the nearest future. Of course, the presented model is oversimplified and it is not possible to establish a one-to-one correspondence between the real spectrum of the system and these idealized vibrations. But we believe that this model preserves the main features of the regarded complex as it takes into account both type of vibrations.

Figure 10.8 shows the intervalence absorption band for the investigated compound calculated at low and room temperature. One can see a good correlation between the shape and the position of the experimental and calculated curves. Temperature increasing causes the intervalence absorption band to be broader. The position of the maximum of the theoretical curve is independent of the temperature which is in a good agreement with the experiment.

It should be mentioned that although we have many parameters (double exchange, vibronic coupling parameters with PKS and Piepho vibrations) all of them can be more or less accurately obtained from the comparison between the experimental and theoretical data because their influence on the position and the shape of the intervalence absorption band is different (see Table 10.1). The increase of all of these parameters shifts the position of the maximum of the intervalence band to high energy region but the bigger value of the double exchange results in smaller band width while the growth of coupling

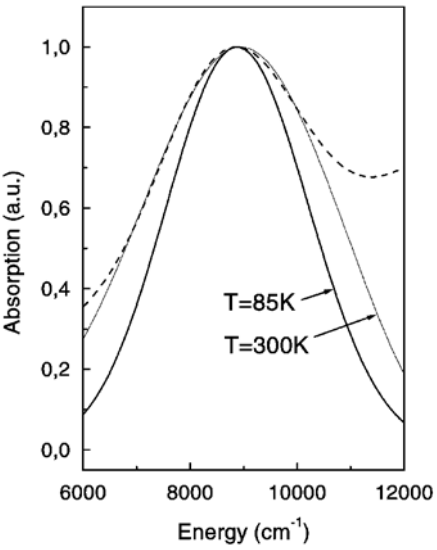

Fig. 10.8. Intervalence absorption band (*dotted curve*, $T = 300\,\mathrm{K}$) [19] and theoretical fit (*solid curves*): $B = 260\,\mathrm{cm}^{-1}$, $\omega = 310\,\mathrm{cm}^{-1}$, $v = 3\,\omega$, $\Omega = 125\,\mathrm{cm}^{-1}$, $\lambda_0 = \Omega$, $W = 0$

Table 10.1. The effects of double exchange (B), PKS (v) and Piepho (λ_0) vibronic coupling parameters on the shape and the position of the intervalence absorption band (IAB) and delocalization degree of the itinerant extra electron (I = increase and D = decrease)

	Energy of the maximum of IAB	Width of IAB	Delocalization degree
B	I	D	I
v	I	I	D
λ_0	I	I	I

parameters leads to a broad band contour with a decrease of the degree of delocalization in the case of PKS vibrations and an increase of the degree of delocalization for the Piepho vibrations.

The obtained value of the double exchange parameter ($B = 260\,\mathrm{cm}^{-1}$) looks rather small as compared to the previous considerations [13, 17–19] and needs some explanations. In the presence of Piepho coupling B is the initial value of double exchange parameter which corresponds to the interaction of metal centers with the interionic distance r_0 (r_0 is the metal–metal distance for the system without extra electron). Piepho type vibrations change this metal–metal distance and, as a result, the double exchange parameter is modified (see (10.6)). The real (effective) value of the double exchange has to be calculated by substituting in (10.6) new nuclear coordinates. An effective increase of the double exchange parameter occurs.

The adiabatic potentials for the investigated compound are shown in Fig. 10.9. As it was found in [16] depending on the relative values of the key parameters of the system several qualitatively different types of the adi-

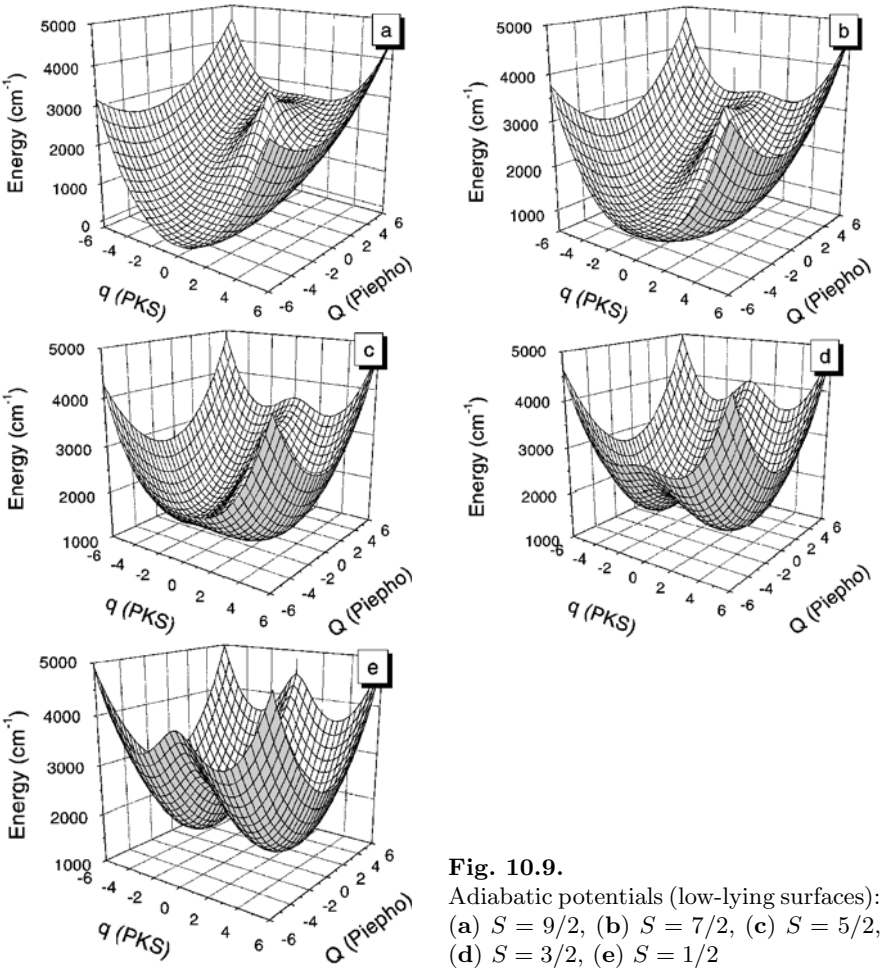

Fig. 10.9.
Adiabatic potentials (low-lying surfaces): (**a**) $S = 9/2$, (**b**) $S = 7/2$, (**c**) $S = 5/2$, (**d**) $S = 3/2$, (**e**) $S = 1/2$

abatic surfaces should be distinguished. For $S = 9/2$ we have the situation when Piepho coupling exceeds the PKS coupling and the double exchange is relatively strong $\left(B\left(S+1/2\right) > \lambda^2\left(S\right)/\Omega - v^2/\omega\right)$. In this case the adiabatic potential has a single deep minimum in $\{0, -\lambda\left(S\right)/\Omega\}$ position (Fig. 10.9a). The extra electron in this minimum is fully delocalized. The effective value of the double exchange parameter calculated in this minimum (10.6) is equal to $885\,\mathrm{cm}^{-1}$ which is in a good agreement with the previously reported result ($B = 820\,\mathrm{cm}^{-1}$ in [13]).

For the adiabatic potentials corresponding to other values of the total spin of the dimer the situation is as follows: both double exchange interaction and vibronic coupling with Piepho type of vibrations are spin dependent and become smaller with spin decreasing while the PKS interaction is spin inde-

pendent and remains the same for all spin states. The relationship between the key parameters of the system changes. For the $S = 7/2$ adiabatic potential we already have the situation which can be characterized as a case of strong PKS coupling and comparatively strong double exchange. The shape of the corresponding adiabatic potential differs from the shape of $S = 9/2$ adiabatic surface but the main peculiarities are the same: a single deep minimum with the fully delocalized extra electron (Fig. 10.9b).

The $S = 5/2$, $3/2$ and $1/2$ adiabatic potentials correspond to the case of strong PKS coupling and comparatively weak double exchange. As it was shown in [16] this type of adiabatic potentials possesses two equivalent minima. The position and deepness of these minima as well as the degree of delocalization of the extra electron depend on the key parameters of the system. As one can see from Figs. 10.9c–e with the total spin value decreasing these minima become deeper, the barrier between them increases and the extra electron becomes more and more localized.

To understand the influence of different spin states on the behavior of the regarded compound we calculated the relative population of the adiabatic surfaces minima at room temperature. For the $S = 7/2$ adiabatic potential this value is about 2.9%. The relative population for the minima of the adiabatic surfaces corresponding to the other (smaller) values of the total spin is less than 0.3% and their effect on the properties of the system is negligible small.

10.5.3 Magnetic behavior

To explain the magnetic properties of the regarded compound we included in the hamiltonian (10.7) zero-field splitting for the ferromagnetic ground state (only axial component D_{gr} of zero-field splitting tensor is assumed to be non zero). The excited states with the other (smaller) values of the total spin are high in energy and their splitting in the zero field is not significant for the magnetic properties of the investigated complex. The temperature dependence of the magnetic susceptibility can be computed using the well-known Van Vleck equation:

$$\chi_{\text{Van Vleck}}(T,\vartheta) = \frac{N\sum\limits_{S}\sum\limits_{M}\sum\limits_{\nu=0}^{\infty}\left[\frac{\left(E_{SM}^{(1)}(\nu)\right)^2}{k_BT} - 2E_{SM}^{(2)}(\nu)\right]\exp\left(-\frac{E_{SM}^{(0)}(\nu)}{k_BT}\right)}{\sum\limits_{S}\sum\limits_{M}\sum\limits_{\nu=0}^{\infty}\exp\left(-\frac{E_{SM}^{(0)}(\nu)}{k_BT}\right)}, \tag{10.21}$$

where $E_{SM}^{(0)}(\nu)$ is the energy of vibronic level ν in zero field, $E_{SM}^{(1)}(\nu)$ and $E_{SM}^{(2)}(\nu)$ are first- and second-order Zeeman coefficients respectively. The summation in (10.21) runs over all values of total spin S, magnetic quantum numbers M and all vibronic levels. The magnetic susceptibility is a function of the angle ϑ between the applied magnetic field and the principle axis of ZFS

tensor (it is significant mostly for the low temperature region) [20]. To find the powder-average magnetic susceptibility it is necessary to integrate (10.21) over ϑ:

$$\chi(T) = \frac{1}{2}\int_0^{\pi} \chi(T,\vartheta)\sin\vartheta \mathrm{d}\vartheta \,. \tag{10.22}$$

The experimental magnetic properties of the regarded compound are shown in Fig. 10.10 as well as the theoretical fit (relative error is about 0.4%). The value of the effective magnetic moment at low temperature (but more than 30 K) indicates a ferromagnetic ground state. In the temperature region 50 K – 300 K the magnetic moment slightly depends on the temperature. The high temperature magnetic behavior is very sensitive to the isotropic exchange parameter (at given values of the double exchange and vibronic coupling parameters) and allows us to determine this value very accurately. The sharp decrease of the effective magnetic moment below 30 K is explained by the positive value of the axial component of the zero field splitting tensor for the ferromagnetic ground state. In our calculations we found $J = -5\,\mathrm{cm}^{-1}$ and $D_{gr} = 4\,\mathrm{cm}^{-1}$ which are in a good agreement with the values obtained in [13].

Figure 10.11 shows the probability distribution in the configuration space for the investigated compound at low and at room temperature. At low temperature the probability distribution in configuration space represents a sharp peak at the position of the minimum of $S = 9/2$ adiabatic surface. It corresponds to the most probable configuration in which both subunits are equivalent and have the equal oxidation degree. The extra electron is fully delocalized. With the temperature increasing this peak becomes lower and the probability to find the system at configuration with smaller absolute values of

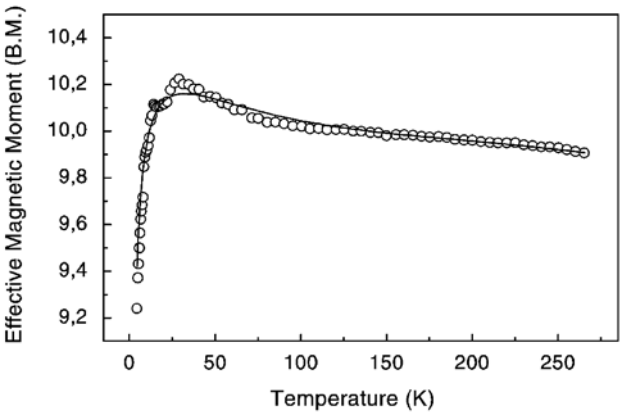

Fig. 10.10. Effective magnetic moment (*open circles* represent the experimental values, *solid curve* – best fit obtained with $B = 260\,\mathrm{cm}^{-1}$, $J = -5\,\mathrm{cm}^{-1}$, $\omega = 310\,\mathrm{cm}^{-1}$, $v = 3\,\omega$, $\Omega = 125\ \mathrm{cm}^{-1}$, $\lambda_0 = \Omega$, $D_{gr} = 4\,\mathrm{cm}^{-1}$, $g_{\|} = 1.8$, $g_{\perp} = 2.1$)

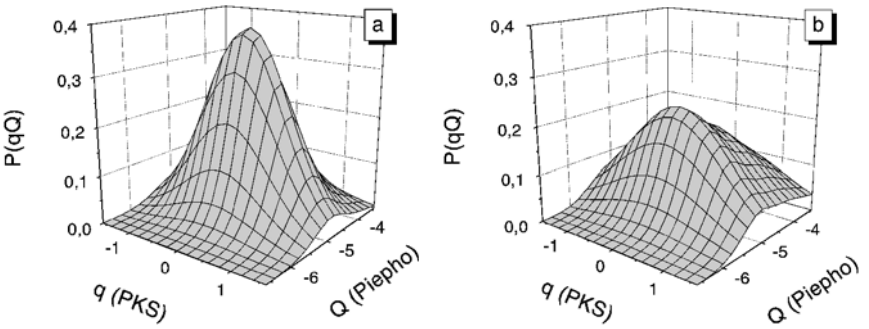

Fig. 10.11. Probability distribution in configuration space: (**a**) $T = 30\,\mathrm{K}$, $\overline{\beta_\mathrm{d}^2} = 0.97$; (**b**) $T = 300\,\mathrm{K}$, $\overline{\beta_\mathrm{d}^2} = 0.90$

Q increases (it corresponds to the thermal elongation of Fe-Fe distance). The extra electron remains fully delocalized. This is the untrapped case. The regarded complex belongs to Class III in Robin and Day classification scheme. Respective degrees of delocalization of the extra electron are $\overline{\beta_\mathrm{d}^2} = 0.97$ at $T = 30\,\mathrm{K}$ and $\overline{\beta_\mathrm{d}^2} = 0.90$ at $T = 300\,\mathrm{K}$.

10.6 Summary

The behavior of MV dimers is determined by a strong competition between several processes: double exchange and vibronic coupling with different type of vibrations. The double exchange (or spin dependent electron delocalization) in dimeric compounds always leads to a symmetric splitting of the spin states, which is larger as the spin increases. As a result, a strong stabilization of the ferromagnetic spin state occurs independently of the sign of the double exchange parameter. The fully delocalized situation is rarely achieved in MV systems due to vibronic coupling. In the framework of the PKS model vibronic interaction represents a trapping effect that tends to localize the extra electron. This term leads to an effective reduction of the double exchange parameter. Taking into account multicenter vibrations the transfer integral is modified by the motion of the metal ions. The resulting effect of this mode is the effective increasing of the double exchange parameter and the extra electron delocalization.

Acknowledgements. The author thanks Professors B. S. Tsukerblat and W. Haase for fruitful discussions. The research work was supported by the Deutsche Forschungsgemeinschaft (project Ha 782/43-1).

References

1. E. L. Bominaar, C. Achim, S. A. Borshch, J.-J. Girerd, E. Münck: Inorg. Chem. **36**, 3689 (1997)
2. C. Achim, E. L. Bominaar, E. Münck: J. Bioinorg. Chem. **3**, 126 (1998)
3. V. Papaefthymiou, J.-J. Girerd, I. Moura, J. J. G. Moura, E. Münck: J. Am. Chem. Soc. **109**, 4703 (1987)
4. L. Noodleman, D. A. Case: Adv. Inorg. Chem. **38**, 423 (1992)
5. D. R. Gamelin, E. L. Bominaar, M. L. Kirk, K. Wieghardt, E. I. Solomon: J. Am. Chem. Soc. **118**, 8085 (1996)
6. D. R. Gamelin, E. L. Bominaar, C. Mathoniere, M. L. Kirk, K. Wieghardt, J.-J. Girerd, E. I. Solomon: Inorg. Chem. **35**, 4323 (1996)
7. C. Zener: Phys. Rev. **82**, 403 (1951)
8. P. W. Anderson, H. Hasegawa: Phys. Rev. **100**, 675 (1955)
9. S. B. Piepho, E. R. Krausz, P. N. Schatz: J. Am. Chem. Soc. **100**, 2996 (1978)
10. P. N. Schatz: In: *Mixed-Valence Compounds*, ed. by D. B. Brown (Riedel, Dordrecht 1980), p. 115
11. K. Y. Wong, P. N. Schatz: Prog. Inorg. Chem. **28**, 369 (1981)
12. M. B. Robin, P. Day: Adv. Inorg. Radiochem. **10**, 247 (1967)
13. S. M. Ostrovsky, R. Werner, K. Nag, W. Haase: Chem. Phys. Lett. **320**, 295 (2000)
14. S. B. Piepho: J. Am. Chem. Soc. **110**, 6319 (1988)
15. S. B. Piepho: J. Am. Chem. Soc. **112**, 4197 (1990)
16. J. J. Borras-Almenar, E. Coronado, S. M. Ostrovsky, A. V. Palii, B. S. Tsukerblat: Chem. Phys. **240**, 149 (1999)
17. C. Saal, S. Mohanta, K. Nag, S. K. Dutta, R. Werner, W. Haase, E. Duin, M. K. Johnson: Ber. Buns. Phys. Chem. **100**, 2086 (1996)
18. S. K. Dutta, J. Ensling, R. Werner, U. Flörke, W. Haase, P. Gütlich, K. Nag: Angew. Chem. **109**, 107 (1997)
19. C. Saal: PhD Thesis, Darmstadt University of Technology, Darmstadt (1998)
20. O. Kahn: *Molecular Magnetism* (VCH, Weinheim 1993)

Part IV

Relaxation Phenomena in High-T_c Superconducting Systems, Nonlinear Optical Polymers and Metallic Glasses

11

High-T_c Superconductors

11.1 Superconductivity suppression and critical currents in the $R_{1-x}Pr_xBa_2Cu_3O_{7-\delta}$ systems (R = Ho, Y)

Z. Tomkowicz and M. Bałanda

11.1.1 Introduction

One of the most intensively studied topics in the field of high temperature superconductivity was the superconductivity suppression by Pr substitution in the $R_{1-x}Pr_xBa_2Cu_3O_{7-\delta}$ systems (R = Y, rare earth). Pr is the only suppressing dopant, which forms the solid solution $R_{1-x}Pr_xBa_2Cu_3O_{7-\delta}$ in the whole concentration range without any change in the crystal structure. Three basic mechanisms of this suppression were considered [1]: (i) hole filling due to possible near 4^+ valency of Pr-ion, (ii) magnetic pair breaking mechanism of Abrikosov-Gor'kov, and (iii) hole localization through disorder. It has been recently shown that $PrBa_2Cu_3O_{7-\delta}$ can be superconducting [2], but still it is not clear whether this is an intrinsic property or this is due to some defects. In any case the superconductivity suppression in $R_{1-x}Pr_xBa_2Cu_3O_{7-\delta}$ for low Pr doping seems to be a legitimate property. Fehrenbacher and Rice (F-R) [3] explained the lack of superconductivity in $PrBa_2Cu_3O_{7-\delta}$ through the localization of holes in hybridized Pr4f-O2p_π orbitals. According to F-R there are two kinds of Pr-ions: Pr^{III} and Pr^{IV}, which appear in almost equal proportions. The first of them is a normal ionic state $Pr^{3+}(4f^2)$, the second is a mixture of the ionic state $Pr^{4+}(4f^1)$ and $Pr^{3+}(4f^2L)$ state, where L denotes a hole residing on the ligand. The resulting hybridized F-R state has the wave function of the form

$$|\Psi\rangle = \alpha \left|4f^1p^6\right\rangle + \beta \left|4f^2p^5\right\rangle \quad . \tag{11.1}$$

When the weight of the second component β is dominant then Pr^{IV}-ion is seen in many experiments as Pr^{3+}-ion.

For the most studied system $Y_{1-x}Pr_xBa_2Cu_3O_{7-\delta}$ superconductivity disappears at the critical concentration $x_c \sim 0.6$. In general, x_c depends on the ionic radius r of R^{3+}-ion. The greater is r, the smaller is x_c. The case of R = Ho seems to be particularly interesting, because $r(Ho^{3+}) = r(Y^{3+})$, however, while Y^{3+}-ion is diamagnetic, the Ho^{3+}-ion possesses a big magnetic moment. Thus, it is interesting to check whether this big magnetic moment plays a role in superconductivity suppression. In this work two systems with R = Y and R = Ho were investigated and their critical temperatures T_c of transition into superconducting state were compared as a function of Pr concentration. In addition, inter- and intra-grain critical currents were determined from magnetic AC and DC measurements, respectively.

This section is a review based on published results.

11.1.2 Experimental

All samples of the $Ho_{1-x}Pr_xBa_2Cu_3O_{7-\delta}$ and $Y_{1-x}Pr_xBa_2Cu_3O_{7-\delta}$ systems were prepared by the solid state reaction method. Starting components were high purity oxides and $BaCO_3$, appropriate amounts of which were mixed, hand pressed into pellets and calcined in an alumina boat in air at 900 °C for 24 h. Then the samples were crushed, ground, pressed into pellets under press and sintered at 930 °C for 30 h under flowing oxygen and subsequently cooled in oxygen. This process was repeated several times and the sintering temperature was slightly varied according to Pr concentration. During the last process the samples were kept 6 h in an oxygen stream at 450 °C before cooling to room temperature.

Good quality of the samples was confirmed by means of an X-ray powder diffractometer. The samples had a pronounced texture with the preferred orientation of c-axis perpendicular to the surface of pellets. The density of samples was approximately 85% of the theoretical value for the doped samples and $\sim$ 80% for the undoped samples. For most measurements the samples were cut along their diameter into bars of approximately $2.5 \times 2 \times 10\,\mathrm{mm}^3$.

DC electrical resistance was measured by means of the four points method. Measurements of AC magnetic susceptibility (ACS) $\chi = \chi' - i\chi''$ were performed with a Lake Shore susceptometer, model 7225 as a function of temperature T, frequency f and amplitude of the driving magnetic field H_{AC}. Magnetization hysteresis loops were obtained with the same instrument using the extraction method.

The demagnetization factor for whole samples was estimated roughly to be about $0.1 \cdot 4\pi$.

11.1.3 Electrical resistance study and discussion of the mechanism of the superconductivity suppression

The temperature dependences of resistance were measured for the samples of the $Ho_{1-x}Pr_xBa_2Cu_3O_{7-\delta}$ and $Y_{1-x}Pr_xBa_2Cu_3O_{7-\delta}$ systems. The obtained results are similar for both systems and are shown in Fig. 11.1 for

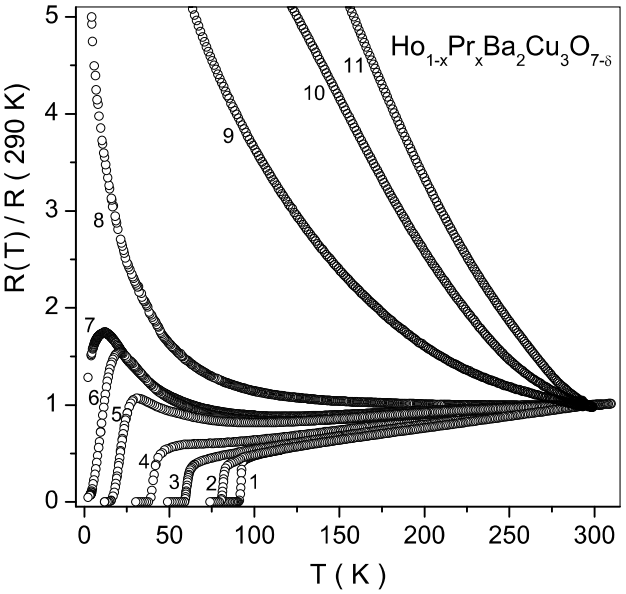

Fig. 11.1. Temperature dependences of electrical resistance for the $Ho_{1-x}Pr_x$ $Ba_2Cu_3O_{7-\delta}$ system. The *curves* are normalized to the value of resistance at 290 K. The numbers denote concentrations: 1: $x = 0$, 2: $x = 0.15$, 3: $x = 0.30$, 4: $x = 0.45$, 5: $x = 0.55$, 6: $x = 0.57$, 7: $x = 0.60$, 8: $x = 0.65$, 9: $x = 0.80$, 10: $x = 0.90$, 11: $x = 1.0$. From [4]

the $Ho_{1-x}Pr_xBa_2Cu_3O_{7-\delta}$ system. It is seen in the figure that samples with $x < 0.60$ show a superconducting transition. The width of transition increases with Pr concentration, which seems to be an intrinsic property of the studied system, because nothing changes when a sample is subjected to the additional preparation stage. For x close to 0.60 and more, a semiconducting-like character appears. Critical temperature T_c of transition to the superconducting state was taken at the middle of transition. Concentration dependences of T_c for both systems are shown in Fig. 11.2. It is seen that both dependences are practically the same. The common critical concentration x_c equals 0.58 ± 0.004 obtained by fitting the end part of $T_c(x)$ dependence to $A(x_c - x)^{1/2}$.

With the mechanisms of superconductivity suppression, considered up to date, it was not possible to describe satisfactorily the $T_c(x)$ curve in the whole superconducting concentration range up to x_c. The mechanism described in this work (see also [4]) is based on the F-R unusual model of the electronic structure of $PrBa_2Cu_3O_{7-\delta}$ (see Sect. 11.1.1). In this model only Pr^{IV}-ions are suppressing the superconductivity. In our model we allow the relative number of Pr^{IV}-ions to change with concentration. If we assume that there is about 80–90% of Pr^{IV}-ions (with respect to the whole number of Pr-ions) in the low x region, i.e. $\nu_0 = 0.80$–0.90 and this percent varies with Pr concentration as

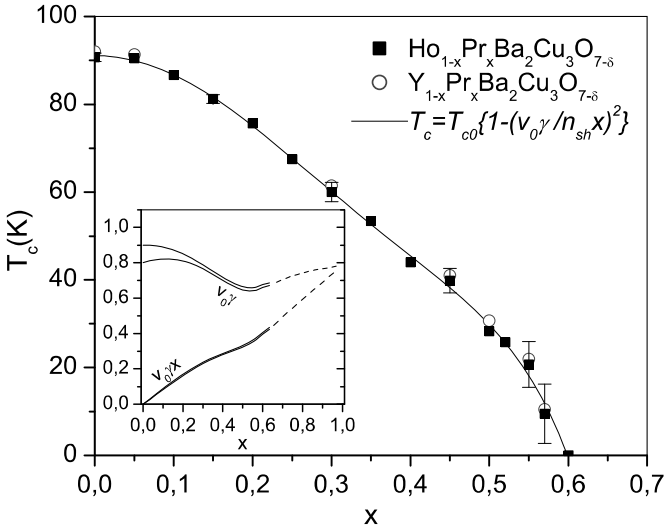

Fig. 11.2. Critical temperatures vs. Pr concentration for the $Ho_{1-x}Pr_xBa_2Cu_3O_{7-\delta}$ and for the $Y_{1-x}Pr_xBa_2Cu_3O_{7-\delta}$ systems. The *line* is a polynomial fit through the points for the $Ho_{1-x}Pr_xBa_2Cu_3O_{7-\delta}$ system to guide the eye. *Vertical bars* denote widths of transition for this system. *Inset*: concentration dependence of the relative number $\nu_0\gamma$ of Pr^{IV}-ions (with respect to all Pr-ions) and of $\nu_0\gamma x$ (relative number of Pr^{IV}-ions with respect to all R-ions) being equal to the number of trapped holes. There are two curves – one is for $\nu_0 = 0.8$ and the second for $\nu_0 = 0.9$. *Dashed lines* for x above 0.6 are hypothetical (see text)

described by parameter γ, normalized to 1 for $x = 0$, then $T_c(x)$ curve can be described by the following formula

$$T_c = T_{c0}\left\{1 - \left(\frac{\nu_0\gamma(x)}{n_{sh}}\,x\right)^2\right\} \quad . \tag{11.2}$$

The predicted $\nu_0\gamma(x)$ dependence, needed for description of $T_c(x)$ curve is shown in the inset to Fig. 11.2. Unfortunately, our model does not predict the value of $\nu_0\gamma$ for x above 0.6. The dashed line for $x > 0.6$ is a hypothetical dependence. We assume the value of $\nu_0\gamma(1) = 0.8$ in accordance with the number of all trapped holes in $PrBa_2Cu_3O_{7-\delta}$ [5].

Also the $\nu_0\gamma x$ product is shown in Fig. 11.2. This quantity has interpretation of the relative number of Pr^{IV}-ions with respect to all rare earth ions, or of the number of holes trapped by F-R states. It is seen that all sheet holes are trapped already at $x = 0.6$. Above this concentration the holes transferred from chains are trapped too until $x = 1$, in accordance with the theoretical model of electronic structure of $Y_{1-x}Pr_xBa_2Cu_3O_{7-\delta}$ published by Wang et al. [6].

Thus, the superconductivity suppression in the $Ho_{1-x}Pr_xBa_2Cu_3O_{7-\delta}$ system is understood by the hole localization at Pr^{IV}-ions, the relative number of which changes with the concentration. The M-I transition in Cu-O_2 planes at $x = x_c$ is the natural consequence of trapping all sheet holes.

11.1.4 AC magnetic susceptibility studies

It is expected that Pr produces flux pinning centers (due to the local suppression of the superconducting order parameter). Thus for small x values in the range of the plateau of the $T_c(x)$ curve the critical current can be greater. Indeed, there were some reports that Pr doping improves the intragrain critical current for small x values in the $Y_{1-x}Pr_xBa_2Cu_3O_{7-\delta}$ system [7–9]. Concerning intergrain critical current, no improvement of this current was observed with Pr doping as reported by Widder et al. [10] for the $Y_{1-x}Pr_xBa_2Cu_3O_{7-\delta}$ system in the concentration range $0 \leq x \leq 0.3$. These authors used the AC magnetic susceptibility method and analyzed their data in the frame of the critical state model. It is still interesting to study AC susceptibility behavior for the higher concentration range.

In Fig. 11.3 temperature dependences of χ' and χ'', obtained for different Pr concentrations, are shown. Usually, the onset of a diamagnetic signal is observed at the offset of resistance. With increasing Pr doping the temperature of this onset deviates more from T_c determined in the resistive way. For $x = 0.52$ the value of the amplitude $H_{AC} = 0.002$ Oe is probably still too high and the screening is not complete. How $\chi(T)$ evolves with H_{AC} is shown in Fig. 11.4. Two cases: $x = 0.25$ and $x = 0.52$ are compared. This strong amplitude dependence allows to analyze the data in terms of the critical state model.

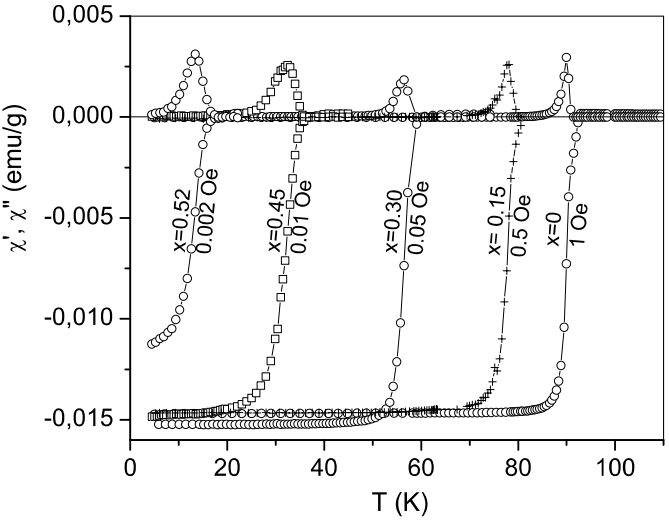

Fig. 11.3. χ vs. T dependences for the $Ho_{1-x}Pr_xBa_2Cu_3O_{7-\delta}$ system. From [13]

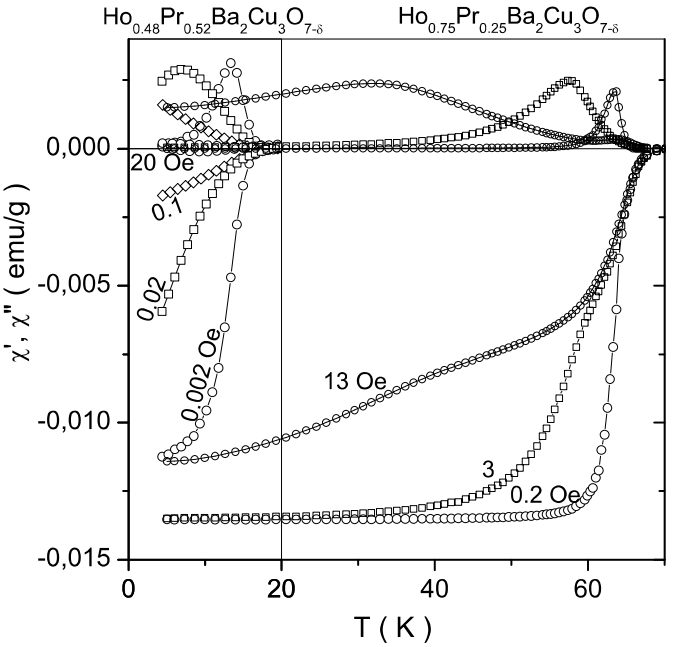

Fig. 11.4. χ vs. T curves for $Ho_{0.75}Pr_{0.25}Ba_2Cu_3O_{7-\delta}$ and $Ho_{0.48}Pr_{0.52}Ba_2Cu_3O_{7-\delta}$ taken at different amplitudes of the driving AC field. Curves for $Ho_{0.48}Pr_{0.52}Ba_2Cu_3O_{7-\delta}$ are presented only below 20 K

The $\chi(H_{\mathrm{AC}})$ dependences were measured for different concentrations. Exemplary results obtained at different temperatures for two concentrations $x = 0.40$ and $x = 0.15$ are shown in Fig. 11.5. For a correspondingly high field a plateau is observed on the $\chi'(H_{\mathrm{AC}})$ curve, from which a value of the effective permeability μ_{eff} of granular material [11] can be estimated as $1+\chi'_{pl}$, were χ'_{pl} is taken at the plateau region. These values of μ_{eff} are dependent on T and x. The T dependence should result from the temperature dependence of the London penetration depth $\lambda_g(T)$, when it is comparable with the grain dimension r_g. Instead, the x dependence should result from the expected increase of λ_g with x [12]. Thus, it may be concluded that $\mu_{\mathrm{eff}}(x)$ increases not because of increasing volume fraction of nonsuperconducting matrix, but because of decreasing r_g/λ_g ratio. This conclusion is in agreement with SEM studies, which showed that the material is homogeneous and that the grain diameter does not vary with Pr doping [13]. Of course, for detailed calculation of μ_{eff} one should take into account the anisotropy of λ_g and of grain dimension. The estimated values of μ_{eff} (extrapolated to 0 K) were contained in the interval: 0.30–0.67 for x between 0 and 0.40, respectively.

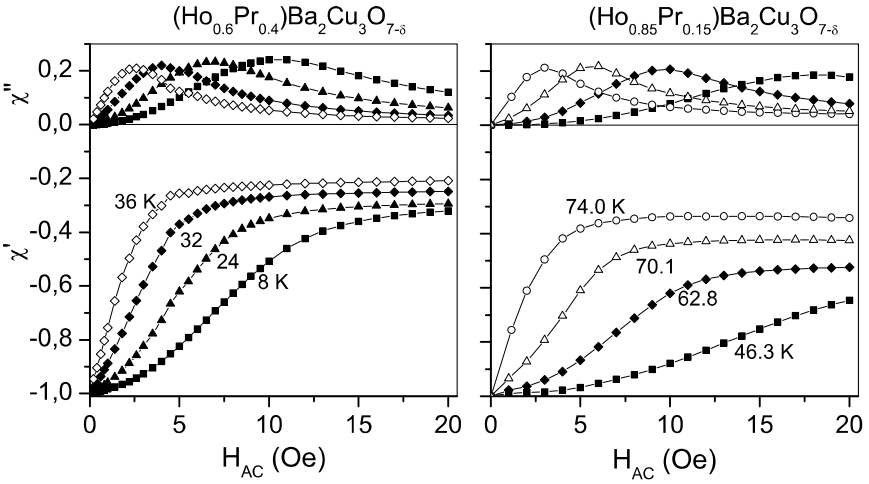

Fig. 11.5. χ vs. amplitude of the driving field for $Ho_{0.60}Pr_{0.40}Ba_2Cu_3O_{7-\delta}$ and $Ho_{0.85}Pr_{0.15}Ba_2Cu_3O_{7-\delta}$ taken at different temperatures. From [13]

11.1.4.1 Intergrain critical currents

In order to obtain information about critical currents the following equation of the critical state model can be used

$$J_c = \frac{H_p - H_{c1}}{r}, \tag{11.3}$$

where H_p is the so-called full penetration field, i.e. the field at which the supercurrent penetrates to the center of the sample, H_{c1} is the first critical field and r is the sample radius.

In the Kim critical state model [14] for long samples of square cross section, H_p nearly equals $H_{\rm AC}$ at the temperature of $\chi''_{\rm max}$. Thus, measuring the position $H_{\rm AC}$ of $\chi''_{\rm max}$ on $\chi''(H_{\rm AC})$ curves, the value of $H_p(T)$ is obtained. Similarly, measuring the position T of $\chi''_{\rm max}$ on $\chi''(T)$ curves, the temperature T_p is obtained at which $H_{\rm AC} = H_p(T_p)$. The values of current obtained from both kinds of dependences overlapped in the intermediary temperature range. In Fig. 11.6 these values are drawn by black and open points, respectively. It is seen in Fig. 11.6 that J_c for the Ho-system is a monotonically decreasing function of Pr doping, which is in agreement with the results of Widder et al. [10] for the $Y_{1-x}Pr_xBa_2Cu_3O_{7-\delta}$ system ($0 \le x \le 0.3$). In ceramic materials the critical current is limited mainly by junctions. For low Pr doping the junctions of the S-I-S (superconductor-insulator-superconductor) type are expected, but at higher doping $J_c(T)$ dependences suggest junctions of other type, possibly S-N-S. These $J_c(T)$ dependences were fitted assuming above types of junctions. For S-I-S type Ambegaokar-Baratoff [15, 16] formula was used and for S-N-S type the formula of Yu and Sayer [17] was used.

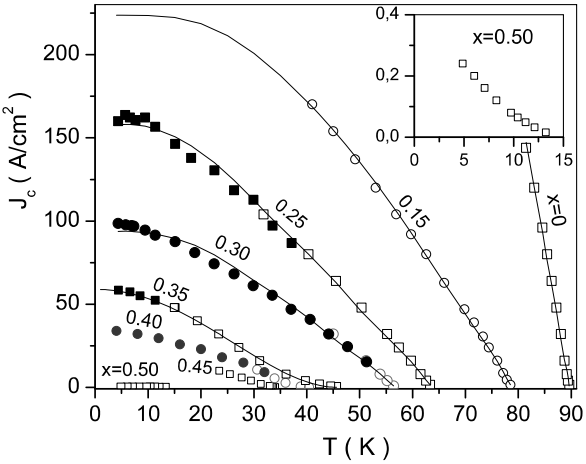

Fig. 11.6. Intergranular critical currents vs. T for the $Ho_{1-x}Pr_xBa_2Cu_3O_{7-\delta}$ system. *Solid lines* for $x = 0$, 0.15, 0.25 and 0.30 are fits to the S-I-S model and *solid line* for $x = 0.35$ is a fit to the S-N-S model. *Solid* and *open symbols* refer to two different kinds of experiments (see text). *Inset* shows the result for the concentration $x = 0.50$ in an enlargement. From [13]

For low concentrations x ($x \leq 0.25$) the obtained $J_c(T)$ curves could be well fitted using the S-I-S model. This is in agreement with Widder et al. [10], who also interpreted their results for the $Y_{1-x}Pr_xBa_2Cu_3O_{7-\delta}$ system ($0 \leq x \leq 0.3$) in terms of S-I-S junctions. Although for higher x ($x = 0.35$ and $x = 0.40$) good fits could be obtained with S-N-S model, see Fig. 11.6, these fits were not reliable because of correlation between parameters. The fitting parameters point at very thin intergrain boundaries. Such possibility can be accepted, when a number of nonsuperconducting percolating clusters, rich in Pr-ions, increases in grains with Pr doping. Then they can play a role of additional grain boundaries of the S-N-S type influencing results of fitting.

It should be noted that the decrease of critical current with Pr doping is a consequence of the global decrease of the condensation energy. Both the above discussed junction models are consistent with this statement. However, the particular form of $J_c(T)$ dependence can result not only from the character of weak junctions. At $T > 0$ K the flux creep can superimpose. Anderson flux creep theory [18, 19] predicts a linear $J_c(T)$ dependence at low temperatures. It would be interesting to know if the role of flux creep increases with Pr doping. Unfortunately, the flux contribution cannot be derived from the data obtained from the critical state model.

11.1.4.2 Study of the flux creep

The shift in the susceptibility, observed in ceramic materials with varying frequency f can be explained in terms of the flux creep at the grain boundaries.

This shift can be described by the Arrhenius relation

$$f = f_0 e^{-E_a/k_B T}, \tag{11.4}$$

where E_a is the activation energy. It can be shown [20, 21] that for small values of H_{AC} the parameter E_a can be approximated by the pinning energy U_0 of the flux lines.

The ACS frequency characteristics were studied for two compositions $Ho_{0.65}Pr_{0.35}Ba_2Cu_3O_{7-\delta}$ and $Ho_{0.50}Pr_{0.50}Ba_2Cu_3O_{7-\delta}$.

Exemplary $\chi(T)$ curves obtained at different frequencies f are shown in the inset to Fig. 11.7 for the sample with $x = 0.35$. The small temperature shift of χ'' peak with frequency is well seen. This temperature shift can be described by (11.4) with $T = T_p$, position of a peak maximum. The main Fig. 11.7 shows $\ln f$ vs. $1/T_p$ dependences obtained for $x = 0.35$ at DC magnetic fields of 10 Oe and for $x = 0.50$ at DC magnetic field of 0 and 10 Oe. The linear character of these dependences confirms the correctness of analysis in terms of the flux creep model without invoking an activation energy distribution. However, the obtained values of f_0 ($\sim 10^{63}$) are without physical sense. Taking into account the temperature dependence of the activation energy [22] $U(T) = U_0(1 - T/T_c)$, the simplest one, but compatible with the Arrhenius law, the reasonable values of f_0 were obtained: $1.7{\cdot}10^{10}$ Hz for $x = 0.35$ and $8.6{\cdot}10^6$ Hz for $x = 0.50$ at $H_{\mathrm{DC}} = 10$ Oe or $3.2{\cdot}10^7$ Hz for $x = 0.50$ at $H_{\mathrm{DC}} = 0$ Oe. The corresponding values of U_0 were 7099 K, 155 K or 242 K. The first value can be compared with that obtained from our resistance measurements,

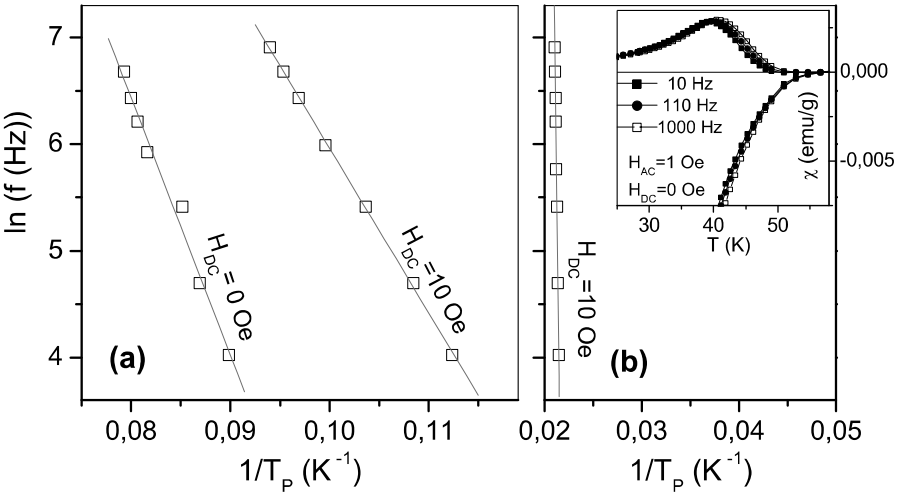

Fig. 11.7. $\ln f$ vs. reciprocal temperature for $Ho_{0.50}Pr_{0.50}Ba_2Cu_3O_{7-\delta}$ (**a**) and $Ho_{0.65}Pr_{0.35}Ba_2Cu_3O_{7-\delta}$ (**b**). *Lines* are linear fits to the data. *Inset*: χ vs. T curves for $Ho_{0.65}Pr_{0.35}Ba_2Cu_3O_{7-\delta}$ taken at different frequencies of the driving AC field. Both (**a**) and (**b**) diagrams are drawn in the same scale. From [13]

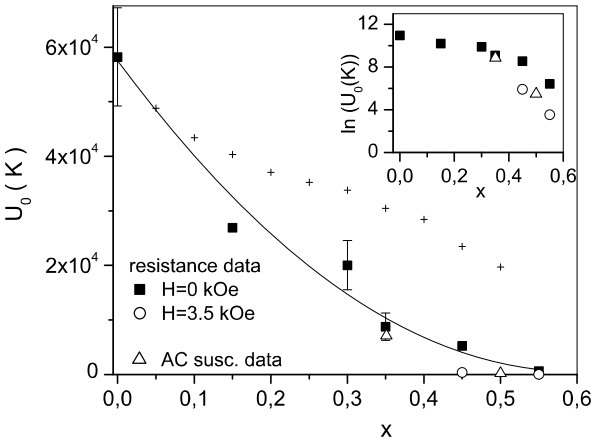

Fig. 11.8. Concentration dependence of the intergranular pinning energy for the $Ho_{1-x}Pr_xBa_2Cu_3O_{7-\delta}$ system. The same is on the *inset* in the logarithmic scale. The *solid line* is a guide for the eye. The *crosses* represent $U_0(x)$ dependence after elimination of the decrease of the condensation energy (see text). From [13]

which is 8753 K. For comparison, we also quote the value U_0 $138{\cdot}10^3$ K found by Nikolo and Goldfarb for polycrystalline $YBa_2Cu_3O_{7-\delta}$ in zero field limit using ACS method [23]. In Fig. 11.8 all results for U_0 (including resistance data) as a function of Pr concentration are shown. As is seen, U_0 strongly decreases with Pr doping. One can roughly eliminate the change of condensation energy by dividing $U_0(x)$ dependence by $T_c^2(x)$ [24]. The resulting dependence is a decreasing function of Pr concentration. Thus the flux creep at grain boundaries should really increase with Pr concentration. Because of flux creep it is not possible to state unequivocally whether for $x > 0.25$ weak junctions change character from S-I-S to S-N-S.

The high values of U_0, marked in Fig. 11.8 for small Pr doping, seem to be in discordance with the low transport critical current in these materials. But it was shown [20, 26, 27] that the critical current density is not determined by the pinning potential only but by the pinning force density U_0/Va, where V is the activation volume and a is the hop distance. Both V and a are comparable with dimensions of grains between which intergranular Josephson vortices penetrate.

11.1.5 Hysteresis loops and intragranular critical current

As already known, both intergranular critical current and flux pinning energy strongly decrease with Pr doping into $HoBa_2Cu_3O_{7-\delta}$. However, an enhancement of the intragranular critical current J_{cg}, with Pr doping is expected, similarly as observed in the $Y_{1-x}Pr_xBa_2Cu_3O_{7-\delta}$ system [7].

In this section hysteresis loops for the $Ho_{1-x}Pr_xBa_2Cu_3O_{7-\delta}$ system obtained at 4.3 K are presented for different Pr concentrations. Because of strong magnetism of Ho we present also the loops for the $Y_{1-x}Pr_xBa_2Cu_3O_{7-\delta}$ system in order to show the pure effect of Pr.

The hysteresis loops for $Ho_{1-x}Pr_xBa_2Cu_3O_{7-\delta}$ ($x = 0$, 0.35) are presented in Fig. 11.9 , where also the loops for $YBa_2Cu_3O_{7-\delta}$ and $Y_{0.45}Pr_{0.55}Ba_2Cu_3O_{7-\delta}$ are shown for comparison. The loop for $x = 0.55$ is very thin, so that in the scale of figure its width seems to be equal zero, but it does not close even at 50 kOe. The loops for Ho-system are tilted because of paramagnetism of Ho^{3+}-ions and the loop for $Y_{0.45}Pr_{0.55}Ba_2Cu_3O_{7-\delta}$ is tilted mainly because of paramagnetism of Pr-ions. For estimation of intragranular critical current densities the following formula, derived from the Bean model [28], was used

$$J_{cg} = \frac{15\left|M^+ - M^-\right|}{r_g} \tag{11.5}$$

(in CGS units; M^+, M^- in emu/cm^3), where r_g is the average grain radius. The values of M^+ and M^- were taken for $H = 3$ T, for r_g the value of $2{\cdot}10^{-4}$ cm was assumed [13]. We did not take into account the correction for paramagnetism [29] for the Ho-system, which can lead to about 20% of error.

The obtained concentration dependence of J_{cg} is shown in Fig. 11.10. No remarkable enhancement of the intragrain critical current is seen for the

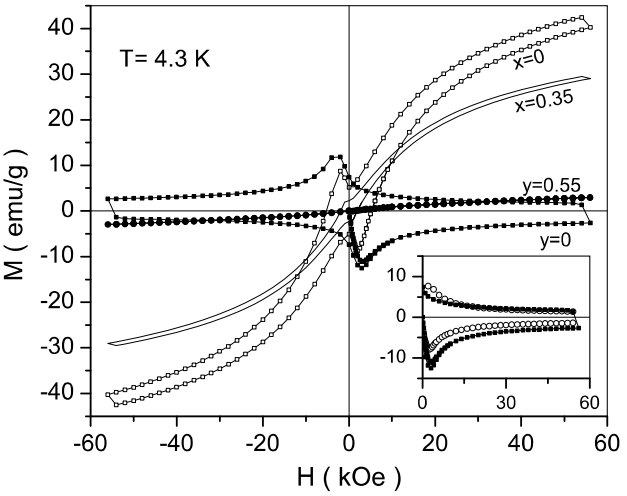

Fig. 11.9. Magnetization hysteresis loops for two samples of the $Ho_{1-x}Pr_xBa_2Cu_3O_{7-\delta}$ system with $x = 0$ and $x = 0.35$ and for two samples of the $Y_{1-x}Pr_xBa_2Cu_3O_{7-\delta}$ system with $x = 0$, 0.55. All loops were measured at 4.3 K. In the *inset*, the halves of the loops of $YBa_2Cu_3O_{7-\delta}$ (*black symbols*) and of $HoBa_2Cu_3O_{7-\delta}$ with subtracted paramagnetic contribution (*open symbols*) are compared. From [13]

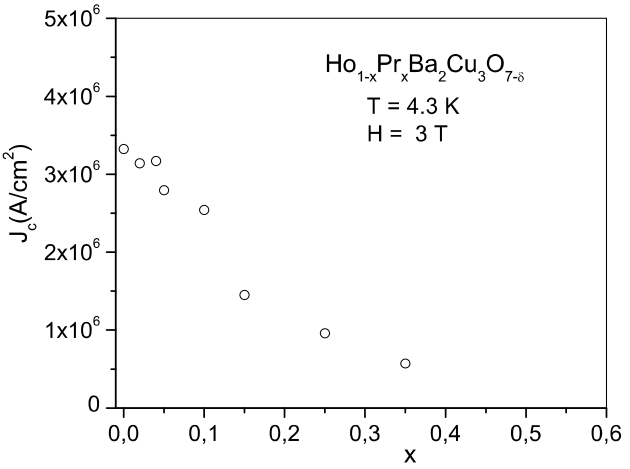

Fig. 11.10. Intragranular critical current density vs. Pr concentration. From [13]

$Ho_{1-x}Pr_xBa_2Cu_3O_{7-\delta}$ system in the concentration region $0 \leq x \leq 0.1$. This is discordant with the literature results for the $Y_{1-x}Pr_xBa_2Cu_3O_{7-\delta}$ system [7–9]. The reasons of this discordance can be different: the magnetic moment of the Ho-ion, conditions of measurements (e.g. $T = 10$ K, selffield in [7]) or conditions of synthesis.

11.1.6 Concluding remarks

Superconducting properties of the $Ho_{1-x}Pr_xBa_2Cu_3O_{7-\delta}$ system were studied by measurements of electric resistance, AC magnetic susceptibility and magnetization hysteresis loops.

It was shown that Pr concentration dependence of critical temperature for the $Ho_{1-x}Pr_xBa_2Cu_3O_{7-\delta}$ system is the same as for the $Y_{1-x}Pr_xBa_2Cu_3O_{7-\delta}$ system. The mechanism of superconductivity suppression by Pr substitution was proposed, which is based on the hole trapping.

Intergranular critical currents and adequate pinning energies for the $Ho_{1-x}Pr_xBa_2Cu_3O_{7-\delta}$ system strongly decrease with increasing Pr concentration. For low Pr concentration the critical current is limited by S-I-S junctions. For higher concentration it is limited by junctions and flux creep along grain boundaries. Intragranular critical currents at 4.3 K were obtained from magnetization loops as a function of Pr doping. No enhancement of these currents for small Pr doping was observed.

Acknowledgements. We are grateful to Elsevier Science publisher and the authors who kindly agreed for the reproduction of figures.

References

1. H.B Radousky: J. Mater Res. **7**, 1917 (1992), review article
2. Z. Zou, J. Ye, K. Oka, Y. Nishihara: Phys. Rev. Lett. **80**, 1074 (1998)
3. R. Fehrenbacher, T.M. Rice: Phys. Rev. Lett. **70**, 3471 (1993)
4. Z. Tomkowicz: Physica C **320**, 173 (1999)
5. H.-C.I. Kao, F.C. Yu, W. Guan: Physica C **292**, 53 (1997)
6. Y. Wang, H. Rushan, Z.-B. Su: Phys. Rev. **14**, 10350 (1994)
7. L.M. Paulius, C.C. Almasan, M.B. Maple: Phys. Rev. B **47**, 11627 (1993)
8. K. Sekizawa, Y. Takano, T. Endo: Physica C **235–240**, 2909 (1994)
9. A.K. Pradhan, S.B. Roy, P. Chaddah, C. Chen, B.M. Wanklyn: Physica C **225**, 369 (1994)
10. W. Widder, L. Bauernfeind, M. Stebani, H.F. Braun: Physica C **249**, 78 (1995)
11. Q.H. Lam, C.D. Jeffries: Physica C **194**, 47 (1992)
12. C.L. Seaman, J.J. Neumeier, M.B. Maple, L.P. Le, G.M. Luke, B.J. Sternlieb, Y.J. Uemura, J.H. Brewer, R. Kadono, R.F. Kiefl, S.R. Krietzman, T.M. Riseman: Phys. Rev. B **42**, 6801 (1990)
13. Z. Tomkowicz, M. Bałanda, A.J. Zaleski: Physica C **370**, 259 (2002)
14. D.-X. Chen, J. Nogues, K.V. Rao: Cryogenics **29**, 800 (1989)
15. V. Ambegaokar, A. Baratoff: Phys. Rev. Lett. **10**, 486 (1963)
16. V. Ambegaokar, A. Baratoff: Phys. Rev. Lett. **11**, 104 (1963)
17. X.-J. Yu, M. Sayer: Phys. Rev. B **44**, 2348 (1991)
18. M. Tinkham: *Introduction to Superconductivity* (McGraw-Hill, New York 1996)
19. M. Tinkham: Helv. Phys. Acta **61**, 443 (1988)
20. K.-H. Miller: Physica C **168**, 585 (1990)
21. B.V. Kumaraswamy, R. Lal, A.V. Narlikar: Phys. Rev. **52**, 1320 (1995)
22. T.T.M. Palstra, B. Batlogg, R.B. van Dover, L.F. Schneemeyer, J.V. Waszczak: Phys. Rev. B **41**, 6621 (1990)
23. M. Nikolo, R.B. Goldfarb: Phys. Rev. B **39**, 6615 (1989)
24. Another relevant parameter is the density of states at the Fermi level. The relative change of its bulk value for $Y_{1-x}Pr_xBa_2Cu_3O_{7-\delta}$ is small $1.92 \div 1.31$, when x changes from 0 to 0.5 – J.L. Peng, P. Klavins, R.N. Shelton, H.B. Radousky, P.A. Hahn, L. Bernardez: Phys. Rev. B **40**, 4517 (1989)
25. C.P. Dhard, S.N. Bhatia: J. Magn. Magn. Mater. **146**, 198 (1995)
26. M.P. Maley, M.E. McHenry, J.O. Willis, M. McElfresh: Physica C **162–164**, 701 (1989)
27. K.-H. Müller, M. Nikolo, R. Driver: Phys. Rev. B **43**, 7976 (1991)
28. W.A. Fietz, W.W. Webb: Phys. Rev. **178**, 657 (1969)
29. M.J. Qin, Z.X. Shi, H.L. Ji, X. Jin, X.X. Yao, H.C. Li, X.S. Rong: J. Appl. Phys. B **40**, 4517 (1989)

11.2 Vortex dynamics and magnetic relaxation in high-T_c superconductors

M. Bałanda

11.2.1 Introduction

Magnetic properties of a type-II superconductor in the presence of a magnetic field larger than the lower critical field H_{c1} and less than the upper critical field H_{c2} are determined by static and dynamic properties of vortices. In comparison to conventional superconductors, the vortex state in high-T_c materials is more complex and its dynamics is more pronounced. This is due to the layered structure, a very short coherence length, random pinning and high operating temperatures (T_c of about 100 K) for copper-oxide superconductors. Below, we give a short description of the vortex state for the classical superconductors (Abrikosov flux line lattice) and for the HT_c superconductors (HTSC) and raise the main points of difference.

11.2.1.1 Abrikosov flux line lattice

Vortices, called also flux lines, consist of a normal core with a radius, roughly equal to the coherence length ξ, and a tiny supercurrent circulating around the core. Each flux line carries one quantum of magnetic flux $\Phi_o (= h/2e = 2.07 \times 10^{-15}\,\mathrm{Tm}^2)$. Flux density connected with the vortex spreads over a distance equal roughly to the penetration depth λ. As predicted by Abrikosov [1], in the absence of defects and thermal fluctuations the vortices, due to their mutual interactions arrange themselves into a perfect triangular flux line lattice (FLL). The FLL spacing is $a_0 = (\Phi_0/B)^{1/2}$, where $\mathbf{B}$ is a magnetic flux density (for example, $a_0 \cong 0.3\,\mu\mathrm{m}$ when $B = 200$ Gs). Such a periodic stable flux line lattice does not disturb superconductivity. As the field is increased, the distance between vortices decreases and at $H = H_{c2} = \Phi_0/2\mu_0\pi\xi^2$ the cores overlap and superconductivity disappears. The equilibrium FLL can only appear in single crystal samples with no transport current and in a uniform applied field, otherwise the FLL is deformed and defective. For the detailed course on magnetic flux structures in connection with the time dependent phenomena see [2].

The FLL distortions caused by structural defects or by thermal fluctuations can be calculated from linear elasticity theory with the help of three main **elastic moduli**: c_{11}(uniaxial compression), c_{66} (shear) and c_{44} (tilt). The modulus for isotropic compression (bulk modulus) is $c_{11} - c_{66}$. The elastic response of the FLL is nonlocal because, in most cases, the range of the vortex interaction λ exceeds the vortex spacing a_0 [3]. When thermal displacements $\langle u^2\rangle^{1/2} \approx (k_B T/\sqrt{B c_{66}})^{1/2}$ become large enough compared to a_0 (**Lindemann criterion**) the FLL melts into a vortex liquid phase via a thermally induced first-order transition [4]. For conventional superconductors this

occurs only in an immeasurably small region near T_c. To minimize the free energy of a superconductor, the normal cores of the vortices tend to couple to regions where correlation energy is reduced compared to the fully superconducting state. Coupling to such regions, called **pinning centres**, gives a pinning force f_p, which is proportional to $H_c^2\xi$ (core interaction) and to H_{c1}/λ (in case of magnetic interaction), where $H_{c1}H_{c2} = H_c^2 \ln\kappa, \kappa = \lambda/\xi$. To get the bulk pinning force F_p, contributions of the individual pinning centres must be summed over the distribution of pinning centres. The average pin energy is $U_p = F_p L_c a_0^2 \xi$, where L_c is a length of a vortex line. Pinning is responsible for **irreversible properties** of a material (among others, for a hysteresis of the magnetization curve $M(H)$), as it traps vortices and prevents (or impedes) the flux lattice movement under the influence of a driving force. A source of a driving force may be either a Lorentz force due to the transport current j, a flux density gradient or a flux line curvature and a temperature gradient. The Lorentz force acting on the unit volume of the isolated vortex is $\boldsymbol{F} = \boldsymbol{j} \times \boldsymbol{B}$. If F exceeds the pinning force, the vortex drift dissipates energy and leads to the flux-flow resistivity, while there will be no flux motion if F is balanced with the overall pinning force F_p. Thus, the overall pinning force F_p, preventing a flux-flow under the influence of Lorentz force, determines the value of the critical current j_c in the material, due to the equality

$$F_p = j_c B. \tag{11.6}$$

11.2.1.2 Vortices in layered HTSC

The layered structure of cuprate superconductors and a very short coherence length gives rise to the large anisotropy of superconducting parameters. As reviewed in [5], the anisotropy ratio $\Gamma = \lambda_c/\lambda_{ab} = \xi_{ab}/\xi_c = (m_c/m_{ab})^{1/2}$ equals $\cong 4$ for $YBa_2Cu_3O_7$ ($\xi_{ab} \cong 15\,\text{Å}$, $\xi_c \cong 4\,\text{Å}$) and 150 for $Bi_2Sr_2CaCu_2O_8$ ($\xi_{ab} \cong 20\,\text{Å}$, $\xi_c \cong 0.15\,\text{Å}$). HTSC materials are considered as consisting of superconducting CuO layers interacting via the Josephson coupling. While the properties of YBCO show a quasi-three-dimensional (3D) character, the properties of BSCCO have to be regarded as quasi-two-dimensional (2D). Due to the high κ they are extreme type-II superconductors. Vortices formed in such a medium are soft (big λ) and have thin cores (small ξ). The possibility for an unconventional symmetry of the pairing state in HTSC raises also a question about the structure of a vortex in a non-s-wave superconductor. A modification of the core of a flux line in a $d_{x^2-y^2}$ superconductor has been considered in [6].

Pinning in HT_c granular materials occurs at defects in the superconducting layers, i.e. oxygen vacancies, at dislocations, twin planes and at normal precipitations. Besides the bulk pinning, flux pinning on sample surface (Bean-Livingston surface barrier, edge-shape barrier [7]) and at grain boundaries takes place. Inhomogeneous pinning and thermal fluctuations give rise to

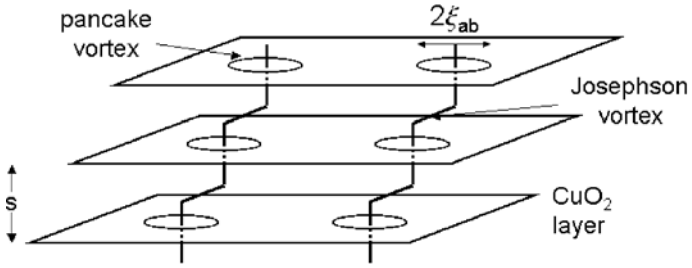

Fig. 11.11. Vortices in a strongly layered superconductor. The vortex consists of pancake vortices located within the superconducting layers and connected across the layers by Josephson vortices

vortex deformations (curved, entangled or even crossed and looped vortices). Besides, in HTSC **new forms of vortices** are observed, such as pancake (or point) vortices and Josephson vortex lines (see Fig. 11.11). When the applied field $\boldsymbol{H}_a$ is nearly parallel to the c-axis the flux lines formally consist of strings of 2D **pancake vortices** in each superconducting layer, with only weak, temperature dependent correlations between vortices in different layers. As correlation between adjacent layers decays when approaching irreversibility line from low temperatures, vortex lines should decompose into vortex pancakes, which can move freely in the CuO plane. Appearing of vortices of this specific form is most probable in most anisotropic compounds. The field of a single point vortex is confined to a layer of thickness $\approx 2\lambda_{ab}$. When H_a is aligned close to the *ab*-plane, the vortex core prefers to run between the CuO layers. The current circulating around the core is a Josephson tunneling current. The width of the **Josephson vortex** core is $\lambda_J = \Gamma * s$ and its thickness is s, where s is the distance between the copper oxide layers. For the field nearly parallel to the *ab*-plane the "lock-in transition" is observed consisting in switching $\boldsymbol{B}$ exactly into the *ab*-plane [8].

As follows from above, the picture of a regular vortex lattice is not appropriate for HTSC. More relevant could be the old "vortex slush" conception of Larkin and Ovchinnikov [9] or, a more suitable, "**vortex glass**" model postulated by Fisher, Fisher and Huse [10]. According to [10], the competition between vortex–vortex interactions and the random pinning potential results in a phase in which the vortices are frozen into a particular random pattern. The phase is characterized by a vanishing linear resistance in the limit of zero current density and a spin-glass-like order parameter. In the vortex glass model there is a true phase transition at $T = T_g$ between the non-superconducting vortex fluid and the vortex glass phase. Associated with this transition there is a diverging correlation length given by $l_{vg} \propto (T - T_g)^{-\nu}$. The experimental evidence supporting the vortex glass picture emerged from transport I-V measurements [11, 12], from which the glass transition temperature T_g could be determined. In the weak field region the vortex state for

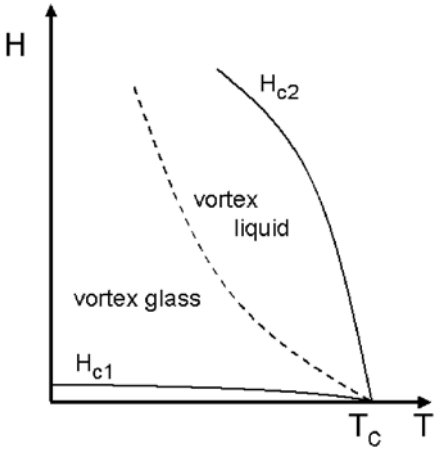

Fig. 11.12. Schematic phase diagram for a high-T_c superconductor. The irreversibility line (*dotted curve*) separates the truly superconducting vortex glass from the dissipative vortex liquid phase

a superconductor with point defects can show the positional ordering. The possibility of such a "Bragg glass" phase was noticed first in [13].

The most characteristic feature of the (H, T) phase diagram of HTSC shown in Fig. 11.12 is a pronounced **reversible region**, contained between an **irreversibility line** and a *$H_{c2}(T)$ line*. The reversible region separates the truly superconducting irreversible region from the normal state. In order to improve transport properties, the irreversibility line should be shifted upward by introducing an artificial pinning to the material, for example, the irradiation defects [14]. Another idea is to produce films with a grid of submicrometer holes, for which a pronounced increase of the pinning force at the matching fields has been observed [15]. Recently, besides non-magnetic artificial pinning centres, the effect of ferromagnetic pinning arrays has been investigated [16].

11.2.2 Dynamics of vortices

11.2.2.1 Flux creep

At nonzero temperatures flux lines can move from one pinning region to an adjacent one by thermally activated hopping. The jumping rate can be described by an Arrhenius type expression

$$\nu = \nu_0 \exp(-U_{\text{eff}}(j)/k_B T), \tag{11.7}$$

where ν_0 is an attempt frequency of the order of 10^5 to $10^{11}\,\text{s}^{-1}$ and $U_{\text{eff}}(j)$ is the effective activation energy. When there is no force acting on flux lines, it is as likely to jump in one direction as in the other. Under the influence of the driving force, which results from the current passed through the sample or a flux density gradient, jumps of the vortices in the direction of the force are most probable. The flux lines actually jump as bundles of vortices of

a correlated volume V_c. This results in a net flow of flux lines, e.g. **flux creep**.

Motion of vortices leads to energy dissipation and manifests itself as a decay with time of superconducting currents, i.e. as **relaxation of magnetization**. A phenomenon of thermally activated flux motion (TAFM) was already known in conventional superconductors although it was observed only at temperatures close to T_c and on much smaller scale. The extraordinary decay of the magnetization and the big broadening of the resistive transition in a magnetic field observed in high-T_c superconductors reveal the strong flux creep active in these materials.

The very first report on large magnetic relaxation by Müller et al. [17] attributed its origin to a superconducting glassy state, visualized as an assembly of weakly coupled superconducting grains. Later, the observation of a similar large relaxation in single crystals led some authors [18] to use the name of a "giant" flux creep for the vortex motion with much lower activation energy, as compared to conventional superconductors.

11.2.2.2 The critical state

Dynamic phenomena in the flux line lattice are analyzed in terms of the critical state model, generally referred to as the Bean model [19]. The Bean model describes how the distribution of magnetic flux in the sample changes when the applied field or current do change. The flux is prevented from moving into the interior by pinning centres. According to [19], no flux moves into or out of a sample unless the force F connected with the field gradient, exerted on the vortex, exceeds the pinning force F_p. When $F = F_p$, the sample is in the critical state and the effective barrier for flux motion is zero. In the simplest, one-dimensional case the force $F = \frac{dH}{dx}B$.
Comparing F with F_p given by (1) one gets

$$F = \frac{dH}{dx}B = j_c B. \tag{11.8}$$

Thus, the stronger pinning, the larger is the field gradient, which, in turn, determines the critical current of the sample. On the other hand, if $F > F_p$, the vortex creep occurs, which gradually reduces the flux density gradient. Upon decreasing the field, the pinning forces keep the flux trapped in the sample until the appropriate opposite is applied. From the obtained hysteresis loop one can determine the critical current density j_c, which is proportional to the hysteresis width ΔM. Figure 11.13 illustrates a distribution of a magnetic field induction inside a superconducting slab of thickness d for various field intensities. For $H \geq H^*$ the whole volume is penetrated by vortices and the superconductor is said to be in the critical state. In the Bean model j_c is considered as independent of the local flux density. In the Anderson–Kim model [20] j_c decreases with increasing local field

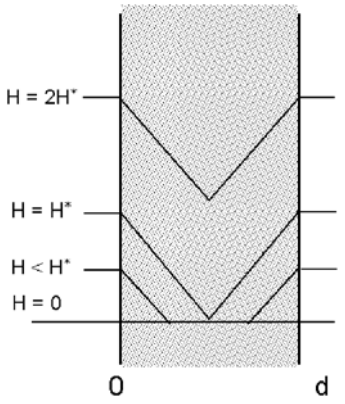

Fig. 11.13. Magnetic field profile inside a superconducting slab according to Bean's critical state model; H^*–full penetration field

$$j_c(H) = \frac{k}{|H| + H_0}, \tag{11.9}$$

where H_0 is a constant and k is a temperature dependent pinning force density.

11.2.2.3 Relaxation effects in hysteresis loop

According to Sect. 11.2.2.2, the critical current density j_c can be inferred from a magnetization loop of a superconductor using the Bean model. However, the shape and width of hysteretic magnetization curves strongly depend on the relaxation processes occurring in the sample during a field sweep. Figure 11.14a presents magnetization curves for $(Y_{0.9}Pr_{0.1})Ba_2Cu_3O_{7-\delta}$ at $T = 4.3$ K, 20 K and 30 K, measured with the extended time of measurement, i.e. M value for each H value was detected every 15 s within 5 min. At $T = 4.3$ K for $H < 0.5$ kOe, diamagnetic M increases linearly with H and its value at given H does not depend on time. Starting from $H_{c1} \cong 0.6$ kOe, $M(H)$ is no longer linear and the dependence on time begins. At $H^* = 2.8$ kOe, which is the field of full penetration, the diamagnetic shielding is maximum. Figure 11.14b gives the data from Fig. 11.14a normalized to the appropriate full penetration value. The time decay of magnetization is easily noticeable. The full penetration field decreases with temperature and so does the difference ΔM between the branches for rising and declining field (see Fig. 11.14c). It can be expected from Fig. 11.14c that the hysteresis for the different field sweep rate will change and will become smaller for slower sweep.

The dependence of the shape of hysteretic magnetization curves on the relaxation processes occurring in the sample during a field sweep has been discussed in [21]. It appears that the critical current density inferred from the magnetization loop is significantly influenced by the time scale of the experiment. As a result, the value $j_c \ll j_{c0}$ is obtained, where j_{c0} is the non-relaxed value. The only way of probing j_{c0} directly is by keeping the

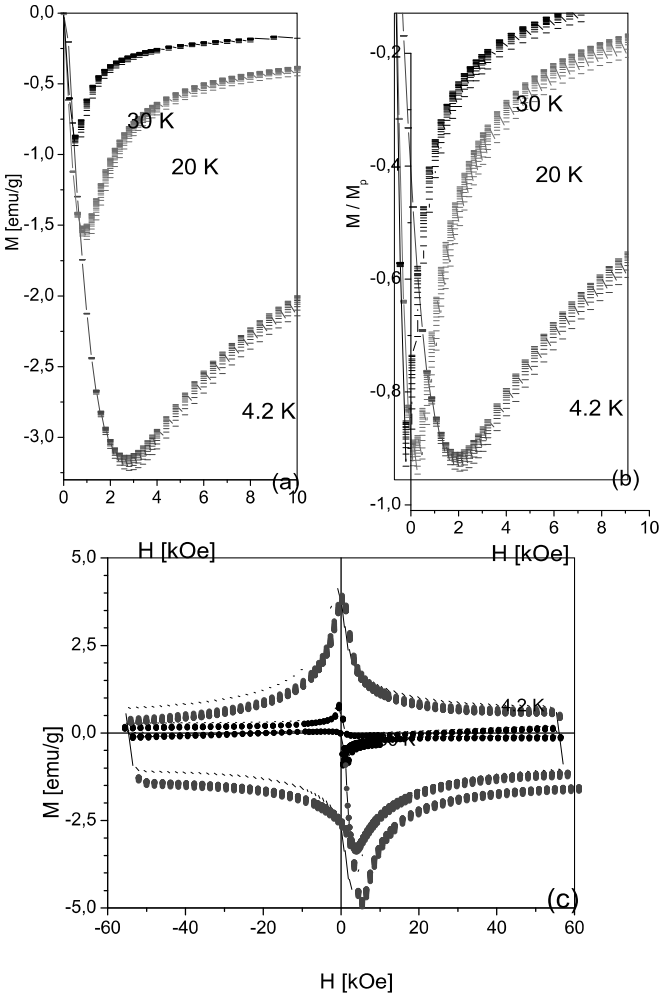

Fig. 11.14. Relaxation effects in hysteresis loops for $(Y_{0.9}Pr_{0.1})Ba_2Cu_3O_{7-\delta}$. (**a**) magnetization curves at $T = 4.2$ K, 20 K and 30 K, where M for subsequent H was detected every 15 s within the extended time of 5 min; (**b**) results from (**a**) normalized to the value at the full penetration field $M_p = M(H^*)$; (**c**) full hysteresis loops at 4.2 K and 30 K

time scale of the experiment as short as possible so that the vortex state has very little time to relax. Very short measuring times are realized in the pulsed field magnetization measurements [22], which, additionally, penetrate a large $H - T$ region. Measurements of the dynamic relaxation rate $Q = d(\ln M(t))/d\ln(dH/dt)$ were first performed in [23], while correspondence between $M(t)$ and $M(dH/dt)$ has been derived in [24]. The two dependences

were found to correspond with each other in Taylor expansions of effective activation energy $U_{\text{eff}}(j)$.

11.2.3 Logarithmic dependence of magnetization on time for limited H, T and t

11.2.3.1 TAFM model, linear $U(j)$

The effective activation energy U_{eff}, which appears in (11.7), is a crucial value for the thermally activated flux motion. The dependence of U_{eff} on the current j (transport current or shielding current) is complicated and different functional dependences $U_{\text{eff}}(j)$ have been proposed to account for the measured relaxation data. In the TAFM model, introduced by Anderson [20] for conventional superconductors, the activation energy is given by:

$$U_{\text{eff}}(j) = U_0(1 - j/j_c) = U_0 - jV_cBx, \tag{11.10}$$

where x is a hop distance and U_0 is a pinning energy. As flux motion proceeds, the system creeps away from the critical state, the flux density gradient decreases and gives the characteristic logarithmic time dependence of the flowing current

$$j(t) = j_c[1 - (k_BT/U_0)\ln(t/\tau)], \tag{11.11}$$

($\tau = 1/\nu_0$), and a monotonic increase of the effective barrier $U_{\text{eff}}(j)$. The shielding current is reflected in the magnetization, thus one gets also the logarithmic decay of magnetization

$$M(t) = M(t = 0)[1 - (k_BT/U_0)\ln(t/\tau)]. \tag{11.12}$$

The logarithmic dependence on time implies that the same change of magnetization occurs between, for example, 1 s and 1000 s as between 1 year and 1000 years. In the critical state $U_0 = j_cV_cBx$. Taking into account that for an isolated flux line $V_cB = \Phi_0L_c$, where L_c is the longitudinal correlation length depending on the disorder of the flux line lattice, and assuming $\xi < L_c < a_0$, one obtains $j_c\Phi_0\xi^2 \leq U_0 \leq j_c\Phi_0a_0\xi$. This expression shows that the short coherence length in HTSC gives a small activation energy for flux motion and hence, is a reason for the large magnetization decay. The other factor facilitating an easy flux motion is a large FLL flexibility (due to large λ) and an anisotropy, which can lead to breaking the vortices into short segments or point vortices. Such segments would then depin individually with a very small activation energy.

To avoid a divergence for $t = 0$ one uses a modified form [25] of (11.12):

$$M(t, T, B) = M(0, T, B)[1 - (k_BT/U_0(B))\ln(1 + t/\tau)], \tag{11.13}$$

which, depending on a value of t, can be approximated by three functions:

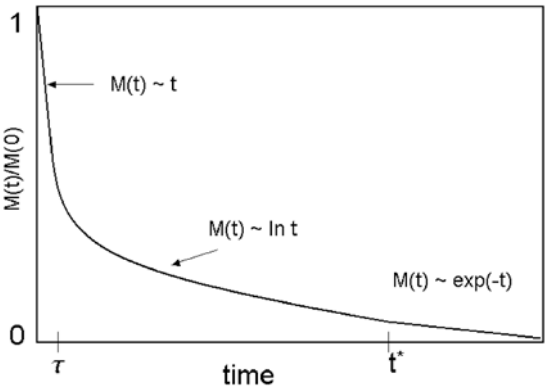

Fig. 11.15. Schematic presentation of the magnetization decay of a superconductor, where $t^* = \tau \exp(U_0/k_BT)$ (see text and [25])

a) for very short observation time, $t \leq \tau$, (11.12) extrapolates to

$$M(t) = M_0[1 - (k_BT/U_0)(t/\tau)]; \tag{11.14}$$

b) for $\tau \ll t < t^*$ one obtains a famous logarithmic law (11.12);
c) for very long times $t \gg t^*$ one gets an exponential diffusion, given by:

$$M(t) = M_0(2k_BT/U_0)\exp(-2(t/\tau)\exp(-U_0/k_BT)), \tag{11.15}$$

where $t^* = \tau \exp(U_0/k_BT)$. Figure 11.15 demonstrates schematically the above regions (after Griessen et al. [25]).

11.2.3.2 Magnetization relaxation rate

A big number of experimental results has been reported (see, for example, [26–29]) on the logarithmic relaxation in granular or single crystal samples of high-T_c superconductors for the magnetic fields $H < 5$ kOe, temperature $T < 40$ K and observation time up to 3 decades. The change of magnetization with time at constant temperature is usually detected for the zero-field cooled (ZFC) sample or by measuring the decay of the trapped flux for the field cooled sample. Figure 11.16 shows results of a simple relaxation experiment performed for $Y_{0.9}Pr_{0.1}Ba_2Cu_3O_{7-\delta}$, the same sample, for which hysteresis loops (see Fig. 11.14a–c) were measured. For every temperature shown, the dependence of magnetization on time was recorded first after switching the field on (lower part of Fig. 11.14 a and Fig. 11.14b) and then, after switching the field off (upper part of Fig. 11.16 a and Fig. 11.16c). The applied field was 3 kOe, little above the full penetration field for $T = 4.2$ K determined from Fig. 11.14a. In this way Fig. 11.16b reflects the penetration of vortices into the sample, while Fig. 11.16c shows movement of vortices out of the sample. One can see that for $T \leq 24$ K $M(t)$ is a logarithmic function and the rate of

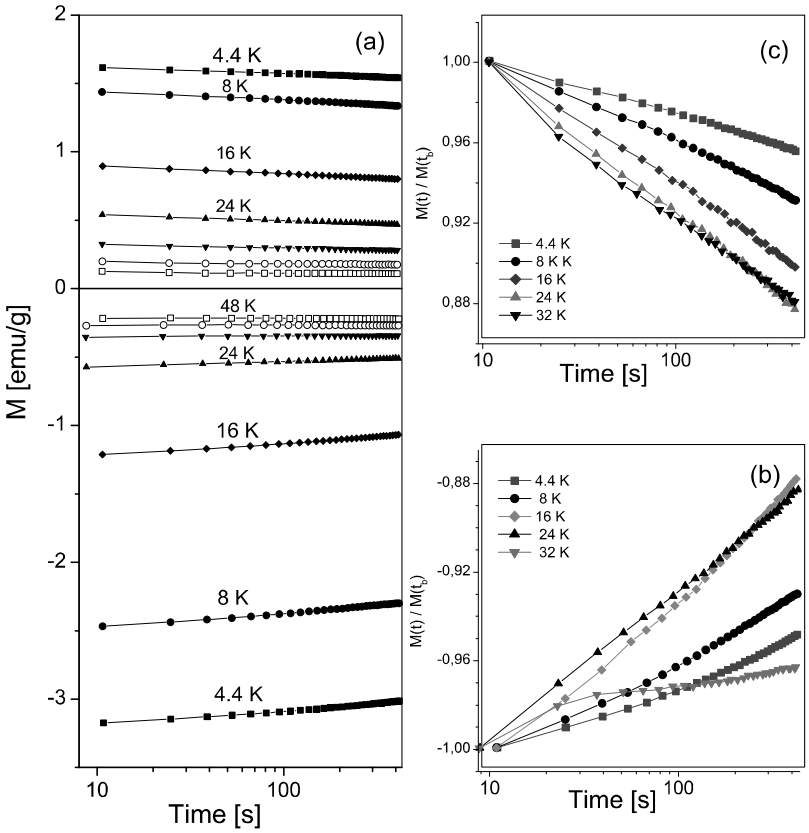

Fig. 11.16. Demonstrative relaxation experiment for $(Y_{0.9}Pr_{0.1})Ba_2Cu_3O_{7-\delta}$ in $H = 3$ kOe; (**a**) time dependences of M after switching the field on (*lower part*) and after switching the field off (*upper part*) at the temperatures from 4.4 K up to 48 K; (**b**) $M(t)$ for flux penetrating the sample normalized to the beginning value; (**c**) normalized $M(t)$ for flux leaving the sample

a magnetization change increases with temperature. For T equal about 32 K, $M(t)$ is no longer logarithmic and changes less in our experimental window, as the main magnetization decay has occurred already before beginning of the measurement (t less than 10 s).

The commonly used normalized decay rate of magnetization, derived as

$$S = \left(-\frac{1}{M(t_b)}\right)\left(\frac{dM}{d\ln(t)}\right) \cong -\frac{d\ln(M)}{d\ln(t)} \tag{11.16}$$

depends on temperature and on magnetic field. It follows from (11.12) that the decay rate is a linear function of temperature, and hence, the pinning barrier is given:

$$U_0 \cong k_B T/S + k_B T \ln(t_b/\tau), \tag{11.17}$$

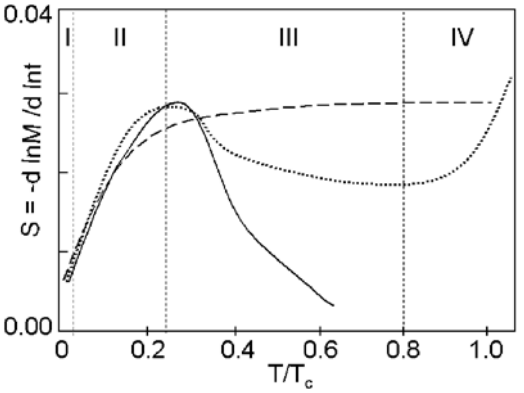

Fig. 11.17. Schematic temperature dependences of the magnetization decay rate with four regions: (I) quantum tunneling of vortices; (II) TAFM; (III) not explicable by TAFM; (IV) vortex liquid state

where t_b is the start time of the measurement after switching on the field. The simple linear proportionality $S \propto T$ is obeyed only in the low temperature range. Generally, the experimentally obtained temperature dependences of the relaxation rate shows different dependence on temperature. Usually, $S(T)$ increases monotonically up to the value of 0.02–0.035 and then can have a plateau, can exhibit a peak, or can show a flat maximum followed by an increase close to T_c. Such three possibilities are depicted in Fig. 11.17. A similar value reached by $S(T)$ at plateau, irrespective of applied field strength, field orientation or material properties represented by the samples, has been explained in [30] on the basis of a vortex glass approach as the universality of flux creep, connected with a strongly nonlinear (exponential) $I - V$ characteristics (see Chap. 4).

The energy barriers U_0 obtained for low T from relaxation experiments (see, for example, [26, 28, 29, 31]) are between 30 and 70 meV, what is one order of magnitude smaller than for conventional superconductors and also smaller than the values extracted for HTSC from resistivity measurements in a magnetic field. For $T > 30$ K, U_0 determined from (11.17) displays a strong increase with temperature. This groundless increase of activation energy, which originates from the shape of the $S(T)$ curve (both peaks [32] or plateaus [33, 34] have been found), points to the fact that TAFM model holds only in the limited low temperature region.

A model of a superconductor with the spectrum of activation energies was proposed by Hagen and Griessen in [35]. According to [35], at the given T and time t_b, the minimum barrier which is able to pin vortex is approximately

$$E^* = k_B T \ln(t_b/\tau), \tag{11.18}$$

as the jumps over the weaker barriers have already occurred. For a polycrystalline YBCO, the distribution of activation energies determined by means of

the "inversion scheme" proposed in [35], resembles the log-normal distribution function and has a maximum at $E^* = 60$ meV.

In [36, 37] observations were done that even at the very lowest temperatures, down to the mK range, it was possible to measure significant relaxation of magnetization. The relaxation rate was found to be temperature independent and could be extrapolated to a finite value at $T = 0$. These results imply that quantum tunneling process has to be included in the low-temperature description of vortex motion.

There are no much data on relaxation in the temperature region close to T_c. This is due to enlarged experimental difficulty for measuring small magnetization values. The extensive and comparative study of critical current, magnetization relaxation and activation energies for $YBa_2Cu_3O_7$ (YBCO) and $YBa_2Cu_4O_8$ films was done in [38]. The measurements of the dynamic relaxation rate Q performed by means of sensitive torque magnetometer at temperatures between 2 K and 70 K have been completed with the results obtained from transport $I-V$ measurements. At fields up to 5 kOe, Q exhibited a plateau at $Q \cong 0.06$ for YBCO and 0.04 for $YBa_2Cu_4O_8$, with a sharp increase up to $Q \approx 1$ on approaching the irreversibility line. An influence of the quantum creep was seen up to ≈ 13 K.

The whole temperature range $0 < T < T_c$ of the $S(T)$ dependence can be divided into four regions, shown schematically in Fig. 11.17, where (I) – quantum tunnelling of vortices, (II) – well described by TAFM, (III) – not explicable by TAFM and (IV) – vortex liquid state.

Experimental data show that the actual $S(T)$ shape depends on the form of the material (single crystal, ceramic powder, thin film, ...) [33]. A correlation between the shape of the $S(T)$ curve and the filamentary phase separation in YBCO and TlBCCO thin films has been found in [39]. This phase separation is connected with the relative amount of an underdoped phase to that of an optimally doped one. Two of them have different dependence of the critical current: of a Ginzburg-Landau type, with $J_c(T) \propto (T_c - T)^{3/2}$ and of a Ambegaokar-Baratoff type [40], characteristic for Josephson tunneling. The results revealed that when the amount of the underdoped phase increases above a certain threshold value, a peak appears in $S(T)$ at $T \cong 20$–30 K. As the dependence of the relaxation rate on the magnetic field is concerned, it has been found that the field is responsible for a reduction of the peak's magnitude and its shift to lower temperatures.

11.2.4 Non-logarithmic magnetization decay for extended H, T and t

11.2.4.1 Non-linear $U(j)$

For $M(t)$ data collected over a long measuring time (22 h [41], 100 h [42]), departures from a logarithmic dependence have been found. The non-linear logarithmic decay, especially visible at higher temperatures, was reported for

single crystals of $Bi_2Sr_2CaCu_2O_x$ [33, 41, 43, 44] and for as-grown and proton-irradiated crystals of YBCO [34, 42]. Analysis of the strongly non-logarithmic data [33] by means of the Hagen-Griessen model revealed the high energy tails in the pinning energy distribution. In order to explain the non-logarithmic $M(t)$ dependence, the plateau at the $S(T)$ curve and, also, big discrepancies between values of activation energies extracted from magnetic relaxation and from the transport data, different approaches have been used. The efforts concentrated on finding the correct form of the $U(j)$ function.

The linear $U(j)$ (11.10) holds only for a saw-tooth pinning potential. For a smooth and continuously differentiable potential (e.g. a sinusoidal pinning potential) a good estimation can be $U(j) = U_0(1 - j/j_c)^{3/2}$ [45]. In general, $U(j)$ is nonlinear and grows with decreasing j. The difference between results obtained for U_0 from magnetic and transport measurements comes from the fact that magnetization begins its decay from the critical state, and this is why the barriers observed are small. By contrast, the resistive measurements [46] are generally performed for $j \ll j_c$, and hence the higher effective energies are recorded. Figure 11.18 gives a schematic representation of an arbitrary non-linear effective potential versus $\Delta M \propto j$, with two tangent lines showing the results obtained from measurements at different j (or T).

A method of direct determination of $U(j)$, avoiding the a priori assumption of any model, was proposed by Maley et al. [47]. In Maley's approach one uses the expression

$$U(j)/k = -T \ln |dM/dt| + T \ln(B\nu x/\pi d), \tag{11.19}$$

which emerges from the TAFM rate equation [48]

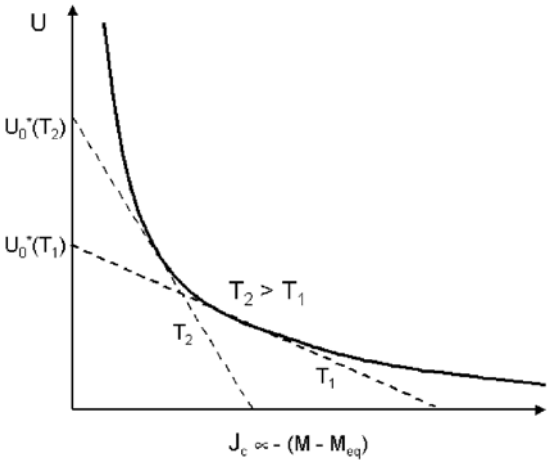

Fig. 11.18. Arbitrary nonlinear energy barrier $U(j)$ with two tangent lines showing the resulting apparent U_0^* obtained from measurements at different j or T, where $T_2 > T_1$

$$d(M - M_{eq})/dt = (B\nu x/\pi d)\exp(-U/k_BT), \tag{11.20}$$

where d is the average grain diameter. Plotting the relaxation data obtained at different temperatures in the form of $T\ln(dM/dt)$ vs. $M - M_{eq}$ and fitting the $\ln(B\nu x/\pi d)$ term (usually equal to 14–18) one obtains a smooth $U(j)$ dependence.

Based on an analysis of resistive transitions in a magnetic field at different current densities for YBCO films near T_c, Zeldov et al. [49] proposed a logarithmic form of $U(j)$ given

$$U(j) = U_0 \ln(j_c/j), \tag{11.21}$$

for which $j = j_c(t/\tau_0)^{-k_BT/U}$. That form has been confirmed in [50], where the time dependence and spatial distribution of the magnetic induction in YBCO crystals were measured with a novel Hall probe technique. Using this technique, the logarithmic time scale, τ, as a function of temperature was for the first time obtained.

11.2.4.2 Collective flux creep model

A theory which predicts a non-logarithmic magnetization decay implying a power-law for the dependence of the effective barrier on current density is the collective flux creep theory introduced by Feigel'man, Geshkenbein, Larkin and Vinokur (FGLV) [51]. The FGLV theory, like the vortex glass model, describes the dynamics of the vortex state with a collective pinning. In [51] relaxation at currents $j < j_c$ and $j \ll j_c$ is considered. General expressions for the activation energy and magnetization decay is:

$$U(j) = (U_0/\mu)[(j_c/j)^\mu - 1]. \tag{11.22}$$

The form of $U(j)$ provides a rapidly increasing U at small j, so the linear electrical resistivity vanishes in the limit $j \to 0$ giving a "true" superconducting state.

In contrast to the vortex glass model [10], where μ is a universal exponent less than 1, in the FGLV theory the exponent μ depends on the dimensionality of the system and the particular flux creep regime. In a 3D low-temperature limit for a weak field $\mu = 1/7$ and the creep is dominated by the motion of individual flux lines. At higher fields, a collective creep of small, less than λ, bundles gives $\mu = 3/2$, and it is a maximum value, as for still higher fields and temperatures μ is expected to decrease. The value $\mu = 7/9$ corresponds to a large bundle size at high temperatures and high fields. For two-dimensional systems $\mu = 9/8$ for collective pinning at large currents and $\mu = 1/2$ for larger bundle size and smaller currents. The change of μ with temperature or with current density observed experimentally [42] reflects the transition between corresponding regimes during the creep process. Figure 11.19 shows three different types of potentials discussed. The straight line corresponds

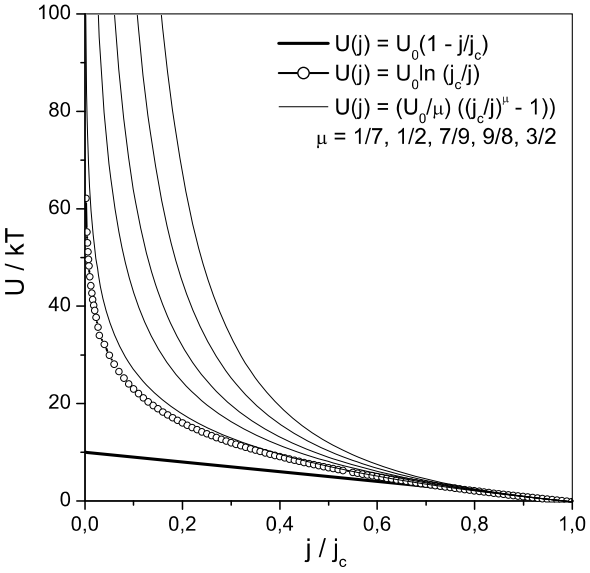

Fig. 11.19. Three different types of $U(j)$ discussed (see text): the *straight line* – linear (TAFM); the *pointed line* – logarithmic [49]; *thin lines* – the power law [51], for the top curve $\mu = 3/2$. All curves have a common tangent at $j = j_c$

to $U(j) = U_0(1 - j/j_c)$ (TAFM, [20]), the dashed line corresponds to the logarithmic potential $U(j) = U_0 \ln(j_c/j)$ (Zeldov, [49]). The five upper curves are the power-law potentials [51] $U(j) = (U_0/\mu)[(j_c/j)^\mu - 1]$ for $\mu = 1/7$, $1/2$, $7/9$, $9/8$ and $3/2$, respectively (for the lowest curve $\mu = 1/7$). Value of $U_0 = 10\ k_BT$ is the same for all potentials. It can be seen that all curves have a common tangent at $j = j_c$.

From [51] the time dependent magnetization reads

$$M(t) = M_0/[1 + (\mu k_B T/U_0) \ln (t/\tau)]^{1/\mu} . \tag{11.23}$$

The latter expression is referred to as the "**interpolation formula**" because, depending on μ value, it interpolates between the low-temperature Anderson's form and a high temperature behavior. Interpolation formula describes very well numerous experimental $M(t)$ results. As mentioned above, the long-lasting measurements performed in [42] fit extremely well to (11.23) with the μ parameter changing with temperature. However, sometimes, for a good fit only one μ value is needed. For example, the exponents determined in [38] are intermediate between the single vortex value and the small bundle volume and equal $\mu = 0.62$ for YBCO and $\mu = 0.54$ for $YBa_2Cu_4O_8$ in the whole current range down to $j/j_c \cong 0.15$. From (11.23) a formula for a normalized relaxation rate at long times arises

$$S = T/[U_0 + \mu k_B T \ln (t/\tau)] \approx 1/\mu \ln (t/\tau). \tag{11.24}$$

As already mentioned, this result displays the universality of magnetic relaxation, because S depends here only on μ and on the observation time. According to [30, 52], for $\mu = 1$, $t = 1000$ s, $\tau = 10^{-10}$ s one gets $S \cong 0.03$ in remarkable agreement with experiment. The last, important success of collective pinning theory is a prediction of a crossover to a power-law $I - V$ behavior above the vortex glass transition.

11.2.5 Complex AC susceptibility of HT_c superconductors

11.2.5.1 Intra- and intergranular contributions to χ' and χ''

Complex AC susceptibility, $\chi_{AC} = \chi' - i\chi''$, where χ' is the in-phase and χ'' is the out-of-phase component [53], is very useful for characterizing high-T_c superconductors and also in studying magnetic flux dynamics in these granular materials. A sintered HT_c superconductor can be modeled as a system of weakly coupled superconducting grains. Grain boundaries act like Josephson junctions. When applied magnetic field is low, only intergranular weak-link network is penetrated, while for the field stronger than H_{c1g} – magnetic flux penetrates also the grains. In the oscillating field the critical state profile (Fig. 11.13) depends both on the amplitude $H_{\rm AC}$ of the AC field and on the value of a superimposed DC field. In such granular materials, $\chi_{\rm AC}$ has both intrinsic and coupling components. It has been shown [54] that AC susceptibility data can be understood in terms of a critical state model [19] with pinning force density k_J for intergranular Josephson vortices and k_g, for intragranular Abrikosov vortices. The real part of AC susceptibility (χ') is an inductive component, as it corresponds to the magnetic shielding generated by supercurrents. The imaginary part (χ'') is related to losses. The experimentally measured $\chi_{\rm AC}$ comes both from the **intragrain** (χ'_g, χ''_g) and the **intergranular** susceptibility (χ'_J, χ''_J): $\chi' = f_g\chi'_g + f_J\chi'_J$ and $\chi'' = f_g\chi''_g + f_J\chi''_J$. Here, f_g is the volume fraction of superconducting grains and $f_J = 1 - f_g$ is the volume fraction of intergranular region.

Figure 11.20 presents the temperature variation of both components measured for Zn-substituted YBCO with the help of Lake Shore 7225 AC susceptometer. The amplitude of the driving field $H_{\rm AC}$ changes from 0.025 Oe to 10 Oe, while the frequency $f = 110$ Hz. The critical temperature T_c of 48 K is determined as the onset temperature of the diamagnetic χ' signal. Very close to T_c there is no distinct χ' dependence on $H_{\rm AC}$, but upon further cooling the diamagnetic response becomes extremely sensitive to $H_{\rm AC}$. The amplitude-sensitive χ' results from the shielding effect limited by Josephson current between the grains, while the χ' signal in the large amplitude limit comes from the Meissner effect in the grains. The χ'' component is associated with energy dissipation. Energy dissipation takes place when Josephson vortices move in and out of the weak-links and/or when Abrikosov vortices move in and out of the superconducting grains. Therefore, the χ'' maximum occurs when the current induced by the AC field is equal to the Josephson

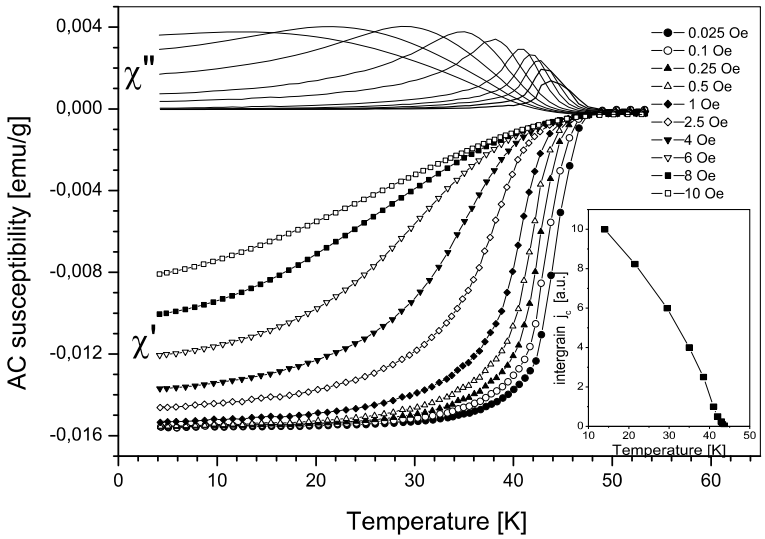

Fig. 11.20. AC susceptibility of the sintered $YBa_2(Cu_{0.94}Zn_{0.06})_3O_{7-\delta}$ measured with different amplitude of the oscillating field (shown). For χ'', H_{AC} changes from right to left. *Inset*: temperature dependence of intergrain j_c determined from the positions of the χ'' peak maximum

super-current. One can see in Fig. 11.20 that with increasing H_{AC}, the χ'' maximums broaden and shift to lower temperatures. This shift correlates with the temperature dependence of the intergranular critical current (see inset in Fig. 11.20). The actual temperature dependence of the intergrain critical current is determined by the type of the junctions: S-N-S or S-I-S, where S – superconductor, N – normal, I – insulating. It should be noted that the intergrain χ''_J contribution to χ_{AC} disappears upon powdering the sample.

Besides χ''_J, the intragranular losses, χ''_g, connected with depinning Abrikosov vortices, appear for magnetic fields exceeding the lower critical field H_{c1g} for grains. The intragranular peak can be seen in Fig. 11.21 close to T_c for H_{AC} large enough (here $H_{AC} = 10$ Oe), when χ''_J maximum is well in the low temperature region. Assuming the proper volume fraction of superconducting grains and proper temperature dependence of the pinning force density $k(T)$ (11.9), one can calculate $\chi'(T)$ and $\chi''(T)$ using a critical state model.

A very good agreement of the calculated and measured χ' and χ'' curves has been obtained for a complex (Tl,Sr)BCO superconductor ($T_c = 120$ K) [55] using the pinning force density of the form: $k_g(T) = k_g(0)(1-(T/T_{cg})^2)^2$ and $k_J(T) = k_J(0)(1-T/T_{cJ})^{1.2}$ for the grains and intergranular regions respectively. Like in [55], both contributions to χ' and χ'' for our $(Ho_{0.7}Pr_{0.3})$BCO sintered sample are illustrated in Fig. 11.21. Sometimes, the third loss peak can be observed [56], which is the intrinsic peak, associated with London field penetration. All three peaks shift to lower temperature as the magnetic

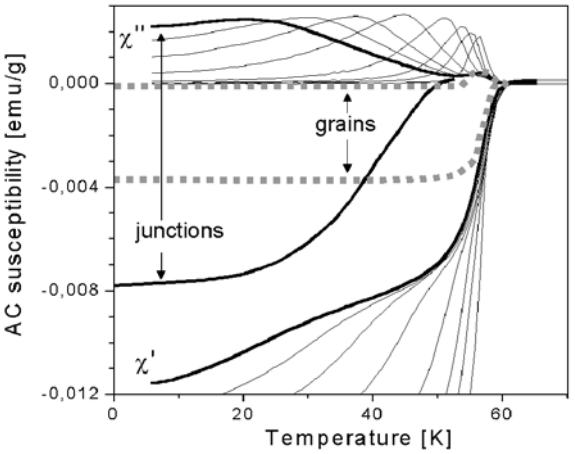

Fig. 11.21. Intragrain and intergrain (junctions) contributions to the AC susceptibility of the sintered $(Ho_{0.7}Pr_{0.3})Ba_2Cu_3O_{7-\delta}$ sample

field increases. The intergranular peak is the most temperature sensitive, due to the weak pinning forces, the intragrain peak–not as much, because the granular pinning forces are stronger. The intrinsic peak reflects the field dependence of T_c.

11.2.5.2 Frequency dependence and flux creep at grain boundaries

It has been found that the loss peak in HT_c superconductors shifts slightly to higher temperatures with increasing frequency of the AC magnetic field. The frequency dependence reflects the relaxation of the superconducting state due to the flux creep at grain boundaries. The effect of flux motion in the AC experiment for a thin slab of the granular superconductor with the average grain diameter of R_g and the slab thickness of D has been considered in [57]. The flux creep term is included into the pinning force density as following

$$F_p = \frac{1}{dV_b}(U_0 + k_B T \ln(\nu/\nu_0)), \tag{11.25}$$

where $d-$ half width of the pinning potential well, V_b – the bundle volume of Josephson vortices. The critical state equation (5) becomes modified

$$\frac{dH}{dx} = \pm\left(a\frac{H_0}{|H| + H_0} + b\right), \tag{11.26}$$

a and b are temperature dependent and $b = \frac{k_B T}{2R_g^2\Phi_0}\ln(\nu/\nu_0)$. It follows from [57] that χ'' has its maximum at a temperature T_p, for which $H_{\rm AC} = (j_c(T_p) + b'T_p\ln(f/\nu_0))D/2$. A strong frequency dependence is expected for materials with small grain size and weak density of boundary junctions.

Assuming the linear temperature dependence $j_c(T) = j_c(0)(1 - T/T_c)$, the author obtains the approximate form of the activation energy of $U_{\text{eff}} \simeq U_0(T = 0, H_{\text{AC}}) - j_c(T_p)\mu_0 H_{\text{AC}} V_b d/2$.

Figure 11.22 gives the χ' and χ'' data for frequency ranged from 10 Hz to 1000 Hz for the sintered $(Ho_{0.65}Pr_{0.35})$BCO sample ($T_c = 53$ K). The effective activation energy determined from the frequency shift (see inset) is 9660 K (832 meV). This is the large value in comparison with the values obtained from DC magnetization measurements and with low intensity of intergranular transport currents found for such materials. However, there is no superimposed DC field for the case in Fig. 11.22 and one should remember that j_c is determined by the pinning force density, which is small, as V (the activation volume) and a (the hop distance) are comparable with dimensions of the grains, between which Josephson vortices penetrate. The activation energy determined in the same way for the sample with the increased concentration of praseodymium (and the decreased H^*) $(Ho_{0.5}Pr_{0.5})$BCO ($T_c = 17$ K) is much lower and clearly dependent on H_{AC}. Figure 11.23a and Fig. 11.23b show a much stronger dependence of χ' and χ'' on frequency and for $H_{\text{DC}} = 10$ Oe one gets $U_{\text{eff}} = 151$ K and $U_{\text{eff}} = 58$ K for $H_{\text{AC}} = 0.01$ and 0.02 Oe respectively. Dependence of U_{eff} on concentration in the rare earth sublattice of the superconductivity suppressing Pr-ions has been determined in [59].

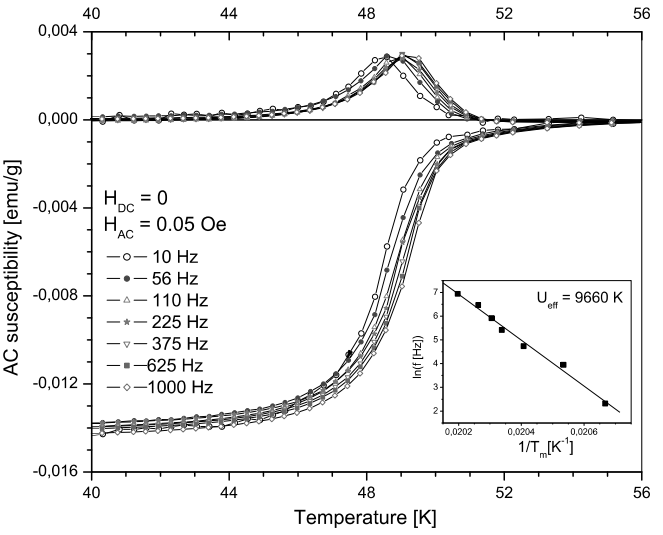

Fig. 11.22. Frequency dependent AC susceptibility of the sintered $(Ho_{0.65}Pr_{0.35})Ba_2Cu_3O_{7-\delta}$ sample. *Inset*: plot of $\ln f$ vs. $1/T$ of the χ'' peak maximum with the aim to determine U_{eff}

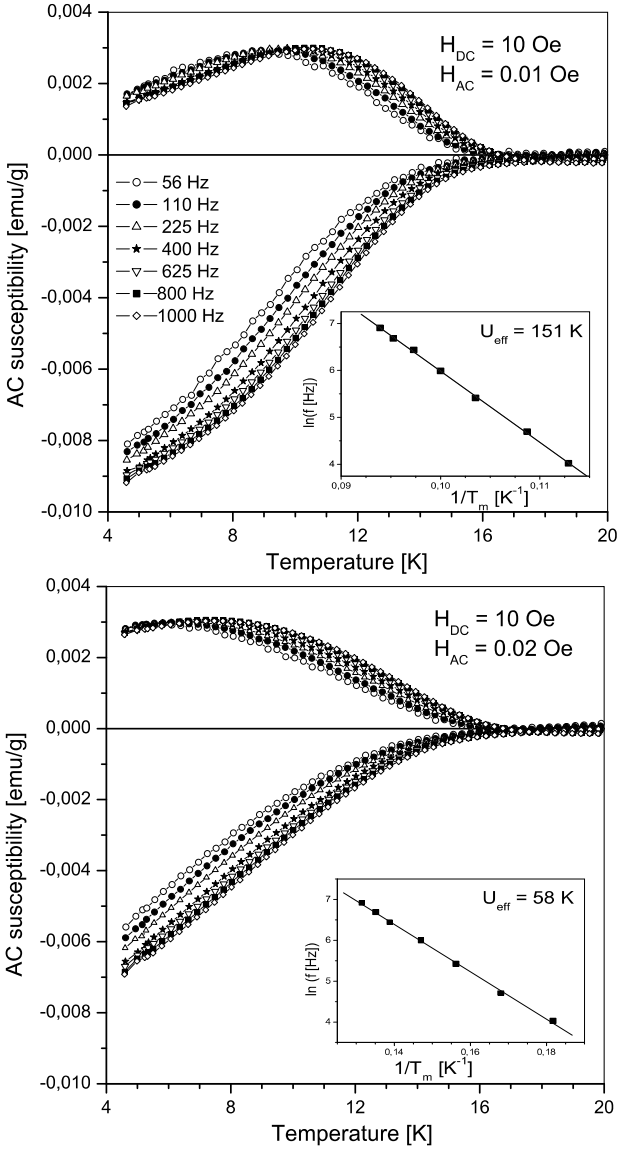

Fig. 11.23. Frequency dependent AC susceptibility of heavily Pr-doped YBCO ($T_c = 17$ K) in the applied field of 10 Oe and for the amplitude of the oscillating field of 0.01 Oe (*upper*) and 0.02 Oe (*lower*). *Insets*: determination of the U_{eff} by means of the Arrhenius plots

11.2.5.3 AC response in strong DC magnetic field

Frequency dependence of the AC susceptibility measured with varied amplitude H_{AC} and at different values of the superimposed DC field can supply full

information on the dynamics of vortices in the mixed state. In comparison to conventional relaxation measurements AC technique offers the time window extended towards shorter time of 10^{-5}–10^{-3} s.

A detailed study has been performed for the partially melt processed $TlSr_2Ca_2Cu_3O_y$ superconductor [59]. The dependence of the energy barrier on temperature, DC field and on the current density $U(T, H, j)$ has been investigated as a complex function $U(T)U_0(H)U_0'(H_{AC})$ in a series of experimental runs. The irreversibility line close to T_c, determined by the temperatures of the χ'' peaks at different DC fields, was of the form $H \propto [1 - T/T_c]^{3/2}$. It appeared that for DC fields up to 10 kOe the frequency effect on the position of χ'' maximums could be expressed as linear functions in the $\ln f$ versus $[1-(T/T_c)^2]^{3/2}/T$ diagram. For all the lines the common fitting parameter T_c of 117 K and the attempt time τ of 2×10^{-6} s was obtained. The slopes of the lines depended on the DC magnetic field as $H^{-3/4}$. The dependence on j was obtained by measurements using different H_{AC}, as $j = CH_{AC}/d$, where C – constant, d – a half grain dimension. The obtained result $U_0 \propto j^{-0.64}$ showed that the flux motion barrier would increase infinitely as j decreased. This result is the evidence for the collective creep inherent for the investigated superconductor (see (11.22)); the vortex glass exponent is $\mu = 0.64$. Thus, the flux pinning barrier was found to have the form

$$U(j, H, T) \propto j^{-0.64} H^{-3/4} [1 - (T/T_c)^2]^{3/2}. \tag{11.27}$$

The emerging function for the current decay is $j(t) = A(T)[\ln(t/\tau)]^{-1/\mu}$. From $j(t)$ one gets the normalized relaxation rate $S = -d \ln j / d \ln t = 1/(\mu \ln[t/\tau])$, which confirms that S is universal according to the collective creep theory and to many of the magnetization relaxation experiments.

11.2.6 Summary

Motion of the magnetic flux in a superconductor leads to energy dissipation and manifests itself as a time decay of magnetization, i.e. magnetic relaxation. Flux motion occurs by hopping of flux lines (vortices) or bundles of flux lines between adjacent pinning centers. The jump rate is thermally activated with the energy barrier $U_{eff}(j)$ dependent on pinning energy U_0 and on applied or induced current j. Magnetic relaxation is much more pronounced in high-T_c than in conventional type II superconductors. This difference is due to short coherence length, high operating temperatures, layered structure and random pinning of vortices in the HT_c cuprates. A variety of pinning centers, randomly distributed, leads to the vortex glass rather than to the vortex lattice. In the (H, T) phase diagram of the HT_c superconductor the vortex glass state and vortex liquid state (dissipative) are separated by the irreversibility line. Dynamics of vortices affects transport properties of a material, i.e. the critical current j_c, which is field and temperature dependent.

Two basic experimental approaches, which can deliver information on flux dynamics and on critical current have been described. These are the time dependent magnetization and AC susceptibility measurements. From a measurement of the temperature dependence of the relaxation rate of magnetization $S = -dM/d(\ln t)$, the apparent activation energy can be extracted. Experimentally measured magnetization decay rates depend on temperature and show the following regimes: I) quantum flux creep at the lowest temperatures (up to about 10 K); II) thermally activated regime (ca. 10 K up to ca. 30 K) with the activation energies dependent on current in a highly nonlinear way; III) decrease, plateau or increase, depending on the intergranular phase; IV) high temperature regime with the sharp increase of the decay rate in the vortex fluid state. The full $U(j)$ dependence can be obtained only from the extended-time-scale experiment reaching the non-logarithmic regime. On the other hand, the AC magnetic susceptibility of a granular HT_c superconductor, measured with the different driving-field amplitude and frequency, can supply information on the temperature dependence of j_c and help to understand the nature of coupling between the grains. The real part, χ', originates from magnetic shielding while the imaginary part, χ'' is related to losses. These come from flux penetration to the grain boundaries and weak links (intergranular losses) and from depinning of vortices inside the grains (intragranular losses).

The most relevant picture of the HT_c mixed state, which accounts for the experimentally observed magnetization decay in the full (from $T = 0$ K up to $T \leq T_c$) temperature range is the vortex glass model with its collective flux creep and the energy barrier $U(j) \approx U_0[(j_c/j)^\mu - 1]$, where μ changes with the dimensionality of the system and may depend on the particular flux creep regime.

References

1. A.A. Abrikosov: Zh. Eksp. Teor. Fiz. **32**, 1442 (1957)
2. R.P. Huebener: *Magnetic Flux Structures in Superconductors* (Springer-Verlag, Berlin, Heidelberg 1979)
3. E.H. Brandt: In: *Phase Transitions and Relaxation in Systems with Competing Energy Scales*, ed. by T. Riste, D. Sherrington (Kluwer Academic Publishers, Dordrecht 1993)
4. E. Zeldov, D. Majer, M. Konczykowski, V.B. Geshkenbein, V.M. Vinokur, H. Shtrikman: Nature **375**, 373 (1995)
5. M. Cyrot, D. Pavuna: *Introduction to Superconductivity and High-T_c Materials* (World Scientific, Singapore 1992); K. Kadowaki, Y. Songliu, K. Kitazawa: Supercond. Sci. Technol. **7**, 519 (1994); M. Tinkham: Physica C **235–240**, 3 (1994)
6. P.I. Soininen, C. Kallin, A.J. Berlinsky: Physica C **235–240**, 2593(1994)
7. Ming Xu, D.K. Finnemore, G.W. Crabtree, V.M. Vinokur, B. Dabrowski, D.G. Hinks, K. Zhang: Phys. Rev. B **48**, 10630 (1993); M.V. Indenbom, G. D'Anna, M.-O. André, V.V. Kabanov, W. Benoit: Physica C **235–240**, 201 (1994)

8. S. Koleśnik, T. Skośkiewicz, J. Igalson, Z. Tarnawski: Physica C **235–240**, 2569 (1994); M. Oussena, P.A.J. de Groot, R. Gagnon, L. Taillefer: Physica C **235–240**, 2771 (1994)
9. A.I. Larkin, Yu.N. Ovchinnikov: J. Low. Temp. Phys. **34**, 409 (1979)
10. D.S. Fisher, M.P.A. Fisher, D.A. Huse: Phys. Rev. B **43**, 130 (1991); D.A. Huse, M.P.A. Fisher, D.S. Fisher: Nature **358**, 553 (1992)
11. P.L. Gammel, L.F. Schneemeyer, D.J. Bishop: Phys. Rev. Lett. **66**, 953 (1991)
12. H. Safar, P.L. Gammel, D.J. Bishop, D.B. Mitzi, A. Kapitulnik: Phys. Rev. Lett. **68**, 2672 (1992)
13. T. Giamarchi, P. Le Doussal: Phys. Rev. Lett. **72**, 1530 (1994)
14. M. Konczykowski: Phys. Rev. Lett. **67**, 7167 (1991) L. Civale, L. Krusin-Elbaum, J.R. Thompson, R. Wheeler, M.A. Kirk, C. Feil: Physica C **235–240**, 2969 (1994)
15. M. Baert, V.V. Metlushko, C.D. Potter, E. Rossel, R. Jonckheere, V.V. Moshchalkov, Y. Bruynseraede: Physica C **235–240**, 2789 and 2791 (1994)
16. M.J. Van Bael, L. Van Look, M. Lange, J. Bekaert, S.J. Bending, A.N. Grigorenko, K. Ternst, V.V. Moshchalkov, Y. Bruynseraede: Physica C **369**, 97 (2002)
17. K.A. Müller, M. Takashige, J.G. Bednorz: Phys. Rev. Lett. **58**, 1143 (1987)
18. Y. Yeshurun, A.P. Malozemoff: Phys. Rev. Lett. **60**, 2202 (1988)
19. C.P. Bean: Phys. Rev. Lett. **8**, 250 (1962); C.P. Bean: Rev. Mod. Phys. **36**, 31 (1964)
20. P.W. Anderson: Phys. Rev. Lett. **9**, 309 (1962); P.W. Anderson, Y.B. Kim: Rev. Mod. Phys. **36**, 39 (1964)
21. H.G. Schnack, R. Griessen, J.G. Lensink, C.J. van der Beek, P.K. Kes: Physica C **197**, 337 (1992)
22. K. Rossel, J. Vanacken, L. Trappeniers, H.H. Wen, W. Boon, F. Herlach, V.V. Moshchalkov, Y. Bruynseraede: Physica C **337**, 265 (2000)
23. L. Pust: Supercond. Sci. Technol. **3**, 598 (1990); M. Jirsa, L. Pust, H.G. Schnack, R. Griessen: Physica C **207**, 85 (1993)
24. S.A. Aruna, H.M. Shao, J.C. Shen, Y. Rui, H.L. Ji, X.N. Xu, X.X. Yao: Physica C **341–348**, 1153 (2000)
25. C.W. Hagen R. Griessen, E. Salomons: Physica C **157**, 199 (1989); R. Griessen, J.G. Lensink, A.M. Schröder, B. Dam: Cryogenics **30**, 563 (1990); R. Griessen: In *Concise Encyclopedia of Magnetic and Superconducting Materials*, ed. by J.E. Evetts (Pergamon Press, Oxford 1991)
26. M. Tuominen, A.M. Goldman, M.L. McCartney: Phys. Rev. B **37**, 548 (1988)
27. D. Shi, M. Xu, A. Umezawa, R.F. Fox: Phys. Rev. B **42**, 2062 (1990)
28. M. Mittag, R. Job, M. Rosenberg: Physica C **174**, 101 (1991)
29. M. Bałanda, A. Bajorek, A. Szytuła, Z. Tomkowicz: Physica C **191**, 515 (1992)
30. A.P. Malozemoff, M.P.A. Fisher: Phys. Rev. B **42**, 6784 (1990)
31. D. Shi, S. Salem-Sugui, Jr.: Phys. Rev. B **44**, 7647 (1991)
32. M. Tuominen, A.M. Goldman, M.L. McCartney: Physica C **153–155**, 324 (1988)
33. D. Hu, W. Paul, J. Rhyner: Physica C **200**, 359 (1992)
34. J.R. Thompson, Y.R. Sun, L. Civale, A.P. Malozemoff, M.W. McElfresh, A.D. Marwick, F. Holtzberg: Phys. Rev. B **47**, 14440 (1993)
35. C.W. Hagen, R. Griessen: Phys. Rev. Lett. **62**, 2857 (1989)

36. R. Griessen, J.G. Lensink, H.G. Schnack: Physica C **185–189**, 337 (1991); L. Fruchter. A.P. Malozemoff, I.A. Campbell, I. Sanchez, M. Konczykowski, R. Griessen, F. Holtzberg: Phys. Rev. B **43**, 8709 (1991)
37. G.T. Seidler, T.F. Rosenbaum, K.M. Beauchamp, H.M. Jaeger, G.W. Crabtree, U. Welp, V.M. Vinokur: Phys. Rev. Lett. **74**, 1442 (1995)
38. H. Wen, H.G. Schnack, R. Griessen, B. Dam, J. Rector: Physica C **241**, 353 (1995)
39. J. Jung, H. Yau, H. Darhmaoui, W.K. Kwok: Physica C **332**, 207 (2000)
40. V. Ambegaokar, A. Baratoff: Phys. Rev. Lett. **10**, 486 (1963)
41. D. Shi, M. Xu: Phys. Rev. B **44**, 4548 (1991)
42. J.R. Thompson, Y.R. Sun, D.K. Christaen, L. Civale, A.D. Marwick, F. Holtzberg: Phys. Rev. B **49**, 13287 (1994)
43. P. Svedlindh, C. Rossel, K. Niskanen, P. Norling, P. Nordblad, L. Lundgren, G.V. Chandrashekhar: Physica C **176**, 336 (1991)
44. S. Sengupta, D. Shi, Z. Wang, M.E. Smith, S. Salem-Sugui, Jr., P.J. McGinn: Phys. Rev. B **47**, 5414 (1993)
45. V.B. Geshkenbein, A.I. Larkin: Zh. Eksp. Teor. Fiz. **95**, 1108 (1987); R. Griesse: Physica C **172**, 441 (1991)
46. T.T.M. Palstra, B. Batlogg, R.B. van Dover, L.F. Schneemeyer, J.V. Waszczak: Phys. Rev. B **41**, 6621 (1990)
47. M.P. Maley, J.O. Willis, H. Lessure, M.E. McHenry: Phys. Rev. B **42**, 2639 (1990)
48. M.R. Beasley, R. Labush, W.W. Webb: Phys. Rev. **181**, 682 (1969)
49. E. Zeldov, N.M. Amer, G. Koren, A. Gupta, M.W. Mc Elfresh, R.J. Gambino: Phys. Rev. Lett. **62**, 3093 (1989)
50. Y. Abulafia, A. Shaulov, Y. Wolfus, R. Prozorov, L. Burlachkov, Y. Yeshurun, D. Majer, E. Zeldov, V.M. Vinokur: Phys. Rev. Lett. **75**, 2404 (1995)
51. M.V. Feigel'man, V.B. Geshkenbein, A.I. Larkin, V.M. Vinokur: Phys. Rev. Lett. **63**, 2303 (1989)
52. A.P. Malozemoff: Physica C **185–189**, 264 (1991)
53. See, for example, M. Bałanda: *Dynamic susceptibility of paramagnetic and exchange-coupled spin systems,* (Sect. 2.1) in this volume
54. K.-H. Müller: Physica C **159**, 717 (1989)
55. J.H. Lee, Y.C. Kim, B.J. Kim, D.Y. Jeong: Physica C **350**, 83 (2001)
56. E.M. Ferreira, J.A. Aguiar, J.M. Ferreira: Physica C **349**, 235 (2001)
57. K.-H. Müller: Physica C **168**, 585 (1990)
58. Z. Tomkowicz, M. Bałanda, A.J. Zaleski: Physica C **370**, 259 (2002)
59. S.Y. Ding, G.Q. Wang, X.X. Yao, H.T. Peng, Q.Y. Peng, S.H. Zhou: Phys. Rev. B **51**, 9107 (1995)

12

Relaxation Phenomena in Nonlinear Optical Polymers

T. Weyrauch and W. Haase

12.1 Introduction

Polymeric non-linear optical (NLO) materials have attracted much attention during the last two decades because of their potential to surpass the performance of current inorganic materials such as $LiNbO_3$ in integrated high-speed electro-optic devices. Since the optical nonlinearity in polymers is based on molecular properties of chromophorers, molecular design allows to tailor the material properties and thus to achieve high electro-optic coefficients. Other important advantages of polymers are the low dispersion between carrier and modulation frequency (allowing high-speed operation), their compatibility with many substrates, a flexibility of fabrication methods, and therefore the prospect of large-scale low-cost integration (see e.g. [1, 2]).

The polar symmetry that is required for second-order (quadratic) non-linear optical properties has been a main point of interest since the first description of such properties in polymers [3], because the non-centrosymmetry has to be induced for amorphous polymers by a poling process: The polymers are cooled down from temperatures above to well below the glass transition point while a high d.c. electric field is applied and a frozen-in polar order of dipolar chromophores remains even after the d.c. poling field is switched off. However, the glassy state allows for structural relaxations and a decay of quadratic NLO properties can be observed. Investigations on the poling and its relaxation processes have thus been major topics in research and development of NLO polymer materials and devices. The activity in this field led also to the development of new experimental techniques that are now used far beyond their original scope.

In this paper we will briefly review the basic principles of NLO polymers. Then experimental techniques and results performed to study the relaxation of polar order will be presented. We will show that the observed relaxation behavior can be described in terms of a relaxation model for structural relaxations in the glassy state. Finally the application of electroabsorption spectroscopy for evaluation of relaxation processes will be discussed.

12.2 Physical background

12.2.1 NLO susceptibility and effects

In nonlinear optical media the linear relationship between an electric field $\boldsymbol{E}$ and the induced polarization $\boldsymbol{P}$ must be replaced by a nonlinear expression, e.g. a Taylor series expansion:

$$P_i = P_i^{(0)} + \sum_j \chi_{ij}^{(1)} E_j + \sum_{jk} \chi_{ijk}^{(2)} E_j E_k + \sum_{jkl} \chi_{jkl}^{(3)} E_j E_k E_l + \ldots \tag{12.1}$$

Here the indices i, j, k, l denote the vector components in the laboratory frame, $\boldsymbol{P}^{(0)}$ is a permanent polarization that may be present in the material, $\chi^{(\mathbf{1})}$ is the linear optical susceptibility and $\chi^{(\mathbf{2})}$, $\chi^{(\mathbf{3})}, \ldots$ are the nonlinear susceptibilities of second, third, ... order, respectively. For quadratic effects we have to take into account only the term containing $\chi^{(\mathbf{2})}$ and we obtain for the related quadratic polarization

$$P_i^{(2)} = \sum_{jk} \chi_{ijk}^{(2)} E_j E_k \; . \tag{12.2}$$

Quadratic effects require a non-centrosymmetric material structure. Otherwise, an inversion operator applied to (12.2) would invert the sign of the electric polarization vector component $P_i^{(2)}$ and the electric field vector components E_j and E_k, but not of the $\chi^{(\mathbf{2})}$ tensor, a contradiction that can only be solved if all components of $\chi^{(\mathbf{2})}$ are zero. For non-centrosymmetric materials however the inversion operator will also change the sign of the $\chi^{(\mathbf{2})}$ components.

Equation (12.2) describes the interaction of three waves. This can be seen best considering the total electric field applied to the material consisting of two Fourier components $E(\omega_1)$ and $E(\omega_2)$:

$$P_i^{(2)}(\omega_3) = \sum_{jk} \chi_{ijk}^{(2)}(\omega_3; \omega_1, \omega_2) E_j(\omega_1) E_k(\omega_2) + \ldots \tag{12.3}$$

Thus, the nonlinear $\chi^{(\mathbf{2})}$ term is the origin of the generation of the sum and the difference frequencies $\omega_3 = \omega_1 + \omega_2$, $\omega_3' = \omega_1 - \omega_2$. Two special cases deserve special attention: First, in the case $\omega_1 = \omega_2$ we have frequency doubling (second harmonic generation, SHG), which may occur as the self-interaction of a single optical wave. Second, if one electric field is an optical wave and the other is a static (or quasi-static low frequency) field the interaction appears as a (static or low-frequency) refractive index variation for the light beam. This is known as Pockels effect and the basis for interferometric electrooptic modulators.

12.2.2 Organic NLO materials

In organic materials the origin of the optical nonlinearity is the nonlinear behavior on the molecular level. The dipole moment of a molecule under a local electric field $\boldsymbol{E}^{\text{loc}}$ may be described similar to (12.1) as a Taylor expansion:

$$\mu_I = \mu_I^0 + \sum_J \alpha_{IJ} E_J + \sum_{JK} \beta_{IJK} E_J E_K + \sum_{JKL} \gamma_{JKL} E_J E_K E_L + \dots \quad (12.4)$$

Here μ^0 is the permanent dipole moment, α is the linear polarizability and β, γ are the quadratic and cubic hyperpolarizabilities, respectively. A well known type of molecules, representing materials with high quadratic hyperpolarizability, are extended π-electron systems with donor and acceptor substituting groups (Fig. 12.1). The π-electron system may be realized e.g. by phenyl, stilbene or azobenzene groups. The nitro and the dialkylamino groups are often used as donor and acceptor groups, respectively. The β tensor of such rod-like NLO molecules has one dominant component β_{ZZZ}, where Z is the molecular longitudinal axis. Other components are much smaller and can usually be neglected.

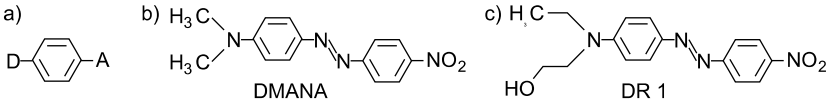

Fig. 12.1. Quadratic NLO chromophores. (**a**) General structure (D = donor group, A = acceptor group). (**b**),(**c**) Example molecules

In organic materials intramolecular forces are much higher than intermolecular forces and the macroscopic susceptibility may easily be calculated from the hyperpolarizabilities of the molecules in the ensemble by considering their orientational average [4–6]:

$$\chi^{(2)}_{ijk}(-\omega_3;\omega_1,\omega_2) = (N/V) f_i^{\omega_3} f_j^{\omega_1} f_k^{\omega_2} \langle \beta_{IJK} \cos\xi_{iI} \cos\xi_{jJ} \cos\xi_{kK} \rangle \quad (12.5)$$

N/V is the number of molecules per volume unit, $\xi_{iI} = \angle(i,I)$, $\xi_{jJ} = \angle(j,J)$ and $\xi_{kK} = \angle(k,K)$ describe the relative orientation of the molecular frame (I,J,K) and the laboratory frame (i,j,k). The angle brackets $\langle \dots \rangle$ denote averaging over all molecules in the ensemble. The local field correction factors f_i^{ω} describe the relation between the externally applied field $\boldsymbol{E}$ and the local field $\boldsymbol{E}^{\text{loc}}$ sensed by the molecules.

12.2.3 Poled NLO polymers

A poling procedure is necessary to introduce a non-centrosymmetric structure in amorphous polymers. For thermal poling (as shown in Fig. 12.2a) the

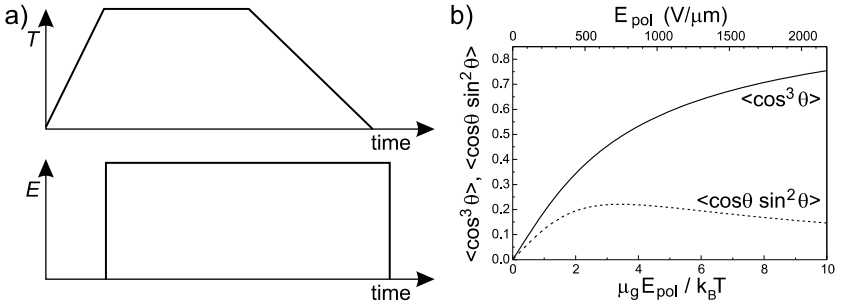

Fig. 12.2. Thermal poling. (**a**) Schematic of the evolution of temperature T and electric poling field E. (**b**) Expectation values for the polar order parameters $\langle\cos^3\theta\rangle$ and $\langle\cos\theta\sin^2\theta\rangle$

polymer is heated to or above the glass transition point and a high electric field is applied. Subsequently the polymer is cooled down to room temperature under the field. At low temperatures the induced polar structure is frozen in and the external electric field can be switched off. The resulting structure of the polymer has an ∞mm symmetry and the $\chi^{(\mathbf{2})}$ tensor has only two independent elements $\chi^{(2)}_{zzz}$ and $\chi^{(2)}_{zxx}$ (if additional symmetry considerations are valid [7]). Thus (12.5) results in

$$\chi^{(2)}_{zzz}(-\omega_3;\omega_1,\omega_2) = (N/V) f_z^{\omega_3} f_z^{\omega_1} f_z^{\omega_2} \beta_{ZZZ} \langle\cos^3\theta\rangle \tag{12.6}$$

$$\chi^{(2)}_{zxx}(-\omega_3;\omega_1,\omega_2) = 0.5(N/V) f_z^{\omega_3} f_x^{\omega_1} f_x^{\omega_2} \beta_{ZZZ} \langle\cos\theta\sin^2\theta\rangle \ , \tag{12.7}$$

where the terms $\langle\cos^3\theta\rangle$ and $\langle\cos\theta\sin^2\theta\rangle$ are the relevant polar order parameters. Their expectation values can be calculated from the Maxwell–Boltzmann distribution of the dipoles in the poling field [5, 8]. Figure 12.2b shows the order parameters in dependence on the Boltzmann factor $\mu_g E^{\rm loc}_{\rm pol}/k_B T$ (μ_g = permanent dipole moment, $E^{\rm loc}_{\rm pol}$ = local electric poling field, k_B = Boltzmann constant, T = temperature). The scale for the electric field refers to an example of $\mu_g = 7\,$Debye and $T = 100\,^\circ$C. Note that a local field correction factor $f^0 = f^{\omega=0}$ describes the relation between external and local poling field. The Onsager and the Lorentz–Lorenz models have been widely used for the calculation of f^0 and f^ω, the d.c. and optical local electric field correction, respectively [5, 9], but alternative models, that consider the anisotropic shape of molecules, e.g. [10], deliver non-negligible different results. The uncertainty in the determination of the correction factors is in general a problem for the exact calculation of the relationship between molecular and macroscopic NLO properties.

12.2.4 Stark effect (Electroabsorption)

In quadratic NLO materials the absorption is influenced by an electric field simultaneously to the refractive index (electroabsorption and electrooptic effect,

or Stark effect and Pockels effect , respectively) and both effects are connected due to the Kramers–Kronig relation. Thus the Stark effect may be discussed in terms of the imaginary parts of the nonlinear optical tensors $\chi^{(2)}$, β, $\chi^{(3)}$ and γ for the linear and the quadratic effect, respectively [11]. We use here a description, where the Stark effect is immediately related to relevant molecular properties of the chromophores, i.e. the differences of dipole moment ($\Delta\mu$) and linear polarizability ($\Delta\alpha$) in the ground and the electronically excited state [12]. The shift $\Delta\tilde{\nu}$ of the wave number of the absorption band of an orientationally fixed molecule by application of an electric field $\boldsymbol{E}$ is given by

$$(h/c)\Delta\tilde{\nu} = \Delta\mu\,\boldsymbol{E}^{\mathrm{loc}} - (1/2)\Delta\alpha\boldsymbol{E}^{\mathrm{loc}}\boldsymbol{E}^{\mathrm{loc}} \tag{12.8}$$

(c = light velocity, h = Planck constant). Note, that (12.8) contains the local electric field $\boldsymbol{E}^{\mathrm{loc}} = f\boldsymbol{E}$; again a local field correction factor f is required to obtain it from the external field $\boldsymbol{E}$. $\Delta\tilde{\nu}$ is usually too small (especially in comparison to the width of the absorption band) to be measured directly. We rather consider the change of the extinction $\Delta\varepsilon(\tilde{\nu})$ at fixed $\tilde{\nu}$ and derive from (12.8) for a single molecule [12]

$$\Delta\varepsilon(\tilde{\nu}) = \frac{\Delta\mu}{hc}\boldsymbol{E}\tilde{\nu}\frac{\mathrm{d}(\varepsilon/\tilde{\nu})}{\mathrm{d}\tilde{\nu}} + \frac{(\Delta\mu\,\boldsymbol{E})^2}{2(hc)^2}\tilde{\nu}\frac{\mathrm{d}^2(\varepsilon/\tilde{\nu})}{\mathrm{d}\nu^2} + \frac{(\Delta\alpha\boldsymbol{E})\boldsymbol{E}}{2hc}\tilde{\nu}\frac{\mathrm{d}(\varepsilon/\tilde{\nu})}{\mathrm{d}\tilde{\nu}}\,. \tag{12.9}$$

We can calculate the electric induced absorption change $\Delta A(\tilde{\nu})$ of a macroscopic sample by averaging (12.9) over all molecules in the ensemble considering of the molecules' orientational distribution in respect to the electric field and the light propagation direction:

$$\begin{aligned}\Delta A(\tilde{\nu}) = {} & F_1\frac{\Delta\mu\,E}{hc}\mathcal{A}'(\tilde{\nu}) + \frac{1}{2}\frac{E^2}{hc}\left[\Delta\alpha_l(1-F_2) + \Delta\alpha_t F_2\right]\mathcal{A}'(\tilde{\nu}) \\ & + \frac{1}{2}\left(\frac{\Delta\mu\,E}{hc}\right)^2 F_2\mathcal{A}''(\tilde{\nu}),\end{aligned} \tag{12.10}$$

where $\mathcal{A}'(\tilde{\nu})$ and $\mathcal{A}''(\tilde{\nu})$ are abbreviations for the derivative terms

$$\mathcal{A}'(\tilde{\nu}) = \tilde{\nu}\frac{\mathrm{d}(A/\tilde{\nu})}{\mathrm{d}\tilde{\nu}} \quad \text{and} \quad \mathcal{A}''(\tilde{\nu}) = \tilde{\nu}\frac{\mathrm{d}^2(A/\tilde{\nu})}{\mathrm{d}\tilde{\nu}^2} \tag{12.11}$$

of the absorption spectrum $A(\tilde{\nu})$ of the sample. $\Delta\alpha_l$ is the longitudinal component of the polarizability difference, $\Delta\alpha_t$ is the transversal component and F_1 and F_2 are order parameters given by

$$F_1 = \frac{\langle\cos\theta\sin^2\theta\rangle}{\langle\sin^2\theta\rangle} \quad \text{and} \quad F_2 = \frac{\langle\cos^2\theta\sin^2\theta\rangle}{\langle\sin^2\theta\rangle}. \tag{12.12}$$

θ is the angle between the dipole moment and the propagation direction of the light. The angle brackets $\langle\ldots\rangle$ denote averaging over all molecules in the sample. F_1 is a polar order parameter, consequently the linear Stark effect

described by the first term of (12.10) can be observed only in polar samples. Since F_2 is a non-polar order parameter the quadratic effect [second and third term in (12.10)] occurs also in unpoled samples. The expectation value of F_2 can be calculated easily to 1/5 for isotropic materials, but differs even for poled samples only insignificantly from this value. We can therefore simplify (12.10) by neglecting this small difference as well as the then meaningless polarizability anisotropy by replacing F_2 with 1/5 and using $\Delta\alpha = \Delta\alpha_l = \Delta\alpha_t$.

12.2.5 Piezoelectric effect

Quadratic NLO polymers have a macroscopic polarization due to a frozen-in polar orientation of dipolar chromophores. They can thus be considered as molecular dipole electrets with additional polarization-related properties as e.g. piezo- and pyroelectricity. We paid some attention to the characterization of poling stability by the piezoelectric effect because rather simple experimental techniques (acoustoelectric measurements) may be used. Broadhurst et al. provided a theoretical description of the piezoelectricity in molecular dipole electrets [13, 14]. We present their results here briefly: The frozen-in polarization P of a molecular dipole electret is given by

$$P = \frac{N}{V}\langle m\rangle \ , \tag{12.13}$$

where N/V is the number of dipoles per volume and $\langle m\rangle$ is the effective molecular dipole moment, which is composed from the permanent dipole moment μ_g and an internal-field-induced contribution. Calculation of $\langle m\rangle$ results in

$$P = \frac{N}{V}\frac{\epsilon_\infty + 2}{3}\mu_g\langle\cos\theta\rangle \ , \tag{12.14}$$

with the dielectric constant ϵ_∞ at optical frequencies and the average $\langle\cos\theta\rangle$ of the angle between individual molecular dipoles and the polar axis of the material. Rather than the variation of the polarization P that is induced by a change of the pressure p, one measures experimentally the change of the compensation charges Q on the electrode area A of the sample, i.e.

$$d_p^{\exp} = \frac{1}{A}\frac{\partial Q}{\partial p}, \tag{12.15}$$

which can be approximately described by

$$d_p^{\exp} = -P\beta\frac{\epsilon_\infty}{3} = -\beta\frac{N}{V}\frac{(\epsilon_\infty + 2)\epsilon_\infty}{9}\mu_g\langle\cos\theta\rangle \ , \tag{12.16}$$

where $\beta = -(\mathrm{d}V/\mathrm{d}p)/V$ is the volume compressibility. The piezoelectric coefficient is proportional to the induced polarization, i.e. to the average value $\langle\cos\theta\rangle$. This is a different dependency on molecular order than in the case of the nonlinear optical susceptibilities, where higher order terms are used (12.6). Thus one can't necessarily expect a similar relaxation behavior of NLO and piezoelectric properties.

12.3 The stability of polar order after poling

12.3.1 Experimental methods

Sample preparation and poling

Investigations on NLO polymers require very often thin film samples, prepared using the spin coating technique, where the polymer is dissolved in an appropriate solvent and the solution is spread onto a substrate, e.g. glass, mounted on top of a rotating table. The film thickness can be set from the sub-micrometer range until several micrometers by varying the polymer concentration and the rotation speed. For drying one usually keeps the films after their preparation for several hours under room ambient conditions and subsequently heats them under vacuum to remove the remaining solvent.

In most cases poling field is applied perpendicular to the film plane and the substrate must comprehend a conductive layer used as an electrode. If a transparent substrate is required, the electrode usually consists of indium tin oxide (ITO). Two different poling techniques, electrode poling and corona poling, have been used. For the first an additional electrode layer must be provided, e.g. by sputtering a thin metal layer onto the polymer film or attaching a second ITO covered substrate onto the polymer film using an epoxy resin [12]. The demand for a sophisticated sample preparation is one central problem of electrode poling. Any defect in the film (originated from dust or impurities in polymer or solvent) may lead to an electric short circuit when a high poling voltage at an elevated temperature is applied and thus destroy the sample. The absorption of metal electrodes, although semi-transparent for sufficiently thin layers, raise another problem for experiments where higher light intensities are necessary as e.g. in SHG measurements.

Corona poling does not require a second electrode, but uses the corona discharge at a needle tip or a thin wire connected to a high voltage U_{HV} (about 10 kV) to generate ions above a polymer sample (see Fig. 12.3). Grounding the ITO electrode of the sample forces the ions to follow the electric field onto the polymer film's surface, where they remain for some time until they are

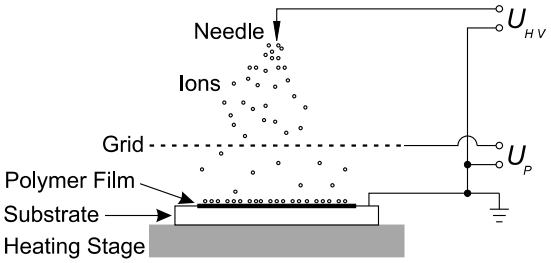

Fig. 12.3. Schematics of a corona poling setup (U_{HV} high voltage, U_P poling voltage)

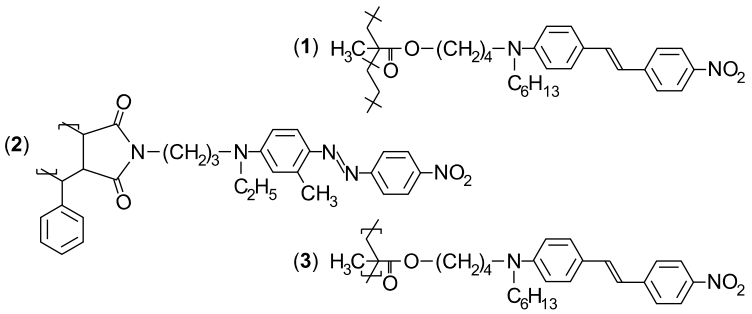

Fig. 12.4. Chemical structure of polymers used for poling and relaxation experiments

neutralized. Hence a rather high voltage is applied across the polymer film. In a more sophisticated version of the technique an additional grid is used between the corona and the film that allows to control the poling voltage, which will not exceed the intermediate voltage U_P applied to the grid. The major advantage of corona poling is the much less demanding sample preparation: Local defects do not destroy the whole sample because of the low lateral conductivity for the ions on the polymer surface and the remaining part of the film can be poled without damage. A disadvantage of corona poling is a possible impairment of the surface quality through the ion bombardment. The ions may also induce chemical reactions with the polymer or the NLO chromophores and thus deteriorate the sample. Controlling the corona poling atmosphere, esp. using an oxygen-free gas, can reduce the negative effects [15].

We present here results that were obtained from measurements on the polymers depicted in Fig. 12.4. Polymer **1** is a copolymer of ethylene and methacrylate units, the latter are attached by an $O(CH_2)_4$ spacer to an amino nitrostilbene NLO chromophore. The ratio of ethylene and methacrylate is 9:1; the glass transition temperature is about 103 °C. The poly(styrene-maleic anhydride) polymer **2** with a chemically attached Disperse Red 1 side group was provided by Sandoz Optoelectronics (Huningue, France). The glass transition is at 137 °C. The polymethacrylate **3** has an amino nitrostilbene NLO side group and a glass transition temperature of about 66 °C. Polymers **1** and **3** were provided by Merck KGaA (Darmstadt, Germany).

Second harmonic generation

We used the Maker-fringe technique [16] to determine the stability of the optical nonlinearity in poled polymers. The pulsed laser beam of a Nd-YAG laser ($\lambda = 1064$ nm) was directed to the sample (the polymer film on a glass substrate), which was mounted on a rotation stage to allow a variation of the angle of incidence α (Fig. 12.5a). After blocking the fundamental wave the signal strength of the second harmonic light ($\lambda = 532$ nm) was measured

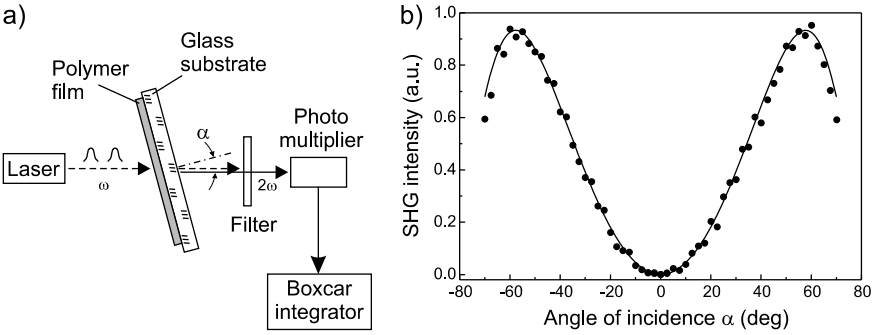

Fig. 12.5. (**a**) Schematics of a SHG experiment using the Maker-fringe technique. (**b**) Experimental curves of SH intensity vs. angle of incidence α

using a photomultiplier and a Boxcar integrator that measured the signal only during the 10 ns pulses to increase the signal-to-noise ratio. To avoid errors due to fluctuations of the energy of the pulses of the fundamental wave, the polymer second harmonic signal was measured in respect to a reference signal obtained from a quartz crystal. A sample curve of second harmonic intensity versus angle of incidence is shown in Fig. 12.5b. We omit here a discussion of the shape of the curve $I_{2\omega}(\alpha)$, which depends not only on the nonlinear susceptibility tensor elements $\chi^{(2)}_{zzz}$ and $\chi^{(2)}_{zxx}$, but also on the refractive indices for the fundamental and second harmonic in polymer and substrate as well as on the sample thickness [5, 8]. For relaxation measurements only the relative signal strength at different times after the poling is relevant and we were able to use the experimental signals directly rather than calculating the nonlinear susceptibility $\chi^{(2)}$. Keeping the angle of incidence α constant allowed for mounting of a corona-poling setup onto the optical table and thus for in situ measurements of the second harmonic intensity during the poling.

Acoustoelectric measurements

To compare the relaxation of NLO properties and piezoelectricity, we developed acoustoelectric methods for the measurement of the relaxation behaviour of the piezoelectric effect [15, 17]. Both are based on the fact that acoustic waves with relatively moderate pressure suffice to generate an electric response that can be measured by lock-in technique. As shown in Fig. 12.6 the differential pressure of the acoustic sound wave may be applied either transversal (a) or longitudinal (b) to the polar axis of the polymer. Samples for the transversal configuration are prepared by pressing a melted drop of the polymer between two ITO coated glass plates until it reaches the thickness of the spacers that defines the desired distance between the glass plates (typically about 100 μm). The advantage is the very small amount of polymer that is required for sample preparation, which requires however some experience to avoid parasitic signals (e.g.

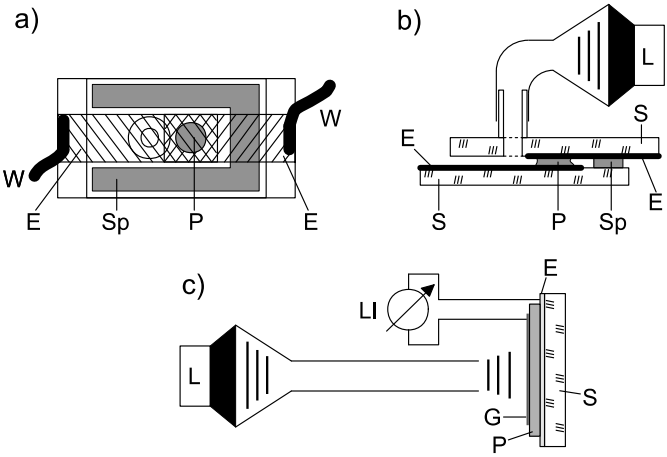

Fig. 12.6. Acoustoelectric measurements on poled NLO polymers in (**a**),(**b**) transversal and (**c**) longitudinal geometry (E = electrode, G = gold electrode, L = loudspeaker, LI = lock-in amplifier, P = polymer, S = substrate, Sp = spacer, W = wires)

from the spacers). The disadvantage is the relatively small part of the sample along the edge of the polymer that is deformed by the acoustic pressure and thus contributes to the signal. As shown in [17] the active area corresponds to an annular plate with a width in the order of 2/3 of the sample thickness.

Measurements in the longitudinal configuration were performed on spin-casted films with a sputtered top gold electrode. During the poling process the samples were cooled down to the temperature of measurement with a rate of 3 K/min under electric field (corona poling was used for the SHG experiment). For the piezoelectric measurements the electrodes were short-circuited for a few seconds to allow for the discharge of the sample capacitance. The sound signal was generated using the internal signal generator of the lock-in amplifier, an amplifier and a loudspeaker. A funnel and a pipe were used to guide the acoustic wave to the sample.

12.3.2 The relaxation of SHG and acoustoelectric response

In in-situ corona poling and SHG experiments we observed two different processes that contribute to the relaxation of second order NLO properties after poling. Figure 12.7a shows the second harmonic power $P(2\omega)$ during and shortly after corona poling of polymer **1** (Fig. 12.4) at different temperatures. A steep decrease of the SHG signal takes place immediately after switching off the high voltage (at $t-t_0 = 0$), followed by a slower relaxation. The time scale of the faster process is in the order of 1 minute and is generally attributed to the decay of surface charges on the polymer sample. The presence of surface

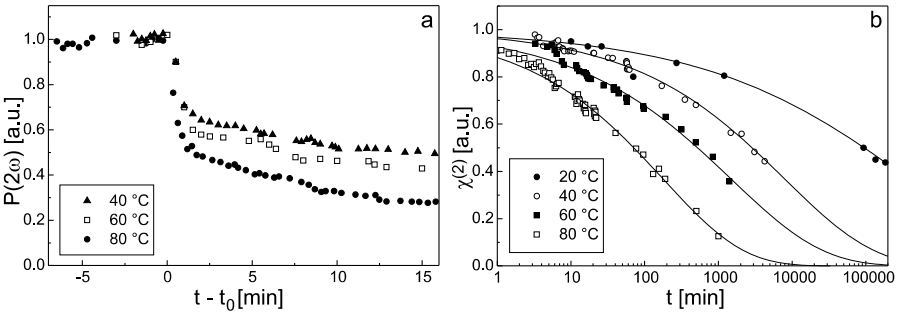

Fig. 12.7. (**a**) SHG signal $P(2\omega)$ during and immediately after corona poling of the nitrostilbene side-chain polymer **1**. (**b**) Nonlinear susceptibility $\chi^{(2)}$ measured in long time experiments at different temperatures

charges, and thus of a poling field, increases the SHG signal by stabilization of the chromophores' polar order in the external d.c. field as well as through higher order nonlinear terms, i.e. from $\chi^{(3)}(E_{2\omega}; E_\omega, E_\omega, E_0)$ tensor elements that correspond to the interaction of the d.c. field E_0 and the optical field E_ω.

Figure 12.7b shows the long term behavior of the nonlinear susceptibility $\chi^{(2)}$ of polymer **1** at different temperatures. To describe the measured data analytically we tested several different relaxation functions (exponential, bi-exponential, and exponential functions with a time dependent constant as proposed in [18]), but we received the best results using the stretched exponential function

$$u(t) = u_0 \exp[-(t/\tau_0)^\beta] \,, \tag{12.17}$$

also known as the Kohlrausch–Williams–Watt (KWW) function, where the exponent β $(0 < \beta \leq 1)$ describes an asymmetrical broadening of the relaxation time distribution. The average relaxation time $\tau_m = \langle\tau\rangle$ is different from the nominal value τ_0 and is given by $\tau_m = (\tau_0/\beta)\Gamma(\beta^{-1})$, where Γ is the Euler gamma function [19]. The lines in Fig. 12.7b were obtained by fitting KWW functions to the experimental data.

We found a very similar relaxation behavior in acoustoelectric measurements of the piezolectric effect (Fig. 12.8). Since electrode poling was used for these experiments, the faster process cannot be explained by the presence of ions on the surface, but by charge distributions that are generated due to charge injection at the polymer electrode interfaces. The influence of such charges on the acoustoelectric signal is however different from NLO experiments, because rather high piezoelectric signals my arise from asymmetric volume charge distributions directly, i.e. even without a polar order of the NLO chromophores. Indeed, we observed rather high acoustoelectric signal amplitudes during the fast process immediately after the poling ended, esp. in case of the transversal experiment (cf. Fig. 12.8a, where the sample is deformed non-homogeneously). The decay times of these fast processes are comparable

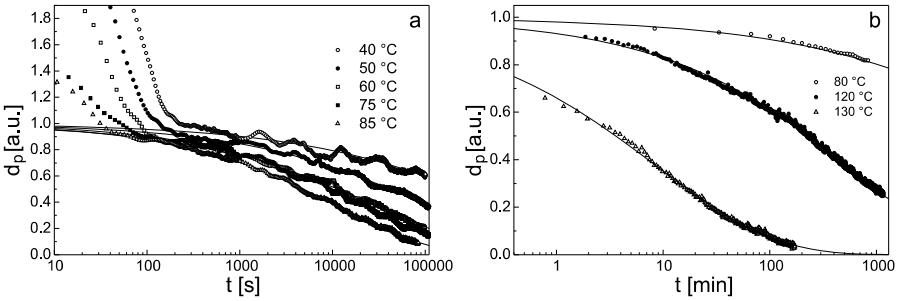

Fig. 12.8. Relaxation of the piezoelectric signal d_p in acoustoelectric experiments (**a**) measured in transversal geometry on a sample of polymer **1**, (**b**) obtained from longitudinal experiments on polymer **2**

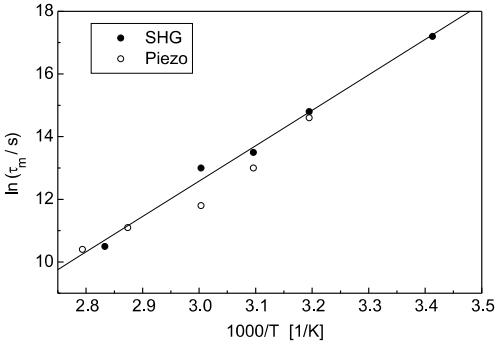

Fig. 12.9. Temperature dependence of the average relaxation time τ_m of the polymer **1** obtained from relaxation data of SHG and piezoelectric (acoustoelectric) effect

to those observed in transient depolarization current measurements [15, 20], which is another indication for their relation to charge distributions.

Fitting the KWW function to experimental curves of both, the piezoelectric effect and SHG measured on samples of the polymer **1** we found values for β in the range from 0.35 to 0.45 for the temperature between 40 °C and 85 °C. An example for the temperature dependence of the average relaxation time τ_m is shown in Fig. 12.9. The experimental values of τ_m follow in a good approximation an Arrhenius-type temperature behavior [15, 21].

12.3.3 Discussion of poling stability

An interpretation of the experimental results is possible in terms of semi-empirical phenomenological models, which describe the glass transition as a relaxational phenomenon: Below the transition temperature the characteristic time constant of the structural relaxations of the polymer chains exceeds the time scale set by the experiment, thus the polymer appears as rigid. Above

the glass transition temperature a deviation from Arrhenius behavior is observed for the α relaxation, i.e. the large scale microbrownian motion of the chains, with a strong slowing down of the relaxation when approaching the glass transition temperature. This temperature dependence of the relaxation time τ is often described by the equation given by Williams, Landel and Ferry

$$\ln\left[\frac{\tau_m(T)}{\tau(T_g)}\right] = \frac{-C_1(T-T_g)}{C_2+(T-T_g)}, \tag{12.18}$$

known as WLF behavior, where $\tau(T_g)$ is the relaxation time constant at the glass transition temperature T_g, and C_1 and C_2 are material constants, which are very often close to the "standard" values $C_1 = 17$ and $C_2 = 52$ K [22]. Equation (12.18) implies an infinitively large relaxation time for the temperature $T_g - C_2$. Therefore its validity is typically limited to the temperature range above $T_g + 10$ K. A theoretical foundation for the WLF behavior (Adams–Gibbs–DiMarzio theory) was presented in [23, 24] and based on calculations of the configuration entropy. $T_0 = T_g - C_2$ was identified as the temperature where the configuration entropy becomes zero.

In the glassy state the relaxation time τ depends, in general, not only on T but also on the material history, hence the material is not in an thermal equilibrium. Non-equilibrium behavior is often described by means of the fictive temperature T_f introduced by Tool [25]. It corresponds to the temperature of an equilibrium state, which is fictive and could be reached only by infinitively slow cooling, and is equivalent to the actual non-equilibrium state of the material. Figure 12.10 illustrates the fictive temperature concepts by means of the generalized temperature dependence of a thermodynamical quantity ϕ. The measurable temperature dependence $\phi(T)$ has distinctively different slopes above and below the glass transition temperature (a) and (c), respectively, with a transition region (b) around T_g. The exact shape of (b) and (c) depends on the history of the material (cooling rate, aging, etc.).

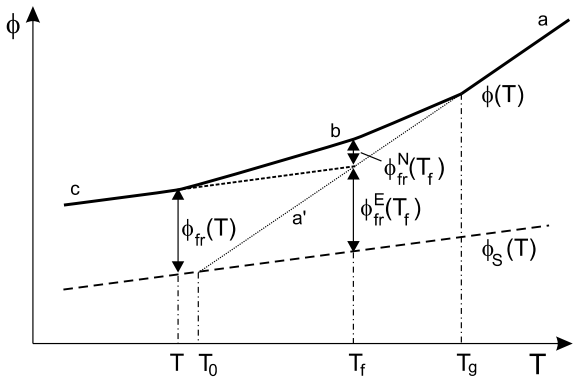

Fig. 12.10. Schematic of the temperature dependence of a thermodynamical quantity ϕ for a glass forming material

Curves (a) and (a′) describe the material in an equilibrium state, the extrapolation (a′) is however a fictive curve for infinitively slow cooling, which is required to allow for slow structural relaxations. This extrapolation ends at the intersection with curve $\phi_S(T)$, which is valid for a fictive equilibrium solid state. The free part ϕ_{fr}, i.e. the portion of ϕ that can be attributed to structural relaxation, is given by the difference between $\phi(T)$ and $\phi_S(T)$, and can be divided into an equilibrium part ϕ_{fr}^E below (a′) and a non-equilibrium part ϕ_{fr}^N above (a′). The fictive temperature T_f for a given state $\phi(T)$ is defined by $\phi_{fr}^E(T) = \phi_{fr}(T)$.

If we identify the quantity ϕ with the enthalpy H, then the slopes of the curve parts (a) and (b) are the heat capacities c_p^l and c_p^g for the liquid and glassy state, respectively, and may be obtained by extrapolation of an experimental $c_p(T)$ curve. The fictive temperature may thus be calculated from experimental data by numerical integration of the equation

$$\frac{dT_f(T)}{dT} = \frac{c_p(T) - c_p^g(T)}{c_p^l(T) - c_p^g(T)}. \tag{12.19}$$

We used differential scanning calorimetry (DSC) to measure $c_p(T)$. In Fig. 12.11a two different experimental curves are shown, obtained after annealing the polymer **1** at 80 °C for 20 and 75 minutes. Using (12.19) we obtained the curves for the fictive temperatures $T_f(T)$ shown in Fig. 12.11b. They demonstrate that the fictive temperature is mainly determined by the material-history-dependent magnitude of the DSC nose at the glass transition and is nearly independent from T below T_g.

Scherer used the fictive temperature to derive an analytic description of relaxation processes in the glassy state by extending the Adams–Gibbs–DiMarzio theory considering the fictive temperature for the calculation of the configurational entropy [26]. This Adam–Gibbs–Scherer (AGS) model results in the

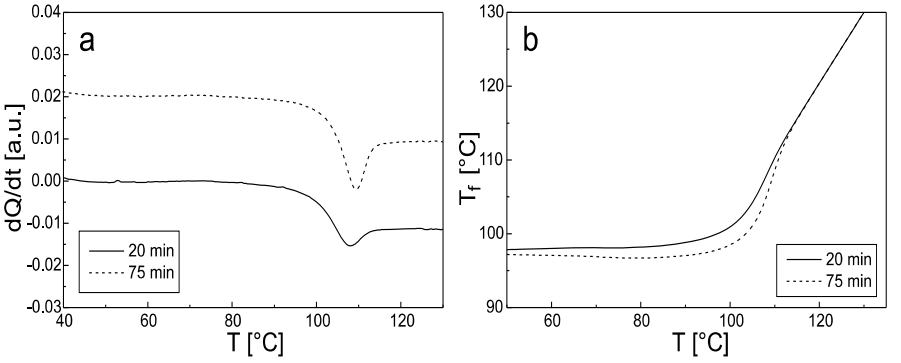

Fig. 12.11. (**a**) DSC curves (shifted by an offset for better visualization) and (**b**) calculated temperature dependence of the fictive temperature of polymer **1** after annealing at different temperatures

following expression for the time-temperature dependence of the relaxation process (in terms of the WLF notation) [15, 27]:

$$\ln\left[\frac{\tau_m(T, T_f(T))}{\tau(T_g)}\right] = \frac{C_1 C_2}{T\left(1 - \dfrac{T_g - C_2}{T_f(T)}\right)} - C_1 \,. \tag{12.20}$$

For the case of a constant T_f, which is nearly the case according to DSC experiments (Fig. 12.11b), this equation predicts indeed the Arrhenius-type behavior of $\tau_m(T)$ in the glassy state that was found in SHG and acoustoelectric measurements. The AGS model is also in accordance with relaxation behavior measured above and below the glass transition temperature as shown in Fig. 12.12. The temperature dependence of relaxation times observed on the side-chain NLO polymer **3** with dielectric spectroscopy above [20] and by SHG below the glass transition are well described by the AGS model (solid line).

In conclusion, our experiments showed a similar relaxation behavior for second order nonlinear optical and piezoelectric properties, although they are determined by different polar order parameters, and confirmed the theoretical prediction in [28]. The observed Arrhenius type temperature dependence of the relaxation time constants (also reported e.g. in [19, 29]) can be explained by the AGS model, which was discussed in similar way in [27, 30]. One may conclude from this result that a NLO polymer is the better suitable for application in electrooptic devices the higher its glass transition temperature is. A high T_g implicates however such problems as a reduced poling efficiency (because of the Boltzmann factor) and the chemical instability of NLO chromophores at high temperatures. Alternative approaches to stabilize the polar order have been discussed: Cross linking of the NLO polymers during poling [31, 32] may improve the poling stability but on the cost of disadvantages

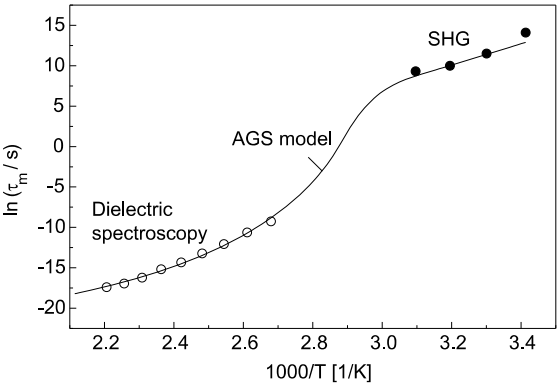

Fig. 12.12. Temperature dependence of relaxation time constants of the polymer **3** measured with dielectric spectroscopy and SHG above and below T_g, respectively, (*dots*) and a fit of the AGS model (*solid line*)

as a worse processability or a reduced polar order [33]. Enforcing the polar order by application of a permanent high d.c. voltage [34] is probably impracticable for real devices. Hence, the selection of the appropriate material for electrooptic devices is not only a question of the poling stability but a trade-off between several important material properties and some decrease of the electrooptic coefficient may be acceptable and compensated by an increase of the driving voltage.

12.4 Electroabsorption spectroscopy as a tool for relaxation measurements

12.4.1 Experimental technique

The detected signals in an electro-absorption spectrometer are the static component I and the electric field induced change ΔI of the transmitted light intensity (Fig. 12.13). Since $\Delta I \ll I$ the absorption change can be approximated by $\Delta A = -\Delta I / I \ln 10$. It makes the measurement insensitive to any specific spectral dependencies of the detector and allows for a comparable simple experimental set-up without sophisticated spectral calibration. A comparison of spectra obtained with and without a d.c. electric field applied does usually not suffice to determine the Stark effect because ΔA is small and might not exceed the noise level. The signal-to-noise ratio can be improved by several orders of magnitude using an a.c. electric field and a lock-in amplifier. If an electric field $E(t) = E_0 \sin(\Omega t)$ with a modulation frequency $f = \Omega/2\pi$ is applied to the sample, the linear effect will also be observed at f. The quadratic effect is proportional to $E^2(t)$ and has, because of $E_0^2 \sin^2(\Omega t) = 0.5 E_0^2 [1 - \cos(2\Omega t)]$, a d.c. component and a component at $2f = \Omega/\pi$. Since a lock-in amplifier typically delivers effective values in both the f and the $2f$ measurement mode, it is convenient to express the magnitude of all a.c. signals as effective values. We have thus for the linear effect

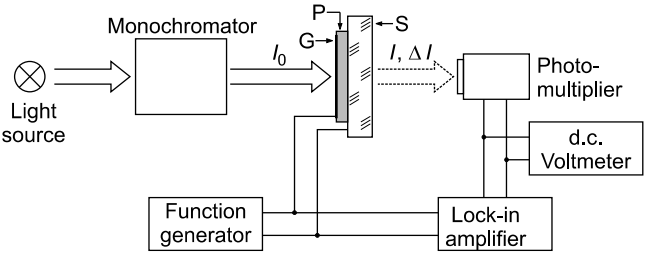

Fig. 12.13. Schematics of an electroabsorption spectroscopy experiment (G = semitransparent gold electrode, P = polymer film, S = glass substrate with transparent ITO electrode), I_0 incoming light intensity; I, ΔI see text

$$\Delta A_{\text{eff}}(f) = F_1 \frac{\Delta\mu\, E_{\text{eff}}(f)}{hc} \mathcal{A}'(\tilde{\nu}), \tag{12.21}$$

and for the quadratic effect

$$\Delta A_{\text{eff}}(2f) = \frac{E_{\text{eff}}^2}{\sqrt{2}} \left[\frac{\Delta\alpha}{2hc} \mathcal{A}'(\tilde{\nu}) + \frac{(\Delta\mu)^2}{10h^2c^2} \mathcal{A}''(\tilde{\nu}) \right]. \tag{12.22}$$

Using measured absorption spectra $A(\tilde{\nu})$ one can calculate the derivative terms $\mathcal{A}'(\tilde{\nu})$ and $\mathcal{A}''(\tilde{\nu})$ numerically. Fitting an equation of the form $\Delta A(\tilde{\nu}) = C_1\mathcal{A}'(\tilde{\nu}) + C_2\mathcal{A}''(\tilde{\nu})$ with variable parameters C_1 and C_2 to an experimental quadratic electroabsorption spectrum $\Delta A_{\text{eff}}^{2\omega}(\tilde{\nu})$ allows to determine the molecular parameters $\Delta\mu$ and $\Delta\alpha$. The knowledge of the value of $\Delta\mu$ allows then for the determination of the polar order parameter F_1 after fitting an equation of the form $\Delta A(\tilde{\nu}) = C_L\mathcal{A}'(\tilde{\nu})$ to the measured linear electroabsorption spectrum $\Delta A_{\text{eff}}^{\omega}(\tilde{\nu})$ of a polar sample. Note that the polar order parameter can be calculated from

$$F_1 = \frac{C_L U_{\text{eff}}^{\text{qu}}}{\sqrt{10\sqrt{2}C_2} U_{\text{eff}}^{\text{lin}}}\,, \tag{12.23}$$

where $U_{\text{eff}}^{\text{qu}}$ and $U_{\text{eff}}^{\text{lin}}$ are the modulation voltages used in the quadratic and linear experiment, respectively. F_1 can therefore be determined without measuring the film thickness and without any assumption about the correction factors for the local field; esp. the latter reduces the error for the polar order parameter significantly and is a valuable advantage in comparison with other NLO measurements [35].

12.4.2 Electroabsorption spectroscopy with variable modulation frequency

It has been desirable to study relaxation processes of NLO chromophores in polymers above and below the glass transition temperature, i.e. over several orders of magnitude in timescale, observing only one single physical property. New experimental techniques, often referred to as chi-electric relaxation measurements, have thus been developed for the observation of fast dynamics above the glass transition using quadratic NLO properties as e.g. SHG. The polar orientation of the chromophores is induced by a time dependent electric field E_p applied to the sample. The variation of the temporal relation between probing laser pulses and poling field allows to measure the temporal response of the NLO chromophore to the electric field. Figure 12.14 depicts the principles of two of the methods for chi-electric relaxation measurements. In Fig. 12.14a measurements are performed in the time domain [30]: E_p is a pulse of duration t_d and induces a second-order nonlinear susceptibility $\chi^{(2)}$ that follows the electric field with a characteristic response time. The variation of the delay t_m between probing laser pulse I_ω and E_p allows to determine

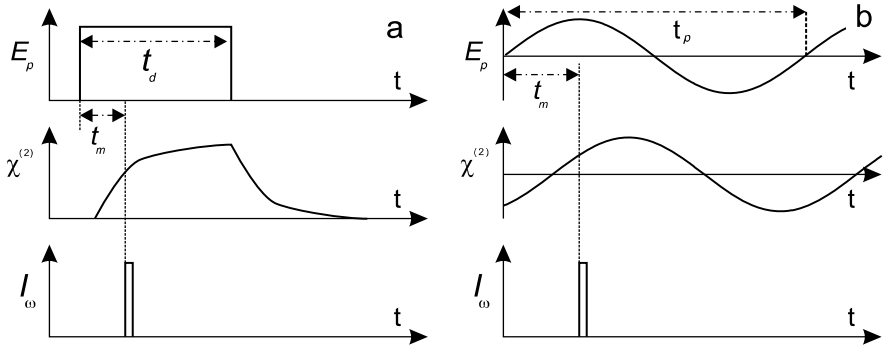

Fig. 12.14. Methods for chi-electric relaxation measurements in (**a**) time domain and (**b**) frequency domain (*top*: applied electric field, *middle*: response of nonlinear susceptibility χ^2, *bottom*: probing laser pulse intensity)

the response characteristics of the field induced $\chi^{(2)}$. As shown in Fig. 12.14b a sinusoidal E_p (with oscillation time t_p) induces a $\chi^{(2)}$ response that is also sinusoidal and, in general, phase shifted [36]. Variation of the delay time t_m for the synchronization of the probing laser pulses with E_p allows to scan the SHG response and thus to determine the amplitude and phase shift of $\chi^{(2)}$ (with respect to E_p). Repeating the measurements at a number of different frequencies $f = 1/t_p$ in the interesting frequency range allows to characterize the response characteristics of the NLO chromophores in the frequency domain. The measured SHG signal in both methods is however in fact the sum of $\chi^{(2)}$ and $\chi^{(3)}$ effects, where one of the field components in the $\chi^{(3)}$ term of (12.1) is from the electric field E_p, whereas the other two components are from the electric field of the laser pulse. This $\chi^{(3)}$ contribution to the apparent effect doesn't require reorientation of the chromophores, is much faster due to its electronic nature and appears thus as a constant offset.

The method for the measurement of the $\chi^{(2)}$ response is not limited to SHG; the electrooptic (Pockels) effect or the electroabsorption (Stark) effect may be used as well. Both effects are the optical response (in dispersion and absorption, respectively) to an electric field. Measurements in the frequency domain may thus be performed using a sinusoidal electric field for both, inducing the polar order and measuring the electrooptic or electroabsorption response. Our research in this direction has been focused on the Stark effect after we observed the influence of an electric field on the electroabsorption signal due to reorientation of chromophores [37].

Electroabsorption spectroscopy as described above allows in general to distinguish between the $\chi^{(2)}$ and the $\chi^{(3)}$ contributions, which correspond to the linear and quadratic Stark effect, respectively, due to their different wavenumber dependency. As described in (12.12) and (12.21) the linear electroabsorption effect can be observed at the first harmonic $f = \Omega/2\pi$ of the modulation field $E(t) = E\exp(\mathrm{i}\Omega t)$ and is proportional to the polar order

parameter F_1, whereas the quadratic effect is observable at the second harmonic $2f$ and is (in good approximation) independent of F_1. The linear effect doesn't contribute to the signal at $2f$ if the orientation of the chromophores is fixed. In the case of a sufficient rotational mobility at the frequency f a time dependent dipolar order may be induced by the modulation field E_m. In this case the polar order parameter F_1 oscillates with the frequency f, i.e.

$$F_1(t) = M_1 E \exp(\mathrm{i}\Omega t) = \sqrt{2} M_1 E_{\mathrm{eff}} \exp(\mathrm{i}\Omega t)\,, \tag{12.24}$$

where M_1 describes the magnitude of the chromophores' reorientation in the electric modulation field $E_m(f)$ at the frequency f.

Another contribution to the apparent electroabsorption spectrum is based on the absorbance change through the reorientation itself. The electric field gives a slight preference for molecules oriented in the direction of the light propagation (z axis) and thus reduces the absorbance of the sample, which is proportional to the expectation value $\langle \sin^2\theta \rangle$ for the angle between the molecular long axis and the z axis. The effect is (in contrast to the linear and quadratic Stark effect) proportional to the absorption spectrum $A(\tilde{\nu})$ itself and is quadratic in the electric modulation field E_m. Both, the oscillating polar order and the electro-orientation introduce additional contributions to the electroabsorption response at $2f$. Thus the electroabsorption spectrum can be described by

$$\Delta A_{\mathrm{eff}}(2f) = \frac{E_{\mathrm{eff}}^2}{\sqrt{2}} \left[\frac{2M_1 \Delta\mu + \Delta\alpha}{2hc} \mathcal{A}'(\tilde{\nu}) + \frac{(\Delta\mu)^2}{10h^2c^2} \mathcal{A}''(\tilde{\nu}) + M_0 A(\tilde{\nu}) \right]. \tag{12.25}$$

Taking into account the maximum values for both coefficients M_1 and M_0 according to the Boltzmann distribution of dipoles μ_g in the electric field E, we can write

$$M_1 = \frac{1}{5}\eta \frac{\mu_g}{k_B T} \quad \text{and} \quad M_0 = \frac{1}{15}\eta \left(\frac{\mu_g}{k_B T} \right)^2 , \tag{12.26}$$

where η is the relative response function that describes the reorientation magnitude in respect to its maximum ($\eta = 0$ for orientational fixed chromophores, $\eta = 1$ for chromophores that fully follow the modulation field E).

Figure 12.15a shows the electroabsorption spectra of Disperse Red 1 (DR1, Fig. 12.1) in polymethylmethacrylate (PMMA) measured with modulation frequencies $f = 2$ Hz and 2 kHz [38]. At $f = 2$ kHz the chromophores are not able to follow the modulation field, whereas for $f = 2$ Hz the reorientation of the chromophores is possible; the signal has thus a different amplitude and wavenumber dependency. The reorientation magnitude η can be evaluated by analyzing the relative magnitude of the different spectral contributions (A, $\mathcal{A}'$, $\mathcal{A}''$) to the experimental electroabsorption spectra $\Delta A(\tilde{\nu})$. After fitting an equation of the form $\Delta A(\tilde{\nu}) = C_0 A(\tilde{\nu}) + C_1 \mathcal{A}'(\tilde{\nu}) + C_2 \mathcal{A}''(\tilde{\nu})$ to experimental data, η is obtained by comparing the fit parameters C_0 and C_1 with the

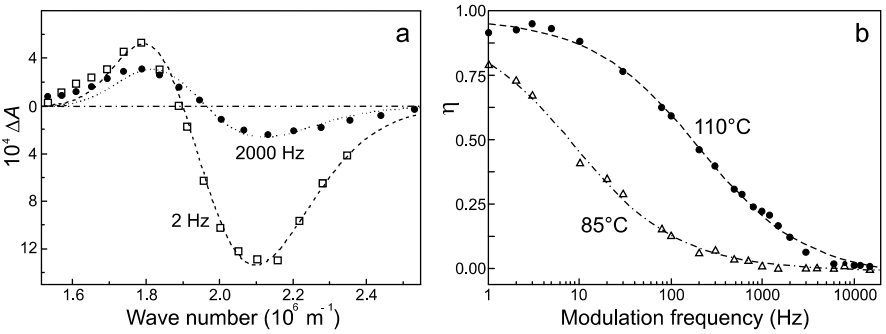

Fig. 12.15. Electroabsorption spectroscopy with variable modulation frequency. (**a**) Spectrum for Disperse Red 1 in PMMA for $f = 2$ Hz and 2 kHz. (**b**) Frequency dependence of the reorientation magnitude η for two temperatures

expressions of the corresponding coefficients given in (12.25). In experiments we found C_0 more significant than C_1 because of the magnitude of this contribution and its direct proportionality to η. To determine the mean relaxation frequency and the relaxation frequency distribution one has to repeat the measurement of the electroabsorption spectra several times at different modulation frequencies f and calculate the corresponding η value. Figure 12.15b shows as an example the results obtained for DR1 in PMMA at two different temperatures. More detailed analyses have shown that the curves $\eta(f)$ can be described by well-known frequency-domain relaxation functions (the dashed curves in Fig. 12.15b were obtained by fitting the Cole–Cole model). The corresponding mean relaxation frequencies are in agreement with results obtained by other techniques as chi-electric measurements [39–41].

Hence, electroabsorption spectroscopy with variable modulation frequency proved to be an alternative to other methods for the measurement of molecular orientation relaxation. The non-ambiguous attribution of the measured effect to the chromophore relaxation is a very important advantage over bulk measurements as dielectric spectroscopy and might be interesting for investigations on other materials besides quadratic NLO polymers, e.g. low-T_g photorefractive polymers. Electroabsorption measurements are also possible on samples with very low chromophore concentration, which may be important to exclude or even study effects of aggregation. A certain disadvantage of this method is the requirement to measure full spectra $\Delta A(\tilde{\nu})$ for a number of different modulation frequencies. However, in many cases it might be sufficient to determine the modulation frequency dependence of electroabsorption at a fixed wave number $\tilde{\nu}$. E.g. in Fig. 12.15a the response at $\tilde{\nu} = 2.1 \times 10^6\,\mathrm{m}^{-1}$ would be a good choice, because the signal magnitude is (besides a small frequency-independent offset) almost proportional to η.

12.4.3 Internal electric field in NLO films

In Sect. 12.3 we discussed briefly the influence of charges on the SHG or acoustoelectric signals. However, little attention (with some exceptions, see e.g. [42]) has been paid to understand effects related to charge transport and storage as well as non-uniform electric field distributions in NLO polymers, although these phenomena are relevant for both, preparation and operation of NLO polymer devices. From special importance is the knowledge of the internal electric field distribution from an externally applied voltage for poling [43, 44] or adjustment of retardation in modulators in Mach–Zehnder interferometer configuration [45]. Waveguide modulators consist usually of three different polymer layers, where the active layer (the NLO polymer) is embedded between two NLO inactive cladding layers. Since there is no method to measure the field distribution directly, one has to estimate it from its effect on other phenomena. To determine the electric field E_0 within the active layer one may measure NLO properties but their field dependence may be unclear because a mixture of $\chi^{(2)}$ and $\chi^{(3)}$ effects is observed. An effect that is directly proportional to the field in the NLO active layer is thus very helpful for the investigation and understanding of the processes in polymeric sandwich structures under electric field. In the following we will show that electroabsorption is especially suitable for this task and present measurements that demonstrate the behavior of a nonuniform field distribution in a double-layer polymer film.

Above we discussed electroabsorption spectroscopy in terms of the linear Stark effect (observed at the frequency f) of the modulation field E_f and the quadratic Stark effect, which can be measured at $2f$. In the presence of a d.c. electric field E_0 (from an externally applied d.c. voltage or as result of internal polarization) the quadratic effect will however also contribute to the signal at f. It will be referred to as *quasilinear Stark effect* and is described by

$$\Delta A_{\text{eff}}^{\text{ql}}(f) = 2E_{\text{eff}}^2 E_0 \left[\frac{\Delta\alpha}{2hc} \mathcal{A}'(\tilde{\nu}) + \frac{(\Delta\mu)^2}{10h^2c^2} \mathcal{A}''(\tilde{\nu}) \right] , \tag{12.27}$$

i.e. it has the same wave number dependency as the quadratic effect (12.22). If the sample is polar the electroabsorption spectrum measured at f is the sum of the linear and the quasilinear effects. Figure 12.16 shows as an example the quasilinear and the linear electroabsorption spectrum of the NLO chromophore DMANA (Fig. 12.1) in polycarbonate [38]. Note two important points in the spectra: At wave number $\tilde{\nu}_A$ the quasilinear effect is zero and only the linear effect contributes to the signal, whereas at $\tilde{\nu}_B$ only the quasilinear effect will be measured. Since the latter is proportional to the electric field strength E_0, one may determine the magnitude and the temporal evolution of the internal field E_0 by measuring the Stark signal at $\tilde{\nu}_B$ [46, 47].

To demonstrate the usefulness of the method we performed experiments on double-layer sandwich structures (one active and one inactive layer,

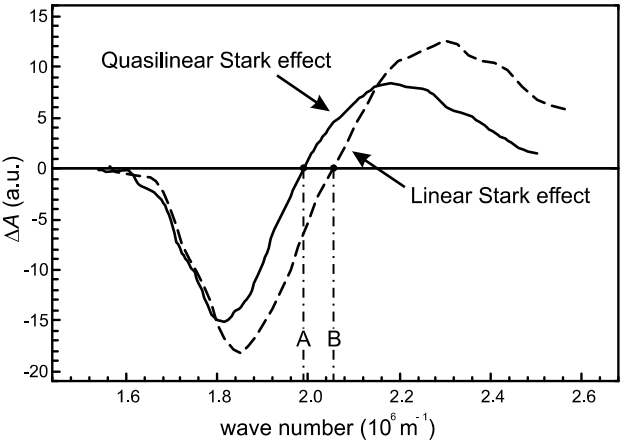

Fig. 12.16. Quasilinear and linear electroabsorption spectrum of the chromophore DMANA in polycarbonate. $\tilde{\nu}_A$ corresponds to $\lambda = 501$ nm, $\tilde{\nu}_B$ to 488 nm

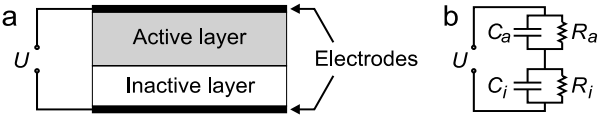

Fig. 12.17. Double polymer layer sandwich structure and simple equivalent circuit

Fig. 12.17a). The active layer consisted of 4 μm polycarbonate bisphenol-A containing 2 weight-% of the NLO chromophore DMANA, for the 8.5 μm thick inactive layer the polyimide PI 2566 was used. Figure 12.18 shows the evolution of the electroabsorption response measured with the modulation frequency f at 488 nm ($\widehat{=}\,\tilde{\nu}_B$), where the linear effect is zero [38]. During the first 500 seconds no d.c. voltage was applied to the sample and the response is zero within error range. At $t = 0$ s the d.c. voltage was switched on and we observed an immediate response followed by a slower increase of the signal magnitude. A fast signal jump (in opposite direction) was also observed when the d.c. voltage was switched off at $t = 1000$ s. The signal returns however not to zero but relaxes slowly with approximately the same time constant of $\tau \approx 430$ s as observed at the process between $t = 0$ s and 1000 s.

The equivalent circuit shown in Fig. 12.17b is the simplest model to describe the observed behavior. It considers that the layers have in general different resistance and capacitance, depending on the conductivity, dielectric constant and thickness of the respective layer. Immediately after a d.c. voltage U is applied to the electrodes of the sandwich structure at $t = 0$ the voltage U_a^0 across the active layer is determined by the capacitances of the layers, i.e. $U_a^0 = UC_a/(C_a + C_i)$. Then the conductivity of the layers allow charges to accumulate at the interface between active and cladding layer until the voltage U_a^∞ across the active layer for $t \to \infty$ is determined

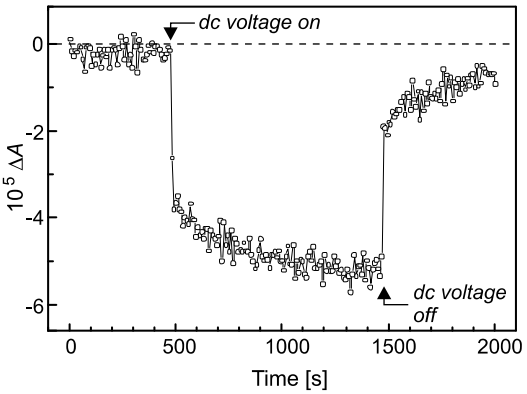

Fig. 12.18. Quasilinear Stark effect measured on a two-layer polymer sample

by the resistances, i.e. $U_a^\infty = UR_a/(R_a + R_i)$. According to the equivalent circuit the transition between U_a^0 and U_a^∞ follows an exponential behavior $U_a(t) = U_a^\infty - (U_a^0 - U_a^\infty)\exp(-t/\tau)$ with $\tau = (C_a + C_i)/(R_a^{-1} + R_i^{-1})$. Considering the dielectric constants of the polymers, thickness of the layers, the measured capacitance and resistance of the sample we find that the measured time constant ($\tau \approx 430$ s) is in accordance with the two-layer equivalent circuit.

Comparable measurements on single-layer films reveal that an internal electric field may also be induced by charging effects on the polymer-electrode interface [47]. Such effects are important for the understanding of the properties of other sandwich structures, esp. organic light emitting diodes and solar cells. Electroabsorption spectroscopy has recently been used to determine the internal electric field in both structures [48, 49].

12.5 Summary

We presented investigations on relaxation phenomena in nonlinear optical polymers with focus on the stability of polar order after poling and the application of electroabsorption spectroscopy for relaxation measurements. The decay of the second order nonlinear optical susceptibility $\chi^{(2)}$ in the glassy state of the polymers was measured by SHG and compared with piezoelectric measurements. The relaxation behavior for both cases was similar and could be described by an Arrhenius-type temperature dependence of the mean relaxation time. This result can be understood in frames of Scherer's extension of the Adams–Gibbs–DiMarzio theory for the glassy state.

We demonstrated that the electroabsorption spectra of NLO chromophores in polymers depend on the the modulation frequency f used in the electroabsorption spectrometer if f is in the range of the chromophores' orientational relaxation frequency. The relaxation time constant can thus be obtained by

analyzing the spectra for a number of different suitable f values. This method allows one to measure chromophore relaxation abovse or in the glass transition region optically (i.e. in absorption) and is hence only sensitive to the absorbing chromophores. It can be considered as a valuable supplement to other techniques (e.g. dielectric spectroscopy) and can be compared with chi-electric relaxation measurements.

We also showed that anisotropic field distributions – especially in multilayer polymer films – and their evolution can be studied by the Stark effect. For the appropriate wavelength the Stark effect is directly proportional to the internal electric field in the polymer layer that contains the NLO chromophores. It can thus be used to determine the response of the internal field to changes of the externally applied voltage. This is of specific importance for optimized poling, in polymeric light-emitting diodes and solar cells, where polarization effects at layer interfaces strongly influence the device performance.

Acknowledgment. Several co-workers of the authors contributed due to their experimental work: S. Großmann investigated double-layer polymer films, E. Jakob performed dielectric spectroscopy measurements and S. Saal developed the variable-modulation-frequency electroabsorption spectroscopy experiments. Valuable discussions with S.V. Yablonskii and L.M. Blinov are gratefully acknowledged. Part of the work was supported by the Volkswagen-Stiftung.

References

1. D. Chen, H.R. Fetterman, A. Chen, W.H. Steier, L.R. Dalton, W. Wang, Y. Shi: Appl. Phys. Lett. **70**, 3335 (1997)
2. Y. Shi, W. Lin, D.J. Olson, J.H. Bechtel, H. Zhang, W.H. Steier, C. Zhang: Science **288**, 119 (2000)
3. G.R. Meredith, J.G. VanDusen, D.J. Williams: Macromolecules **15**, 1385 (1982)
4. J. Zyss, J.L. Oudar: Phys. Rev. A **26**, 2028 (1982)
5. K.D. Singer, M.G. Kuzyk, J.E. Sohn: J. Opt. Soc. Am. B **4**, 968 (1987)
6. A.F. Garito, C.C. Teng, K.Y. Wong, O. Zammani'Khamiri: Mol. Cryst. Liq. Cryst. **106**, 219 (1984)
7. D.A. Kleinman: Phys. Rev. **126**, 1977 (1962)
8. K.D. Singer, J.E. Sohn, S.J. Lalama: Appl. Phys. Lett. **49**, 248 (1986)
9. K.D. Singer, A.F. Garito: J. Chem. Phys. **75**, 3572 (1981)
10. W.F. Brown: In: *Dielektrika, Handbuch der Physik, Vol. XVII*, ed. by S. Flügge (Springer, Berlin 1956), pp. 1–154
11. C. Poga, T.M. Brown, M.G. Kuzyk, C.W. Dirk: J. Opt. Soc. Am. B **12**, 531 (1995)
12. M.I. Barnik, L.M. Blinov, T. Weyrauch, S.P. Palto, A.A. Tevosov, W. Haase: 'Stark Spectroscopy as a Tool for the Characterization of Poled Polymers for Nonlinear Optics'. In: *Polymers for Second-Order Nonlinear Optics*, ACS Symposium Series, Vol. 601, ed. by G.A. Lindsay, K.D. Singer (American Chemical Society, Washington, DC 1995), pp. 288–303

13. M.G. Broadhurst, G.T. Davis: In *Electrets*, Topics in Applied Physics, Vol. 33, 2nd edition, ed. by G.M. Sessler (Springer, Berlin 1987), pp. 285–319
14. F.I. Mopsik, M.G. Broadhurst: J. Appl. Phys. **46**, 4204 (1975)
15. T. Weyrauch: 'Untersuchungen zur Polung und Relaxation nichtlinearer optischer Polymere.' PhD Thesis, Technische Hochschule Darmstadt, Darmstadt (1997)
16. P.D. Maker, R.W. Terhune, M. Nisenoff, C.M. Savage: Phys. Rev. Lett. **8**, 21 (1962)
17. S.V. Yablonskii, E.I. Kats, M.V. Kozlovskii, T. Weyrauch, E.A. Soto Bustamante, D.B. Subachius, W. Haase: Mol. Mater. **3**, 311 (1994)
18. C.P.J.M. van der Vorst, R.A.P. van Gassel: Macromol. Symp. **90**, 47 (1995)
19. A. Dhinojwala, G.K. Wong, J.M. Torkelson: Macromolecules **26**, 5943 (1993)
20. E. Jakob, T. Weyrauch, T. Hanemann, W. Haase: 'Relaxation Studies on a Polymethylmethacrylate with a Nitrostilbene Side Chain for Nonlinear Optics'. In: *Organic Materials for Nonlinear Optics III*, ed. by G.J. Ashwell, D. Bloor (Royal Society of Chemistry, Cambridge 1993), pp. 163–169
21. T. Weyrauch, R. Willner, E. Jakob, W. Haase: 'Relaxation of Piezoelectricity and Nonlinear Optical Properties of Poled Polymers'. In: *Nonlinear Optical Properties of Organic Materials VI*, Proc. SPIE 2025, ed. by G.R. Möhlmann (SPIE, Bellingham, WA 1993), pp. 211–220
22. M.L. Williams, R.F. Landel, J.D. Ferry: J. Amer. Chem. Soc. **77**, 3701 (1955)
23. G. Adams, J.H. Gibbs: J. Chem. Phys. **43**, 139 (1965)
24. J.H. Gibbs, E.A. DiMarzio: J. Chem. Phys. **28**, 373 (1958)
25. A.Q. Tool: J. Am. Ceram. Soc. **29**, 240 (1946)
26. G.W. Scherer: J. Am. Ceram. Soc. **67**, 504 (1984)
27. H.-J. Winkelhahn, Th.K. Servay, D. Neher: Ber. Bunsenges. Phys. Chem. **100**, 123 (1996)
28. J.W. Wu: J. Opt. Soc. Am. B **8**, 142 (1991)
29. Ph. Prêtre, P.G. Kaatz, U. Meier, P. Günther, B. Zysset, M. Ahlheim, M. Stähelin, F. Lehr: Polymer Preprints **35**, 136 (1994)
30. R.D. Dureiko, D.E. Schuele, K.D. Singer: J. Opt. Soc. Am. B **15**, 338 (1998)
31. M. Eich, B. Reck, D.Y. Yoon, C.G. Willson, G.C. Bjorklund: J. Appl. Phys. **66**, 3241 (1989)
32. T. Hanemann, C. Noel, W. Haase: Adv. Mater. **7**, 465 (1995)
33. J.D. Bewsher, G.R. Mitchell: Appl. Opt. **36**, 7760 (1997)
34. A. Chen, V. Chuyanov, S. Garner, H. Zhang, W.H. Steier, J. Chen, J. Zhu, F. Wang, M. He, H. Mao, L.R. Dalton: Opt. Lett. **23**, 478 (1998)
35. S. Großmann, T. Weyrauch, W. Haase: J. Opt. Soc. Am. B **15**, 414 (1998)
36. W.N. Herman, J.A. Cline: J. Opt. Soc. Am. B **15**, 351 (1998)
37. L.M. Blinov, S.P. Palto, A.A. Tevosov, M.I. Barnik, T. Weyrauch, W. Haase: Mol. Mater. **5**, 311 (1995)
38. S. Großmann, T. Weyrauch, S. Saal, W. Haase: 'Characterization of NLO Materials for Photonic Application'. In *Anisotropic Organic Materials – Approaches to Polar Order*, ACS Symposium Series, Volume 798, ed. by R. Glaser and P. Kaszynski (American Chemical Society, Washington, DC 2001) pp. 2–15
39. W. Haase, S. Saal, S. Großmann, T. Weyrauch: 'Mobility of Dyes in Polymer Matrix: Frequency-dependent Electroabsoption'. In: *Organic Photonic Materials and Devices*, Proc. SPIE 3623, ed. by B. Kippelen (SPIE, Bellingham, WA 1999), pp. 159–166

40. S. Saal, W. Haase: Chem. Phys. Lett. **278**, 127 (1997)
41. S. Saal: 'Elektroabsorptionsspektroskopie zur Charakterisierung der Rotationsmobilität von Farbstoffmolekülen in polymeren Matrizes'. PhD Thesis, Technische Universität Darmstadt, Darmstadt (1999)
42. R. Blum, M. Sprave, J. Sablotny, M. Eich: J. Opt. Soc. Am. B **15**, 318 (1998)
43. D.G. Girton, W.W. Anderson, J.A. Marley, T.E. Van Eck, S. Ermer: In *Organic Thin Films for Photonics Applications*, OSA Technical Digest Series, Vol. 21, (Optical Society of America, Washington DC 1995), pp. 470–473
44. V. Ricci, G.I. Stegeman, K.P. Chan: J. Opt. Soc. Am. B **17**, 1349 (2000)
45. H. Park, W.-Y. Hwang, J.-J. Kim, Appl. Phys. Lett. **70**, 2796, (1997)
46. S. Großmann, T. Weyrauch, S. Saal, W. Haase: Opt. Mat. **9**, 236 (1998)
47. S. Großmann, T. Weyrauch, W. Haase: Nonlinear Optics **20**, 223 (1999)
48. T.M. Brown, J.S. Kim, R.H. Friend, F. Cacialli, R. Daik, W.J. Feast: Synthetic Metals **111–112**, 285 (2000)
49. P.A. Lane, J. Rostalski, C. Giebeler, S.J. Martin, D.D.C. Bradley, D. Meissner: Solar Energy Materials & Solar Cells **63**, 3 (2000)

13

Relaxation Processes in Two- and Three-Component Metallic Glasses

M. Davidović and P. Tomić

13.1 Introduction

As long as the stability of amorphous structure occurs to be a very important property it is necessary to study the relaxation phenomena, i.e. the process of crystallization as a function of time. One of the methods to obtain the amorphous phase one-way is the rapid quenching (cooling) of the liquid alloy [1]. By combining the amorphous with the metallic structure, a new quality can be achieved when the system contains paramagnetic 3d elements. The content of transition metal component, like Fe, Co and Ni is usually about to 80% while the metalloid components: B, C, Si, P and Al share about 20%. This system is more complex comparing with regular glass. In this study a ferromagnetic amorphous glass – having nearly isotropic properties with small hysteresis loops and high permeability – has been developed.

Thermally activated processes lead to the transformation from a disordered amorphous phase, which is the low temperature phase, into an ordered crystal [2]. By studying the low-temperature relaxations it is possible to determine T_c of the ferromagnetic transition temperature and observe its functional correlation with the relaxation mechanism [3]. In this temperature region the dynamics of the "low free volume" has also been studied. On the other hand, at higher temperatures ($T > T_k$, T_k being crystallization temperature, Fig. 13.1b), the crystallization phenomenon and its parameters, such as the activation energy E_a, have been investigated. It is also possible to evaluate the thermal stability of amorphous metals and the lifetime of the glasses state at different temperatures. This kind of information can be obtained by annealing of metallic glasses [4]. The changes are generally attributed to the microscopic processes, which provide reliable evidence of the structural rearrangement. Investigation of the crystallization phenomena includes then determination of the activation energy of crystallization (E_a). It is also possible to define the coefficient n, which is connected with the mechanism of crystallization responsible for crystallization dynamics as well as the characteristic time of crystallization $\tau(t)$. These parameters, as it is well known, give

information about the stability of amorphous structure. Annealing treatment causes changes in many physical properties, which depend on both temperature and time. An easy way to follow these changes is neutron diffraction through the evaluation of the structure factor $S(Q)$ after several annealing treatments [5], Q is the so-called scattering vector.

The transformations, that correspond to the solid-state reaction, can be described in detail by the JMAK (Johnson–Melh–Avrami–Kolmogorov) kinetic model for non-isothermal conditions [6, 7] as follows:

$$\mathrm{d}\alpha/\mathrm{d}t = A \cdot n(1-\alpha)[-\ln(1-\alpha)]^{n-1/n} \exp(-E_a/RT)) \,, \tag{13.1}$$

where α is the transforming fraction, t – time, T – absolute temperature, R – gas constant, n – kinetic exponent and A – pre-exponential factor. Drawing the quantity $\ln[-\ln(1-\alpha)]$ as a function of 1/T, one gets straight lines with the coefficient $n \cdot E_a$. With a given value of E_a, it is easy to determine the coefficient n. Combining the JMAK model with the so-called Kissinger method [8] it is also possible to determine the activation energies E_a from the equation:

$$\ln(T_m^2/\beta) = E_a/RT + \text{const.} \,, \tag{13.2}$$

where T_m is the temperature which corresponds to the maximum of the reaction, i.e. when $\mathrm{d}(\mathrm{d}\alpha/\mathrm{d}t)\mathrm{d}t = 0$ and β is the linear heating rate equal to $\mathrm{d}\alpha/\mathrm{d}t$. The activation energy E_a and the coefficient n can be simultaneously determined. Using the method suggested by Kissinger, where the experimental results are plotted as $\ln(T_m^2/\beta)$ against $1/T_m$, straight lines with the coefficient E_a/R are obtained. These lines are called Kissinger's straight lines for the amorphous alloy studied and they characterize the crystallization kinetics. From the JMAK model represented by (13.2), and applying Doyl's approximation [9], one can obtain n and E_a:

$$\ln[\ln(1/1-\alpha)] = n \cdot \ln(AE_a/\beta R) + C_1 + C_2 \,, \tag{13.3}$$

where C_1 and C_2 are constants proportional to n and $n \cdot E_a$ [10], respectively. With a given value of E_a it is easy to determine the coefficient n, the nature of which is rather complex as it depends on the crystal growth morphology [11]. In accordance with other authors [7, 12], for different nucleation mechanisms and crystal grain growth it is possible to interpret the crystallization as a sum of two sub-processes:

$$n = a + bp \,, \tag{13.4}$$

where a is the parameter responsible for the nucleation process and its value varies from 0 (nucleons annealed) to 1 (constant speed of nucleation). The b coefficient with the values 1, 2 or 3 represents the dimensionality of the crystal grain grown. The p coefficient describes the mechanism of the crystal

grain growth: if $p = 0.5$ then we have a diffusion controlled parabolic process, and $p = 1$ means interfacial controlled growth, where growth is linear in time.

The crystallization rate can generally be described in terms of two processes: nucleation and growth [11, 12]. The structure relaxation is classified into two types of short range ordering in a metal-metalloid system. One of the processes is called topological short range ordering (TSRO) and corresponds to an irreversible atomic rearrangement such as the annihilation of quenched-in free volume. Another type is connected with the reversible change in the physical properties with annealing temperature. It is also known as the compositional, i.e. chemical short range ordering (CSRO), which is formed through chemical interaction amid constituent atoms.

Different amorphous alloys as Al-Y-Ni [13], Fe-Si-B [14], and Cu-Zr [15], were prepared using a self-made apparatus [16]. The Co-B ribbon tape was obtained from NIST [17] (USA). The ribbon was of uniform geometry with a thickness varying from 20 to 25 μm and width between 5 and 6 mm. It is worth noting that no sharp Bragg's peaks were observed in X-ray diffractograms, obtained by an APD 1700 automated diffractometer, substantiating amorphous structure of the sample. Very similar results were obtained using neutron diffraction [17].

Crystallization rate can generally be described in terms of nucleation and growth [6].

13.2 Description of the relaxation phenomena

There are two classes of physical properties of amorphous materials: one class is connected with the transition from a melt to an amorphous structure and the other is related to the crystallization. The first class incorporates the change in the specific heat $C_p(T)$, shown in Fig. 13.1a, which takes place at the glass forming temperature T_g, also shown in Fig. 13.1b. The latter is usually determined by the inflection point of the specific heat curve and T_k is an ideal glass transition temperature [18].

Between the T_m and T_g temperatures the liquid is a thermodynamically supercooled state [19], varying from one composition to the other. It is generally known that the amorphous alloy with a wide supercooled liquid region or a high reduced glass transition temperature T_g/T_m, where T_m is a melting temperature, has an excellent glass forming ability. In many cases the temperature behavior of the specific heat $C_p(T)$ near T_g exhibits discontinuities (Fig. 13.1b).

In scope of this work two types of investigations on a cobalt-boron system have been undertaken to better understand the crystallization kinetics of metallic glasses. First, the neutron diffraction studies of the eighty-twenty metal–metalloid composition were performed by the neutron scattering experiments at the ISIS spallation neutron source at the Rutherford Appleton Laboratory to follow crystallization kinetics by applying JMAK kinetic

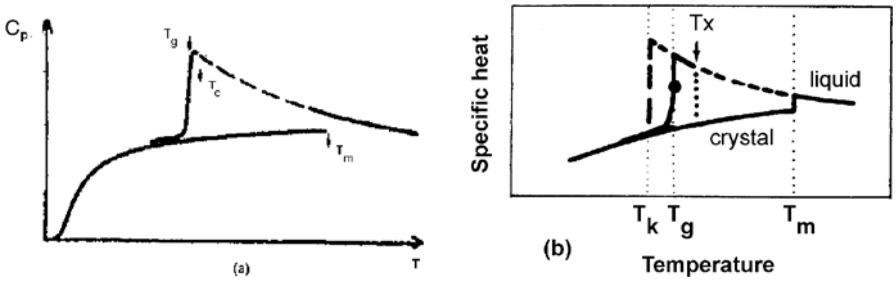

Fig. 13.1. (a) Specific heat C_p in the vicinity of the T_g glass forming temperature, **(b)** thermodynamic melting temperature T_m and a wide supercooled liquid region $\mathrm{d}T_x = T_x - T_g$ shown on the same figure

relation. The samples were annealed and the evolution time of the diffraction pattern measured with an aim to calculate the Avrami coefficient n and the scaling parameter $\tau(t)$. By simultaneously applying the JMAK relation and the results of DSC measurements, the values of activation energy E_a, and of the coefficient n, responsible for the nucleation process crystallization, and kinetics of the spin glasses, were determined. Using the Vogel–Fulcher–Tammann relation, the scaling parameter $\tau(t)$ was extracted, too. Comparing the results obtained with those reported by other authors a good agreement was found. The results suggest that the mechanism of crystallization kinetics [17] of the amorphous alloy studied is diffusion controlled.

Stability of the amorphous structure is a very important property indispensable for understanding many different successful applications of metal glasses. In order to know the stability of an amorphous structure, it is necessary to study the relaxation phenomena completely, i.e. the time development of the crystallization process. Namely, thermally activated processes lead to the transformation of a disordered amorphous state into an ordered crystal structure [2]. Investigation of the crystallization phenomena consists in determination of the activation energy of crystallization (E_a) responsible for crystallization dynamics. The second parameter to be evaluated is the coefficient n, which depends on the mechanism of crystallization responsible for crystallization dynamics. Last but not least, the characteristic time of crystallization $\tau(t)$ is also of great interest. These parameters, as it is well known, give information on the stability of amorphous structure.

This kind of information can be also obtained by annealing of the metallic glass [5]. Such a treatment causes changes of many physical properties, which depend on both temperature and time. These changes are generally attributed to microscopic processes referred to as relaxation phenomena. Reliable direct evidence of the structure rearrangement can also be obtained by neutron

diffraction study through the evaluation of the structure factor $S(Q)$ after several annealing treatments [5].

Using the combination of the Arrhenius and Vogel–Fulcher–Tammann equation, which are systematically analyzed in [2], the relaxation time, $\tau(t)$, can be described as follows:

$$\tau^{-1} = \tau_0^{-1} \exp\left[E_a / k_B \left(T - T_g\right)\right] \ , \tag{13.5}$$

where k_B – the Boltzmann constant and T_g – the glass transition temperature. For a given activation energy E_a, the characteristic time of crystallization τ_0 in isothermal conditions can be determined, and the obtained values compared to those of dynamic relaxation conditions in metallic glasses.

13.3 Experimental

In order to introduce the relaxation phenomena for two and three component alloys, the thermal procedure was extensively used to study the kinetics of chemical reactions and crystallization of glasses. As already mentioned, the mechanism of crystallization is extremely important for the determination of the activation energy of crystal growth from the DSC data.

One of the aims of the present study is to apply DSC, i.e. the kinetic of crystallization and phenomena related to them. This procedure enables us to separate the activation energy of crystallization originated from the nucleation and growth of different two- and three-component metallic glasses, respectively.

Mainly amorphous alloys were studied before and after thermal annealing [19]. The results for two- and three-component alloys are shown in Table 13.1. The values of T_x temperatures, shown in the last column depend on the cooling rate, which is usually of the order of 10 K/min.

Table 13.1. Values of activation energy and n parameter for various two- and three-components amorphous alloys

Components	E_a**(kJ/mol)**	n	T_x**[K]**	**Ref**
$Al_{87}Y_8Ni_5$	182	–	726	13
$Co_{80}B_{20}$	202	2.48	863	17
$Fe_{40}Ni_{40}B_{20}$	316	2.1	838	20
$Fe_{80}B_{10}Si_{10}$	350	2.3	764	14
$Cu_{60}Zr_{40}$	530	–	823	16
Ni – Zr	296	–	779	20

The numerical factor n dependent on crystallization mechanisms can have different values:

If $n = 2 \Rightarrow$ 1 Instant nucleation in one-dimensional medium
2 Instant nucleation in two-dimensional medium
3 Instant nucleation in three-dimensional medium,

depending on crystallization mechanism.

The Kissinger's straight lines [21] for two observed amorphous alloys are shown in Fig. 13.2.

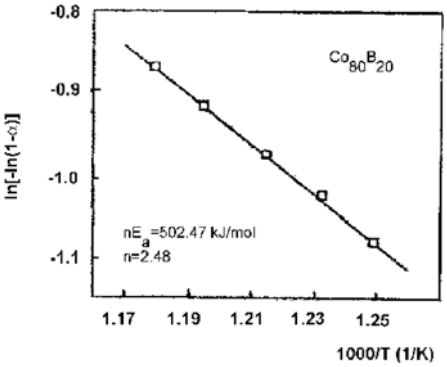

a

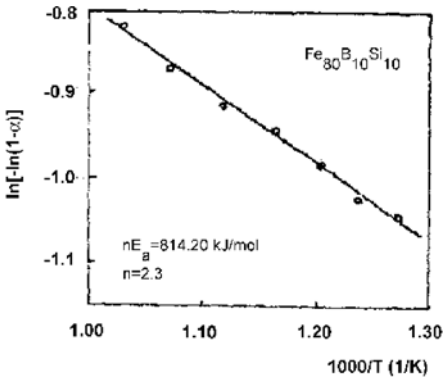

b

Fig. 13.2. Kissinger's diagrams for different two- and three-component amorphous alloys

13.4 Results and discussion

The $Fe_{67}Co_{18}Si_1B_{14}$ metallic glass samples were prepared [23] by rapid solidification of the melt on a single-roll spinning copper wheel in an argon atmosphere. They were in the form of a continuous ribbon (2.5 cm wide and 40 μm thick).

The crystallization kinetics of glassy alloys was studied using a Perkin Elmer DSC-800 system. First, the samples were heated at various heating rates to study the non-isothermal kinetics, and then, isothermal annealing was performed at a chosen temperature for various time intervals to separate the nucleation from the growth.

The heat flow vs. temperature curve, presented in Fig. 13.3 for one of the samples, shows two exothermic processes.

The low temperature process near 380 °C exhibits the appearance of crystallization of the α-Fe structure (BCC) located in the amorphous matrix. When the temperature is raised to 480 °C, the α-phase increases and new phases Fe_3B and Co_2B are being formed while the amorphous phase almost disappears. Our results are consistent with the investigations of structural changes in the process of crystallization of $Fe_{60}Co_{18}Si_9B_{13}$ glass using of positron life time measurement [23]. The experimental data on crystallization have been interpreted using modified Kissinger's equation [8, 22] for the determination of activation energy and fractional crystallization method [14, 24] to ascertain the mechanism.

From the equation discussed in [21] for non-isothermal crystallization, the activation energy of crystallization E_c can be evaluated as:

$$\ln[-\ln(1-x)] = -n\ln(\alpha) - 1.052mE_c/RT + \text{const}\,, \tag{13.6}$$

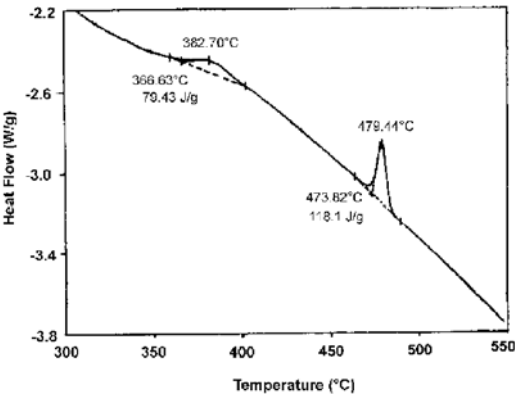

Fig. 13.3. Crystallization thermogram of the $Fe_{60}Co_{18}Si_9B_{13}$ metallic glass obtained at a heating rate of 1 K/min

where x is the fractional crystallization at any temperature T raised at a uniform rate.

For the evaluation of the order parameter n, $\ln[-\ln(1-x)]$ was plotted as a function of $\ln(\alpha)$, see (Fig. 13.4). The average value of n derived from the plots at various temperatures was found to be 3.81 for the first and 5.44 for the second crystallization peak. Normally, n should not exceed 4, i.e. the value for the three-dimensional bulk nucleation. In the present case, it is assumed that the surface-induced abnormal grain growth expected for the Fe-based alloys [25] is responsible for the high value of n for this multicomponent glass in the second stage crystallization. Similar, high values of n (i.e., $n = 6$) were reported for a ternary halogenide glass [26].

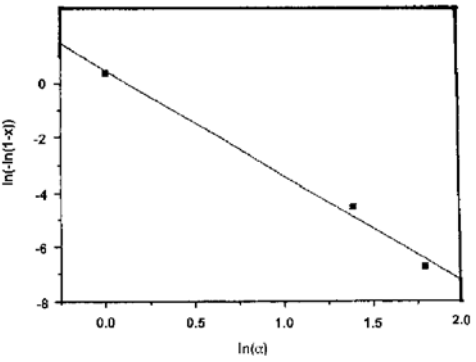

Fig. 13.4. $\ln[-\ln(1-x)]$ versus $\ln(x)$ for the first crystallization peak presented in Fig. 13.3

Since no particular heat treatment was applied to nucleate the samples before thermal analysis, the dimensionality of growth m is taken to be equal to $(n-1)$. In the present case, the evaluated value of n is not an integer. This means that the crystallization occurs with fractal dimensionality and the dimensionality of growth $m = (n-1) = 2.809$ for the first crystallization peak and $m = 4.44$ for the second peak. Fractal dimensionality of the order of 4 in the case of surface scattering from particles of colloidal aggregate of silica using X-rays has already been reported [26, 27]. Recently, the growth dynamics of fractal Ge clusters in Au layer has been observed [28].

For the evaluation of the activation energy of crystallization E_c, the modified Kissinger equation [22] is used,

$$\ln(\alpha^n/T_p^2) = -mE_c/RT_p + \ln K \ , \tag{13.7}$$

where the shift in peak crystallization temperature T_p with heating rate α is used to determine E_c and m; the latter being the dimensionality of growth. Using the value of the order parameter $n = 3.81$ and the dimensionality of growth $m = 2.81$ for the first crystallization peak event and the corresponding values of $n = 5.44$ and $m = 4.44$ for the second peak of crystallization, E_c is computed from the slope of $\ln(\alpha^n/T_p^2)$ versus $(1/T_p)$. The plots are

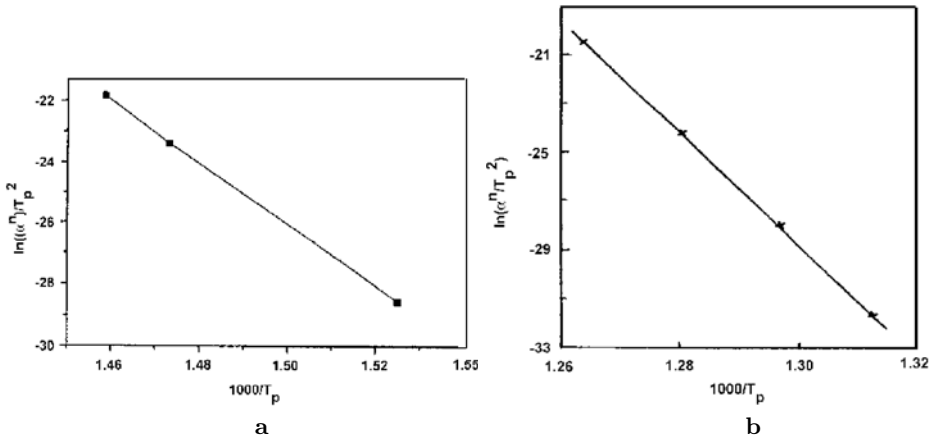

a **b**

Fig. 13.5. $\ln(\alpha^n/T_p^2)$ versus $(1/T_p)$ (**a**) for the first and the (**b**) for the second crystallization peak

shown in Figs. 13.5a and 13.5b, respectively, for the first and the second crystallization peak shown in Fig. 13.3. The corresponding values of E_c derived from the first and the second peak come out to be 299.15 and 440 kJ/mol, respectively. The values reported earlier [24] for the two-step crystallization of a glass, having very close composition ($Fe_{65}Co_{18}B_{16}Si_1$), are 260.06 and 394.9 kJ/mol for the first and the second step, respectively. The closeness of the activation energy values shows the singularity of recrystallization of the two systems. The higher values of E_c for the second step show that the first stage crystallization is easily reached compared to the second one.

An alternative approach was also applied to calculate $(m/n)E_c$ from the slope of the $\ln\alpha$ versus $1/T_p$ plot. Figure 13.6 shows $\ln\alpha$ versus $1/T_p$ for the second peak.

The value of E_c for the second stage crystallization evaluated knowing m and n is 433.3 kJ/mol, which is quite close to the value derived from the modified Kissinger equation (440.4 kJ/mol). From the slope of the $\ln[-\ln(1-x)]$ versus $(1/T_p)$ curve (Fig. 13.7a,b), mE_c was calculated using (13.1) and mE_c was found to be dependent on the heating rate. For the first stage using the E_c value obtained using (13.2), various m values corresponding to different heating rates were derived. For the first stage, the m values at heating rates of 1 K/min and 2 K/min are 2.33 and 2.22, respectively. The decreasing trend of m with increasing heating rate for the first peak shows decreasing dimensionality of nucleation with increasing heating rate. It means that at lower heating rate the particles grow with higher dimensionality. The m values for the second peak are listed in Table 13.2. Initially the m values decrease with increasing rate, but this trend changes and increasing m from 4.22 to 5.31 shows an enhanced sur-

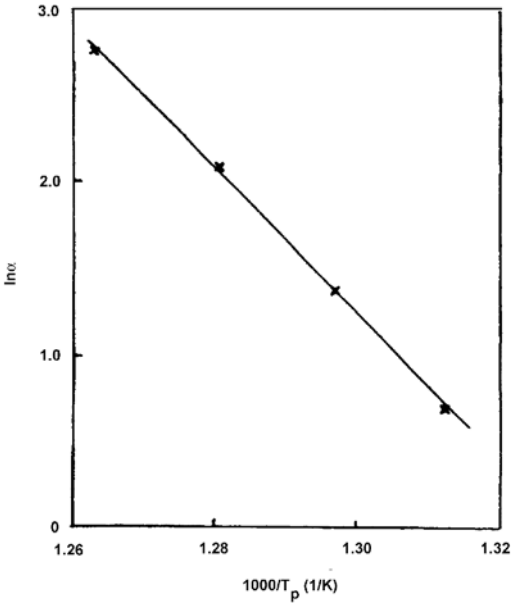

Fig. 13.6. $\ln \alpha$ as a function of $(1/T_p)$ for the second peak presented in Fig. 13.3

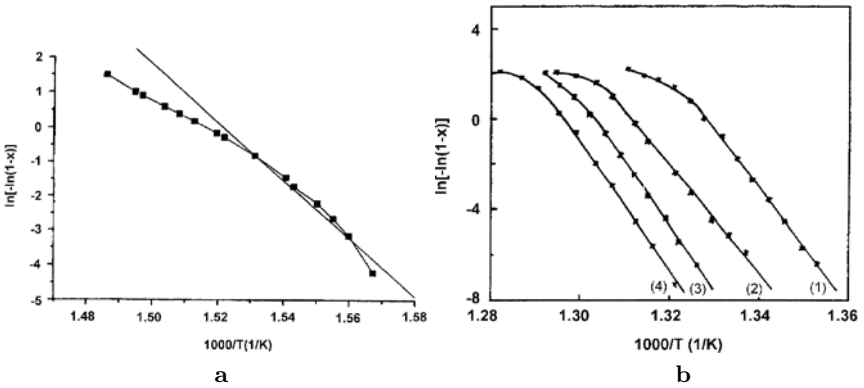

Fig. 13.7. $\ln(\alpha^n/T_p^2)$ versus $(1/T_p)$ (**a**) $\ln[-\ln(1-x)]$ for the first peak at various temperatures and typical heating rate of 1 K/min, (**b**) $\ln[-\ln(1-x)]$ for the second peak at various temperatures and heating rates in degree/min indicated in parentheses for each curve

face-induced abnormal grain growth at higher heating rates. Such a gradual increase in surface crystallization with increasing heating rate has already been reported [29].

In order to obtain the activation energy of growth (E_g) from the second crystallization peak, the samples were first annealed at 470 °C (i.e. at the

Table 13.2. Heating rate dependence of dimensionality

From $\ln[-\ln(1-x)]$ versus $1/T$ curve

Heating rate (K/min)	$\boldsymbol{mE_c}$ **(kJ/mol)**	$\boldsymbol{m}$
1	2144.5	4.63
2	1955.3	4.22
3	2292.4	4.95
4	2462.2	5.31

temperature just before the major crystallization process) for the following time intervals: 10, 15, 20, and 25 min. It was found that the peak temperature (T_p) decreases with the pre-annealed time.

The value of activation energy, calculated by the modified Kissinger method, for the samples annealed for various times was plotted against pre-annealed time (Fig. 13.8). As seen it tends to decrease with pre-annealed time reaching a minimum value denoted as E_g, which comes out to be 310 kJ/mol. The activation energy of nucleation was then deduced from the proposed expression [30, 31]:

$$E_c = \frac{aE_n - rbE_g}{a + rb} \,, \tag{13.8}$$

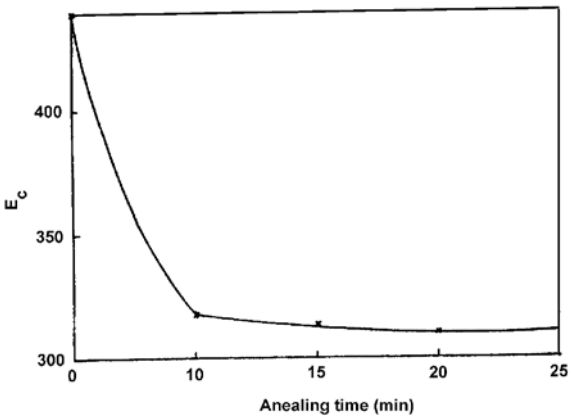

Fig. 13.8. E_c versus annealing time for the second crystallization peak seen in Fig. 13.3

where $r = 1$ for linear growth, $r = 1/2$ for parabolic growth, $b = 1, 2, 3$ for one-, two-, three-dimensional growth, respectively, $a = 0$ for nucleation and $a = 1$ for constant crystallization. For the system studied the following parameters: $r = 1/2$, $a = 1$ and $b = 4.44$ (fractal dimensionality) were taken. From these values, experimentally determined E_c and E_g values and using (13.3), the value of E_n was finally found to be 729.88 kJ/mol.

13.5 Summary and conclusion

The relaxation processes in two- and three-component amorphous metallic alloys were studied in the low temperature relaxation region, i.e. $T < T_x$ (T_x being the crystallization temperature), as well as in the region of crystallization.

The samples have been prepared using a laboratory made "melt spinning" device. The samples have been characterized by XRD, DSC, dilatation measurements as well as measurements of the changes of the electrical resistivity.

In the low temperature region we have explored the dynamics of annealing of "excess free volume" effect, which causes the change in topological-TSRO and chemical-ordering CSRO of examined metallic alloys, as well as the corresponding activation energy of relaxation for "ideal glass". In addition, we have studied the influence of doping by hydrogen on the relaxation processes. This kind of metastable structure results from the formation of corresponding hybrid bonds.

By isothermal and dynamic treatment and by studying the crystallization phenomena, the corresponding activation energy and the exponent n were determined from the JMAK kinetic equation. The value of n gives some information about controlled processes, going on during the crystal growth with one or three dimensions. The characteristic time of crystallization τ has been computed.

The crystallization parameters of various glasses were calculated by the Kissinger equation. The non-isothermal kinetics using the method [14, 22] provides consistent crystallization curves and important information regarding the mechanisms of nucleation and growth. The mathematical approaches for the description of the relaxation processes used together are correct. The present Fe-based multicomponent amorphous alloy seems to nucleate with fractal dimensionality owing to an abnormal grain growth expected in this system.

References

1. A.E. Oven: *Glass transition, Amorphous Solid and the Liquid State*, ed. by N. March, R. Street, M. Tosi (Plenum Press, London 1985)
2. S.R. Elliott: *Physics of Amorphous Materials*, Chap. 2 (Longman Inc. New York 1983)
3. C.A. Angell, K.L. Ngai, G.B. McKenna, P.F. MvMillan, S.W. Martin: Appl. Phys. Reviews, J. Appl. Phys. **88**(6), 3113 (2000)
4. Y. Waseda, T. Egami: J. Mater. Sci. **14**, 1249 (1979)
5. S. Katano, Y. Morii, M. Iizumi, H.R. Child, R.N. Nicklow: J. Phys. Soc. Japan **56**, 96 (1987)
6. C. Rawers, R.A.M. Cune, A. Adams: J. Mater. Sci. Lett. **7**, 958 (1988)
7. J. Sestak: Thermo. Phys. Prop. of Solid. Thermal Anal., Vol. XII (North Holland, Amsterdam 1984)
8. H.E. Kissinger: Anal. Chem. **29**, 1702 (1957)
9. C.D. Doyle: J. Appl. Polym. Sci. **6**, 639 (1962)
10. J.M. Criado, A. Ortega: Acta Metall. **35**, 1715 (1987)
11. J.W. Christian: *The Theory of Transformations in Metals and Alloys*, 2nd edn. (Pergamon Press, New York 1975)
12. H.A. Davies: Phys. Chem. Glasses **17**, 159 (1976)
13. P. Tomić, M. Davidović: Proceedings for Natural Sciences, No. 85, (Matica Srpska, Novi Sad 1993) pp. 377–381
14. P. Tomić, M. Davidović: J. Non-Crystal. Solids **204**, 32 (1996)
15. P. Tomić, M. Davidović, B. Arsenović: Submitted for publication (2003)
16. P. Tomić, M. Davidović: Rapid Quenched and Metastable Materials RQ9, Supplement, 1–4 (Elsevier, Bratislava 1996)
17. M. Davidović, J. Rhyne, S.W. Howells: *Structure Relaxation in Amorphous Materials*, A58.ISIS. (1988)
18. P.R. Okamoto, N.Q. Lam, L.E. Rehn: Solid State Phys. **52**, 1 (1999)
19. P. Tomić, M. Davidović, A. Kuršumović, M. Jeremić: Contemporary studies in Advanced Materials and Processes, Trans. Tech. Publications (2002) p. 65
20. K. Matusita, S. Sakka, Y. Matsui: J. Mater. Sci. **10**, 961 (1975)
21. M. Davidović, P. Tomić: *Relaxation of Amorphous Metallic Alloys, Solid State Phenomena*, Vols. 61–62 (Scitec Publications, Switzerland 1998) pp. 67–74
22. J. Filipecki, E. Jakuboczyk, Z. Mardecki (eds.) *Nanostructural and non-crystalline materials* (World Scientific, Singapore 1995) p. 369
23. Z. Vejnović, M. Davidović, P. Tomić: *Proceedings of the Symposium on Condensed Matter Physics* (Arandjelovc, Yugoslavia, October 3–5 2001) SFIW.XV (A1) 129, Belgrad (2002)
24. K. Matusita, S. Sakka: J. Non-Crystal. Solids **38–39**, 741 (1980)
25. K. Matusita, S. Sakka: Phys. Chem. Glasses **20**, 81 (1979)
26. R.W. Cahn (ed.): *Physical metallurgy* (North Holland, Amsterdam 1970)
27. S. Mahaderm, A. Giridhar, A.H. Sigoh: J. Non-Crystal. Solids **88**, 11 (1986)
28. D.W. Shoefen, K.D. Keefen: Phys. Rev. Lett. **53**, 1383 (1984)
29. M.D. Baro, S. Seninoch, J.A. Diego, M.T. Clovagera-Mero, N. Clovagera: Mater. Sci. Eng. **A133**, 807 (1991)
30. H. Vogel, M. Van Haimendahl: Mater. Sci. Energy **57**, 171 (1983)
31. J.J. Lu, K. Wang: J. Mater. Sci. **23**, 3001 (1988)

Index

α-relaxation 244, 246, 253
Abrikosov lattice 642
absorbance components 451, 452
absorbance profile 446
AC magnetic susceptibility 90, 101–110, 551, 554, 570, 574–577, 579–582, 584, 657–661
AC susceptibility for superconductor 657–663
AC susceptometer 92–95, 551, 573
achiral interactions 271
acoustoelectric measurements 675
activation energy 75, 79, 81, 173, 179, 183, 200, 250, 251, 694, 696, 697, 702, 703
activation enthalpy 75, 79, 81, 183, 200
activation volume 75, 79, 81, 183, 199, 200, 638, 661
Adam–Gibbs model 368
Adam–Gibbs–Scherer model 680, 681
Adam–Gibbs–DiMarzio model 679, 680, 689
adiabatic potential 611, 621
adiabatic susceptibility 5, 93–95, 97, 98
alcohol-water systems 42
alignment layer 28, 31, 305–307
amorphous metals 693
amplitudon mode 324–326, 357, 498, *see* soft mode
anisotropic fluids 168
annealing 696
anticlinic order 267–269, 332–358
antiferroelectric liquid crystals 15, 21, 257–272, 294, 328–330, 332–358, 445–447, 454–466, 468–507
antiferroelectric ordering 207, 261, 262, 269
antiferroelectric polarization 262
antiferroelectric switching 412
antiferromagnetic correlation 147, 148
antiferromagnetic coupling 531, 549
antiferromagnetic ordering 148, 155
antiferromagnetic structure 148
antiferromagnets 99
Argand diagram 5, 23, 93–94, 96, 104, 106, 108, 166
Arrhenius behavior 99, 481, 498, 500, 507, 679, 681
Arrhenius equation 79, 99, 173, 250, 366, 637
Arrhenius plot 178, 542
attenuated total reflection method (ATR) 450
attractive interaction 75
Avrami coefficient 696
axial pair distribution function 225

β-relaxation 244–246
B_2 phase 412, 414, 415
B_3 phase 413
B_4 phase 414, 415
B_6 phase 416
B_7 phase 417
B_8 phase 418
B_X phase 418

banana/bent shaped molecules 208, 400–420
bellows cell 73
bent shaped/banana molecules 208, 400–420
bias voltage 475, 495–497
biasing parameters of 12OBBB8 454, 456
biaxial liquid crystalline phases 168
biaxial SmA phase 412
bilayer structure 262, 263
birefringence 349, 429, 430
bistability 275, 280, 282, 283, 291, 294
blocking anomaly 579, 582, 584
blocking temperature for superparamagnets 108, 581, 582
Boltzmann distribution 51, 558, 670
bond orientational order 320, 321
Brillouin function 556
bulk mode 289

Casimir–du Pré model 93, 95
cavity field 164
CCN-55 26
$CeAl_3$ 114, 128
$CeCu_2Ge_2$ 120, 123
$CeCu_2Si_2$ 114, 119, 121, 123
$CeNi_2Ge_2$ 120, 125
$CeNi_2Si_2$ 119, 122
CeNiSn 127
$CeOs_2$ 119
$CeOs_3$ 114
$CePd_3$ 114, 119
$CeRu_2Si_2$ 120, 125
chemical affinity 61
chemical relaxation 6, 63, 66–70
chemical reaction 6, 60, 65
chi-electric spectroscopy 684, 686
chiral interactions 275–522
chiral smectic 275, 284, 286, 291
chromophores, dyes 236–241, 248–253, 669, 674, 681, 683–690
Clausius–Clapeyron equation 74
Clausius–Mossotti equation 55, 163
coercive field 578, 579
Cole–Cole diagram 5, 17, 18, 20, 21, 23, 26, 28, 38, 58–60, 64, 166, 193, 194, 439, 472
Cole–Cole equation 78, 94, 95, 166, 181, 188, 346, 363, 403, 497, 686
Cole–Davidson equation 21, 78, 166, 346, 363
collective relaxation processes 13, 20, 170, 441, 487, 498–500, 507
columnar ferroelectric 511, 522–528
columnar phases 511, 522–528, 530–545
complex dielectric permittivity 4, 13–15, 17, 18, 29, 31, 36, 165
composite 376–397
compressibility 79, 80
computer simulations 204–233
conductivity 14, 20–21, 27–30, 43, 46, 243, 404, 469, 478, 497, 530, 539
configurational entropy 74, 680
confined film/geometry 280, 381
conformational changes 403, 418
continuous model 268–270
contrast ratio 376, 383–387, 389
copper(II) trimers 549-566
corona poling 673
correlation function 146, 168, 171, 204
correlation length 146, 148, 595, 596, 602, 603
critical current 629, 630, 635, 643, 646, 653, 657
  intergranular 636, 638, 640
critical Pr-concentration 630, 631
critical state 646, 649, 661
critical state model 634, 635
critical temperature 147, 571, 579, 581, 588, 598
crystal field 95, 121, 123, 553
crystal structure 137, 146
crystallization dynamics 693, 696
crystallization kinetics 699
CuO_2 planes 137
Curie temperature T_c 95, 105, 501, 551
Curie–Weiss behaviour 498, 551, 552, 556

δ-relaxation 244–252
DC electric resistance 630
DC magnetic susceptibility 555, 570
DC magnetization 551
de Vries eigenmodes 307
Debye diffusion model 171

Debye equation 4, 5, 15, 16, 18, 28, 78
Debye model 15, 40, 43, 58
Debye relaxation 95, 174, 178, 189
Debye screening radius 288
Debye–Pellat equations 166, 167
Debye-type process 183, 193, 195, 438, 500, 507
deformed helix 278–280
degree of delocalization 618
depolarization factor 313
depolarization field 310, 312, 313
dichroic dyes, chromophores 237–241, 248–253, 669, 674, 681, 683–690
dielectric absorption 4
dielectric anisotropy 177, 280
dielectric increment 16, 20, 61, 165, 181, 346, 395, 471
dielectric investigations 531, 537
dielectric dispersion 4
dielectric permittivity 4, 13–14, 29, 39, 43, 54, 61, 64, 168
dielectric relaxation 3, 4, 75, 78, 181, 202, 242, 244, 246, 248, 250, 362, 363, 393–397, 499, 507, 514, 539–542
dielectric relaxation spectra 38, 80–81, 184, 192, 202, 469
dielectric relaxation under pressure 71–84, 198–201
dielectric response 165, 427
dielectric spectroscopy 14, 288, 468, 487, 489, 492, 493, 681
dielectric strength 16, 20, 61, 165, 181, 346, 395, 471
dielectric susceptibility 4, 261, 314, 316
differential scanning calorimetry 72, 240–242, 342, 472, 490, 532, 680
diffusion coefficient 31
diffusion controlled parabolic process 695
diffusion length 280
dilational entropy 74
dimensionality of growth 700
dipolar interaction 587–607
dipolar ordering 205
dipolar polymers 164
dipole auto-correlation 167
dipole correlation
  antiparallel 401
dipole correlation functions 173
dipole moment 17, 53–56, 67, 68, 164, 213, 669, 671
dipole-dipole interactions 57, 194, 204, 208, 210, 571, 582, 588, 591, 597, 604
director 185, 205
director azimuth motion 275
discotic liquid crystals 208, 522-528, 530, 545
discotic metallomesogens 522, 531–545
discrete model 257, 263, 265, 273, 469
dislocation wall 274, 283–287, 291, 293–295
distribution of relaxation times 166, 194
  asymmetrical 677
domain, focal conic 378, 379, 382, 383
domain modes 288
domain wall
  displacement 97, 101
  susceptibility 98
  width 97
domain width 286, 287, 294
double exchange 609–625
droplets 376, 378–384, 386–394, 396, 397
dyes, chromophores 236–241, 248–253, 669, 674, 681, 683–690
dynamic magnetic susceptibility 89–131
dynamics of the molecular reorientation in FLCs 462

effective activation energy 645, 648
effective magnetic moment 536, 570, 571
elastic constant 259, 311, 395, 442
elastic energy 389, 395–397
electrets 672
electric field gradient 140
electrical resistance 630
  of $Ho_{1-x}Pr_xBa_2Cu_3O_{7-\delta}$ 631
electrically controlled phase retarder 381
electro-optical switching process 275, 278, 280, 293, 297, 305, 390–392, 545

electroabsorption 670–672
electroabsorption spectroscopy 667, 682–684, 686, 687, 689, 690
electrode poling 673
electron delocalization 609–625
electron density 140
electron diffusion in ferrites 98–100
electron spin resonance 113–131, 558–564
electronic band 147
electronic polarization 164
electrooptic modulation 443
electrooptic response 376, 391
energy barrier 189, 197
enthalpy 74
entropy change 74
entropy separation 74
equation of state 73
equilibrium, constant 6, 61, 65
Euler angles 169
Ewald summation technique 217–219
exchange integral 537, 552, 562, 564, 566, 591, 599
exchange interaction 97, 113, 537, 552, 556, 564, 566 591, 599
exchange narrowing 116
excluded volumen 74
external circuit elements 305

Far-infrared spectra 563
Fermi liquid 112, 120–126
ferrimagnetic chains 570, 571, 583, 595
ferrimagnets 99
ferrites 99
ferroelectric clusters 412
ferroelectric domains 275, 284, 286, 290, 291, 294
ferroelectric liquid crystal 15, 17, 19, 27–30, 257–528
ferroelectric order 262
ferroelectric short range order 411, 416, 418
ferroelectricity 15
ferromagetic state 570, 579
ferromagnetic coupling 535, 537, 554, 588
ferromagnetic resonance in ferrites 99
ferromagnetism 99, 582, 584, 588
field cooling 555, 573, 576
field of full penetration 635
flexible molecules 164
flexoelectric coefficient 286, 442
flexoelectric coupling 260, 268, 269
flux creep 636–638, 640, 645, 646, 652, 659
  collective 655
flux line lattice 642, 649
flux pinning centers 633
flux pinning energy 638
Fourier transform infrared spectroscopy 445–447, 467
Fourier transformation 22, 35–37
fractional crystallization 699, 700
free charges 286, 287
freezing temperature in spin-glasses 105
frequency domain dielectric spectroscopy 13, 15, 19, 25, 489, 497, 538
frequency domain of IR response 465
frequency response analyser 23, 28, 365, 513, 538
Fuoss–Kirkwood model 21, 167, 243, 245

Gay–Berne potential 173, 204, 209, 211, 212–216, 223, 227–232
$Gd_{1-x}Sr_xTiO_3$ 130
glass transition 361, 362, 366, 368–371, 375, 679–681
glass transition temperature 366, 368, 679–681
gold electrode 23, 25, 676
Goldstone mode 18, 310, 314, 317, 319, 320, 346, 366, 371 393, 394, 427, 468, 471, 475, 476, 483, 495–501
grain growth 694, 700, 702

Haller formula 189, 191
Hamiltonian 139, 148, 552
  anisotropic spin 551
hard magnets 101
Havriliak–Negami equation 21, 78, 166, 346, 363, 369, 515
heavy-fermion 112, 118
helicoidal modulation 272
helicoidal structure 310, 311, 312, 314, 316–319, 513, 523, 528

hexatic 310, 320
high frequency ESR spectra 558
high frequency process 192, 469, *see* reorientation around long axes, L-process
high pressure ESR spectra 561
high spin molecule 108, 109
High-T_c superconductors 137–157
higher harmonic susceptibility 573, 579
homeotropic alignment 291, 292, 481
hybridization gap 122
hyperfine interactions 138
hysteresis, apparent 545
hysteresis loop 578, 579, 581, 630
  for superconductors 639, 640, 646–648

Impedance Analyzer 16, 23, 24, 242, 363, 502, 513, 538
inelastic neutron scattering 145
in-plane polarization 262
indicatrix 443
induced polarization 269
insulator 137
insulator-metal transition 155
inter-layer diffusion 267, 268
inter-layer interactions 257, 260, 264, 267–269, 271, 273
inter-valence absorption band 613, 619–623
interaction potential 75
interchain coupling 571, 591
interdigitation 333
intermediate valence 113, 118, 609
intermolecular potential 73
internal electric field 687
internal field factors 164
intra-layer interaction 264, 265
intralayer spacing 602
inversion frequency 305, 307
ionic dopant 290
irreversibility line for superconductors 644, 645
Ising ferromagnet 104
isobaric 73
isochoric 73
isomer shift 140
isothermal 73
isothermal susceptibility 5, 93–95, 97
isotropic fluids 163–168, 188, 189, 192, 194–198, 365
ITO electrodes 27, 28, 346, 492, 673

Johnson–Melh–Avrami–Kolmogorov model 694
Jonscher description 21, 78, 167
Josephson vortices 638

Kalmykov–Coffey approach 190
Kirkwood correlation factor 164, 167
Kissinger method 694, 699, 700, 703
Kohlrausch–Williams–Watts equation 369, 677
Kondo effect 113
Kondo insulator 114, 118, 127
Kondo lattice 113, 116, 119
Korringa relaxation 117
Kramers–Kronig relation 3, 5, 671

L-process 15, 27, 498–501, *see* reorientation around long axes, high-frequency process
La_2CuO_4 146
Langevin function 52
Langevin saturation 57, 59, 63
Laplace transform 4, 167
Larmor frequency 141
Lennard–Jones interaction 211
Lesli coefficient 297
libration of dipoles 404
librational relaxation 174
Lifshitz term 259, 268, 311
light scattering 376, 381, 382, 385, 397
light transmittance 293, 299–305, 382–387
light-emitting diodes 690
liquid crystal dimers 176
liquid crystal mixtures 176
liquid crystal polymers 177, 236, 238, 244
liquid crystals 14, 15, 23, 34, 80–84, 163–545
liquid-like phases 181
local magnetic ordering 138
London penetration depth 634
longitudinal relaxation time 6
Lorentz force 643

Lorentz–Lorenz equation 670
low frequency process 185, 192, 469, *see* reorientation around short axes, S-process

Mössbauer effect, spectra 138, 148, 153–156
Mach–Zehnder interferometer 687
macroscopic relaxation time 1
magnetic absorption 5, 91
magnetic dispersion 5, 91
magnetic domains 600
magnetic dynamic susceptibility 89–112
  adiabatic 5, 93, 94
  frequency dependence 106, 107
  isothermal 5, 93, 94
  measurement of 92
  nonlinear 91
magnetic fluctuation 151
magnetic moment 148, 536
magnetic ordering 151
magnetic ordering 3D 588, 589
magnetic phase transitions in rare earth metals 102, 103
magnetic properties 537, 549, 569–571, 581, 583, 587
magnetic relaxation 109, 137
magnetic structure 145, 150
magnetic susceptibility 5, 90–110, 138, 536, 537, 551–556, 574–581, 590, 603, 624
magnetization 5, 89, 557, 581
magnetization curve 557, 577–579
magnetization decay rates 662
magnetization density 146
magnetization relaxation rate for superconductor 650–653, 656
Maier–Meier equation 169
Maier–Saupe model 75
Maier–Saupe potential 185, 187, 246
Maker-fringe technique 674
Manganese(III)-Porphyrin-TCNE-systems 107, 569–584, 589–591, 595–602
Maxwell equation 18, 296
Maxwell–Wagner relaxation 27, 30, 438
metallic glasses 693, 695, 697
metallomesogens 511–529, 531–546
metastable smectic phase 73
microconfined FLC (MFLC) 376, 377, 381, 393, 394, 396, 397
microscopic relaxation time 1
mixed-valence systems 609–625
molecular conformation of 12OBBB8 455
molecular dynamics 213, 216
molecular dynamics simulations 173, 216, 221
molecular processes 493, 500
molecular relaxation 26
molecular reorientation of 12OBBB8 452, 466
molecule-based magnets 587
Monte Carlo method 213, 216, 582
motion about the long axis 173
Mott–Hubbard transition 114
Mott-insulator 130
multipole moments 210
muon spin rotation spectroscopy 138, 142, 156

Néel temperature T_N 146, 148, 151, 582
nearest neighboring layers 257, 264, 266, 269, 335
nematic liquid crystal 72, 80–84, 174–177, 183–202, 205, 469, 481
nematic order 74
nematic potential 75, 173, 175, 185, 246
neutron diffraction 145, 696
neutron scattering 117, 125
neutron scattering, inelastic 145
Newton–Raphson method 41, 45
next nearest layers 269, 270, 335
NLO chromophores 674, 677, 681, 683, 684, 689, 690
NLO materials 667, 669
NLO polymers 667–690
NLO susceptibility 668, 669, 684
non-cancellation mode 480, 498–501
non-chiral bent-shaped molecules 400
nonlinear dielectric relaxation 57, 60, 68
nonlinear dielectric spectroscopy 7, 51, 53, 64

nonlinear trimers 554, 556, 558, 564
Nordio, Rigatti and Segre theory 171, 184, 244
NPT ensemble 221
nuclear magnetic resonance 113, 117, 124–125
NVT ensemble 221

odd-even effect 176
Onsager equation 163, 169
Onsager model 16, 53–55, 217, 219, 670
optical axis 443
optical response 434
optical rotatory power 337, 351
optical transmittance 293, 299–305, 376, 382–387, 388, 390
Orbach process 96, 104
order parameter 75, 169–172, 175, 184, 187–189, 191, 192, 222, 244, 246, 247, 452, 700
order parameter, antiferroelectric 262, 329, 486
order parameter, ferroelectric 262, 329, 486
orientational diffusion 279, 280, 304
orientational distribution function 452, 458
orientational elasticity 275, 277
orientational kink 277
orientational order parameters S and D 452
orientational relaxation 63, 67, 69
orientational relaxation frequency 297
orientationally disordered crystal, ODIC 532, 533, 539, 543

pair distribution 221, 224
pair potential 209–211
paraelectric phase 468
parallel ordering of dipoles 164
paramagnetic Curie temperature T_c 97, 105, 551
paramagnetic linear trimers 549, 551, 554
paramagnetic moment of trimers 537, 551
paramagnetic spin 141
periodic boundary conditions 216
perovskite titanates 130
phase diagram 80, 148, 488
phase fluctuation 457
phase retardation 299, 305
phase shift 18–20, 91
phase transition 284, 286, 291, 292, 490–492
phase transition temperature 241, 252, 488
phason mode 324–326, 348, 357, 498, *see* Goldstone mode
photoconductivity 530
Piepho model 614
piezo-modulus 275, 286, 291
piezoelectric coupling 260, 266, 268, 335
piezoelectric effect 672
pinned helix 312, 314
pinning centres in superconductor 642, 643
pinning energy 637, 638, 642, 649, 651, 652
pinning force 643, 646, 658
pitch 395, 396
PKS model 611
planar alignment 291, 431
planar orientation 376, 388
Pockels effect 668, 671, 684
polar anchoring 281
polar order parameter 206, 333, 671, 681, 683
polarizability 164, 669, 671, 672
  cubic 669
  linear 669
  quadratic 669
polarization 3, 4, 13, 52, 53, 57, 59, 68, 168, 257–259, 266, 270, 273, 275, 283–287, 311, 334, 486, 668, 672
  apparent spontaneous 543
  atomic 164
polarization mode 357
polarization of light 382
polarization order parameter 257, 265, 486
polarization reversal current method 502, 543–545
polarization reversal process 274–277, 284, 295
polarizational helix 275

Poley absorption 23, 27
poling 669, 689
  corona 673, 674
  electrode 673
poling stability 672, 678, 681, 682
polymer dispersed FLC (PDFLC) 376–397
polymer 236–252, 667–690
positional correlation 267
positional order 205, 415
positive dipole correlation 409, 419
precession about the director 174
precessional motion 172
pressure dependence 562
  of T_c 571
pressure induced 72
pressure limited 72
principal order parameter 171
pVT measurements 73

quadrupolar interaction 139, 272
quadrupolar ordering 257, 261, 268
quadrupolar splitting 140
quantum fluctuations 148
quantum tunneling for high-spin clusters 109
quantum tunneling of vortices in superconductors 652, 662
quartet spin state 549, 566

rare earth metals 101, 148–155
reaction field 53, 54, 163, 164, 217
reaction field method 219
reentrant spin glass transition 570, 580
reflection method 38, 44
relaxation frequency 1, 288, 290–292, 297, 363
relaxation function 1, 22
relaxation of magnetization for superconductor 645, 648, 650, 651
relaxation process 1, 5, 8, 35, 104, 181, 183–185, 192, 194, 198, 202, 569
relaxation time 1, 21, 59, 75, 89, 93, 94, 98, 181, 183, 185, 187, 189–199
  distribution of 94
  in spin glasses 106
relaxation time of copper trimers 558, 564
remanence field 578
remanent magnetization 578
reorientation around the long axes, L- or high frequency process 15, 27, 172, 192–195, 369, 405, 406, 417, 419, 499–501
reorientation around the short axes, S- or low frequency process 15, 172, 185, 189, 244–253, 369, 407, 419, 469, 481, 499–501
reorientation dynamics 462, 466
reorientational motion 192
repulsive interaction 75
resonance field 558, 560, 566
resonance shift 559, 561, 566
response function 2
response time 279, 280
reversal current method 502, 543–545
rod-like molecule 183, 400
rotational dynamics 171
rotational viscosity 390, 392, 393, 395
rubbing cell 293, 294

S-process 15, 490–501, *see* reorientation around short axes, low frequency process
saturation voltage 387–390, 396
scattering function 146
second harmonic generation (SHG) 435, 673, 674, 676, 687
segmental tilt angles of the molecule 446
Shannon sampling theorem 36
short range dipole-dipole interactions 164
singlet distribution functions 222
skewed Cole–Cole plot 166
Sm A 181–183, 194–197, 206–207, 418, 515–516
Sm $\tilde{A}$ 207
Sm A^* 258, 261, 309, 315–317, 365, 412, 419, 420, 435, 519–522
Sm A_1 201
Sm A_2 207
Sm A_d 182, 198, 207
SmB_6 compound 129
Sm B/Cr B 183, 195–197

SmC 182, 183, 258, 418, 514
SmC$^*_A$ 261–264, 272, 345, 435, 477–480, 495
Sm C$^*_\alpha$ 333, 334, 340, 343, 356–358, 468–484, 489
Sm C$^*_\gamma$ 261
Sm C$^*_{FI1}$ 272, 333, 334, 339, 340, 344, 345, 349, 350, 352, 354, 356, 358, 470, 489
Sm C$^*_{FI2}$ 272, 333, 334, 338, 339, 344, 470, 489
Sm E/Cr E 73, 183, 198–201
Sm F* 310, 321
Sm F$^*_A$ 310
Sm F/Cr F 195
Sm G/Cr G 195
Sm I* 321–328
Sm I$^*_A$ 310, 504–506
smectic planes 283, 285–287, 291, 293
Smoluchowski equation 280
soft mode 309, 317, 346, 394, 428, 468, 471, 473–476, 479, 483, 495–501
solid-like phases 181
soliton 104
space charge relaxation frequency 297
spatial correlation function 164
specific heat 138, 680, 695
spin canting 582
spin flop 578
spin glass 105–108, 147, 155, 556, 696
spin Hamiltonian 537, 556
spin relaxation 117, 137
spin reorientation 100, 102
spin-lattice relaxation 5, 89, 95, 96, 104
  time 6, 95, 96
spin-orbit coupling 6, 95
spin-phonon coupling 566
spin-spin relaxation 6, 89, 96, 104
spontaneous polarization 274, 275, 284, 286, 287, 290, 291, 305, 344, 390, 489, 492, 500–502, 504, 505, 507
SQUID magnetometer 551
Stark effect 671, 682, 684, 685, 687, 689, 690
  linear 685, 687
  quadratic 682, 685
  quasilinear 687
static dielectric constant 78
static dielectric permittivity 470
steric effects 75
stochastic model 141
stretched exponential function 369, 677
striped texture 293
strong electric field 56, 57, 60, 62
strongly correlated system 147
sub-hertz dielectric relaxation 30, 31
superconducting compounds 137
superconducting critical temperature 631, 632, 640
superconducting state 137, 150
superconducting-magnetic phase diagram 152
superconductivity suppression 629–631, 633, 640
supercooled 73
superparamagnet 108, 109, 579
superparamagnetic relaxation 580, 582
superpressurized 73
superspins 595, 596, 603
surface anchoring 275, 284, 293
surface mode 289
surface stabilized ferroelectric liquid crystal (SSFLC) 425
surface tension 281, 282, 291, 294
surface treatments 168
switching process 274–307, 376, 390–393
switching time of 12OBBB8 467
symmetric dimers 176
symmetric distribution of relaxation times 167, 176
synclinic order 267, 332–359
synclinic SmC* 263, 332, 357

TAFM 645, 648, 652, 657, 662
temperature gradient cell 293
thermal expansion 79
thermal poling 669, 670
thermally induced phase separation 378, 379, 381, 384
thermoremanent magnetization 577, 578
thickness mode 317, 319, 320
thin film 673
three-dimensional bulk nucleation 700

tilt angle 275, 278, 281, 284–286, 292, 299, 307, 343, 505
tilt order parameter 273, 311, 333, 486
tilt vector 262
time domain spectroscopy 9, 26, 35–50, 495, 500
time-resolved spectra 462
transient method 35
transition-metal oxides 131
transmission method 40–44
transmittance 293, 299–305, 382–387
transversal pair distribution function 225
triple point 72
triplet correlations 222
triplet distribution function 226
tunneling of magnetization 581
twisted structure 310, 312, 313, 316
two-phonon processes 562

uniaxial director 170
URu_2Si_2 114, 126

V-shaped switching 293, 294, 296, 304, 305, 506
Van der Waals interaction 209, 265, 267, 335
Van Vleck paramagnetism 551
vanadyl complexes 514, 530
vibronic coupling 611–618
viscosity 442
viscosity coefficient 275, 297
Vogel–Fulcher–Tammann equation 106, 362, 368, 526, 696, 697
Vogel temperature 366
voltage divider 307
volume steps 74
vortex glass model 644, 655, 656, 663
vortices in high T_c superconductors 643, 644

weak correlated system 147
weak ferromagnet 591, 601
weak magnet 104, 105
Williams–Landel–Ferry equation, behaviour 542, 545, 679, 681

X-band ESR spectra 551
X-ray diffraction 401, 531, 534
X-ray powder patterns 551, 561, 563

Zeeman interaction 115, 141
zero field cooling 555, 573, 576, 579, 582
zero field splitting 552, 556, 566, 623
ZLI-3654 mixture 447, 449